International Association of Geodesy Symposia
143

Chris Rizos
Pascal Willis *Editors*

IAG 150 Years

Proceedings of the 2013 IAG Scientific Assembly, Potsdam, Germany, 1–6 September, 2013

Springer

International Association of Geodesy Symposia

Chris Rizos, Series Editor
Pascal Willis, Series Associate Editor

International Association of Geodesy Symposia

Chris Rizos, Series Editor
Pascal Willis, Series Associate Editor

More information about this series at http://www.springer.com/series/1345

IAG 150 Years

Proceedings of the 2013 IAG Scientific Assembly, Potsdam, Germany, 1–6 September, 2013

Edited by

Chris Rizos
Pascal Willis

Springer

Volume Editors
Chris Rizos
School of Civil & Environmental Engineering
University of New South Wales
Sydney
Australia

Pascal Willis
Institut national de l'Information
géographique et forestière
Direction de la Recherche
et de l'Enseignement
Marne-la-Vallée
France

Series Editor
Chris Rizos
School of Civil & Environmental Engineering
University of New South Wales
Sydney
Australia

Associate Editor
Pascal Willis
Institut national de l'Information
géographique et forestière
Direction de la Recherche
et de l'Enseignement
Marne-la-Vallée
France

ISSN 0939-9585
International Association of Geodesy Symposia
ISBN 978-3-319-24603-1
DOI 10.1007/978-3-319-30895-1

ISSN 2197-9359 (electronic)

ISBN 978-3-319-30895-1 (eBook)

Library of Congress Control Number: 2016939265

© Springer International Publishing Switzerland 2016
This work is subject to copyright. All rights are reserved by the Publisher, whether the whole or part of the material is concerned, specifically the rights of translation, reprinting, reuse of illustrations, recitation, broadcasting, reproduction on microfilms or in any other physical way, and transmission or information storage and retrieval, electronic adaptation, computer software, or by similar or dissimilar methodology now known or hereafter developed. The use of general descriptive names, registered names, trademarks, service marks, etc. in this publication does not imply, even in the absence of a specific statement, that such names are exempt from the relevant protective laws and regulations and therefore free for general use.
The publisher, the authors and the editors are safe to assume that the advice and information in this book are believed to be true and accurate at the date of publication. Neither the publisher nor the authors or the editors give a warranty, express or implied, with respect to the material contained herein or for any errors or omissions that may have been made.

Printed on acid-free paper

This Springer imprint is published by Springer Nature
The registered company is Springer International Publishing AG Switzerland

Preface

In 1862, the Prussian General Johann Jacob Baeyer initiated the Central European Arc Measurement ("Mitteleuropäische Gradmessung") project. By the end of that year, 15 countries had affirmed their participation, and in 1864, the first General Conference was held in Berlin. This was a great success and the start of an organised international collaboration in geodesy. The IAG counts this international scientific initiative, and the organisation it spawned, as its origin. The IAG celebrated its 150th anniversary with a Scientific Assembly in Potsdam, Germany, 2–6 September 2013.

This volume contains the proceedings of selected papers from sessions organised under the six themes listed below (with the names of their associate editors):

Theme 1: Definition, Implementation and Scientific Applications of Reference Frames
Main Editor: Tonie van Dam
Associate Editors: Zuheir Altamimi, Joao Torres
Theme 2: Gravity Field Determination and Applications
Main Editor: Urs Marti
Associate Editors: Hussein Abd-Elmotaal, Xiaoli Deng, Annette Eicker, Jianliang Huang, Roland Pail, Laura Sanchez
Theme 3: Observing, Understanding and Assessing Earth Hazards
Main Editor: Manabu Hashimoto
Associate Editor: Jeff Freymueller
Theme 4: Science and Applications of Earth Rotation and Dynamics
Main Editor: Richard Gross
Theme 5: Observation Systems and Services
Main Editor: Hansjörg Kutterer
Associate Editor: Urs Hugentobler
Theme 6: Imaging and Positioning Techniques and Applications
Main Editor: Dorot Grejner-Brzenzinska
Associate Editors: Allison Kealy, Pawel Wielgosz

The symposium was a tremendous success, attracting 533 delegates from 46 countries and 13 national and international sponsors. There were 241 oral papers and 234 posters presented over the 5 days of the symposium. From the presentations and the papers accepted for these proceedings, a number of observations can be made:

- The most popular theme was Gravity Field Determination and Applications. The recent gravity field mapping satellites (first CHAMP and then the GRACE and GOCE missions) continue to produce exciting results in support of a wide range of geoscience applications, including geoid determination, physical oceanography, hydrology and geophysical and atmospheric sciences. *The gravimetric community waits eagerly for the GRACE follow-on mission*.
- On the other hand, the value of reference frames to the broader navigation, geospatial and global change communities continues to rise. The International Terrestrial Reference Frame (ITRF) is a highly valued product of modern geodesy. The ITRF is increasingly recognised

as the fundamental datum for national and regional mapping, as well as global change studies. *The current ITRF2008 will be superseded by ITRF2014*.

- The Global Navigation Satellite System (GNSS) continues to be the workhorse of geodesy; not only is it the quintessential 3D (and also 4D) geodetic positioning technology, but it also provides invaluable measurement data for the determination and maintenance of the ITRF and easy connection to the ITRF and supports precise orbit determination for many Earth observation satellite missions. *High-precision GNSS is by far the most advanced, and accessible, geodetic tool ever developed*.
- Modern geodesy is very dependent on the satellite missions launched by a handful of space agencies. In addition to GNSS and gravity field mapping missions, there are many Earth observation satellites including those for magnetic field mapping; topographic, sea and ice surface mapping; timing; relativity probes; and Earth imaging. *The challenge is to "operationalise" what are often once-off science missions, so as to ensure long time series of observations of many Earth system parameters*.
- The IAG is fortunate to have launched a range of services in the 1990s and is now reaping the reward in terms of increased accuracy and resolution in the geometric and gravimetric mapping of the dynamic Earth. The challenge for the IAG in the coming decade is the realisation of an integrated Global Geodetic Observing System (GGOS). Such a synoptic observing system will contribute to unified measurement modelling and analysis – that will deliver a *quantum increase in accuracy and stability for the time, gravitational and spatial reference frames underpinning today's geodetic enterprises*.
- The International GNSS Service (IGS) is the most visible of the IAG services because its products and expertise support the ever-growing range of GNSS applications in science and engineering. *In 2014, the IGS celebrated the 20^{th} anniversary of its founding*.

Pascal Willis, the IAG Symposium Series associate editor, guided the reviews of the submitted papers, communicated with the symposium editors and the paper reviewers and finally accepted the papers that comprise this volume. I am personally indebted to him, for I could not have put this volume together without his invaluable assistance and extraordinary tenacity.

I wish to also acknowledge the generous support of the Helmholtz Centre Potsdam – GFZ German Research Centre for Geosciences. It is very fitting that the 150th anniversary of the founding of the IAG's forerunner is celebrated in Potsdam. In 1864, a "Central Bureau of European Arc Measurement" was established under Baeyer's presidency in Berlin. During the following years, the maturing association developed into the European (1867) and later into the International (1886) Arc Measurement. The significant role of Berlin and Potsdam in the history of geodesy is further marked by the foundation of the Royal Prussian Geodetic Institute, which was established upon Baeyer's proposal in Berlin in 1870. The institute moved into its own new building on the site of the Royal Prussian Observatories on the Telegraph Hill in Potsdam in 1891. To this day, the building is the domicile of the Department of "Geodesy and Remote Sensing" of the German Research Centre for Geosciences.

Last, but definitively not least, I wish to thank all participating scientists, and those who made oral and poster presentations, who came to Potsdam and made our Scientific Assembly a great success. International geodesy has come a long way in 150 years, and we can proudly claim that "geodesy matters, now more than ever". We all wish the IAG a long and productive future.

Sydney, NSW, Australia — Chris Rizos
18 November 2014

Contents

Part III Gravity Field Determination and Applications

Part I

History Session

From a Regional Project to an International Organization: The "Baeyer-Helmert-Era" of the International Association of Geodesy 1862–1916

Wolfgang Torge

Abstract

The following paper describes the first epoch of organized international collaboration in geodesy, which started about 150 years ago and finally led to today's "International Association of Geodesy". This development may be regarded as a consequence of the refined definition of the figure of the Earth, originating at the end of the seventeenth century and leading from the rotational ellipsoid to the equipotential surfaces of the gravity field, close to mean sea level. An increasing number of geodetic enterprises based on astronomic, geodetic and gravimetric measurements followed until the middle of the nineteenth century, in order to determine the curvature of the Earth's figure at different regions of the world. The arc measurement based on triangulation played a special role at these endeavours, because this method was now increasingly used as the basis for national mapping. In 1861, the retired Prussian General Johann Jacob Baeyer took up earlier ideas from Schumacher, Gauss, Bessel, Struve and others, and proposed an arc measurement project for central Europe in order to systematically study the figure of the Earth in this region. The proposed network ranged from southern Italy to Norway, and from France to Poland, and its survey and evaluation naturally required international cooperation. Baeyer's initiative immediately got the support from the Prussian government, and the enthusiastic collaboration of the European countries soon reached far beyond the original project. Consequently, the name of this "governmental" scientific organization changed from "Mitteleuropäische Gradmessung" to "Europäische Gradmessung", and the scientific program widened significantly by including levelling, mean sea level investigations, standardization of length and time measures, and gravity observations. Baeyer remained the dominating person of the "European Arc Measurement" until his death (1885), keeping a strong position as the President of the Association's Central Bureau hosted at the newly established Prussian Geodetic Institute. The following epoch is governed by Friedrich Robert Helmert, well-known by a fundamental monograph on "Higher Geodesy", who became appointed Director of the Geodetic Institute and the Central Bureau in 1886. The regional organization immediately extended to the global "Internationale Erdmessung" ("Association Géodésique Internationale"), and the scientific program was enlarged significantly, with strong accent on physical geodesy and geophysics including investigations on temporal variations. This epoch ended due to the First World

W. Torge (✉)
Institut für Erdmessung, Leibniz Universität Hannover, Schneiderberg 50, 30167 Hannover, Germany
e-mail: torge@ife.uni-hannover.de

© Springer International Publishing Switzerland 2015

C. Rizos, P. Willis (eds.), *IAG 150 Years*, International Association of Geodesy Symposia 143,
DOI 10.1007/1345_2015_42

War, when the governmental convention on the Association was not extended. Although a reduced association among neutral nations succeeded in keeping the Latitude Service alive, the next era of international cooperation in geodesy only followed in 1922, within the frame of the non-governmental "International Union of Geodesy and Geophysics".

Keywords
Arc measurements • Baeyer • Figure of the Earth • Geodetic Institute Potsdam • Helmert • History of geodesy • International Association of Geodesy • Internationale Erdmessung • Mitteleuropäische Gradmessung

1 The "Figure of the Earth": A Challenge for Modern Geodesy

Since the time of Aristotle (384–322 B.C.), at the latest, the *sphere* had been generally accepted as the "Figure of the Earth". The Earth's radius as the sphere's parameter was first provided by Eratosthenes (276–195 B.C.), introducing the arc measurement as a combination of astronomic and geodetic observations. At the beginning of the modern age, the reviving interest in the Earth's dimension led to new determinations of the Earth's radius, which benefited from improved technology and the introduction of triangulation as an efficient geodetic method. For the history of geodesy we refer to Perrier (1939) and Bialas (1982), short introductions can be found in geodetic textbooks, e.g. Torge and Müller (2012).

A revolution for geodesy occurred in the last decades of the seventeenth century, when a new definition of the Earth's figure arose from physics and astronomy. The heliocentric world system with the annual revolution of the Earth around the Sun and the daily rotation of the Earth had been accepted at that time, Jean-Dominique Cassini had observed the polar flattening of Jupiter (1666), and Richer had found the latitude-dependence of gravity by pendulum measurements (1672/1673). These observations supported the new Earth model based on the theory of hydrostatic equilibrium for a rotating fluid, which postulated the Earth's figure to be flattened at the poles (I. Newton 1687: "Philosophiae Naturalis Principia Mathematica", C. Huygens 1690: "Discours de la Cause de la Pesanteur"). This was a great challenge for geodesy: to prove the polar flattening by geometric methods and to determine the parameters of such an Earth model! For a rotational *ellipsoid*, e.g., these parameters would be the semi-major axis and the flattening. After lengthy disputes on the results of more recent arc measurements, the problem of the flattened Earth was finally solved by the famous *arc measurements* in Lapland (1736/1737, Maupertuis et al.) and in the Spanish Vice-Kingdom of Peru (today Ecuador; 1735–1744, LaCondamine, Bouguer, Godin, and the Spanish officers Jorge Juan and Antonio de Ulloa), initiated and

Fig. 1 Pierre–Louis Moreau de Maupertuis "flattens the Earth". Engraving by R. de Tournières, from Perrier (1939)

organized by the French Academy of Sciences (Fig. 1). Other arc measurements at different latitudes followed, as the repeated measurement along the Paris meridian. Started by Jean Picard in 1669/1670, these measurements are since 1683 about one century connected with the Cassini family, which over four generations provided the director of the Paris observatory. The connection to the Greenwich observatory in 1787 and the following triangulation of Great Britain carried out by General W. Roy and others finally completed an arc running from Spain to the Shetland Islands. Great importance for the determination of the figure of the Earth and as a basis for national mapping also obtained "The Great Arc" and other triangulation chains in India (Lambdon, Everest,

Fig. 2 Wilhelm Struve. Portrait by Eduard Hau (1837, https://commons.wikimedia.org/wiki/File:Wilhelm_Struve._1837.jpg)

(a) (b)

Fig. 3 (**a**) Heinrich Christian Schumacher. Lithography by Otto Speckter (1853, https://commons.wikimedia.org/wiki/File:Heinrich_Christian_Schumacher,_von_Otto_Speckter_1853.jpg). (**b**) Carl Friedrich Gauss. Oil-painting by Gottlieb Biermann (1887), after an original portrait by Christian Albrecht Jensen. Copy Göttinger Universitätssternwarte, Gauß-Gesellschaft Göttingen

1803–1850), and the "Struve-Arc" (since 2005 included in the UNESCO world heritage list) running along the 27° East meridian from northern Norway through Russia until the Black Sea (W. Struve, Director of Tartu Observatory, Estonia, General Tenner, and Prof. Hansteen, Director of Christiana Observatory), to mention just a few of these large enterprises (Fig. 2). The combination of different arcs revealed a large scattering of the ellipsoidal parameters, around 1800 the flattening values, e.g., varied between 1/144 and 1/352. There were even attempts to derive the flattening from the gravimetric method, according to the theorem which Clairaut had derived already in 1743. Although values like 1/321 and 1/336, derived in 1799 by Laplace from only 15 pendulum measurements, fitted into the broad range of the astrogeodetic results, this did not contribute to its explanation. After lengthy discussions, a new definition of the "Figure of the Earth" was accepted finally, taking the actual gravity field of the Earth into account. Following Gauss (1828) and Bessel (1837), the *mathematical surface* of the Earth is defined now as the equilibrium surface of the gravity field coinciding with mean sea level, and continued below the continents, i. e. the level surface which we call "*geoid*" today.

Compared with the large-scale triangulation chains established in western and eastern Europe, in India and elsewhere, the situation in *central Europe* is less favourable in the first half of the nineteenth century. This is due to the strong separation into local territorial units, which is especially pronounced in Germany (for the history of geodesy in Germany we refer to Torge 2009). Nevertheless, a number of high quality triangulations are carried out as a contribution for determining the figure of the Earth and for local or national mapping (e.g. Torge 2012). An early impetus for solving the geodetic problem for central Europe came from the astronomer Franz Xaver von Zach, who – at the turn from the eighteenth to the nineteenth century – developed the Gotha Observatory to a centre of scientific exchange in astronomy and geodesy (Brosche 2001). Although – with the revival of the war between France and Germany – his plan of an arc measurement in the centre of Germany abruptly ended in 1806, Zach's ideas and first measurements influenced – among others – Gauss and the Prussian General von Müffling. The latter one started in 1814 a systematic triangulation of Prussia, connected to the French geodetic system and directed by the General Staff (Torge 2002). Here, Johann Jacob Baeyer (at that time Lieutenant) appears the first time, as a scientific collaborator of Müffling. More important – from the scientific point of view – becomes the Hannover arc measurement (1821–1823) of Carl Friedrich Gauss, connecting the astronomical observatories of Altona close to Hamburg, and Göttingen where Gauss holds the chair for astronomy since 1807. This project is initiated by the Danish astronomer Heinrich Christian Schumacher, Director of the Altona Observatory and in charge of a new triangulation of Denmark, based on a north-south directed arc measurement (Fig. 3). In 1816, Schumacher suggests to Gauss to extend the Danish arc through the Kingdom of Hannover and possibly via Hesse and Bavaria until Italy, and Gauss immediately responds very positively. The subsequent arc measurement through Hannover is carried out by Gauss himself, and – together with the following triangulation of the whole kingdom – considered by him as part of a future trigonometric network covering Europe, connecting the existing astronomical observatories (Gauss 1828; Großmann 1955). Another local, but outstanding geodetic contribution from central Europe is due to Friedrich Wilhelm Bessel, Professor at the University of Königsberg in Eastern Prussia and Director

Fig. 4 Friedrich Wilhelm Bessel. Portrait by Christian Albrecht Jensen (1839, https://commons.wikimedia.org/wiki/File:Friedrich_Wilhelm_Bessel_(1839_painting).jpg)

Fig. 5 Johann Jacob Baeyer, founder of the "Mitteleuropäische Gradmessung". Oil painting by P. Stankiewicz, Deutsches Geoforschungszentrum, Potsdam, from Buschmann (1994)

of the astronomical observatory. He widens the Russian proposal (1829) to connect the triangulation in the Baltic provinces with the triangulation of the Prussian General Staff, to a proper arc measurement (1831–1836), which sets new standards for triangulation (Bessel and Baeyer 1838). Like Gauss, Bessel clearly states the idea of a *European* contribution to the determination of the figure of the Earth, considering his arc measurement as part of it (Fig. 4). It is the arc measurement in Eastern Prussia where we meet Baeyer (now Captain) again (see below Baeyer's course of life). As an experienced observer detached from the Prussian General Staff, he learns from the ingenious astronomer and geodesist Bessel, and high quality triangulation and the figure of the Earth problem decisively coin the following 50 years of his life (Hamel and Buschmann 1996).

2 The "Central European Arc Measurement" – Idea and Realization: The Baeyer-Epoch" 1861–1885

It is the (now) General Baeyer, who in 1861 takes up the manifold ideas for a central European contribution to the determination of the figure of the Earth, by defining and realizing a corresponding project, which from the very beginning is based on a scientific program and an efficient organization. The program immediately expands from the original regional project to a more general research enterprise covering all kind of available geodetic methods and triggering new ones. Based on the enthusiasm of the participating persons, the well organized program soon extends over the whole of Europe, and becomes attractive overseas. Over 25 years, Baeyer is the leading person at this new international geodetic organization, which requires to remember some stations of Baeyer's curriculum vitae (Buschmann 1994).

Johann Jacob Baeyer was born 1794 in the village of Müggelheim close to Köpenick, now part of Berlin. Sponsored by the local parson, the peasant's son receives a thorough secondary education. In 1813, with the beginning of the war against Napoleon, he voluntarily enters the Prussian army, and decides to start a military career. Having graduated from the military academy, he enters the Topographical Bureau directed by General Müffling, where he gets first experiences in topographic and trigonometric measurements, as well as in geodetic computations. Detached to the Prussian General Staff in 1820, his career in the Trigonometric Bureau (since 1822) leads him from Prime Lieutenant to Major General (1852), directing that bureau from 1843 until his retirement (1857), Fig. 5. His geodetic abilities are acknowledged soon, for example by Alexander von Humboldt, the famous naturalist, to whom he is introduced in 1823. Humboldt even proposes Baeyer's participation in his planned expedition to central Russia and Siberia. Although this cooperation does not come off, Humboldt continues to observe Baeyer's career. In a letter directed to the King of Prussia in 1837, e.g., Humboldt characterizes Baeyer as one of the most experienced officers who could be found in any army. Meanwhile, Baeyer's collaboration with Bessel at the famous arc

measurement in Eastern Prussia (see above) has significantly improved and widened Baeyer's geodetic background. This is well documented by the final publication, where we find the above mentioned statement on the geodetic connection of the astronomic observatories in Europe. The following two decades are characterized by a number of outstanding geodetic projects carried out or directed by Baeyer. New triangulation chains are spread out over Prussia following the high standards set by Bessel, and connected to neighbouring countries like Denmark and Russia. Additional baselines improve the scale of the Prussian triangulations, and scale comparisons between Prussian and Russian baselines as well as studies on the mean sea level of the Baltic Sea already indicate focal points of the later "Mitteleuropäische Gradmessung". A trigonometric height transfer from the Baltic Sea level to Berlin is suggested by Humboldt and carried out by Baeyer in 1835, in order to correctly reduce Bessel's absolute pendulum measurements to mean sea level, and herewith connected studies of atmospheric refraction also continue to keep Baeyer's interest over the next 20 years.

In 1857, a break occurs in Baeyer's career. Having advanced until the rank of a Major General, he was supposed to stand back to the practical military service, and take the leadership of a brigade. Supported by Humboldt ("the King of Prussia owned sufficient officers for commanding a brigade, but only one Baeyer") he asks the King to allow the continuation of his scientific work by setting him in an adequate position. A rather unpleasant development follows, which can be traced back until 1851. In that year, Baeyer had proposed a radical reorganization of the surveying and mapping activities in Prussia, on a higher technical level and with a centralized organization, where a large-scale map should be based on a state-wide geodetic survey, and serve civilian and military purposes. This proposal is strongly attacked by the responsible authorities and not successful. A short-lived construction finally answers Baeyer's petition, but does not end his quarrel with the General Staff, which since 1857 is led by Helmuth von Moltke. Baeyer now becomes "characterized" (i. e. obtaining the corresponding rank but remaining with the wages of the previous position) as Lieutenant-General and put to the disposition of the Chief of the General Staff. He is charged with the Prussian part of an international arc measurement project along the 52° N parallel, again initiated by Wilhelm Struve, now Director of the recently established Pulkovo Observatory (Dick 1996). Unfortunately, the support from the General Staff for this project is rather weak, and this is accompanied by conflicts with the much younger Otto Struve who follows his father in Pulkovo. About 1860, Baeyer probably reflects the first time upon an arc measurement in central Europe. This becomes visible, e.g., through a dedicated voyage to Munich, where he meets an obvious interest at the Bavarian General Staff and the cadastral administration, the idea of a memorandum for realizing such a project originates here (Pieper 1996).

In April 1861, Baeyer presents the "*Entwurf zu einer Mitteleuropäischen Gradmessung*" to the Prussian Minister of War (Fig. 6a). The objective of this project is the determination of the deflections of the vertical – and thus the relative structure of the geoid – in central Europe. This shall be achieved by exploiting the available triangulations and astronomic observations, and by performing new measurements if necessary. High quality standards are set for the data to be included into the corresponding computations – this will later lead to severe dispute with the Prussian General Staff. A memorandum (Baeyer 1861) explains the project in detail and provides a thorough scientific foundation. The project contains more than 30 astronomic observatories, covering an area of about 16° of difference in longitude and 22° difference in latitude, ranging from Brussels to Warsaw and from Palermo to Christiana (now Oslo), respectively (Fig. 6b). The main objective – determination of the curvature anomalies of the Earth's figure – is extended by including the interpretation of the results. This is specified by examples, as the effect of the Alps on the deflections of the vertical, and an eventually anomalous gravity field behaviour at the European border seas: the geophysical-geological interpretation of the geodetic results is already a component part of the project!

On 20th June 1861 – only 2 months after presenting his memorandum! – Baeyer's plan is approved by order of the Prussian Royal Cabinet, and the Prussian Foreign Ministry asks the governments of the other central European states or countries for collaboration (Laitko 1996). Already in April 1862, first negotiations between representatives of Prussia, Austria and Saxony take place in Berlin, with the following participants: Johann Jacob Baeyer, Lieutenant-General z.D., Prussia; August von Fligely, Major-General and Director of the Military-Geographic Institute Vienna, Austria; Carl von Littrow, Director of the Astronomic Observatory Vienna, Austria; Josef Herr, Professor for Spherical Astronomy and Higher Geodesy, Polytechnical School Vienna, Austria; Julius Ludwig Weisbach, Professor for Mathematics at the Royal Montanistic Academy Freiberg, Saxony; Christian August Nagel, Professor of Geodesy, Polytechnic School Dresden, Saxony; Carl Christian Bruhns, Professor of Astronomy, University of Leipzig, Saxony.

At the end of 1862, Baeyer presents a General Report on the state of the "*Mitteleuropäische Gradmessung*" ("Central European Arc Measurement"), with 16 states or countries having declared their participation (Sadebeck 1883; Levallois 1980; Torge 2005). These are the seven German states (Germany is not yet united!) Baden, Bavaria, Hannover, Mecklenburg, Prussia, Saxony and Saxony-Gotha, as well as Austria, Belgium, Denmark, France (allows the use of data necessary for the project), Italy, The Netherlands, Poland

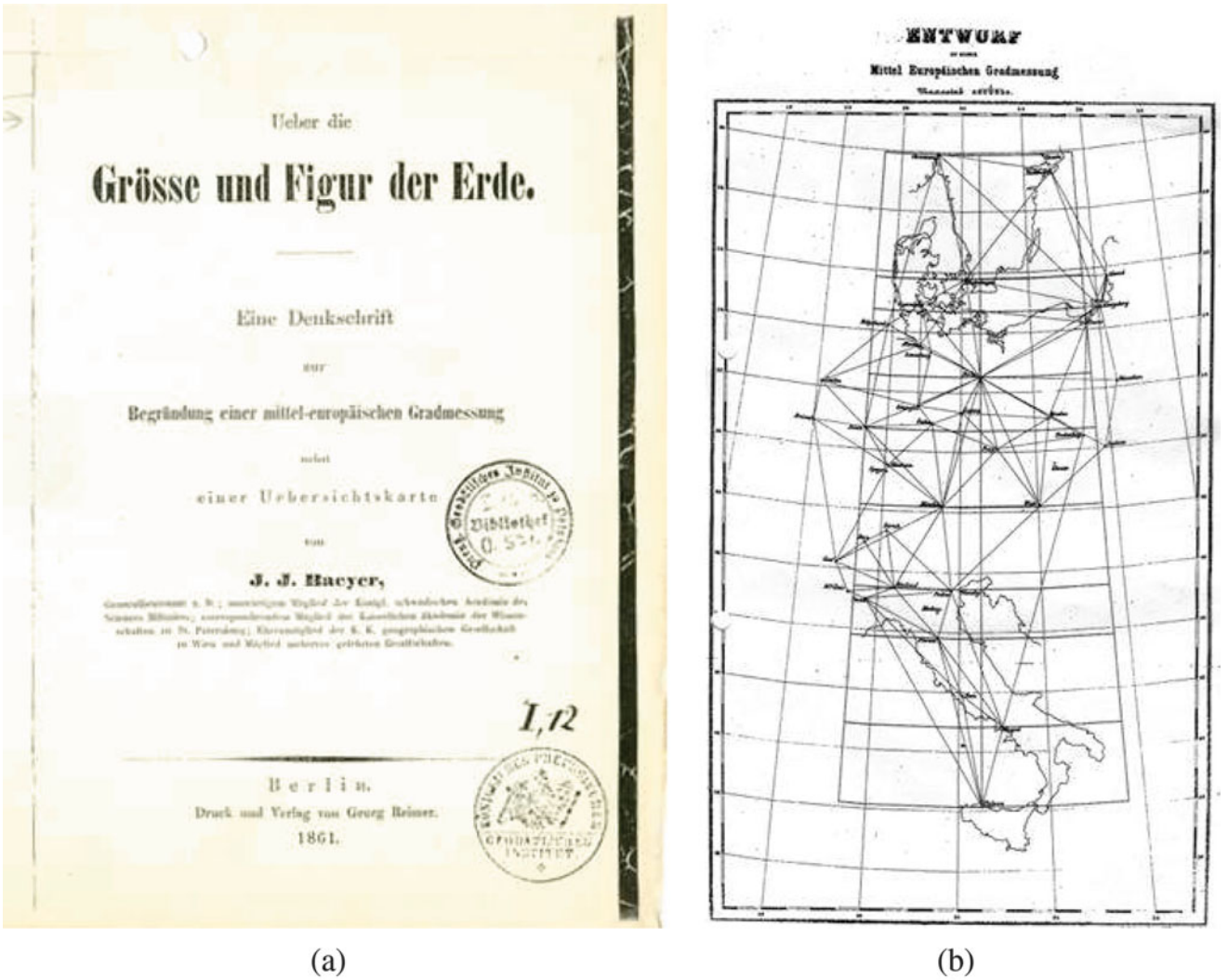

Fig. 6 Baeyer (1861): Memorandum for the foundation of a "Mitteleuropäische Gradmessung", Deutsches Geoforschungszentrum. (**a**) Frontpage, (**b**) network sketch: astronomical observatories and geodesics to be computed from triangulations

(through Russia), Sweden and Norway (in personal union), and Switzerland. This is a great success: an international collaboration for a scientific project reaching far beyond central Europe has been approved by the respective governments, and is carried by leading representatives of science and military geography. The next step to be taken comprises the formation of an effective organization and a more specified definition of the problems to be attacked. In 1864, the first *General Conference* of the Representatives to the "Central European Arc Measurement" takes place in Berlin. The conference fixes the administrative structure as well as the research program of this "governmental" scientific organization, following Baeyer's suggestions in his General Report. The organization includes the *Permanent Commission*, meeting annually and responsible for the scientific management, the *Central Bureau* as an executive, and *General Conferences* meeting at 3-year intervals. The scientific program includes the examination of existing triangulations including baselines, the execution of new triangulations and connections between neighbouring countries, the introduction of a uniform reference ellipsoid, the comparison of length units and the definition of a common standard, first order levelling and mean sea level determination, pendulum measurements, and the development of accuracy standards.

The membership list of the first General Conference naturally shows the predominance of the representatives of the German states, and until the 1880s the German influence is also visible in the location of the General Conferences (Berlin 1864 and 1867, Vienna 1871, Dresden 1874, Stuttgart 1877, Munich 1880, Rome 1883). But already in 1867, after Portugal, Spain and Russia had joined the project, the name of the organization is changed to "*Europäische Gradmessung*". The Central Bureau is located in Berlin and starts work in 1866, with Baeyer as president. He is assisted

Fig. 7 Presidents of the Permanent Commission 1864–1886. (**a**) Peter Andreas Hansen. Photography around 1865 (https://commons.wikimedia.org/wiki/File:P.A.Hansen.jpg), (**b**) General August von Fligely. Bundesamt für Eich- und Vermessungswesen, Wien (Drewes 2013), (**c**) General Carlos Ibáñez e Ibáñez de Ibero. Instituto Geográfico Nacional, Madrid (Drewes 2013)

by Wilhelm Foerster, Director of the Berlin Observatory, but further support is rather low. This situation changes radically in 1870, when the *Prussian Geodetic Institute* is established, following a "Promemoria" prepared by Baeyer and Foerster in 1867, and a further (1869) memorandum, where Baeyer drastically describes the situation of the Central Bureau and the benefit of a national scientific institute for geodesy. Consequently, the new institute (until 1891 located in Berlin) is entrusted with the Prussian part of the Arc Measurement program, on the one hand, and with the operation of the Central Bureau, on the other; Baeyer becomes its Director with the title "President". The presidents of the *Permanent Commission* naturally also play an important role during this first epoch of organized international cooperation, these were as follows: Peter Andreas Hansen, Director of the Gotha Observatory, Thuringia (1864–1868, Fig. 7a); General August von Fligely, Vienna (1869–1874, Fig. 7b), already known from the first meeting in Berlin (see above); General Carlos Ibáñez e Ibáñez de Ibero, Director of the Geographical and Statistical Institute, Madrid, Spain (1874–1886, Fig. 7c).

It is remarkable that the "Arc Measurement" organization developed so rapidly in the 1860s and 1870s, even though this period is characterized by a number of wars in central Europe. There was the Italian war of unification in the 1850s, with participation of France and Austria, the war of Prussia and Austria against Denmark in 1864, the war between Prussia and Austria in 1866, with smaller German states mainly on the side of Austria and Italy on the side of Prussia, and the war of Prussia and the other German states against France in 1870/1871, which finally led to the unification of Germany and a German empire under Prussian leadership. The Permanent Commission, for instance, met 1867 in Vienna and 1875 in Paris, i. e. only a relatively short time after military actions. This fact clearly indicates the scientific interest in the geodetic problems attacked by the Arc Measurement organization, but also the understanding of the countries' administration for solid geodetic fundamentals, required for mapping and planning, with the military demands playing a special role. In addition, the conflict of the Prussian General Baeyer with the Prussian General Staff (see below) might have brought this dominating person of the "Arc Measurement" some additional sympathy, especially from the military representatives of several neighbouring countries, where the Prussian army was not too popular.

We now shortly describe some of the major achievements of this first epoch of the Association (Torge 2005, 2012). Following the original project definition, *triangulation* is progressing rapidly in the European countries. The number of first order trigonometric points increased, e.g., from 2010 in the year 1862 to more than 3500 in 1880, and reached more than 5500 in 1912 (Fig. 8). The number of baselines available grew from 57 to 109, between 1862 and 1889. The quality of the triangulation improves significantly, where General Annibale Ferrero, Director of the Istituto Geografico Militare in Florence, plays an important role. Outstanding examples are the first order triangulation of the Kingdom of Saxony (1867–1878) directed by Professor Nagel (Fig. 9a), and the new triangulation of Prussia (1875–1895). The latter one is characterized by the radical improvements introduced by the (later) General Oscar Schreiber (Fig. 9b), since 1875 leading the Trigonometric Department of the newly established "Königlich Preußische Landesaufnahme", and since 1888 chief of that institution which is under the direct responsibility of the General Staff. A remarkable enterprise is the connection of the Spanish triangulation with Algeria (1879), where triangles with a maximum side length of 270 km are observed from mountain stations, under the direction of

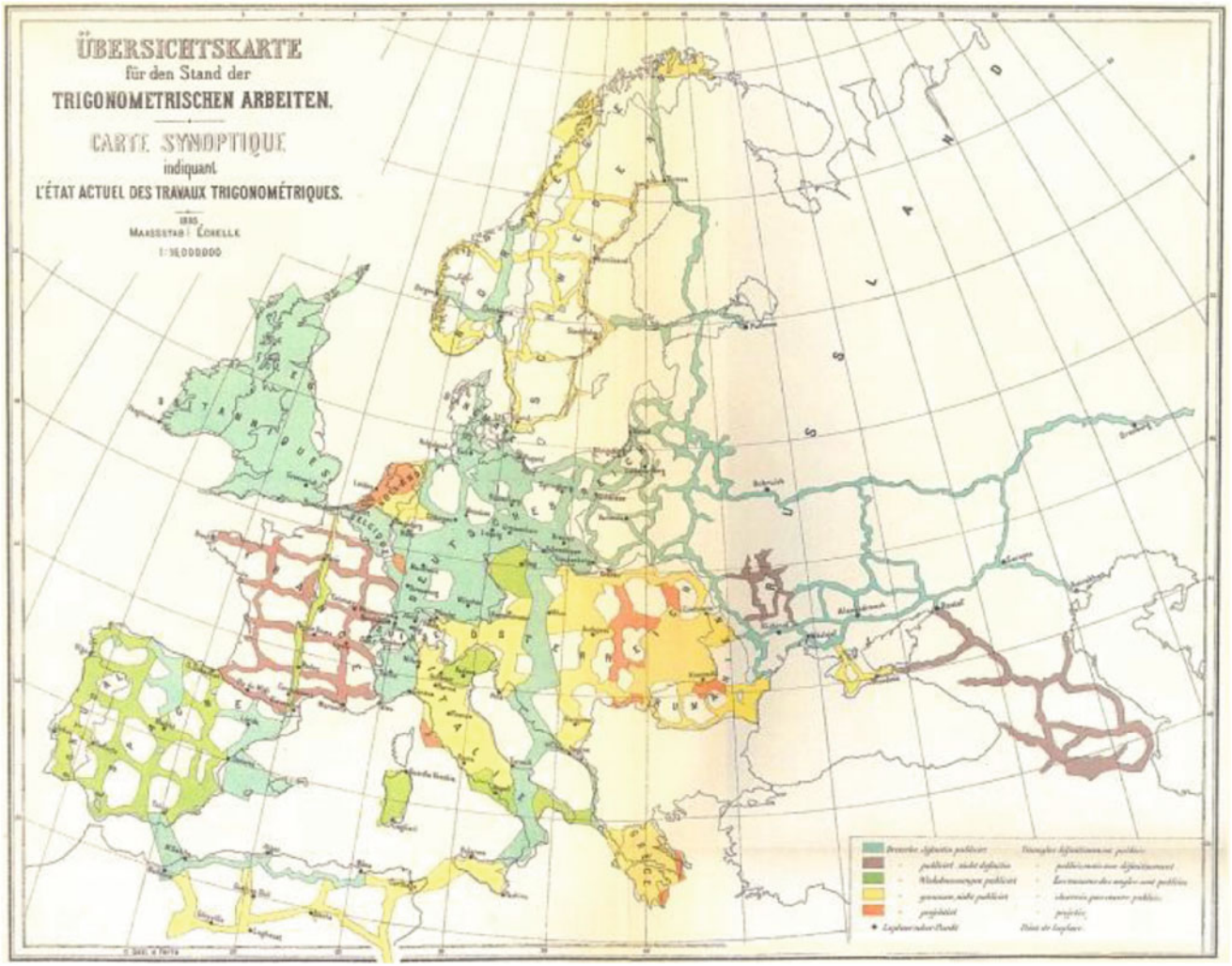

Fig. 8 State of the triangulation in Europe 1911, Verhandlungen der 17. Allgemeinen Conferenz der Internationalen Erdmessung, II. Theil. Georg Reimer, Berlin 1914

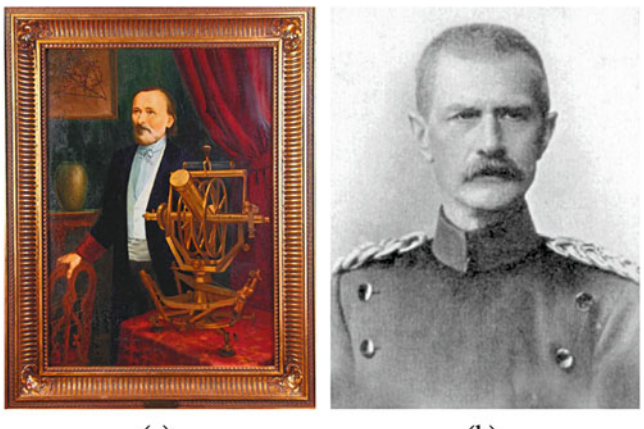

Fig. 9 (**a**) Professor Christian August Nagel. (**b**) Oil painting (private collection). General Oscar Schreiber (Torge 2009)

General Ibáñez and Major François Perrier from the Geodetic Section of the French General Staff.

In Prussia, curiously enough, severe problems arise at realizing the high standards set by the Arc Measurement for triangulation. This is due to the fact, that with the foundation of the Prussian Geodetic Institute two different state agencies exist for triangulation and levelling. The General Staff is responsible for providing the geodetic fundamentals for mapping the country, while the geodetic Institute collects and examines existing data for use at the Arc Measurement project, and carries out own measurements if necessary. In this connection, Baeyer declares that all measurements of the General Staff carried out since 1858 (Baeyer had retired in 1857!) did not satisfy the scientific demands of the project. The following confrontation between Baeyer and the General Staff involves several members of the Permanent

Commission, and lasts until Baeyer's death (Pieper 1996). The conflict is settled finally by an agreement between Baeyer's successor Helmert and Schreiber, with the exclusive responsibility of the "Landesaufnahme" for first order triangulation and levelling.

The comparison of the length units used in different countries finally led to a decision which reached far beyond geodesy. While the General Conference in 1864 still proposed the Bessel toise as a uniform *length standard* for the Arc Measurement, the meter was recommended in 1867, and the establishment of an international bureau recommended for the realization of a corresponding prototype. An International Meter Convention was signed 1875 in Paris, and the new International Bureau for Weights and Measures (Bureau International des Poids et Mesures, BIPM) in Sèvres close to Paris became responsible for constructing a stable meter standard and distributing copies to the countries that had signed the convention.

A remarkable step forward also occurred at the survey of the third dimension. First order geometric *levelling* now started in most European countries, based on the experience from France and Switzerland. With the "Nivellement général de la France" (NGF), a first countrywide levelling network had been established (1857–1864), under the direction of Paul-Adrien Bordalouë. Remarkable improvements including error investigations are due to Charles Lallemand responsible for the NGF since 1884. Following this example, about 64000 km first order levelling lines were surveyed in central, western and southern Europe until 1880, with proper junctions between the countries. A larger number of connections to mean sea level (MSL) as derived from tide gauges (with recording mareographs at many places) allowed first investigations on the relation of MSL to a gravity field equipotential surface. An important conclusion followed in 1890, namely to not yet introduce a common sea-level related height datum for Europe. This decision was based on the comparison of levelling results with MSL observations around Europe, revealing differences of 10–30 cm between levelling and MSL, which could be due to real discrepancies between MSL and a level surface of the gravity field, but also to systematic errors inherent in levelling over large distances.

The original project's definition also required a sufficient number of *astronomic* latitude, longitude and azimuth determinations. This was attacked with different intenseness, where longitude determinations played a special role, with time differences transferred through telegraphy introduced since the 1850s. Adjustments of a Central European Longitude Network started in the 1870s by Theodor Albrecht at the Geodetic Institute Potsdam, and a final adjustment including 80 stations was presented by him in 1905. It was the longitude problem which again was of high interest for the public in general, especially through the increasing global traffic and commerce. In 1882, the Senate and the Geographic Society of the city of Hamburg asked the Permanent Commission to deal with the unification of the geographic longitudes by selecting one *zero meridian* and to suggest a corresponding decision. This question was discussed at the General Conference in Rome 1883, which was also attended by observers from Great Britain and the United States as countries extremely interested in this problem. The Conference decided to select the Greenwich meridian as the zero meridian for longitude, with the Universal Time referred to it. At the 1884 Meridian Conference in Washington, a general agreement on this definition was obtained, and gradually all countries referred their longitudes to the Greenwich meridian.

With the inclusion of *gravity measurements* into the programme of the "Arc Measurement" this physical tool again came into the focus of geodesy, after the world-wide activities along geodetic arcs and at ship-borne expeditions during the first three decades of the century. The Repsold workshop in Hamburg was asked to construct a transportable reversible pendulum. A limited number of gravity measurements was carried out until about 1900, but the results were not satisfactory. This was due – among other reasons – to the effects of co-oscillation (detected by C. S. Peirce from the U.S. Coast and Geodetic Survey) between the pendulum, its support and the ground, and led to a multitude of investigations on the theory of the reversible pendulum. A real progress in gravity measurement techniques only happened in the following epoch of the Association (see below).

The 1880s may be regarded also a certain closing at the development of modern *geodesy* as a *proper science*, with a clearly defined objective, an established research program, and dedicated university educational programs. Geodesy is now not only lectured from astronomers, mathematicians, and at military academies, but also at Institutes of Technology, outstanding examples being the early chairs for geodesy at the Polytechnic Schools in Dresden/Saxony (Professor Nagel, since 1852) and in Aachen/Prussia (Professor Helmert, since 1870). Among the fundamental literature of that time we have the two volumes monograph "Die mathematischen und physikalischen Theorieen der höheren Geodäsie" by Helmert (1880/1884, Fig. 10a) and the widespread textbook "Geodesy" by Colonel A. R. Clarke (first edition 1880). A remarkable step towards the combined vista of geometrical and physical geodesy is due to Heinrich Bruns, Professor of Mathematics at the University of Berlin. Triggered by the geodetic activities of the European Arc Measurement, he publishes a study on the fundamental

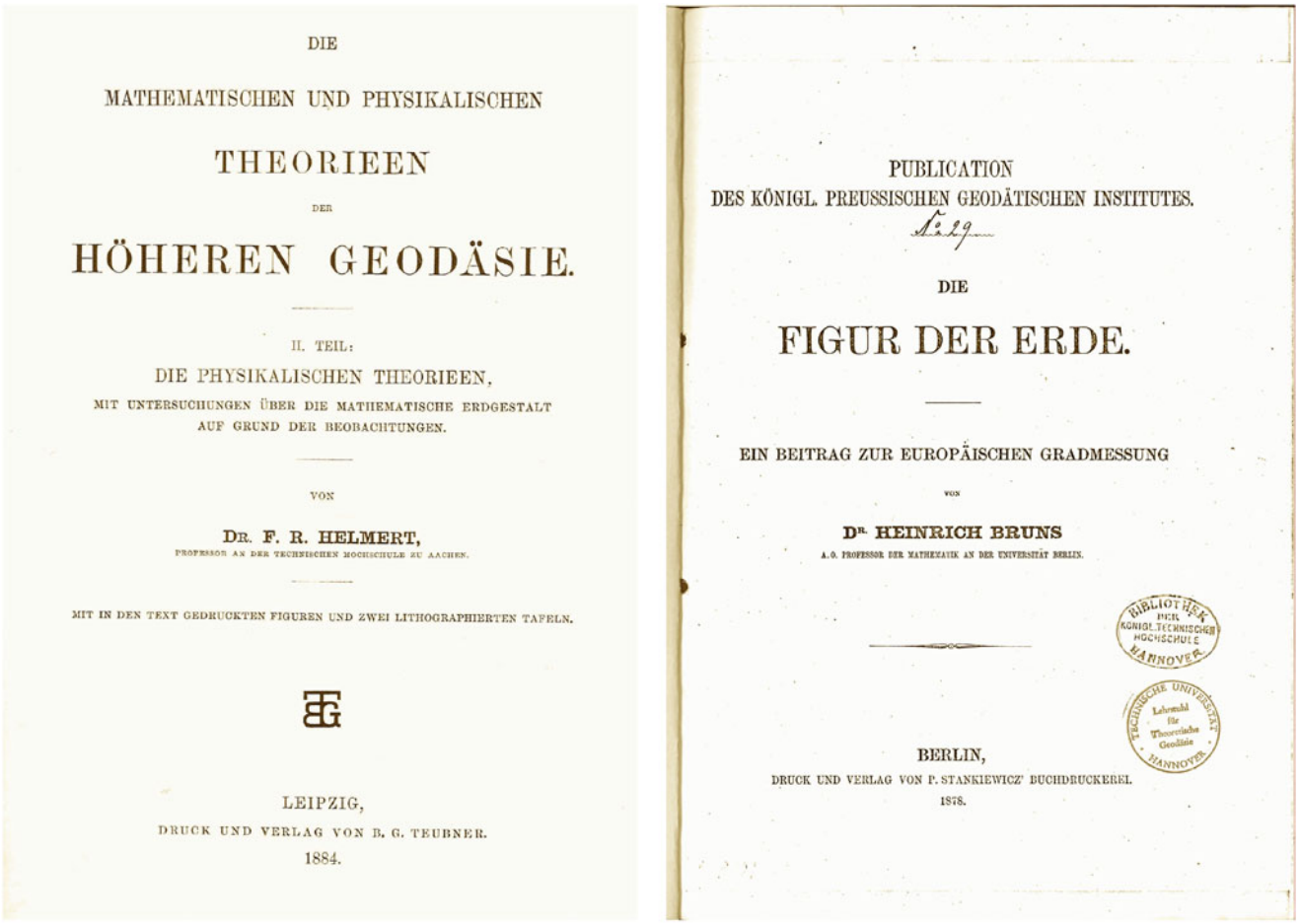

Fig. 10 (**a**) Frontpage of F. R. Helmert: Die mathematischen und physikalischen Theorieen der höheren Geodäsie. II. Teil, Leipzig 1884 and (**b**) frontpage of H. Bruns: Die Figur der Erde, Berlin 1878

problem of geodesy which looks far into the future and contains conclusions for the scientific programme of the organization (Bruns 1878, Fig. 10b).

The death (1885) of Baeyer finishes the first epoch of organized international collaboration in scientific geodesy. Among the many honours which Baeyer has obtained we especially mention the gold medal given to him (and in absentia accepted by Helmholtz) by the Italian Arc Measurement Commission, at the General Conference in Rome 1883. It is here, where a first step to observing the Earth as a dynamic system in space can be recognized. The Italian astronomer Emmanuele Fergola, Director of the Naples Observatory, proposes to monitor the Earth's rotational axis with respect to the solid Earth by astronomic latitude observations on the same parallel. Friedrich Küstner from the Berlin observatory observes the predicted latitude changes in 1884/1885, and this leads us to the organized polar motion observations, starting in the next epoch of the international cooperation in geodesy.

3 The "International Geodetic Association" – Global Extension and Deepening: The "Helmert-Epoch" 1886–1916

The first General Conference of the "European Arc Measurement" after the death of Baeyer was held in Berlin in 1886, with the astronomer Wilhelm Foerster as Chairman. The conference brought a new convention on the organization, which was now called "*Internationale Erdmessung*" ("*Association Géodésique Internationale*" in French, and translated into English "*International Geodetic Association*"). Until 1899, the United States of America, Mexico, Chile, Argentine and Japan agreed with the new convention, and Great Britain joined the Association in 1898. The General Conference, composed of the delegates from the membership countries, remained the leading structure of the Association. It became strengthened at the General Conference 1895, where

Fig. 11 Presidents of the Permanent Commission 1892–1916. (**a**) Hervè Faye (Drewes 2013), (**b**) General Jean Bassot (Drewes 2013)

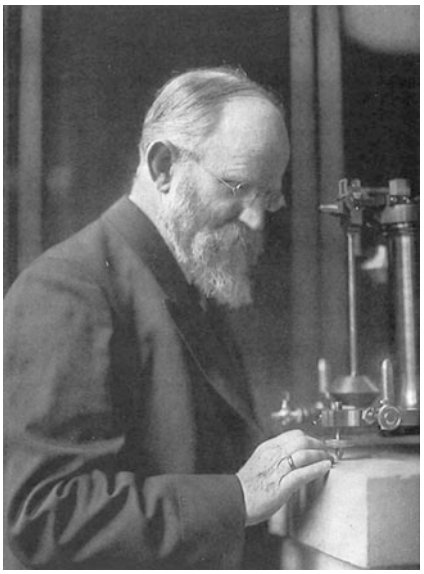

Fig. 12 Friedrich Robert Helmert with relative pendulum apparatus. Geoforschungszentrum Potsdam (Helmert 1993, p. 36)

the Permanent Commission's responsibility was reduced to administrative matters. An annual financial contribution from the countries stabilized the Association, and the performance of the Association's work was improved by the strong positions of the Director of the Central Bureau and a newly established Permanent Secretary. Voting at the General Conferences now followed the principle of one voice per country, which reduced the overwhelming influence of the German states. The more international character of the Association can be seen also from the locations of the *General Conferences*: Paris (1889), Brussels (1892), Berlin (1895), Stuttgart (1898), Paris (1900), Copenhagen (1903), Budapest (1906), London and Cambridge (1909), and Hamburg (1912).

Under the new conventions, the elected *Presidents* of the Permanent Commission and the Association, resp., were as follows: General Ibáñez de Ibero (1887–1891), Hervè Faye (Fig. 11a), President of the Bureau des Longitudes, Paris (1892–1902), and General Jean Bassot (Fig. 11b), Chief Geodetic Section, Service Geographique de l'Armeè/Director Nice Observatory (1903–1916). As *Permanent Secretaries* we have Adolphe Hirsch, Director of the Neuchatel Observatory, Switzerland (1886–1900) and H. G. van de Sande Bakhuizen, Director of the Leiden Observatory, The Netherlands (1900–1916). Director of the *Central Bureau* becomes F. R. Helmert, and it is he who – as the President of the Prussian Geodetic Institute hosting the Central Bureau – especially stamps the "Internationale Erdmessung" between 1886 and 1916 (Helmert 1913a,b).

Friedrich Robert Helmert was born in 1843 in Freiberg/Saxony, as the son of a foundation cashier. He studied surveying engineering and geodesy at the Polytechnic School Dresden (1859–1863); with Professor Nagel as the main teacher. During the next 3 years he assisted Prof. Nagel, enlarging his own knowledge and deepening his understanding for geodesy, including the participation at the new triangulation of the Kingdom (see above). An additional study of mathematics and astronomy (1866/1867) followed at the University of Leipzig, where he was promoted with the degree of a Dr.phil. in 1868. After different employments (geodesist at the state triangulation, secondary school teacher for mathematics, observer at the Hamburg astronomical observatory) he was appointed teacher (1870) and full professor (1872) at the newly established Polytechnic School in Aachen/Prussia. It was here where he published the fundamental monograph on the mathematical and physical theories of higher geodesy (see above), but also a leading textbook on least squares adjustment and a number of papers on different topics in geodesy and surveying engineering. He held the chair of geodesy until 1886, when he was appointed Director of the Prussian Geodetic Institute and simultaneously Professor of Higher Geodesy at the University of Berlin (Fig. 12). He systematically develops the Institute and extends the range of the scientific research, especially with respect to physical geodesy and geophysics (Buschmann 1993). This attracts a number of talented scientists, and is of extreme benefit for the Geodetic Association, as an overwhelming part of the research work is related to the demands of the Central Bureau. A remarkable step forward occurs in 1892, when the Institute can move to a new central building and related observation sites on the Telegraphenberg Potsdam (Fig. 13), leaving its previous seat at different private houses in Berlin. Helmert himself is strongly engaged in the planning of the Institute's facilities, examples being the temperature-stabilized pendulum room in the main building and the "Helmert"-tower for angular measurements (Löschner 1970; Wolf 1970, 1993).

Fig. 13 Central Building, Prussian Geodetic Institute, Potsdam Telegraphenberg, Geoforschungszentrum Potsdam

Among the main achievements of the Helmert epoch naturally we have the continuing collection of *horizontal control* data, documented, e.g., by more than 9200 first order trigonometric points worldwide in the member countries of the Association. This is followed by network adjustments and the calculation of geodetic lines between the increasing number of astronomic control points. Arc measurements along meridians and parallel circles were carried out either as part of national geodetic surveys or/and as contribution to the determination of the figure of the Earth. We mention the completion of the 52° parallel, initiated in the 1850s by W. Struve (see above), the remeasurement of the Paris meridian arc (Bassot, Defforges, Perrier) from the 1870s to the 1890s, with connections to Great Britain, Spain, and Algeria (see above), and the remeasurement of the classical "Peru-arc" (1899–1906) through French officers including Georges Perrier from the "Service géographique de l'Armée". A remarkable enterprise is the African 30° meridian arc measurement between the Cape and Cairo, finished only in the 1950s. It is initiated in 1883 by Sir David Gill, Her Majesty's Astronomer at the Royal Observatory at the Cape of Good Hope, in connection with the geodetic survey of South Africa. Triangulation chains reach Lake Tanganyika in 1907, and simultaneously triangulation starts in Egypt and in Uganda. The triangulation of the United States of America (carried out by the Coast and Geodetic Survey, directed from 1900 to 1915 by Otto H. Tittmann, and since 1898 with John F. Hayford as Inspector of Geodetic Work and Chief of Computing Division, followed in 1909 by William Bowie) becomes an outstanding example for the sophisticated treatment of a geodetic network of large dimensions. Based on several extended geodetic arcs and a number of more local triangulations, a common adjustment is carried out and referred to one fundamental station and a single reference ellipsoid; a multitude of observed astronomical latitudes, longitudes, and azimuths is also available around 1900. A minimum condition applied on the deflections of the vertical then leads to a datum shift and a best-fitting ellipsoid, where topographic-isostatic reductions of the deflections of the vertical play an essential role (see below).

The growing number of observed *deflections of the vertical* leads to an increased discussion on the magnitude and behaviour of these gravity field quantities, which contain local and regional disturbances, resulting from topography and isostasy. Gradually it becomes obvious that these local data, available only at larger distances on the continents, can not deliver a unique global result with respect to the figure of the Earth (gravity field, ellipsoid). Nevertheless, the computation of reference ellipsoids from triangulation results continues, an important result being the Hayford-Ellipsoid of 1909. It is calculated from topographic-isostatic reduced vertical deflections in the United States of America, and will be later recommended by the Geodetic Association as "International Ellipsoid 1924". There are, on the other hand, first attempts to get more detailed insight into the *local* gravity field structure. This is achieved by a dense vertical deflection survey, with station distances of about 10 km or less. Astronomic levelling, as proposed by A. J. Yvon-Villarceau 1871/1875 and by Helmert in 1884, then allows to determine the local *geoid* structures, as demonstrated by Galle in the Harz mountains in central Germany. A sophisticated step forward towards a local gravity field

survey is due to the Hungarian professor Loránd Eötvös, who since 1890 develops and continuously improves a torsion balance to be used in the field. As demonstrated at the General Conference in 1906, this instrument delivers the geoid curvature and the horizontal gravity gradient; in the 1920s it gained great importance for oil exploration. First investigations on the *global* structure of the geoid again are carried out by Helmert. He first estimates the geoid heights from continental topography to be not larger than 400 m, but reducing to a mean variation of ±27 m at isostatic compensation. He also risks a first geoid estimate based on the gravimetric method, as derived by Georges Gabriel Stokes in 1849. As the insufficient coverage of the Earth with gravity data at that time does not allow a more detailed evaluation of Stokes's surface integral, Helmert assumes a mean variation of ±35 mGal for the gravity anomalies and thus obtains ±50 m for the geoid variation, a rather realistic estimate.

Gravity measurements, from local to global scale, experience a great progress in the Helmert epoch. This development is driven by the geodetic possibilities inherent in the gravimetric method (see above), but also by the geophysical information provided by the gravity field, where the isostatic behaviour of the different parts of the Earth receives special interest. In 1887, Colonel Robert von Sterneck from the Military Geographic Institute Vienna presents a transportable relative pendulum apparatus delivering an accuracy of a few mGal. This leads to a rapid increase in the number of relative gravity stations and the problem of connecting them to the few and less accurate absolute stations. The problem is solved in several steps, starting with a new absolute determination with several reversible pendulums in the Potsdam Geodetic Institute, carried out by Kühnen and Furtwängler between 1898 and 1904. This is followed by worldwide ties between twenty fundamental stations and Potsdam. A subsequent adjustment is carried out by Borrass and references all available relative data (about 2400) to the Potsdam value. The 1909 General Conference introduces this "*Potsdam Gravity System*" as international gravity standard, which remains valid until a new definition in 1971. Sponsored by the Association, first world-wide *gravity measurements on sea* are carried out between 1901 and 1909 by Oscar Hecker from the Geodetic Institute. Gravity is derived from the differences between the results of several mercury barometers and hypsometers, at shipborne expeditions on the Atlantic, the Indian and the Pacific Oceans, and the Black Sea. Although the accuracy is limited (±30 mGal), the results confirm the theory that the oceans in general are isostatically compensated, with the exception of tectonically disturbed areas. These surveys are also used for investigating the "Eötvös-effect", due to the movement of the gravity sensor on the rotating Earth.

The geodetic contribution to *geodynamic research* is recognized more and more during this epoch. Recent crustal movements produced by an earthquake are investigated by the US Coast and Geodetic Survey, by reobserving a selected triangulation network in the area of the 1906 San Francisco earthquake. The results of repeated levelling are also discussed early with respect to vertical movements. Significant changes were observed after the 1891 No-Bi earthquake in Japan, while the isostatically caused land uplift in Fennoscandia was first derived from sea level records. The development of a horizontal pendulum by E. v. Rebeur-Paschwitz allowed the first observations of Earth tides (1889–1893), with more regular measurements carried out in Potsdam by Hecker (since 1910). It is here where W. Schweydar in 1914 also observes the gravimetric Earth tides, and there are even first attempts (1909) to establish a global observing system for studies of crustal movements, jointly with the International Association for Earthquake Research.

A successful story is the determination of *polar motion*, following the first proposals and observations made in the early 1880s (see above). An international service for a continuous astronomic monitoring of polar motion is proposed by W. J. Foerster in 1888, and simultaneous observations in Berlin, Potsdam and Prague (1889–1890) clearly show the "Chandler" period of about 427 days, detected by S. C. Chandler in 1891. This result is strengthened by an expedition to Honolulu (A. Marcuse, 1891–1892), with parallel observations in Berlin and other places (Fig. 14). The *International Latitude Service* (ILS) is now established by the Association and starts regular observations in 1899, at Mizusawa, Japan (Director H. Kimura), Carloforte, Italy, Gaithersburg and Ukiah, USA, all located on the 39° 08′ parallel and equipped with specially designed zenith telescopes. The service is later joined by the observatories at Tschardjui (later moved to Kitab, Russia, now Uzbekistan) and Cincinatti, USA, and more observatories follow during the next decades. The evaluation of the observations is performed at the Central Bureau in Potsdam, and continued throughout and after the First World War (see below).

4 End and Survival of the "Internationale Erdmessung": The Transition Time 1917–1922

The convention of the "Internationale Erdmessung" expired at the end of 1916, and was not extended due to the First World War. The situation was rendered more difficult through the dead of some of the leading officers of the Association, among them the President, Bassot, from France (1917), the Vice-President, O. Backlund, from Russia (1916), and the

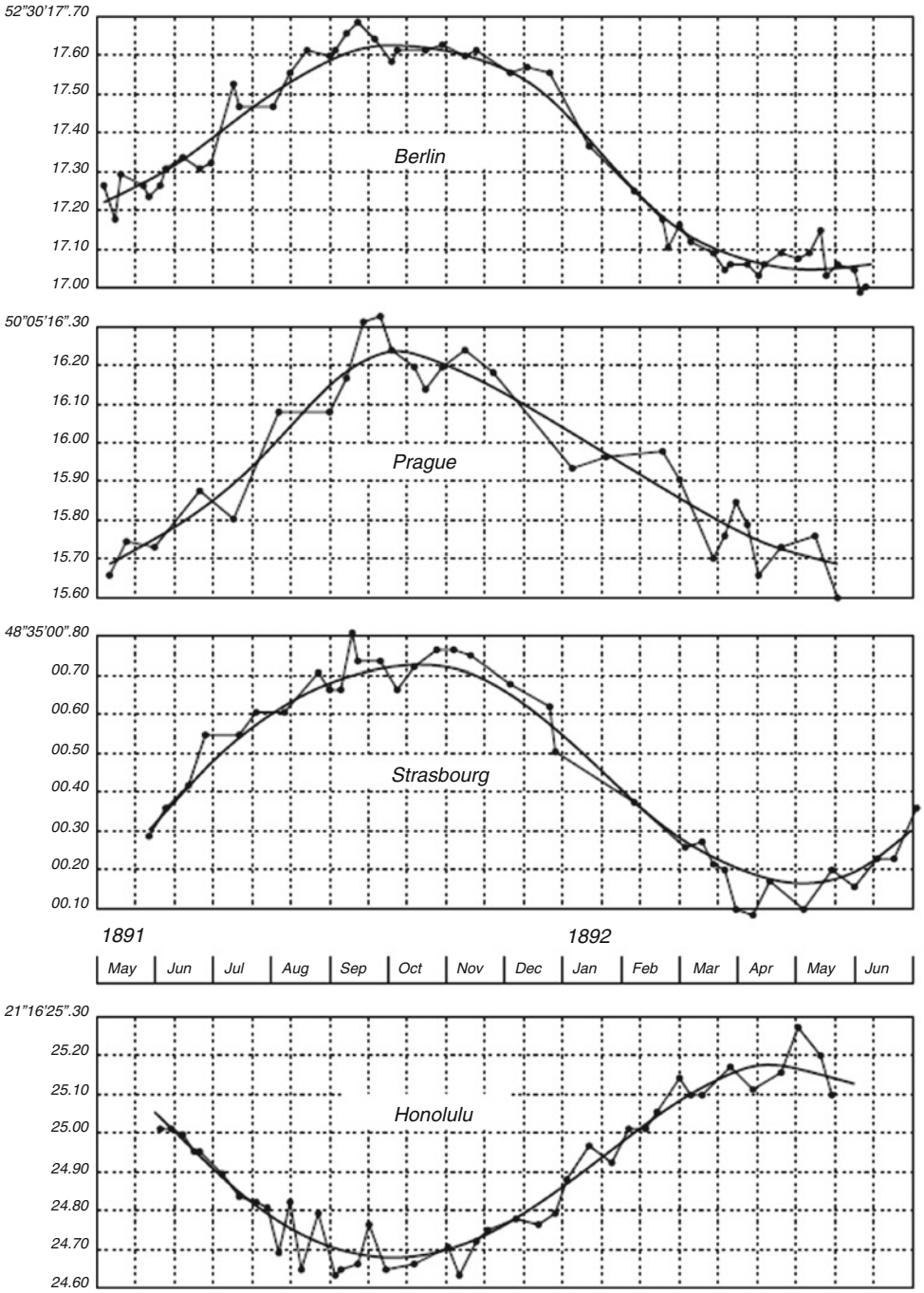

Fig. 14 Simultaneous latitude observations at Berlin, Prague, Strasbourg and Honolulu, from May 1891 to June 1892. From: Albrecht, Th., Central Bureau Internationale Erdmessung, Berlin 1892

Director of the Central Bureau, Helmert, from Germany (1917). Fortunately some of the activities of the Association could be continued, especially the Latitude Service. This is due to the efforts of two men from neutral countries, namely Raoul Gautier (Fig. 15a), Director of the Geneva Observatory, Switzerland, and the Association's Secretary Hendrikeus Gerardus van de Sande Bakhuizen (see above, Fig. 15b). They proposed that the neutral nations "maintain the existence of the Association under the terms of the old convention…for a period that cannot be precisely defined at present". A "*reduced geodetic Association among Neutral Nations*" was formed accordingly, comprising Denmark, The Netherlands, Norway, Spain, Sweden, Switzerland, and the United States until its entry into the war in 1917. The Central Bureau continued (reduced) operation, and received data through the Secretary. Naturally, it was further on located at the Geodetic Institute Potsdam, which was directed by Louis Krüger between 1917 and 1922. Some research on Earth tides, gravity field features and isostatic reductions could be carried out, but the main task

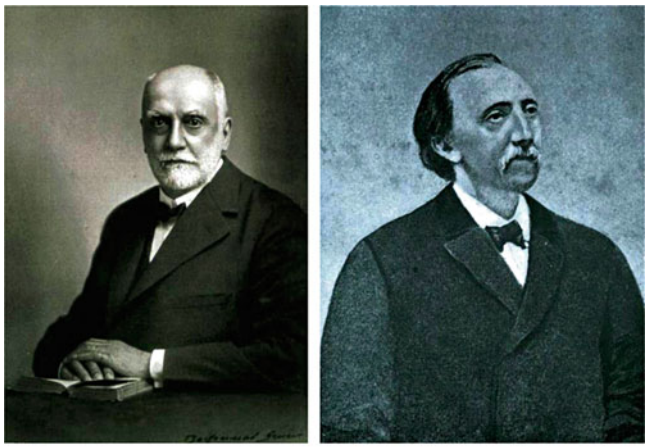

(a) (b)

Fig. 15 (**a**) Raoul Gautier, Observatoire de Genève. (**b**) Hendrikeus Gerardus van de Sande Bakhuizen, photography 1898 (Drewes 2013)

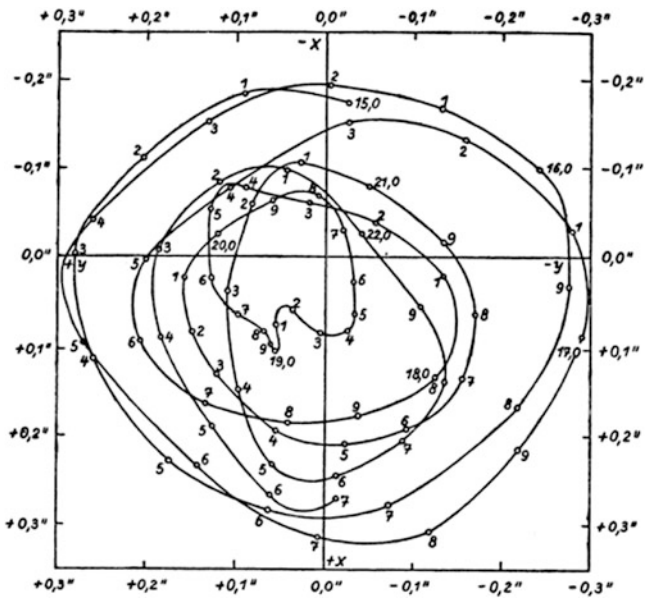

Fig. 16 Polar motion 1915.0–1922.7. From: Jordan-Eggert: Handbuch der Vermessungskunde III/2. 8. Auflage, Stuttgart 1941, S. 525

was the collection and evaluation of the polar motion data, obtained from the International Latitude Service. In this way, polar motion could be continuously derived until 1923 (Fig. 16).

The end of the First World War also was the beginning of an international non-governmental organization of a multitude of scientific disciplines. A "Conseil International des Recherches" was founded in Brussels in 1919, which included the "*International Union of Geodesy and Geophysics*" (IUGG). At the first IUGG General Assembly in Rome 1922, a "Section of Geodesy" was established, with W. Bowie from the U.S. Coast and Geodetic Survey serving as President until 1933. For this next epoch of the IAG history see the following paper by Boucher and Willis (2015).

References

Baeyer JJ (1861) Über die Größe und Figur der Erde: eine Denkschrift zur Begründung einer mittel-europäischen Gradmessung. G. Reimer, Berlin (in German)

Bessel FW (1837) Über den Einfluß der Unregelmäßigkeiten der Figur der Erde, auf geodätische Arbeiten und ihre Vergleichung mit den astronomischen Bestimmungen. Astronomische Nachrichten 14:269–312 (in German)

Bessel FW, Baeyer JJ (1838) Gradmessung in Ostpreussen und ihre Verbindung mit Preussischen und Russischen Dreiecksketten. Gedruckt in der Druckerei der Königlichen Akademie der Wissenschaften 1838, in Commission bei F. Dümmler (in German)

Bialas V (1982) Erdgestalt, Kosmologie und Weltanschauung. K. Wittwer, Stuttgart (in German)

Boucher C, Willis P (2015) IAG history, the years of the World wars and aftermath (1917–1959). In: IAG Symposia Vol. 143

Brosche P (2001) Der Astronom der Herzogin – Leben und Werk von Franz Xaver von Zach. Harri Deutsch, Frankfurt am Main (in German)

Bruns H (1878) Die Figur der Erde – Ein Beitrag zur europäischen Gradmessung. P. Stankiewicz, Berlin (in German)

Buschmann E (1993) Ein Jahrhundert Geodäsie in Potsdam. Allgemeine Vermessungs-Nachrichten 100(7):247–265 (in German)

Buschmann E (ed) (1994) Aus Leben und Werk von Johann Jacob Baeyer. Institut für Angewandte Geodäsie, Frankfurt am Main (in German)

Dick WR (1996) Zur Vorgeschichte der Mitteleuropäischen Gradmessung. In: Beiträge zum J. J. Baeyer-Symposium, Berlin-Köpenick, 5.–6.11.1994. Deutsche Geodätische Kommission, Reihe E Nr. 25, Frankfurt am Main, pp 15–27 (in German)

Drewes H (2013) IAG History: Photos of the Presidents and Secretaries. http://iag.dgfi.badw.de/index.php?id=311

Gauss CF (1828) Bestimmung des Breitenunterschiedes zwischen den Sternwarten von Göttingen und Altona. Carl Friedrich Gauß Werke, Bd. IX. Teubner, Leipzig (1903) (in German)

Großmann W (1955) Niedersächsische Vermessungsgeschichte im 18. und 19. Jahrhundert. In: Gauß und die Landesvermessung in Niedersachsen, Hrsg. Niedersächsische Vermessungs- und Katasterverwaltung, Niedersächsisches Landesvermessungsamt, Hannover (in German)

Hamel J, Buschmann E (1996) Friedrich Wilhelm Bessels und Johann Jacob Baeyers Zusammenwirken bei der "Ostpreußischen Gradmessung" 1830–1838. In: Beiträge zum J. J. Baeyer-Symposium, Berlin-Köpenick, 5.–6.11.1994. Deutsche Geodätische Kommission, Reihe E Nr. 25, Frankfurt am Main, pp 45–57 (in German)

Helmert FR (1880/1884) Die mathematischen und physikalischen Theorieen der höheren Geodäsie. Teubner, Leipzig, [reprint Minerva GmbH, Frankfurt am Main, 1961] (in German)

Helmert FR (1913a) Das Zentralbureau während der ersten fünfzig Jahre der Internationalen Erdmessung. In: Verhandlungen der siebzehnten Allgemeinen Conferenz der Internationalen Erdmessung, I. Theil, Beilage A.I, G. Reimer, Berlin, pp 129–164 (in German)

Helmert FR (1913b) Die Internationale Erdmessung in den ersten fünfzig Jahren ihres Bestehens. Internat Monatsschrift für Wissenschaft, Kunst und Technik 4(7):397–424 (in German)

Helmert FR (1993) Akademie-Vorträge. Nachrichten aus dem Karten- und Vermessungswesen, Reihe I, No. 109, Verlag des Institut für angewandte Geodäsie, Frankfurt am Main (in German)

Laitko H (1996) Johann Jakob Baeyer, die internationale Stellung des Preußischen Vermessungswesens und die Mitteleuropäische Gradmessung. In: Dahlemer Archivgespräche Band I, Archiv der Max-Planck-Gesellschaft, Berlin, pp 58–78 (in German)

Levallois JJ (1980) The history of the International Association of Geodesy. Bull Geod 54(3):248–313

Löschner F (1970) Helmert's Entwicklung und Bedeutung als Lehrer der Praktischen Geometrie, Deutsche Geodätische Kommission, Reihe E, Nr. 12, Aachen, pp 1–14 (in German)

Perrier G (1939) Petit Histoire de la Géodésie: Comment l'homme a mesuré et pesé la terre. Alcan, Presses Universitaires de France, Paris, [German translation by E. Gigas (1950): Wie der Mensch die Erde gemessen und gewogen hat – Kurze Geschichte der Geodäsie. Bamberger Verlagshaus Meisenbach, Bamberg]

Pieper H (1996) Johann Jacob Baeyer. In: Beiträge zum J. J. Baeyer-Symposium, Berlin-Köpenick, 5.–6.11.1994. Deutsche Geodätische Kommission, Reihe E Nr. 25, Frankfurt am Main, pp 89–119 (in German)

Sadebeck M (1883) Register der Protokolle, Verhandlungen und Generalberichte für die Europäische Gradmessung vom Jahre 1861 bis zum Jahre 1880. Publ. des Königl. Preußischen Geodätischen Instituts, Berlin (in German)

Torge W (2002) Müfflings geodätisches Wirken in der Umbruchepoche vom 18. zum 19. Jahrhundert. Zeitschrift für Vermessungswesen 127(2):97–108 (in German)

Torge W (2005) The International Association of Geodesy 1862 to 1922: from a regional project to an international organization. J Geod 78(9):558–568

Torge W (2009) Geschichte der Geodäsie in Deutschland, 2nd edn. de Gruyter, Berlin – New York (in German)

Torge W (2012) 150 years of international cooperation in geodesy: precursors and the development of Baeyer's project to a scientific organization. Zeitschrift für Vermessungswesen 137(3):166–175

Torge W, Müller J (2012) Geodesy, 4th edn. de Gruyter, Berlin/Boston

Wolf H (1970) Die wissenschaftliche Ausstrahlung Helmert's in die Gegenwart, Deutsche Geodätische Kommission, Reihe E, Nr. 12, Aachen, pp 15–28 (in German)

Wolf H (1993) Friedrich Robert Helmert – sein Leben und Wirken. Zeitschrift für Vermessungswesen 118(12):582–590 (in German)

IAG History: The Years of World Wars and Aftermath (1917–1959)

Claude Boucher and Pascal Willis

Abstract

In the frame of the celebration of the 150th birthday of the International Association of Geodesy (IAG), this contribution is devoted to the period 1917–1959, starting at the move of the IAG Central Bureau from Potsdam to Paris, up to the occurrence of space technology. Among important aspects, the evolution of international cooperation is presented, with crucial geopolitical aspects (mostly around World Wars I and II) as well as drastic technological innovations. A particular important issue is the creation of the International Union of Geodesy and Geophysics (IUGG) and the inclusion of IAG. The evolution of the IAG structure and organization is presented, as well as its links with other scientific entities.

Keywords

Central Bureau • General Assemblies • History • International Association of Geodesy

1 Introduction

This paper was written in the frame of the celebration of the 150th anniversary of the International Association of Geodesy (IAG) by the two participants of the last IAG Central Bureau located in France (1917–1995), Claude Boucher (general secretary) and Pascal Willis (assistant secretary).

The two main goals of the paper are to provide a written document corresponding to the speech of Claude Boucher during the celebration organized on September 2013 in the frame of the IAG Scientific Assembly in Potsdam (Germany), together with Prof W. Torge for early years (Torge in press) and Prof I.I. Mueller for the space age, both former IAG presidents. Quite a few articles are available in the scientific literature on these historical aspects of the IAG: Levallois 1980; Angus-Leppan 1984; Whitten 1988; Louis 1992; Torge 1996; Beutler et al. 2004; Torge 2005; Adam 2008.

The second goal is to give some basic information on the IAG Central Bureau while it was located in France and to pay a well-deserved tribute to our well-known predecessors. While a more exhaustive study related to Geodesy in France since the eighteenth century (Perrier 1939; Levallois 1988), nothing really exists for the more recent years.

The start and end dates of the analysed period were selected to reflect these arrangements. 1917 is the start of the IAG Secretariat, later called IAG Central Bureau, in France. 1957 is the year of the launch of the first artificial satellite Sputnik I, symbolically initiating the beginning of the space era in geodesy in the 1960s.

Such an historical work can be undertaken using different approaches. For example, we can mention: chronology of major events, biography of people involved in the IAG (officers, chairs of various working groups, individual geodesists), description of the internal organization of IAG and evolution of its activities (meetings, publications, new structures such as projects and services, etc.), relationship with other organizations: the International Union for Geodesy

C. Boucher
Observatoire de Paris, SYRTE, Paris, France

P. Willis (✉)
IGN, Direction de la Recherche et de l'Enseignement, Saint-Mande, France

IPGP, UMR 7154, Gravimétrie et géodésie, Université Paris Diderot, Sorbonne Paris Cité, Paris, France
e-mail: pascal.willis@ign.fr

© Springer International Publishing Switzerland 2015

C. Rizos, P. Willis (eds.), *IAG 150 Years*, International Association of Geodesy Symposia 143,
DOI 10.1007/1345_2015_96

and Geophysics (IUGG), the International Astronomical Union (IAU), the United Nations Educational and Cultural Organization (UNESCO), the *Fédération Internationale des Géomètres* (International Federation of Surveyors, FIG), the *Bureau International des Poids et Mesures* (International Bureau for Weights and Measures, BIPM), etc.

Taking into consideration all these different approaches, which are difficult to reconcile in a linear presentation, this paper is organized as follows. In a first step, we will present the chronological aspects related to the IAG general meetings and subsequent changes in its internal organization. We will then focus on the history of the Central Bureau in Paris. Then, we will discuss relations of IAG with other organizations. Finally, we will present the development of the IAG services and their increased role in the Association.

2 Chronology: IAG Assemblies and Evolution of the IAG Structure

This chronological survey starts at the year 1917. During World War I, the old IAG organization still existed, however with some minimal activity. In 1917, a major change occurred following the death during this year of both leading officers, namely the President, general Antonin Léon Bassot (France), the vice-President Sir Georges Darwin and the Director of the IAG Central Bureau Friedrich Robert Helmert (Germany). As mentioned by Angus-Leppan (1984), "it is remarkable that the association managed to survive".

In order to maintain some continuity, seven neutral countries decided to continue cooperative geodetic activities and elected as president of this reduced IAG Raoul Gautier from Switzerland (see Angus-Leppan 1984). The "Reduced Geodetic Association among Neutral Nations" was then established. Some tasks performed before continued, however at a lower level of activity.

After the end of the World War I, intense international scientific cooperation was deployed again. The main starting event was the creation of an International Research Council (ICSU), during a meeting in Brussels in July 1919. Major scientific domains were organized into Unions, which were direct members of ICSU. Like astronomy, which gave birth to the International Astronomical Union (IAU), geosciences were organized through an International Union of Geodesy and Geophysics (IUGG).

As explicitly expressed in its name, IUGG was in particular covering geodesy. A Geodesy section was therefore established, ensuring a complete continuity with the pre-war IAG. A first bureau was elected: President: William Bowie (USA) (Fig. 1), Vice-president: Vincenzo Reina (Italy), General secretary: Georges Perrier (France) (Fig. 5) (Figs. 2 and 3). See also De Martonne 1946.

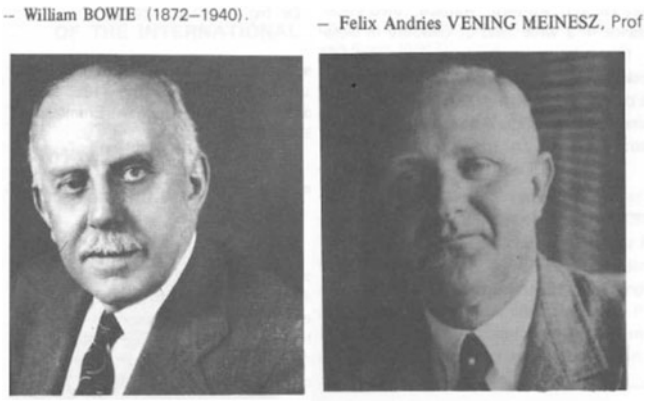

Fig. 1 *Left*: William Bowie, IAG President (1919–1933) and *Right*: Felix A. Vening-Meinesz, IAG President (1933–1945)

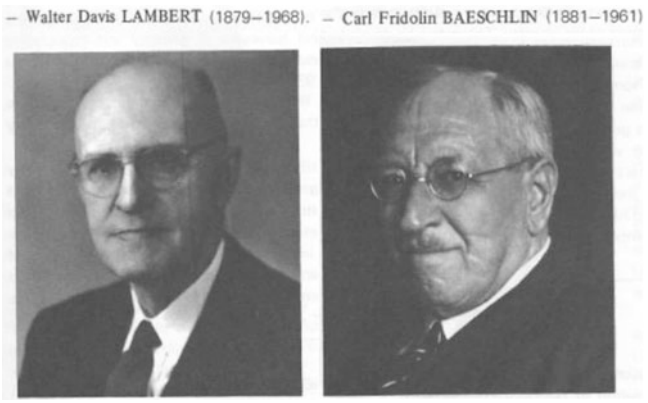

Fig. 2 *Left*: Walter Davis Lambert, IAG President (1945–1951) and *Right*: Carl Fridolin Baeschlin, IAG President (1951–1954)

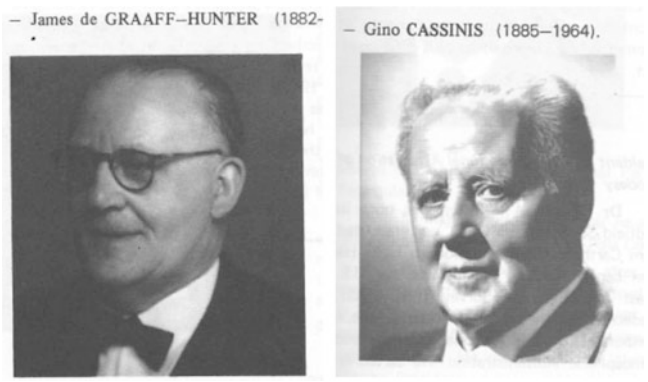

Fig. 3 *Left*: James de Graaf Hunter, IAG President (1954–1957) and *Right*: Gino Cassinis, IAG President (1957–1960)

A complete list of the IAG Presidents during the considered period can be found in Table 1.

The first IUGG general assembly was organized 3 years later in Rome from May 2 to 10, 1922. IAG organized there a general assembly as well as several executive committee meetings. A complete list of the IAG General Assembly is provided below for the 1917–1960 period:

Table 1 IAG Presidents (1917–1959)

Period	Name	Country
1917–1918	Raoul Gautier	Switzerland
1919–1933	William Bowie	USA
1933–1945	Felix A Vening-Meinesz	The Netherlands
1945–1951	Walter D Lambert	USA
1951–1954	Carl F Baeschlin	Switzerland
1954–1957	James de Graaf Hunter	UK
1957–1960	Gino Cassinis	Italy

- 1919: Brussels, Belgium where the creation of the new IAG happened.
- 1922: Rome, Italy. This is the official meeting of the new IAG organization.
- 1924: Madrid, Spain. The adoption of the Hayford ellipsoid occurred.
- 1927: Prague, Czechoslovakia
- 1930: Stockholm, Sweeden
- 1933: Lisbon, Portugal
- 1936: Edinburgh, UK
- 1939: Washington DC, USA. This corresponds to the first IAG meeting of this type outside Europe.
- 1946, Cambridge, UK
- 1948: Oslo, Norway
- 1951: Brussels, Belgium. The creation of Sections was decided.
- 1954: Rome, Italy
- 1957: Toronto, Canada
- 1960: Helsinki, Finland

A much more exhaustive list of these General Assemblies, as well as of the Scientific Assemblies of the Association can be found in Adam (1984).

As the vice-president Vincenzo Reina died late 1919, a new one was elected, namely Raoul Gautier (France). This choice was mainly done to smoothly ensure the proper inclusion into IAG of the activities of the organization reduced to neutral countries mentioned before.

During the 1919 assembly, the different domains of geodesy were also defined. For each of them, general reporters were appointed. Their main role was to collect information and to present synthetic reports, based on information coming from all parts of the world, to future assemblies. These major domains included: basis and triangulations (G. Perrier), precise levelling (C. Lallemand), geodetic astronomy, deflections of vertical, gravimetry, isostasy, variations of latitudes, map projections, Earth tides, stability of the Earth as time keeper (this last topic was later cancelled later, as considered as mostly related to astronomy).

The next assembly was held in 1924 in Madrid (Spain), mainly leading to the adoption of numerous organizational

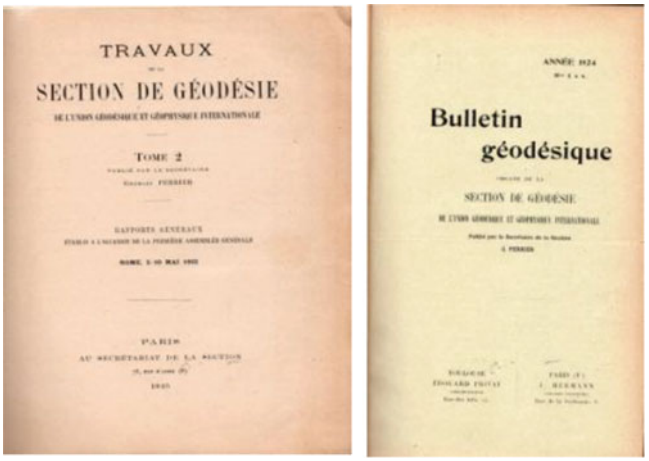

Fig. 4 Publications of the International Association of Geodesy: (*left*) *Travaux* and (*right*) Bulletin Géodésique

issues related to IAG: adoption of the statutes for the section of geodesy, (prepared by the general secretary G. Perrier), setting up of the IAG publication system including the *Bulletin géodésique*, which later became the official Journal of the IAG as Journal of Geodesy, after being merged with Manuascripta Geoadetica, and the *Travaux* (general and national reports) (Fig. 4), the creation of the library of the Central Bureau in Paris (mainly based on a worldwide exchange policy between IAG publications and various international journals and report series), creation of the International Geodetic Bibliography (IGB), creation of commissions (as listed Table 2). The role itself of the Association was also slightly different, trying to promote new projects instead of coordinating them as in the past (Angus-Leppan 1984).

On a more technical point of view, an important resolution from the Madrid meeting was the adoption of the Hayford 1909 ellipsoid, later named International ellipsoid (1924). At the assembly of Stockholm in 1930, following a proposal of the section of Geodesy, all IUGG sections were renamed Associations. IAG was therefore explicitly renamed "International Association of Geodesy" one component of the IUGG.

The last assembly organized before World War II was in Washington DC (USA) in 1939. It must be noticed that it was the first time an IAG assembly was held outside Europe. Some difficulties related to travel problems disturbed the meeting and lowered its attendance. As an example, even the IAG general secretary was not able to attend this meeting due to these travel difficulties.

The next significant event was the first meeting after the end of the Second War, during the IUGG extraordinary meeting held in Cambridge (UK) in December 1945, followed by an IAG executive committee meeting in Oxford (UK) held on July 1946. New officers were elected: Walter

Table 2 Permanent Commissions (1924)

Number	Designation
1	Finances
2	Trigonometric tables
3	Invar
4	Gravity
5	Latitudes
6	Map projections
7	Earth tides
8	Common topics with seismology and volcanology
9	International rules for geodetic surveys
10	AGU proposal for extension of topographic and oceanographic mapping
11	Junction of Belgian and French triangulations
12	Junction of French and Italian triangulations
13	Junction of triangulations of Sardinia and Liguria through Corsica
14	Junction of the Arc of Cape to Cairo to European triangulations through the African coasts in Mediterranean sea
15	Arc of meridian from arctic glacial ocean to Mediterranean sea, extended to Africa
16	Junction of Spanish and French triangulations in Morocco
17	Arc of meridian in Siam and neighbouring countries
18	Longitudes

Table 3 Evolution of IAG structure (1917–1959)

Period	Structures
1922	Reports
1924	Commissions
1951	Sections
1954	Study groups
1954	Permanent commissions

Fig. 5 *Left*: le general Georges Perrier, IAG General Secretary (1919-1946) and *Right*: Pierre Tardi, IAG General Secretary (1946–1960)

D. Lambert (USA) as President (Fig. 2) and Pierre Tardi (France) as General Secretary, after the death of Georges Perrier (1872-1946) (Fig. 1). Statutes and by-laws of the IAG were also changed and maintained as parallel and compatible as possible from those of IUGG. The name of the IAG Secretariat was also changed to the more recent terminology, as Central Bureau.

The IAG assembly held in Brussels in 1951 was the place where several important events occurred for IAG: the election of a new president C.F. Baeschlin (Switzerland) (Fig. 2), the adoption of new IAG by-laws, the adoption of a new structure in sessions and commissions. The sections covering geodesy were defined as follows: (1) Triangulation, (2) Precise leveling, (3) Geodetic astronomy, (4) Gravity, (5) Geoid.

During the next assembly in Rome in 1954, James de Graaf Hunter (UK) was elected as new president, and the organization was modified by replacing the old commissions by two new types of structures: study groups and permanent commissions (Fig. 3).

The following permanent commissions were therefore created during the Rome meeting: the International gravity commission, the European triangulations (RETRIG), later leading to the EUREF Commission (Bruyninx et al. 2012), the European levelling, the geodetic bibliography, the International world longitude geodetic commission.

As presented in Table 3, the organization of the IAG has regularly changed with time, defining new types of structures in size an in duration.

3 IAG Central Bureau in Paris (1917–1995)

After the first period of the history of IAG (Torge in press), during which the Central Bureau was established in Potsdam (Germany), a new location of the bureau was selected during the World War I in Paris (France) by Georges Perrier. The national mapping organization of France, initially *Service Géographique de l'Armée* (Military Geographic Division), later transformed during World War II into a civilian organization, *Institut Géographique National* (IGN), provided permanently the necessary resources (office and human resources) up to the end in 1995 at the General Assembly of Boulder (Figs. 5 and 6).

The list of French officers who worked in this central bureau is given in Table 4.

Fig. 6 *Left*: Jean-Jacques Levallois, IAG General Secretary (1965-1975) and *Right*: Michel Louis, IAG General Secretary (1975–1991)

Table 4 IAG central bureau organization (1919–1995)

Period	General Secretary	Assistant Secretary
1919–1946	Georges Perrier	N/A
1946–1960	Pierre Tardi	N/A
1961–1975	Jean-Jacques Levallois	Michel Louis
1975–1991	Michel Louis	Claude Boucher
1991–1995	Claude Boucher	Pascal Willis

The archives and the library of the Central Bureau remain archived in France, even after its relocation in Copenhagen, after the election of Christian Tscherning as IAG Secretary General in 1995.

4 IAG Relationship to External Bodies

The development of international organizations and the continuous efforts of IAG to give visibility to geodesy are the guiding forces to the relations of IAG with several external bodies.

First of all, we must mention the direct relations with IUGG since its creation in 1919.

A second important issue was the development of agreements between International Council for Science (ICSU) and UNESCO discussed during the Extraordinary Assembly of IUGG in Cambridge (UK) in 1946. This agreement included a funding plan from UNESCO, which would be dedicated to the emerging IAG services, at that time the International Latitude Service (ILS), the *Bureau International de l'Heure* (International Time Bureau, BIH) and the Isostatic Institute.

Without going into details here, one must also mention the relations with other ICSU unions, such as the International Astronomical Unions (IAU) or the International Geographical Union (IGU).

5 The Birth of IAG Services

This period was also the time when service activities started to develop. Various field of geodesy require high quality and permanent observing systems (data collection, processing, archiving and worldwide dissemination). This activity is done primarily for scientific research, but also for technological and societal uses. A more detailed study on these aspects can be found in Mueller (1990) and Mueller (1992).

In particular, the measurements require international cooperation either for establishing global observing networks or for specifying methods for in situ measurements.

The first service to be developed by the IAG was the International Latitude Service (ILS). Its activity even continued during World War I, under the supervision of the reduced IAG. ILS was formally reincorporated within the new IAG organization in 1922. ILS was then relocated in Misuzawa (Japan) with H. Kimura as Director.

The next created service was the Bureau International de l'Heure (BIH). The decision was taken in 1912, but its formal creation was only done in 1919, just after the end of World War I. Since the beginning, the BIH was hosted by the Paris Observatory (France). See Guinot 2000.

The Isostatic Institute of Helsinki (Finland) was then created.

The *Bureau Gravimétrique International* (International Gravity Bureau, BGI) was created in Paris in 1951 with the R.P. Lejay as first director.

Finally, the International Center for Earth Tide (ICET) was created in Brussels (Belgium) in 1958, with Prof Paul Melchior as first director.

These services can be considered as the predecessors of a multitude of future IAG Services, now mostly based on satellite data, and providing the necessary tools to build the vision of the Global Geodetic Observing System (GGOS, Plag and Pearlman 2009), previously called Integrated Global Geodetic Observing System (IGGOS, Rummel et al. 2002).

References

Adam J (2008) The international association of geodesy. Update of the history of the international association of geodesy. J Geod 82(11):662–674

Angus-Leppan PV (1984) A note on the history of the international association of geodesy. The geodesist's handbook 1984. Bull Geod 58(3):224–229

Beutler G, Drewes H, Verdun A (2004) The new structure of the international association of geodesy (IAG) viewed from the perspective of history. The geodesist's handbook 2004. J Geod 77(10-11):566–575

Bruyninx C, Habrich H, Soehne W, Kenyeres A, Stangl G, Volksen C (2012) Enhancement of the EUREF permanent network services and products. IAG Symp 136:27–34

De Martonne E (1946) Le Général Georges Perrier (1872–1946). Ann Geogr 55(299):161–163
Guinot B (2000) History of the Bureau International de l'Heure. In: Dick S, McCarthy D, Luzum B (eds) Polar motion: historical and scientific problems. ASP Conf Series 208
Levallois JJ (1980) The history of the international association of geodesy. The geodesist's handbook 1980. Bull Geod 54(3):249–313
Levallois JJ (1988) Mesurer la Terre. Trois cent ans de géodésie française, AFT, Paris (in French)
Louis M (1992) History of the international association of geodesy. The geodesist's handbook 1992. Bull Géod 66(2):79–81
Mueller II (1990) 125 years of international cooperation in geodesy. IAG Symp 102:421–432
Mueller II (1992) The role of the international association of geodesy in establishing user services. IAG Symp 112(3-4)
Perrier G (1939) Petit Histoire de la Géodésie: Comment l'homme a mesuré et pesé la terre. Alcan, Presses Universitaires de France, Paris (in French)
Plag HP, Pearlman M (2009) Global geodetic observing system, meeting the requirements of a global society on a changing planet in 2020. Springer, Berlin
Rummel R, Drewes H, Beutler G (2002) Integrated global geodetic observing system, a candidate IAG project. IAG Symp 125:609–614
Torge W (1996) The international association of geodesy (IAG) – more than 130 years of international cooperation. The geodesist's handbook 1996. J Geod 70(12):840–845
Torge W (2005) The international association of geodesy 1862 to 1922: from a regional project to an international organization. J Geod 78(9):558–568
Torge W. From a regional project to an international organization: the "Baeyer-Helmert-Era" of the International Association of Geodesy 1862–1916, IAG Symp, 143, same issue, in press
Whitten CH (1988) History of the international association of geodesy. The geodesist's handbook 1988. Bull Geod 62(3):197–206

Part II

Definition, Implementation and Scientific Applications of Reference Frames

Epoch Reference Frames as Short-Term Realizations of the ITRS

Datum Stability Versus Sampling

Mathis Bloßfeld, Manuela Seitz, and Detlef Angermann

Abstract

The IAG (International Association of Geodesy) and the IERS (International Earth Rotation and Reference Systems Service) Joint Working Group (JWG) on "Modeling environmental loading effects for reference frame realizations" currently investigates the effect of correcting station positions for non-linear loading displacements on the realization of the International Terrestrial Reference System (ITRS). Another IAG/IERS JWG works on strategies for the frequent realization of single-technique and combined short-term reference frames, which are called epoch reference frames (ERFs). Both approaches are able to resolve the lack of parametrization which occurs when only taking linear velocities of geodetic observation sites into account (conventional parametrization). ERFs can account for any non-linear station motion (periodic signals, abrupt position changes, non-linear regional deformations, instrumental-related motions, etc.) on a regional as well as on a global basis.

In this study, combined ERFs using the geodetic space techniques GPS, VLBI, SLR with different temporal resolutions (7-, 14- and 28-day) are compared to conventional multi-year/long-term realizations of the ITRS w.r.t. the datum stability and the ability to sample non-linear station motions. The 7-/14-day ERFs are able to monitor short-term station motions but the realization of the datum is not as stable as for the long-term reference frames. The 28-day ERFs have a more stable datum but are only able to monitor very slow long-term motions such as post-seismic deformations.

Keywords

Epoch reference frame • ERF • ITRF • MRF • Non-linear station motions

1 Introduction

Terrestrial Reference Frames (TRFs) nowadays are used for a broad variety of applications in geosciences and practice. In the geosciences, a precisely defined TRF is needed, e.g., for quantifying Earth rotation, geocenter motion, Earth gravity field, sea level rise, post-glacial rebound, tectonic motion and crustal deformation, atmospheric and hydrological loading, large scale deformations due to earthquakes and local subsidence. Practical applications are, e.g., surveying, engineering, mapping or geographical information systems (GIS).

The current official TRF realization of the International Earth Rotation and Reference Systems Service (IERS) is the International Terrestrial Reference Frame 2008 (ITRF2008) (Altamimi et al. 2011). It describes regularized station positions X_R which are already corrected for geophysical effects like solid Earth and ocean tides (Petit and Luzum 2010). The ITRF2008 is a secular TRF, where the station positions are parametrized as a constant value X_S at a reference epoch t_0

M. Bloßfeld (✉) • M. Seitz • D. Angermann
Deutsches Geodätisches Forschungsinstitut (DGFI), Munich, Germany
e-mail: mathis.blossfeld@tum.de

© Springer International Publishing Switzerland 2015

C. Rizos, P. Willis (eds.), *IAG 150 Years*, International Association of Geodesy Symposia 143,
DOI 10.1007/1345_2015_91

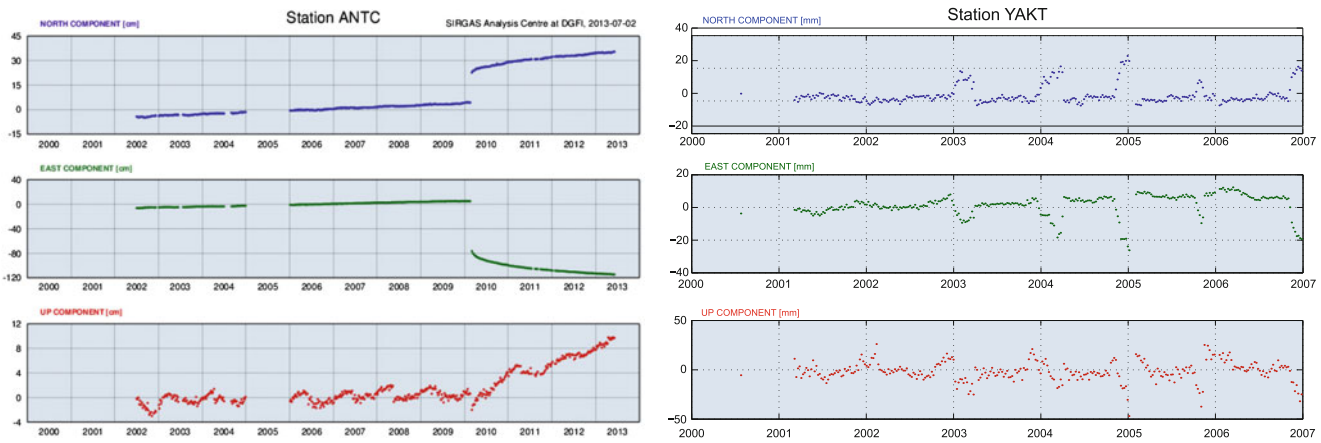

Fig. 1 Absolute position changes in GPS-only weekly coordinate solution series for the stations ANTC (Los Angeles, Chile) and YAKT (Yakutsk, Russia) w.r.t. a mean position. The ANTC time series is taken from the website of SIRGAS (Systema de Referencia Geocéntrico para Las Américas; www.sirgas.org) (Sánchez et al. 2012), the YAKT time series was computed at DGFI

and a constant velocity $\dot{X}$. This kind of TRF is called a multi-year reference frame (MRF) (Bloßfeld et al. 2014).

Since not all geophysical processes are known or can be modeled perfectly, X_R moves not purely linearly over time (Bloßfeld et al. 2014). Examples for un-modeled effects include atmospheric or hydrological loading (Tregoning and van Dam 2005), the elastic response of the lithosphere due to mass variations in a flowing river system (Bevis et al. 2005) or, e.g., anthropogenic periodic effects due to groundwater withdrawal (Bawden et al. 2001). The neglect of these effects cause mis-modeled station positions in the current TRF realizations. To overcome this deficiency, in general three different possibilities exist:

- **Extended parametrization**. In addition to the current linear model, parameters of periodic functions or splines can be estimated to account for the observed seasonal station position variations.
- **Improved geophysical modeling**. Currently un-modeled effects like atmospheric or hydrological loading remain in the position estimates. The IAG (International Association of Geodesy) and IERS Joint Working Group (JWG) 1.2 *"Modeling environmental loading effects for reference frame realizations"* investigates approaches to model these effects and validate the results.
- **Frequent estimation of station positions** $\tilde{X}$. If the regularized station position is estimated frequently (e.g. every 1, 7, 14 or 28 days), the non-linear station motions are approximated automatically (Bloßfeld et al. 2014). This TRF realization is called an epoch reference frame (ERF). The IAG/IERS JWG 1.4 *"Strategies for epoch reference frames"* investigates strategies for the computation of the ERFs.

All these approaches are also investigated by the research group *"Space-time reference systems for monitoring global change and for precise navigation"* (FOR 1503) of the German Research Foundation (DFG) (Nothnagel et al. 2010).

In this paper, we discuss the frequent estimation of station positions. In total, four different time series of ERFs are computed with a different sampling interval. We compare a daily GPS-only solution and 7-, 14- and 28-day combined ERF time series with two consistent GPS-only and combined MRF solutions. All combined TRFs are based on a combination of the geodetic space techniques GPS, SLR and VLBI.

Figure 1 shows two examples of neglected non-linear station motions. Both examples show the absolute position change w.r.t. a mean coordinate. In addition to a linear velocity change following the Maule earthquake in 2010, the station ANTC (Chile) clearly shows a non-linear post-seismic behavior. This effect can last over decades (Freymueller 2010). Furthermore, the height component varies seasonally by about a few mm. In the case of the YAKT (Russia) time series, no clear seasonal behavior show up in any component. The station shows abrupt deflections up to 25 mm from autumn to spring due to the snow coverage during the winter months. If not manually removed, the snow could remain for months on the antenna (IGSSTATION email 365). This effect cannot be handled in global or regional models.

2 Epoch Reference Frames

This section describes the computation algorithm and the three different ERF solutions used for the analysis in Sect. 3. A much more detailed description of the used data, the datum realization, the LT selection and the processing strategy of the ERFs is given in Bloßfeld et al. (2014).

2.1 Computation Algorithm

The DGFI computation algorithm for global TRF solutions is based on the combination of different techniques at the level of normal equations (NEQs) (Bloßfeld et al. 2014; Seitz et al.

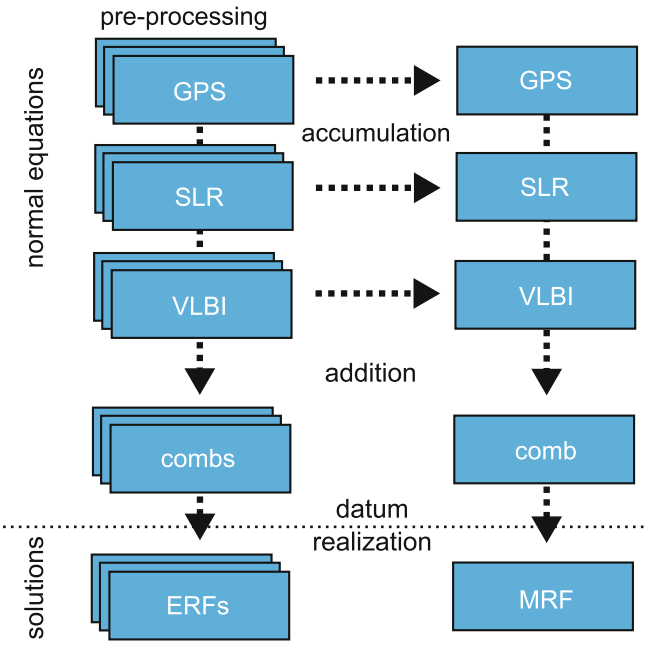

Fig. 2 Algorithm for computing global TRF solutions from a combination of GPS, SLR and VLBI at the normal equation level at DGFI

2012). A schematic overview of the computation algorithm is shown in Fig. 2. In the pre-processing, the input NEQs are solved and the time series of station coordinates are analyzed w.r.t. outliers and discontinuities. For the MRF computation, the pre-processed NEQs are accumulated per technique and station velocities are introduced. Then, the technique-specific NEQs are summed up by applying weighting factors of 1.0 for SLR and VLBI and 0.23 for GPS (due to corrupted stochastic model Bloßfeld et al. 2014), local ties (LTs) are introduced as pseudo observations and the geodetic datum is realized. Thereby, the origin is defined by SLR, the orientation is realized via a No-Net-Rotation (NNR) condition over a subnet of globally distributed GPS stations and the scale is a weighted mean scale of SLR and VLBI. The ERFs are based on identical NEQs. After the pre-processing, the NEQs of all techniques are summed up epoch-wise. Then, the LTs are introduced epoch-wise and the geodetic datum is realized in the same way as for the MRF. The combined MRF contains station coordinates, velocities and EOP. The combined ERFs contain station coordinates and EOP.

2.2 Sampling of Non-linear Station Motions

The sampling interval of the station motions can be chosen freely. Since the standard SLR arc length is 7 days, we chose at least a sampling of 7 days. Additionally, we computed 14- and 28-day ERF solutions in order to investigate the effect of the sampling on the stability and quality of the TRFs. To compute the 14- and 28-day ERFs, the 7-day SLR arcs are combined. Within an ERF solution, the station position $\tilde{X}$ is assumed to be constant. This means, that for a 28-day solution, the position error due to the secular motion of a station is larger than the error for the 7-day solution. An extreme value for this error can be computed, e.g., for the GPS station ISPA (Easter Island) in the ITRF2008 with a linear motion in x-direction of 4.9 mm in 28 days.

3 Comparison of ERF and MRF

All TRFs are validated w.r.t. DTRF2008 (Seitz et al. 2012) using 14-parameter similarity transformations for the MRFs and 7-parameter similarity transformations for the ERFs. The results (Bloßfeld et al. 2014) show that all TRFs are comparable to state-of-the-art TRFs as the ITRF2008 and DTRF2008. To compare the station coordinates and the datum stability of the ERFs, 7-parameter similarity transformations between the combined MRF and the combined ERFs are performed. In this study, we used a subnet of GPS stations (and a subnet of SLR stations) for these transformations since then, the transformation is the most stable (due to globally well distributed stations) and the network effect is limited. Furthermore, the GPS-based transformation allows to analyze the origin and scale transfer from SLR/VLBI to GPS. For all NNR conditions and similarity transformations, the same GPS subnet is used. The recently published paper (Bloßfeld et al. 2014) gives the transformation parameter time series of the weekly combined ERFs w.r.t. the MRF also for other space techniques. Figure 6 in Bloßfeld et al. (2014) shows the time series of the weekly transformation parameters (GPS subnet), the translation and scale parameters for the SLR-only ERFs and the scale time series for the VLBI-only ERFs. The transformation parameters (three translations/rotations, one scale factor) are equal to the common motions of all stations in the subnet (Sect. 3.1) whereas the transformation residuals are equal to individually station motions (Sect. 3.2). The datum stability of the subnets of the combined ERFs depends strongly on the spatial geometry of the technique-specific networks and on the number, quality and spatial distribution of the LTs. If only a few LTs are introduced in the combination, the RMS of a similarity transformation would increase and the network integration would be less stable (Seitz et al. 2012). The quality of the LTs is controlled by a selection process. Thereby, the 3D difference vector between the single-technique solutions is compared to the corresponding LT. If the difference is less than 30 mm, the LT is introduced with a weight of 1.0 mm in the combined NEQ. This selection process was adopted from the MRF computations at DGFI (Seitz et al. 2012; Bloßfeld et al. 2014). In future, this issue will be investigated also for the ERF computations in more detail. The amount of LTs and their global distribution depend indirectly on the length of the

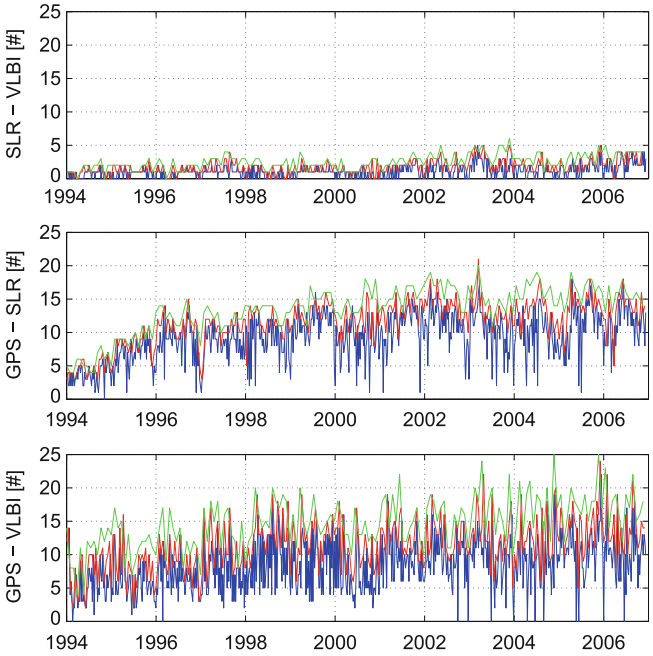

Fig. 3 Number of LTs in the 7- (*blue*), 14- (*red*) and 28-day (*green*) ERF solutions (see also Fig. 3)

Table 1 Mean number of different local ties in the weekly, 14- and 28-day solutions

LT type	7-day	14-day	28-day
SLR-VLBI	1	2	3
GPS-SLR	9	12	14
GPS-VLBI	8	12	15

combination interval. The longer the combination interval is, the more dense is usually the global observing station network. Figure 3 shows the different number of LTs in the ERF solutions, the mean values are summarized in Table 1. For the weekly solutions, the station network is sometimes so sparse that not enough LTs (at least three are needed) between the techniques can be selected. The result is a NEQ which has a rank deficiency. For the 14-day solutions, the situation improves. At least three LTs are available between SLR and GPS and therefore, each NEQ is invertible. The small number of SLR-VLBI LTs can be compensated by the LTs of SLR and VLBI with GPS. This fact emphasizes the importance of GPS in the TRF computation. The most LTs are introduced in the 28-day solutions. Therein, on average three SLR-VLBI, 14 GPS-SLR and 15 GPS-VLBI LTs are introduced in the ERF solutions.

Figure 3 contains no information about the global distribution of the LTs. For example, if three LTs to link two techniques are only available in Europe, the number of LTs is enough to transfer the datum information between the networks but the spatial information is poor. Therefore, the estimated TRF would not have a stable datum and an outlier in the time series might occur.

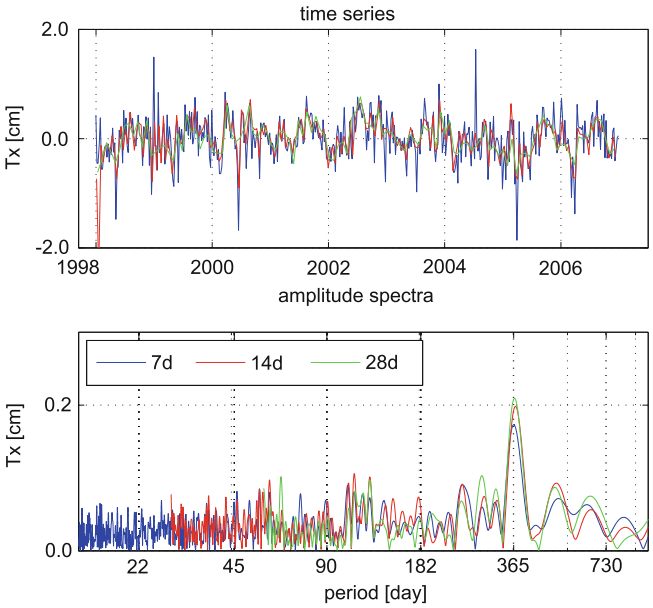

Fig. 4 Time series and spectra of the x-translations between the combined MRF and the time series of combined ERFs for different combination intervals based on a GPS subnet

3.1 Common Motions of Stations

Figure 4 shows the time series and spectra of the translations in x-direction between the combined MRF and the time series of combined ERFs (GPS subnet). Since the other parameters show a similar behavior, their time series and spectra are not shown. The time series shows an annual variation with an amplitude of 1.8 mm which can be identified in the spectra. The variation is caused by the fact that the MRF contains linear motions only, whereas in the ERFs, non-linear variations are allowed. A part of this variation is a common translation of the transformation stations (Bloßfeld et al. 2014). For the annual amplitudes of the weekly SLR-only time series, see Table 7 in Bloßfeld et al. (2014). The spectra in Fig. 4 clearly shows, that signals with frequencies below twice the computation interval cannot be sampled correctly. This means, the 7-, 14- and 28-day ERFs are not able to sample signals below 14, 28 and 56 days. Table 2 summarizes the annual amplitudes and phases of the time series of the translation and scale parameters for the three different combination intervals. The rotation parameters are not shown since the orientation was fixed by an NNR-condition to the a priori network. In the second-right column of Table 2, the scatter (RMS values) of each parameter time series, after the annual signal is removed, are shown. All translations have a significant ($|A| > 3\sigma$) annual variation with an amplitude between 1.7 mm and 2.7 mm. For comparison, the top-right column shows the RMS values for the weekly SLR subnet of the combined ERFs w.r.t. the combined MRF. The RMS values of the VLBI subnet are not shown here since the

Table 2 Annual amplitudes A and phases Φ of the time series of translation and scale parameters between the combined MRF and ERFs for different combination intervals based on a GPS subnet

Parameter	A [mm]	Φ [days]	RMS[a] [mm]	RMS[b] [mm]
Tx (7d)	1.7 ± 0.2	193.4 ± 5.1	3.8	4.9
Tx (14d)	1.8 ± 0.3	211.9 ± 2.3	3.2	3.1
Tx (28d)	1.9 ± 0.2	219.0 ± 0.6	2.3	2.7
Ty (7d)	2.7 ± 0.1	303.7 ± 6.3	3.9	4.2
Ty (14d)	2.6 ± 0.1	304.3 ± 7.2	3.6	2.6
Ty (28d)	2.7 ± 0.0	306.3 ± 5.6	2.5	2.0
Tz (7d)	2.0 ± 0.6	245.9 ± 6.0	8.1	10.0
Tz (14d)	2.2 ± 0.5	245.9 ± 5.2	6.4	7.0
Tz (28d)	2.2 ± 0.4	257.4 ± 7.5	5.6	6.1
Sc (7d)	1.1 ± 0.2	183.3 ± 8.6	3.3	3.9
Sc (14d)	1.0 ± 0.2	188.2 ± 8.5	2.6	2.5
Sc (28d)	1.2 ± 0.1	190.8 ± 4.7	1.9	2.2

In the top-right column, the parameters based on an SLR subnet w.r.t. the combined MRF are shown. A and Φ are defined by $A \sin(2\pi f \cdot (t - 2000.0) + \Phi)$ with t in years and frequency f in cycles/year. The two right columns shows the RMS of time series after an annual signal is removed
Combined ERF: [a]GPS subnet, [b]SLR subnet

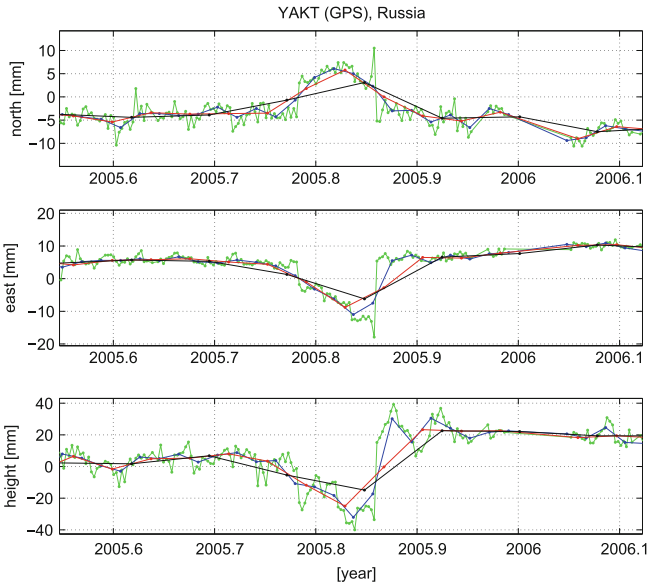

Fig. 5 Daily individual GPS-only (green) time series of the station Yakutsk. In addition, the 7- (*blue*), 14- (*red*) and 28-day (*black*) individual time series of the combined ERFs are shown. A longer time series of weekly GPS-only solutions w.r.t. a mean position is shown in the right panel of Fig. 1

main datum information is transferred from SLR to GPS (for the weekly VLBI-only RMS values, see Bloßfeld et al. 2014). The amplitudes and phases of the 7-, 14- and 28-day solutions for each parameter agree very well (within their standard deviation). With an increase of the combination interval, also the datum stability of the SLR subnet increases. This fact proofs that a more stable datum of the combined ERFs is achieved by a better geometry. As a consequence of the improved network, the number of LTs increases ensuring a more stable datum transfer from SLR to the other networks.

3.2 Individual Motions of Stations

As an example for the individual station motions, Fig. 5 shows the transformation residuals for the GPS station YAKT for four different solutions (daily GPS-only and three combined ERFs). The geodetic datum of the daily GPS-only solution is realized in a different way than the datum of the combined ERFs. Since the major part of the datum differences is expressed by common motions to all stations, the spurious YAKT motions are individual station motions. Therefore, they are comparable to the motions of the combined ERFs and can be seen as a good approximation of the real station motion. By comparing the residuals, we can evaluate the combined ERFs for their ability to sample this motion. The 7-day solution gives the best approximation of the station motion. The 14-day solution already causes errors of e.g. 10 mm in the east and height component at the epoch 2,005.85. The 28-day solution is not able to sample the variations between 2,005.7 and 2,006.0 in any component (error increases to 20 mm). Nevertheless, a big advantage of the 28-day solution are the nearly continuous time series of station positions. If a station does not observe during a week due to e.g. operational issues, it will not be present in the weekly solution. In the 28-day solution, it will not be present only if the station does not observe during four consecutive weeks. The results confirm that the longer the combination interval is, the less accurate is the sampling of short-term motions. In contrast to this, the long-term motions can be sampled very well with all sampling intervals.

4 Conclusions

ERFs are valuable to study the non-linear station motions which are suppressed in the conventional secular TRF. From the results shown in Sect. 3 we can conclude that the larger the sampling interval for the ERFs is, the better is the network geometry and therefore, the more LTs are introduced. These improvements contribute to a more stable realized geodetic datum. However, the shorter the sampling interval for the ERFs is, the better the short-term motions can be sampled. The characteristics of the different TRF realizations are summarized in Table 3 and some examples for suitable applications are given. We can conclude that:

– MRFs (e.g. ITRF2008 Altamimi et al. 2011) are optimal for monitoring long-term changes in the Earth system such as sea level rise or tectonic plate motion.

Table 3 Properties of the different TRF approaches. The lower part gives examples for applications of the TRF realizations

	MRF	ERF
Stability	Long-term	Short-term
Parametrization	$X_S(t_0)$, $\dot{X}$	$\tilde{X}(t_i)$
Estimated positions	Precise (formal errors)	Accurate (geometry)
Position latency after earthquakes	$\geq$ 2.5 years	Few epochs
Non-linear station motions	Suppressed	Frequently sampled
Station network	Dense (VLBI, SLR)	Sparse (VLBI, SLR)
Number of LTs	High	Low
Suitable to monitor e.g.	Long-term changes, sea level rise, plate motions	28d: annual variations, post-seismic deformations 7d/14d: abrupt motions, short-term local environmental effects

– The ERFs (28-day sampling) are able to monitor annual variations and post-seismic deformations. They provide a higher datum stability than the 7- or 14-day ERFs. Their accuracy is nearly consistent over time and they provide continuous time series of station positions for nearly every station. One disadvantage is the assumption of a constant position over 28 days which causes an error due to the neglected secular motion. The maximal error of 3 mm is obtained for the GPS station Easter Island (site velocity in ITRF2008 is ca. 5 mm per 28 days).
– The ERFs (7-/14-day sampling) are able to monitor short-term station variations such as local environmental effects at costs of the datum stability due to the sparse station networks and the low number of local ties per epoch. The sparse networks also cause gaps in some station position time series since not all stations observed every 7/14 days. The lower datum stability is especially a problem in the early 1990s, when the station networks in general have not been homogeneously distributed.

A possibility to solve the datum problems in the short-term ERFs would be a denser network with more co-location sites and more frequently (accurately) measured LTs. Especially VLBI and SLR would benefit from larger networks. To improve SLR, observations to more satellites (only Etalon 1/2 and LAGEOS 1/2 are currently used for TRFs Bloßfeld et al. 2013) might also help.

Acknowledgements The work contributes to the research group 'Space-Time Reference Systems for Monitoring Global Change and for Precise Navigation' (FOR 1503) Nothnagel et al. (2010) of the German Research Foundation. The authors want to thank the three reviewers and the editor for their suggestions.

References

Altamimi Z, Collilieux X, Métivier L (2011) ITRF2008: an improved solution of the international terrestrial reference frame. J Geod 85(8):457–473. doi:10.1007/s00190-011-0444-4

Bawden GW, Thatcher W, Stein RS, Hudnut KW, Peltzer G (2001) Tectonic contraction across Los Angeles after removal of groundwater pumping effects. Lett Nat 412:812–815. doi:10.1038/35090558

Bevis M, Alsdorf D, Kendrick E, Fortes LP, Forsberg B, Smalley R. Jr, Becker J (2005) Seasonal fluctuations in the mass of the Amazon river system and earth's elastic response. Geophys Res Lett 32:(L16308). doi:10.1029/2005GL023491

Bloßfeld M, Seitz M, Angermann D (2014) Non-linear station motions in epoch and multi-year reference frames. J Geod 88(1):45–63. doi:10.1007/s00190-013-0668-6

Bloßfeld M, Štefka V, Müller H, Gerstl M (2013) Satellite Laser Ranging - A tool to realize GGOS? in this issue

Freymueller JT (2010) Active tectonics of plate boundary zones and the continuity of plate boundary deformation from Asia to North America. Curr Sci 99(12):1719–1732. ISSN: 0011-3891

Nothnagel A, Angermann D, Börger K, Dietrich R, Drewes H, Görres B, Hugentobler U, Ihde J, Müller J, Oberst J, Pätzold M, Richter B, Rothacher M, Schreiber U, Schuh H, Soffel M (2010) Space-time reference systems for monitoring global change and for precise navigation. Mitteilungen des Bundesamtes für Kartographie und Geodäsie, Band 44, Verlag des Bundesamtes für Kartographie und Geodäsie, ISBN: 978-3-89888-920-9

Petit G, Luzum B (2010) IERS Conventions(2010). IERS Technical Note No. 36, Verlag des Bundesamtes für Kartographie und Geodäsie, ISBN: 978-3-89888-989-6

Sánchez L, Seemüller W, Seitz M (2012) Combination of the weekly solutions delivered by the SIRGAS processing centres for the SIRGAS-CON reference frame. In: Kenyon S, Pacino MC, Marti U (eds) Geodesy for planet earth. IAG symposia, vol 136, pp 845–851. Springer, Berlin. doi:10.1007/978-3-642-20338-1_106

Seitz M, Angermann D, Bloßfeld M, Drewes H, Gerstl M (2012) The DGFI Realization of ITRS: DTRF2008. J Geod 86(12):1097–1123. doi:10.1007/s00190-012-0567-2

Tregoning P, van Dam T (2005) Effects of atmospheric pressure loading and seven-parameter transformations on estimates of geocenter motion and station heights from space geodetic observations. J Geophys Res 110:(B3). doi:10.1029/2004JB003334

Status of the IGS-TIGA Tide Gauge Data Reprocessing at GFZ

Zhiguo Deng, Gerd Gendt, and Tilo Schöne

Abstract

The International GNSS Service (IGS) Tide Gauge Benchmark Monitoring Working Group (TIGA-WG) is responsible for analyzing GNSS data from stations at or near tide gauges (TG) on a preferably continuous basis and to provide information specifically for the vertical rates. The position and vertical velocity results of the stations can be applied in several geodetic and geophysical applications, such as global and regional sea-level change, calibration of satellite altimeters and the unification of height systems. As one of the TIGA Analysis Centers the German Research Centre for Geosciences (GFZ) is contributing to the IGS TIGA Reprocessing Campaign (TIGA REPRO2). The solutions of the GFZ TIGA REPRO2 will also contribute to IGS second Data Reprocessing Campaign (IGS REPRO2) with the GFZ IGS REPRO2 solution. Following the first IGS reprocessing finished in 2010 some improvements were implemented into the latest GFZ software version EPOS.P8: reference frame IGb08 based on ITRF2008, antenna calibration igs08.atx, geopotential model (EGM2008), higher-order ionospheric effects, new a priori meteorological model (GPT2), VMF mapping function, and other minor improvements. GNSS data of the globally distributed tracking network of 794 stations for the time span from 1994 until end of 2012 are used for the GFZ TIGA REPRO2. To handle such large networks a new processing strategy is developed and described in detail. In the GFZ TIGA REPRO2 the GNSS@TG data are processed in precise point positioning (PPP) mode to clean data using the GFZ IGS REPRO2 orbit and clock products. To validate the quality of the PPP coordinate results the rates of 80 GNSS@TG station vertical movement are estimated from the PPP results using Maximum Likelihood Estimation (MLE) method. The rates are compared with the solution of University of La Rochelle Consortium (ULR) (named ULR5). 56 of the 80 stations have a difference of the vertical velocities below 1 mm/year. The error bars of PPP rates are significantly larger than those of ULR5, which indicates large time correlated noise in the PPP solutions.

Keywords

PPP • Reprocessing • TIGA

Z. Deng (✉) • T. Schöne
Section 1.2: Global Geomonitoring and Gravity Field, Helmholtz Centre Potsdam, GFZ German Research Centre for Geosciences, Telegrafenberg, 14473 Potsdam, Germany
e-mail: deng@gfz-potsdam.de; tschoene@gfz-potsdam.de

G. Gendt
Section 1.1: GPS/Galileo Earth Observation, Helmholtz Centre Potsdam, GFZ German Research Centre for Geosciences, Telegrafenberg, 14473 Potsdam, Germany
e-mail: gendt@gfz-potsdam.de

© Springer International Publishing Switzerland 2015

C. Rizos, P. Willis (eds.), *IAG 150 Years*, International Association of Geodesy Symposia 143,
DOI 10.1007/1345_2015_156

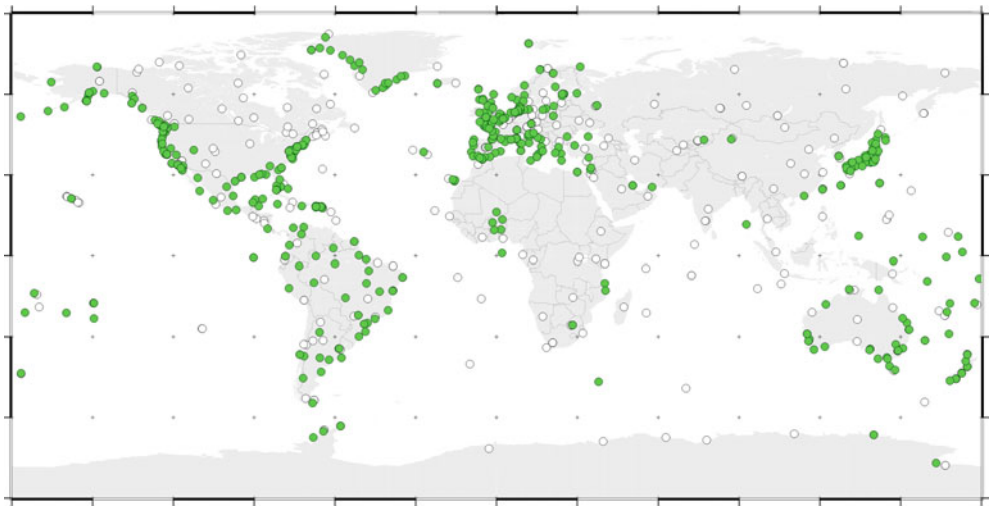

Fig. 1 Global distribution of the TIGA reprocessed GNSS@TG stations for GFZ IGS REPRO2 (*dots*, 307 stations) and TIGA-only (*green dots*, 487 stations)

1 Introduction

To analyse tide gauge measurements for the purpose of global long-term sea level change research a well-defined reference frame is required by the oceanographic community. To create such a reference frame the data from a global GNSS network located at or near tide gauges are used. The required accuracy of the station coordinate solutions is about 5–10 mm and <1 mm/year for horizontal positions and vertical motions, respectively (Schöne et al. 2009). Several TIGA Analysis Centers (TACs) around the world have been involved in the TIGA Working Group. Recent studies have demonstrated the improvement of the sea level rate consistency by using GPS solutions (Wöppelmann and Marcos 2012; Rudenko et al. 2013). As one of the TACs GFZ is processing data from 794 globally distributed GNSS stations for the time span from 2 January 1994 until 29 December 2012. The up-to-date models and processing strategies are applied for the reprocessing. This paper describes the strategy and the stream lining of the TIGA data processing at GFZ. The GFZ TIGA REPRO2 uses the same software and strategy as the GFZ IGS REPRO2. The quality of the GFZ IGS REPRO2 satellite orbits will be assessed by comparison with the first IGS reprocessing campaign orbits and the IGS operational orbits. In addition the IGS REPRO2 orbit overlaps are checked.

The large number of GNSS@TG stations significantly increases the computational burden of a network solution. Currently, to reduce the time of a network processing, the GNSS@TG stations have to be divided into several clusters. As an alternative the PPP mode can be used to overcome the computational burden. The PPP allows analyzing data from hundreds or thousands of sites in parallel, with results of comparable quality to the simultaneous analysis of all data. In order to evaluate the performance of the PPP results the quality of the TIGA PPP solutions using GFZ IGS REPRO2 products are compared with the ULR5 solutions (Santamaría-Gómez et al. 2012a).

2 GPS Network and Processing Scheme

For the GFZ TIGA REPRO2 GPS data of a global network with 794 stations covering the time span 2 January 1994 to 29 December 2012 (the GPS weeks 730 to 1,720) were processed. The global network of GPS stations used for the reprocessing is given in Fig. 1. For the GFZ TIGA REPRO2 the software package EPOS.P8 developed at GFZ is used. The data processing is performed on the local Linux cluster with a maximum number of 30 computers/servers. With EPOS.P8 a high degree of automatization of the individual processing jobs can be achieved.

The number of reprocessed GPS satellites is given in Fig. 2, it increases from 24 in the beginning years to 32 in 2011. Since the processed number of GNSS@TG stations can reach up to 560 daily (Fig. 2) and EPOS.P8 can process up to 250 stations in a single job, the GNSS@TG stations must be split into several sub-networks. One of the sub-networks is the GFZ IGS REPRO2 network, which has a processing scheme similar to GFZ routine analysis. A flow diagram of the GFZ TIGA REPRO2 is shown in Fig. 3. The GFZ TIGA REPRO2 is done in two steps, first precise satellite clocks, orbits and 1-day normal equations are generated from the GFZ IGS REPRO2 using the IGS stations. In the second step the GNSS@TG stations, which are not already included in the GFZ IGS REPRO2, named TIGA-only stations, are processed; the GFZ IGS REPRO2 satellite

clock and orbit products are introduced and fixed to clean the observation data in PPP mode. Due to the large number of the TIGA-only stations up to 2 sub-networks are build and processed in network mode. The final solution is the result of a Normal Equation (NEQ) stacking of all sub-networks. For connecting the sub-networks 30 globally distributed GFZ IGS REPRO2 stations are selected and processed together with the TIGA-only sub-networks. The connecting stations are different for each sub-network and are selected automatically from the GFZ IGS REPRO2 stations for each day according to their distribution and post fit. If the number of GFZ TIGA REPRO2 stations is smaller than 250, the TIGA-only stations will be processed with the GFZ IGS REPRO2 stations together as final solution, and no sub-network is needed.

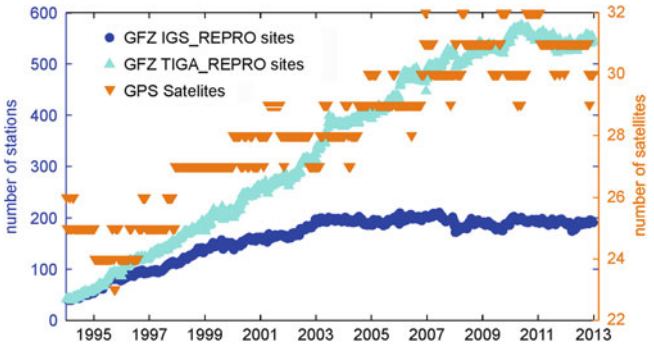

Fig. 2 Weekly number of stations and satellites included in the GFZ IGS/TIGA REPRO2. The GFZ TIGA REPRO2 is based on the same set of GFZ IGS stations, so that the difference to the GFZ IGS REPRO2 shows the number of processed TIGA-only stations

Since the initial coordinates of most TIGA-only stations have insufficient accuracy (>2 cm) for the data analysis, the estimated station coordinates from the PPP data clean step are used to generated new initial coordinates and velocities. The used models and algorithms in GFZ IGS REPRO2 are listed below.

Observation data:

- Ionosphere-free linear combination, undifferenced carrier phase and pseudo-range observables
- Sampling rate: 5 min; elevation cut-off angle: 7°
- Elevation depended weighting: 1/2sin(e) for e < 30°

Measurement models:

- Satellite and ground antenna phase center offsets (PCOs) and phase center variations (PCVs) from igs08_1730.ATX file
- Ocean tide loading: FES2004 (CoM corr. applied)
- Tidal effects: IERS Conventions 2010 (Petit and Luzum 2010)
- Loading due to S1 and S2 atmosphere pressure tides
- ARP eccentricities from site-logs/igs.snx
- Troposphere: a priori zenith delay from Saastamoinen, Global Pressure and Temperature model (GPT2) and Vienna Mapping Function (VMF) (Boehm et al. 2008)

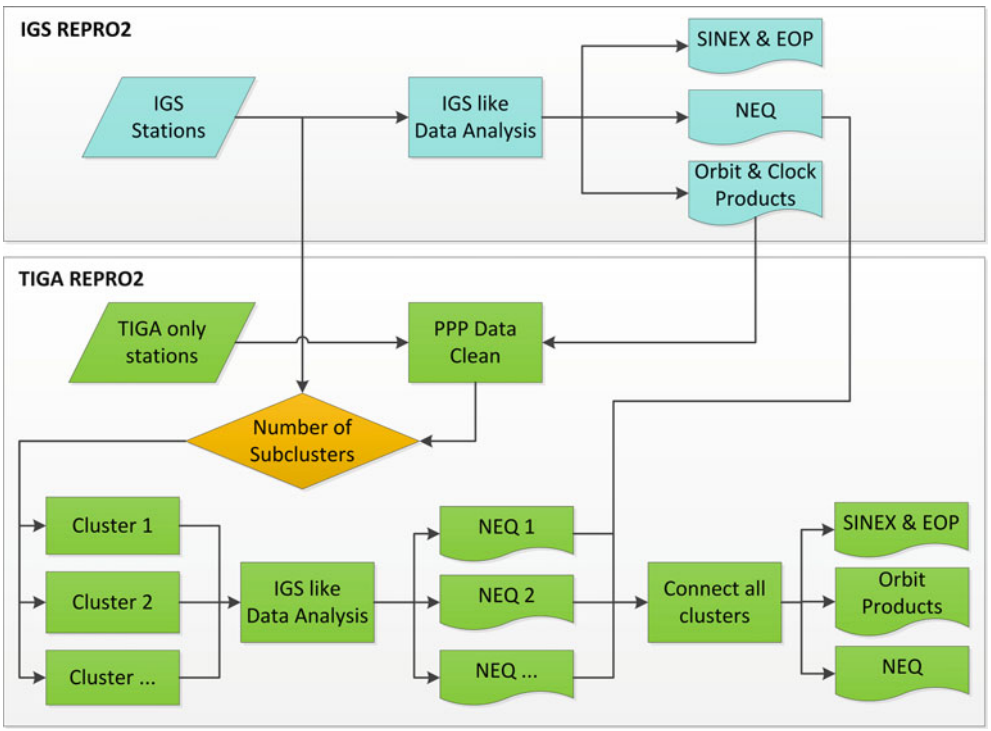

Fig. 3 The GFZ IGS REPRO2 scheme is similar to GFZ routine analysis processing scheme. Its orbit and clock products are introduced and fixed for GFZ TIGA REPRO2 to clean the data. The final solution is the result of a NEQ stacking (clusters + GFZ IGS REPRO2)

– Ionosphere: include second order ionosphere correction (Petit and Luzum 2010)

Reference frames:

– Terrestrial: IGS realization of ITRF2008 (IGb08)
– IAU 2000A Precision-Nutation model
– Bulletin A EOPs as a priori values

Orbit models:

– Gravity field: EGM2008 (12×12) with temporal variations
– Geopotential ocean tide model: FES2004 (Petit and Luzum 2010)
– Third-Body: JPL planetary ephemeris DE405
– Solar radiation pressure: a priori none
– Albedo and antenna thrust acceleration: model from Rodriguez-Solano et al. (2012)
– Earth shadow model: penumbra
– Attitude model: Bar-Sever, based on nom. yaw-rates (Bar-Sever 1996)
– Relativistic effects: Schwarzschild and Lense-Thirring dynamical correction and gravitational time delay

Estimated parameters (Least Square Adj.):

– Station coordinates
– Clocks of satellites and receivers per epoch
– Orbits (position, velocity, solar radiation pressure, stochastic impulses, y-bias, yaw-rate) per day
– Troposphere: ZTD per hour, gradients per 24 h
– Ambiguities: fixed
– ERPs: pole coordinates and rates, LOD per day

3 Orbit Results and Comparisons

In the GFZ TIGA REPRO2 the precise satellite clocks and orbits are generated in the GFZ IGS REPRO2 firstly. Since the IGS REPRO2 combination solutions are not available, the quality of the reprocessed GPS satellite orbits is assessed by comparison with the first reprocessing campaign (REPRO1) orbits (Uhlemann et al. 2010) and IGS Final orbits by 7-parameter similarity transformations. The mean RMS of the transformed reprocessed orbits w.r.t. the REPRO1/IGS orbits is shown in Fig. 4. The RMS decreases rapidly from about 15 cm in 1994 to about 2 cm in the mid of 1995. To quantify the internal consistency of the GPS satellite orbits, the overlap of 2 consecutive 1-day orbit arcs was checked. The daily mean RMS of the overlaps serve as quality indicator and are shown in Fig. 5. In the first year the RMS is on a level of 15–50 cm and falls later below 10 cm.

4 PPP Results

Due to the steadily increasing number of GNSS@TG stations the computational burden of the network solution is becoming larger. In the GFZ TIGA REPRO2 to reduce the computational burden of the data processing in the network mode and to overcome the computer memory limitation, the processed stations have to be divided into clusters. By stacking the NEQs from all clusters the final TIGA solution is generated. The PPP mode provides an alternative solution. Using precise satellite orbit and clock products the precise station coordinates can be estimated in PPP mode for a single station. So a large number of stations can be processed in parallel. The GFZ IGS REPRO2 orbit and clock products are in reference frame IGb08 (aligned to ITRF2008) (Rebischung 2012). With the fixed SP3 products the TIGA PPP are applied. It guarantees that the estimated PPP coordinates are in the same reference frame as the SP3. In order to evaluate the performance of the TIGA PPP results the quality of the vertical velocities from 80 stations are compared with the ULR5 solutions (Santamaría-Gómez et al. 2012b). All the 80 stations have time series longer than 2.5 year and no obvious trend changes. The PPP mode estimated Cartesian station coordinates are converted to longitude, latitude and height using the WGS84 ellipsoid. The vertical linear trends and the seasonal component are estimated by fitting the height time series using the CATS software, which is provided by Williams (2008). In the CATS software the MLE method (Zhang et al. 1997; Mao et al. 1999) is applied for the coordinate time-series analysis. The PPP coordinates with residuals larger than 3 times the standard error are treated as outliers and removed in the linear regression. The known offsets are estimated together with other parameters e.g. trend, bias and seasonal signals. In Table 1 the vertical trends of the 80 stations for PPP and ULR5 are given. For comparison the differences of the trends are shown in the table. For 56 of the 80 common stations the difference of the vertical velocities are below 1 mm/year. The stations with larger differences, as WGTN and LYTT, will be studied by comparison with the GFZ TIGA REPRO2 network solution in the further study. The error of PPP vertical velocities are significant larger than those of ULR5, which is possibly caused by large time correlated noise in the PPP solutions. This good agreement indicates that the trend from the PPP mode has almost the same high-quality as the network solution. Already the height time series from the PPP solutions can be used to correct tide gauge data for estimation of regional and global sea level changes.

5 Summary

As one of the TIGA ACs GFZ is contributing to the IGS TIGA Reprocessing Campaign. The globally distributed GPS tracking network of 794 stations for the time span from 1994 until end of 2012 is reprocessed with up-to-date models and processing strategies. The precise initial

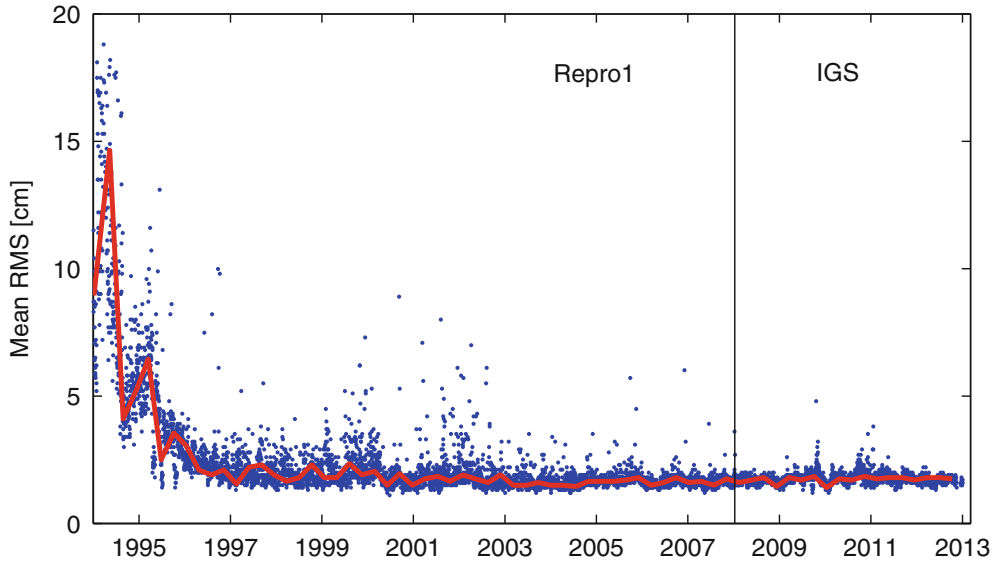

Fig. 4 Mean RMS of transformed GFZ IGS REPRO2 orbits w.r.t. the REPRO1 (1994.0–2008.0) and the IGS Final orbits (2008.0–2013.0). The *solid line* represents a 100-day median

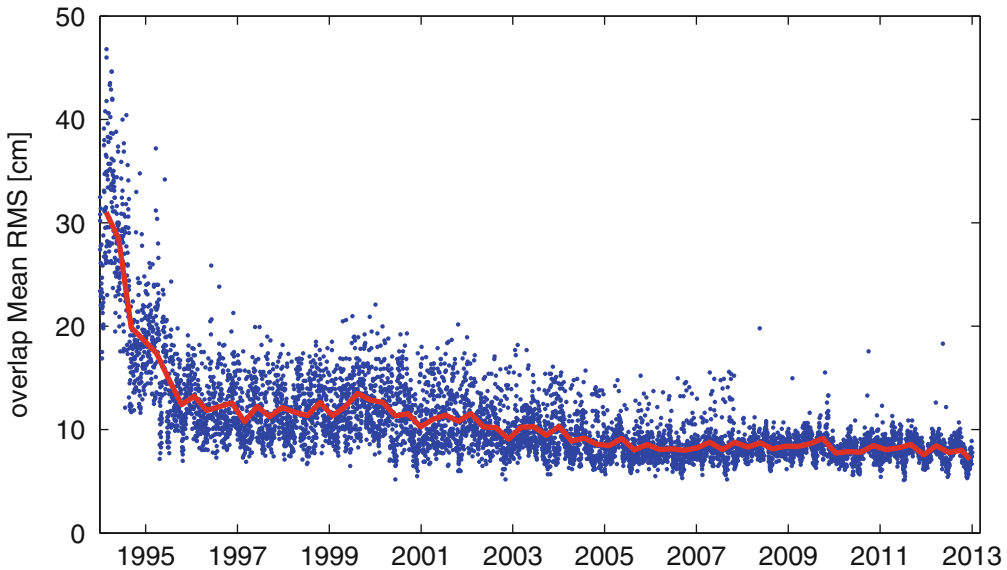

Fig. 5 Mean RMS values of GFZ IGS REPRO2 orbit overlaps (4 h).The *solid line* represents a 100-day median

coordinates and velocities (in ITRF2008 coordinate frame) of the TIGA-only stations are estimated in PPP mode with the orbit and clock products from the GFZ IGS REPRO2. The quality of the GFZ IGS REPRO2 satellite orbits are assessed by checking orbit overlaps as well as comparison with the IGS REPRO1/Final orbits. The daily mean RMS of the overlaps is on a level of 15–50 cm in the first years and falls below 10 cm. In the orbit comparisons the mean RMS of the transformed reprocessed orbits w.r.t. the IGS REPRO1/Final orbits decreases rapidly from about 15 cm in 1994 to about 2 cm in the mid of 1995. Using the GFZ IGS REPRO2 orbit and clock products about 500 TIGA-only stations are processed in PPP mode. The vertical trends of 80 GNSS@TG stations are calculated from the PPP estimated coordinates and compared with the ULR5 solution. The PPP vertical trends of 70% of the stations have a difference smaller than 1 mm/year compared to ULR5 network solution. The results verify that the trend estimated from the PPP results has almost the same high-quality as from a network solution. For the TIGA data processing, the PPP can be used to reduce computational burden. In the next step the TIGA-only stations will be processed in the network mode. Together with the solution of GFZ IGS REPRO2 the GFZ TIGA final network products will be generated.

Table 1 Linear height trends at 80 GNSS@TG stations

		Time span (year)			PPP	ULR	
Site	DOMES	Begin	End	Data	Trend (mm/year)		Diff.
0194	21752S001	1999.175	2012.994	98.5	2.57±0.94	3.65±0.28	−1.08
ABER	13231M001	2005.917	2012.994	70.2	0.37±0.98	0.87±0.11	−0.50
ACOR	13434M001	2003.887	2012.994	95.8	−2.89±0.77	−2.38±0.14	−0.51
ADE1	50109S001	2003.002	2011.556	85.1	−1.42±0.95	−0.95±0.28	−0.47
AJAC	10077M005	2000.060	2009.794	82.8	−0.24±0.78	0.28±0.14	−0.52
ALAC	13433M001	1999.591	2012.994	95.8	2.22±0.66	0.39±0.14	1.83
ALEX	30102M001	2001.882	2008.081	87.1	0.72±1.76	0.05±0.28	0.67
ALME	13437M001	2007.120	2012.994	99.0	−1.62±1.40	1.24±0.19	−2.86
ANDE	19966M001	2007.498	2012.000	79.3	2.23±1.28	1.56±0.19	0.67
ANP1	49908S101	2001.468	2007.745	93.0	−0.65±1.41	−1.49±0.40	0.84
ANP5	99992M001	2007.750	2012.994	84.3	−1.83±1.42	−1.49±0.37	−0.34
ARP3	49878S003	1996.030	2006.386	79.0	−1.81±0.96	−1.28±0.37	−0.53
BHR1	99928M001	2003.002	2009.646	93.9	−0.32±1.27	0.06±0.28	−0.38
BREW	40473M001	2001.876	2012.994	98.7	−0.80±0.55	−0.63±0.26	−0.17
CAGL	12725M003	2004.183	2012.994	98.1	0.15±0.93	−0.44±0.14	0.59
CAGZ	12725M004	2002.424	2012.994	93.5	−0.27±0.83	−0.45±0.19	0.18
CASC	13909S001	1998.331	2012.994	92.8	−0.53±0.50	0.36±0.28	−0.89
CHTI	50242M001	2007.945	2012.994	83.3	−3.16±1.55	−2.17±0.52	−0.99
COYQ	41715S001	2009.038	2012.248	79.8	−2.60±3.15	−1.05±0.35	−1.55
CRAO	12337M002	2004.647	2012.994	89.2	1.38±1.26	0.41±0.26	0.97
DJOU	32708M001	2005.646	2011.161	81.9	−0.24±1.78	−1.99±0.42	1.75
DUNT	50212S001	2004.125	2011.605	68.9	−1.59±1.06	−0.94±0.20	−0.65
ESBH	10115M002	2004.868	2012.994	89.2	0.47±0.81	−1.17±0.35	1.64
FTS1	49893S001	1999.005	2008.232	97.9	2.91±0.71	2.13±0.34	0.78
GAO1	33503M001	2005.660	2010.246	74.5	0.54±1.73	−0.61±0.69	1.15
GCGT	80401M001	2005.438	2011.898	78.7	−0.65±2.03	−2.37±0.21	1.72
GESR	10116M002	2004.822	2012.994	89.9	0.35±0.68	0.76±0.31	−0.41
GLPT	49467M001	1999.030	2006.567	95.0	−3.03±1.26	−2.29±0.78	−0.74
GRIS	99998M001	2005.682	2012.994	75.0	−5.70±1.35	−8.00±0.19	2.30
HELG	14264M001	1999.857	2012.994	98.4	−0.35±0.57	0.50±0.19	−0.85
HIRS	10106M002	2004.863	2012.994	90.1	2.25±0.65	2.80±0.21	−0.55
HUEL	13451M001	2007.539	2012.994	99.2	−1.27±1.21	−1.86±0.53	0.59
IBIZ	13454S001	2004.786	2012.994	69.2	−1.54±0.85	−1.12±0.20	−0.42
IGM1	41505M003	2003.961	2012.994	87.4	0.28±1.32	−0.31±0.56	0.59
KELS	49662M001	2002.756	2007.693	97.5	−1.88±1.33	−0.89±0.26	−0.99
KGNI	21704S005	2001.758	2011.098	90.4	0.53±1.19	0.91±0.22	−0.38
KULU	99999M001	2003.947	2012.994	80.2	9.22±0.68	6.60±0.43	2.62
KYW1	49852S001	1997.002	2007.778	85.4	−0.13±1.16	−0.63±0.40	0.50
LAGO	13903M001	2004.674	2012.994	96.8	−1.35±0.76	−0.44±0.25	−0.91
LYTT	50214S001	2003.904	2009.586	85.4	−7.86±1.48	−1.53±0.20	−6.33
MAT1	12734M009	2001.378	2012.994	96.0	1.26±0.70	0.85±0.23	0.41
MDSI	99910M001	2007.641	2012.923	75.3	−2.11±1.54	−2.81±0.28	0.70
MOB1	49863S001	1996.275	2009.939	84.4	−2.53±0.75	−3.05±0.39	0.52
MOBS	50182M001	2006.131	2012.994	96.4	−1.35±0.94	−0.99±0.18	−0.36
NEAH	40139M001	2004.065	2012.994	97.2	1.52±0.84	2.63±0.25	−1.11
NEIA	41620M001	2002.493	2012.994	84.3	4.12±1.55	0.51±0.33	3.61
NICA	10012M002	2007.002	2012.994	81.4	−1.09±1.22	−0.17±0.28	−0.92
NOT1	12717M004	2004.396	2012.994	94.1	−1.05±1.00	−0.57±0.20	−0.48
NPRI	49684S001	1999.594	2007.742	95.9	−0.38±0.93	−0.32±0.18	−0.06

(continued)

Table 1 Continued.

		Time span (year)			PPP	ULR	
Site	DOMES	Begin	End	Data	Trend (mm/year)		Diff.
OSN1	23904S001	1999.709	2009.534	80.8	−0.02±0.99	0.96±0.22	−0.98
OUAG	33101M001	2006.410	2012.994	66.4	−0.88±1.57	−0.94±0.47	0.06
P102	21754S001	2003.284	2011.115	99.1	−4.37±1.24	−4.36±0.25	−0.01
P103	21755S001	2003.249	2011.191	99.0	2.20±1.10	1.41±0.16	0.79
P104	21756S001	2003.419	2011.183	96.5	4.09±1.03	3.38±0.20	0.71
P115	21767S001	2006.180	2011.441	98.4	−3.44±1.85	−4.73±0.22	1.29
P116	21768S001	2005.876	2012.994	97.7	6.84±1.46	6.11±0.41	0.73
P117	21715S002	2003.449	2011.230	96.5	4.88±1.27	4.54±0.17	0.34
PLO5	99913M001	2006.435	2012.994	83.2	−1.39±1.45	−3.23±0.17	1.84
PNGM	51006M001	2002.331	2012.663	91.2	−2.05±1.52	−0.95±0.44	−1.10
POR4	49842S004	1999.569	2004.841	92.3	−0.74±1.69	−0.78±0.29	0.04
PRE1	30310S001	1999.194	2012.262	86.2	0.33±0.81	−0.53±0.36	0.86
REYK	10202M001	2003.309	2012.994	97.2	3.39±0.58	0.31±0.19	3.08
SABL	10063M001	2007.002	2012.994	73.0	0.53±1.39	−0.02±0.23	0.55
SEAT	40457M002	2002.490	2011.487	97.6	−1.46±0.67	−1.34±0.23	−0.12
SHEE	13236M001	2003.156	2012.994	81.0	2.26±0.80	1.03±0.25	1.23
STAS	10330M001	2000.830	2012.994	98.2	1.79±0.50	1.84±0.17	−0.05
TERS	13534M001	2000.360	2012.994	99.4	−0.29±0.50	−0.15±0.11	−0.14
TNML	23604S001	2008.341	2012.994	80.9	−1.23±2.46	−0.31±0.28	−0.92
TORS	10108S001	2003.109	2005.504	95.3	1.96±3.03	0.05±1.41	1.91
TRDS	10331M001	2000.830	2012.994	97.3	3.76±0.62	4.03±0.19	−0.27
TSEA	49448S001	2004.284	2012.994	91.9	6.43±0.76	6.11±0.26	0.32
USN3	40451S007	2004.535	2012.994	99.5	−0.19±0.88	−0.81±0.24	0.62
USNO	40451S003	2002.942	2012.994	95.1	1.26±0.79	−0.81±0.16	2.07
VAAS	10511M001	1999.164	2012.994	95.3	9.42±0.64	8.46±0.13	0.96
VARS	10322M002	2000.830	2012.994	98.0	3.37±0.62	2.96±0.22	0.41
VBCA	41512M001	1999.394	2012.994	84.2	−0.49±0.73	1.01±0.23	−1.50
VIKH	99922M001	2009.865	2012.994	99.4	6.81±2.59	0.56±0.60	6.25
VIMS	49880S001	2001.052	2009.265	89.7	−2.86±0.99	−3.82±0.46	0.96
WGTN	50208M003	1996.398	2012.994	88.9	−16.07±0.64	−2.31±0.24	−13.76
WGTT	50208S004	1999.953	2012.994	94.9	−3.92±0.93	−2.83±0.33	−1.09

The beginning and the end of the PPP time series are given. The column "Data" gives the percentage of data in the time series

Acknowledgements We would like to thank the IGS and the SONEL data center (www.sonel.org) for providing GNSS observation data.

References

Bar-Sever Y (1996) A new model for GPS yaw attitude. J Geodesy 70(11):714–723. doi:10.1007/BF00867149

Boehm J, Kouba J, Schuh H (2008) Forecast Vienna mapping functions 1 for real-time analysis of space geodetic observations. J Geodesy. doi:10.1007/s00190-008-0216-y

Mao A, Harrison CGA, Dixon TH (1999) Noise in GPS coordinate time series. J Geophys Res 104:2797–2816

Petit G, Luzum B (2010) IERS technical note No 36. Technical Report, IERS Convention Centre

Rebischung P (2012) IGSMAIL-6663. http://igscb.jpl.nasa.gov/pipermail/igsmail/2012/006655.html

Rodriguez-Solano C, Hugentobler U, Steigenberger P, Lutz S (2012) Impact of Earth radiation pressure on GPS position estimates. J Geodesy 86(5):309–317. doi:10.1007/s00190-011-0517-4

Rudenko S, Schön N, Uhlemann M, Gendt G (2013) Reprocessed height time series for GPS stations. Solid Earth 4(1):23–41. doi:10.5194/se-4-23-2013

Santamaría-Gómez A, Bouin MN, Wöppelmann G (2012a) Improved GPS data analysis strategy for tide gauge benchmark monitoring. In: Kenyon S, Pacino MC, Marti U (eds) Geodesy for planet Earth. International association of geodesy symposia, vol 136. Springer, Berlin/Heidelberg, pp 11–18. doi:10.1007/978-3-642-20338-1-2

Santamaría-Gómez A, Gravelle M, Collilieux X, Guichard M, Martín Míguez B, Tiphaneau P, Wöppelmann G (2012b) Mitigating the effects of vertical land motion in tide gauge records using a state-of-the-art GPS velocity field. Global Planet Chang 98-99:6–17. doi:j.gloplacha.2012.07.007

Schöne T, Schön N, Thaller D (2009) IGS tide gauge benchmark monitoring pilot project (TIGA): scientific benefits. J Geodesy 83:249–261. doi:10.1007/s00190-008-0269-y

Uhlemann M, Rudenko S, Nischan T, Gendt G (2010) GFZ results of the first IGS data reprocessing campaign. IGS Workshop, Newcastle. ftp://stella.ncl.ac.uk/pub/IGSposters/Uhlemann.pdf

Williams S (2008) Cats: GPS coordinate time series analysis software. GPS Solutions 12(2):147–153. doi:10.1007/s10291-007-0086-4

Wöppelmann G, Marcos M (2012) Coastal sea level rise in southern Europe and the nonclimate contribution of vertical land motion. J Geophys Res Oceans 117(C1). doi:10.1029/2011JC007469

Zhang J, Bock Y, Johnson H, Fang P, Williams S, Genrich J, Wdowinski S, Behr J (1997) Southern California permanent GPS geodetic array: error analysis of daily position estimates and site velocities. J Geophys Res Solid Earth 102(B8):18035–18055. doi:10.1029/97JB01380. http://dx.doi.org/10.1029/97JB01380

On the Impact of Correlation Information on the Orientation Parameters Between Celestial Reference Frame Realizations

Yulia Sokolova and Zinovy Malkin

Abstract

In this study, we compared results of determination of the orientation angles between celestial reference frames realized by radio source position catalogues using three methods of accounting for correlation information: using the position errors only, using additionally the correlations between the right ascension and declination (RA/DE correlations) reported in radio source position catalogues published in the IERS format, and using the full covariance matrix. The computations were performed with nine catalogues computed at eight analysis centres. Our analysis has shown that using the RA/DE correlations only slightly influences the computed rotational angles, whereas using the full correlation matrices leads to substantial change in the orientation parameters between the compared catalogues.

Keywords

Celestial reference frame • CRF orientation • ICRF • Radio source position catalogues • VLBI

1 Introduction

Catalogues of radio source positions derived from VLBI observations are used by the International Astronomical Union (IAU) to establish the International Celestial Reference Frame (ICRF) since 1998 (Ma et al. 1998, 2009; Feissel and Mignard 1998). In addition to the official ICRF catalogues International VLBI Service for Geodesy and Astrometry (IVS) analysis centres routinely publish radio source catalogues (RSC), hereafter referred to as individual catalogues, which, generally speaking, represent independent celestial reference frame (CRF) realizations. Comparison of these catalogues both among themselves and with the ICRF is important for quality assessment of the ICRF. The primary interest is to investigate the mutual orientation of these individual systems, which can be represented by rotation around three Cartesian axes by the angles A1, A2, A3. In this study we investigate the impact of correlations between radio source positions on determination of these angles, which is an extension of the first study on the subject of Jacobs et al. (2010).

2 Method Used

For transformation of a radio source vector (X, Y, Z) from one system to another we can write for small rotation angles:

$$\begin{pmatrix} X_1 \\ Y_1 \\ Z_1 \end{pmatrix} = \begin{pmatrix} 1 & A_3 & -A_2 \\ -A_3 & 1 & A_1 \\ A_2 & -A_1 & 1 \end{pmatrix} \begin{pmatrix} X_2 \\ Y_2 \\ Z_2 \end{pmatrix}. \quad (1)$$

Y. Sokolova (✉)
Pulkovo Observatory, St. Petersburg, Russia
e-mail: Julia.rs07@hotmail.com

Z. Malkin
Pulkovo Observatory, St. Petersburg, Russia

St. Petersburg State University, St. Petersburg, Russia
e-mail: malkin@gao.spb.ru

© Springer International Publishing Switzerland 2015

C. Rizos, P. Willis (eds.), *IAG 150 Years*, International Association of Geodesy Symposia 143,
DOI 10.1007/1345_2015_179

Then, taking into account that

$$\begin{pmatrix} \mathrm{X} \\ \mathrm{Y} \\ \mathrm{Z} \end{pmatrix} = \begin{pmatrix} \cos\alpha\cos\delta \\ \sin\alpha\cos\delta \\ \sin\delta \end{pmatrix}, \tag{2}$$

where α is the right ascension and δ is the declination of the source, we find for the difference of radio source coordinates in the compared catalogues $\Delta\alpha = \alpha_1 - \alpha_2$ and $\Delta\delta = \delta_1 - \delta_2$:

$$\begin{aligned} \Delta\alpha\cos\delta &= A_1\cos\alpha\sin\delta + A_2\sin\alpha\sin\delta - A_3\cos\delta, \\ \Delta\delta &= -A_1\sin\alpha + A_2\cos\ \alpha. \end{aligned} \tag{3}$$

The rotation angles A_1, A_2, and A_3 are obtained by applying the least squares method for the Eq. (3) on all sources or selected group of sources. In our investigation we used all common sources between compared catalogues.

This method was used by the International Earth Rotation and Reference Systems Service (IERS) for comparison and combination of individual radio source catalogues in the 1980s and 1990s, before adopting the official version of the ICRF (Arias et al. 1988). Although systematic differences between individual catalogues are much more complicated than represented by the simple rotation model (Sokolova and Malkin 2007), determining orientation of the frames is a fundamental part of the constructing ICRF, like it was done for ICRF and ICRF2 (Ma et al. 1998, 2009). In both cases the computation of the final reference frame was conducted in two steps. First, the catalogue was calculated as a result of the global VLBI solution in its own independent system, and in the second step the catalogue was transferred to the IERS95 system in the case of ICRF and to the ICRF system in the case of ICRF2 applying the rotation model on a set of defining sources.

In order to obtain parameters of the rotation model (3) the following system is solved by least squares:

$$\mathbf{Bx} + \boldsymbol{\varepsilon} = \mathbf{l}, \tag{4}$$

where $\mathbf{B}$ is the coefficient matrix of dimension $2n \times 3$, $\mathbf{x} = (\mathrm{A}_1, \mathrm{A}_2, \mathrm{A}_3)'$ is the vector of unknowns, $\boldsymbol{\varepsilon}$ is the vector of errors with length $2n$, $\mathbf{l} = (\triangle\alpha_1\cos\delta_1, \triangle\delta_1, \ldots, \triangle\alpha_\mathrm{n}\cos\delta_\mathrm{n}, \triangle\delta_\mathrm{n})'$ is the vector of length $2n$ of coordinate differences, n is the number of sources used, and prime denotes the transpose of a matrix. Note that since we have two Eq. (3) for each source, the dimension of corresponding arrays is $2n$.

The covariance matrix for coordinate differences is given by

$$\mathbf{Q} = \mathbf{Q_1} + \mathbf{Q_2}, \tag{5}$$

where $\mathbf{Q}_1$ and $\mathbf{Q}_2$ are the covariance matrices of the compared catalogues of dimension $2n \times 2n$. Each of them may be either a diagonal matrix if only position uncertainties are used or a two-diagonal matrix if the correlations between the right ascension and declination estimates for each source (RA/DE correlations) are taken into account or a full matrix when available. Strictly speaking the Eq. (5) is correct if the catalogues are independent. But the investigation of source coordinate correlations between catalogues is a separate nontrivial task, which is not addressed here. A possible approach to its solution is discussed by Malkin (2013), but not all problems are solved yet.

Finally, the solution of the system (4) is

$$\mathbf{x} = \left(\mathbf{B}'\mathbf{Q}^{-1}\mathbf{B}\right)^{-1}\mathbf{B}'\mathbf{Q}^{-1}\mathbf{l}. \tag{6}$$

Traditionally, the system (4) is solved with weights of condition equations (3) inversely proportional to the position uncertainties reported in the catalogues. In other words, a diagonal covariance matrix is used in the least square solution. However, Jacobs et al. (2010) showed that accounting for correlations between the source positions derived from VLBI global solution changes significantly the orientation parameters between CRF realizations if a microarcsecond level of accuracy is required. In their work, catalogues with diagonal covariance matrix and with full covariance matrix were used for an investigation of the impact of correlation information on the orientation angles.

Currently, the IVS analysis centres mostly provide their individual CRF solutions in a standard IERS format, where the RA/DE correlations for each source are reported together with radio source positions and other relevant information. The ICRF2 catalogue is also published in the same format. So, in this case we only can use a two-diagonal covariance matrix in the least square solution. This case not considered by Jacobs et al. (2010) is also important to investigate, since such a research has not been done yet.

Recently some IVS analysis centres have started producing results of global solutions in the SINEX format, where the full covariance matrix is presented. For our work, we used two such solutions provided by Vienna University of Technology, Austria and NASA Goddard Space Flight Center, USA. Thus we could undertake a detailed comparison of commonly used rotational alignment models with three methods of accounting for the covariance information: using the position errors only (diagonal covariance matrix), using additionally RA/DE correlations available for the catalogues in the IERS format (two-diagonal covariance matrix), and using the full covariance matrices from SINEX files.

Table 1 CRF solutions used in this study

Catalogue	Analysis centre	Software	Time span	Number of sources	Format
aus2012b	AUS	Occam	1980–2012	2,892	ICRF
bkg2011a	BKG	Calc/Solve	1984–2011	3,214	ICRF
cgs2012a	CGS	Calc/Solve	1980–2011	842	ICRF
gsf2011a	GSF	Calc/Solve	1979–2011	1,340	SINEX
gsf2012a	GSF	Calc/Solve	1979–2012	3,708	ICRF
vie2012a	VIE	VieVS	1984–2011	860	SINEX
opa2012a	OPA	Calc/Solve	1979–2012	3,482	ICRF
sha2012b	SHA	Calc/Solve	1979–2012	3,470	ICRF
usn2012a	USN	Calc/Solve	1979–2012	793	ICRF

Table 2 Orientation parameters between individual CRF solutions and ICRF2 computed with diagonal (first line) and two-diagonal (second line) covariance matrices

Catalogue and source number	A1	A2	A3
aus2012b	-26.5 ± 4.5	2.1 ± 4.6	1.7 ± 4.0
936	-26.5 ± 4.5	2.3 ± 4.5	2.5 ± 3.9
bkg2011a	25.6 ± 3.1	17.0 ± 3.1	-10.5 ± 2.7
936	25.5 ± 3.0	17.1 ± 3.1	-12.9 ± 2.6
cgs2012a	11.9 ± 3.5	-1.1 ± 3.5	-13.0 ± 3.1
795	12.0 ± 3.5	-0.2 ± 5.5	-18.2 ± 3.0
gsf2012a	-0.9 ± 2.3	6.0 ± 2.3	-4.9 ± 2.0
936	-1.0 ± 2.3	5.8 ± 2.3	-3.7 ± 2.0
opa2012a	-4.7 ± 2.1	10.8 ± 2.1	-10.0 ± 1.8
936	-5.0 ± 2.1	10.9 ± 2.1	-10.5 ± 1.8
sha2012b	-4.4 ± 2.2	2.3 ± 2.2	-5.2 ± 1.9
936	-4.4 ± 2.1	2.4 ± 2.2	-5.1 ± 1.9
usn2012a	-2.5 ± 2.6	10.5 ± 2.6	-6.5 ± 2.3
780	-2.9 ± 2.6	10.7 ± 2.6	-5.6 ± 2.3

The number of common sources between the individual catalogue and ICRF2 is given below the catalogue name. Unit: μas

3 Results of Computations

Nine CRF solutions from eight IVS analysis centres have been used for our investigation (Table 1): AUS (Geoscience Australia), BKG (Federal Agency for Cartography and Geodesy, Germany), CGS (Space Geodesy Centre, Italy), GSFC (NASA Goddard Space Flight Center, USA), VIE (Vienna University of Technology, Austria), OPA (Paris Observatory, France), and SHA (Shanghai Astronomical Observatory, China).

The results of computation of the orientation angles between seven catalogues published in the IERS format and ICRF2 are shown in Table 2. In this test, diagonal or two-diagonal covariance matrices $\mathbf{Q}_1$ and $\mathbf{Q}_2$ were used.

Table 3 Orientation parameters between individual CRF solutions and ICRF2 computed with diagonal (first line), two-diagonal (second line), and full (third line) covariance matrices

Catalogue	A1	A2	A3
gsf2011a	-9.2 ± 2.3	3.5 ± 2.3	2.2 ± 2.0
1171	-9.3 ± 2.3	3.7 ± 2.3	2.0 ± 1.9
	-4.4 ± 3.1	2.8 ± 3.1	0.3 ± 2.3
vie2012b	13.3 ± 3.0	11.3 ± 3.0	-1.1 ± 2.4
856	13.2 ± 3.0	11.5 ± 3.0	-0.8 ± 2.3
	2.6 ± 4.1	7.0 ± 4.3	-0.9 ± 2.4

The number of common sources between the catalogue and ICRF2 is given below the catalogue name. Unit: μas

Table 4 Orientation parameters between gsfc2011a and vie2012b catalogues computed with diagonal (first line), two-diagonal (second line), and full (third line) covariance matrices

Catalogues	A1	A2	A3
gsfc2011a	-24.0 ± 2.1	-5.4 ± 2.2	6.0 ± 1.1
vie2012b	-23.9 ± 2.1	-5.2 ± 2.2	5.7 ± 1.1
854	-0.6 ± 2.5	3.4 ± 3.5	0.7 ± 1.2

The number of common sources between the catalogues is given below the catalogue name. Unit: μas

Table 3 shows the results of computation of the orientation angles between two catalogues with full covariance matrices and ICRF2. In this test, we used diagonal, two-diagonal, or full covariance matrices for GSF and VIE catalogues and diagonal or two-diagonal covariance matrix for ICRF2.

Table 4 presents results of comparisons of two catalogues with full covariance matrices to each other. In this test we used all three modes of covariance matrices for both catalogues.

Obtained results have shown that the off-diagonal elements of the catalogue covariance matrix have large impact on the results of computation of the orientation parameters. Figure 1 gives an impression of how large these correlations can be. Although generally the off-diagonal correlations are small, some can exceed 0.9.

4 Summary

Our analysis revealed substantial differences between rotation parameters between CRF realizations (radio source position catalogues) computed without accounting for correlation information and using full covariance matrices of individual catalogues. The difference in the rotation angles may exceed 20 μas (see Table 4). Thus our findings confirm result of Jacobs et al. (2010) based on different catalogues and comparison scheme. Therefore, it is necessary to account for the full covariance information during comparison, combination and analyses of modern CRF solutions.

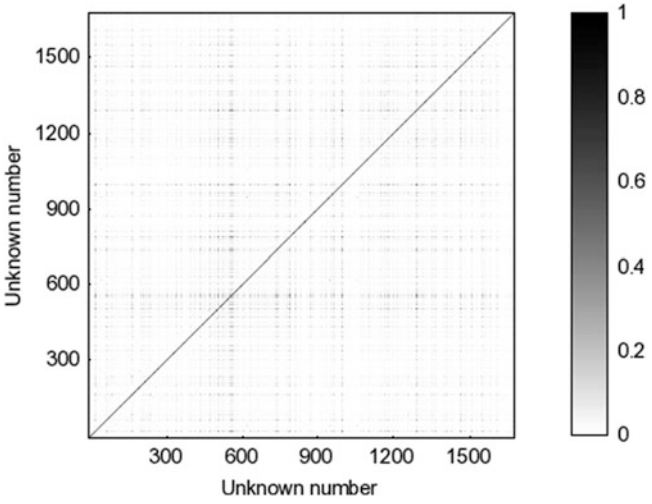

Fig. 1 Correlation matrix of the catalogue gsfc2011a for sources used in the computations presented in Table 4. For better visibility, the absolute values of correlations are depicted. The odd unknown numbers correspond to the right ascension (RA) of the sources sorted by the RA; the even unknown numbers correspond to the declination of the sources

On the other hand, accounting for RA/DE correlations only, the differences in rotation parameters are found to be at a level below 1σ, i.e. practically insignificant (cf. the first two lines in Tables 2, 3, and 4).

It should be noted that accounting for a full correlation matrix may be essential not only for definition of mutual orientation, but also for decomposition of the coordinate differences by orthogonal functions. If it is the case, the full correlation information should be accounted for during calculation of a combined catalogue as proposed by Sokolova and Malkin (2007). Corresponding investigations are underway.

Indeed, the results obtained in this study can be applied also to determination of orientation parameters between other reference frames, such as TRF solutions from space geodesy techniques or optical source position catalogues.

Acknowledgements The authors are grateful to all the VLBI data analysts, who made their catalogues available for this study either via public access or via personal contact. We thank the anonymous referees for careful reading of the manuscript and useful comments and suggestions.

References

Arias EF, Lestrade J-F, Feissel M (1988) Comparison of VLBI celestial reference frames. Astron Astrophys 199:357–363

Feissel M, Mignard F (1998) The adoption of ICRS on 1 January 1998: meaning and consequences. Astron Astrophys 331:L33–L36

Jacobs CS, Heflin MB, Lanyi GE, Sovers OJ, Steppe JA (2010) Rotational alignment altered by source position correlations. In: Behrend D, Baver KD (eds) Proceedings of the IVS 2010 general meeting, pp 305–309

Ma C, Arias EF, Eubanks TM, Fey AL, Gontier A-M, Jacobs CS, Sovers OJ, Archinal BA, Charlot P (1998) The international celestial reference frame as realized by very long baseline interferometry. Astron J 116:516–546

Ma C, Arias EF, Bianco G, Boboltz DA, Bolotin SL, Charlot P, Engelhardt G, Fey AL, Gaume RA, Gontier AM, Heinkelmann R, Jacobs CS, Kurdubov S, Lambert SB, Malkin ZM, Nothnagel A, Petrov L, Skurikhina E, Sokolova JR, Souchay J, Sovers OJ, Tesmer V, Titov OA, Wang G, Zharov VE, Barache C, Boeckmann S, Collioud A, Gipson JM, Gordon D, Lytvyn SO, MacMillan DS, Ojha R (2009) The second realization of the international celestial reference frame by very long baseline interferometry. In: Fey AL, Gordon D, Jacobs CS (eds) IERS technical note No. 35. Verlag des Bundesamts für Kartographie und Geodäsie, Frankfurt am Main

Malkin Z (2013) A new approach to the assessment of stochastic errors of radio source position catalogues. Astron Astrophys 558:A29. doi:10.1051/0004-6361/201322334

Sokolova J, Malkin Z (2007) On comparison and combination of catalogues of radio source positions. Astron Astrophys 474:665–670. doi:10.1051/0004-6361:20077450

Quality Evaluation of the Weekly Vertical Loading Effects Induced from Continental Water Storage Models

Z. Li, T. van Dam, X. Collilieux, Z. Altamimi, P. Rebischung, and S. Nahmani

Abstract

To remove continental water storage (CWS) signals from the GPS data, CWS mass models are needed to obtain predicted surface displacements. We compared weekly GPS height time series with five CWS models: (1) the monthly and (2) three-hourly Global Land Data Assimilation System (GLDAS); (3) the monthly and (4) one-hourly Modern-Era Retrospective Analysis for Research and Applications (MERRA); (5) the six-hourly National Centers for Environmental Prediction-Department of Energy (NCEP-DOE) global reanalysis products (NCEP-R-2). We find that of the 344 selected global IGS stations, more than 77% of stations have their weighted root mean square (WRMS) reduced in the weekly GPS height by using both the GLDAS and MERRA CWS products to model the surface displacement, and the best improvement concentrate mainly in North America and Eurasia. We find that the one-hourly MERRA-Land dataset is the most appropriate product for modeling weekly vertical surface displacement caused by CWS variations. The three-hourly GLDAS data ranks the second, while the GLDAS and MERRA monthly products rank the third. The higher spatial resolution MERRA product improves the performance of the CWS model in reducing the scatter of the GPS height by about 2–6% compared with the GLDAS. Under the same spatial resolution, the higher temporal resolution could also improve the performance by almost the same magnitude. We also confirm that removing the ATML and NTOL effects from the weekly GPS height would remarkably improve the performance of CWS model in correcting the GPS height by at least 10%, especially for coastal and island stations. Since the GLDAS product has a much greater latency than the MERRA product, MERRA would be a better choice to model surface displacements from CWS. Finally, we find that the NCEP-R-2 data is not sufficiently precise to be used for this application. Further work is still required to determine the reason.

Keywords

Continental water storage • GLDAS • GPS height • MERRA • NCEP

1 Introduction

Previous research has confirmed the strong correlation between Continental Water Storage (CWS) induced vertical surface displacement and the global positioning system (GPS) height time series (van Dam et al. 2001, 2007; Tregoning et al. 2009; Fritsche et al. 2012). This environmentally driven displacement adds noise to the

Z. Li (✉) • T. van Dam
Faculté des Science, de la Technologie et de la Communication, University of Luxembourg, 6 rue Richard Coudenhove-Kalergi L-1359, Luxembourg, Luxembourg
e-mail: zhao.li@uni.lu

X. Collilieux • Z. Altamimi • P. Rebischung • S. Nahmani
IGN/LAREG and GRGS, Univ Paris Diderot, Sorbonne Paris Cité, Paris, France

© Springer International Publishing Switzerland 2015

C. Rizos, P. Willis (eds.), *IAG 150 Years*, International Association of Geodesy Symposia 143,
DOI 10.1007/1345_2015_174

GPS data being used for geodynamic investigations, such as postglacial rebound, sea level rise, etc. To remove this environmental signal from the GPS data, the CWS mass models are required to predict surface displacements. However, these CWS model induced vertical surface displacement are often not consistent with one another and with the seasonal changes in the position of the GPS markers (Jiang et al. 2013).

Currently, the most frequent used CWS mass models are the soil moisture (SM) plus snow water equivalent (SWE) from the monthly Global Land Data Assimilation System (GLDAS)[1] (Rui 2011) and the six-hourly National Centers for Environmental Prediction-National Center for Atmospheric Research (NCEP-NCAR) global reanalysis datasets (R-1) (Kalnay et al. 1996), with spatial resolutions as $1^\circ \times 1^\circ$ and $1.875^\circ \times (1.8889 - 1.9048)^\circ$ respectively. It is well known that the CWS model in the R-1 are inaccurate (Kanamitsu et al. 2002), and (Jiang et al. 2013) found that the vertical loading time series from the R-1 CWS model were not fit well with the GPS height. To fix the known errors and also update the parameterizations of physical processes in R-1,the NCEP-Department of Energy (NCEP-DOE) global reanalysis products (NCEP-R-2) came into being[2] (Kanamitsu et al. 2002). Are the temporal or spatial resolutions of the CWS model from the GLDAS and the NCEP-R-2 sufficient for correcting the GPS height time series?

Since 2012, the Modern-Era Retrospective Analysis for Research and Applications (MERRA) published an improved land surface data product called MERRA-Land reanalysis[3] (Reichle et al. 2011; Reichle 2012). It provides both monthly and one-hourly CWS estimates for snow mass (SNOMAS) and SM with spatial resolution as $1^\circ/2^\circ \times 2^\circ/3^\circ$ in latitude and longitude. In addition, GLDAS also provides three-hourly CWS estimates. Whether these higher temporal and spatial resolution products would improve the correlation between the CWS driven displacement and the GPS height is the motivation for this research.

In this paper, we assess the quality of five CWS mass model induced vertical surface displacements, that is the CWS estimates from the monthly and three-hourly GLDAS, monthly and hourly MERRA-Land, together with the six-hourly NCEP-R-2 products, by inter-comparing similar models with each other and with the latest International GNSS service (IGS; Dow et al. 2009) combined weekly GPS coordinate time series. We test whether higher spatial or temporal resolution CWS products are better at reducing the scatter in the GPS height.

[1] http://disc.sci.gsfc.nasa.gov/services/grads-gds/gldas.

[2] http://www.esrl.noaa.gov/psd/data/gridded/data.ncep.reanalysis2.html.

[3] http://gmao.gsfc.nasa.gov/pubs/office_notes/.

2 Data Processing

2.1 Farrell's Green's Function Approach

The predicted vertical displacement of a point on the Earth's surface driven by changes in CWS can be determined by convolving Farrell's Green's functions (Farrell 1972) with a surface mass model over the surface of the Earth (van Dam and Wahr 1987). The basic equation can be written as:

$$d_u(\theta, \phi) = \sum_{i=1}^{nlon} \sum_{j=1}^{nlat} \triangle P_{i,j} G^u_{i,j} A_{i,j} \quad (1)$$

where i and j denote a unique loading grid point from given CWS model, $nlon$ and $nlat$ represent the number of CWS grid unit increment in longitude and latitude respectively, and $G^u_{i,j}$ denotes the Green's function for the vertical component of surface displacement. $\triangle P_{i,j}$ is the CWS variation at the grid point and $A_{i,j}$ is the area of the loading grid point. Here we choose the Green's function derived in the center of figure (CF) frame to maintain consistency between the predicted loading and GPS heights (Dong et al. 1997; Blewitt 2003).

2.2 Data Description

Here, we model the vertical surface displacements for 344 global IGS stations using the above five different CWS models. The time period we consider runs from January 01, 2000 to December 31, 2010. For both GLDAS monthly and three-hourly products, we use the one degree Noah-Version 1 SM and SWE data.[4] We did not include the SWE data above the latitude of 60.5N. This area includes Greenland and most Arctic regions; GLDAS does not model snow dynamics well in these regions (Rui 2011; Jiang et al. 2013).

For the monthly and hourly MERRA-Land products, we use the variables called the total profile soil moisture content (PRMC) and the SNOMAS, which represent the SM and SWE respectively (tavg1_2d_mld_Nx[5]). To convert PRMC into equivalent water height, a corresponding constant file that describes the thickness of the soil layer is also needed (const_2d_mld_Nx[6]).

The last CWS model we use is the volumetric soil moisture (VSM) and the water equivalent of accumulated snow

[4] ftp://hydro1.sci.gsfc.nasa.gov/data/s4pa/GLDAS_V1.

[5] http://disc.sci.gsfc.nasa.gov/daac-bin/DataHoldings.pl?LOOKUPID_List=MST1NXMLD.

[6] http://disc.sci.gsfc.nasa.gov/daac-bin/DataHoldings.pl?LOOKUPID_List=MSC0NXMLD.

Table 1 Details of the five CWS models used

Model	Data source	Unit	Temporal resolution	Spatial resolution (degree)	Latency
GLDAS-A (NOAH)	SM (4 layers)	kg/m^2	Monthly	1×1	1–4 months
	SWE	kg/m^2			
NCEP-R-2	SM (2 layers)	m^3/m^3	6-hourly	$1.875 \times (1.8889 - 1.9048)$	3–4 days
	SWE	kg/m^2			
GLDAS-B (NOAH)	SM (4 layers)	kg/m^2	3-hourly	1×1	1–4 months
	SWE	kg/m^2			
MERRA-A	PRMC	m^3/m^3	Monthly	$2/3 \times 1/2$	1–2 months
	SNOMAS	kg/m^2			
MERRA-B	PRMC	m^3/m^3	1-hourly	$2/3 \times 1/2$	1–2 months
	SNOMAS	kg/m^2			

depth (SD) from the NCEP-R-2 products.[7] Table 1 shows the details of each CWS model. Note that the groundwater component are excluded from all the five CWS models (Rui 2011; Reichle 2012; Kanamitsu et al. 2002), and all the five CWS models use the soil moisture and the snow water equivalence as the input for calculating the CWS loading time series, although the name of the variables are different from model to model. This condition makes our results more comparable to each other.

For comparison, the latest IGS combined weekly GPS coordinate time series until the year 2011 is applied to evaluate the performance of each CWS model in correcting the GPS height. These data include homogeneously reprocessed coordinates from the first IGS reprocessing campaign (Chen et al. 2013). The reprocessed individual solutions from each IGS analysis center (AC) are then recombined using the combination strategy of the new IGS combination center (Rebischung et al. 2012). Compared with previous products, the advantage of this IGS combined solution is that it implements the absolute antenna calibrations for both satellites and receivers. However, it still has some limitations, for example, the higher-order ionospheric delay together with the diurnal and semi-diurnal atmospheric tides are not considered during the data processing.[8]

Because the applied GPS weekly height time series include the surface displacement caused by atmospheric tides, together with the impacts of non-tidal ocean loading (NTOL) and atmospheric loading (ATML) effects, here we also model stations' displacement induced by atmospheric and oceanic loading effects using Farrell's Green's function approach, to investigate whether the comparison between CWS loading and GPS height would be changed or not if these two kinds of loading effects are removed from the GPS observations first. The MERRA provided global 6-hourly surface pressure grid[9] is used for modeling the ATML, while the 12-hourly ocean bottom pressure (OBP) from the estimating the circulation and climate of the ocean (ECCO) global model from the JPL kf080 analysis[10] is used for modeling the NTOL. The spatial resolution for these two selected products are at $1°/2° \times 2°/3°$ and $(1 - 0.3)° \times 1°$ in latitude and longitude respectively.

During the loading calculation, we firstly remove a 10-year mean of the total CWS from 2000 to 2009 for each CWS model. Then, the residual CWS is convolved with the Farrell's Green's function to obtain the vertical surface displacement. The data are then detrended, averaged or interpolated into daily solutions corresponding to decimal year, or weekly solutions corresponding to the GPS week. For the ATML and NTOL, we follow the same procedure as the CWS loading calculation except that there is no need to remove the linear trend in the obtained ATML time series. Note that we assume that the total mass of the atmosphere, continental water together with ocean is constant, and simply sum up individual loading effects to obtain a stations displacement caused by total loads (Jiang et al. 2013). The gravitational consistency and mass conservation on surface loads are not considered here (Clarke et al. 2005). We state that this is a limitation of this investigation.

Before comparison with the detrended loading results, offsets in both the weekly GPS height time series should be carefully detected and removed. Then a linear trend should also be removed from the GPS observations. When implementing the comparison, we interpolate (for monthly products) or average (for subdaily products) the loading corrections for each station into each epoch of the GPS weekly time series to obtain load-corrected GPS data (Jiang et al. 2013). The red dots in Fig. 1 show the spatial distribution of the 344 stations used (Wessel and Smith 2013).

[7] http://www.esrl.noaa.gov/psd/cgi-bin/db_search/SearchMenus.pl?Dataset=NCEP/DOE+AMIP-II+Reanalysis+(Reanalysis-2)&group=1.

[8] http://acc.igs.org/reprocess.html.

[9] http://disc.sci.gsfc.nasa.gov/daac-bin/FTPSubset.pl?LOOKUPID_List=MAI6NVANA.

[10] http://ecco.jpl.nasa.gov/thredds/catalog/las/kf080/catalog.html.

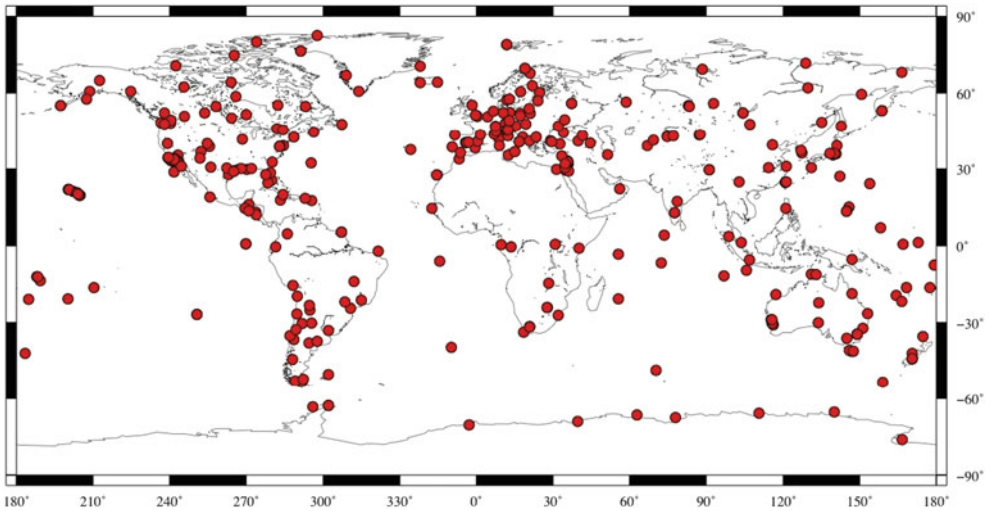

Fig. 1 Spatial distribution of the 344 IGS stations used in this analysis

3 Results and Discussion

3.1 Comparison of the Weekly Loading Time Series Between Models

Figure 2 shows an example of the detrended weekly loading time series for BRAZ (Brasilia, Brazil) and POTS (Potsdam, Germany) generated from our five CWS models. The detrended GPS time series is shown as black curve in the figure. Since the GPS time series include the ATML and NTOL effects, we also show the total weekly loading time series here (see the bottom panels for each station). For combination of the three loading effects, please refer to (Jiang et al. 2013) for detail. To address the difference between NCEP-R-1 and NCEP-R-2, the detrended loading time series from NCEP-R-1 is also shown as yellow curve. Note that of the five models listed in Table 1, only the loading time series from the GLDAS model exhibits a significant linear trend that is known to be artificial and should be removed (van Dam et al. 2001). For the MERRA and NCEP datasets, the linear trend is very small for most of the stations and can be neglected.

From Fig. 2 we observe that predicted heights from GLDAS and MERRA models track the trend of the GPS height time series better as compared with the two NCEP models, of which the NCEP-R-1 sometimes over estimates station's vertical displacement, while the NCEP-R-2 could only yield very small surface displacement. For the same spatial resolution, we observe that the temporal resolution differences, i.e. three-hourly versus monthly GLDAS, are only slightly different at the weekly samples shown here. Thus, when comparing the models to one another, we will plot the results from the higher temporal resolution data sets GLDAS-B and MERRA-B hereafter. If we look at the difference among CWS models at the daily sampling, however, there would be bigger difference between different temporal resolution products.

From Fig. 2 we also notice that after considering the ATML and NTOL effects, the fitting between each CWS model and the weekly GPS height exhibits some difference, in particular for station POTS. Both the phase and amplitude of the CWS model become more closer with the applied GPS height. This result indicates that ATML and NTOL would have some impact on the performance of CWS modeling in correcting the GPS height time series.

An analysis of the two stations in Fig. 2 does not allow us to determine whether the GLDAS or MERRA model is better. The left panels of Fig. 3 show the standard deviation (STD) of the weekly loading time series for the 344 stations derived from GLDAS-B, MERRA-B and NCEP-R-2 model. In general, we can observe that the MERRA model yields a slightly bigger scatter than the GLDAS model across the continents, in particular for the stations above the latitude of 60.5 degree. The lower scatter in the GLDAS data at high latitudes is because we removed the SWE value in these regions when modeling the displacement from GLDAS. Quite different from the MERRA and GLDAS model, the NCEP-R-2 model yields very small STD value at most of places around the globe, while the STD of the NCEP-R-1 model is very large, especially for the central North America and Eurasia. Since our results on the NCEP-R-1 model is quite similar as that from (Jiang et al. 2013), we only show the results from the NCEP-R-2 model only hereafter. The

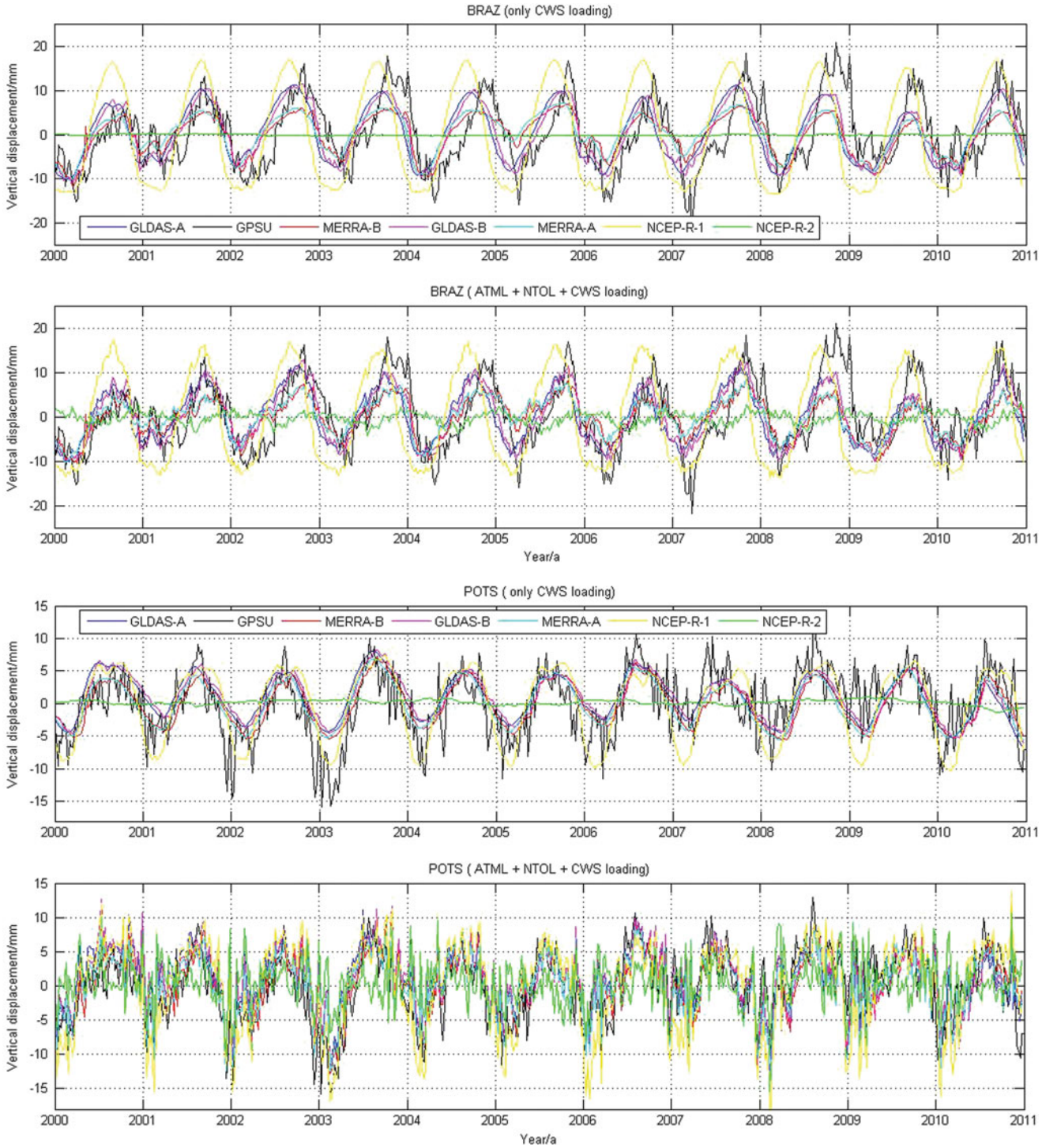

Fig. 2 Weekly vertical displacement of station BRAZ and POTS generated from different CWS models. Unit of the displacement is in mm

right panels of Fig. 3 show the correlations for GLDAS-B, MERRA-B and NCEP-R-2 with GLDAS-A. We can see that GLDAS-B has the largest correlation with GLDAS-A. However, MERRA-B and NCEP-R-2 do not correlate well with the GLDAS-A. This is particularly true for coastal and ocean areas.

3.2 Comparison Between Loading and GPS Height Time Series

To evaluate the quality of the CWS induced weekly vertical loading displacement, we calculate the Weighted Root Mean Square (WRMS) reduction of the GPS height time

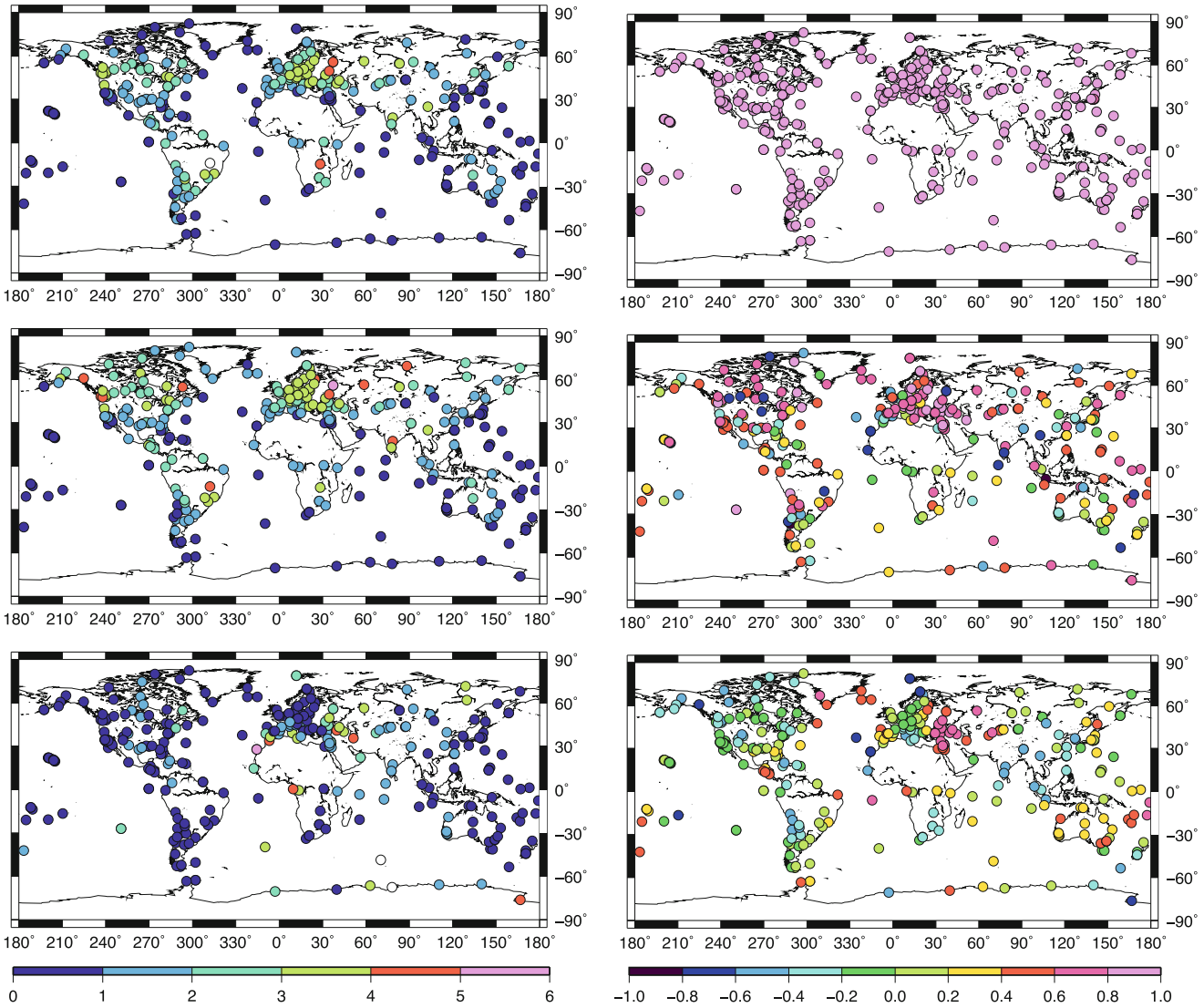

Fig. 3 Spatial distribution of the STD different CWS models (*left*) and their correlation with the reference model GLDAS-A (*right*). From top to bottom are GLDAS-B, MERRA-B and NCEP-R-2. Unit of the STD is in mm. The *white dots* in the figure indicate that the STD value for the station is larger than the maximum value on the scale

series using the CWS models (Jiang et al. 2013) and the correlation coefficients between each CWS model and the GPS height. Some statistics of the WRMS and correlation results are shown in Table 2. The left panels of Fig. 4 show the WRMS results for GLDAS-B, MERRA-B and the NCEP-R-2 model. The reddish colors in the panels on the left hand side of the figure indicate that the station's WRMS was reduced when the model was applied; bluish colors indicate the WRMS of the heights increased. Black dots indicate that a station's WRMS increase exceeds the lower limit of the scale. The right panels of Fig. 4 illustrate the correlation of the models with the GPS height time series. The higher the correlation and WRMS reduction, the better the model is in correcting the GPS height for CWS effects.

From Fig. 4 and Table 2, we observe that the MERRA product has slightly higher correlations with GPS heights than the GLDAS model. More than 40 and 33% of the stations have correlations with the GPS heights larger than +0.5 for the MERRA-B and GLDAS-B models respectively. Those stations with stronger correlations are found mainly in central North America and Eurasia. The NCEP-R-2 model, however, has a very poor correlation with the weekly GPS height.

As for the WRMS reduction, MERRA-B and GLDAS-B reduce the scatter on 88 and 82% of the weekly GPS height respectively. The stations with the largest reductions in scatter (on the order of 10%) are mostly in North America and Europe. Compared to GLDAS-B, MERRA-B improves the WRMS of the IGS stations to a greater extent in

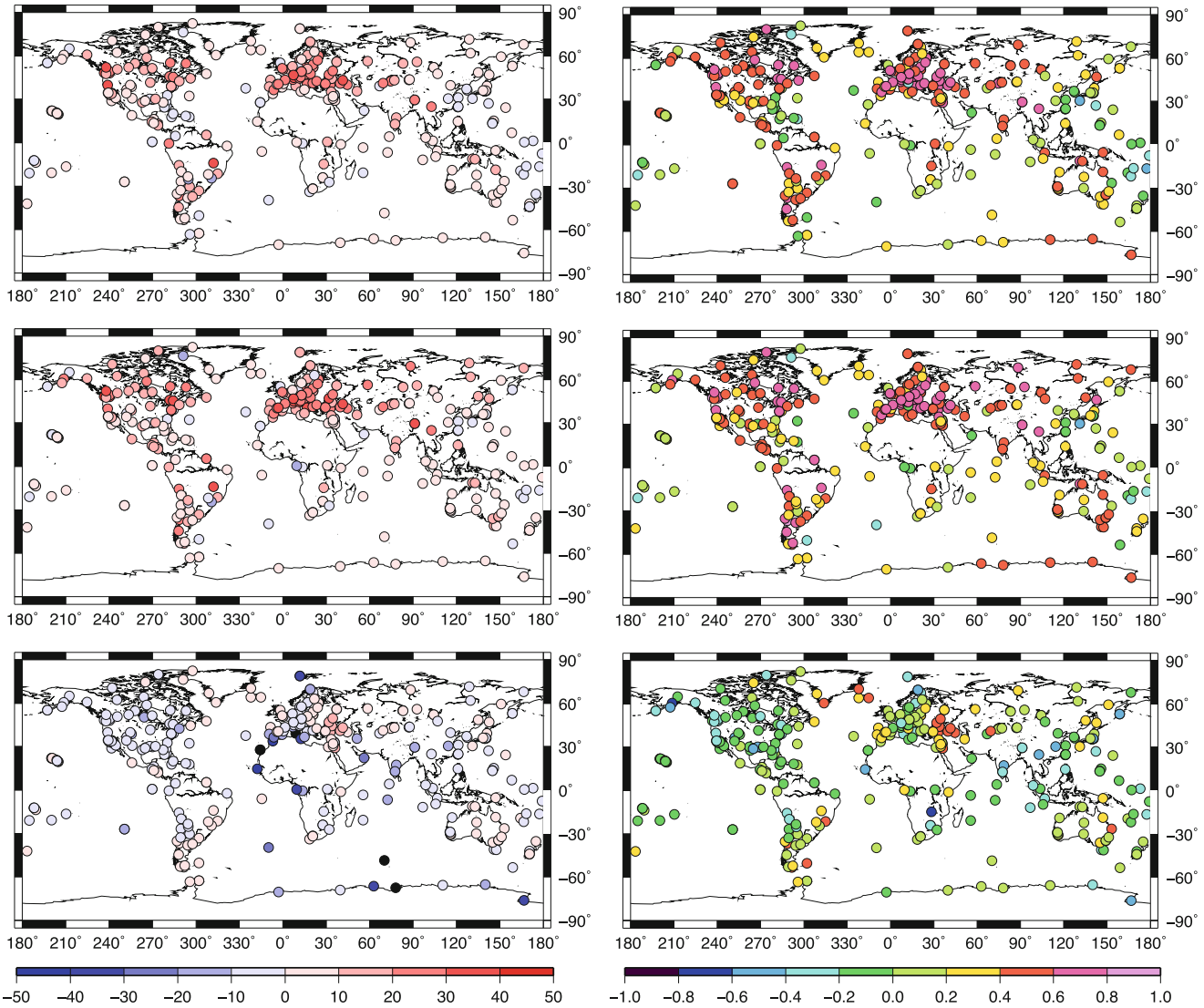

Fig. 4 Spatial distribution of the WRMS reduction rate using different CWS loading corrections (*left*) and their correlation with GPS height (*right*). From *top to bottom* are GLDAS-B, MERRA-B and NCEP-R-2. The *black dots* in the figure indicate that the WRMS reduction for the station is smaller than the minimum value on the scale. Unit of the WRMS reduction is in %

Table 2 Statistics of the correlation coefficients and the WRMS from the 5 CWS models

	Percentage of stations whose correlation with GPS is higher than +0.5 before considering ATML and NTOL effects (%)	Percentage of stations whose correlation with GPS is higher than +0.5 after considering ATML and NTOL effects (%)	Percentage of stations with WRMS reduced before considering ATML and NTOL effects (%)	Percentage of stations with WRMS reduced after considering ATML and NTOL effects (%)
GLDAS-A	30	51	78	88
GLDAS-B	34	53	82	89
MERRA-A	35.6	52	80	88
MERRA-B	41.8	55	88	89
NCEP-R-2	4	24	36	63

South America, southeast Asia, and those close to the Pacific Ocean. Note that although the SWE data above the latitude of 60.5 degree is included when modeling the displacement using the MERRA-B model, it has no advantage over the GLDAS-B model in reducing the WRMS of stations in Greenland.

MERRA-A and GLDAS-A also reduce the WRMS to a reasonable extent, although the WRMS reduction is not

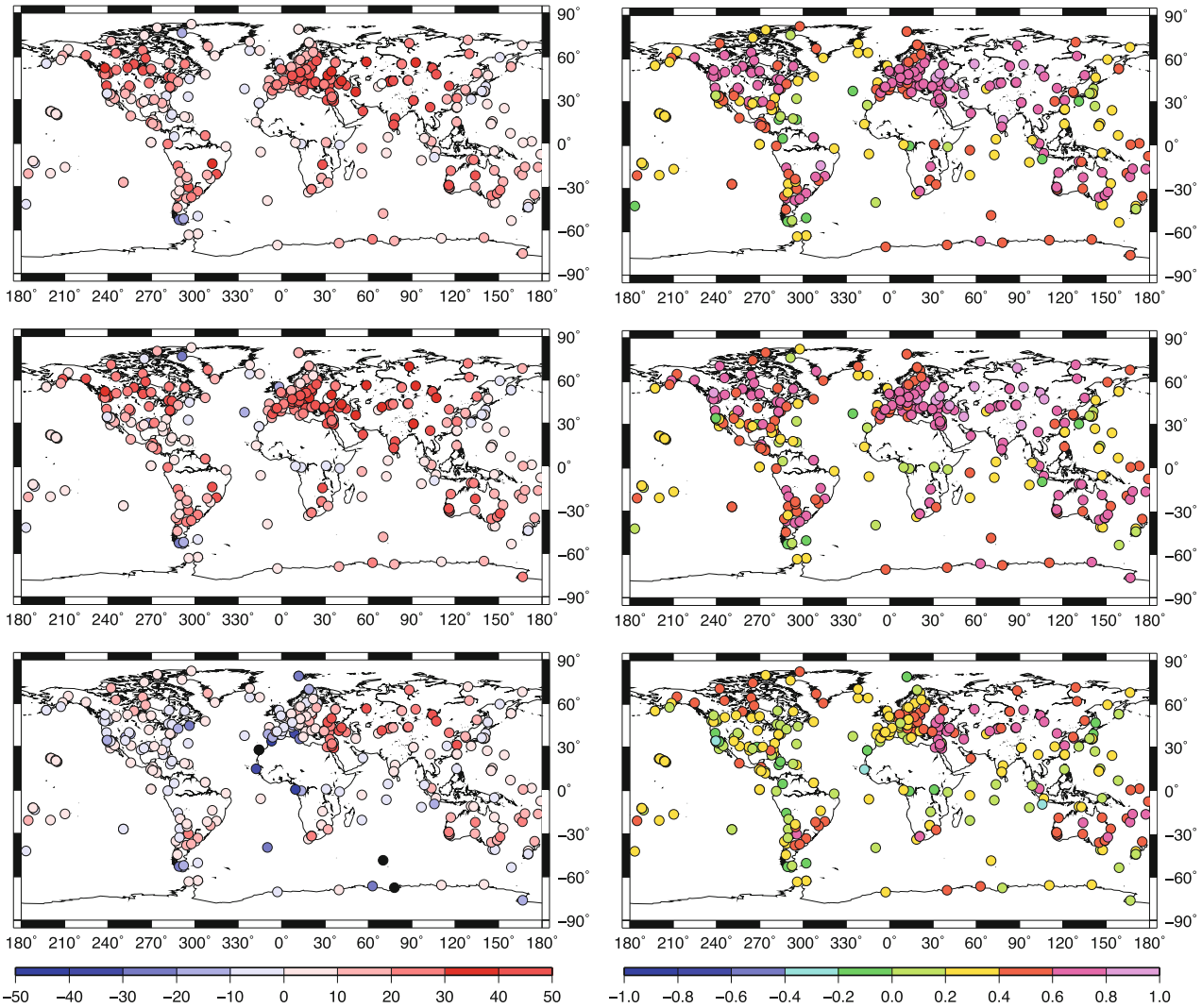

Fig. 5 Spatial distribution of the WRMS reduction rate using different CWS loading corrections (*left*) and their correlation with GPS height (*right*) after removing the ATML and NTOL effects. From *top to bottom* are GLDAS-B, MERRA-B and NCEP-R-2. The *black dots* in the figure indicate that the WRMS reduction for the station is smaller than the minimum value on the scale, while the *white dots* means the WRMS reduction is larger than the maximum value. Unit of the WRMS reduction is in %

as good as for the higher temporal resolution products. Compared with GLDAS and MERRA model, however, the NCEP-R-2 model could only reduce 36% of the stations' WRMS, and the biggest improvement is found mainly in Europe. This is even much worse than the NCEP-R-1 model (Jiang et al. 2013). Therefore, we conclude that the CWS data from both the GLDAS and MERRA products could be used for correcting the GPS height to some extent, among which the higher spatial resolution product MERRA does slightly better performance. This mainly due to the scientific and technical improvement of the MERRA-Land product itself. Under the same spatial resolution, the higher temporal resolution model could also improve its correlation with the weekly GPS height by about 2–6%, together with its performance in reducing the WRMS. Better fitting results would be expected when comparing the three-hourly or hourly CWS model with higher temporal resolution GPS height time series. Similar as the NCEP-R-1 model, the NCEP-R-2 model may also not be suitable in this kind of application.

Since ATML and NTOL may affect the comparison results (see Fig. 2), we recalculate the WRMS and the correlation coefficients after removing the ATML and the NTOL effects from the weekly GPS height. The left panels Fig. 5 show the WRMS results for GLDAS-B, MERRA-B and the NCEP-R-2 model, while the right panels show their correlation with the ATML and NTOL-removed GPS height. We also show some of the statistics of each CWS model in Table 2 for the ATML and NTOL removed results. We find that MERRA-B performs slightly better than GLDAS-B

in correcting the weekly GPS height, while MERRA-A and GLDAS-A rank the third and fourth respectively. The NCEP-R-2 model could also reduce the WRMS of 63% of the stations after removing the ATML and NTOL effects, especially for East Europe and central Asia.

Compared Fig. 5 with Fig. 4, we confirm that ATML and NTOL have a significant impact on the comparison between CWS model and the GPS height generally. After removing the ATML and NTOL effects, the correlation between each CWS model and the weekly GPS height improved by about 13–20% at most stations, and the WRMS reduction for most stations also improved by at least 10%, in particular for those located along coast or in the oceans. Hence, to make a more realistic comparison between CWS loading and GPS time series, the effects of ATML and NTOL would better be removed first.

4 Conclusions

We compare the weekly vertical surface displacements from five CWS models. We inter-compare the models with each other and then compare all the models with a set of weekly GPS height time series. We find that overall the higher spatial resolution MERRA products are better at correcting the weekly GPS height than the GLDAS products. This result is mainly due to the scientific and technical improvement of the MERRA-Land data itself. Under the same spatial resolution, the CWS models with higher temporal resolution performs slightly better than that with a coarser resolution by about 2–6%. We also confirm that removing the ATML and NTOL effects from the weekly GPS height would improve the correlation between CWS model and the GPS height by about 13–20% at most stations, and the WRMS reduction could also improve by at least 10%, especially for coastal and island stations.

We find that the one-hourly soil moisture and snow mass data from the improved MERRA-Land datasets is the most appropriate product for modeling vertical surface displacement by CWS variations. The three-hourly GLDAS data also does well in reducing the WRMS in the GPS height. Considering that the GLDAS products have a higher latency than the MERRA products, MERRA would be a better choice for modeling CWS surface displacements. Further work is still required to determine the reliability and precision of the CWS products. We confirm that the NCEP-R-2 data is also insufficient for applying this correction. Note that all these results are obtained using GPS coordinate time series obtained without considering the impacts of atmospheric tides and higher-order ionospheric delay, we claim that this is one of the limitations of this research. After the 2nd IGS reprocessing has been done, different conclusions may be drawn.

Until now, the GLDAS also provides 0.25 degree product from February 2, 2000 to the present. Due to this model's higher spatial resolution, better results would be expected if we use this type of product to predict surface displacement. Also, the recent reprocessed Jet Propulsion Laboratory (JPL) daily GPS coordinate time series with seasonal signal restored is available now.[11] The vertical loading displacement induced from the 3-hourly GLDAS and 1-hourly MERRA products should perform much better at correcting the daily GPS height time series than the most frequently used monthly CWS products.

Acknowledgements We thank the NASA and NOAA for making the MERRA-LAND, GLDAS and NCEP data freely available. Figures are plotted with the GMT and MATLAB software.

References

Blewitt G (2003) Self-consistency in reference frames, geocenter definition, and surface loading of the solid Earth. J Geophys Res 108(B2):2103. doi:10.1029/2002JB002082

Chen Q, van Dam T, Sneeuw N, Collilieux X, Weigelt M, Rebischung P (2013) Singular spectrum analysis for modeling seasonal signals from GPS time series. J Geodyn. doi:10.1016/j.jog.2013.05.005

Clarke P, Lavalle D, Blewitt G, van Dam T, Wahr J (2005) Effect of gravitational consistency and mass conservation on seasonal surface mass loading models. Geophys Res Lett 32(L08306):1–5. doi:10.1029/2005GL022441

van Dam T, Wahr J (1987) Displacements of the Earth's surface due to atmospheric loading: effects on gravity and baseline measurements. J Geophys Res 92(B2):1281–1286. doi:10.1029/JB092iB02p01281

van Dam T, Wahr J, Milly PCD, Shmakin AB, Blewitt G, Lavallée D, Larson KM (2001) Crustal displacements due to continental water loading. Geophys Res Lett 28(4):651–654. doi:10.1029/2000GL012120

van Dam T, Wahr J, Lavallée D (2007) A comparison of annual vertical crustal displacements from GPS and gravity recovery and climate experiment (GRACE) over Europe. J Geophys Res 112(B3):B03,404. doi:10.1029/2006JB004335

Dong D, Dickey JO, Chao Y, Cheng MK (1997) Geocenter variations caused by atmosphere, ocean and surface ground water. Geophys Res Lett 24(15):1867–1870. doi:10.1029/97GL01849

Dow JM, Neilan R, Rizos C (2009) The International GNSS Service in a changing landscape of global navigation satellite systems. J Geod 83:191–198. doi:10.1007/s00190-008-0300-3

Farrell WE (1972) Deformation of the Earth by surface loads. Rev Geophys 10(3):761–797. doi:10.1029/RG010i003p00761

Fritsche M, Döll P, Dietrich R (2012) Global-scale validation of model-based load deformation of the Earth's crust from continental watermass and atmospheric pressure variations using GPS. J Geodyn 59–60(0):133–142. doi:10.1016/j.jog.2011.04.001

Jiang W, Li Z, van Dam T, Ding W (2013) Comparative analysis of different environmental loading methods and their impacts on the GPS height time series. J Geod 1–17. doi:10.1007/s00190-013-0642-3

Kalnay E, Kanamitsu M, Kistler R, Collins W, Deaven D, Gandin L, Iredell M, Saha S, White G, Woollen J, Zhu Y, Chelliah M, Ebisuzaki W, Higgins W, Janowiak J, Mo K, Ropelewski C, Wang J, Leetmaa

[11] http://sideshow.jpl.nasa.gov/post/series.html.

A, Reynolds R, Jenne R, Joseph D (1996) The NCEP/NCAR 40-year reanalysis project. Bull Am Meteorol Soc 77(3):437–471. doi:10.1175/1520-0477(1996)077<0437:TNYRP>2.0.CO;2

Kanamitsu M, Ebisuzaki W, Woollen J, Yang Sk, Hnilo JJ, Fiorino M, Potter GL (2002) Ncep-doe amip-ii reanalysis (r-2). Bull Am Meteorol Soc 83(83):1631–1643. doi:http://dx.doi.org/10.1175/BAMS-83-11-1631

Rebischung P, Griffiths P, Ray J, Schmid J, Collilieux X, Garayt B (2012) IGS08:the IGS realization of ITRF2008. GPS Solutions 16:483–494. doi:10.1007/s10291-011-0248-2

Reichle RH (2012) The MERRA-Land Data Product. GMAO Office Note No. 3 (version 1.2), 38 pp

Reichle RH, Koster RD, De Lannoy GJM, Forman BA, Liu Q, Mahanama SPP, Tour A (2011) Assessment and enhancement of MERRA Land surface hydrology estimates. J Climate 24(24):6322–6338. doi:10.1175/JCLI-D-10-05033.1

Rui H (2011) README document for global land data assimilation system version 1 (GLDAS-1) products. http://disc.sci.gsfc.nasa.gov/services/grads-gds/gldas, GSFC online document, 34 pp

Tregoning P, Watson C, Ramillien G, McQueen H, Zhang J (2009) Detecting hydrologic deformation using GRACE and GPS. Geophys Res Lett 36(15):L15,401. doi:10.1029/2009GL038718

Wessel P, Smith WH (2013) The generic mapping tools technical reference and cookbook (version 4.5.11). https://www.soest.hawaii.edu/gmt/gmt/pdf/GMT_Docs.pdf, GMT online document, 250 pp

Impact of Time Variable Gravity on Annual Sea Level Variability from Altimetry

Saskia Esselborn, Tilo Schöne, and Sergei Rudenko

Abstract

This study investigates seasonal to interannual changes in regional sea level caused by the recent replacement of the geopotential model EIGEN-GL04S_annual by the model EIGEN-6S for the precise orbit determination of satellite altimeters. We have analysed the radial orbit components for the Envisat, ERS-2 and TOPEX missions originating from two orbit solutions processed at the GeoForschungsZentrum (GFZ). These orbits were computed almost identically except for the use of the two different geopotential models mentioned above. An alternative orbit solution for Envisat provided by the European Space Operations Centre based on the model EIGEN-6C has been analysed as well. Empirical Orthogonal Functions (EOF) of the detrended radial orbit differences have been applied to study the typical spatio-temporal scales. The dominant EOF modes for all orbit differences exhibit large-scale bipolar patterns with opposite phase suggestive of apparent shifts of the origins of the different orbit solutions. In case the geopotential model is replaced the detrended radial orbit differences for all three missions are dominated by annual oscillations. The spatial patterns of these annual oscillations are similar for all three missions, with the TOPEX patterns and the ERS-2/Envisat patterns being out of phase. The annual amplitude reaches 5 mm at its maxima which corresponds to up to ∼10% of the annual sea level signal itself for some locations. In addition, it accounts for annual changes of the height gradient between the two maxima of the first EOF-patterns of up to 1 cm with inverse changes for TOPEX and ERS-2/Envisat.

Keywords

Altimetry • Annual cycle • Orbit errors • Precise orbit determination • Sea level • Time variable gravity

1 Introduction

Since the start of the first radar altimetry mission precise orbit determination (POD) has been a basic prerequisite for the derivation of accurate sea level records (Tapley et al. 1994). Since the 1990s the accuracy of orbit solutions has been improved from about 10 cm for the radial error to nowadays better than 1 cm (Bertiger et al. 2010). One of the main drivers for this progress has been the increased knowledge of the Earth's gravity field – brought forward especially by the spaceborne gravimetric CHAMP and GRACE missions – as

S. Esselborn (✉) • T. Schöne
GFZ German Research Centre for Geosciences, Telegrafenberg, D-14473 Potsdam, Germany
e-mail: Saskia.Esselborn@gfz-potsdam.de; tschoene@gfz-potsdam.de

S. Rudenko
GFZ German Research Centre for Geosciences, Telegrafenberg, D-14473 Potsdam, Germany

Technische Universität Berlin, Straße des 17. Juni 135, D-10623 Berlin, Germany
e-mail: rudenko@gfz-potsdam.de

© Springer International Publishing Switzerland 2015

C. Rizos, P. Willis (eds.), *IAG 150 Years*, International Association of Geodesy Symposia 143,
DOI 10.1007/1345_2015_103

well as improvements in the satellite tracking systems, the terrestrial reference frame realization, and force models. Based on enhanced orbit processing standards (including improved geopotential models) orbit reprocessing for multiple missions has been and is performed, e.g., for ERS-1 and ERS-2 in the ESA project REAPER (Rudenko et al. 2012) and more recently for TOPEX, Jason-1 and Jason-2 in the framework of the NASA Making Earth Science Data Records for Use in Research Environments (MEaSUREs) Program (Lemoine et al. 2011). For the most recent multi-mission reprocessing effort, within the ESA's Climate Change Initiative Sea Level project (Larnicol et al. 2013; Ollivier et al. 2012), the POD is based on the time variable geopotential model EIGEN-6S (Förste et al. 2011). EIGEN-6S is a time variable geopotential model that accounts for semi-annual, annual and secular variations of the geopotential, which stem from the mass redistribution in the Earth system caused by processes as atmospheric and hydrological variations, ocean circulation changes, melting of ice sheets and glacial isostatic adjustment (Lemoine et al. 2010). The previous POD processing standards (Cerri et al. 2010) were based on the stationary geopotential model EIGEN-GL04S_annual (Lemoine et al. 2007) which includes annual and semi-annual components, but no drift terms of the geopotential coefficients.

The substitution of the geopotential model EIGEN-GL04S_annual by the EIGEN-6S model in the POD processing leads to considerable changes of the radial orbit component. Two time series of the difference of the radial orbit components based on these two geopotential models at two locations with strong signal (32°S/42°E east of Durban, and 15°N/155°W south of Hawaii) are shown in Fig. 1. The most striking features are the opposing trends of almost 3 mm/year at those two locations. This phenomenon has been investigated in detail by Lemoine et al. (2011), Zelensky et al. (2012) and Rudenko et al. (2014) and can be related to the application or omission of the trends for the geopotential coefficients. In addition, annual signals with amplitudes of about 0.5 cm are superimposed to the trends at these two specific locations.

Seasonal differences between the radial components from different orbit solutions have been investigated by Melachroinos et al. (2013). In their analysis most of the observed differences could be explained by errors in the origin of the tracking station network. However, some of the seasonal differences seemed to be related to the time variable geopotential models used. The present paper studies the spatio-temporal characteristics of the differences between the radial components of orbits based on the geopotential models EIGEN-GL04S_annual and EIGEN-6S for TOPEX, ERS-2, and Envisat for seasonal timescales. The goal is to track potential temporal inhomogeneities between different missions related to the substitution of the model EIGEN-GL04S_annual by the model EIGEN-6S for the POD. Even though the detrended radial orbit differences are only of the order of 0.5 cm they might introduce spurious signals when assimilating the sea level data in ocean circulation models depending on their spatial characteristics.

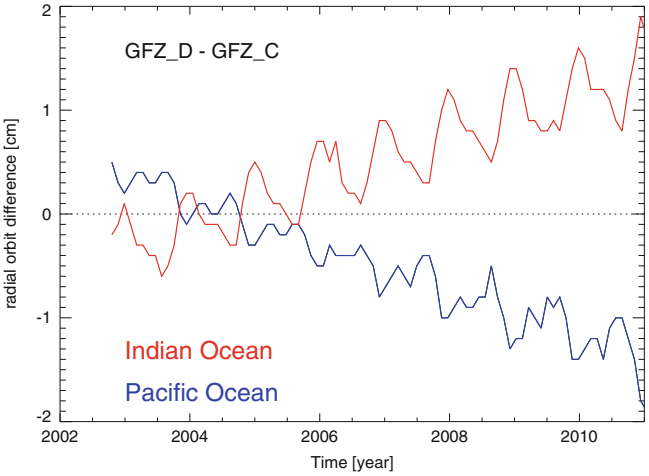

Fig. 1 Time series of Envisat radial orbit differences for two sites located at areas of high RMS: 32°S/42°E and 15°N/155°W (positions marked in Fig. 2). Both orbits originate from GFZ and differ only by the geopotential field used (EIGEN-GL04S_annual and EIGEN-6S). These time series are equivalent to sea level changes when updating the orbit model

2 Data and Analysis Methods

In order to quantify the changes in sea level height arising from the substitution of the geopotential model for the POD we have analyzed the differences between the radial orbit components of different orbit solutions. The radial orbit components map directly to the derived sea surface heights. We use two different orbit solutions for each of the TOPEX, ERS-2 and Envisat missions computed at GFZ which span the periods 3/1993 to 5/2004 (TOPEX), 5/1995 to 6/2003 (ERS-2) and 10/2002 to 12/2010 (Envisat). These orbit solutions were computed at the GeoForschungsZentrum (GFZ) and differ by the underlying geopotential model only. The orbit solutions denoted as GFZ_D are based on the time variable geopotential model EIGEN-6S which is part of the Jason-2 data processing standard GDR-D (OSTM/Jason-2 user handbook, 2011). The other orbit solutions denoted as GFZ_C are based on the model EIGEN-GL04S_annual which corresponds to the previous processing standard geophysical data record-C(GDR-C) (Cerri et al. 2010). The geopotential model EIGEN-GL04S_annual is a stationary model, i.e. a static model augmented by annual and semi-annual variations of the geopotential coefficients for degree and order 2–50. These seasonal terms were derived from

Table 1 List of the main models used to compute GFZ_C, GFZ_D and ESOC_D orbits

Parameter/orbit	GFZ_C	GFZ_D	ESOC_D
DORIS station coordinates	DPOD2008 (Willis et al. 2009)		
SLR station coordinates	ITRF2008 (Altamimi et al. 2011)		
Polar motion and UT1	IERS EOP 08 C04 series with IERS 2003 daily and sub-daily corrections		
Static gravity field	EIGEN-GL04S_annual (Lemoine et al. 2007)	EIGEN-6S (Förste et al. 2011)	EIGEN-6C (Shako et al. 2014)
Time varying gravity field	– Annual and semi-annual variations (d/o 2–50 terms)	– Annual and semi-annual variations (d/o 2–50 terms) – Constant linear drift (d/o 2–50 terms) – sine correction for $C_{2,0}$ (18.6-year)	– Annual and semi-annual variations (d/o 2–50 terms) – Constant linear drift (d/o 2–50 terms)
Non-tidal atmospheric gravity	ECMWF 6-hourly fields up to degree and order 50 (Dobslaw et al. 2013)		AGRA service at GSFC, up to d/o 20
Solid Earth tides	IERS Conventions (2010)		IERS Conventions (2004)
Ocean tides	EOT10A (Mayer-Gürr et al. 2012), all constituents up to degree and order 50		FES2004 (Letellier 2005), all principal constituents up to d/o 50
Third bodies	Sun, Moon, all major planets (DE-421) (Folkner et al. 2008)		Sun, Moon, all major planets (DE-405) (Standish 1998)
Radiation pressure model	GFZ EPOS-OC box/wing model		ANGARA model (Doornbos et al. 2002)
Earth radiation	Knocke and Ries (1987)		ANGARA model (Doornbos et al. 2002)
Atmospheric density model	MSIS-86 (Hedin 1987)		MSIS-90 (Hedin 1991)
Drag coefficients	Estimated eight times per day		Estimated ten times per day
Along-track and cross-track empirical accelerations	Estimated 1–2 times per day (once per revolution)		Estimated once per day (once per revolution)
Software	EPOS-OC (Zhu et al. 2004, ver. 06.69)		Napeos 3.6 2011

2 years of LAGEOS and GRACE data. EIGEN-6S is the more recent model which incorporates GRACE data as well as GOCE data for the mean field. Semi-annual and annual components as well as trends for the geopotential coefficients for degree and order 2–50 were derived from 8 years of GRACE and LAGEOS data. The trend terms were included in EIGEN-6S to account for decadal and secular changes in the mass distribution of the Earth system as caused by decadal climate variability, melting of ice sheets, and glacial isostatic adjustment. For the GFZ_D orbit solutions an additional nodal correction for the $C_{2,0}$ spherical harmonic term with an 18.6 years period has been applied. To investigate the changes to be expected when performing the POD with the same geopotential model but slightly different models for other perturbation forces, parameterization and a different software package, an additional orbit solution for Envisat provided by the European Space Operations Centre ESOC (Otten et al. 2010) is analysed for the period 5/2002 to 12/2009. This orbit solution denoted as ESOC_D is based on the geopotential model EIGEN-6C, which is almost identical to EIGEN-6S at the spatial scales relevant here. A list of the main models exploited to derive the orbits used in this study is given in Table 1. A comprehensive description of the GFZ orbits is given in Rudenko et al. (2014). All orbit solutions analysed here are integrated in the GFZ's Altimeter Data System (ADS Central) (Schöne et al. 2010).

The differences of the radial orbit components at the time of the altimetry measurement (1 Hz, ~6.7 km on ground) are calculated and interpolated to a 1°×1° grid for every 35 day cycle for ERS-2 and Envisat and for every 10 day cycle for TOPEX. Since we are aiming at seasonal to interannual time scales the resulting time series of gridded height differences has been detrended. Typical spatio-temporal patterns are calculated using decomposition to Empirical Orthogonal

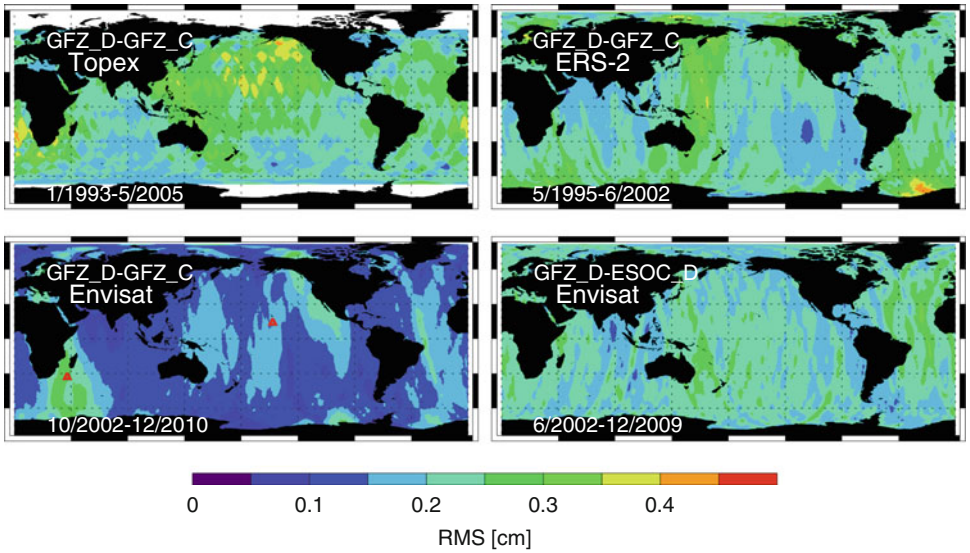

Fig. 2 RMS of the detrended radial differences between GFZ_C and GFZ_D orbits for ERS-2, TOPEX and Envisat. The RMS of the Envisat —ESOC_D minus GFZ_D— orbit differences is at the *lower right*. GFZ_D and ESOC_D orbits are based on EIGEN-6S, GFZ_C orbits are based on EIGEN-GL04S_annual. The positions of the two time series in Fig. 1 are marked by *red triangles* in the *lower left panel*

Functions (EOF) (Hannachi et al. 2007). By solving for the eigenvectors of the covariance matrix orthogonal basis functions are found that minimize the residual variance. For each spatial pattern the principal component (PC) is derived which describes the temporal fluctuations of the corresponding EOF-pattern. In order to identify recurrent signals in the radial orbit differences a spectral analysis of the two leading PCs is performed.

3 Results

To study the size and the spatial characteristics of the orbit differences their Root Mean Square (RMS) has been calculated. The regional distribution of the RMS values of the detrended radial orbit differences (GFZ_D minus GFZ_C) for all three missions is shown in Fig. 2. The regional RMS values reach up to 4 mm which corresponds to up to 10% of the local sea level signal. The strongest RMS value of the orbit differences can be observed for the TOPEX orbits, the smallest one occurs for the Envisat orbits. The RMS values of the radial differences between the GFZ_D and the ESOC_D orbits for Envisat amount for around 2 mm – about the same order of magnitude as the RMS values for the GFZ orbit differences. That demonstrates that even after detrending the replacement of the geopotential model for the POD still causes orbit changes of the same magnitude as the POD based on slightly different models, parameterization, and another software package.

To gain insight into the typical spatio-temporal characteristics of the radial orbit differences for the three missions we have applied classical EOF analysis. The two leading EOF-patterns and the corresponding PC time series are shown in Fig. 3 for TOPEX and ERS-2 and in Fig. 4 for Envisat. Between 40% and 70% of the total variance of the radial orbit differences can be explained by the first two modes which are all large-scale and hint to apparent shifts between the origins of the orbit solutions. The first EOF of the GFZ_D minus GFZ_C orbits is similar for all three missions and shows a pronounced east/west gradient with quasi-annual behavior with maximum peak to peak values of almost 1 cm (locally up to ∼10% of annual sea level signal). The pattern derived from the TOPEX orbits seems to be opposite in phase to the patterns derived from the ERS-2 and Envisat orbits. Note, that these patterns resemble the patterns of the trend differences that have been eliminated from the data before (not shown). The GFZ_D minus ESOC_D radial orbit differences exhibit large-scale variability as well, but none of the corresponding PCs shows a pronounced annual signal.

The results of the mean of the spectral analysis of the leading two PCs for each set of orbit differences are shown in Fig. 5. The PCs for the GFZ_D minus GFZ_C orbits show distinct peaks for periods around 180 and 365 days for all three missions. The PCs for the GFZ_D minus ESOC_D Envisat radial orbit differences contain increased power for the temporal ranges between 70 and 130 days, between 180 and 365 days and around 3 years. The most plausible source for the increased power at the periods between 70 and 130

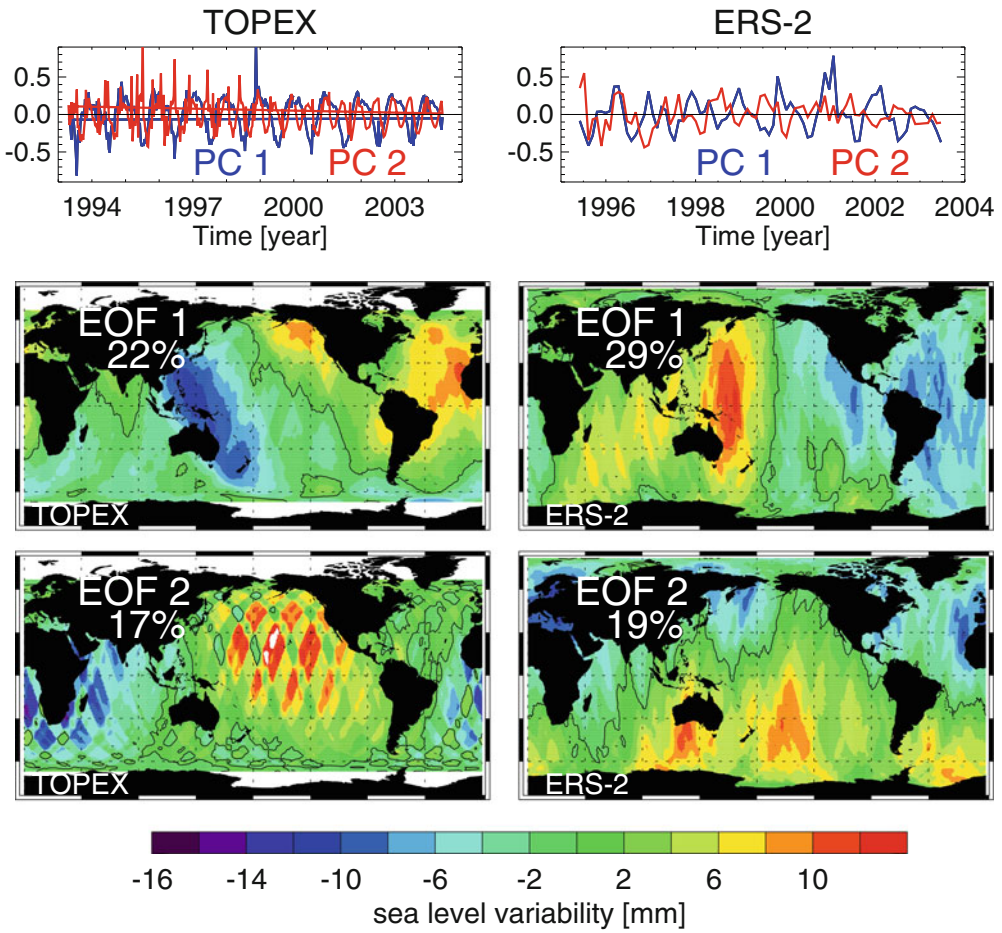

Fig. 3 The two dominant PCs (*top*) and EOFs (*bottom*) of the radial orbit differences GFZ_D minus GFZ_C (*left*: TOPEX, *right*: ERS-2)

days are differences between the used ocean tide models (ESOC: FES2004 and GFZ: EOT10A). Since the draconitic period for the sun-synchronous Envisat is 365 days, the peaks at periods of 180 and 365 days are most probably related to differences in the modeling of the solar radiation pressure for these two solutions.

4 Discussion

The replacement of the geopotential model EIGEN-GL04S_annual by the model EIGEN-6S in the POD processing leads to large-scale changes of the radial orbit component which are in the order of several millimeters. The annual amplitude of the orbit differences reaches up to 5 mm. Its patterns are in phase opposition between TOPEX and ERS-2/Envisat. From the analyses performed here no statement can be made whether the semi-annual and annual components of EIGEN-GL04S_annual or of EIGEN-6S lead to better orbits solutions. The annual and semi-annual components from EIGEN-6S are based on more data and hence are more reliable than the ones of the EIGEN-GL04S_annual. However, it remains an open question whether annual and semi-annual components of the geopotential will stay constant over the time-frame of decades. They are caused by seasonal mass changes in the hydrosphere and the cryosphere which are prone to interannual to decadal variability. Strong seasonal mass changes of continental water storage are located at the equatorial band. It seems to be plausible that changes in these regions might give rise to large-scale shifts which are oriented along the East–West axis. It might be possible to identify the most reliable orbit solution by checking the consistency between the annual sea level signal from TOPEX on the one hand and ERS-2/Envisat on the other hand at regions with maximum annual signal of the radial orbit differences.

From the EOF-analyses there is a strong indication for apparent shifts between the origins of the orbit solutions. The trend analyses and multi-mission crossover analyses by Rudenko et al. (2014) give as well strong evidence for the existence of such apparent shifts in the origins of the orbits. We can only speculate about the causes. Errors, especially if they are systematic, of the satellite tracking data together

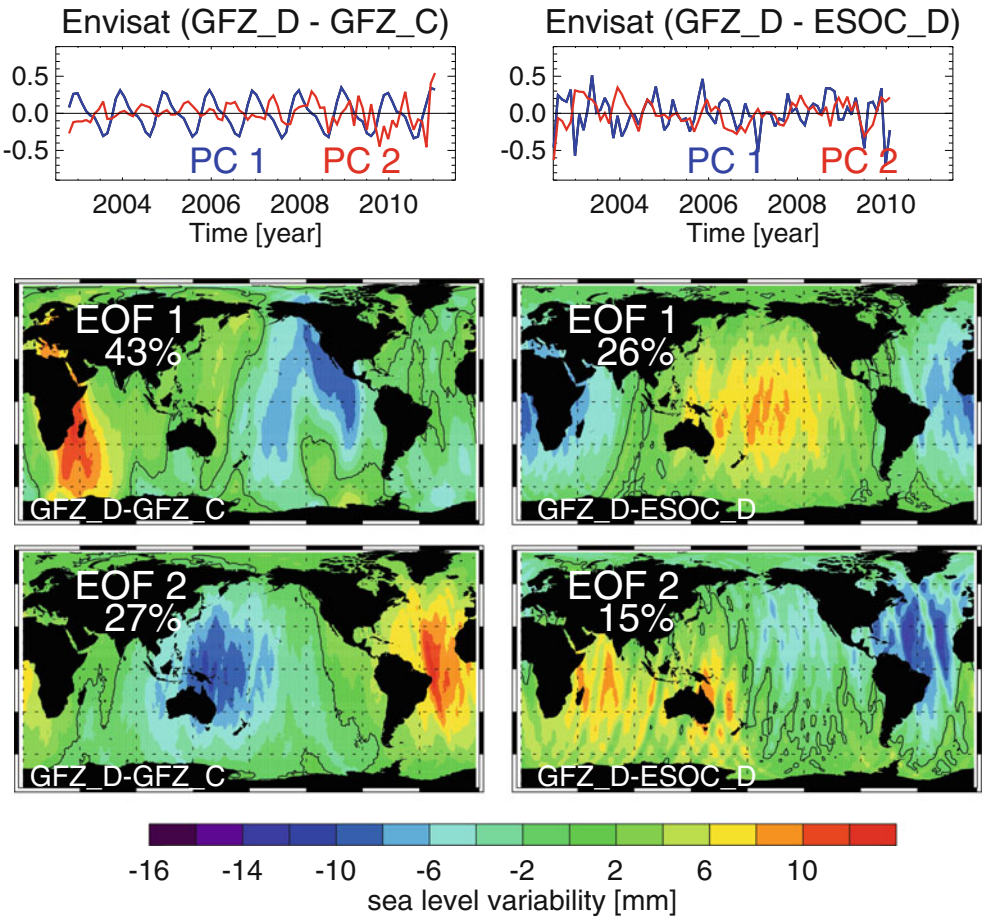

Fig. 4 The two dominant PCs (*top*) and EOFs (*bottom*) of the radial orbit differences for Envisat (*left*: GFZ_D minus GFZ_C, *right*: GFZ_D minus ESOC_D. PC is in blue, PC2 in red.)

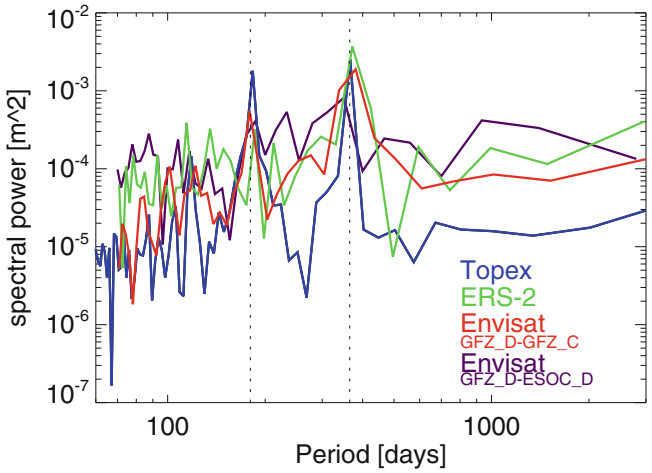

Fig. 5 Mean spectral power over the first two PCs of radial orbit differences for Envisat, TOPEX and ERS-2. Periods of 180 and 365 days are marked by *dashed lines*

with remaining errors of the geopotential models will probably result in the apparent shifts of the orbit origins. The degree to which the orbit reacts to these errors is complex and dependent on the orbit solution strategy. GPS-based reduced dynamic orbit solutions are less prone to error in the dynamic models and more prone to the errors of the tracking observations (Fu and Haines 2013). However, no GPS observations are available for ERS-2, Envisat and very few for TOPEX. Inclusion of annual centre of mass variations to the reference station coordinates can improve orbit solutions as well (Melachroinos et al. 2013).

5 Conclusions

We investigated the changes in regional sea level caused by the recent replacement of the geopotential model EIGEN-GL04S_annual by the model EIGEN-6S for the POD with focus on seasonal frequencies. Therefore, we have analysed orbit heights for Envisat, ERS-2 and TOPEX from two GFZ orbit solutions. Those were computed based on the same models and parametrisation with the exception that the two above-mentioned geopotential models were used. To investigate the changes to be expected when basing the POD on the same geopotential model but slightly different models for other perturbation forces, parameterizations and a different software package, an additional orbit solution for Envisat provided by ESOC has been analysed as well.

Since this paper is focusing on seasonal changes the time series of radial orbit differences have been detrended. An EOF-analysis has been applied to study the typical spatio-temporal scales. The dominant EOF modes for all orbit differences exhibit large-scale bipolar patterns with opposite phase which are suggestive of apparent shifts between the origins of the different orbit solutions. For the replacement of the geopotential model – as done for the GFZ solutions – the first EOF-modes of the radial orbit differences are similar for all three missions and show predominantly annual oscillations. One center of the corresponding EOF-pattern is over the Western Pacific and the Indian Ocean, the other over the Eastern Pacific and the Atlantic Ocean. While the phases of the ERS-2 and Envisat patterns are very close to each other, the TOPEX derived pattern has a phase shift of about 180° relative to them. The annual amplitude of the radial orbit differences reaches 5 mm at the maxima. Depending on the location this corresponds to up to ∼10% of the annual sea level signal itself. In addition, it accounts for annual changes of the height difference between the two centers of the first EOF-patterns of up to 10 mm with inverse changes for TOPEX and ERS-2/Envisat. In contrast, the patterns derived from the differences between the ESOC and the GFZ orbit solutions based on basically the same geopotential model have their power distributed over a wide range of frequencies.

Even though the signals are quite small compared to the sea level variability, they are predominantly coherent on large spatial scales. Therefore, they might introduce spurious signals when assimilating the derived sea level data in ocean circulation models. In addition, inhomogeneities might be introduced when merging sea level data from different missions. From the analyses presented here it is not possible to decide which orbit solution performs best. An evaluation of the annual components of the radial orbit components for various time spans and based on different geopotential models is hence needed in order to distinguish between inter-ocean sea level changes and orbit error. Even though the signals are quite small it might be possible to validate them by inter-mission comparisons between TOPEX and ERS-2/Envisat.

Acknowledgements We thank the anonymous reviewers for their valuable comments. We thank ESOC for providing Envisat solution v8 orbits (ftp://dgn6.esoc.esa.int/envisat/sol8/envisat.sol8.txt). This work was partly supported by the European Space Agency within the Climate Change Initiative Sea Level Project, by the Helmholtz Climate Initiative REKLIM and by DFG within the project UHR-GravDat.

References

Altamimi Z, Collilieux X, Métivier L (2011) ITRF2008: an improved solution of the international terrestrial reference frame. J Geod 85:457–473. doi:10.1007/s00190-011-0444-4

Bertiger W, Desai SD, Dorsey A, Haines BJ, Harvey N, Kuang D, Sibthorpe A, Weiss JP (2010) Sub-centimeter precision orbit determination with GPS for ocean altimetry. Mar Geod 33:363–378. doi:10.1080/01490419.2010.487800

Cerri L, Berthias JP, Bertiger WI, Haines BJ, Lemoine FG, Mercier F, Ries JC, Willis P, Zelensky NP, Ziebart M (2010) Precision orbit determination standards for the Jason series of altimeter missions. Mar Geod 33:379–418. doi:10.1080/01490419.2010.488966

IERS Conventions 2003 (2004). Dennis D. McCarthy and Gérard Petit (eds). IERS technical note no. 32, Verlag des Bundesamts für Kartographie und Geodäsie, Frankfurt am Main, ISBN 3-89888-884-3

Dobslaw H, Flechtner F, Bergmann-Wolf I, Dahle C, Dill R, Esselborn S, Sasgen I, Thomas M (2013) Simulating high-frequency atmosphere-ocean mass variability for de-aliasing of satellite gravity observations: AOD1B RL05. J Geophys Res Ocean 118:3704–37011. doi:10.1002/jgrc.20271

Doornbos E, Scharroo R, Klinkrad H, Zandbergen R, Fritsche B (2002) Improved modelling of surface forces in the orbit determination of ERS and ENVISAT. Can J Remote Sens 28:535–543. doi:10.5589/m02-055

Folkner WM, Williams JG, Boggs DH (2008) The planetary and lunar ephemeris DE 421. IPN Progress Report 42–178

Förste C, Bruinsma S, Shako R, Marty J-C, Flechtner F, Abrykosov O, Dahle C, Lemoine J-M, Neumayer K-H, Biancale R (2011) EIGEN-6 – a new combined global gravity field model including GOCE data from the collaboration of GFZ Potsdam and GRGS Toulouse. Geophys Res Abstr 13: EGU2011-3242-2 (EGU General Assembly. Conference Abstracts, p 3242)

Fu L-L, Haines BJ (2013) The challenges in long-term altimetry calibration for addressing the problem of global sea level change. Adv Space Res 51:1284–1300. doi:10.1016/j.asr.2012.06.005

Hannachi A, Jolliffe IT, Stephenson DB (2007) Empirical orthogonal functions and related techniques in atmospheric science: a review. Int J Climatol 27:1119–1152. doi:10.1002/joc.1499

Hedin AE (1987) MSIS-86 thermospheric model. J Geophy Res Space Phys 92:4649–4662. doi:10.1029/JA092iA05p04649

Hedin AE (1991) Extension of the MSIS thermosphere model into the middle and lower atmosphere. J Geophys Res 96:1159–1172. doi:10.1029/90JA02125

Knocke P, Ries J (1987) Earth radiation pressure effects on satellites. Technical Memorandum CSR-TM-87-01. Center for Space Research, the University of Texas at Austin, USA

Larnicol G, Cazenave A, Faugère Y, Ablain M, Johannessen J, Stammer D, Timms G, Knudsen P, Cipolini P, Roca M, Rudenko S, Fernandes J, Balmaseda M, Guinle T, Benveniste J (2013) ESA sea level climate change initiative. http://www.esa-sealevel-cci.org/webfm_send/123. Accessed Oct 2013

Lemoine J-M, Bruinsma S, Loyer S, Biancale R, Marty J-C, Perosanz F, Balmino G (2007) Temporal gravity field models inferred from GRACE data. Adv Space Res 39:1620–1629. doi:10.1016/j.asr.2007.03.062

Lemoine FG, Zelensky NP, Chinn DS, Pavlis DE, Rowlands DD, Beckley BD, Luthcke SB, Willis P, Ziebart M, Sibthorpe A, Boy JP, Luceri V (2010) Towards development of a consistent orbit series for TOPEX, Jason-1, and Jason-2. Adv Space Res 46:1513–1540. doi:10.1016/j.asr.2010.05.007

Lemoine F, Zelensky NP, Melachroinos S, Chin DS, Beckley BD, Rowlands DD, Luthcke SB (2011) GSFC OSTM (Jason-2), Jason-1 & TOPEX POD Update, OSTST Meeting, San Diego. http://www.aviso.oceanobs.com/fileadmin/documents/OSTST/2011/oral/02_Thursday/Splinter%203%20POD/03%20rev%20Lemoine_etal_SWT2011_v01.pdf. Accessed Oct 2013

Letellier T (2005) Etude des ondes de marée sur les plateaux continentaux. These doctorale, Universite de Toulouse III, Ecole Doctorale des Sciences de l'Univers, de l'Environnement et de l'Espace, p 237

Mayer-Gürr T, Savcenko R, Bosch W, Daras I, Flechtner F, Dahle C (2012) Ocean tides from satellite altimetry and GRACE. J Geodyn 59–60:28–38. doi:10.1016/j.jog.2011.10.009

Melachroinos SA, Lemoine FG, Zelensky NP, Rowlands DD, Luthcke SB, Bordyugov O (2013) The effect of geocenter motion on Jason-2 orbits and the mean sea level. Adv Space Res 51:1323–1334. doi:10.1016/j.asr.2012.06.004

Ollivier A, Faugere Y, Picot N, Ablain M, Femenias P, Benveniste J (2012) Envisat ocean altimeter becoming relevant for mean sea level trend studies. Mar Geod 35:118–136. doi:10.1080/01490419.2012.721632

Otten M, Flohrer C, Springer T, Dow J (2010) DORIS processing at the European Space Operations Centre. Adv Space Res 46:1606–1613. doi:10.1016/j.asr.2010.04.024

Rudenko S, Otten M, Visser P, Scharroo R, Schöne T, Esselborn S (2012) New improved orbit solutions for the ERS-1 and ERS-2 satellites. Adv Space Res 49:1229–1244. doi:10.1016/j.asr.2012.01.021

Rudenko S, Dettmering D, Esselborn S, Schöne T, Förste C, Lemoine J-M, Ablain M, Alexandre D, Neumayer K-H (2014) Influence of time variable geopotential models on precise orbits of altimetry satellites, global and regional mean sea level trends. Adv Space Res. doi:10.1016/j.asr.2014.03.010

Schöne T, Esselborn S, Rudenko S, Raimondo J-C (2010) Radar altimetry derived sea level anomalies – the benefit of new orbits and harmonization. In: Flechtner FM, Gruber T, Güntner A et al (eds) System earth via geodetic-geophysical space techniques. Springer, Berlin, pp 317–324

Shako R, Förste C, Abrikosov O, Bruinsma S, Marty J-C, Lemoine J-M, Flechtner F, Neumayer H, Dahle C (2014) EIGEN-6C: a high-resolution global gravity combination model including GOCE data. In: Flechtner F, Sneeuw N, Schuh W-D (eds) Observation of the system earth from space - CHAMP, GRACE, GOCE and future missions. Springer, Berlin, pp 155–161. doi:10.1007/978-3-642-32135-1

Standish EM (1998) JPL planetary and lunar ephemerides, DE405/LE405, JPL IOM 312.F-98-048

Tapley BD, Ries JC, Davis GW, Eanes RJ, Schutz BE, Shum CK, Watkins MM, Marshall JA, Nerem RS, Putney BH, Klosko SM, Luthcke SB, Pavlis D, Williamson RG, Zelensky NP (1994) Precision orbit determination for TOPEX/POSEIDON. J Geophys Res 99:24383–24404. doi:10.1029/94JC01645

Willis P, Ries JC, Zelensky NP, Soudarin L, Fagard H, Pavlis EC, Lemoine FG (2009) DPOD2005: an extension of ITRF2005 for precise orbit determination. Adv Space Res 44:535–544. doi:10.1016/j.asr.2009.04.018

Zelensky N, Lemoine FG, Beckley BD, Chinn DS, Melachroinos S, Luthcke SB, Mitchum G, Bordyugov O (2012) Improved modeling of time variable gravity for altimeter satellite POD., OSTST 2012, Venice. http://www.aviso.oceanobs.com/fileadmin/documents/OSTST/2012/posters/Zelensky_TVG_modelling_for_POD.pdf. Accessed Jan 2014

Zhu S, Reigber C, König R (2004) Integrated adjustment of CHAMP, GRACE, and GPS data. J Geod 78:103–108. doi:10.1007/s00190-004-0379-0

Development of a Combination Procedure for Celestial Reference Frame Determination

A. Iddink, T. Artz, and A. Nothnagel

Abstract

The currently existing realizations of the International Celestial Reference System (ICRS), the International Celestial Reference Frame 1 (ICRF1) and ICRF2, are based on solutions estimated by one VLBI group. In contrast, the International Terrestrial Reference Frame (ITRF) is based on a multi-technique combination with contributions from different geodetic space techniques. Furthermore, these individual technique-specific solutions are generated in an intra-technique combination. To overcome the shortcomings of the past ICRF determination, one of the main goals for the upcoming realizations of the ICRS and ITRS is an entirely consistent and simultaneous computation of both frames. This includes inter- as well as intra-technique combinations.

In this paper, a concept for the generation of a VLBI intra-combined CRF is shown. Focusing on consistency between different VLBI solutions is the first necessary step before passing on to multiple space techniques. The requirements, difficulties and individual steps of the intra-technique combination procedure are explained and highlighted. Furthermore, the concept of a combination software with several special features is illustrated. These features will become indispensable for the next ICRF and in any future investigations. Preliminary results confirm the proper functioning of the combination procedure and the corresponding software developed at the Institute of Geodesy and Geoinformation (IGG).

Keywords

Datum-free normal equations • ICRF • Intra-technique combination • VLBI

1 Introduction

Presently, the two existing fundamental frames, the International Terrestrial Reference Frame (ITRF) and the International Celestial Reference Frame (ICRF), are generated by various institutions and are based on different input data.

The ITRF is computed by an inter-technique combination, based on contributions from the geodetic space techniques Global Navigation Satellite Systems (GNSS), Satellite Laser Ranging (SLR), Doppler Orbitography and Radiopositioning Integrated by Satellite (DORIS), and Very Long Baseline Interferometry (VLBI). Each of these geodetic space techniques complement each other in order to overcome the technique-specific shortcomings and to profit from the advantages of the individual technique. Moreover, these individual solutions are again generated in intra-technique combinations of different analysis centers (ACs) (see e.g., Böckmann et al. 2010a; Kouba 2009; Pavlis et al. 2009; Willis et al. 2010).

A. Iddink (✉) • T. Artz • A. Nothnagel
Institute of Geodesy and Geoinformation, University of Bonn, Nussallee 17, D-53115 Bonn, Germany
e-mail: aiddink@uni-bonn.de; artz@igg.uni-bonn.de; nothnagel@uni-bonn.de

© Springer International Publishing Switzerland 2015

C. Rizos, P. Willis (eds.), *IAG 150 Years*, International Association of Geodesy Symposia 143,
DOI 10.1007/1345_2015_22

In contrast, the previous realizations of the ICRS, the ICRF1 and ICRF2 (e.g., Fey et al. 2009), are single monolithic solutions generated by the VLBI group at the Goddard Space Flight Center (GSFC) using the Calc/Solve software package. Thus, the ICRF2 is only consistent to the GSFC specific TRF, which is aligned with the VLBI Terrestrial Reference Frame 2008 (VTRF2008) (Böckmann et al. 2010b), and corresponding Earth Orientation Parameters (EOPs).

Consequently, the previous realizations of the ICRS and ITRS, as well as their related EOP series are not fully consistent. To overcome this shortcoming, both frames should be estimated simultaneously and entirely consistent in the upcoming realizations. This includes also a simultaneous estimation of the EOP series, due to the fact that the EOPs are the direct link between both frames.

VLBI is the unique geodetic space technique which provides source parameters for the CRF determination. Presently, only the TRF and the corresponding EOPs are estimated in a rigorous VLBI intra-technique combination. In several studies it has already been shown that the use of this intra-technique combination in the context of TRF and EOPs estimations improves the stability and robustness of the results in comparison to single solutions (Böckmann et al. 2010b). By adding source parameters to the rigorous intra-technique combination process, these benefits are also exploited for the CRF combination. The new approach including source positions in the VLBI intra-technique combination enables the computation of a fully consistent VLBI output for EOPs, station coordinates and source positions.

The proposed sequence of operations can be summarized as follows:

1. VLBI solutions of several ACs containing CRF, EOP and TRF parameters

   Input: Raw VLBI observables
   Output: Session-wise datum-free VLBI normal equation systems

2. VLBI intra-technique combination for CRF, EOP and TRF

   Input: Session-wise datum-free VLBI normal equation systems
   Output: Complete VLBI normal equation system with all CRF, EOP and TRF components

3. inter-technique combination of VLBI data with GNSS, SLR and DORIS data

   Input: Complete VLBI Normal equation system with all CRF, EOP and TRF components; idem for the other techniques and their corresponding components
   Output: Consistent CRF, EOP and TRF solution

In this paper we focus on the consistency within the VLBI intra-technique combination as a first step towards upcoming ICRS and ITRS realizations.

2 The Combination Procedure

2.1 Process and Data Characteristics

Basically, a rigorous combination of contributions from different ACs or geodetic space techniques can be performed at three different levels: At the level of solutions, normal equations or observation equations. Considering the goal, that we want to achieve consistency within the VLBI intra-technique combination, the combination at the level of datum-free normal equation is the most obvious strategy. At this level of combination, it is guaranteed that the contributions are not distorted by any constraints before combining them. The underlying datum for TRF and CRF can be applied during the combination process. Consequently it can be ensured that the same datum reference frames are applied and an identical datum is used in the whole process for all input series. Even more important is that using this combination strategy, the full variance-covariance information of all parameters and all individual input contributions is rigorously transferred. In the subsequent step of the inter-technique combination, the full variance-covariance is then also available which is another advantage of the concept. Compared to the combination at the level of observations the size of the data sets is essentially smaller. This type of combination would require software packages suitable for a giant number of observations and would complicate the distributed processing within the international services.

In general, the intra-technique combination leads to several substantial positive effects compared to using a single independent solution. The combination enables the analysis of differences, the uncovering of systematic effects and the detection of outliers. Through the final combination, the stability and robustness of the final product is improved and the analyst's noise is reduced (Böckmann et al. 2010b).

The following requirements have to be fulfilled to be technically able to combine a CRF but also to achieve sensible and reliable combined results. At first it is mandatory that all contributing datum-free normal equations contain the entire set of parameters, including EOPs, all station coordinates and all source positions. The EOPs are composed of the nutation parameters, the pole offsets and UT1 as well as their corresponding time derivatives. The delivery and exchange of these normal equations is based on the Solution Independent Exchange Format (SINEX). Ideally the contributing solutions should be stable and independent (Böckmann et al. 2010c). Although the different contributions

Table 1 Contributing ACs with their used software packages and supported parameters

AC	Institution	Software	Sources	EOPs	Stations
BKG	Federal Agency for Cartography and Geo.	Calc/Solve	✓	Offset/Rate	✓
DGFI	German Geodetic Research Institute	OCCAM	–	Offset/Rate	✓
GSFC	Goddard Space Flight Center	Calc/Solve	✓	Offset/Rate	✓
IAA	Institute of Applied Astronomy	QUASAR	–	Offset/Rate	✓
OPA	Paris Observatory	Calc/Solve	✓	Offset/Rate	✓
TUW	Vienna University of Technology	VieVS	✓	CPWLF	✓
USNO	United States Naval Observatory	Calc/Solve	✓	Offset/Rate	✓

are determined from identical sets of raw observations, they are treated as being independent without taking any correlations into consideration. This is due to the fact that various analysis software packages including many possible analysis options are being used. A small drawback is that in this procedure individual systematics and other shortcomings may be mixed together which cannot be identified or isolated again afterwards. However, the benefit not to be forced to define one AC as clearly better than the others outweighs the downside of a mixed solution.

At present, six ACs regularly contribute their independent solutions to the International VLBI Service for Geodesy and Astrometry (IVS) for the computation of combined products such as EOP time series (Behrend 2013). Not all of these contributions support source parameters in their normal equations yet. Hence only four out of the official six IVS contributing ACs are used for our initial CRF investigations and developments. Ongoing efforts of several ACs give reason to expect more ACs containing source parameters in the future. In addition to the official IVS ACs, the solution of the Vienna University of Technology (TUW) contains all necessary parameters, thus it is involved in our investigations as well. The integration of the TUW solutions is a big gain for the whole combination since a completely new and independent software called VieVS (Böhm et al. 2012) is used for the analysis.

In Table 1 the most important properties of the official IVS ACs in the context of combination and the additional AC TUW are summarized. This comprises the software packages used and the supported parameters including the type of the EOP parameterization. The latter aspect becomes crucial because the parameters have to be adapted to each other before we are able to stack them.

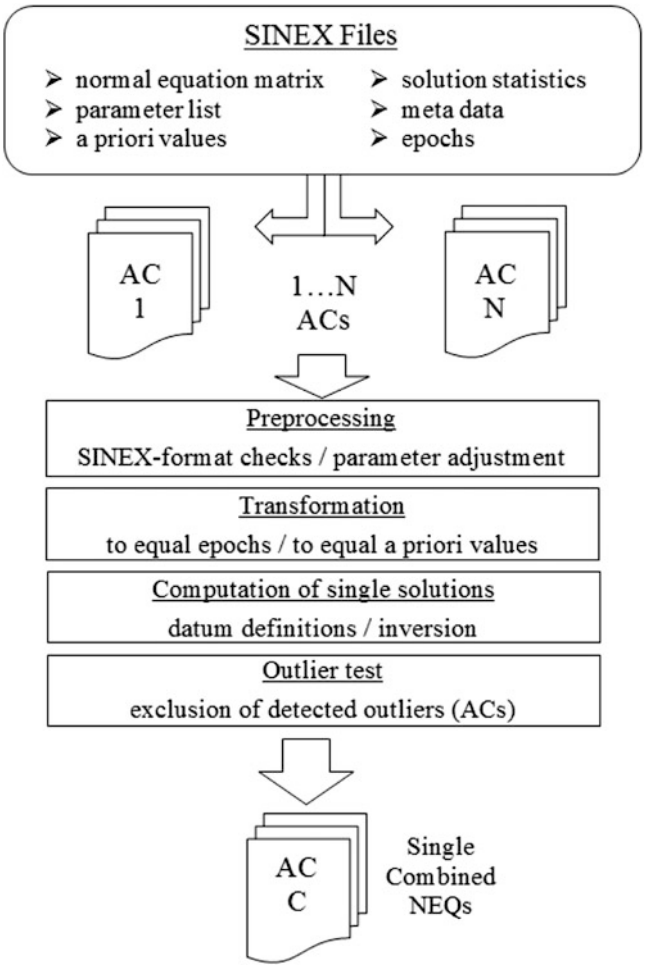

Fig. 1 Flowchart of the combination process

2.2 Methodology

The general procedure of the combination is divided into several steps illustrated in Fig. 1. High precision geodetic VLBI is operating since 1979 and over 5,000 sessions were observed, analysed and submitted so far. Multiplying this with the number of contributing ACs, several tens of thousands of datasets need to be organized and handled in the combination process. Not all of these sessions are suitable for the determination of the desired parameters, thus affected sessions can already be excluded at this point. In the preprocessing step, discrepancies and irregularities in the SINEX files are detected and fixed. Furthermore, the continuous piecewise linear (CPWL) parameterization for

the EOP is transformed to the Offset/Rate parameterization to enable the TUW solution to contribute to the combination. Due to the fact that the used epochs and a priori values of the different ACs are oftentimes slightly different, transformations to identical aprioris and epochs need to be done in the next step.

Although one of our main goals is to generate a single intra-technique datum-free normal equation system for step 3 (combination with the other techniques), we can insert an intermediate step where we define a datum and calculate single solutions. This is necessary to detect and to exclude outliers. In order to take account of the different qualities of the individual contributions, a variance component estimation is used to determine weighting factors for each submission (Böckmann and Nothnagel 2008). In the next step, the results of the combination process illustrated at the bottom of Fig. 1 are session-wise combined datum-free normal equations. Based on the combined and AC's specific normal equations we are able to perform comparisons and to generate several intermediate products. For example while performing a global solution the corresponding time series could be displayed during the processing as an intermediate product. The whole combination procedure is realized in our software environment called BonnSolutionCombination (BoSC). The capabilities and the basic structure of BoSC are shown in Fig. 2. The first option is to stack all single combined normal equations to one monolithic datum-free normal equation. Subsequently, we are able to freely choose whether a session should contribute to the final product or not. Furthermore, a parameter can be set up as an arc or a global parameter. This offers for instance the opportunity to parameterize special parameters such as special handling source positions more appropriately than done in the previous realizations of the ICRS. For example the positions of special handling sources could be parameterized with continuous piecewise linear functions or other convenient functions.

The second option which is supported by BoSC, is the determination and illustration of parameter time series. For instance, while investigating the stability of source positions or the residuals of ACs, we can benefit from this feature. In order to analyse the position variations of selected sources, the time series with respect to right ascension and declination can be visualized. Before contributing to the inter-technique combination it is necessary to check the consistency within the VLBI data sets. This is supported by the third feature of BoSC, computing a consistent VLBI intra-technique CRF, TRF and corresponding EOP series. For this purpose, it is required to define a datum in order to remove the rank deficiency of the normal equation matrix.

In order not to be restricted by a couple of default datum definitions, BoSC supports a complete customizable datum definition for every single parameter. Different constraints such as the no net translation (NNT) and the no net rotation (NNR) condition can be applied to a selected set of parameters while other parameters remain unconstrained. Furthermore, parameters can be eliminated, fixed or reduced. All upcoming CRF investigations can profit from this wide spectrum of possibilities. Hence the combination procedure and its related software are not only suitable to generate a combined CRF but also to facilitate any studies and analyses required beforehand.

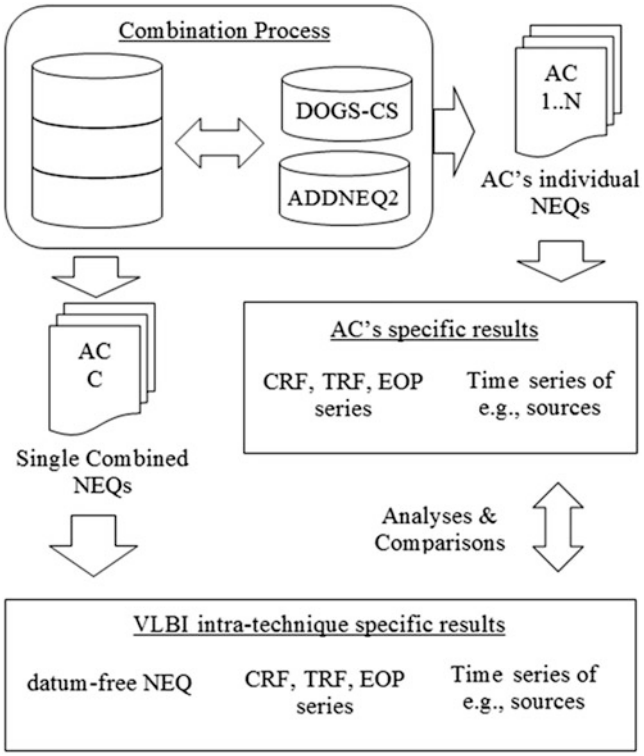

Fig. 2 Capabilities and final products of BoSC, including combined results and AC's individual outcomes

One additional special feature of the developed procedure is, that the combination can be performed either with DOGS-CS, a software developed at the DGFI, or ADDNEQ2, a subprogram of the Bernese GNSS software. Both are used to stack and constrain the parameters of the normal equations. This feature offers the opportunity to detect and analyse differences, individual shortcomings or numerical problems solely founded in the applied stacking program.

3 Results

In order to confirm the general functionality of the combination procedure and its related software, a combination of a selected source was performed. Since the source 0552+398 is the most observed one in VLBI experiments with about 350,000 observations in over 4,000 sessions, it is predestined

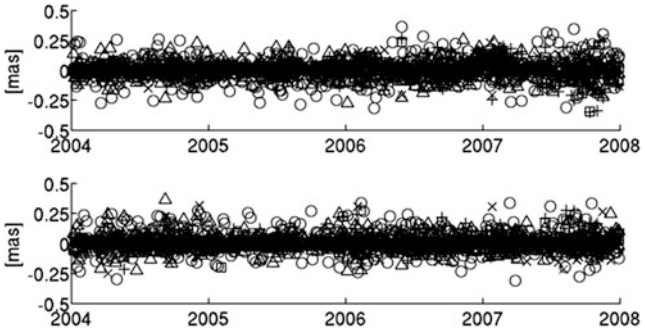

Fig. 3 Right ascension (*up*) and declination (*down*) residuals of the defining source 0552+398. Contributing ACs [BKG (*Circle*), GSFC (*Cross*), OPA (*Plus*), USNO (*Square*), TUW (*Triangle*)] w.r.t. combined AC

Table 2 Statistical information of the performed combination

AC	Bias [μas]	σ [μas]	#Ses
BKG	2	120	201
GSFC	−4	75	205
OPA	12	80	203
USNO	9	91	205
TUW	7	81	204

for initial investigations and tests. 0552+398 is a defining source and no inherent variability in the position is expected. Using the developed flexible datum definition, an NNR condition on the defining sources except the selected one and a free estimation of the remaining sources were set up. Furthermore, the station positions were fixed to the epoch transformed a priori ITRF2008 coordinates and the EOPs were freely estimated. To generate a time series, the selected source was parameterized as an arc parameter and the combination was performed in single session mode. All ACs supporting source parameters (see Table 1) contributed to this combined solution. In Fig. 3 and corresponding Table 2 the results of this combination are shown.

The results should only demonstrate the proper function of our combination procedure. The variations of the residuals match the expectations with no significant systematics recognizable. Hence it can be assumed that the rigorous combination software developed here which now also includes source parameters seems to operate correctly. Further studies, analyses and comparisons have to be performed in the future.

4 Conclusion and Outlook

In this paper, a combination procedure for CRF determination has been presented. The capabilities of the corresponding combination software BoSC developed at the Institute of Geodesy and Geoinformation were illustrated and the general functionality has been described.

In order to generate a consistent TRF and CRF, investigations concerning the features and properties of a CRF combined from several VLBI solutions have to be made in upcoming studies. Our combination software enables these investigations. Individual CRFs based on solutions generated by the different ACs are planned to be compared among themselves and to the official ICRF2. In this context, the impact of the additional data, which became available after the ICRF2 was published, should be examined as well. Based on comparisons between combined and individual CRFs we expect that a combined CRF provides improvements in terms of stability and robustness.

References

Behrend D (2013) Data handling within the international VLBI service. Data Sci J 12:WDS81–WDS84. ISSN 1683–1470. doi: 10.2481/dsj.WDS-011

Böckmann S, Nothnagel A (2008) The variance component approach in the IVS combination. In: Finkelstein A, Behrend D (eds) International VLBI service for geodesy and astrometry, measuring the future, general meeting proceedings, pp 329–334, ISBN 978-5-02-025332-2

Böckmann S, Artz T, Nothnagel A (2010a) VLBI terrestrial reference frame contributions to ITRF2008. J Geod 84:201–219. doi: 10.1007/s00190-009-0357-7

Böckmann S, Artz T, Nothnagel A, Tesmer V (2010b) International VLBI service for geodesy and astrometry: earth orientation parameter combination methodology and quality of the combined products. J Geophys Res 115:B04404. doi:10.1029/2009JB006465

Böckmann S, Artz T, Nothnagel A (2010c) Correlations between the contributions of individual IVS analysis centers. In: Behrend D, Baver KD (eds) International VLBI service for geodesy and astrometry, general meeting proceedings, NASA/CP-2010-215864, Greenbelt MD, pp 222–226

Böhm J, Böhm S, Nilsson T, Pany A, Plank L, Spicakova H, Teke K, Schuh H (2012) The new Vienna VLBI software VieVS. In: Kenyon S, Pacino MC, Marti U (eds) Proceedings of IAG scientific assembly 2009. International association of geodesy symposia series, vol 136, pp 1007–1011, doi:10.1007/978-3-642-20338-1_126

IERS (2009) The second realization of the international celestial reference frame by very long baseline interferometry. In: Fey AL, Gordon D, Jacobs CS (eds) IERS technical note 35, presented on behalf of the IERS/IVS working group, Verlag des Bundesamtes für Geodäsie und Kartographie, Frankfurt am Main

Kouba J (2009) A guide to using international GNSS service (IGS) products. Natural Resources Canada. Online available: http://igscb.jpl.nasa.gov/components/usage.html, February 2014

Pavlis EC, Luceri V, Sciarretta C, Kelm R (2009) The ILRS contribution to ITRF2008. Geophysical research abstracts, vol 11, EGU2009-6564, EGU General Assembly 2009, held 19–24 April 2009 in Vienna, Austria

Willis P, Fagard H, Ferrage P, Lemoine FG, Noll CE, Noomen R, Otten M, Ries JC, Rothacher M, Soudarin L, Tavernier G, Valette JJ (2010) The international DORIS service, toward maturity. In: Willis P (ed) DORIS: scientific applications in geodesy and geodynamics. Advances in space research, vol 45, issue 12, pp 1408–1420, doi: 10.1016/j.asr.2009.11.018

Improved Parameter Estimation of Zenith Wet Delays Using an Inequality Constrained Least Squares Method

Sebastian Halsig, Lutz Roese-Koerner, Thomas Artz, Axel Nothnagel, and Wolf-Dieter Schuh

Abstract

The path of signals from space geodetic techniques, such as Very Long Baseline Interferometry (VLBI) or Global Navigation Satellite Systems (GNSS), is affected by refractivity variations in the neutral atmosphere. This tropospheric delay, which represents a major contribution to the error budget of space geodetic observations, is generally considered by applying an adequate model (hydrostatic component) and by additionally estimating tropospheric parameters (wet component). Sometimes, the standard approach may lead to negative tropospheric parameters. Due to the fact, that there is nothing like negative water vapour, these negative estimates do not reflect the meteorological conditions in a plausible way.

In this paper, we introduce an Inequality Constrained Least Squares (ICLS) method from the field of convex optimization to constrain the tropospheric parameters to non-negative values. We applied this new methodology to 17 years of VLBI sessions. For about 20% of these sessions the method automatically applied inequality constraints. For many sessions the procedure is successful. However, deficiencies in the hydrostatic modeling also lead to worse results for a few sessions. Thus, the methodology is applicable to VLBI data analyses if the a priori modeling is correct which is not always the case for the data set available at the moment.

Keywords

Inequality Constrained Least Squares • Refractivity variations • Tropospheric delay • VLBI

1 Introduction

Refractivity variations in the neutral atmosphere are the major error source in space geodetic techniques such as Very Long Baseline Interferometry (VLBI) or Global Navigation Satellite Systems (GNSS). They are the limiting factor for any further improvements in the accuracy of the derived parameters. Generally, in the VLBI analysis an Ordinary Least Squares (OLS) adjustment is used to estimate terrestrial positions, source coordinates, Earth system parameters as well as clock and atmospheric model parameters.

Concerning the atmospheric parameters, the total slant tropospheric delay (STD) can be divided into a hydrostatic (index h) and a wet (index w) part (Davis et al. 1985). Each of these terms can be described as the product of the zenith delay (*ZHD* and *ZWD*) and the corresponding mapping function ($mf_{h(e)}$ and $mf_{w(e)}$), referring the zenith delay to the elevation angle e,

$$STD \quad mf_h(e)\, ZHD + mf_w(e)\, ZWD. \tag{1}$$

S. Halsig (✉) • L. Roese-Koerner • T. Artz • A. Nothnagel • W.-D. Schuh
Institute of Geodesy and Geoinformation, University of Bonn, Nussallee 17, 53115 Bonn, Germany
e-mail: halsig@igg.uni-bonn.de; roese-koerner@igg.uni-bonn.de; artz@igg.uni-bonn.de; nothnagel@igg.uni-bonn.de; schuh@igg.uni-bonn.de

© Springer International Publishing Switzerland 2015

C. Rizos, P. Willis (eds.), *IAG 150 Years*, International Association of Geodesy Symposia 143,
DOI 10.1007/1345_2015_171

The zenith hydrostatic delay (ZHD) on the one hand is taken into account by applying an adequate model (Davis et al. 1985) mainly depending on the surface air pressure. On the other hand, the wet part is influenced by water vapour in the atmosphere which is highly variable in space and time. For this purpose, the zenith wet delay (ZWD) is estimated within the VLBI analysis. In total, the zenith tropospheric delays have a precision of about 2–4 mm (Heinkelmann et al. 2011).

From a meteorological point of view, the ZWD parameters should always be positive, as negative values do not correspond to actual meteorological conditions and physical properties. This can be explained by the fact, that, according to physics of the atmosphere, there is very little water vapour content at temperatures below 0°C (and there is nothing like negative water vapour which could produce a negative delay contribution). However, when estimating ZWD parameters using the ZHDs as a priori information in an OLS adjustment, sometimes negative values are present. Assuming correct hydrostatic modeling, one could argue that un-modeled non-tropospheric effects are absorbed by the ZWDs, which should be avoided.

As a new method, we present an Inequality Constrained Least Squares (ICLS) adjustment to estimate tropospheric parameters from VLBI observations. The introduction of inequality constraints allows for a reliable modeling of physical properties and meteorological conditions. Using algorithms from the field of convex optimization (Boyd and Vandenberghe 2004) it is possible to constrain quantities to a fixed interval, i.e., positive ZWDs in our case.

However, deficiencies in the a priori ZHDs, for example due to missing or incomplete pressure data (cf. Heinkelmann et al. 2011), are compensated by the ZWD estimates. For instance, a wrong surface pressure of +1 hPa would lead to a ZHD which is too large by about 2.3 mm (using the hydrostatic delay model, cf. Davis et al. 1985). As the ZWDs compensate ZHD mis-modeling to about 100%, the corresponding estimated ZWD would be −2 mm in this case. In this study, the hydrostatic delay is based on numerical weather models (e.g., of the European Centre for Medium-Range Weather Forecasts, ECMWF). Although the differences to meteorological in-situ observations could reach a few millimeters (Snajdrova et al. 2006), homogeneous time series of meteorological data could be guaranteed. If the ZWD parameters are now constrained to be positive in the ICLS adjustment, erroneous a priori delays are not compensated for any more. As a consequence, the ZWD estimates themselves as well as highly correlated parameters, such as the vertical positions, are affected. Thus, it is of utmost importance that the ZHD a priori information is adequately modeled. In addition to bad a priori information, wrong mapping functions could also be compensated for by the ZWD estimates, although, the compensation of this effect is not significant.

For our investigations, we assume correct hydrostatic modeling and show that the new methodology is promising for VLBI analysis. However, this assumption is not always true and needs further investigations.

2 Inequality Constrained Least Squares

In a linear Gauss Markov model of the form

$$\mathbf{l} = \mathbf{A}\mathbf{x} + \mathbf{v}, \tag{2}$$

$\mathbf{l}$ is the $n \times 1$ vector of observations, $\mathbf{v}$ the vector of residuals, and vector $\mathbf{x}$ contains the m unknown parameters to be estimated. The matrix $\mathbf{A}$ is the $n \times m$ design matrix containing the partial derivatives of the observation equations with respect to the parameters. Minimizing the (possibly weighted) sum of squared residuals

$$\mathbf{v}(\mathbf{x})^T \boldsymbol{\Sigma}^{-1} \mathbf{v}(\mathbf{x}) \ldots \text{ min} \tag{3}$$

with the variance covariance matrix $\boldsymbol{\Sigma}$ of the observations yields an Ordinary Least Squares (OLS) estimate $\mathbf{x}_{OLS}$. In Fig. 1a, the contour lines of the objective function of an example problem as well as the corresponding OLS estimate are illustrated. This problem is extended to an Inequality Constrained Least Squares (ICLS) problem by adding p linear inequality constraints of the form

$$\mathbf{B}^T \mathbf{x} \leq \mathbf{b}, \tag{4}$$

which have to be fulfilled strictly. This leads to the following model:

INEQUALITY CONSTRAINED LEAST SQUARES

objective funct.: $\mathbf{v}(\mathbf{x})^T \boldsymbol{\Sigma}^{-1} \mathbf{v}(\mathbf{x}) \ldots \text{Min}$

constraints: $\mathbf{B}^T \mathbf{x} \leq \mathbf{b}$

optim. variable: $\mathbf{x} \in R^m$ (5)

$\mathbf{B}$ is the $m \times p$ matrix of constraints and $\mathbf{b}$ the corresponding $p \times 1$ right-hand side. The contour lines of the objective function and the ICLS estimate for an example problem are shown in Fig. 1b. The inequality constraints ($x_1 \leq 3, x_2 \geq 2, x_1 + x_2 \geq 2$, gray lines) limit the feasible region (gray shaded area). Further, the initial solution $\mathbf{x}^{(0)}$, the interim solution $\mathbf{x}^{(1)}$ and the final solution $\mathbf{x}_{ICLS}$ of the ICLS problem are shown as black dots. For comparison, the OLS solution $\mathbf{x}_{OLS}$ (gray cross) in the infeasible region is illustrated once again.

In order to solve an ICLS problem, there exist only iterative methods. It is not known in the beginning which

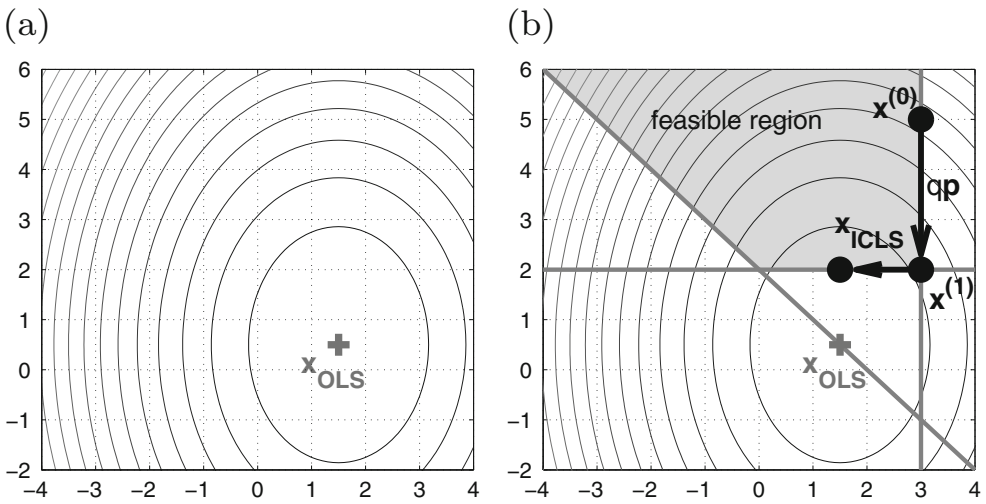

Fig. 1 Contour lines of the objective function and (**a**) OLS and (**b**) ICLS estimates for an example problem. The inequality constraints ($x_1 \leq 3, x_2 \geq 2$, $x_1 + x_2 \geq 2$, *gray lines*) limit the feasible region (*gray shaded area*). Initial solution $\mathbf{x}^{(0)}$, interim solution $\mathbf{x}^{(1)}$ and final solution $\mathbf{x}_{ICLS}$ of the active set method are shown as *black dots*. The OLS solution $\mathbf{x}_{OLS}$ (*gray cross*) in the infeasible region is shown for comparison

inequality constraints will influence the result. Therefore, the sets of active and inactive constraints change iteratively. In the next section, one of these iterative methods will be explained in some detail.

2.1 Active Set Method

The Active Set method (Gill et al. 1981, pp. 167–173) is a simplex-type algorithm for solving ICLS problems. The basic idea is to follow the boundary of the feasible set (e.g., the set where all inequality constraints are fulfilled, gray shaded region in Fig. 1b) until the optimal solution $\mathbf{x}_{ICLS}$ is reached. The algorithm can be subdivided into four main steps which are described briefly below (cf. Roese-Koerner et al. 2012b).

Step 1. Choose initial point and find active constraints: In a first step, an initial point $\mathbf{x}^{(0)}$ is chosen, which fulfills all constraints. Subsequently, the set of constraints is subdivided into active constraints, which hold as equality constraints $\mathbf{W}^T\mathbf{x}^{(i)} = \mathbf{w}$ and inactive constraints which hold as strict inequalities $\mathbf{V}^T\mathbf{x}^{(i)} < \mathbf{v}$. That means, if $x_j = 0$, the jth inequality constraint $x_j \leq 0$ is called active at point $\mathbf{x}$. Further, if $x_j < 0$, we say the constraint $x_j \leq 0$ is inactive. Otherwise, if a constraint is neither active, nor inactive, $x_j > 0$ is valid and we say the constraint is violated (iteration indices were neglected). This is essential, as only active constraints have an influence on the result.

Step 2. Compute search direction: The gradient

$$\mathbf{g} = \mathbf{N}\mathbf{x}^{(i)} - \mathbf{n} \tag{6}$$

in point $\mathbf{x}^{(i)}$ is computed using the normal equations

$$\mathbf{N} = \mathbf{A}^T\boldsymbol{\Sigma}^{-1}\mathbf{A} \qquad \text{and} \qquad \mathbf{n} = \mathbf{A}^T\boldsymbol{\Sigma}^{-1}\mathbf{l}. \tag{7}$$

Subsequently, the negative gradient is projected in the nullspace of the set of active constraints to ensure that the boundary of the feasible set is followed, resulting in search direction

$$\mathbf{p}^{(i)} = -\Pi^N_{S^\perp(\mathbf{W})}\,\mathbf{g}. \tag{8}$$

Step 3. Compute step length: The distance to all inactive constraints in search direction is computed to determine the maximal feasible step length $q^{(i)}$.

Step 4. Update parameters and active set: With search direction $\mathbf{p}$ and step length q at hand, an update of the parameters can be computed

$$\mathbf{x}^{(i+1)} = \mathbf{x}^{(i)} + q^{(i)}\mathbf{p}^{(i)} \tag{9}$$

and the corresponding Lagrange multipliers of the extended objective function

$$\Phi\,(\mathbf{x}, \mathbf{k}) = \mathbf{x}^T\mathbf{N}\mathbf{x} - 2\mathbf{n}^T\mathbf{x} + \mathbf{k}^T(\mathbf{B}^T\mathbf{x} - \mathbf{b}) \tag{10}$$

are computed (iteration indices were neglected). If all Lagrange multipliers linked with active constraints are non-negative, the optimal solution is found and the algorithm terminates. Otherwise all constraints with negative Lagrange multipliers are removed from the set of active constraints and the algorithm is started again.

2.2 Stochastic Description

In contrast to classic adjustment procedures, there exists no analytic relationship between parameters and observation in the ICLS case. Therefore, variance propagation cannot be applied. In order to derive a measure for the quality of the

estimated quantities, Monte Carlo methods can be utilized to derive a discrete approximation of the a posteriori probability density function (pdf, cf. Roese-Koerner et al. 2012a). As the introduction of inequality constraints often leads to asymmetric pdfs, highest probability density (HPD) intervals are computed instead of (symmetric) standard deviations.

3 Solution Setup

In the following, the VLBI modeling and estimation process will be briefly described. Based on observations involving several VLBI stations and different radio sources, the required parameters, such as coordinates of stations or sources, Earth orientation parameters as well as clock and tropospheric model parameter corrections, are estimated. For this purpose, we made use of 2,333 VLBI databases from 1993 to 2010 provided by the International VLBI Service for Geodesy and Astrometry (IVS, Schuh and Behrend 2012). These are initially processed with the VLBI analysis software Calc/Solve (Ma et al. 1990) which implements an OLS adjustment. We modified Calc/Solve to export the OLS equation system. In a second step, we use a C++ backend to perform the OLS adjustment and to implement and solve the ICLS problem.

A typical parametrization for single session VLBI analysis has been chosen. We fixed source positions to their positions in the current version of the International Celestial Reference Frame (ICRF2, Fey et al. 2009). This means that we focus on the estimation of terrestrial positions, Earth orientation parameters, clock behaviour and tropospheric delays. For this purpose, the clock parameters are modeled by a quadratic polynomial. Additionally, we set up continuous piecewise linear functions (CPWLF), i.e., linear splines (de Boor 1978), with a temporal resolution of 60 min. ZWDs are parametrized by CPWLF with a temporal resolution of 60 min and daily Earth orientation parameters are estimated with offsets and rates. Troposphere gradients are estimated as CPWLF with a temporal resolution of 6 h. In order to stabilize the equation system, the clock and tropospheric parameters are supplemented by soft constraints in the form of pseudo observations, which are, compared to hard constraints, less heavily weighted (e.g., $\sigma_{clock} = 2 \cdot 10^{-14} \frac{s}{s}$, $\sigma_{ZWD} = 15 \frac{mm}{h}$, $\sigma_{grad_1} = 2 \frac{mm}{day}$, $\sigma_{grad_2} = 0.5$ mm). Further, additional equations of hard constraints, including a no-net-translation (NNT) and a no-net-rotation (NNR) condition with three equations each, are needed to remove the natural VLBI rank deficiency and to prevent the system of equations from singularities (Angermann et al. 2004). In the following, the term constraint will always only refer to inequalities concerning the ICLS method and not to the measures for the stabilization of the equation system. The stabilizing pseudo observations are always applied.

Concerning the estimation of ZWDs, the Vienna mapping function (VMF1, Böhm et al. 2006) is used. To receive homogeneous time series of meteorological data, the hydrostatic delay is also modeled using the VMF1 data, which are computed using reanalysis data of the numerical weather model of the European Centre for Medium-Range Weather Forecasts (ECMWF). This has been done although in-situ surface pressure is included in the IVS databases. However, these are not always correct and would, thus, lead to errors in our solution as described in Sect. 1. As the VMF1 files contain information only in intervals of 6 h, we loose precision (from the pressure values at the epoch of each observation) but gain a higher accuracy.

In the following, an adequate a priori model is assumed and an Inequality Constrained Least Squares adjustment (cf. Sect. 2) is applied to the VLBI modeling procedure, complementing the Ordinary Least Squares solution described above. For this purpose, we have imposed the constraint, that all ZWD estimates must be greater than or equal to 0 mm (i.e., $x_i \geq 0$ mm).

4 Results

The long term solution with 2,333 VLBI databases from 1993 to 2010 has been solved in an OLS and an ICLS adjustment. In 454 out of these databases at least one constraint is active, that means in about 20% of cases. For both the OLS (gray asterisks) and the ICLS (black points) adjustment, the baseline repeatabilities, which occur in at least 30 sessions, as well as the baseline repeatabilities for only those sessions, for which, in addition, inequality constraints are applied, are shown in Fig. 2a, b, respectively. Further, a quadratic polynomial is fitted to the data. Regarding these baseline repeatabilities, the ICLS solution (black line) is slightly more precise than the OLS solution (gray dashed line, Fig. 2b). The application of ICLS improves 9% of the baseline repeatabilities for at least 1 mm (black bars in Fig. 3) while 1% get worse for at least 1 mm (dark gray bars) and 90% remain unchanged (light gray bars). However, within this paper the general effects of the new solution should be demonstrated. Thus, the long term series is not analyzed in more depth and we concentrate on the effects which can be seen in a single session. In the following, we will demonstrate the application of the ICLS algorithm to a VLBI analysis. First results are shown comparing the tropospheric parameters to the OLS solution and discussing their influence on other parameter types.

As negative ZWD estimates are the least plausible in cold regions, we have exemplarily chosen the station Ny Ålesund (Spitsbergen, Norway, January 17, 2002) to demonstrate the consequences of introducing inequality constraints to model physical properties. For this purpose, an adequate hydrostatic model is assumed. In Fig. 4, both the OLS (gray asterisks)

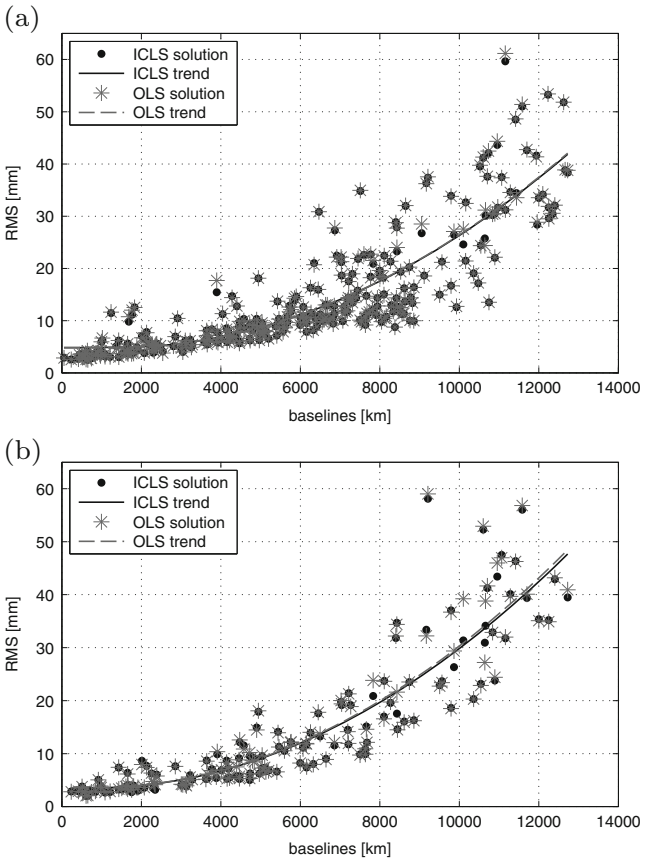

Fig. 2 Baseline repeatabilities for (**a**) VLBI data from 1993 to 2010 and (**b**) those sessions, for which constraints are active, w.r.t. the OLS (*gray asterisks*) and the ICLS (*black points*) solution. A quadratic polynomial is fitted to the data

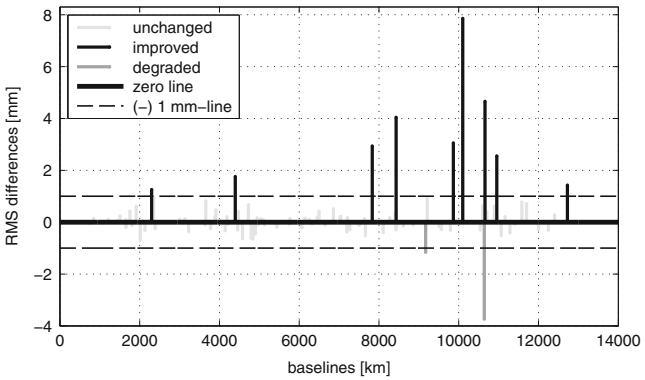

Fig. 3 Difference in baseline repeatabilities (OLS-ICLS)

and ICLS (black points) tropospheric parameter estimates as well as the constraints (gray line) of the ICLS problem are shown. The negative OLS parameters, for which a constraint is active, are turned into non-negative estimates in the ICLS adjustment. All the other ICLS estimates remain positive anyway.

Furthermore, it is notable that in this case all ICLS parameter values have increased compared to the OLS estimates,

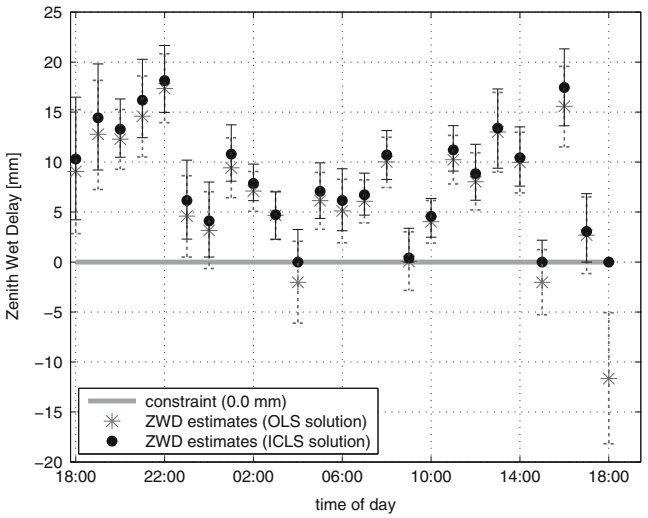

Fig. 4 Tropospheric ZWD estimates, analyzed by an OLS (*gray asterisks*) and an ICLS (*black points*) adjustment. The negative OLS parameters are turned into non-negative estimates (due to the constraints $x_i \geq 0$ mm, *gray line*) in the ICLS adjustment. HPD intervals are depicted as *dashed* (OLS) and *solid* (ICLS) error bars

which follows directly from the positive correlations between the tropospheric parameters. That means, if the correlations between the parameters with active constraints and these with inactive constraints are positive, all parameters increase in value. As described in Sect. 3, the ZWDs are parametrized by CPWLF, which is equivalent to a representation using an offset and rates. If now a single ZWD parameter is wrongly estimated, both the (adjacent) rates and the offset would be changed. Assuming the hydrostatic delay to be calibrated correctly, that would actually imply that also those non-negative parameters were wrongly estimated with the OLS method. This is healed by the ICLS method.

The impact of the ICLS adjustment on the whole set of parameters is illustrated in Fig. 5. When considering the differences between both solution approaches, the OLS and the ICLS, it is obvious that not only the constrained ZWDs (black bars) have changed up to the level of a centimeter, but also the other tropospheric estimates (gray bars) of the same station differ from the OLS solution in the range of a few millimeters (cf. Fig. 5a). However, the effect on the ZWD parameters of the other stations of the network is an order of magnitude smaller. As an example, Fig. 5c shows the differences in the estimated atmosphere parameters of Wettzell (Bavarian Forest, Germany). The same tendency can be observed regarding the station coordinates: whereas the influence on position vectors of other stations is comparatively small (not shown here), we see significant differences in the station coordinates of Ny Ålesund (cf. Fig. 5b). The general experience from the 2,333 sessions analyzed so far is that the inequality constraints affect only the coordinates of that station that is affected by inequality constraints in

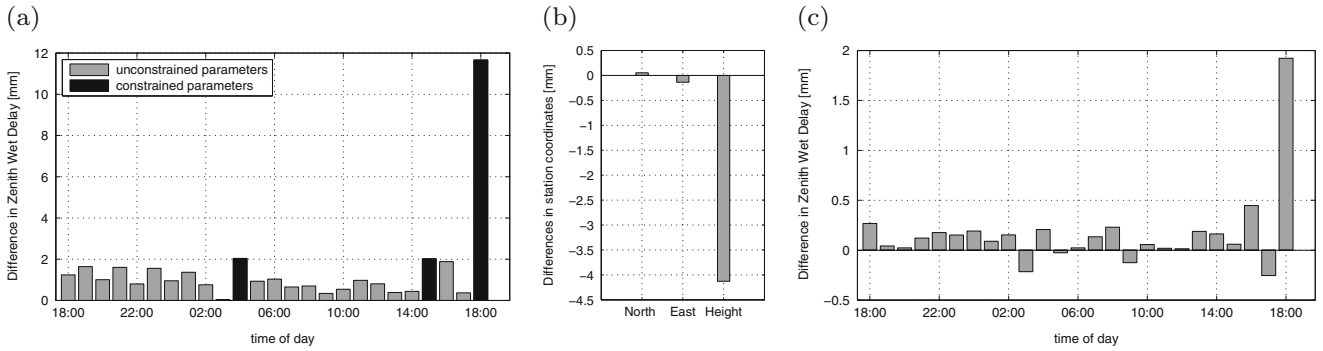

Fig. 5 Differences between the OLS and ICLS solution of the ZWD estimates for Ny Ålesund (Spitsbergen, Norway) on January 17, 2002 (**a**). *Black bars* indicate, that the constraint associated with the parameter is active. Influence of these constraints on (**b**) the station coordinates (North, East, Height) and on (**c**) atmosphere parameters of other stations (e.g., Wettzell, Bavarian Forest, Germany). Please note, that different scales are used

tropospheric ZWD. In particular, the vertical component changes noticeably in the order of several millimeters.

5 Conclusion and Outlook

In this study, an Inequality Constrained Least Squares adjustment has been introduced for the estimation of tropospheric parameters. Only under the assumption that the a priori ZHD parameters are correct, this leads to a more reliable modeling of some general meteorological and physical conditions, such as the non-negativity of these parameters. In order to introduce the ICLS method in the VLBI estimation procedure, preliminary results have been illustrated. The differences to an Ordinary Least Squares solution as well as the effect of the constraints on different parameter types have been investigated exemplarily for the station Ny Ålesund (Spitsbergen, Norway) in January, 2002. Up to today, the ICLS method cannot yet be used operationally in the VLBI analysis. Particularly due to missing or incomplete pressure data, the hydrostatic a priori information cannot be modeled with sufficient accuracy. As a consequence, these mismodelings would be compensated for by the ZWD parameter in the OLS estimation process, which would be not the case for the ICLS solution any more.

Thus, new strategies have to be developed to ensure an adequate handling of the hydrostatic a priori model. That means, that we need to know how to deal with missing and incorrect meteorological observations, and whether and to what extent model data could be used instead of these data. As a next step, further investigations will be performed to evaluate the influence of the inequality constraints on terrestrial reference frames.

Acknowledgements The authors thank the German Research Foundation (Deutsche Forschungsgemeinschaft) for its financial support (NO 318/10-1).

References

Angermann D, Drewes H, Krügel M, Meisel B, Gerstl M, Kelm R, Müller H, Seemüller W Tesmer V (2004) ITRS combination center at DGFI: a terrestrial reference frame realization 2003. Deutsche Geodätische Kommission Bayer. Akad. Wiss. München, Reihe B 313:1–141

Böhm J, Werl B, Schuh H (2006) Troposphere mapping functions for GPS and very long baseline interferometry from European centre for medium-range weather forecasts operational analysis data. J Geophys Res 111:B02406. doi:10.1029/2005JB003629

Boyd S, Vandenberghe L (2004) Convex optimization. Cambridge University Press, Cambridge

Davis JL, Herring TA, Shapiro II, Rogers AEE, Elgered G (1985) Geodesy by radio interferometry: effects of atmospheric modeling errors on estimates of baseline length. Radio Sci 20(6):1593–1607

de Boor C (1978) A practical guide to splines. Applied mathematical sciences, vol 27. Springer, New York

Fey A, Gordon D, Jacobs CS (2009) The second realization of the international celestial reference frame by very long baseline interferometry, IERS Technical Note 35, Verlag des Bundesamtes für Kartographie und Geodäsie, Frankfurt am Main

Gill PE, Murray W, Wright MH (1981) Practical optimization. Academic, London

Heinkelmann R, Böhm J, Bolotin S, Engelhardt G, Haas R, Lanotte R, MacMillan DS, Negusini M, Skurikhina E, Titov O, Schuh H (2011) VLBI-derived tropospheric parameters during CONT08. J Geodesy 85:377–393. doi:10.1007/s00190-011-0459-x

Ma C, Sauber JM, Clark TA, Ryan JW, Bell LJ, Gordon D, Himwich WE (1990) Measurement of horizontal motions in Alaska using very long baseline interferometry. J Geophys Res 95(B13):21991–22011. doi:10.1029/JB095iB13p21991

Roese-Koerner L, Devaraju B, Sneeuw N, Schuh WD (2012a) A stochastic framework for inequality constrained estimation. J Geodesy 86(11):1005–1018. doi:10.1007/s00190-012-0560-9

Roese-Koerner L, Krasbutter I, Schuh WD (2012b) A constrained quadratic programming technique for data-adaptive design of decorrelation filters. In: VII Hotine-Marussi symposium on mathematical geodesy. Springer, Berlin/Heidelberg, pp 165–170

Schuh H, Behrend D (2012) VLBI: a fascinating technique for geodesy and astrometry. J Geodyn 61:68–80. doi:10.1016/j.jog.2012.07.007

Snajdrova AJ, Böhm J, Willis P, Haas R, Schuh H (2006) Multitechnique comparison of tropospheric zenith delays derived during the CONT02 campaign. J Geodesy 79:613–623. doi:10.1007/s00190-005-0010-z

The Realization of a Semi-Kinematic Datum in Greece Including a New Velocity Model

Miltiadis Chatzinikos, Aristeidis Fotiou, Christos Pikridas, and Dimitrios Rossikopoulos

Abstract

The current geodetic network in Greece, which is realised by both the official Hellenic Geodetic Reference System of 1987 (HGRS87) and the GPS permanent network of the contemporary static Hellenic Terrestrial Reference System of 2007 (HTRS07), experience significant inhomogeneous ground displacements. As time passes, the distortion of both networks results in increasing degradation of positioning accuracy and datum stability. For these reasons the velocity field of the Earth's crust in Greece has to be rigorously estimated and taken into account.

In order to achieve a stable geodetic datum, independent of time and coping with the problems of the serious inhomogeneous crustal displacements, the implementation of a semi-kinematic datum for Greece is proposed. The new datum will be referred to a specific epoch, absorbing crustal displacement using an estimated velocity model. This model has been created by dividing Greece into stable crustal blocks by applying the Euler Pole model and statistical criteria. In addition the Least Squares Collocation was applied at the residuals of Euler Pole model in order to predict the previous estimated residuals separately for each one block, integrating in this way the new estimated velocity model.

Keywords

Euler pole • Greek area • Least squares collocation • Semi kinematic-datum • Velocity model

1 Introduction

The Earth's crust in Greece is one of the most tectonically active and complex regions in the world. It cannot be characterized as a solid body but rather as a fragmented area where all kinds of faults exist (Fig. 1). According to Papazachos et al. (1984) the main tectonic features are the normal faults in the mainland of Greece (Thessaly, Gulf of Corinth, Gulf of Patras), the thrust faults in the Northwestern Greece (western of the island of Corfu up to Lefkada) and along the mountain range of Pindos, the dextral strike slip faults along the North Aegean Trough (NAT), the Kefalonia transform fault and the Hellenic Arc. All of these different kinds of faults arise from the complex collisional tectonic setting of the Earth's crust in the Southeastern Europe. Specifically, the structure of the Earth's crust of Greece is the result of the collision among the Eurasian, Nubian and Anatolian plates. Consequently, the velocities in the area of Greece relative to the Eurasian plate vary from a few mm/year in Northern Greece up to almost 35 mm/year in Southern Peloponnisos and Crete (McClusky et al. 2000; Hollenstein et al. 2008; Müller et al. 2013). Other studies (Nyst and Thatcher 2004; Reilinger et al. 2006; Floyd et al. 2010), illustrate the inhomogeneity of the velocity field in Greece

M. Chatzinikos (✉) • A. Fotiou • C. Pikridas • D. Rossikopoulos
Department of Geodesy and Surveying, Aristotle University of Thessaloniki, Thessaloniki, Greece
e-mail: mchatzin@topo.auth.gr

© Springer International Publishing Switzerland 2015

C. Rizos, P. Willis (eds.), *IAG 150 Years*, International Association of Geodesy Symposia 143,
DOI 10.1007/1345_2015_93

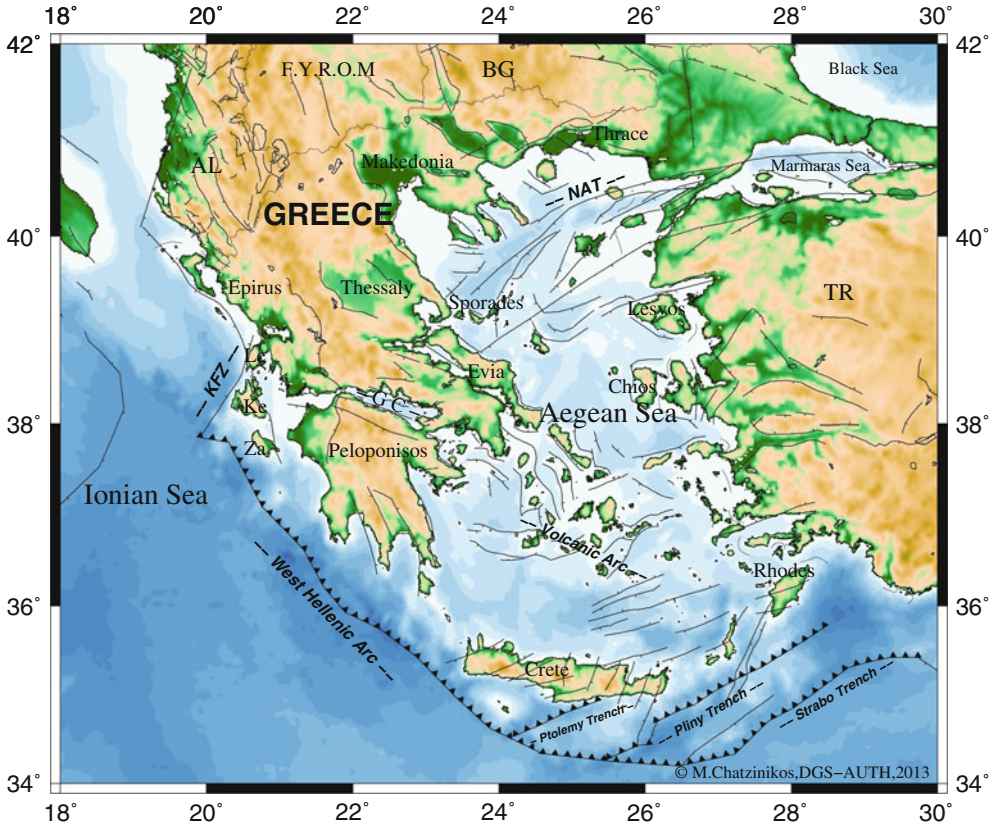

Fig. 1 Tectonic settings of the Earth's crust in Greece (source of trace faults: Howe and Bird 2010)

by the division of the crust in several continental blocks or microplates, rotating each one with different angular velocity.

Since the 1980s, Greece has adopted a local static horizontal geodetic datum, named HGRS87, implemented mostly by classical observations (angles, distances, azimuths). Moreover satellite data have been used for some points in order to improve the accuracy of the network's scale and orientation and help in the determination of datum transformation parameters with respect to the International Terrestrial Reference System (Fotiou 2007). In order to exploit the use of the modern satellite techniques (GPS/GNSS), the Greek National Cadastre and Mapping Agency (NCMA S.A.) established a static geocentric reference system (Katsampalos et al. 2009), named HTRS07, as a realization of ETRS89 (European Terrestrial Reference System 1989) in Greece at epoch 2007.5. HTRS07 was implemented through a GPS network of 98 permanent stations (Gianniou 2009) and used for the coordinate transformation from ETRS89 to HGRS87.

Ongoing tectonic deformation degrades positioning accuracy and causes incompatibility problems to geodetic and surveying applications. By ignoring relative deformation in Greece a relative positioning error e.g. 100 cm between North and South Greece will become obvious over a time period of about 30 years, a period that approaches the age of HGRS87. Significant relative errors can be determined throughout Greece where the orientation of the velocities changes dramatically (Fig. 2). In order to overcome the above deficiencies, we propose the implementation of a semi-kinematic datum for Greece, as New Zealand (Blick et al. 2006) and Japan (Tanaka et al. 2007) have done.

The realization of a semi-kinematic datum for Greece can be based on a new velocity model which will model crustal displacement consistently over time. The construction of the new estimated velocity model consists of two main steps. In the first step the Earth's crust is divided into stable crustal blocks applying the Euler Pole model and statistical criteria. The second step predicts the residuals of the Euler's Pole model in each block using Least Squares Collocation (LSC), integrating the new velocity model.

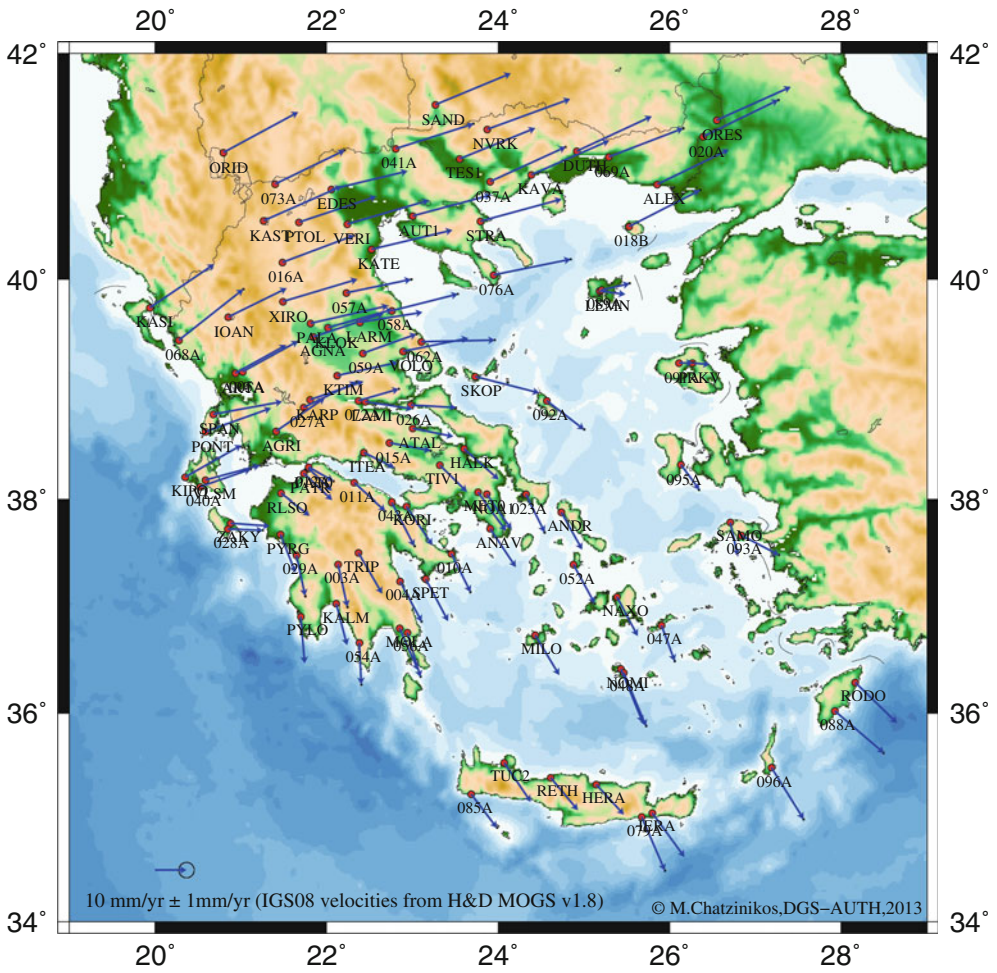

Fig. 2 The site velocities of GRNET in Greece relative to IGS08 reference frame. Error ellipses correspond to 99% confidence level

2 GPS Data Processing and Velocity Estimation

It is only recently that accurate estimation of velocities has been possible in Greece by means of a well distributed permanent GPS network, GRNET. This network covers almost all the major tectonic features of Greece and is formed by a combination of four different GPS permanent networks, i.e. LEICA SMARTNET GREECE, HEPOS, NOANET and HERMES (Fotiou and Pikridas 2012). GRNET consists of 105 stations supplemented with 17 permanent IGS stations (Dow et al. 2005). The time interval of data varies from 3 to 6 years in the range 2007–2013.

Daily GPS data were processed using Bernese GPS software v5.0 (Dach et al. 2007) following the standard method. Absolute antenna phase center corrections (IGS05.atx) were applied before 17/4/2011 and similarly for the rest period (IGS08.atx). Two different ambiguity resolution strategies were used depending on the length of baselines (SIGMA: <200 km, QIF: >200 km), where the average percentage of the resolved ambiguities was 92%. IGS final orbits and the associated earth orientation parameters where held fixed. In addition IGS station coordinates were minimally constrained by imposing a no-net translation condition. Each one of the final daily solutions was derived using the ionosphere free linear combination, estimating daily coordinates and 12 tropospheric parameters. The average a-posteriori Root Mean Square (RMS) error of the GRNET daily solutions was 1.4 mm.

The estimation of site velocities was carried out in two main steps in order to generate an equivalent frame solution overcoming the artificial discontinuities which may be caused by the change from the IGS05 reference frame (igs05.atx) to the IGS08 (igs08.atx). In the first step, as Rebischung et al. 2011 proposed, we estimated the Station Specific Corrections (SSC) in order to evaluate the antenna calibrations updates from the igs05.atx to igs08.atx. The SSC were derived from the mean average position differences between two cumulative Precise Point Positioning (PPP)

solutions. The two cumulative PPP solutions were done applying the same options, setting up two PPP solutions every 3 months for the time period 1/1/2007 to 17/4/2011, following the standard method, where the only different option between these two cumulative solutions was the antenna calibration model (using igs05.atx for the 1st PPP and igs08.atx for the 2nd). The SSC were estimated subtracting the average stations position of the 2nd PPP cumulative solution from the 1st. The average values of the GRNET SSC are 1.5, 0.2 and −1.3 mm for the north, east and up component respectively. Then, each station specific correction was applied on the coordinates of its corresponding time series for the time interval 1/1/2007 to 17/4/2011. In addition, Helmert transformations were setting up between each updated daily solution and the IGS08 cumulative solution for the time interval 2007–2013. Finally the time series for each station were obtained in a uniform and consistent reference frame adding the daily transformation parameters to the daily updated stations' positions.

In the second step, the site velocities were estimated with the help of a modified version of the new developed H&D MOGS (Hourly and Daily Monitoring Of GNSS Stations) software package (Chatzinikos et al. 2013). The algorithm used estimates the linear vector of site velocity $\overrightarrow{V}$, simultaneously for all stations, applying least squares adjustment. Input data are the vectors of each station topocentric $\overrightarrow{X}$(t) daily coordinates (from the first step) and the according daily covariance matrixes. The algorithm also determines the magnitude $\overrightarrow{\Delta X}_{\mathrm{i}}$ of $\mathrm{m}_{\Delta X}$ predefined discontinuities and the parameters $\mathrm{a_j}$, $\mathrm{b_j}$ of $\mathrm{m_s}$ periodic (ω_j) signals, using the model (Perfetti 2006):

$$X(t) = X(t_0) + (t - t_0) \cdot V + \sum_{i=1}^{m_{\Delta X}} (\Delta X_i \cdot k_{\Delta X,i}(t)) + \sum_{j=1}^{m_s} \left(\left[a_j \cdot \sin\left(\omega_j \cdot \Delta t\right) + b_j \cdot \cos\left(\omega_j \cdot \Delta t\right) \right] \right) \quad (1)$$

where t is the measurement epoch, t_0 the reference epoch and $\overrightarrow{X}(t_0)$ the topocentric coordinates at the reference epoch. The $\mathrm{k}_{\Delta X,i}$(t) values in Eq. (1) are set to zero in case the measurement epoch t is before the discontinuity epoch, otherwise are set to one.

Taking into account the predefined discontinuities and the annual and semi-annual signals of the coordinates' time series, the linear site velocities of GRNET stations were estimated. It should be mentioned that the predefined discontinuities correspond to GPS equipment changes and geophysical reasons, e.g. earthquakes.

The daily coordinate repeatabilities of GRNET stations were estimated 1.6, 1.4 and 5.2 with respect to north, east and up topocentric components. In Fig. 2 the site velocities of the GRNET stations are depicted relative to IGS08.

3 A New Velocity Model for Greece

3.1 Division into Stable Crustal Blocks

The division of the Earth's crust in Greece into stable crustal blocks was derived statistically, using the estimated site velocities. This study has not attempted to identify physical microplates or divide Greece into continental blocks like those referred by Nyst and Thatcher (2004), Reilinger et al. (2006) and Floyd et al. (2010). Instead, the definition of stable crustal blocks was obtained using a deterministic model, as the Euler Pole. Due to the limited time span of data only horizontal velocities were considered. Least squares adjustment was applied in order to identify the clusters of GRNET stations that are rotating in accordance to the Euler Pole model. The minimization of the horizontal velocities in each one cluster was performed using the equation:

$$\begin{bmatrix} v_n \\ v_e \end{bmatrix}_i = r_e \cdot \begin{bmatrix} \sin\lambda & -\cos\lambda & 0 \\ -\sin\varphi\cdot\cos\lambda & -\sin\varphi\cdot\sin\lambda & \cos\varphi \end{bmatrix}_i \cdot \begin{bmatrix} \omega_x \\ \omega_y \\ \omega_z \end{bmatrix} + \begin{bmatrix} u_n \\ u_e \end{bmatrix}_i \quad (2)$$

or

$$\overrightarrow{v}_i = A_i \overrightarrow{x} + \overrightarrow{u}_i \quad (3)$$

where, v_n, v_e are the north and east components of the velocity vector $\overrightarrow{v}$ of a station i with φ and λ its geodetic latitude and longitude, r_e is the radius of the Earth, $\omega_x, \omega_y, \omega_z$ are the rotation rates of the Euler vector $\overrightarrow{x}$, u_n, u_e are the residuals and A_i the rotation matrix of the station i.

The definition of the clusters was based on statistical test, ignoring the traces of the faults, in an iterative process. After each iteration the normalized residual for any station i is estimated and tested by the data snooping technique,

$$r_i^2 = \frac{\widehat{u}_i^T Q_i^{-1} \widehat{u}_i}{2\widehat{\sigma}^2}, \; F_i = r_i^2 \frac{f-2}{f-2r_i^2} \le F^a_{2,\,f-2} \quad (4)$$

where, $\widehat{u}_i = v_i - A_i\widehat{x}$, $Q_i = [Q_{\hat{u}}]_{ii}$ is the 2×2 diagonal part of $Q_{\hat{u}}$ covariance matrix of the residuals $\hat{u}$ and f the degrees of freedom.

After a definition of a cluster, its stations are excluded from the following step for new cluster identification, except for those stations located at the boundary zones between two adjacent clusters. The boundaries of the stable crustal blocks are finally defined by the stations located parametrically.

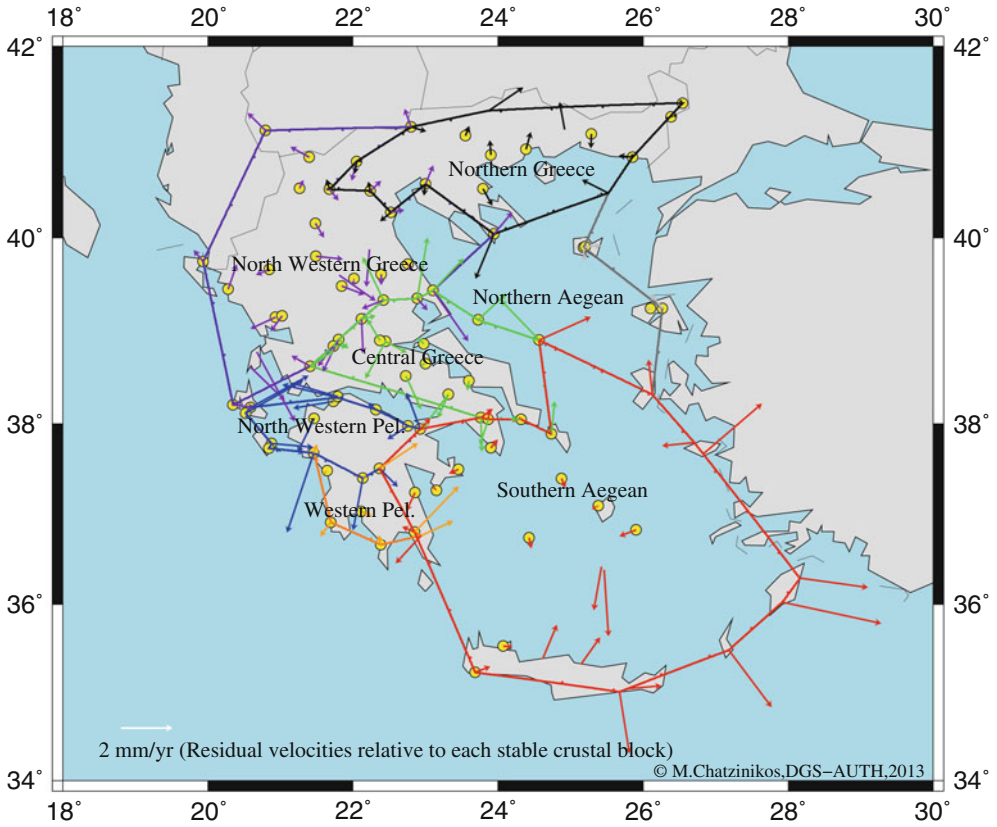

Fig. 3 Residual velocities of GRNET: *Colored vectors* referred to each one block, *yellow dots* depict GPS stations participating in the estimation of Euler Pole vector in each block and *colored polygons* define the boundaries of the seven stable crustal blocks

Table 1 The parameters of Euler Pole for the seven stable crustal blocks of Greece relative to IGS08

Stable crustal block	Num. GPS stations	ϕ (degree)	λ (degree)	ω (degree/Myr)	RMS[a] (mm/year)
Northern Greece	14	55.321	14.645	0.862	±1.0
		±0.698	±0.153	±0.103	
Northwestern Greece	26	−33.445	204.786	1.737	±1.4
		±0.428	±0.024	±0.135	
Central Greece	21	−37.168	202.653	4.677	±2.2
		±0.355	±0.007	±0.299	
Northwestern Peloponnesus	13	−36.840	200.833	4.500	±3.3
		±0.851	±0.018	±0.693	
Western Peloponnesus	6	−35.951	195.721	1.436	±0.8
		±1.546	±0.173	±0.405	
Northern Aegean	4	−36.442	205.814	1.148	±1.2
		±3.028	±0.035	±0.625	
Southern Aegean	17	29.717	124.876	0.129	±0.8
		±1.942	±3.878	±0.016	

[a]The square root of sum of squares of the residuals divided by the number of degrees of freedom

Following the above algorithmic process seven stable crustal blocks were defined (Fig. 3), where its' Euler Pole parameters relative to IGS08 are given in Table 1.

Figure 3 illustrates the residual velocities of GRNET stations in north and east component after the adjustment with the Euler Pole model in each block. Colored polygons define the boundaries of the seven stable crustal blocks and yellow dots present sites included in the estimation of Euler Pole parameters. Some stations in the boundaries between two blocks passed the statistical test and belong

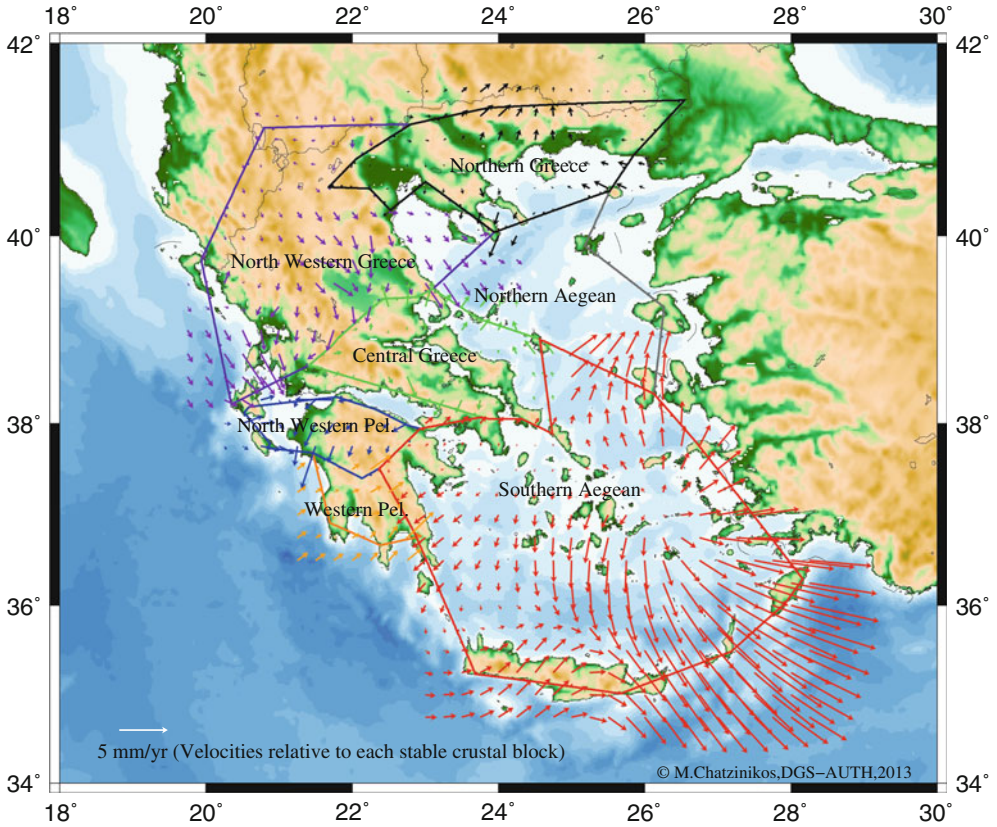

Fig. 4 Predicted signals for the six stable crustal blocks in Greece

to both of them. A percentage of 74% range between −2 to +2 mm/year and 18% between −4 to −2 and 2 to 4 mm/year whereas ±2.9 mm/year is the 2-D RMS.

The biggest residuals were found at the islands of the Ionian Sea, in Northwestern Peloponnesus, along the NAT and in Southeastern Greece (Rhodes, Kalymnos, Eastern Crete and Santorini). Specifically, Southeastern Greece seems to move in a different way than Southern Aegean but the limited number of stations did not allow the definition of one more stable crustal block.

3.2 Least Squares Collocation

In this study a detailed analysis in the residuals of the Euler's Pole model in Greece is presented, using LSC (Dermanis 1985; El-Fiky and Kato 1999; Egli et al. 2007) at the horizontal residuals of all stations within each one of the six stable crustal blocks individually. The Northern Aegean block was excluded from this procedure due to the limited number of GPS stations. The purpose is to consider the displacements of the sites which were not included in the estimation of Euler vectors. In the exact LSC method we used the equations:

$$u' = C_{u'u} C_u^{-1} \widehat{u} \tag{5}$$

where, $\widehat{u}_i = v_i - A_i \widehat{x}$ are the estimated residuals of the Euler's Pole model, u' the predicted residuals at any point and $C_{u'u}$ and C_u the covariance matrices where their elements are computed by a selected covariance function. Assuming that each one of the six blocks is characterized by a homogeneous and isotropic field, the covariance function of signals is only a function of the spherical distance d among the stations. The selected covariances function of the signals:

$$C(d) = \frac{C_o}{1 + \left(d / r\right)^2} \tag{6}$$

is fitted to the estimated residuals with distance interval 15 km for each one of the divided regions separately, where C_o is the variance and r the spatial correlation length varying from 15 to 25 km for five blocks except Southern Aegean block where r = 145 km.

Applying Eq. (5) separately on six grid points (15′ × 15′) for all blocks the result is shown in Fig. 4.

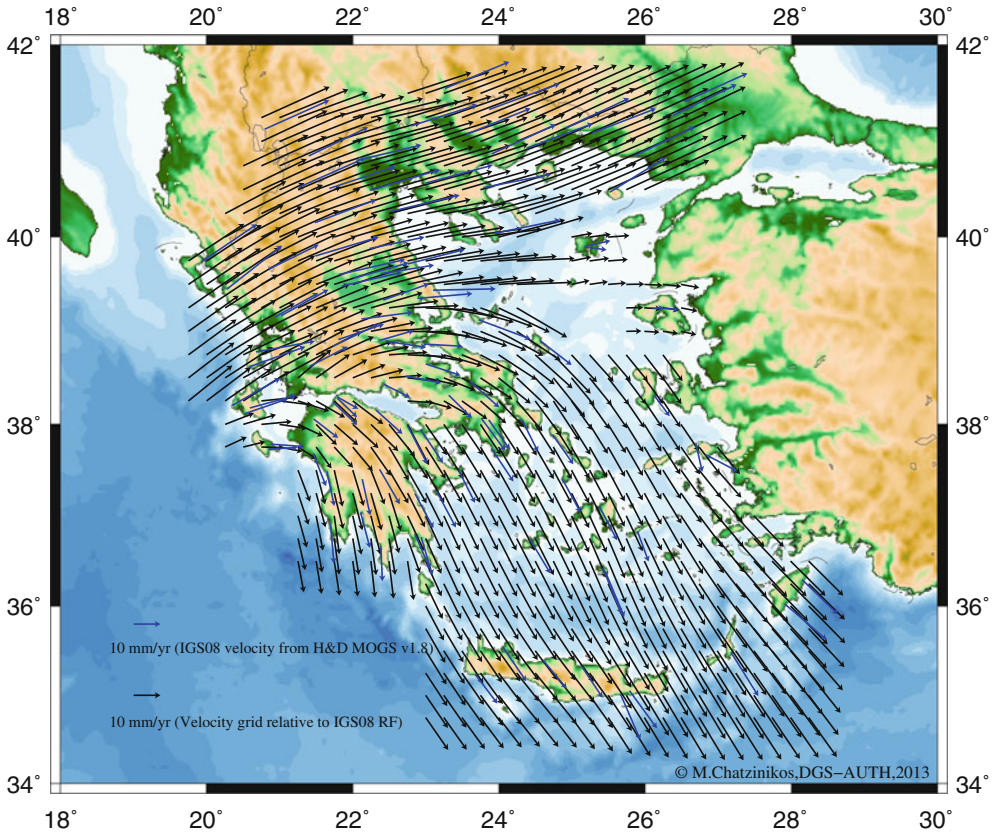

Fig. 5 The Hellenic Geodetic Velocity Model 2013 (*black* and *blue arrows* depict relative to IGS08 the gridded deformation model and the GRNET stations' velocities respectively)

3.3 The Hellenic Geodetic Velocity Model 2013

The new estimated horizontal velocity model for Greece, named the Hellenic Geodetic Velocity Model 2013 (HGVM2013), is the combination of the Euler vectors and the predicted residuals of LSC. Based on Eqs. (2) and (3) the velocity matrix $V_{(j)_i}^{IGS08}$ relative to IGS08 reference frame of a point i at the block j is given by:

$$\mathrm{V}_{(\mathrm{j})_\mathrm{i}}^{\mathrm{IGS08}} = \mathrm{A_i}\ \omega_{(\mathrm{j})}^{\mathrm{IGS08}} + \mathrm{U_i'^{(j)}} \tag{7}$$

where A_i is the rotation matrix of a point i, $\omega_{(j)}^{IGS08}$ is the matrix of angular velocity at block j and $U'^{(j)}_i$ is the predicted signal matrix of the point i according to Eq. (5). It should be noted that applying Eq. (7) for the 105 sites in the GRNET with known velocities, the HGVM2013 estimated these site velocities with a precision of ±1.7 mm/year at 95% confidence. Furthermore, applying Eq. (7) on a grid with dimension ($15' \times 15'$), which mainly covers the mainland of Greece, it has as a result the creation of a gridded deformation model (Fig. 5). The grid represents the final form of the HGVM2013, where the estimation of a point velocity could be derived applying the b-linear method at the four nearest points of the grid.

4 The Proposed Semi-Kinematic Datum for Greece

Greece needs a new geodetic datum which would be characterized by uniform stability and accuracy overcoming the serious positioning problems introduced by unmodelled tectonic deformation. For this reason we propose the implementation of a semi-kinematic datum. According to the presented analysis the new datum, called here Hellenic Semi-Kinematic Datum 2010 (HSKD2010), is a realization of IGS08 using the new estimated velocity model HGVM2013. It should be mentioned that the realization could be also considered with respect to ETRS89 reducing the rotation rates of the seven stable crustal blocks relative to Eurasian plate applying its Euler Pole parameters (Boucher and Altamimi 2011).

The implementation of HSKD2010 follows the next steps:

- The coordinates of the GRNET stations will be referred to IGS08 and at the epoch 1/1/2010 (mean epoch of used

observations). These reference epoch coordinates will be held fixed.
- Positioning for any point will be performed in IGS08 and at the measurement epoch, taking into account the current coordinates of the reference stations as derived using the velocities of the estimated velocity model and the time span from the reference epoch.
- The computation of HSKD2010 coordinates of any point will be obtained by the translation of its estimated current coordinates back to the reference epoch (1/1/2010) using the interpolated velocities from HGVM2013 and the corresponding time span.

The stability of HSKD2010 depends on the accuracy of the estimated velocity model (HGVM2013) and the time interval between the reference and the measurement epoch. The new velocity model of Greece should be updated and assessed normally every few years. In case of unexpected events, like strong earthquakes and landslides, the effect to the velocity model should be investigated. In that case, the HGVM2013 should be revised at the spot of the event, due to coseismic deformation, applying a patch model as for example Tanaka et al. 2007 proposed.

5 Summary

The realization of a semi-kinematic datum for Greece, called HSKD2010, has been presented. The implementation of HSKD2010 will provide users with an accurate and stable geodetic datum, overcoming the instability of the HGSR87 static geodetic datum. Moreover the HSKD2010 could be adopted by the Real Time Kinematic networks of Greece providing significant benefits regarding the position of a reference station in relation to the rover point. The HSKD2010 is realized in terms of the IGS08 reference frame and depends on the new estimated velocity model of Greece (HGVM2013).

The new velocity model was created in two steps and it refers to the horizontal level. Firstly, the Earth's crust in Greece was divided into seven stable crustal blocks using the Euler Pole model, statistical test and the site velocities of GRNET. The accuracy of the Euler Pole model was estimated at ± 2.9 mm/year. In addition, the local deformations of the blocks with respect to Euler vectors were modeled applying LSC on the residuals of the Euler Pole model. The combination of the Euler Pole model with the LSC constructed the new gridded deformation model of Greece (HGVM2013).

Finally, longer duration of GPS data will enable estimation of the vertical component of the datum realization and its implementation.

Acknowledgements Dr. A. Ganas from National Observatory of Athens, Dr. M. Gianniou from NCMA S.A. and Mr. A. Antonakakis from METRICA S.A. are acknowledged for providing the GPS data which were used in this study from the networks NOANET, HEPOS and SMARTNET GREECE respectively. Moreover, an anonymous reviewer is acknowledged for his suggestions which helped in the improvement of this paper.

References

Blick G, Crook C, Grant D, Beavan J (2006) Implementation of a semi-dynamic datum for New Zealand. International Association of Geodesy Symposia, vol. 128, A window on the future of geodesy. Proceedings of the International Association of Geodesy, IAG General Assembly, June 30–July 11, 2003, Sapporo, Japan

Boucher C, Altamimi Z (2011) Memo: specifications for reference frame fixing in the analysis of a EUREF GPS campaign. http://etrs89.ensg.ign.fr/memo-V8.pdf

Chatzinikos M, Fotiou A, Pikridas C, Rossikopoulos D (2013) New results of the velocity field in Greece by an automatic process of a permanent GPS network. Presented at the EUREF Annual Symposium, May 29–31 2013, Budapest, Hungary

Dach R, Hugentobler U, Fridez P, Meindl M (2007) Bernese GPS software version 5.0. Astronomical Institute, University of Bern, Switzerland

Dermanis A (1985) Geodetic applications of interpolation and prediction. Eratosthenes 22:229–262

Dow JM, Neilan RE, Gendt G (2005) The international GPS service: celebrating the 10th anniversary and looking to the next decade. Adv Space Res 36:320–326

Egli R, Geiger A, Wiget A, Kahle HG (2007) A modified least squares collocation for the determination of crustal deformation: first results in the Swiss Alps. Geophys J Int 168:1–12

El-Fiky GS, Kato T (1999) Continuous distribution of the horizontal strain in the Tohoku district, Japan, predicted by least-squares collocation. J Geodyn 27:213–236

Floyd MA, Billiris H, Paradissis D et al (2010) A new velocity field for Greece: implications for the kinematics and dynamics of the Aegean. J Geophys Res 115:B10403

Fotiou A (2007) Geometric geodesy, theory and practice. Ziti, Thessaloniki (in Greek)

Fotiou A, Pikridas C (2012) GPS and geodetic applications, 2nd edn. Ziti, Thessaloniki (in Greek)

Gianniou M (2009) National report of Greece to EUREF 2009. Presented at the EUREF Annual Symposium, May 27–30 2009, Florence, Italy

Hollenstein C, Müller MD, Geiger A, Kahle HG (2008) Crustal motion and deformation in Greece from a decade of GPS measurements, 1993–2003. Tectonophysics 449:17–40

Howe TM, Bird P (2010) Exploratory models of long-term crustal flow and resulting seismicity across the Alpine-Aegean orogen. Tectonics 29:TC4023

Katsampalos K, Kotsakis C, Gianniou M (2009) Hellenic terrestrial reference system 2007 (HTRS07): a regional densification of ETRS89 over Greece in support of HEPOS. EUREF 2009 Symposium, May 27–30 2009, Florence, Italy

McClusky S, Balassanian S, Barka A et al (2000) Global positioning system constraints on plate kinematics and dynamics in the eastern Mediterranean and Caucasus. J Geophys Res 105:5695–5719

Müller MD, Geiger A, Kahle HG, Veis G, Billiris H, Paradisis D, Felekis S (2013) Velocity and deformation fields in the North Aegean domain, Greece, and implications for fault kinematics, derived from GPS data 1993–2009. Tectonophysics 597–598:34–49

Nyst M, Thatcher W (2004) New constraints on the active tectonic deformation of the Aegean. J Geophys Res 109:B11406

Papazachos BC, Kiratzi AA, Hatzidimitriou PM, Rocca AC (1984) Seismic faults in the Aegean area. Tectonophysics 106:71–85

Perfetti N (2006) Detection of station coordinate discontinuities within the Italian GPS Fiducial Network. J Geod 80(7):381–396

Rebischung P, Griffiths J, Ray J, Schmid R, Collilieux X, Garayt B (2011) IGS08: the IGS realization of ITRF2008. GPS Solut 1–12. doi:10.1007/s10291-011-0248-2

Reilinger R, McClusky S, Vernant P et al (2006) GPS constraints on continental deformation in the Africa-Arabia-Eurasia continental collision zone and implications for the dynamics of plate interactions. J Geophys Res 111:B05411

Tanaka Y, Saita H, Sugawara J et al (2007) Efficient maintenance of the Japanese geodetic datum 2000 using crustal deformation models – PatchJGD & semi-dynamic datum. Bull Geogr Surv Inst 54:49–59

Simulated VLBI Satellite Tracking of the GNSS Constellation: Observing Strategies

Lucia Plank, Johannes Böhm, and Harald Schuh

Abstract

Very Long Baseline Interferometry (VLBI) observations to satellite targets is a promising technique to improve future realizations of terrestrial reference frames (TRF). The high number of available satellites of Global Navigation Satellite Systems (GNSS) provides an attractive existing infrastructure that could be utilized for such observations. The Vienna VLBI Software (VieVS) was extended for the possibilities of scheduling, simulating, and processing VLBI observations to GNSS satellites, allowing to give information on expected accuracies of derived station coordinates. Assuming the GNSS signals to be measured with a precision of 30 ps, we find weekly station position repeatabilities at the centimeter level or better for simulated observations to satellite targets only. Adequate scheduling strategies have to be applied, e.g. in terms of a fast switching between the observed satellites. Even better solutions of about 5 mm in mean 3D position rms after one day are achieved when integrating the satellite observations into standard VLBI sessions to extragalactic radio sources. Further, this combined approach allows the determination of a frame tie between the satellite system and the VLBI system in terms of relative Earth rotation parameters and a scale with a precision of about 1–2 mm at the Earth's surface.

Keywords

Co-location • Inter-technique frame ties • Very long baseline interferometry • VLBI satellite tracking

1 Introduction

VLBI satellite tracking is defined as using the Very Long Baseline Interferometry (VLBI) technique to observe close, Earth-orbiting satellites instead of distant extragalactic radio sources. Early examples for such applications, either for the use of orbit determination or positioning, were presented by Preston et al. (1972), Rosenbaum (1972), or Counselman and Gourevitch (1981). More recently, in order to test newly developed hardware and software, VLBI tracking to satellites was performed prior to the VLBI tracking of the lunar probes SELENE and Chang'E (Hanada et al. 2008; Huang et al. 2006). Huang et al. (2011) also mention this technique for supporting the orbit determination of the COMPASS/BeiDou system. The successful realization of VLBI observations to satellites of the GNSS was shown by Tornatore et al. (2014), tracking GLONASS satellites at L-Band.

Aside the goal of improved orbit determination, the co-location of different sensors and observation types aboard a satellite, including VLBI satellite tracking, has the potential to improve the future Global Geodetic Observing System

L. Plank (✉) • J. Böhm
Vienna University of Technology, Gußhausstraße 27-29, 1040 Vienna, Austria

Present address of L. Plank: University of Tasmania, Private Bag 37, Hobart 7001, Australia
e-mail: Lucia.Plank@utas.edu.au

H. Schuh
DeutschesGeoForschungsZentrum GFZ, Telegrafenberg, A17, 14473 Potsdam, Germany

© Springer International Publishing Switzerland 2015

C. Rizos, P. Willis (eds.), *IAG 150 Years*, International Association of Geodesy Symposia 143,
DOI 10.1007/1345_2015_87

(Rothacher et al. 2009). Thus, the observation of GNSS satellites with VLBI would allow to directly tie the GNSS transmitters to the International Celestial Reference Frame (ICRF) (Hase 1999). It also enables the determination of the Earth's center of mass in the ICRF, what is not possible with classical VLBI (Dickey 2010). Improvements are expected in the area of inter-technique frame ties, which is the link between the various space geodetic techniques used for the derivation of the International Terrestrial Reference Frame (ITRF2008; Altamimi et al. 2011). There are several ideas for dedicated new satellites, as e.g. the proposed GRASP mission (Geodetic Reference Antenna in Space; Bar-Sever et al. 2009), combining all techniques by the installation of adequate technique-specific sensors on a single satellite platform, realizing a so-called space tie. Finally, the interaction of the terrestrial and the celestial reference frame, being topic of IAG Sub-Commission 1.4,[1] as well as the consistency of the whole product range of CRF, the Earth orientation parameters (EOP), and TRF is thought to profit from VLBI satellite observations. All in all, numerous applications for geodetic purposes ask for more detailed investigations of this technique.

2 Composition of the Study

The results presented in this contribution are based on simulated observations, generated and processed with the Vienna VLBI Software (VieVS; Böhm et al. 2012). These VLBI observations to satellites are used to determine positions of the observing radio telescopes in the satellite system. On the other hand, the antenna positions in the VLBI system can be derived from classical VLBI observations to radio sources. In the end, a comparison between the two systems in terms of Earth rotation parameters (ERP) and a scale component gives the frame tie between them.

2.1 Software Realization in VieVS

VieVS is state-of-the-art geodetic VLBI analysis software. For the purpose of studying VLBI observations to satellites, new amendments allow for the scheduling, simulation, and analysis of such observations (Plank et al. 2014). At the moment, the scheduling only meets basic requirements that are necessary for simulations. This means, that observations are scheduled at distinct epochs without consideration of an observation duration or actual capabilities of the radio telescopes, e.g. in terms of slewing speed. Based on a given antenna network and the satellite orbit(s), observations are scheduled whenever the selected satellite is visible from at least two radio telescopes, according to the chosen observation interval. The generated observation file is the input to the analysis part, where the observations are simulated following the strategy described by Pany et al. (2010). Besides the geometrical delay, the artificially generated observations include the most dominant stochastic errors due to the troposphere τ^{12}_{trp}, accounting for tropospheric turbulence at each station $i = 1, 2$, clock errors τ^{12}_{clk}, and a measurement error τ^{bl}_{wn} modeled as white noise per baseline. A rather turbulent troposphere was assumed with a structure constant of $2.5 \cdot 10^{-7}\mathrm{m}^{1/3}$ and an effective height of 2,000 km at all stations (Nilsson et al. 2007). Concerning the other simulated errors, a clock error corresponding to an Allan standard deviation of $1 \cdot 10^{-14}$ at 50 min and a measurement noise of 30 ps was used. Systematic errors due to insufficient knowledge of the target's position, such as orbit errors or signal emission of different antenna elements of the GNSS satellites, respectively source structure effects of the observed quasars (e.g. Shabala et al. 2014) were not included in our simulation. In the processing, the geometrical delay for satellite observations is calculated following the model for VLBI observations of Earth satellites by Klioner (1991). When analyzing the simulated observations, this geometrical delay falls out and the remaining observed minus computed value $(o-c)$ for each observation consists of the simulated errors only (Eq. 1).

$$o - c = \tau^{12}_{trp} + \tau^{12}_{clk} + \tau^{bl}_{wn} \tag{1}$$

We use standard settings for the analysis, estimating station clocks and zenith wet delays as piecewise linear offsets using loose relative constraints, and determining station coordinates (dr, de, dn) once per 24 h session. All stations contributed to the datum, minimizing the squared differences between the a priori and the estimated station coordinates. This implies that translation and rotation between the a priori and estimated coordinates vanish (no-net-translation and no-net-rotation condition). EOP were estimated once per session. Any estimated values represent a distortion from the a priori system.

2.2 Station Position Repeatability

To generate and analyze the artificial observations, we use Monte Carlo simulations. A sample of 30 repetitions of the simulation allows for a statistical analysis, in terms of station position repeatability. The standard deviation of 30 simulation runs gives a measure for the precision that can be expected for the determination of station coordinates. We use the standard deviation in three components: radial (σ_{dr}), east (σ_{de}), and north (σ_{dn}). The 3D position root mean square

[1] http://iag.geo.tuwien.ac.at.

(rms) is then defined as:

$$3\text{D position rms} = \sqrt{\sigma_{dr}^2 + \sigma_{de}^2 + \sigma_{dn}^2} \qquad (2)$$

The 3D position rms solely includes stochastic errors varying for each of the 30 simulation runs. The influence of systematic errors was tested for the satellite orbits, using various orbit solutions provided by the IGS (International GNSS Service; Dow et al. 2009). For the simulated observations the final orbits were used and in the analysis the satellites' positions were taken from the ultra-rapid, respectively rapid orbits. While the 3D position rms did not change significantly (< 0.5 mm), mean 3D position offsets up to 2 mm were found. The effect of orbit errors on the repeatability of the frame tie (see Sect. 4) was maximal 4 µas respectively 0.4 µs for the ERP and smaller than 0.05 ppb in scale.

3 Observing GNSS Satellites with VLBI

With the existing and upcoming GNSS, in the next years the number of available satellites will increase from about 50–60 today to 100–120 active GNSS satellites in orbit. For observations with VLBI, where in contrast to GNSS only one target is observed from a set of receiving telescopes at a certain time epoch, a careful selection of the observed satellites is needed. Some general ideas for the so-called scheduling are given in Sect. 3.2. In terms of the technical realization of VLBI observations to satellites of the GNSS, namely the actual tracking with the radio telescopes and the reception and processing of the available signals, research is ongoing. With regard to the observed signal, Tornatore and Haas (2009) concluded that the GNSS signals can be observed with a group delay precision of about 28 ps. Kodet et al. (2013) showed that the reception of the strong L-band signals may be even possible with the standard S-band receivers, while compatibility with the upcoming VLBI2010 Global Observing System (VGOS) is not guaranteed. Aside these practical issues to be solved, the purpose of this contribution is to give some information about possible observing strategies and expected accuracies of the results. For the subsequent examples we selected six satellites of the Global Positioning System (GPS) assuming that they can be observed with existing and possible upcoming radio telescopes of the IVS (International VLBI Service for Geodesy and Astrometry; Schuh and Behrend 2012) network with a precision of 30 ps.

3.1 Weekly Solution

We chose a global network, consisting of 16 either real or fictitious VLBI stations well distributed around the globe (Fig. 1). For the six selected GPS satellites, observations were scheduled whenever the satellite is visible from at least two stations. Each satellite is observed at most once every 10 min, while the minimum observation interval is 1 min. The cutoff elevation angle was set to 10°. A typical sequence of the schedule is shown in Table 1, with all six satellites being visible for the selected time of observation. For this kind of observing schedule covering 24 h, a mean 3D position rms of 2.8 cm is found for the Monte Carlo simulations.

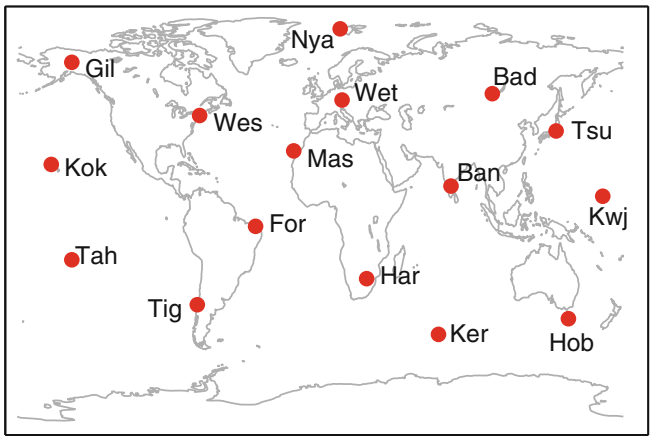

Fig. 1 Map of the fictitious global 16 station network

Table 1 A typical sequence of observations (hh:mm) using the applied scheduling strategy

Sat1	Sat2	Sat3	Sat4	Sat5	Sat6
13:00	13:01	13:02	13:03	13:04	13:05
13:10	13:11	13:12	13:13	13:14	13:15
...	...	...	...	...	...

When all six satellites (Sat1-Sat6) are visible, the maximum of six observations within a 10 min interval is scheduled at one station

One possibility to improve our results is the concept of weekly solutions. At the moment, the IGS and the International SLR Service (ILRS; Pearlman et al. 2002) produce weekly station coordinates and also the GRASP concept follows this strategy. When we simulated and processed VLBI observations to the six GPS satellites for seven consecutive days and combined the normal equation matrices of each 24 h session within a global solution (Krásná et al. 2014), we obtained the results presented in Fig. 2. The 3D position rms is shown for each station, as well as the expected precision in each component, height, east, and north. The results are arranged following the mean total number of observations per station per day, as indicated by the red line. Although a slight relation between higher precision and increasing number of observations is visible, also other factors like the location of the station within the network and the geometry between the observing baselines and the satellite orbit

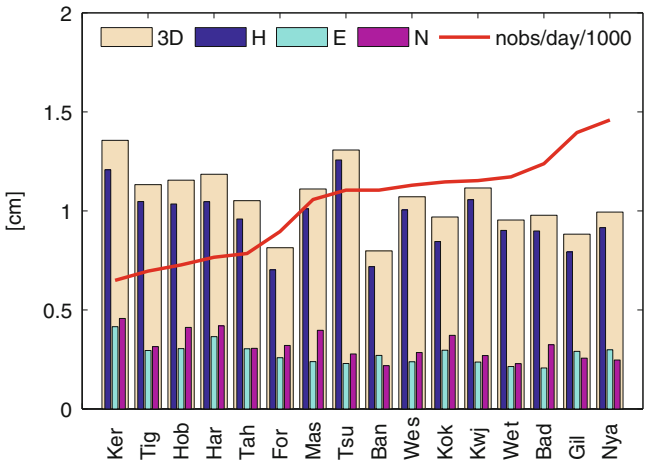

Fig. 2 Station position repeatabilities after one week if six GPS satellites were observed with a 16 station network. For each station, the 3D position rms is shown with a beige bar, the height component in *blue*, the east component in *cyan* and the north component in *pink*. The *red line* is an indicator for the mean number of observations per station per day

Fig. 3 One day skyplot of station Svetloe when applying the fast switching (*left*) and the continuous observation (*right*) scheduling strategy as explained in the text. Each colored *circle* represents one observation and *black* lines are drawn between consecutive observations

influence the results. Hence, despite station Tsukuba (Tsu) and Bangalo (Ban) have a similar number of observations, their expected station position repeatabilities are quite different. This is due to a considerably worse sky coverage at Tsukuba compared to that at Bangalo. Clearly evident is the dominating error in the height component, an indication for a poorly determined troposphere. The resulting mean weekly 3D position rms is 1.0 cm, about three times better than for the 24 h session. We want to point out, that systematic errors due to tropospheric correlation between consecutive days were not taken into account in the weekly solution.

3.2 Scheduling

A careful scheduling prior to the observation is an essential part of a VLBI experiment and has impact on the results. Considering the capabilities in sensitivity and slewing of the participating antennas, together with the signal strengths of the radio sources, today's geodetic VLBI observations are usually scheduled following the sky coverage optimization (e.g. Petrov et al. 2009). To minimize the correlation between the estimated station heights, clock parameters, and troposphere delays, it is necessary to have observations in different directions and elevations above each station. With the prospect of future VGOS radio telescopes equipped with high slew speeds (e.g. Schuh and Behrend 2012) and assuming a relatively strong signal from the satellites, in our scheduling the observation interval, including observation and slewing, was fixed to 1 min and antenna specifications were not taken into account.

In terms of the scheduling strategy, we find that a switching of the target satellite yields better results than the continuous tracking of one satellite. This was tested with simulated observations in a regional European network, where six GPS satellites were observed from seven stations during one week using two different scheduling strategies. The first option was the one described above, using a minimal interval of 1 min, fast switching between all six satellites, and the restriction that the same satellite is not observed twice within 10 min. In the second option the observation interval was also fixed to one minute but the target was selected to be the satellite best visible from all participating stations. This resulted in long continuous tracking periods for one satellite until another appeared high in the sky above the network. Showing the sky coverage after 24 h for station Svetloe, these two schedules are visualized in Fig. 3. Although when following one satellite the mean number of observations per station is about six times higher than for the first option, the achieved weekly mean 3D position rms of 5 mm for the switching schedule is considerably better than the 3.3 cm for the second schedule. This clearly shows the importance of a thorough scheduling, an important topic that is not investigated more deeply here.

4 Frame tie between VLBI and GNSS

So far, the presented results were achieved by simulating observations solely to satellite targets, revealing good results only for long observation durations, e.g. one week. Presuming that the radio telescopes are capable to receive both signals, the artificial satellite signal as well as the emission by extragalactic radio sources, the possibility of combined schedules is investigated next. Therefore, we took the schedules of two geodetic VLBI sessions to radio sources:

– IVS-R1594 on July 16, 2013. This is a standard 24 h session including eight stations.

Table 2 Mean 3D position rms after 24 h, as determined in the combined (c) approach with common zenith wet delays and clocks and the separate solution (sep)

Mean 3D position rms	R1594	CONT11-1
Satellite (c) (mm)	6	5
Radio source (c) (mm)	5	4
Satellite + Radio source (c) (mm)	3	3
Satellite (sep) (mm)	42	31
Radio source (sep) (mm)	13	10

– CONT11-1 on September 15, 2011. This is the first 24 h session of the continuous VLBI campaign 2011 (CONT11), including 13 stations.

For the same periods and antenna networks, observations to six GPS satellites were scheduled, following the switching strategy described above (Sect. 3.2). Both schedules, i.e. the observations to the extragalactic radio sources and to the satellites, were combined, again disregarding actual antenna capabilities, observing time, and slewing. After simulation, the analysis was performed following a combined approach: while all observations were used to determine the zenith wet delays and clocks for the individual stations, the estimation of antenna site coordinates was done separately for (a) the observations to the satellites and (b) the classical observations to the radio sources. Consequently, two sets of coordinates were derived, in the satellite system and in the VLBI system realized by the positions of the extragalactic radio sources. For the investigated schedules, we got mean 3D position rms of $4-6$ mm for both solutions, solving for station coordinates in the satellite system or in the classical VLBI way (Table. 2). If we included all observations in the estimation of station coordinates, an even better mean 3D position rms of 3 mm after 24 h was achieved. For comparison, also a completely separate analysis of satellite only, respectively radio source only observations was performed, yielding significantly worse results of a few centimeters.

In order to quantify the agreement between the two sets of station positions, we compared the estimated ERP. We also determined the scale difference in a 7-parameter Helmert transformation. This was done for a sample of 30 simulated sessions. The standard deviation of each parameter gives a measure of the expected accuracy. The corresponding values are shown in Table 3.

The combined approach allows the determination of the frame tie in terms of ERP after one day at the level of 10–30 µas in x_p and y_p, respectively 1–2 µs in $dUT1$. The maximal difference in the scale component is 0.3 ppb. On global scale, these values correspond to a relative alignment of the two systems at the level of 1–2 mm. As shown in Table 3, the completely separate solutions (sep) show much worse results. This is due to the fact, that the satellite observations alone are not suitable to determine ERP precisely.

Table 3 Expected accuracy in terms of the standard deviations of 30 simulated sessions of the difference in ERP and the scale between the satellite and the VLBI system

	x_p (µas)	y_p (µas)	$dUT1$ (µs)	Scale (ppb)
R1 (c)	26	18	2	0.3
R1 (sep)	248	178	17	1.3
CONT11-1 (c)	16	17	1	0.2
CONT11-1 (sep)	159	109	8	0.7

The frame tie was calculated for the two sessions using the combined solution (c). For a comparison, also the frame tie of the completely separate approach (sep) is shown

This so-called frame tie shows the agreement between the two target systems, as determined via the estimation of the ERP. When using real observations, any larger discrepancies in these parameters could indicate systematic errors between the GPS and the VLBI frames, an important task for future improvements of the ITRF.

5 Conclusions

Investigating the possibilities of VLBI satellite tracking to improve the future ITRF, the Vienna VLBI Software VieVS was extended allowing for simulations of VLBI observations to satellite targets. A constellation of six GPS satellites serves as representative for the whole GNSS, with observations scheduled from global networks of VLBI radio telescopes. For satellite only observations, we find expected station position repeatabilities of a few centimeters after 24 h and at the 1 cm level after one week of observations. Scheduling strategies like fast switching between the tracked satellites, can considerably improve the expected results. For these observations, significantly worse results for the height component are found, indicating insufficient determination of the troposphere. Assuming adequate signals and receiving telescopes, we recommend the combination of VLBI satellite observations with standard VLBI sessions to extragalactic radio sources. Solving for a combined troposphere, the separate determination of station coordinates and ERP in the satellite system on the one hand and in the VLBI (radio source) system on the other, realizes a precise frame tie.

The results of our simulations confirm the potential of VLBI satellite observations for the establishment of frame ties and for future improvements of the TRF. Applying a previously probed simulation method, this work represents a first insight into this topic, opening the field for future research, as e.g. including orbital errors of the target satellites into the simulations or detailed investigations on scheduling optimization. Further, the role of the EOP, as e.g. applied during orbit estimation in GNSS or for the derivation of the a priori reference frames, needs to be investigated more deeply. Actual results of VLBI tracking of GNSS satellites will also

strongly rely on the observability of the GNSS signal, a subject of current research.

Acknowledgements The research was done within project D-VLBI (SCHU 1103/4-1) as part of the DFG Research Unit *Space-Time Reference Systems for Monitoring Global Change and for Precise Navigation in Space* funded by the German Research Foundation (FOR 1503). The authors acknowledge the IVS and all contributors to the CONT11 campaign. We thank the three reviewers for their useful comments.

References

Altamimi Z, Collilieux X, Métivier L (2011) ITRF2008: an improved solution of the international terrestrial reference frame. J Geod 85(8):457–473

Bar-Sever Y, Haines B, Bertiger W, Desai S, Wu S (2009) Geodetic reference antenna in space (GRASP) - a mission to enhance space-based geodesy. In: COSPAR Colloquium, Padua 2009

Böhm J, Böhm S, Nilsson T, Pany A, Plank L, Spicakova H, Teke K, Schuh H (2012) The new Vienna VLBI software VieVS. In: IAG Symp 136, pp 1007–1011

Counselman C, Gourevitch SA (1981) Miniature interferometer terminals for earth surveying: ambiguity and multipath with global positioning system. IEEE Trans Geosc Rem Sens GE-19(4):244–252

Dickey JM (2010) How and Why do VLBI on GPS. In: Proceedings of IVS 2010, pp 65–69, NASA/CP 2010-215864

Dow JM, Neilan RE, Rizos C (2009) The international GNSS service in a changing landscape of global navigation satellite systems. J Geod 83:191–198

Hanada H, et al. (2008) VLBI for better gravimetry in SELENE. Adv Space Res 42:341–346

Hase H (1999) Phase Centre Determinations at GPS-Satellites with VLBI. In: Proceedings of 13th EVGA, pp 273–277

Huang Y, Hu X, Huang C, Jiang D, Zheng W, Zhang X (2006) Orbit determination of satellite "Tance 1" with VLBI data. Chin Astr Astroph 30:318–329

Huang Y, Hu X, Zhang X, Jiang D, Guo R, Wang H, Shi S (2011) Improvement of orbit determination for geostationary satellites with VLBI tracking. Chin Sci Bull 56:2765–2772

Klioner SA (1991) General relativistic model of VLBI observables. In: Proceedings of AGU Chapman Conference on Geodetic VLBI: Monitoring Global Change, pp 188–202, NOAA Techn Rep NOS 137 NGS 49

Kodet J, Plötz C, Schreiber KU, Neidhardt A, Pogrebenko S, Haas R, Molera G, Prochazka I (2013) Co-location of space geodetic techniques in space and on the ground. In: Proceedings of 21st EVGA, pp 223–226

Krásná H, Böhm J, Plank L, Nilsson T, Schuh H (2014) Atmospheric effects on VLBI-derived terrestrial and celestial reference frames. In: IAG Symposium 139. Doi: 10.1007/978-3-642-37222-3__26

Nilsson T, Haas R, Elgered G (2007) Simulations of atmospheric path delays using turbulence models. In: Proceedings of 18th EVGA, pp 175–180

Pany A, Böhm J, MacMillan DS, Schuh H, Nilsson T, Wresnik J (2010) Monte Carlo simulations of the impact of troposphere, clock and measurement errors on the repeatability of VLBI positions. J Geod 85:1:39–50

Pearlman MR, Degnan JJ, Bosworth JM (2002) The international laser ranging service. Adv Space Res 30:2:135–143

Petrov L, Gordon D, Gipson J, MacMillan D, Ma C, Fomalont E, Walker RC, Carabajal C (2009) Precise geodesy with the very long baseline array. J Geod 83:859–876

Plank L, Böhm J, Schuh H, (2014) Precise station positions from VLBI observations to satellites - a simulation study. J Geod. Doi:10.1007/s00190-014-0712-1

Preston RA, et al. (1972) Interferometric observations of an artificial satellite. Science 178-4059:407–409

Rosenbaum B (1972) The VLBI time delay function for synchronous orbits. NASA/TM-X-66122 GSFC

Rothacher M, et al. (2009) The future global geodetic observing system. In: Plag HP, Pearlman M (eds) Global geodetic observing system. Springer, Berlin/Heidelberg, pp 237–272

Schuh H, Behrend D (2012) VLBI: a fascinating technique for geodesy and astrometry. J Geod 61:68–80

Shabala S, McCallum J, Plank L, Böhm J (2014) Simulating the effects of quasar structure on parameters from geodetic VLBI. Submitted to J Geod

Tornatore V, Haas R (2009) Considerations on the observation of GNSS-signals with the VLBI2010 system. In: Proceedings on 19^{th} EVGA, pp 151–155

Tornatore V, Haas R, Casey S, Duev D, Pogrebenko S, Molera Calvés G (2014) Direct VLBI observations of global navigation satellite system signals. In: IAG Symposium 139. Doi: 10.1007/978-3-642-3722-3__32

On the Development and Implementation of a Semi-Dynamic Datum for Indonesia

Hasanuddin Z. Abidin, Susilo Susilo, Irwan Meilano, Cecep Subarya, Kosasih Prijatna, M. Arief Syafi'i, Edwin Hendrayana, Joni Effendi, and Dodi Sukmayadi

Abstract

Since the nineteenth century, several local topocentric geodetic datums have been used for surveying and mapping in Indonesia. In 1975 the Indonesian Datum 1974, which is a national topocentric datum, was introduced and then replaced by the National Geodetic Datum 1995 which is a static geocentric datum realized using GPS observations. In recent years it has been realized that, due to on-going active tectonics in the Indonesian region, the National Geodetic Datum 1995 is inadequate for surveying and mapping in some regions of Indonesia, and also for some current and emerging applications. Initial studies suggested that a semi-dynamic geocentric datum is suitable for Indonesia. The adopted new datum uses the ITRF2008 reference frame with a reference epoch of 1 January 2012. It incorporates several major deformation blocks of Indonesia, and several micro blocks to model specific deformation events such as large earthquakes. Realization of this new semi-dynamic datum will be primarily based on existing data coming from many previous national GPS campaigns that have been conducted by the Geospatial Agency of Indonesia, and from existing GPS CORS stations across Indonesia.

Keywords

Deformation block • Geocentric datum • Geodetic datum • GPS • Indonesia • ITRF2008 • Reference frames • Semi-dynamic datum • Topocentric datum

1 Introduction

Indonesia is a maritime continent with a complex and active tectonic setting (see Fig. 1), and therefore prone to various natural hazards, such as earthquakes, tsunamis, volcanic eruptions, landslides, flooding and land subsidence. The surface deformation caused by these hazards, coupled with tectonic plate motion in and around the Indonesian region, will cause the geocentric coordinates of many geodetic benchmarks and monuments in Indonesia to change with time. Accordingly, the adopted geodetic datum for Indonesia should take into account the active nature of Indonesian geodynamics.

Since the nineteenth century, several local topocentric geodetic datums have been used for surveying and mapping in Indonesia (Schepers and Schulte 1931). All of these local datums used the Bessel 1841 ellipsoid as the reference ellipsoid, with different datum origin points. In 1975, the Indonesian Datum 1974 (ID 1974), a national topocentric datum, was introduced (Rais 1975) and then replaced by the National Geodetic Datum 1995 (DGN 1995) which is a static geocentric datum realized using GPS observations (Subarya

H.Z. Abidin (✉) • I. Meilano • K. Prijatna
Geodesy Research Group, Faculty of Earth Science and Technology, Institute of Technology Bandung (ITB), Jl. Ganesha 10, Bandung, Indonesia
e-mail: hzabidin@gd.itb.ac.id

S. Susilo • M.A. Syafi'i • E. Hendrayana • J. Effendi • D. Sukmayadi
Geospatial Agency of Indonesia (BIG), Jl. Raya Jakarta – Bogor Km. 46, Cibinong, Indonesia

C. Subarya
Previously with Geospatial Agency of Indonesia (BIG), Jl. Raya Jakarta – Bogor Km. 46, Cibinong, Indonesia

© Springer International Publishing Switzerland 2016

C. Rizos, P. Willis (eds.), *IAG 150 Years*, International Association of Geodesy Symposia 143,
DOI 10.1007/1345_2015_83

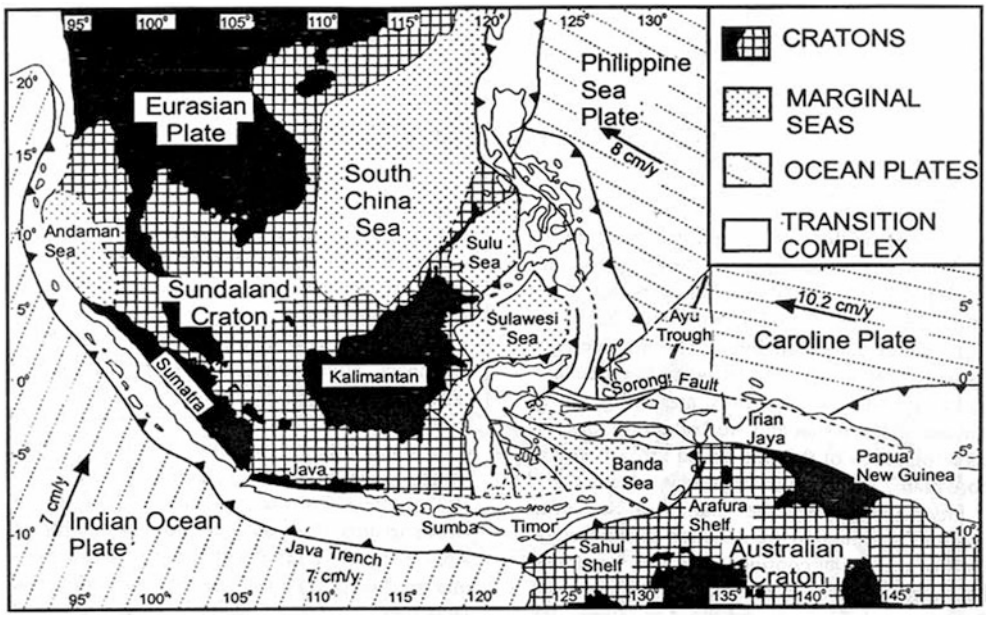

Fig. 1 Complex tectonic characteristics of the Indonesian region, from Simandjuntak and Barber (1996)

and Matindas 1996). In recent years it has been realized that, due to on-going active tectonics in the Indonesian region, DGN 1995 is inadequate for surveying and mapping in some areas of Indonesia and also for some current and emerging applications in positioning, navigation, scientific applications and spatial data management. Moreover, with the use of space geodetic techniques with mm to cm level positioning accuracy, the need for a more accurate and global geocentric datums is required for Indonesia.

Table 1 Triangulation Network in Indonesia

Region	Started	Datum
Java and Madura	1862	G. Genuk (Batavia)
Sumatera	1883	G. Genuk (Batavia)
Bangka	1917	Bukit Rimpah
Sulawesi	1913	Moncong Lowe
Flores	1960	G. Genuk (Batavia)

2 Historical Background

Positioning and mapping activities in Indonesia began in 1862. In these activities, the horizontal geodetic control network was established mainly using triangulation. The triangulation was started in the Java and Madura islands of Indonesia, which are the most populated islands in Indonesia. This first triangulation campaign started in 1862 and was completed in 1880. The measurements were then extended to other islands (see Table 1). The coordinates of the triangulation monuments were based on various local (topocentric) datums (see Fig. 2). All of these topocentric datums, except for the T21 Sorong datum, used the Bessel 1841 reference ellipsoid.

The various local topocentric datums used by the triangulation measurements in Indonesia are shown in Fig. 2. Datum unification started in 1974 using measurements from the *Navy Navigation Satellite System* (*NNSS*) or Doppler satellites. In the period 1974 to 1982, 378 Doppler stations were established. At the end of 1986 there were 966 Doppler stations throughout Indonesia. This new datum was named the Indonesian Datum 1974 (ID 1974) and can be considered as the first national topocentric datum of Indonesia. This datum, which adopted the GRS 1967 reference ellipsoid, used a certain monument in Padang (West Sumatra) as the datum origin point, and is therefore sometimes called the Padang Datum (Rais 1979).

Since 1989, the Geospatial Agency of Indonesia (BIG), formerly BAKOSURTANAL, began establishing geodetic networks for geodynamics studies in Sumatra using precise GPS campaigns, through the GPS–GPS (Global Positioning System For Geodynamic Project in Sumatra) programme which lasted till 1994. With this programme, the zeroth order geodetic network of Indonesia was established, and then expanded to other regions. In 1995, the National Geodetic Datum 1995 (DGN 1995) was declared as the new geodetic datum for Indonesia. This is a geocentric datum realized using precise GPS observations and WGS-84 as the reference ellipsoid. The DGN 1995 datum is realized by the zeroth and first order National Geodetic Control Network (NGCN), of which there were initially around 60 and 460 monuments,

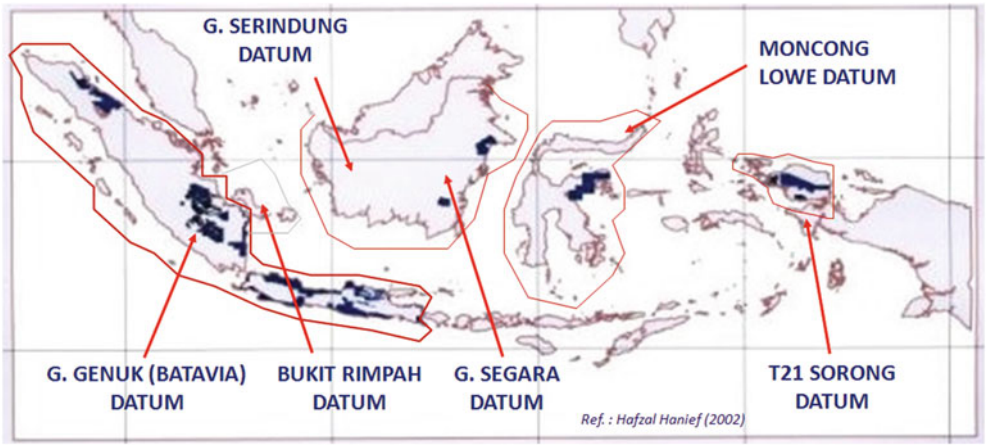

Fig. 2 Main local (topocentric) datums in Indonesia

respectively. Since 2004, after the readjusment process, the DGN 1995 coordinates of those monuments have been given in ITRF2000 at reference epoch 1998.0.

3 Reasons to Update the Geodetic Datum

Since the DGN 1995 datum was adopted in 1996, it can be expected that, due to tectonic (plates and blocks) motion and earthquake related deformation (e.g. Sumatra-Andaman 2004, Nias 2005, and Bengkulu 2007, and other earthquakes in other part of Indonesia), the coordinates of the DGN 1995 reference frame have changed (see Fig. 3). Since 1996, the total magnitude of 3D coordinate displacements due to the combined effects of block motion and earthquake deformation in the Indonesia region varied spatially from about 31 cm to 6.3 m. The largest contribution comes from the Sumatra-Andaman 2004 earthquake (Vigny et al. 2005; Subarya et al. 2006). Nowadays, these changes in coordinates can be precisely monitored using GNSS CORS networks. Moreover, many new applications (e.g. early warning systems for natural hazards, location based services, and precise photogrammetric mapping) need real time coordinates in a global reference system. Since the Indonesian region will always be affected by tectonic motion and earthquakes, changing the DGN 1995 datum into a more dynamic datum is both necessary and strategic for Indonesia.

4 New Semi-Dynamic Geodetic Datum

There are three basic kinds of datums that could be used for Indonesia: a static datum, a semi-dynamic datum and a dynamic. The main features and differences between these types of datums are summarized in Table 2.

Considering the active geodynamic nature of the Indonesian region, a static geodetic datum is not suitable for Indonesia. However, a dynamic datum is also not appropriate at present due to the vast area of the Indonesian region with its large differences in positioning infrastructures. Many positioning and mapping stakeholders, such as cadastral, boundary surveying, engineering and construction surveying, will be troubled and confused by the complexity of a dynamic datum. Therefore, the most appropriate datum to be adopted at present is a semi-dynamic datum.

On 11 October 2013, BIG launched a new geocentric datum named the Indonesian Geospatial Reference System 2013 (IGRS 2013). This new datum is a semi-dynamic datum in nature, which uses the global ITRF2008 reference frame (Altamimi et al. 2011) with a reference epoch of 1 January 2012. A velocity model, which incorporates tectonic motion and earthquake related deformation, is used to transform coordinates at an observation epoch to or from this reference epoch. In order to convert the 3D geocentric Cartesian coordinates into geodetic ellipsoidal coordinates, IGRS 2013 adopted the WGS-84 reference ellipsoid. If a new version of the ITRF reference frame becomes available, then the IGRS reference frame will also be updated accordingly. The reference epoch may also be changed. The procedure for updating the reference frame and reference epoch is still under studied by BIG.

For its initial implementation, the velocity model of IGRS 2013 considers an initial deformation model setting based on four tectonic plates (e.g. Eurasian, Australian, Pacific and Philliphine Sea), and seven tectonic blocks (e.g. Burma, Sunda, Molucca, Banda, Timor, Bird Head and Maoke) as illustrated in Fig. 4, and also 126 earthquakes. With this deformation model setting, if the plate motion model MORVEL (DeMets et al. 2010) is used, then the computed horizontal deformation rates in Indonesia are as shown in Fig. 5. Later, several more micro blocks will

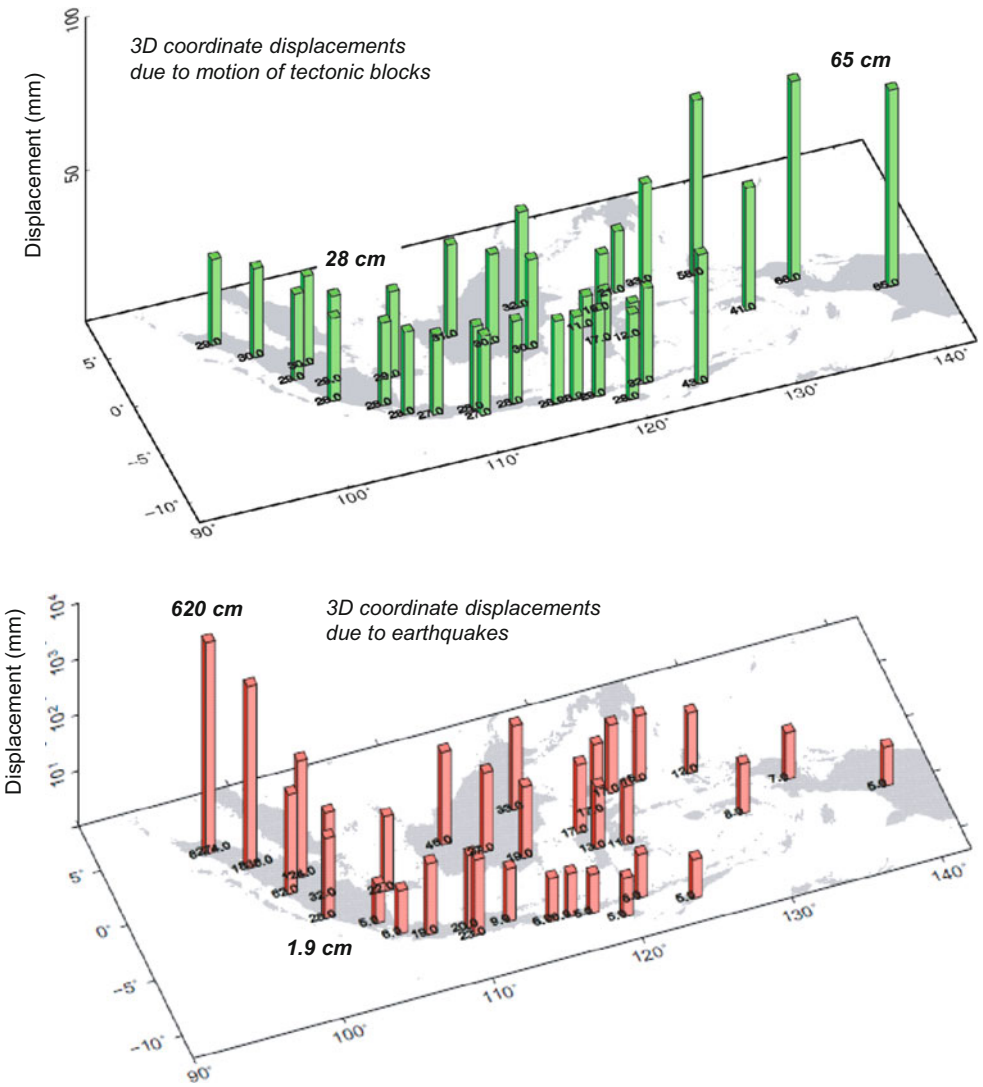

Fig. 3 The total magnitude of 3D coordinate displacements due to block motion (*upper chart*) and earthquakes (*lower chart*) since 1996, from GPS observations; courtesy of Susilo (ITB). The ranges of 3D coordinate displacements due to block motion and earthquake are 28–65 cm, and 1.9–6.2 m, respectively

Table 2 Main features of static, semi-dynamic, and dynamic datums (Grant and Blick 1998; Tregoning and Jackson 1999; Grant et al. 1999)

Static datum	Semi-dynamic datum	Dynamic datum
• The datum is defined by the coordinates of main geodetic stations	• The datum is defined by its relationship to a dynamic global reference system (e.g. ITRS) at a specified reference epoch	• The datum is defined by its continuous relationship to a dynamic global reference system (e.g. ITRS)
• The coordinates of those stations are held fixed or unchanging with time	• A time-dependent velocity model is used to transform coordinates at an observation epoch to or from the reference epoch	• Time dependencies of the datum are included in station velocities and rates of change for transformation parameters
	• The coordinates of geodetic stations are given in a dynamic global reference frame (e.g. ITRF) at the reference epoch	• The coordinates and velocities of geodetic stations are given in dynamic global reference frame (e.g. ITRF)

be also added to account for specific deformation events such as large earthquakes. In this case, only earthquakes with magnitudes larger than 6.0 will be considered in the deformation model. Localized deformation models explained in (Jordan et al. 2007; Winefield et al. 2010) will be considered in IGRS 2013, in order to take into account deformation associated with localised events such as the aforementioned earthquakes, landslides and land subsidences.

At present, the velocity model of IGRS 2013 will be mainly realized using the GPS-derived rates at passive and continuous GPS stations maintained by BIG and BPN (see Figs. 6, 7, and 8). The status of its development is explained in the following section.

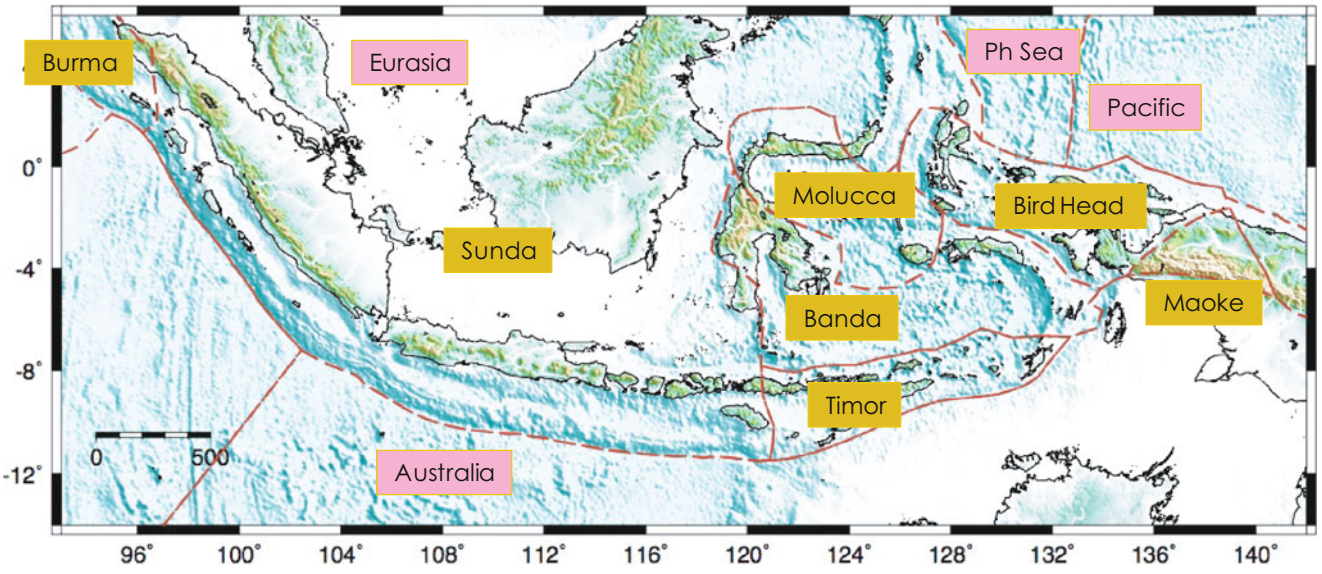

Fig. 4 Deformation model setting of Indonesia, after DeMets et al. (2010). In this Figure, *pink boxes* indicate the tectonic plates and *yellow boxes* indicate the tectonic blocks

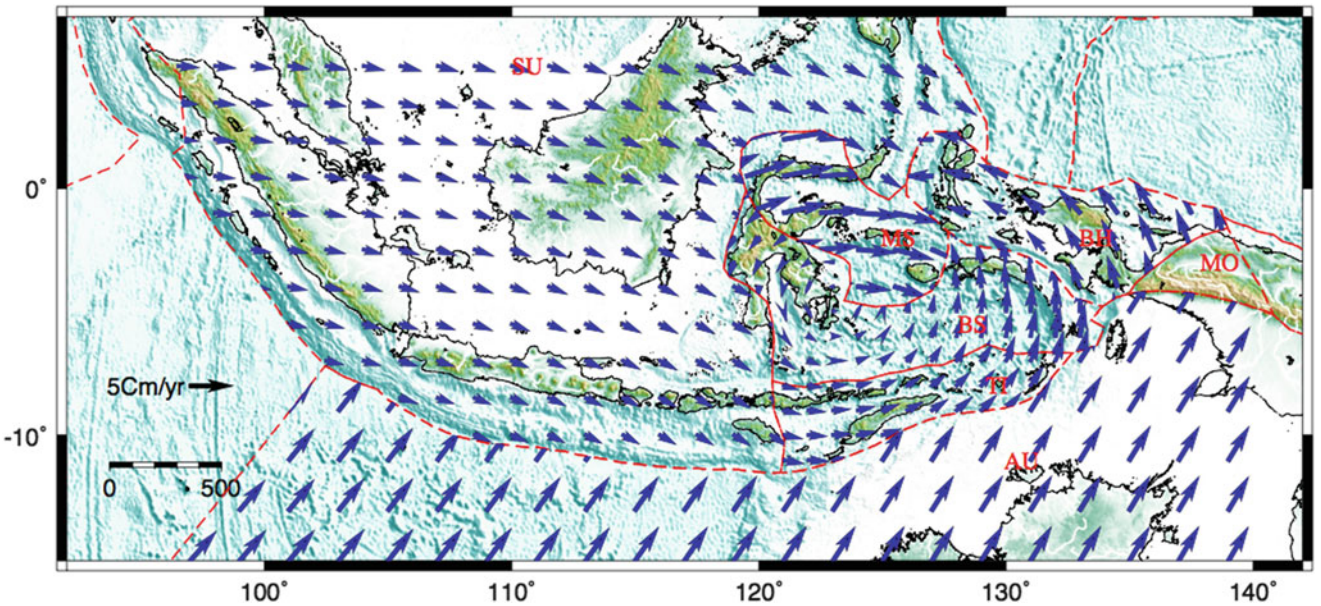

Fig. 5 Initial model for horizontal deformation rates in Indonesia, courtesy of Irwan Meilano (ITB) and Susilo (BIG). It is derived using the plate motion model MORVEL (DeMets et al. 2010)

5 Realization of New Geodetic Datum

IGRS 2013 will be realized in the field by the National Geodetic Control Network (NGCN) stations, consisting of continuous GPS stations (GPS CORS) and passive GPS survey stations (pGPS), covering the Indonesian region. In this case, the coordinates of NGCN stations are given in the ITRF2008 reference frame at the reference epoch of 2012.0. At present, BIG has 118 GPS CORS stations and about 1,350 passive geodetic monuments that have been positioning using precise GPS surveys (see Figs. 6 and 7). The National Land Agency of Indonesia (BPN) also operates 183 GPS CORS Stations (see Fig. 8), and has also established thousands of GPS-positioned passive monuments across Indonesia (Abidin et al. 2011, 2012). Besides the GPS CORS maintained by BIG and BPN, there is also the SUGAR (Sumatera GPS Array) network, consisting of 32 continuous GPS stations (Caltech 2013), which is maintained by the Indonesian Institute of Sciences (LIPI) in collaboration with the California Institute of Technology (Caltech) and the Earth Observatory of Singapore (EOS). All of these

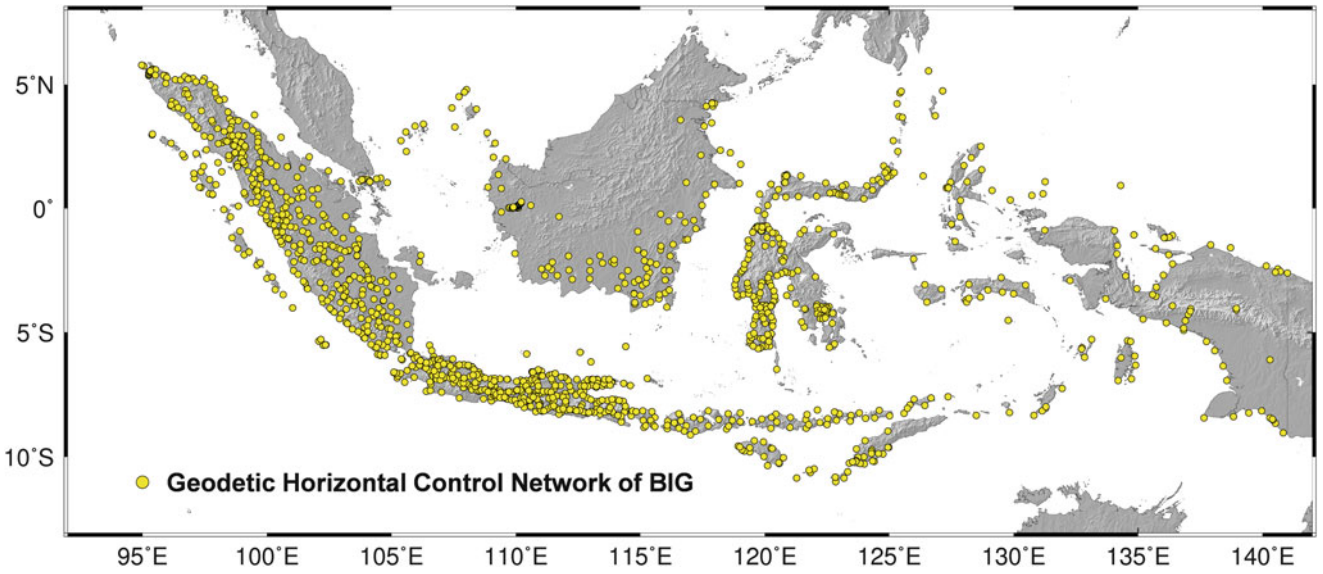

Fig. 6 Distribution of passive (pGPS) geodetic control stations established by Geospatial Agency of Indonesia (BIG) using episodic GPS surveys. Total number of established stations up to 2013 is 1,350 stations

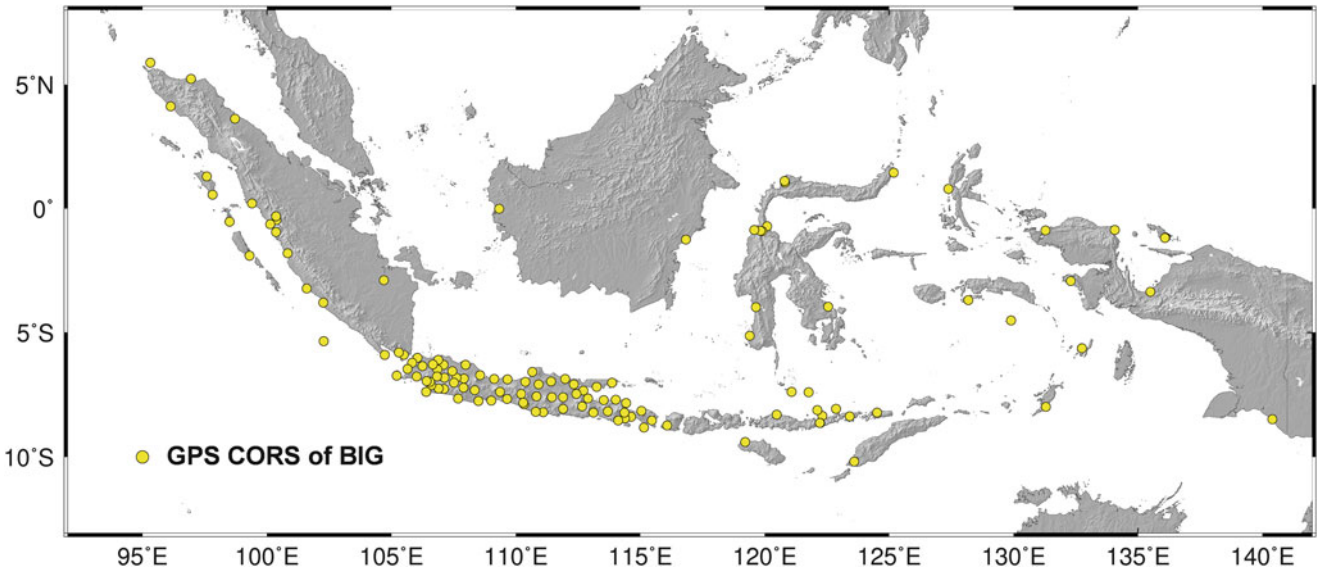

Fig. 7 Distribution of GPS CORS stations in Indonesia maintained by the Geospatial Agency of Indonesia (BIG). Total number of established stations up to 2013 is 118 stations

pGPS and GPS CORS stations can be utilized as part of the IGRS 2013 reference frame.

Presently, BIG has estimated the ITRF2008 velocities at sGPS and GPS CORS stations using pGPS data from 2007 to 2009 campaigns, GPS CORS data from 2010 to 2013, and data from more than 250 globally distributed IGS stations. In total the data from around 790 pGPS and GPS CORS stations in the Indonesian region have been processed so far using GAMIT/GLOBK software (Herring et al. 2010). The processing is done based on dynamic network processing method. In this case, GPS data is firstly processed in daily basis, which one-day data itself is divided into several networks processing consisting of related cGPS and IGS stations. These network solutions are then combined to yield a daily solution. After quality assessment, the daily solutions are then combined into weekly solution. The final coordinates and velocities are then estimated from the weekly solutions.

The obtained velocities at GPS CORS stations are shown in Fig. 9. The velocities at pGPS stations are not yet established, waiting for data from more passive GPS campaigns to be conducted in order to have more reliable velocities. The Helmert transformation parameters of the coordinates given by GAMIT/GLOBK solution with respect to ITRF2008

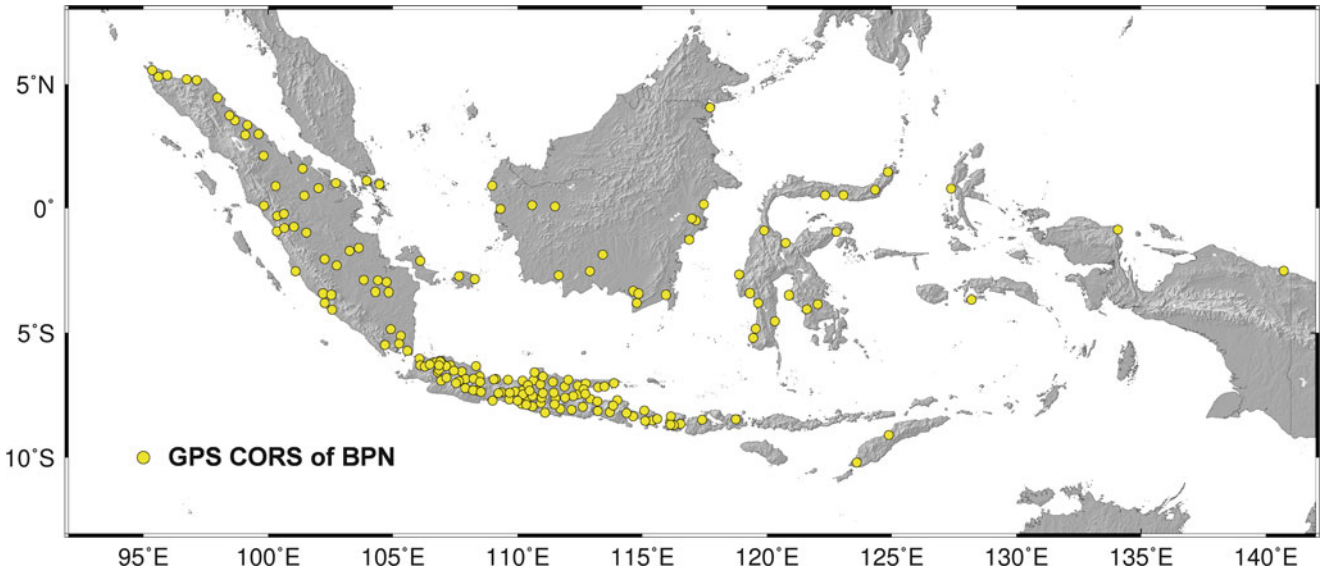

Fig. 8 Distribution of GPS CORS stations in Indonesia maintained by the National Land Agency of Indonesia (BPN). Total number of established stations up to 2013 is 183 stations

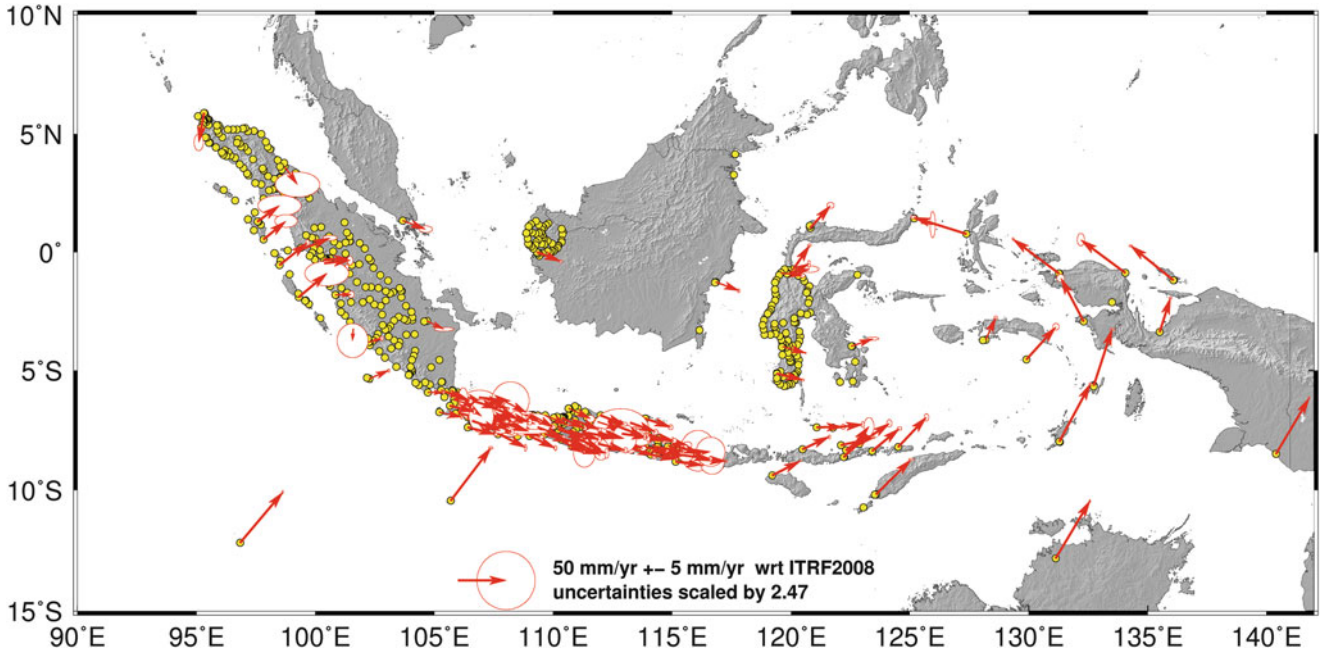

Fig. 9 ITRF 2008 velocities and their error ellipses at the GPS CORS stations maintained by BIG computed using GPS CORS data from 2010 to 2013; courtesy of Susilo (BIG). The velocities at pGPS stations are not yet shown, waiting for more GPS campaigns to be conducted in order to have more reliable velocities

epoch 2005.0 are shown in Fig. 10. The values of transformation parameters are relatively small, which in general translation <5 cm, rotation <0.4 mas, and scale <0.5 ppb. The values indicate the relatively good realization of IGRS 2013 reference frame. The preliminary Euler pole parameters of the involved tectonic plates and blocks have also been estimated from the GPS CORS solutions, as given in Table 3. These Euler pole parameters can then be utilized to estimate the velocities at locations outside the GPS CORS stations

In the next processing stage, the velocity field shown in Fig. 9 will be densified by processing more data of pGPS and GPS CORS stations maintained by BIG, i.e. data observed since 2000. Moreover, data from GPS CORS maintained by BPN will also be included in data processing.

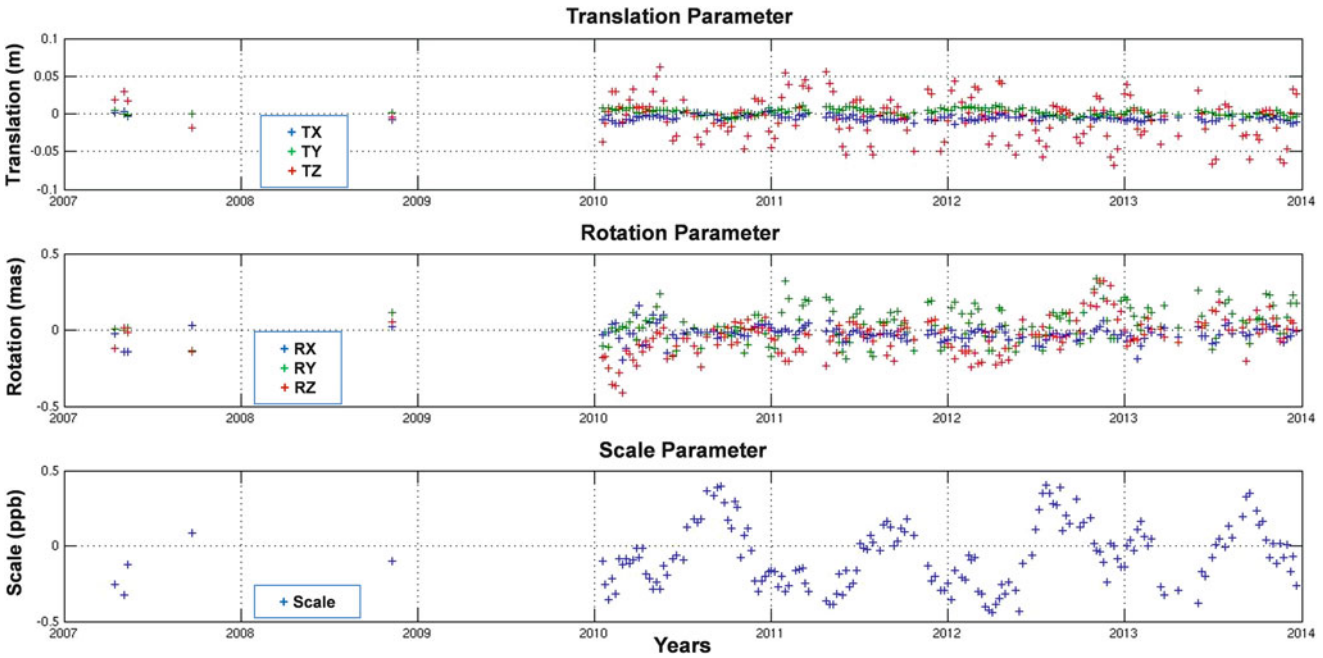

Fig. 10 The Helmert transformation parameters of the estimated GAMIT/GLOBK coordinates solution with respect to ITRF2008 epoch 2005

Table 3 Preliminary Euler pole parameters as estimated from GPS CORS solutions in Indonesia

Plate	Latitude (deg)	Longitude (deg)	Rate (deg/Myr)	Semi Major (deg)	Semi Minor (deg)	Azimuth (deg)	Rate uncertainty (deg/Myr)	wrms (mm/year) N	wrms (mm/year) E
AU	32.119	37.615	0.635	0.18	0.04	106.0	0.0006	0.44	0.83
BS	0.271	120.474	2.083	0.36	0.03	348.3	0.0918	1.04	1.41
BH	−52.415	54.260	0.536	5.33	0.12	85.7	0.0037	0.20	1.42
MO	8.015	−49.090	1.198	1.99	0.11	55.1	0.1774	0.06	0.05
SU	45.162	128.115	0.313	1.42	0.14	27.8	0.0052	0.70	0.97
TI	2.461	113.389	1.350	0.27	0.02	322.3	0.0260	2.64	0.72

In this Table, *AU* Australian plate, *BS* Banda Sea block, *BH* Birds Head block, *MO* Molucca Sea block, *SU* Sunda block, *TI* Timor block

6 Closing Remarks

The new semi-dynamic datum of Indonesia (IGRS 2013) was officially launched by the Geospatial Agency of Indonesia (BIG) on 11 October 2013. However, several things related to this IGRS 2013 realization are still under investigation and development. This includes how to synergize the velocity model derived using the plate motion model (e.g. MORVEL) with the velocity field estimated using pGPS and GPS CORS data. There would still be a question whether the existing plate and block motion model would be able to accurately predict the velocity field for all over Indonesia. In this case, the interplate coupling models for all plates and blocks interfaces in Indonesian region should also be established. As an example, (Hanifa et al. 2014) has recently proposed an interplate coupling model of the Australia-Java plate interface off the southwestern coast of Java, which will be useful in establishing the accurate deformation model of IGRS 2013. Moreover, detail mechanisms on handling secular trends, earthquakes offsets (co-seismic deformation), and post-earthquakes motion (post-seismic deformation) should also be established for accurate realization of IGRS 2013.

In the first year of datum transition from DGN 1995 to IGRS 2013, education of all positioning and mapping stakeholders in Indonesia should be conducted to ensure users are not confused by the datum change. Therefore, fast and reliable web-based and online service systems must be provided as soon as possible for the implementation of the new datum across the entire region of Indonesia. Presently, BIG has initiated a web-based service that enables users to access the ITRF2008 coordinates (at reference epoch 2012.0) and their rates of change for all NGCN stations. Coordination with the BPN is also being carried out in order to integrate the coordinates of all pGPS and GPS CORS stations maintained by BPN into IGRS 2013.

BIG should also densify its GPS CORS network to cover all of Indonesia, especially Borneo Island and the eastern parts of Indonesia. With a denser GPS CORS network, the deformation model of IGRS 2013 can be estimated more reliably and in more detail. Cooperation and coordination with all related positioning and mapping institution in Indonesia (e.g. BPN, Army Topographic Agency, Navy Hydrographic Agency) should also be maintained by BIG throughout the implementation process of IGRS 2013.

References

Abidin HZ, Andreas H, Gumilar I, Adiyanto FH, Rusmawar W, Firmansyah (2011) On the use of GPS CORS for Cadastral Survey in Indonesia. In: Proceedings of the FIG working week 2011, TS03B – GNSS CORS Networks Case Studies, Marrakech, Morocco, 18–22 May, http://www.fig.net/pub/fig2011/techprog.htm

Abidin HZ, Haroen TS, Mudita I, Adiyanto FH (2012) Implementation of GPS CORS for Cadastral survey and mapping in Indonesia: status, constraints and opportunities. In: Proceedings of the FIG 2012 Working Week, TS06C – GNSS CORS infrastructure and applications II, Rome, Italy, 6–10 May, http://www.fig.net/pub/fig2012/techprog.htm

Altamimi Z, Collilieux X, Metivier L (2011) ITRF2008: an improved solution of the International Terrestrial Reference Frame. J Geodesy 85(8):457–473. doi:10.1007/s00190-011-0444-4

Caltech (2013) Website of the Sumatran Plate Boundary Project, California Institute of Technology (Caltech). http://www.tectonics.caltech.edu/sumatra/index.html, Accessed 14 Nov 2013

DeMets C, Gordon RG, Argus DF (2010) Geologically current plate motions. Geophys J Int 181:1–80. doi:10.1111/j.1365-246X.2009.04491.x

Grant DB, Blick GH (1998) A new geocentric datum for New Zealand. New Zealand Surveyor 288:40–42

Grant DB, Blick GH, Pearse MB, Beavan RJ, Morgan PJ (1999) The development and implementation of New Zealand Geodetic Datum 2000. Paper presented at IUGG99 General Assembly, Birmingham UK, 18–30 July

Hanifa NR, Sagiya T, Kimata F, Efendi J, Abidin HZ, Meilano I (2014) Interplate coupling model off the southwestern coast of Java, Indonesia, based on continuous GPS data in 2008–2010. Earth Planet Sci Lett 401:159–171

Herring TA, King RW, McClusky SC (2010) Introduction to GAMIT/GLOBK, Release 10.4, Department of Earth, Atmospheric, and Planetary Sciences, Massachusetts Institute of Technology. http://www-gpsg.mit.edu/~simon/gtgk/docs.htm

Jordan A, Denys P, Blick G (2007) Implementing localised deformation models into a semi-dynamic datum. In: Dynamic Planet, Springer, Berlin/Heidelberg, pp 631–637

Rais J (1975) The problems of datum selection for surveys and mapping. Document No.03/1975, National Agency for Surveying and Mapping (Bakosurtanal), Indonesia

Rais J (1979) Doppler surveying in Indonesia (1974–1979). Paper at IAG Symp., General Assembly XVII IUGG, Canberra, Australia

Schepers JHG, Schulte FCA (1931) Geodetic Survey in the Netherlands East Indies. Report to Section Geodesy, IUGG

Simandjuntak TO, Barber AJ (1996) Contrasting tectonic styles in the Neogene orogenic belts of Indonesia. In: Hall R, Blundell DJ (eds) Tectonic evolution of Southeast Asia, Geological Society Special Publication No. 106, pp 185–201

Subarya C, Matindas RWM (1996) Geocentric Indonesian Datum 1995. Publication of the National Agency for Surveying and Mapping (Bakosurtanal), Indonesia

Subarya C, Chlieh M, Prawirodirdjo L, Avouac J-P, Bock Y, Sieh K, Meltzner AJ, Natawidjaja DH, McCaffrey R (2006) Plate-boundary deformation associated with the great Sumatra–Andaman earthquake. Nature 440. doi:10.1038/nature04522

Tregoning P, Jackson R (1999) The need for dynamic datums. Geomatics Res Australasia 71:87–102

Vigny C, Simons WJF, Abu S, Bamphenyu R, Satirapod C, Choosakul N, Subarya C, Socquet A, Omar K, Abidin HZ, Ambrosius BAC (2005) Insight into the 2004 Sumatra–Andaman earthquake from GPS measurements in Southeast Asia. Nature 436. doi:10.1038/nature03937

Winefield R, Crook C, Beavan J (2010) The application of a localised deformation model after an earthquake. In: Proceedings of the FIG Working Week 2010, FS 2C – Positioning Measurement Techniques and Applications I, Sydney, Australia, 11–16 April, http://www.fig.net/pub/fig2010/techprog.htm

Regional Model to Estimate Vertical Deformations Due to Loading Seasonal Changes

Romina Galván, Mauricio Gende, and Claudio Brunini

Abstract

Surface mass transfer produces changes in the terrestrial geometric reference frame that are clearly detectable by GNSS techniques. These deformations are mainly observed in the vertical coordinate component and show periodic behavior with seasonal cycles. Therefore, the assumption that the kinematics of the reference frame has a linear behavior is no longer sufficient.

This study focuses on a model of crustal vertical deformations caused by surface loading variations in the South American region. Thirty-four locations were analyzed in order to adjust a parametric exponential function that relates height changes with mass pressure variations.

This parametric function depends on regional rheological properties. Crustal deformations were characterized using multi-annual GPS time series provided by SIRGAS and the surface loading information was derived from GRACE spherical harmonic coefficients provided by GRGS (Release 2). The proposed parametric model was able to properly reproduce inter-annual variations observed in vertical displacement in a 9-year time-span (2003–2012). This study will contribute to a better understanding the kinematics of the reference frame and the elastic parameters on a regional scale.

Keywords

Geodesy • GPS • GRACE • Gravity • Green function • Seasonal variations • Surface loading • Vertical deformation

1 Introduction

Accurate time series of coordinates achieved by GNSS have allowed us to observe seasonal variations mainly in the vertical component (van Dam et al. 2001; Blewitt et al. 2001; Dong et al. 2002). Data from GRACE satellite mission has also shown seasonal variations in the Earth's gravity field (Tapley et al. 2004; Wahr et al. 2004). Both effects are caused by the same geophysical phenomenon: mass redistribution on the Earth's surface or around it. Several authors have studied how mass exchange affects the Earth system using both sources of data: GPS and GRACE, and they have concluded that temporal loading variations produce geometric deformations on the Earth's surface (e.g. Tregoning et al. 2009; Tesmer et al. 2011; Fu et al. 2012).

Global and regional reference frames are materialized by a set of fiducial stations with known positions for a given epoch and constant velocities. They are transformed to other epochs by means of applying linear coordinate changes (Altamimi et al. 2011; Brunini et al. 2009).

The representation of the kinematics of fiducial stations using a linear model, i.e. neglecting surface loading effects, will have an impact on the reference frame realization (e.g.

R. Galván • M. Gende • C.Brunini (✉)
Geodesia Espacial y Aeronomía, Facultad de Ciencias Astronómicas y Geofísicas, CONICET, Paseo del Bosque s/n, La Plata, Argentina.
e-mail: rgalvan@fcaglp.unlp.edu.ar

© Springer International Publishing Switzerland 2015

C. Rizos, P. Willis (eds.), *IAG 150 Years*, International Association of Geodesy Symposia 143,
DOI 10.1007/1345_2015_101

Poutanen et al. 2002; Freymueller 2009; Collilieux et al. 2010, 2012; Zou et al. 2014).

In continental regions, the most relevant temporal loading variations are due to atmospheric (van Dam and Wahr 1987; Tregoning and Watson 2009), non-tidal ocean (Williams and Penna 2011; van Dam et al. 2012), and hydrological loads like water, snow and ice loads (e.g. Bettinelli et al. 2008; Fu and Freymueller 2012).

Those variations produce vertical displacements in geodetic benchmarks that can reach several centimeters in amplitude (e.g. van Dam 1998; Biessy et al. 2011). Therefore, GPS is well designed for estimating the effect of loads in the Earth's crust and determining a new model of elastic response for fiducial stations.

The classical approach used to convert surface loading into geometric deformations (e.g. van Dam 1998; van Dam and Wahr 1987; Kusche and Schrama 2005; Fu and Freymueller 2012; Fu et al. 2012) is based on a function that characterizes the Earth's response to loading, which depends on load Love numbers (Longman 1962; Farrell 1972). Those models do not take into consideration changes in the Earth's crust behavior due to local variations of the rheological properties.

We have investigated the possibility of using a variant to this conventional methodology which defines the Earth's response by a parametric and exponential function that considers different elastic properties of the crustal material. This function was first introduced by Seitz and Krügel (2009). In order to obtain a regional model to estimate vertical deformations produced by loading seasonal changes, we applied this methodology on a regional scale using GRACE data and GPS time series and tested it in the South American region. Although the distribution of GPS data over the Earth is not uniform, today in South America there is a very dense network of continuously operating sites that provide a unique opportunity.

2 Applied Methodology

Temporal loading variations applied on the Earth's surface produce geometric deformation changes in nearby regions where loading is applied. Those deformations are modeled by a function that addresses how those deformations change as we move away from the point where the load is applied. Usually, the displacements observed at P affected by a load applied at Q are described by the following function (Longman 1962; Farrell 1972; Moritz and Mueller 1987)

$$d_r(P) = \frac{R_E^3}{M} \int\int q_Q \sum h'_n P_n(\cos\varphi_{PQ}) d\sigma_Q, \qquad (1)$$

where φ_{PQ} stands for the spherical distance between P and Q, P_n and h'_n are the Normalized Legendre Polynomials and the loading Love numbers of degree n, respectively; R_E represents the mean radius of the Earth and M is the total mass of the Earth. The expression

$$G(\varphi_{PQ}) = \frac{R_E}{M} \sum h'_n P_n(\cos\varphi_{PQ}), \qquad (2)$$

represents the Green's function for vertical displacements (Longman 1962). This function depends on the loading Love numbers which change according to P and S body velocities, and ρ densities for a spherically-symmetric non-rotating elastic isotropic Earth model, SNREI such as PREM, iasp91, ak135, etc.

Due to crustal material inhomogeneities, Green's function does not handle variations of the physical behavior of the Earth's crust for loads in surrounding regions correctly. Our aim was to replace this Green's function with an exponential function that depends on the site where the deformation is calculated (Seitz and Krügel 2009)

$$F(\varphi_{PQ}) = 10^{-17} a \exp^{-b\varphi_{PQ}}, \qquad (3)$$

where a and b are unknown physical parameters that represent crustal inhomogeneities. The parameter a provides a measure of the vertical deformation of a cell when it is loaded by a certain mass, while b shows to what extent a given mass can affect the Earth's surface. The parameter a has units of [m/Kg] and it is related to the Young's modulus E for the area where the load is applied, while b is dimensionless and depends on the elastic parameters of the neighboring cells.

When replacing this function in Eq. (1), the vertical displacement can be estimated by the following function:

$$d_r(P) = 10^{-17} \sum_{k/\varphi_{PQ}<R} q_{Q_k} A_{Q_k} a \exp^{-b\varphi_{PQ}}, \qquad (4)$$

where A_{Q_k} represents the area of the cell k, which depends on the spatial resolution of the loading data. The summation is set for all cells within a radius R where mass loads affect the deformation observed in P. The method has been tested in the Amazon region where we can observe the most relevant annual vertical deformations due to the temporal variations in the Amazon River and its affluents.

The geometric deformations have been characterized with SIRGAS GPS time series of the region, while loading variations have been estimated with the GRACE satellite mission.

In order to estimate numerical values for a and b parameters, we linearized the problem [Eq. (4)] and performed an iterative least square adjustment where we set initial values for the parameters.

With the estimated parameters, we calculated a weekly vertical deformation of the surface and we compared it with the displacements observed for the selected GPS sites.

3 Data Sources

In order to estimate both the geometrical deformation of the Earth's surface and the temporal loading variations in the South American region, we have used GPS time series of SIRGAS Continuously Operating Network (SIRGAS-CON) and spherical harmonic coefficients of the Earth's gravity field estimated from GRACE data.

3.1 GPS Data

SIRGAS is the Geocentric Reference System for Latin America and the Caribbean (Brunini et al. 2009) and it is a regional densification of ITRF. Its definition corresponds to the IERS International Terrestrial Reference System (ITRS) and it is realized by a network of 368 continuously operating GNSS stations (Fig. 1). It is processed on a weekly basis by the SIRGAS analysis centers, which generate weekly solutions for station positions. Each GNSS station is aligned to the current ITRF reference stations. The accuracy of the positions in the reference epoch is estimated to be better than 1.0 mm in the horizontal component and 2.9 mm in the vertical component. These GPS data are available at http://www.sirgas.org.

The analysis was carried out with Bernese 5.1 software (Dach et al. 2007) and a 30-s interval was used for every station. The elevation mask was set to 3° and an elevation angle dependent function weighing between 3° and 5° was applied. Also, ocean tide loading was modeled according to the FES2004 ocean tide model (Letellier 2005). The Niell (1996) dry mapping function was applied to map the a priori zenith delay (dry part), which is modeled using the Saastamoinen (1973) model. The wet part of the zenith delay was estimated at a 2-h interval within the network adjustment and it was mapped using the Niell wet mapping function (Niell 1996).

We have used weekly solutions of the GPS time series from every station within the network. These stations are aligned to the IGS05 reference frame using a six parameter similarity transformation: no-net-rotation (NNR), no-net-translation (NNT) (Brunini et al. 2012).

Figure 2 shows the displacements observed for a SIRGAS-CON station located in the Amazon Basin. The first and second plots correspond to horizontal displacements, while the red dots correspond to the vertical ones. As we can observe, the horizontal components have a mostly linear behavior. However, this is not true for the vertical component, where the movements reported the biggest amplitudes with a strong seasonal variation. This is why our work focuses only on the vertical component.

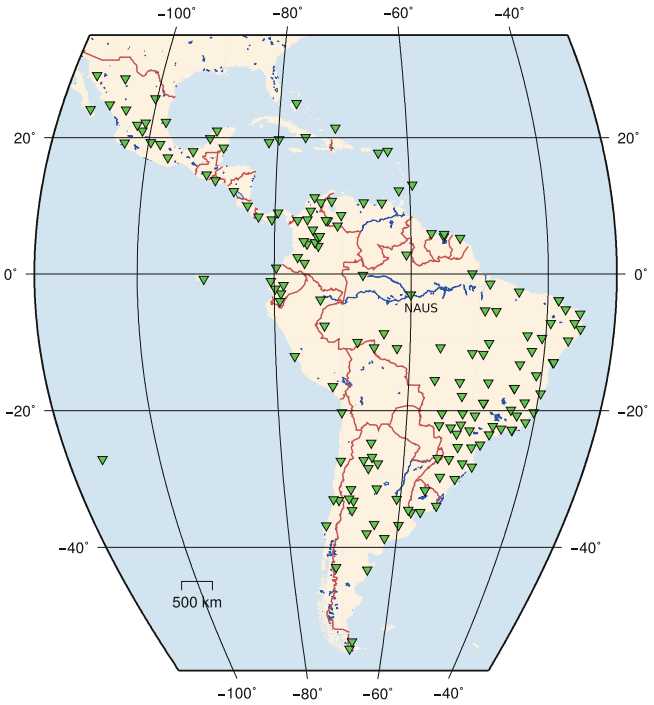

Fig. 1 SIRGAS-CON network

In order to test the model, we started with a sample of 368 stations and we selected only those whose time span was longer than 3 years, those whose vertical components had visible seasonal variations and we checked that a similar behavior was observed in nearby stations. Additionally, we did not take into account those stations which had sudden changes or trend variations caused by earthquakes, extensive data gaps, those cases where local effects dominated the signal, or those when the signal was very noisy. After ruling out those stations, a group of 34 South American GPS sites was considered. We used, when available, GPS weekly solutions between 2003 and 2012 so that they matched the time interval of GRACE data. We removed the linear trend of the time series and we applied a low-pass filter assuming that periods shorter than 4 months were not related with the loading effects we tried to model. We used samples of 343 observations on average.

3.2 GRACE Data

GRACE is designed to monitor temporal variations in the fluid mass on the Earth's surface (Tapley et al. 2004). The GRACE geopotential solution can be used to recover time changes in water storage. There are four main GRACE data centers that provide temporal variations of the harmonic

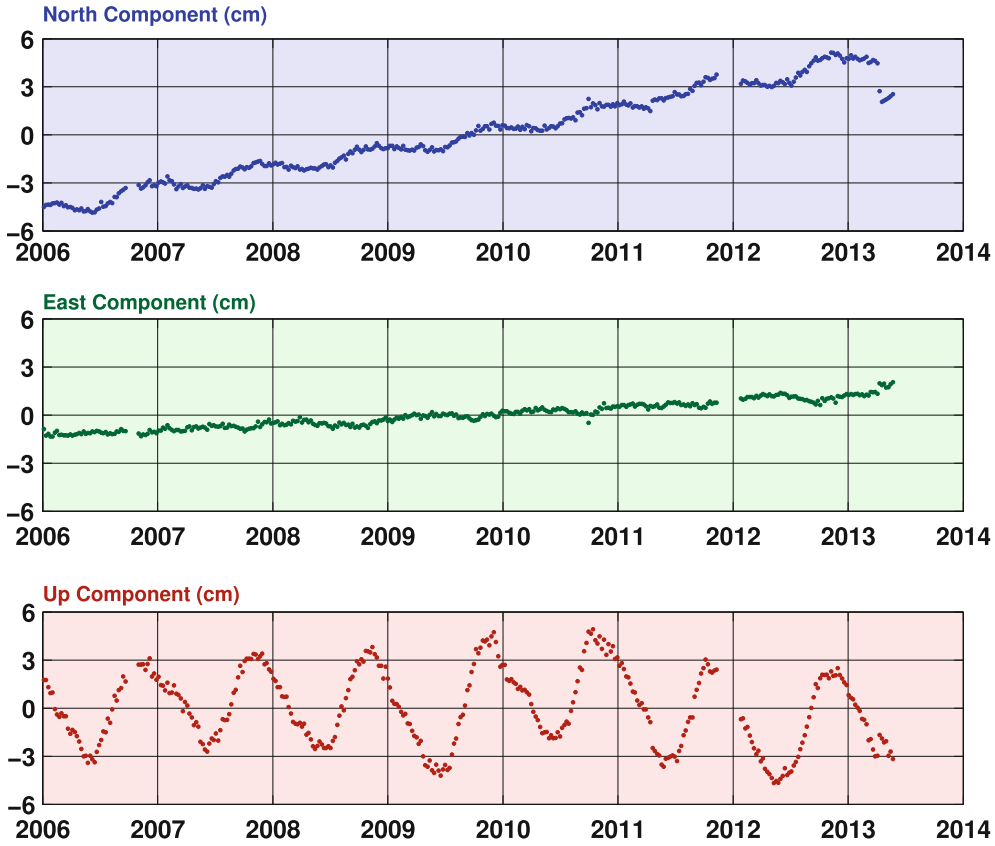

Fig. 2 GPS time series for a SIRGAS-CON station (NAUS)

coefficients: CSR (University of Texas, Center for Space Research), GFZ (GeoForschung Zentrum, Potsdam), JPL (Jet Propulsion Laboratory, NASA) and GRGS (Space Geodesy Research Group). They have different temporal resolution: CSR, JPL and GFZ provide monthly harmonic coefficients while GRGS offers data with a 10-day resolution. The main difference of the GRGS center is the solution strategy adopted. The constraint applied in the inversion method produces a better reduction of the North-South stripes. Consequently, a post-processing filtering or smoothing was not needed. Additionally, this center added harmonics of very low degree, in particular degrees 2 and 3, from Lageos data observations because they cannot be estimated accurately with GRACE data only. Although higher temporal resolution usually means noisier data, the noise associated with GRGS solution is comparable with the GRACE project solutions. For details, see Bruinsma et al. (2010).

We used this center latest improved releases, that is, the GRGS series of the gravity field model expressed in normalized spherical harmonic coefficients from degree 2 to 50. Given that the effects of atmospheric and non-tidal ocean loads have been removed from GRACE signal, but they are still present in GPS data, we have restored those effects to GRACE spherical harmonic solutions in order to maintain consistency. We have added GRACE's Atmosphere and Ocean De-aliasing Level-1B (AOD1B) solution that is based on 6-hourly ECMWF analysis data and output from the baroclinic ocean model for circulation and tides (OMCT). This product contains spherical harmonic coefficients up to degree and order 100 for four 6-hourly time stamps (0, 6, 12 and 18 h). We applied a time interpolation and we calculated spherical harmonic coefficients for a 10-day resolution so that they would be consistent with the time resolution of GRGS's data. It is also important to note that equivalent water height values, deduced from GRACE measurements, were corrected for the gravitational effect induced by crust geometric displacement as a response to water loading using an elastic Earth hypothesis as explained in Wahr et al. (1998).

We used the results to construct the equivalent water height at every point in a 1°-×-1° global grid. We filtered the signal in time as we did with GPS signals using the same assumption and we interpolated it and calculated weekly values so that they could be compared with GPS epochs.

Figure 3 shows an example of equivalent water height on a global scale for a given epoch. The amplitude of the Amazon Basin is large, as might be expected from the gravity and surface mass signals (Tapley et al. 2004).

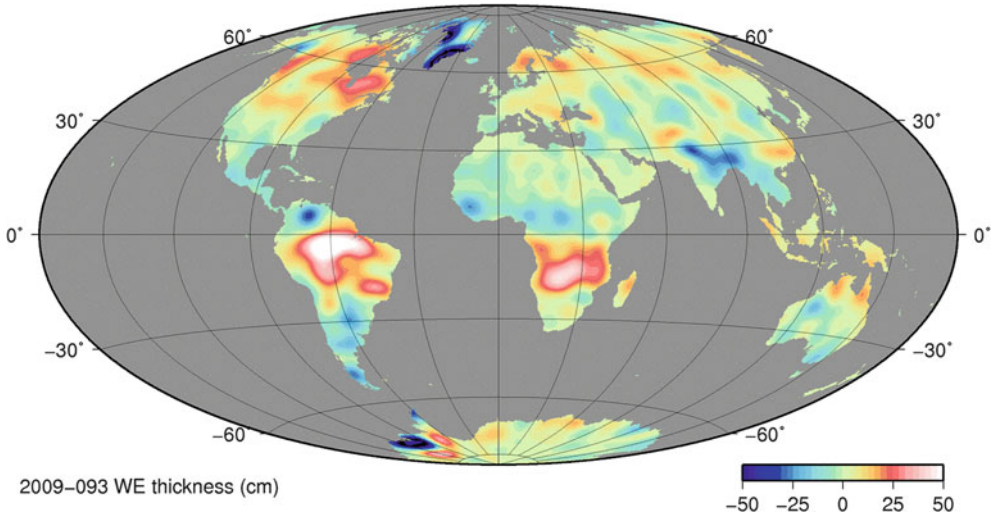

Fig. 3 EWH from GRGS center

4 Correlation Coefficient and Parameter Adjustment

If we superimpose EWH and vertical displacements for a station located in the Amazon basin, when EWH grows, the vertical displacement is expected to decrease and vice-versa.

Figure 4 shows both signals for NAUS station. This figure demonstrates that GRACE is very sensitive to hydrological loading. It is worth noting that we are observing two different effects with different vertical scales, where EWH is represented in green and the vertical displacements in blue. The former effect has amplitudes of about 100 cm while the latter reaches 5 cm.

Nevertheless, we would expect the correlation coefficients between both effects to be close to -1. We calculated the correlation coefficients for every selected station as we explained in Sect. 3.1 (34 GPS sites) and we decided on modeling only those stations whose correlation was lower than -0.75. Figure 5 shows the correlation coefficient for the 20 stations that fulfill the above requirement. At middle latitudes, the correlation coefficients are systematically large given their proximity to the Amazon River.

We estimated the numerical values of a and b parameters by applying the inversion method based on an iterative least square adjustment using Eq. (4). Each of the GPS-derived vertical displacements and the corresponding EWH for grid cells within a radius R, both with respect to weekly time values were taken as observations.

5 Results

The least squares adjustment of the parameters was performed for data between 2003 and 2012, taking into account that crustal deformations measured in a point P are caused by loads within a radius R of 200 km from P, according to Bevis et al. (2005) and Seitz and Krügel (2009). We defined as initial values for unknown parameters those proposed by Seitz and Krügel (2009), $a = -12.5$ and $b = -35$ that were obtained by fitting a function to the mentioned Green's function.

We found mean values of -16 and -27 for a and b, respectively. These values are consistent with those adjusted by Seitz and Krügel (2009).

A weighting function for each station using the best fit parameters was calculated. Also, we compared it with both the function obtained by Seitz and Krügel (2009) for the region and Green's function based on global values of load Love numbers for continental crust up to degree $n = 2{,}000$. In Fig. 6, all fitted weighting functions are plotted as a blue continuous line, the red line represents the initial function that best fits Green's functions, and Green's function for a normal continental crust was plotted in black.

The adjusted functions F differ slightly from those proposed initially and they seem to agree with Green's function. We estimated displacements due to loading variations for each station and we compared them with the observed displacements in GPS sites. Figures 7 and 8 show estimated displacements in blue and observed displacements in red dots for two stations. We have selected an example of a station with a strong harmonic behavior and another example in which interannual variations are visible.

In order to assess whether varying these parameters is a significant improvement or not, standard deviation (STD) between computed displacements and observed displacements was calculated and we compared it with that STD obtained using the Farrell's method. Figure 9 shows those results.

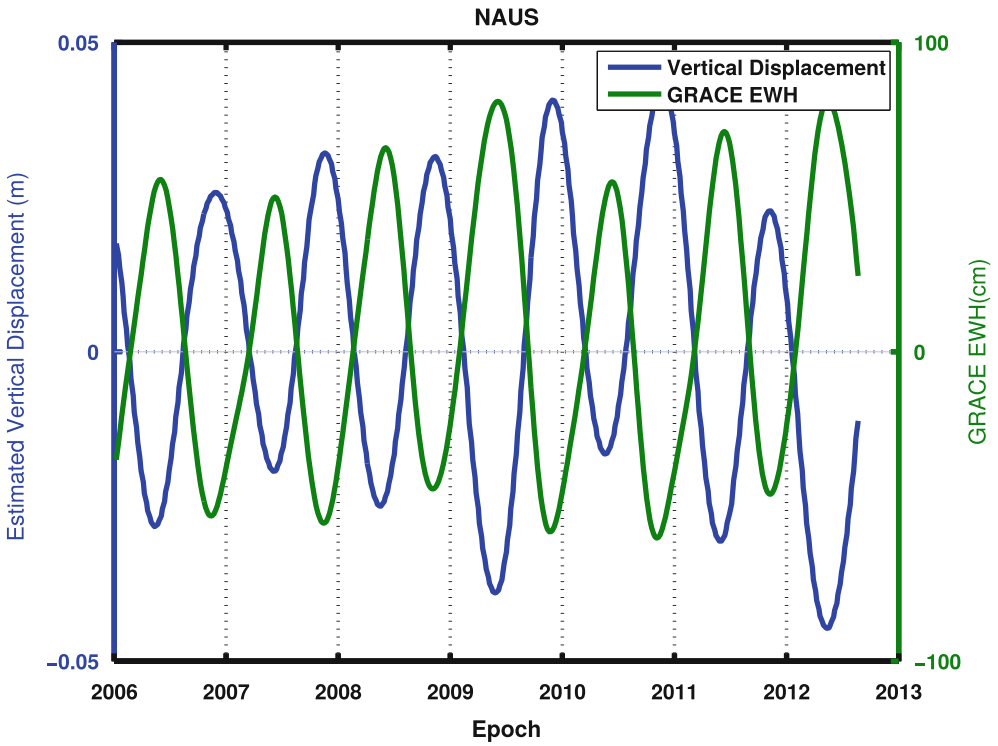

Fig. 4 EWH vs vertical displacements for a station located in the Amazon basin (NAUS)

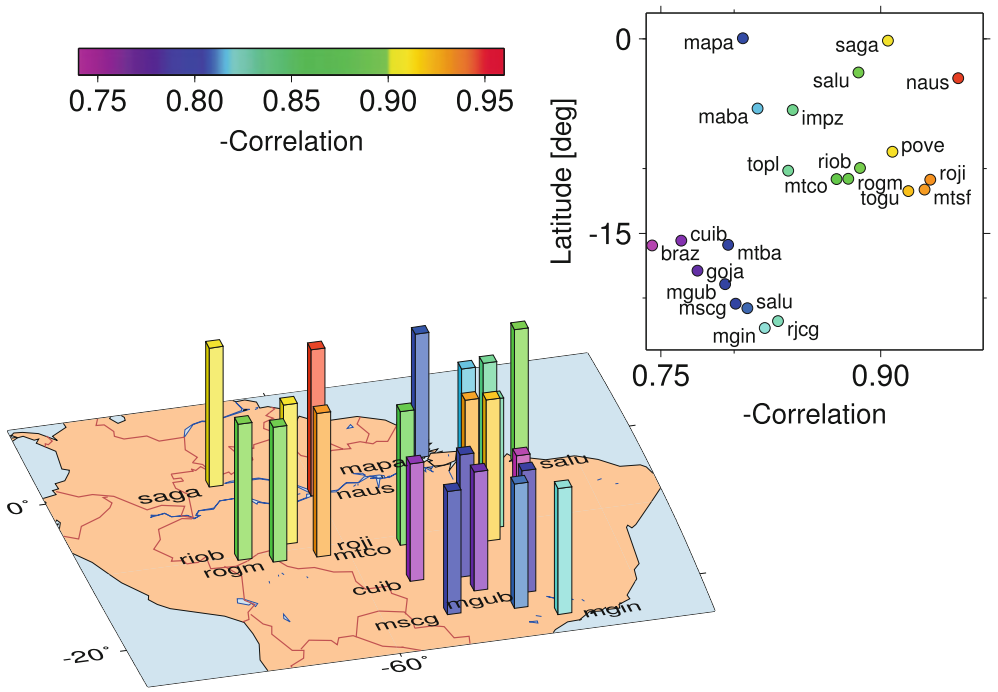

Fig. 5 Correlations between loading variations (EWH) and vertical displacements for South America

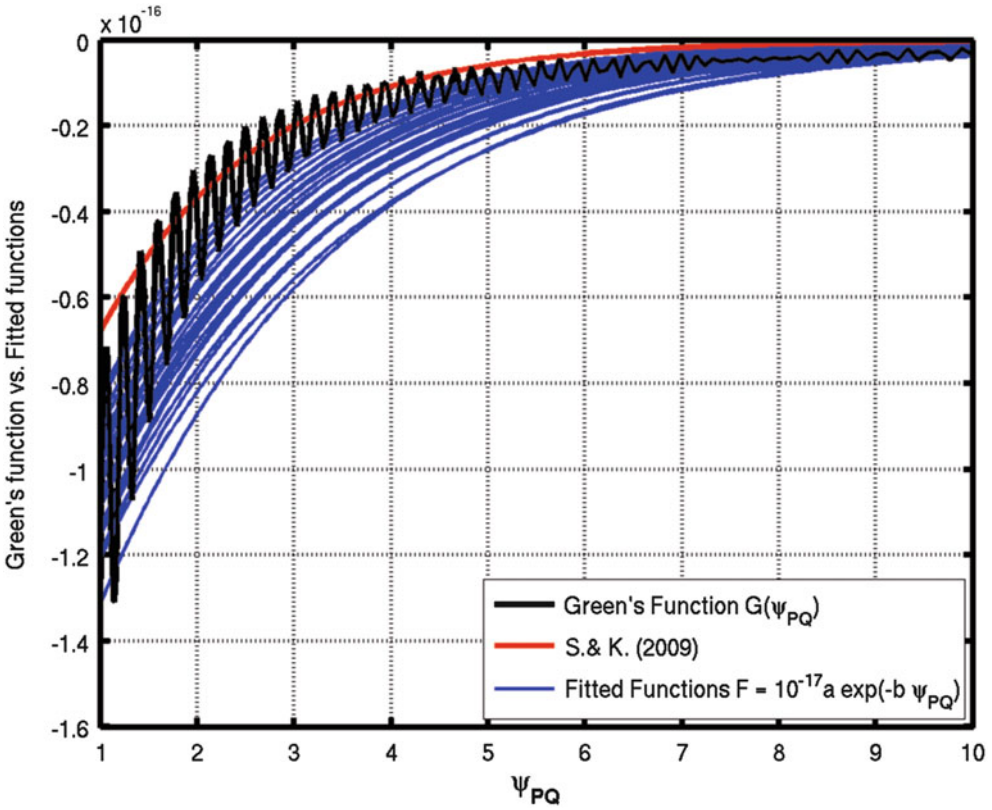

Fig. 6 Comparison between weighting functions

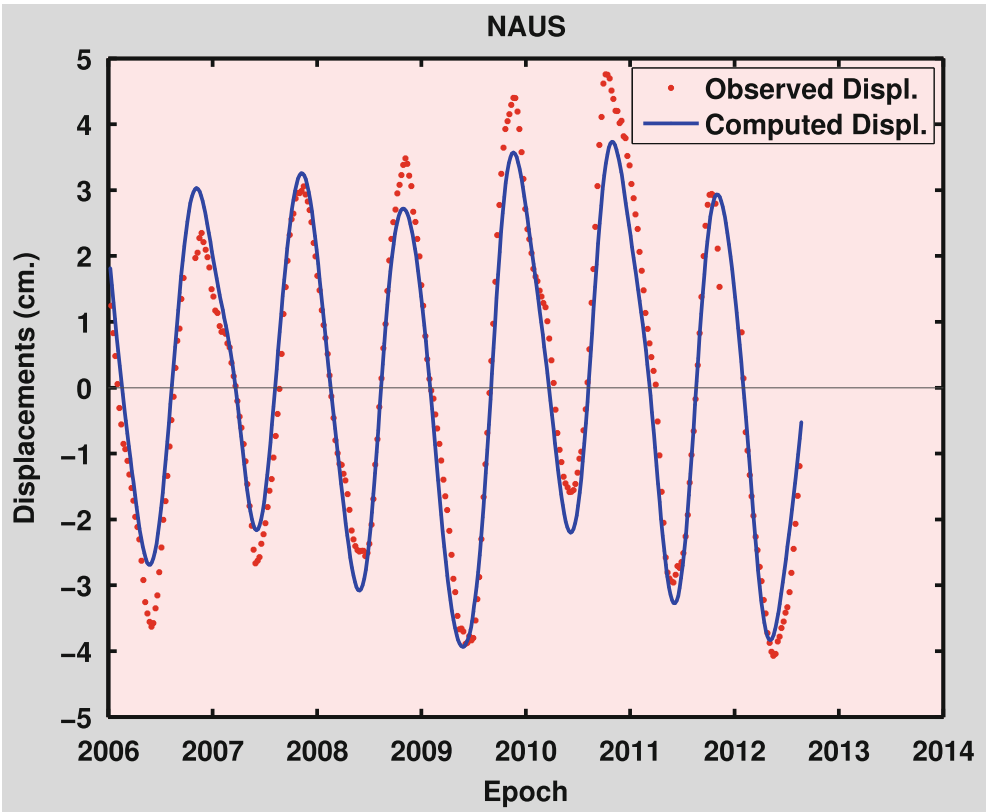

Fig. 7 Comparison between observed (red dots) and calculated (blue line) displacement for a station with strong harmonic behavior (NAUS)

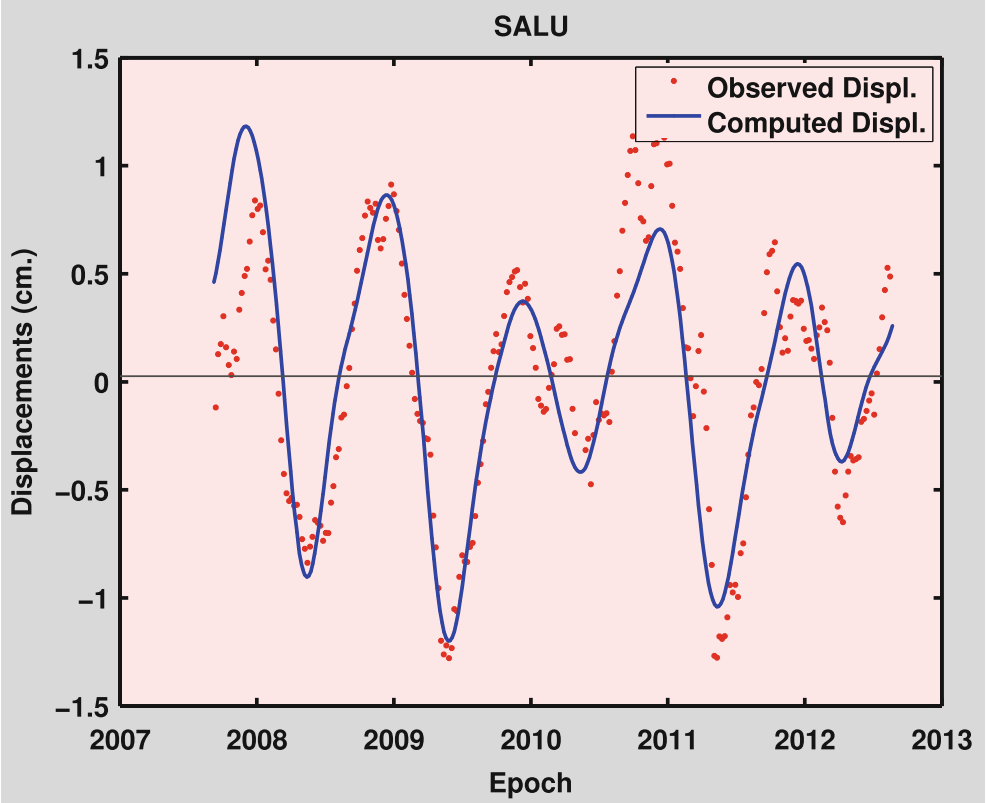

Fig. 8 Comparison between observed (red dots) and calculated (blue line) displacement for a station with visible interannual variations (SALU)

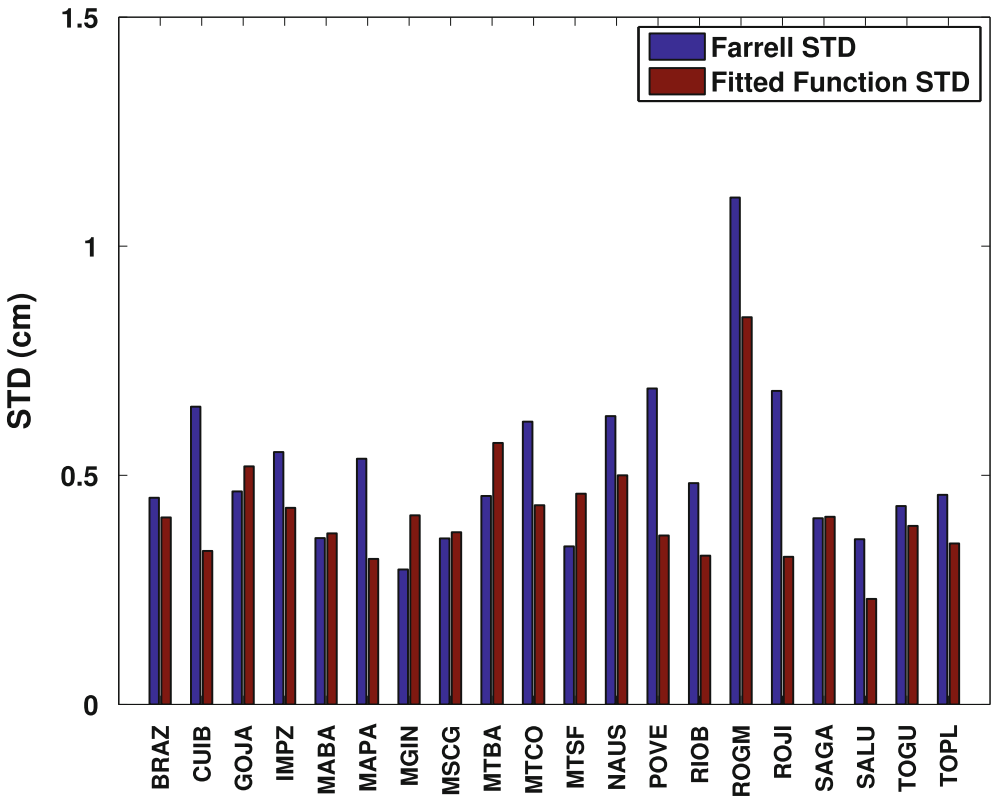

Fig. 9 STD for GPS stations

6 Summary and Outlook

This paper focused on a regional model of crustal vertical deformations caused by surface loading variations. We have used GPS data and GRACE data in order to quantify vertical surface displacements and temporal loading variations.

For those sites where the surface exhibits harmonic motion, the estimated displacements were very similar to those estimated with Farrell's method. For the remaining stations, the modeled displacements were capable of representing anomalous changes in time with good agreement. The observed displacements are dominated by a large annual continental mass signal and the differences in amplitudes between different years depend on local climate changes like *El niño* and *La niña*, etc.

These comparisons demonstrate that a physical mechanism is responsible for the correlation between both geodetic signals. We were capable of modeling changes in the surface due to load changes that differ from an annual or semiannual behavior, like flooding and dry seasons.

The main differences between the modeled and observed displacements are related to differences in maximum and minimum displacements. These may happen because GRACE can recover temporal variations of the Earth's gravity field due to mass redistribution that are spatially smoothed with a given resolution, while GPS data represents discrete point observations.

We have compared EHW values from the GRGS with those from CSR for the region of interest and we have not found significant differences in the solutions. Therefore, the use of any other GRACE data center is not expected to alter the main results presented in this work.

In this paper, we present a way to estimate vertical variations in GPS sites produced by persisting effects in current models. This method can be applied to other similar regions in order to achieve a better knowledge of the surface behavior.

Acknowledgements We thank SIRGAS-CON and GRGS centers for sharing the stations GPS data and spherical harmonic coefficients respectively. We are also grateful to the reviewers for valuable comments and suggestions that improved the manuscript. Also, the first author would like to thank Erasmus Mundus Program for giving her the opportunity to attend the IAG meeting. This research was supported by CONICET.

References

Altamimi Z, Collilieux X, Métivier L (2011) ITRF2008: an improved solution of the international terrestrial reference frame. J Geodesy 85:457–473. doi:10.1007/s00190-011-0444-4

Bettinelli P, Avouac JP, Flouzat M, Bollinger L, Ramillien G, Rajaure S, Sapkota S (2008) Seasonal variations of seismicity and geodetic strain in the Himalaya induced by surface hydrology. Earth Planet Sci Lett 266:332–344. doi:10.1016/j.epsl.2007.11.021

Bevis M, Alsdorf D, Kendrick E, Fortes LP, Forsberg B, Smalley R, Becker J (2005) Seasonal fluctuations in the mass of the Amazon river system and Earth's elastic response. Geophys Res Lett 32:L16308. doi:10.1029/2005GL023491

Biessy G, Moreau F, Dauteuil O, Bour O (2011) Surface deformation of an intraplate area from {GPS} time series. J Geodyn 52(1):24–33. doi:http://dx.doi.org/10.1016/j.jog.2010.11.005. http://www.sciencedirect.com/science/article/pii/S0264370710001572

Blewitt G, Lavallée D, Clarke P, Nurutdinov K (2001) A new global mode of earth deformation: seasonal cycle detected. Science 294:2342–2345. doi:10.1126/science.1065328

Bruinsma S, Lemoine JM, Biancale R, Valès N (2010) CNES/GRGS 10-day gravity field models (release 2) and their evaluation. Adv Space Res 45:587–601. doi:10.1016/j.asr.2009.10.012

Brunini C, Costa S, Mackern V, Martínez W, Sánchez L, Seemüller W, da Silva A (2009) SIRGAS: ITRF densification in Latin America and the Caribbean. In: Arabelos DN, Tscherning CC (eds) EGU general assembly conference abstracts, vol 11, p 2105

Brunini C, Sanchez L, Drewes H, Costa S, Mackern V, Martínez W, Seemuller W, Silva A (2012) Improved analysis strategy and accessibility of the sirgas reference frame. In: Kenyon S, Pacino MC, Marti U (eds) Geodesy for planet earth, international association of geodesy symposia, vol 136. Springer, Berlin/Heidelberg, pp 3–10. doi:10.1007/978-3-642-20338-1_1. http://dx.doi.org/10.1007/978-3-642-20338-1_1

Collilieux X, Altamimi Z, Coulot D, van Dam T, Ray J (2010) Impact of loading effects on determination of the international terrestrial reference frame. Adv Space Res 45:144–154. doi:10.1016/j.asr.2009.08.024

Collilieux X, van Dam T, Ray J, Coulot D, Métivier L, Altamimi Z (2012) Strategies to mitigate aliasing of loading signals while estimating GPS frame parameters. J Geodesy 86:1–14. doi:10.1007/s00190-011-0487-6

Dach R, Hugentobler U, Fridez P, Meindl M (2007) Bernese GPS Software, Version 5.0. Astronomical Institute, University of Bern. http://www.bernese.unibe.ch/docs/DOCU50.pdf

Dong D, Fang P, Bock Y, Cheng MK, Miyazaki S (2002) Anatomy of apparent seasonal variations from gps derived site position time series. J Geophys Res Solid Earth 107(B4). doi:10.1029/2001jb000573. <Go to ISI>://WOS:000178917000010, n/a

Farrell WE (1972) Deformation of the earth by surface loads. Rev Geophy 10(3):761–797. doi:10.1029/RG010i003p00761. http://dx.doi.org/10.1029/RG010i003p00761

Freymueller J (2009) Seasonal position variations and regional reference frame realization. In: Drewes H (ed) Geodetic reference frames, international association of geodesy symposia, vol 134. Springer, Berlin/Heidelberg, pp 191–196. doi:10.1007/978-3-642-00860-3_30. http://dx.doi.org/10.1007/978-3-642-00860-3_30

Fu Y, Freymueller JT (2012) Seasonal and long-term vertical deformation in the Nepal Himalaya constrained by GPS and GRACE measurements. J Geophys Res Solid Earth 117(B16):B03407. doi:10.1029/2011JB008925

Fu Y, Freymueller JT, Jensen T (2012) Seasonal hydrological loading in southern Alaska observed by GPS and GRACE. Geophys Res Lett 39:L15310. doi:10.1029/2012GL052453

Kusche J, Schrama EJO (2005) Surface mass redistribution inversion from global GPS deformation and gravity recovery and climate experiment (GRACE) gravity data. J Geophys Res Solid Earth 110:B09409. doi:10.1029/2004JB003556

Letellier T (2005) Etude des ondes de marée sur les plateaux continentaux. http://books.google.de/books?id=_3UEOgAACAAJ

Longman IM (1962) A green's function for determining the deformation of the earth under surface mass loads, 1, theory. J Geophys Res 67:845–850. doi:10.1029/JZ067i002p00845

Moritz H, Mueller II (1987) Earth rotation: theory and observation, Earth: Rotation, Provided by the SAO/NASA Astrophysics Data System, New York, Unga. http://adsabs.harvard.edu/abs/1987erto.book.....M

Niell AE (1996) Global mapping functions for the atmosphere delay at radio wavelengths. J Geophys Res Solid Earth 101(B2):3227–3246. doi:10.1029/95JB03048. http://dx.doi.org/10.1029/95JB03048

Poutanen M, Koivula H, Ollikainen M (2002) On periodicity of gps time series. In: Adam J, Schwarz KP (eds) Vistas for geodesy in the new millennium. International association of geodesy symposia, vol 125. Springer, Berlin, pp 388–392

Saastamoinen J (1973) Contributions to the theory of atmospheric refraction. Bull Géod 107(1):13–34. doi:10.1007/BF02522083. http://dx.doi.org/10.1007/BF02522083

Seitz F, Krügel M (2009) Inverse model approach for vertical load deformations in consideration of crustal inhomogeneities. In: Drewes H (ed) Geodetic reference frames, IAG symposia, vol 134. Springer, pp 23–29. doi:10.1007/978-3-642-00860-3_4

Tapley BD, Bettadpur S, Watkins M, Reigber C (2004) The gravity recovery and climate experiment: mission overview and early results. Geophys Res Lett 31:9607–+. doi:10.1029/2004GL019920

Tesmer V, Steigenberger P, van Dam T, Mayer-Gürr T (2011) Vertical deformations from homogeneously processed GRACE and global GPS long-term series. J Geodesy 85:291–310 doi:10.1007/s00190-010-0437-8

Tregoning P, Watson C (2009) Atmospheric effects and spurious signals in GPS analyses. J Geophys Res Solid Earth 114:B09403. doi:10.1029/2009JB006344

Tregoning P, Watson C, Ramillien G, McQueen H, Zhang J (2009) Detecting hydrologic deformation using GRACE and GPS. Geophys Res Lett 36:15401. doi:10.1029/2009GL038718

van Dam T (1998) Modeling environment loading effects: a review. Phys Chem Earth 23:1077–1087. doi:10.1016/S0079-1946(98)00147-5

van Dam TM, Wahr JM (1987) Displacements of the earth's surface due to atmospheric loading - effects of gravity and baseline measurements. J Geophys Res 92:1281–1286. doi:10.1029/JB092iB02p01281

van Dam T, Wahr J, Milly PCD, Shmakin AB, Blewitt G, Lavallée D, Larson KM (2001) Crustal displacements due to continental water loading. Geophys Res Lett 28:651–654. doi:10.1029/2000GL012120

van Dam T, Collilieux X, Wuite J, Altamimi Z, Ray J (2012) Nontidal ocean loading: amplitudes and potential effects in GPS height time series. J Geodesy 86:1043–1057. doi:10.1007/s00190-012-0564-5

Wahr J, Molenaar M, Bryan F (1998) Time variability of the earth's gravity field: hydrological and oceanic effects and their possible detection using GRACE. J Geophy Res Solid Earth 103(B12):30205–30229. doi:10.1029/98JB02844. http://dx.doi.org/10.1029/98JB02844

Wahr JM, Swenson S, Zlotnicki V, Velicogna I (2004) Time-variable gravity from grace: first results. Geophys Res Lett 31:11501. doi:10.1029/2004GL019779. http://adsabs.harvard.edu/abs/2004GeoRL..3111501W

Williams SDP, Penna NT (2011) Non-tidal ocean loading effects on geodetic GPS heights. Geophys Res Lett 38:L09314. doi:10.1029/2011GL046940

Zou R, Freymueller JT, Ding K, Yang S, Wang Q (2014) Evaluating seasonal loading models and their impact on global and regional reference frame alignment. J Geophys Res Solid Earth 119:1337–1358. doi:10.1002/2013JB010186

Expression of the Local GPS Solution in the Regional Reference Frame ETRF2000

Violeta Vasilić and Dragan Blagojević

Abstract

Station coordinates of a Local GPS permanent network (National permanent network of Serbia – AGROS and national permanent network of Former Yugoslav Republic of Macedonia – MAKPOS) were computed and expressed by aligning them to ITRF2005 using selected high quality Eurasian Plate EPN stations that were included in the GPS processing, which form part of the ITRF2005 realization. By application of transformation formulae, this network solution was transformed into ETRF2000. The minimum constraints approach has been applied preserving original characteristic of the local GPS solution, and in the same time, the local GPS solution was expressed in the regional reference frame through the mathematical definition of the ETRS89.

Keywords

GPS • Minimum constraints approach • Terrestrial Reference Frame

1 Introduction

According to the general rules given in the Law on the State Survey and Cadastre (LSSC) of Serbia, the European Terrestrial Reference System 1989 (ETRS89) was adopted as a basis of national geodetic system. Therefore, the Ministry of Civil Engineering and Urban Planning of Serbia and, consequently, of Republic Geodetic Authority (RGA) of Serbia, had to implement ETRS89. The GPS measurement campaign was realized in Republic of Serbia in 2010 in order to fulfill the regulations in LSSC and to be included in the EUREF (IAG – International Association of Geodesy – Reference Frame Sub-commission for Europe), Campaign Database. The campaign included 20 EPN (EUREF Permanent Network) stations, 48 stations from national permanent networks (Serbia, Former Yugoslav Republic of Macedonia, Bulgaria and Hungary) and 19 field points (Fig. 1). Station coordinates covered by this campaign were computed and expressed as a local GPS network, and then aligned to ITRF2005. This alignment was performed using EPN stations of high quality in the region of the Eurasian plate that were included in GPS processing, which are themselves part of the ITRF2005. By applying of Memo transformation formulae (Boucher and Altamimi 2009), this network solution was transformed into ETRF2000 as the basic frame of the ETRS89 realization. Given the configuration of a local network it is very important to carefully select the sub-set of EPN stations for application of minimum constraints approach which preserves original characteristic of the local GPS solution. The connection between local/regional solution and ITRF is provided through a selection of a set of ITRF stations which are part of the local network. The selection criteria for ITRF stations (also applied to the EPN stations) were applied as in (Altamimi 2003) for aligning a local/regional solution to the ITRF:

- A certain number of ITRF stations of high quality, surrounding the implied network, should be included in the GPS processing;
- A long observing history is preferred (at least 3 years);

V. Vasilić (✉) • D. Blagojević
Department of Geodesy and Geoinformatics, The University of Belgrade, 73 Boulevard king's Aleksandar, 11000 Belgrade, Serbia
e-mail: tatic@grf.bg.ac.rs; bdragan@grf.bg.ac.rs

© Springer International Publishing Switzerland 2015

C. Rizos, P. Willis (eds.), *IAG 150 Years*, International Association of Geodesy Symposia 143,
DOI 10.1007/1345_2015_34

Fig. 1 Distribution of sites in the EUREF Serbia 2010 Campaign

- The ITRF residuals should be less than 5 (eventually 10) mm for positions and 3 mm/year for velocities for at least three different solutions contributed to ITRF generation.

In addition to the above criteria, optimal estimation was carried out in accordance with the Guidelines for EUREF Densification (Bruyninx et al. 2010) and categorization of EPN station as reference stations in Class A taking into account the station quality and the length of available observation time span (Kenyeres 2011). EPN stations are categorized in Class A if they have positions at the 1 cm precision and velocities at the 1 mm/year precision at all epochs.

The establishment and development of a new geodetic reference system in Serbia was initiated primarily to provide support for geo-referencing activities, but what is particularly important is the support of scientific research. To achieve this goal however it is necessary to improve cooperation and coherence between national reference systems within EUREF.

2 ETRS89 Definition and Realization

A Terrestrial Reference System (TRS) co-rotates with the Earth in its diurnal motion in space. In a TRS positions of points attached to the solid surface of the Earth have coordinates which experience only small variations with time, due to geophysical effects (tectonic or tidal deformations). In the physical model adopted in Astronomy and Geodesy, a TRS is modeled as a reference trihedron close to the Earth and co-rotating with it. A Terrestrial Reference Frame (TRF) as the realization of a TRS, is also designated as a crust-based TRF. The main characteristic of both a TRS, at the theoretical level, and its corresponding TRF at the realization level are the origin, the scale, the orientation and their time evolution. The most commonly used terrestrial reference system is the IERS Terrestrial Reference System (ITRS) and its various realizations, known as International Terrestrial Reference Frames (ITRF). These frames are based on combinations of solutions from a four space based techniques: Very Long Baseline Interferometry (VLBI), Doppler Orbitography and Radiopositioning Integrated by Satellite (DORIS), Global Positioning System (GPS) and Satellite Laser Ranging (SLR). The individual solutions of station positions and velocities together with full variance matrices provided by each of these techniques represent a realization of a particular reference frame. The combination model used to generate ITRF solution contains 14 parameters, so-called "datum definition" parameters, which represent the ITRF origin, scale, orientation and time evolution (Petit and Luzum 2010). The EUREF Technical Working Group (TWG) decided at its Budapest meeting in 2009 to schedule updating of densification of the ITRF each 15 weeks by a new EUREF realizations using all EPN stations. ETRS89 was defined and adopted by EUREF in 1990 and has been

used by most European countries as the basis of their national geodetic systems. Advantage of adoption of the ETRS2000 as a conventional frame of the ETRS89 realization is to minimize the coordinate shifts at epochs posterior to 1989.0 between different implementations of the ETRS89 in Europe (Bruyninx et al. 2010). ETRS89 definition consists of two conditions: the reference system which coincides with ITRS at epoch 1989.0 and which is fixed to the stable part of the Eurasian tectonic plate (Altamimi 2009).

The general transformation of the Cartesian coordinates of any point close to the Earth from TRS (A) to TRS (B) is given by a three-dimensional similarity

$$\vec{X}_B = \vec{X}_A + \vec{T} + D\vec{X}_A + R\vec{X}_A \tag{1}$$

where $\vec{T}$ is a translation vector, D is a scale factor and R is a rotation matrix.

It is assumed that Eq. (1) is linear for sets of station coordinates provided by space geodesy techniques. Origin differences are about a few hundred meters, and differences in scale and orientation are at the level of 10^{-5}. Generally, $\vec{X}_A$, $\vec{X}_B$, $\vec{T}$, D and R are function of time, thus differentiating Eq. (1) with respect to time and excluding the terms that are negligible gives

$$\dot{\vec{X}}_B = \dot{\vec{X}}_A + \dot{\vec{T}} + \dot{D}\vec{X}_A + \dot{R}\vec{X}_A \tag{2}$$

The ETRS89 has been realized through the transformation formulae from ITRF yy to ETRF yy which means that to change the frame parameters of the departure frame (ITRF yy) at any epoch t_c to define the parameters (origin, scale, orientation) of the target frame (ETRF yy). The ETRS89 definition allows specifying rigorously the mathematical transformation formulae between the two systems:

$$\vec{X}^E(t_c) = \vec{X}^I_{yy}(t_c) + \vec{T}_{yy} + \begin{bmatrix} 0 & -\dot{R}3_{yy} & \dot{R}2_{yy} \\ \dot{R}3_{yy} & 0 & -\dot{R}1_{yy} \\ -\dot{R}2_{yy} & \dot{R}1_{yy} & 0 \end{bmatrix} \times \vec{X}^I_{yy}(t_c) \cdot (t_c - 1989.0) \tag{3}$$

3 EUREF Serbia 2010 Campaign

The "EUREF Serbia 2010 Campaign" was realized by RGA during the summer of 2010 covering an observation period of 5 weeks. The campaign included 20 EPN stations, 48 stations from national permanent networks (Serbia, FYRO Macedonia, Bulgaria and Hungary) and 19 field points, i.e., 87 stations in total. The local network is within a radius of about 600 km in the N–S direction for area Serbia and FYRO Macedonia. For a datum definition the following 18 EPN stations were considered: AUT1, BACA, BAIA, BUCU, BZRG, DEVA, DUBR, GRAZ, GSR1, ISTA, MATE, ORID, OROS, OSJE, PADO, PENC, SRJV, and ZIMM. Datum definition was provided in ITRF2005 with seven EPN/ITRF2005 stations BUCU, GRAZ, ISTA, MATE, PADO, PENC and ZIMM. Due to the lack of EPN stations surrounding the campaign network, the stations: BAIA, BUCU, DEVA, ISTA, SRJV were not excluded from processing, although they had coordinate time series with large periodic signals with an amplitude exceeding 1 cm. The stations SOFI and WTZR had antenna replacements after the publication of ITRF2005 so they were processed but they were excluded from datum reference list as recommended in (Habrich 2008). The network processing was carried out using the Bernese Software v.-5.0 following the Guidelines for EPN Analysis Centers (Bruyninx et al. 2010). For the final network solution the minimum constraints were applied to the translation parameters on the reference EPN stations which were located on the stable part of Eurasian plate and whose precise velocities were available. After that, transformation from campaign reference frame ITRF2005, epoch 2010.63 to ETRF2000 was performed using the online transformation service available on EPN-CB web page. The EUREF campaign in Serbia 2010 was accepted as Class B standard by EUREF Technical Working Group as an improvement and extension of EUREF in Serbia (EUREF Resolutions 2011).

4 Realization of Regional Reference Frame in Republic of Serbia

Realization ETRF2000 in Republic of Serbia was obtained using the Memo transformation formulas (Boucher and Altamimi 2009) from the source system (ITRF2005) into the target system (ETRF2000) in two steps:

1. Transformation of ITRF2005 coordinates into ITRF2000 using IERS/ITRF published values;
2. Application of the above mentioned formula to transform from ITRF2000 into ETRF2000.

The correctness of the datum-realization depends on the quality and distribution of the EPN reference stations. As we reproduce a global reference frame with a local network the so-called network effect cannot be avoided, and that is visible through the differences in all components. The estimated EPN station coordinates from the final combined solution were compared with EPN station coordinates from the actually available cumulative solution EPN_A_ITRF2005_C1600.SNX. The differences in the results along all components are up to 4 mm (Figs. 2, 3 and 4) and the RMS of the differences are: 0.9, 1.6 and 1.9 mm for the North, East and Up component, respectively (Veljković and Lazić 2011). The largest differences at ITRF station

Fig. 2 Differences of reference EPN stations latitude and longitude

Fig. 3 Differences of reference EPN stations height

positions are at ISTA and MATE and in height at stations GRAZ and PENC (Table 1). These differences are less than 10 mm for all reference stations, so they were used to verify the agreement of the estimated positions of the EPN reference stations with EPN_A_ITRF2005 values. To reduce the network effect, more stations that are in ITRF and properly distributed around the campaign network should be used.

Permanent network stations of Serbia have no true absolute antenna calibration models yet (example of the antenna types used in the permanent network of Serbia: TRM41249.00, TRM55971.00, LEIAT504GG), therefore for each antenna type the relative NGS (National Geodetic Survey) antenna calibration model was converted to absolute one, and used for the processing. It is not a robust way to define a national datum since the relationship between the antenna phase centre and fixed monument is not known. The question is to ensure the sustainability of the national datum after the antenna change.

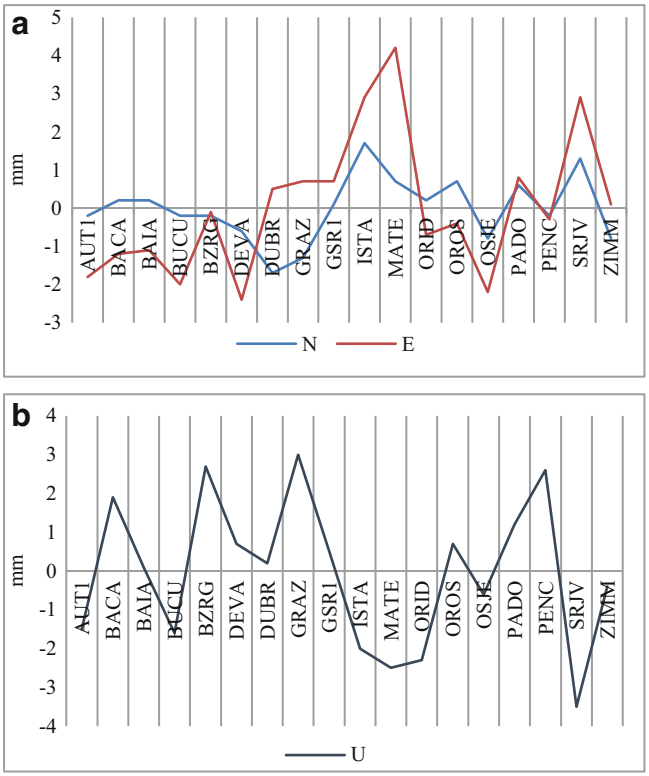

Fig. 4 (**a**) Differences of reference EPN stations for N and E components. (**b**) Differences of reference EPN stations for U component

Table 1 Differences between ITRF2005 coordinate values for reference EPN stations (ITRF stations are in bold)

Station	North (mm)	East (mm)	Up (mm)
AUT1	−0.2	−1.6	−1.5
BACA	0.2	−1.4	1.9
BAIA	0.2	−1.3	0.1
BUCU	**−0.2**	**−1.8**	**−1.6**
BZRG	−0.2	0.1	2.7
DEVA	−0.6	−1.8	0.7
DUBR	−1.7	2.2	0.2
GRAZ	**−1.3**	**2.0**	**3.0**
GSR1	0.1	0.6	0.5
ISTA	**1.7**	**1.2**	**−2.0**
MATE	**0.7**	**3.5**	**−2.5**
ORID	0.2	−0.9	−2.3
OROS	0.7	−1.1	0.7
OSJE	−0.8	−1.4	−0.6
PADO	**0.6**	**0.2**	**1.2**
PENC	**−0.2**	**−0.1**	**2.6**
SRJV	1.3	1.6	−3.5
ZIMM	**−0.8**	**0.9**	**−0.4**
RMS	0.9	1.6	1.9

Therefore, it is particularly important to isolate, detect and investigate all kind of discontinuities in coordinate time series because any change in station position (offset, noise or

Table 2 Station coordinates from national permanent networks of Campaign network in the ETRF2000

Station	X (m)	Y (m)	Z (m)
BAJI	4,332,494.7638	1,540,226.6512	4,405,782.7753
BALE	4,184,409.8245	1,435,900.9861	4,579,323.5811
BEOG	4,246,572.4886	1,585,753.4773	4,472,178.5797
BERO	4,395,121.3996	1,852,322.0471	4,221,826.7415
BITO	4,489,050.7610	1,753,409.5351	4,164,880.5858
BLAG	4,365,251.9516	1,861,898.4779	4,247,666.9158
BOR_	4,252,559.7314	1,726,576.9005	4,414,702.3888
BOSI	4,352,527.5356	1,800,358.1263	4,287,319.7273
BUJA	4,377,012.6688	1,747,681.0365	4,283,713.0166
DEBA	4,479,215.9295	1,677,227.7540	4,206,430.4444
DIMI	4,306,825.8415	1,808,482.4875	4,329,154.1658
GMIL	4,304,059.8737	1,605,810.7119	4,410,324.2988
GROC	4,250,871.8243	1,610,726.6056	4,459,349.2229
HALA	4,151,633.5998	1,469,027.3406	4,598,530.0041
INDJ	4,239,594.1599	1,549,817.8560	4,491,191.8813
IVAN	4,342,572.6451	1,600,353.5468	4,374,843.0699
KICE	4,467,288.2550	1,711,204.5770	4,205,358.3951
KIKI	4,171,106.3311	1,556,486.2147	4,552,146.1967
KLAD	4,198,525.6804	1,748,784.5689	4,456,702.4141
KNJA	4,284,174.9368	1,753,166.2810	4,373,521.7226
KRPA	4,377,111.2877	1,798,384.9812	4,263,084.4483
KRUS	4,310,927.6888	1,683,242.1277	4,374,596.2920
KUMA	4,400,896.4223	1,752,888.5720	4,257,110.0542
KURS	4,344,218.6011	1,691,248.3411	4,338,960.2993
LESK	4,333,721.6290	1,746,352.5819	4,327,504.7041
LOZN	4,300,140.5663	1,499,531.4014	4,450,807.1418
MONT	4,264,436.8720	1,829,947.2037	4,361,298.9874
NEGM	4,434,095.6994	1,799,508.2347	4,202,961.4281
NEGO	4,228,641.9626	1,754,177.1389	4,426,206.3829
NPAZ	4,365,991.2578	1,634,053.0454	4,339,210.5008
PLAN	4,197,325.5604	1,621,400.1455	4,505,445.4586
PRIJ	4,372,826.4645	1,560,748.5146	4,359,082.1023
PRIL	4,460,456.5897	1,762,385.7536	4,191,613.6298
SABA	4,271,111.9045	1,529,000.3223	4,468,514.4320
SID_	4,256,180.8775	1,484,331.9848	4,497,564.8158
SKOP	4,419,733.9778	1,732,735.6939	4,245,785.5397
SOMB	4,210,757.2214	1,459,275.7754	4,547,875.6709
SRBO	4,210,389.2122	1,515,090.6539	4,530,038.1659
SRED	4,310,640.3513	1,862,714.4503	4,302,583.1992
SUBO	4,172,027.2639	1,491,099.4418	4,573,052.0490
SZEG	4,147,508.7230	1,522,034.2672	4,585,018.5197
TETO	4,432,297.3230	1,698,764.1458	4,246,735.7316
VALA	4,430,250.1043	1,840,818.3373	4,189,158.3323
VALJ	4,301,920.2855	1,555,888.4956	4,429,917.4273
VELE	4,427,996.0603	1,768,429.5684	4,222,454.8639
VGRA	4,219,786.4010	1,663,918.3501	4,469,057.0106
VINI	4,393,777.5205	1,820,368.5165	4,236,330.064
ZITI	4,194,384.9594	1,572,394.8626	4,525,379.4716

seasonal signal) can degrade the characteristics of the time series, and seriously degrade the quality of estimated positions and velocities. The minimum time-span of observation data series is 2.5 year (Blewit and Lavallée 2002). Stations included in the campaign network were categorized as Class B stations with positions at the 1 cm precision at the epoch of minimal position variance of each station except for the stations with low quality antenna: BOSI, INDJ, GMIL, PLAN, SID_, and SRBO. In any case, inspection of irregularities in coordinate time series should be carried out independently of the campaign and certainly before the next campaign. Table 2 shows the station coordinates from national permanent network of Serbia, Former Yugoslav Republic of Macedonia, Bulgaria and Hungary in the Regional reference frame ETRF2000, epoch 2010.63. The Table 2 does not contain information about the formal uncertainties of station coordinates although general measure of uncertainty for all stations is at the mm level (RGA, personal communication).

5 Conclusion

The adoption of the ETRS89 reference system, defined by EUREF is an important step towards the improvement of cooperation and coherence of national reference frames within Europe. For the optimal expression of the Serbian national GPS solution inthe ETRF2000 Regional Reference Frame, the minimum constraints approach was applied over the translation parameters of the EPN reference stations. In order to improve the agreement with ITRF more datum stations around the campaign network should be used.

The EUREF Serbia 2010 campaign was accepted as Class B standard by the EUREF TWG as an improvement and extension of ETRS89 in Serbia. The quality of ETRF2000 realization depends upon the geometry and number of stations of the EPN reference stations chosen as well as on reliability of permanent networks stations included in the campaign. To improve and assess the stability of national TRF, it could be advantageous to use regular official update of realization, as well as to remove all kinds of irregularities in GPS coordinate time series of continuous permanent network of Serbia independently of the campaign.

References

Altamimi Z (2003) Discussion on how to express a regional GPS solution in the ITRF. EUREF Publication No. 12.Verlag des Bundesamts für Kartographie und Geodäsie, Frankfurt am Main, pp 162–167

Altamimi Z (2009). ETRS89 realization: current status, ETRF2005 and future development. Bull Geod Geomat LXVIII(3)

Blewit G, Lavallée D (2002) Effect of annual signals on geodetic velocity. J Geophys Res 107(B7)

Boucher C, Altamimi Z (2009) Memo: specifications for reference frame fixing in the analysis of a EUREF GPS campaign.V. 7. http://etrs89.ensg.ign.fr/

Bruyninx C et al (2010) Guidelines for EUREF densifications. ftp://epncb.oma.be/pub/general/

Habrich H (2008) EPN analysis – products and report. EUREF symposium. Brussels, Belgium

Kenyeres A (2011) Categorizaton of permanent GNSS reference stations. Bull Geod Sci LXIX(2–3):375–390

Law on the State Survey and Cadastre. Ministry of Civil Engineering and Urban Planning of the Government of the Republic of Serbia. Official Gazette RS, br. 72/2009, 18/2010, 65/2013

Petit G, Luzum B (2010) IERS conventions (2010). IERS Technical Note No. 36. Verlag des Bundesamts für Kartographie und Geodäsie, Frankfurt am Main. http://www.iers.org/TN36/

Resolutions of the XIXth EUREF Symposium (2011). Chisinau, Moldova. http://www.euref.eu/symposia/2011Chisinau/08-01-Resolution/

Veljković Z, Lazić S (2011) EUREF Serbia 2010 – final report. XIXth EUREF symposium, Chisinau, Moldova

Impact of Antenna Phase Centre Calibrations on Position Time Series: Preliminary Results

D. Sidorov and F.N. Teferle

Abstract

Advances in GPS error modelling and the continued effort of re-processing have considerably decreased the scatter in position estimates over the last decade. The associated reduction of noise in derived position time series has revealed the presence of previously undetected periodic signals. It has been shown that these signals have frequencies related to the orbits of the GPS satellites. A number of potential sources for these periodicities at the draconitic frequency and its harmonics have already been suggested in the literature and include, e.g., errors in the sub-daily tidal models, multipath and unresolved integer ambiguities.

Due to the geometrical relationship between the observing site and the orbiting satellite, deficiencies in the modelling of electromagnetic phase centres of receiving antennas have the potential to also contribute to the discovered periodic signals. The change from relative to absolute type mean antenna/radome calibrations within the International GNSS Service (IGS) led to a significant improvement, but the use of individual calibrations could possibly add further refinements to computed solutions. However, at this stage providing individual calibrations for all IGS stations is not feasible. Furthermore, antenna near-field electromagnetic effects might outweigh the benefits of individual calibrations once an antenna is permanently installed.

In this study, we investigate the differences between position estimates obtained using individual and type mean antenna/radome calibrations as used by the IGS community. We employ position time series derived from precise point positioning (PPP) as implemented in two scientific GNSS software packages. Our results suggest that the calibration differences propagate directly into the position estimates, affecting both sub-daily and daily results and yielding periodic variations.

The sub-daily variations have periods close to half a sidereal day and one sidereal day with peak-to-peak amplitudes of up to 10 mm in all position components. The stacked power spectra of the daily difference time series reveal peaks at the GPS draconitic frequency and its harmonics with peak-to-peak amplitudes of up to 1 mm. Although these results are still preliminary, they confirm that small differences between individual and type

D. Sidorov (✉)
Geophysics Laboratory, University of Luxembourg, 6 rue Richard Coudenhove-KalergiL-1359, Luxembourg City, Luxembourg

Present address: Astronomical Institute, University of Bern, Sidlerstrasse 5, CH-3012 Bern, Switzerland
e-mail: dmitry.sidorov@aiub.unibe.ch

F.N. Teferle
Geophysics Laboratory, University of Luxembourg, 6 rue Richard Coudenhove-KalergiL-1359, Luxembourg City, Luxembourg

© Springer International Publishing Switzerland 2016

C. Rizos, P. Willis (eds.), *IAG 150 Years*, International Association of Geodesy Symposia 143,
DOI 10.1007/1345_2015_216

mean antenna/radome calibrations propagate into position time series and may be partly responsible for the spurious signals with draconitic frequency and its harmonics.

Keywords
Antenna phase centre calibration • Global positioning system • GPS draconitic year • Spurious signals

1 Introduction

Advances in processing of Global Navigation Satellite System (GNSS) measurements, in particular of the Global Positioning System (GPS), and refinements in the applied error models during the last decade have resulted in an outstanding reduction of background noise both in the satellite products and station position time series of the International GNSS Service (IGS; Dow et al. 2009). These improvements enabled more detailed studies of geophysical processes, resulting in further discoveries and revealing processing artifacts. The identification and precise estimation of the latter is essential in confirming geophysical models and, consequently, deeper understanding of the underlying geophysical processes.

Ray et al. (2008) examined the residuals of the GPS position time series, which were generated during the combination of the International Terrestrial Reference Frame (ITRF) realization 2005, and discovered a periodic signal at 1.04 cpy, followed by 6 overtones. Similar signals could be found in the reprocessed ITRF2008 solution (Collilieux et al. 2011). The discovery of Ray et al. (2008) gave an impulse to an extensive research, revealing the factors contributing to the generation of these signals, and linking them to the earlier work by Penna et al. (2007). The latter showed how errors in the tidal models propagate into coordinate solutions, because of the linearisation performed in the least squares estimation, as described by Stewart et al. (2005).

Later, Tregoning and Watson (2009) demonstrated the generation of harmonic signals at draconitic frequencies in position time series due to unmodelled atmospheric loading deformation. Rodriguez-Solano et al. (2012) reported that some power of the draconitic signals can be attributed to insufficient modelling of the Earth radiation pressure. Finally, Griffiths and Ray (2013), investigating the effects of errors in sub-daily EOP tides, showed that the latter propagate into the GPS orbits. In addition, Tregoning and Watson (2009) as well as King and Watson (2010) reported that unresolved ambiguities may also contribute to the power at the draconitic frequencies. However, this effect may be small as integer ambiguities are resolved routinely with high success rates by the various IGS analysis centers.

Other factors that add power at the draconitic frequencies in GPS position time series, are site-specific and consist mainly of multipath (King and Watson 2010) and electromagnetic (EM) coupling between the antenna and the monument (e.g., Dilßner et al. 2008; King et al. 2012). Both effects can be interpreted as an amplification of the antenna phase centre modelling errors, as from a geometrical point of view these effects are similar to those from mismodelling phase centres. Although the site-specific effects are difficult to quantify, the resulting errors may noticeably contribute to the unexplained periodic signals observed by Ray et al. (2008) and Collilieux et al. (2011).

In 2006, the IGS switched from relative to absolute type mean antenna/radome calibrations within its products, which led to a significant improvement in computed station positions (Dow et al. 2009), but the use of individual calibrations could possibly add further refinements to computed solutions. However, at this stage providing individual calibrations for all IGS stations is not feasible. In this study, we show how a change from type mean to individual antenna phase centre variation models affects position time series on sub-daily and daily time scales. However, this effect is potentially much smaller than the one caused by site-specific effects, including EM coupling between antenna and monument as well as multipath, as also reported by, e.g., Steigenberger et al. (2013). We highlight the importance of antenna/radome modelling errors by demonstrating how they propagate into harmonic signals in coordinate solutions.

2 Antenna Calibrations

The electromagnetic centre of a GNSS antenna does not coincide with the physical one, therefore, for high-precision applications antenna phase centre models are employed (Schmid et al. 2007). These models include an antenna phase centre offset (PCO) with respect to the antenna reference point and phase centre variations (PCV) depending on azimuth and elevation, which are unique for each individual antenna including the radome, if present (Fig. 1). For brevity, the combination of PCO and PCV will be denoted as phase centre correction (PCC) hereinafter.

The existing calibration procedures require mounting the antenna on a robot (e.g., Wübbena et al. 2006; Bilich and Mader 2010) or placing it into an anechoic chamber (e.g., Görres et al. 2006; Zeimetz and Kuhlmann 2008). Considering that an on-site calibration is not possible yet, the

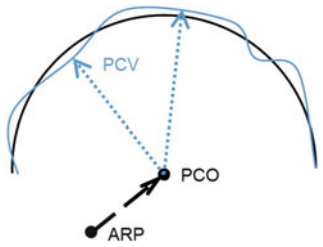

Fig. 1 Antenna reference point (ARP), phase centre offset (PCO) and phase centre variations (PCV)

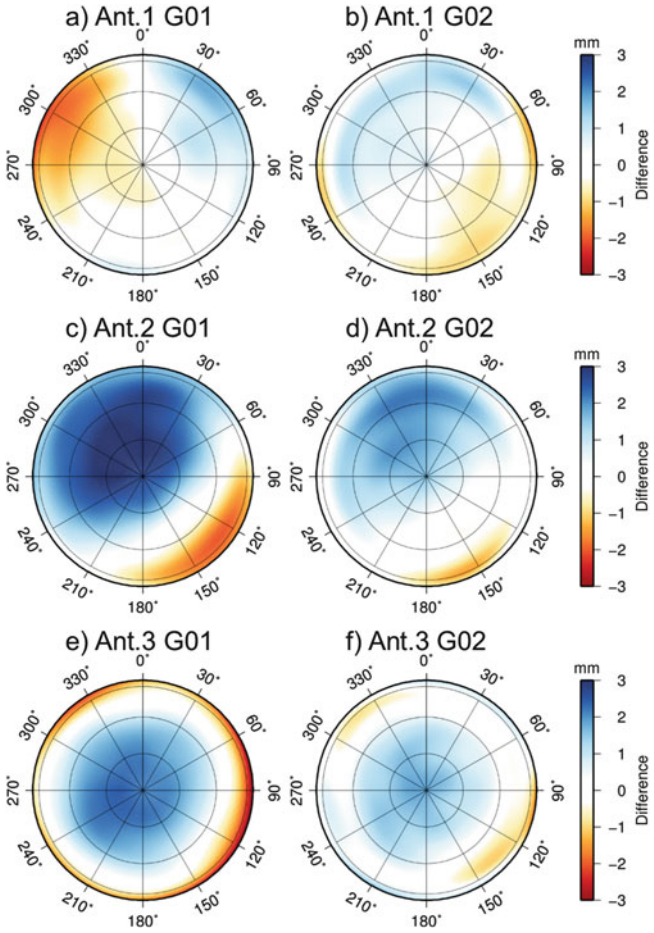

Fig. 2 Skyplots of the differences between type mean PCCs and individual antenna calibrations for three IGS-standard choke ring antennas for the GPS frequencies G01 (**a**), (**c**), and (**e**), and G02 (**b**), (**d**) and (**f**), respectively. (**a**), (**b**), (**c**) and (**d**) correspond to the same antenna model

calibration of already installed antennas and radomes would inevitably result in discontinuities in the position time series through the removal and replacement of the antenna after calibration. However, due to the fact that the individual calibrations for an antenna/radome combination show fairly consistent PCCs across all combinations of the same antenna type, the geodetic community currently employs averaged ("type mean") rather than individual calibrations for high-accuracy GNSS data processing.

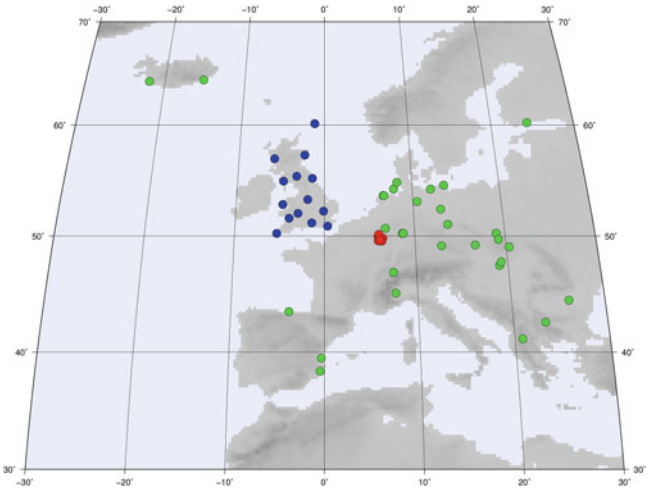

Fig. 3 The processed network, consisting of EUREF, BIGF, ACT and NRCan sites (not shown), marked by *green, blue and red dots*, respectively

In contrast to the common assumption that the PCCs of individual antennas do not deviate much from the type mean model, Fig. 2 shows the PCC differences for three IGS-standard choke ring antennas. Two of them (Fig. 2a–d), being of the same model, are installed in Luxembourg within the national real-time kinematic (RTK) network. Robot-based individual PCC models are available for both stations. The differences between the type mean and individual PCCs for these two antennas reach 2 mm, whereas the differences between the two individual ones reach 4 mm. This suggests that using type mean antenna calibrations may lead to PCC-specific errors during parameter estimation.

3 Methodology

In order to investigate this effect further, we carried out two parallel precise point positioning (PPP; Zumberge et al. 1997) runs, in which all processing options were kept identical except for the antenna/radome calibrations employed. The PPP technique was selected to reveal the antenna/radome effects at each site, minimizing any influence from neighbouring sites. We performed this processing using two scientific software packages: the Bernese GNSS Software ver. 5.2 (BSW; Dach et al. 2007; BSWteam 2012) and the NAvigation Package for Earth Observation Satellites ver. 3.3.1 (NAPEOS; Springer 2009), using the IGS final products. Integer ambiguities were not resolved, as this is not possible with BSW5.2, and as NAPEOS' ambiguity resolution is based on a baseline-by-baseline approach.

In total we were able to consider 54 sites, mostly located in Europe (Fig. 3) and contributing to the International

Table 1 Antenna/radome combinations within the processed network together with the calibration facilities for the individual calibrations

Antenna	Radome	Number of stns	Calibr. facility	Antenna	Radome	Number of stns	Calibr. facility
AOAD/M_T	NONE	2	Geo++[a]	TPSCR.G3	TPSH	1	Geo++
JAV_RINGANT_G3T	NONE	1	AMK Bonn[b]	TPSCR3_GGD	CONE	7	Geo++
LEIAR25	LEIT	13	Geo++	TRM29659.00	NONE	2	Geo++
LEIAR25.R3	LEIT	14	Geo++	TRM29659.00	SNOW	2	Geo++
LEIAR25.R3	NONE	1	Geo++	TRM33429.20+GP	NONE	2	Geo++
LEIAR25.R4	LEIT	3	Geo++	TRM41249.00	NONE	2	Geo++
LEIAT504	LEIS	1	Geo++	TRM41249.00	TZGD	1	Geo++
LEIAT504	SCIT	2	Geo++	TRM55971.00	NONE	1	Geo++
LEIAT504GG	LEIS	7	Geo++, SenStadt Berlin[c]	TRM55971.00	TZGD	4	SenStadt Berlin, LWa(TU-Dresden)[d]
NOV750.R4	NONE	2	Geo++	TRM59800.00	NONE	1	Geo++

[a]Geo++: Gesellschaft für satellitengestützte geodätische und navigatorische Technologien mbH, Garbsen, Germany
[b]Antennenmesskammer, University of Bonn
[c]Senate Department for Urban Development and the Environment, Berlin
[d]Calibrations performed by Lambert Wanninger, Technische Universität Dresden

Association of Geodesy (IAG) Reference Frame Sub-Commission for Europe (EUREF), the British Isles continuous GNSS Facility (BIGF), the Natural Resources Canada (NRCan) and l'Administration du Cadastre et de la Topographie (ACT), Luxembourg. The processing was performed for the period between July 2002 and December 2011. As some antennas were exchanged during that period, the actual number of examined antenna/radome combinations is obviously larger than the number of sites. However we have selected only those antenna/radome combinations with time series of 1 year or longer. Overall 69 antenna/radome combinations were investigated (see Table 1).

First, a PPP run using type mean PCCs was carried out in order to estimate station coordinates and zenith tropospheric delays (ZTD). Due to the correlation between PCCs and ZTDs, and in order to highlight the pure effect of the applied PCCs on the estimated station coordinates, the ZTD estimates from the "type mean" run were fixed in the second PPP run, in which individual antenna PCCs were applied. After obtaining the position solutions from both PPP runs, we computed their differences epoch by epoch.

In this study we made the assumption that all error sources remained identical in both PPP runs, suggesting that the differences in the final coordinate solutions were only affected by variations in the applied antenna/radome calibrations.

4 Results: Sub-daily Position Estimates

Pseudo-kinematic 15-min PPP solutions for 1 week (GPS week 1667) were obtained for six stations of the RTK network in Luxembourg using the BSW5.2. Following the methodology described above, Fig. 4 shows the differences between the position solutions applying type mean and individual antenna/radome calibrations, respectively. The difference time series in Fig. 4 correspond to the antenna shown in Fig. 2a, b. An elevation mask of 10° was applied at the receiver level, therefore the PCC differences in low elevations of Fig. 2a, b do not have an impact.

For clarity, constant biases have been removed from all difference time series presented in this paper, however they are still reported as the median values and the corresponding interquartile ranges in Fig. 4. For the six investigated stations constant biases of up to 5 mm can be observed in all three components. Additionally, the position differences exhibit periodic variations at diurnal and semi-diurnal frequencies with peak-to-peak amplitudes of up to 10 mm. A frequency analysis shows that the variations in the position differences have periods close to 11 h 58 min, which corresponds to the orbital period of the GPS satellites or half a sidereal day.

Stewart et al. (2005) showed that unmodelled sub-daily periodic site displacements would result in longer wavelength periodic signals. The observed ~11 h 58 m periodic signal resulting from the PCC errors can be interpreted as an artificial unmodelled displacement that has the potential to produce aliased longer wavelength signals when sampled at 24 h intervals. As all six sites of the RTK network in Luxembourg exhibited similar periodic patterns in their position differences, it is suggested that similar effects may also be observed for other stations with deficiencies in the antenna/radome correction models.

5 Results: Daily Position Estimates

For our daily results we used both the BSW5.2 and NAPEOS3.31 to guarantee that the observed effects are not software-dependent. After obtaining nearly identical

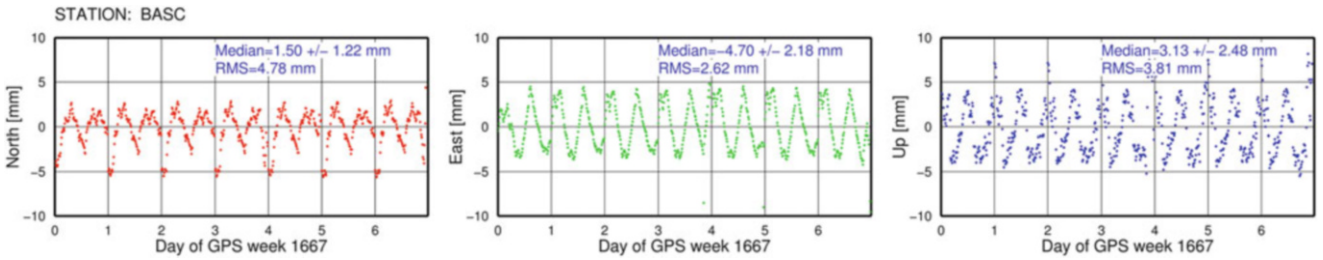

Fig. 4 Differences in the north (*red*), east (*green*) and up (*blue*) coordinate components between individual and type mean PCCs from the BSW 15-min pseudo-kinematic PPP solutions for ACT station BASC equipped with the antenna from Fig. 2a, b

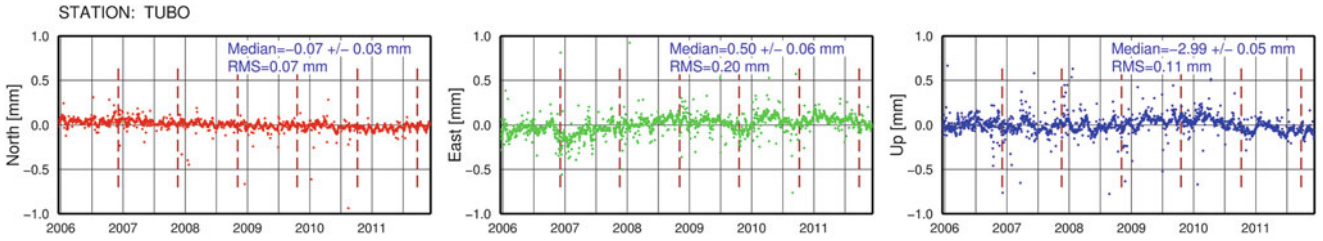

Fig. 5 Differences in the north (*red*), east (*green*) and up (*blue*) coordinate components between individual and type mean PCCs from the NAPEOS daily PPP solutions for EUREF station TUBO equipped with the antenna from Fig. 2e, f. The *vertical dashed brown lines* indicate the GPS draconitic years from the beginning of the time series and correspond to 351.2 days, 702.4 days, 1053.6 days, etc.

difference time series from the daily position estimates of both software packages, we only consider NAPEOS results in the following.

Figure 5 shows the difference time series derived from the daily PPP solutions for EUREF station TUBO equipped with the antenna shown in Fig. 2e, f. Of importance are constant biases as expressed by the median values of up to 3 mm (up component) and the harmonic signals visible for the east and up components.

As a result of the changes in the applied PCC models, the north component shows a small trend of about −0.02 mm/year. King and Watson (2010) suggested that such a phenomenon may be explainable by the evolving GPS constellation, or, alternatively, could be a long wavelength periodic signal. The observed phenomenon is an indication that estimated site velocities may be affected by imperfections in the applied PCC models.

Biases and harmonic signals, with peak-to-peak amplitudes of up to 1 mm, can be observed in the difference time series of the majority of the investigated antenna/radome combinations. However, due to the high noise level, the corresponding frequency analysis does not reveal clear peaks.

To identify common periodic signals in the daily position differences, we computed the Lomb-Scargle periodogram (Scargle 1982) for each station. Then we stacked the obtained individual power spectra after normalizing them to 1 mm^2 variance. This leads to the stacked power spectra for the

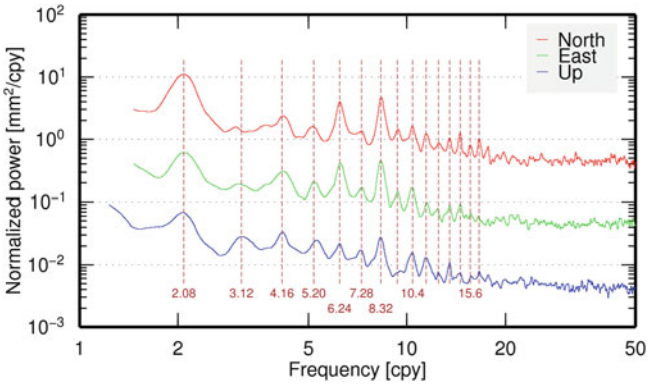

Fig. 6 Stacked power spectra for the difference time series of 69 investigated antenna/radome combinations, having more than 365 daily observations between 2002 and 2012. For clarity the *curves* of the north and east components have been shifted

north, east and up components shown in Fig. 6. By analyzing these results the power of the periodic signals is identified at frequencies that match the overtones of the GPS draconitic year ($1.04 \times n$ cpy, where $n = 2, 3, 4, \ldots$). The power of the overtones, observable for $n \leq 16$, tends to decrease with growing n. Generally, the spectra follow the power law and become flat, i.e. white at about 20 cpy. This rule, however, is not completely applicable to the power spectra of the horizontal components, which show large peaks at the sixth and eighth harmonic. Besides, odd harmonics generally have less power than even ones.

6 Conclusions

We have investigated the effect of antenna/radome phase centre models on GPS position time series. The results suggest that differences between model-specific (type mean) and antenna-specific (individual) phase centre corrections may result in significant deviations in the computed station position on sub-daily and daily time scales. The analysis of sub-daily position differences from two PPP processing runs using type mean and individual PCCs revealed the presence of biases and harmonic signals with large amplitudes and periods equal to the GPS orbital repeat (11 h 58 min). Rapid changes in the position differences of up to 1 cm during half a day were observed in both horizontal and vertical components. The analysis of daily position differences also revealed the presence of biases and harmonic signals. The latter may be produced due to the sampling of the aforementioned sub-daily harmonic signals at 24 h intervals and, thus, the generation of aliased longer wavelength periodic signals.

The analysis of stacked power spectra of the differences in the daily PPP position estimates between using type mean and individual PCCs indicated the presence of harmonic signals at frequencies that match the overtones of the GPS draconitic year, corresponding to the multiples of 1.04 cpy. Thus, mm-level deviations between type mean and individual antenna/radome PCCs lead to biases and substantial temporal variations of computed positions. As a consequence, this results in a contribution to the draconitic signals in GPS position time series.

Finally, the effect of the imperfections in the PCC models may be underestimated in this study due to possible electromagnetic coupling between the antenna and the monument, which may result in a further deviation of the PCC model from the actual antenna phase centre. On the other hand, integer ambiguity resolution, which was not performed here, may reduce the power of the spurious signals. Clarification of these two aspects will be part of future work.

Acknowledgements The authors are grateful to the editors and two anonymous reviewers for their constructive comments and criticism. We would also like to thank the IGS, EUREF, Natural Resources Canada, the British Isles continuous GNSS Facility and Administration du Cadastre et de la Topographie, Luxembourg, for providing products and data for this study.

References

Bilich A, Mader GL (2010) GNSS absolute antenna calibration at the National Geodetic Survey. In: Proceedings of ION GNSS 2010, Portland, pp 1369–1377

BSWteam (2012) BSW electronic mail #0310. Release of the new Bernese version 5.2. ftp://ftp.unibe.ch/aiub/bswmail/bswmail.0310

Collilieux X, Métivier L, Altamimi Z, van Dam T, Ray J (2011) Quality assessment of GPS reprocessed terrestrial reference frame. GPS Solutions 15(3):219–231. doi:10.1007/s10291-010-0184-6

Dach R, Hugentobler U, Fridez P, Meindl M (eds) (2007) Bernese GPS Software Version 5.0. Astronomical Institute, University of Bern. http://www.bernese.unibe.ch/docs50/DOCU50.pdf

Dilßner F, Seeber G, Wübbena G, Schmitz M (2008) Impact of near-field effects on the GNSS position solution. In: Proceedings of ION GNSS 2008, Savannah, pp 612–624

Dow JM, Neilan RE, Rizos C (2009) The international GNSS service in a changing landscape of global navigation satellite systems. J Geod 83(3–4):191–198. doi:10.1007/s00190-008-0300-3

Görres B, Campbell J, Becker M, Siemes M (2006) Absolute calibration of GPS antennas: laboratory results and comparison with field and robot techniques. GPS Solutions 10(2):136–145. doi:10.1007/s10291-005-0015-3

Griffiths J, Ray JR (2013) Sub-daily alias and draconitic errors in the IGS orbits. GPS Solutions 17(3):413–422. doi:10.1007/s10291-012-0289-1

King MA, Watson CS (2010) Long GPS coordinate time series: multipath and geometry effects. J Geophys Res 115(B4):B04403. doi:10.1029/2009JB006543

King MA, Bevis M, Wilson T, Johns B, Blume F (2012) Monument-antenna effects on GPS coordinate time series with application to vertical rates in Antarctica. J Geod 86(1):53–63. doi:10.1007/s00190-011-0491-x

Penna NT, King MA, Stewart MP (2007) GPS height time series: short-period origins of spurious long-period signals. J Geophys Res 112(B2):B02402. doi:10.1029/2005JB004047

Ray J, Altamimi Z, Collilieux X, van Dam T (2008) Anomalous harmonics in the spectra of GPS position estimates. GPS Solutions 12(1):55–64. doi:10.1007/s10291-007-0067-7

Rodriguez-Solano CJ, Hugentobler U, Steigenberger P, Lutz S (2012) Impact of Earth radiation pressure on GPS position estimates. J Geod 86(5):309–317. doi:10.1007/s00190-011-0517-4

Scargle JD (1982) Studies in astronomical time series analysis. II - Statistical aspects of spectral analysis of unevenly spaced data. Astrophys J 263:835–853. doi:10.1086/160554

Schmid R, Steigenberger P, Gendt G, Ge M, Rothacher M (2007) Generation of a consistent absolute phase center correction model for GPS receiver and satellite antennas. J Geod 81(12):781–798. doi:10.1007/s00190-007-0148-y

Springer TA (2009) NAPEOS - mathematical models and algorithms. Technical report, DOPS-SYS-TN-0100-OPS-GN, issue 1.0, ESA-ESOC. ftp://dgn6.esoc.esa.int/napeos/DOPS-SYS-TN-0100-OPS-GN-MathModels.pdf

Steigenberger P, Hugentobler U, Schmid R, Hessels U, Klügel T, Seitz M (2013) GPS-specific local effects at the geodetic observatory Wettzell. In: Altamimi Z, Collilieux X (eds) Reference frames for applications in geosciences. IAG symposia, vol 138, pp 125–130. doi:10.1007/978-3-642-32998-2_20

Stewart MP, Penna NT, Lichti DD (2005) Investigating the propagation mechanism of unmodelled systematic errors on coordinate time series estimated using least squares. J Geod 79(8):479–489. doi:10.1007/s00190-005-0478-6

Tregoning P, Watson C (2009) Atmospheric effects and spurious signals in GPS analyses. J Geophys Res 114(B9):B09403. doi:10.1029/2009JB006344

Wübbena G, Schmitz M, Boettcher G, Schumann C (2006) Absolute GNSS antenna calibration with a robot: repeatability of phase variations, calibration of GLONASS and determination of carrier-to-noise pattern. In: Proceedings of IGS workshop 2006: perspectives and visions for 2010 and beyond, Darmstadt

Zeimetz P, Kuhlmann H (2008) On the accuracy of absolute GNSS antenna calibration and the conception of a new anechoic chamber. In: Integrating generations, FIG working week 2008, Stockholm

Zumberge JF, Heflin MB, Jefferson DC, Watkins MM, Webb FH (1997) Precise point positioning for the efficient and robust analysis of GPS data from large networks. J Geophys Res 102(B3):5005–5017. doi:10.1029/96JB03860

Optimized Parameterization of VLBI Auxiliary Parameters in Least-Squares Adjustment: Preliminary Results

Emine Tanır Kayıkçı, Robert Heinkelmann, Maria Karbon, Tobias Nilsson, Virginia Raposo-Pulido, Benedikt Soja, and Harald Schuh

Abstract

In a general parameter estimation model, a priori information is used to linearize the system of equations being solved so that just offsets to the a priori values need to be estimated. A priori information used in Very Long Baseline Interferometry (VLBI) data analysis is additionally needed for modeling and constraining the auxiliary parameters, i.e. zenith wet delays, clocks, and troposphere gradients, in order to stabilize the parameter estimation. In our study we investigate the modelling of the auxiliary parameters.

In order to improve the currently used parameterization in the VLBI software VieVS used by many International VLBI Service for Geodesy and Astrometry – IVS Analysis Centers we consider three different approaches. In the first one the choice of the length of the time interval is made relatively to the temporal behavior of parameters (*approach1*), in the second one we do not estimate parameters in gaps in the observation sessions (*approach2*), and in the third one the time interval is choosen relatively to the number of observations (*approach3*). The preliminary results show that *approach2* and *approach3* provide results better than the *standard approach* (currently used parameterization in VieVS software) for VLBI single session analysis with the least squares solution of the Vienna VLBI Software (VieVS). The impacts of *approach2* and *approach3* on various VLBI solutions with VieVS were assessed by descriptive statistics and remarks for future studies are given. The optimization depending on *approach1* will be investigated in future.

Keywords

Atmospheric gradients • Clock • Parameterization • VLBI • Zenith wet delay (ZWD)

1 Introduction

The adjustment of Very Long Baseline Interferometry (VLBI) data can be carried out using different methods such as Kalman Filter (KF), least-squares method (LSM), and least-squares collocation method (LSCM). The functional model of LSM, based on the Gauss-Markov Model, in the VLBI data analysis contains time delay observations and pseudo-observations (constraints). Within this model, the standard geodetic parameters like station coordinates and Earth orientation parameters can be estimated. In order to avoid numerical problems and to stabilize the estimation, constraints (pseudo observations) for the coefficients of the

E.Tanır Kayıkçı (✉)
Department of Geomatics Engineering, Karadeniz Technical University, 61080 Trabzon, Turkey

GFZ German Research Centre for Geosciences, 14473, Potsdam, Germany
e-mail: etanir@ktu.edu.tr

R. Heinkelmann • M. Karbon • T. Nilsson • V. Raposo-Pulido • B. Soja • H. Schuh
GFZ German Research Centre for Geosciences, 14473, Potsdam, Germany

© Springer International Publishing Switzerland 2015

C. Rizos, P. Willis (eds.), *IAG 150 Years*, International Association of Geodesy Symposia 143,
DOI 10.1007/1345_2015_80

continuous piecewise linear functions of the clocks (clk) and the tropospheric zenith delays (ZWD) have to be included (Kutterer 2003). These parameters are defined as piecewise linear offsets and the offsets are estimated at certain time intervals, e.g. every 60 min (Titov et al. 2004; Teke et al. 2009). Auxiliary parameters like the coefficients of the continuous piecewise linear functions for the clocks (clk), the tropospheric zenith delays (ZWD), and the north and east troposphere gradients (NGR, EGR) are usually of little interest for geodetic purposes. However, it is important to model them accurately in order to obtain precise results of the geodetic parameters. The temporal variations of the auxiliary parameters are restricted to stay within predefined limits. In addition, the gradients are sometimes directly constrained, i.e. constrained to be close to their a priori values. Due to the direct constraints, precise VLBI solutions depend on the exact knowledge and application of a priori gradients.

The auxiliary parameters in space geodetic least-squares analysis are not standardized as several reduction models are recommended by the IERS Conventions (2010). Yet, the parameterization can have a significant effect on the results; sometimes it can even be the largest effect causing significant differences between various VLBI data analyses of the same data set (c.f. Heinkelmann et al. 2011). Most VLBI analysts apply a kind of standard parameterization (called *standard approach* later on) to the auxiliary parameters with empirically assessed numerical values for time intervals and constraints. In principle, it would be possible to determine these numerical values by analyzing the physics of the processes modeled by the various auxiliary parameters. However, apart from the physics there are also mathematical restrictions given by the equation system, for example the number of observations per time. In practice the mathematical restrictions are much more stringent than the ones derivable through physical models. Hence, in this work we propose three different methods (*approach1*, *approach2*, *approach3)* for choosing the time intervals of the auxiliary parameters. In the entire article the constraints are kept constant, i.e. if the interval length of an auxiliary parameter is changed the size of its constraint is changed accordingly so that the constraining effect remains constant over time. Within this paper, the performance of two of them (*approach2*, *approach3)* was investigated by analyzing VLBI data with the Vienna VLBI Software (VieVS) (Böhm et al. 2012) and the results were presented. The evaluation of *approach1* will be performed in ongoing investigations.

2 Methods

The current version of VieVS applies in its *standard approach* the least-squares method weighting the observations with their formal errors from the correlations plus a noise floor of 1 cm. A standard parameterization for the auxiliary parameters is used, i.e. a piece-wise linear representation with a default temporal resolution of 60 min for clocks and ZWD and 6 h for the gradients. Loose relative constraints are applied to all these parameters. From the physical point of view, the interval length should be as short as possible to optimally represent the high frequency variations of the underlying processes. From the mathematical point of view, however, the interval length should be long enough to achieve an appropriate redundancy required to estimate stable parameters. In the subsections below, two of the new approaches (*approach2*, *approach3*) for achieving optimized parameterizations of the auxiliary parameters for each station and session are described and investigated. The general idea and determination of *approach1* is presented in section of *Conclusions and Future Work*. The *approach1* realizes the idea of a flexible parameter definition interval depending on the variability of the parameters determined with a priori estimation featuring an equally spaced standard parameterization.

2.1 Solution Intervals Considering Data Gaps

A significant number of VLBI sessions show gaps between successive observations at a certain station. Figures 1 shows the time differences between successive observations at station WETTZELL during the session 08AUG24 (CONT08-Continuous VLBI Campaign 2008). For example, during the CONT08 session WETTZELL stopped and performed an intensive VLBI session of about one hour duration together with another network station. Before and after the intensive session additional time was needed for test and the antenna system reset until the station could again join the CONT08 schedule. Since the intensive observations are not included in the CONT08 database, an observational gap is found within the CONT08 data (Fig. 1). Currently, VLBI group delay observations are based on a few minutes of coherent integration. Consequently, between successive observations there is always a time difference usually of several minutes or more. Thus, it is necessary to define a data gap based on a minimal time difference between successive observations. As empirically assessed in this study, we define a time difference of greater or equal 45 min between successive observations at a station as a data gap.

With our second approach (*approach2*) we want to define the auxiliary parameters strictly outside of data gaps. A parameter defined inside a data gap is determined by the soft constraint (the non-singularity of the equation system is ensured by the constraint) and probably only a few observations will contribute to its determination. This ‘unsupported’ parameter does not improve the solution but decreases the

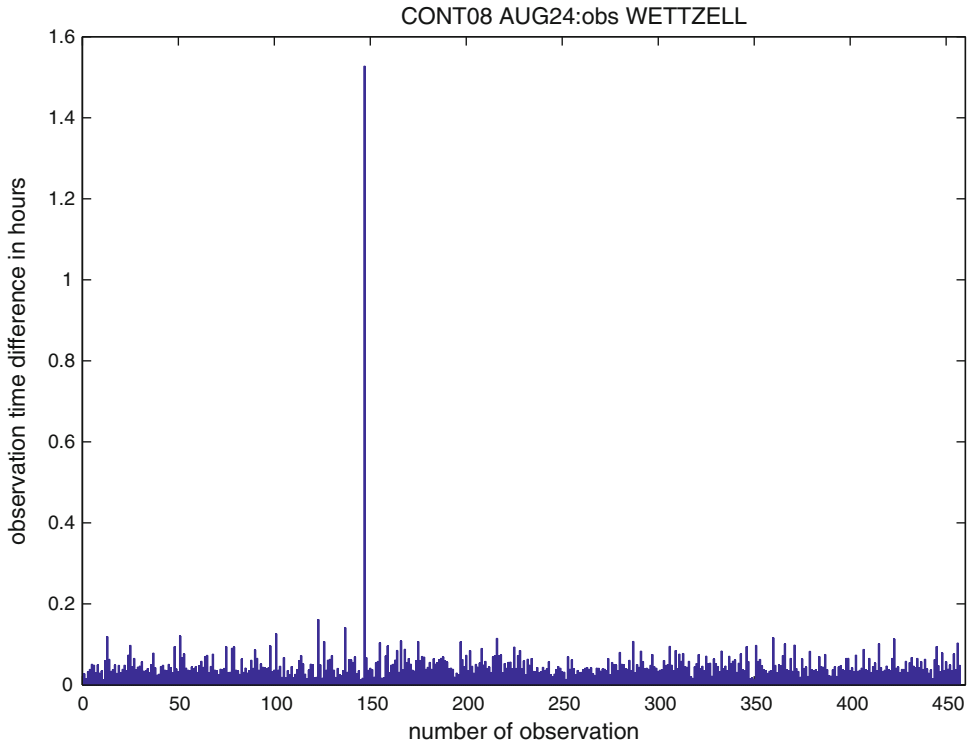

Fig. 1 Time difference (hours) between successive observations at station WETTZELL during session 08AUG24 (CONT08)

redundancy and thus might degrade the solution. To be more specific, in case of a data gap between observations, the node within the gap is removed and replaced by one at beginning and one at the end of the gap.

2.2 Consideration of the Time Interval Relatively to the Number of Observations

With our third approach (*approach3*) we want to realize the largest possible flexibility for the definition of auxiliary parameter interval lengths. Therefore, we define the interval lengths solely depending on the number of supporting observations. With this approach it is possible to obtain an equal partial redundancy for each auxiliary parameter, i.e. each parameter is determined by the same number of observations. Figure 2 shows how much the total number of observations supporting an auxiliary parameter will vary if the auxiliary parameter time intervals are defined as equally spaced by the standard parameterization. Because the parameterization is identical for ZWD and clk as well as for NGR and EGR, only the number of observations used to estimate clk and NGR parameters are displayed in Fig. 2 at a variety of VLBI stations during session 02NOV05.

From Fig. 3 it is obvious that there is a significant relation between the formal error of an estimated parameter and the corresponding total number of observations supporting this parameter. However, since we are not interested in the auxiliary parameters themselves, we will not take care about their formal errors. Nevertheless, we will further investigate this issue making sure that it does not cause numerical problems

3 Results

The *approach*2, in Fig. 4, slightly decreases the resulting formal errors of the auxiliary parameters around the gaps and the estimated values of parameters with *approach2* agree with the results of the *standard approach* (currently used for the parameterization in the VieVS software providing the standard VLBI least-squares solution), at station OHIGGINS. Further comparisons for this method can be performed on the basis of baseline length repeatability for multi-session analysis in future studies.

Different parameterization options (presented as *par.1*, *par.2*, *par.3, par.4,* and *par.5,* in Table 1) were used applying VieVS to investigate the effect of *approach3* on the resulting parameter estimation. The different parameterization options differ in the total number of supporting observations (column 2 of Table 1) at each parameter estimation interval.

Table 1 shows that using shorter time intervals for the ZWD/clk/NGR/EGR parameters results in a smaller chi-square calculated for the constraints and the observations. The corresponding loss of redundancy does obviously not play a significant role for the quality of the solution. It should be mentioned that in this session one of the stations has a

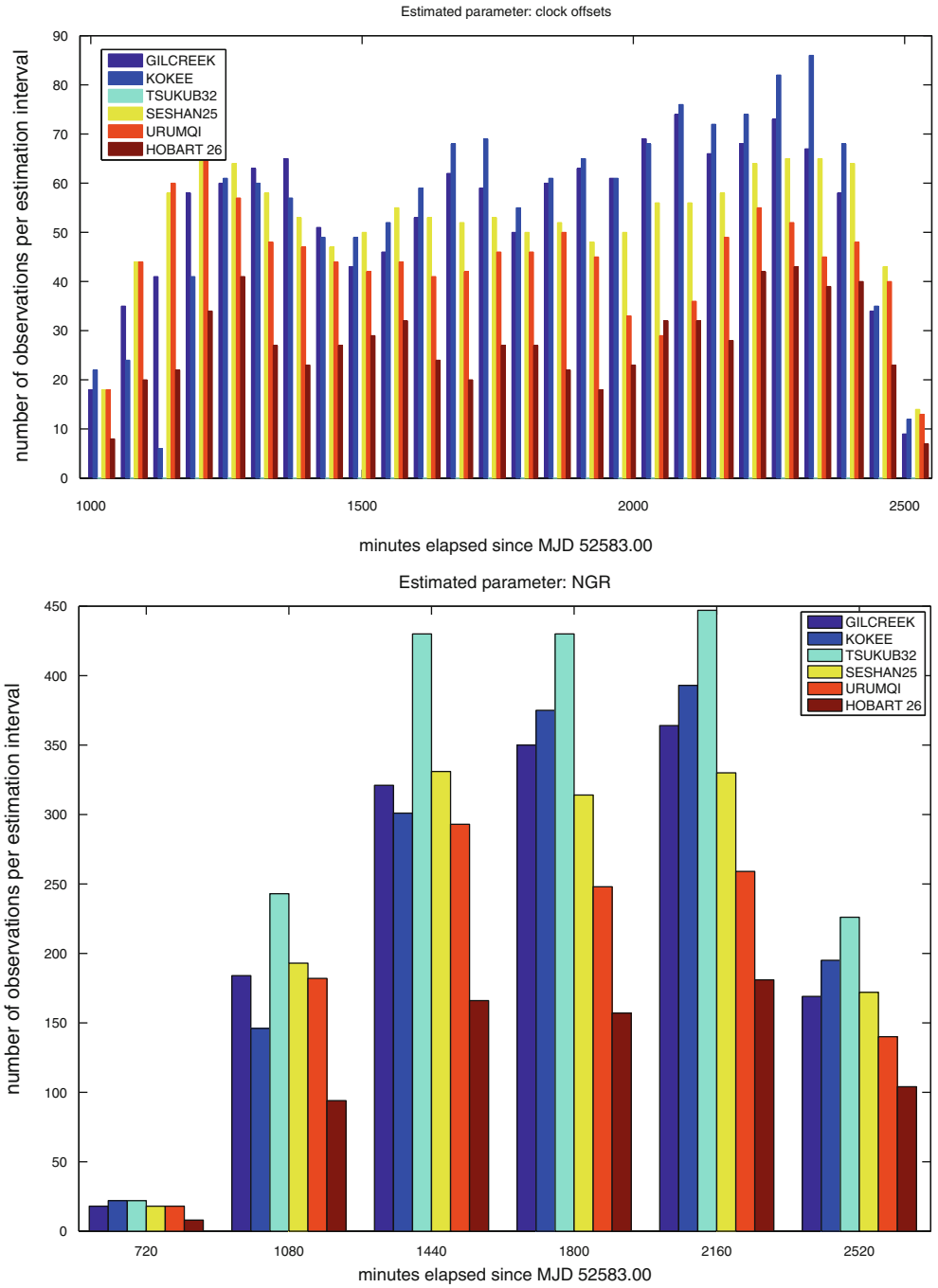

Fig. 2 Total number of observations supporting an auxiliary parameter with standard parameterization: upper plot: clk (60 min intervals), lower plot: NGR (360 min intervals each) during session 02NOV05

large diurnal clock variation, what is not well modelled by a piece-wise linear function if the interval length is too large. The significant improvement of chi-square of the overall solution (a posteriori variance factor) is thus expected. For other sessions, the improvement may not be as large as for this session.

Figure 5 shows that options *par. 2* and *par. 5* provide almost equivalent results.

4 Conclusions and Future Work

In this article we presented two ideas on how to improve the parameterization of auxiliary parameters zenith delays, clocks, and north and east troposphere gradients.

- Our preliminary results show that *approach2* and *approach3* provide results better than the *standard*

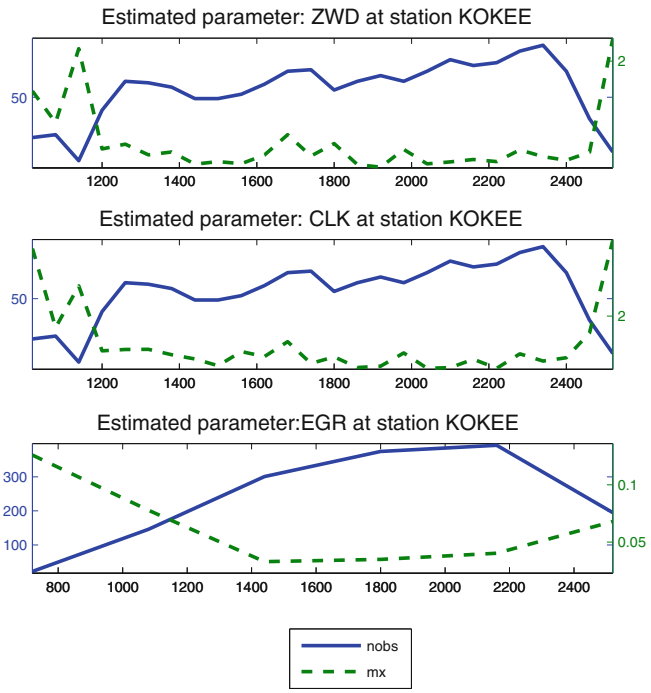

Fig. 3 The total number of observations (nobs) supporting the specific parameter and the formal errors (*mx* in cm) of the auxiliary parameters zwd, clock, and egr (*top down*) at station KOKEE during session 02NOV05

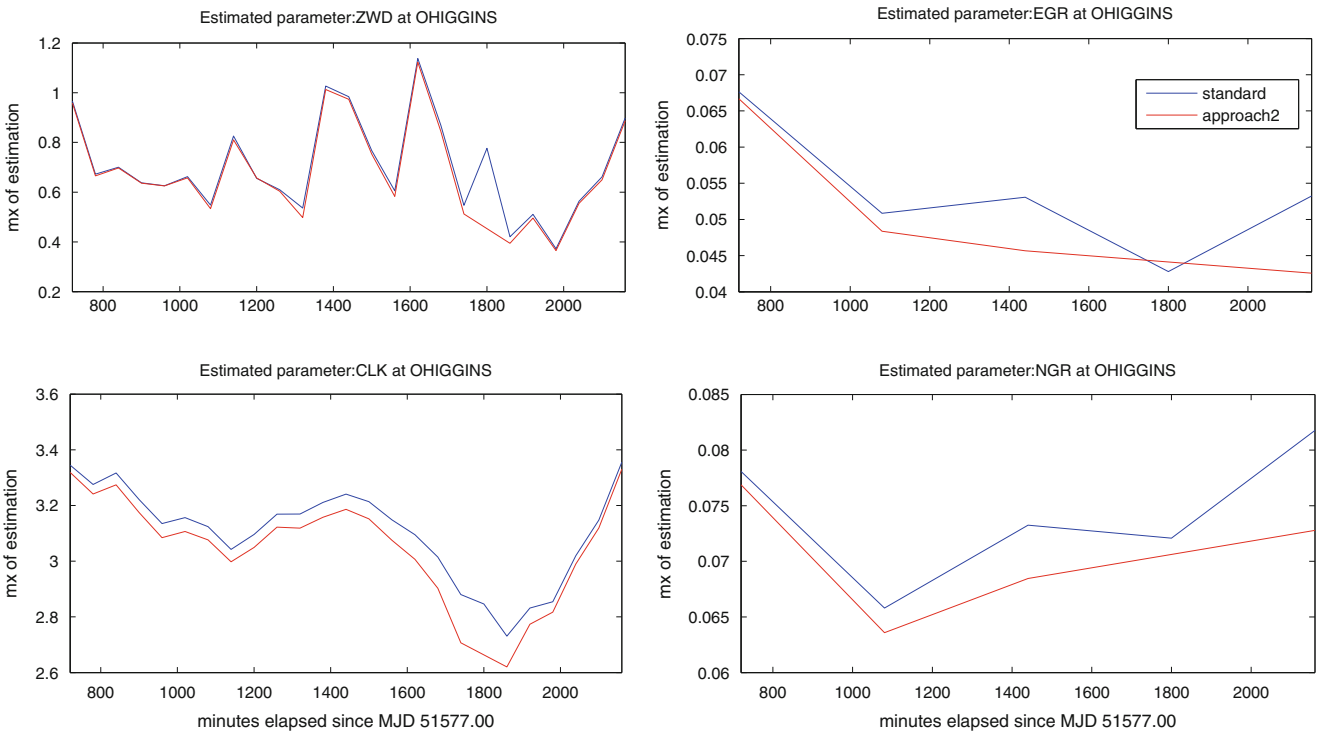

Fig. 4 The impact of *approach2* on formal errors (*mx* in cm) of the estimated parameters

approach for VLBI single session analysis with smaller chi-square statistics by least-squares solution of VieVS software.

- The next step will be to practically assess *approach1*, i.e. choice of the interval length relatively to the behavior of parameters. In the standard VLBI least-squares solution, the interval lengths of auxiliary parameters are usually set to be evenly spaced in time because there is no a priori information about the variability available. Consequently, our first optimization (*approach1*) would realize the idea of a flexible parameter definition interval depending on the variability of the parameters determined with a priori

Table 1 Parameterizations applied in the analysis of session 02NOV05

Parameterization	Number of at each interval observations	Chi-square of overall solution (cm^2)	Used relative constraints (cm/interval)
par.1	10–20 for zwd and clock	2.0031	zwd: 1.086
	40–50 for gradients		clock: 0.942
			gradients: 0.030
par.2	5–10 for zwd and clock	0.518	zwd: 0.791
	40–50 for gradients		clock: 0.686
			gradients: 0.030
par.3	5–10 for zwd and clock	0.5254	zwd: 0.791
	50–60 for gradients		clock: 0.686
			gradients: 0.033
par.4	10–20 for zwd and clock	2.164	zwd: 1.086
	60–70 for gradients		clock: 0.942
			gradients: 0.037
par.5	5–10 for zwd and clock	0.5017	zwd: 0.791
	20–30 for gradients		clock: 0.686
			gradients: 0.021
standard	Changes in each interval	4.0623	zwd: 1.5
			clock: 1.3
			gradients: 0.05

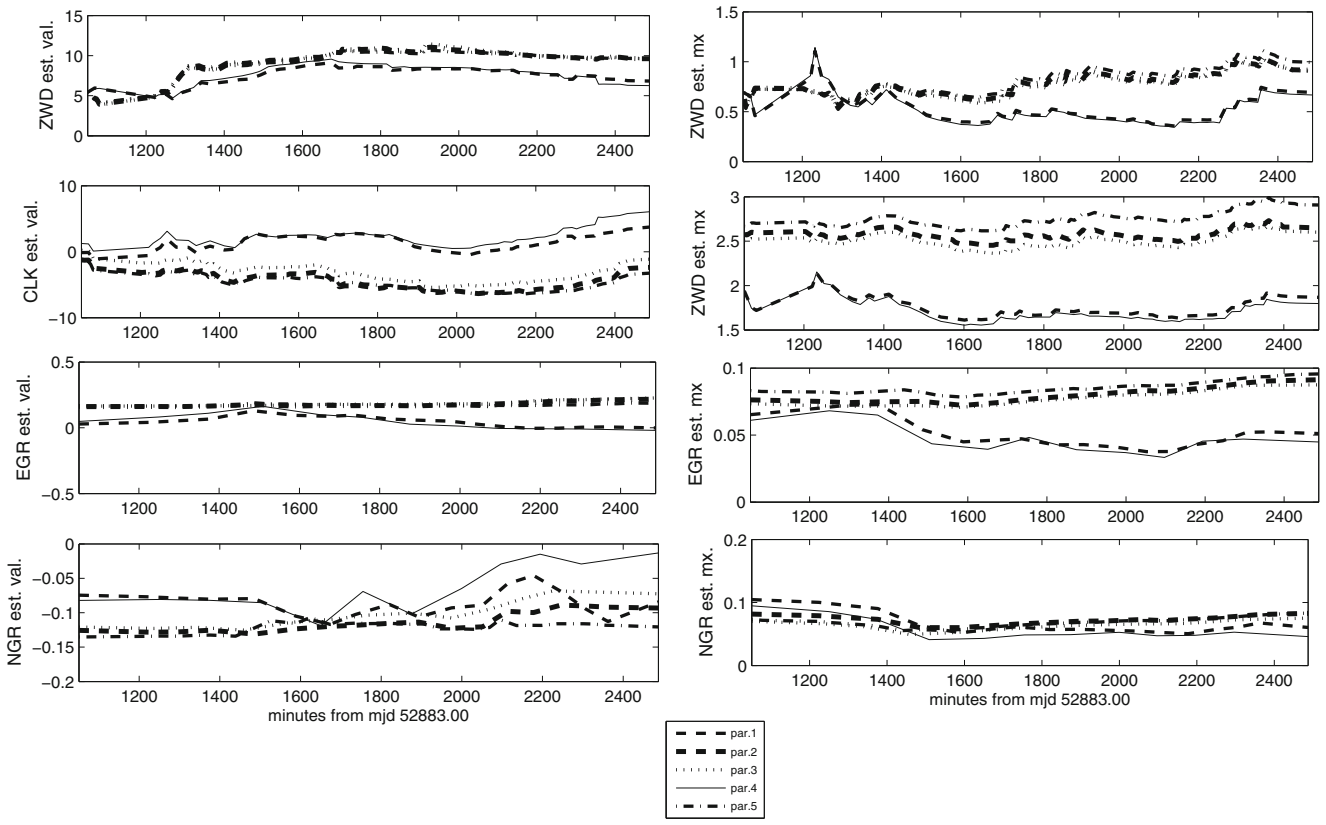

Fig. 5 Estimates and formal errors (in cm) of parameters with different parameterizations obtained by *approach3* at station KOKEE during session 02NOV05

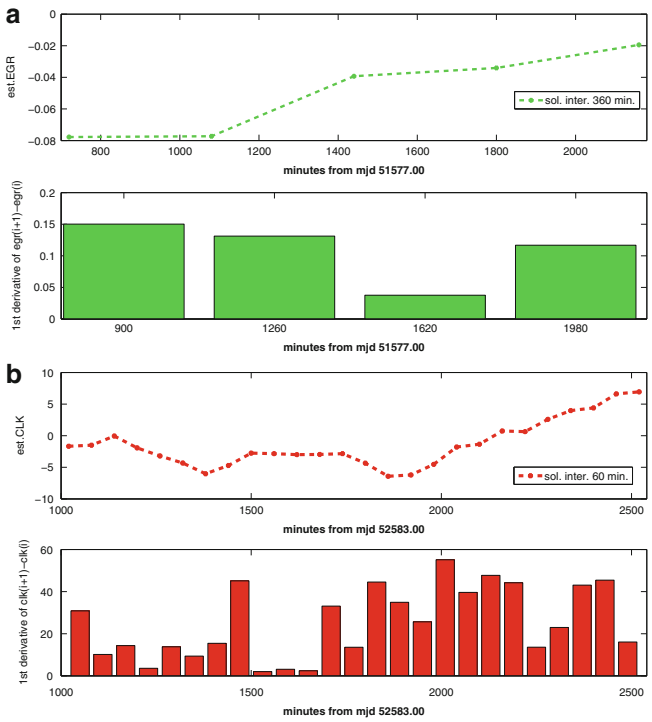

Fig. 6 An example for the time dependent variations of auxiliary parameters: a) egr at FORTLEZA for session 00FEB03 (OHIG-10), b) clock at GILCREEK for session 02NOV05 (APSG-11)

estimation featuring an equally spaced standard parameterization. Thus, if the variation is relatively large, the length of the estimation interval will be shortened allowing for a larger degree of freedom for this specific parameter over this interval. The bottom part of Fig. 6a illustrates this idea. The larger first time derivatives of successive differences for the first three parameters are shown; for the interval between minutes 1,000 and 1,200 of modified Julian date (mjd) 51577 more than one parameter is estimated, what is shown in the upper part of Fig. 6a. If the temporal variation of a parameter over a certain interval is relatively small, the interval length of the parameter will be increased for the successive estimation. As shown in Fig. 6b around minutes 1,600 of mjd 52583, five estimated parameters have almost the same values and show relatively small time dependent variation of the successive parameter differences. As a consequence of this temporal behavior, only one parameter will be estimated instead of five parameters. Estimating one parameter instead of five immediately increases the redundancy and since the variations over time are relatively small the residuals of the observations supporting this parameter will not increase significantly. At the same time the gained redundancy can be utilized to set up more parameters where larger variations were found. Thus, this will reduce the residuals of observations where bigger variations are present.

With this approach it is possible to flexibly handle the parameter definition time interval according to a first standard solution while keeping the overall number of parameters constant. It would also be possible to repeat the application of *approach1* in an iterative way whenever the session is reanalyzed. This iterative optimization will be investigated in future.

Furthermore, it remains to study the size of the constraints. We plan to develop an automatic optimized parameterization for auxiliary parameters in VLBI single session least-squares analyses probably combining all three approaches.

Acknowledgements The authors thank the International VLBI Service for Geodesy and Astrometry - IVS (Schuh and Behrend 2012) for scheduling, observing, correlating, and providing the VLBI data used in this work. The first author, Emine TANIR KAYIKCI, acknowledges the Council of Higher Education of Turkey (YOK) for the financial support of her research stay at GFZ.

References

Böhm J, Böhm S, Nilsson T, Pany A, Plank L, Spicakova H, Teke K, Schuh H (2012) The new Vienna VLBI Software. In: Kenyon S, Pacino MC, Marti U (eds) Proceedings of the IAG Scientific Assembly 2009, Buenos Aires/Argentina, International Association of Geodesy Symposia Series, vol 136. pp 1007–1011. doi:10.1007/978-3-642-20338-1_126

IERS Conventions, Petit G, Luzum B (eds) (2010) IERS Technical Note 36, Verlag des Bundesamts für Kartografie und Geodäsie, Frankfurt am Main, p 179

Heinkelmann R, Böhm J, Bolotin S, Engelhardt G, Haas R, Lanotte R, MacMillan DS, Negusini M, Skurikhina E, Titov O, Schuh H (2011) VLBI-derived troposphere parameters during CONT08. J Geodesy 85(7):377–393. doi:10.1007/s00190-011-0459-x

Kutterer H (2003) The role of parameter constraints in VLBI analysis. In: Schwegmann W, Thorandt V (eds) Proceedings of the 16th working meeting on European VLBI for Geodesy and Astrometry, Bundesamt für Kartographie und Geodäsie, Leipzig/Frankfurt am Main, pp 171–179

Schuh H, Behrend D (2012) VLBI: A fascinating technique for geodesy and astrometry. J Geodyn 61:68–80. doi:10.1016/j.jog.2012.07.00

Teke K, Boehm J, Tanır E, Schuh H (2009) Piecewise linear offsets for VLBI parameter estimation. In: Bourda G, Charlot P, Collioud A (eds) Proceedings of the 19th European VLBI for Geodesy and Astrometry working meeting, Universite Bordeaux1-CNRS, Bordeaux, France, pp 63–67

Titov O, Tesmer V, Boehm J (2004) OCCAM v. 6.0 software for VLBI data analysis. In: Vandenberg NR, Baver KD (eds) Proceedings of the international VLBI Service for Geodesy and Astrometry 2004 general meeting, NASA/CP-2004-212255, pp 267–271

The Antarctic Regional GPS Network Densification: Status and Results

Axel Rülke, Reinhard Dietrich, Alessandro Capra, Jan Cisak, E. Dongchen, Trond Eiken, Adrian Fox, Larry D. Hothem, Gary Johnston, E.C. Malaimani, Alexey J. Matveev, Gennadi Milinevsky, Hans-Werner Schenke, Kazuo Shibuya, Lars E. Sjöberg, Andrés Zakrajsek, Mathias Fritsche, Andreas Groh, Christoph Knöfel, and Mirko Scheinert

Abstract

We report on the activities related to the IAG Subcommission 1.3f "Regional Reference Frame for Antarctica". Campaign-style GPS observations have been carried out since 1995. Based on the Bernese GNSS Software the latest analysis yields results for about 30 stations aligned to the terrestrial reference frame solution IGS08. The obtained station motions are discussed in the context of plate kinematics and glacial-isostatic adjustment. It is demonstrated that the activities are a valuable contribution both to the ITRF densification in Antarctica and to geodynamic research.

Keywords

Antarctica • Crustal deformation • Euler pole • GIA • Reference frame

1 Introduction

In 1994, at the XXIII Meeting of the Scientific Committee on Antarctic Research (SCAR) in Rome it was decided to start geodetic GPS observations in Antarctica. GPS campaigns were carried out on an annual basis in order to realize and to densify the Antarctic GPS network and to link Antarctica

A. Rülke (✉)
Federal Agency for Cartography and Geodesy, Frankfurt/Main, Germany
e-mail: axel.ruelke@bkg.bund.de

R. Dietrich • A. Groh • C. Knöfel • M. Scheinert
TU Dresden, Institut für Planetare Geodäsie, Dresden, Germany
e-mail: reinhard.dietrich@tu-dresden.de

A. Capra
Department of Engineering "Enzo Ferrari", University of Modena and Reggio Emilia, Modena, Italy

J. Cisak
Instytut Geodezji i Kartografii, Warsaw, Poland

E. Dongchen
Chinese Antarctic Center of Surveying and Mapping, Wuhan University, Wuhan, China

T. Eiken
Department of Geosciences, University of Oslo, Oslo, Norway

A. Fox
British Antarctic Survey, Cambridge, UK

L.D. Hothem
U.S. Geological Survey, Reston, VA 20192, USA

G. Johnston
Geoscience Australia, Canberra, ACT 2601, Australia

E.C. Malaimani
National Geophysical Research Institute (NGRI), Hyderabad, India

A.J. Matveev
OAO Aerogeodezia, St. Petersburg, Russia

G. Milinevsky
Taras Shevchenko National University of Kyiv, Kyiv, Ukraine

H.-W. Schenke
Alfred-Wegener-Institut Helmholtz-Zentrum für Polar- und Meeresforschung, Bremerhaven, Germany

K. Shibuya
National Institute of Polar Research, Tokyo, Japan

L.E. Sjöberg
Royal Institute of Technology, Stockholm, Sweden

A. Zakrajsek
Instituto Antártico Argentino, Buenos Aires, Argentina

M. Fritsche
Helmholtz-Zentrum Potsdam, Deutsches GeoForschungsZentrum GFZ, Potsdam, Germany

© Springer International Publishing Switzerland 2015

C. Rizos, P. Willis (eds.), *IAG 150 Years*, International Association of Geodesy Symposia 143,
DOI 10.1007/1345_2015_79

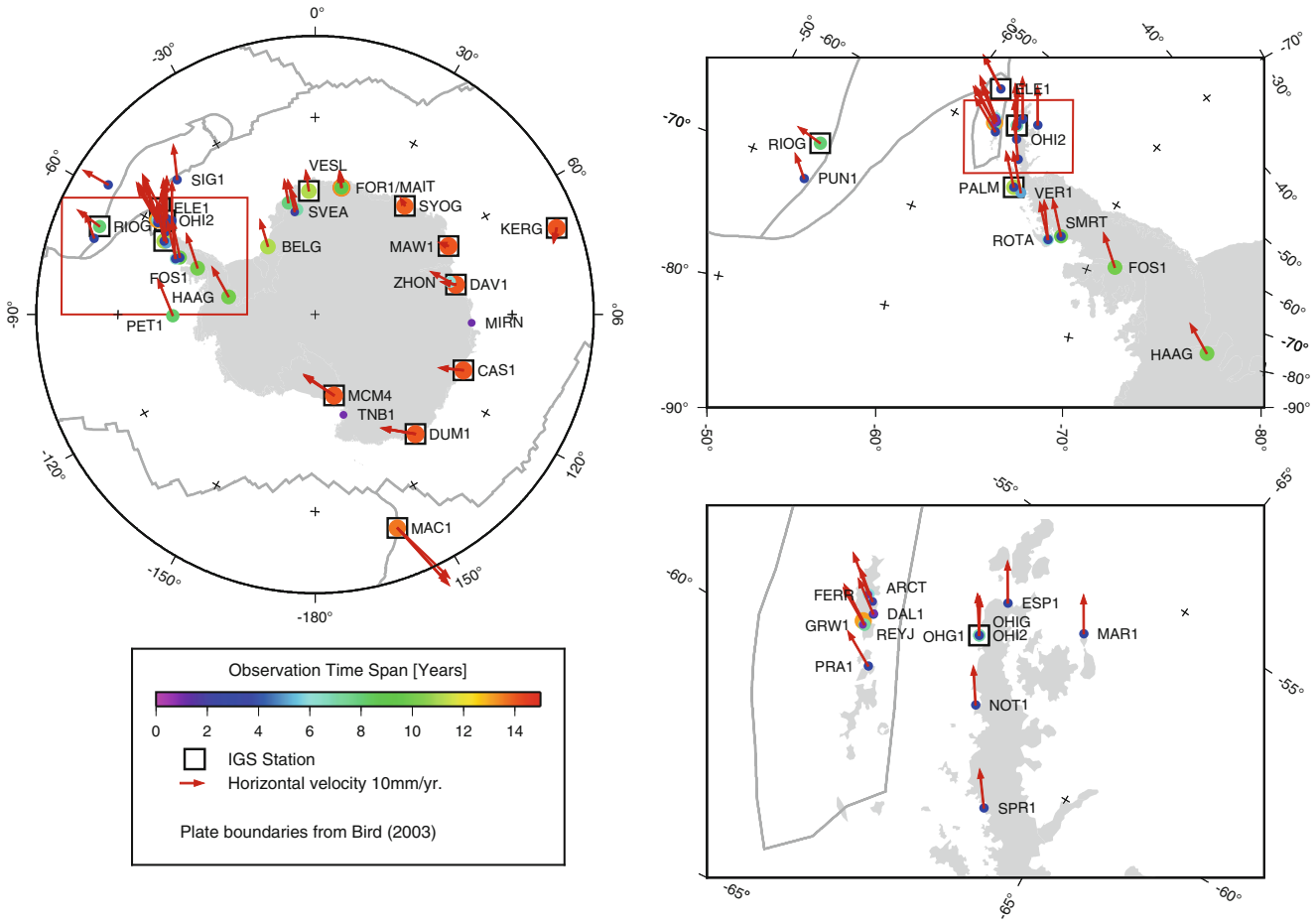

Fig. 1 Horizontal velocity field estimated for the Antarctic network. Only velocities from observation time spans of more than two years are shown here. Size and color of the circles depend on the time span covered by observations. The permanent IGS sites are marked by a *black square*. *Right*: Zoom of the areas marked by the *red* rectangles. Plate boundaries are taken from (Bird 2003)

to the global terrestrial reference frame (ITRF). For this purpose a project group was established. In 2003 the International Association of Geodesy (IAG) decided to establish subcommissions for regional reference frames. Concurrently to the SCAR affiliation the project group became Subcommission 1.3f within the IAG. Closely linked to the permanent GPS stations in Antarctica contributing to the International GNSS Service (IGS, Dow et al. 2009), over the years the campaign stations have been providing valuable geodetic information with a lot of significant geophysical implications (Dietrich et al. 2004). On a regular basis reports were delivered both to SCAR and to IAG. In the following we summarize these activities related to GPS observations in Antarctica and present their major results and conclusions.

2 Campaign Organization and Observations

During the 1990ies, because of the shortage of permanent sites in Antarctica, the campaign observations were coordinated to take place between January 20 and February 10 each Antarctic summer. With an increasing number of permanent sites this coordinated schedule for the campaigns became obsolete. The number of participating stations increased rapidly. A total of about 30 stations contributed observations (Fig. 1, Table 1). The observational data as well as the corresponding meta data are archived within a database located at TU Dresden, Germany. To maintain consistency the observations of permanents sites used in this analysis are limited to the time spans covered by observations of the campaign sites.

3 Data Analyses and Results

The acquired data of the Antarctic GPS sites and of a selected number of permanent IGS stations in the Southern hemisphere were homogeneously analyzed using a modified version of the Bernese GNSS Software 5.0 (Dach et al. 2007). Satellite orbits and Earth orientation parameters were taken from a homogeneous reprocessing (Steigenberger et al.

Table 1 Estimated velocities of the Antarctic network sites. (ΔT: time span covered by observations; v_n, v_e, v_u: estimated velocities in north, east and vertical directions. $\sigma_{n,e}$ and σ_u: respective uncertainties; v_u^{el}: vertical deformation caused by the elastic effect; v_u^{W12a} and v_u^{IJ05R2}: vertical rates predicted by the GIA model W12a (Whitehouse et al. 2012) and IJ05R2 (Ivins et al. 2013), resp., cf. Fig 4)

Station	Lat. [deg]	Lon. [deg]	ΔT [yrs]	v_n [mm/yr]	v_e	v_u	$\sigma_{vn,e}$	σ_{vu}	v_u^{el}	v_u^{W12a}	v_u^{IJ05R2}
ARCT 66016M001	−62.16	−58.47	2.1	12.7	8.8	7.9	2	5	0.4	1.3	−0.1
ART1 66017M001	−62.18	−58.90	13.1	15.9	8.6	−1.1	1	2	0.4	1.4	−0.1
BELG 66018M002	−77.87	−34.63	11.0	11.7	3.7	0.6	1	2	−0.2	0.1	1.3
CAS1 66011M001	−66.28	110.52	14.6	−10.4	2.5	2.1	1	2	0.8	2.4	0.7
DAL1 66019M001	−62.24	−58.68	3.1	14.1	9.0	5.6	2	4	0.4	1.4	−0.1
DALL 66019M002	−62.24	−58.66	1.1	18.8	8.0	−8.9	4	9	0.4	1.4	−0.1
DAV1 66010M001	−68.58	77.97	14.6	−6.2	−2.4	−0.1	1	2	0.5	0.7	1.0
DUM1 91501M001	−66.67	140.00	14.0	−11.7	9.2	1.1	1	2	0.2	1.3	1.6
EACF 66015M002	−62.08	−58.39	1.2	17.9	9.9	−4.7	4	9	0.4	1.3	−0.1
ELE1 66021M001	−61.48	−55.63	3.1	14.9	7.1	−0.6	2	4	0.2	1.0	−0.3
ESP1 66022M001	−63.40	−57.00	3.1	10.9	14.8	21.6	2	4	0.8	1.7	−0.2
FERR 66015M001	−62.09	−58.39	5.9	15.9	11.0	−10.5	1	2	0.4	1.3	−0.1
FOR1 66023M001	−70.78	11.83	14.0	6.9	−2.4	0.9	1	2	1.3	1.2	0.4
FOR2 66023M002	−70.77	11.84	13.2	6.9	−1.9	1.0	1	2	1.3	1.2	0.4
FOS1 66024M001	−71.31	−68.32	9.9	10.4	11.9	−1.7	1	2	−0.2	0.3	3.3
GRW1 66012M001	−62.22	−58.96	7.1	16.6	8.2	−3.7	1	2	0.4	1.4	−0.1
HAAG 66025M001	−77.04	−78.29	10.0	9.9	11.2	7.5	1	2	−1.2	5.6	4.3
KERG 91201M002	−49.35	70.26	14.2	−4.3	5.1	2.4	1	2	-	-	-
KOTA 66027M001	−74.30	−9.76	7.0	9.2	−1.0	0.6	1	2	−1.3	0.6	0.5
MAIT 66028M001	−70.77	11.74	9.1	6.0	−1.8	0.2	1	2	1.3	1.2	0.4
MAR1 66029M001	−64.24	−56.66	3.1	10.1	13.6	8.0	2	4	0.6	1.8	−0.2
MAW1 66004M001	−67.60	62.87	14.0	−3.4	−3.4	0.6	1	2	0.1	1.0	0.9
MCM4 66001M003	−77.84	166.67	14.0	−12.1	10.5	0.9	1	2	0.5	4.3	−0.1
MIRN	−66.55	93.01	1.2	−1.2	−0.8	29.2	4	9	−0.2	0.4	0.7
NOT1 66031M001	−63.67	−59.21	3.1	10.2	13.4	6.9	2	4	0.7	2.0	0.1
OHG1 66008M003	−63.32	−57.90	3.1	11.0	14.3	3.8	2	4	1.2	1.8	−0.1
OHI2 66008M005	−63.32	−57.90	7.0	9.7	14.1	4.8	1	2	1.2	1.8	−0.1
OHIG 66008M001	−63.32	−57.90	6.9	9.2	13.7	5.7	1	2	1.2	1.8	−0.1
PAL1 66005M001	−64.77	−64.05	3.1	11.4	15.4	4.5	2	4	1.6	2.0	0.5
PALM 66005M002	−64.78	−64.05	11.0	10.4	12.0	4.5	1	2	1.6	2.0	0.5
PET1 66032M001	−68.86	−90.43	8.1	6.9	15.9	2.2	1	2	0.4	0.0	−0.7
PRA1 66033M001	−62.48	−59.65	3.1	15.8	7.8	4.5	2	4	0.5	1.6	0.0
PUN1 41718M001	−53.63	−70.92	3.1	8.2	8.2	1.3	2	4	-	-	-
REYJ 66012M002	−62.20	−58.98	1.1	13.1	16.6	9.3	4	9	0.4	1.4	−0.1
RIOG 41507M004	−53.79	−67.75	8.0	11.8	2.4	2.8	1	2	-	-	-
ROT1 66007M001	−67.57	−68.13	3.1	8.4	15.0	3.8	2	4	1.2	2.0	0.8
ROTH 66007M003	−67.57	−68.13	6.1	9.8	13.3	2.9	1	2	1.2	2.0	0.8
SIG1 30607M001	−60.71	−45.59	3.1	12.5	8.9	1.6	2	4	0.1	0.0	−0.4
SMR1 66034M001	−68.13	−67.10	3.0	12.1	14.4	−0.6	2	4	2.2	1.5	1.5
SMRT	−68.13	−67.10	9.8	10.1	13.2	2.1	1	2	2.2	1.5	1.5
SPR1 66035M001	−64.30	−61.05	3.1	10.4	13.3	6.2	2	4	2.0	2.2	0.4
SVEA	−74.58	−11.23	3.0	14.2	−0.2	−3.9	2	4	−1.4	0.5	0.6
SYOG 66006S002	−69.01	39.58	13.9	1.7	−4.0	2.9	1	2	−0.3	1.1	0.8
TNB1 66036M001	−74.70	164.10	1.1	−15.0	11.7	6.1	4	9	1.1	1.8	−0.3
VER1 66038M001	−65.25	−64.25	5.1	11.4	14.0	3.1	2	3	2.5	2.1	0.6
VESL 66009M001	−71.67	−2.84	11.0	9.2	−0.9	2.2	1	2	0.5	1.4	0.4
WASA 66039M001	−73.04	−13.41	7.9	10.4	0.5	3.2	1	2	−1.2	1.3	0.7
ZHON 66030M001	−69.37	76.37	6.1	−7.5	−6.2	−4.7	1	2	1.0	0.7	1.5

2006). A tropospheric model based on ECMWF weather data (Vey et al. 2006), higher-order ionospheric corrections (Fritsche et al. 2005), absolute antenna phase center corrections and ocean tide loading corrections according to the FES2004 model were applied.

The daily solutions were combined at the normal equation level to estimate a set of station coordinates and velocities. In the analysis we considered inhomogeneities due to geophysical events such as earthquakes or due to antenna changes. In such cases new station coordinates were adopted. If possible, station velocities before and after the event were jointly estimated by introducing appropriate constraints (Rülke et al. 2008). The velocities of stations located close to each other were separately estimated, e.g. FOR1 and FOR2 or OHIG, OHG1 and OHI2. The final solution is aligned to the IGS08 reference frame by a minimum constraining condition on the IGS stations. The estimated station velocities are plotted in Fig. 1 and compiled in Table 1.

We computed daily coordinate solutions for each campaign. The averaged daily repeatability of all station coordinates is 6 mm for the vertical and 2 mm for the horizontal components. The assumption of a white noise error model for the daily coordinate solution and an average observation time span of 20 days for each campaign yields formal errors of 1.3 mm and 0.4 mm. A more realistic power noise model considers the correlations between the daily solutions and scales the error measures by a factor of 2 to 5 (Zhang et al. 1997; Mao et al. 1999; Williams 2003; Williams et al. 2004). Thus, a factor of 4.5 results in error estimates of 6 mm for the vertical and 2 mm for the horizontal coordinate components for an individual campaign solution. Then, the station velocity error estimates are computed by error propagation. The effect of the reference frame realization noise adds another 1 mm/yr uncertainty to these values (Dietrich et al. 2001; Bevis and Brown 2014). The individual error estimates are listed in Table 1.

Independent velocity errors are computed for individual points at co-located sites such as FOR1 and FOR2 or OHIG, OHG1 and OHI2. This enables a further check of the achieved uncertainties. However, it needs to be considered that station velocities may change over time in the Antarctic Peninsula region (Thomas et al. 2011).

4 Geophysical Implications

4.1 Horizontal Motion and Plate Kinematics

From a geological point of view the Antarctic plate cannot be regarded as a homogeneous block. While East Antarctica consists of a stable craton, West Antarctica is considered to consist of a multitude of tectonic fractions entities which may move relatively to each other or with respect to East Antarctica (Dalziel and Elliot 1982). Figure 2 shows changes of the

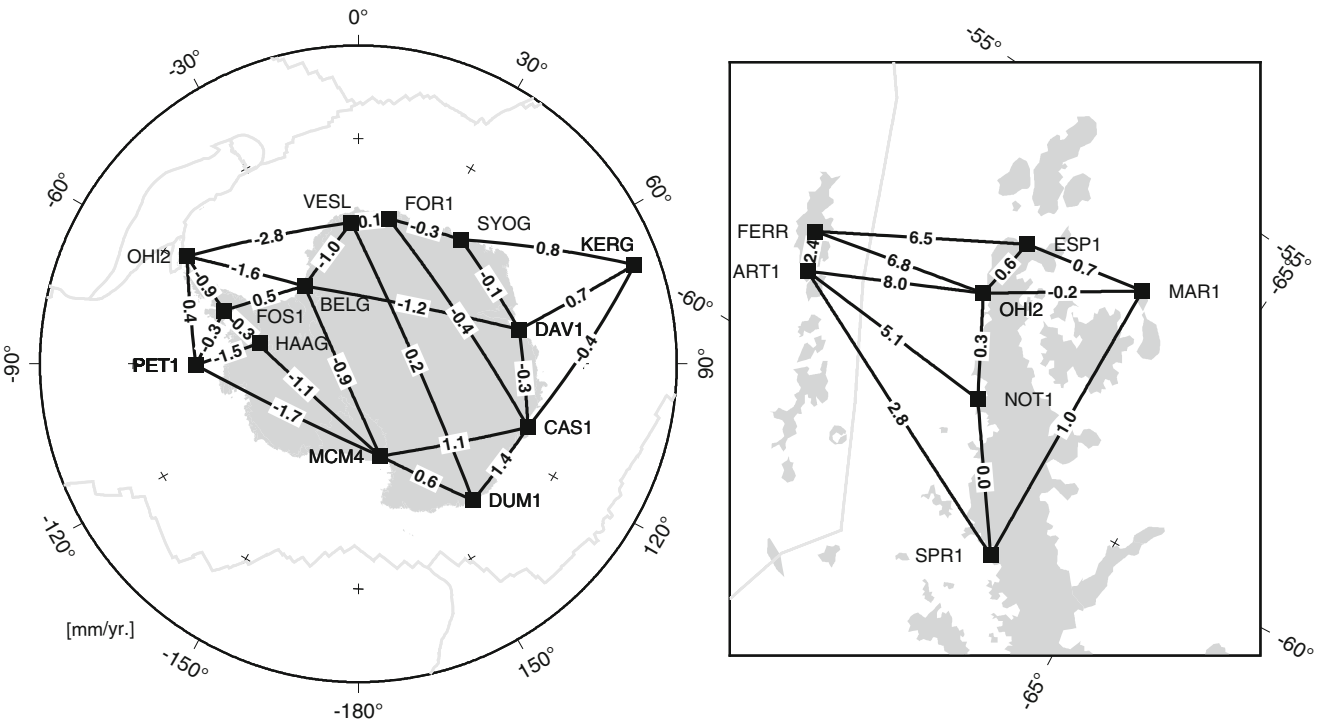

Fig. 2 Changes of spherical distance for selected station pairs in Antarctica [mm/yr]. The *right* figure depicts an enlargement of the northern tip of the Antarctic Peninsula, the Bransfield Strait and the South Shetland Islands

spherical distances between station pairs across the Antarctic Plate. The accuracy of these distance rates propagated from the accuracy of the horizontal station velocities (cf. Table 1) is estimated to be 1 to 2 mm/yr. The deformation rates in East Antarctica are small and do not exceed 1 mm/yr for most station pairs including the Kerguelen Islands. The majority of station pairs in West Antarctica also show small values of less than 1 mm/yr. This includes a coherent motion of Peter I. Island and the Antarctic Plate. The right subfigure of Fig. 2 clearly shows the opening of the Bransfield Strait between the Antarctic Peninsula and the South Shetland Islands. From our analyses we inferred a value of about 7 mm/yr for this opening rate. This result agrees with seismological evidence in that region which suggests an opening rate of less than 10 mm/yr (Maurice et al. 2003).

A shortening of −2.8 mm/yr can be found for the baseline between O'Higgins (OHI2) at the northern tip of the Antarctic Peninsula and SANAE IV (VESL) in East Antarctica which is in good agreement with Argus et al. (2011). Figure 3 displays the residual motions of the northern Antarctic Peninsula and its offshore islands after subtracting the plate motion of the Antarctic plate (red arrows). Knowledge of the tectonic activity in the Bransfield Strait helps to explain the shortening of the spherical distance between the Antarctic Peninsula and East Antarctica mentioned already by Mayer et al. (2000). The residual motion of the observation sites in the Antarctic Peninsula are systematically directed eastwards. This suggests that the spreading process in the Bransfield Strait has an impact on the motion not only of the South Shetland Island block but also of the northern part of the Antarctic Peninsula. A relative Euler pole of this part with respect to the Antarctic Plate is located at (67.1±15.5)°S and (292.3±10.4)°E. The rotation rate is estimated to be (0.20±0.19)°/Ma. The residuals of this Euler pole estimation are shown in Fig. 3 (in blue). Due to the small area the three components of the Euler pole are highly correlated resulting in large error estimates.

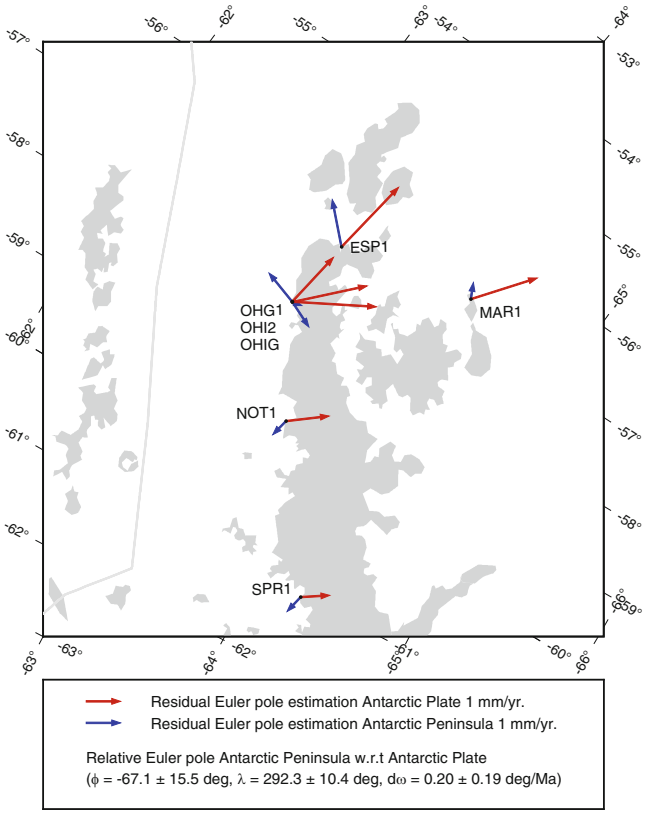

Fig. 3 Estimation of the Euler pole for the Antarctic Plate. The *red arrows* indicate the residuals of the Euler pole estimation. Additionally, an Euler pole of the northern tip of the Antarctic Peninsula was estimated. The respective residuals are indicated in *blue*

4.2 Vertical Motion and Glacial-Isostatic Adjustment

Past ice-mass changes in Antarctica are the cause a glacial-isostatic adjustment (GIA) of the solid Earth. Therefore, the vertical rates of the GPS sites contain valuable information about GIA and can be used to validate respective models. In Fig. 4 and in Table 1 (last columns) the observed rates are compared with those predicted by two recent GIA models (Ivins et al. 2013; Whitehouse et al. 2012). For comparison the observed vertical rates have to be reduced by the elastic effect caused by present-day ice-mass changes. The elastic uplift is computed based on ICESat observations (Groh et al. 2014). The GPS results and the GIA model predictions are related to the center of mass (CM) of the whole Earth system and the center of solid Earth (CE), respectively. However, this effect does not exceed 0.2 mm/yr and can be neglected here (Thomas et al. 2011).

It can be seen that along the coast of East Antarctica there is a good agreement between both models and the observations. On the contrary, there are remarkable differences between both model predictions in the region of the Antarctic Peninsula. At some sites the GPS rates also reveal larger differences with the model predictions. More GPS sites can certainly help to provide further constraints to improve the GIA modeling.

5 Summary and Outlook

We have shown that the SCAR GPS Campaigns provided valuable data for the ITRF densification in Antarctica. The geophysical interpretation of site motions in the context of plate kinematics and GIA demand highest accuracies. It has already been demonstrated that different software packages incorporating the same data may lead to small differences

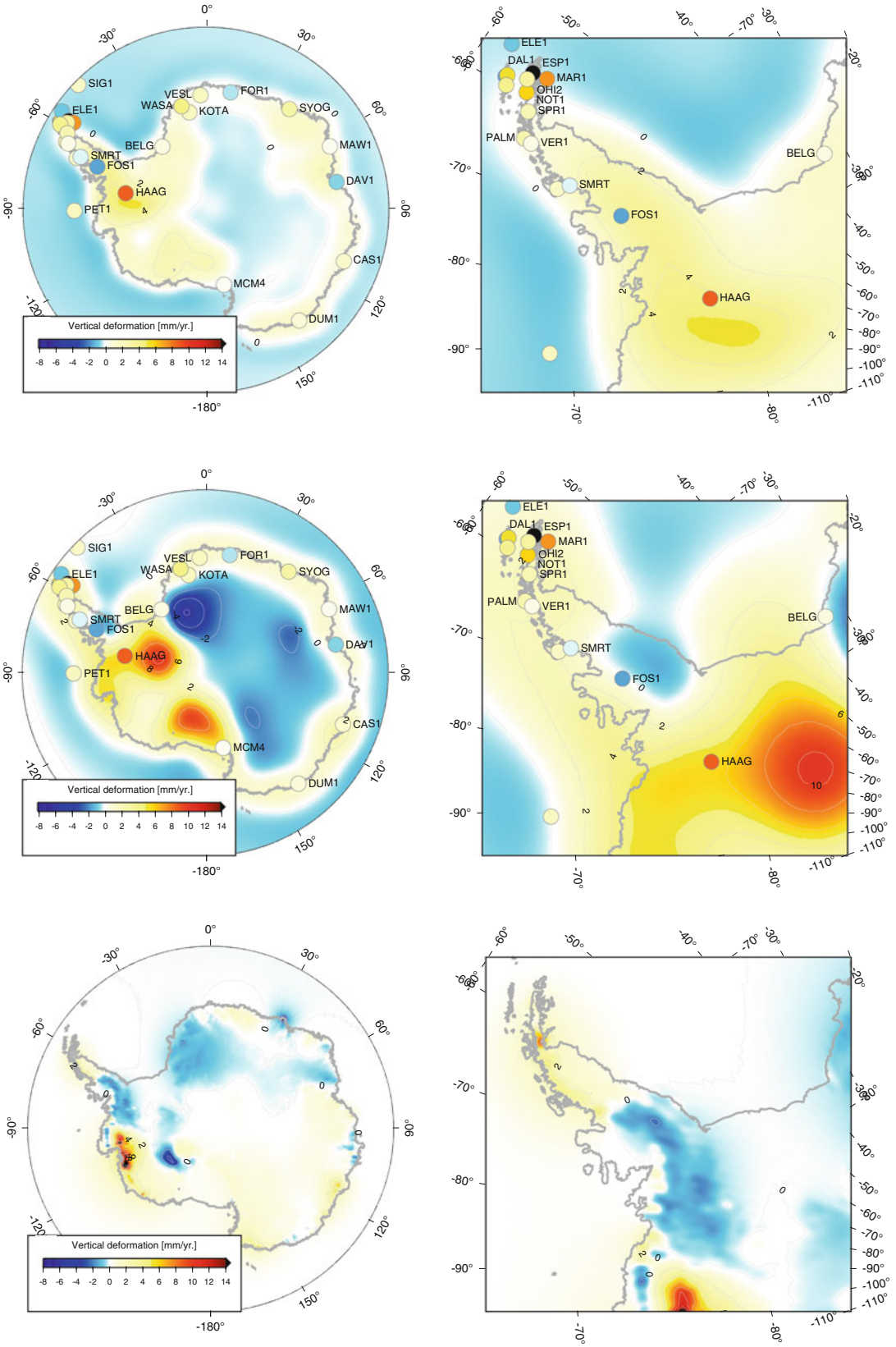

Fig. 4 Comparison of the vertical deformations observed by GPS and predicted by two GIA models. The GPS results have been reduced by the modeled elastic uplift effect and are plotted by color-coded circles. The respective GIA model prediction is shown in the background. *Top*: IJ05R2, 65 km lithospheric thickness (cf. Ivins et al. 2013, Fig. 5). *Center*: W12a (Whitehouse et al. 2012). *Bottom*: Elastic uplift effect caused by present-day ice mass changes (Groh et al. 2014)

in the results (Dietrich et al. 2001). Since there exist several national GNSS projects in Antarctica (Bevis and Kendrick 2009; Capra et al. 2008; Groh et al. 2012; Scheinert et al. 2006; Tregoning et al. 2000) it is a future challenge to generate homogeneous and consistent results with respect to the global reference frame in order to gain the most reliable information on the GIA in Antarctica. In our opinion, this forms also an important prerequisite to achieve improved estimates of the Antarctic ice-mass balance by means of satellite gravimetry (Groh et al. 2014, 2012).

Acknowledgements We would like to thank all nations, agencies and persons who contributed to the SCAR GPS Campaigns and provided data. Special thanks go to the leaders and the staff of the Antarctic stations for their support of our work. We thank the three reviewers for their comments which helped us to improve the manuscript.

References

Argus DF, Blewitt G, Peltier WR, Kreemer C (2011) Rise of the ellsworth mountains and parts of the east antarctic coast observed with GPS. Geophys Res Lett 38:16303. Doi:10.1029/2011GL048025

Bevis M, Brown A (2014) Trajectory models and reference frames for crustal motion geodesy. J Geodesy 88(3):283–311. Doi:10.1007/s00190-013-0685-5

Bevis M, Kendrick E (2009) Geodetic measurements of vertical crustal velocity in West Antarctica and the implications for ice mass balance. Geochem Geophy Geosy 10(10):1–11. Doi:10.1029/2009GC002642

Bird P (2003) An updated digital model of plate boundaries. Geochem Geophy Geosy 4(3):52. Doi:10.1029/2001GC000,252

Capra A, Dubbini M, Galeandro A, Gusella L, Zanutta A, Casula G, Negusini M, Vittuari L, Sarti P, Mancini F, Gandolfi S, Montaguti, M, Bitelli G (2008) VLNDEF project for geodetic infrastructure definition of Northern Victoria Land, Antarctica, Springer, Berlin/Heidelberg, pp 37–72

Dach R, Hugentobler U, Fridez P, Meindl M (eds) (2007) Bernese GPS Software Version 5.0. Astronomical Institute, University of Bern, Switzerland

Dalziel I, Elliot D (1982) West Antarctica: problem child of gondwanaland. Tectonics 1(1):3–19

Dietrich R, Dach R, Engelhardt G, Ihde J, Korth W, Kutterer HJ, Lindner K, Mayer M, Menge F, Miller H, Müller C, Niemeier W, Perlt J, Pohl M, Salbach H, Schenke HW, Schöne T, Seeber G, Veit A, Völksen C (2001) ITRF coordinates and plate velocities from repeated GPS campaigns in Antarctica - an analysis based on different individual solutions. J Geodesy 74(11/12):756–766

Dietrich R, Rülke A, Ihde J, Lindner K, Miller H, Niemeier W, Schenke HW, Seeber G (2004) Plate kinematics and deformation status of the antarctic peninsula based on GPS. Global Planet Chang 42:313–321

Dow JM, Neilan RE, Rizos C (2009) The International GNSS service in a changing landscape of global navigation satellite systems. J Geodesy 83:191–198. Doi:10.1007/s00190-008-0300-3

Fritsche M, Dietrich R, Knöfel C, Rülke A, Vey S, Rothacher M, Steigenberger P (2005) Impact of higher-order ionospheric terms on GPS estimates. Geophys Res Lett 32:L23311. Doi:10.1029/2005GL024342

Groh A, Ewert H, Fritsche M, Rülke A, Rosenau R, Scheinert M, Dietrich R (2014) Assessing the current evolution of the Greenland ice sheet by means of Satellite and ground-based observations. Surv Geophys. 35(6):1459–1480. Doi:10.1007/s10712-014-9287-x

Groh A, Ewert H, Scheinert M, Fritsche M, Rülke A, Richter A, Rosenau R, Dietrich R (2012) An investigation of Glacial Isostatic Adjustment over the Amundsen Sea sector, West Antarctica. Global Planet Change 98–99:45–53. Doi: 10.1016/j.gloplacha.2012.08.001

Ivins E, James T, Wahr J, Schrama EO, Landerer F, Simon K (2013) Antarctic contribution to sea level rise observed by GRACE with improved GIA correction. J Geophys Res Solid Earth 118(6):3126–3141. Doi: 10.1002/jgrb.50208

Mao A, Harrison CGA, Dixon TH (1999) Noise in GPS coordinate time series. J Geophys Res 104(B2):2797–2816. Doi: 10.1029/1998JB900033

Maurice SDR, Wiens DA, Shore PJ, Vera E, Dorman LM (2003) Seismicity and tectonics of the South Shetland Islands and Bransfield Strait from a regional broadband seismograph deployment. J Geophys Res 108(B10):2461. Doi: 10.1029/2003JB002,416

Mayer M, Lindner K, Kutterer H, Heck B (2000) Deformationsanalyse zur Aufdeckung von Punkt- und Blockbewegungen im Bereich der Antarktischen Halbinsel. In: Dietrich R (ed) Deutsche Beiträge zu GPS-Kampagnen des Scientific Committee on Antarctic Research (SCAR) 1995–1998, no. 310 in Series B, pp. 127–144. Verlag der Bayerischen Akademie der Wissenschaften in Kommission beim Verlag C. H. Beck

Rülke A, Dietrich R, Fritsche M, Rothacher M, Steigenberger P (2008) Realization of the Terrestrial Reference System by a reprocessed global GPS network. J Geophys Res 113:B08403, doi 10.1029/2007JB005231

Scheinert, M., Ivins, E., Dietrich, R., Rülke, A Vertical Crustal Deformations in Dronning Maud Land, Antarctica: Observations versus Model Predictions In: Fütterer, D, Damaske D, Kleinschmidt G, Miller H, Tessensohn F (eds) Antarctica – Contributions to Global Earth Sciences (Proc. of ISAES IX, Potsdam, September 8–12, 2003), pp. 357–360. Springer Berlin – Heidelberg – New York (2006)

Steigenberger, P., Rothacher, M., Dietrich, R., Fritsche, M., Rülke, A., Vey, S.: Reprocessing of a global GPS network. J Geophys Res 111 (2006). B05402, DOI 10.1029/2005JB003747

Thomas ID, King MA, Bentley MJ, Whitehouse PL, Penna NT, Williams SDP, Riva REM, Lavallée DA, Clarke PJ, King EC, Hindmarsh RCA, Koivula H (2011) Widespread low rates of Antarctic glacial isostatic adjustment revealed by GPS observations. Geophys Res Lett 38(22), Doi: 10.1029/2011GL049277

Tregoning P, Welsh A, McQueen H, Lambeck K (2000) The search for postglacial rebound near the Lambert Glacier, Antarctica. Earth Planets Space 52:1037–1041

Vey S, Dietrich R, Fritsche M, Rülke A, Rothacher M, Steigenberger P (2006) Influence of mapping function parameters on global GPS network analyses: comparisons between NMF and IMF. Geophys Res Lett 33:L01814. Doi:10.1029/2005GL024361

Whitehouse PL, Bentley MJ, Milne GA, King MA, Thomas ID (2012) A new glacial isostatic adjustment model for Antarctica: calibrated and tested using observations of relative sea-level change and present-day uplift rates. Geophys J Int 190(3):1464–1482 Doi:10.1111/j.1365-246X.2012.05557.x

Williams SDP (2003) The effect of coloured noise on the uncertainties of rates estimated from geodetic time series. J Geod 76:483–494. Doi:10.1007/s00,190–002–0283–4

Williams SDP, Bock Y, Fang P, Jamason P, Nikolaidis RM, Prawirodirdjo L, Miller M, Johnson DJ (2004) Error analysis of continuous GPS position time series. J Geophys Res 109:B03,412. Doi: 10.1029/2003JB002,741

Zhang J, Bock Y, Johnson H, Fang P, Williams S, Genrich J, Wdowinski S, Behr J (1997) Southern California permanent GPS geodetic array: error analysis of daily position estimates and site velocities. J Geophys Res 102(B8):18,035–18,055

Impact of Celestial Datum Definition on EOP Estimation and CRF Orientation in the Global VLBI Session IYA09

V. Raposo-Pulido, R. Heinkelmann, T. Nilsson, M. Karbon, B. Soja, E. Tanir Kayikci, C. Lu, J. Mora-Diaz, and H. Schuh

Abstract

Earth Orientation Parameters (EOP) provide the rotation of the International Terrestrial Reference System (ITRS) to the Geocentric Celestial Reference System (GCRS) as a function of time. When estimating a Celestial Reference Frame (CRF) usually a number of radio sources with a long history of observations and stable positions are included in the datum used to define the orientation of the frame. How many and which radio sources are taken into account for the datum definition has a significant effect on the estimated EOP. In this study we analyze the effects of different options for the celestial datum definition on the precision of the EOP and on the agreement w.r.t the last realization of the International Celestial Reference Frame (ICRF2; Fey et al., The second realization of the international celestial reference frame by very long baseline interferometry, IERS Technical Note No. 35, 2009). The resulting EOP of the special VLBI session IYA09 are compared to the C04 08 EOP series (Bizouard and Gambis, The combined solution C04 for Earth orientation parameters consistent with international terrestrial reference frame 2008, IERS Notice 2011, 2011). The analysis shows that the smallest uncertainties for EOP are achieved when the maximum number of defining sources is chosen for the datum. Comparing with a typical VLBI session, the precision of the EOP and the agreement of the axes w.r.t. ICRF2 could be improved if more defining sources, especially in the southern hemisphere, were considered.

Keywords

Celestial datum • Earth orientation parameters (EOP) • Geodetic very long baseline interferometry (VLBI) • International celestial reference frame (ICRF) • Reference systems • Vienna VLBI software (VieVS)

1 Introduction

The special session IYA09 was observed in the International Year of Astronomy from 2009-11-18 at 18:00 UTC to 2009-11-19 at 18:00 UTC. The goal was to observe as many of the 295 ICRF2 defining sources as possible in a single

V. Raposo-Pulido (✉)
IGN, National Geographic Institute, Madrid, Spain
Department 1: Geodesy and Remote Sensing, Helmholtz Centre Potsdam, GFZ German Research Centre for Geosciences, 14473 Potsdam, Germany
e-mail: raposo@gfz-potsdam.de; v.raposo@oan.es

E. Tanir Kayikci
Department of Geomatics Engineering, Karadeniz Technical University, 61080 Trabzon, Turkey

R. Heinkelmann • T. Nilsson • M. Karbon • B. Soja • C. Lu • J. Mora-Diaz • H. Schuh
Department 1: Geodesy and Remote Sensing, Helmholtz Centre Potsdam, GFZ German Research Centre for Geosciences, 14473 Potsdam, Germany

© Springer International Publishing Switzerland 2015

C. Rizos, P. Willis (eds.), *IAG 150 Years*, International Association of Geodesy Symposia 143,
DOI 10.1007/1345_2015_106

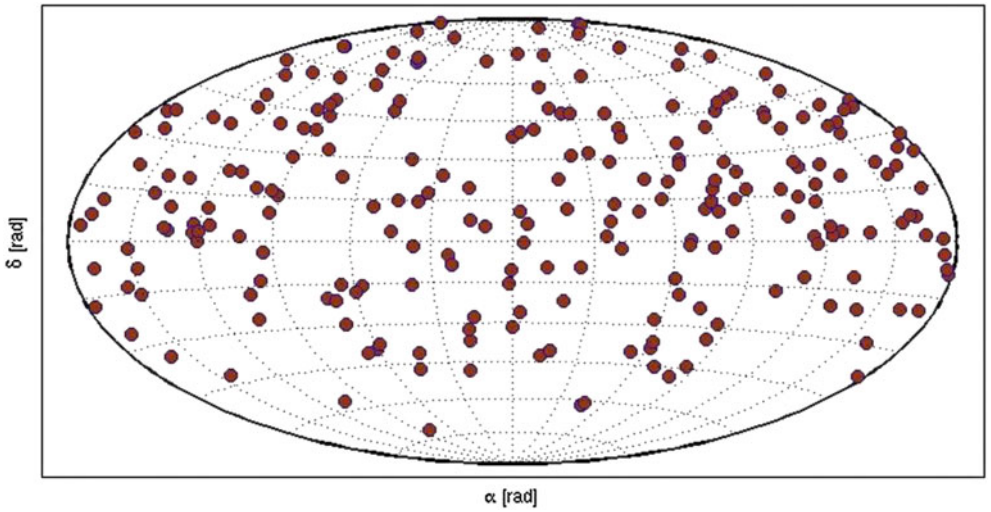

Fig. 1 Distribution of radio sources observed (Table 1)

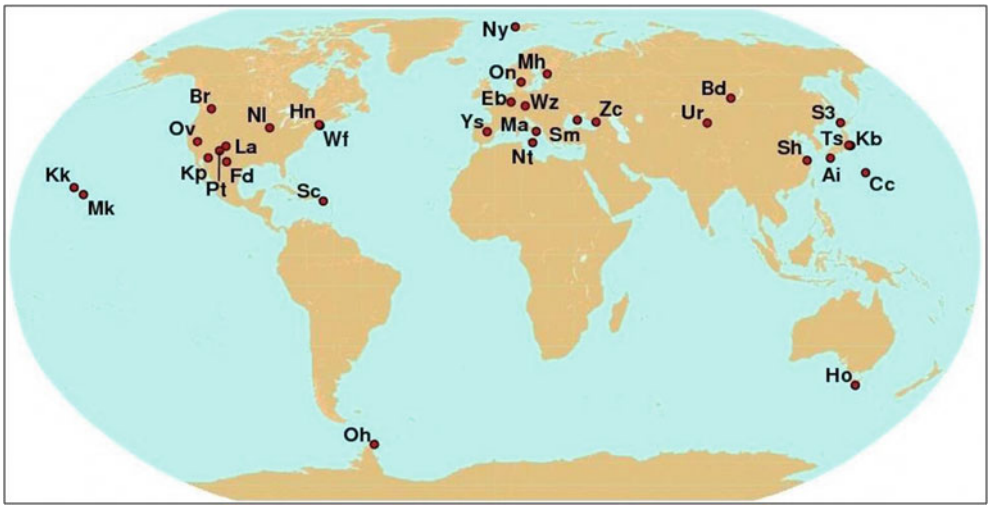

Fig. 2 The VLBI station network observed (Table 1). Modified from http://ivscc.gsfc.nasa.gov/program/iya09

24-h session with the highest possible number of stations, in order to acquire unique data on these radio sources. In a typical geodetic VLBI session only a subset of the ICRF2 defining sources is observed. This means that in order to have observations of all ICRF2 defining sources with typical geodetic VLBI sessions, several of these sessions need to be combined. These sessions must have subsets of common radio sources so that it becomes possible to relate all defining sources by concatenating all observations in these sessions. In particular, since there are only few VLBI stations in the southern hemisphere, it is difficult to link the northern and southern sky from session to session. The advantage of session IYA09 is that it is possible to determine the arc lengths between radio sources without relying on source overlaps between different VLBI sessions. The station network in the southern hemisphere is in general sparse and this is also true for this session. However, although it means that some southern sources will be missed, with this session we have the opportunity to strengthen the frame.

Nowadays, in a typical geodetic VLBI session 50–70 radio sources are observed with a network of 7–11 stations, while the IYA09 includes 237 radio sources (162 in the northern hemisphere and 75 in the southern hemisphere, see Fig. 1) and 32 stations (23 geodetic VLBI stations and 9 VLBA stations, see Fig. 2). Three out of thirty five scheduled stations were dropped. SVETLOE had hardware problems, DSS13 had problems with one of the X-band channels and TIGOCONC had only 66 observations, most of them with very low SNR (Gipson et al. 2010). Unfortunately, 58 out of 295 ICRF2 defining sources could not be observed due to the proximity to the sun or the sparseness of stations in the southern hemisphere (see Fig. 2).

Table 1 Description of the session IYA09

	Scheduled	Observed	Used in this study
Stations	35	32	29
Radio sources	243	237	237
Observations	37,236	26,696	25,492

Table 1 summarizes what data were scheduled, actually observed, and used in this study (explanation for the exclusion of stations is given below). In the case of the radio sources all the observed ones were considered and used in this study. However, as we will see, depending on the analysis criteria, we are going to have different number of radio sources in our analysis.

In general it can be imagined that the reliability of a celestial datum should increase with an increasing number of radio sources that is used for the datum definition. However, this requires that the radio sources have the same quality in terms of accurate and stable coordinates. Since this is not the case, an increase in the number of radio sources means that also less accurate radio sources will be used for the datum definition. Thus, the celestial datum could be degraded instead.

Another question is how to handle radio sources that have been observed only once or twice during a VLBI session. The coordinates of these radio sources cannot be estimated from the data due to the too low redundancy. One possibility is to fix the coordinates of these radio sources, but it only makes sense if they have stable positions.

The first realization of the International Celestial Reference Frame (ICRF1) was adopted in 1998-01-01 (Ma et al. 1998). To estimate the ICRF2, a no-net-rotation (NNR) constraint was imposed on 205 out of the 212 ICRF1 defining sources to align their positions with the original ICRF1 defining sources. The remaining seven were special handling sources, i.e., radio sources with large positional variations. The ICRF2 consists of 3,414 radio sources where the datum is formed by the 295 defining sources determined in the ICRF2 analysis process. These radio sources satisfy a number of specific conditions, e.g. having more than 20 observations or coordinates differences smaller than 500 μas w.r.t. ICRF1 (Fey et al. 2009). However, as mentioned before, in standard geodetic VLBI sessions not all of these radio sources are observed, and thus different datum definitions need to be considered. In this study we assess the impact of different celestial datum definitions on EOP results from geodetic VLBI. We focus on the IYA09 session and use the VieVS software (Böhm et al. 2012) following the current IERS Conventions (Petit and Luzum 2010).

Table 2 Celestial datum configurations

	Datum conditions	Radio sources to define the datum
A	Fixed to ICRF2	ICRF2 defining sources (237)
B	NNR condition	ICRF2 defining sources (229)
C	NNR condition	F-V sources (103)
D	NNR condition	Random sources (156)

Feissel-Vernier (F-V) sources are radio sources selected by Allan standard deviation

2 Parameterization and Analysis Options

We analyzed the IYA09 session using the following analysis approach. Piecewise-linear offsets were estimated for the clocks (60 min interval, 0.5 ps^2/s relative constraints) with WETTZELL as reference clock, zenith wet delays (60 min interval, 0.7 ps^2/s relative constraints), troposphere gradients (360 min interval, 2 mm/day relative constraints and 1 mm absolute constraints), and EOP (1,440 min interval, 0.1 ∼ μas/day relative constraints). For each EOP three values were estimated, at 00:00 UTC before, during, and after the session. However, due to the tight constraints applied, all three will be equal, thus practically a constant value is estimated for each EOP. One offset was estimated for each station coordinate and for each radio source coordinate. The datum definition of the station network was realized by applying no-net-translation (NNT) and NNR conditions for the stations with no breaks before the session and coordinates from the a priori VTRF2008 catalogue (Böckmann et al. 2010). Following this criterion, EFLSBERG, TSUKUB32, and YEBES40M were not included in the datum.

The celestial datum definitions were realized by applying NNR conditions including different subsets of radio sources. Within approach A, all 237 radio sources of the session were fixed to their a priori ICRF2 coordinates. In approach B, radio source coordinates were estimated imposing NNR constraints on ICRF2 defining sources. For approach C, radio source coordinates were estimated imposing NNR constraints on Feissel-Vernier (F-V) sources, which are stable radio sources selected by Allan standard deviation of radio source coordinates. The F-V sources have no time-varying behavior and accordingly they support the maintenance of the frame they materialize (Feissel-Vernier 2003). Finally, for approach D, radio source coordinates were estimated imposing NNR constraints on a set of random radio sources which were selected to assess the significance of the number of radio sources in the datum (see Table 2

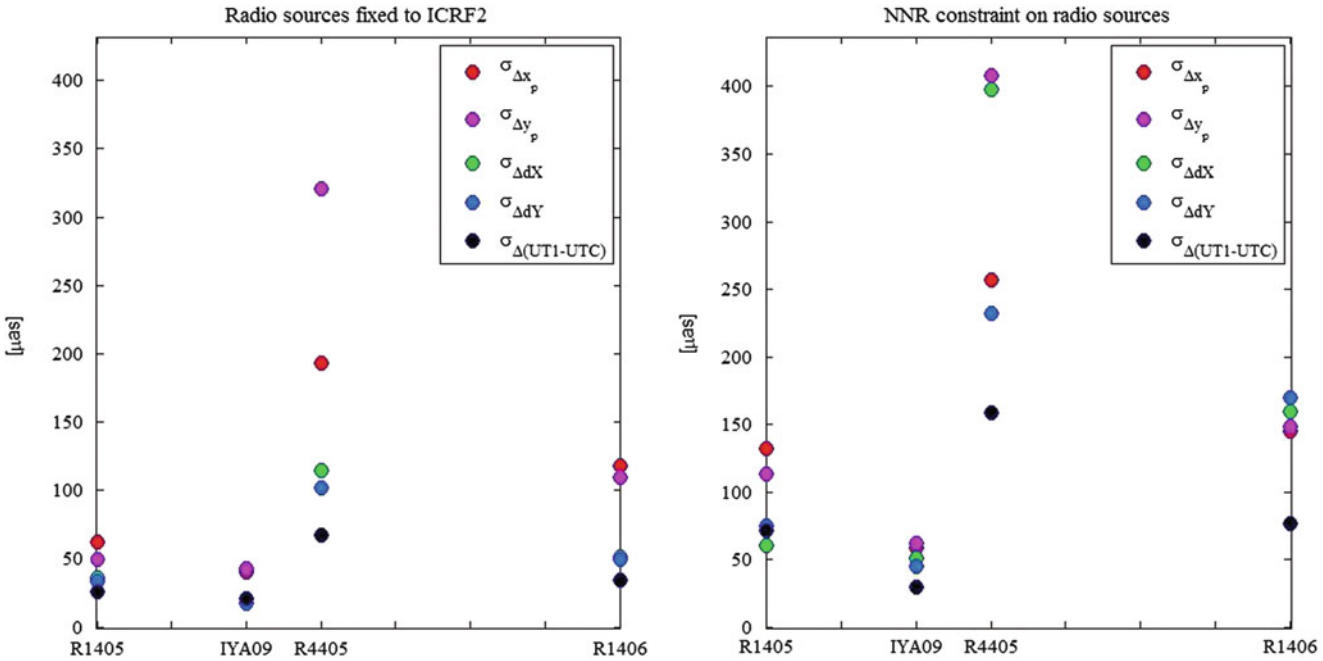

Fig. 3 Formal errors (in μas) of the EOP adjustments estimated for four VLBI sessions when radio sources are fixed (*left graph*, approach A), and estimated (*right graph*, approach B)

and Fig. 4). In the cases B, C, and D radio sources with only one or two observations (8 out of 237) were excluded. Large outlying observations were removed (95 out of 25,587 $\sim$ 0.37%) when the absolute value of the residuals were larger than five times the root-mean-square of all residuals. The Japanese stations AIRA, CHICHI10, and SINTOTU3 were excluded due to the high scatter of the post-fit residuals.

3 Effect of the Choice of Datum Sources on the EOP

The IERS C04 08 series (Bizouard and Gambis 2011) is the international reference time series for the EOP provided by the Earth Orientation Center of the IERS located at Paris Observatory. This EOP series, consistent with the ITRF2008, is obtained from the combination of operational EOP series derived from five different astro-geodetic techniques: Lunar Laser Ranging (LLR), Satellite Laser Ranging (SLR), Very Long Baseline Interferometry (VLBI), Global Navigation Satellite Systems (GNSS), and Doppler Orbitography by Radiopositioning Integrated on Satellite (DORIS). The C04, given at integer MJD (UTC), includes the International VLBI Service (IVS) operational rapid combination solution and the Paris Observatory (OPA) VLBI solution (Lambert and Barache 2013). The OPA VLBI solution included the IYA09 session, but the IVS combined solution did not include it because only two IVS Analysis Centers (AC) had provided solutions for it. Figure 3 shows a comparison of the formal errors of the EOP adjustments for four different kind of sessions: R1405 (09NOV16XA), IYA09 (09NOV18XA), R4405 (09NOV19XE), and R1406 (09 NOV23XA). R1 and R4 are typical modern VLBI sessions observed adjacent to the IYA09 session. Two analyses were considered: radio sources fixed to ICRF2 (analysis approach A) and radio sources estimated (analysis approach B). In both cases the smallest uncertainties are reached with the IYA09 session (see Fig. 3).

In the following we discuss the results for the EOP that were derived using the different celestial datum definitions described in the previous section. As a reference for the comparisons we use the EOP of the IERS C04 08 series.

Table 3 shows the estimated EOP adjustments relative to IERS C04 08 as well as their formal errors. To accurately determine the origin of right ascension (α), a good coverage in α range is necessary. The adjustments for UT1-UTC (which are strongly correlated with the right ascension origin) agree with the a priori uncertainty (see Table 3), being smaller when the radio sources are estimated. The x_p adjustments show values smaller than the uncertainties of the a priori values, while the y_p adjustments are larger (see Table 3). This effect is independent of the celestial datum configuration. The EOP x_p is sensitive to baselines in north-south direction along the great circle from the poles through Greenwich (and 180°) longitude. The EOP y_p is

Table 3 A priori uncertainties from the combined EOP series and adjustments for Universal Time (UT1-UTC), pole coordinates (x_p, y_p) and celestial pole offsets (dX, dY) at 00:00 UTC, 2009-11-19 (MJD 55154)

A priori uncertainties, MJD 55154	UT1-UTC[μs]	x_p[μas]	y_p[μas]	dX[μas]	dY [μas]
C04 08 EOP series	7.1	40	41	32	23
Adjustments and formal errors, MJD 55154	△(UT1-UTC)[μs]	$\triangle x_p$[μas]	$\triangle y_p$[μas]	△dX[μas]	△dY[μas]
IYA09 (A)	-7.7 ± 1.4	-5.4 ± 39.9	363.2 ± 42.8	20.1 ± 17.2	-46.7 ± 17.4
IYA09 (B)	-2.8 ± 2.0	-16.8 ± 58.6	248.4 ± 62.4	32.1 ± 51.2	-150.9 ± 44.8
IYA09 (C)	-2.4 ± 2.3	-16.8 ± 58.6	248.4 ± 62.4	50.2 ± 61.3	-123.5 ± 51.7
IYA09 (D)	-2.8 ± 2.0	-16.8 ± 58.6	248.4 ± 62.4	10.1 ± 54.8	-126.8 ± 46.2

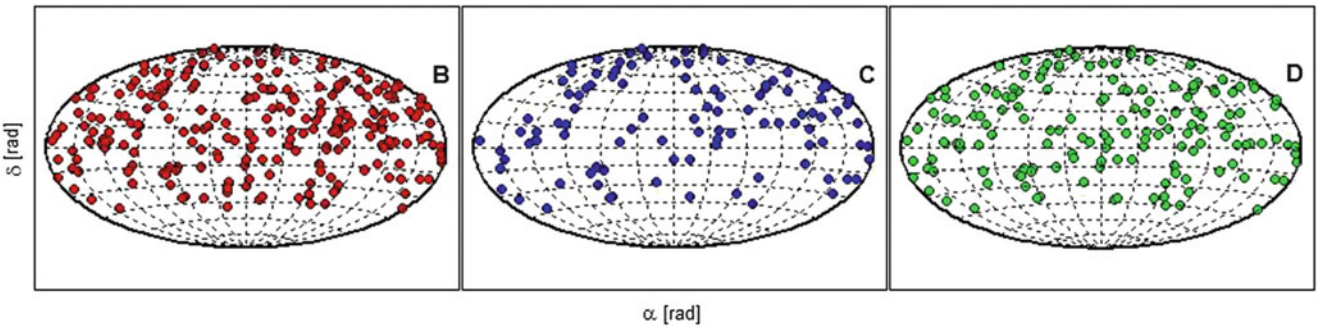

Fig. 4 Celestial datum approaches (Table 2)

sensitive to baselines in north-south direction along the great circle from the poles through 90° (and 270°) longitude. In the vicinity of the 0° longitude we find most of the European stations. For the vicinity of the 270° longitude we find the stations in North America, where PIETOWN, a station with strong nonlinear variations, is included. For that reason the y_p adjustments are not as good as for x_p. In both cases we find a small number of stations in the south. For B, C, and D the adjustments for x_p and y_p show identical values within the rounding, unlike approach A. The reason is that the station network and the datum definition included in the analysis is always the same, but approach A has a higher number of observations because all the sources were included (although fixed) and the radio sources with one or two observations were not excluded. This is also the case of △(UT1-UTC) when approach A is compared with approaches B, C, and D. The celestial pole offset △dY depends on the distribution of radio sources along the celestial meridian defined by the y-axis. The poor distribution of radio sources in the southern hemisphere (see Fig. 1) explains why the dY adjustments are larger than the uncertainty of the a priori value for all the cases. The approaches C and D are subsets of the datum B, but covering almost the same declination and right ascension range (see Fig. 4). For that reason, the EOP adjustments agree within 40 μas for these three approaches (see Table 3). If the number of datum sources is largest (B), the celestial datum is most stable and thus, formal errors of the EOP adjustments are smallest (see Table 3).

4 CRF Orientation Depending on the Celestial Datum

In this section we want to assess the effect of different sets of radio sources on the orientation of the celestial frame. By definition, the relative orientation of two celestial reference frames (CRF) can be modeled by three rotation angles (A_1, A_2, A_3) around the axes of the equatorial coordinate system and systematic effects by three deformation parameters such as shearing (D_α, D_δ) and bias in declination (dz), (see Fig. 5). Parameters D_α and D_δ represent slopes in right ascension and in declination as functions of declination, for $\delta_o = 0$ (Li and Wang 2000). The deformations $D_\alpha\delta$ and $D_\delta\delta$ are zero on the equator and increase with increasing declination. The dz parameter reflects systematic differences in declination that may be caused by inaccuracy of the tropospheric gradient modelling for radio sources observed at low elevations. However, in this study we do not consider dz because the tropospheric gradients were estimated, which have been shown to absorb systematic declination differences (MacMillan and Ma 1997). The five parameters were estimated by the equations:

$$d\alpha = A_1 \tan\delta \cos\alpha + A_2 \tan\delta \sin\alpha - A_3 + D_\alpha(\delta - \delta_o) \quad (1)$$

$$d\delta = -A_1 \sin\alpha + A_2 \cos\alpha + D_\delta(\delta - \delta_o) + dz \quad (2)$$

Equations (1) and (2) were weighted by using the inverse of the variances of the offsets ($\sigma^2_{d\alpha}, \sigma^2_{d\delta}$). We compared the

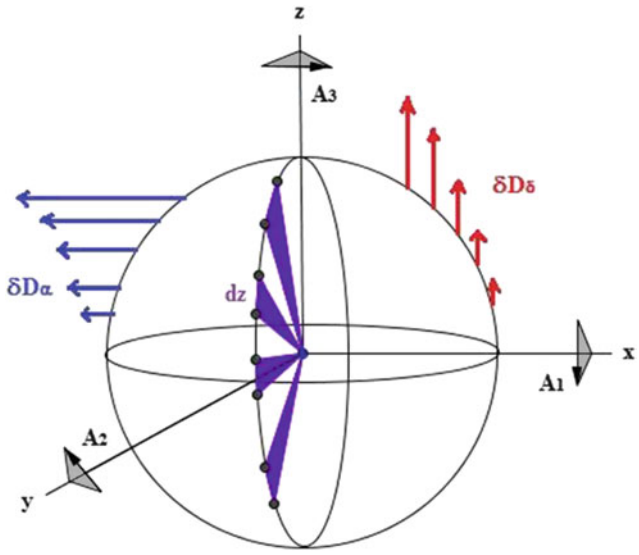

Fig. 5 Rotation and deformation parameters

Table 4 Rotation angles and deformation parameters derived from the comparison based on datum sources

	IYA09 (B)	IYA09 (C)	IYA09 (D)
A_1 [μas]	−69.5±21.2	−68.2±27.3	−38.6±24.7
A_2 [μas]	−18.7±22.1	−39.6±29.7	3.0±26.6
A_3 [μas]	−9.8±19.2	−23.3±28.5	4.3±22.7
D_α [μas/degree]	0.3 ± 0.7	−1.5 ± 1.0	−0.2 ± 0.8
D_δ [μas/degree]	−0.4 ± 0.4	−0.5 ± 0.5	−0.9 ± 0.5

estimated source coordinates obtained by the approaches B, C, and D with the respective ICRF2 positions for assessing the stability of the obtained solutions (see Table 4). This was done by evaluating Eqs. (1) and (2) for the respective subsets of estimated radio sources (B, C, and D). The results show the largest values for the rotation angles A_1 (up to 70 μas), which are directly related to the △dY value of the previous section, because it means a rotation of the axis *y*. Angles A_2 and A_3 show values smaller than 40 μas. The deformation parameter D_α increases up to 1.5 μas/degree when the subset C is considered (five times worse than B) because of the sparseness of radio sources along the right ascension range.

5 Summary

The formal errors of the EOP improve when the radio sources are fixed. If we estimate the EOP together with the radio sources, the smallest formal errors for the EOP are reached when more radio sources are included in the datum (approach B).

When radio source positions were estimated, we compared three VLBI solutions (IYA(B), IYA(C), and IYA(D)) to the ICRF2 by using the datum sources (B, C, and D respectively). The analysis approach C shows the largest uncertainty values for the determined rotation angles and deformation parameters because it contains the smallest number of defining sources to define the directions of the axes. The rotation angles reach the smallest values when the approach D was chosen, with an improvement up to 31 μas w.r.t. the other approaches. The deformation parameters D_i, considered together, are minimum when the approach B was considered. The smallest uncertainties for the rotations A_i and the deformations D_i are achieved when the approach B was used (formal error on the order of 19–22 μas and 0.4–1 μas/degree respectively). Compared with B, the uncertainties of the rotation angles given by the approaches C and D are larger by up to 9 μas.

6 Conclusions

This study shows that increasing the number of radio sources in a VLBI session (as e.g. in the IYA09 session, see Fig. 3), and in particular in the celestial datum (see Table 3), allows the celestial pole offsets to be estimated with higher quality with no detriment of the other EOP.

In IERS Technical Note No. 34 (Gontier et al. 2006) individual VLBI frames are compared with ICRF-Ext.2 (Fey et al. 2004) by using common ICRF defining sources. These comparisons show rotation angles with values between −32 μas and 50 μas and uncertainties between 18 μas and 31 μas. The deformation parameters show values between −1.8 μas/degree and 0.4 μas/degree with uncertainties between 0.4 μas/degree and 1 μas/degree. In our study (see Table 4), we get rotation angles with values between −69.5 μas and 4.3 μas with uncertainties between 19.2 μas and 29.7 μas. The deformation parameters show values between −1.5 μas/degree and 0.3 μas/degree with uncertainties between 0.4 μas/degree and 1 μas/degree. The comparisons given by Gontier et al. work with celestial catalogues obtained by global solutions, but the results given here are valid for only one session (IYA09). In both cases the values have the same order of magnitude, concluding the excellent performance of the IYA09 session.

For that reason, more sessions with these characteristics should be considered and performed for further investigations related to the EOP and the CRF. Increasing the number of observations of radio sources in the south and including more radio sources, not necessarily ICRF2 defining sources, could give us the opportunity to study new approaches for the datum definition.

Acknowledgements The first author acknowledges IGN for its support. We acknowledge IVS for providing the data analyzed in this study, in particular all stations which took part at the IYA09 session. We greatly acknowledge the three reviewers for their detailed comments and suggestions.

References

Bizouard C, Gambis D (2011) The combined solution C04 for Earth orientation parameters consistent with international terrestrial reference frame 2008. IERS Notice 2011. ftp://hpiers.obspm.fr/iers/eop/eopc04/C04.guide.pdf

Böckmann S, Artz T, Nothnagel A (2010) VLBI terrestrial reference frame contributions to ITRF2008. J Geodesy 84:201–219. doi:10.1007/s00190-009-0357-7

Böhm J, Böhm S, Nilsson T, Pany A, Plank L, Spicakova H, Teke K, Schuh H (2012) The new vienna VLBI software VieVS. In: Kenyon S et al. (eds) Geodesy for planet earth, international association of geodesy symposia 136. Springer, Berlin/Heidelberg. doi:10.1007/978-3-642-20338-1_126

Feissel-Vernier M (2003) Selecting stable extragalactic compact radio sources from the permanent astrogeodetic VLBI program. Astron Astrophys 403:105–110. doi:10.1051/0004-6361:20030348

Fey AL, Ma C, Arias EF, Charlot P, Feissel-Vernier M, Gontier A-M, Jacobs CS, Li J, MacMillan DS (2004) The second extension of the international celestial reference frame: ICRF-EXT-1. Astron J 127:3587–3608

Fey AL, Gordon D, Jacobs CS (eds) (2009) The second realization of the international celestial reference frame by very long baseline interferometry. Presented on behalf of the IERS/IVS working group(IERS Technical Note No. 35). Frankfurt am Main: Verlag des Bundesamts für Kartographie und Geodäsie, p 204. ISBN 3-89888-918-6

Gipson J, Behrend D, Gordon D, Himwich E, MacMillan D, Titus M, Corey B (2010) Coordinating, scheduling, processing and analyzing IYA09. In: IVS 2010 general meeting proceedings, pp 90–94

Gontier A-M, Arias EF, Barache C (2006) Maintenance of the ICRF using teh most stable sources. (IERS Technical Note No. 34, pp 7–19). Frankfurt am Main: Verlag des Bundesamts für Kartographie und Geodäsie, p 137. ISBN 3-89888-802-9

Lambert S, Barache C (2013) OPA2013a solution. http://ivsopar.obspm.fr/earth/glo/rapid/opa2013a.eops

Li J, Wang G (2000) Global solution of VLBI observations and assessments. Earth Planets Space 52:731–733

Ma C, Arias EF, Eubanks TM, Fey AL, Gontier A-M, Jacobs CS, Sovers OJ, Archinal BA, Charlot P (1998) The international celestial reference frame as realized by very long baseline interferometry. Astron J 116:516–546

MacMillan DS, Ma C (1997) Atmospheric gradients and the VLBI terrestrial and celestial reference frames. Geophys Res Lett 24(4):453–456

Petit G, Luzum B (2010) IERS conventions (2010) (IERS Technical Note No. 36) Frankfurt am Main: Verlag des Bundesamts für Kartographie und Geodäsie, p 179. ISBN 3-89888-989-6

A High-Precision Deformation Model to Support Geodetic Datum Modernisation in Australia

R. Stanaway and C. Roberts

Abstract

This paper describes a gridded kinematic representation of a deformation model that can be used to support kinematic geodetic datum applications for high precision users. The kinematic model is comprised of a site velocity model (for coordinate prediction and to model inter-seismic deformation and plate motion) and an epoch correction (patch) model. The epoch correction model estimates distortion between reference frames at the reference epoch and can include episodic deformation arising from seismic activity.

The kinematic model presented enables seamless interaction between precision GNSS positioning and related systems, GIS and static spatial datasets within a kinematic coordinate environment with centimetre precision.

The next generation Australian Geodetic Datum will be realised within a kinematic reference frame in order to capture the highest resolution deformation of the Australian tectonic plate. This represents a paradigm shift from classical geodetic datums which are realised by coordinates of geodetic monuments fixed at a specified reference epoch (static geodetic datums). Centimetre precision positioning will be available to the mass market in the near future and the disparity between static geodetic datums (and spatial data products derived from them) and ITRF due to the effects of Earth deformation will be become more apparent. As development of deformation models within GIS is still in its infancy, there is still an ongoing requirement to provide static coordinates to users to enable positioning within a kinematic reference frame to maintain alignment with existing spatial datasets (e.g., cadastral, utilities, roads, infrastructure, mining, precision agriculture, imagery and LiDar). Furthermore, a four-dimensional GIS, when developed, will still require a precise deformation or kinematic model to enable spatial data collected at different epochs to be integrated harmoniously.

The current strategy used in Australia to transform between a specified epoch of ITRF and GDA94 (the current ITRF aligned geodetic datum fixed at epoch 1994.0) is to use a 14 parameter conformal transformation but approach does not capture the full complexity and variation of the deformation field at the highest resolution for some users, and so a variable resolution gridded deformation model is proposed here as an alternative.

Keywords

Reference Frame • Deformation Model • GNSS • kinematic datum

R. Stanaway (✉) • C. Roberts
School of Civil and Environmental Engineering, University of New South Wales, Sydney, NSW 2052, Australia
e-mail: richard.stanaway@student.unsw.edu.au; c.roberts@unsw.edu.au

1 Introduction

Increasingly, precise positioning services e.g., AusPOS (Commonwealth of Australia 2013), NRCan-PPP (Government of Canada 2013) and OPUS (US Government

© Springer International Publishing Switzerland 2015

C. Rizos, P. Willis (eds.), *IAG 150 Years*, International Association of Geodesy Symposia 143,
DOI 10.1007/1345_2015_31

2013) are providing coordinates within the latest realisation of the International Terrestrial Reference Frame (ITRF), currently ITRF2008, or other global reference frames closely aligned with ITRF such as WGS84 and IGS08. The positional uncertainty of these services is typically less than 10 mm for horizontal coordinates and less than 25 mm for ellipsoidal heights for submitted static dual-frequency carrier phase observations of several hours duration. The application of these services is therefore sensitive to tectonic displacement. Repeat observations made on a geotechnically stable geodetic monument within a time span of even a few months can show centimetre changes in coordinates. Many of the online ITRF based processing services also transform the ITRF coordinates at the epoch of measurement to a localised reference frame where global scale tectonic deformation effects have been largely modelled out (e.g., GDA94 in AusPOS, NAD83(CSRS) in NRCan, and NAD83(2011)/SPCS in OPUS). Removal of the underlying tectonic deformation signal (in particular the absolute plate rotation component) in most instances enables repeatability of coordinate estimation within a localised reference frame over very long periods. Coordinate stability at a specific reference epoch is an essential requirement for integration of spatial data acquired at different epochs within a localised reference frame (Stanaway and Roberts 2011).

This paper presents a gridded kinematic representation of a tectonic deformation model for the Australian continent that can be utilised to project or propagate ITRF coordinates at a kinematic epoch to a fixed reference epoch for applications that require temporally stable centimetre-level absolute positioning accuracy. The current geodetic datum officially adopted in Australia is the Geocentric Datum of Australia 1994 (GDA94) which is a realisation of ITRF92 at epoch 1994.0 (ICSM 2013). In 2012 the realisation of GDA94 was updated in order to reduce the formal uncertainties of the fiducial network from 30 mm (horizontal) and 100 mm (vertical) to less than 10 mm (Commonwealth of Australia 2012). Despite this, many stations in the Australian National Network (ANN) still have uncertainties of up to 300 mm due to distortions in the original geodetic adjustment of the ANN (Haasdyk and Roberts 2013). The proliferation of CORS networks streaming RTK and NRTK in Australia is already highlighting the disparity between GDA94 derived from CORS and the GDA94 coordinates of passive geodetic control in distorted secondary and tertiary networks (Haasdyk and Janssen 2012).

The model described here enables propagation of any epoch of the current ITRF realisation (ITRF2008) to a projected frame that is closely aligned with the current realisation of GDA94 with a precision of 10 mm at 95% Confidence Interval (CI). This level of precision is sufficient for the majority of precision users of the datum. The model can be utilised in GIS, GNSS positioning and GNSS post-processing software. Utilisation of the model in services such as Google Earth and mass-market positioning devices can ensure that precision ITRF position estimation can be aligned closely with an underlying map or image base that is tied to a fixed epoch of ITRF via a local reference frame consistently over periods of several decades. This alleviates the requirement to keep local reference frames in constant alignment with ITRF.

2 Advantages of Gridded Deformation Models Over Conformal Transformation Models

A commonly used strategy to transform ITRF coordinates to a localised reference frame is to apply a Fourteen parameter conformal transformation (seven parameters and their rates of change), or to use a model of rigid plate motion (e.g., Stanaway and Roberts 2010). Fourteen parameter transformation models have been developed between each realisation of ITRF and GDA94 (Dawson and Woods 2010) and these have enabled ITRF coordinates computed from positioning services such as AusPOS to be transformed to GDA94 for submitted observation data within Australia. AusPOS processing is undertaken within the IGS08 reference frame using Bernese software (Dach et al. 2007).

Conformal transformation approaches assume that deformation of the local reference frame with respect to ITRF is secular and well distributed. The major disadvantage of these approaches is that localised and non-conformal deformation is either unaccounted for, or propagates errors into the parameter estimation if monuments located in regions of localised deformation are constrained in a least squares estimation of parameters. Gridded deformation models overcome the limitations of parametric approaches because localised deformation can be isolated within the model. Furthermore, non-linear deformation effects such as complex plate boundary interseismic deformation can be modelled and interpolated with greater precision. In regions of localised deformation, or where positioning tolerances are smaller (e.g., urban areas), a denser deformation grid can be developed (Winefield et al. 2010).

3 Development of a Gridded Kinematic Model for Australia

A gridded kinematic modelling approach using a schema outlined in LINZ (2013) and Stanaway et al. (2014) is presented in this paper for the Australian continent. The approach described separates two modes of deformation; interseismic motion (modelled site velocity) and episodic deformation (coordinate shift at a defined epoch). This approach has been used in Japan (Hiyama et al. 2011) and in New Zealand (Crook and Donnelly 2013). While Australia

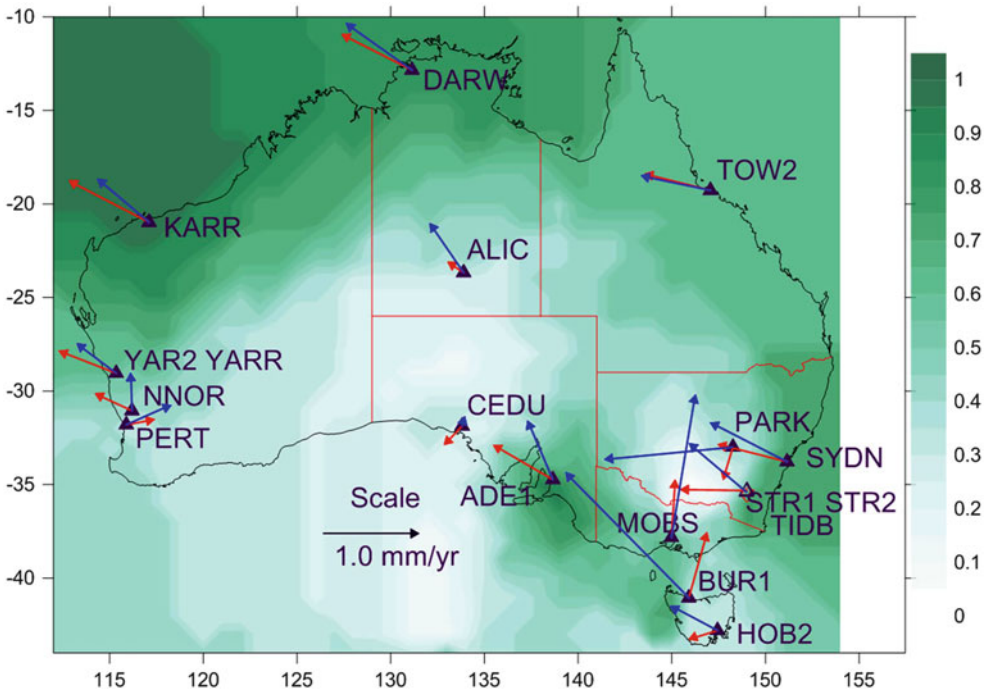

Fig. 1 Differences between published APREF, ITRF2008 GPS velocities and modelled velocities estimated from the ITRF2008 Australian Plate Euler pole at Australian fiducial CORS (*purple triangles*). *Green shading* shows the site velocity differences between the kinematic model (this paper) and velocities estimated from the ITRF2008 Euler pole in mm/year. The *darker blue vectors* show ITRF2008 GPS published velocities minus modelled velocities. The *lighter red vectors* show APREF velocities minus modelled velocities

is more tectonically stable than Japan and New Zealand, there is still observable intraplate deformation that warrants a high precision kinematic model for the highest precision applications. Postseismic deformation is typically exponential in character and a third deformation mode defined by a grid of exponential decay parameters could also be implemented to model non-linear deformation arising from postseismic deformation where this is significant. In the Australian context, the magnitude of postseismic decay from regional earthquakes is at present not sufficiently significant to warrant separate inclusion in the Australian deformation model and is not discussed further.

The Australian continent lies wholly within the stable portion of the Australian tectonic plate. With the exception of isolated intraplate earthquakes e.g., Tennant Creek, Meckering, Newcastle (Leonard et al. 2007), no significant (>1.0 mm/year baseline changes across the continent) intraplate deformation between stable geodetic monuments fixed to bedrock has been observed in the interseismic period. Since the year 2000, large regional earthquakes along the margins of the Australian tectonic plate have resulted in observable far-field deformation at the millimetre level within the Australian Plate (Tregoning et al. 2013). Sites located on regolith and sedimentary basins where groundwater abstraction, coal seam gas extraction and underground mining is occurring are also subject to observable vertical deformation, however this deformation is localised.

The horizontal deformation components of the Australian kinematic model have been derived from the ITRF2008 Euler pole of the Australian plate (Altamimi et al. 2012) which has been computed by inversion of observed site velocities at a selection of geodetic monitoring stations across the Australian plate. These stations comprise of IGS Reference frame GNSS stations, SLR and VLBI stations. As the Australian plate is tectonically stable at the mm/year level, a 1° apriori grid of site velocities (topocentric East and North rates) was computed for each node covering the Australian continental landmass from the ITRF2008 plate model. The 1° grid resolution was chosen as it is the maximum grid size where a planar assumption of an ellipsoid does not propagate error during interpolation of the grid at a significant level. While the Australian continent is sufficiently tectonically stable to support a 1° grid, higher resolution grids are warranted in regions of higher relative deformation, or in urban areas and mines. In the absence of any apparent widespread vertical deformation beyond the 0.05 mm/year level within the Australian continent on geological timescales (Braun et al. 2009), the apriori vertical deformation model has been set to zero for all nodes.

Observed site velocities from 18 CORS comprising all of the fiducial CORS that define the Australian Datum (Geoscience Australia 2013) on the Australian continent (Fig. 1) were then selected to further refine the apriori ITRF2008 plate motion model by kriging of the residuals of observed site velocities (IERS 2014). All CORS selected

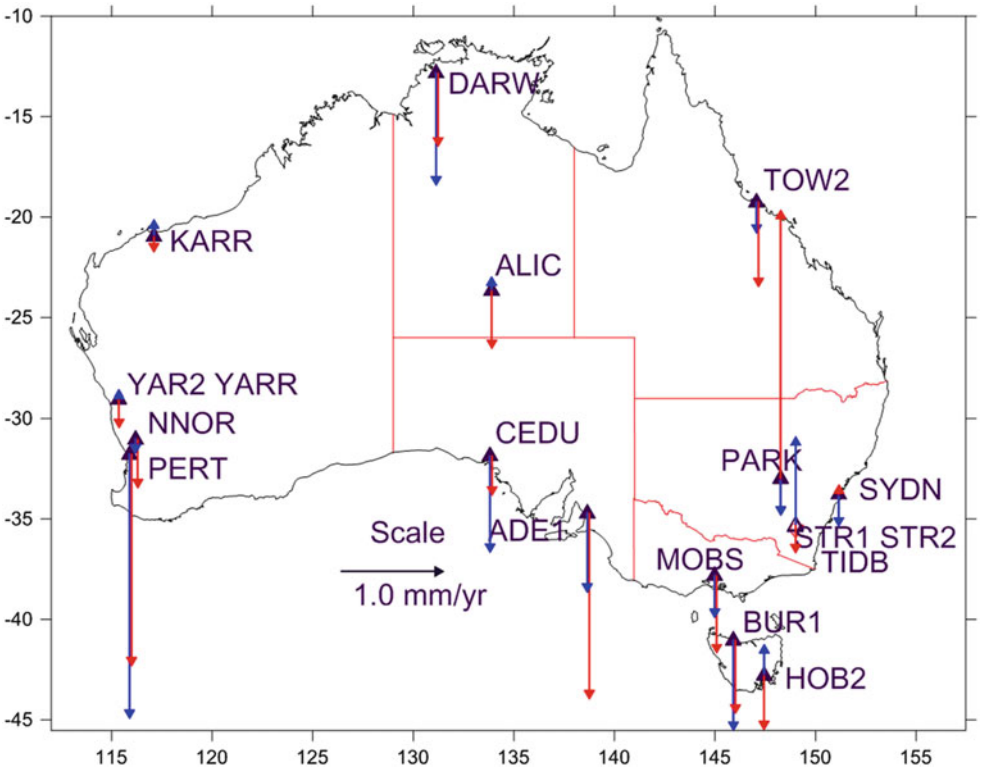

Fig. 2 Observed vertical (UP) velocities at Australian fiducial CORS. The *darker blue vectors* show ITRF2008 GPS published vertical velocities. The *lighter red vectors* show APREF observed vertical velocities

have observation spans greater than 8 years. For each of the CORS locations the site velocity was estimated from the ITRF2008 plate model and compared with the observed site velocity from Geoscience Australia's APREF data analysis (Geoscience Australia 2013).

The maximum differences between APREF and modelled apriori site velocities are 0.9 mm/year. The RMS of APREF site velocity differences is 0.2 mm/year over all of the CORS sites modelled and this provides a global level of uncertainty for site velocities estimated from the deformation model for bedrock locations. Between epochs 2013 and 1994 the site velocity model error has a global uncertainty of 6 mm at 95% CI for propagation back to the GDA94 reference epoch. Kriging using Surfer software (Golden Software 2013) was used to model and propagate site velocity differences over the Australian continent. The standard kriging technique with a variogram slope of 1 was used due to the sparsity of the network of CORS stations used.

The velocity model corrections were then applied to the apriori ITRF2008 plate model derived grid. This approach ensures that site velocities interpolated from the model are consistent with observed velocities of the fiducial CORS network.

Vertical deformation rates over the Australian continent (Fig. 2) are very poorly constrained due to the absence of long time series on a dense network of CORS stations, unmodelled seasonal deformation and other biases in vertical time series. A number of the fiducial CORS in Australia are located on clay-rich regolith or potentially unstable locations such as buildings and jetties (e.g., PERT, MOBS, ADE1, PARK and BUR1) and the vertical rates for these locations are strongly influenced by seasonal ground water and seasonal clay moisture variations. Large areas of the Australian continent are also overlain by clay-rich regolith and there are also extensive aquifers across the continental interior. Vertical deformation rates in these regions have yet to be determined with any precision and any continental scale vertical deformation model is contingent on the availability of accurate and widespread vertical deformation observations.

Figures 3 and 4 show topocentric East and North deformation rates for the Australian continent estimated from the ITRF2008 plate motion model with corrections applied from kriging of the residuals between observed and modelled site velocities at the fiducial CORS stations.

The computed site velocity model was then used to propagate the ITRF2008 APREF solution at epoch 2012.3 to epoch 1994.0 (consistent with the GDA94 reference epoch). The propagated coordinates were then compared with the latest published GDA94 coordinates for the fiducial network. The residuals between ITRF2008 at epoch 1994.0 and published GDA94 coordinates were then used to develop a continental displacement model, also using the kriging technique. The displacement model represents a coordinate shift to be applied to ITRF2008 coordinates at Epoch 1994.0 in order to estimate the equivalent GDA94 coordinates. The model essentially combines distortions and uncertainty in the original realisation of GDA94 with any episodic deformation

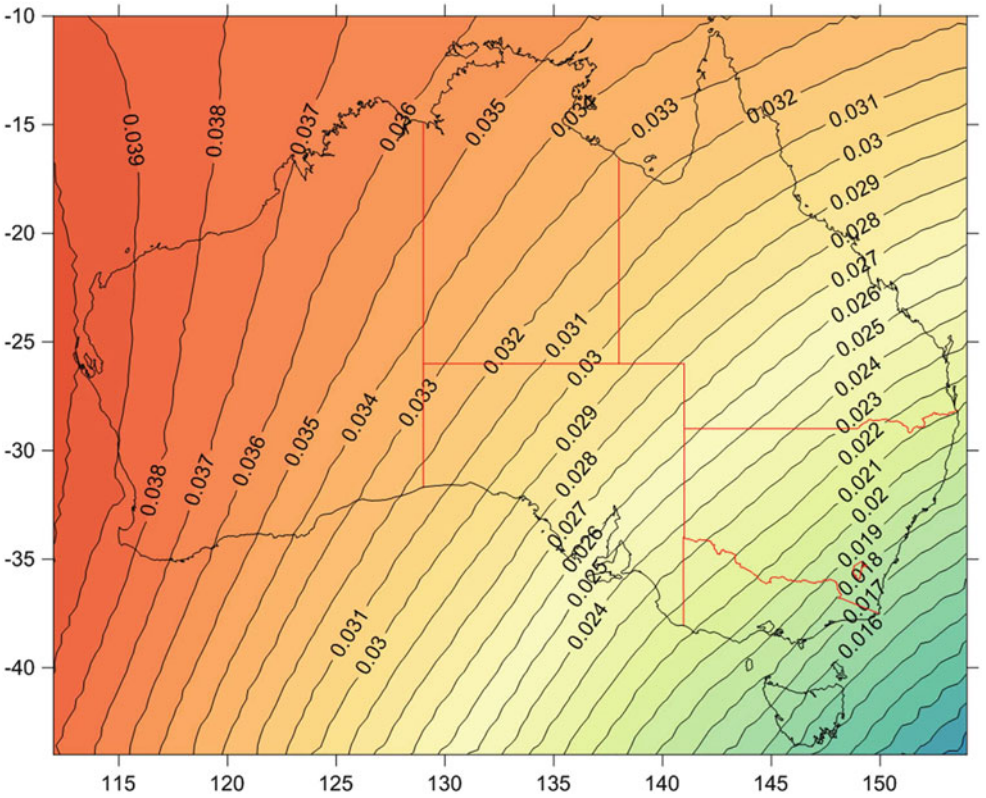

Fig. 3 Australian Kinematic Model – Topocentric East velocity (m/year)

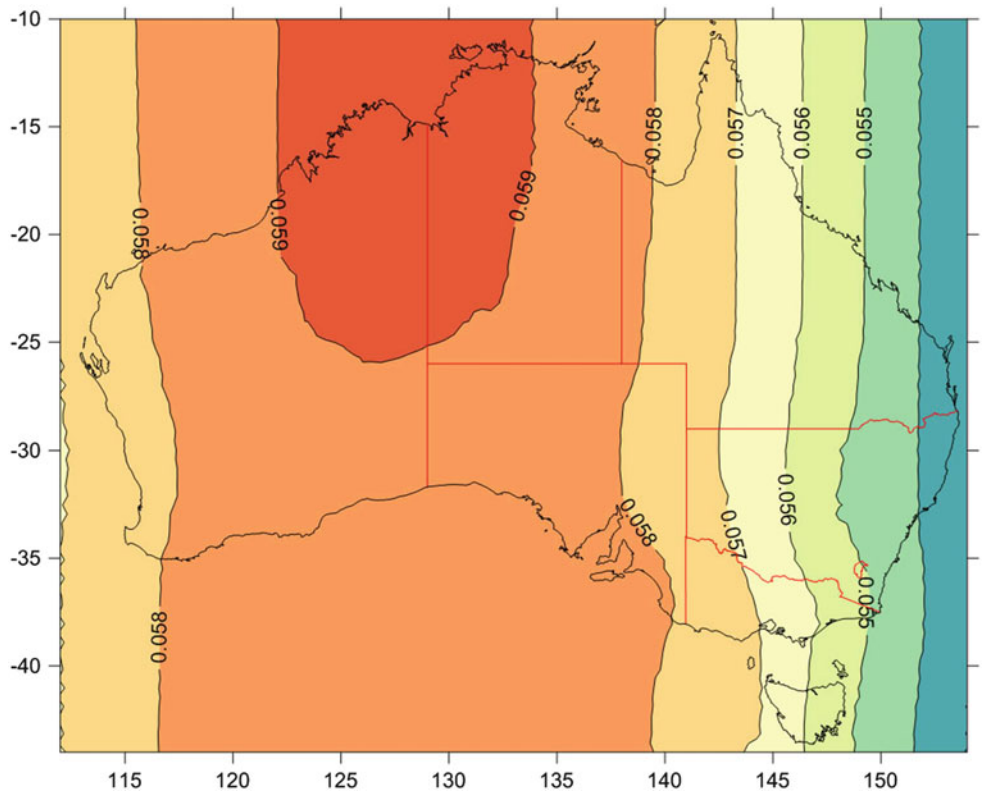

Fig. 4 Australian Kinematic Model – Topocentric North velocity (m/year)

that has occurred between 1994 and 2012, for example deformation arising from subsidence and regional earthquakes. The RMS of the displacement estimation (for bedrock sites) is 3 mm from the kriging analysis. Figures 5, 6, and 7 show the coordinate shift component of the deformation model for ITRF2008 (epoch 2012.3) propagation to published GDA94.

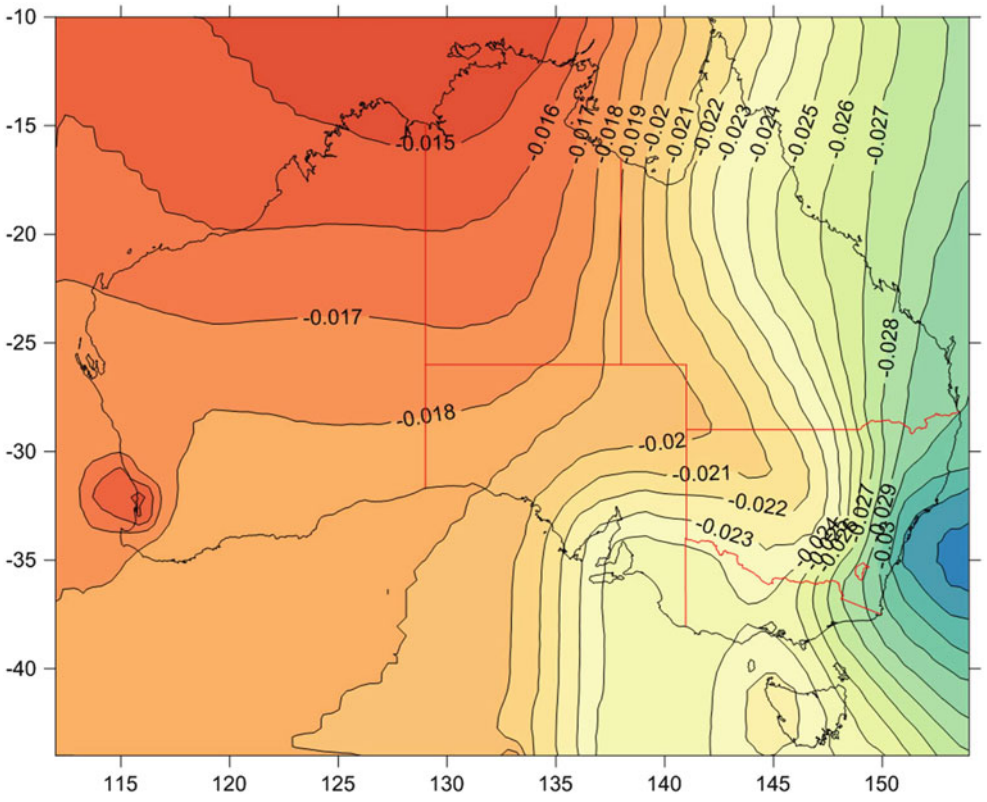

Fig. 5 GDA94 to ITRF2008(1994.0) Coordinate Shift East (m)

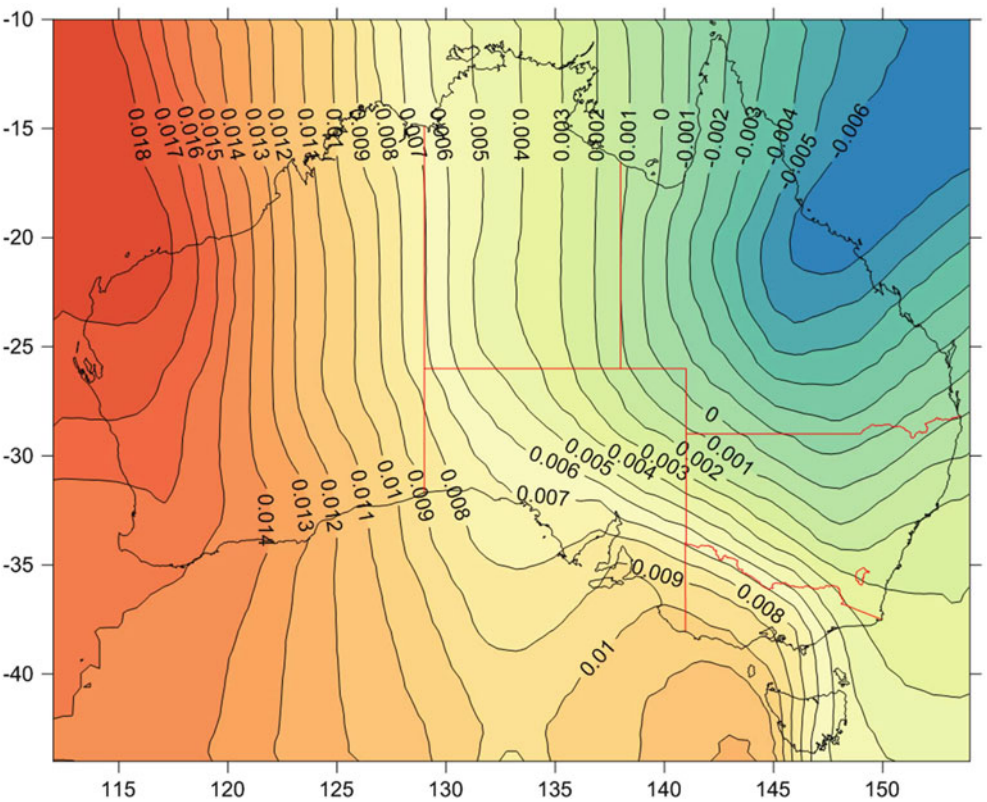

Fig. 6 GDA94 to ITRF2008(1994.0) Coordinate Shift North (m)

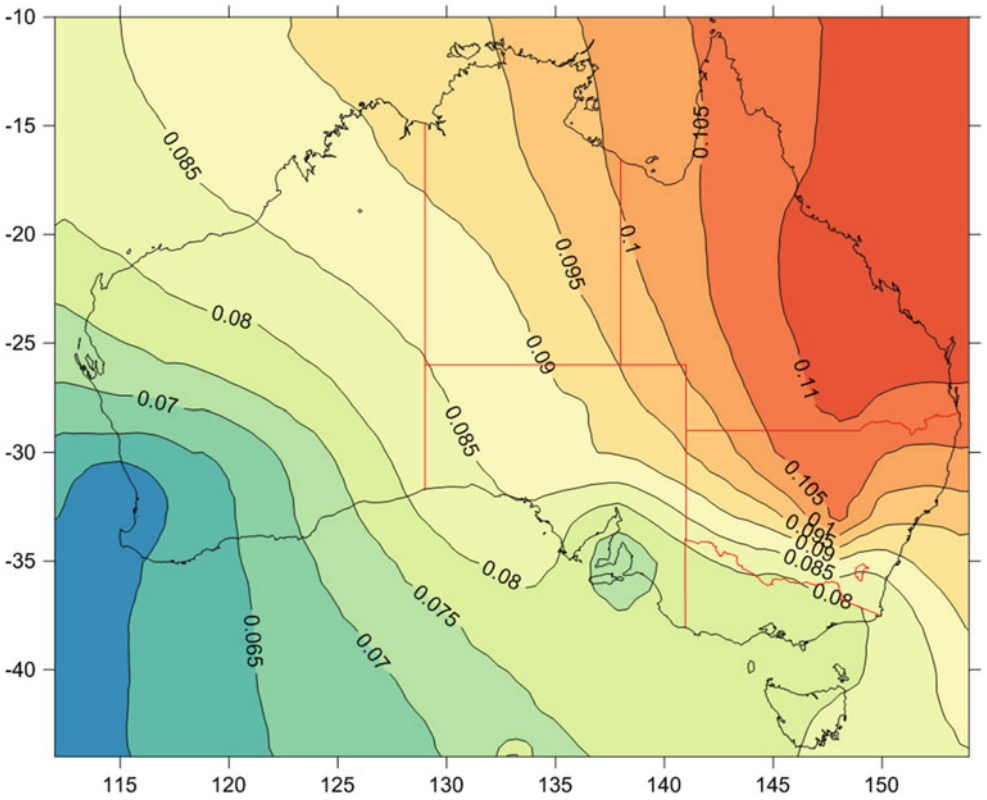

Fig. 7 GDA94 to ITRF2008(1994.0) ellipsoid height correction (Up) (m)

Table 1 Metadata format of the kinematic and displacement components of the model

Model name	Australian site velocity model	GDA94 to ITRF2008(1994.0) displacement model
Model datum (start)	ITRF2008	ITRF2008
Model datum (end)	ITRF2008	GDA94(2012 gazettal)
Model datum epoch (start)	1994.0	1994.0
Model datum epoch (end)	Not defined	1994.0
Grid size	1	1
Grid latitude (degrees) max	−10	−10
Grid latitude (degrees) min	−44	−44
Grid longitude (degrees) max	154	154
Grid longitude (degrees) min	112	112
Coordinate units	Decimal degrees	Decimal degrees
Velocity format	Topocentric	Topocentric
Velocity units	Metres	Metres
Interpolation method	Bi-linear	Bi-linear
Version	Version 201310101	Version 201310101
Release date	10th October 2013	10th October 2013
Model uncertainty at 95% CI	0.0004 m/year	0.005 m

4 Format and Application of the Model

The model is presented in a standard ASCII text format to enable conversion to other text or binary grid formats.

The header of the site velocity deformation grid file contains metadata shown in Table 1.

For each degree node of latitude and longitude, the following deformation data are provided:

Latitude, Longitude, East velocity, North velocity, Up velocity (for the site velocity model component) or Latitude,

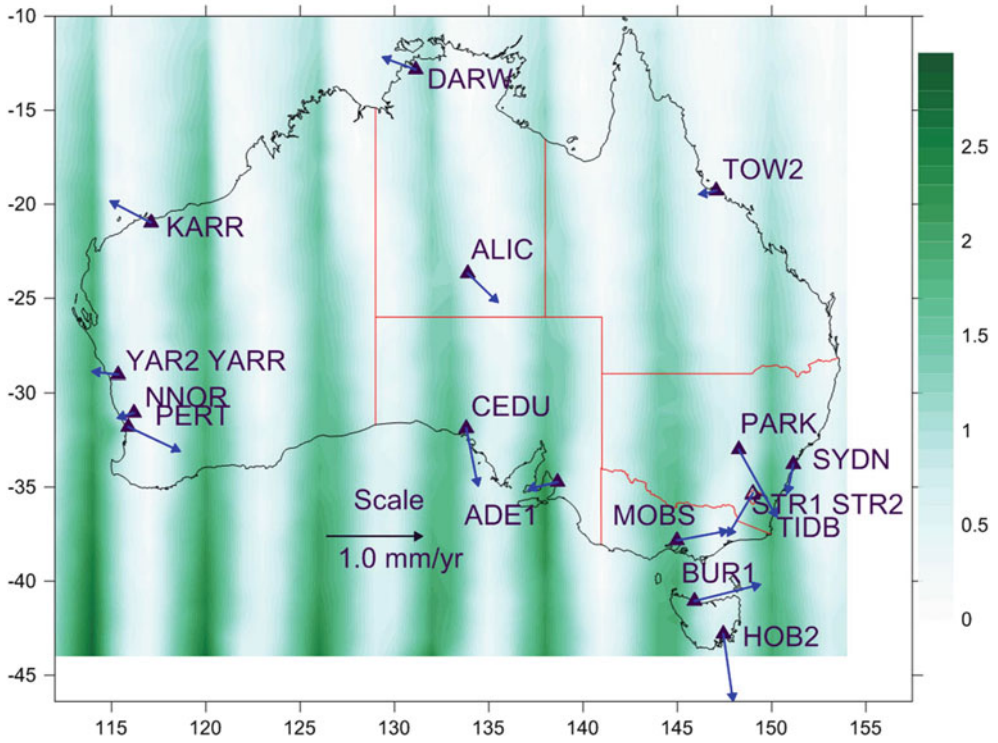

Fig. 8 Comparison of Australian kinematic model with the current 14 parameter model (Dawson and Woods 2010). Site velocity differences are shown by *green shading* (mm/year). *Blue vectors* show APREF site velocities minus velocities estimated from the 14 parameter model

Longitude, East translation, North translation, Up translation (for the displacement model component).

Propagation of ITRF coordinates at a specific epoch to GDA94 is accomplished as follows:

1. ITRF coordinates are converted to decimal degree format
2. The site velocity grid is interpolated (using bi-linear method) to extract the topocentric site velocities for that location
3. The topocentric rates are converted to ellipsoidal (latitude and longitude) coordinate rates
4. The coordinates at epoch 1994 are estimated by applying the computed deformation
5. The patch model grid is interpolated (using bi-linear method) to extract the topocentric shifts
6. The shifts are converted to ellipsoidal (latitude and longitude) format
7. The shift is applied to the 1994 epoch propagation to derive coordinates consistent with GDA94.

Propagation of ITRF coordinates to other epochs can also be accomplished using the site velocity model and other patch models that include net episodic deformation between specified epochs. These patch models would be of a similar format to the one presented here for ITRF to GDA94 propagation.

5 Comparison with Existing Models

The gridded deformation model described was compared with both the ITRF2008 Euler Pole and the latest 14 parameter models (Dawson and Woods 2010). Figure 8 shows the magnitude of site velocity differences between this deformation model and the 14 parameter model.

6 Conclusion

The Australian kinematic model described here enables propagation of ITRF coordinates from any specified epoch to GDA94, which is a realisation of ITRF92 at Epoch 1994.0. Two modes of deformation are represented by the model, secular interseismic motion via a site velocity model, and episodic deformation combined with modelled distortion via a displacement model. The gridded deformation model approach has potential advantages over classical conformal transformation strategies such as the 14-parameter model in that localised deformation can be isolated within the model. The grid approach allows for denser nested grids than the model presented (where sufficient sites with site velocities

are available) to better model deformation where there is a greater requirement for precision, or where deformation is more spatially variable. The gridded approach is also well suited to incorporation in personal navigation devices, GIS and surveying software.

One of the main advantages of a two component deformation model is that it can enable ITRF positioning to be related with centimetre precision to a digital map base or spatial data base fixed at a specified reference epoch. A disadvantage of the 14-parameter model is that localised or non-linear deformation at any sites used in the inversion of the parameter estimation will propagate into the model. In this paper, the stability of the Australian plate can support a fixed reference epoch for a number of decades before the most stringent positioning tolerances are exceeded.

The models can be improved as more quality geodetic data become available. Integrity monitoring at CORS can be achieved by comparing deformation model predictions with the latest ITRF coordinate solutions for the monitoring stations.

References

Altamimi Z, Métivier L, Collilieux X (2012) ITRF2008 plate motion model. J Geophys Res 117, B07402. doi:10.1029/2011JB008930

Braun J, Burbidge D, Gesto F, Sandiford M, Gleadow A, Kohn B, Cummins P (2009) Constraints on the current rate of deformation and surface uplift of the Australian continent from a new seismic database and low-T thermochronological data. Aust J Earth Sci 56:99–110

Commonwealth of Australia (2012) ComLaw, National Measurement Act 1960 - Recognized-value standard of measurement of position (No. 1)

Commonwealth of Australia (2013) Geoscience Australia AUSPOS online GPS processing service. http://www.ga.gov.au/earth-monitoring/geodesy/auspos-online-gps-processing-service.html. Accessed 30 Oct 2013

Crook C, Donnelly N (2013) Updating the NZGD2000 deformation model. Proceedings of the 125th annual conference of the New Zealand Institute of Surveyors (NZIS), 28–31 August 2013, Dunedin, New Zealand

Dach R, Hugentobler U, Fridez P, Meindl M (eds) (2007) Bernese GPS software version 5.0. User manual, Astronomical Institute, University of Bern

Dawson J, Woods A (2010) ITRF to GDA94 coordinate transformations. J Appl Geod 4(4):189–199

Geoscience Australia (2013) APREF network solution. ftp://ftp.ga.gov.au/geodesy-outgoing/gnss/solutions/misc/combination.xyz.vel. Accessed 30 Oct 2013

Golden Software (2013) Surfer 11. Accessed 30 Oct 2013

US Government (2013) National geodetic survey (NGS) OPUS online positioning user service. http://www.ngs.noaa.gov/OPUS/. Accessed 30 Oct 2013

Government of Canada (2013) Natural resources Canada (NRCan) precise point positioning. http://webapp.geod.nrcan.gc.ca/geod/tools-outils/ppp.php. Accessed 30 Oct 2013

Haasdyk J, Janssen V (2012) Site transformation: a block shift in thinking. Proceedings of association of public authority surveyors conference (APAS2012), 19–21 March 2012, Wollongong, Australia, pp 29–47

Haasdyk J, Roberts C (2013) Monitoring station movement using a state-wide simultaneous 'adjustment of everything' – implications for a next-generation Australian datum. Proceedings of IGNSS Symposium 2013 (IGNSS2013), 16–18 July 2013, Gold Coast, Australia, p 15

Hiyama Y, Yamagiwa A, Kawahara T, Iwata M, Fukuzaki Y, Shouji Y, I Sato Y, Yutsudo T, Sasaki T, Shigematsu H, Yamao H, Inukai T, Ohtaki M, Kokado K, Kurihara S, Kimura I, Tsutsumi T, Yahagi T, Furuya Y, Kageyama I, Kawamoto S, Yamaguchi K, I Tsuji H, Matsumura S (2011) Revision of survey results of control points after the 2011 off the Pacific Coast of Tohoku Earthquake. Bull GSI 59, Geospatial Information Authority of Japan

IERS (2014) ITRF 2008 GNSS SSC position and velocity table. http://itrf.ensg.ign.fr/ITRF_solutions/2008/doc/ITRF2008_GNSS.SSC.txt. Accessed 28 Apr 2014

Intergovernmental Committee on Surveying and Mapping (ICSM) (2013) Geocentric datum of Australia 1994 (GDA94). http://www.icsm.gov.au/gda/. Accessed 30 Oct 2013

Land Information New Zealand (LINZ) (2013) NZGD2000 deformation model. http://apps.linz.govt.nz/ftp/geodetic/nzgd2000_deformation_20130801_full.zip. Accessed 30 Oct 2013

Leonard M, Robinson D, Allen T, Schneider J, Clark D, Dhu T, Burbidge D (2007) Toward a better model of earthquake hazard in Australia, continental intraplate earthquakes: science, hazard, and policy issues. The Geological Society of America, Special Paper 425

Stanaway R, Roberts CA (2010) CORS network and datum harmonisation in the Asia-Pacific region, FIG Congress 2010, Sydney, Australia

Stanaway R, Roberts CA (2011) ITRF transformations in deforming zones to support CORS-NRTK applications. Proceedings of the international global navigation satellite systems society (IGNSS) symposium 15–17 November 2011, Sydney, Australia

Stanaway R, Roberts CA, Blick G (2014) Realisation of a geodetic datum using a gridded absolute deformation model (ADM). Willis P (eds) Earth on the edge: science for a sustainable planet proceedings of the IAG General Assembly, Melbourne, Australia, June 28 - July 2, 2011. International Association of Geodesy Symposia, vol 139, Rizos, Chris

Tregoning P, Burgette R, McClusky SC, Lejeune S, McQueen H, Watson CS (2013) A decade of horizontal deformation from great earthquakes. J Geophys Res. doi:10.1002/jgrb.50154

Winefield R, Crook C, Beavan J (2010) The application of a localised deformation model after an earthquake. FIG Congress 2010, Sydney, Australia

Interaction Between Subdaily Earth Rotation Parameters and GPS Orbits

Natalia Panafidina, Urs Hugentobler, and Manuela Seitz

Abstract

In this contribution we study the influence of the subdaily model for Earth rotation parameters (ERPs) on the GPS (Global Positioning System) solution and the dynamical reference frame realized by the GPS orbits. As input data we use a long term time series of daily normal equation systems (NEQ) obtained from GPS observations from 1994 till 2007 where ERPs are set up with 1-h resolution. The subdaily ERP model which was used in the processing in general cannot be replaced on the NEQ-level by another model as long as it is not present in the NEQ explicitly as a set of parameters. In our case the high temporal resolution of the ERPs allows the transformation of the ERPs into tidal terms which then can be kept fixed to new a priori values. To study the influence of individual tidal terms on the solution we change successively a priori values for one tidal term in polar motion and compare the resulting solutions for GPS orbits, station coordinates and ERPs. We show that changes in a priori subdaily polar motion lead to a common rotation of the whole GPS constellation with periods defined by the respective tidal frequencies. Time series of all the estimated parameters also show variations with respective periods.

Keywords

Dynamical reference frame • Earth rotation parameters • Subdaily tidal models • Terrestrial reference frame

1 Introduction

In processing GPS observations the Earth rotation parameters (ERPs) are usually estimated once per day, whereas the subdaily part of the variations in the Earth rotation is kept fixed to an a priori model. Different subdaily models can be used in processing. Currently there is a commonly accepted model recommended by the International Earth Rotation and Reference Systems Service (IERS) which contains terms in polar motion (PM) and Universal Time (UT1) on tidal frequencies (Petit and Luzum 2010). This model represents the theoretically computed effect of ocean tides on the Earth rotation and has errors supposedly up to 20% (Griffiths and Ray 2013) due to uncertainties of the underlying ocean model, it also does not contain the effects of other geophysical phenomena like atmospheric tides, so it may be subjected to changes in the future.

Another issue is the high-frequency part of nutation which is called libration. In accordance with the convention, nutation terms with periods longer than 2 days in the inertial space are taken into account by a nutation model, and nutation terms with shorter periods should be taken into account in terrestrial reference frame (TRF) by the ERPs. Libration terms have periods of half a day in inertial space, what corresponds to daily periods in TRF and contributes

N. Panafidina (✉) • M. Seitz
Deutsches Geodätisches Forschungsinstitut, Afons-Goppel-Str. 11, 80539 Munich, Germany
e-mail: panafidina@dgfi.badw.de

U. Hugentobler
Technische Universität München, Arcisstr. 21, 80333 Munich, Germany

© Springer International Publishing Switzerland 2015

C. Rizos, P. Willis (eds.), *IAG 150 Years*, International Association of Geodesy Symposia 143,
DOI 10.1007/1345_2015_180

to prograde daily PM and semi-daily UT1. The libration is computed theoretically and can be used in processing together with the IERS tidal model for subdaily ERPs. So, besides the possible change in the subdaily ERP model caused by changes in the ocean model, already now different solutions can be based on the IERS subdaily model with the libration effects added to the tidal model or not, what leads to different amplitudes for some tidal terms (Petit and Luzum 2010).

There are also different empirical tidal models computed from space geodetic techniques which can also be used as a priori subdaily models. These empirical models could be considered as a better approximation for the subdaily variations in the Earth rotation than the theoretical IERS tidal model, since space geodetic techniques see the integral effect of all physical phenomena causing Earth rotation variations and not only the effect of the ocean tides. Unfortunately, the empirical models depend noticeably on the processing strategies, contain technique-specific biases and usually show disagreement with each other and with the IERS tidal model (Artz et al. 2011; Panafidina et al. 2012).

In this study we investigate the effect caused by differences in the a priori subdaily models on the GPS solution, and more specifically we consider the question which systematic changes appear in the time series of the estimated parameters (station coordinates, GPS orbits and ERPs with 24 h resolution) when tidal terms in the a priori subdaily ERP model are changed.

2 Data Used and Procedure

The most direct way to study the influence of the a priori subdaily model on the GPS solution would be to compute different solutions starting from the observations using different subdaily models and then compare the solutions. But, since this way is rather time-consuming we chose another approach based on normal equations (NEQs). As data set we used free daily normal equations over the time span 1994–2007 obtained within the GGOS-D project (Rothacher et al. 2011). The parameters explicitly present in these daily NEQs are station coordinates, GPS orbits and ERPs with 1 h resolution. The IERS2003 subdaily ERP model was used and kept fixed in the processing and it is not possible to change the a priori values for this model directly in the initial NEQs, because the subdaily model is not present there as a set of parameters. But in our case, having ERPs with 1 h resolution in the normal equations, we can transform the ERPs into tidal terms because they are linearly dependent on each other (the transformation can be found in Artz et al. 2011). Having done this transformation we obtain the parameters of the subdaily ERP model explicitly in the NEQ, what allows us to change the a priori values for the tidal amplitudes and fix them to the new values (a general description of the NEQ transformation due to changes in a priori values for the parameters can be found in Thaller 2008). In this way we can obtain solutions which will refer to another a priori subdaily model. From each daily normal equation we compute station coordinates, GPS orbits, ERPs estimated as a linear function over 24 h, and in addition the geometrical geocenter was set up and estimated. To define the datum a no-net-rotation and a no-net-translation conditions were applied over a set of stable stations. Since UT1 in an absolute sense cannot be estimated from GPS observations, the value at the beginning of the day for the linear representation of UT1 was fixed to the a priori and the length of day (LOD) was estimated. For the GPS orbits usual constraints described in Springer et al. (1999) were applied: 6 Keplerian elements and 5 radiation pressure parameters (constant terms in three directions: D-direction to the Sun, Y-direction along the satellite solar panels and X-direction perpendicular to D- and Y-directions, as well as the sine and cosine amplitudes of a one-per-revolution acceleration in X-direction) were estimated freely, the sine and cosine amplitudes of one-per-revolution terms in Y- and D-directions were tightly constrained. Additionally stochastic pulses in three directions were set up each 12 h, the pulses in along-track and radial directions were estimated with a loose-constraint, and the pulses in out-of-plane direction were tightly constrained.

Using this procedure we computed from the input NEQs two sets of daily GPS solutions: first one with the standard subdaily model (IERS2010) and the second one with a changed subdaily model. To see a general mechanism how an individual tidal term influences the solution we change successively one term in polar motion by 100 μas and consider the differences in the parameter time series between these two sets of solutions, as well as the systematic changes in the dynamical reference frame realized by the GPS orbits. The value of 100 μas was chosen arbitrary, the only requirement was that the change in the subdaily model is big enough to see all possible effects in the estimated parameters.

3 Effects on the Dynamical Reference Frame Realized by GPS Orbits

In this section we study the systematic effect caused by the change in the subdaily ERP model on the GPS orbits and thus on the dynamical reference frame. Here we consider the Helmert parameters between two GPS orbits: the first one is computed with the standard subdaily model (IERS2010) and the second one with the model where one tidal term in PM was changed by 100 μas. We present results only for the case where the S1 tide (24.00 h) in PM was changed, but the general conclusions hold also for the case when other tidal terms are changed. In Fig. 1 we present the Helmert

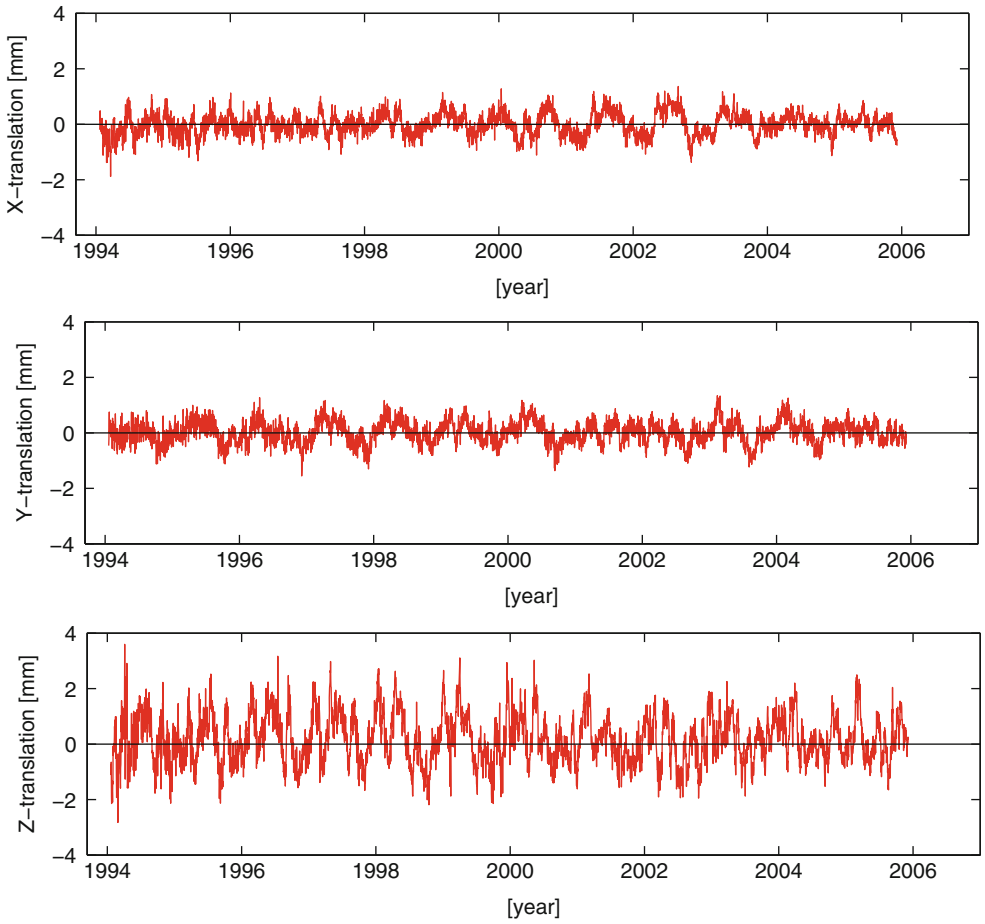

Fig. 1 Helmert parameters between GPS orbits computed with the standard subdaily model (IERS2010) and with a subdaily model with changed S1 term in polar motion: translations

translations between the two described solutions, and in Fig. 2 the Helmert rotations. As we can see, the change in the subdaily ERP model does not influence the position of the geocenter, the translations remain nearly unaffected, whereas the orientation of the satellite constellation as a whole shows noticeable periodic variations in X- and Y-directions. Z-rotation also remains unaffected by the PM change in the subdaily model. This common rotations appear also when other than S1 tidal terms in polar motion are changed, the period of the signal in rotations depend on the period of the changed tidal term.

It is not obvious why a change in the subdaily tidal model causes a common rotation of the whole GPS constellation, but this behavior can be explained if part of the prograde daily signal contained in the subdaily model for polar motion is mistaken in a 1-day solution for a retrograde diurnal signal. That would correspond to a relative periodic change in nutation offsets between GPS solutions with different subdaily models and explain the common rotation of the GPS constellation.

In the next section we consider the influence of this rotation of the dynamical reference frame on the estimated parameters such as station coordinates, GPS orbits and ERPs.

4 Effects on the Time Series of Estimated Parameters

In this section we consider time series of differences in estimated parameters between daily solutions computed with the standard subdaily model (IERS2010) and with the subdaily model where the S1 term in polar motion was changed by 100 μas.

4.1 Changes in the Estimated Orbit Parameters

First we consider the estimated orbit parameters which consist of 6 Keplerian elements and 5 freely-estimated radiation pressure parameters from the CODE radiation pressure model (Springer et al. 1999). Figure 3 shows the time series of differences in Keplerian elements for 3 satellites (PRN2, PRN5 and PRN22) from one orbital plane and Fig. 4 shows time series of differences in radiation pressure parameters for the same 3 satellites. As can be seen from the time series of differences in Keplerian elements the

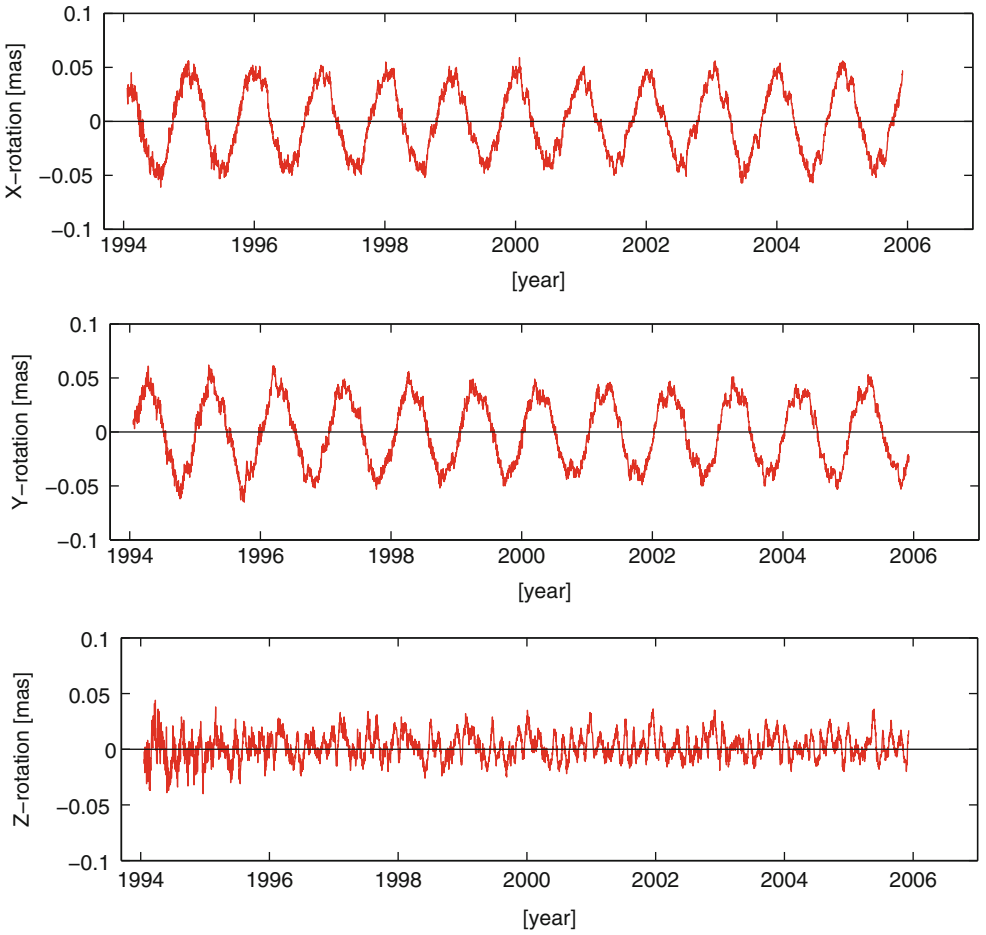

Fig. 2 Helmert parameters between GPS orbits computed with the standard subdaily model (IERS2010) and with a subdaily model with changed S1 term in polar motion: rotations

parameters defining the orientation of the orbital plane in space (inclination, right ascension of the ascending node) and argument of latitude are changing consistently for the shown three satellites, whereas the other three parameters are changing differently for different satellites. This consistent change in some Keplerian elements reflects the resulting common rotation of the GPS constellation shown in the previous section. In general, all the parameters, also the ones which change not consistently for different satellites, show systematic signals with periods depending on the period of the common rotation of the orbits. The situation is similar if we consider solutions where other tidal terms from the subdaily model are changed, but the periods of the signal appearing in the time series are different, as was mentioned before. The radiation pressure parameters show consistent changes only for the constant term in X-direction, other radiation pressure parameters seem not to contribute to the common rotation.

Another question is, whether the periodic signals observed in the parameter time series are significant or if they are below the noise level and can be neglected. The amplitude of the signal in, e.g., the semi-major axis is about 2 cm (see Fig. 3). That is a noticeable value, but the change in S1 tide in PM was also too big (100 μas) to be realistic, since we studied here only the general effect of the subdaily ERP model on GPS solutions. To estimate the possible realistic values of the changes in the subdaily model we have computed several empirical tidal models from GPS and VLBI observations and compared them with the IERS2010 tidal model, with each other and with some empirical models published by other authors. We found that there is a set of tidal terms which show big differences of about 10–30 μas for all considered solutions, these terms were S1 (24.00 h), K1 (23.93 h), S2 (12.00 h), K2 (11.97 h), M2 (12.42 h). We computed a test solution with the subdaily model where these terms were changed by 10–20 μas and compared it with the solution computed with the standard subdaily model. The amplitude of the signal in semi-major axis became respectively smaller, about 5 mm. This is below the current accuracy of the orbit determination, which is 2.5 cm (http://igscb.jpl.nasa.gov/components/prods.html), but it is above the noise-level of the time series of the semi-major axis estimates. A similar conclusion can be drawn for the signals seen in the other orbit parameters. That means that realistic changes in the subdaily ERP model are not of practical importance for the quality of the GPS solutions,

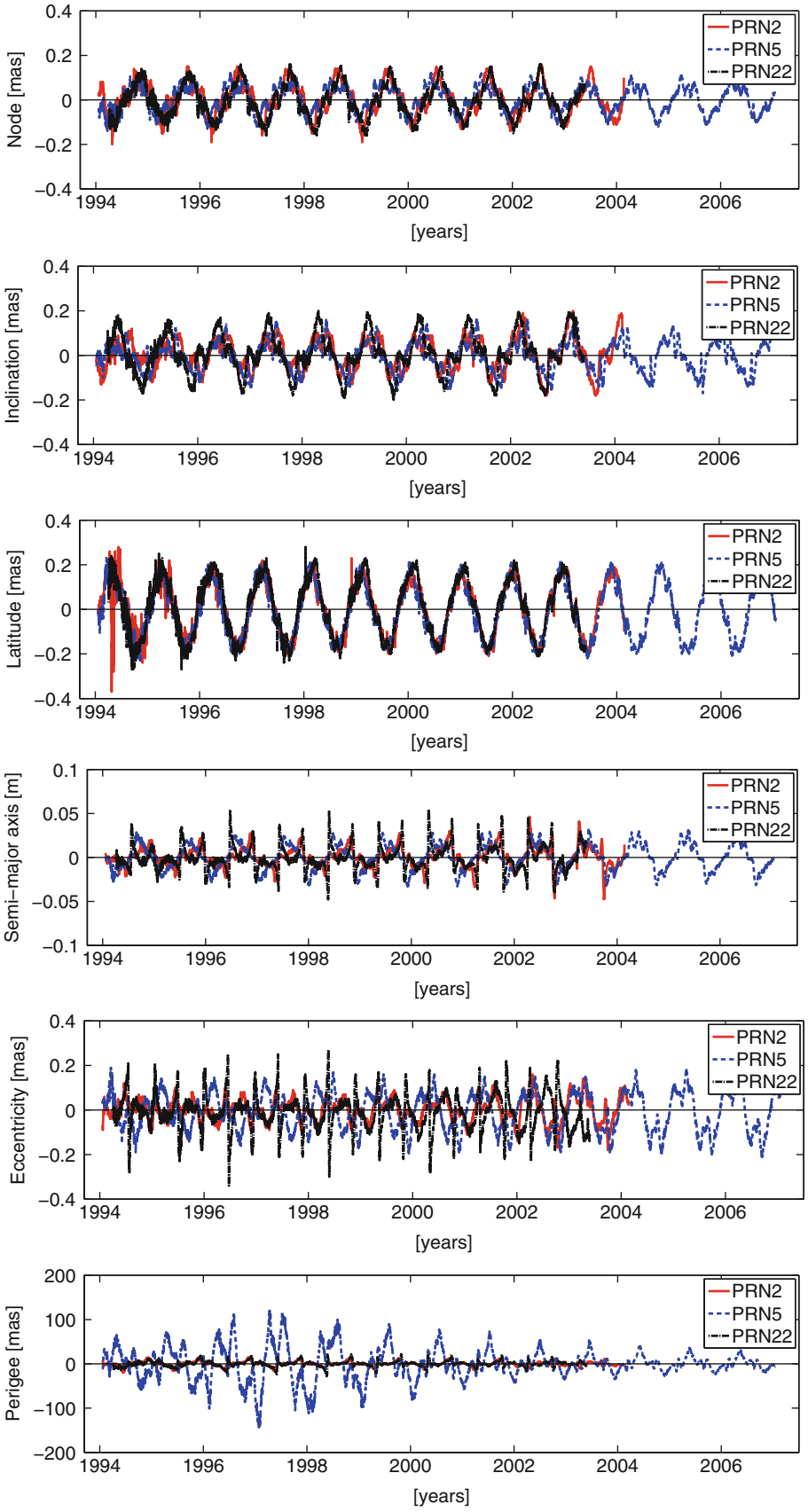

Fig. 3 Differences in Keplerian elements between GPS orbits computed with the standard subdaily model (IERS2010) and with a subdaily model with changed S1 term in polar motion: PRN2, PRN5, PRN22

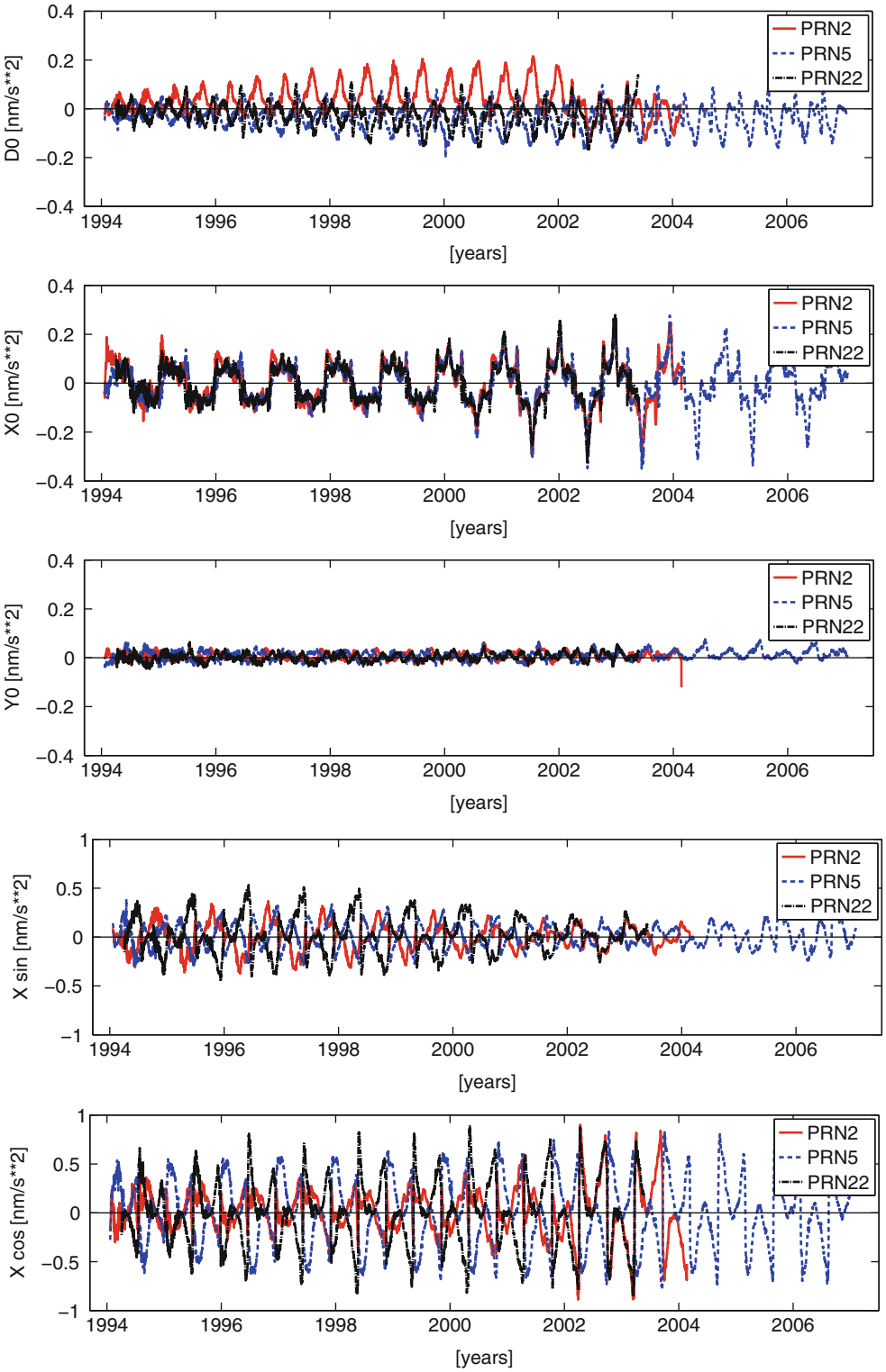

Fig. 4 Differences in radiation pressure parameters between GPS orbits computed with the standard subdaily model (IERS2010) and with a subdaily model with changed S1 term in polar motion: PRN2, PRN5, PRN22

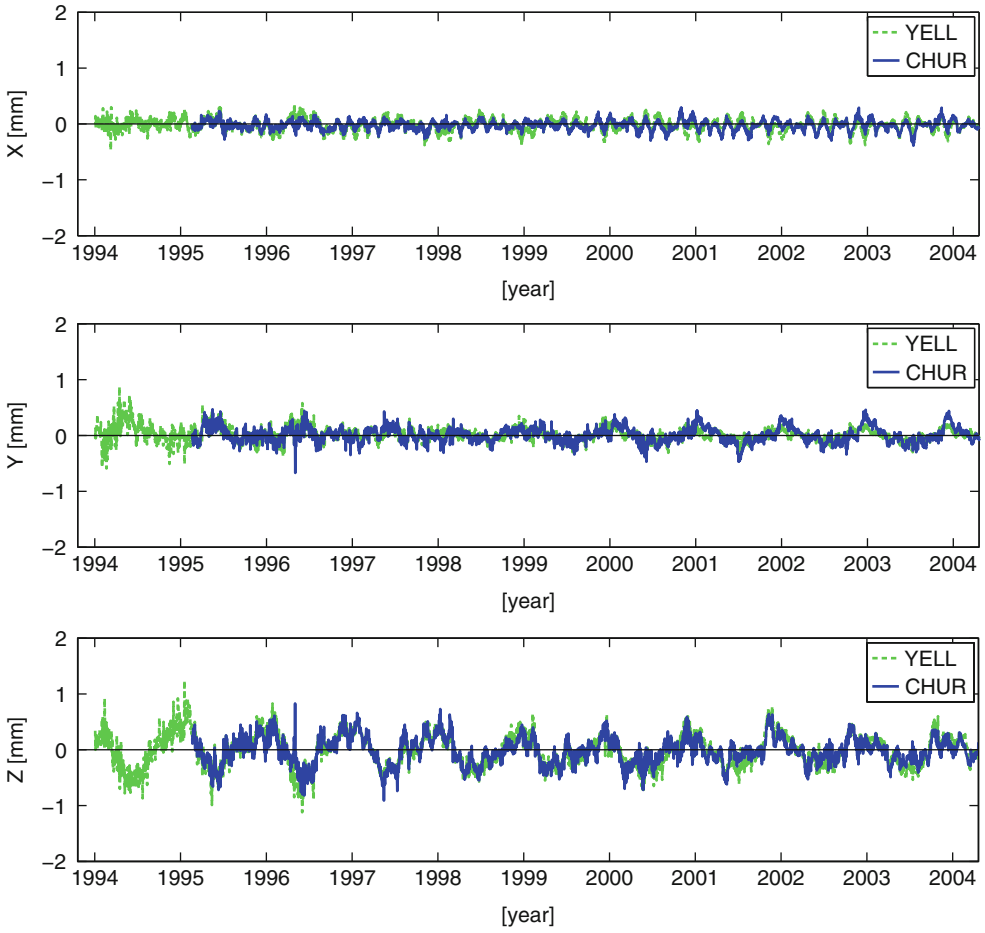

Fig. 5 Differences in station coordinates between GPS solutions computed with the standard subdaily model (IERS2010) and with a subdaily model with changed S1 term in polar motion: stations in Canada YELL and CHUR

but the comparison between estimated orbit parameters will demonstrate noticeable periodic differences.

4.2 Changes in the Estimated Station Coordinates

To see the influence of the changes in the subdaily ERP model on station coordinates we first consider the effect on the geometrical geocenter which was set up as a parameter and estimated from each daily NEQ. We have found that there is no noticeable signal in the time series of geocenter differences, so we may make a conclusion that there is no net-effect on the terrestrial reference frame caused by the changes in subdaily ERP model. When the differences in station coordinates are considered, we find that there is a small but systematic change with the same period as the period seen in the rotations of the GPS orbits. This change is very similar for stations located relatively close to each other in one region, and different for stations located in different regions. This leads to a conclusion that changes in subdaily model cause a global deformation in the estimated station coordinates. To demonstrate this effect we show in Fig. 5 coordinate differences for two stations Yellowknife (YELL) and Churchill (CHUR) both located in Canada, and in Fig. 6 coordinate differences for two stations Kokee Park (KOKB) and Mauna Kea (MKEA) both located in Hawaii. As we can see the changes are rather different for these two regions: for Canada the biggest variation appears in Z-component, for Hawaii the most prominent variation is in Y-component, but these variations are consistent within each region. On the other hand, the amplitude of the coordinate variations is very small (about 1 mm) even when the S1 tide in the subdaily model was changed by 100 μas. In the case of realistic changes in the subdaily model described in the previous subsection the coordinate differences would not be bigger than 0.3 mm.

4.3 Changes in the Estimated Earth Rotation Parameters

The Earth rotation parameters were estimated as a linear function over 24 h, what is equivalent to estimating one offset and one rate per day. In general, there are systematic variations in the estimated offsets and rates for polar motion with

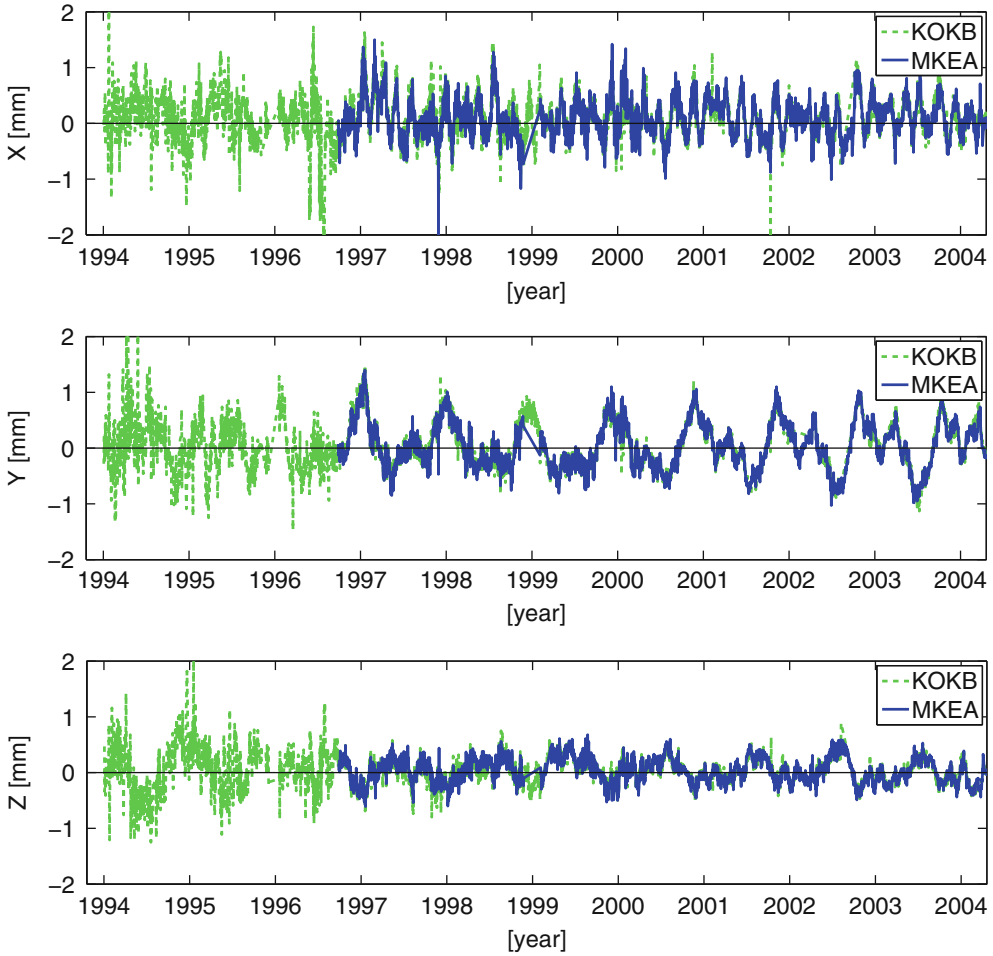

Fig. 6 Differences in station coordinates between GPS orbits computed with the standard subdaily model (IERS2010) and with a subdaily model with changed S1 term in polar motion: stations in Hawaii KOKB and MKEA

the period of the changed tidal term sampled each 24 h, while LOD estimates remain unaffected. The rates are affected noticeably on the level of 0.3 mas/day, whereas the offsets show smaller variations with amplitudes of 10 μas. Since the S1 term has a period of exactly 24 h, the changes in the daily ERPs estimates caused by the changed S1 term in the subdaily model are showing a constant shift in both offsets and rates. To demonstrate the periodic effects in the ERPs we show in Fig. 7 the differences in the estimated x-pole offsets and rates for the case where the P1 term (24.066 h) was changed, for this tidal term the signal appearing in the time series of x- and y-pole coordinates has a period of about a year.

5 Conclusions

For a 1-day GPS solution a change in the amplitude of some tidal terms for polar motion in subdaily ERP model does not affect the geocenter seen by the GPS constellation, but causes a common periodic rotation in the satellite orbits. In this way it causes periodic changes in the orientation of the dynamic reference frame realized by the orbits. The period of the signal depends on the period of the changed tidal terms, the observed period for the case when only the S1 term in polar motion is changed is about 365 days.

All the estimated parameters are sensitive to changes in the a priori ERP tidal model: there is a periodic signal seen in station coordinates, daily ERP offsets and rates and orbital parameters computed with different subdaily models. The amplitudes of the periodic signal in the orbit parameters are significant for the test case considered here with the S1 tide changed by 100 μas, e.g., the amplitude in semi-major axis is about 2 cm. In the case of realistic changes in the subdaily model of 10–20 μas for several major tidal terms the signal amplitudes become noticeably smaller and below the current accuracy of orbit determination. At the same time the amplitudes remain slightly above the noise level of the estimated orbit parameters. This means that the overall quality of the GPS solution will not be affected by a possible

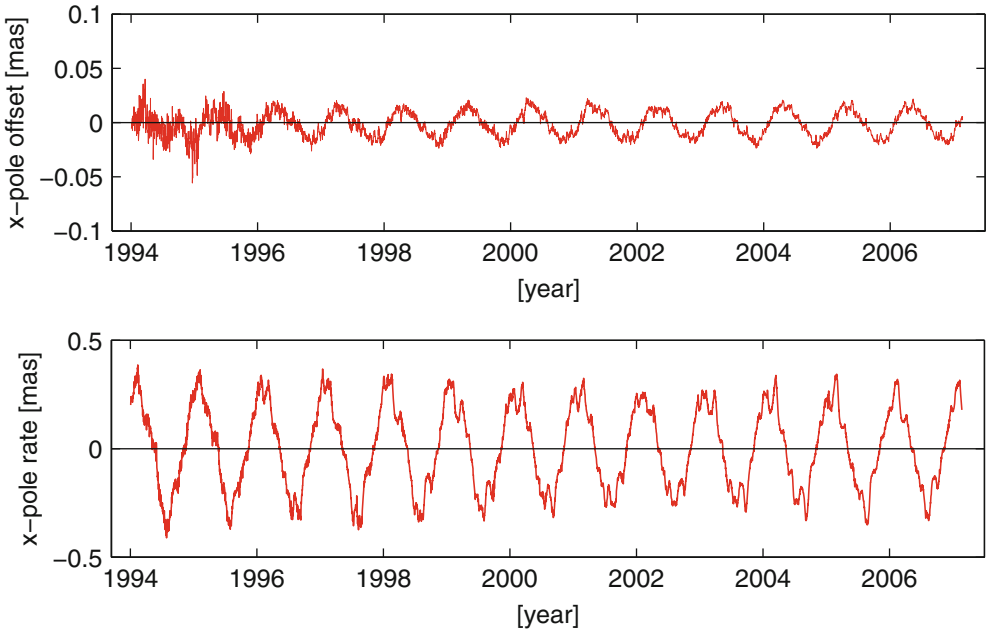

Fig. 7 Differences in x-pole offsets and rates between GPS solutions computed with the standard subdaily model (IERS2010) and with a subdaily model with changed P1 term in polar motion

(realistic) change in the subdaily model, but the comparison between solutions computed with different subdaily models will show noticeable periodic differences in the estimated parameters.

The periodic signals seen in station coordinates are showing a small but systematic global deformation, where the stations in the same regions are affected by the changes in subdaily model in a similar and consistent way. The amplitudes of this global deformation are small, 1 mm in our test case, and so will be well below 1 mm and negligible in the case of realistic changes in the subdaily model. The differences in the estimated geometrical geocenter show that there is no net-effect on the station coordinates.

The Earth rotation parameters show systematic changes in the daily estimates for polar motion, especially noticeable in the rates. The LOD estimates remain basically unaffected by the changes in polar motion of the subdaily model.

Acknowledgements This work was done within the research unit "Space-time reference systems for monitoring global change and for precise navigation in space" (FOR 1503) of the German Research Foundation (DFG) (Nothnagel et al. 2010).

References

Petit G, Luzum B (2010) IERS Conventions 2010, Verlag des Bundesamts für Kartographie und Geodäsie

Griffiths J, Ray J (2013) Sub-daily alias and draconitic errors in the IGS orbits. GPS Solution doi:10.1007/s10291-012-0289-1

Artz T, Tesmez nee Boeckmann S, Nothnagel A (2011) Assessment of periodic sub-diurnal Earth rotation variations at tidal frequencies through transformation of VLBI normal equation systems. J Geod doi:10.1007/s00190-011-0457-z

Panafidina N, Kurdubov S, Rothacher M (2012) Empirical model of subdaily variations in the Earth rotation from GPS and its stability. In: Proceedings of the "Journées 2011 Systèmes de Référence Spatio-Temporels", pp 148–151. Vienna University of Technology, Observatoire de Paris

Rothacher M, Angermann D, Artz T, Bosch W, Drewes H, Gerstl M, Kelm R, Koenig D, Koenig R, Meisel B, Mueller H, Nothnagel A, Panafidina N, Richter B, Rudenko S, Schwegmann W, Seitz M, Steigenberger P, Tesmer S, Tesmer V, Thaller D (2011) GGOS-D: homogeneous reprocessing and rigorous combination of space geodetic observations. J Geod. doi:10.1007/s00190-011-0475-x

Thaller D (2008) Inter-technique combination based on homogeneous normal equation systems including station coordinates, Earth orientation and troposphere parameters, Dissertation, Scientific Technical Report STR 08/15, Deutsches GeoForschungsZentrum, ISSN 1610-0956. doi:10.2312/GFZ.b103-08153

Springer T, Beutler G, Rothacher M (1999) Improving the orbit estimates of GPS satellites. J Geod. doi:10.1007/s001900050230

Nothnagel A, Angermann D, Börger K, Dietrich R, Drewes H, Görres B, Hugentobler U, Ihde J, Müller J, Oberst J, Pätzold M, Richter B, Rothacher M, Schreiber U, Schuh H, Soffel M (2010) Space-time reference systems for monitoring global change and for precise navigation. Mitteilungen des Bundesamtes für Kartographie und Geodäsie, Band 44, Verlag des Bundesamtes für Kartographie und Geodäsie, ISBN: 978-3-89888-920-9

A Geocenter Time Series from a Combination of LAGEOS and GRACE Observations

Rolf König, Christoph Dahle, Margarita Vei, and Karl-Hans Neumayer

Abstract

The geocenter motion can be inferred by evaluating Satellite Laser Ranging (SLR) observations to the LAGEOS satellites. Within the dynamic orbit determination process the degree 1 coefficients of a spherical harmonic expansion of the Earth's gravity field are estimated. In a combined approach covering the years 2006–2011, GRACE mission GPS, K-band inter-satellite range-rate, and SLR observations are added to the LAGEOS solution via normal equations to examine possible improvements of the geocenter estimates. The particular effects on the estimates by each of the GRACE observation types are analyzed and the combined solutions are assessed and discussed. It turns out that adding GRACE data degrades the LAGEOS geocenter time series while at the same time consuming considerable computational resources.

Keywords

Geocenter • GPS • GRACE • K-band inter-satellite ranging • LAGEOS • SLR

1 Introduction

Satellite Laser Ranging (SLR) observations to the LAGEOS (ILRS 2013) satellites are being evaluated for the determination of the geocenter motion since Watkins and Eanes (1997), a recent time series is published by Cheng et al. (2013). Geocenter motion is the result of mass redistributions in the Earth system, solutions of geocenter motion are therefore a valuable means to monitor seasonal variations (driven e.g. by atmosphere) and secular trends (driven e.g. by post-glacial uplift). The cannonball shaped satellite LAGEOS orbits the Earth since 1976. Its orbit is characterized by a semi-major axis of 12,270 km, an inclination of 109.8°, and an eccentricity of 0.004. Its twin LAGEOS-2 launched in late 1992 follows an orbit with a semi-major axis of 12,160 km, an inclination of 52.6°, and an eccentricity of 0.014.

R. König (✉) • C. Dahle • M. Vei • K.-H. Neumayer
GFZ German Research Centre for Geosciences, c/o DLR Oberpfaffenhofen, 82234 Wessling, Germany
e-mail: koenigr@gfz-potsdam.de

Based on LAGEOS SLR data we perform Precise Orbit and parameter Determination (POD) by our software system EPOS-OC (see Zhu et al. 2004). EPOS-OC employs a differential orbit and parameter improvement process where all the dynamic, geometric and measurement models are set up. This way the parameters of interest can be estimated along with the orbit. In order to derive the geocenter motion we take the dynamic approach and solve for the degree 1 terms of the gravity field. The C(1,1), S(1,1), and C(1,0) parameters represent the dynamic geocenter solution and correspond to X, Y, and Z coordinates of the geocenter relative to the network origin of a geometric solution. The dynamic geocenter parameters monitor the motion of the center of mass relative to the origin of the network. The problem coming along with this approach is that C(1,1), S(1,1), and C(1,0) become different from zero, therefore inertial space is left and centrifugal, Euler and Coriolis corrections need to be applied. Following König et al. (2015) these corrections are omitted here as we focus on seasonal variations where significant differences to those of a geometric solution are not observed.

© Springer International Publishing Switzerland 2015

C. Rizos, P. Willis (eds.), *IAG 150 Years*, International Association of Geodesy Symposia 143,
DOI 10.1007/1345_2015_24

Once the time series from LAGEOS data is available data from the twin satellite mission GRACE (Tapley et al. 2004) gathered over the period 2006–2011 are added to the LAGEOS solution. In principle GRACE data are available since 2002, but in view of the enormous amount of processing resources the analysis is restricted to 6 years which should allow deducing reliable numbers of annual and semi-annual variations. The idea is to check whether this Low Earth Orbiters (LEOs) could improve the geocenter estimates. Kang et al. (2007) conclude geocenter determination by GPS tracking of the GRACE satellites is possible to some extent. The weak point behind adopting LEO data in geocenter determination is that the LEOs are subject to much higher perturbing forces than the LAGEOS satellites which can hide or possibly destroy the geocenter signal. The GRACE twins are in orbit since 2002. They follow an orbit with a semi-major axis of 6,800 km, an inclination of 89.0°, and an eccentricity of 0.005.

The inclusion of the GRACE data into our LAGEOS geocenter solution is done in subsequent steps, firstly onboard GPS tracking data, then K-band inter-satellite range-rate (KRR) data, and finally SLR observations to the GRACE satellites are added. Proceeding this way the effect of each observation type can be assessed. We end with a comparison and conclusions.

2 Approach and Data

For LAGEOS POD the standards are chosen according to the International Earth Rotation and Reference Systems Service (IERS 2013) Conventions 2010 (Petit and Luzum 2010). Deviating from this we take for the gravity field model the static part of EIGEN-6C (Shako et al. 2014), for the a priori station coordinates the SLRF2008 (ILRS 2013) which is the adoption of the ITRF2008 (Altamimi et al. 2011) by the International Laser Ranging Service (ILRS, Pearlman et al. 2002), and for the Earth orientation parameters the "EOP 08 C04 (IAU2000)" series (IERS 2013). It should be emphasized that no mass variations due to non-tidal atmospheric pressure variations are modelled. Also station deformations due to atmospheric loading are not modelled.

For each arc (15-day arcs until 1992, 7-day arcs from 1993 onwards) Normal Equations (NEQs) are formed which among other parameters contain all the station coordinates involved and the degree 1 harmonic coefficients of the gravity field relevant for the time span of the arc. Also the degree 2–5 spherical harmonics are solved for in each arc. The degree 2 to 5 spherical harmonics are accumulated to monthly solutions, the degree 3 to 5 spherical harmonics and the station coordinates are accumulated to global solutions. The degree 2 coefficients are also solved for monthly because over the time span of the LAGEOS mission considerable variations are present (see Cheng and Tapley 2004) that need to be modelled.

As the degree 1 harmonics and the station coordinates are solved for concurrently a datum defect of six arises. So six Helmert conditions for translation and rotation are applied to all stations occurring over the analysis time span from 1983 to 2011. This leads to a solution in the SLRF2008 Terrestrial Reference Frame (TRF). It should be noted that global biases in the geocenter time series depend on the choice of the datum points (König et al. 2015).

As in König et al. (2015) 1,750,000 SLR Normal Points to LAGEOS from 1983 to 2011, and 1,165,000 to LAGEOS-2 from 1992 to 2011 are adopted for this analysis. The orbital fits of the operational analysis ranges around the centimeter from the advent of LAGEOS-2 onwards.

For GRACE POD standards identical to those for LAGEOS are adopted with one exception. As the GRACE orbits are determined with given GPS satellite ephemerides and clocks the TRF for GRACE is defined by the TRF used in the GPS POD. For GPS POD we use in general the IGS08 TRF (Rebischung et al. 2012) which is the adoption of ITRF2008 by the International GNSS Service (IGS, Dow et al. 2009). Though formally both SLRF2008 and IGS08 refer to the same TRF, namely the ITRF2008, differences between the two (and therefore between the LAGEOS and GRACE solutions) can not be excluded as the adoptions concern station discontinuities, station velocities and old or new stations not being part of ITRF2008. Also the mixture of errors in the GPS clocks, orbits and parameters such as tropospheric delays, radiation pressure mis-modelling etc. introduce biases in the datum implementation, some of which have long-wavelength nature and will ruin the consistency of the GPS-orbits-implied frame versus that defined by SLR and show up as long-wavelength artifacts.

The computational effort to include GRACE data is anyway quite noticeable. On a 2.5 GHz machine POD of one GRACE arc takes about 6 min and the generation of the NEQ about 12 min. So for a 1 year analysis where some 400 arcs (normally 1-day arcs but fraction of day arcs when GRACE observations show gaps) need to be processed, computation time amounts to nearly 5 days. For the 6 years of GRACE data over the period 2006–2011 24,000,000 space-borne GPS code and phase observations, 6,000,000 K-band inter-satellite range-rate observations, and 60,000 SLR Normal Points to the GRACE satellites are adopted. Counting the three observation type scenarios all in all about 90 days of computation time are spent.

The consecutive inclusion of the different GRACE observation types is realized via weighting. Those observation types that should not contribute to the solution are given an extremely large a priori sigma that implicitly leads to a weight close to zero. The weighting of the GRACE observation types is compiled in Table 1 below. The GRACE NEQs

Table 1 A priori weighting of GRACE data and a posteriori orbital fit RMS

	GRACE observation types used		
	GPS	GPS+KRR	GPS+KRR+SLR
A Priori sigma			
Code (cm)	70.0	70.0	70.0
Phase (mm)	7.0	7.0	7.0
KRR (μm/s)	∞	0.1	0.1
SLR (cm)	n.a.	∞	1.0
Orbital fit RMS			
Code (cm)	35.5	36.1	36.1
Phase (mm)	3.9	4.9	4.9
KRR (μm/s)	358	0.35	0.35
SLR (cm)	n.a.	4.3	1.0

from the daily and sub-daily arcs are accumulated to a NEQ that has essentially the same entries as the final LAGEOS NEQ: monthly degree 1 and 2 harmonics, and global SLR station coordinates. In the last step the GRACE NEQ is added as is to the LAGEOS NEQ and the combined NEQ is inverted eventually.

3 The Geocenter Solutions

Firstly we present the LAGEOS only geocenter solution. The full time series of geocenter estimates from 1993 onwards is given in Fig. 1.

Figure 2 provides for the GRACE analysis period 2006–2011 a visual comparison to the Cheng et al. (2013) time series where biases in both series are removed. The Cheng et al. (2013) time series is the one denoted RL05 from the GRACE Tellus site (GRACE 2013). The series agree obviously well in seasonal variation except for the period around New year 2010. Also our time series shows large extremal values for the C(1,0) or Z component in the early periods.

In order to quantify the different solutions, annual harmonic functions are fitted to the time series and compiled in Table 2. Fitting of semi-annual amplitudes and phases in addition to the annual ones does not lead to significantly different results. The fits are restricted to the GRACE analysis period 2006–2011. The Cheng et al. (2013) time series for this period and our LAGEOS solution are significantly different in amplitudes except for S(1,1) but agree in phases. It should be noted that the Cheng et al. (2013) time series analyzed here shows also significant differences in amplitude when compared to their originally published analysis values. From independent analysis one would expect values of around 3 mm in X, Y, and 5–6 mm in Z, from GPS, ocean bottom pressure, and GRACE data combinations something like 2–4 mm in X and Y, and 4–5 mm in Z (Wu et al. 2006), or 1–5 mm in X and Y, and 2–6 mm in Z (Rietbroek et al. 2012). The differences in amplitudes between the Cheng et al. (2013) and our time series can be attributed to the differences around New Year 2010, in case of C(1,0) also to the large extremal values of our solution. These large

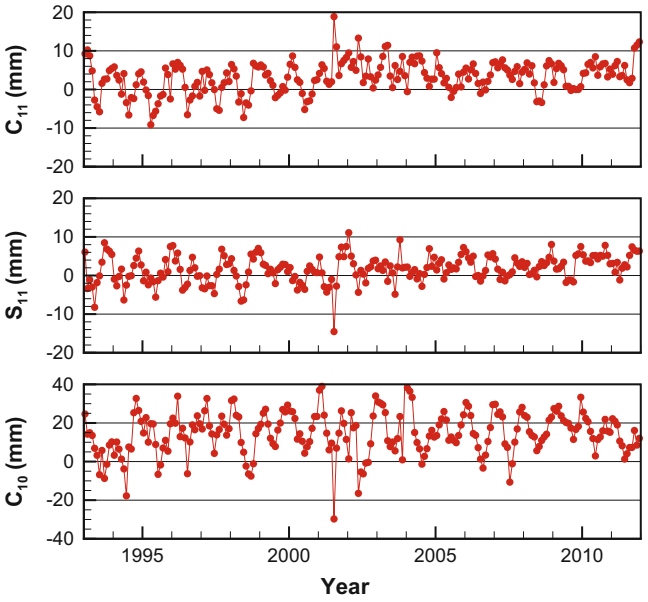

Fig. 1 The LAGEOS only geocenter time series

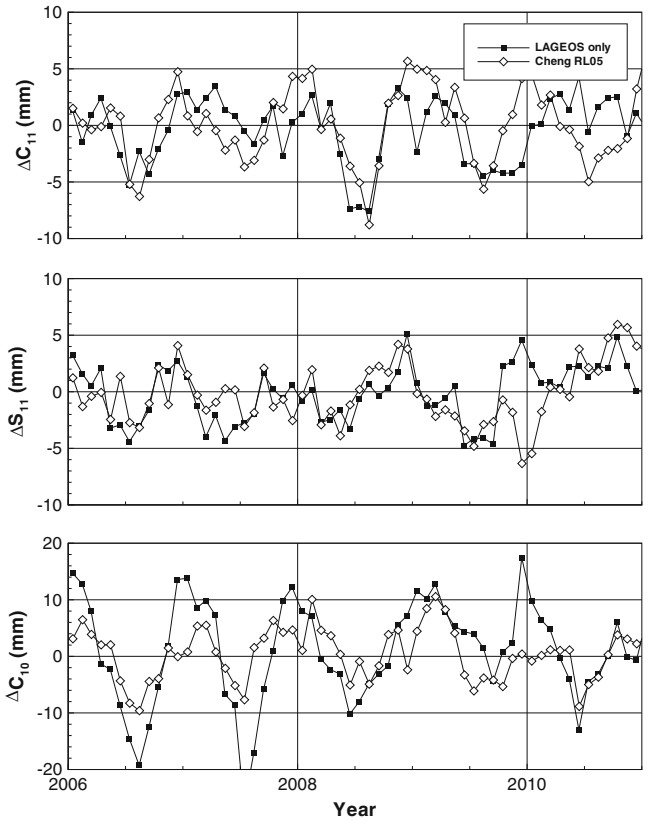

Fig. 2 The Cheng et al. (2013) time series and this LAGEOS solution

Table 2 Comparison of the LAGEOS and the LAGEOS+GRACE and the Cheng et al. (2013) solutions

	Cheng et al.	Cheng et al.	LAGEOS	LAGEOS+	LAGEOS+	LAGEOS+
	Article	RL05		GRACE.	GRACE.	GRACE.
	Monthly	Here		GPS	GPS.KRR	GPS.KRR.SLR
Ampl. $C_{1,1}$	2.9 ± 0.4	4.1 ± 0.4	1.9 ± 0.8	1.7 ± 0.3	1.6 ± 0.7	1.7 ± 0.6
Ampl. $S_{1,1}$	2.6 ± 0.2	1.5 ± 0.5	1.9 ± 0.6	1.8 ± 0.5	2.2 ± 0.6	2.3 ± 0.8
Ampl. $C_{1,0}$	4.2 ± 0.3	5.9 ± 1.4	10.4 ± 1.2	2.8 ± 0.7	2.1 ± 0.9	2.4 ± 0.8
Phase $C_{1,1}$	35 ± 3	61 ±5	50 ± 25	46 ± 12	57 ± 25	60 ± 21
Phase $S_{1,1}$	306 ± 2	323 ± 18	303 ± 17	310 ± 15	283 ± 16	289 ± 20
Phase $C_{1,0}$	33 ± 2	57 ± 13	71 ±7	63 ± 13	33 ± 25	50 ± 19

Amplitudes and their standard deviations are given in (mm), phases and their standard deviations in (degrees) relative to January 1

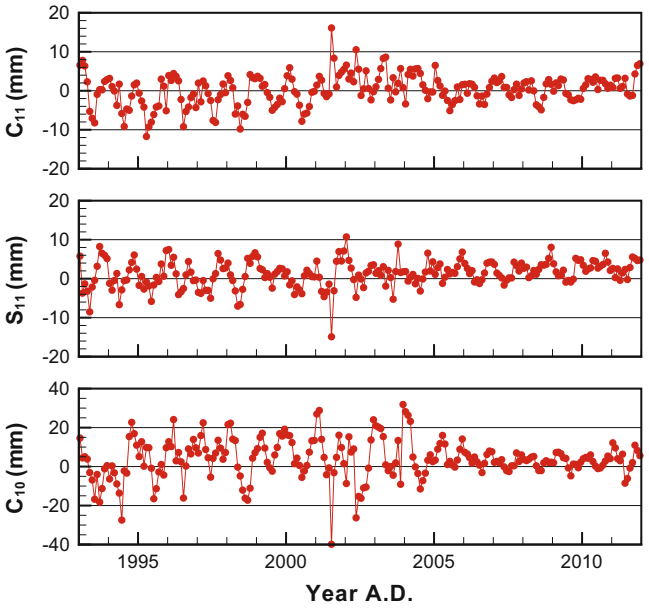

Fig. 3 The LAGEOS plus GRACE-GPS geocenter time series

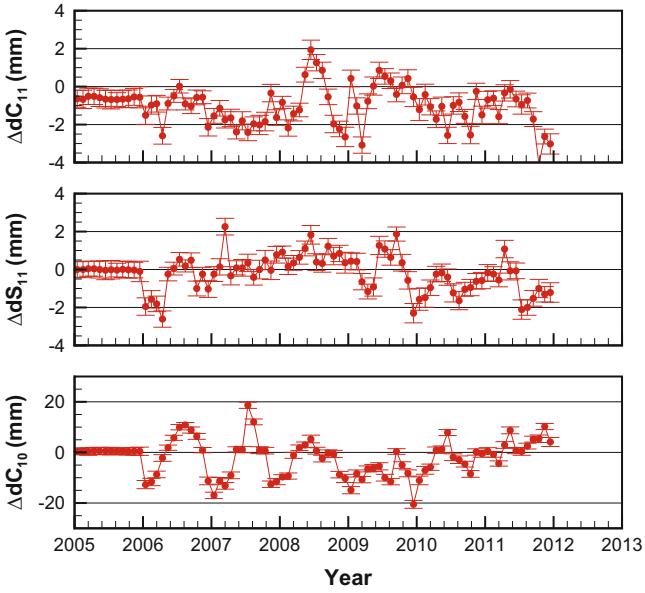

Fig. 4 Differences of the LAGEOS only to the LAGEOS plus GRACE-GPS geocenter time series

extremal values seem to appear individually during peak seasons, the reason for this being not clear but probably coming from some network effects in conjunction with some sensitivity of this approach.

The time series of geocenter solutions when GRACE-GPS data are added are given in Fig. 3. One can clearly see the differences for the GRACE analysis period 2006–2011. In particular all axes get dampened in amplitudes. The signal of the LAGEOS solution does not get completely destroyed as still significant annual amplitudes remain. Distinctly the C(1,0) series shows now amplitudes comparable in size to the other axes.

In order to make the differences more clear Fig. 4 displays just the differences of the LAGEOS only to the LAGEOS plus GRACE-GPS solutions. The variations of the differences are as large as the amplitudes of the LAGEOS only solution. The C(1,1) and S(1,1) differences look random mostly. The C(1,0) differences look like a seasonal signal in the first 3 years but change to random for the last 3 years. The conclusion from this is that the GRACE GPS observations just add more noise to the already noisy LAGEOS geocenter solution.

Figure 5 shows the differences of the LAGEOS only to the LAGEOS plus GRACE-GPS and -K-band geocenter solutions. The character of the differences time series remains similar to that in Fig. 4 where however variations are increased. Disastrously a significant change of the bias becomes obvious when looking at the differences for year 2005 where no GRACE data are employed. This means that adding of the GRACE data and specifically the K-band data has a significant impact on the datum now. The reason could come from the difference of the TRFs of the LAGEOS and the GRACE solutions as indicated previously, even when the culprit data are not present, only through the correlations.

Figure 6 presents the differences of the LAGEOS only to the LAGEOS plus GRACE-GPS and -K-band and -SLR

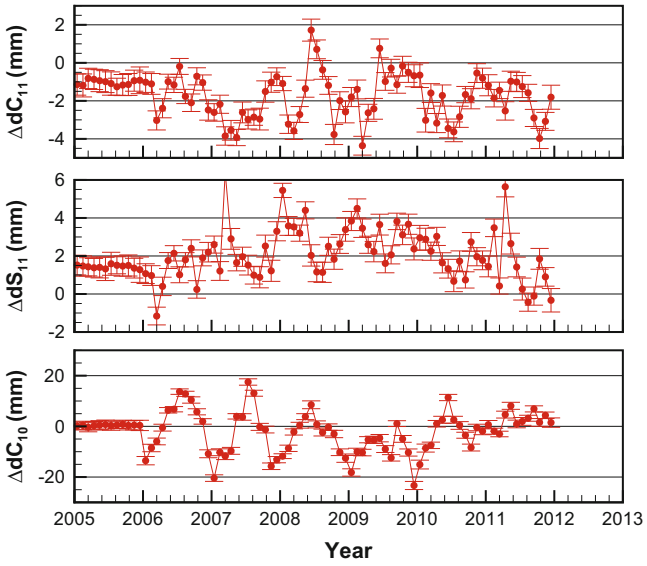

Fig. 5 Differences of the LAGEOS only to the LAGEOS plus GRACE-GPS and -K-band geocenter time series

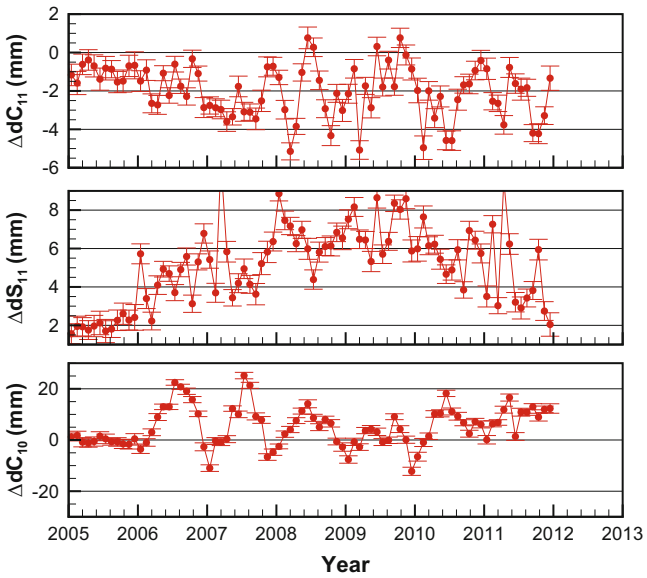

Fig. 6 Differences of the LAGEOS only to the LAGEOS plus GRACE-GPS, -K-band and -SLR geocenter time series

geocenter solutions. The character of the differences time series again remains similar to those in Figs. 4 and 5 with even more pronounced deviations. So all in all concluding from the differences it seems that adding GRACE data this way has a adverse impact on the LAGEOS geocenter time series.

Figure 7 exhibits the orbital fits of all GRACE observations types for all arcs where all GRACE observation types are taking place in the adjustment process. The overall RMS values of the GPS code observations, the GPS phase observations, the K-band range-rates, and the SLR ranges are compiled in Table 1 for the consecutive steps of the analysis together with the a priori weighting. It can be seen that code and phase RMS are slightly increased when K-band and SLR observations are added. Indeed K-band and SLR observations take a prominent role what is underlined by their a posteriori RMS values. From the difference in SLR fits one sees that the two orbits GPS+KRR and GPS+KRR+SLR, are markedly different and most likely not just in terms of the mean, but also in higher frequencies. In turn this transfers into the geocenter time series. The long-term periodic variations in code and phase RMS (also partly visible in the SLR RMS) are induced by mis-modelled solar radiation effects on the GPS ephemerides and clocks. Also this transfers into the geocenter time series.

When GRACE data are added to the LAGEOS solution the amplitudes in the C(1,0) component drop down to the size of the amplitudes in the other components. Unlike the case presented by Kang et al. (2007), where the Z component can not be recovered from GRACE GPS tracking data only, still a significant signal remains in the combined LAGEOS and GRACE solutions.

All phases reported in Table 2 agree well given their large uncertainties. In contrast to Kang et al. (2007), who report problems in determining the phases from GRACE GPS tracking only, here the LAGEOS solution is strong enough to not let the GRACE data change the phases significantly.

4 Conclusions

LAGEOS and LAGEOS-2 data up to 2011 are processed in order to derive a geocenter time series expressed in the dynamic parameters C(1,1), S(1,1) and C(1,0). GRACE data over the period 2006–2011, in sequence GPS tracking data, K-band range-rate data, and SLR data, are added to the LAGEOS solution. In all cases the GRACE data do not lead to an improvement of the LAGEOS geocenter solution. Indeed the LAGEOS geocenter signal gets considerably degraded. Also changes in biases of the geocenter series become evident seemingly implied by long-term biases in the GPS TRF implementation transferred through correlations by the GRACE data.

Acknowledgements GPS and SLR data, station coordinates and Earth orientation parameters are provided by IGS, ILRS, and IERS of the International Association of Geodesy (IAG). We would like to thank the German Space Operations Center (GSOC) of the German Aerospace Center (DLR) for providing continuously and nearly 100% of the raw telemetry data of the twin GRACE satellites.

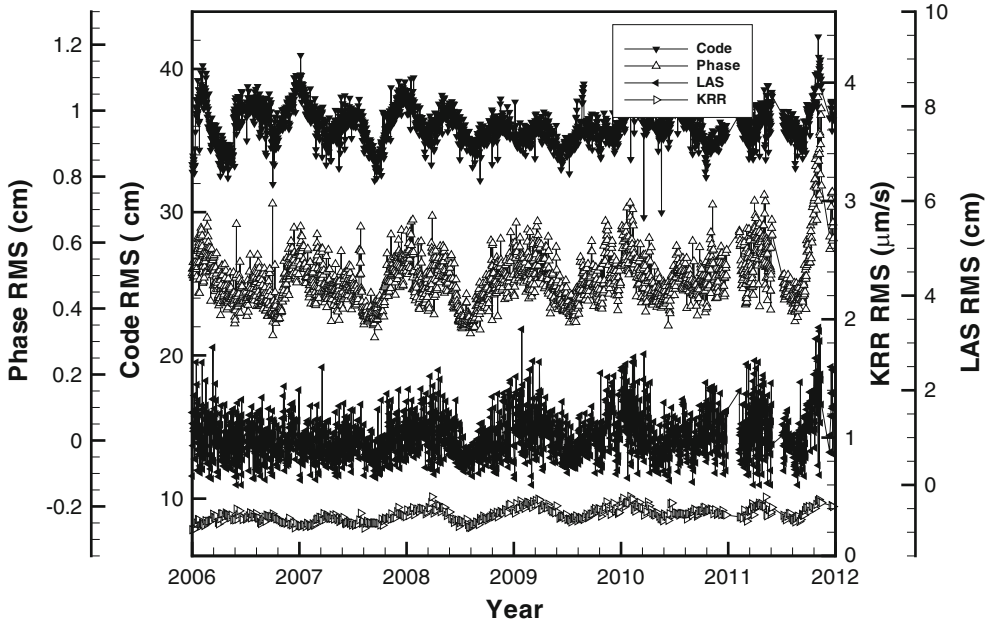

Fig. 7 Orbital fits of the GRACE-GPS, -K-band and -SLR operational solution

References

Altamimi Z, Collilieux X, Metivier L (2011) ITRF 2008: an improved solution of the international terrestrial reference frame. J Geod 85(8):457–473

Cheng MK, Tapley BD (2004) Variations in the Earth's oblateness during the past 28 years. J Geophys Res 109(B9):B09402

Cheng MK, Ries JC, Tapley BD (2013) Geocenter variations from analysis of SLR data. In: Altamimi Z, Collilieux X (eds) Reference frames for applications in geosciences. International association of geodesy symposia, vol 138. Springer, Berlin, pp 19–26

Dow JM, Neilan RE, Rizos C (2009) The international GNSS service in a changing landscape of global navigation satellite systems. J Geod 83(3):191–198

GRACE (2013) GRACE Tellus web site. http://grace.jpl.nasa.gov. Accessed 29 Nov 2013

IERS (2013) International Earth rotation and reference systems service web site. http://www.iers.org. Accessed 29 Nov 2013

ILRS (2013) International laser ranging service web site. http://ilrs.gsfc.nasa.gov. Accessed 29 Nov 2013

Kang Z, Tapley B, Chen J, Ries J, Bettadpur S (2007) Geocenter variations derived from GPS tracking of the GRACE satellites. J Geod 83:895–901

König R, Flechtner F, Raimondo J-C, Vei M (2015) Atmospheric loading and mass variation effects on the SLR-defined geocenter. In: International association of geodesy symposia. Springer [ISSN: 0939-9585] (accepted)

Pearlman MR, Degnan JJ, Bosworth JM (2002) The international laser ranging service. Adv Space Res 30(2):135–143

Petit G, Luzum B (2010) IERS conventions (2010) Bundesamts für Kartographie und Geodäsie, Frankfurt am Main. http://www.iers.org/TN36. Accessed 16 Sept 2013

Rebischung P, Griffiths J, Ray J, Schmid R, Collilieux X, Garayt B (2012) IGS08: the IGS realization of ITRF2008. GPS Solut 16:483–494

Rietbroek R, Fritsche M, Brunnabend S-E, Daras I, Kusche J, Schröter J, Flechtner F, Dietrich R (2011) Global surface mass from a new combination of GRACE, modelled OBP and reprocessed GPS data. J Geodyn 59–60:64–71

Shako R, Förste C, Abrykosov O, Bruinsma S, Marty J-C, Lemoine J-M, Flechtner F, Neumayer K-H, Dahle C (2014) EIGEN-6C: A high-resolution global gravity combination model including GOCE data. In: Flechtner F, Sneeuw N, Schuh W-D (eds) Observation of the system Earth from space - CHAMP, GRACE, GOCE and future missions, (GEOTECHNOLOGIEN Science report; No. 20; advanced technologies in Earth sciences). Springer, Berlin, pp 155–161

Tapley BD, Bettadpur S, Watkins M, Reigber C (2004) The gravity recovery and climate experiment: mission overview and early results. Geophys Res Lett 31:L09607

Watkins MM, Eanes RJ (1997) Observations of tidally coherent diurnal and semidiurnal variations in the geocenter. Geophys Res Lett 24(17):2231–2234

Wu X, Heflin MB, Ivins ER, Fukumori I (2006) Seasonal and interannual global surface mass variations from multisatellite geodetic data. J Geophys Res 111:B09401

Zhu S, Reigber C, König R (2004) Integrated adjustment of CHAMP, GRACE and GPS data. J Geod 78(1–2):103–108

DPOD2008: A DORIS-Oriented Terrestrial Reference Frame for Precise Orbit Determination

Pascal Willis, Nikita P. Zelensky, John Ries, Laurent Soudarin, Luca Cerri, Guilhem Moreaux, Frank G. Lemoine, Michiel Otten, Donald F. Argus, and Michael B. Heflin

Abstract

While accuracy of tracking station coordinates is of key importance for Precise Orbit Determination (POD) for altimeter satellites, reliability and operationality are also of great concern. In particular, while recent ITRF realizations should be the most accurate at the time of their computation, they cannot be directly used by the POD groups for operational consideration for several reasons such as new stations appearing in the network or new discontinuities affecting station coordinates. For POD purposes, we computed a new DORIS terrestrial frame called DPOD2008 derived from ITRF2008 (as previously done by DPOD2005 with regards to ITRF2005). In a first step, we will present the method used to validate the past ITRF2008 using more recent DORIS data and to derive new station positions and velocities, when needed. In particular, discontinuities in DORIS station positions and/or velocities are discussed. To derive new DORIS station coordinates, we used recent DORIS weekly time series of coordinates, recent GPS relevant time series at co-located sites and also dedicated GPS campaigns performed by IGN when installing new DORIS beacons. DPOD2008 also contains additional metadata that are useful when processing DORIS data, for example, periods during which DORIS data should not be used or at least for which data should be downweighted. In several cases, a physical explanation can be found for such temporary antenna instability. We then demonstrate improvements seen when using different reference frames, such as the original ITRF2008 solution, for precise orbit determination of altimeter satellites TOPEX/Poseidon and Jason-2 over selected periods spanning 1993–2013.

Keywords

DORIS • Jason-2 • Terrestrial Reference Frame • Tracking network

P. Willis (✉)
IGN, Direction de la Recherche et de l'Enseignement, Saint-Mande, France

IPGP, UMR 7154, Gravimétrie et géodésie, Université Paris Diderot, Sorbonne Paris Cité, Paris, France
e-mail: pascal.willis@ign.fr

N.P. Zelensky
SGT, Greenbelt, MD, USA

J. Ries
University of Texas, Center for Space Research, Austin, TX, USA

L. Soudarin • G. Moreaux
CLS, Toulouse, France

L. Cerri
CNES, Toulouse, France

F.G. Lemoine
GSFC, Greenbelt, MD, USA

M. Otten
ESA, Darmstadt, Germany

D.F. Argus • M.B. Heflin
JPL, Caltech, Pasadena, CA, USA

© Springer International Publishing Switzerland 2015

C. Rizos, P. Willis (eds.), *IAG 150 Years*, International Association of Geodesy Symposia 143,
DOI 10.1007/1345_2015_125

1 Introduction

Altimetry missions such as TOPEX/Poseidon, Jason-1&2 and others (Fu and Haines 2013) now provide key scientific observations for regional and global mean sea level determination. All such missions require Precise Orbit Determination (POD) based on satellite geodetic techniques such as Satellite Laser Ranging (SLR), DORIS (Doppler Orbitography and Radiopositioning Integrated by Satellite) and GPS (Global Positioning System), as discussed by Cerri et al. (2010), Lemoine et al. (2010), and Zelensky et al. (2010). To avoid any systematic errors between altimetry data sets, such orbit determination must be done in the same terrestrial reference frame (TRF). While all these techniques participate in the elaboration of the successive International Terrestrial Reference Frames (ITRFs, e.g. Altamimi et al. 2005), POD groups cannot directly use the latest ITRF coordinates and velocities for the tracking stations for the following reasons:

- some stations are regularly added to the tracking network after the realization of the latest ITRF;
- even if the station coordinates are the most precise realization at the time of realization of the latest ITRF, because of inherent uncertainties in the velocities, the precision of these coordinates slowly degrades with time and may then degrade POD results when used long after (several years) the ITRF computation;
- some stations may be affected by coordinate and/or velocity discontinuities that could happen after the realization of the latest ITRF;
- some problems in geodetic technique data processing may be found after the computation of the ITRF solution (Willis et al. in press).

This work is also done in conjunction with the International DORIS Service (Tavernier et al. 2002; Willis et al. 2010b) as it provides a priori coordinates for all past and existing DORIS stations, even the most recent ones. This is important for all DORIS Analysis Centers as well as for the Combination Center (Valette et al. 2010), especially when metadata, such as epoch of coordinates and/or velocities discontinuities, are provided with the TRF or periods during which some DORIS data should be disregarded or down-weighted for a specific tracking station. As such, it is important to point out that DORIS Analysis Centers adopt the updated DPOD solution for their operational processing, and as a basis for their contributions to the generation of a new ITRF.

The goal of this paper is to document the realization of the DPOD2008 solution, which is a DORIS datum based on the latest ITRF2008 coordinates and velocities (Altamimi et al. 2011; Seitz et al. 2012). In a first step, we will explain how this terrestrial reference frame (TRF) was obtained. We will then present some POD results using recent data and discuss possible continuation of such a work.

2 Description of DPOD2008

DPOD2008 consists of a data set of station coordinates expressed for each DORIS tracking station as piecewise linear model (3D coordinates in 2000.0, conventionally used as reference epoch, and 3D velocities). It is the continuation of previous work done: DPOD2000 (Willis and Ries 2005) and DPOD2005 (Willis et al. 2009). This new model is available in text format and in SINEX format at the following URL: http://www.ipgp.fr/~willis/DPOD2008. As these coordinates will be used as fixed in POD computations, unlike ITRF solutions, no correlation matrix is provided between station components, nor between stations.

The effect of errors in station positions on derived mean sea level is twofold: a global error as defined in the parameter transformation (3 translations, 3 rotations and 1 scale factor) and regional or local errors in station coordinates. The first type of error is mainly driven by an error in the Z-component (value or time-derived) as discussed by Morel and Willis (2005) and later demonstrated by Beckley et al. (2007). It can be minimized by adopting a TRF as close as possible, or even directly linked to the latest ITRF. This is why all DPOD solutions are aligned on the most recent ITRF solutions. The second type of error is more difficult to deal with as it depends on the geographic location of the closest tracking station as well as on the North-East orientation of the satellite ground tracks. However, the order of magnitude of such effects in the case of the DORIS network (Morel and Willis 2002) shows that a 5 cm error in any station coordinate (or velocity), assuming that such errors are station-independent, should not map into more than 0.2 mm in derived mean sea level (or sea level rate). While such a requirement is easy to deal with for geodesists when actual data are available, it is a bit more difficult to achieve when the requirement applies outside the observation period. Figure 1 displays the precision (formal errors) of DORIS station velocities as provided in the original ITRF2008 data set (Altamimi et al. 2011). It can be seen that a few stations are far less precise than others, usually because they had less observations at the time of the ITRF2008 computation. Coordinates for such stations would not meet a 5 cm requirement for precision in 2013, due to these uncertainties in velocity.

In a first step, we identified in ITRF2008 all stations for which the velocity formal errors would map to station coordinate uncertainties of more than 5 cm when computed in 2015. We also identified new stations that were not considered in ITRF2008, usually because they did not provide sufficient data at that time or because they were added to

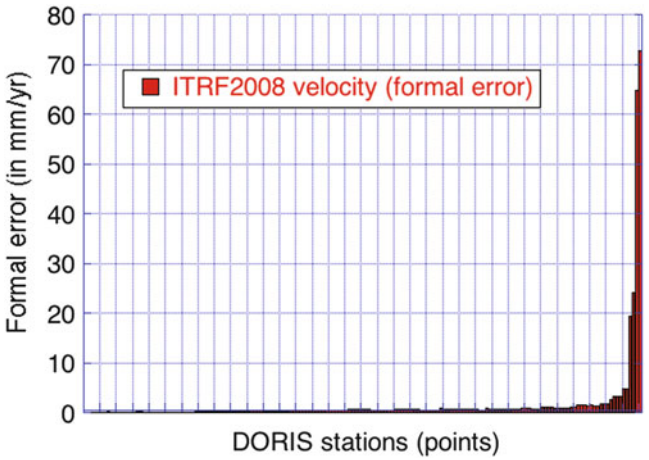

Fig. 1 Formal error of DORIS station velocities in ITRF2008 solution

the network at a later date. Only 3 stations (FAIB, GAVB, REZB), out of 170, have a velocity formal error larger than 5 mm/year. We also considered that stations, which were affected by discontinuities in the time series of coordinates after 2008, needed to be re-estimated (new linear model after the discontinuity).

To derive such new coordinates, we adopted the following strategy but always verified our results with at least several weeks of actual DORIS data and results from several DORIS solutions expressed in ITRF2008 (Willis et al. 2010a):

- In the case of a station relocation (a new antenna is placed a few hundred meters within the previous antenna position after change in equipment), we used the geodetic local tie provided by IGN (Fagard 2006) and the original velocity from ITRF2008. At worst, we used the original ITRF2008 velocity and determined the coordinates at an epoch of reference using actual DORIS data.
- Otherwise, we fixed the velocity to a reliable GPS solution (JPL PPP solution using new processing strategy from Bertiger et al. 2010 and Heflin et al. 2011; available at http://sideshow.jpl.nasa.gov/post/series.html) or to a recent plate model (GEODVEL, from Argus et al. 2010) and used all available DORIS observations to derive the position at the epoch of reference (2000.0 by convention).

One of the characteristics of the DPOD solution is also that it is a dynamic frame, evolving with time when new stations appear in the ground network or, less frequent, when an error is found in some of the station coordinates. DPOD2008 is then associated with a version number, the latest one being 1.13 (September 22, 2013). Another advantage is that a new realization of DPOD2008 does not change coordinates of all stations, as would any ITRF-type solution because a complete recomputation would be involved. For DPOD, only a few stations coordinates, usually the most recent ones, are modified between two successive versions. This is an interesting point for testing software packages, as tests done with an old data set would not be affected by such a modification and should provide exactly the same results. However, data processing using data from the most recent stations could be done using the same TRF. This is done at JPL on a regular basis, as a sample of old DORIS data in 2003 are processed automatically for verification purposes every time a new GIPSY-OASIS II executable (http://gipsy-oasis.jpl.nasa.gov/gipsy/software.html) is built, which could happen more than once a day in some cases. Impact on regular modifications of the software package can then be monitored on a systematic basis, allowing easy detection of potential gross errors.

3 Discussion on a Few Examples

As identified in more details in Willis et al. (2009), several DORIS station coordinates cannot be modeled with a unique linear model due to known geophysical effects: Socorro Island (Mexico) is affected by successive displacements related to volcano subsidence and submarine eruptions (Briole et al. 2009), while Fairbanks (Alaska) on 3 November 2002 and Arequipa (Peru) on 23 June 2001 are affected by nearby earthquakes (Eberhardt-Phillips et al. 2003; Perfettini et al. 2005; Williams and Willis 2006) modifying the station positions by tens of centimeters during the co-seismic displacement and also modifying the long-term velocity during the post-seismic relaxation.

Table 1 provides more information on how the piecewise linear model was derived for these three cases. In this table, when the position and velocity are both estimated, they are derived using only DORIS data from this time interval. When the position is not estimated, we forced the consecutive linear models to be continuous by using the geodetic local tie information between successive DORIS beacons, or used external information, such as GPS-derived velocity.

Other types of displacements can be related to extreme weather conditions (severe snow storm for Ottawa, Canada) or manmade displacements (hit by a car for Kourou, Guyana). More information is documented on a station-by-station basis (one page per beacon) in the metadata available online at http://www.ipgp.fr/~willis/DPOD2008 with the DPOD2008 solutions.

From the 110 DORIS stations provided in the original ITRF2008, 72 were used without any modification for DPOD2008, 38 were recomputed because: for 9 of them the velocity was not precise enough (ARLA, ARMA, FAIA, FAIB, GAVB, KRAB, REYA, REYB, REZB); for 10, a possible data analysis problem affecting the DORIS station coordinate in the South Atlantic Anomaly region (AREA, AREB, ARFB, CACB, CADB, KRUB, KRVB, SANA, SANB, SAOB, Willis et al. 2004) was found after

Table 1 DPOD2008 estimation for piecewise linear model: interval definition (day.month.year) and parameter estimation

Station	Acronym	Start	End	Position estimated	Velocity estimated
Socorro Island	SOCA	09.06.1989	15.09.1990	Yes	No (plate motion)
Socorro Island	SODA	08.02.1991	02.01.1993	No	No (plate motion)
Socorro Island	SODA	03.01.1993	26.12.1995	No	Yes
Socorro Island	SODA	27.12.1995	20.12.1997	No	Yes
Socorro Island	SODB	21.05.1998	02.10.2002	No	No (from SODA)
Socorro Island	SODB	03.10.2002	...	Yes	No (plate motion)
Fairbanks	FAIA	25.10.1990	05.10.1999	Yes	Yes
Fairbanks	FAIB	08.10.1999	02.11.2002	No	No (from GPS)
Fairbanks	FAIB	03.11.2002	31.12.2003	Yes	No (from GPS)
Fairbanks	FAIB	01.01.2004	07.10.2010	Yes	No (from GPS)
Arequipa	AREA	01.02.1990	22.06.2001	Yes	No (from GPS)
Arequipa	AREA	23.06.2001	20.11.2001	Yes	No (from GPS)
Arequipa	AREB	21.11.2001	31.12.2001	Yes	No (from GPS)
Arequipa	AREB	01.01.2002	01.08.2006	Yes	No (from GPS)
Arequipa	ARFB	02.08.2006	...	Yes	No (from GPS)

the realization of ITRF2008, affecting the SPOT5 data (Stepanek et al. 2013); for 17, discontinuities provided in ITRF2008 were ignored, as found as not significant for this work (COLA, DIOA, DIOB, DJIB, EVEB, HELB, KESB, REUB, ROTA, SAKA, SAKB, STJB, TRIA, TRIB, WAIA, WALA); for 2, new discontinuities were added. Furthermore, 49 DORIS stations were added to the original ITRF2008 solution: 22 older stations which were not provided by the IDS combination center for the ITRF2008 computation, usually because too few data were available by then (AJAB, CRAB, DJCB, FLOA, GR2B, GR3B, HUAA, HVOA, IQUB, KRUA, LIFB, OTTA, OTTB, RICA, SAMB, SIGA, SOCA, SODA, SODB, TANB, TROA, WETB); and 27 new stations recently added in the network (ADGB, AMVB, ASEB, BETB, CIDB, COBB, CRQB, FUBB, GRFB, HBLB, JIVB, KRBB, KRWB, LAOB, MAIB, MEUB, MOSB, NOXB, PASB, PAUB, RIKB, RILB, RIMB, RIRB, ROVB, STJB, TRJB).

4 Validation Using POD Tests

The DORIS ITRF2008 and DPOD2008 station complements were used to compute TOPEX/Poseidon (TP) and Jason-2 (J2) DORIS-only orbits in a series of controlled tests at the CNES and GSFC altimeter satellite POD analysis centers. The tests applied the latest GDR-D comparable POD modeling standards and include SLR-only and GPS-only orbits for comparison.

The collective effect of the improvements made to DPOD2008 (Sect. 2) is shown in the POD comparison to ITRF2008 as: (a) an increase in the number of stations and data, (b) a decrease in the DORIS residuals (mismatch between the observed and modeled tracking observation) indicating a reduction in station coordinate error, and (c) an improvement in the orbit shown with the improved SLR residuals (Table 2 and Fig. 2). It must be emphasized that the SLR and the xover tests are independent.

The very small differences between the altimeter crossover residuals are much less telling of the orbit quality when compared to the significant total orbit improvement seen with the SLR data (slant range) residuals for DPOD2008 (Table 2). In these tests, the SLR data and altimeter crossover residuals are independent. We note incidentally that the Jason-2 satellite benefits from the DGXX multi-channel receiver (Auriol and Tourain 2010), which provides much more DORIS data then the single-channel receiver used on TOPEX, so that the consistency with the independent SLR data is improved. The analysis summarized in Table 2 follows Lemoine et al. (2010) with updates to the station complement and the background geopotential modelling.

The ITRF2008 complement was computed with DORIS data spanning 1993–2008 and did not include all available stations, whereas DPOD2008 is historically complete and includes new stations from 2009. Table 2 is divided into three periods and spans 1993–2010. Thus DPOD2008 is shown to provide more data over the ITRF2008 solution span, and increasingly more data following 2008. All three periods show an improvement in the DORIS and independent SLR residuals for DPOD2008 (Table 2). The SLR residual improvement for DPOD2008 continues to be seen through the latest mid-2013 period (Fig. 2).

An error on the Z-component of the network origin is directly expressed as a mis-centering in Z in the derived orbit (Morel and Willis 2005). Figure 3 indicates

Table 2 DORIS ITRF2008 and DPOD2008 station complement performance over time

DORIS ITRF2008/DPOD2008 complement performance over time						
				Average residuals per cycle		
Period	Test DORIS-only	Number stations	Average points/cycle	Doris (mm/s)	slr (cm)	xover (cm)
Apr 19, 1993 – Jul 17, 1993 (TP cycles 22–30)	**TP ITRF2008**	42	54,342	0.5391	4.90	5.942
	DPOD2008_1.12	45	57,135	0.5385	4.71	5.945
Jan 15, 2002 – Aug 11, 2002 (TP cycles 344–364)	**TP ITRF2008**	51	56,015	0.4736	4.20	5.621
	DPOD2008_1.12	53	57,365	0.4729	3.96	5.628
Jul 11, 2008 – Jan 28, 2010 (J2 cycles 1–57)	**J2 ITRF2008**	53	154,874	0.3726	2.32	5.551
	DPOD2008_1.12	62	170,924	0.3659	2.28	5.558

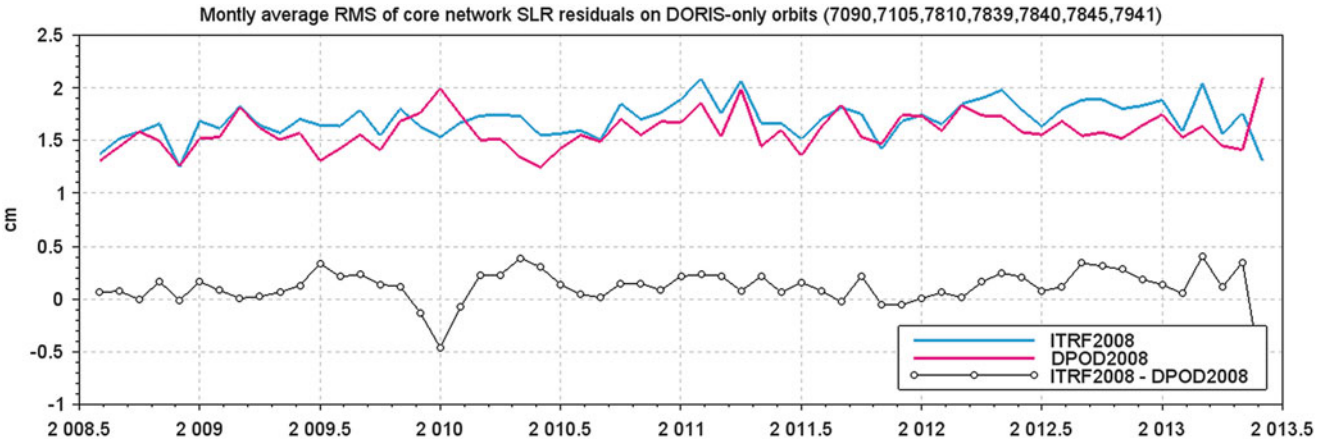

Fig. 2 Jason-2 independent SLR residuals computed from ITRF2008 and DPOD2008 DORIS-only orbits at the CNES POD Center

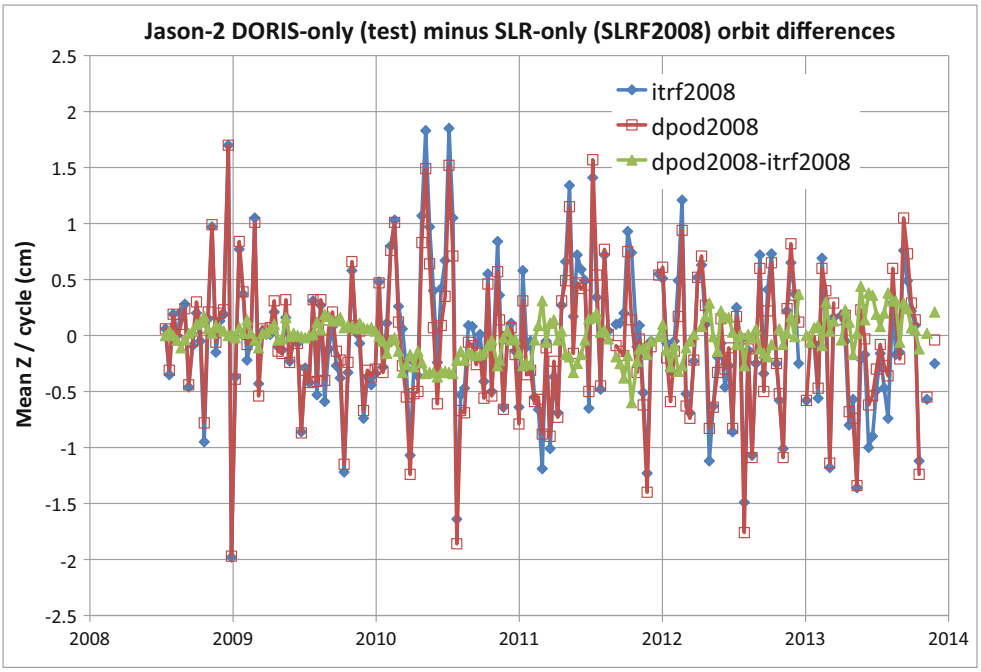

Fig. 3 Jason-2 DORIS-only minus SLR-only mean Z orbit differences shown in *blue* and *red*, and in *green* the differences between the two DORIS-only orbits (ITRF2008)

both the ITRF2008 and DPOD2008 origin are consistent with SLRF2008 (ILRS update to ITRF2008, http://ilrs.gsfc.nasa.gov/science/awg/SLRF2008.html). We compare DORIS-only orbits computed using ITRF2008 and DPOD2008 with SLR-only orbits computed with SLRF2008. While the orbits are consistent in Z on average,

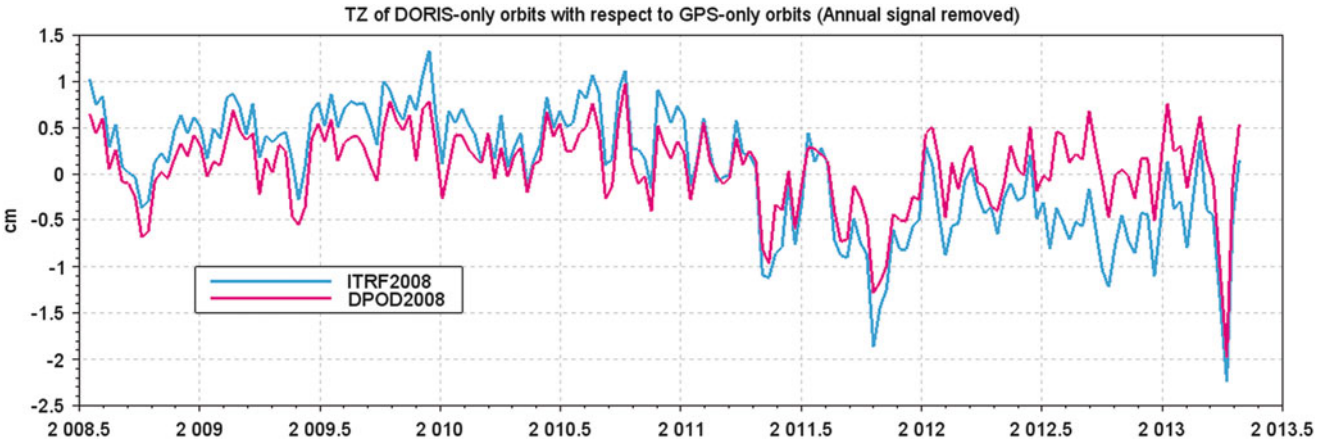

Fig. 4 Jason-2 DORIS-only minus GPS-only mean Z orbit differences

the larger scatter can be attributed to the sparseness of the SLR network (a relatively small core set of stations provide the bulk of the tracking) and the inability to track in unfavorable weather conditions. The differences between the two DORIS-only orbits begins to increase following 2010, as can be expected with the progressive coverage degradation of the ITF2008 complement relative to DPOD2008 (Fig. 3).

A more robust test is provided by comparing the DORIS-only orbits with external GPS-only based Jason-2 orbits, using JPL's orbits and clocks referenced to the IGS08 network (Rebischung et al. 2012). After removal of an annual signal, Fig. 4 shows the Z-translation of DORIS-only orbits computed with ITRF2008 and DPOD2008, where the DPOD2008-determined orbits are shown to be better centered. For two stations (THUB and SANB), a new discontinuity was introduced in the coordinate time series.

5 Conclusions and Plans for the Future

Following ITRF2008, a terrestrial reference frame (DPOD2008) was derived, using most of the station coordinates and velocities from ITRF2008 solution and providing coordinates and velocities for all DORIS stations since the start of the system in 1990 and up to now. This frame is continuously updated when new stations appear in the DORIS tracking station or when geophysical, manmade or technical problems require some modification. In September 2013, version 1.13 is available in text and SINEX format at the following Website http://www.ipgp.fr/~willis/DPOD2008/. Additional metadata are also available there. As demonstrated in this article, such a terrestrial reference frame is well suited for Precise Orbit Determination and is operationally used by several groups for major altimetric missions.

Acknowledgements Part of this work was supported by the Centre National d'Etudes Spatiales (CNES). It is based on observations with DORIS receivers on the SPOT satellites, TOPEX/Poseidon, Envisat, Jason-2 and Cryosat-2. FG Lemoine and NP Zelensky were supported by the NASA Ocean Surface Topography Science Team (OSTST) and the NASA Interdisciplinary Research in Earth Science/Sea Level Change. The work of Don Argus and Mike Heflin was performed at the Jet Propulsion Laboratory, California Institute of Technology under contract with the National Aeronautics and Space Administration (NASA). This paper is IPGP contribution number 3477.

References

Altamimi Z, Boucher C, Willis P (2005) Terrestrial reference frame requirements within GGOS perspective. J Geodyn 40(4–5):363–374

Altamimi Z, Collilieux X, Metivier L (2011) ITRF2008, an improved solution of the International Terrestrial Reference Frame. J Geod 85(8):457–473

Argus DF, Gordon RG, Heflin MB, Ma C, Eanes R, Willis P, Peltier WR, Owen S (2010) The angular velocities of the plates and the velocity of the Earth's Center from Space Geodesy. Geophys J Int 180(3):916–960

Auriol A, Tourain C (2010) DORIS system, the new age. Adv Space Res 46(12):1484–1496

Beckley BD, Lemoine FG, Luthcke SB, Ray RD, Zelensky NP (2007) A reassessment of global and regional mean sea level trends from TOPEX and Jason-1 altimetry based on revised reference frame and orbits. Geophys Res Lett 34(14) art L14608. doi:10.1029/2007GL030002

Bertiger W, Desai SD, Haines B, Harvey N, Moore AW, Owen S, Weiss JP (2010) Single receiver phase ambiguity resolution with GPS data. J Geod 84(5):327–337

Briole P, Willis P, Dubois J, Charade O (2009) Potential volcanic applications of the DORIS system, a geodetic study of the Socorro Island (Mexico) coordinate time series. Geophys J Int 178(1): 581–590

Cerri L, Berthias JP, Bertiger WI, Haines BK, Lemoine FG, Mercier F, Ries JC, Willis P, Zelensky NP, Ziebart M (2010) Precision orbit determination standards for the Jason Series of Altimeter Missions. Marine Geod 33(S1):379–418

Eberhardt-Phillips D, Haeussler PJ, Freymueller JT, Frankel AD, Rubin CM, Craw P, Rathovski NA, Anderson G, Carver GA, Crone AJ, Dawson TE, Flectcher H, Hansen R, Harp EL, Harris RA, Hill DP, Hreinsdottir S, Jibson RW, Jones LM, Kayen R, Keefer DK,

Larsen CF, Moran SC, Personius SF, Plafker G, Sherrod B, Sieh K, Sitar N, Wallace WK (2003) The 2002 Denali faul earthquake, Alaska, A large magnitude, slip-partitioned event. Science 300(5622): 1113–1118

Fagard H (2006) Twenty years of evolution of the DORIS permanent network, from its initial deployment to its renovation. J Geod 80(8–11):429–456

Fu LL, Haines BJ (2013) The challenges in long-term altimetry calibration for addressing the problem of global sea level change. Adv Space Res 51(8):1284–1300

Heflin MB, Moore AW, Owen SE (2011) Impact of ambiguity resolution on the global reference frame, AGU Fall Meeting Abstracts, 2011AGUFM.G53A0879H

Lemoine FG, Zelensky N, Chinn D, Pavlis D, Beckley B, Luthcke SB, Willis P, Ziebart M, Sibthorpe A, Boy JP, Luceri V (2010) Towards development of a consistent orbit determination, TOPEX/Poseidon, Jason-1 and Jason-2. Adv Space Res 46(12):1513–1540

Morel L, Willis P (2002) Parameter sensitivity of TOPEX orbit and derived mean sea level to DORIS station coordinates. Adv Space Res 30(2):255–263

Morel L, Willis P (2005) Terrestrial reference frame effects on sea level rise determined by TOPEX/Poseidon. Adv Space Res 36(3):358–368

Perfettini H, Avouac JP, Ruegg JC (2005) Geodetic displacements and aftershocks following the 2001 Mw = 8.4 Peru earthquake, Implications for the mechanics of the earthquake cycle along subduction zones. J Geophys Res 110(B9) art B09404. doi:10.1029/2004JB0003522

Rebischung P, Griffiths J, Ray J, Schmid R, Collilieux X, Garaut B (2012) IGS08, the IGS realization of ITRF2008. GPS Solut 16(4):483–494

Seitz M, Angermann D, Blossfeld M, Drewes M, Gerstl M (2012) The 2008 DGFI realization of the ITRS, DTRF2008. J Geod 86(12):1097–1123

Stepanek P, Dousa J, Filler V (2013) SPOT-5 DORIS oscillator instability due to South Atlantic Anomaly, mapping the effect and application of data corrective model. Adv Space Res 52(7): 1355–1365

Tavernier G, Soudarin L, Larson K, Noll C, Ries JC, Willis P (2002) Current status of the DORIS Pilot Experiment and the future international DORIS Service. Adv Space Res 30(2):151–155

Valette JJ, Lemoine FG, Ferrage P, Yaya P, Altamimi Z, Willis P, Soudarin L (2010) IDS contribution to ITRF2008. Adv Space Res 46(12):1614–1632

Williams SDP, Willis P (2006) Error analysis of weekly station coordinates in the DORIS network. J Geod 80(8–11):525–539

Willis P, Ries JC (2005) Defining a DORIS core network for Jason-1 Precise Orbit Determination based on ITRF2000, methods and realization. J Geod 79(6–7):370–378

Willis P, Haines B, Berthias JP, Sengenes P, Le Mouel JL (2004) Behavior of the DORIS/Jason oscillator over the South Atlantic Anomaly. CR Geosci 336(9):839–846

Willis P, Ries JC, Zelensky NP, Soudarin L, Fagard H, Pavlis EC, Lemoine FG (2009) Realization of a DORIS terrestrial reference frame for precise orbit determination. Adv Space Res 44(5):535–544

Willis P, Boucher C, Fagard H, Garayt B, Gobinddass ML (2010a) Contributions of the French Institut Geographique National (IGN) to the International DORIS Service. Adv Space Res 45(12):1470–1480

Willis P, Fagard H, Ferrage P, Lemoine FG, Noll CE, Noomen R, Otten M, Ries JC, Rothacher M, Soudarin L, Tavernier G, Valette JJ (2010b) The International DORIS Service (IDS), toward maturity. Adv Space Res 45(12):1408–1420

Willis P, Lemoine FG, Moreaux G, Soudarin L, Ferrage P, Ries J, Otten M, Saunier J, Noll C, Biancale R, Luzum B (in press) The International DORIS Service (IDS), recent developments in preparation of ITRF2013. In: IAG Symp 143, DOI: 10.1007/1345_2015_164

Zelensky N, Lemoine FG, Chinn D, Rowlands D, Luthcke S, Beckley B, Pavlis D, Klosko S, Ziebart M, Sibthorpe AJ, Willis P, Luceri V (2010) DORIS/SLR POD modeling improvements for Jason-1 and Jason-2. Adv Space Res 46(12):1541–1558

SIRGAS Core Network Stability

L. Sánchez, H. Drewes, C. Brunini, M.V. Mackern, and W. Martínez-Díaz

Abstract

The main objective of SIRGAS (*Sistema de Referencia Geocéntrico para las Américas*) is to provide an accurate spatial and time-referenced infrastructure as a basis for Earth System research and to support scientific and practical applications based on high-precise positioning. Following this purpose, significant achievements related to the extension, analysis, and maintenance of this reference frame have been reached during the last years. However, there are still unresolved problems hindering the attainment of the best possible precision. In particular, the assimilation of seismic-related deformations and non-lineal station movements is very difficult and its omission considerably reduces the reliability of SIRGAS as a high precision reference frame. To advance in the solution of these inconveniences, this paper presents the first kinematic model of the SIRGAS reference frame computed after the strong earthquake occurred in the Chilean region of Maule in February 2010. This model is based on the combination of weekly free normal equations covering the time span from April 18, 2010 to June 15, 2013. Computed station positions and velocities refer to the IGb08 reference frame (the IGS realisation of the ITRF2008), epoch 2012.0. The averaged rms precision is ± 1.4 mm horizontally and ± 2.5 mm vertically for the station positions at the reference epoch, and ± 0.8 mm/year horizontally and ± 1.2 mm/year vertically for the constant velocities. Comparisons with reference frames based on measurements before the earthquake (like ITRF2008 or former SIRGAS solutions) make evident the strong deformation caused by this earthquake and the necessity of updating accordingly the reference frames in the affected region.

Keywords

ITRF densifications • Regional reference frames • Seismic effects on reference frames • SIRGAS

1 Introduction

The realisation of SIRGAS (*Sistema de Referencia Geocéntrico para las Américas*) is a regional densification of the International Terrestrial Reference Frame (ITRF)

IAG Symposia Series (IAG General Assembly 2013), accepted for publication, 2014

L. Sánchez (✉) • H. Drewes
Deutsches Geodätisches Forschungsinstitut (DGFI), Alfons-Goppel-Str. 11, 80539 Munich, Germany
e-mail: sanchez@dgfi.badw.de

C. Brunini
Consejo Nacional de Investigaciones Científicas y Técnicas (CONICET), Universidad Nacional de la Plata (UNLP), La Plata, Argentina

M.V. Mackern
Universidad Nacional de Cuyo, Universidad Juan A. Maza, Mendoza, Argentina

W. Martínez-Díaz
Instituto Geográfico Agustín Codazzi, Bogotá, Colombia

© Springer International Publishing Switzerland 2015

C. Rizos, P. Willis (eds.), *IAG 150 Years*, International Association of Geodesy Symposia 143,
DOI 10.1007/1345_2015_143

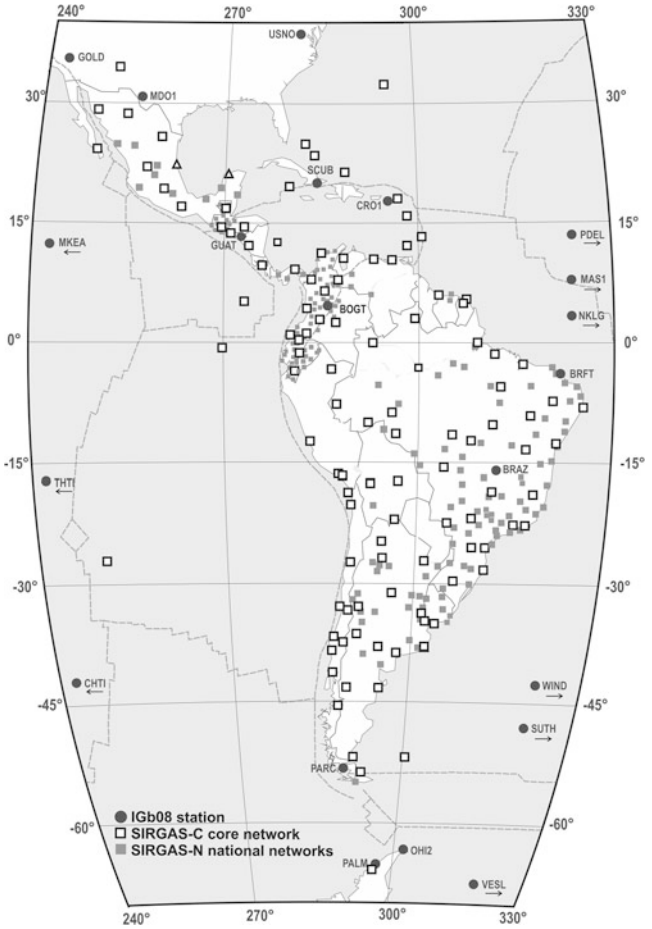

Fig. 1 SIRGAS reference frame (as of October 2013)

(e.g. SIRGAS 1997; Drewes et al. 2005; Sánchez and Brunini 2009). At present, it is composed of GNSS stations only. Stations determined using other space geodetic techniques like VLBI, SLR or DORIS are not included yet. SIRGAS comprises two hierarchical levels (Fig. 1):

(a) One core network (SIRGAS-C) composed by a set of geographically well-distributed and consistently reliable reference stations. The main purpose of the SIRGAS-C network is to ensure the long-term stability of the reference frame, and it is understood to be the primary densification of the ITRF in Latin America and the Caribbean.
(b) National reference networks (SIRGAS-N) as further densifications of the core network. The central purposes of these densifications are to provide accessibility to the reference frame at national and local levels and to facilitate the integration of new reference stations into SIRGAS (mainly those installed by the national agencies responsible for the local reference networks).

The SIRGAS reference frame is calculated weekly. The SIRGAS-C network is processed by the *Deutsches Geodätisches Forschungsinstitut* (DGFI, Germany) since this institute acts as the *IGS Regional Network Associate Analysis Centre for SIRGAS* (IGS-RNAAC-SIR, Sánchez 2012, 2013). The SIRGAS-N networks are computed by the SIRGAS Local Processing Centres, which at present are:

– CEPGE: *Centro de Procesamiento de datos GNSS del Ecuador, Instituto Geográfico Militar* (Ecuador),
– CPAGS-LUZ: *Centro de Procesamiento y Análisis GNSS SIRGAS, Universidad del Zulia* (Venezuela),
– IBGE: *Instituto Brasileiro de Geografia e Estatistica* (Brazil),
– IGAC: *Instituto Geográfico Agustín Codazzi* (Colombia),
– IGM-Cl: *Instituto Geográfico Militar* (Chile),
– IGN-Ar: *Instituto Geográfico Nacional* (Argentina),
– INEGI: *Instituto Nacional de Estadística y Geografía* (Mexico),
– SGM-Uy: *Servicio Geográfico Militar* (Uruguay).

These processing centres deliver loosely constrained weekly solutions for the SIRGAS-N national networks, which are combined with the SIRGAS-C core network to generate station positions aligned to the ITRF for the entire network. The individual solutions are combined by the SIRGAS Combination Centres currently operated by the IGS-RNAAC-SIR (i.e., DGFI, Germany) and IBGE (Brazil). The final solutions are provided by the IGS-RNAAC-SIR through www.sirgas.org. It should be mentioned that stations belonging to the core network or to the national densifications satisfy the same operational requirements and each one is included in three solutions to get the necessary redundancy for the combination of the individual normal equation systems.

2 Weekly Analysis of the SIRGAS Reference Frame

The SIRGAS processing centres follow unified standards for the computation of the loosely constrained solutions (e.g. Costa et al. 2012a; Natali et al. 2009; Seemüller et al. 2012). These standards are based in general on the conventions outlined by the *International Earth Rotation and Reference Systems Service* (IERS) and the GNSS-specific guidelines defined by the *International GNSS Service* (IGS); with the exception that in the individual SIRGAS solutions the satellite orbits, satellite clock offsets, and Earth orientation parameters (EOP) are fixed to the final weekly IGS values (SIRGAS does not compute these parameters). Positions for all stations are constrained to ± 1 m to generate the loosely constrained solutions in SINEX format. INEGI (Mexico) and IGN-Ar (Argentina) work with the GAMIT/GLOBK software (Herring et al. 2010) while the other local processing centres use the Bernese GPS Software V5.0 (Dach et al. 2007). At the moment, the SIRGAS Local Processing Centres are aligning their procedures to the new standards described in the IERS Conventions 2010 (Petit

and Luzum 2010) and to the characteristics specified for the second reprocessing of the IGS global network (http://acc.igs.org/reprocess2.html). Since July 2013 the IGS-RNAAC-SIR has applied these new standards and it is working with the Bernese GNSS Software V5.2 (Dach et al. 2013). It is expected that the other processing centres will start delivering solutions based on the new standards in January 2014.

The combination of the individual solutions is made at the normal equation level by IBGE using the Bernese GPS Software V5.0 IBGE (Costa et al. 2012b) and by DGFI using the Bernese GNSS Software V5.2 (Sánchez et al. 2012). The internal consistency of the weekly SIRGAS station positions is estimated to be about ±1.0 mm in the horizontal component and about ±3.0 mm in the vertical one, while their reliability (external precision) is about ±2.0 mm in the horizontal and ±4.0 mm in the vertical (Sánchez 2013).

Strictly speaking, the weekly solutions of the SIRGAS reference frame are computed with respect to the IGS reference frame because it is the basis for the IGS products included in the SIRGAS network processing. An *IGS Reference Frame* usually corresponds to a subset of ITRF positions and velocities for a specified set of long-term stable and globally well-distributed reference stations; for instance, the IGS08 reference frame (Rebischung et al. 2012) corresponds to the ITRF2008 (Altamimi et al. 2011). When an IGS reference frame is refined (e.g. by including or excluding some stations), its name is changed accordingly; i.e., for the IGS08 reference frame there is the improved version IGb08 (see http://igscb.jpl.nasa.gov/pipermail/igsmail/2012/007853.html). The main difference between the ITRF2008 and the IGS08/IGb08 is associated to the model applied for the correction of the antenna phase centre variations. While ITRF2008 coordinates are consistent with the igs05.atx set of calibrations (Schmid et al. 2007), the IGb08 is consistent with the updated igs08.atx model (Schmid 2011). Consequently, the IGS08/IGb08 position of some stations differs by some millimetres with respect to the ITRF2008; coordinates of remaining stations are the same as in ITRF2008 (more details in Rebischung et al. 2012 and http://igscb.jpl.nasa.gov/pipermail/igsmail/2012/007853.html). The IGS08/IGb08 coordinates are internally more consistent than the original ITRF values and there is not any translation, rotation or scale between both realisations. Thus the IGS final products and those computations based on them, like the SIRGAS solutions, can be considered to be nominally in the current ITRF2008. However, it should be mentioned that the results presented in this study refer to the IGb08 reference frame.

3 Kinematics of the SIRGAS Reference Frame

To estimate the kinematics of the SIRGAS reference frame, a cumulative (multi-year) solution is computed (updated) every year, providing epoch positions and constant velocities for stations operating longer than two years; stations active during shorter time spans are omitted from the cumulative solutions. The coordinates of the multi-year solutions refer to the latest available IGS reference frame and to a common reference epoch, e.g., the most recent released SIRGAS multi-year solution SIR11P01 refers to IGS08 (ITRF2008), epoch 2005.0 (Sánchez and Seitz 2011). It includes weekly normal equations from January 2, 2000 to April 16, 2011 for 230 stations with 269 occupations. Its averaged rms precision is estimated to be ±1.0 mm horizontally and ±2.4 mm vertically for the station positions at the reference epoch, and ±0.7 mm/year horizontally and ±1.1 mm/year vertically for the constant velocities.

Because the switch to the ITRF2008 (i.e. IGS08/IGb08) for the generation of the IGS products caused a discontinuity of some millimetres in the station position time series, the computation of multi-year solutions for the SIRGAS reference frame was discontinued until getting weekly normal equations referenced to the IGS08/IGb08 and covering a time span of at least three years. Indeed, it was decided that the entire SIRGAS network will be reprocessed from January 1997 to present using the latest IERS/IGS procedures and standards. However, while the SIRGAS Local Processing Centres are unable to apply these, a new multi-year solution was computed for the SIRGAS-C core network only, i.e., for the stations processed routinely by the IGS-RNAAC-SIR. The main objective of this multi-year solution is to identify possible secular effects in the kinematics of the SIRGAS reference frame caused by the Maule earthquake of February 2010 (Sánchez et al. 2013).

4 New Processing Standards for the SIRGAS Reference Frame

The input for the SIRGAS cumulative solutions are weekly free normal equations, which for this study were calculated using the following characteristics:

- Basic observable: ionosphere-free linear combination;
- Sampling rate: 30 s;
- Elevation cut-off angle: 3°;

- Elevation-dependent weighting of observations: $\frac{1}{cos^2 z}$, where z is the zenith distance;
- Satellite orbits, satellite clock offsets, and EOP fixed to the combined IGS weekly solutions (Dow et al. 2009, www.igs.org/components/prods.html). Since the IGS products have used IGS08/IGb08 only since April 2011 (GPS week 1632), the normal equations for previous weeks (back until April 2010) were computed using the IGb08-based satellite products and EOP generated by the IGS processing centre CODE (*Centre for Orbit Determination in Europe*, ftp://ftp.unibe.ch/aiub/CODE/);
- Application of antenna phase centre offsets and direction-dependent phase centre variation values from model igs08.atx (Schmid 2011, http://igscb.jpl.nasa.gov/igscb/station/general/pcv_archive/) for both satellite transmitting and ground receiving antennas;
- Antenna radome calibrations applied if given in the model igs08.atx. Otherwise, the radome effect is neglected and the standard antenna model (radome NONE) is used;
- Phase ambiguities for L1 and L2 solved after the quasi-ionosphere free (QIF) strategy described in Dach et al. (2007). The ionosphere models of CODE (ftp://ftp.unibe.ch/aiub/CODE/) are used as input to increase the number of solved ambiguities;
- The tropospheric zenith delay is modelled using the *Vienna Mapping Function 1* (VMF1, Böhm et al. 2006). The a-priori values (∼dry part) are derived from gridded coefficients based on the climate numerical weather models of ECMWF (*European Centre for Medium-Range Weather Forecasts*) and made available by J. Böhm, TU Vienna, at http://ggosatm.hg.tuwien.ac.at/DELAY/GRID/VMFG/. These a-priori values are refined by computing partial derivatives of the troposphere zenith delay parameters (∼wet part) in a 2-h interval (also using VMF1) within the network adjustment. In addition, to model azimuthal asymmetries, horizontal gradient parameters are estimated using the model described by Chen and Herring (1997);
- Corrections for the solid Earth tide, permanent tide, and solid Earth pole tide are applied as described in Petit and Luzum (2010). The ocean tide loading is estimated with the FES2004 model (Letellier 2004) and the atmospheric tide loading caused by the semidiurnal constituents S1 and S2 is estimated following the model of van Dam and Ray (2010). The coefficients for the ocean tide loading are provided by M.S. Bos and H.-G. Scherneck at http://holt.oso.chalmers.se/loading/. The coefficients for the atmospheric tide loading are provided by T. van Dam at http://geophy.uni.lu/ggfc-atmosphere/tide-loading-calculator.html;
- Ocean or atmospheric tide geocentre coefficients are not applied since this correction is already contained in the final IGS (and CODE) products;
- Non-tidal loading such as atmospheric pressure, ocean bottom pressure, and surface hydrology are not reduced;
- Daily free normal equations are computed by applying the double difference strategy using the Bernese GNSS Software V5.2. The baselines are formed by maximising the number of common observations for the associated stations;
- The seven daily free normal equations corresponding to a GPS week are combined into a weekly free normal equation. Stations with large residuals in any daily normal equation (more than ±20 mm in the horizontal or more than ±30 mm in the vertical) are removed from the corresponding daily equation and the weekly combination is recomputed.

5 Multi-Year Solution SIR13P01

The input data for this new cumulative solution are the weekly free normal equations (computed as described in the previous section) covering the time span from April 18, 2010 (GPS week 1580) to June 15, 2013 (GPS week 1744). Given that most of the existing ITRF stations in South America are affected by the earthquake in Chile in February 2010 (see e.g. Sánchez et al. 2013), further stations located in Europe, Africa, Oceania and North America (Fig. 2) are included in the SIRGAS computations to increase the availability of fiducial points.

Before combining the weekly normal equations, a time series analysis was performed to identify outliers and discontinuities in the station positions. For that, the weekly normal equations are solved separately applying no-net-rotation (NNR) and no-net-translation (NNT) conditions with respect to the IGb08 core stations included in the SIRGAS network (Fig. 2). To generate residual position time series, the weekly solutions were transformed to an a-priori SIRGAS reference frame (i.e. the current SIRGAS reference frame SIR11P01) by 7-parameter similarity transformations. The residual time series of station positions were evaluated and outliers removed and detected discontinuities taken into account for the computation of the new multi-year solution. The thresholds for outliers are defined by ±15 mm for North/East and ±30 mm for height (about fourfold the mean rms). If outliers appear sporadically (without pattern), the station is removed from the respective free normal equation.

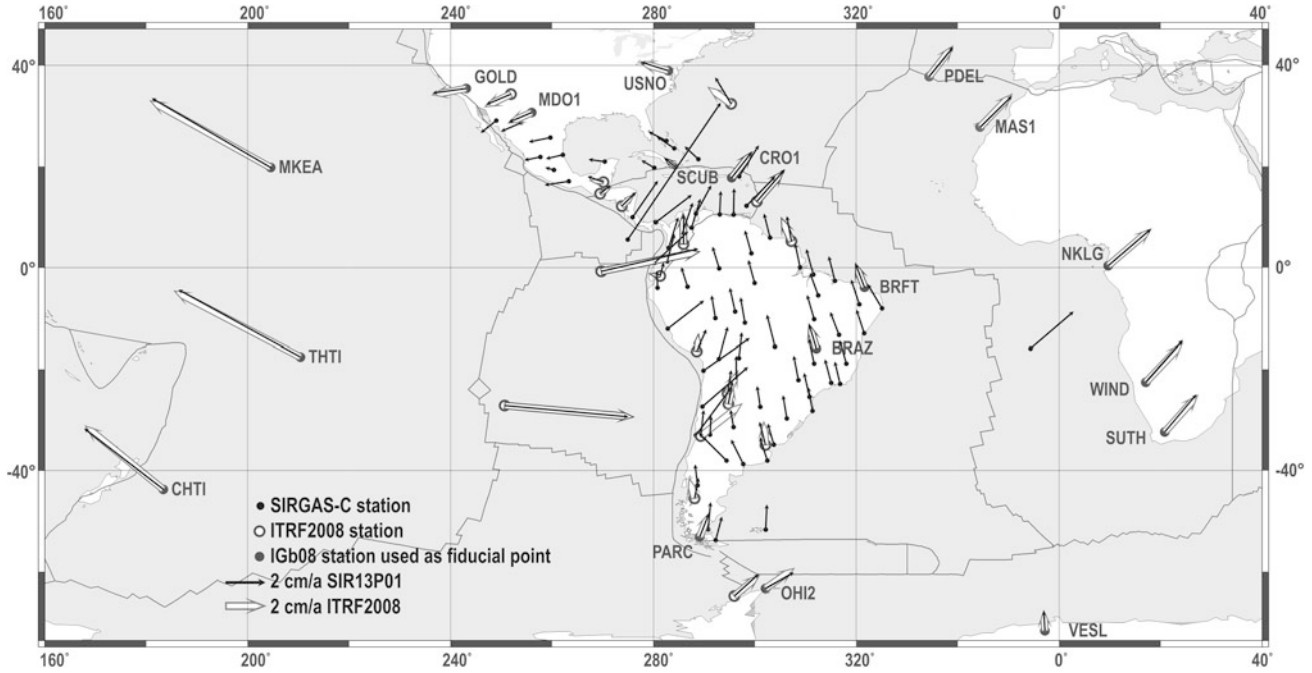

Fig. 2 Horizontal velocities of the SIRGAS multi-year solution SIR13P01: it covers the time span from April 18, 2010 to June 15, 2013, includes 108 SIRGAS core stations and refers to IGb08, epoch 2012.0. (Stations with labels are fiducial points)

If outliers reflect a discontinuity, a new position is estimated for the station.

Once outliers are removed and discontinuities are identified, the weekly normal equations are combined to a multi-year solution with station velocities. The estimated velocities represent linear station position variations only. Seasonal signals (e.g. hydrologic loading) are not considered. The geodetic datum is realised by applying NNR and NNT conditions with respect to the IGb08 coordinates of the selected reference stations (Fig. 2). After this first computation, new station position residual time series are generated by transforming the weekly solutions to this new SIRGAS reference frame. Discontinuity detection and outlier removal is repeated and the new information is introduced into the computation of a refined reference frame. This iterative process is repeated until no outliers and discontinuities remain. The procedure is carried out using the Bernese GNSS Software V5.2.

The result of this computation is called the SIR13P01 solution (Fig. 2). It includes positions and velocities for 108 SIRGAS core stations referring to IGb08, epoch 2012.0. Its averaged rms precision is ±1.4 mm horizontally and ±2.5 mm vertically for the station positions at the reference epoch, and ±0.8 mm/year horizontally and ±1.2 mm/year vertically for the constant velocities. Stations CONZ (Concepción, Chile) and ANTC (Antuco, Chile) are excluded from these computations, because their post-seismic movements are very irregular and the modelling by means of constant velocities is not adequate.

6 Comparison of the New Multi-Year Solution SIR13P01 with Former Solutions of Reference Frames in the SIRGAS Region

To evaluate the reliability of SIR13P01, different comparisons were performed. The first comparison examines the dissimilarities of the station positions and velocities at the fiducial points, i.e. the IGb08 coordinates are compared with the values obtained in the SIR13P01 solution for the reference stations. The same procedure is repeated in a second comparison, but taking into account the ITRF2008 coordinates for all ITRF stations included in the SIR13P01 solution. Finally, the third comparison collates station position and velocities of the present solution with those values estimated in the last SIRGAS multi-year solution computed before the earthquake of February 2010 (i.e. the SIR10P01 solution in Seemüller et al. 2010). For these comparisons, all the station coordinates (IGb08, ITRF2008, SIR10P01, and SIR13P01) are given at the epoch 2005.0 and the solution SIR10P01 is transformed from IGS05 to IGb08 applying the transformation parameters presented in Rebischung et al. (2012). Table 1 summarizes the main statistical indexes of these comparisons and Figs. 3 and 4 show the geographical distribution of the horizontal discrepancies.

The discrepancies (for station positions and velocities) at the fiducial points are in the same magnitude of the coordinate accuracy in the IGb08 solution and one could conclude

Table 1 Differences between the new SIR13P01 solution and the IGb08, the ITRF2008, and the former solution SIR10P01 (computed before the Chilean earthquake in February 2010). All the coordinates refer to the epoch 2005.0

Index	Positions (cm)			Velocities (cm/year)		
	N	E	Up	N	E	Up
Comparison with IGb08, fiducial points only (18 stations)						
rms	±0.27	±0.19	±0.34	±0.06	±0.11	±0.13
Mean	0.26	−0.13	0.03	−0.03	−0.01	0.06
Min	−0.20	−0.47	−0.72	−0.18	−0.20	−0.23
Max	1.03	0.24	0.68	0.18	0.19	0.24
Comparison with ITRF2008 (41 stations)						
rms	±2.20	±2.90	±2.81	±0.18	±0.48	±0.37
Mean	1.08	0.85	0.02	−0.10	0.06	0.09
Min	−0.21	−1.56	−4.47	−0.63	−0.74	−1.06
Max	13.96	17.62	13.55	0.31	1.98	0.89
Comparison with SIR10P01 (transformed from IGS05 to IGb08, 81 stations)						
RMS	±1.72	±2.40	±2.28	±0.19	±0.37	±0.34
Mean	1.50	0.82	−0.30	−0.10	0.06	0.11
Min	−2.03	−5.33	−4.53	−0.72	−1.06	−1.06
Max	13.93	17.88	12.76	0.44	1.91	0.80

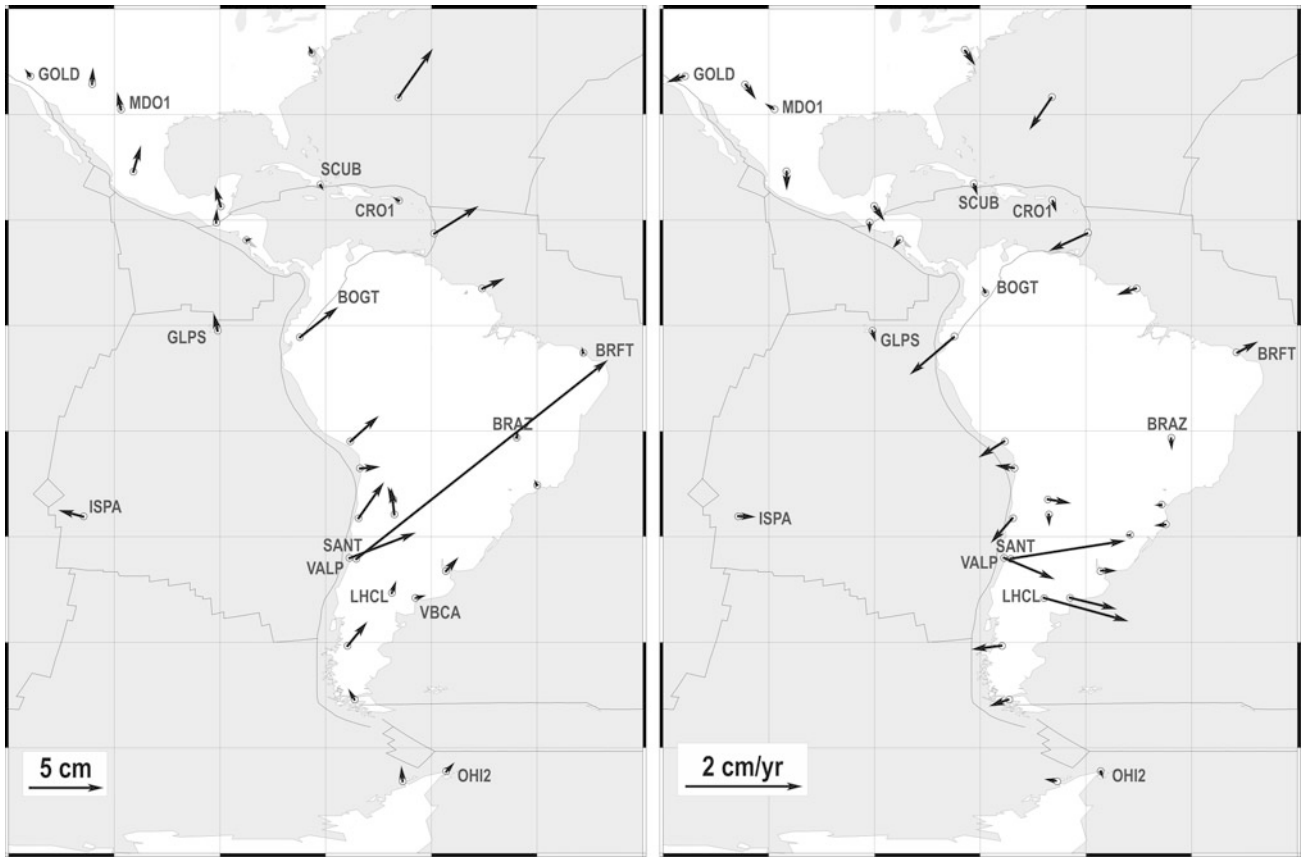

Fig. 3 Horizontal position difference vectors (*left*) and horizontal velocity difference vectors (*right*) between the ITRF2008 and SIR13P01 (all station coordinates refer to epoch 2005.0)

that the new SIRGAS solution is appropriately aligned to this frame and it can be considered as its regional densification in Latin America and the Caribbean. On the contrary, the magnitudes obtained from the other two comparisons are very large, in particular in the East component. This means that the past reference frame solutions (ITRF2008

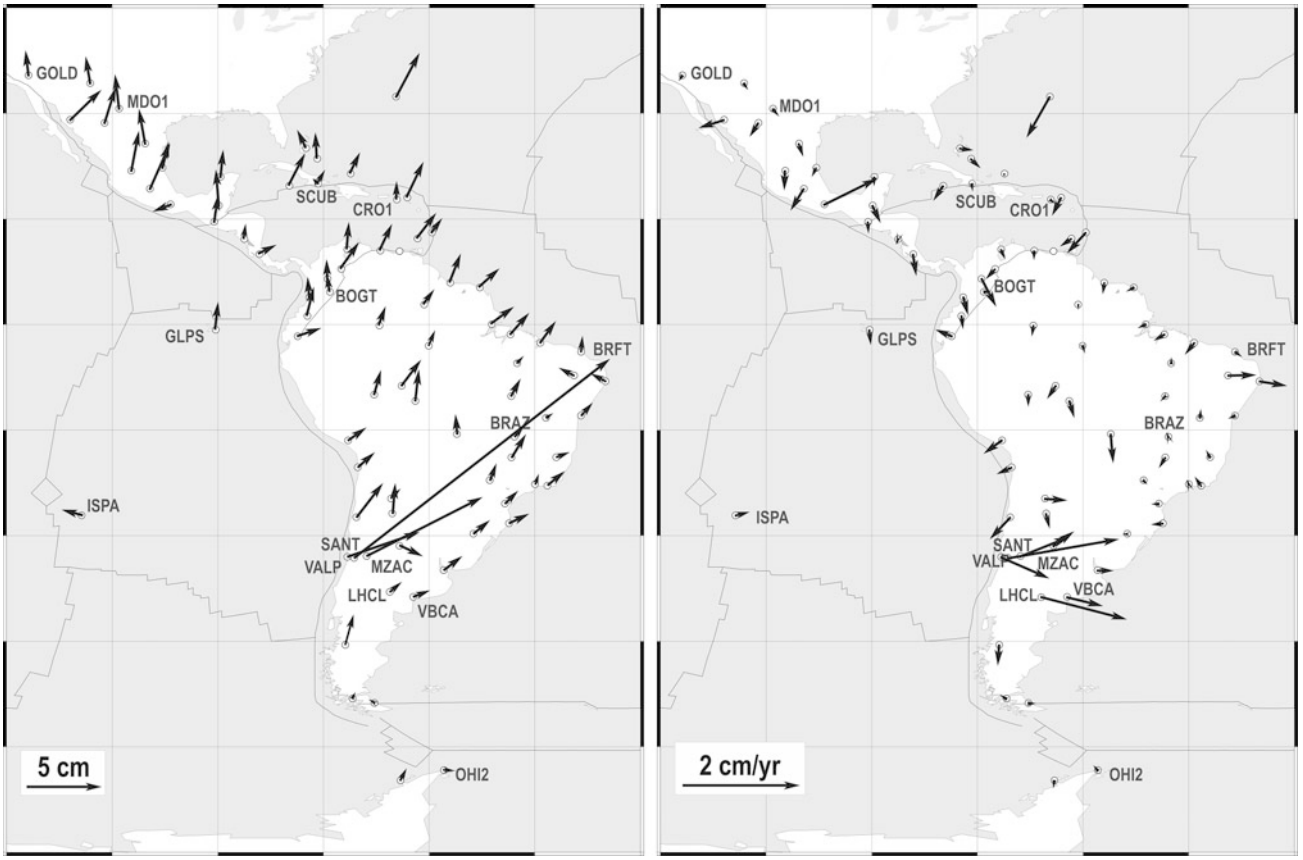

Fig. 4 Horizontal position difference vectors (*left*) and horizontal velocity difference vectors (*right*) between SIR10P01 (before the earthquake of February 2010) and SIR13P01 (all station coordinates refer to epoch 2005.0)

and SIR10P01) disagree significantly with respect to the new one. Main reasons for this disagreement are:

- ITRF2008 and SIR10P01 do not reflect the effects (co-seismic and post-seismic movements) caused by the seism of February 2010 in the Southern part of South America;
- The input weekly solutions for ITRF2008 and SIR10P01 are computed with respect to the IGS05 frame, while SIR13P01 is computed with respect to the IGS08/IGb08 frame. This affects, for instance, the model applied for the corrections of the antenna phase centre variations;
- Troposphere effects in SIR10P01 and SIR13P01 are modelled differently. Although the atmosphere parameters estimated within the network adjustment (∼wet part) are very similar (some millimetres of discrepancy), the a-priori zenith delay values (∼dry part) differ up to 5 cm, especially at those stations located in the tropical region. This decreases the reliability of the vertical coordinates in the former solution;
- The uncertainty of the station velocities reduces the reliability of the SIR13P01 station positions, since an extrapolation from 2012.0 (reference epoch) to 2005.0 (epoch of comparison with the other solutions) is necessary;

The datum realisation in SIR10P01 and SIR13P01 is based on different fiducial points. While the old solution includes reference stations located in Latin America only, the new solution comprises reference stations located far away (some thousands of kilometres). This could help to reduce the dependence of the regional network on the radial effects associated to the GNSS positioning (i.e. the larger the geographical extension of the network the smaller the dependence on radial effects, i.e. higher reliability in the vertical coordinate). However, the non-availability of fiducial points in the internal regions of the network reduces the reliability of the coordinates estimated at the remote stations.

7 Conclusions and Outlook

A new multi-year solution of the SIRGAS reference frame is computed for the time after the large Maule earthquake in Chile (February 2010). The input normal equations are based on the new standards outlined by the IERS and the IGS. Although the internal consistency of the solution is under the expected limits (at mm level), the estimation of its reliability

is very complicated, since existing reference frame solutions (like ITRF2008) do not reflect the deformations caused by the mentioned earthquake. To improve our knowledge about the real effects generated by this earthquake in the SIRGAS frame, it is necessary to re-compute all the weekly normal equations previous to February 2010 applying the same standards and trying to maintain the geometry of the network, i.e., the far away fiducial points used in this computation must also be included in the reprocessing of the SIRGAS network. Another important aspect is the necessity of more fiducial points in the SIRGAS region. For that, a set of continuously operating SIRGAS stations was proposed to be included in the second IGS reprocessing. From 70 stations initially suggested, the IGS Reference Frame Working Group and the IGS Global Analysis Centres decided to include 40 SIRGAS stations not only in the IGS reprocessing but also in the present routine IGS processing. With this, the next solution of the ITRF will include more and better distributed stations in Latin America and the Caribbean. This will improve the accuracy and long-term stability of the SIRGAS reference frame.

References

Altamimi Z, Collilieux X, Métivier L (2011) ITRF2008: an improved solution of the international terrestrial reference frame. J Geod 85(8):457–473. doi:10.1007/s00190-011-0444-4

Böhm J, Werl B, Schuh H (2006) Troposphere mapping functions for GPS and very long baseline interferometry from European Centre for Medium-Range Weather Forecasts operational analysis data. J Geophys Res 111, B02406. doi:10.1029/2005JB003629

Chen G, Herring TA (1997) Effects of atmospheric azimuthal asymmetry on the analysis of space geodetic data. J Geophys Res 102(B9):20489–20502. doi:10.1029/97JB01739

Costa SMA, Silva AL, Vaz JA (2012a) Processing evaluation of SIRGAS-CON network by IBGE Analysis Center. In: Geodesy for Planet Earth, IAG Symposia, vol 136. pp 859–868. doi:10.1007/978-3-642-20338-1_108

Costa SMA, Silva AL, Vaz JA (2012) Report on the SIRGAS-CON combined solution by IBGE Analysis Center. In: Geodesy for Planet Earth, IAG Symposia, vol 136. pp 853–857. doi:10.1007/978-3-642-20338-1_107

Dach R, Hugentobler U, Fridez P, Meindl M (eds) (2007) Bernese GPS Software Version 5.0 – Documentation. Astronomical Institute, University of Berne, Berne, 640 pp

Dach R et al (2013) Bernese GPS Software: new features in version 5.2. http://www.bernese.unibe.ch/docs/BSW52_newFeatures.pdf

Dow JM, Neilan RE, Rizos C (2009) The International GNSS Service in a hanging landscape of Global Navigation Satellite Systems. J Geod 83:191–198. doi:10.1007/s00190-008-0300-3

Drewes H, Kaniuth K, Voelksen C, Alves Costa SM, Souto Fortes LP (2005) Results of the SIRGAS campaign 2000 and coordinates variations with respect to the 1995 South American geocentric reference frame. In: A window on the future of geodesy, IAG Symposia, vol 128. pp 32–37. doi:10.1007/3-540-27432-4_6

Herring TA, King RW, McClusky SC (2010) Introduction to GAMIT/GLOBK, Release 10.4, Massachusetts Institue of Technology. http://www-gpsg.mit.edu/~simon/gtgk/Intro_GG.pdf

Letellier T (2004) Etude des ondes de marée sur les plateux continentaux. Thèse doctorale, Université de Toulouse III, Ecole Doctorale des Sciences de l'Univers, de l'Environnement et de l'Espace, 237 pp (in French)

Natali MP, Mueller M, Fernández L, Brunini C (2009) CPLat: first operational experimental processing center for SIRGAS in Argentina. J Geodesy 83:219–226. doi:10.1007/s00190-008-0270-5

Petit G, Luzum B (eds) (2010) IERS Conventions 2010. IERS Technical Note 36. Verlag des Bundesamtes für Kartographie und Geodäsie, Frankfurt a.M

Rebischung P, Griffiths J, Ray J, Schmid R, Collilieux X, Garayt B (2012) IGS08: the IGS realization of ITRF2008. GPS Solutions 16(4):483–494. doi:10.1007/s10291-011-0248-2

Sánchez L (2012) IGS Regional Network Associate Analysis Centre for SIRGAS (IGS RNAAC SIR). Report of activities 2011, pp 107–115

Sánchez L (2013) IGS Regional Network Associate Analysis Centre for SIRGAS (IGS RNAAC SIR). International GNSS Service Technical Report 2012, pp 111–120

Sánchez L, Brunini C (2009) Achievements and challenges of SIRGAS. In: Geodetic Reference Frames, IAG Symposia, vol 134. pp 161–166. doi:10.1007/978-3-642-00860-3_25

Sánchez L, Seitz M (2011) Recent activities of the IGS Regional Network Associate Analysis Centre for SIRGAS (IGS RNAAC SIR). DGFI Report No. 87

Sánchez L, Seemüller W, Seitz M (2012) Combination of the weekly solutions delivered by the SIRGAS processing centres for the SIRGAS-CON reference frame. In: Geodesy for Planet Earth, IAG Symposia, vol 136. pp 845–851. doi:10.1007/978-3-642-20338-1_106

Sánchez L, Seemüller W, Drewes H, Mateo L, González G, Silva A, Pampillón J, Martínez W, Cioce V, Cisneros D, Cimbaro S (2013) Long-term stability of the SIRGAS reference frame and episodic station movements caused by the seismic activity in the SIRGAS region. In: Reference frames for applications in geosciences, IAG Symposia, vol 138. pp 153–161. doi:10.1007/978-3-642-32998-2_24

Schmid R (2011) Upcoming switch to IGS08/igs08.atx – Details on igs08.atx. IGSMAIL-6355. (http://igs.org/pipermail/igsmail/2011/006347.html

Schmid R, Steigenberger P, Gendt G, Ge M, Rothacher M (2007) Generation of a consistent absolute phase center correction model for GPS receiver and satellite antennas. J Geod 81(12):781–798. doi:10.1007/s00190-007-0148-y

Seemüller W, Sánchez L, Seitz M, Drewes H (2010) The position and velocity solution SIR10P01 of the IGS Regional Network Associate Analysis Centre for SIRGAS (IGS RNAAC SIR). DGFI Report No. 86

Seemüller W, Seitz M, Sánchez L, Drewes H (2012) The new multi-year position and velocity solution SIR09P01 of the IGS Regional Network Associate Analysis Centre (IGS RNAAC SIR). In: Geodesy for Planet Earth, IAG Symposia, vol 136. pp 877–883. doi: 10.1007/978-3-642-20338-1_110

SIRGAS (1997) SIRGAS Final Report; Working Groups I and II IBGE, Rio de Janeiro; 96 p. www.sirgas.org

van Dam T, Ray R (2010) S1 and S2 atmospheric tide loading effects for geodetic applications. http://geophy.uni.lu/ggfc-atmosphere/tide-loading-calculator.html. Accessed 1 June 2013

Part III

Gravity Field Determination and Applications

Numerical Computation of Point Values, Derivatives, and Integrals of Associated Legendre Function of the First Kind and Point Values and Derivatives of Oblate Spheroidal Harmonics of the Second Kind of High Degree and Order

Toshio Fukushima

Abstract

This article reviews the recent works of the author on the numerical computation of the point values, the derivatives, and the integrals of the associated Legendre function (ALF) of the first kind as well as the point values and the derivatives of the oblate spheroidal harmonics of the second kind (Fukushima T, 2012a, J. Geodesy, 86, 271; ibid., 2012b, J. Geodesy, 86, 745; ibid., 2012c, J. Geodesy, 86, 1019; ibid., 2012d, Comp. Geosci., 49, 1; ibid., 2013, J. Geodesy, 87, 303; ibid., 2014, Comp. Geosci., 63,17. First, a sort of exponent extension of the floating point numbers, named the X-number formulation, resolved the underflow problem in the computation of the point values of the fully-normalized ALF of the first kind of high degree and order such as 216 000 or more. Similarly, the formulation precisely computes their derivatives and integrals. Second, a dynamic switch from the X-number to the ordinary floating point number during the fixed-order increasing-degree recursions significantly reduces the increase in the CPU time caused by the exponent extension. Third, the sectorial integrals obtained by the forward recursion cause no troubles in the subsequent non-sectorial recursions. Fourth, the fixed-order increasing-degree recursions can be accelerated on PCs with multiple or many cores by the folded parallel computation, namely by the parallel computation the load balance of which is equalized by pairing the recursion of orders m and $M-m$, where M is the maximum order to be computed. Finally, a recursive formulation is developed to compute the point values and the derivatives of the oblate spheroidal harmonics of the second kind, i.e. the unnormalized ALF of the second kind with a pure imaginary argument. The relating Fortran programs as well as the output examples are available at the author's WEB page in ResearchGate:
https://www.researchgate.net/profile/Toshio_Fukushima/

Keywords

Associated Legendre function • Exponent extension of arithmetics • Oblate spheroidal harmonics • Spherical harmonics • Underflow problem

1 Introduction

The spherical and the oblate spheroidal[1] harmonic expansions are widely used in geodesy and geophysics (Heiskanen and Moritz 1967; Maus 2010; Pavlis et al.

[1]We reserve the word 'ellipsoidal' for an ellipsoid with three different axes (Lowes and Winch 2012; Wang and Yang 2013).

T. Fukushima (✉)
National Astronomical Observatory of Japan, 2-21-1, Ohsawa, Mitaka, Tokyo 181-8588, Japan
e-mail: Toshio.Fukushima@nao.ac.jp

© Springer International Publishing Switzerland 2015

C. Rizos, P. Willis (eds.), *IAG 150 Years*, International Association of Geodesy Symposia 143,
DOI 10.1007/1345_2015_124

2012; Lowes and Winch 2012). However, their numerical computations face with some obstacles when degree/order is high. One problem in the spherical case (Holmes and Featherstone 2002) is an underflow during the computation of $\overline{P}_{nm}(t)$, the 4π fully-normalized Associated Legendre Function (ALF) of the first kind (Heiskanen and Moritz 1967, Sect. 1–14). Here $t \equiv \cos\theta$ while θ is the geocentric colatitude. Additional issue in the oblate spheroidal case (Sona 1995) is the difficulty in computing $Q_{nm}(ix)$, the unnormalized ALF of the second kind with a pure imaginary argument (Olver et al. 2010, Sect. 14.2). This article reviews recent solutions to these problems and related issues (Fukushima 2012a,b,c,d, 2013, 2014).

2 X-Number Formulation

An underflow occurs in the forward sectorial recursion of $\overline{P}_{nm}(t)$ since it is a sequence of multiplications of small factors. For example, when $\theta = 60°$, an underflow happens when $m > 1030$ in the double precision environment of the IEEE 754 standard (IEEE 2008) where the minimum representable number is $2^{-1023} \approx 1.1 \times 10^{-308}$. Once an underflow occurs, all the subsequent sectorial values are regarded as exact zeros in the computers. This ruins the non-sectorial recursions of $\overline{P}_{nm}(t)$ starting from them, which would recover the diminished ALFs to the level of the order of unity *if* the sectorial values remain to be non-zero even if they are extremely tiny. Thus, the underflow results a significant loss of precision in the computation of not only the point values when the maximum order M is as high as 2700 (Fukushima 2012a, Fig. 5) but also the low-order derivatives and the integrals (Fukushima 2014, Fig. 1).

This trouble is solved by the so-called X-number formulation (Fukushima 2012a) or other similar devices (Wittwer et al. 2008; Nesvadba 2008). The X-number formulation represents a real number X by a pair of a floating point number (termed F-number) x and a signed integer i_X such that $X = xB^{i_X}$ where B is a power of 2. If (1) x is an IEEE 754 double precision F-number, (2) i_X is a 32 bit signed integer, and (3) $B \equiv 2^{960}$, the minimum representable number becomes as tiny as $\approx 1.2 \times 10^{-6.2\times 10^{12}}$ (Fukushima 2014, §1). As a result, almost no underflow occurs in the computation of $\overline{P}_{nm}(t)$. Thus, the formulation enables the correct computation of not only the point values of the ALF but also their low-order derivatives and integrals of high degree and order such as 216 000 or more (Fukushima 2012a,c, 2014).

As an illustration, some sample values of them for the case $n = 216\,000$, $m = 108\,000$, $\theta_1 = 60°$, and $\theta_2 = 30°$ are listed below:

$$\overline{P}_{nm}(t_1) = -3.105\,584\,633\,08(1\,662), \tag{1}$$

$$\left[d\overline{P}_{nm}/d\theta\right](t_1) = -6.327\,420\,821\,20(2\,954) \times 10^4, \tag{2}$$

$$\left[d^2\overline{P}_{nm}/d\theta^2\right](t_1) = +6.287\,479\,684\,91(0\,149) \times 10^9, \tag{3}$$

$$\overline{I}_{nm}(t_1, t_2) = +4.839\,192\,555\,12(2\,765) \times 10^{-3}, \tag{4}$$

where the erroneous digits, determined from the comparison with the quadruple precision X-number computation, are shown in parentheses.

3 Acceleration of ALF Computation

In general, the X-number formulation results an increase in the CPU time of a factor 2–3. As already reported in Jekeli et al. (2007), $\overline{P}_{nm}(t)$ starts to oscillate with respect to n when n is sufficiently larger than m (Fukushima 2014, Fig. 2). This suggests a possible switch from the X- to F-number computations during the recursion. The switch is dynamically conducted when both $\overline{P}_{n-1,m}(t)$ and $\overline{P}_{n-2,m}(t)$ can be regarded as F-numbers, namely when both i_X of $\overline{P}_{n-1,m}(t)$ and i_X of $\overline{P}_{n-2,m}(t)$ are 0. This device reduces significantly the CPU time increase (Fukushima 2014, Fig. 6).

Another technique to accelerate the computation of ALFs is the folded parallel computation (Fukushima 2012d). A pairing of the fixed-order increasing-degree recursions of order m and $M - m$, where M is the maximum order, equalizes the computational load of different-order recursions conducted in parallel at multiple processor units. Consequently, its simple implementation by the OpenMP architecture (OpenMP ARB 2011) achieves the acceleration factor being the same as the number of processor units (Fukushima 2012d, Fig. 1).

4 Effect of Underflow of Sectorial Integrals on Non-sectorial Integrals

During the investigation of the computation of the integral of the ALF of the first kind, $\overline{I}_{nm}(t_1, t_2) \equiv \int_{t_1}^{t_2} \overline{P}_{nm}(t)dt$, it is noticed that an underflow, which might occur during the forward recursion of the sectorial integrals (Fukushima 2014, Eq. (A.10)), causes no problem in the subsequent non-sectorial computation (Fukushima 2014).

The reason of this phenomenon becomes clear by examining the dependence of the non-sectorial integral on the sectorial one. The fixed-order increasing-degree recurrence

formulas of $\overline{I}_{nm}$ are expressed (Fukushima 2014, Eqs. (A.2) and (A.8)) as

$$\overline{I}_{m+1,m} = -\overline{J}_{m+1,m},\ \overline{I}_{nm} = f_{nm}\overline{I}_{n-2,m} - \overline{J}_{nm},\ (n \geq m+2) \tag{5}$$

where (1) $\overline{J}_{nm}$ is a partial integral computed from $\overline{P}_{nm}$ at the two end points of the integration interval as

$$\overline{J}_{nm} \equiv \sqrt{\frac{(2n+1)(2n-1)}{(n+m)(n-m)}}\left(\frac{u_2^2\overline{P}_{nm}(t_2) - u_1^2\overline{P}_{nm}(t_1)}{n+1}\right), \tag{6}$$

while $u \equiv \sin\theta$, (2) f_{nm} is a numerical constant defined as

$$f_{nm} \equiv \frac{n-2}{n+1}\sqrt{\frac{(2n+1)(n+m-1)(n-m-1)}{(2n-3)(n+m)(n-m)}},$$
$$(n \geq m+2 \geq 2) \tag{7}$$

and (3) the arguments t_1 and t_2 are omitted where no confusion is introduced.

Thus, $\overline{I}_{nm}$ is a linear function of $\overline{I}_{mm}$ and a group of $\overline{P}_{\ell m}(t_j)$ where $m+1 \leq \ell \leq n$ and $j = 1$ and 2. If $n-m$ is odd, $\overline{I}_{nm}$ does not depend on $\overline{I}_{mm}$ at all. Meanwhile, if $n-m$ is even, $\overline{I}_{nm}$ linearly depends on $\overline{I}_{mm}$ with a product of $f_{\ell m}$ as its proportional coefficient. Namely

$$\left(\frac{\partial\overline{I}_{m+2k-1,m}}{\partial\overline{I}_{mm}}\right)_{\overline{P}_{nm}} = 0,$$
$$\left(\frac{\partial\overline{I}_{m+2k,m}}{\partial\overline{I}_{mm}}\right)_{\overline{P}_{nm}} = \prod_{j=1}^{k} f_{m+2j,m}.\ (k \geq 1) \tag{8}$$

The coefficient is less than unity since $0 < f_{nm} < 1$ when $n \geq m+2 \geq 2$. This means that the absolute error of the sectorial integral contributes to a smaller absolute error of the non-sectorial one. In other words, not the relative error but the absolute error must be worried in the sectorial integral computation. For this purpose, the simple forward recursion (Fukushima 2014, Eq. (A.2)) is sufficient. At any rate, this fact enables one to avoid the existing complicated approach to obtain the sectorial integrals by the backward recursion starting from the two seed values computed by the hypergeometric series (Paul 1978; Gerstl 1980; Gleason 1985).

When $|t_2 - t_1|$ is small, the direct evaluation of $\overline{J}_{nm}$ suffers from a heavy cancellation, and therefore results a precision loss of $\overline{I}_{nm}$. This is eminent when n and m are rather small, say less than 30 or so (Fukushima 2012b, Figs. 1 and 2). In that case, a computing method based on the cancellation-error-free evaluation of the finite differences is effective (Fukushima 2012b).

5 Recursive Computation of Oblate Spheroidal Harmonics of the Second Kind

In addition to the problem of $\overline{P}_{nm}(t)$ computation, another type of problem arises in the computation of oblate spheroidal harmonic expansion. The non-angular component of the expansion is a ratio of $Q_{nm}(ix)$, the ALF of the second kind with a pure imaginary argument (Heiskanen and Moritz 1967). The computational difficulty of $Q_{nm}(ix)$ is caused by the fact that it is the minimal solution of a second-order difference equation (Gil and Segura 1998). As a result, the increasing-degree recursion to obtain $Q_{nm}(ix)$ is fragile against the contamination of the initially tiny but rapidly inflating component, $P_{nm}(ix)$, and therefore becomes quite erroneous (Sona 1995).

Thus, a various forms of hypergeometric functions have been developed instead. However, except that used in Martinec and Graferend (1997), all other forms (Hobson 1931; Jekeli 1988; Petrovskaya and Vershkov 2000; Vershkov 2002; Sebera et al. 2012; Petrovskaya and Vershkov 2013) are inappropriate for high degree and/or order (Fukushima 2013, Fig. 1) due to the cancellation problems. Meanwhile, a method using the backward recursion already exists (Gil and Segura 1998). It uses the Wronskian relation to obtain the seed values of $Q_{nm}(ix)$ from the values of $P_{nm}(ix)$ computed by the forward recursion. However, this method faces the overflow problem in the recursive computation of $P_{nm}(ix)$ (Gil and Segura 1998, Tables 1 and 2).

In order to overcome this situation, a new method based on the backward recursion is developed (Fukushima 2013). The key point of the new method is the usage of a hypergeometric series to evaluate $Q_{nm}(ix)$ developed by Petrovskaya and Vershkov (2000). Although it is not suitable for general values of n and m, it rapidly converges when m is sufficiently small, say $m = 0$ and 1. Thus, it can be used in obtaining the three seed values of the backward recursion. Also, the derivative computation is achieved by recursion. As a result, the new method is sufficiently precise and yet much faster than the existing method in the computation of the point values and low-order derivatives of the ratio of $Q_{nm}(ix)$ (Fukushima 2013, Fig. 2).

Sample values of the ratio, $q_{nm}(x) \equiv Q_{nm}(ix)/Q_{nm}(x_0)$, and its low-order derivatives with respect to x for the case $n = 216\,000$, $m = 108\,000$, $x_0 = b/E$, and $x = (b + 0.1\ \text{km})/E$, while b and $E \equiv ae$ are those of the GRS80 system, are listed below:

$$q_{nm}(x) = +3.392\,092\,979\,84(8\,901) \times 10^{-2}, \tag{9}$$

$$dq_{nm}(x)/dx = -5.989\,743\,102\,88(4\,788) \times 10^2, \quad (10)$$

$$d^2q_{nm}(x)/dx^2 = +1.057\,671\,120\,81(9\,206) \times 10^7. \quad (11)$$

6 Summary and Future Issues

The so-called X-number formulation (Fukushima 2012a,c, 2014) resolves not only the underflow problem but also the overflow problem in any kind of computation. For example, the *unnormalized* ALF of the first kind, $P_{nm}(t)$ or $P_{nm}(ix)$, can be computed by this formulation without suffering from the overflow problem.

The formulation is significantly accelerated by the dynamic switch from X- to F-numbers during the fixed-order increased-degree recursions of $\overline{P}_{nm}(t)$. Also, if a suitable parallel computing environment is available, a further speed-up is achieved by the folded parallel execution of fixed-order recursions (Fukushima 2012d).

Consequently, the formulation realizes an accurate, precise, and fast computation of the point values, the derivatives, and the integrals of the ALF of the first kind. This enables us to conduct not only the spherical harmonic synthesis but also the spherical harmonic analysis of high degree and order as 216 000 or more.

On the other hand, a backward recursive formulation computes the point values of $Q_{nm}(ix)$ precisely and quickly (Fukushima 2013). This has lowered the computational difficulty of the oblate spheroidal harmonic synthesis to the level of the popular spherical harmonic synthesis. Thus, the next problem to be investigated is the oblate spheroidal harmonic analysis (Wang and Yang 2013). If that is completed, there will be 'nothing to fear from oblate spheroidal harmonics' (Nesvadba 2011).

The Fortran 77/90 programs of these computations as well as output examples are available from the following website:
https://www.researchgate.net/profile/Toshio_Fukushima/

The author appreciates many valuable suggestions by Dr. J. Sebera and two anonymous referees.

References

Fukushima T (2012a) Numerical computation of spherical harmonics of arbitrary degree and order by extending exponent of floating point numbers. J Geod 86:271–285

Fukushima T (2012b) Recursive computation of finite difference of associated Legendre functions. J Geod 86:745–754

Fukushima T (2012c) Numerical computation of spherical harmonics of arbitrary degree and order by extending exponent of floating point numbers: II first-, second-, and third-order derivatives. J Geod 86:1019–1028

Fukushima T (2012d) Parallel computation of satellite orbit acceleration. Comp Geosci 49:1–9

Fukushima T (2013) Recursive computation of oblate spheroidal harmonics of the second kind and their first-, second-, and third-order derivatives. J Geod 87:303–309

Fukushima T (2014) Numerical computation of spherical harmonics of arbitrary degree and order by extending exponent of floating point numbers: III integral. Comput Geosci 63:17–21

Gerstl M (1980) On the recursive computation of the integrals of the associated Legendre functions. Manuscr Geod 5:181–199

Gil A, Segura J (1998) A code to evaluate prolate and oblate spheroidal harmonics. Comput Phys Commun 108:267–278

Gleason DM (1985) Partial sums of Legendre series via Clenshaw summation. Manuscr Geod 10:115–130

Heiskanen WA, Moritz H (1967) Physical geodesy. Freeman and Co, San Francisco

Hobson EW (1931) The theory of spherical and spheroidal harmonics. Cambridge University Press, Cambridge

Holmes SA, Featherstone WE (2002) A unified approach to the Clenshaw summation and the recursive computation of very high degree and order normalized associated Legendre functions. J Geod 76:279–299

IEEE Computing Society (2008) 754-2008 – IEEE Standard for Floating-Point Arithmetic. doi:10.1109/IEEESTD.2008.4610935

Jekeli C (1988) The exact transformation between ellipsoidal and spherical harmonic expansions. Manuscr Geod 13:106–113

Jekeli C, Lee JK, Kwon JH (2007) On the computation and approximation of ultra-high-degree spherical harmonic series. J Geod 81:603–615

Lowes FJ, Winch DE (2012) Orthogonality of harmonic potentials and fields in spheroidal and ellipsoidal coordinates: application to geomagnetism and geodesy. Geophys J Int 191:491–507

Martinec Z, Grafarend EW (1997) Solution to the stokes boundary value problem on an ellipsoid of revolution. Stud Geophys Geod 41:103–129

Maus S (2010) An ellipsoidal harmonic representation of Earth's lithospheric magnetic field to degree and order 720. Geochem Geophys Geosyst 11:Q06015

Nesvadba O (2008) Towards the numerical evaluation of high degree and order associated Legendre functions as in EGM08. In: GGEO symposium, Chania, 23–27 June 2008

Nesvadba O (2011) Nothing to fear from ellipsoidal harmonics. In: General assembly of the European Geosciences Union, Vienna, 3–8 April 2011

Olver FWJ, Lozier DW, Boisvert RF, Clark, CW (eds) (2010) NIST handbook of mathematical functions. Cambridge University Press, Cambridge. http://dlmf.nist.gov/

OpenMP Architecture Review Board (2011) OpenMP 3.1 API Fortran Syntax Quick Reference Card. http://openmp.org/mp-docmments/S

Paul MK (1978) Recurrence relations for integrals of associated Legendre functions. Bull Geod 52:177–190

Pavlis NK, Holmes SA, Kenyon SC, Factor JK (2012) The development and evaluation of the Earth Gravitational Model 2008 (EGM2008). J Geophys Res 117:B04406

Petrovskaya MS, Vershkov AN (2000) Simplified relations between the ellipsoidal and spherical harmonic coefficients of the external earth's potential. Bollettino di Geodesia e Scienze Affini 59:57–72

Petrovskaya MS, Vershkov AN (2013) Improved expressions for the ellipsoidal harmonic series representing the Earth gravitational potential and its first and second derivatives on and outside the reference ellipsoid of revolution. Stud Geophys Geod 57:353–368

Sebera J, Bouman J, Bosch W (2012) On computing ellipsoidal harmonics using Jekeli's renormalization. J Geod 86:713–726

Sona G (1995) Numerical problems in the computation of ellipsoidal harmonics. J Geod 70:117–126

Vershkov AN (2002) Determination of the spherical harmonic coefficients from the ellipsoidal harmonic coefficients of the Earth's external potential. Artif Satell 37:157–168

Wang YM, Yang X (2013) On the spherical and spheroidal harmonic expansion of the gravitational potential of the topographic masses. J Geod 87:909–921

Wittwer T, Klees R, Seitz K, Heck B (2008) Ultra-high degree spherical harmonic analysis and synthesis using extended-range arithmetic. J Geod 82:223–229

Developments in the Implementation and Use of Least-Squares Collocation

C.C. Tscherning

Abstract

The method of Least-Squares Collocation (LSC) was developed in the 1960s based on theoretical advances by T. Krarup and H. Moritz. The method may be used for the determination of approximations to the anomalous gravity potential (T) and associated parameters like biases or tilts. All gravity field observabels which may be related to T through a linear functional may be predicted and error-estimates computed. The method has primarily been used in local or regional applications, due to the fact that a system of equations with as many unknowns as the number of observations need to be established and solved. The problem has been solved due to the use of multiprocessing in the current GRAVSOFT implementation of GEOCOL.

The method has been implemented using isotropic reproducing kernels fitted to empirical covariance functions. The Kernels are harmonic outside a so-called Bjerhammar-sphere, which must be inside the volume bounded by the location of the used data. This problem has been overcome by initially lifting the data in Polar areas 20 km, thereby enabling global LSC solutions in the form of spherical harmonic expansions.

The theoretical possibility of computing error-estimates does not give good results due to the isotropy of the kernels used. The error estimates primarily shows where good data are located or where data are missing. However due to the advent of global gravity gradients from the ESA Gravity and Ocean Circulation Explorer (GOCE) mission it is possible to compute nearly everywhere local signal variances which can be used to tune the otherwise uniform estimates.

Keywords

Error-estimates • GEOCOL program • Gravity • GRAVSOFT package • Least-squares collocation • Reproducing kernels

1 Introduction

The method of Least-Squares Collocation (LSC) was developed in the 1960s based on theoretical advances by T. Krarup (1969) and H. Moritz (1965, 1980). It gives the optimal (best) linear approximation in a reproducing kernel Hilbert-Space of harmonic functions or in an equivalent stochastic process. A minimum norm solution is obtained.

LSC is optimal so it gives the best results using less data. An example is the comparison with reduced point masses (RPM, a Radial basis-function) and LSC used in

C.C. Tscherning (✉)
Niels Bohr Institute, University of Copenhagen, Copenhagen, Denmark
e-mail: cct@gfy.ku.dk

It is with great sadness that we report that Professor Carl Christian Tscherning, former General Secretary of the International Association of Geodesy, and a charismatic, outspoken, and giant of geodesy, passed away on October 24, 2014, at the age of 72 years.

© Springer International Publishing Switzerland 2015

C. Rizos, P. Willis (eds.), *IAG 150 Years*, International Association of Geodesy Symposia 143,
DOI 10.1007/1345_2015_54

Table 1 Computation time for Cholesky reduction of normal equations with N unknows

N	37,971	22,464	22,464
Processors	22	22	4
Time (s)	440	136	391

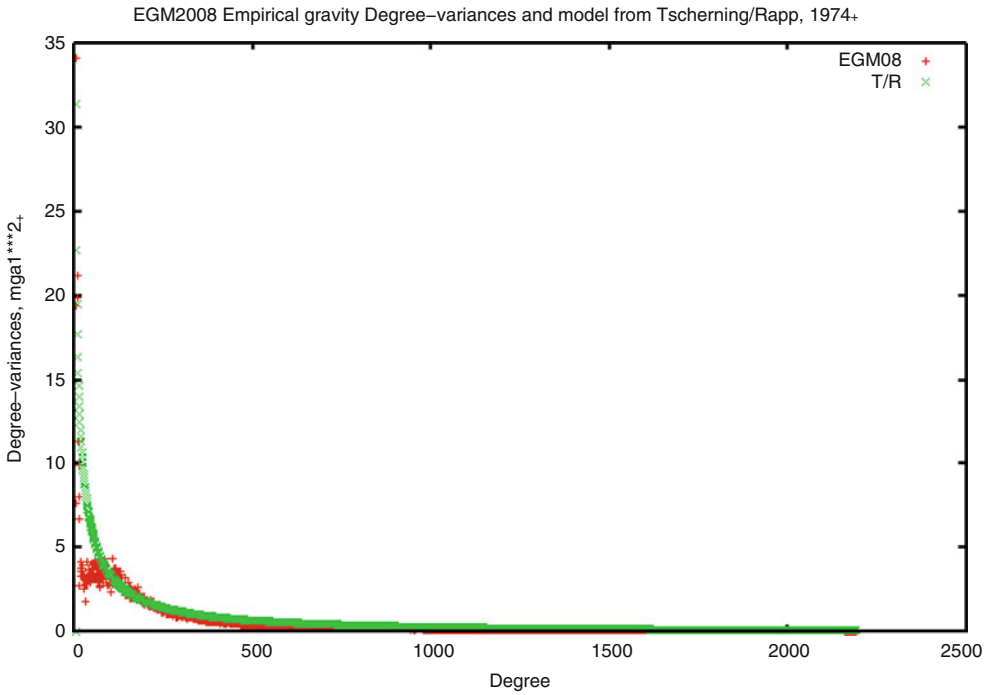

Fig. 1 EGM2008 and T/R degree-variances (mGal^2)

GOCINA test area with GOCE T_{zz} data, see Herceg et al. (2012).

The method may be used for the determination of approximations to the anomalous gravity potential (T) and associated parameters like biases or tilts. All gravity field observables which may be related to T through a linear functional may be predicted and error-estimates computed.

The convergence of the method has been proven for increasing number of (noisy) data, see Tscherning (1978), Sansò and Tscherning (1980), Sansò and Venuti (2012).

Despite these positive properties, a number of problems had to be solved before an operational, effective, method was developed. In the following is discussed the most important of these developments, many of which are due to results or software developed by other scientists. See the acknowledgements below. The following discussion will be limited to the 3D-implementation. For 2D LSC see Forsberg (1984). For more details about applications and theory see Sansò and Sideris (2013).

2 Solution of Equations

The method has primarily been used in local or regional applications, due to the fact that a system of equations with as many unknowns as the number of observations need to be established and solved. The problem has been solved due to the use of multiprocessing in the current GRAVSOFT implementation of GEOCOL, Forsberg and Tscherning (2008), Kaas et al. (2013). It is available from http://cct.gfy.ku.dk/software/geocol19.htm. In Table 1 is given an example of the time (in seconds) needed for solving a typical system of equations with N observations using a 2.40 GHz Intel® computer for a different number of processors.

3 Covariance Function Representation

The method has in GRAVSOFT been implemented using isotropic reproducing kernels fitted to empirical covariance functions (Tscherning 1972a, b; Knudsen 1987). The Kernels are harmonic outside a so-called Bjerhammar-sphere, which must be inside the volume bounded by the location of the used data. If spherical approximation is used, then this causes no problem. But for global use the best fitting model has an associated radius smaller than the semi-major axis, see Tscherning and Rapp (1974). This old covariance function representation is surprisingly still valid despite it was estimated using very few data. The model fits very well the degree-variances computed from EGM2008 (Pavlis et al. 2012), see Fig. 1.

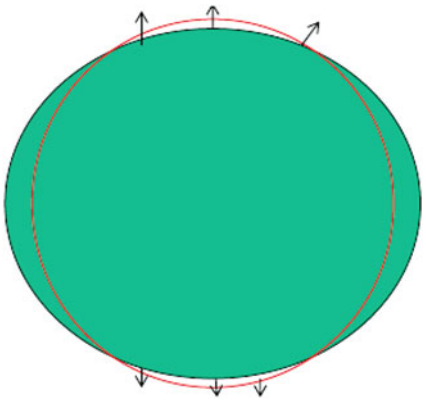

Fig. 2 Moving data at the poles outside the best fitting Bjerhammar sphere

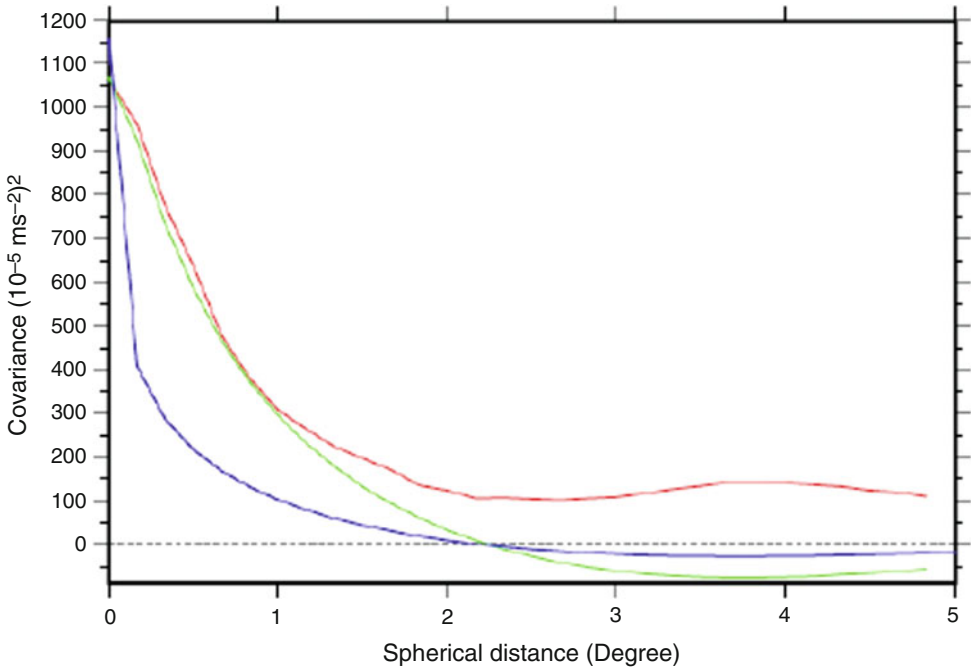

Fig. 3 Disagreement between the analytic models determined from the data, *blue*: T_{zz}, *red*: empirical Δg, *green*: analytic from gravity (Arabelos et al. 2013)

The Bjerhammar-sphere problem has been overcome by initially lifting the data in Polar areas 20 km, thereby enabling global LSC solutions in the form of spherical harmonic expansions, as illustrated in Fig. 2, see the following section.

The basic model is isotropic, and this causes difficulties when LSC is applied in areas with a strongly non-isotropic gravity field such as along a mountain chain or a fault. However, the removal of the cause of anisotropies – both in long and short wavelengths – has been succesful using the remove-restore method, Forsberg and Tscherning (1981), Migliaccio et al. (2005). But this obviously requires that reliable topographis data are available.

Recent development using anisotropic functions are described in Pertusini et al. (2007) and in Reguzzoni and Gatti (2013).

Another difficult situation arises if the ground data is unreliable which for example may be detected using a simple tool as a histogram, or if data does not exist. The last excuse is happily not applicble anymore, due to the advent of global data especially from GOCE. This is illustrated in Fig. 3, where a covariance model has been estimated using ground data and GOCE T_{zz} data.

4 Applications of LSC

4.1 Regional or Local Applications

The method has been used extensively for regional geoid (height anomaly) determination. It is not possible to list all the references here. A good example is the computation of the geoid of Pakistan (Sadiq et al. 2010). A comparison of LSC with other regional procedures is published in Yildiz et al. (2012). Other important applications have been the use for the gridding and calibration of GOCE data Bouman et al. (2004), Pail et al. (2011) and the prediction of gravity anomalies from satellite altimeter data (Andersen et al. 1996).

Table 2 Unitless estimate and error estimate for coefficient $\overline{C}(100, 100)*10^8$

Model	N, Number of observations	Estimate	Error-estimate
EGM96		0.111	0.036
EGM2008		0.100	0.012
GOCE TIM2	>10,000,000	0.105	0.015
LSC 1° grid	42,219	0.120	0.054
LSC 0.5° grid	164,212	0.106	0.028
LSC 0.25° grid	~650,000	?	0.014

Data distributed in the LSC solutions in an approximate equal-area grid

4.2 Global LSC

A recent development is the use LSC globally for the estimation of spherical harmonic coefficients (Tscherning 2001) using GOCE Terrestrial Reference Frame (TRF) T_{zz} data (HPF 2010) and gravity anomalies at the poles. The results are shown in Table 2 for various global gravity field models.

Considering the associated error-estimates it should be possible to use LSC in order to obtain an error similar to the one obtained using many more data.

5 Computation of Error Estimates

The theoretical possibility of computing error-estimates does not give good results due to the isotropy of the kernels used. The error estimates primarily shows where good data are located or where data are missing (see for example Fig. 8). However due to the advent of global gravity gradient from the ESA GOCE mission it is possible to compute local signal variances (see Fig. 8) where no ground data are available, which can be used to tune the otherwise uniform estimates. An example is the use of this method (still being developed) for the improvement of error-estimates of grids of gravity anomalies computed from GOCE T_{zz} data in the trench area south of Japan, see Figs. 4, 5, 6, 7, 8, and 9.

It is obvious (comparing Figs. 6 and 9) that the scaled error-estimates improves the reliability of the estimates. However, the procedure is still under development. More details are found in Tscherning (2013).

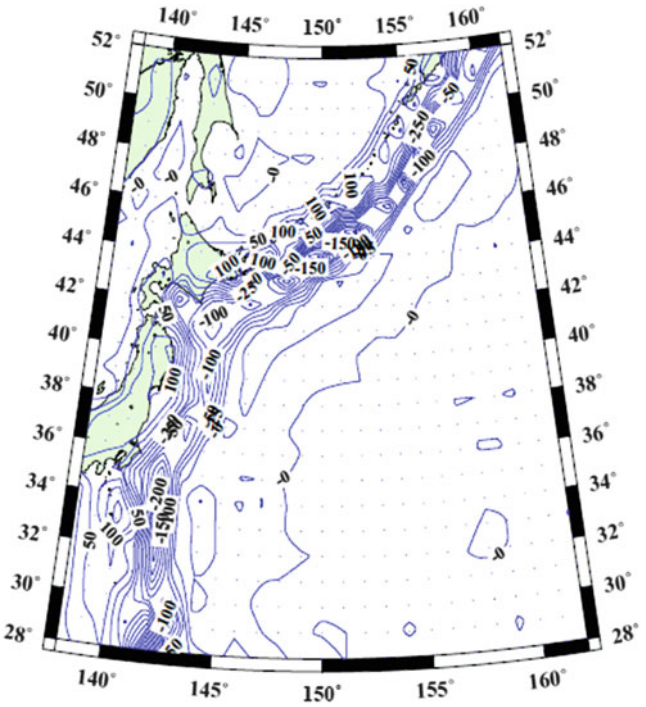

Fig. 4 Gavity anomalies from GOCE T_{zz} & EGM2008 to 512 (ITG-Grace2010c, (Mayer-Guerr et al. 2010) to 36 subtracted everywhere), units: mGal

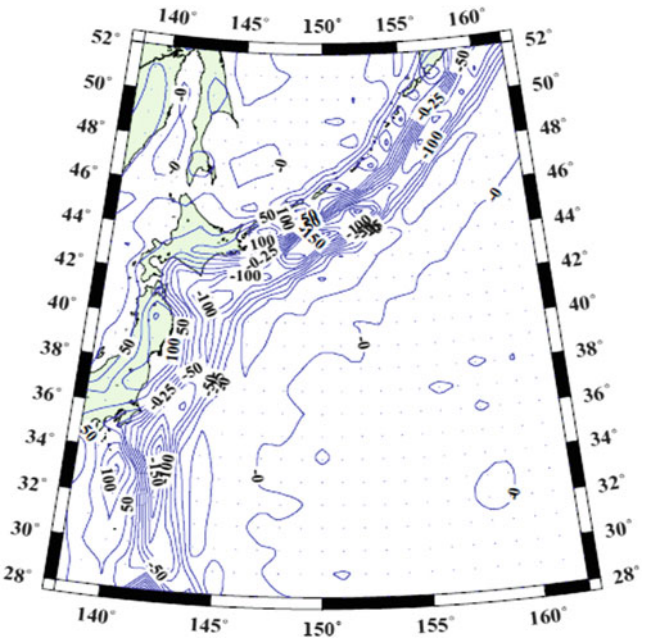

Fig. 5 Gravity anomalies from GOCE T_{zz} & EGM2008 to 512 (ITG-Grace2010c, (Mayer-Guerr et al. 2010) to 36 subtracted everywhere), units: mGal

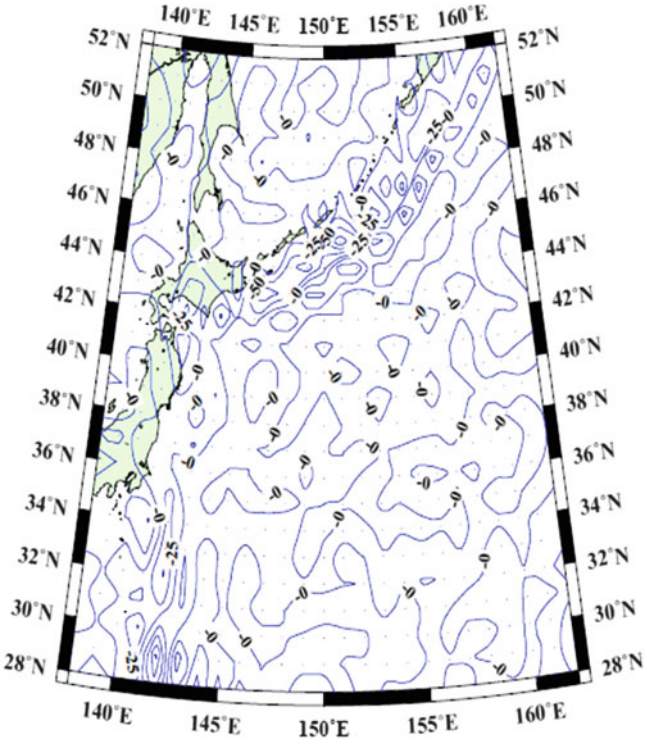

Fig. 6 Differences gravity (mGal) from GOCE T_{zz}-EGM2008 to 512 and LSC error estimates

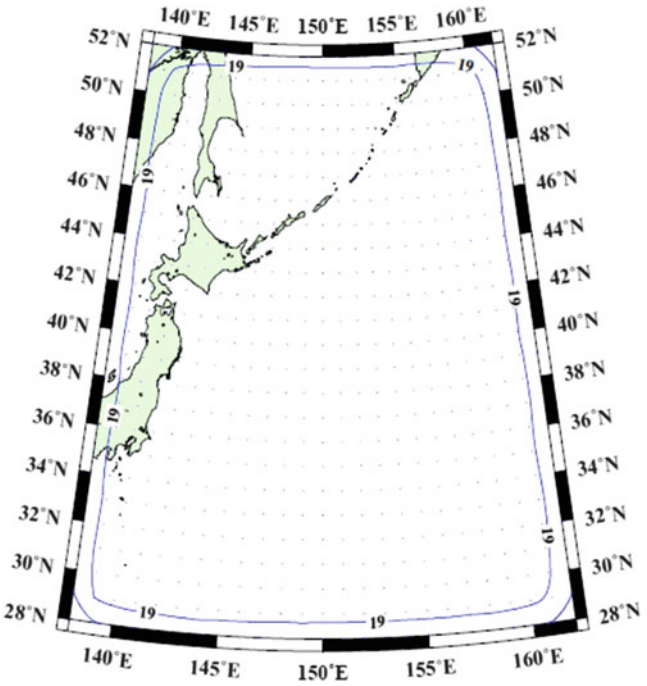

Fig. 7 Differences gravity (mGal) from GOCE T_{zz}-EGM2008 to 512 and LSC error estimates

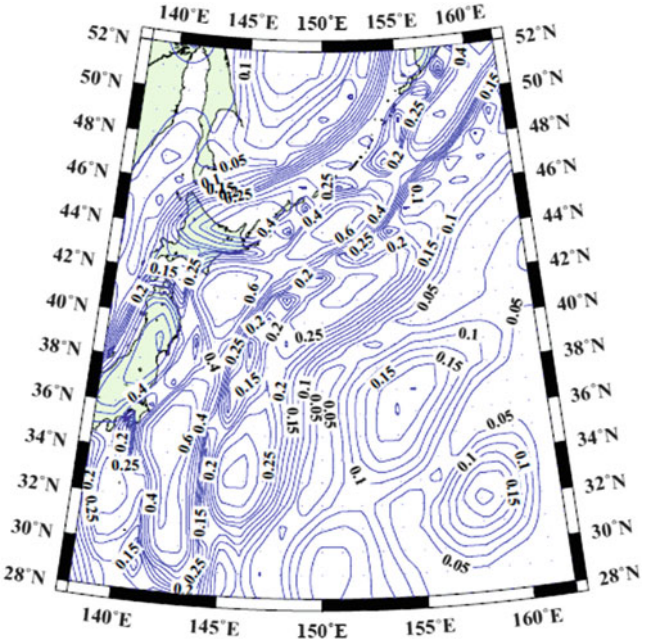

Fig. 8 T_{zz} RMS (E) and scaled error estimates (mGal)

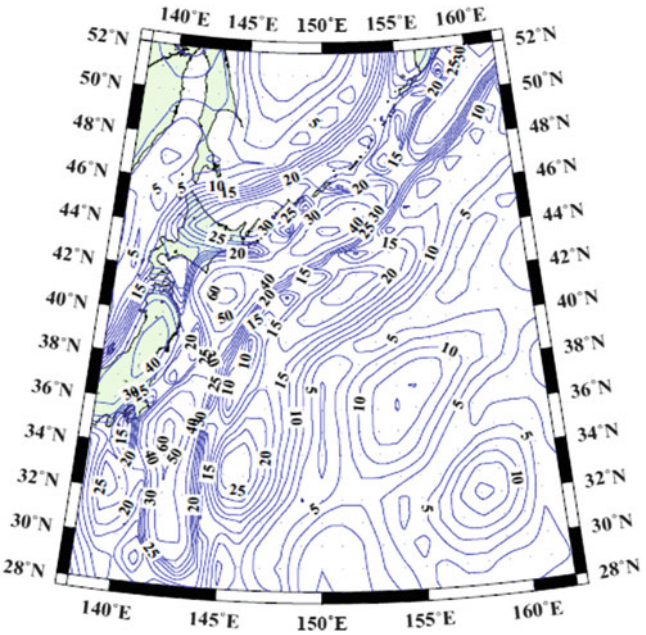

Fig. 9 T_{zz} RMS (E) and scaled error estimates (mGal)

6 Software Development

The first general program was written in Algol in 1972 (Tscherning 1972a, b). A general FORTRAN program was written in 1974 for 3D LSC (Tscherning 1974), geocol, now

geocol19. A 2D LSC program, gpcol, was developed by R. Forsberg. Both programs are available for scientific or teaching purpose free of charge.

Programs have also been developed at TUGraz, POLIMI and UHannover.

7 Conclusion

LSC is not anymore restricted due to large number of observations if multiprocessing can be used. Analytic ellipsoidal or anisotropic kernels are under development or already developed. Software is available in the GRAVSOFT package. The scaling of LSC derived error-estimates improves the error estimates, so that the variation of the error due to changing local signal standard deviation is seen. The development and use have involved many colleagues, whom the author is grateful to acknowledge, see the incomplete list below.

Acknowledgement Thanks to those who have contributed to the development: D. Arabelos, M. Reguzzoni, F. Sansò, M. Sideris, K.P. Schwarz, R. Rummel, R. Barzaghi, R.H. Rapp, P. Holota, H. Sünkel, P. Knudsen, R. Forsberg, M. Veicherts, B. Sørensen, G. Moreaux, S. Heitz, E. Grafarend.

References

Andersen OB, Knudsen P, Tscherning CC (1996) Investigation of methods for global gravity field recovery from dense ERS-1 geodetic mission altimetry. In: Rapp RH, Cazenave AA, Nerem RS (eds) Global gravity field and its temporal variations. IAG Symposia, vol 116. Springer, pp 218–226

Arabelos D, Reguzzoni M, Tscherning CC (2013) Global grids of gravity anomalies and vertical gravity gradients at 10 km altitude fromGOCE gradient data 2009–2011 and polar gravity. Newtons Bull. http://www.isgeoid.polimi.it/Newton/Online_First/Newton_cct2208.pdf

Bouman J, Koop R, Tscherning CC, Visser P (2004) Calibration of GOCE SGG data using high-low SST, terrestrial gravity data, and global gravity field models. J Geod 78:1–2. doi:10.1007/s00190-004-383-5

Forsberg R (1984) Local covariance functions and density distributions. Reports of the Department of Geodetic Science and Surveying No. 356, The Ohio State University, Columbus

Forsberg R, Tscherning CC (1981) The use of height data in gravity field approximation by collocation. J Geophys Res 86(B9):7843–7854

Forsberg R, Tscherning CC (2008) An overview manual for the GRAVSOFT geodetic gravity field modelling programs, 2nd edn. Contract report for JUPEM

Herceg M, Knudsen P, Tscherning CC (2012) GOCE data for local geoid enhancement. Accepted proceedings international symposium on gravity, geoid and height systems 2012, Venice, Italy

HPF (2010) GOCE level 2 product data handbook, GO-MA-HPF-GS-0110, Issue 4.3, 9 Dec 2010

Kaas E, Sørensen B, Tscherning CC, Veichert M (2013) Multiprocessing least squares collocation applications to gravity field analysis. J Geod Sci 3(3):219–223. doi:10.2478/jogs-2013-0025

Knudsen P (1987) Estimation and modelling of the local empirical covariance function using gravity and satellite altimeter data. Bull Geod 61:145–160

Krarup T (1969) A contribution to the mathematical foundation of physical geodesy. Meddelelse no. 44, Geodætisk Institut, København

Mayer-Guerr T, Kurtenbach E, Eicker A (2010) The satellite-only gravity field model ITG-grace2010s. http://www.igg.uni-bonn.de/apmg/index.php?id=itg-grace2010

Migliaccio F, Reguzzoni M, Sansò F, Tscherning CC (2005) The performance of the space-wise approach to GOCE data analysis, whenstatistical homogenization is applied. Newton Bull 2. http://www.isgeoid.polimi.it/Newton/Newton_2/Migliaccio.pdf

Moritz H (1965) Schwerevorhesage und Ausgelichungsrechnung. Z Vermessungswesen 90:181–184

Moritz H (1980) Advanced physical geodesy. H. Wichmann, Karlsruhe

Pail R, Bruinsma S, Migliaccio F, Förste C, Goiginger H, Schuh W-D, Höck E, Reguzzoni M, Brockmann JM, Abrikosov O, Veicherts M, Fecher T, Mayrhofer R, Krasbutter I, Sansò F, Tscherning CC (2011) First GOCE gravity field models derived by three different approaches. J Geod 85:819–843. doi:10.1007/s00190-011-0467-x

Pavlis NK, Holmes SA, Kenyon SC, Factor JK (2012) The development and evaluation of the earth gravitational model 2008 (EGM2008). J Geophys Res Solid Earth 117:B04406. doi:10.1029/2011JB008916

Pertusini L, Reguzzoni M, Sansò F, Sona G (2007) Ellipsoidal collocation. Presented XXIV IUGG General Assembly, Perugia

Reguzzoni M, Gatti A (2013) Anisotropic covariance modelling based on locally adapted coefficient variances in gravity field estimation. Submitted proceedings HM2013

Sadiq M, Tscherning CC, Zulfiqar A (2010) Regional gravity field model in Pakistan area from the combination of CHAMP, GRACE and ground data using least squares collocation: A case study. J Adv Space Res 46(11):1466–1476. doi:10.1016/jasr.2010.07.004

Sansò F, Sideris MG (eds) (2013) Geoid determination, vol 110, Lecture notes in earth system science. Springer, Berlin-Heidelberg. doi:10.1007/978-3-540-74700-0_7

Sansò F, Tscherning CC (1980) Notes on convergence problems in Collocation theory. Bull Geod Sci Affi XXXIX(2):221–252

Sansò F, Venuti G (2012) The convergence problem of collocation solutions in the framework of the stochastic. VII Hotine-Marussi symposium on mathematical geodesy, vol 137. Proceedings of the symposium in Rome, 6–10 June, 2009. Springer

Tscherning CC (1972) An Algol-program for prediction of height anomalies, gravity anomalies and deflections of the vertical. The Danish Geodetic Institute Internal Rep. No. 2

Tscherning CC (1972) Representation of covariance functions related tothe anomalous potential of the earth using reproducing kernels. The Danish Geodetic Institute Internal Rep. No. 3

Tscherning CC (1974) A FORTRAN IV program for the determination of the anomalous potential using stepwise least squares collocation. Reports of the Department of Geodetic Science No. 212, The Ohio State University, Columbus, Ohio

Tscherning CC (1978) On the convergence of least squares collocation. Bull Geod Sci Affi XXXIII(2–3):507–516

Tscherning CC (2001) Computation of spherical harmonic coefficients and their error estimates using least squares collocation. J Geod 75:14–18

Tscherning CC (2013) Improvement of least-squares collocation error x estimates using local GOCE Tzz signal standard deviations. Submitted proceedings HM2013

Tscherning CC, Rapp RH (1974) Closed covariance expressions for gravity anomalies, geoid undulations, and deflections of the vertical implied by anomaly degree-variance models. Reports of the Department of Geodetic Science No. 208, The Ohio State University, Columbus, Ohio

Yildiz H, Forsberg R, Aagren J, Tscherning CC, Sjoeberg LE (2012) Comparison of remove-compute-restore and least squares modification of Stokes formula techniques to quasi-geoid determination over the Auvergne test area. J Geod Sci 2(1):1–12. doi:10.2478/v10156-011-0024-9

The Impact of Using Jason-1 and Cryosat-2 Geodetic Mission Altimetry for Gravity Field Modeling

Ole Baltazar Andersen, Maulik Jain, and Per Knudsen

Abstract

Since the release of the Danish Technical University DTU10 global marine gravity field in 2010, the amount of geodetic mission altimetry data has nearly tripled. The Cryosat-2 satellite have provided data along its 369 day near repeat since 2010 and as of May 2012 the Jason-1 satellite has been operating in a geodetic mission as part its end of life mission.

In this presentation, we perform an investigation of the impact of the Cryosat-2 and Jason-1 geodetic missions on high resolution marine gravity field mapping through comparison with recent high quality marine gravity measured by the United States Naval Ship Bowditch in the Western Pacific Ocean in 2006. Comparisons of pre and post Cryosat-2/Jason-1 gravity fields illustrated the importance of these new geodetic missions for altimeter marine gravity field mapping.

Altimetric gravity derived using 1 year of either Cryosat-2 or Jason-1 is nearly 10% better than gravity derived from retracked and reprocessed combined ERS-1 and Geosat in terms of lower standard deviation with marine gravity. The combination of data from all four geodetic mission data improves the agreement from around 4.1 mGal to around 3.1 mGal. Accounting for an error estimate of around 1 mGal in the marine gravity observations, it is concluded that for this particularly gravity survey region, the new gravity field from four geodetic missions has an accuracy of about 2 mGal.

Keywords

Gravity anomalies • Marine gravity • Satellite altimetry

1 Introduction

During 1985/1986 Geosat performed a 15 months geodetic mission resulting in an irregular roughly 6 km track spacing at the Equator. In 1994/1995 the ERS-1 satellite performed a similar geodetic mission lasting 11 months resulting in a regular 8 km across track pattern. Since 1995 various missions have be measuring along exact repeat track for oceanography (i.e., the 9.91 days repeat track by TOPEX/Poseidon and Jason). However, these exact repeat tracks are not particularly useful to gravity field determination, as they do not provide the essential dense track coverage. However with the availability of Cryosat-2 and the Jason-1 end-of-life missions, three times as many geodetic mission altimetric data have now become available to the scientific community.

Of equal importance is the fact, that the Cryosat-2 and Jason-1 are new generations of satellite altimeters offering increased range precision compared with the older ERS-1 and Geosat generation satellites. Increased range precision improves local mapping of the Ocean's height field which will improve local marine gravity field mapping. The Cryosat-2 pre-launch specifications indicated a factor of two in range precision compared with the older geodetic mission. This could in principle lead to a twofold improvement in

O.B. Andersen (✉) • M. Jain • P. Knudsen
DTU Space, Technical University of Denmark, Elektrovej 328, 2800 Kgs Lyngby, Denmark
e-mail: oa@space.dtu.dk

© Springer International Publishing Switzerland 2015

C. Rizos, P. Willis (eds.), *IAG 150 Years*, International Association of Geodesy Symposia 143,
DOI 10.1007/1345_2015_95

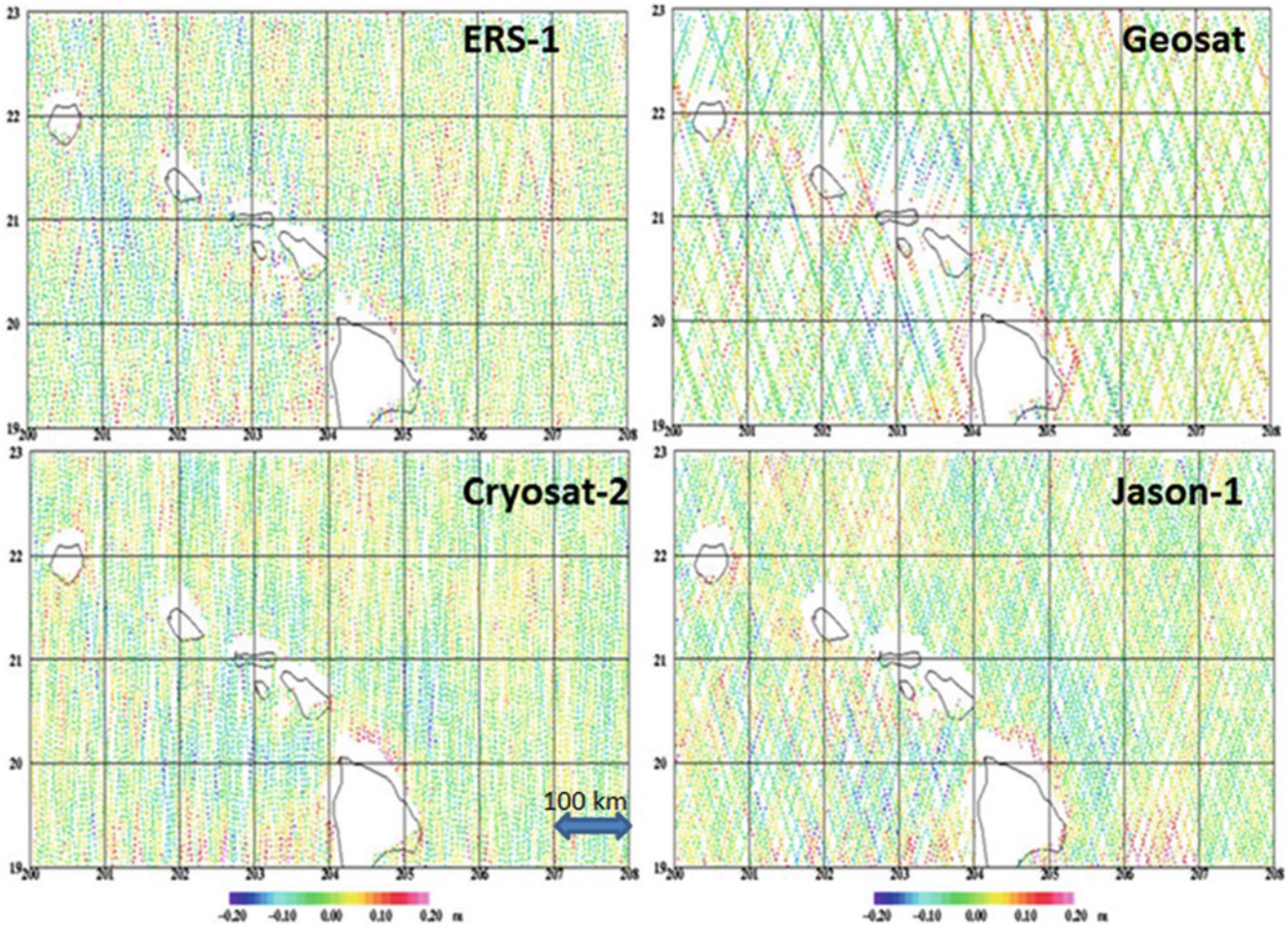

Fig. 1 Residual geoid height relative to EGM2008 (in meters) derived from 1 year of various geodetic missions around the Hawaiian island chain in the Pacific Ocean. *Upper left*: ERS-1 (11 month); *Upper right*: Geosat; *Lower left*: Cryosat-2; *Lower right*: Jason-1. One degree in longitude on the x-axis corresponds to roughly 100 km at the given latitudes, as illustrated in the lower left figure. An old version of the NGDC coastline is shown to outline the Hawaiian island chain

gravity field modeling (Sandwell et al. 2013). However, retracking of the old geodetic mission data (Sandwell and Smith 2005; Andersen et al. 2010) has significantly improved the range precision of these older missions by a factor of 1.5 (Sandwell et al. 2009) which means that the expected improvement with Cryosat-2 and Jason-1 will be less than a factor of two.

Here we will assess the improvement in gravity field determination that these new data offers through a comparison with highly accurate marine gravity observations in the Pacific Ocean. The structure of the paper is such that the next session describes the new altimeter data. The following section describes the marine gravity data and the comparison between marine gravity observations and altimetric gravity field prediction.

2 Altimetry Data

2.1 Conventional ERS-1 and Geosat Geodetic Missions

The ERS-1 and Geosat geodetic missions had for 15 years been the only available geodetic missions for gravity field determination. Consequent, these have been extensively investigated, reprocessed (Lillibridge et al. 2004) and retracked with respect to gravity field determination (i.e. Andersen et al. 2010; Maus et al. 1998; Sandwell and Smith 2005). Figure 1 shows the so-called along track residual geoid height for each geodetic mission relative to EGM2008. The residual geoid height is derived from the corrected and

crossover adjusted data following the method of Andersen and Knudsen (1998). In the upper left the ERS-1 GM data are shown and in the upper right the Geosat GM data are shown.

2.2 Cryosat-2 "Geodetic Mission" Data

CryoSat-2 was successfully launched by ESA in February 2010 focusing on collecting altimetry over the cryosphere (Wingham et al. 2006). However several studies have demonstrated its importance for ocean and land as well (i.e., Stenseng and Andersen 2012). The satellite has a near 369-day repeat cycle resulting in an average ground track spacing of 7 km at the equator. Such long repeating cycle make it extremely useful for geodetic purposes and hence it's called a geodetic mission. The altimeter onboard Cryosat-2 is capable of operating like other nadir looking altimeters (called LRM or low resolution mode). It can also operate in SAR mode where the along track resolution is increased from 7 km to around 300 m and in SAR-in mode (Wingham et al. 2006) where two antennas are applied. The operation mode changes dynamically with time and is defined by the mode mask found at earth.esa.int. For this investigation we have solely used the Cryosat-2 LRM taken from the Radar Altimetry Data System (RADS) processed with the standard set of range and geophysical corrections (Andersen and Scharroo 2011). The processed Cryosat-2 data for 1 year (2011) are shown in the lower left part of Fig. 1. Cryosat-2 measures all the way to 200 km from the North Pole (inclination of 88°). Consequently, the tracks will be more north–south going than any of the other geodetic missions and consequently the satellite will have fewer crossing point locations at low latitude. Cryosat-2 has now been operating more than 3 years performing three complete repeats of 369 days data. More years of Cryosat-2 data will naturally continue to improve gravity field further in the future by the increased number of observations. In this investigation we have treated each track individually and not examined the potential of averaging of repeat tracks to lower sea surface variability and its effect on gravity field modelling.

2.3 Jason-1 End of Life Geodetic Mission

The Jason-1 satellite was launched in 2001 to replace the aging TOPEX/Poseidon satellite. After many years of successful observations, the satellite was taken out of normal operation and put into an End-of-Life orbit in 2012. To avoid a potential collision between Jason 1 and TOPEX, the Jason-1 satellite was moved into a lower orbit with a long repeat time of 406 days resulting in an average ground-track spacing of 7 km at the Equator. Jason-1 has the lowest inclination of all satellites (66°). This nicely complements the higher inclination orbits of i.e., ERS-1 (82°) and Cryosat-2 (88°), as it creates a high number of crossing locations for the cross-over adjustment. Jason-1 failed just 4 days after completing its 406-day geodetic phase in June 2013. The Jason-1 data are shown in the lower right part of Fig. 1.

Figure 1 illustrates the residual geoid signal (relative to EGM2008) derived from roughly 1 year of each geodetic missions. This signal is subsequent used for the gravity field computation. For the given region this signal varies between −15 and 15 cm, as the Hawaiian island chain is a region of very large gravity anomalies. It illustrates that ERS-1 and Geosat data has higher noise than particularly the newer Cryosat-2 and Jason-1 satellites (more salt and pepper type noise). A careful inspection the figure illustrates, that the different inclination for the different satellites result in slightly different cross-over adjustment, which in turn will result in slightly different gravity anomalies. As an example, a region of higher residual geoid is seen bounded by 19–19.5° N and 206–207° E for Jason-1). This highlights the importance of having more satellites to stabilize the cross-over adjustment as this consequently leads to a more accurate marine gravity field.

3 Impact of New Altimeter Missions

A direct way of assessing the improvement in accuracy gained by introducing the two new geodetic missions is through a comparison with accurate marine gravity observations. We have used a recent survey by the United States Naval Ship (USNS) Bowditch in the western Pacific Ocean. This marine gravity survey was carried out to map the western insular margins and the 2,500-m isobath of Guam and the northern Marianas islands. The northern part of the survey used here is outlined in blue in the left part of Fig. 2 and bounded by latitude 15° N to 22° N and longitude 141° E to 144° E. Location of the southern survey is outlined with yellow colors. A total of 66.291 marine gravity observations along 74 tracks were measured with a maximum gravity anomaly reaching 148 mGal. The survey used GPS navigation and the BM-5 gravity instrumentation. So, the accuracy is expected to be around 1 mGal (Gardner 2006) though it might be higher. The data have been downloaded from the National Ocean and Atmosphere Administration (NOAA) National Geophysical Data Center (NGDC) web site.

In order to initially evaluate the impact of the "new generation" Cryosat-2 and Jason-1 satellites, altimetry from 1 year from each individual geodetic mission (except for 11 month for ERS-1) was processed and used to compute altimetric gravity field for the region. The altimetric gravity was computed using the methods described in Andersen (2010), Andersen et al. (2010), and Andersen and Knudsen

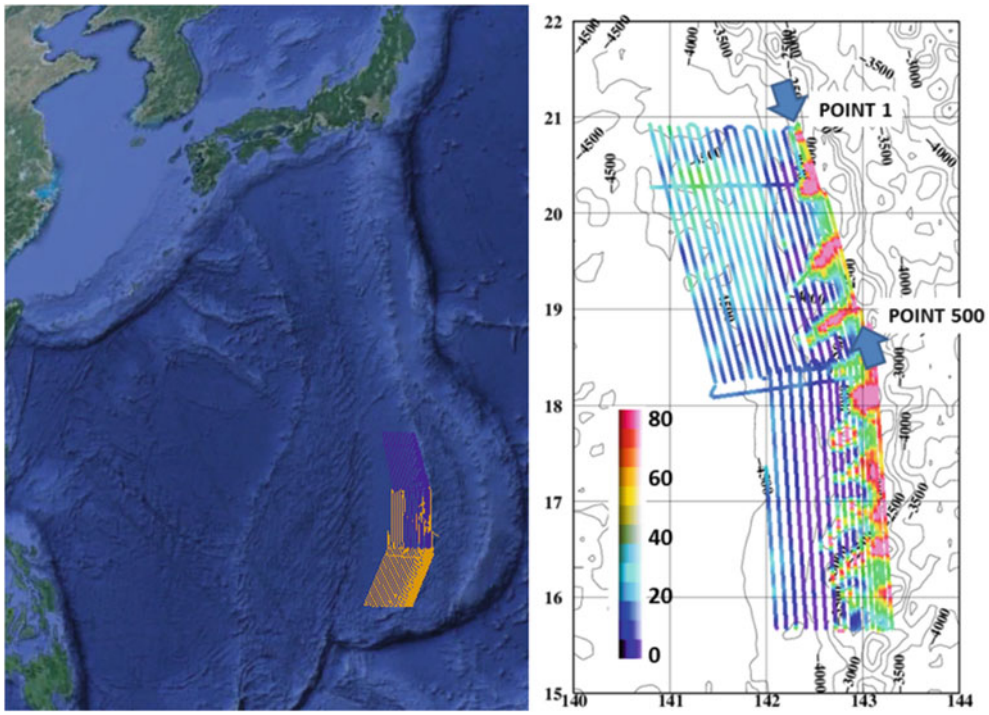

Fig. 2 The USNS Bowditch marine gravity survey. The *left part* of the figure illustrates the location of the northern and southern parts of the survey (in *blue* and *yellow*) and the *right part* of the figure illustrates the measured gravity anomalies (scale is in mGal) for the northern survey. The profile used for the detailed gravity comparison is marked with *arrows*

(1998) using altimetric sea surface height observations. The process of deriving gravity from the sea surface height applies a remove-restore technique relative to EGM2008 and the dynamic topography DOT07A (Pavlis et al. 2012) to account for the long wavelengths. Iterative local editing of the altimetric data is performed to ensure that there will be no outliers present. Subsequently a crossover adjustment is applied to remove ocean variability. This is followed by optimal interpolation onto a regular 1 min grid using a covariance function with a correlation length of 6.5 km. Finally, gravity is computed using Fast Fourier methods. As the conversion from geoid height to gravity enhances short wavelengths, a Wiener filter is applied to filter out wavelength shorter than 7 km. The setup is similar to that used for the derivation of the DTU10 gravity field. However, two important differences are implemented. The correlation length in the interpolation of geoid residuals (values shown in Fig. 1) was lowered from 9 to 6.5 km and the Wiener filter cut-off wavelength where the filter reaches 0.5 was lowered from 12 to 7 km. These values were determined empirically where the resulting gravity fits the best with the Bowditch marine gravity observations. The lowering of the correlation length and the cut-off wavelength will allow significantly shorter wavelength gravity signal to be present in the new gravity field which again increases the fit with marine gravity. The ability to lower the filtering is a consequence of the increased number of data and less noise in the new Cryosat-2 and Jason-1 sea surface height observations.

The comparison with the USNS Bowditch gravity observations and the derived gravity field from each geodetic mission and combination of various geodetic missions are shown in Table 1. Gravity derived from the 1 year of ERS-1 or Geosat both show a standard deviation with the marine data of around 4.2 mGal. By combining these two old geodetic mission datasets the standard deviation is lowered to 4.05 mGal. This number hereinafter called the "Old GM limit" (GM = geodetic mission), as these are the data that were available for the derivation of the DTU10, Sandwell and Smith (SSV18.1) and EGM2008. For reference these fields compare with the Bowditch data at 4.16, 4.09 and 4.21 mGal for DTU10, SS 18.1 and EGM2008.

The comparisons with Bowditch using gravity derived from 1 year of either Cryosat-2 or Jason-1 missions are considerably lower at around 3.7 mGal. The conclusion is, that altimetry from only 1 year of either Cryosat-2 or Jason-1 already lowers the standard deviation with the Bowditch data by 7% compared with the "Old GM limit" of gravity from the combined ERS-1 and Geosat missions. The maximum difference between observed and estimated gravity also decreases, supporting that the Cryosat-2 and Jason-1 derived gravity is actually getting closer to the measured marine gravity.

Table 1 Comparison with the USNS Bowditch 66219 marine gravity observations and interpolated gravity field from each geodetic mission and from a combination of various geodetic missions

	Std. dev of difference (mGal)	Maximum difference (mGal)
ERS-1	4.23	49.1
Geosat	4.21	49.0
ERS-1 + Geosat (DTU10)	4.05	46.9
Cryosat-2 (1 year)	3.77	41.8
Jason-1 (1 year)	3.73	41.5
Cryosat-2 (3 year)	3.42	39.8
C2 (3Y) + J1 (1 year)	3.30	37.6
All (DTU13)	3.14	36.1

Values are given in mGal

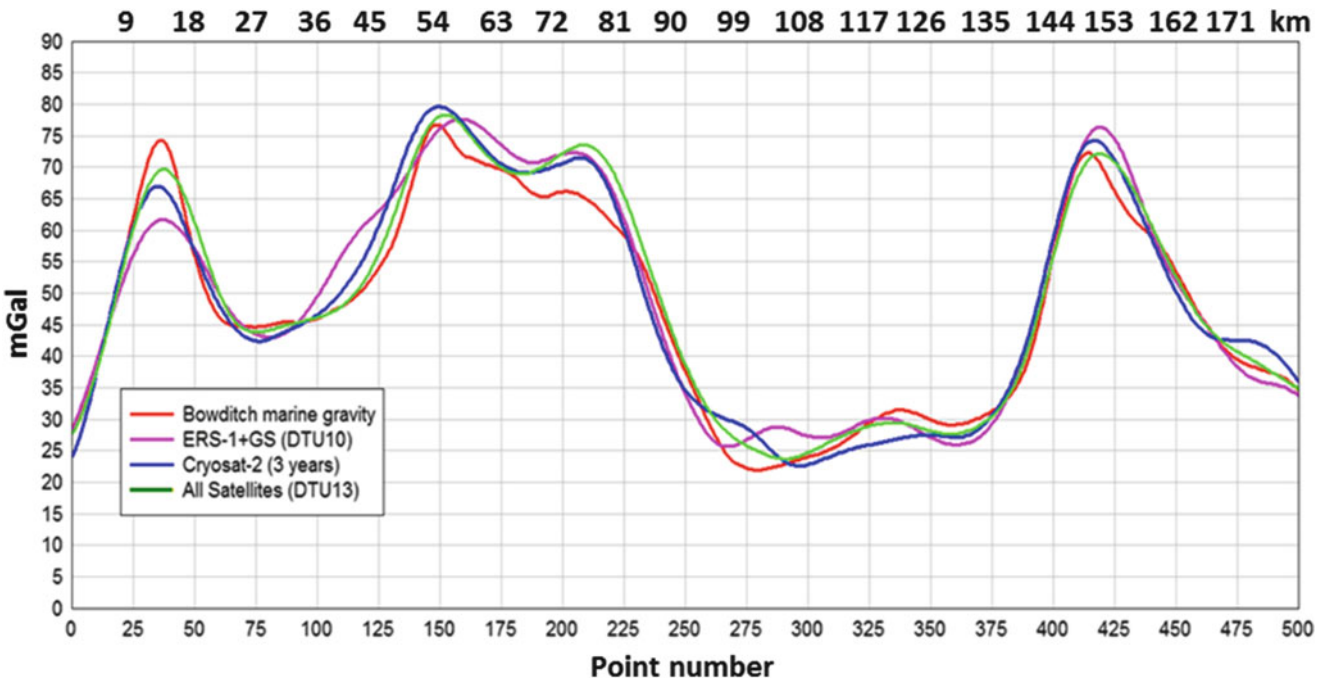

Fig. 3 A direct comparison with one of the Bowditch marine gravity tracks shown in Fig. 2 going from 20.9° N, 142.3° E to 18.6° N, 142.9° E. The Bowditch marine gravity is shown in *red*, the ERS-1/Geosat gravity delineated in *purple*. Cryosat-2 derived gravity field is shown in *blue* and the gravity field from all four geodetic missions is delineated in *green*. The scale in the *upper part* of the picture is the equivalent distance in km assuming a constant speed of the ship

By increasing the number of Cryosat-2 data to 3 years further increases the agreement to 3.42 mGal, and by introducing 1 year of Jason-1 data the number is further lowered to 3.30 mGal. Again, the conclusion is supported by a similar decrease in maximum deviation with the observed marine gravity. The result is even more impressive when the assumed 1 mGal error in the marine gravity data is accounted for. The final inclusion of all four geodetic missions lowers the standard deviation to 3.15 mGal being almost 1 mGal better than the "Old GM limit".

It is interesting, that the inclusion of the old geodetic missions, still improves the gravity field compared to a combined Cryosat-2 and Jason-1 gravity field. This is most likely a result of the additional data stabilizing the crossover adjustment and at the same time increasing the number of data. By accounting for an error of around 1 mGal in the marine gravity observations, it can be concluded, that for this particularly gravity survey, the new derived altimetric gravity field has an accuracy of about 2 mGal.

A detailed investigation along a profile consisting of 500 points in the marine gravity file going northwest to southeast from (20.9° N, 142.3° E to 18.6° N, 142.9° E) is shown in Fig. 3. For reference, the values are labeled 62,911,903 to 62,920,830 and the profile is marked with arrows in Fig. 2. In Fig. 3, both the point-number and the associated distance along the profile are shown assuming a constant speed of the vessel.

The Bowditch marine gravity is shown in red, the ERS-1 + Geosat gravity is delineated in purple. The Cryosat-2 alone gravity field from 3 years of data is shown in blue and the gravity field from all four satellites is delineated with green. The first peak in the figure occurs at point 40 and the measured gravity reaches 75 mGal. The pre "old GM limit" gravity derived from ERS-1 and Geosat data only reaches 60 mGal and hence was nearly 15 mGal of the measured gravity. However, the gravity field using all four geodetic missions reaches 70 mGal being less than 5 mGal of the measured gravity field anomaly. As data have been processed using identical setup, this illustrates how shorter wavelengths in the gravity field are significantly better mapped with the inclusion of the two new geodetic missions.

Significantly differences are particularly seen between point number 150 and 225 where the differences exceed 6 mGal at several locations. A comparison with the DTU10 and SSV18.1 gravity fields showed similar consistent differences. This discrepancy is currently under investigations, but it leads to the conclusion that the assumption of a 1 mGal error on the Bowditch data is most likely too optimistic.

4 Summary

With the launch of Cryosat-2 and the Jason-1 end-of-life geodetic mission two new geodetic missions have become available to marine gravity field determination. The impact of these new geodetic mission data on global marine gravity field is highlighted through comparison with high quality recent ship borne gravity onboard the USNS Bowditch in the Western Pacific Ocean. Altimetric gravity derived using 1 year of either Cryosat-2 or Jason-1 is nearly 10% better than gravity derived from retracked and reprocessed combined ERS-1 and Geosat in terms of lower standard deviation with marine gravity. This improvement increases further if one accounts for the internal error in the marine gravity of around 1mGal.

The final inclusion of all four geodetic missions (ERS-1, Geosat, Cryosat-2 and Jason-1) lowers the standard deviation to 3.15 mGal being almost 1 mGal better than what could be achieved using ERS-1 and Geosat. It is found that the inclusion of the old ERS-1 and Geosat geodetic missions with the new geodetic mission still improves gravity compared with a field derived using the new geodetic missions alone. This is explained by the fact that the old geodetic missions stabilize the crossover adjustment and also increase the number of data. Detailed comparison with the Bowditch survey along a profile illustrates the importance of the new geodetic mission data but also highlighted potential significant errors in the survey.

Ongoing investigations can and will improve the gravity field further in the near future. One improvement is expected from the retracking of the Cryosat-2 and Jason-1 geodetic mission as this previously significantly improved the older ERS-1 and Geosat geodetic missions. A second improvement might come from the use of more years of Cryosat-2 as the mission continues to operate for hopefully many years.

Acknowledgements The authors would like to thank the RADS (rads.tudelft.nl) team for making altimetric data as well as corrections readily available to the user. Also the authors would like to acknowledge the NOAA National Geophysical Data Center for making the Bowditch marine gravity data available to the scientific community.

References

Andersen OB (2010) The DTU10 global gravity field and mean sea surface – improvements in the Arctic. Presented at the 2nd international gravity field service symposium, Fairbanks, Alaska

Andersen OB, Knudsen P (1998) Global marine gravity field from the ERS-1 and GEOSAT geodetic mission altimetry. J Geophys Res 103:8129–8137

Andersen OB, Scharroo R (2011) Range and geophysical corrections in coastal regions: and implications for mean sea surface determination. In: Vignudelli S et al (eds) Coastal altimetry. Springer, Berlin, pp 103–145. doi:10.1007/978-3-642-12796-0_5

Andersen OB, Knudsen P, Berry PAM (2010) The DNSC08GRA global marine gravity field from double retracked satellite altimetry. J Geod 84:191–199. doi:10.1007/s00190-009-0355-9

Gardner JV (2006) Cruise report, USNS Bowditch: U.S. Law of the Sea cruise to map the western insular margin and 2500-m isobath of Guam and the Northern Marianas Islands: Cruise BD06-1, UNH-CCOM/JHC Tech Rep 06–100

Lillibridge JL, Smith WHF, Scharrroo R, Sandwell DT (2004) The Geosat geodetic mission 20th anniversary data product, AGU, 85(47), Fall Meet. Suppl., Abs SF43A–0786

Maus S, Green CM, Fairhead D (1998) Improved ocean-geoid resolution from retracked ERS-1 satellite altimeter waveforms. Geophys J Int 134(1):243–253

Pavlis NK, Holmes SA, Kenyon SC, Factor JK (2012) The development and evaluation of the earth gravitational model 2008 (EGM2008). J Geophys Res 117:B4

Sandwell DT, Smith WHF (2005) Retracking ERS-1 altimeter waveforms for optimal gravity field recovery. Geophys J Int 163:79–89. doi:10.1111/j.1365-246X.2005.02724

Sandwell DT, Smith WHF (2009) Global marine gravity from retracked Geosat and ERS-1 altimetry: ridge segmentation versus spreading rate. J Geophys Res 114:B01411. doi:10.1029/2008JB006008

Sandwell DT, Garcia E, Soofi K, Wessel P, Chandler M, Smith WHF (2013) Towards 1-mGal accuracy in global marine gravity from Cryosat-2, Envisat and Jason-1. The Leading Edge, Houston, pp 892–898

Stenseng L, Andersen OB (2012) Preliminary gravity recovery from CryoSat-2 data in the Baffin Bay. Adv Space Res 50(8):1158–1163

Wingham D et al (2006) CryoSat-2: a mission to determine the fluctuations in Earths land and marine ice fields. Adv Space Res 37(4):841–871

Mohorovicic Discontinuity Depth Analysis Beneath North Patagonian Massif

María Laura Gómez Dacal, Claudia Tocho, and Eugenio Aragón

Abstract

The Mohorovicic discontinuity (Moho) is the surface that limits the Earth's crust and mantle. It is of paramount importance in understanding and investigating the dynamics of the Earth's interior. The GEMMA project (GOCE Exploitation for Moho Modeling and Applications), funded by the European Space Agency and Politecnico di Milano, has provided a high resolution map of the Moho surface (GEMMA Model), based on the inversion of homogeneous, well-distributed gravimetric data measured by the Steady-State Ocean Circulation Explorer (GOCE), which ensures a global coverage using gravity field. In the current paper, this Moho depth estimation (Riccardo Barzaghi, personal communication, April 20, 2012) is compared with other models based on both seismic and gravity observations, under the North Patagonian Massif (NPM). Said massif is an Argentinean plateau that stands out 500 to 700 m higher in altitude than the surrounding topography and was created by a sudden uplift without noticeable internal deformation (Aragón et al. (2011b) Upper mantle geodynamic constrains beneath the north patagonian massif, Argentina). The features described led us to analyze the crustal thickness in the area. The work describes different Moho models available in the area under study and their comparison with the GEMMA Model. The aim is to validate this well distributed, homogeneous data model in this area with sparse seismic data and check its usefulness to get more information about the Moho. According to comparisons with the different models, the crustal thickness in the study area varies between 36 and 46 km. The good agreement between the GEMMA Model and some of the other Moho models may account for the use of such model to study this little known area.

Keywords

GOCE • Mohorovicic discontinuity (Moho) • Moho models • North Patagonian Massif

1 Introduction

The Mohorovicic discontinuity is the boundary between the crust and the mantle. It is defined by seismologists as the depth at which the P-wave velocity exceeds 7.6 km/s; therefore, it depends on the density and elastic properties of crustal and mantle rocks (Lowrie 2007). The Moho plays a fundamental role in the Earth's dynamics. In particular, it helps to understand the isostatic compensation state of an area and consequently its epeirogenic movements. It also proves to be useful to construct a gravity model.

M.L. Gómez Dacal (✉) • C. Tocho
Facultad de Ciencias Astronómicas y Geofísicas, Departamento de Gravimetría, Universidad Nacional de La Plata, Paseo del Bosque s/n, B1900FWA, Argentina
e-mail: gomezdacal@fcaglp.unlp.edu.ar

M.L. Gómez Dacal • E. Aragón
Consejo Nacional de Investigaciones Científicas y Técnicas, Av. Rivadavia nº 1917, C1033AAJ, Argentina

E. Aragón
Facultad de Ciencias Naturales y Museo, Universidad Nacional de La Plata, Centro de Investigaciones Geológicas, 1 nº 644, B1900FWA, Argentina

© Springer International Publishing Switzerland 2015

C. Rizos, P. Willis (eds.), *IAG 150 Years*, International Association of Geodesy Symposia 143,
DOI 10.1007/1345_2015_89

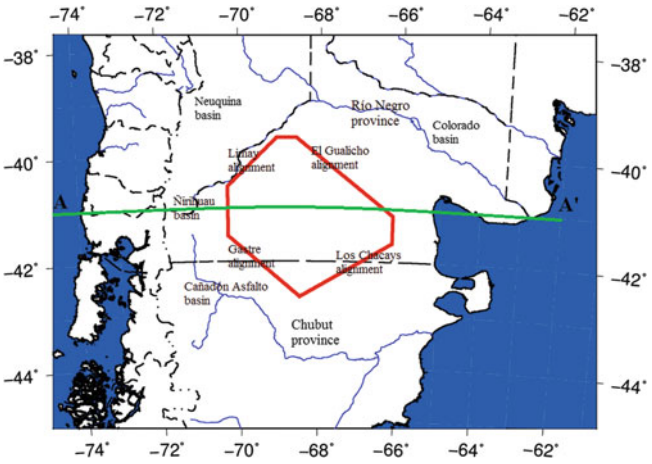

Fig. 1 Geographical location of the North patagonian massif

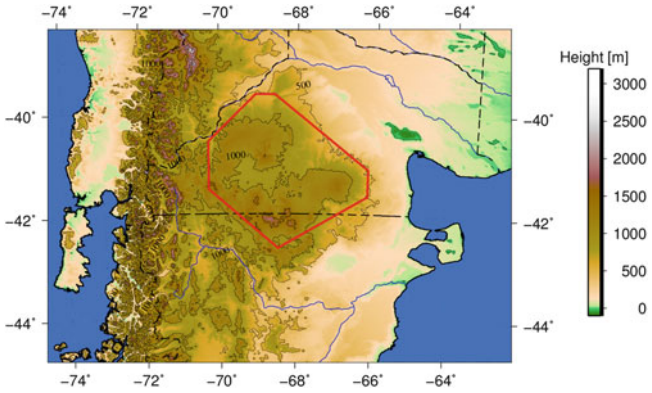

Fig. 2 Topography of the North patagonian massif and the surrounding areas

The GEMMA Model -a global, high-resolution map of the Moho using GOCE gravity satellite data- was derived by Barzaghi et al. (2014). Comparisons between this model and other Moho models are analyzed for the North Patagonian Massif both to test the GEMMA Model and to learn more about the Moho in this area. Five models are compared: two of these were created with seismic information (Feng et al. 2007; Bassin et al. 2000); others were made with a combination of both gravity and seismic techniques (Assumpção et al. 2012; Tassara and Echaurren 2012) and the last one is an inversion of gravity data of the area under study. This gravity data inversion is also presented in this work.

The North Patagonian Massif (NPM) is an Argentinean area that is sparsely studied and has interesting characteristics. Specifically, the area of study is located between the alignments Limay, Gastre, Los Chacays and Gualicho, and is called the NPM core. This area of low relief and great height constitutes a plateau that is surrounded by Neuquina, Colorado, Ñirihuau and Cañadon Asfalto basins (Aragón et al. 2011b; Fig. 1). This plateau is a 100.000 km^2, subrectangular, area that has a height of about 1,200 m above sea level and stands out 500 to 700 m higher in altitude than the surrounding topography (Aragón et al. 2010; Gómez Dacal 2012; Fig. 2).

The NPM corresponds to a morpho-structural region having a different tectonic behavior than its surrounding areas because it suffered a sudden uplift from heights below sea level to heights around 1,200 m in a brief geological time. This uplift is considered to have been generated by an epeirogenic movement because the marine sediments from the Cretaceous-Tertiary boundary lay without noticeable internal deformation at 1,100 m above sea level; however, in the surrounding areas, the sediments of the same formation are at a height between 300 and 500 m above sea level and show deformation (Aragón et al. 2010, 2011a). Such different mechanical response between the massif plateau and the surrounding back arc and the short time in which this process took place raise questions about the geodynamic behavior of the study area.

The particular features of the NPM led us to investigate the Moho and validate the GEMMA Model for this area.

2 Description of Models of Mohorovicic Discontinuity

The Moho models are mainly based on seismic or gravimetric data of an area; hence, numerous data of this kind are required to create a model. Seismic data allows to create a more accurate regional model of the Moho surface. The NPM is an area with lack of seismic data and in, consequence it is difficult to create a good regional Moho model. For this reason, global models of the Mohorovicic discontinuity seem appropriate to describe the study zone. There are many Moho models at a global scale that can be used; however in this work, the performance of the GEMMA Model (Barzaghi et al. 2014) for the study area is investigated. This model was chosen because it has been globally computed using GOCE data, thus ensuring well-distributed and homogeneous global coverage. The authors reduced the data by subtracting the contribution of the normal potential, then corrected it for the effect of topography and bathymetry and made a spherical harmonics analysis of the residual field to obtain the coefficients of the residual gravity field. After that, they related the coefficients already found to the product between Moho depth and density contrast (between mantle and crust) with a linear relationship. Taking the density contrast as a constant and equal to 630 kg/m^3 (homogeneous crust of density 2,670 kg/m^3 and a homogeneous mantle of 3,270 kg/m^3), they get the Moho depth (Sampietro and Reguzzoni 2011). The model has a resolution of 30 min. Figure 3 shows the mapping of the model in the NPM area (delimited in red) and its surroundings. It can be observed

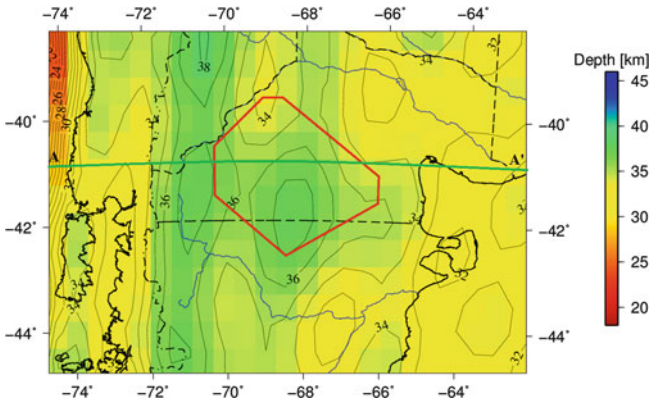

Fig. 3 GEMMA model (Barzaghi et al. 2014)

that the Moho depth varies from 34 to 36 km in the NPM area and it is thinner on its North, East and South surroundings whereas the West boundary shows the opposite.

The Global Moho model described has been compared with a set of Moho models at different scales (from global to local ones) and with different origins (based on different data and compiled with different methods) as shown in Table 1. We expect that the GEMMA Model fits correctly with these models, which constitute the only information available about the Moho surface for the interest area.

As can be observed from the figures, the Moho models for the study area have the following characteristics:

- Model A (CRUST 2.0; Fig. 4) presents a Moho depth between 36 and 40 km for the study area and it is surrounded by areas of thinner crust on the South and East boundaries and by areas of thicker crust on the other two boundaries. It should be noted that the model has a poor resolution and there are few data used for generating the model in the area under study, i.e the model is an interpolation of data available in surrounding areas. This model was chosen to make the comparison because is one of the most well-known and spread model inside the geoscience community in spite of its low resolution and it was used as the mean Moho depth for the derivation of the GEMMA Model (Reguzzoni et al. 2013).
- The Moho depth for Model B in the study zone is between 36 and 45 km and it is surrounded on the North, East and North-West boundaries by a thinner crust, on its West boundary by a thicker crust and on the South boundary there is an area with no model coverage. This can be seen in Fig. 5. There are no point estimates of the Moho depth in the NPM area to constrain this model (Fig. 5). The resolution of Model B is 2 minutes.
- According to Model C (Fig. 6), the Moho depth beneath NPM is between 32 and 38 km and in accordance with the previously described model, it is surrounded by a thinner crust on the North, East and North-West boundaries, by a thicker crust on the West boundary, and on the South boundary, there is an area with no model coverage. It is important to highlight that in the NPM area there are no point estimates of the Moho depth and there is only one point estimate near the mentioned area (Fig. 6), hence this model is mainly based on gravity data Moho estimates (from Tassara and Echaurren (2012)) for the NPM region and could be weakly defined. Nevertheless, Model C is the one with the largest database of all analyzed models.
- In Fig. 7 it can be seen that the Moho depth for Model D is between 35 and 37 km and it is surrounded by areas of thinner crust on the North, East and South boundary and by areas of thicker crust on the West boundary. Model D is the result of an adaptation of the Moho surface from a three dimensional density model of the NPM (Gómez Dacal 2012). Forward modelling was performed using the software IGMAS+ (Interactive Gravity and Magnetic Application System) and Bouguer anomalies from EGM2008, through the triangulation of sections separated 0.5°, which means a longitudinal resolution of 25 km. In the original model (Tassara and Echaurren 2012), the Moho was constrained using receiver function points and refraction profiles but there are some areas without constraints. For these regions, the Moho was shaped by fitting the intermediate wavelength of the Bouguer anomaly and under the assumption that the orogenic topography is primarily compensated by a crustal root (Tassara and Echaurren 2012). In the NPM area, the model does not have independent data to constrain the Moho surface (Fig. 7) and therefore it could be poorly defined.
- According to Model E (Fig. 8), the Moho depth beneath the NPM region is between 39 and 46 km and is surrounded by thinner crust areas on the North, East and South boundaries and by a thicker crust on the West boundary. This model was derived using Lithoflex software (Braitenberg et al. 2007), Bouguer anomalies from EGM2008 (Pavlis et al. 2012) and a cutoff wavelength of 200 km. The gravity data selected is consistent with those used in Models B and C, and the cutoff wavelength was chosen so as not to project superficial masses at Moho level in order to be consistent with the other models that show a long wavelength. The physical parameters used in the inversion were: 36 km for the reference depth and 340 kg/m^3 for the density contrast. The choice of the reference depth was based on the coincidence of several Moho models out of the NPM area; the density contrast was calculated with density values extracted from xenolithes for the lower crust and upper mantle and the upper crust values from literature values (Castro et al. 2011; Kliger 2010; Kostadinoff and Schillizi 1996; Kostadinoff and Gelós 1994). Moho depths in Model E have been obtained without taking into account the topography or any isostatic hypothesis. The

Table 1 Moho models used in this study

Model	Coverage	Description	Figure	Reference
Model A CRUST 2.0	Global.	Seismic data: reflection, refraction and receiver function studies; Specified in $2°x2°$ grid; Available online	Figure 4	Bassin et al. (2000) http://www.igppweb.ucsd.edu/gabi/~crust2.html
Model B	Regional model: South America.	Seismic data: joint inversion of regional S and Rayleigh waveforms and fundamental mode Rayleigh wave group velocities. There is a refraction profile at 39° South Latitude	Figure 5	Feng et al. (2007)
Model C	Regional model: South America.	Seismic data: point estimates from seismic refraction experiments, receiver function analysis, surface-wave dispersion (there is the same refraction profile as Model B and a point estimate) and gravity based estimates from Tassara and Echaurren (2012) to cover gaps in seismic information; interpolated with surface-wave tomography	Figure 6	Assumpção et al. (2012)
Model D	Regional model: Central and South Andes.	Three-dimensional density model constrained by independent data (mainly seismic; in the area, it integrates the profile of Model B): Moho surface extracted from the adaptation to the study area using *IGMAS+* software (Götze 1978, 1984; Götze and Lahmeyer 1988; Schmidt and Götze 1998)	Figure 7	Tassara and Echaurren (2012)
Model E	Local model: NPM area.	Inversion of gravity data (Lithoflex software Braitenberg et al. 2007): Bouguer anomalies extracted from EGM2008 geopotential model (Pavlis et al. 2012)	Figure 8	———————-

standard deviations of the differences between GEMMA and Model E is ±2.57 km (Table 2).

3 Comparison of Moho Models

To evaluate the performance of the GEMMA Model (Barzaghi et al. 2014) in the study area, comparisons with other models have been made:

- The differences, in absolute value, between the GEMMA Model and the models described in Sect. 2 are depicted in Figs. 9, 10, 11, 12 and 13, respectively.
- A profile crossing the study area has been chosen to compare the different Moho models (Fig. 14). The profile is at 41° S because it crosses the middle of the North Patagonian Massif (Fig. 1).

Crossing the NPM from West to East (from A to A'), the Moho depth varies by more than 20 km for different models, ranging from a relatively shallow depth (around 25 km), deepening down to about 40 km between 72° and 66° West longitude, and rising up again to about 35 km depth in the East.

Overall, the following characteristics can be observed:

- Model A differs significantly from the GEMMA Model with an standard deviation of 4.53 km (Fig. 9, Table 2).

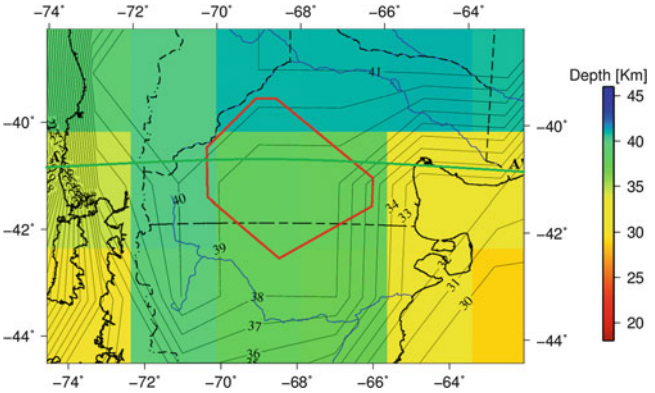

Fig. 4 Model A: CRUST 2.0 (Bassin et al. 2000)

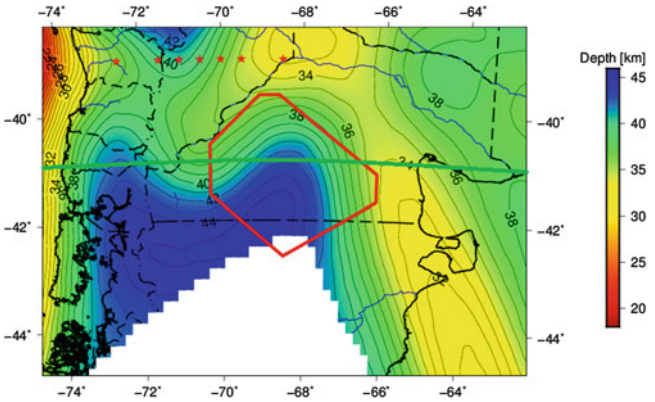

Fig. 5 Model B (Feng et al. 2007). *White area* indicates no model coverage and *red stars* constrain data

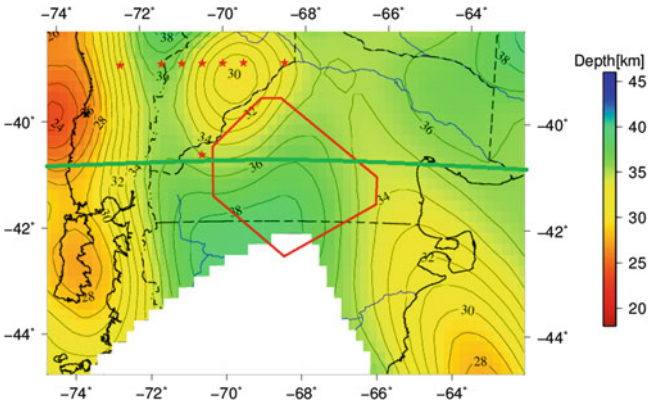

Fig. 6 Model C (Assumpção et al. 2012). *White area* indicates no model coverage and *red stars* constrain data

Nevertheless, more meaningful is the difference between the mentioned model and all the other models. The difference can be observed in Fig. 14. This fact make this model unreliable for the area. The differences between Model A and the other models could be caused by the poor resolution of Model A and, the few data in which the model was based to interpolate the Moho in the study area.

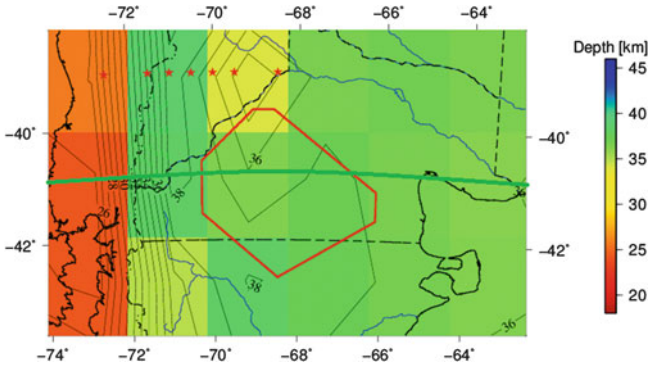

Fig. 7 Model D (Tassara and Echaurren 2012). *Red stars* indicate constrain data

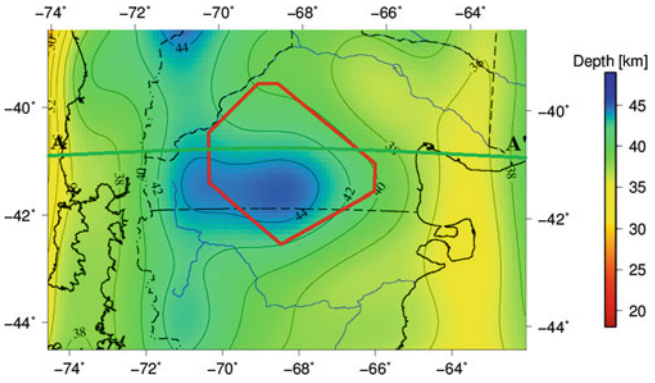

Fig. 8 Model E: made from the inversion of gravity data

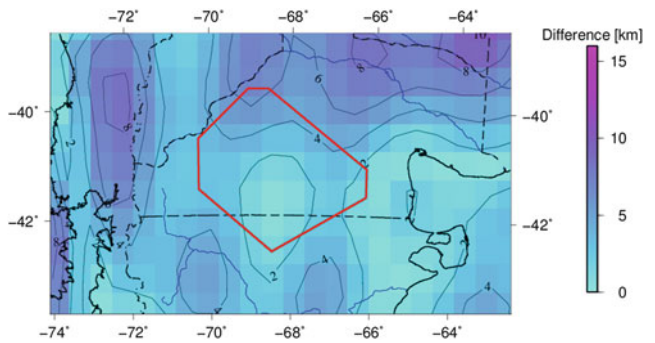

Fig. 9 Difference between the GEMMA model and model A

- Figure 10 shows that Model B differs from the GEMMA Model essentially in the NPM and the West boundary, but it is similar in the other surroundings. Figure 14 shows that Model B Moho is considerably deeper (in almost every place of the profile) than the other models, except for Model E. Model A and B are the only ones made with only seismic data; however, Model A is not worth considering as it has poor resolution.
- Figure 11 shows the opposite situation. Model C seems to be more similar to the GEMMA Model in the NPM area and different from it in the surroundings. Model

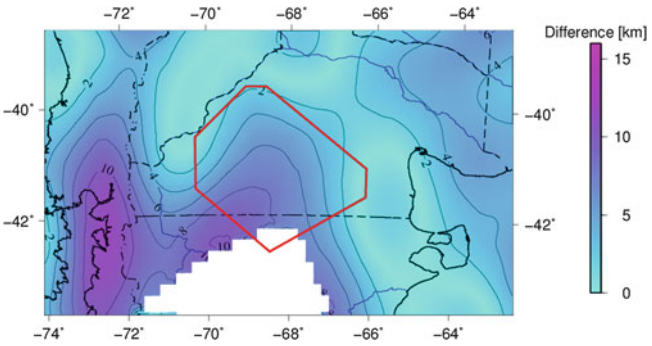

Fig. 10 Difference between GEMMA model and model B

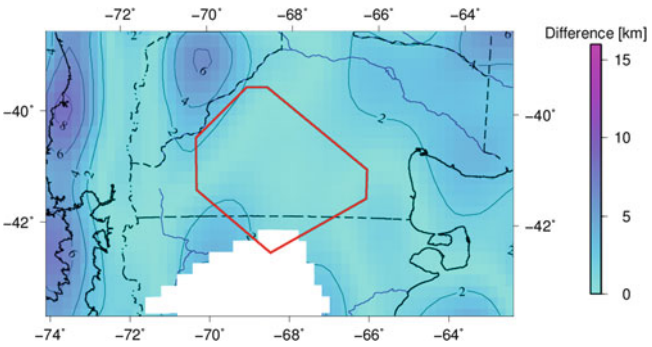

Fig. 11 Difference between the GEMMA model and model C

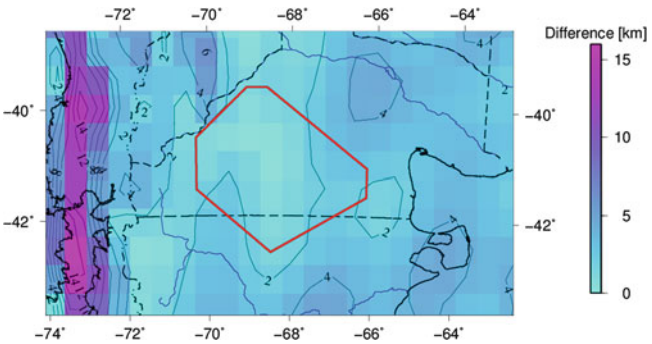

Fig. 12 Difference between the GEMMA model and model D

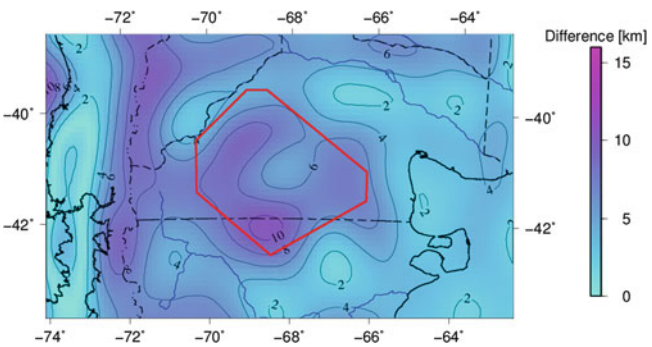

Fig. 13 Difference between the GEMMA model and model E

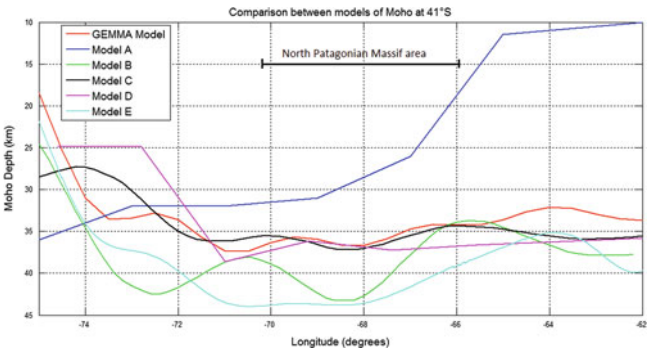

Fig. 14 Comparisons of Moho models crossing NPM along the 41°S parallel

Table 2 Standard deviations of the differences between the regional or local models and GEMMA model

Model comparison	Standard deviation [km]
Model A - GEMMA	4.53
Model B - GEMMA	3.07
Model C - GEMMA	3.08
Model D - GEMMA	6.94
Model E - GEMMA	2.56

C is the most similar to the GEMMA model (Fig. 14). This information is relevant considering that Model C is the one with the largest database. Nevertheless, it does not have any point of Moho estimate in the NPM. The similarity in the comparison between Model C and GEMMA Model in the study area can be cause by more seismic points interpolated with surface-wave tomography and complemented with the gravity-based crustal model of Tassara and Echaurren (2012). Model C includes more seismic crustal thicknesses points compared to the previous point constraints from Model B. The differences between GEMMA and Model B and C show similar error standard deviations of 3.07 and 3.08 km, respectively (Table 2).

- Model D has values similar to those of the GEMMA Model in the NPM area (Fig. 12). This could also be seen in Fig. 14. Nevertheless, the difference between this model and GEMMA Model shows the largest standard deviation of ±6.94 km as can be seen in Table 2.
- Model E has great differences with the GEMMA Model, especially in the NPM area as shown in Fig. 13. This difference can be caused by the selection of the inversion parameters. Model E values are more similar to Model B (Fig. 14).

4 Conclusions

In this study, the high resolution, homogeneous and well-distributed GEMMA Model inferred from satellite gravity observations provided by the GOCE mission (Barzaghi et al. 2014) has been compared with five other models based on seismic and/or gravity data to evaluate its quality. One of them was derived from the inversion of Bouguer gravity anomalies (Model E). The analysis has been performed on the North Patagonian Massif area (Argentina).

Most of the models show a Moho depth between 36 and 38 km (GEMMA Model and Models A, C and D) evidencing a good correlation of these models with the GEMMA Model for the area under study. Model A has poor resolution and few data to derive the model in the area of study; therefore, it is unreliable for such area. In the agreement of Models C, D and the GEMMA Model, the influence of gravity data could be observed. Models B and E show a deeper Moho discontinuity reaching 46 km. It can be caused by the different data source employed (only seismic data) in Model B, and by the more realistic density contrast of 340 kg/m^3 and the reference depth of 36 km selected for the inversion in Model E. Model C, which has been recently derived using the largest database, shows the best correlation to the GEMMA Model of all the analyzed models. All the models have discrepancies towards the West where the boundary of the continent and subduction take place.

Crustal models are useful for studies of isostasy, dynamic topography, and for the understanding of geodynamic processes at different spatial and time-scales. The study was done in a massif with no noticiable internal deformation observed; therefore, it is not expected to find any special feature in the Moho shape or depth in terms of isostasy. Nevertheless, most of the Moho models selected have shown a thickened crust below the NPM, which shows a more complex geodynamic setting than expected. This should be investigated in detail in the future.

The overall conclusion is that the model derived from GOCE data (GEMMA Model) seems to be an important contribution because it has a good agreement with some of the regional models in the North Patagonian Massif in southern Argentina. This may account for the use of such model in the NPM area.

As the GEMMA Model is a high resolution, homogeneous, well-distributed Moho model, and has shown a good correlation with the most updated regional seismic/gravity models for South America (Model C and D), at least in the NPM area, it might be used to get information about this surface in other areas with few data. On the other hand, the GOCE gravimetric model could be improved incorporating local/regional more realistic density models and seismic data.

Acknowledgements We would like to thank Dr. Riccardo Barzaghi for providing the global Moho model using GOCE data (GEMMA Model).

References

Aragón E, Aguilera Y, Cavarozzi CE, Ribot A (2010) The north patagonian altiplano and the somún curá basaltic plateau. Geociencias 29:527–532. Doi:10.1016/j.tecto.2011.06.012

Aragón E, Brunelli D, Castro A, Rivalenti G, Varela R, Rabbia O, Spackman W, Cavarozzi CE, Aguilera Y, Ribot A, Mazzucchelli M, D'Eramo F, Demartis ML (2011a) Tectono-magmatic response to major convergence changes in the north patagonian suprasubduction system: the paleogene subduction-transcurrent plate margin transition. Tectonophysics. http://dx.doi.org/101016/jtecto201106012

Aragón E, Tassara A, Tocho C, Mendoza LPM, Spackman W, Rabbia O, Perdomo R, Bertotto WG (2011b) Upper mantle geodynamic constrains beneath the north patagonian massif, Argentina

Assumpção M, Feng M, Tassara A, Juliàă J (2012) Models of crustal thickness for south america from seismic refraction, receiver functions and surface wave tomography. Tectonophysics (0), Doi:http://dx.doi.org/10.1016/j.tecto.2012.11.014, URL http://www.sciencedirect.com/science/article/pii/S0040195112007330

Barzaghi R, Reguzzoni M, Borghi A, De Gaetani C, Sampietro D, Marotta AM (2014) Global to local Moho estimate based on GOCE geopotential model and local gravity data. In: Proceedings of the VIII Hotine-Marussi Symposium - IAG Symposia, Springer

Bassin C, Laske G, Masters G (2000) The current limits of resolution for surface wave tomography in North America, vol 81, p F897

Braitenberg C, Wienecke S, Ebbing J, Born W, Redfield T (2007) Joint gravity and isostatic analysis for basement studies - a novel tool. Extend ended abstracts

Castro A, Aragón E, Díaz-Alvarado J, Blanco I, García-Casco A, Vogt K, Liuf DY (2011) Age and composition of granulite xenoliths from paso de indios, chubut province, Argentina. J S Am Earth Sci. http://dx.doi.org/101016/jjsames201106001

Feng M, Van der Lee S, Assumpção M (2007) Upper mantle structure of south america from joint inversion of waveforms and fundamental mode group velocities of rayleigh waves. J Geophys Res 112 Doi:10.1029/2006JB004449

Gómez Dacal ML (2012) Modelado gravimétrico tridimensional del macizo norpatagónico. Degree thesis. Facultad de ciencias astronómicas y geofísicas, Universidad Nacional de La Plata

Götze HJ (1978) Ein numerisches verfahren zur berechnung der gravimetrischen feldgröben dreidimensionaler modellköper. TU Clausthal

Götze HJ (1984) Uber den einsatz interaktiver computergrafik in rahmen3 dimensionaler interpretationstechniken in gravimetrie und magnetik habiltationsschrift. Arch Meteorol Geophys Bioklimatol A

Götze HJ, Lahmeyer B (1988) Application of three-dimensional interactive modeling in gravity and magnetict. Geophysics 53:1096–1108. http://dx.doi.org/10.1190/1.1442546

Kliger FL (2010) Estudio gravi-magnetométrico en el macizo norpatagónico. PhD thesis, Universidad Nacional de San Juan

Kostadinoff J, Gelós EM (1994) Análisis de las mediciones gravimagnetométricas realizadas entre el fuerte y arroyo verde, provincia de río negro. Rev Asoc Geol Arg 49:19–25

Kostadinoff J, Schillizi R (1996) Características geofísicas del litoral atlántico entre el rio chubut y puerto camarones. Rev Asoc Geol Arg 51:387–392

Lowrie W (2007) Fundamentals of geophysics. Cambridge University Press, Cambridge. http://dx.doi.org/10.1017/CBO9780511807107

Pavlis NK, Holmes SA, Kenyon SC, Factor JK (2012) The development and evaluation of the earth gravitational model 2008 (egm2008). J Geophys Res. http://dx.doi.org/101029/2011JB008916117

Reguzzoni M, Sampietro D, Sanso F (2013) Global Moho from the combination of the CRUST2.0 model and GOCE data. Geophys J Int. Doi:10.1093/gji/ggt247.

Sampietro D, Reguzzoni M (2011) Global Moho from the combination of the CRUST 2.0 model and GOCE data. GNGTS

Schmidt S, Götze HJ (1998) Interactive visualization and modification of 3d models using gis functions. Phys Chem Earth. http://dx.doi.org/101016/S0079-1946(98)00027-523

Tassara A, Echaurren A (2012) Anatomy of the chilean subduction zone: Three-dimensional density model upgraded and compared against global-scale models. Geophys J Int. Doi:10.1111/j.1365-246X.2012.05397.x

The A10 Gravimeter Total Uncertainty Budget Estimation: A Case Study Using the A10-020

P. Dykowski, J. Krynski, and M. Sękowski

Abstract

A10 absolute gravimeters are in active use for more than 10 years. This type of gravimeter has proven to be a very efficient tool for absolute gravity determinations, both in field and in laboratory conditions. In order to get full assessment of the gravimeter performance, study on the total uncertainty budget is required. It is especially important when the gravity determinations with the A10 are to be compared with gravity determinations using other types of absolute gravimeters, e.g. during absolute gravimeter comparison campaigns such as ICAG, ECAG or other similar local surveys. With the uncertainty estimated, the reliability of the A10 gravimeter required for gravity control establishment can further be evaluated.

Uncertainty budget components provided by the manufacturer need to be revised in order to estimate the experimental uncertainty of gravity determinations with the A10. The budget itself can be divided into three main components: correction/reduction models, instrument related issues, and statistical uncertainty.

As the A10 gravimeter is used in laboratory and field conditions two uncertainty estimates were considered. In addition, the sensitivity of the A10 gravimeter with respect to local hydrology has been discussed.

Studies and estimates were performed based on numerous surveys with the A10-020 on the stations of the gravity control in Poland. The most interesting material comes from the repeated regular absolute gravity determinations with the A10-020 at three stations in Borowa Gora Geodetic-Geophysical Observatory. Additional information is provided by absolute gravimeter comparison campaigns and calibrations of metrological parameters performed from October 2008.

Keywords

A10 absolute gravimeter • Metrology • Uncertainty budget estimation

1 Introduction

Contribution of A10 absolute gravimeters to absolute gravity determinations is growing in the last decade. Currently the number of A10 absolute gravimeters in use exceeds 30. Portability and measurement efficiency make the A10 a very useful tool for a wide range of precise field gravimetric surveys, from validating satellite gravity missions (Falk et al. 2012; Pettersen et al. 2012), through e.g. geothermal reservoir monitoring (Fukuda et al. 2010; Sofyan et al. 2012) to gravity control and gravimetric calibration baseline maintenance (Sousa and Santos 2010; Dykowski et al. 2012b). A10 gravimeters were used in particular for modernization and maintenance of gravity control in France (Duquenne et al. 2005), Spain (Pujol 2005), Finland (Mäkinen et al.

P. Dykowski (✉) • J. Krynski • M. Sękowski
Institute of Geodesy and Cartography, 27 Modzelewskiego St., 02-679 Warsaw, Poland
e-mail: przemyslaw.dykowski@igik.edu.pl

© Springer International Publishing Switzerland 2015

C. Rizos, P. Willis (eds.), *IAG 150 Years*, International Association of Geodesy Symposia 143,
DOI 10.1007/1345_2015_98

2010; Krynski and Rogowski 2011), Denmark, Sweden and Norway (Krynski and Rogowski 2012, 2013; Pettersen et al. 2012), and recently in Poland (Krynski and Dykowski 2013).

Each A10 absolute gravimeter manufactured by Micro-g is a unique measuring device and requires specific study of its performance in different measurement conditions. To investigate the performance of the A10-020 absolute gravimeter regular monthly gravity measurements (more than 200 single set-ups) along with control of metrological parameters of the meter are carried out in the Borowa Gora (BG) Geodetic-Geophysical Observatory of the Institute of Geodesy and Cartography (IGiK) for more than 4 years on three sites (A-BG, BG-G2, 156). Two of the stations (A-BG and BG-G2) are located in stable laboratory conditions while the station 156 is located in the open field.

Schmerge and Francis (2006) analysed the results of calibrations of the rubidium clock and laser of the A10-008 gravimeter. They found no significant effect of the change of calibrated parameters on the determined gravity as long as laser modes drift symmetrically. First results of the study of the effect of laser and clock stability on gravity surveyed with the A10-020 were presented in 2011 (Sękowski et al. 2012) and then in 2012 (Dykowski et al. 2012a, 2012b). The experience gained allows a reliable study on the A10-020 uncertainty budget estimation. The authors are convinced that the uncertainty budget provided by the manufacturer is overestimated at least for the A10-020, and may indicate that the performance of A10 gravimeters is better than the prescribed one. The estimation of the total uncertainty budget is an essential part of all absolute gravity determinations. Its importance is especially underlined during ICAG (International Comparison of Absolute Gravimeters) and ECAG (European Comparison of Absolute Gravimeters) campaigns. The estimate of the uncertainty budget is in fact no less important than the measured gravity value itself since it describes the reliability of the absolute gravimeter.

Until now no study of this kind for any A10 gravimeter had been presented although A10 gravimeters participated (Jiang et al. 2012; Francis et al. 2012) and will participate in both ICAG and ECAG campaigns. This paper presents the revision of the total uncertainty (*T.U.*) budget provided by the manufacturer in order to estimate the uncertainty that more reliably describes the performance of the A10-020. The revision includes the decomposition of *T.U.* into three components of corrections/reductions models (model uncertainty), instrument related issues (system uncertainty), and statistical uncertainties. Each of those components is described for the A10-020 and evaluated based on long-term experience with the meter. Corrections/reductions are site dependent. Instrumental issues are related to the components of the instrument, mainly length (ML-1 laser) and frequency standards (Symmetricom X-72 rubidium oscillator). Consequent calibrations of these components allow to estimate their long- and short-term stability and their further influence on the determined gravity values.

2 Components of the A10 Gravimeter Uncertainty Budget

The total uncertainty budget can be considered as a measure of the reliability of the gravity value provided by the gravimeter. As an absolute gravimeter is a very complicated device the total uncertainty budget should include multiple components which describe all parts of the determination of the gravity value. Basic decomposition of the *T.U.* budget

$$T.U. = \sqrt{\sigma_{\text{stat}}^2 + \sigma_{\text{sys}}^2 + \sigma^2{}_{\text{mod}}}$$

consists of the following components

- site related statistics of the gravity determination (statistical uncertainty – σ_{stat}),
- instrumental related issues (system uncertainty – σ_{sys}),
- model described corrections and reductions to the determined value (model uncertainty – σ_{mod})

Consecutive sub-sections of the article describe the components of *T.U.* providing the suggested/estimated uncertainty levels.

2.1 Statistical Uncertainty

In the calculation of the uncertainty budget the statistical component is described as set scatter (standard deviation of performed sets) divided by the square root of the number of sets. The statistical "behaviour" of the measurement depends on the gravimeter as well as on the site on which the measurement is performed. The site noise in most cases depends on the time of day and time of week affects the estimate of statistical uncertainty. No less important is the measurement strategy applied. The strategy developed at IGiK and applied when using the A10-020 consists of two independent measurements/set-ups of eight sets. Each set consists of 120 drops, one drop per second. Two independent set-ups are performed to allow gross error detection and to ensure good reliability of obtained gravity (Sękowski et al. 2012).

The magnitude of statistical uncertainty (measurement precision) ranges from 0.3 to 3.6 μGal with the average of 1.1 μGal (typical value) and drop scatter (standard deviation of the performed drops) within a set from 20 to 120 μGal. Naturally the set scatter strongly depends on the drop scatter. The lower the drop scatter the more stable is the final result. Figure 1 presents the set scatter dependence on the time of

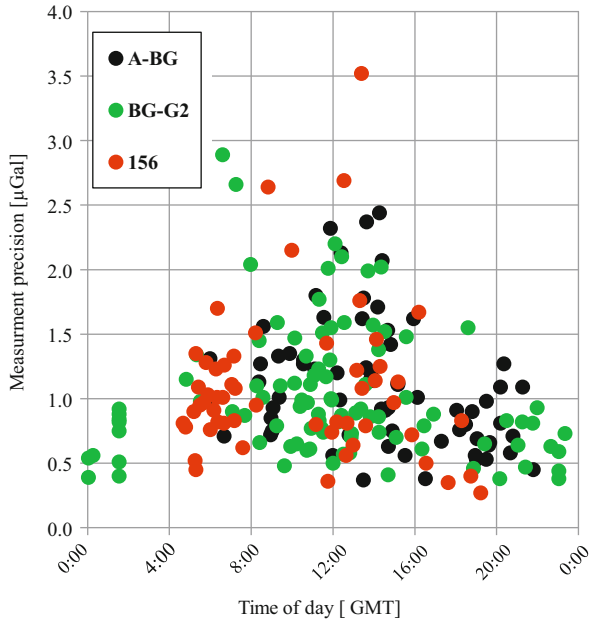

Fig. 1 Measurement precision as a function of the time of day at Borowa Gora Observatory

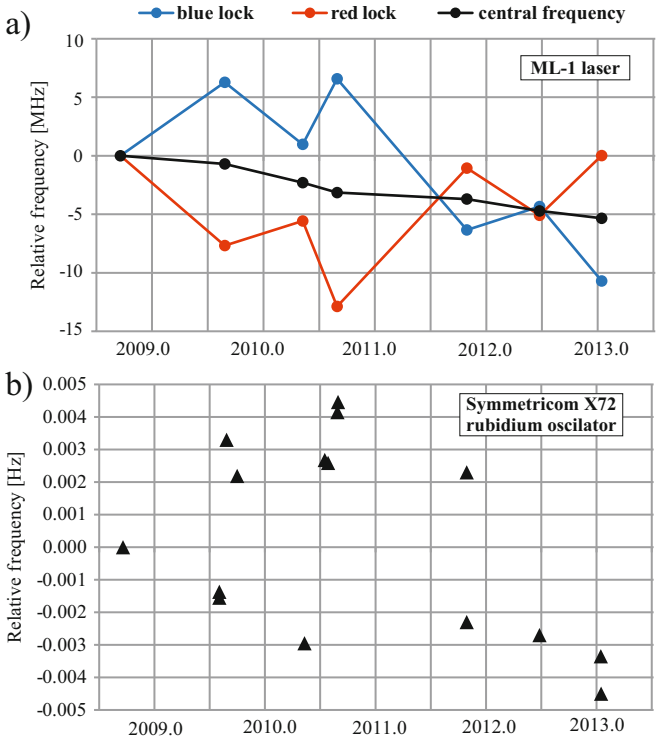

Fig. 2 Long-term stability of the laser lock frequencies (**a**) and clock frequency (**b**)

the day at Borowa Gora Observatory, showing distinctive increase during day hours comparing to the calm night conditions.

Certain effect of temperature on the behaviour of the A10 has also been observed. The range of the observed values of statistical uncertainty shows that it might contribute significantly to the estimated total uncertainty. Therefore, it is vital to assure measurement conditions as good as possible not only in terms of seismic noise but also temperature conditions.

2.2 System Uncertainty

The system uncertainty can be divided into 4 main components: laser, clock, system model and set-up. Other components clearly related to the measurement system include Self Attraction Correction (SAC) and Diffraction Correction (DC) uncertainties. Manufacturer based uncertainties are taken from the g8/g9 manual (Micro-g Inc. 2008, 2012).

Laser uncertainty is described by short- and long-term stability of the blue/red lock wavelengths (frequencies). Long-term stability of the A10-020 laser frequency is shown in Fig. 2a. Over the 5 years the laser frequency drift has reached the level of 5 MHz which corresponds to 10 μGal. Short-term stability can be described by single calibration accuracy (typically 0.3 MHz per red/blue lock which corresponds to nearly 0.7 μGal in gravity uncertainty). The maximum daily change (dynamic) of the interpolated blue/red lock frequency value is nearly 0.07 μGal. Combining these values, the laser uncertainty can be estimated as 0.7 μGal instead of a very optimistic 0.1 μGal suggested by the manufacturer. Uncertainty due to influence of change of temperature on laser frequency is assumed negligible because of the construction of the ML-1 laser (Micro-g Inc. 2005) and the previous investigations (Dykowski et al. 2012a).

Clock is also described by short- and long-term stability of the frequency standard. The stability of the A10-020 frequency standard is presented in Fig. 2b. All calibrated values are within the range of ±0.005 Hz (±1 μGal). The standard deviation of all calibrated clock frequency values is 0.003 Hz (0.6 μGal). Typical calibration error in terms of the gravity uncertainty value is 0.2 μGal. Therefore, the combined value for experimental clock uncertainty is set at 0.66 μGal.

System model uncertainty for each gravimeter is recommended by the manufacturer. For the A10 it is set by Micro-g at 10 μGal. This value reflects the uncertainty due to all effects affecting the survey with the gravimeter which were not taken into account when estimating the total uncertainty budget. The best way to evaluate this component would be to conduct regular measurement tests with the meter. The 4 years long time series at three stations in Borowa Gora Observatory provide more than sufficient data to evaluate the representative statistics, in particular the standard deviation which the authors consider as the experimental system

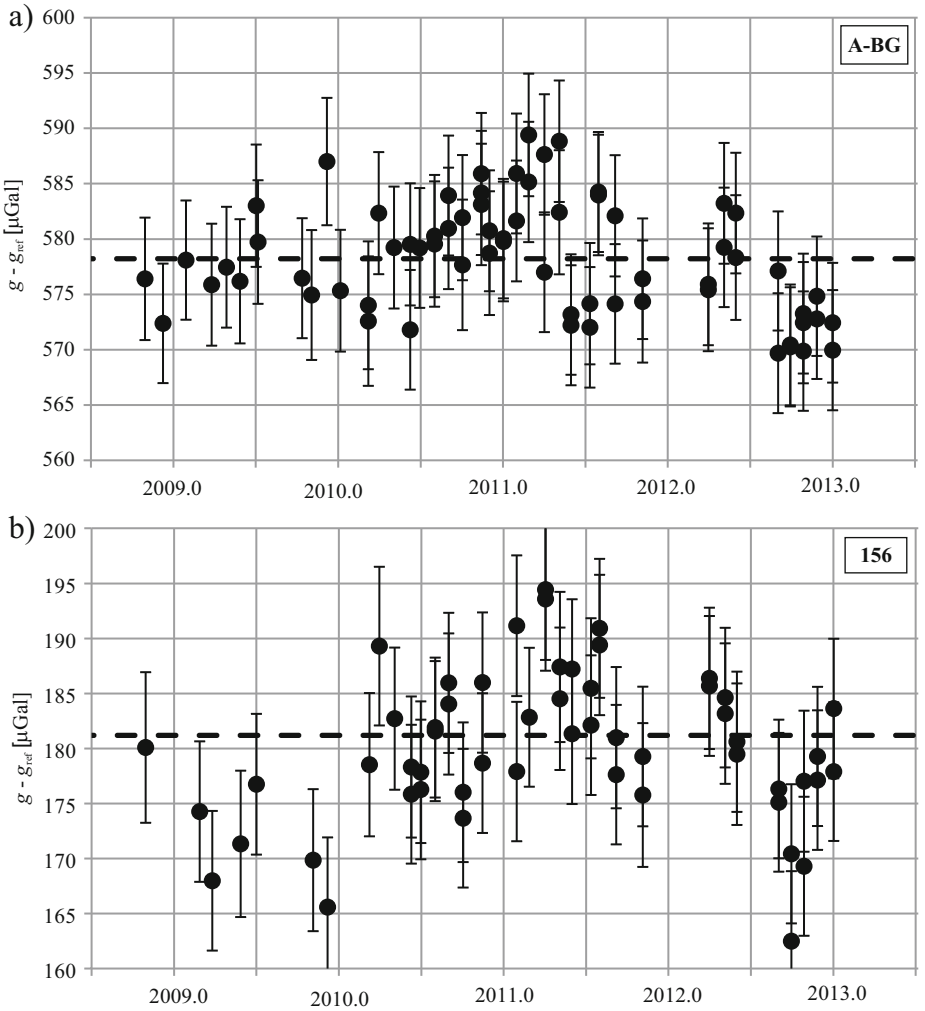

Fig. 3 Gravity determination time series at A-BG (*top*) and 156 (*bottom*) station, *dotted line* corresponds to the average gravity value ($g_{ref} = 981{,}250{,}000$ µGal)

model uncertainty. Figure 3 shows a time series of gravity determination at the laboratory station A-BG (a) and the field station 156 (b) with revised *T.U.* values as error bars. The results obtained indicate that system model uncertainty for the A10 should be estimated separately for stable laboratory conditions and for field conditions, which is typically much less stable due to variations of temperature, seismic noise and others. As the A10 is a portable gravimeter used mostly in field conditions the proper uncertainty estimation for the field conditions is required. On the other hand for the absolute gravimeter comparison type measurements, which are always held in laboratory conditions the second kind of uncertainty should be used.

Values of uncertainties for both laboratory and field conditions were determined from data not corrected for hydrological effects, either local or global. Correlation between water table changes and gravity changes is sufficiently large to allow a reliable estimate of correction due to this effect. Applying the correction reduces the standard deviation values by nearly 30% providing uncertainty values of 3.5 and 4.8 µGal, respectively, for laboratory and field conditions. Applying the local hydrological influence correction is an important step to estimate the uncertainty related strictly to the gravimeter.

Set-up uncertainty value is initially set at 3 µGal. The verification of this value is estimated from set-up to set-up within single measurement survey with the A10-020 and is assured by the use of the measurement strategy developed in IGiK. Data collected in Borowa Gora Observatory (consistent on all three stations) allows to determine this value at an average of 3.21 µGal. Yet it needs to be noted that the set-up to set-up agreement ranges from near 0 to 9 µGal. Differences exceeding 10 µGal are adopted as a limit beyond which further set-up is required. The estimated 3.21 µGal is a typical result. It would, however, be recommended to use a value related to the set-up agreement observed at the station.

SAC and **DC** uncertainties are not initially specified within the manual of g8 but are added to the g9 software as an option since they are essential uncertainty quantities required for ICAG and ECAG campaigns. Since they were not yet studied by the authors, their estimates were taken from other

Table 1 Manufacturer provided and experimental system uncertainties [μGal]

Uncertainty component	Manufacturer provided	Experimental $k = 1$
Laser	0.10	0.70
Clock	0.50	0.66
System model	10.00	3.50 (lab)
		4.80 (field)
Set-up	3.00	3.21
SAC	–	0.30
DC	–	0.50
Total (σ_{sys})	10.45	4.88 (lab)
		5.88 (field)

Table 2 Manufacturer provided and experimental model uncertainties [μGal]

Uncertainty component	Manufacturer provided	Experimental $k = 1$
Tide	0.10	0.10
Ocean	0.01	0.01
Baro	1.00	1.00
Polar	0.05	0.05
Gradient	2.10	2.00 (lab)
		2.90 (field)
Total (σ_{mod})	2.33	2.24 (lab)
		3.07 (field)

works (Jiang et al. 2012). The uncertainty values used in this study are 0.3 and 0.5 μGal for SAC and DC, respectively.

Table 1 presents a summary of system uncertainties. As one can clearly see the system model uncertainty is a dominating factor and the performed revision reduced the estimate by more than 50%.

2.3 Model Uncertainty

Model uncertainty is the most difficult component to be reliably estimated because it is strictly site related. Its estimation can only be performed at stations with supporting gravity recordings (tidal measurements). Since a dominating part of the A10-020 measurements is done in "new" measurement conditions on new field sites, instant models for local corrections cannot be developed due to the lack of supporting measurements. Thus the uncertainty provided by the manufacturer must be used.

Model uncertainty can be decomposed into a set of corrections and reductions. These are tidal, ocean loading, barometric, polar motion corrections and the reduction for the vertical gravity gradient.

In local, regional and international absolute gravity campaigns corrections mentioned above are very well observed and modelled with the use of supporting SG (Superconducting Gravimeter) measurements. Uncertainty due to these corrections is very small and might be considered negligible in case of the A10 *T.U.* budget estimate.

In the case of the vertical gravity gradient determination the authors consider also two types of uncertainty, one related to laboratory conditions, and second to field conditions. For laboratory conditions in Borowa Gora Observatory (Dykowski 2012) the estimated uncertainty of the vertical gravity gradient consists of 2.0 μGal for reduction to the benchmark level and 0.01 μGal for the measurement itself (performing a single drop). For field conditions, experience gained during the establishment of a new gravity control in Poland can be mentioned (Krynski and Dykowski 2013). At each station, the vertical gravity gradient determination is performed two times with LaCoste&Romberg G gravimeter, providing two independent gradient values. The average agreement between two determinations at first 50 stations already surveyed is 5.8 μGal. For uncertainty estimate the authors will assume half of that value, i.e. 2.9 μGal for the reduction of gravity to the benchmark level and 0.02 μGal for the measurement. This is a typical result but the best solution for an uncertainty estimate at any given station will be to use the gradient uncertainty related to the station.

Table 2 presents a summary concerning model uncertainties. Although the experimental model uncertainty for laboratory conditions does not differ much from the one suggested by the manufacturer, a significant change for vertical gradient uncertainty estimate is due to determining the gradient in field conditions on a new station.

3 Total Uncertainty

The typical uncertainty values for the A10-020 in laboratory and field conditions at Borowa Gora Observatory and the total uncertainty is presented in Table 3. Actua measurement uncertainty values may of course vary depending on the station (its location, weather conditions etc.). Among the reviewed A10 uncertainty components the most significant is the system uncertainty. It is related to a particular gravimeter, while the two remaining components are site related.

For $k = 1$, at 67% confidence level the estimated total uncertainty is 5.5 μGal for laboratory conditions and 6.7 μGal for field conditions. Consequently, for $k = 2$, *T.U.* at 95% confidence level is 11 μGal which is very close to a $k = 1$ uncertainty suggested by the manufacturer.

Reviewing the total uncertainty values for ICAG2009 and ECAG2011 the authors obtained for the A10-020 a *T.U.* value of 5.1 μGal at 67% confidence level and 10.2 μGal at 95% confidence level. The uncertainty estimated in this paper

Table 3 Total uncertainty estimates for the A10-020 [μGal]

	Manufacturer provided	Confidence level 67% $k = 1$	Confidence level 95% $k = 2$
σ_{stat}	1.10	1.10	2.20
σ_{sys}	10.45	4.88 (lab)	9.76 (lab)
		5.88 (field)	11.76 (field)
σ_{mod}	2.33	2.24 (lab)	4.48 (lab)
		3.07 (field)	6.14 (field)
T.U.	10.76	5.48 (lab)	10.96 (lab)
		6.72 (field)	13.44 (field)

proves to be a good estimate with respect to the determined offsets in the ICAG2009 (+4.3 μGal – Jiang et al. 2012) and ECAG2011 (−5.8 μGal – Francis et al. 2013) campaigns. Also the *T.U.* estimates for the A10-020 correspond to *T.U.* values determined for the A10-005 and A10-014 at the ICAG2009 (Jiang et al. 2012). Yet the estimation procedures for these meters were not widely presented. The final *T.U.* estimates prove to be very optimistic as the manufacturer based uncertainty is nearly twice bigger.

4 Conclusions

Initial approach to the total uncertainty budget estimation for the A10-020 gravimeter presented in the paper proved to be valuable source of information on its performance. With more than 900,000 drops performed the meter's long- term reliability and efficiency is also confirmed.

The *T.U.* evaluations improved from the 10.8 to 5.5 μGal. The most significant change in the uncertainty estimates was observed in the system uncertainty. On one hand the estimates for the laser and clock uncertainties were larger than the manufacturer suggested. Yet on the other hand the most dominant component of 10 μGal (system model uncertainty) has been replaced with the long term standard deviation of results at Borowa Gora Observatory. Values of 3.5 μGal (lab conditions) and 4.8 μGal (field conditions) had a profound influence on the *T.U.* estimate. Yet further work on the *T.U.* estimates is needed to further understand the behaviour of the gravimeter. More detailed studies can be performed for the A10-020 with respect to Niebauer et al. (1995) detailed description of possible influences. In future work they might explain the small, yet visible difference between the laboratory and field system model uncertainty values.

Evaluation of the uncertainty parameters and their stability for the A10-020 absolute gravimeter is especially important as it is one of the basic tools for the currently realized establishment of the new gravity control in Poland. As the A10-020 is used to survey gravity at base stations (field locations) the distinction for the laboratory (for absolute gravimeter comparison campaigns) and field (for the new gravity control stations) total uncertainty value is required. Participation of the A10-020 in ICAG2009, ECAG2011 campaign and the upcoming ICAG2013 is the essential part of the establishment of the gravity control.

Acknowledgements The research was supported by the Polish Ministry of Science and Higher Education. This work was carried out within the grant No N N526 160340 research. Some parts of the project had been carried out within the statutory project of the Institute of Geodesy and Cartography, Warsaw, "Problems of geodesy and geodynamics".

References

Duquenne F, Duquenne H, Gattacceca T (2005) Gravity measurements on the French geodetic network, Symposium of the IAG Subcommission for Europe (EUREF) held in Vienna. Austria, 1-4 June 2005. http://www.euref-iag.net/symposia/2005Vienna/7-02.pdf.

Dykowski P (2012) Vertical gravity gradient determination for the needs of contemporary absolute gravity measurements – first results. Rep Geod 1(92):23–35 (Warsaw University of Technology)

Dykowski P, Sękowski M, Krynski J (2012a) Stability of metrological parameters and performance of the A10 absolute gravimeter, EGU GA 2012, 22–27 April, 2012, Vienna, Austria

Dykowski P, Sękowski M, Krynski J (2012b) Testing the suitability of the A10-020 absolute gravimeter for the establishment of new gravity control in Poland, IAG Symposia, vol 140. In: Willis P (eds) Symposium gravity, geoid and height systems GGHS2012, Venice, Italy, 9–12 October 2012

Falk R, Müller J, Lux N, Wilmes H, Wzionek H (2012) Precise gravimetric surveys with the field absolute gravimeter A-10. IAG Symp 136:273–279. doi:10.1007/978-3-642-20338-1_33

Francis O et al (2012) Final report of the regional key comparison EURAMET.M.G-K1: European Comparison of Absolute Gravimeters ECAG-2011. Metrologia 49(1A):07–014. doi:10.1088/0026-1394/49/1A/07014

Francis O et al (2013) The European Comparison of Absolute Gravimeters 2011 (ECAG-2011) in Walferdange, Luxembourg: results and recommendations. Metrologia 50:257–268. doi:10.1088/0026-1394/50/3/257

Fukuda Y, Nishijima J, Hasegawal T, Sofyan Y, Taniguchi M (2010) Monitoring groundwater variations using A10 absolute gravimeter. Proceedings IAG symposium on terrestrial gravimetry: static and mobile measurements (TG-SMM2010) 22–25 June 2010, Russia, Saint Petersburg

Jiang Z et al (2012) The 8th international comparison of absolute gravimeters 2009: the first key comparison (CCM.G-K1) in the field of absolute gravimetry. Metrologia 49(6):666–684. doi:10.1088/0026-1394/49/6/666

Krynski J, Dykowski P (2013) Establishment of a new gravity control in Poland – current status, IAG Scientific Assembly 2013, Potsdam

Krynski J, Rogowski JB (2011) National report of Poland to EUREF 2012, IAG Subcommission for Europe (EUREF), Chisinau, Moldova, 25–28 June 2011

Krynski J, Rogowski JB (2012) National report of Poland to EUREF 2012, IAG Subcommission for Europe (EUREF), Paris, France, 6–8 June 2012

Krynski J, Rogowski JB (2013) National report of Poland to EUREF 2013, IAG Subcommission for Europe (EUREF), Budapest, Hungary, 29–31 May 2013

Mäkinen J, Sękowski M, Kryński J (2010) The use of the A10-020 gravimeter for the modernization of the Finnish First Order Gravity Network. Geoinform Issue 2(1):5–17

Micro-g LaCoste Inc. (2005) ML-1 polarization stabilized laser, November 2008, p 13

Micro-g LaCoste Inc. (2008) g8 user's manual, March 2008, p 48

Micro-g LaCoste Inc. (2012) g9 user's manual, April 2012, p 54

Niebauer TM, Sasagawa GS, Faller JE, Hilt R, Klopping F (1995) A new generation of absolute gravimeters. Metrologia 32:159–180

Pettersen BR, Sprlak M, Omang OCD, Lysaker DI, Sękowski M, Dykowski P (2012) Comparison of GOCE gravity field models to test fields in Norway, IAG Symposia, vol 140. In:Willis P (ed) Symposium gravity, geoid and height systems GGHS2012, Venice, Italy, 9–12 October 2012

Pujol E (2005) Absolute gravity network in Spain. Fisica de la Tierra 17:147–163

Schmerge D, Francis O (2006) Set standard deviation, repeatability and offset of absolute gravimeter A10-008. Metrologia 43:414–418

Sękowski M, Krynski J, Dykowski P, Mäkinen J (2012) Effect of laser and clock stability and meteorological conditions on gravity surveyed with the A10 free-fall gravimeter – first results. Rep Geod 1(92):47–59 (Warsaw University of Technology)

Sofyan Y, Daud Y, Supriyanto, Yani A, Herdiansyah T, Nishijima J, Fujimitsu Y, Ehara S, Fukuda Y (2012) Declined mass trends of unbalanced production to recharge activity in Kamojang geothermal field, Indonesia: a continuous monitoring with hybrid gravimetry. Proceedings 37th workshop on geothermal reservoir engineering, Stanford Univeristy, Stanford, California, 30 January–1 February 2012

Sousa M, Santos A (2010) Absolute gravimetry on the Agulhas Negras calibration line. Rev Brasil Geofis 28(2):165–174

Analysis of the Discrepancies Between the Brazilian Vertical Reference Frame and GOCE-Based Geopotential Model

Vagner G. Ferreira, Sílvio R.C. de Freitas, and Bernhard Heck

Abstract

In this study we estimate the discrepancies between the Brazilian vertical network, realized in the system of normal-orthometric heights, and a global quasi-geoid model. We consider the GNSS-leveling and a global quasi-geoid model derived from the *Gravity field and steady-state Ocean Circulation Explorer* (GOCE) mission enhanced by high degree components of the Earth Gravitational Model 2008 (EGM2008). The results indicate that the enhanced geopotential model fits the GNSS-leveling with a root mean square error of 20.2 cm. The estimated bias of -0.4 ± 0.6 cm (w.r.t. the centroid of the network) implies that any future changes to the geopotential value W_0 ($62636856.0\,\mathrm{m^2\,s^{-2}}$) should be minor for the Brazilian Height System (BHS). However, since the GNSS-leveling based "height anomalies" refer to the Brazilian Vertical Datum at Imbituba harbor (BVD-I), Southern Brazil, the results of the comparisons may be an indicator of the mean bias of the national leveling network due to the effect of Mean Dynamic Topography (MDT) at the BVD-I.

Keywords

Brazilian vertical reference frame • EGM2008 • GNSS-leveling benchmarks • GOCE GGM • Normal-orthometric height • Vertical datum

1 Introduction

Brazil occupies approximately 47% of the South American continent and borders all other its countries except Ecuador and Chile. Due to its geographical extension, it plays an important role in the solution of the vertical datum problem among the South American states. The Brazilian Height System (BHS) is materialized by a leveling network with a current extension of about four times the Earth's circumference (considering double-run leveling this number doubles). The Brazilian vertical reference frame has spatio-temporal heterogeneities with large distortions because of its realization starting from South to Northeast (1945–1969 and 1981–2005) and later from Central-West to the North (1970–1980) (Luz et al. 2009).

The major part of the BHS leveling network is linked to the Brazilian Vertical Datum at Imbituba harbor (BVD-I), Southern Brazil, derived from 9 years of sea level observations, centered in 1953. The BHS is based on spirit leveling corrected for the non-parallelism of normal equipotential surfaces. From the practical point of view, the BHS is a normal-orthometric height system. Thus, the BHS does not have a rigorous physical meaning, i.e., a defined reference surface (e.g., geoid or quasi-geoid) does not exist. As such, the BHS is not able to support precise height determination based on ellipsoidal heights obtained by Global Navigation Satellite

V.G. Ferreira (✉)
School of Earth Sciences and Engineering, Hohai University, Nanjing, China
e-mail: vagnergf@hhu.edu.cn

S.R.C. de Freitas
Department of Geomatics, Federal University of Paraná, Curitiba, Brazil

B. Heck
Geodetic Institute, Karlsruhe Institute of Technology, Karlsruhe, Germany

© Springer International Publishing Switzerland 2016

C. Rizos, P. Willis (eds.), *IAG 150 Years*, International Association of Geodesy Symposia 143,
DOI 10.1007/1345_2015_20

Systems (GNSS) (Ihde and Sánchez 2005). Nevertheless, the BHS-based normal-orthometric heights may be considered as approximations of normal heights (Wolf 1974).

Although BHS has served Brazil well since its adoption in 1945, its modernization is a necessary and inevitable task at medium to longer term. A modern height system should enable the determination of heights with a complete physical meaning everywhere across the country by using GNSS technologies (e.g., Global Positioning System - GPS). Apart from the fact that the BHS is not fully compatible with a normal height system, the current (quasi-)geoid model over Brazil, MAPGEO2010 (de Matos et al. 2012), still contains uncertainties of around 5 dm or more for crucial regions in the country like in the North (Amazon region) and Northeast (Melo and de Freitas 2012).

The state-of-the-art geopotential models derived from the observations of *Gravity field and steady-state Ocean Circulation Explorer* (GOCE) have achieved high accuracy as reported in the literature (see, e.g., Yi and Rummel 2014, and references therein). One of the main scientific objectives of GOCE is the worldwide unification of height systems (Rummel 2012). Following Rummel (2002), the main task in connecting two vertical datums is to determine their potential difference at a datum point or the mean offset between the networks. If GOCE can provide a common reference surface for connecting local vertical datums, we can compare national networks to this surface for determining distortions. This paper aims to analyze the discrepancy between the Brazilian vertical network and a GOCE-based global quasi-geoid model. The present study is an attempt to contribute to the modernization of the BHS by considering the systematic leveling errors of the vertical network.

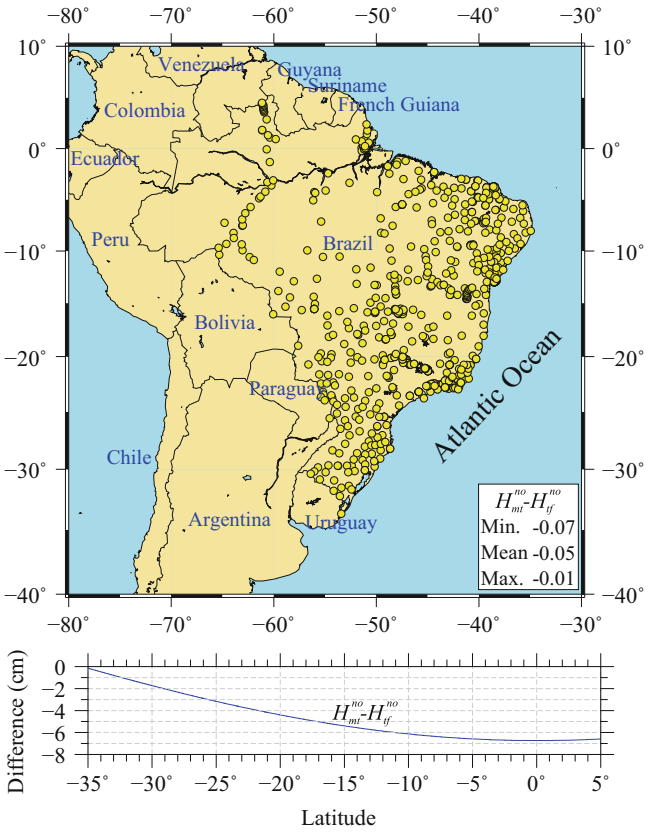

Fig. 1 Distribution of 683 GPS-leveling benchmarks (*top panel*). The graphic (*bottom panel*) shows the differences between the heights in the mean-tide (*mt*) and tide-free (*tf*) systems on a latitudinal profile over the study area

2 Methodology

2.1 Data Sets

For our numerical investigations 683 GPS-leveling points in Brazil were used (Fig. 1, top panel). The ellipsoidal heights (h) and normal-orthometric heights H^{no} (from the 2011 BHS realization) are defined in the tide-free (*tf*) and mean-tide (*mt*) systems, respectively. In Fig. 1 (bottom panel) the differences between both tidal systems are shown. In contrast to MAPGEO's official evaluation presented in de Matos et al. (2012), here we considered the differences in the treatment of the tidal systems.

The used Global Geopotential Models (GGMs) are the fourth release of the time-wise model (TIM-R4) (Pail et al. 2011) and the Earth Gravitational Model 2008 (EGM2008) (Pavlis et al. 2012). In an independent study, Ferreira et al. (2013) found that over Southern Brazil TIM-R4 is slightly more accurate than the fourth generation of the direct approach model (DIR-R4). All data sets were homogenized and transformed to the tide-free system, adopting the Geodetic Reference System 1980 (GRS80) as reference system. Although the International Association of Geodesy in its resolution No. 16 of 1983 recommends the zero-tide convention, we adopted the tide-free system in our comparisons due to its wide use in the GNSS community; the comparison is not influenced by this choice due to differencing. The spherical harmonic series of the GGMs were evaluated at the points of the Earth's surface as suggested by Hirt et al. (2010). The constant term $\zeta_0 = -44.28\,\text{cm}$ was used to re-scale the height anomalies over the study region by considering the geopotential reference value W_0 as $62636856.0\,\text{m}^2\,\text{s}^{-2}$ (Groten 2004).

2.2 Normal and Normal-Orthometric Height Systems

The normal height H^n is defined as (Heck 2003, p. 291):

$$H^n = \frac{C}{\bar{\gamma}}, \tag{1}$$

where C is the geopotential number and $\bar{\gamma}$ is the mean value of the normal gravity along the normal plumb line between the level ellipsoid and the evaluation point on the telluroid. With the geopotential numbers C replaced by normal potential numbers C' (also known as spheropotential numbers), we can write the normal-orthometric height H^{no} as (Heck 2003, p. 294):

$$H^{no} = \frac{C'}{\bar{\gamma}'}, \tag{2}$$

where $\bar{\gamma}'$ is the mean value of the normal gravity along the normal plumbline between the level ellipsoid and the evaluation point at normal-orthometric height.

The difference between the normal and normal-orthometric heights yields

$$\delta H = H^{n} - H^{no} \approx \frac{C - C'}{\bar{\gamma}'}, \tag{3}$$

by considering $\bar{\gamma}' \approx \bar{\gamma}$, where the normal height H^{n} refers to the global quasi-geoid model while H^{no} refers to the unknown reference surface of the BHS. It follows from (3) that

$$\delta H \approx \frac{(W_0 - W_P) - (U_0^{no} - U_P)}{\bar{\gamma}'}. \tag{4}$$

Decomposing $U_0^{no} = U_g + \delta U$ and inserting into (4) yields

$$\delta H \approx \frac{(W_0 - U_g) - (W_P - U_P) + \delta U}{\bar{\gamma}'}, \tag{5}$$

which results in the expression

$$\delta H \approx \frac{T_g - T_P}{\bar{\gamma}'} + \frac{\delta U}{\bar{\gamma}'}, \tag{6}$$

where $T_g = W_0 - U_g$ and $T_P = W_P - U_P$ refer to the disturbing potentials at the geoid and P, respectively. W_P and U_P denote the geopotential and the normal potential at point P, respectively; U_0^{no} is the normal potential at the zero reference for the normal-orthometric heights; U_g is the normal potential at the geoid; and δU is the unknown normal potential difference between the zero reference for H^{no} (U_0^{no}) and the geoid (U_g).

The relation (6) can be re-written as:

$$\delta H \approx \frac{\gamma_0}{\bar{\gamma}'}(N - \zeta) - \frac{T_P}{\bar{\gamma}'}\left(1 - \frac{\gamma_0}{\gamma_Q}\right) + \frac{\delta U}{\bar{\gamma}'}, \tag{7}$$

where γ_0 and γ_Q are the normal gravity at the reference ellipsoid and at the telluroid, respectively; N is the geoidal height and ζ is the height anomaly (or quasi-geoid height). The difference $N - \zeta$ is the same as the difference between the normal height and the orthometric height and can be computed, for example, from Eq. (10a) of Sjöberg (2010). If GNSS-leveling data are available, the height difference (3) can also be expressed as:

$$\delta H = H^{n} - H^{no} = (h - \zeta) - (h - \eta) = \eta - \zeta, \tag{8}$$

where η denotes the height of the unknown BHS reference level above the ellipsoid; the difference between normal and normal-orthometric heights is neglected.

2.3 Combined Geopotential Model

By relation (8) it is possible to analyze the BHS discrepancy with respect to global or local quasi-geoid models by using either the potential differences or offsets. However, we need to choose a suitable representation for the quasi-geoid model. GOCE-only geopotential models may be not sufficient to accomplish this task due to its omission error. Rülke et al. (2012) pointed out that high resolution models (e.g., EGM2008) or regional models (e.g., MAPGEO2010) can be used to reduce omission error. Hence, we enhanced TIM-R4 with EGM2008 by applying a least-squares combination approach (Huang and Véronneau 2013):

$$C_{nm}^{\mathrm{C}} = \frac{(\sigma_{nm}^{\mathrm{A}})^2}{(\sigma_{nm}^{\mathrm{A}})^2 + (\sigma_{nm}^{\mathrm{B}})^2} C_{nm}^{\mathrm{B}} + \frac{(\sigma_{nm}^{\mathrm{B}})^2}{(\sigma_{nm}^{\mathrm{A}})^2 + (\sigma_{nm}^{\mathrm{B}})^2} C_{nm}^{\mathrm{A}}. \tag{9}$$

C_{nm}^{A} and C_{nm}^{B} are the TIM-R4 and EGM2008's cosine coefficients of degree n and order m, respectively. σ_{nm}^{A} and σ_{nm}^{B} are their respective coefficient standard deviations. The same holds for the sine coefficients S_{nm} and their uncertainties (except for the case $m = 0$).

2.4 Treatment of Systematic Errors in the Data

The offsets at the GPS-leveling benchmarks of the leveling network, computed according to Eq. (8), contain systematic and random measurements errors, as well as errors from the GGMs (Kotsakis et al. 2012). To remove the systematic effects in the height simultaneously with the estimation of the offsets, an extended observation equation can be used according to Kotsakis et al. (2012):

$$\delta H_P + \mathbf{a}_P^{\mathrm{T}}\mathbf{x} + v_P = \eta_P - \zeta_P \tag{10}$$

where the term $\mathbf{a}_P^{\mathrm{T}}\mathbf{x}$ absorbs the systematic errors through $n \times 1$ vectors of parameters $\mathbf{x}$ and known coefficients $\mathbf{a}_P$ of a pre-selected model, while v_P is a stochastic term related to the remaining random errors in the height data.

The observation equation (10) can be implemented with the following options for its "bias corrector" term (Kotsakis et al. 2012):

– *Null model:*

$$\mathbf{a}_P^{\mathrm{T}}\mathbf{x} = 0, \tag{11}$$

– *Model 1:*

$$\mathbf{a}_P^{\mathrm{T}}\mathbf{x} = \delta s H_P, \tag{12}$$

– *Model 2:*

$$\mathbf{a}_P^{\mathrm{T}}\mathbf{x} = x_1(\varphi_P - \varphi_0) + x_2(\lambda_P - \lambda_0)\cos\varphi_P \tag{13}$$

and

– *Combined model:*

$$\mathbf{a}_P^{\mathrm{T}}\mathbf{x} = x_1(\varphi_P - \varphi_0) + x_2(\lambda_P - \lambda_0)\cos\varphi_P + \delta s H_P. \tag{14}$$

The parameters x_1 and x_2 represent the spatial tilt between the corresponding reference surfaces consisting of a north-south component and a west-east component, respectively, with respect to the centroid (φ_0, λ_0) of the test network. The parameter δs is a scale factor that accounts for the potential correlation between the raw residuals $\eta_P - \zeta_P$ and the topographic heights.

3 Results and Discussions

As suggested by Gruber et al. (2011), the steepness of the slopes of the root mean square error (RMSE) values is useful to identify at which degree a GGM starts to lose power. Figure 2 shows the RMSEs of the "height anomaly"[1] differences, calculated at 683 points according to Eq. (8), increasing the degree 1 by 1 starting from 60 up to the GGM's maximum degree (no significant differences between degree 2 and 59 were found). As a result, EGM2008 slightly outperforms the official geoid model in Brazil at degree and order (d/o) 360 by approximately 3.5% in terms of RMSE. The improvement rates are given in terms of the RMSE and refer to the MAPGEO2010 comparison. It is worth mentioning that MAPGEO2010 uses EGM2008 up to d/o 150 and more terrestrial gravity anomalies in Brazil than those available to EGM2008's Development Team.

The gravity anomaly values used for the EGM2008 project were of proprietary nature or unavailable (e.g., Amazon region) and their use was restricted to a resolution of 15 arc-minute mean values (Pavlis et al. 2012). This

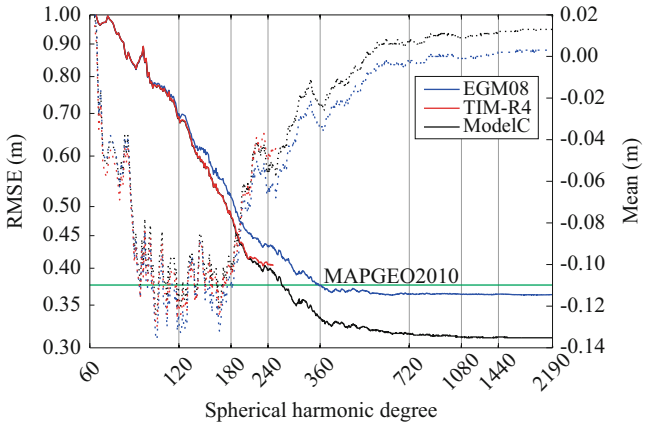

Fig. 2 RMSE values (*solid lines*) and mean values (*dashed lines*) of the "height anomaly" differences according to Eq. (8) for the selected truncation degrees for TIM-R4, EGM2008 and ModelC

resolution would allow a representation of the Earth's gravity field up to d/o 720. However, a post-processing analysis has shown that EGM2008 incorporated the proprietary gravity data information up to a maximum harmonic d/o 900 which corresponds approximately to 12 arc-minute resolution (Pavlis et al. 2013). Beyond d/o 900 "fill-in" gravity anomalies were applied, which implies that over Brazil EGM2008-derived height anomalies would have less accuracy in comparison with MAPGEO2010.

The evaluation of the GOCE-only satellite model TIM-R4 shows evidence of improvement of the Earth's static gravity field determination over Brazil in comparison with the pre-GOCE-era (Hirt et al. 2011). The RMSE value for TIM-R4 is 0.404 m at its maximum degree of expansion while for EGM2008 it is 0.429 m at the same degree (i.e., 250). The improvement within the frequency band between degrees 96 and 250 (Fig. 2) amounts to an average value of 5% with a maximum improvement of 9.1% at degree 206 with respect to EGM2008. The EGM2008 was based on a satellite model up to d/o 180, and beyond gravity anomalies and satellite altimetry data were used. However, it can be noted that TIM-R4 within the band 180–250 presents more power than EGM2008 which possesses an enhanced signal by using terrestrial gravity anomalies.

We combined TIM-R4 and EGM2008 by using the least-squares approach proposed by Huang and Véronneau (2013). The combined model (ModelC) outperforms EGM2008 and MAPGEO2010 by 14.4% and 17.4%, respectively, in terms of RMSE. Surprisingly, there is an improvement of ModelC with respect to TIM-R4 from degree 210 up to 250, amounting to 2.9% at degree 250. Probably the gravity anomalies used in EGM2008 enhanced the TIM-R4 model and improved the spectral content at that band. Furthermore, it seems that ModelC also improved the "fill-in" band (901–2190). The slope of the RMSE function is −0.002 mm

[1]We used the quotation marks in order to indicate that the normal heights have been approximated by normal-orthometric heights.

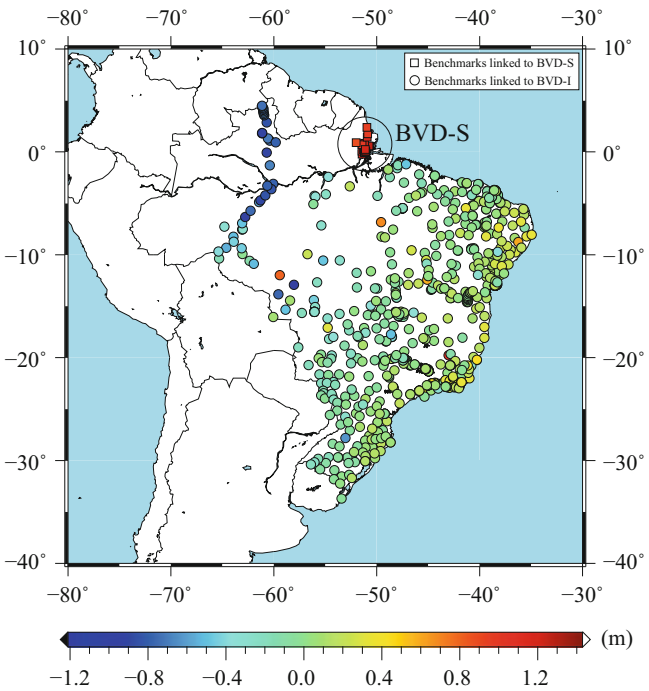

Fig. 3 "Height anomaly" differences ($\eta_P - \zeta_P$) in meters for the Brazilian vertical datum at Imbituba (BVD-I) and Santana (BVD-S) GPS-leveling benchmarks

Table 1 Estimated offsets and parameters corresponding to various bias corrector models in Eq. (10) and their respective RMSEs of the adjusted residuals (goodness of model fit). The coordinates of the centroid of the network are 15.5932°S and 46.1879°W

Model	δH (cm)	x_1 (cm/degree)	x_2 (cm/degree)	δs	RMSE (cm)
Null	-0.2 ± 0.8	–	–	–	20.2
Model 1	-1.0 ± 1.3	–	–	$1.96 \times 10^{-5} \pm 2.48 \times 10^{-5}$	20.2
Model 2	-0.4 ± 0.6	-0.90 ± 0.08	2.27 ± 0.10	–	14.7
Combined	-1.0 ± 1.0	-0.88 ± 0.08	2.27 ± 0.10	$1.37 \times 10^{-5} \pm 1.93 \times 10^{-5}$	14.7

and −0.001 mm per degree of expansion for ModelC and EGM2008, respectively. Furthermore, above degree 1600 the use of ModelC's spherical harmonic coefficients provided an almost constant RMSE.

Figure 2 also shows the behavior of the mean value as a function of the degree. A mean difference between GPS-leveling "height anomalies" and the GOCE gravity field model indicates a height system offset. The impact of the omission error on the height system offset is investigated by comparing mean values resulting from either taking into account the omission error or not (Fig. 2). It has to be noted that the mean value starts to be nearly constant above degree 720 which implies that for vertical datum connection the omission error (coefficients beyond the maximum degree of the GOCE-based models) cannot be neglected.

We examined the systematic effects and their impact on the estimated discrepancy between BHS and a global quasi-geoid model computed from the spherical harmonic coefficients of ModelC. The "height anomaly" differences according to Eq. (8) are presented in Fig. 3 in order to emphasize the systematic spatial tilt present in the GPS-leveling network. Figure 3 shows that there is a significant east-west tilt whereas the north-south tilt appears to be less important. The residuals related to the Brazilian Vertical Datum at Santana (BVD-S) are explained by a shift between the two segments of BHS referred to BVD-I and BVD-S. Montecino and de Freitas (2014) estimated that the BVD-S is located in the range of 1.32–1.43 m above the BVD-I.

The offsets δH and the parameters values (x_1, x_2 and δs) computed by using the adjusted "height anomaly" differences, after the removal of 20 outliers and 17 points related to the BVD-S, are presented in Table 1 for each of the four bias corrector models (Sect. 2.4). We estimated the parameters by using 646 points of the network, and the RMSE values were calculated by using the adjusted residuals from the least-squares estimation.

The *Null* and *Model 1* for the "bias corrector" show almost the same RMSE which means that the consideration of a scale factor δs does not provide any improvement. However, the use of *Model 2* shows a significant improvement of 5 cm in terms of RMSE when compared to the *Null* and *Model 1*. Additionally, the scale factor in the *Combined* model does not provide any improvement over *Model 2*. Over the test area, there is no correlation between the topographic heights and the residuals ($\eta_P - \zeta_P$). This means that *Model 2* can be considered sufficient for explaining the spatial tilts found in

the network. Considering the GPS-leveling distribution over the test area, the north-south and the west-east tilts evaluated with *Model 2* are −0.9 cm/degree and 2.3 cm/degree, respectively. The tilts in both directions are in agreement with the Brazilian leveling specification of $4\,\mathrm{mm}\sqrt{k}$ where k is the length of the leveled line in km (or ∼4.2 cm/degree at the equator). Additionally, considering the signal-to-noise ratio, the offsets δH estimated by the four models presented in Table 1 are insignificant.

4 Conclusions

Using the GOCE-based geopotential model (i.e. TIM-R4) spectrally enhanced with the high-resolution model EGM2008 we found a predominant tilt in the west-east direction in the BHS network linked to BVD-I. The tilt of 2.3 cm/degree in the west-east direction (with respect to the centroid of the network) could be attributed to the characteristics of the spatial and temporal realization of the leveling network. The comparisons indicated that the combined model (ModelC) fits to the GPS-leveling stations better than 20.2 cm in RMSE (after removal of outliers) and shows an offset of -0.4 ± 0.6 cm w.r.t. the centroid of the network, which is insignificant. However, since GPS-leveling based "height anomalies" refer to BVD-I in the present case, the results of the comparisons may be an indicator of the mean bias of the local network due to the effect of Mean Dynamic Topography (MDT) at BVD-I. Future work will mainly refine our results by using the modeled MDT (satellite altimetry and tide gauges) to test its influence on the BHS and to confirm our preliminary result for the bias in the Brazilian vertical reference frame.

Acknowledgements V.G. Ferreira acknowledges the National Natural Science Foundation of China (Grant No. 41204016). S.R.C. de Freitas acknowledges the National Council for Scientifics and Technological Development (Grant No. 301797/2008-0). We would like to thank the Brazilian Institute of Geography and Statistic (IBGE) for providing the GPS-leveling data. Finally, we acknowledge the Associate Editor and three reviewers for their remarks which helped to improve the manuscript.

References

de Matos ACOC, Blitzkow D, Guimarães GN, Lobianco MCB, Costa SMA (2012) Validação do MAPGEO2010 e comparação com modelos do geopotencial recentes (in Portuguese). Bol Cienc Geod 18(1):101–122. doi:10.1590/S1982-21702012000100006

Ferreira VG, Zhang Y, de Freitas SRC (2013) Validation of GOCE gravity field models using GPS-leveling data and EGM08: a case study in Brazil. J Geod Sci 3(3):209–218. doi:10.2478/jogs-2013-0027

Groten E (2004) Fundamental parameters and current (2004) best estimates of the parameters of common relevance to astronomy, geodesy, and geodynamics. J Geod 77(10–11):724–797. doi:10.1007/s00190-003-0373-y

Gruber T, Visser PNAM, Ackermann C, Hosse M (2011) Validation of GOCE gravity field models by means of orbit residuals and geoid comparisons. J Geod 85(11):845–860. doi:10.1007/s00190-011-0486-7

Heck B (2003) Rechenverfahren und Auswertemodelle der Landesvermessung: Klassische und moderne Methoden (in German), 3rd edn. Wichmann, Karlsruhe

Hirt C, Featherstone WE, Marti U (2010) Combining EGM2008 and SRTM/DTM2006.0 residual terrain model data to improve quasigeoid computations in mountainous areas devoid of gravity data. J Geod 84(9):557–567. doi:10.1007/s00190-010-0395-1

Hirt C, Gruber T, Featherstone WE (2011) Evaluation of the first GOCE static gravity field models using terrestrial gravity, vertical deflections and EGM2008 quasigeoid heights. J Geod 85(10):723–740. doi:10.1007/s00190-011-0482-y

Huang J, Véronneau M (2013) Canadian gravimetric geoid model 2010. J Geod 87(8):771–790. doi:10.1007/s00190-013-0645-0

Ihde J, Sánchez L (2005) A unified global height reference system as a basis for IGGOS. J Geodyn 40(4–5):400–413. doi:10.1016/j.jog.2005.06.015

Kotsakis C, Katsambalos K, Ampatzidis D (2012) Estimation of the zero-height geopotential level W_o^{LVD} in a local vertical datum from inversion of co-located GPS, leveling and geoid heights: a case study in the Hellenic islands. J Geod 86(6):423–439. doi:10.1007/s00190-011-0530-7

Luz R, de Freitas SRC, Heck B, Bosch W (2009) Challenges and first results towards the realization of a consistent height system in brazil. In: Geodetic reference frames. IAG Symposia, vol 134, pp 291–296. doi:10.1007/978-3-642-00860-3_45

Melo LFS, de Freitas SRC (2012) Avaliação de modelos globais do geopotencial para os estados do Maranhão e Piauí (in Portuguese). Bol Cienc Geod 18(2):203–224. doi:10.1590/S1982-21702012000200003

Montecino H, de Freitas SRC (2014) Strategies for connecting Imbituba and Santana Brazilian datums based on satellite gravimetry and residual terrain model. In: Earth on the edge: science for a sustainable planet. IAG Symposia, vol 139, pp 543–549. doi:10.1007/978-3-642-37222-3_72

Pail R, Bruinsma S, Migliaccio F, Förste C, Goiginger H, Schuh WD, Höck E, Reguzzoni M, Brockmann JM, Abrikosov O et al (2011) First GOCE gravity field models derived by three different approaches. J Geod 85(11):819–843. doi:10.1007/s00190-011-0467-x

Pavlis NK, Holmes SA, Kenyon SC, Factor JK (2012) The development and evaluation of the earth gravitational model 2008 (EGM2008). J Geophys Res 117(B4):B04406. doi:10.1029/2011JB008916

Pavlis NK, Holmes SA, Kenyon SC, Factor JK (2013) Correction to "The development and evaluation of the earth gravitational model 2008 (EGM2008)". J Geophys Res 118(5):2633–2633. doi:10.1002/jgrb.50167

Rülke A, Liebsch G, Sacher M, Schäfer U, Schirme U, Ihde J (2012) Unification of European height system realizations. J Geod Sci 2(4):343–354. doi:10.2478/v10156-011-0048-1

Rummel R (2002) Global unification of height systems and GOCE. In: Gravity, geoid and geodynamics 2000. IAG Symposia, vol 123, pp 13–20. doi:10.1007/978-3-662-04827-6_3

Rummel R (2012) Height unification using GOCE. J Geod Sci 2(4):355–362. doi:10.2478/v10156-011-0047-2

Sjöberg L (2010) A strict formula for geoid-to-quasigeoid separation. J Geod 84(11):699–702. doi:10.1007/s00190-010-0407-1

Wolf H (1974) Über die Einführung von Normalhöhen (in German). Zeitschrift für Vermessungswesen (ZfV) 99:1–5

Yi W, Rummel R (2014) A comparison of GOCE gravitational models with EGM2008. J Geodyn 73:14–22. doi:10.1016/j.jog.2013.10.004

Regional Gravity Field Modeling by Radially Optimized Point Masses: Case Studies with Synthetic Data

Miao Lin, Heiner Denker, and Jürgen Müller

Abstract

A two-step point mass method with free depths is presented for regional gravity field modeling based on the remove-compute-restore technique. Three numerical test cases were studied using synthetic data with different noise levels. The point masses are searched one by one in the first step with a simultaneous determination of the depth and magnitude by the Quasi-Newton algorithm L-BFGS-B. In the second step, the magnitudes of all searched point masses are readjusted with known positions by solving a linear system in the least-squares sense. Tikhonov regularization with an identity regularization matrix is employed if ill-posedness exists. One empirical and two heuristic methods for choosing proper regularization parameters are compared. In addition, the solutions computed from standard and regularized least-squares collocation are presented as references.

Keywords

Free depths • Least-squares collocation • Point mass method • Regional gravity field modeling • Tikhonov regularization

1 Introduction

The numerical integration method and least-squares collocation (LSC) together with the remove-compute-restore (RCR) technique are standard methods for regional gravity field modeling. In recent years, the parameter estimation method using radial basis functions have been used extensively in gravity field modeling, e.g. based on the robust basis function (e.g. Bjerhammar 1986), the radial multipoles (e.g. Marchenko et al. 2001), the Blackman kernel (e.g. Schmidt et al. 2007; Bentel et al. 2013), the Poisson wavelet (e.g. Klees et al. 2008; Tenzer and Klees 2008), the spherical spline kernel (e.g. Eicker 2008) as well as the point mass (e.g. Barthelmes 1986; Lehmann 1993; Claessens et al. 2001; Antunes et al. 2003). Compared to the integration method, the estimation method is more flexible, and it usually requires fewer unknowns to be estimated in comparison to LSC. A critical issue in the estimation method is how to assemble the radial basis functions in a reasonable way.

In this study, a two-step point mass method with free depths is proposed on the basis of the concept of free-positioned point masses (e.g. Barthelmes 1986). The applicability and performance of the method is demonstrated by three case studies using synthetic data with different noise levels. The LSC method serves as reference for the gravity field computations and the corresponding results are presented for comparison. The proposed method and LSC are briefly described in Sect. 2. Three numerical test cases with synthetic data are conducted and discussed in Sect. 3. Finally, Sect. 4 gives the conclusions drawn from the numerical results.

M. Lin (✉) • H. Denker • J. Müller
Institut für Erdmessung (IfE), Leibniz Universität Hannover, Hannover, Germany
e-mail: linmiao@ife.uni-hannover.de

© Springer International Publishing Switzerland 2015

C. Rizos, P. Willis (eds.), *IAG 150 Years*, International Association of Geodesy Symposia 143,
DOI 10.1007/1345_2015_92

2 Method

2.1 Two-Step Point Mass Method with Free Depths

The disturbing potential T at the i-th computation point exterior to the Earth's surface can be represented by a set of N point masses as

$$T_i = \sum_{j=1}^{N} \mu_j \phi_{ij}^T \left(r_i, \varphi_i, \lambda_i, r_j, \varphi_j, \lambda_j\right), \tag{1}$$

where μ_j is the magnitude of the j-th point mass; r, φ and λ are the radial distance, geocentric latitude and longitude, respectively, and ϕ_{ij}^T stands for the point mass basis function which is expressed as the reciprocal of the distance between the i-th computation point and the j-th point mass:

$$\phi_{ij}^T = \frac{1}{l_{ij}} = \sum_{n=0}^{\infty} \frac{1}{r_i} \left(\frac{r_j}{r_i}\right)^n P_n\left(\cos\psi_{ij}\right), \tag{2}$$

where P_n are the Legendre polynomials. For other gravity field quantities (e.g. gravity anomaly, geoid height, etc.), the related ϕ_{ij} are given as the corresponding derivatives of ϕ_{ij}^T.

In contrast to the frequently used point mass method with fixed positions, the unknown parameters are not just the magnitudes but also the depths, leading to a nonlinear least-squares problem. In this case, the vector of the model parameters for N point masses is $\mathbf{m} = (\mu_1, r_1, \ldots, \mu_N, r_N)^{\mathrm{T}}$, and the objective function to be minimized is given as

$$\Psi(\mathbf{m}) = (\mathbf{d}_{\mathrm{obs}} - \mathbf{F}(\mathbf{m}))^{\mathrm{T}} \mathbf{P} (\mathbf{d}_{\mathrm{obs}} - \mathbf{F}(\mathbf{m})), \tag{3}$$

where $\mathbf{d}_{\mathrm{obs}}$ is the data vector, $\mathbf{F}(\mathbf{m})$ can be expressed by Eq. (1) or its derivatives, depending on the data types, and $\mathbf{P}$ denotes the weight matrix of the input data which is an identity matrix $\mathbf{I}$ in this study, as the accuracy of all input data is assumed to be the same. When the model parameters are bounded, then the constraints $\mathbf{m}_{\min} \leq \mathbf{m} \leq \mathbf{m}_{\max}$ will be included in Eq. (3), where $\mathbf{m}_{\min}$ and $\mathbf{m}_{\max}$ are lower and upper bounds.

In practice, there usually are two strategies to estimate the point mass depths and magnitudes. The first strategy is that we give the initial positions (i.e. horizontal locations and depths) and magnitudes of a given number of point masses first, and then improve the model parameters iteratively to minimize the objective function shown in Eq. (3). In this case, the number of point masses should be smaller than half the number of observations, as the number of model parameters are two times the point mass number. Furthermore, the numerical instability is very serious in the case of a large number of point masses. In the second strategy, a point-wise procedure is applied for searching the point masses. For each new point mass, its depth and magnitude are estimated iteratively (e.g. Barthelmes 1986; Lehmann 1993; Claessens et al. 2001), see also Fig. 1.

In this study, a two-step method is proposed according to the above mentioned point-wise procedure (abbreviated as '2SPM_FD' in the rest of the paper). Figure 1 shows the detailed procedure of the method which is used in the following computations. In the first step of 2SPM_FD, the point masses are searched and optimized one by one. In order to reach a good representation of the gravity field, all searched point masses are restricted to a layer with defined upper and lower bounds. The Quasi-Newton algorithm L-BFGS-B (e.g. Zhu et al. 1994; Byrd et al. 1995; Nocedal and Wright 1999) is employed to solve the nonlinear problem with bound constraints on the depths. When the first step is finished by satisfying a defined maximum number of point masses or by satisfying a limit for the data misfit, the resulting point masses are considered as being located at reasonable positions. Then a further readjustment of the magnitudes for all searched masses with known positions is conducted in the second step. Tikhonov regularization with an identity regularization matrix (e.g. Tikhonov 1963; Bouman 1998) is introduced to solve the ill-posedness which may be caused by large point mass depths, masses in close proximity, or data gaps. In this case, the regularization parameters are determined by one empirical method, i.e. (1) minimizing the root mean square (RMS) of the differences between predicted and observed values on a set of control points, see e.g. Tenzer and Klees (2008); and two heuristic methods, i.e. (2) generalized cross validation (GCV), see e.g. Bouman (1998), Kusche and Klees (2002); (3) variance component estimation (VCE), see e.g. Koch and Kusche (2002).

2.2 Least-Squares Collocation

The formula of the standard LSC for the prediction of signals based on noisy data can be expressed as (e.g. Moritz 1980)

$$\hat{\mathbf{s}} = \mathbf{C}_{st}(\mathbf{C}_{tt} + \mathbf{C}_{ee})^{-1}\mathbf{l}, \tag{4}$$

where $\hat{\mathbf{s}}$ denotes the estimated signal vector, $\mathbf{C}_{st}$ and $\mathbf{C}_{tt}$ are the cross- and auto-covariance matrices of the signals, $\mathbf{l}$ is the observation vector, consisting of a signal and a noise component, and $\mathbf{C}_{ee}$ is the noise covariance matrix, defining the amount of smoothing. Eq. (4) can be considered as being equivalent to Tikhonov regularization with signal constraints, where the regularization parameter equals 1 (e.g. Bouman 1998). Generally, the standard LSC can provide stable solutions for ill-posed problems. However, in some cases the amount of smoothing provided by the

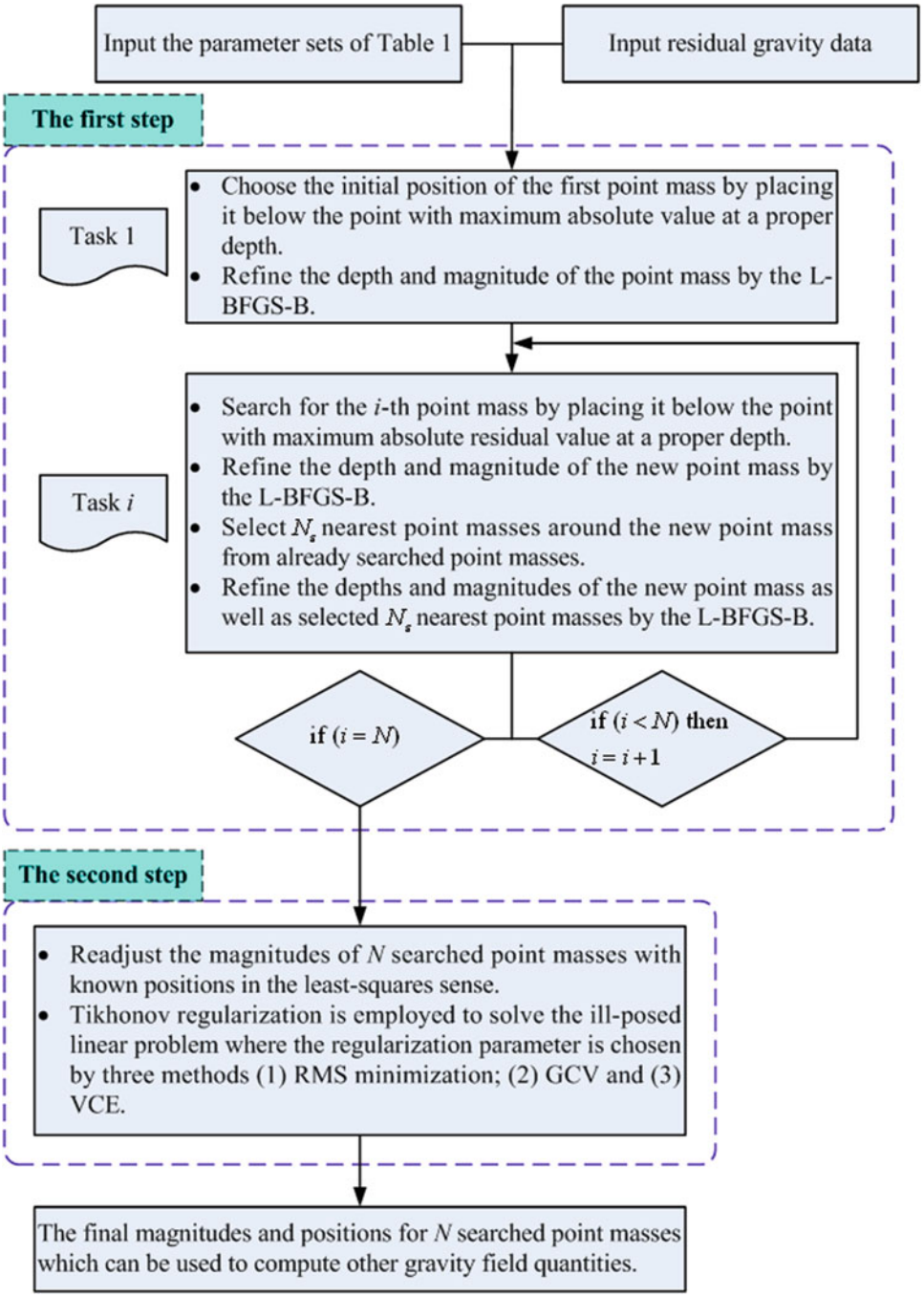

Fig. 1 Computation procedure of the two-step point mass method with free depths

noise covariance matrix is not enough, then an additional regularization parameter α has to be introduced into Eq. (4), leading to the regularized LSC (e.g. Marchenko et al. 2001)

$$\widehat{\mathbf{s}} = \mathbf{C}_{st}(\mathbf{C}_{tt} + \alpha\mathbf{C}_{ee})^{-1}\mathbf{l}. \tag{5}$$

If $\alpha = 1$, Eq. (5) becomes Eq. (4). The regularization parameter α can be determined based on the following formula derived from the so-called misclosure principle (e.g. Ameti 2006)

$$\alpha = 1 + \sqrt{1 + \frac{trace\,(\mathbf{C}_{tt}\mathbf{C}_{ee})}{trace\,(\mathbf{C}_{ee}\mathbf{C}_{ee})}}. \tag{6}$$

Suppose that (1) only one data type is used; (2) the noise covariance matrix $\mathbf{C}_{ee}$ can be represented as $\mathbf{C}_{ee} = \sigma_e^2\mathbf{I}$, where σ_e^2 is the variance of the noise and (3) the

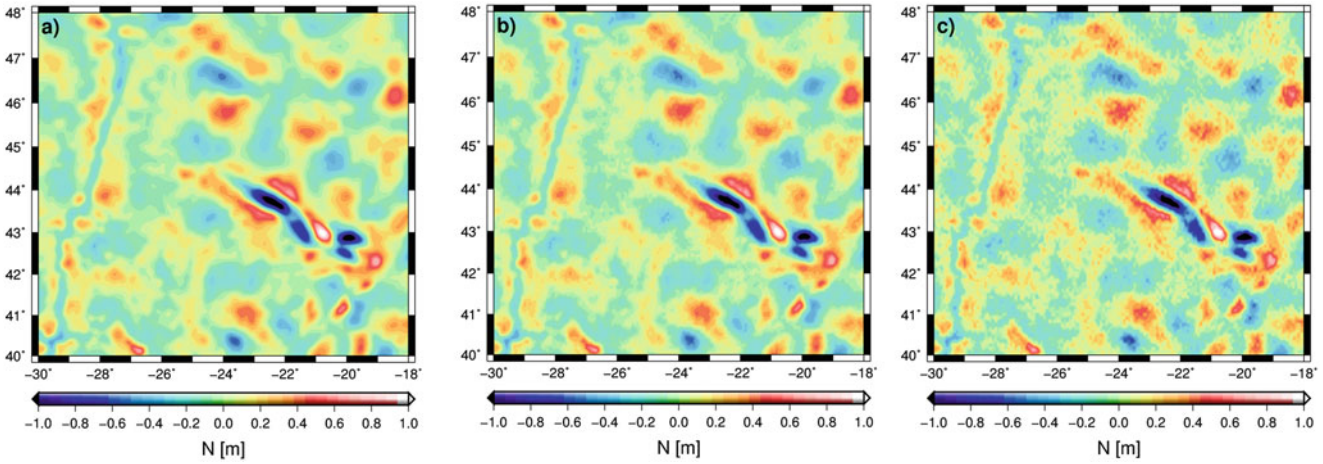

Fig. 2 Simulated residual geoid heights over the test area. (**a**) error-free data; (**b**) white noise added, with a standard deviation of 0.02 m and (**c**) white noise added, with a standard deviation of 0.05 m

auto-covariance matrix $\mathbf{C}_{tt}$ can be approximately written as $\mathbf{C}_{tt} = \sigma_t^2\mathbf{I}$, where σ_t^2 is the variance of the signals, then Eq. (6) can be approximated as (e.g. Marchenko and Tartachynska 2003)

$$\alpha = 1 + \sqrt{1 + \frac{\sigma_t^2}{\sigma_e^2}}. \tag{7}$$

It should be noted that Eq. (7) only provides a possible upper limit of α.

3 Numerical Tests

Three numerical test cases are conducted to investigate the performance of 2SPM_FD by comparing the results to corresponding LSC results. For all test cases, synthetic data with different noise levels are used for the gravity field modeling in one test area.

3.1 Data Sets

The test area is located in the North Atlantic Ocean with an extent from −30° to −18°E and 40° to 48°N. The data set (a) consists of 14065 error-free residual geoid heights which are computed by the EGM2008 model (Pavlis et al. 2012) up to d/o 2160 with the removal of the long-wavelength contributions from the GOCO03S model (Mayer-Gürr et al. 2012) up to d/o 250. The input residuals are located at grid points with a resolution of 5′ and the height for each point is 0 m. The data sets (b) and (c) are obtained by adding white noise with the standard deviations (STD) of 0.02 and 0.05 m to data set (a). All three sets of residual geoid heights are illustrated in Fig. 2. In addition, 11305 residual gravity anomalies located at grid points with true values are used as control points to assess the modeled gravity anomalies in each test case. The grids for the control points coincide with the ones for the observations but have a smaller extent. As the test area is in the ocean area, the test cases can be considered as analogue to gravity anomaly recovery from altimeter data.

3.2 Results and Discussions

Before the computation by using 2SPM_FD, several parameter sets (e.g. initial depth, depth limits, etc.) have to be chosen appropriately. An empirical rule for choosing the initial depth and depth limits is applied here (Lin et al. 2014): the initial depth is chosen to be the one at which the half width (i.e. the spherical distance where the basis function attains half of its maximum value) of the point mass basis function is equal to the correlation length of the empirical covariance function of the observations and the upper depth limit is chosen to be 0.8–0.9 times this value while being larger than the average data spacing (e.g. about 9 km in our test cases); the lower depth limit can be determined from the simple formula $D = R/(n-1)$ as given in Bowin (1983), where D means the depth, R denotes a mean Earth radius, and n stands for the maximum spherical harmonic degree of the reference field, but it should be smaller than the maximum resolution of the reference field (e.g. about 80 km in our test cases). Figure 3 gives the empirical covariance function and the fitted analytical Tscherning-Rapp covariance function model (e.g. Tscherning and Rapp 1974) for data set (a). The latter one is used in LSC. The covariance functions for the other two data sets are not shown here as they are similar. As a result, the correlation lengths are about 0.240°, 0.238° and 0.227° for the three data sets, resulting in an

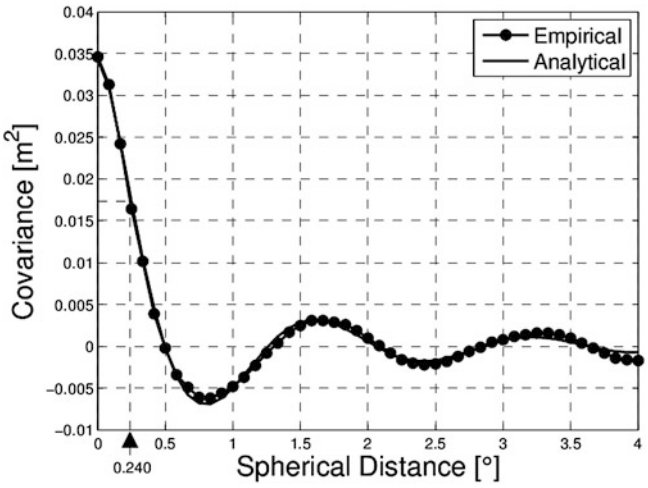

Fig. 3 Empirical covariance function and the fitted analytical Tscherning-Rapp covariance function model for data set (a). The value of 0.240 means the correlation length of the empirical covariance function

initial depth of about 15.5 km for all test cases. The chosen upper depth limit is about 0.9 times the initial depth and the lower depth limit is computed from Bowin's formula using $R = 6{,}371.0$ km and $n = 250$, resulting in a point mass layer with the upper depth of 14 km and the lower depth of 25 km. Figure 4 shows the histograms of the depths for the searched point masses in each test case. Most of the point masses are located around the depth limits (about 80–90%). The point masses around the lower depth limit contribute to the long-wavelength signals, while the short-wavelength signals are mostly represented by the masses close to the upper depth limit. As 2SPM_FD is implemented together with the RCR technique, the input data are residuals which are obtained by subtracting the contributions of a global gravity field model complete to degree n_{ref} and of the topography from a digital terrain model. Therefore, the summation of the series expansion in Eq. (2) starting with $n_{\min} = 0$ (i.e. the original basis function) does not seem to be a good choice. Often, $n_{\min} = n_{\text{ref}} + 1$ is chosen, as one assumes that the input residuals do not contain enough signals below degree $n_{\text{ref}} + 1$ (Klees et al. 2008). In practice, the above assumption is not satisfying totally because there usually are some long-wavelength errors in the residuals. Therefore, the summation in Eq. (2) starting with $1 < n_{\min} \leq n_{\text{ref}} + 1$ is preferred (i.e. the reduced basis function). In this paper, the original basis function and the reduced basis function with $n_{\min} = 101$ are compared. All parameter sets used for the following computations are given in Table 1. For more details about these parameter sets, one can refer to Claessens et al. (2001).

No regularization is applied in the second step of 2SPM_FD for the test case with data set (a), while Tikhonov regularization with an identity regularization matrix is employed in the other two test cases. The regularization parameters determined by the three methods are given in Table 2. Obviously the chosen parameters are nearly the same with the use of the original and reduced basis functions for each method in each test case. When the input data contains larger errors (e.g. test case (c)), a larger regularization parameter is chosen to reduce the effects of the errors in the solutions. In addition, the regularization parameter α of the regularized LSC for test cases (b) and (c) are determined by Eq. (7), resulting in values of 6.25 and 4.0, respectively.

The solutions computed by 2SPM_FD following from the computation procedure described in Fig. 1 as well as the LSC solutions are validated by a set of control points with true values for each test case. The statistics of modeled gravity anomaly errors are listed in Tables 3, 4, and 5. It can be seen that, when the input data are error-free (i.e. Table 3), the solutions of 2SPM_FD without regularization are close to the standard LSC solutions with an accuracy of about 1 mGal. When the input data are noisy (i.e. Tables 4 and 5), the application of Tikhonov regularization in 2SPM_FD improves the solutions marginally in test case (b), e.g. with an accuracy from about 2.7 to 2.5 mGal, but significant improvements can be achieved in test case (c), e.g. with an accuracy from about 5.8 to 3.9 mGal. The standard LSC solutions are seriously affected by the data noise (i.e. Tables 4 and 5), indicating that the amount of smoothing only defined by the noise covariance matrix $\mathbf{C}_{ee}$ is not enough. Better results can be obtained by introducing a regularization parameter $\alpha > 1$ (i.e. 6.25 and 4.0) into the regularized LSC.

The performance of the three methods for choosing proper regularization parameters in 2SPM_FD is different. The parameters determined by the empirical method are the most proper among the three methods according to the numerical results, and the ones associated with the other two methods are smaller, meaning that the effects caused by the data noise in the solutions are larger. Furthermore, the VCE determined parameters are much closer to the ones determined by the empirical method than the GCV determined parameters, resulting in better solutions (see Tables 2, 4, and 5). The square roots of the variance components of data sets (b) and (c) estimated by VCE are about 0.0197 and 0.0490 m, which are slightly smaller than the known data noise, i.e. 0.02 and 0.05 m, meaning that the noise in both data sets is slightly underestimated. This is the reason why the VCE determined regularization parameters are smaller than the ones derived from the empirical method.

The original and reduced point mass basis functions in 2SPM_FD give similar gravity solutions in our test cases. One possible reason is that the modeled gravity field quantities are gravity anomalies which are not very sensitive to

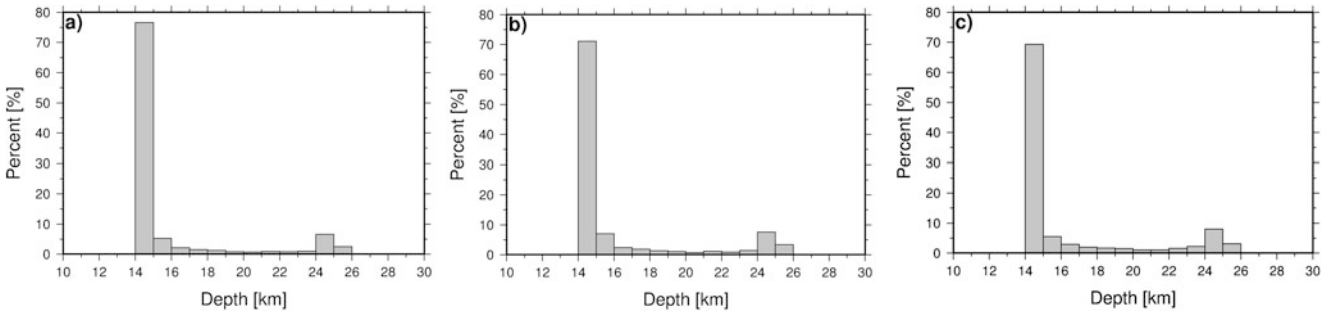

Fig. 4 Histograms of the depths for the searched point masses in the test cases (**a**) with data set (a), (**b**) with data set (b) and (**c**) with data set (c)

Table 1 Parameter sets used in the numerical test cases

Type of basis functions	Original Reduced, $n_{\min} = 101$
Optimization direction	Radial direction
Initial depth [km]	15.5
Depth limits [km]	14–25
Number of nearest point masses	10
Number of point masses	3,000
Iterations for each added point mass	20

Table 2 Regularization parameters in 2SPM_FD obtained by three methods associated with the original and reduced point mass basis functions for test cases (b) and (c)

	Test Case (b)		Test Case (c)	
Method	Original	Reduced	Original	Reduced
Empirical	3.981×10^{-13}	3.981×10^{-13}	2.512×10^{-12}	2.512×10^{-12}
GCV	1.000×10^{-14}	1.000×10^{-14}	1.000×10^{-13}	1.000×10^{-13}
VCE	2.261×10^{-13}	2.267×10^{-13}	1.311×10^{-12}	1.307×10^{-12}

Table 3 Statistics of modeled gravity anomaly errors (mGal) at 11305 control points for test case (a). The first and second rows of 2SPM_FD correspond to the solutions associated with the original and reduced point mass basis functions

Method	Mean	STD	RMS	Min	Max
No regularization	−0.051	1.154	1.155	−5.396	5.472
	0.004	1.164	1.164	−5.382	5.525
Standard LSC	−0.498	0.869	1.019	−4.352	2.917

Table 4 The same as in Table 3, but for test case (b)

Method	Mean	STD	RMS	Min	Max
No regularization	−0.025	2.738	2.738	−18.649	12.760
	0.006	2.740	2.740	−19.070	12.738
Empirical	−0.027	2.481	2.481	−13.921	11.826
	0.009	2.480	2.480	−13.948	11.591
GCV	−0.039	2.675	2.675	−13.759	11.874
	0.006	2.674	2.674	−13.587	11.780
VCE	−0.031	2.492	2.492	−13.325	12.101
	0.008	2.491	2.491	−13.350	11.820
Standard LSC	−0.197	5.074	5.078	−22.375	19.196
Regularized LSC	−0.055	2.420	2.421	−10.343	9.936

Table 5 The same as in Tables 3 and 4, but for test case (c)

Method	Mean	STD	RMS	Min	Max
No regularization	−0.028	5.839	5.839	−34.933	32.801
	0.012	5.840	5.840	−34.955	32.949
Empirical	−0.012	3.909	3.908	−16.886	22.329
	0.019	3.911	3.911	−16.721	22.393
GCV	−0.033	5.022	5.022	−21.940	24.289
	0.013	5.024	5.024	−21.974	24.247
VCE	−0.017	3.986	3.986	−16.395	19.138
	0.017	3.989	3.989	−16.205	19.238
Standard LSC	−0.047	5.568	5.568	−21.451	22.113
Regularized LSC	−0.005	3.596	3.596	−16.902	18.750

the long-wavelength contributions. In principle, the reduced basis functions are recommended when the RCR technique is applied.

4 Summary and Conclusions

The performance of the proposed two-step point mass method with free depths together with the RCR technique has been demonstrated by three numerical test cases for gravity anomaly recovery from simulated geoid heights with different noise levels. If the parameter sets are chosen appropriately and the input data are error-free, the solutions can be achieved close to the LSC solutions. The implementation of Tikhonov regularization in the second step of 2SPM_FD guarantees stable solutions if ill-posedness exists. By comparing three methods for choosing proper regularization parameters in our test cases, the empirical method proves to be the best, then VCE follows. Often, the empirical method is hard to be applied in practical applications with a large amount of input data or in the absence of control points. Then

VCE is an alternative method. Furthermore, it also provides the variance components of the input data which can be interpreted as the posterior errors of the data.

Although GCV gives the worst regularization parameters in our test cases, it does not mean it can not provide better parameters in other applications. The solutions of the standard LSC are found to suffer from the data noise. Therefore, a regularization parameter $\alpha > 1$ is required to further reduce the effects of the data noise in the solutions, resulting in the best results for test cases (b) and (c). The regularized LSC can be a complement to the standard LSC.

Acknowledgements Three anonymous reviewers are acknowledged for their valuable comments which improved the original manuscript. The first author is financially supported by China Scholarship Council (CSC) for his PhD study in Germany.

References

Ameti P (2006) Downward continuation of Geopotential in Switzerland. PhD Thesis, TU Darmstadt, Darmstadt, Germany

Antunes C, Pail R, Catalão J (2003) Point mass method applied to the regional gravimetric determination of the geoid. Stud Geophys Geod 47:495–509

Barthelmes F (1986) Untersuchungen zur approximation des äußeren Schwerefeldes der Erde durch Punktmassen mit optimierten Positionen. Report Nr. 92, Veröffentlichungen des Zentralinstitut Physik der Erde, Potsdam, Germany

Bentel K, Schmidt M, Gerlach C (2013) Different radial basis functions and their applicability for regional gravity field representation on the sphere. GEM Int J Geomath 4:67–96

Bjerhammar A (1986) Megatrend solutions in physical geodesy. NOAA Technical Report No. 116 NGS 34, National Oceanic and Atmospheric Administration, USA

Bouman J (1998) Quality of regularization method. DEOS Report Nr. 98.2, Delft Institute for Earth-Orient Space Research, Delft University of Technology, Delft, Netherlands

Bowin C (1983) Depth of principal mass anomalies contributing to the earth's geoidal undulations and gravity anonalies. Mar Geod 7:61–100

Byrd RH, Lu P, Nocedal J, Zhu C (1995) A limited memory algorithm for bound constrained optimization. SIAM J Sci Comput 16:1190–1208

Claessens SJ, Featherstone WE, Barthelmes F (2001) Experiences with point-mass gravity field modeling in the Perth Region, Western Australia. Geomet Res Aust 75:53–86

Eicker A (2008) Gravity field refinement by radial basis functions from in-situ satellite data. PhD Thesis, University of Bonn, Bonn, Germany

Klees R, Tenzer R, Prutkin I, Wittwer T (2008) A data-driven approach to local gravity field modeling using spherical radial basis functions. J Geod 82:457–471

Koch K-R, Kusche J (2002) Regularization of geopotential determination from satellite data by variance components. J Geod 76:259–268

Kusche J, Klees R (2002) Regularization of gravity field estimation from satellite gravity gradients. J Geod 76:359–368

Lehmann R (1993) The method of free-positioned point masses-geoid studies on the Gulf of Bothnia. Bull Géod 67:31–40

Lin M, Denker H, Müller J (2014) Regional gravity field modeling using free-positioned point masses. Stud Geophys Geod. doi:10.1007/s11200-013-1145-7

Marchenko AN, Tartachynska ZR (2003) Gravity anomalies in the Black sea area derived from the inversion of GEOSAT, TOPEX/POSEIDON and ERS-2 altimetry. Bull Geod Sci Affini LXII:50–62

Marchenko AN, Barthelmes F, Mayer U, Schwintzer P (2001) Regional geoid determination: an application to airborne gravity data in the Skagerrak. Scientific Technical Report No. 01/07, GFZ, Potsdam, Germany

Mayer-Gürr T, Rieser D, Höck E, Brockmann JM, Schuh W, Krasbutter I, Kusche J, Maier A, Krauss S, Hausleitner W, Baur O, Jäggi A, Meyer U, Prange L, Pail R, Fecher T, Gruber T (2012) The new combined satellite only model GOCO03s. International Symposium on Gravity, Geoid and Height Systems, Venice, Italy, October 9–12 (oral presentation)

Moritz H (1980) Advanced physical geodesy. Herbert Wichman, Karlsruhe

Nocedal J, Wright SJ (1999) Numerical optimization. Springer, New York

Pavlis NK, Holmes SA, Kenyon SC, Factor JK (2012) The development and evaluation of the earth gravitational model 2008 (EGM2008). J Geophys Res 117:B04406. doi:10.1029/2011JB008916

Schmidt M, Fengler M, Mayer-Guerr T, Eicker A, Kusche J, Sanchez L, Han S (2007) Regional gravity field modeling in terms of spherical base functions. J Geod 81:17–38

Tenzer R, Klees R (2008) The choice of the spherical radial basis functions in local gravity field modeling. Stud Geophys Geod 52:287–304

Tikhonov AN (1963) Solution of incorrectly formulated problems and the regularization method. Soviet Math Dokl 4:1035–1038

Tscherning CC, Rapp RH (1974) Closed covariance expressions for gravity anomalies, geoid undulations and deflections of the vertical implied by anomaly degree variance models. OSU Report 208, Department of Geodetic Science and Surveying, Ohio State University, Columbus, Ohio, USA

Zhu C, Byrd RH, Lu P, Nocedal J (1994) LBFGS-B: fortran subroutines for large-scale bound constrained optimization. Report NAM-11, EECS Department, Northwestern University, Evanston, IL, USA

Covariance Analysis and Sensitivity Studies for GRACE Assimilation into WGHM

Maike Schumacher, Annette Eicker, Jürgen Kusche, Hannes Müller Schmied, and Petra Döll

Abstract

An ensemble Kalman filter approach for improving the WaterGAP Global Hydrology Model (WGHM) has been developed, which assimilates Gravity Recovery And Climate Experiment (GRACE) data and calibrates the model parameters, simultaneously. The method uses the model-derived states and satellite measurements and their error information to determine updated water storage states. However, due to the fact that hydrological models do not provide any error information, an empirical covariance matrix needs to be calculated. In this paper, therefore, we analyse the combined state and parameter covariance matrix of WGHM. We found that high correlations of up to 0.75 exist between calibration parameters and storage compartments, and that these allow for an efficient calibration. In addition, a sensitivity analysis is performed to identify those parameters that the water compartments are most sensitive to. The performed analysis is important, since GRACE cannot observe the model parameters directly. We found that those parameters, which the water storage is most sensitive to, differ not only regionally, but also with respect to the water compartments. Not unexpected, some climate input multipliers implemented in our model version have an overall strong influence. We also found that the degree of sensitivity changes temporally, e.g. between 0 (in summer) and 0.5 (in winter) for the snow storage.

Keywords

Assimilation • Calibration • GRACE • Sensitivity • WGHM

1 Introduction

The global water cycle is one of the most important processes that ensure life on Earth. Modelling of continental hydrology contributes to its understanding and quantification. A global representation of the terrestrial water cycle is, e.g. provided by the WaterGAP Global Hydrology Model (WGHM), which models the vertical and horizontal water fluxes on a 0.5° grid over the land area. A detailed description of the model can be found e.g. in Döll et al. (2003) and Müller Schmied et al. (2014). However, the degree of a successful representation of the reality is limited due to the simplified representation of hydrological processes and due to the uncertainties of input data, e.g. empirical model parameters, climate forcing and water use data. On the other hand, the Gravity Recovery And Climate Experiment (GRACE) satellite mission (Tapley et al. 2004) observes the Earth's time variable gravity field and methods have been developed that allow one to separate the column-integrated sum of the terrestrial water storage from the total mass signal. Therefore, these measurements can be used to improve hydrological models by calibrating their parameters or adjusting their states to the observations.

M. Schumacher (✉) • A. Eicker • J. Kusche
Astronomical, Physical and Mathematical Geodesy Group, University of Bonn, Nussallee 17, 53115 Bonn, Germany
e-mail: schumacher@geod.uni-bonn.de

H. Müller Schmied • P. Döll
Institute of Physical Geography, University of Frankfurt/Main, Altenhöferallee 1, 60438 Frankfurt am Main, Germany

© Springer International Publishing Switzerland 2015

C. Rizos, P. Willis (eds.), *IAG 150 Years*, International Association of Geodesy Symposia 143,
DOI 10.1007/1345_2015_119

Two main approaches exist so far for the improvement of a hydrological model by using GRACE measurements. Werth and Günthner (2009) used filtered basin means of GRACE total water storage (TWS) changes to improve WGHM. Their aim was the calibration of the model parameters. Zaitchik et al. (2008) used the same kind of observations to improve NASA's catchment land surface model (CLSM) by assimilating GRACE data into it. To this end, they used an ensemble Kalman smoother method.

An ensemble Kalman filter (EnKF) that simultaneously calibrates the parameters of WGHM and assimilates GRACE data into it has been proposed in Schumacher (2012). In contrast to the previous studies, the approach presented here uses TWS changes from GRACE defined on a grid for the calibration and assimilation. Furthermore, the full spatio-temporal GRACE TWS changes error information was considered in the method. For implementing a Kalman filter approach, an empirical model covariance matrix of WGHM has to be determined. This is due to the fact that hydrological models do not provide error information by default. A detailed description of the method is given by Eicker et al. (2014) in which investigations on the Kalman filter gain matrix are presented.

In this paper, we focus on the analysis of the combined model parameter-state covariance matrix to identify those parameters that the water compartments are most sensitive to. The results are presented with respect to the Mississippi River Basin. In addition, a detailed sensitivity analysis was performed with the aim (a) to assess the results of the local model covariance matrix and (b) to identify those parameters with the highest model sensitivity for the 33 largest river basins in the world. These results are compared to those in Werth and Günthner (2009). Additionally, we carried out investigations on the water compartments and on the evolution of sensitivity over time.

2 Data

2.1 WGHM

Within the EnKF approach, the modeled water storages of canopy, snow, soil, river, surface water bodies and groundwater from the current WaterGAP version 2.2 (Müller Schmied et al. 2014) are integrated with the observed TWS changes from GRACE. To determine improved water storage values, the error information of model and measurements are weighted against each other (Schumacher 2012). Since WGHM does not provide error information, an empirical model covariance matrix has to be determined. Here, the influence of the empirical model input parameters on the modeled water storages is considered. Some of these parameters describe physio-geographic characteristics, e.g. the lake depth. Other parameters are conceptual, such as the groundwater outflow coefficient. Whereas it is common that only one parameter associated with the soil compartment (runoff coefficient γ) is used for calibration to fit mean annual discharge to observed one (Döll et al. 2003), Werth and Günthner (2009) used the six to eight most sensitive ones per river basin. Those calibration parameters, which are considered in our EnKF approach, are listed in Table 1.

Table 1 Calibration parameters of WGHM with identification number (IN) and original value

IN	Calibration parameter	Value
1*	Root depth multiplier	1
2*	River roughness coefficient multiplier	1
3	Lake depth	5 m
4	Wetland depth	2 m
5	Surface water outflow coefficient	0.01/day
6*	Net radiation multiplier	1
7	Priestley-Taylor coefficient (humid)	1.26
8	Priestley-Taylor coefficient (arid)	1.74
9	Max. daily potential evapotranspiration	15 mm/day
10	Max. canopy water height per leaf area	0.3 mm
11*	Specific leaf area multiplier	1
12	Snow freeze temperature	0°C
13	Snow melt temperature	0°C
14*	Degree day factor multiplier	1
15	Temperature gradient	0.006°C/m
16*	Groundwater factor multiplier	1
17*	Max. groundwater recharge multiplier	1
18	Critical precipitation for groundwater recharge	10 mm/day
19	Groundwater outflow coefficient	0.01/day
20*	Net abstraction surface water multiplier	1
21*	Net abstraction groundwater multiplier	1
22*	Precipitation multiplier	1

Parameters, marked with (*), are not integrated in the original WaterGAP 2.2 version, but are extra parameters within the adapted version used here

2.2 GRACE TWS Changes

For the calibration and assimilation approach the ITG-GRACE2010 monthly GRACE solutions were used for which the full error information is available (http://www.igg.uni-bonn.de/apmg/index.php?id=itg-grace2010). 0.5°× 0.5° TWS grids are derived following Wahr et al. (1998). The full monthly covariances of potential coefficients were propagated to TWS. A suitable filter technique and an approach to account for leakage effects due to filtering are under investigations and will be reported in future work. However, these choices do not affect the results presented here.

3 Method

3.1 Empirical Model Covariance Matrix

To estimate a combined empirical covariance matrix of the states and parameters, first of all, a priori probability density functions (PDF) have been chosen based on literature (Kaspar 2004) and our own experience of more than 10 years of model development for the model parameters. One of the parameters was assumed to be uniformly distributed, the others were assumed to have a triangular distribution, which can be symmetric or asymmetric. An ensemble of $N = 60$ calibration parameter sets was generated by using a Monte Carlo approach taking into consideration the above mentioned PDFs. For each ensemble member, the model was run globally from 2002 to 2009 for which ITG-GRACE2010 solutions are also available. Identical start values of the cell water storage compartments were used for each run. Time series of monthly averaged water storage states corresponding to each grid cell were obtained as model output for each ensemble member. The monthly regional empirical covariance matrix $\mathbf{C}_e$ for one specific river basin was calculated by using the parameter $\mathbf{p}$ and model state $\mathbf{s}$ ensembles (e.g., Evensen 2009)

$$\mathbf{C}_e = \frac{1}{N-1}\mathbf{X}'(\mathbf{X}')^T. \tag{1}$$

The mean reduced model prediction matrix $\mathbf{X}'$ contains the storage in all compartments for each grid cell in the specific basin and the calibration parameter values for each of the ensemble members in its columns. The covariance matrix consists of three blocks

$$\mathbf{C}_e = \begin{bmatrix} \mathbf{C}_e(\mathbf{s}^-, \mathbf{s}^-) & \mathbf{C}_e(\mathbf{s}^-, \mathbf{p}^-) \\ \mathbf{C}_e(\mathbf{p}^-, \mathbf{s}^-) & \mathbf{C}_e(\mathbf{p}^-, \mathbf{p}^-) \end{bmatrix}. \tag{2}$$

The first block $\mathbf{C}_e(\mathbf{s}^-, \mathbf{s}^-)$ contains the error information with respect to the predicted model states, the second block $\mathbf{C}_e(\mathbf{p}^-, \mathbf{p}^-)$ is related to the parameters. The last block $\mathbf{C}_e(\mathbf{s}^-, \mathbf{p}^-)$ contains the relation between the model states and parameters. To determine those parameters, which the model compartments are most sensitive to, the correlations between each parameter and the basin averaged water compartments were calculated. Since GRACE does not observe the parameters directly, the correlations justify whether the observations will contribute in calibrating the model parameters.

3.2 Sensitivity Analysis

Another possibility to identify those conceptual parameters that relate to large model sensitivities can be derived by performing a sensitivity analysis (e.g., Hamby 1994). Here, the sensitivity index (SI), which is a simple approach, and the Spearman's rank correlation coefficient (SRCC), which was used in Güntner et al. (2007), are chosen as a measure of sensitivity. To determine the SI, first realisations of a single model parameter are generated while considering the others as constant. The SI measures the influence of one single input parameter on the model output. Therefore, the interpretation of the SI is straight forward: It corresponds to a model covariance matrix for which only one calibration parameter set is introduced while the others are constant (not shown here). Note that in contrast, ensembles of all model parameters were generated simultaneously when using the SRCC for assessment of sensitivity. Here, the correlations of the model parameters are considered. This corresponds to the information in the empirical model covariance matrix, which is calculated after running the model with an ensemble of all input parameters (Sect. 1).

3.2.1 Sensitivity Index

The SI is a measure that reflects the relative difference between the minimum and maximum model outputs $S_{\min}$ and $S_{\max}$ when generating an ensemble of one model input parameter with the others being constant (Hoffman and Gardner 1983). SI is calculated by scaling the difference between the minimum and maximum water storage output within the ensemble as

$$SI = \frac{S_{\max} - S_{\min}}{S_{\max}}. \tag{3}$$

Although SI is a simple approach to identify parameters, which the water compartments are most sensitive to, its disadvantage is that it does not take the correlations between parameters into account.

3.2.2 Spearman's Rank Correlation Coefficient

Unlike SI, the SRCC also considers the correlations between the calibration parameters. Further, it allows one to account for nonlinear model equations by performing a rank transformation of the parameters and states (Iman and Conover 1979). To apply this approach, sets of all parameters were generated by using their given PDFs simultaneously. The calibration parameter values and model output are sorted in ascending order by their values leading to their ranks. Finally, the Pearson's correlation coefficient is determined with the exception that the ranks of the i-th parameter R_{P_i} and the water states R_S are used instead of their values (Hamby 1994)

$$\rho_i = \frac{\sum_{n=1}^{N}(R_{P_{in}} - \overline{R_{P_i}})(R_{S_n} - \overline{R_S})}{\sqrt{\sum_{n=1}^{N}(R_{P_{in}} - \overline{R_{P_i}})^2 \sum_{n=1}^{N}(R_{S_n} - \overline{R_S})^2}}. \tag{4}$$

The results of the sensitivity analyses can be used to verify the parameter-state correlations, which are empirically determined as entries of the model covariance matrix.

4 Results and Discussion

The analysis of the model covariance matrix and the sensitivity analysis has been performed for all water compartments in the Mississippi River Basin. The results are shown for the snow and soil compartment to provide an example.

4.1 Correlations Between Model States and Parameters

The correlations between the 22 calibration parameters and the snow water storage for each grid cell in the Mississippi River Basin were determined for the winter (Fig. 1a) and the summer season (Fig. 1b). During winter, a high positive correlation was identified with two of the parameters and in most of the cells. Negative correlations were identified between a few parameters and some of the cells. During summer, nearly no correlations were found, since there is usually no snow in the Mississippi Basin. To identify those parameters, which the water compartments are most sensitive to, the empirical covariance matrices were calculated for each month of 2008 considered as the start of the integration of GRACE data. Then a basin mean of the water compartments was determined. The time evolution of the correlations between the parameters and the averaged snow and soil compartment are shown in Fig. 2. Between the snow compartment and the snow melt temperature, precipitation multiplier, and groundwater factor multiplier, high correlations exist during winter (Fig. 2a). The precipitation multiplier represents a calibration factor applied to the observed daily precipitation values. Scaled precipitation, which was stored as snow, melts when the actual temperature is higher than the snow melt temperature. The groundwater factor multiplier represents a scaling factor for the calculated groundwater recharge. Between the soil compartment and the root depth multiplier, a calibration factor for the average root depth of plants, and two parameters to determine the potential evapotranspiration, high correlations were found all over the year (Fig. 2b). In the original model version all multipliers are one, i.e. the factors are now introduced for model calibration. Note that regarding Fig. 2a, one observes almost no ensemble spread over the months 4–10, since there is usually no snow in the Basin (see Fig. 1b). This means that these parameters can only be updated during winter. In contrast, the parameters with respect to the soil compartment can be calibrated during all seasons. This indicates nicely that the influence of GRACE differs in each month, since the degree of sensitivity changes over time. In addition, these results suggest that the parameters have to be calibrated at least for a full year, since the determination of e.g., an updated snow melt or freeze temperature during summer is not possible.

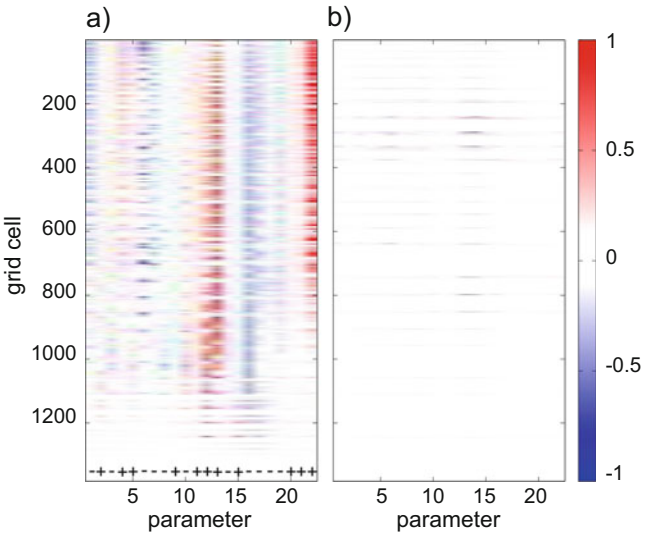

Fig. 1 Correlations between the 22 model parameters and the snow storage in each cell of the Mississippi River Basin for the (**a**) winter and (**b**) summer season. See Table 1 for parameter names. In (**a**) the *plus* and *minus signs* indicate whether the correlation is positive or negative

4.2 Regional Sensitivity Analysis

By using the SI, the high correlation between the snow storage and the snow melt temperature, and precipitation multiplier respectively was confirmed (Fig. 2c). We found, however, that the groundwater factor multiplier has no impact on the snow storage when measured by the SI. The magnitude of the correlations, when evaluating the model covariance matrix or the SI, is different: e.g. the maximum correlation value concerning the snow melt temperature is 0.5 (Fig. 2a) or 0.8 (Fig. 2c) respectively. This is mainly due to the fact that in case of the first method sets of all parameters were generated, while only a set of one parameter is generated in case of the SI. However, the interpretation of both approaches is the same: The snow melt temperature is the most important parameter with respect to the snow compartment. In summer, it is not possible to update parameters that are directly associated with the snow storage, since no correlations exist. For the soil compartment, the parameters, which were identified by analysing the covariance matrix, were also confirmed by evaluating the SI (Fig. 2d).

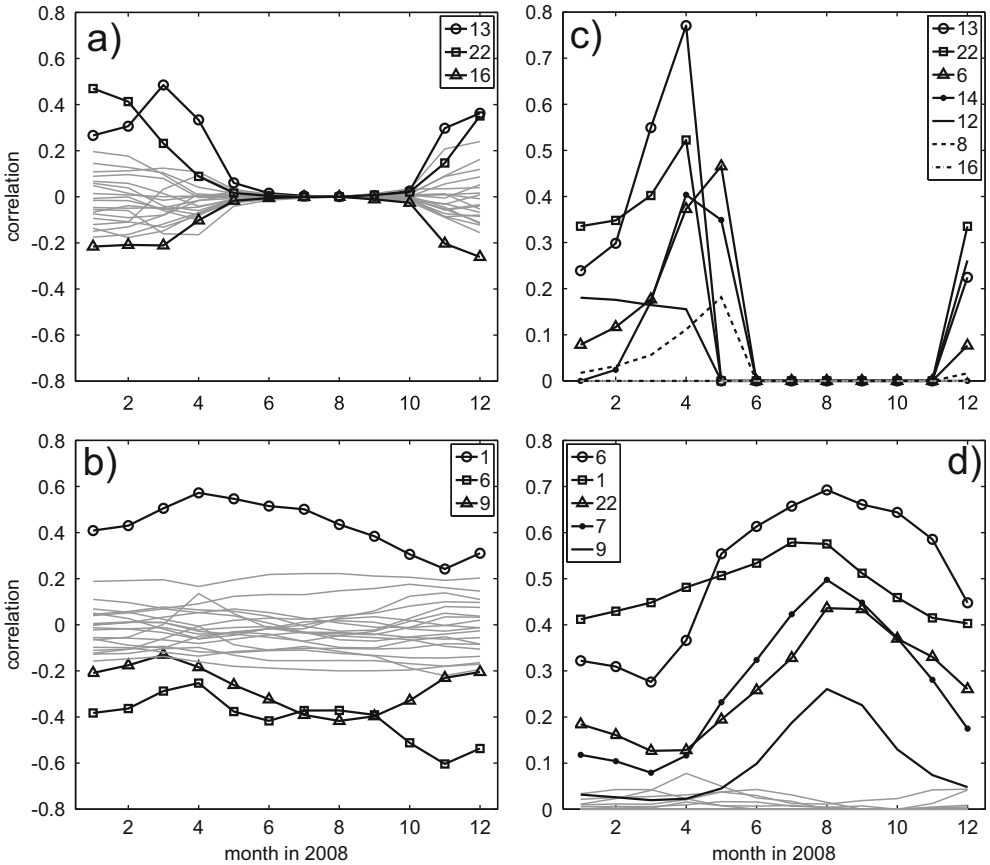

Fig. 2 Time evolution of the correlations between the 22 model parameters and the basin mean of the (**a**, **c**) snow and (**b**, **d**) soil compartment evaluating the empirical model covariance matrix (**a**, **b**) and using the sensitivity index (**c**, **d**). The parameters, which have the highest correlations regarding the averaged compartment states, are listed in the legend. The *gray lines* belong to the other parameters. See Table 1 for parameter names

Considering the SRCC, all parameters with high correlations for the snow and soil compartment were confirmed (not shown here). This includes even the groundwater factor multiplier for the snow. It appears this correlation is introduced through joint dependence on the other perturbed parameters, and thus invisible for the SI.

In the developed EnKF approach, the empirical model covariance matrix, which is computed by first generating an ensemble of all model input parameters, is used in order to determine the updated model states and calibration parameters. This allows the consideration of the parameter, state, and parameter-state correlations in the assimilation and calibration procedure.

4.3 Global Sensitivity Analysis

In addition to the regional analysis, we also performed a global sensitivity analysis to identify the parameters with the highest model sensitivity for the 33 largest river basins in the world. Here, the SRCC was calculated between the calibration parameters and the mean TWS. Different parameters, which the modeled TWS output is most sensitive to, were found for the basins (Figs. 3 and 4). For example, the TWS in the Mississippi River Basin reacts the most sensitive to the net radiation multiplier, as in numerous of the basins. It seems that this calibration parameter has, along with the river roughness coefficient and precipitation multiplier, an overall strong influence. To make the results comparable to the studies of Güntner et al. (2007) and Werth and Günthner (2009), the SRCC was also determined between the calibration parameters and the mean annual amplitude of TWS as a measure for sensitivity (not shown here). Our results confirm some of those parameters with large model sensitivity in the world's largest river basins that were found in these studies, e.g. the root depth multiplier and snow melt temperature regarding the Mississippi River Basin. In contrast to these studies, in which neither a net radiation nor a precipitation multiplier were introduced, a strong dependence of the TWS on the climate input was found here.

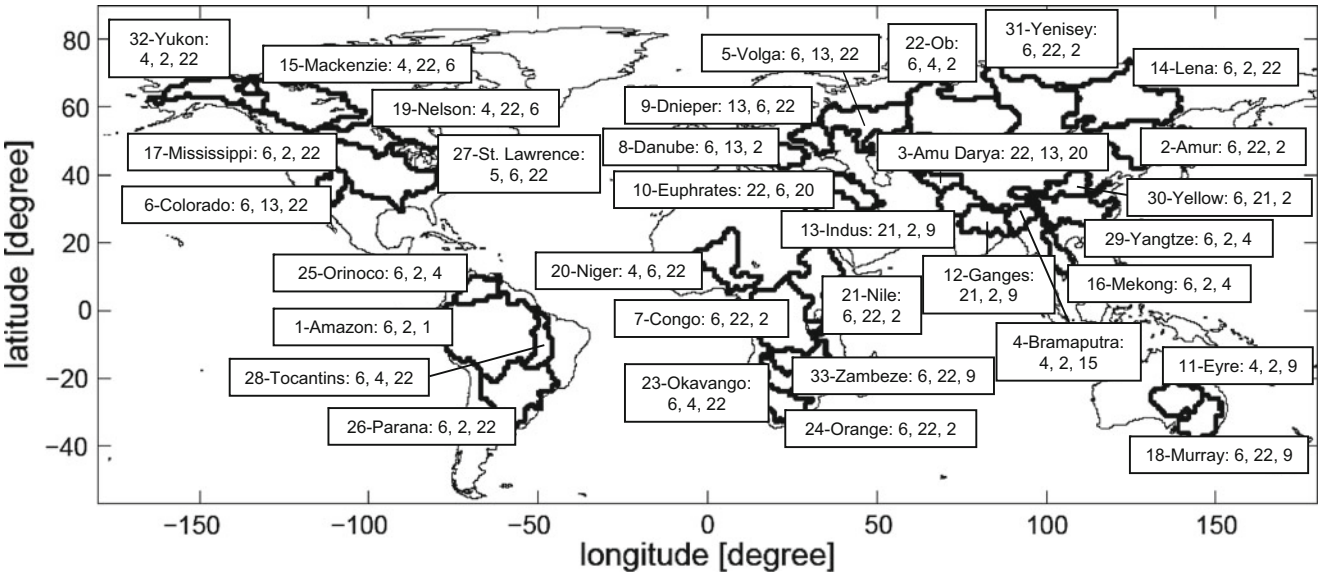

Fig. 3 The three parameters, which the monthly mean TWS output of WGHM is most sensitive to, in the 33 largest river basins of the world. See Table 1 for parameter names. The in the adapted model version introduced river roughness coefficient (2), net radiation (6) and precipitation (22) multipliers have, overall, a strong influence

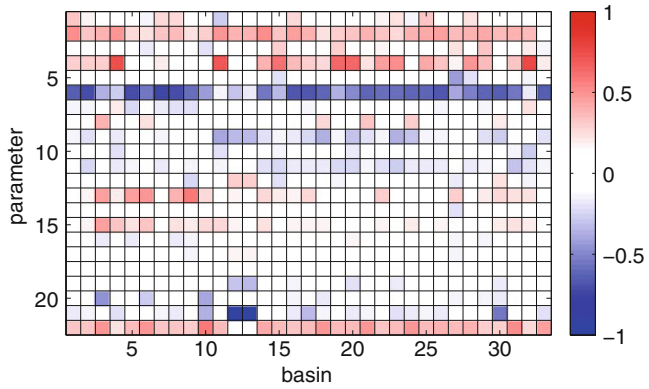

Fig. 4 Spearman's rank correlation coefficient between the calibration parameters and the mean TWS in the 33 largest river basins of the world. See Table 1 for parameter and Fig. 3 for basin names. The correlation between the mean TWS and the humid (7) and arid (8) Priestley-Taylor coefficient is shown for humid and arid regions, respectively

5 Conclusions and Outlook

The analysis of the combined model covariance matrix, as well as the performed sensitivity analysis, indicates that the correlations between the model states and parameters enable the parameter calibration by GRACE measurements. Moreover, these investigations could confirm some parameters which were identified to be most sensitive in previous studies (Güntner et al. 2007; Werth and Günthner 2009). Based on the global sensitivity analysis, a basin-wise parameter calibration seems appropriate. By performing the regional analysis, we found that the compartments are sensitive to different model parameters. The time evolution of the parameter-state correlations indicates that the impact of GRACE changes over time. We plan to validate our calibration results by performing a calibration run for 1 year. Afterwards, the model will run for the following year, both with the standard model parameters and the calibrated values. The model states of both versions will then be compared to the GRACE observations. One can also consider independent data sets, e.g. discharge measurements, for validation. Along with the parameter uncertainties, the uncertainties of climate forcing and water use data will be included to obtain a more realistic representation of the model covariance matrix. Model improvement may also be affected by errors of the background models for other Earth system components that are used for separating TWS from the total mass signal observed by GRACE (see e.g., Forootan et al. 2014). Investigations regarding these errors will be conducted in further work.

Acknowledgements The support of the German Research Foundation (DFG) within the framework of the Special Priority Program "Mass transport and mass distribution in the system Earth" (SPP1257) under the project REGHYDRO is gratefully acknowledged.

References

Döll P, Kaspar F, Lehner B (2003) A global hydrological model for deriving water availability indicators: model tuning and validation. J Hydrol 207:105–134

Eicker A, Schumacher M, Kusche J, Döll P, Müller Schmied H (2014) Calibration/Data Assimilation Approach for Integrating GRACE Data into the WaterGAP Global Hydrology Model (WGHM) Using an Ensemble Kalman Filter: First Results. Surve Geophys 35(6):1285–1309

Evensen G (2009) Data assimilation. The Ensemble Kalman Filter. Springer, Berlin/Heidelberg

Forootan E, Didova O, Schumacher M, Kusche J, Elsaka B (2014) Comparisons of atmospheric mass variations derived from ECMWF reanalysis and operational fields, over 2003 to 2011. J Geod 88(5):503–514

Güntner A, Stuck J, Werth S, Döll P, Verzano K, Merz B (2007) A global analysis of temporal and spatial variations in continental water storage. Water Resour Res 43:W05416

Hamby DM (1994) A review of techniques for parameter sensitivity analysis of environmental models. Environ Monit Assess 32:135–154

Hoffman FO, Gardner RH (1983) Evaluation of uncertainties in environmental radiological assessment models. In: Till JE, Meyer HR (eds) Radiological assessment: a textbook on environmental dose assessment. U.S. Nuclear Regulatory Commission, Washington, DC. Report No. NUREG/CR-3332

Iman RL, Conover WJ (1979) The use of the rank transform in regression. Technometrics 21:499–509

Kaspar F (2004) Entwicklung und Unsicherheitsanalyse eines globalen hydrologischen Modells (in German). Dissertation, University of Kassel

Müller Schmied H, Eisner S, Franz D, Wattenbach M, Portmann FT, Flörke M, Döll P (2014) Sensitivity of simulated global-scale freshwater fluxes and storages to input data, hydrological model structure, human water use and calibration. Hydrol Earth Syst Sci 18:3511–3538

Schumacher M (2012) Assimilation of GRACE data into a global hydrological model using an ensemble Kalman filter. Master Thesis, University of Bonn

Tapley BD, Bettadpur S, Watkins M, Reigber C (2004) The gravity recovery and climate experiment: mission overview and early results. Geophys Res Lett 31:L09607

Wahr JM, Molenaar M, Bryan F (1998) Time variability of the Earth's gravity field: hydrological and oceanic effects and their possible detection using GRACE. J Geophys Res 108(B12):30205–30229

Werth S, Güntner A (2009) Calibration analysis for water storage variability of the global hydrological model WGHM. Hydrol Earth Syst Sci 14:59–78

Zaitchik BF, Rodell M, Reichle RH (2008) Assimilation of GRACE terrestrial water storage data into a land surface model: results for the mississippi river basin. J Hydrometeorol 9(3):535–548

Accuracy Estimation of the IfE Gravimeters Micro-g LaCoste gPhone-98 and ZLS Burris Gravity Meter B-64

Manuel Schilling and Olga Gitlein

Abstract

Presently, modern spring gravimeters are the most flexible, technically simple, and comparatively cheap solution for recordings over extended time periods in contrast to superconducting gravimeters. We investigate the accuracy of the state-of-the-art spring gravimeters Micro-g LaCoste gPhone-98 and ZLS Burris Gravity Meter B-64 of the Institut für Erdmessung (IfE). With both instruments gravity was recorded for periods of several months at five stations with high and low microseismic noise. Simultaneous measurements with both instruments as well as the parallel recording of the ZLS Burris gravimeter with the GWR Instruments Observatory Superconducting Gravimeter OSG-054 in Onsala (Sweden) are investigated. Tidal analysis is used to assess the quality of the time series. Diurnal and semi-diurnal amplitude factors agree at the level of 1‰ and better from recordings of Burris and OSG gravimeters in Onsala.

In addition to gravity recordings a number of calibration experiments were carried out to test the long-term stability of the meters. The linear calibration factor of both gravimeters is stable to 3×10^{-4}. The drift of the gPhone-98 decreased over time and is currently reduced with a linear factor of $\approx$90 nm/s^2 per day. The instrumental drift of Burris B-64 on the other hand can currently not be reduced with a linear factor.

Keywords

gPhone • Instrumental accuracy • Relative gravimetry • Tidal analysis • ZLS Burris

1 Introduction

Modern spring-based gravimeters are a versatile tool in gravimetry. The possible applications include Earth tide recordings, monitoring of geophysical phenomena, and microgravimetric measurements supporting absolute gravimetry. Especially when recording gravity these instruments are limited by the continuous variation of spring tension, which causes a drift effect. Gravity changes due to Earth tides can reach more than 2,000 nm/s^2. Other changes of gravity are orders of magnitude smaller, e.g. changes in the groundwater can be in the order of a few to some 10 nm/s^2 over a few days to weeks. These small signals might not be revealed due to instrumental drift. Therefore, it is necessary that the instrumental drift is easy to model, preferably linear, and stable over time. All metal alloy- or quarz-spring based gravimeters are affected by instrumental drift, independent of their respective design. For example Timmen and Gitlein (2004) reported a drift of $\approx$2.7 µm/s^2 per day for the Scintrex CG3-4492, which uses a vertical quartz spring.

This work focuses on two instruments employed by the IfE. The gPhone-98 is in use for 2 years and the Burris B-64 for 1 year by now. The gPhone has been in use almost continuously at different stations. We present Earth tide recordings made at four stations which have been made in preparation of a future geophysical project and to examine

M. Schilling (✉) • O. Gitlein
Institut für Erdmessung, Leibniz Universität Hannover, Schneiderberg 50, 30167 Hannover, Germany
e-mail: schilling@ife.uni-hannover.de

© Springer International Publishing Switzerland 2015

C. Rizos, P. Willis (eds.), *IAG 150 Years*, International Association of Geodesy Symposia 143,
DOI 10.1007/1345_2015_29

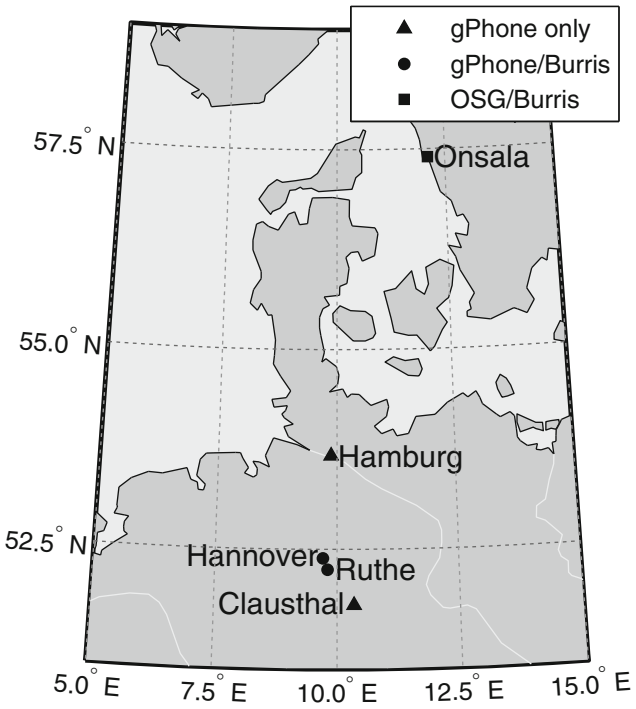

Fig. 1 Stations and co-locations of instruments in Germany and Sweden

the instrument. Other observations were used as a reference in the development of recording atomic gravimeters in Hannover and Berlin. The Burris has been recording Earth tides at three stations.

The stations visited have very different characteristics, e.g. concerning the influence of nearby waterbodies and man made microseisms. The measurements were performed in Onsala, Hamburg, Hannover, Ruthe, and Clausthal (Fig. 1). The stations Hannover (Leibniz Universität Hannover) and Clausthal (Clausthal University of Technology), both with a history of gravity measurements dating back to 1986, are briefly described by Timmen (2010). The gravimetry laboratory in Hannover is located in an university building next to a parking lot, a 20 story building and tram lines near by. The laboratory is equipped with three dedicated pillars for absolute and relative gravimeters. Ruthe is located 20 km south of Hannover in a rural area and has four pillars in a climate controlled container. The station in Hamburg is located in a residential district close to the Elbe river with water level changes of 3–4 m over 12 h due to the direct connection to the North Sea. The measurements were conducted in the basement of an empty building. The aforementioned three stations are located on glacial sediments. Clausthal is located in the Harz mountains and the pillar is directly connected to bedrock. This station is characterized by low natural and man made ground noise. Onsala, Sweden, is located 40 km south of Gothenburg at the Onsala Space Observatory, Chalmers University Gothenburg (Scherneck 2008) close to the Kattegat coast. The measurements were performed in a building equipped with a superconducting gravimeter on a pillar connected to bedrock.

2 Characterization of the Instruments

The gravimeters gPhone-98 and Burris B-64 operate by the same basic principle. Both instruments use the LaCoste & Romberg design for spring based gravimeters and a metal alloy spring. The relationship between LaCoste & Romberg Model D and G instruments and the Burris gravimeter is obvious by its appearance (LaCoste and Romberg 2004; ZLS Corporation 2011), and the gPhone is based on the LaCoste & Romberg Model G gravimeter (Micro-g LaCoste 2008).

The instruments were placed in styrofoam boxes to reduce the effects of room temperature variations at all stations. These variations are likely to affect the tilt of the instruments. In case of the gPhone the electronic levels are recorded along with gravity. Inside the box the daily variation of the temperature is typically below 0.5°C. However, over the duration of several weeks the mean temperature changed slowly by 2°C and more at stations without climate control.

2.1 gPhone

The gPhone is specifically designed for gravity recordings. The sensor offers an electronic feedback range of $\pm 500\,\mu m/s^2$, a resolution of $1\,nm/s^2$, and is housed in a double oven for temperature stabilization (Micro-g LaCoste 2008). Reranging the sensor within its $7\,cm/s^2$ range and clamping is done with the software gMonitor (Version 1.09.10.12) installed on a Laptop, which records data and controls the instrument. The sensor is connected to the electronic box, which houses an uninterruptible power supply and a timing module (rubidium clock). A GPS antenna can be connected to the timing module as well. gMonitor records a variety of instrumental and environmental data in addition to gravity, which include the electronic levels of the sensor, ambient and sensor air pressure and temperature. The data recorded at 1 Hz is unfiltered. gMonitor also records 300 s filtered data, which is not used in this paper.

2.2 Burris

The Burris gravimeter is used for point-wise measurements and the recording of time series. The range of the electronic feedback system is $\pm 250\,\mu m/s^2$. The analog gravity output is filtered with a low pass filter, which adds a 0.6 s phase delay (ZLS Corporation 2011). The range of the instrument

is 7 cm/s^2 and the reranging of the feedback system has to be done manually. The Burris B-64 has a non calibrated micrometer screw for this purpose. Gravity differences exceeding the range of the electronic feedback system have to be divided into smaller differences with the Burris B-64. A calibrated screw has calibration points at a 500 µm/s^2 interval and allows the measurement of gravity differences exceeding 500 µm/s^2 in one step. Jentzsch (2008) reported the precision of the calibration points to be ±150 nm/s^2 for the Burris B-25.

The Burris is controlled with a handheld computer running Palm OS 9 and the UltraGrav software. The handheld computer is connected with Bluetooth or a cable to the gravimeter. UltraGrav is capable of continuous gravity recording with a user defined sample rate and digital filter as well as network measurements. A level correction is calculated and recorded using the electronic levels of the instrument. The measurements in this study were recorded with the software FSUGrav provided by the company Gravity Consult. The software is installed on a standard Laptop connected with Bluetooth to the gravimeter. In addition to gravity readings the software records ambient air pressure with a digital barometer. The electronic levels or a level correction is not recorded by FSUGrav. The time is obtained using either a GPS time receiver or a connection to a NTP server. FSUGrav records gravity and air pressure data in a fixed 10 s interval. The gravity recordings are filtered using a 600 s zero-phase filter, which allows no further adjustments.

2.3 Calibration

The gravimeters are regularly calibrated on the vertical calibration system Hannover (Timmen 2010), which offers, among others, a 160 µm/s^2 gravity difference between the 1st and 17th floor of an university building. The electronic levels of the gravimeters were calibrated and the linear calibration factors were determined prior to all deployments to a different station. The results are listed in Table 1 and the linear term is time stable for both gravimeters at the level of 3×10^{-4}. For a signal with an amplitude of 3,000 nm/s^2 the effect of omitting the differences in the linear calibration factors is below 1 nm/s^2. A quadratic term has been determined for the Burris during some of the calibrations and was found to be below $\pm 0.5 \times 10^{-9}$, which agrees with the measurements of Jentzsch (2008).

Table 1 Linear calibration factors

gPhone-98			Burris B-64		
Date	Linear factor	δ (10^{-3})	Date	Linear factor	δ (10^{-3})
12/2011	1.00240	0.015	04/2012	0.99974	−0.354
04/2012	1.00206	0.366	04/2012	0.99953	−0.138
08/2012	1.00247	−0.122	05/2012	0.99944	−0.059
02/2013	1.00268	−0.259	09/2012	0.99895	0.441
			11/2012	0.99937	0.042
			01/2013	0.99961	−0.222
			02/2013	0.99963	−0.237
			05/2013	0.99946	−0.169
			07/2013	0.99870	0.692
Mean	1.00242±0.00027			0.99939±0.00033	

δ is the difference to the mean linear calibration factor

Table 2 Overview of gravity time series

	Location	Start mm/yy	Days	Drift (nm/s^2/day)	σ (nm/s^2) 1 s
gPhone-98	Hannover	10/11	55	191.2 ± 12.5	730.9
	Hamburg	01/12	84	126.2 ± 4.6	528.2
	Clausthal	05/12	98	117.1 ± 2.6	150.6
	Ruthe	02/13	152	93.9 ± 1.8	446.9
	Location	Start mm/yy	Days	Drift (nm/s^2 /day)	σ (nm/s^2) 10 s
Burris B-64	Onsala	06/12	48	−209.4 ± 61.2	3.1
		07/12	49	−155.4 ± 39.2	4.0
	Hannover	09/12	45	−177.4 ± 15.0	3.7
	Ruthe	03/13	45	43.0 ± 75.9	3.6
		05/13	21	−10.4 ± 44.5	3.7

Drift is estimated by a sequence of linear fitted lines with a length of 7 days. The standard deviation σ is estimated for the numerical differentiated gravity residuals

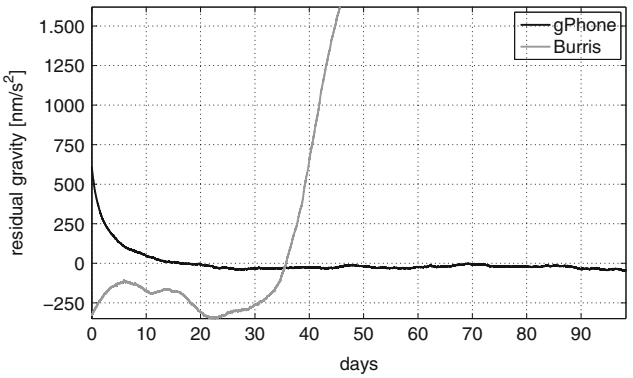

Fig. 2 Example of residual gravity of gPhone-98 (116.8 nm/s^2 per day linear trend removed) and Burris B-64

2.4 Instrumental Drift

The instrumental drift for the different time series is estimated by a piecewise linear approximation of 7 day intervals. The mean linear drift factors are listed in Table 2. After a recording of the gPhone-98 is started the instrument shows a non linear behavior during the first 2–3 weeks, hence the first 2 weeks are excluded from the determination of the drift. An example of gPhone gravity residuals is depicted in the black plot of Fig. 2. However, after this initial run-in phase the drift

seems to be linear. The instrumental drift of gPhone-98 is listed in the upper part of Table 2. During the 2 years, the measurements for this study were recorded, the instrumental drift as well as its variation decreased. Currently, the drift is at ≈90 nm/s^2 per day. Riccardi et al. (2011) reported an instrumental drift at the level of 50 nm/s^2 per day for the gPhone-54 in a 300 day time series. The grey plot in Fig. 2 shows an example of the gravity residuals of a Burris time series. The initial run-in phase lasts a few hours but does not converge into a predictable behavior. The lower part of Table 2 shows that currently neither the drift nor its variation decrease over time when estimated by a piecewise linear approximation.

2.5 Additional Investigations of Burris

The influence of non gravitational air pressure changes on the Burris were tested in a pressure chamber. In a series of tests gravity was recorded while the air pressure was lowered and raised by 70 hPa. This variation can be encountered when measuring a gravity network which covers over 600 m in height. This resulted in a change of the measured gravity by 8–12 nm/s^2. A linear coefficient of ≈0.14 nm/s^2 per hPa has been found for the instrumental air pressure effect. The recordings of the Burris instrument were corrected for this effect. The gPhone was not tested in our pressure chamber due to the size of the instrument. According to the manufacturer the sensor is placed inside two pressure tight chambers. And, as opposed to the Burris, there are no mechanical elements (e. g. a measuring screw) reaching into the sensor chamber (Micro-g LaCoste 2008). The sensor air pressure is recorded and no correlation with ambient air pressure has been found. The sensor pressure of the gPhone-98 decreases with 0.055 hPa/day. This effect would be interpreted as a linear drift component to the overall instrumental drift.

The instrumental phase lag has been determined for the Burris using the step response method described in Richter and Wenzel (1991). The time lag was 3 s on average which results in a phase lag of 0.012° for diurnal and 0.024° for semi diurnal tidal waves. This phase lag is considered in the tidal analysis in Sect. 4.

The Burris has been used along with the Scintrex CG3-4492 (Timmen and Gitlein 2004) in a small scale gravity network consisting of 13 points. Over a period of 3.5 days 160 connections were measured with the Burris and 125 with the CG3 using the step method and hand transport with a maximum of 10 min time for transport. The CG3 achieved a standard deviation 43 nm/s^2 for a single gravity difference and 17 nm/s^2 as the mean standard deviation of the adjusted gravity values. The Burris achieved standard deviations of 23 nm/s^2 and 10 nm/s^2 respectively. This agrees with the results reported by Jiang et al. (2012) using the B-20 and B-25 in the relative gravimeter campaign associated with the ICAG 2009 at the BIPM, Paris.

3 Comparison of Instruments and Stations

The data of both instruments were processed in the same manner. Gravity changes due to Earth tides and polar motion were corrected. If not stated otherwise the synthetic tide model including ocean loading of Timmen and Wenzel (1995) was used. Additionally, time variable gravity changes due to atmospheric masses were reduced using a single admittance factor for each station. For the Burris the instrumental air pressure effect was accounted for by using the factor described in the previous section. Earthquakes, spikes, and steps have been removed using Tsoft (Van Camp and Vauterin 2005). The data was calibrated using the factors listed in Table 1. The level correction was applied for gPhone.

The quality of data depends on the gravimeters and the stations. We compare the data of the instruments and stations using the standard deviation of the numerically differentiated gravity residuals at the sampling rate originally provided by the instrument at 1 or 10 s. Table 2 includes the standard deviations for all stations. Figure 3 shows an example of 3 days uncorrected data of the gPhone and Burris in Hannover. Due to its location the gPhone data in Fig. 3a is dominated by kinematic accelerations caused by natural and man made microseism. In addition, a filtered version is contained in the plot in light grey. For the complete time series the standard deviation of the gravity residuals is 730.9 nm/s^2. The Burris is less affected by the microseismic characteristics of the station. The residuals of the data recorded at a 1 s interval (Fig. 3b) using the handheld computer has a standard deviation of 16.3 nm/s^2. Comparing this dataset with the gPhone data shows the effect of the analog lowpass filter built into the Burris. The gPhone on the other hand does not apply any filtering, which allows the study of high frequency signals. Except for this example the FSUGrav software with a fixed 10 s sampling interval and 600 s digital filter is used (Fig. 3c). The gravity residuals of this time series have a standard deviation of 3.7 nm/s^2. The Burris gravimeter achieves the same standard deviations of ≈4 nm/s^2 for the 10 s data at all stations visited. This is probably due to the filtering performed by the FSUGrav software. The standard deviations of the gPhone data is clearly dependent on the station and its environment as well as seasonal effects allowing further investigations of station characteristics and the study of a variety of higher frequency signals. Comparing all stations within this work, Hannover has the highest influence due to man made microseismic activity. The station with the lowest noise level is Clausthal in the Harz mountains.

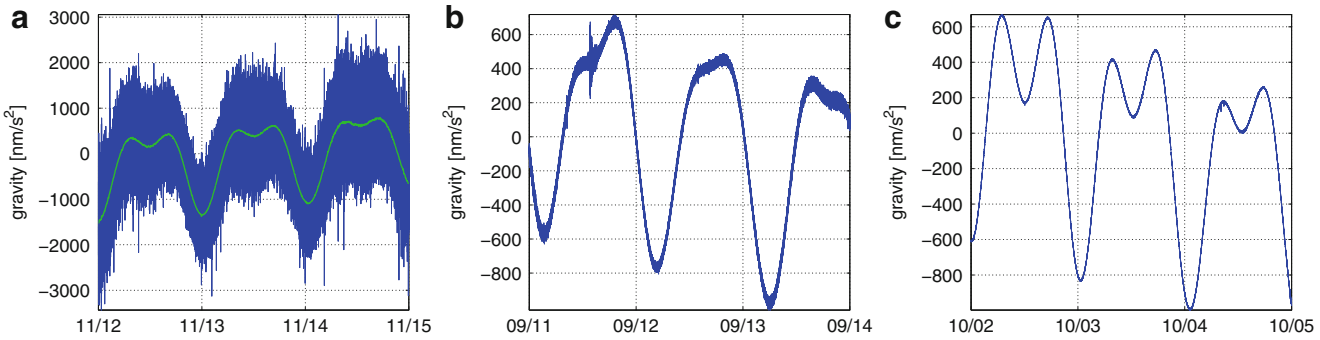

Fig. 3 Examples of raw data from gPhone-98 and Burris B-64 gravimeters for the length of 3 days in Hannover. (**a**) gPhone 1 s raw data (*black*) and 600 s filtered data (*light grey*). (**b**) Burris 1s raw data recorded with handheld computer. (**c**) Burris 10 s raw data recorded with FSUGrav

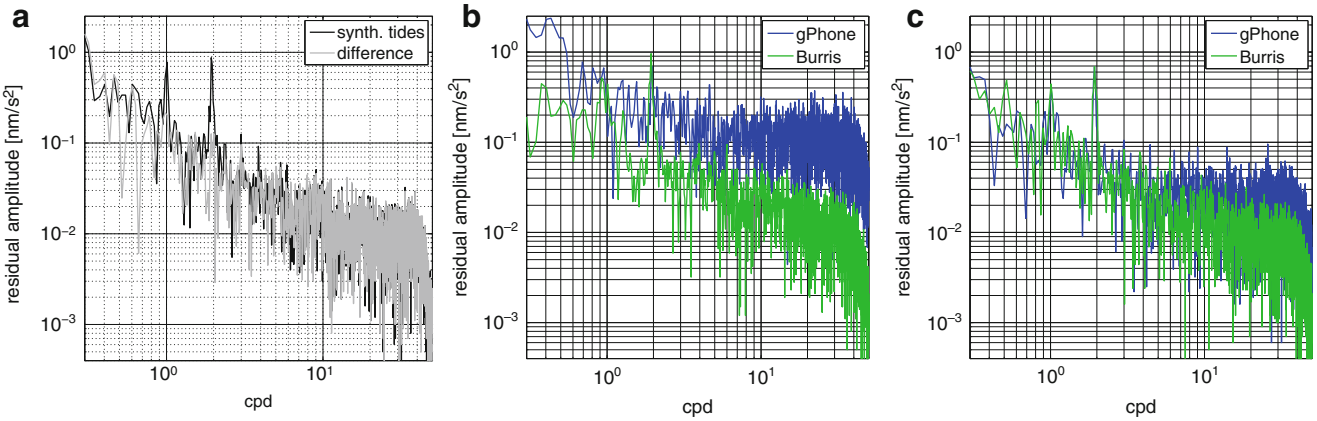

Fig. 4 Fourier spectra of Burris and gPhone gravity residuals at different stations are displayed up to 50 cpd to emphasize the lower frequencies. (**a**) Onsala: Burris data corrected with synth. tidal parameters and difference of observations of Burris and OSG. (**b**) Hannover: observations corrected with synthetic tidal parameters. (**c**) Ruthe: simultaneous recordings corrected with synthetic tidal parameters

For all following comparisons we use gravity recordings resampled to a 300 s interval using the DECIMATE program of the ETERNA 3.4 package (Wenzel 1996). The Burris recorded simultaneously with an instrument of higher accuracy, a superconducting gravimeter (precision of a few tenths of a nm/s^2 and drift of a few tens of nm/s^2 per year) in Onsala for a period of 3 months. Preprocessed 10 s data of the GWR OSG-054 was provided by Hans-Georg Scherneck (OSO). Figure 4a shows the Fourier spectrum of the Burris observations corrected using the synthetic tidal parameters (black graph) and the Fourier spectrum of the difference between Burris and OSG observations (grey graph). Using the synthetic tidal parameters, the residual amplitudes are 0.8–0.9 nm/s^2 for diurnal and semi-diurnal frequencies. As the Onsala station is located directly at the coast, these differences to the synthetic tidal parameters are to be expected. The difference of the observations of the two instruments exclude all environmental effects. Instrumental effects, e. g. uncertainties in the calibration, are still included. The spectrum, plotted in grey, shows the remaining periodic signals at semi- and ter-diurnal frequencies with amplitudes below 0.22 nm/s^2. This suggests, that the Burris is capable of recording diurnal, semi-diurnal and maybe even ter-diurnal tidal waves, given a long enough time series.

A direct comparison of gPhone and Burris is possible for the stations Hannover and Ruthe. Figure 4b presents the spectra of the gPhone and Burris gravity residuals from recordings in Hannover. For higher frequencies the average noise is at the level of 0.15 nm/s^2 for the gPhone residuals, one order of magnitude above the Burris. Both instruments display a peak in the spectrum at semi-diurnal frequency of 0.95 nm/s^2. The amplitude of the gPhone residual is 0.25 nm/s^2 lower. At the diurnal waveband the gPhone residuals show noise at the level of 0.7 nm/s^2 with no distinct peak but a number of peaks from 0.7 to 1.5 cpd. The Burris, however, has a more prominent diurnal effect left in the residuals at the order of 0.5 nm/s^2. Due to the location of the gravimetry laboratory this is not necessarily caused by the synthetic tidal model but is induced by the environment. Figure 4c shows the comparison for the simultaneous recordings in Ruthe. Located outside of populated areas measurements in Ruthe are less affected by human activities, which is also reflected in the standard deviations in Table 2. The first obvious difference, when compared to Fig. 4b, is the lower noise

Table 3 Tidal parameters (amplitude factor and phase lag) for selected wave groups estimated from simultaneous gPhone/Burris observations in Ruthe and OSG/Burris observations in Onsala

	Ruthe						Onsala			
Wave	gPhone (152 days)		gPhone (66 days)		Burris (66 days)		OSG-054 (97 days)		Burris (97 days)	
group	Amplitude	Phase (°)	Amplitude	Phase (°)	Amplitude	Phase (°)	Amplitude	Phase (°)	Amplitude	Phase (°)
O1	1.14791	0.1239	1.14804	0.0949	1.14970	0.1823	1.14747	0.1220	1.14722	0.1580
	± 0.00027	± 0.0135	± 0.00041	± 0.0207	± 0.00133	± 0.0663	± 0.00046	± 0.0232	± 0.00061	± 0.0307
K1	1.13524	0.2511	1.13486	0.2654	1.13955	0.2735	1.13910	0.1249	1.13874	0.1234
	± 0.00020	± 0.0102	± 0.00040	± 0.0203	± 0.00133	± 0.0660	± 0.00046	± 0.0232	± 0.00059	± 0.0295
M2	1.18411	1.6932	1.18433	1.6459	1.18626	1.6891	1.18722	1.2148	1.18703	1.2653
	± 0.00026	± 0.0125	± 0.00036	± 0.0175	± 0.00043	± 0.0206	± 0.00032	± 0.0152	± 0.00056	±0.0271
S2	1.18374	0.3918	1.18363	0.3751	1.18877	0.3875	1.17845	0.2812	1.18049	0.3444
	± 0.00061	± 0.0296	± 0.00112	± 0.0550	± 0.00136	± 0.0668	± 0.00096	± 0.0461	± 0.00165	± 0.0789
M3	1.05415	0.4651	1.05275	1.1120	1.09265	−0.9849	1.05960	1.4674	1.05551	0.4487
	± 0.00848	± 0.4610	± 0.01236	± 0.6724	± 0.02490	± 1.3043	± 0.00711	± 0.3842	± 0.02126	± 1.1545
$\bar{\sigma}$	± 0.00034	± 0.0165	± 0.00057	± 0.0284	± 0.00111	± 0.0549	± 0.00055	± 0.0269	± 0.00085	± 0.0416

$\bar{\sigma}$ is the mean standard deviation of the displayed groups O1 to S2

level of the gPhone residuals at 3×10^{-2} nm/s^2. In the tidal waveband periodic effects remain with an amplitude of 0.4 and 0.7 nm/s^2 for the diurnal and semi-diurnal frequencies, with only slightly lower residuals for the gPhone. For the Burris instrument the spectrum for the higher frequencies does not change, which is also suggested by Table 2. The σ of the Burris is unchanged for all stations and the gPhone shows variations of up to factor 5 for the 1 Hz data. Only in Clausthal the noise level of the gPhone residuals at higher frequencies is 1.5×10^{-2} nm/s^2, which is at the same level as the Burris achieves at all stations.

4 Tidal Analysis

Tidal parameters were calculated for the stations Hamburg, Clausthal, Onsala, and Ruthe. The tidal analysis was performed with ETERNA 3.4 using 300 s data. It should be noted, that the gPhone time series are usually 3 months in length, whereas the Burris observations only have 1.5 months of uninterrupted recordings. To ensure a reduction uncertainty of 1 nm/s^2 the tidal parameters should be obtained with accuracy of 1‰ for the amplitude factor and 0.05° for phase lag.

For Ruthe a tidal analysis was conducted on the observations of both instruments and the results for selected tidal waves are listed in the left of Table 3. For gPhone tidal parameters for the entire length of the time series are listed as well as for the same time the Burris observations were taken. The parameters differ by less than 0.4‰ for the amplitude and 0.05° in phase of diurnal and semidiurnal wave groups. M3 differs by 1.3‰ and 0.65°. The difference between gPhone-98 and Burris B-64 is up to 4.2 ‰ in amplitude for groups up to S2. The difference of the phase lag is up to 0.05° for these groups. The standard deviations σ of amplitude as well as phase of the gPhone tidal parameters are at the same level reported by Riccardi et al. (2011) up to the M2 wave. M3 is not well observed compared to the other wave groups. The shorter observation time of the Burris is reflected in its standard deviations. The mean standard deviation $\bar{\sigma}$ of the O1–S2 groups are twice as much as the $\bar{\sigma}$ of the 66 day gPhone time series parameters.

In the right part of Table 3 the results of the tidal analysis for the measurements in Onsala are shown. The data of the OSG was processed analog to the Burris data and tidal parameters are estimated from a time series of equal length. A comparison of the tidal analysis for Onsala and Ruthe from Burris data shows significantly lower standard deviations for O1 and K1 in Onsala. The semi-diurnal waves M2 and S2 have slightly larger standard deviations. The parameters calculated from Burris observations differ by 0.2–0.4 ‰ in amplitude and up to 0.05° in phase from the OSG except for S2, where the deviation is 1.7‰ and 0.06°. The semi-diurnal waves might be affected by a combination of tidal and non-tidal sea level variations of the Kattegat. These variations typically range from 10 to 20 cm in 12 h, but weather conditions might cause a shift of the mean sea level over a period of several days. Olsson et al. (2009) describe the effect of sea surface tilt of the Baltic Sea and calculated the gravitational effect to be 6–9 nm/s^2 for Onsala in two case studies. Mammadov et al. (2011) report on a tidal recording using the Burris B-14 gravimeter for the period of 1 year in Shaki, Azerbaijan reaching slightly higher standard deviations than the B-64 in Onsala.

Due to the proximity of the station in Hamburg to Elbe and North Sea the residuals, after correcting the observations with the synthetic tidal model, still show a periodic effect with 2 cpd and an amplitude of 1.4 nm/s^2. Table 4 summarizes the residual amplitudes at 1 and 2 cpd for all stations. Correcting the observations with the tidal parameters

Table 4 Residual amplitudes in nm/s^2 at 1 and 2 cycles per day from synthetic and observed tidal parameters

		Synthetic tides		Observed tides	
	Station	1 cpd	2 cpd	1 cpd	2 cpd
gPhone	Hamburg	0.66	1.44	0.30	0.16
	Clausthal	0.76	0.69	0.20	0.19
	Ruthe	0.41	0.68	0.18	0.10
Burris	Onsala	0.77	0.87	0.24	0.28
	Ruthe	0.44	0.69	0.24	0.14

estimated in the tidal analysis removes this peak altogether. At 1 cpd the remaining residual is at the noise level. In Clausthal the observed parameters reduce the residuals at diurnal and semi-diurnal frequencies by the factor of about 3.6. The recordings performed at both stations resulted in improved tidal parameters for the gPhone-98. To verify these parameters additional measurements, preferably with a different instrument, are to be taken.

5 Summary

Gravity was recorded with the IfE gravimeters Micro-g LaCoste gPhone-98 and ZLS Burris Gravity Meter B-64 in Hamburg, Hannover, Ruthe, Clausthal and Onsala to determine the tidal parameters and to assess the accuracy of the instruments. The linear calibration factor for both instruments was determined repeatedly and found to be stable to 3×10^{-4}. The drift of the gPhone has decreased with the age of the instrument and is currently at $\approx$90 nm/s^2 per day after a period of 2 weeks at a new station. The Burris currently shows a non-linear drift with high variations within a few weeks. Using the step-response method a phase delay of 3 s is estimated for the Burris. Testing the Burris in a pressure chamber revealed an instrumental air pressure coefficient of 0.14 nm/s^2 per hPa. The adjustment of a gravity network using hand transport from Burris measurements resulted in a mean standard deviation of 10 nm/s^2 of the adjusted gravity values.

The tidal analysis of gPhone-98 recordings in Clausthal and Hamburg resulted in improved tidal parameters for these stations. Especially for Hamburg the improvement is noticeable due to the effect of ocean tides, which are not well estimated by the synthetic tidal model close to the coast. In Ruthe the tidal analysis of both instruments provided mixed results. The gPhone amplitude factors for diurnal and semi-diurnal groups show a mean standard deviation of 0.3×10^{-3} for a time series of 152 days and of 0.6×10^{-3} for a shorter period of 66 days. For the Burris, with an observation time of 66 days, the mean standard deviation is 2–3 times higher when compared to the 66 and 152 day long time series of gPhone. The diurnal and semi-diurnal tidal amplitude factors from both instruments agree to 1.5–4.2 ‰. The tidal analysis of the Burris measurements in Onsala resulted in parameters for O1, K1 and M2 which agree to 0.3‰ and S2 to 1.7‰ with the parameters derived from GWR OSG-054 data of the same time span and processed the same way. Burris B-64 and gPhone-98 gravimeters show satisfactory results better than 1‰ for the amplitude factors and 0.05° for phase lags obtained from the observations of diurnal and semi-diurnal tidal waves. However, the gPhone achieves a lower mean standard deviation of these parameters in a shorter observation time at one station that was occupied with Burris and gPhone at the same time.

Acknowledgements This work was in part funded by the German Research Foundation (DFG, MU 1141/16-1). The Centre for Quantum Engineering and Space-Time-Research (QUEST) provided funding for the gPhone-98. The authors thank Hans-Georg Scherneck and the Onsala Space Observatory for hosting our instrument and providing gravity and environmental data, and the Leibniz Institute for Applied Geophysics for the cooperation in Hamburg.

References

Jentzsch G (2008) The automated Burris Gravity Meter-a new instrument using an old principle. In: Proceedings of symposium on terrestrial gravimetry static and mobile measurements, St Petersburg, pp 20–23

Jiang Z, Pálinkáš V, Francis O, Jousset P, Mäkinen J, Merlet S, Becker M, Coulomb A, Kessler-Schulz KU, Schulz HR, Rothleitner C, Tisserand L, Lequin D (2012) Relative gravity measurement campaign during the 8th International Comparison of Absolute Gravimeters (2009). Metrologia 49(1):95–107. doi:10.1088/0026-1394/49/1/014

LaCoste & Romberg, Inc. (2004) Instruction manual Model G and D gravity meters. LaCoste & Romberg, Inc., Austin

Mammadov S, Jahr T, Jentzsch G, Kadirov F (2011) Primary results of new gravity station Shaki/Azerbaijan. Bull d'Inf Marées Terrest 147:11881–11890

Micro-g LaCoste (2008) gPhone/P.E.T Hardware Manuel V1. Micro-g LaCoste, Lafayette

Olsson PA, Scherneck HG, Ågren J (2009) Effects on gravity from non-tidal sea level variations in the Baltic Sea. J Geodyn 48(3–5):151–156. doi:10.1016/j.jog.2009.09.002

Riccardi U, Rosat S, Hinderer J (2011) Comparison of the Micro-g LaCoste gPhone-054 spring gravimeter and the GWR-C026 superconducting gravimeter in Strasbourg (France) using a 300-day time series. Metrologia 48(1):28–39. doi:10.1088/0026-1394/48/1/003

Richter B, Wenzel HG (1991) Precise instrumental phase lag determination by the step response method. Bull d'Inf Marées Terrest 111:8032–8052

Scherneck HG (2008) Status report to the Global Geodynamics Project: superconducting gravimeter station at the Onsala Space Observatory. The national facility for radio astronomy in Sweden. Technical Report, Onsala Space Observatory

Timmen L (2010) Absolute and relative gravimetry. In: Xu G (ed) Sciences of geodesy - I. Springer, Berlin, pp 1–48. doi:10.1007/978-3-642-11741-1_1

Timmen L, Gitlein O (2004) The capacity of the Scintrex Autograv CG-3M no. 4492 gravimeter for "absolute-scale" surveys. Revista Brasileira de Cartografia 56(2):89–95

Timmen L, Wenzel HG (1995) Worldwide synthetic gravity tide parameters. In: Sünkel H, Marson I (eds) Gravity and geoid. International Association of Geodesy symposia, vol 113. Springer, Berlin, pp 92–101. doi:10.1007/978-3-642-79721-7_11

Van Camp M, Vauterin P (2005) Tsoft: graphical and interactive software for the analysis of time series and earth tides. Comput Geosci 31(5):631–640

Wenzel HG (1996) The nanogal software: Earth tide data processing package ETERNA 3.30. Bull d'Inf Marées Terrest 124:9425–9439

ZLS Corporation (2011) User guide: Burris Gravity Meter and UltraGrav control system. ZLS Corporation, Austin

Least-Squares Prediction of Runoff Over Ungauged Basins

Mohammad J. Tourian, Robin Thor, and Nico Sneeuw

Abstract

One of the major concerns of hydrology is to quantify the hydrological cycle of basins e.g. by means of modeling the hydrological interactions. However, current hydrological models are far from perfect. The main challenge of modeling is the poor spatio-temporal coverage of in situ databases, which are declining steadily over the past few decades. Among the hydrological interactions, river runoff is of great importance, as it represents a catchment's behaviour. In order to deal with the growing lack of in situ runoff data, we estimate river runoff of ungauged basins by least-squares prediction. In this method, runoff is predicted by mapping the runoff characteristics of gauged basins into ungauged ones through statistical correlations of past data. We follow two scenarios to form the covariance matrices out of available past in situ river runoff: (1) at the signal level, and (2) at the residual level after subtracting monthly mean values. Our validation shows that both scenarios are able to capture runoff values with relative errors less than 15 % for 80 % of the 25 catchments under study. We obtain Nash-Sutcliffe coefficients of over 0.4 for about 90 % and of over 0.75 for about 50 % of the catchments under study. We are thus able to avoid the complexity of hydrological modeling and the challenges (e.g. uncertainty) of spaceborne approaches for runoff estimation over ungauged basins.

Keywords

Least-squares prediction • Runoff

1 Introduction

How much freshwater do we have on land? How is groundwater storage changing with time? These are vital questions to answer for human life. Surprisingly, however, we currently cannot answer them properly (Trenberth et al. 2007). Our estimation of freshwater on surface, ground, snow or soil moisture are confined to rough estimates based on ad hoc assumptions. At the surface, knowledge about water surface height variation and bathymetry of rivers and lakes are limited. The depth of soil moisture is not really known at a global scale. Rain gauge measurements do not provide a reasonable areal representation of input to the hydrological cycle. The publicly available global rain gauge and runoff databases are declining steadily over the past few years (Lorenz and Kunstmann 2012; Fekete and Vörösmarty 2007) be it for economical, political or other reasons. The number of available runoff gauging stations went down from about 8000 (pre-1970) to roughly 2000 (around the year 2010). The total monitored annual streamflow has dropped accordingly by about 75 %. Figure 1 visualizes a clear decline between 1970 and 2010 in the number of available gauges for runoff especially over Asia and Africa.

Given the insufficient monitoring from in situ gauge networks, and without any outlook of improvement, alternatives must be investigated. Spaceborne sensors provide realistic alternatives, from which hydrologically meaningful results

M.J. Tourian (✉) • R. Thor • N. Sneeuw
Institute of Geodesy, University of Stuttgart, Stuttgart, Germany
e-mail: tourian@gis.uni-stuttgart.de

© Springer International Publishing Switzerland 2015

C. Rizos, P. Willis (eds.), *IAG 150 Years*, International Association of Geodesy Symposia 143,
DOI 10.1007/1345_2015_170

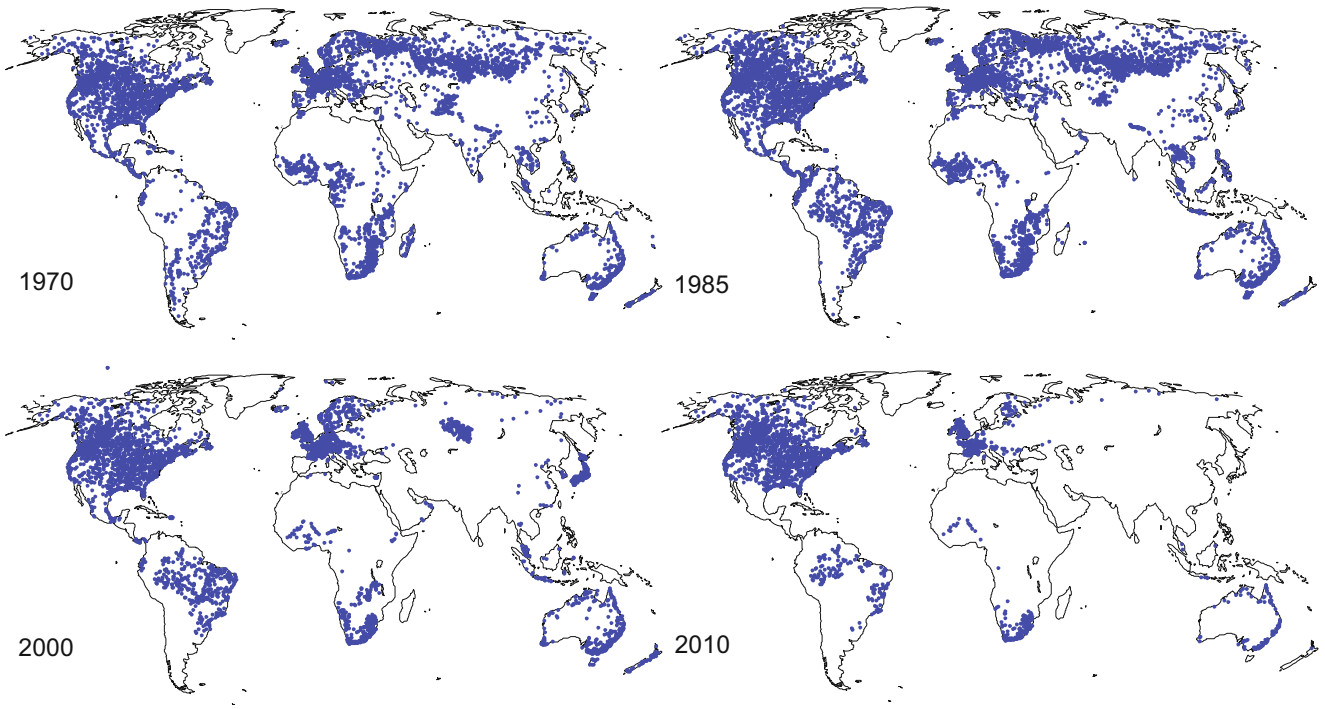

Fig. 1 Spatial distribution of gauges with available runoff data in the data base of GRDC around the world for 1970, 1985, 2000 and 2010

with certain limitations are obtained (Tourian et al. 2013; Sneeuw et al. 2013; Bjerklie et al. 2003). Moreover, hydrological modelling approaches, either stochastic or process-based models, are also commonly used in the hydrological community to predict hydrologic processes e.g. runoff. However, our evidently limited knowledge of the spatial and temporal dynamics of the hydrological cycle often cause large model error, sometimes greater than 100 % (Alsdorf et al. 2007).

Here, we propose a method based on least-squares prediction (Moritz 1989), that avoids the complexity of hydrological modelling and the challenges of spaceborne approaches. The least-squares prediction uses covariance information from past data to predict runoff based on the measurements that have been done in other gauges. This method is particularly effective when runoff correlates well between gauges around the world. In principle, this is the strength of the method, as highly correlated runoff behaviours within different climatic zones are expected. The terminology *prediction* derived from the methodology used here: least-squares prediction. It does not imply projection into the future. We only project current gauge information onto ungauged catchments.

The method is confined to those catchments with available past data, for which the covariance matrices can be generated. This means that the least-squares prediction allow to predict runoff for all gauges that have been ever been measured. In other words, it helps to lift the decaying black curve towards the red line in the Fig. 2.

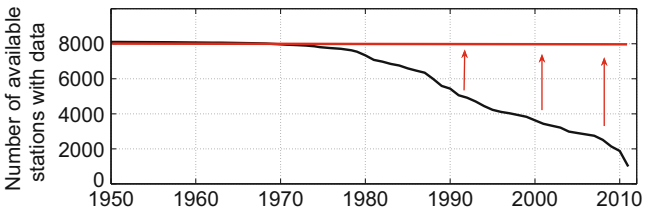

Fig. 2 Number of available stations with discharge data according to GRDC database is depicted for different years. Least-squares prediction helps to reach the *red line* for the number of available stations with runoff data

In the paper at hand, 28 years of data from 25 catchments located in different climatic zones are studied, which will be discussed in Sect. 2. Section 3 describes our methodology, in which we create the covariance matrices through two approaches (signal and residual) from available in situ data. We show the results of the employed method and validation in Sect. 4. Finally, the conclusions are drawn in Sect. 5.

2 Data

Monthly runoff measurements at the outlet gauges of 25 catchments (Fig. 3) in units of m^3/s are collected from different sources: (1) Global Runoff Data Center (GRDC) (2) ArcticRIMS project and (3) ORE HYBAM project. The runoff values are converted to units of mm/month by dividing

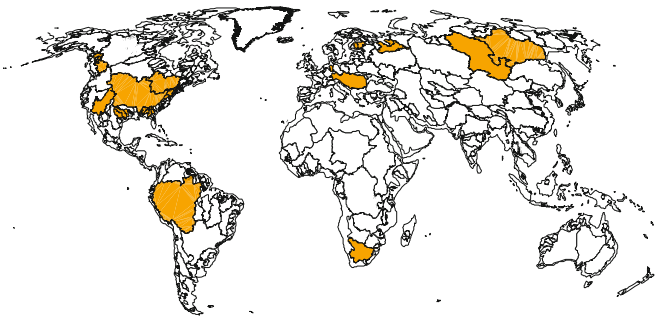

Fig. 3 25 Selected catchments for this study located in different climatic zones

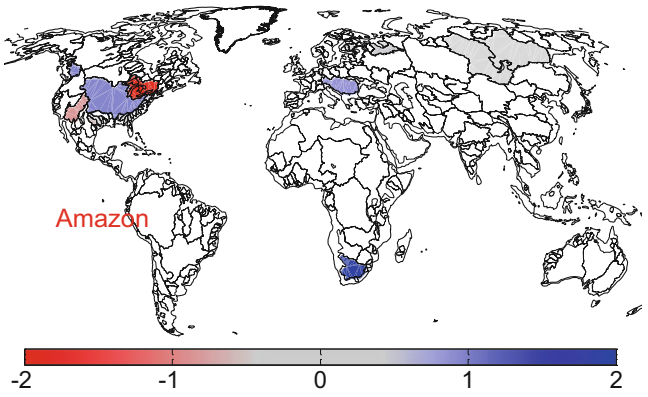

Fig. 4 Contribution of 24 catchments to map the runoff characteristics into Amazon, which are generated through available past data between 1980 and 1990

by the upstream area of the catchment and multiplying by 86.4 (number of seconds per day divided by 1000 for conversion of meter to millimeter). The selected catchments for this study with various size are located in different climatic zones, the largest is Amazon with an area of 4,672,876 km^2 and the smallest one is Potomac River with area of 31,151 km^2.

3 Methodology

Least-squares prediction is discussed in Moritz (1989). In the elementary approach, it is assumed that l is the vector of known measurements (here runoff at gauged catchment) and s is the unknown signal vector (here runoff at ungauged catchment). The signal and measurements are of the same quantity; here runoff. The prediction is linear and unbiased:

$$s = Hl + e \ , \tag{1}$$

where H is prediction model that has to be found by minimizing the covariance matrix of the prediction error e

$$C_{ee} = HC_{ll}H^{\mathrm{T}} - C_{sl}H^{\mathrm{T}} - HC_{sl}^{\mathrm{T}} + C_{ss} \tag{2}$$

where C_{ll} , C_{sl} , and C_{ss} are the covariance matrices of the respective signal and measurements arrays. It can be proven that C_{ee} is minimized for Moritz (1989)

$$H = C_{sl}C_{ll}^{-1} \ . \tag{3}$$

Runoff values are always positive with annual, inter-annual and random variations. In order to apply least-squares prediction to the runoff quantity, we form the C_{sl} and C_{ll} by two approaches:

- Signal approach, removing long-term mean: $\bar{l}_{\mathrm{tr}}$, $\bar{s}_{\mathrm{tr}}$

$$C_{ll} = \frac{1}{T_{\mathrm{tr}}}(l_{\mathrm{tr}} - \bar{l}_{\mathrm{tr}})^{\mathrm{T}}(l_{\mathrm{tr}} - \bar{l}_{\mathrm{tr}}) \ , \quad C_{sl} = \frac{1}{T_{\mathrm{tr}}}(s_{\mathrm{tr}} - \bar{s}_{\mathrm{tr}})^{\mathrm{T}}(l_{\mathrm{tr}} - \bar{l}_{\mathrm{tr}}) \tag{4}$$

- Residual approach, removing seasonal mean: $\tilde{l}_{\mathrm{tr}}$, $\tilde{s}_{\mathrm{tr}}$

$$C_{ll} = \frac{1}{T_{\mathrm{tr}}}(l_{\mathrm{tr}} - \tilde{l}_{\mathrm{tr}})^{\mathrm{T}}(l_{\mathrm{tr}} - \tilde{l}_{\mathrm{tr}}) \ , \quad C_{sl} = \frac{1}{T_{\mathrm{tr}}}(s_{\mathrm{tr}} - \tilde{s}_{\mathrm{tr}})^{\mathrm{T}}(l_{\mathrm{tr}} - \tilde{l}_{\mathrm{tr}}) \tag{5}$$

The index "tr" refers to a training period, for which the runoff data is available for all catchments. T_{tr} represents the length of training period. The equations above are different in terms of the mean (long-term and seasonal) that is removed for computing the covariance matrices. In principle, removing long-term and seasonal mean from a time series provide two different statistical behaviour, which will be reflected on the computed covariance matrices. It is important to note here that C_{ll} and C_{sl} of the aforementioned approaches are obtained by averaging over time, whereas the prediction is done spatially i.e. for each epoch individually. This means that here we assume runoff to be ergodic and cyclo-stationary in time, which is not necessarily valid for all catchments (Milliman et al. 2008).

4 Results and Validation

We employ the two aforementioned approaches over the selected database. In this validation study, we assume the training period between 1980 and 1990, out of which the C_{ll} and C_{sl} and consequently H are generated.

One catchment is selected as *unmeasured* s, while all others go into l. In reality s is measured, too, thus cross-validation is allowed. Such cross-validation is subsequently applied to all catchments. We can thus evaluate the real prediction error. Each row/column in the prediction model matrix H represents the contribution of all other

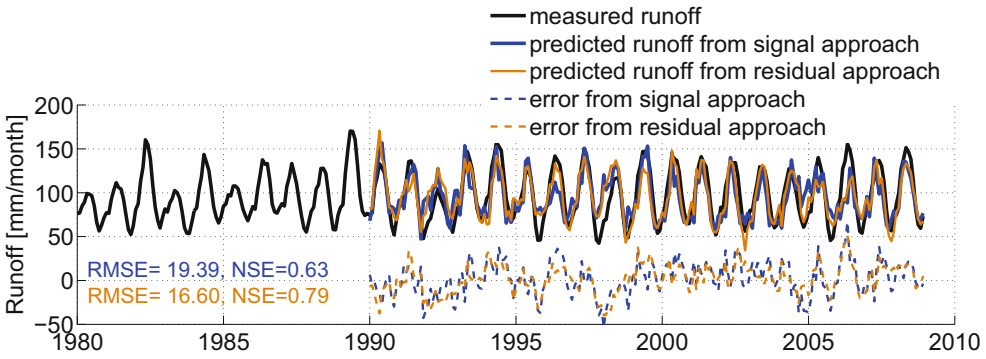

Fig. 5 Prediction of runoff for Amazon with covariance matrices from a training period between 1980 and 1990

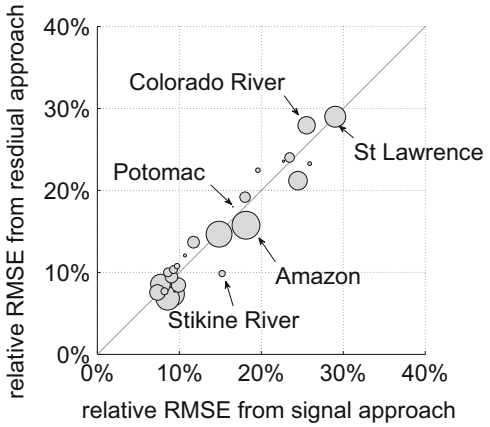

Fig. 6 Computed relative RMSE (RMSE/signal range) from residual approach versus those obtained form signal approach for 25 catchments under study

catchments (in our case 24 catchments) into the selected catchment. For instance, Fig. 4 shows the contribution of 24 catchments for prediction of runoff over Amazon. Among the catchments under study, Orange in southern part of Africa and St Lawrence, Susquehanna River and Potomac River in Eastern part of North America contribute the most. The different climatic behaviour of Amazon as a tropical basin and boreal catchments can be seen in near zero contributions of Lena and Yenisei basins for the prediction of runoff from Amazon. We quantify our validation using metrics of Root Mean Square Error (RMSE) and Nash-Sutcliffe Efficiency (NSE) (Nash and Sutcliffe 1970). Figure 5 shows the least-squares predicted runoff time series of Amazon, for which RMSE values of 19.39 and 16.60 mm/month and NSE coefficients of 0.63 and 0.73 are obtained from the signal and residual approach, respectively. Such RMSE for Amazon corresponds to relative a RMSE (RMSE/signal range) of about 17 %, which is comparable with those from spaceborne approaches (Tourian et al. 2013).

The obtained relative RMSE for all 25 catchments under study are shown in the scatter plot in a condensed form in Fig. 6. It indicates that both signal and residual approaches are able to capture runoff values with an error range less than 15 % for most of the rivers. In terms of relative RMSE neither approach seems to be superior, although in terms of NSE the residual approach provides slightly better results (Fig. 7 right).

The better results of the residual approach were also demonstrated by our spectral analysis (not shown here), where its predicted runoff better captures the seasonal variations. Our validation using NSE shows that least-squares prediction provides NSE larger than 0.5 for most of the catchments, although some exceptions do exist e.g. Orange. Despite the good performance of the least-squares prediction method, it is not able to capture extreme events properly, which is visible from Fig. 5 e.g. October 2006. This can be explicitly explained by the fact that an extreme event does not necessarily follow a statistical long-range relationship. Moreover, our prediction model H contains the average relations of time series within the training period, which is not able to map the extreme events.

5 Conclusion

Least-squares prediction can successfully predict runoff data for ungauged catchment at a given epoch using the covariance information and measurements from other catchments at the same epoch. We validate the performance of the method over a sample dataset of 25 catchments, for which continuous time series are available over 28 years. From this period 10 years were chosen as training period for obtaining the covariance matrices. Overall, both proposed scenarios (signal and residual) lead to error ranges less than 15 % for about 80 % of rivers under study. Our analysis show that the residual approach provides slightly better results

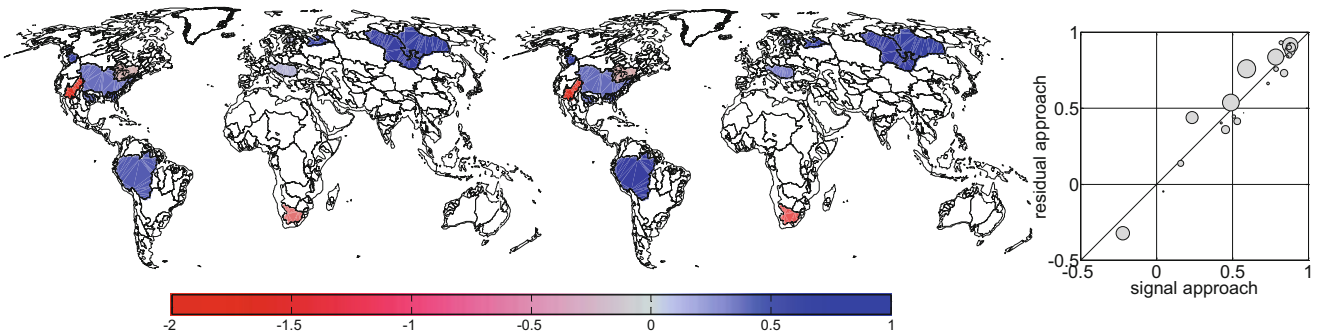

Fig. 7 NSE from signal (*left*) and residual approach (*middle*) and scatter plot of NSE from residual approach versus NSE from signal approach for 25 catchments under study

especially in capturing the seasonality. We have obtained NSE>0.4 for 90 %, NSE>0.75 for 50 % of the 25 selected catchments, which implies a remarkably good performance of the least-squares method. Despite the promising results of this study, we acknowledge that the least-squares prediction method cannot map extreme events and would not represent the true hydrological trend in runoff time series (if any). Such limitation leaves much room for further analysis, where other kind of data like water level from altimetry could be assimilated into the prediction model.

References

Alsdorf D, Rodríguez E, Lettenmaier DP (2007) Measuring surface water from space. Rev Geophys 45:RG2002. doi:10.1029/2006RG000197

Bjerklie DM, Dingman SL, Vörösmarty CJ, Bolster CH, Congalton RG (2003) Evaluating the potential for measuring river discharge from space. J Hydrol 278(1–4):17–38. doi:10.1016/S0022-1694(03)00129-X

Fekete BM, Vörösmarty CJ (2007) The current status of global river discharge monitoring and potential new technologies complementing traditional discharge measurements. In: Predictions in Ungauged Basins: PUB Kick-off (Proceedings of the PUB Kick-off meeting held in Brasilia, 20–22 November 2002) IAHS Publication, p 309

Lorenz C, Kunstmann H (2012) The hydrological cycle in three state-of-the-art reanalyses: intercomparison and performance analysis. J Hydrometeorol 13:1397–1420. doi:10.1175/JHM-D-11-088.1

Milliman J, Farnsworth K, Jones P, Xu K, Smith L (2008) Climatic and anthropogenic factors affecting river discharge to the global ocean, 1951–2000. Glob Planet Chang 62(3-4):187–194. doi:10.1016/j.gloplacha.2008.03.001

Moritz H (1989) Advanced physical geodesy. Wichmann, Karlsruhe

Nash JE, Sutcliffe JV (1970) River flow forecasting through conceptual models: Part 1. A discussion of principles. J Hydrol 10:282–290. doi:10.1016/0022-1694(70)90255-6

Sneeuw N, Lorenz C, Tourian MJ, Devaraju B, Kunstmann H, Bárdossy A (2013) Estimating runoff using hydro-geodetic approaches: status and challenges. Surv Geophys 35:1243-1249

Tourian MJ, Sneeuw N, Bárdossy A (2013) A quantile function approach to discharge estimation from satellite altimetry (ENVISAT). Water Resour Res 49:1–13. doi:10.1002/wrcr.20348

Trenberth KE, Smith L, Qian T, Dai A, Fasullo J (2007) Estimates of the global water budget and its annual cycle using observational and model data. J Hydrometeorol 8:758–769. doi:10.1175/JHM600.1

Improving and Validating Gravity Data Over Ice-Covered Marine Areas

S. Märdla, T. Oja, A. Ellmann, and H. Jürgenson

Abstract

For accurate regional gravity field modelling it is vital to have dense and high quality data coverage. Ice gravimetry is a viable alternative to ship- and airborne gravimetry to help fill gaps over marine areas. A number of factors affect the accuracy of gravimetry on ice, thus special survey and data processing methods are needed. Nevertheless with appropriate methods an accuracy of ± 0.16 mGal was achieved on coastal ice. An efficient method for positioning of survey points is RTK GNSS which takes no more than a few minutes on each point and the accuracy achieved is at least ± 0.15 cm, while 10 min static surveys also yield acceptable results.

This study reports ice gravity surveys proceeded on shore-fast ice in the Väinameri Basin, Estonia. Acquired gravity data agree with existing airborne data while covering a larger area. As a result of the survey it was possible to confirm and specify the extents of an area of positive anomalies. An effort to determine the geoid heights over Väinameri Basin directly via using the GNSS data gathered during gravity surveys on ice was made. For now it proved to be less reliable than classical geoid determination from gravity data.

Keywords

Airborne gravimetry • Baltic sea • GNSS positioning • Gravity anomaly • Ice gravimetry • Relative gravimetry

1 Introduction

Satellite data have resolved the long-wavelength part of the global geoid with an accuracy of a few cm. In particular, thanks to dedicated gravimetric satellite missions (mainly GRACE and GOCE) there is now homogeneous global coverage of long wavelength gravity data with spatial resolution better than 100 km. However, in regional geoid modelling the satellite-only data need to be complemented with high quality and dense regional data across the entire study area. Therefore, when the gravity field is modelled in local scales for geoid computation, large lakes and coastal waters also need to be covered by gravity observations.

Filling gravity data gaps over water bodies is clearly more complicated than on land. Satellite altimetry can be used over open oceans. However, its usability in coastal waters is limited, see e.g. Fernandes et al. (2003), Deng et al. (2002) and references therein. Therefore a special vessel as well as equipment is needed for marine gravity surveys which make such observations expensive and time-demanding. Also, marine gravity data may often be contaminated with systematic errors due to factors of the moving survey environment, instrumental and navigational errors

S. Märdla (✉) • A. Ellmann
Tallinn University of Technology (TUT), Ehitajate tee 5, 19086 Tallinn, Estonia
e-mail: silja.mardla@ttu.ee

T. Oja
Estonian Land Board, TUT, Mustamäe tee 51, 10621 Tallinn, Estonia

H. Jürgenson
Estonian University of Life Sciences, Kreutzwaldi 1a, 51014 Tartu, Estonia

© Springer International Publishing Switzerland 2015

C. Rizos, P. Willis (eds.), *IAG 150 Years*, International Association of Geodesy Symposia 143,
DOI 10.1007/1345_2015_163

(Denker and Roland 2005), that need to be corrected via data processing methods, see e.g. Motao et al. (1999) and references therein.

During the past decade small aircraft have also been used for gravity data acquisition above water bodies, see Forsberg et al. (2001), Hwang et al. (2007) and references therein. However, acquisition of low-elevation airborne data near coasts may be complicated due to the turbulent environment caused by different temperatures of land and water. Therefore both coverage and quality of gravity data collected during marine and aerogravity surveys at shorelines could be quite heterogeneous, which affects subsequent geoid determination accuracy in the coastal regions.

Although not possible everywhere, gravity surveys on shore-fast ice with terrestrial gravimeters is an alternative to marine and airborne surveying. Modern equipment allows for accurate, relatively fast and therefore cost-efficient acquisition of gravity data over ice covered waters. Relative gravity surveys near the coast can easily be connected to the gravimetric network on land, which make them a valuable set of information for validating marine and airborne data.

Gravity surveys on ice were tried already in the 1950s, see a review in Lehmuskoski and Mäkinen (1978). Surveys have been proceeded in the Gulf of Botnia (Lehmuskoski and Mäkinen 1978), at Wanapitei Lake in Canada (Ugalde et al. 2006), Lake Vänern in Sweden (Ågren et al. 2015), on several large Estonian lakes and the Gulf of Riga (Oja et al. 2011). These studies reveal many issues related to mainly wind, ice oscillation and movement, positioning and data processing that affect the quality of gravity observations on ice and thus need to be investigated.

The main objective of this contribution is to assess and compare the quality of gravity data obtained by surveying on marine ice. Emphasis is on methods of evaluation: mainly comparison of gravity surveys on ice with airborne gravimetry, but also using the precise GNSS positioning on top of ice to validate possible geoid modelling improvements.

The paper is structured as follows. The introduction is followed by a review on problems concerning gravity surveys on ice alongside with methods of validating gravity surveys over water. The methods and results of a case study conducted on the Baltic Sea ice are presented. Brief conclusions summarize the contribution.

2 Problems of Gravity Surveys on Ice

According to previous studies (cf. references above) surveying gravity on ice is complicated by moving ice and weather conditions. One problem is the gravimeter tilting due to some compaction of snow as well as melting of ice under the tripod (occurring even with insulation) and the weight of equipment on ice. Modern gravimeters like Scintrex CG5 units have tilt sensors which help correct for the inclination, but only as long as it remains within their working range, thus possible continuous measurement time is limited (Ugalde et al. 2006).

Another problem is strong wind above the ice that shakes the gravimeter (which was one of the main problems on Lake Vänern, see Alm et al. 2011) but also creates noticeable ice oscillation (Kiviniemi 1975). Ice moves and vibrates constantly: high frequency gravity records show peak-to-peak amplitudes of over 150 mGal occurring at frequencies of 0.05–0.35 Hz (at periods of 3–20 s), see Oja et al. (2011), which creates certain challenges for subsequent data processing. Similarly to surveys on land, to obtain reliable ice-gravity results a number of points need to be revisited to allow for gravimeter's drift calculation. A detailed discussion of other possible error sources in ice gravimetry is given in Lehmuskoski and Mäkinen (1978).

Fortunately, visual output of observed high-frequency signal on the screen of some modern gravimeters such as the Scintrex CG5 helps to estimate the quality of surveys on site and adjust the instrument and method accordingly. Hence it has been possible to achieve uncertainties of ±0.15 mGal in recent surveys (Oja et al. 2011; Ågren et al. 2015). The obtained results should be compared with existing gravity datasets.

3 Comparing Gravity Data from Different Sources

Comparing gravity anomaly values from different sources can not be proceeded directly. First, locations of different survey points do not coincide exactly. This can be overcome by interpolating gravity anomaly values of one campaign to the locations of the other. Second, survey altitudes can be different and need to be accounted for. Fortunately, in comparisons of ice gravity data to shipborne surveys the difference in heights is not significant. Conversely, in case of airborne surveys the results at flight level need to be downward continued (DWC) to the sea level.

The problem of DWC is visualized in Fig. 1 that describes comparison of gravity surveys on ice with airborne surveys. The corresponding free air anomalies (Δg) are calculated as follows:

$$\Delta g_{air}(\Omega) = g(r_{air}, \Omega) - \left[\gamma_0(r_e, \Omega) + \frac{\partial \gamma}{\partial h} \cdot H_{air}(\Omega)\right] \quad (1)$$

$$\Delta g_{ice}(\Omega) = g(r_{ice}, \Omega) - \left[\gamma_0(r_e, \Omega) + \frac{\partial \gamma}{\partial h} \cdot H_{ice}(\Omega)\right] \quad (2)$$

where g is measured gravity, γ_0 is the normal gravity on the surface of reference ellipsoid, r is the geocentric radius, Ω is the coordinate pair (latitude, longitude), H is the height with respect to the vertical datum, h is the geodetic

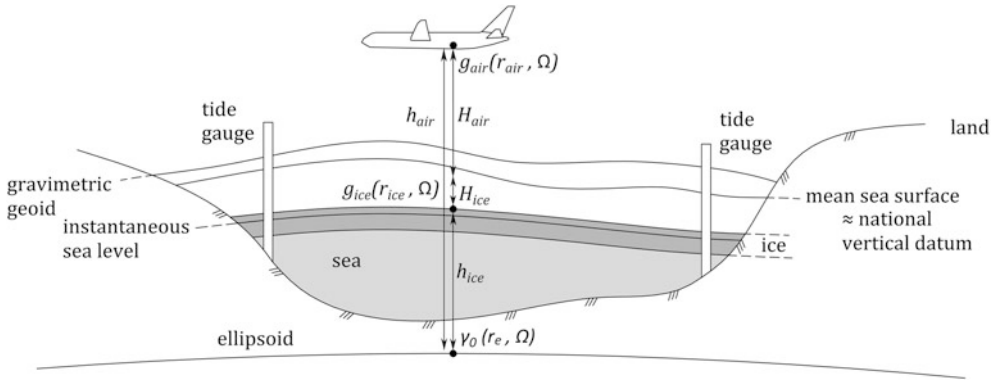

Fig. 1 Comparing gravity surveys on different height levels, the symbols used are explained in the text

height reckoned from the ellipsoid and $\partial\gamma/\partial h$ is the normal gravity gradient. Subscripts ice and air denote parameters acquired during ice and airborne gravity surveys, e refers to the surface of ellipsoid. Note that h can be measured by GNSS during surveys, H_{ice} can be obtained from the sea level data (nearby tide gauges) and H_{air} is conveniently derived in aerogravimetric data processing. To find the difference between gravity anomalies computed in air and on ice Eq. (1) is subtracted from Eq. (2):

$$\begin{aligned}&\Delta g_{air}(\Omega)-\Delta g_{ice}(\Omega) = \\ &g(r_{air},\Omega)-g(r_{ice},\Omega)-\frac{\partial\gamma}{\partial h}\cdot H_{air}(\Omega)+\frac{\partial\gamma}{\partial h}\cdot H_{ice}(\Omega) = \\ &\frac{dg}{dH}\,(r_{air}(\Omega)-r_{ice}(\Omega))-\frac{\partial\gamma}{\partial h}\,(H_{air}(\Omega)-H_{ice}(\Omega))\end{aligned} \quad (3)$$

where dg/dH is the gravity gradient. Since

$$r_{air}(\Omega)-r_{ice}(\Omega) = H_{air}(\Omega)-H_{ice}(\Omega) \approx H_{air}(\Omega) \quad (4)$$

then

$$\Delta g_{air}(\Omega)-\Delta g_{ice}(\Omega) = H_{air}(\Omega)\cdot\left(\frac{dg}{dH}-\frac{\partial\gamma}{\partial h}\right) \quad (5)$$

Eq. (5) represents DWC correction for gravity anomaly and needs to be accounted for in rigorous comparisons of different gravity sets. There are a number of methods to estimate it, see Ellmann (2011) and references therein for an extended discussion.

4 Relation Between Gravity and GNSS Observations

Without accurate positioning all the care taken to measure the gravity signal becomes useless. Considering the gravity gradient of about 0.3 mGal/m: to achieve the accuracy of ±0.05 mGal of gravity values a vertical positioning accuracy of about ±0.15 m has to be achieved. Presently such an accuracy can in most cases be achieved by using RTK (Real Time Kinematic) GNSS positioning. For rapid positioning a reliable VRS (Virtual Reference Stations) service and a cellular data network can be used (where available), otherwise rapid static GNSS observations or other approaches are needed.

Gravity surveys are nowadays accompanied with precise GNSS positioning. The sea ice should reflect quite well the shape of a calm sea surface which in turn should reflect the shape of the geoid. Therefore GNSS positioning provides an additional dataset for validating the geoid model via comparison of heights of survey points situated directly on ice to the geoid model. For this it is important to consider variations of sea level heights during the surveys: ice may be above or below the national vertical datum (cf. Fig. 1 and Sect. 6.3).

5 Case Study on the Väinameri Basin

Due to the large number of islands and islets more than 85% of Estonian borderline is in fact waterfront. Therefore it is vital for Estonian gravity field (and consequent geoid) modelling to have sufficient data available over marine areas. For instance the historic (performed in the 1960s) Gulf of Riga seabottom gravity survey results and the 1999 Baltic Sea airborne gravity campaign (Forsberg et al. 2001) data have been used in earlier geoid modelling studies (Forsberg 2001; Ellmann 2005; Ellmann et al. 2011).

There was evidence however that there may be biases in existing datasets or some important features may be missing from the current gravity field model over marine areas. Since 2009 numerous winter campaigns of relative gravity surveys have been conducted on ice-covered lakes and coastal sea to evaluate the historic datasets and to fill gaps of gravity data in marine areas, the latest of these on the Väinameri Basin of the Baltic Sea in the West Estonian Archipelago.

5.1 Characteristics of the Study Area

The Väinameri Basin is a semi-closed (surrounded by an arc of islands and the mainland) and rather shallow water body with a mean depth of about 5 m. Its area is 2,200 km^2 and it contains hundreds of islets. Compared to the rest of the Baltic Sea the ice cover is formed more frequently and lasts longer (up to 4 months in cold winters). Väinameri, similarly to the rest of the Baltic Sea, is almost tide-less (tides are below a dm level). Instead, the sea level fluctuations are primarily forced by the wind stress and atmospheric pressure changes (Liibusk et al. 2013).

So far there were almost no gravity data except for a few (possibly poorly connected) measurements on the islets (Ellmann et al. 2009) and a single track of the 1999 airborne gravity campaign. Δg of these airborne data were the basis for compiling the anomaly field model used for calculating a recent national gravimetric geoid model GRAV-GEOID2011 (Ellmann et al. 2011), also for Märdla et al. (2015). Thus possible errors in the airborne data strongly affect resulting geoid models.

Indeed, a suspicious "lump" was detected in the anomaly field model over the sea surface of Väinameri (see its location on Fig. 4), showing anomalies up to 9 mGal larger than on surrounding islands. This was in fact one of the main reasons for conducting ice gravity surveys in this particular area. With new gravity data obtained in the surveys it would be possible to verify and improve the gravity anomaly field model.

In the winter of 2013 the Väinameri Basin became covered with a 20…50 cm thick layer of shore-fast ice. The adjacent marine areas were also covered with pack ice. Weather conditions were stable with prevailingly Southern winds well below 5 m/s and steadily high air pressure within the study area during the gravity surveys.

Surveys over the Southern part of the Väinameri Basin were carried out during 4 days in Feb–March 2013, covering about 1,000 km^2. The density (1 point/25 km^2) of surveys (altogether 41 points on ice, additionally 8 points on land) corresponds to that over land. The coverage of ice surveys, however, is more even since it is not constrained to existing roads.

Data collection consisted of relative gravity surveys and point positioning, additionally ice thickness and water depth were recorded (not used in data processing). On ice the team and equipment were transported by a lightweight amphibious crawler (Fig. 2).

Fig. 2 Gravity surveys and GNSS positioning on Väinameri Basin, a lightweight amphibious crawler was used for transport

5.2 Relative Gravimetry

Gravity measurements were performed relative to points on land using a digital Scintrex CG5 spring gravimeter no. 36 (hereafter S36). The benefit of using a CG5 gravimeter is its ability to record readings with a 6 Hz frequency, allowing for study of accelerations created by the vibration of ice surface.

The S36 used has been tested on the Pärnu and Tõravere-Haanja calibration lines in Estonia, an acceptable accuracy of about 200 ppm was concluded (Oja et al. 2010). Since the estimated gravity range in the study area was about 32 mGal, the calibration error of the S36 has an insignificant effect on the survey results (less than 10 μGal).

On each point at least three sets of 60 s readings were taken. Usually, the gravimeters readings in a set on ice were scattered a few mGal from the average (on land the scatter was 0.1…0.2 mGal), the sets agreed with each other within 50 μGal. In case the readings between sets deviated from the average by more than ±0.1 mGal the recording time was extended to 90 or even 120 s. Observations much longer than 120 s tend to be affected by the gravimeter's tilt and consume twice the time, hence were not used.

Gravity surveying was proceeded using loops so that every loop was closed within a day. The starting points on land and one or two additional points were repeated during the same day to estimate the drift parameters of the gravimeter in subsequent data processing. Moreover, on ice at least one point from a previously measured loop was repeated to estimate consistency between the results of different days. The starting points were connected with the national gravity network after the snow and ice melted and the network points were accessible again. Note that different time periods may introduce additional errors into survey results due to changing environmental conditions such as fluctuations in ground water level, sea level variations and so forth.

For gravity data processing and adjustment the GRAVS2 software package developed by the Estonian Land Board was applied. Points of the gravity network were used as reference for the adjustment. Gravity data was processed in much the same way and considering the same issues as in previous ice gravity campaigns in Estonia, see Oja et al. (2011) for more details.

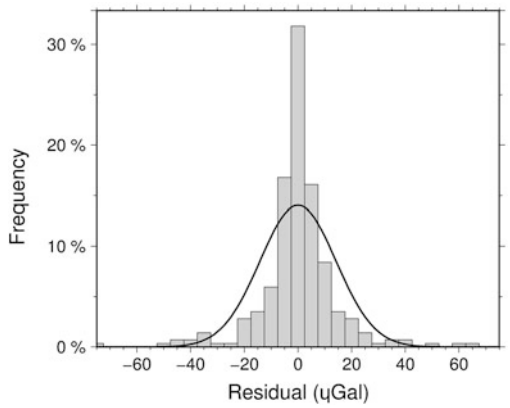

Fig. 3 Histogram of residuals of the adjustment of 286 readings, the bins near the edges and the misfit with the normal distribution curve are apparently connected to the effect of vibration noise on the readings

For comparison of gravity values on revisited points the results were reduced to the height level of the first measurement by applying a free air correction corresponding to the height difference obtained from GNSS data analysis (see Sect. 5.3). The gravitational attraction of changing volume of sea water nor the effect of changing air pressure were accounted for as the effects were estimated to be insignificant (both well below 10 μGal). After the reduction of gravimeter's drift effect on readings the discrepancies on revisited points were less than 20 μGal.

All in all the gravity data obtained on shore-fast ice was reasonably good: the expanded uncertainty multiplied by a coverage factor of k=2 (2-sigma) of ±0.15 mGal was achieved from a least squares adjustment. It can be seen from the histogram of residuals of the adjustment of 286 readings (Fig. 3) that most of the residuals are within 25 μGal. However, the variation of readings on ice is much higher compared to land data, some residuals reach 40…65 μGal. Therefore ice gravity data was weighted down (decreased by a factor of 4) in the adjustment. In addition, the uncertainty of reference points (about 60 μGal) was considered.

Considering also the uncertainty of GNSS height positioning of ±0.15 m (see Sect. 5.3) but neglecting a number of factors with smaller significance mentioned in Lehmuskoski and Mäkinen (1978) the final uncertainty estimation of gravity values amounts to

$$\sigma_g = \pm\sqrt{0.15^2 + (0.15 \cdot 0.3086)^2} = \pm 0.16\ (\text{mGal}) \quad (6)$$

Uncertainty of ±0.16 mGal is close to that of modern gravity data collected on land and better than most data currently available for gravity field modelling. The obtained accuracy is largely sufficient for calculating a geoid model with the accuracy below 1 cm (Ågren and Sjöberg 2015).

5.3 Survey Point Positioning

Positioning of the survey points at Väinameri was proceeded by GNSS methods using a GPS/GLONASS Trimble R8 receiver and a VRS service provided by a commercial CORS (Continuously Operating Reference Stations) network.

A combination of rapid static and kinematic surveys was tested for additional estimation of efficiency and accuracy, also because the availability of cellular network (necessary to obtain corrections via the VRS service) in such a remote area was uncertain before the campaign.

On 18 points a 10 min static measurement was conducted together with at least three kinematic readings of 5 s whereas towards the end of the campaign only kinematic readings were taken. In addition to three evenly distributed CORS 35–50 km away, a dual-frequency Trimble 5800 GPS receiver was set up on the coast about 5 km away and operated as a base point during 5 h of the campaign, covering the static measurement of 9 points in the Western part of the study area.

Data processing, which consisted primarily of baseline processing, was proceeded using a commercial software (Trimble Business Centre). It has to be mentioned that having an additional base point set up did not have a significant effect on the accuracy of positioning. This was revealed from varying baseline processing methods in which the base point position was fixed with different accuracy.

Discrepancies between static and kinematic height results at Väinameri reached +0.03±0.04 m. Although static measurements provided systematically larger height values, distribution of discrepancies does not reveal anything specific (except for a few larger ones in the NE being close to 10 cm).

Additionally differences of height values on revisited points were investigated. On land these were on a cm level, on ice as much as 15 cm. This reflects not only precision of GNSS positioning but also change in the water level during the survey.

In the light of GNSS quality assessment at Väinameri it can be concluded that an uncertainty of ±15 cm can be expected in height values although most points are likely to have a smaller error than this. VRS RTK surveys should be preferred as they are faster, but readiness for static surveys needs to be maintained in case the cellular data network fails in such remote areas.

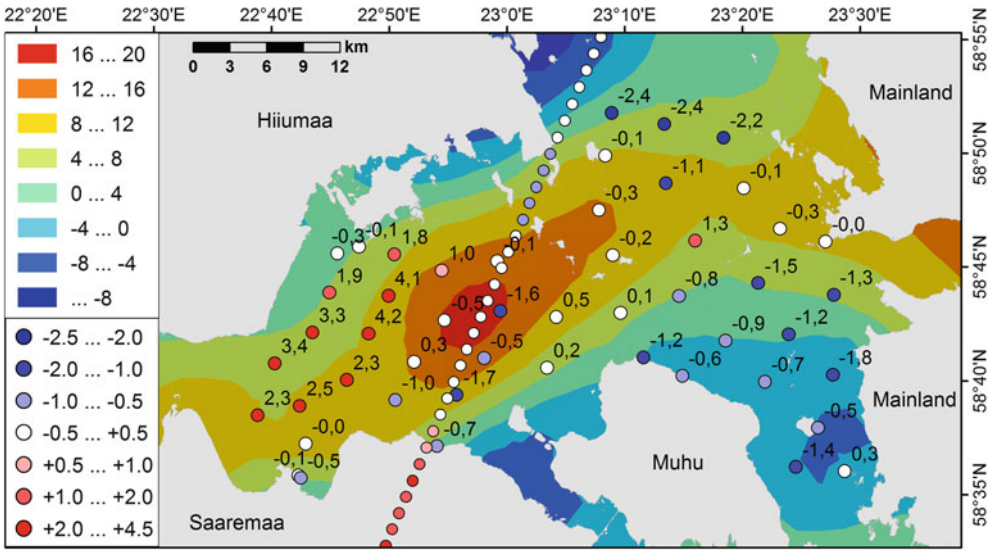

Fig. 4 Locations of air (*line-like sequence*) and ice (*scattered*) gravity points over the Väinameri Basin. The figure is contoured according to the Δg field used for calculating GRAV-GEOID2011, the colour range in mGal is explained in the *top legend*. Differences of $\Delta g_{ice} - \Delta g_{field}$ (shown as values on the figure) and $\Delta g_{air} - \Delta g_{field}$ in mGal are depicted by the *colours* explained in the *bottom legend*

6 Results and Comparisons

The results of the Väinameri campaign were compared to existing data that include (see also Sect. 5.1):

- Baltic Sea aerogravity survey from 1999
- The gravity anomaly field model used to calculate the official gravimetric geoid model of Estonia, GRAV-GEOID2011 (the existing gravity field model)
- The gravimetric geoid GRAV-GEOID2011 itself (the existing geoid model)

6.1 Evaluation of Aerogravity Data

In the Baltic Sea aerogravity survey a precision of ± 2 mGal was achieved (revealed from cross validation between tracks, Forsberg et al. 2001). Gravity anomalies from the Baltic Sea aerogravity data, downward continued to the sea level [see Eq. (1)...(5)] by an approach in Ellmann (2011), were used in this study.

As airborne data is very sparse in the Väinameri area (see the line-like sequence of points on Fig. 4), interpolation does not yield very good results. Therefore only a visual inspection of adjacent points of airborne and ice gravity data was made. Comparisons revealed that the air and ice gravity campaigns do not differ more than 2 mGal which confirms the initial accuracy estimation achieved from cross validation between tracks.

In marine areas off the NW coast of Estonia these airborne data are (and most likely will be for a while) the only data to describe the gravity field. Therefore knowing that airborne data are trustworthy in this area is very important.

6.2 Improvements to the Existing Gravity Field Model

Gravity data obtained in the Väinameri campaign was compared to the existing gravity field model. Although the average difference of ice gravity results from the anomaly field model is only $+0.09$ mGal the standard deviation is as large as ± 1.70 mGal (Fig. 4).

Looking at the distribution of these differences a number of features can be noted. Importantly, the new ice gravity dataset confirmed the existence and magnitude of the area of positive gravity anomalies (the "lump" in the anomaly field) estimated from airborne data. However, it reaches further West than expected. Also, the Eastern part of Väinameri has in fact slightly smaller anomaly values than previously known.

An initial comparison has revealed that the errors in the existing gravity field model in the Väinameri area have an effect of about a cm on the geoid model. Therefore a significant improvement has been made in the light of the attempts to calculate a geod model with an accuracy of 1 cm.

6.3 Evaluation of the Existing Geoid Model Using GNSS Surveys on Ice

The obtained geodetic heights of ice gravity points in the Väinameri Basin are a rather interesting source for verifying

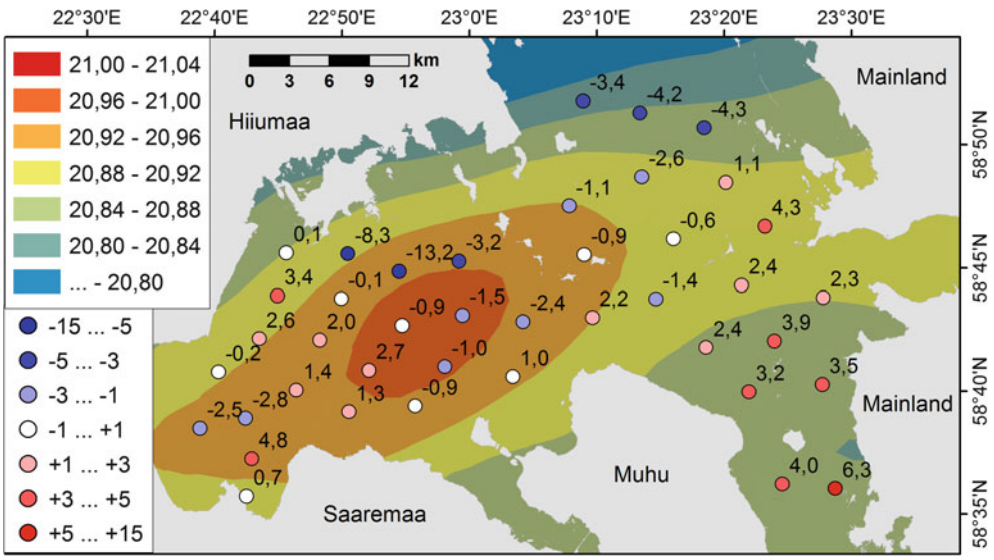

Fig. 5 Contoured GRAV-GEOID2011 model, the colour range in metres is explained in the *top legend*. Discrepancies of GNSS heights with respect to the GRAV-GEOID2011 model (in cm, GNSS-geoid, 1D offset removed) are depicted by *coloured circles* explained in the *bottom legend*

the shape of the marine geoid. In the following discussion RTK heights are used since they exist on all survey points and seem to be at least equally accurate as the static results.

To be able to compare GNSS heights obtained on survey points directly to the gravimetric geoid model heights in the Väinameri Basin some corrections need to be accounted for. During the surveys instantaneous sea level differed from the mean sea level by 30…45 cm (cf. Fig. 1). First, sea level corrections obtained from interpolating values from five surrounding tide gauges (from the online sea level system of Marine Systems Institute, TUT) were applied to surveyed heights. Second, the average difference of +0.375 m between survey point heights and the gravimetric geoid model in the study area was accounted for to simplify comparison. Note that variations in ice top and sea level difference were not accounted for, these could reach no more than 3 cm considering that ice thickness varied from 20…50 cm.

Difference of corrected heights of survey points from the GRAV-GEOID2011 model are depicted in Fig. 5. The standard deviation of differences was ±0.036 m. The largest differences (negative values in NW) appear where the discrepancy between static and kinematic GNSS results was also the largest (up to 10 cm), thus the comparison is not very reliable in that particular area. Although, large deviations could also be due to prevailing Southern winds raising the sea level above average in the area, therefore contradicting the assumption of the ice surface reflecting the geoid surface.

Although differences on adjacent points are similar and the results seem promising they do not match so well with the differences in the anomaly fields (Fig. 4). For example in the East, with addition of ice gravity data, free air anomalies decreased and the height values in NE also decreased but in SE they increased. SE and NE were surveyed on different days which leads to suspect that the points in South could have a systematic error component in GNSS heights.

For now it seems like the GNSS positioning methods used are not accurate enough for direct geoid determination. Nevertheless, higher accuracy of height positioning on sea ice could allow for direct marine geoid determination using height data only.

7 Conclusions

Ice gravimetry is a viable alternative to ship- and airborne gravimetry in areas of shore-fast ice formation – with appropriate survey and data processing methods it is possible to achieve uncertainties of ±0.16 mGal. This is better than most gravity data currently available on land and satisfies easily the accuracy requirements needed for a 1 cm geoid determination.

One source of errors in collecting gravity data can be the positioning of survey points. A preferred method, where available, is RTK GNSS positioning using a VRS service.

Validation and comparison of ice gravimetry can be proceeded after reducing survey results to the same position in space. It was found that in the Väinameri Basin the Baltic Sea 1999 airborne gravity data agree reasonably well (±2 mGal) with new ice survey results.

The survey in Väinameri has revealed important information about the gravity anomaly field, confirming the existence of a local anomaly in the gravity anomaly field, specifying its magnitude and extents.

GNSS positioning on shore-fast ice could become an additional method of determining the shape of the marine geoid. However, the achieved uncertainty of ±0.15 m in height determination seems insufficient for the method to improve the marine geoid model in Väinameri to the same accuracy as gravity data allow.

Acknowledgements This study was funded by the Estonian Science Foundation grant ETF8749 and the Estonian Environmental Technology R&D Programme KESTA project ERMAS AR12052. Transport on ice was provided by the Estonian Environmental Board, access to the VRS RTK service via Trimble VRS Now Estonia by Geosoft Ltd. Mr. E. Grünthal and A. Bloom are thanked for assistance in field works. Conference participation of the prime author was supported by the European Social Funds' program DoRa. The three anonymous reviewers are thanked for their constructive comments.

References

Ågren J, Sjöberg LE (2015, in print) Investigation of gravity data requirements for a 5 mm-quasigeoid model over Sweden. In: Rizos C, Willis P (eds) Gravity, geoid and height systems GGHS2012. IAG Commission 2: Venice, Italy, 9–12 October 2014, IAG symposia proceedings, vol 141. Springer, Berlin/Heidelberg, pp 143–150

Ågren J, Engberg LE, Alm L, Dahlström F, Engfeldt A, Lidberg M (2015, in print) Improving the Swedish quasigeoid by gravity observations on the ice of lake Vänern. In: Rizos C, Willis P (eds) Gravity, geoid and height systems GGHS2012. IAG Commission 2: Venice, Italy, 9–12 October 2014, IAG symposia proceedings, vol 141. Springer, Berlin/Heidelberg, pp 171–178

Alm L, Engberg LE, Dahlström F, Ågren J, Engfeldt A, Lidberg M (2011) Relative gravity measurements on the ice of lake Vänern. In: Symposium of the IAG subcommission for Europe (EUREF), Chisinau, Moldova, 25–28 May 2011. www.euref.eu/symposia/2011Chisinau/p-04-p-Engberg.pdf

Denker H, Roland M (2005) Consistent marine gravity data set surrounding Europe. In: Sansò F (ed) A window on the future of geodesy. In: Proceedings of the IAG general assembly, vol 128, Sapporo, 30 June–11 July 2003. Springer, Berlin/Heidelberg, pp 248–253

Deng X, Featherstone WE, Hwang C, Berry PAM (2002) Estimation of contamination of ERS-2 and POSEIDON satellite radar altimetry close to the coasts of Australia. Mar Geod 25:249–271

Ellmann A (2005) Two deterministic and three stochastic modifications of stokes formula: a case study for the Baltic countries. J Geodesy 79:11–23

Ellmann A (2011) Downward continuation of airborne gravity data using high-resolution global geopotential models. In: Cygas D, Froehner KD (eds) Selected papers of the 8th international conference on environmental engineering, 19–20 May 2011. VGTU Press, Vilnius, Lithuania, pp 1315–1320

Ellmann A, All T, Oja T (2009) Towards unification of terrestrial gravity data sets in Estonia. Estonian J Earth Sci 58(4):229–245

Ellmann A, Oja T, Jürgenson H (2011) Application of space technologies to improve geoid and gravity field models over Estonia (in Estonian). Geodeet 41:22–25

Fernandes MJ, Bastos L, Antunes M (2003) Coastal satellite altimetry – methods for data recovery and validation. In: Tziavos IN (ed) Proceedings of the 3rd meeting of the international gravity and geoid commission (GG2002), Editions ZITI, pp 02–307

Forsberg R (2001) Development of a Nordic cm-geoid with basics of geoid determination. In: Harsson BG (ed) Nordic Geodesy towards the 21st century. Lecture notes for Autumn School, Nordic Geodetic Commission 2001:1. Statens Kartverk, Hønefoss, pp 67–88

Forsberg R, Olesen AV, Keller K, Moeller M, Gidskehaug A, Solheim D (2001) Airborne gravity and geoid surveys in the Arctic and Baltic seas. In: Proceedings of international symposium on kinematic systems in geodesy, geomatics and navigation (KIS-2001), Banff, pp 586–593

Hwang C, Hsiao Y-S, Shih H-C, Yang M, Chen K-H, Forsberg R, Olesen AV (2007) Geodetic and geophysical results from a Taiwan airborne gravity survey: data reduction and accuracy assessment. J Geophys Res 112:B04407

Kiviniemi A (1975) Measurements of wave motion in the ice surface. Technical Report 75:4, Finnish Geodetic Institute

Lehmuskoski P, Mäkinen J (1978) Gravity measurements on the ice of Bothnian Bay. Technical Report, Finnish Geodetic Institute

Liibusk A, Ellmann A, Kõuts T, Jürgenson H (2013) Precise hydrodynamic leveling by using pressure gauges. Mar Geod 36(2): 138–163

Märdla S, Oja T, Ellmann A, Jürgenson H (2015, in print) Modelling the influence of terraced landforms to the Earth's gravity field. In: Rizos C, Willis P (eds) Gravity, geoid and height systems GGHS2012. IAG Commission 2: Venice, Italy, 9–12 October 2014, IAG symposia proceedings, vol 141. Springer, Berlin/Heidelberg, pp. 157–162

Motao H, Zheng G, Guojun Z, Yongzhong O (1999) On the compensation of systematic errors in marine gravity measurements. Mar Geod 22(3):183–194

Oja T, Türk K, Bloom A, Sulaoja M (2010) Gravity surveys on the ice of the Gulf of Riga in 2010 (in Estonian). Technical Report, Reasearch Project ETF7356, pp 71

Oja T, Türk K, Ellmann A, Gruno A, Bloom A, Sulaoja M (2011) Relative gravity surveys on ice-covered water bodies. In: Cygas D, Froehner KD (eds) Selected papers of the 8th international conference on environmental engineering, 19–20 May 2011. VGTU Press, Vilnius, Lithuania, pp 1394–1401

Ugalde HA, L'Heureux E, Lachapelle R, Milkereit B (2006) Measuring gravity on ice: an example from Wanapitei Lake, Ontario, Canada. Geophysics 71(3):J23–J29

Estimation of the Geopotential Value W_0 for the Local Vertical Datum of Argentina Using EGM2008 and GPS/Levelling Data W_0^{LVD}

C. Tocho and G.S. Vergos

Abstract

The main purpose of this paper is to estimate the zero-height geopotential value for the Argentinean Local Vertical Datum (LVD). The methodology is based on the computation of the mean geopotential offset between the value $W_0 = 62{,}636{,}856.0\ m^2\ s^{-2}$, selected as reference in this study, and the unknown geopotential value of the LVD (W_0^{LVD}). This estimation is based on the combination of ellipsoidal heights, levelled heights (referring to the LVD), and some physical parameters derived from the EGM2008 model (namely, geopotential values, gravity values, and geoid undulations). This combination is performed following two approaches: The first one compares levelled heights and geopotential values derived from the EGM2008 model using the Least Squares method to increase the robustness of the adjustment, while the second one analyses the differences between GPS/Levelling and EGM2008 geoid undulations. Both approaches are evaluated at more than 540 benchmarks (BMs) belonging to the vertical network of Argentina. The numerical computations include in addition the assessment of possible correlations of the estimated zero-height geopotential value with the height of the included BMs. The results show that the best possible estimation at present is $62{,}636{,}853.9\ m^2\ s^{-2}$; however, it is necessary to improve these computations by including proper physical heights (instead of the levelled ones) and global gravity models containing GOCE data.

Keywords

Argentinean Local Vertical Datum • Zero-height geopotential value

1 Introduction

The Argentinean Vertical Datum is defined by the mean sea level at the tide gauge station in Mar del Plata, making it a local system that is not tied to a global vertical datum (Bolkas et al. 2012). From that initial point and through spirit and trigonometric levelling, the rest of the benchmarks are tied to the Local Vertical Datum (LVD) origin. Contrary, a global vertical datum is usually defined as a height reference (equipotential) surface for all continents and oceans. Indeed, the International Association of Geodesy (IAG) and its Global Geodetic Observing System (GGOS) aim, via the Working Group on Vertical Datum Standardization,, at the definition and realization of a global reference surface that allows the integration of the existing local vertical datums in a global one (Sanchez 2013). This topic has gained increased focus since the dedicated-gravity satellite missions, like the Gravity Recovery and Climate Experiment (GRACE) and the Gravity field and steady-state Ocean Circulation Explorer (GOCE), support the determination of vertical shifts (either

C. Tocho (✉)
Facultad de Ciencias Astronómicas y Geofísicas, Universidad Nacional de La Plata, Buenos Aires, Argentina
e-mail: ctocho@fcaglp.unlp.edu.ar

G.S. Vergos
Department of Geodesy and Surveying, School of Rural and Surveying Engineering, Aristotle University of Thessaloniki, Thessaloniki, Greece

© Springer International Publishing Switzerland 2015

C. Rizos, P. Willis (eds.), *IAG 150 Years*, International Association of Geodesy Symposia 143,
DOI 10.1007/1345_2015_32

as height or geopotential differences) of regional/national vertical datums with respect to one and the same equipotential surface realized globally (Hayden et al. 2013; Gruber et al. 2012).

As outlined in Grigoriadis et al. (2014), the various methods for the estimation of the zero-height geopotential value can be categorized in two main classes, the first one based on adjusting collocated GPS/Levelling and Global Geopotential Model (GGM) data and the second one employing gravity anomaly data over various LVD areas within a geodetic boundary value problem. In this paper, within the frame of the first methodology, we present two possible approaches for the estimation of the Argentinean LVD zero-level geopotential value W_0^{LVD} using EGM2008 (Pavlis et al. 2012) and GPS/Levelling data over a network of benchmarks (BMs). The first approach consists of an estimator based on a Least Squares (LS) adjustment of Helmert orthometric heights and EGM2008 over the entire GPS/Levelling network of Argentina. In this approach there is no need to use geoid heights in estimating the zero-level geopotential, so the inherent uncertainty for the topographic effects on geoid heights when evaluating them from a GGM is avoided. The second approach is based on the differences between geoid heights from GPS/Levelling measurements and those derived from EGM2008. The estimation of the mean offset can give us a direct link between the Argentinean local vertical datum and a certain W_0 value.

2 Methodology

Lets assume that physical orthometric heights H_i are available over a network of benchmarks (BMs) $i = \{1, 2, 3, \ldots, m\}$, derived by traditional spirit leveling, with their orthometric heights referring to the mean sea level realized by a tide-gauge station. The latter forms the origin of the LVD in the region under study, to which all orthometric heights refer to, with a, generally unknown, zero-level geopotential value W_0^{LVD}. An estimate of W_0^{LVD} can be achieved, following two approaches, when for the same BMs ellipsoidal heights h_i derived by GPS measurements, surface gravity g_i and the geopotential W_i computed from a GGM, are available.

2.1 Approach 1: Combination of Helmert Orthometric Heights, Geopotential Values and Surface Gravity Derived from EGM2008 Using a LS Adjustment

The first approach refers to an estimation of W_0^{LVD} using a LS adjustment scheme, based on the definition of Helmert orthometric heights. The orthometric height is defined by the geopotential number C_i divided by the mean value of gravity $\overline{g}_i$ taken along the plumbline between the LVD and the BM. The orthometric height system is hard to realize perfectly in practice, since the Earth's gravity acceleration at all points along the plumbline need to be known (Heiskanen and Moritz 1967, Eq. 4.4). This requires knowledge of gravity variations or mass-density distribution inside the topography. The orthometric heights are modeled as Helmert type of orthometric heights ($H_i^{Helmert}$), through the estimation of the mean gravity along the plumbline by the Poincaré-Prey reduction using the following equation (Heiskanen and Moritz 1967, pp. 163–167, Eq. 4.26).

$$H_i{}^{Helmert} = \frac{C_i^{LVD}}{\overline{g}_i{}^{Helmert}} = \frac{W_0^{LVD} - W_i}{\overline{g}_i{}^{Helmert}}, \tag{1}$$

where, C_i^{LVD} is the geopotential value, W_i is the actual gravity potential or geopotential and $\overline{g}_i^{Helmert}$ is the mean gravity value at each BM, respectively. Both W_i and $\overline{g}_i^{Helmert}$ can be computed from a GGM. W_i may be synthesized from the gravitational potential Vi, also obtained from the spherical harmonic series expansion plus the centrifugal potential Φi. In this way, Eq. (1) has only one unknown.

$$W_0^{LVD} = H_i{}^{Helmert}\overline{g}_i^{Helmert} + W_i. \tag{2}$$

It is possible to estimate the zero-height geopotential value $\hat{W}_0^{LVD}$ by means of a LS adjustment introducing as observation equation:

$$\widehat{W}_0^{LVD} = \frac{\sum_{i=1}^{m} p_i \left(\overline{g}_i^{Helmert} H_i^{Helmert} + W_i\right)}{\sum_{i=1}^{m} p_i}, \tag{3}$$

and satisfying the condition:

$$\sum_{i=1}^{m} p_i \delta W_i{}^2 = \min. \tag{4}$$

Here p_i represents the weighting of the input data and δW_i^2 is the residual of the unknown W_0^{LVD}.

$\overline{g}_i^{Helmert}$ is related to the gravity measured at the Earth's surface (g_i) according to Heiskanen and Moritz (1967, pp. 163–167).

$$\overline{g}_i^{Helmert} = g_i + 0.0424 H_i. \tag{5}$$

The estimation of g_i in Eq. (5) can be achieved either by available gravity observations at the BM location or can be reconstructed, like in this study, from gravity disturbances

directly computed through the spherical harmonic expansion series as (Filmer et al. 2010):

$$g_i = \gamma_i + T_r^i, \tag{6}$$

where T_r^i is the radial derivative of the disturbing potential. The normal gravity γ_i can be computed with the Eqs. (2.120)–(2.124) of Heiskanen and Moritz (1967).

One advantage of this method is that it does not depend on the evaluation of geoid heights and therefore it is not affected by geoid modelling errors and it is robust with respect to the uncertainties of surface gravity.

Equation (3) is evaluated, in this study, including levelled heights instead of Helmert orthometric heights, since the vertical networks of Argentina were adjusted without including gravity reductions. This omission could generate discrepancies up to several decimeters in comparison with properly computed physical heights.

2.2 Approach 2: Combination of GPS/Levelling with Geoid Undulations Derived from EGM2008

The second approach refers to an estimation of W_0^{LVD} using surface gravity and geoid heights computed from a GGM and GPS/Levelling data. The geopotential number is the potential difference between an equipotential surface (W_i) and a reference equipotential surface (W_0) along a plumb line. The geoid is the traditionally used reference geopotential surface; a local/regional geoid model realizes the origin of a local vertical datum (W_0^{LVD}), while a global geoid model realizes the origin of a global datum (W_0^{CVD}), for a local datum, we talk about a local geoid. In that way, the geopotential number for the same station i can be written as:

$$C^{CVD} = W_0^{CVD} - W_i, \tag{7}$$

$$C_i^{LVD} = W_0^{LVD} - W_i, \tag{8}$$

Consequently, the geopotential number difference at the benchmark can be expressed as:

$$\Delta C_i^{CVD/LVD} = W_0^{CVD} - W_0^{LVD}, \tag{9}$$

By averaging Eq. (9) over the benchmarks, we may determine the zero-height geopotential value for the LVD by:

$$\widehat{W}_0^{LVD} = \frac{\sum_{i=1}^{m} W_0^{LVD}}{m} = W_0^{CVD} - \frac{\sum_{i=1}^{m} \Delta C_i^{CVD/LVD}}{m}, \tag{10}$$

where $\Delta C_i^{CVD/LVD}$ is given by:

$$\Delta C_i^{CVD/LVD} = \left(h_i - H_i^{Helmert} - N_i - N_0\right) \overline{g}_i^{\,Helmert}. \tag{11}$$

N_o represents the contribution of the zero-degree harmonic term to the GGM geoid undulations with respect to a specific reference ellipsoid. In this work, this is computed using Eq. (2.182) of Heiskanen and Moritz (1967):

$$N_0 = \frac{GM - GM_0}{R\gamma} - \frac{W_0 - U_0}{\gamma}. \tag{12}$$

In Eq. (12), the parameters GM_o and U_o correspond to the geocentric gravitational constant of the reference ellipsoid and the normal gravity potential, respectively. The GRS80 ellipsoid is used as the reference ellipsoid for all numerical computations (Moritz 2000), while the Earth's geocentric gravitational constant GM and the gravity potential at the geoid W_o is set to $GM = 398{,}600.4415 \times 10^9$ m^3 s^{-2} and $W_o = 62{,}636{,}856.0$ m^2 s^{-2}, as given by Petit and Luzum (2010). The mean Earth radius R is taken equal to 6,378,136.3 m and the normal gravity γ at the surface of the ellipsoid is computed by the closed formula of Somigliana (Moritz 2000). As in the evaluation of Eq. (3), since the Helmert orthometric heights ($H_i^{Helmert}$) are not available, they are replaced by levelled heights in Eq. (11).

3 Data Availability and Numerical Results for W_0^{LVD}

3.1 Input Data

As already mentioned, the height values $H_i^{Helmert}$ in Eqs. (3) and (11) are replaced by pure levelled heights since no gravity reductions have been considered in the processing of the vertical network of Argentina. This network was installed and is maintained by the Instituto Geográfico Nacional (IGN) using spirit and trigonometric levelling techniques. The zero-height origin is realized by the mean sea level determined at the reference tide gauge Mar del Plata, with an unknown W_0^{LVD} value. Like in most of the countries, no luni-solar tide reduction has been applied to the levelling measurements and therefore, the Argentinean levelled heights are given in Mean Tide (MT) system. To improve the reliability of these computations, these levelled heights are transformed from MT to TF system following Ekman (1989).

$$H^{TF} = H^{MT} - 0.68\left(0.099 - 0.296 sin^2\varphi\right). \tag{13}$$

More details about the vertical data available in Argentina are presented by Tocho et al. (2014).

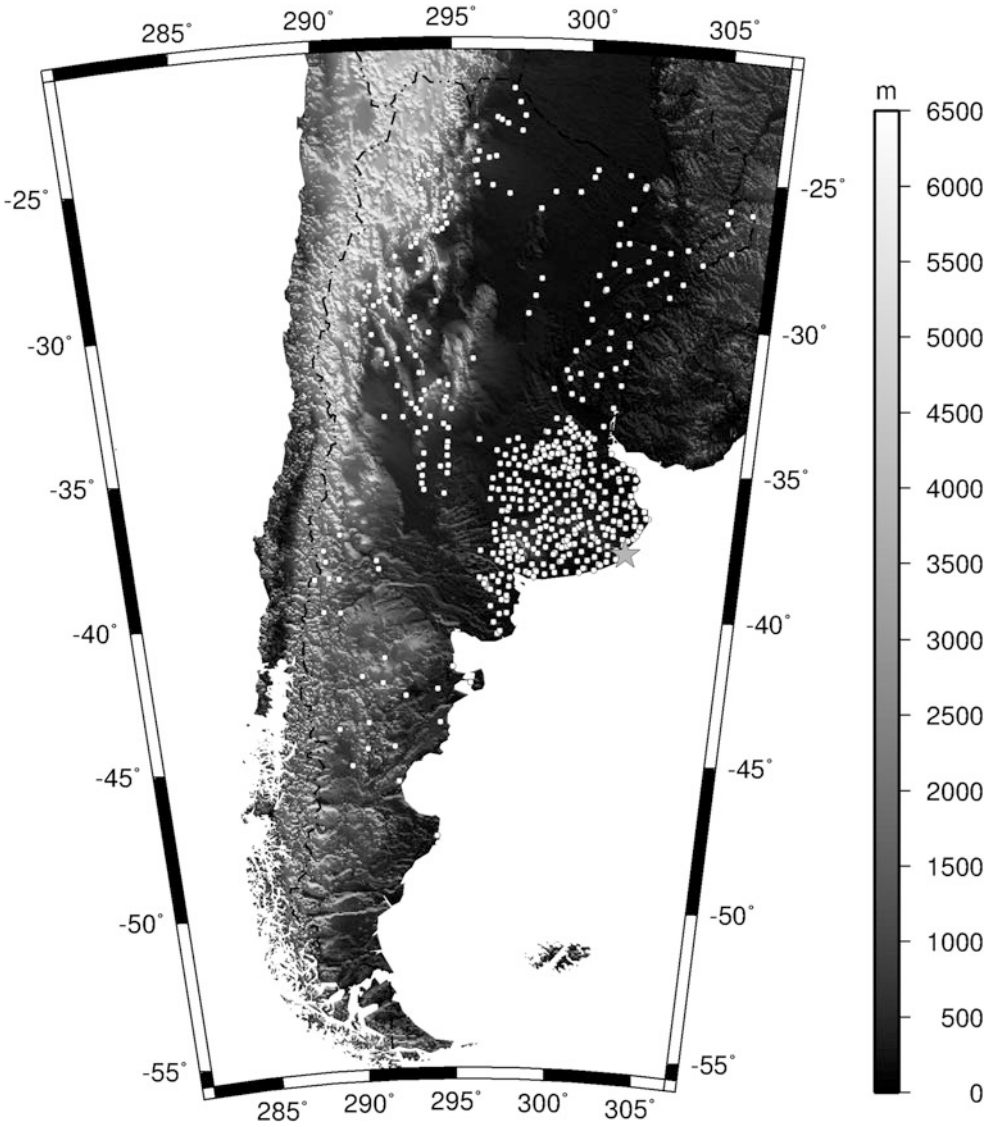

Fig. 1 Geographical distribution of GPS/Levelling BMs in Argentina

For the estimation of W_0^{LVD} with approach 1, the gravity potential values W_i have been computed from EGM2008 (Pavlis et al. 2012) complete to degree and order 2159 and in the TF system. For the computation of the gravitational part of W_i, the harmonic_synth_v02 program has been used and for its centrifugal potential part, the GPS derived spatial coordinates of each station have been used (Grigoriadis et al. 2014). The surface gravity at each BM station, necessary to compute Eq. (5), is also calculated with EGM2008 according to Eq. (6).

To apply Approach 2, we used the traditional technique based on the differences found between geoid heights from 542 GPS/Levelling measurements across Argentina and those derived from EGM2008 with the computation of *No* based on Eq. (12). Figure 1 depicts the distribution of the available GPS/Levelling BMs over Argentina.

3.2 Numerical Results

The results after applying both approaches are summarized in Table 1.

According to Approach 1, the mean geopotential offset between the W_0 value selected as the reference and the estimated $\hat{W}_0^{LVD}$ is about -3.2 m^2 s^{-2}; whereas, the estimation provided by the Approach 2 is -3.0 m^2 s^{-2}. Both results are very similar (only 0.2 m^2 s^{-2} of discrepancy). This is explainable since both approaches are combining the same input data: the same levelled heights, the same GPS positioning data (in form of geocentric coordinates for the first approach and in form of ellipsoidal heights for the second approach), and the same global geopotential model (in form of potential values for the first approach and in form of geoid undulations for the second approach). Indeed, the

Table 1 Estimation of the zero-height geopotential value for Argentina applying different approaches and different weighting functions

Approach 1	Weighting scheme	$\hat{W}_0^{LVD}$	Differences between weighting functions and the un-weighted solution	Number of points	Difference $\hat{W}_0^{LVD}$ with $W_0 = 62{,}636{,}856.0\ m^2\ s^{-2}$
	$p_i = 1$	$62{,}636{,}852.8 \pm 0.04$		542	−3.2
	$p_i = 1/(H_i)$	$62{,}636{,}854.0 \pm 0.02$	$p_i = 1/(H_i) - p_i = 1$ 1.2	542	−2.0
	$p_i = 1/\left(H_i^2\right)$	$62{,}636{,}854.4 \pm 0.01$	$p_i = 1/\left(H_i^2\right) - p_i = 1$ 1.6	542	−1.6
	$p_i = 1/\left(H_i^{0.5}\right)$	$62{,}636{,}853.5 \pm 0.03$	$p_i = 1/\left(H_i^{0.5}\right) - p_i = 1$ 0.7	542	−2.5
Approach 2		62,636,853.0		542	−3.0
Approach 2 − Approach 1 ($p_i = 1$)			0.2	542	−0.2

Unit: $m^2\ s^{-2}$

Table 2 Estimation of the zero-height geopotential value for Argentina using Approach 1 and different elevation threshold

Threshold	Number of points	$\hat{W}_0^{LVD}$	Difference $\hat{W}_0^{LVD}$ with $W_0 = 62{,}636{,}856.0\ m^2\ s^{-2}$
H < 500 m	464	$62{,}636{,}853.3 \pm 0.04$	−2.7
H < 1,500 m	527	$62{,}636{,}853.0 \pm 0.04$	−3.0
H < 3,500 m	542	$62{,}636{,}852.8 \pm 0.04$	−3.2
500 m < H < 1,500 m	63	$62{,}636{,}851.1 \pm 0.15$	−4.9
1,500 m < H < 3,500 m	15	$62{,}636{,}845.1 \pm 1.31$	−10.9

Unit: $[m^2\ s^{-2}]$

only difference between both approaches is that the first one makes the combination in terms of geopotential values, while the second one performs the combination in terms of heights (ellipsoidal, levelled, and geoid heights).

Since the levelled heights are not reduced by gravity effects, it is probably that benchmarks located at large heights (more than 500 m) introduce some biases in the results. In order to confirm this, a weighted LS adjustment is performed applying three different a priori weights, i.e., $p_i = 1/(H_i)$, $p_i = 1/\left(H_i^2\right)$ and $p_i = 1/\left(H_i^{0.5}\right)$. This experiment is carried out using the formulation of Approach 1 (Eqs. 4 and 6) only, but it is expected that Approach 2 produces similar values. The weighted $\hat{W}_0^{LVD}$ estimates present differences between 0.7 to 1.6 $m^2\ s^{-2}$ with respect to the un-weighted adjustment ($p_i = 1$) (Table 1). Assuming that these differences are caused by height-dependent systematic errors, two further adjustments are performed categorizing the available data into height-classes. The first adjustment includes all BMs below a certain elevation threshold (500, 1,500, and 3,500 m), while the second adjustment includes only the BMs available at a certain height-class (i.e., 500–1,500 m, 1,500–3,500 m). The obtained $\hat{W}_0^{LVD}$ estimates are shown in Table 2.

In Table 2, it can be seen that in both cases a strong correlation with height is evident for the estimated zero-height geopotential values. When using the BMs lower than 500 m, the estimate we get is reasonably close to the ones with the weighted scenarios (square root of height inverse and height inverse), since they differ by approximately −0.2 and −0.7 $m^2\ s^{-2}$, respectively. When BMs of higher elevation are used (<1,500 m), then an additional offset of 0.3 $m^2\ s^{-2}$ is added, while when all BMs are included (<3,500 m) then there is an additional offset of 0.2 $m^2\ s^{-2}$. This can be clearly seen, when investigating the determined $\hat{W}_0^{LVD}$ by the BMs available in each height-class solely. When using the BMs between 500 and 1,500 m, the determined $\hat{W}_0^{LVD}$ differs by −2.4 and −2.9 $m^2\ s^{-2}$ with the weighted ones. Finally, the BMs of high altitude (1,500 m < H_i < 3,500 m) contribute the most to the biased estimates, since the determined $\hat{W}_0^{LVD}$ differs as much as −8.4 and −8.9 $m^2\ s^{-2}$ with the weighted ones. This can be also seen in Fig. 2, where we plot the height residuals e_i for the un-weighted solution against height. The height residuals are computed by the following equation:

$$e_i = H_i^{Helmert} - \frac{\widehat{W}_0^{LVD} - W_i}{\overline{g}_i}. \tag{14}$$

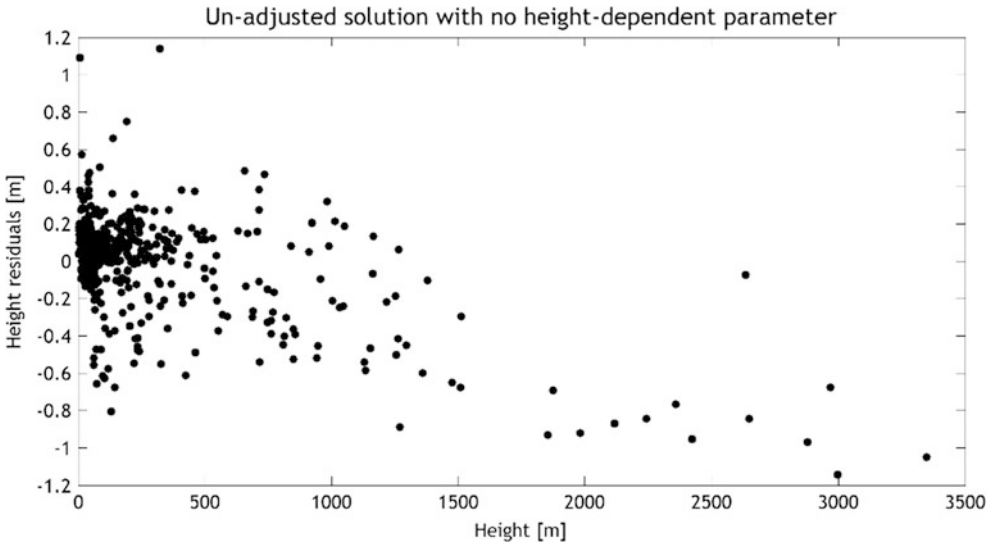

Fig. 2 Heights residuals of the un-weighted solution with no height dependent parameter

Table 3 Estimation of the zero-height geopotential value for Argentina including a height dependent parameter into the data adjustment

Weighting scheme	$\widehat{W}_0^{LVD}$ ($m^2\ s^{-2}$)	$\widehat{\lambda}$	Differences between weighting functions and the un-weighted solution	Number of points	Difference $\hat{W}_0^{LVD}$ with $W_0 = 62{,}636{,}856.0\ m^2\ s^{-2}$.
$p_i = 1$	62,636,853.7 ± 0.05	−3.343E-04 ± 9.600E-06		542	−2.3
$p_i = 1/(H_i)$	62,636,854.2 ± 0.31	−5.300E-04 ± 2.897E-04	$p_i = 1/(H_i) - p_i = 1$	542	−1.8
$p_i = 1/\left(H_i^2\right)$	62,636,854.5 ± 0.91	1.218E-03 ± 4.886E-03	$p_i = 1/\left(H_i^2\right) - p_i = 1$ 0.8	542	−1.5
$p_i = 1/\left(H_i^{0.5}\right)$	62,636,853.9 ± 0.14	−3.654E-04 ± 5.491E-05	$p_i = 1/\left(H_i^{0.5}\right) - p_i = 1$ 0.2	542	−2.1

From Fig. 2, it becomes clear that especially the BMs at high altitude refer to a "different" LVD since their scatter is minimal though around a mean value of ∼−0.8 m.

In order to investigate further this correlation with height and come to a more robust estimate for the zero-level geopotential value, a revised model considering the height-correlated data errors has been investigated by including a height-dependent parameter into the data adjustment as:

$$H_i^{Helmert} = \frac{W_0^{LVD} - W_i}{\overline{g}_i} + \lambda H_i^{Helmert}. \tag{15}$$

The height-dependent parameter λ *in* Eq. (15) describes the linear part of the height-dependent systematic errors. Including the determination of the parameter λ, the height residuals can be computed using:

$$e_i = H_i^{Helmert} - \frac{\widehat{W}_0^{LVD} - W_i}{\overline{g}_i} - \widehat{\lambda} H_i^{Helmert}. \tag{16}$$

Weighted adjustments have been performed with the results being summarized in Table 3, where both the estimated height-dependent parameter λ and the final $\hat{W}_0^{LVD}$ are reported. From the estimated values it becomes apparent that the results are now more robust, since the differences between the un-weighted ($p_i = 1$) and the weighted solutions are smaller, the only exception is the solution with $p_i = 1/\left(H_i^2\right)$ which will be discussed further. The rest of the weighted estimates differ with the un-weighted solution by 0.2 and 0.5 $m^2\ s^{-2}$ only, while the estimated parameters are in good agreement as well.

Table 4 summarizes the statistics of the height residuals from the LS adjustment without and with the height dependent parameter λ Eqs. (15) and (16), respectively). The standard deviation (std) of the height residual without λ is found at the 0.26 m level.

Figures 3 and 4 depict the variation of the estimated $\hat{W}_0^{LVD}$ with height for all weight scenarios, and the differences of the estimated $\hat{W}_0^{LVD}$ from the $p_i = 1/(H_i)$, $p_i = 1/\left(H_i^2\right)$ and

Table 4 Statistics of the height residuals from the LS adjustment: Unit: [m]

e_i	Min	Max	Mean	std
No parameter estimation				
$p_i = 1$	−1.14	1.14	0.000	± 0.26
Un-weighted				
With height dependent parameter estimation λ				
$p_i = 1$	−0.85	1.15	0.00	± 0.21
$p_i = 1/(H_i)$	−0.87	1.18	0.00	± 0.23
$p_i = 1/\left(H_i^2\right)$	−0.82	1.46	−0.11	± 0.34
$p_i = 1/\left(H_i^{0.5}\right)$	−0.86	1.15	−0.00	± 0.21

$p_i = 1/\left(H_i^{0.5}\right)$ solutions with the un-weighted one. Finally, Fig. 5 depicts the derived height residuals for the available BMs after the adjustment. In all figures, some problems with the weighted solution with $p_i = 1/\left(H_i^2\right)$ can be seen. It is noticeable that while the other adjustment solutions manage to improve the residuals for the BMs at high-terrain, the solution with $p_i = 1/\left(H_i^2\right)$ introduces a linear trend in the opposite direction compared to the mean residuals where no linear trend parameter has been estimated. This means that both a bias and a trend are introduced which can be further evidenced from the height residuals presented in Table 4.

After the introduction of the linear height dependent parameter in the observation equations, one would expect that the adjusted residuals would have a zero mean. Indeed, this is the case for all estimates apart from the one with $p_i = 1/\left(H_i^2\right)$ where the mean of the residuals is at the −0.11 m level. This is not a surprising result since the particular weight factor is rather harsh and significantly down-weights most of the available BMs, thus blocking them from the adjustment procedure. In a sense, when the $p_i = 1/\left(H_i^2\right)$ is employed, the high-elevation BMs do not participate in the adjustment at all, hence they have large residuals. But, the over-confidence put on the low-land points does not manage to provide reasonable adjusted residuals heights for the high-elevation BMs. From Fig. 3 it can be seen that the BMs with elevations between 1,000 and 1,800 m provide *Wo* values very close to the estimated ones. Nevertheless, the use of $p_i = 1/\left(H_i^2\right)$ cancels entirely their contribution in the final solution.

Therefore, this weight scheme makes the separation of the $\widehat{\lambda}$ and $\hat{W}_0^{LVD}$ parameters practically impossible. In a practical sense, any of the three robust estimates un-weighted and weighted with $p_i = 1/(H_i)$ and $p_i = 1/\left(H_i^{0.5}\right)$ can be used to provide the $\hat{W}_0^{LVD}$ for Argentina since their differences are within their precision level. To further validate that, if we compare the estimated zero-level geopotential value with Approach 2, we can see that it is closer to the un-weighted solution of Approach 1, without the linear height-dependent parameter (see Table 1, difference of 0.2 $m^2\ s^{-2}$ only). Moreover it differs by 0.7, 1.2 and 0.9 $m^2\ s^{-2}$ with the estimates presented in Table 4. In order to get a more realistic picture of the accuracy of the results we have to consider the bias introduced by EGM2008 itself, through the commission error over spatial wavelengths that exceed the extent of our test network. Given that our area spans 15° × 25°, the

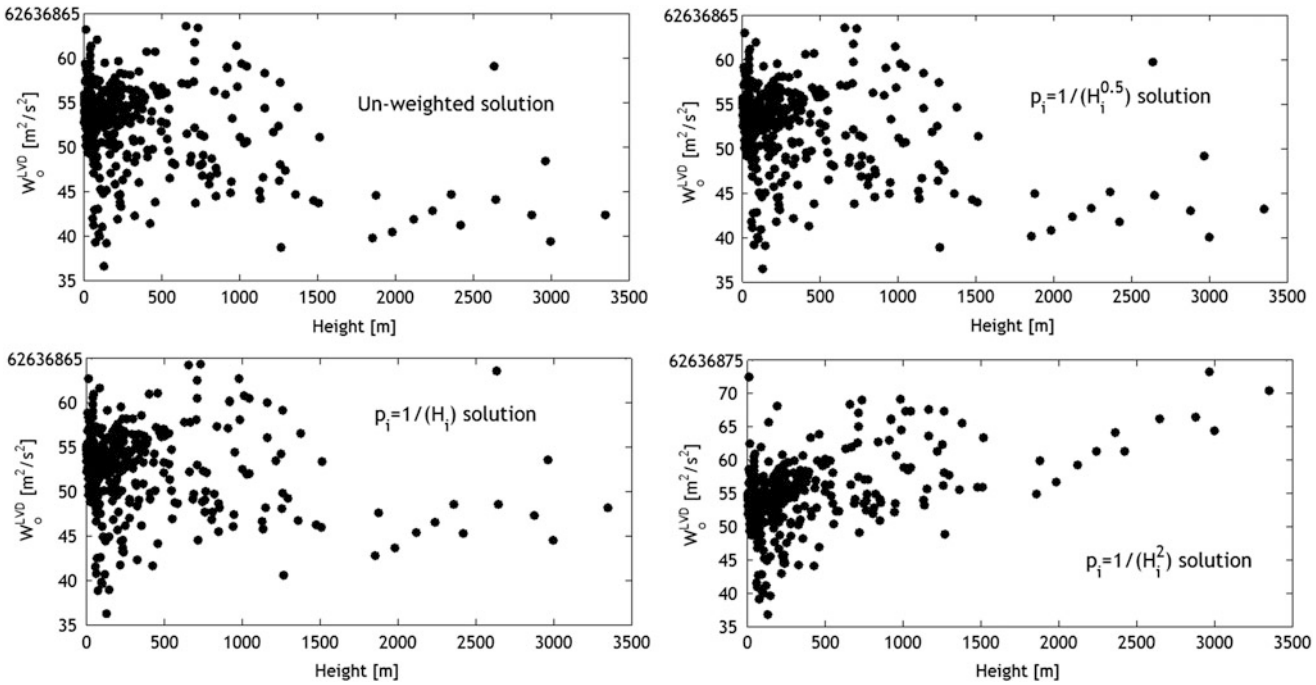

Fig. 3 W_0^{LVD} variations from the un-weighted and the weighted LS adjustment (with height dependent parameter estimation)

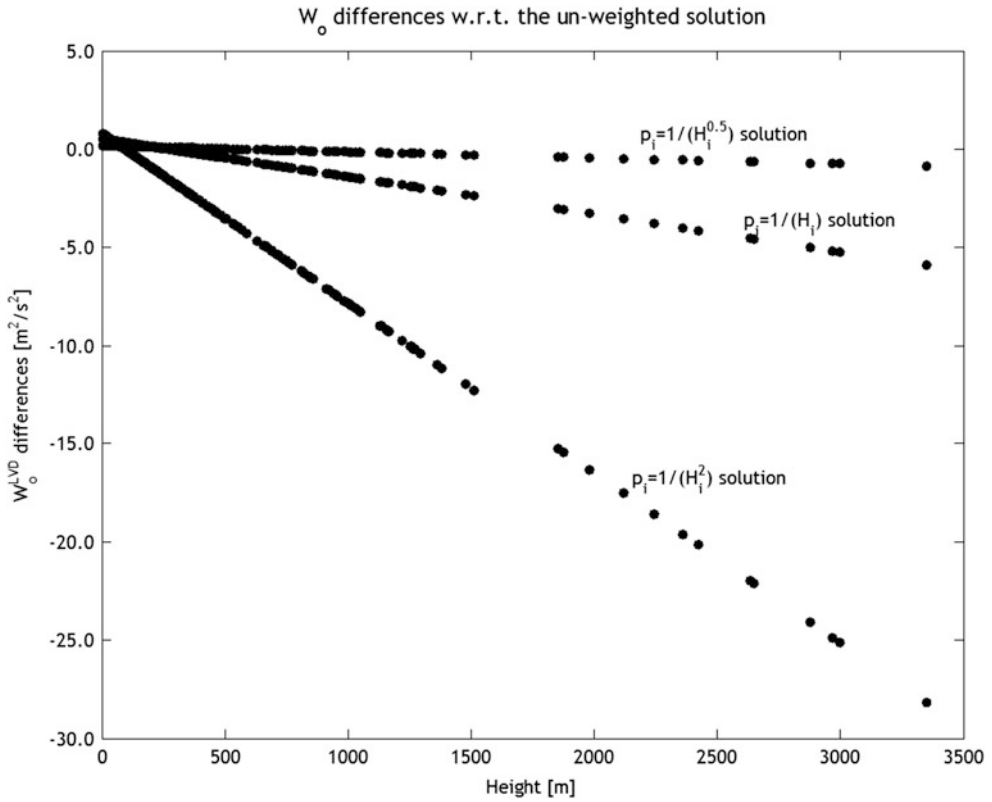

Fig. 4 Differences between the W_0^{LVD} variations between the un-weighted and the weighted LS adjustment (height dependent parameter estimation)

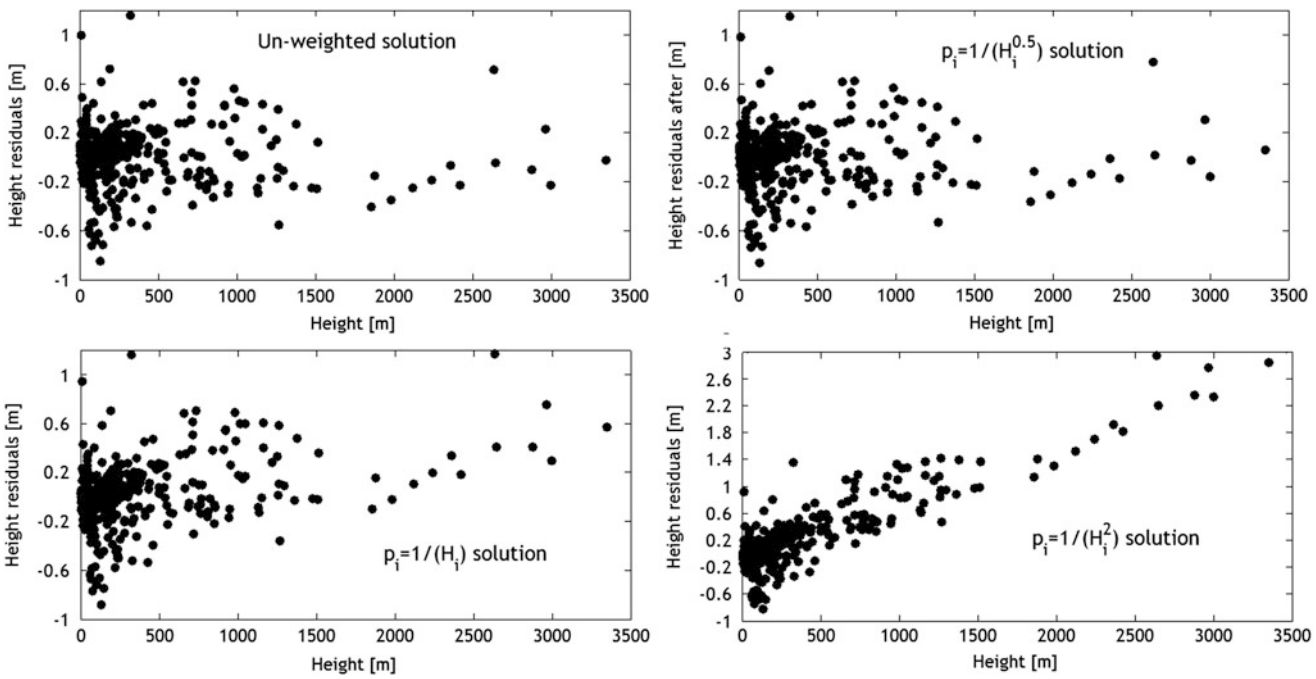

Fig. 5 Residual heights computed from the un-weighted and the weighted LS adjustment (height dependent parameter estimation)

maximum degree of EGM2008 not represented in this test region is selected equal to 10 (∼1,980 full-wavelength), which corresponds to a commission error of 2.8 cm. This error should be added to the formal prediction errors (through error propagation) of the zero-level geopotential values presented in Tables 2 and 3 to get a more realistic picture of the achieved accuracy. Also, given the maximum degree of EGM2008, the omission error is of the order of 2.0 cm following e.g., the Tscherning and Rapp degree variance model (Vergos et al. 2014). So that error should be accounted for in the final estimates and can be probably reduced if proper the contribution of topography is taken into account, e.g., through an RTM model, in the $\hat{W}_0^{LVD}$ estimation.

A final interesting point comes from the comparison of the std of the height residuals with and without the linear height dependent parameter. The original std of the differences between the GPS/Levelling geoid heights and EGM2008 (to its n_{max}) is at the 0.24 m level. When the linear height-dependent parameter is not included in the adjustment, then the std of the mean residuals is at the 0.26 m, so that their difference of 2 cm m is very close to the EGM2008 commission error (2.8 cm) in the $\hat{W}_0^{LVD}$ estimation. On the other hand, when the $\widehat{\lambda}$ and $\hat{W}_0^{LVD}$ parameters are estimated simultaneously, the std of the height residuals drops to the ∼0.21 m level for the most reliable adjustment models $p_i = 1$, $p_i = 1/(H_i)$ and $p_i = 1/\left(H_i^{0.5}\right)$. The latter is another indication that the so-determined $\hat{W}_0^{LVD}$ estimates are indeed robust, since the EGM2008 performance is improved by ∼3 cm. In order to minimize the influence of the EGM2008 commission error to the $\hat{W}_0^{LVD}$ estimation, improved GOCE-based GGMs should and will be investigated in the future.

4 Conclusions

A preliminary determination of W_0 for Argentina is carried out considering a terrestrial network of BMs with collocated levelled heights H and ellipsoidal heights h. A strong correlation with height is evident for BMs of higher elevations a height dependent parameter is introduced in the adjustment for $\hat{W}_0^{LVD}$ estimation. The best estimates achieved are those with $p_i = 1/(H_i)$ and $p_i = 1/\left(H_i^{0.5}\right)$ with the height dependent parameter (Table 4), meanwhile the estimation with $p_i = 1/\left(H_i^2\right)$ is problematic, given the biased residual heights. Any of these two solutions can be used in fact to provide the zero-level geopotential for Argentina, while if a choice would have to be made, then that would be the one with $p_i = 1/\left(H_i^{0.5}\right)$, i.e., 62,636,853.9 $m^2\ s^{-2}$.

Further investigations and the possibility of repeating this study using better input data, like proper physical heights, the original leveling traverses and GOCE/GRACE based GGMs, are still needed to improve the LVD analysis over Argentina.

References

Bolkas D, Fotopoulos G, Sideris MG (2012) Referencing regional geoid-based vertical datums to national tide gauge networks. J Geod Sci 2(4):363–369, http://dx.doi.org/10.2478/v10156-011-0050-7

Ekman M (1989) Impacts of geodynamic phenomena on systems for height and gravity. Bull Géod 63(3):281–296, http://dx.doi.org/10.1007/BF02520477

Filmer MS, Featherstone WE, Kuhn M (2010) The effect of EGM2008-based normal, normal-orthometric and Helmert orthometric height systems on the Australian levelling network. J Geod 84(8):501–513, http://dx.doi.org/10.1007/s00190-010-0388-0

Grigoriadis VN, Kotsakis C, Tziavos IN, Vergos GS (2014) Estimation of the geopotential value Wo for the local vertical datum of continental Greece using EGM08 and GPS/leveling data. International symposium on gravity, geoid and height Systems (GGHS 2012), IAG Symp, vol 141

Gruber T, Gerlach C, Haagmans R (2012) Intercontinental height datum connection with GOCE and GPS-levelling data. J Geod Sci 2(4):270–280, http://dx.doi.org/10.2478/v10156-012-0001-y

Hayden T, Rangelova E, Sideris MG, Véronneau M (2013) Evaluation of W_0 in Canada using tide gauges and GOCE gravity field models. J Geod Sci 2(4):290–301. doi:10.2478/v10156-012-0003-9

Heiskanen WA, Moritz H (1967) Physical geodesy. W.H. Freeman and Company, San Francisco

Moritz H (2000) Geodetic reference system 1980. J Geod 74(1):128–133, http://dx.doi.org/10.1007/s001900050278

Pavlis NK, Holmes SA, Kenyon SC, Factor JK (2012) The development and evaluation of the earth gravitational model 2008 (EGM2008). J Geophys Res 117, B04406, http://dx.doi.org/10.1029/2011JB008916

Petit G, Luzum B (eds) (2010) IERS conventions 2010. IERS Technical Note 36. Verlag des Bundesamts für Kartographie und Geodäsie, Frankfurt a. M, p 179, ISBN 3-89888-989-6

Sanchez L (2013) Towards a vertical datum standardization under the umbrella of global geodetic observing system. J Geod Sci 2(4):325–342. doi:10.2478/v10156-012-0002-x

Tocho C, Vergos GS, Pacino MC (2014) Evaluation of the latest GOCE/GRACE derived global geopotential models over Argentina with collocated GPS/Leveling observations. In: Marti U (ed) Gravity, geoid and height systems, International Association of Geodesy Symposia, vol 141. Springer, Switzerland, pp 75–83. doi:10.1007/978-3-319-10837-7_10

Vergos GS, Grigoriadis VN, Tziavos IN, Kotsakis C (2014) Evaluation of GOCE/GRACE global geopotential models over Greece with collocated GPS/Levelling observations and local gravity data. In: Marti U (ed) Gravity, geoid and height systems, International Association of Geodesy Symposia, vol 141. Springer, Switzerland, pp 85–92. doi:10.1007/978-3-319-10837-7_11

A Feasibility Study on the Unification of the Italian Height Systems Using GNSS-Leveling Data and Global Satellite Gravity Models

R. Barzaghi, D. Carrion, M. Reguzzoni, and G. Venuti

Abstract

Regional height systems are usually referred to the mean sea level at a reference tide gauge. As the mean sea level gravity potential changes from place to place, regional systems refer to different equipotential surfaces and the establishment of a unified datum requires the determination of one bias per region. This is what is referred to as the height datum problem. The possibility to solve this problem by exploiting the nowadays available satellite gravity mission data, the high resolution global gravity potential models, GNSS heights, as well as leveling and gravity data has been explored. A solution strategy and a first error budget have been presented in Gatti et al. (J Geod 87(1):15–22, 2012), showing that an accuracy of about 5 cm can be globally achieved in the bias computation. In the present work, this strategy, with refinements in the error modeling, is applied to the Italian case, where different height systems are used for the mainland and Sicily and Sardinia islands.

Keywords

Height datum problem • Global gravity models • GNSS-leveling • GOCE • GRACE

1 Introduction

The availability of satellite gravity data together with accurate high resolution global gravity models have reopened the possibility to estimate regional height system biases with respect to a common global reference. Different solutions have been explored, for instance by Kotsakis et al. (2012) and Rummel (2012) to solve the problem either on a global or on a local scale. We started from a proposal in Gatti et al. (2012) and performed a first experiment in Italy, where three different height systems are present. The unknown bias of each region reflects in the normal heights of the region itself (Rummel and Teunissen 1988). Height anomalies obtained by differencing GNSS heights and normal heights contain the bias as well. The difference between these biased height anomalies and the corresponding values derived from an unbiased anomalous potential can be therefore modeled as the unknown bias plus errors. When these errors are kept low by an ad hoc combination of satellite-only and high resolution global gravity models, a sufficiently accurate (i.e. with a standard deviation below 5 cm) estimate of the unknowns can be obtained. Although not yet available, Italian normal heights of the main leveling network will be computed in the near future also thanks to a cooperation between the Istituto Geografico Militare (IGM), which is the official institution for creation and maintenance of the Italian geodetic reference network, and the Politecnico di Milano. In particular, normal heights of the GNSS national network will be derived with the corresponding height anomalies, thus allowing for the unification of the Italian height systems. In this work we report the results of a first experiment in this direction, mainly devoted to establish the feasibility of the procedure in terms of accuracy of the solution, when all the available information about the observation errors

R. Barzaghi • D. Carrion • M. Reguzzoni
DICA, Politecnico di Milano, Piazza Leonardo da Vinci 32, Milan, Italy

G. Venuti (✉)
DICA, Politecnico di Milano - Laboratorio di Geomatica del Polo territoriale di Como, Via Valleggio 11, Como, Italy
e-mail: giovanna.venuti@polimi.it

© Springer International Publishing Switzerland 2015

C. Rizos, P. Willis (eds.), *IAG 150 Years*, International Association of Geodesy Symposia 143,
DOI 10.1007/1345_2015_35

is exploited. Moreover, we obtained a preliminary estimate by substituting the needed, but not yet computed normal heights, with the currently official heights, derived from the adjustment of leveling data, without applying any correction accounting for gravity. Well aware that those heights can differ from the required normal ones up to some decimeters, we took into account this systematic error with an increased a priori standard deviation of the leveling observations. We will repeat the same evaluation once the proper observables will be computed and released, but we still consider useful the results of this first attempt.

2 The Height Datum Problem and the Adopted Solution

Global satellite gravity potential models can be profitably used in the solution of the height datum problem. The problem is that of determining the biases between the potential of the equipotential surfaces chosen as regional height references $W = W_0^j$ and that of the geoid $W = W_0$:

$$\delta W^j = W_0 - W_0^j = U_0 - W_0^j \tag{1}$$

where W_0^j is the actual potential of the mean sea surface at the reference tide gauge P_0^j for the region j, W_0 is equal to the normal gravity potential U_0 on the reference ellipsoid. This latter potential is in turn defined by the values of the angular velocity of the Earth ω, its mass M, the ellipsoid semi-major axis a and eccentricity e, which are all well known quantities. The regional bias δW^j in potential reflects in normal heights derived from spirit leveling and gravity observations (cf. Appendix). Height anomalies derived by comparing the nowadays available unbiased ellipsoidal heights h (here unbiased stands for not affected by the potential bias), with the biased normal heights $\tilde{h}^{*j}$ of Eq. (12) will be biased as well:

$$\tilde{\zeta}^j = h - \tilde{h}^{*j} = \zeta - \frac{\delta W^j}{\overline{\gamma}_{P_0^j}}. \tag{2}$$

By exploiting Bruns's formula, for a generic point P of the region j, and recalling Eq. (12), one can write:

$$\tilde{\zeta}^j = \frac{T}{\overline{\gamma}} - h_0^{*j} \tag{3}$$

where $\overline{\gamma}$ is the average value of the normal gravity between the ellipsoid and the telluroid, along the normal to the ellipsoid through P. Provided that an unbiased, sufficiently accurate value of the anomalous potential T is available, Eq. (3) can be used to estimate the regional biases h_0^{*j}. Note that a large uncertainty, say 10 m, in the knowledge of the normal height has a negligible effect on the evaluation of the average values of normal gravity $\overline{\gamma}$. Gatti et al. (2012) proved that a proper combination of the satellite-only global model GOCO (Pail et al. 2010) and the high resolution global model EGM2008 (Pavlis et al. 2012) can give such an unbiased, sufficiently accurate anomalous potential, producing an overall accuracy of 5 cm on the estimated biases. More specifically, one can use satellite-only models up to a degree L, and high resolution models just for the highest degree from $L+1$ to their maximum degree H. While satellite-only models are not biased, high resolution models, computed also from gravity anomalies derived from leveling and gravity measurements, are affected by the regional height biases. Nevertheless, the indirect (i.e. through the gravity anomaly Δg) effects of those biases in the high degree coefficients can be disregarded (Gatti et al. 2012). The boundary degree L in the combination of the low resolution satellite-only model and the high resolution one has to be tuned case-by-case, mainly depending on the size of the involved regions.

3 The Least Squares Estimation: Observation Equations and Observation Error Models

The observation equation in Eq. (3), for a point P belonging to the region j, can be rewritten in the following way:

$$\tilde{\zeta}^j - \frac{T^L + T^H}{\overline{\gamma}} = -h_0^{*j} + \nu \tag{4}$$

where T^L is the prediction of the anomalous potential at the point P derived from the satellite gravity model up to degree L, T^H is the prediction derived from EGM2008 from degree $L+1$ up to degree H and ν is the observation noise. For N_j points in J regions a linear system of $N_j \times J$ equations and J unknowns can be solved by a least squares adjustment, once the observation error covariance matrix C_ν is defined. This matrix has to account for the errors in the ellipsoidal heights derived from GNSS through the covariance matrix C_h, the errors in the normal heights derived from leveling and gravity measurements through $C_{\tilde{h}^*}$, the commission errors of the satellite-only gravity model up to the degree L through C_{T^L} and those in the high resolution model from degree $L+1$ up to degree H through C_{T^H}. It results:

$$C_\nu = C_h + C_{\tilde{h}^*} + C_{T^L} + C_{T^H}. \tag{5}$$

4 The Italian Case

Italy has three different height systems, one for the peninsula and two for Sicily and Sardinia, the tide gauges being in Genova, Catania and Cagliari respectively, for a total

of three unknown biases. To estimate those biases, a set of 1,068 points with known GNSS ellipsoidal heights and leveling derived heights was considered. Among them, 43 points are in Sicily, 48 in Sardinia and the remaining 977 in the mainland. The heights derived from leveling measurements were obtained by a least squares adjustment of the observations without any correction accounting for gravity effects (Betti et al. 2013). GNSS heights are referred to the ETRF89 reference frame, epoch 2006. All the data are made available to us by IGM. The evaluation of normal and orthometric corrections is in progress, also thanks to a cooperation between IGM and the Politecnico di Milano. At the available leveling points, the value of the gravity potential was computed starting from the GOCO-03S satellite-only gravity global model and EGM2008 spherical harmonic coefficients. The GOCO-03S model basically combines the ITG-Bonn GRACE solution with the time-wise GOCE one (release R3, that is the second to the last solution based on 1 year and a half GOCE data) (Pail et al. 2011; Mayer-Gürr 2006); the coefficients were downloaded from the website of the International Center for Global Earth Models (ICGEM). Moreover, we could use the GOCO-03S order-wise block diagonal error covariance matrix, which practically brings the same information as the full error covariance matrix (Gerlach and Fecher 2012). As for EGM2008 spherical harmonic coefficients, the error coefficient variances and a global grid of local geoid error variances are available. Consistently with GNSS data, the coefficients of the two global models are tide-free. As for leveling data, they are referred to the mean sea level at the three tide gauges of Genova, Catania and Cagliari.

5 Reference Frame Transformations

GNSS coordinates, GOCO-03S and EGM2008 data are referred to different frames with different epochs. Therefore, before combining those observations, transformations to a common frame and epoch must be performed. In order to evaluate the impact of those transformations in the GNSS observations, we started by updating the given coordinates to the most recent frame of the GOCE model. The Italian GNSS data are given in ETRF89, epoch 2006, while GOCE data are in ITRF2008, with a not specified epoch between 2010 and 2011. Both transformations from ETRF89-2006 to ITRF2008-2010 and from ETRF89-2006 to ITRF2008-2011 were performed in three steps:

- from ETRF89-2006 to ITRF89-2006 using the EUREF online tool 'ETRS89/ITRS TRANSFORMATION' (http://www.epncb.oma.be/_productsservices/coord_trans/);
- from ITRF89-2006 to ITRF2008-2006 using the transformations and parameters provided by the International Earth Rotation and Reference Systems Service (IERS) (http://itrf.ensg.ign.fr/doc_ITRF/Transfo-ITRF2008_ITRFs.txt);
- from ITRF2008-2006 to ITRF2008 epochs 2010 and 2011, using the mean values of the Italian stations velocities again provided by IERS (http://itrf.ensg.ign.fr/ITRF_solutions/2008/doc/ITRF2008_GNSS.SSC.txt). In particular, the stations of Medicina, Genova, Torino I, Cagliari, Matera, Padova and Perugia were taken into account.

It resulted a change in the planimetric coordinates of about 50 cm and about 1 cm in height. In order to evaluate the impact of such differences in our observations we compared the biased height anomalies $\tilde{\zeta} = h - \tilde{h}^*$ computed from GNSS heights referred to the original reference frame ETRF89 at epoch 2006 with the anomalies computed from GNSS heights referred to ITRF2008 at epochs 2010 and 2011. The statistics of the differences are reported in Table 1. The differences between the two considered epochs are negligible and we expect that this is true also when considering the larger time span of GRACE data. Analogous transformations for the EGM2008 data cannot be applied because the time reference of its gravity database is not available.

Table 1 Statistics of the differences between biased height anomalies computed with the ETRF89 (epoch 2006) GNSS data and with the ITRF2008 epoch 2010 (first row) and epoch 2011 (second row)

Epoch	Mean (cm)	Std (cm)	Min (cm)	Max (cm)
2010	−0.85	0.44	−2.00	0.60
2011	−0.86	0.45	−2.00	0.60

6 Error Budget and the Choice of the Boundary Degree L

In order to set a proper boundary degree in the combination of GOCO-03S and EGM2008 for the solution of the height datum problem, the biases accuracy was evaluated from the available error models. We assumed the set of differences between GNSS and leveling heights to have an uncorrelated noise with a standard deviation $\sigma_{\tilde{\zeta}} = 1$ cm, that is

$$C_{\tilde{\zeta}} = C_h + C_{\tilde{h}^*} = \sigma_{\tilde{\zeta}}^2 \times I \tag{6}$$

where I is the identity matrix. The error covariance matrix C_{T^L} of the set of potential values $\{T^L\}$ predicted in the GNSS-leveling points from GOCO-03S was obtained by propagation from the given order-wise block diagonal error covariance matrix. The covariance matrix C_{T^H} of the set of potential values $\{T^H\}$, computed in the same points from EGM2008, was obtained by propagation from the coefficient error variances properly rescaled accordingly to the geographical map of local geoid errors (Gilardoni et al.

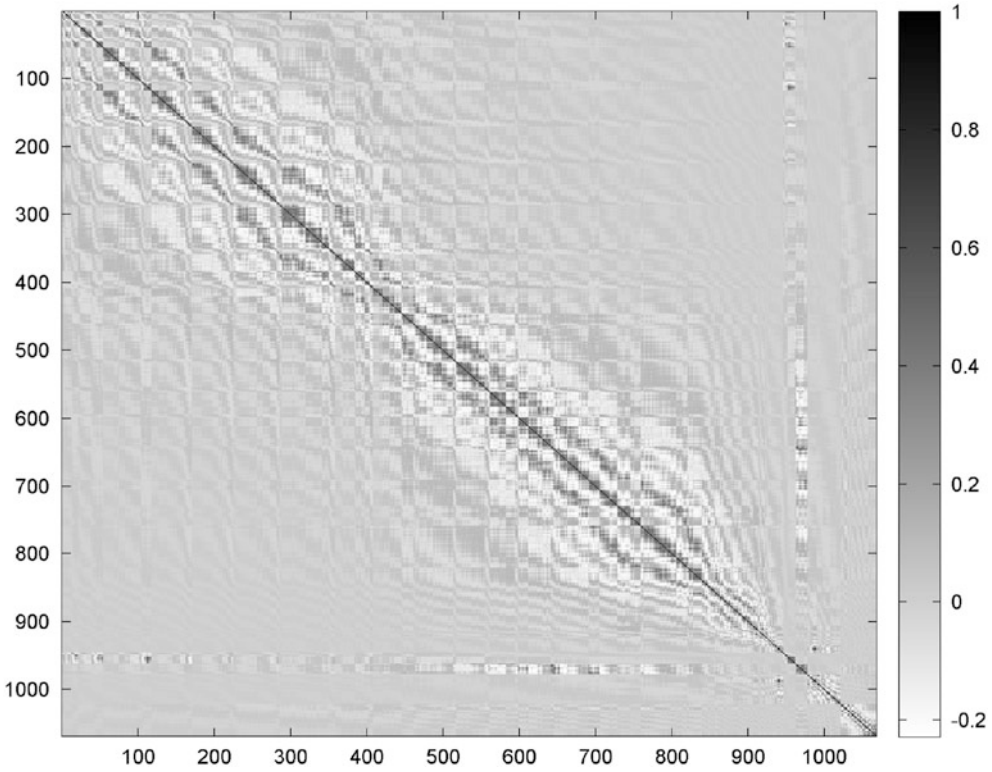

Fig. 1 Correlation matrix of the total error in the case of L = 250. The first 977 observations are mainland points, then the 43 Sicily points and finally the 48 Sardinia points

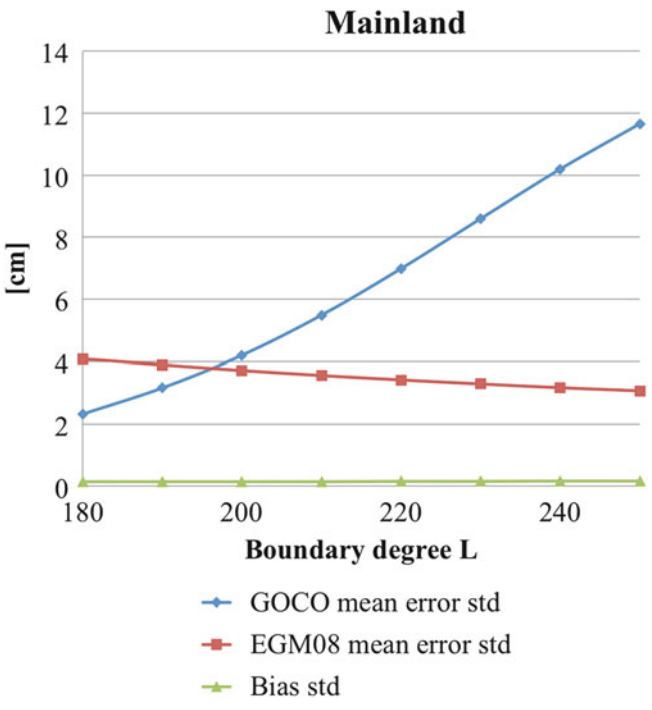

Fig. 2 GOCO-03S and EGM2008 mean error standard deviation versus the boundary degree L and the corresponding accuracy of the mainland bias

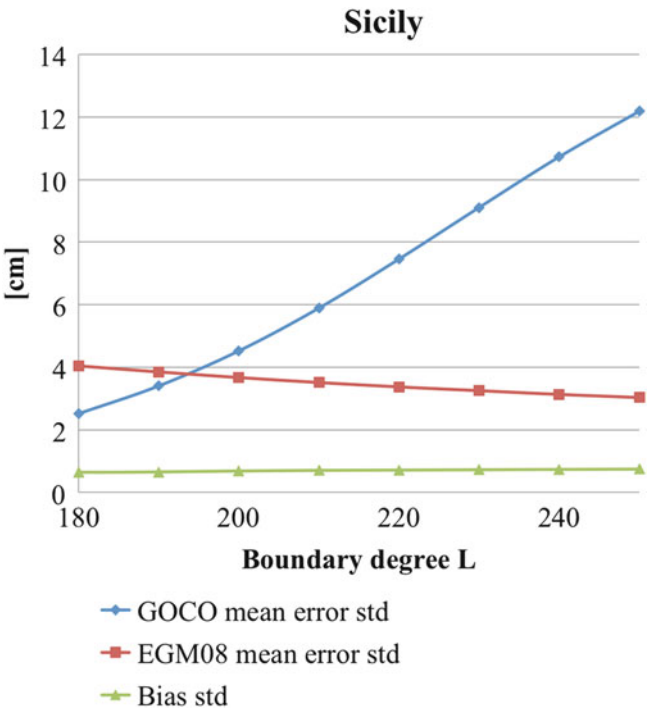

Fig. 3 GOCO-03S and EGM2008 mean error standard deviation versus the boundary degree L and the corresponding accuracy of the Sicily bias

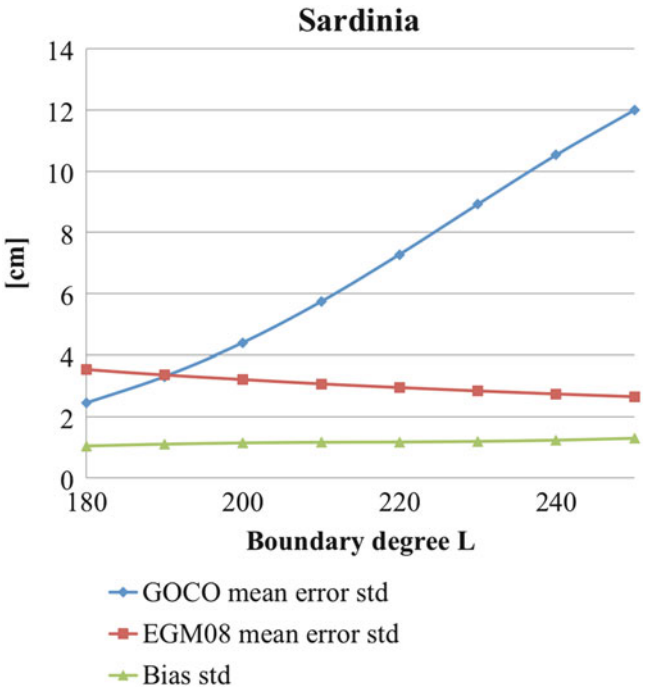

Fig. 4 GOCO-03S and EGM2008 mean error standard deviation versus the boundary degree L and the corresponding accuracy of the Sardinia bias

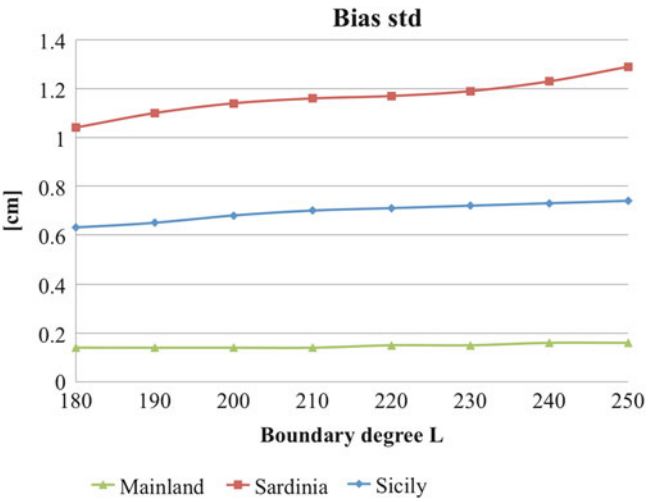

Fig. 5 Mainland, Sicily and Sardinia bias accuracies versus the boundary degree L

2013). The resulting error covariance matrix of Eq. (5) is shown in Fig. 1, for $L = 250$. In Figs. 2, 3 and 4 the GOCO-03S and EGM2008 mean error standard deviations are plotted as functions of L together with the resulting bias standard deviations, for mainland, Sicily and Sardinia respectively. As it can be better appreciated in Fig. 5, where the standard deviations of the three biases are compared, different values of L do not reflect in significant variations of the parameter accuracies. Therefore, we preferred to use GOCO-03S to its highest degree $L = 250$, in order to reduce the height datum secondary effects in EGM2008 (cf. Sect. 2).

Table 2 Estimated biases and corresponding standard deviations for different GNSS-leveling observation error model

$\sigma_{\tilde{\zeta}} = 1$ cm	Mainland	Sicily	Sardinia
$\hat{h}_0^{*j}$ [cm]	82.73	73.25	95.54
$\hat{\sigma}_{\hat{h}_0^{*j}}$ [cm]	0.59	2.75	4.92
$\hat{\sigma}_0^2 = 12.78$, H_0 rejected			
$\sigma_{\tilde{\zeta}} = 5$ cm	Mainland	Sicily	Sardinia
$\hat{h}_0^{*j}$ [cm]	78.98	68.72	97.11
$\hat{\sigma}_{\hat{h}_0^{*j}}$ [cm]	0.51	2.62	3.17
$\hat{\sigma}_0^2 = 3.32$, H_0 rejected			
$\sigma_{\tilde{\zeta}} = 10$ cm	Mainland	Sicily	Sardinia
$\hat{h}_0^{*j}$ [cm]	77.50	67.78	97.84
$\hat{\sigma}_{\hat{h}_0^{*j}}$ [cm]	0.51	2.56	2.77
$\hat{\sigma}_0^2 = 1.37$, H_0 rejected			
$\sigma_{\tilde{\zeta}} = 11$ cm	Mainland	Sicily	Sardinia
$\hat{h}_0^{*j}$ [cm]	77.34	67.59	97.88
$\hat{\sigma}_{\hat{h}_0^{*j}}$ [cm]	0.52	2.57	2.74
$\hat{\sigma}_0^2 = 1.20$, H_0 rejected			
$\sigma_{\tilde{\zeta}} = 12$ cm	Mainland	Sicily	Sardinia
$\hat{h}_0^{*j}$ [cm]	77.22	67.40	97.90
$\hat{\sigma}_{\hat{h}_0^{*j}}$ [cm]	0.52	2.57	2.72
$\hat{\sigma}_0^2 = 1.07$, H_0 accepted			

7 Bias Estimation and Analysis of the Least Squares Residuals

The Italian biases of mainland, Sicily and Sardinia were finally computed via least squares. A first model assessment was then performed by analyzing the adjustment residuals. More specifically, a χ^2 test was done at a significance level of 5%, to verify the null hypothesis $H_0 : \sigma_0^2 = 1$ (Koch 1987). The test was mainly devoted to the evaluation of the observation stochastic model. In particular, we are confident on the global gravity model covariances, but we know that uncorrected leveling derived heights, completely disregarding the effects of gravity, introduce systematic errors. These errors can reach some decimeters in zones like the Alps or the Calabrian Arc, where gravity anomalies undergo to high variations. Although a deeper analysis is required, these values partly justifies the following result. We performed different adjustments of the same observations, each time adopting a different a priori height anomaly accuracy $\sigma_{\tilde{\zeta}}$, looking for that value for which the χ^2 test verifies the null hypothesis. The result of such an approach is that an accuracy of 12 cm can be accepted. A summary of the trials is reported in Table 2. The residuals of the least squares adjustment corresponding to the last trial are reported in Fig. 6.

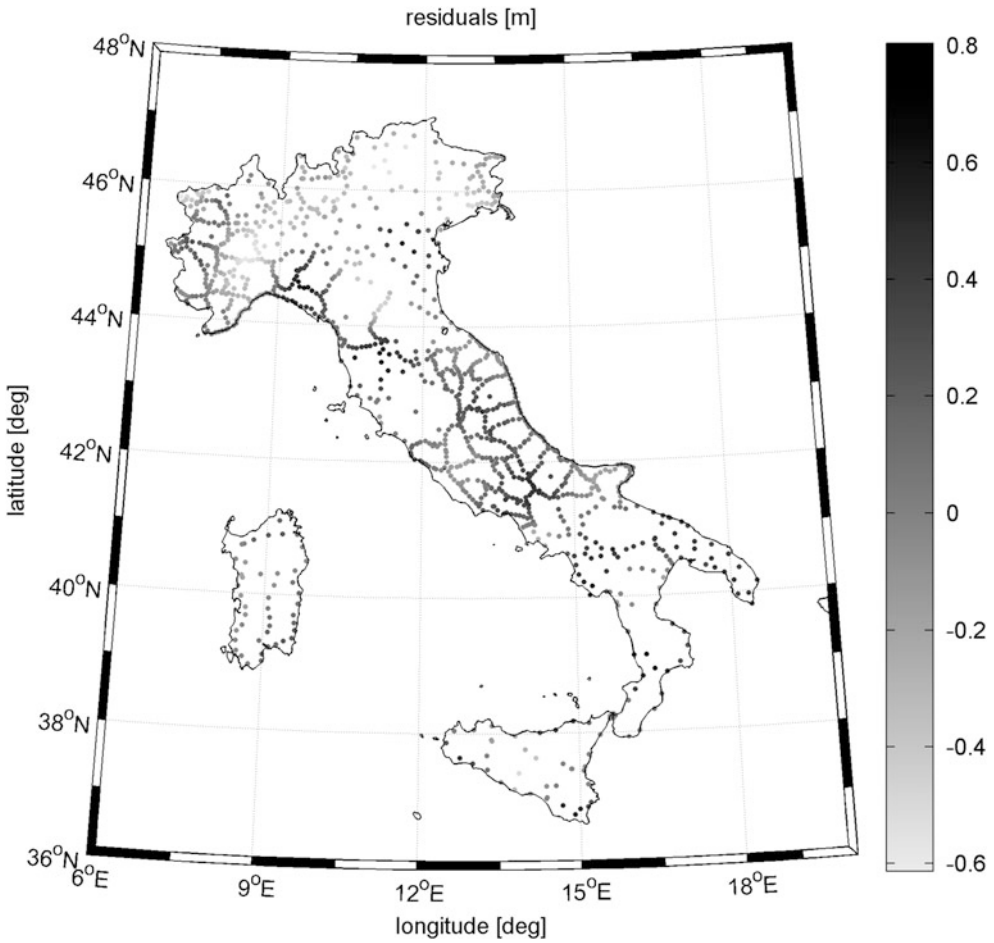

Fig. 6 Estimated residuals in meters of the least squares adjustment, $\sigma_{\tilde{\zeta}} = 12\,\text{cm}$

8 Discussion

A first experiment in the solution of the Italian height datum problem was performed. The main goal was to understand the feasibility of the adopted solution strategy in terms of expected accuracies of the estimates for the best possible error model currently available. The difference between biased and unbiased height anomalies in one height system region can be modeled as the sum of the unknown bias plus a random error, containing from one side the GNSS and leveling/gravity derived height accuracies, from the other side the two global model commission errors. By assuming an accuracy level of 1 cm in the GNSS/leveling data and by using the best error models nowadays available to evaluate the global model commission error covariances, it resulted an accuracy of the estimated biases below 1.5 cm, the highest error being in Sardinia for its smallest extension. This proves the feasibility of such an approach. In other words, the combination of GOCO-03S up to its highest degree $L = 250$ and EGM2008 for the remaining higher degrees proves to have a sufficient resolution to describe the unbiased height anomalies (the omission error is sufficiently low); moreover, the effects of the biases entering EGM2008 through the free air gravity anomalies depending on biased heights can be disregarded. This approach clearly depends on the availability of accurate GNSS and normal heights. The actual Italian height values, in fact, leave high systematic errors in the observation residuals. The poor result obtained in this first estimate could be due also to local errors of the global models especially in areas like the Alps or the Calabrian Arc. In any event a partial confirmation of the proposed approach is given by the difference of biases between Sicily and mainland. This has been estimated by us to have a value of 9.81 cm, with a standard deviation of 2.57 cm. A similar value, namely 14.1 cm (personal communication), was independently derived by IGM, by means of a trigonometric connection across the Messina Strait.

Appendix: Determination of Normal Heights from Spirit Leveling and Gravity Observations

We shortly review here two possible ways for the determination of regional normal heights from gravity and leveling observations. In one case we least squares adjust potential differences of height benchmarks derived from observed gravity g and leveling increments δL [see Heiskanen and Moritz 1967, Eqs. (4–3), page 161]:

$$\Delta W_{AB} = -\sum_{A}^{B} g\delta L \tag{7}$$

by fixing the potential of the reference regional tide gauge to U_0. This introduces a bias in the adjusted potential values equal to the difference between the unknown actual potential of the reference point and U_0:

$$\tilde{W}^j = W - \delta W^j. \tag{8}$$

From these estimated potentials, biased normal heights will be derived as follows:

$$\tilde{h}^{*j} = \frac{\tilde{C}}{\overline{\gamma}} = \frac{W_0 - \tilde{W}^j}{\overline{\gamma}} = \frac{U_0 - W}{\overline{\gamma}} + \frac{\delta W^j}{\overline{\gamma}} = h^* + \frac{\delta W^j}{\overline{\gamma}} \tag{9}$$

where $\tilde{C}$ are the biased geopotential numbers, and $\overline{\gamma}$ is average normal gravity between the reference ellipsoid and the telluroid along the normal to the ellipsoid through the considered benchmark.

In the other case we least squares adjust leveling increments properly corrected (Betti et al. 2013)

$$\Delta L_{AB} + NC = h^*_B - h^*_A, \tag{10}$$

deriving benchmark normal heights with respect to the biased normal height of the reference point P_0^j. This height, which we set equal to zero, by assuming that the point is on the geoid, is actually proportional to the potential bias:

$$h_0^{*j} = \frac{U_0 - W_0^j}{\overline{\gamma}_{P_0^j}} = \frac{U_0 - W_0}{\overline{\gamma}_{P_0^j}} + \frac{\delta W_0^j}{\overline{\gamma}_{P_0^j}} = \frac{\delta W_0^j}{\overline{\gamma}_{P_0^j}}. \tag{11}$$

It follows that the benchmark normal heights are all biased by the normal height of the reference tide gauge:

$$\tilde{h}^{*j} = h^* + \frac{\delta W_0^j}{\overline{\gamma}_{P_0^j}} = h^* + h_0^{*j}. \tag{12}$$

By comparing Eqs. (9) and (12) an inconsistency appears: in the first case the bias δW^j does not reflect in a constant bias in normal heights, while in the second case it does. In the first case, in fact, δW^j is divided by $\overline{\gamma}$, which depends of the point where the height is computed. On the contrary, in the second case, the bias in potential is divided by the average normal gravity of the reference point and the ratio is therefore a constant bias in height. This discrepancy can be attributed to the different approximations done in both formulas and it should be better investigated. Nonetheless, the term $\frac{\delta W^j}{\overline{\gamma}}$ undergoes to variations that are smaller than 1 mm even for heights of 2,000 m, thus making the two solutions practically equivalent. It is clear that the variation of $\overline{\gamma}$ does not compromise the solution of the height datum problem as it was presented here: the least squares system, in fact, can be easily modified considering as unknowns only the involved potential biases δW_0^j and correspondingly modifying the least squares coefficient matrix including the known $\overline{\gamma}$ coefficients.

Acknowledgements The authors would like to thank Roland Pail and Christian Gerlach for kindly providing us the GOCO-03S order-wise block diagonal error covariance matrices.

References

Betti B, Carrion D, Sacerdote F, Venuti G (2013) The observation equation of spirit leveling in Molodensky's context. Presented at the VIII Hotine Marussi symposium in honor of Fernando Sansò, 17–21 June 2013. IAG symposia series. Accepted for publication

Gatti A, Reguzzoni M, Sansò F, Venuti G (2012) The height datum problem and the role of satellite gravity models. J Geod 87(1):15–22. doi:10.1007/s00190-012-0574-3

Gerlach C, Fecher T (2012) Approximations of the GOCE error variance-covariance matrix for least-squares estimation of height datum offsets. J Geod Sci 2(4):247–256. doi:10.2478/v10156-011-0049-0

Gilardoni M, Reguzzoni M, Sampietro D, Sansò F (2013) Combining EGM2008 with GOCE gravity models. Bollettino di Geofisica Teorica ed Applicata. 54(4):285–302. doi:10.4430/bgta0107 (in print)

Heiskanen WA, Moritz H (1967) Physical geodesy. W.H. Freeman, San Francisco

Koch KR (1987) Parameter estimation and hypothesis testing in linear models. Springer, Berlin

Kotsakis C, Katsambalos K, Ampatzidis D (2012) Estimation of the zero-height geopotential level W_0^{LVD} in a local vertical datum from the inversion of co-located GPS, leveling and geoid heights: a case study in the Hellenic islands. J Geod 86(6):423–439. doi:10.1007/s00190-011-0530-7

Mayer-Gürr T (2006) Gravitationsfeldbestimmung aus der Analyse kurzer Bahnbögen am Beispiel der Satellitenmissionen CHAMP und GRACE. Ph.D. Thesis, University of Bonn, Bonn

Pail R, Goiginger H, Schuh W-D, Höck E, Brockmann JM, Fecher T, Gruber T, Mayer-Gürr T, Kusche J, Jäggi A, Rieser D (2010) Combined satellite gravity field model GOCO01S derived from GOCE

and GRACE. Geophys Res Lett 37(20) [American Geophysical Union]. doi:10.1029/2010GL044906

Pail R, Bruinsma S, Migliaccio F, Förste C, Goiginger H, Schuh W-D, Höck E, Reguzzoni M, Brockmann JM, Abrikosov O, Veicherts M, Fecher T, Mayrhofer R, Krasbutter I, Sansò F, Tscherning CC (2011) First GOCE gravity field models derived by three different approaches. J Geod 85(11):819–843. doi:10.1007/s00190-011-0467-x

Pavlis NA, Holmes SA, Kenyon SC, Factor JK, (2012) The development and evaluation of the Earth Gravitational Model 2008 (EGM2008). J Geophys Res (Solid Earth) 117(B16):4406. doi:10.1029/2011JB008916

Rummel R (2012) Height unification using GOCE. J Geod Sci 2(4):355–362. doi:10.2478/v10156-011-0047-2.

Rummel R, Teunissen P (1988) Height datum definition, height datum connection and the role of the geodetic boundary value problem. Bull Géod 62(4):477–498

Analysis of the Discrepancies Between the Vertical Reference Frames of Argentina and Brazil

M.E. Gomez, R.A.D. Pereira, V.G. Ferreira, D. Del Cogliano, R.T. Luz, S.R.C. de Freitas, C. Farias, R. Perdomo, C. Tocho, E. Lauria, and S. Cimbaro

Abstract

The vertical reference frames for Argentina and Brazil present discrepancies due to their different datums and realizations. Thus, since 2008, we have started a series of activities with the aim of unifying the Argentine and Brazilian national vertical networks (NVNs). To achieve this goal, we have connected the two NVNs at three border points by using the geodetic levelling approach. Additionally, the gravity field approach was also applied, based on a suitable representation of the geoid by considering the Earth Gravitational Model (EGM2008) in its full resolution. In this regard, 1266 co-located Global Positioning System (GPS) and levelling benchmarks regularly distributed over Argentina (612) and Brazil (654) were considered. The geodetic levelling approach shows an offset value of 54 cm, which implies that the Argentine vertical reference frame is above that of the Brazilian vertical reference frame. However, the result of the gravimetric approach shows an offset of 57 cm, which implies a difference of approximately 3 cm between both methods. Hence, since Brazil and Argentina represent a significant part of South America, the solution to the datum problem between both countries could point towards a common vertical reference frame for the Atlantic side.

Keywords

Argentine and Brazilian levelling networks • Geodetic levelling approach • Gravity field approach • Vertical datum connection

1 Introduction

1.1 Background

There is an agreement among South American countries to monitor and integrate the National Vertical Networks (NVNs) according to the Geocentric Reference System for the Americas' (SIRGAS) statements (Fortes 1998). A unified vertical datum in South America is important for monitoring common problems related to the environment, engineering, natural resources, land management and cadastral surveying (Ferreira and de Freitas 2011). As part of a bilateral research

M.E. Gomez (✉) • D. Del Cogliano • C. Farias • R. Perdomo • C. Tocho
Facultad de Ciencias Astronómicas y Geofísicas, Universidad Nacional de La Plata, La Plata, Argentina
e-mail: megomez@fcaglp.unlp.edu.ar

R.A.D. Pereira
Federal University of Pelotas, Pelotas, Brazil

V.G. Ferreira
School of Earth Sciences and Engineering, Hohai University, Nanjing, China

R.T. Luz
Brazilian Institute of Geography and Statistics, Rio de Janeiro, Brazil

S.R.C. de Freitas
Department of Geomatics, Federal University of Paraná, Curitiba, Brazil

E. Lauria • S. Cimbaro
Instituto Geográfico Nacional, Buenos Aires, Argentina

© Springer International Publishing Switzerland 2015

C. Rizos, P. Willis (eds.), *IAG 150 Years*, International Association of Geodesy Symposia 143,
DOI 10.1007/1345_2015_75

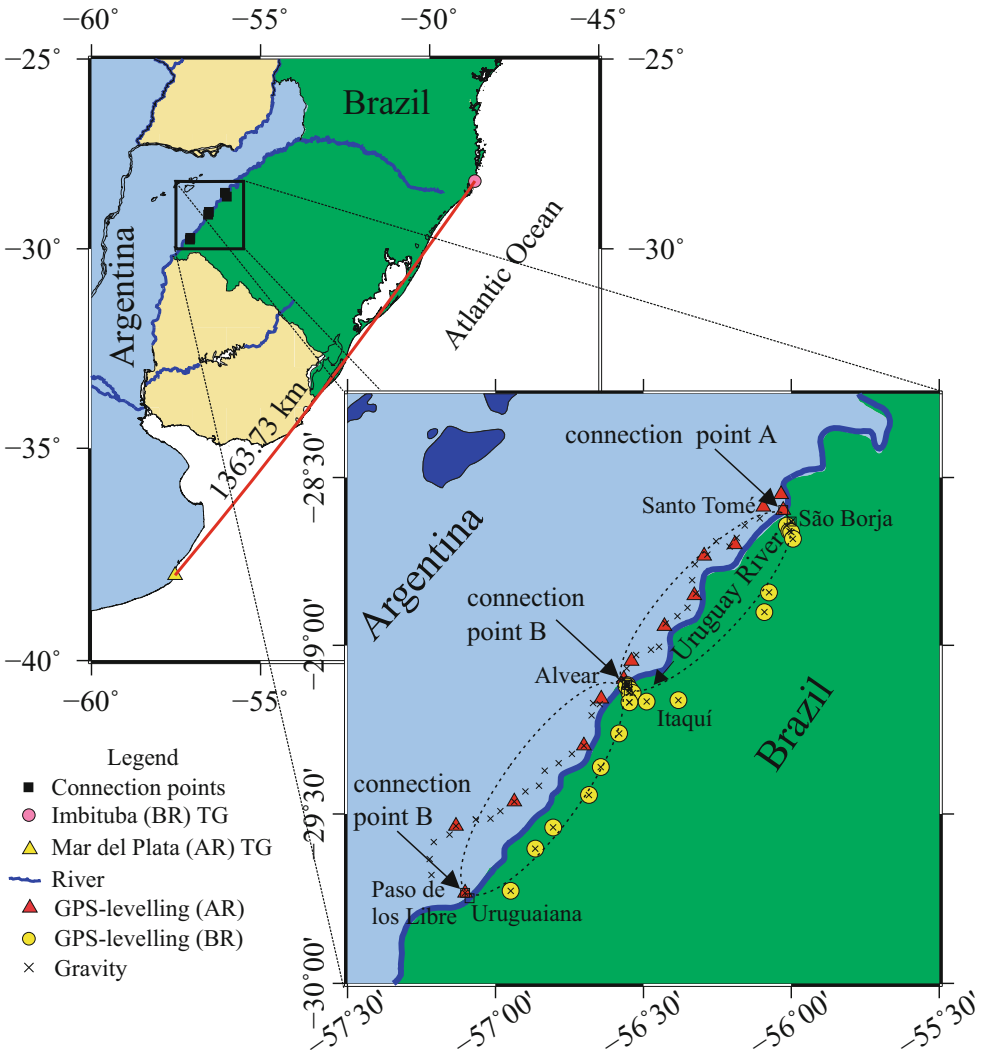

Fig. 1 The study region located in North-east Argentina and Southern Brazil. The *enclosed rectangle* shows the study area with the three connection points (A, B, C) between the two National vertical networks. Additionally, it shows the distance between the two tide gauges (TG) at Mar del Plata (Argentina) and Imbituba (Brazil) and the location of the levelling circuits (*dashed lines*) and the GPS-levelling stations

project between Argentina and Brazil, the Federal University of Parana (UFPR), Brazil and the National University of La Plata (UNLP), Argentina have started a series of activities that aim to connect the Argentine and Brazilian vertical reference frames. The main purpose of this paper is to present the actions to assess the vertical offset between the Argentine and Brazilian NVNs at three points along the border between both countries (Fig. 1).

One of the early studies relating to the connection between the vertical datums by Heck and Rummel (1990) suggested three approaches to connecting independent vertical reference frames: the oceanographic levelling approach, the geodetic levelling approach, and the gravity field approach. As a first attempt to connect the Argentine and Brazilian NVNs, we considered in this study only the geodetic levelling and the gravity field approaches. We carried out precise geodetic levelling as well as Global Positioning System (GPS) surveying on available benchmarks (BMs) in the study region. Additionally, we considered the geoid model derived from Earth Gravitational Model 2008's (EGM2008) spherical harmonic coefficients (Pavlis et al. 2012) and the GPS-levelling dataset for both countries. The particular choice of the EGM2008 was mainly due to its high resolution (5 arc-min). Hence, we were able to determine the offsets by two independent methods, namely, the geodetic levelling and gravity field approaches.

1.2 Argentine and Brazilian National Vertical Networks

Levelling activities in Argentina started in 1899, initially using Riachuelo tide gauge (TG) at the Río de la Plata estuary as reference. In 1923, the mean sea level at Mar del Plata TG

was adopted as the datum of the Argentine height system. In 2012 a readjustment using levelling differences and observed gravity values of the Argentine NVN was carried out by the *Instituto Geográfico Nacional* (National Geographic Institute of Argentina; IGN) to determine geopotential numbers (Cimbaro et al. 2013, "personal communication"). However, this adjustment was not ready at the time of the realization of the present work.

The Brazilian height network was started as an effort by the *Instituto Brasileiro de Geografia e Estatística* (Brazilian Institute of Geography and Statistics; IBGE) in 1945. Two different vertical datums were established resulting in two separate networks: Santana to the north of the Amazon River estuary and Imbituba spreading for almost the whole country (Montecino and de Freitas 2014). The origin at Imbituba TG (Fig. 1) was defined in 1957 after nine years of sea-level observations with the mean value centred in 1953. The NVN related to it was subject to eight sequential adjustments in order to include new levelling lines. However, only three global adjustments were performed in 1959, 1993 and 2011. The heights derived from the 1993 and 2011 adjustment realizations were considered in this work.

It is important to mention that both NVNs were realized using the normal-orthometric height system; that is, only reductions based on the normal gravity field were used before the adjustment of the levelling networks. The normal-orthometric heights are not able to support height determination with the full physical meaning derived from the ellipsoidal heights obtained by the GPS (Ihde and Sánchez 2005). Despite this, we considered the normal-orthometric heights as an approximation to orthometric heights. Further discussion about the differences between normal-orthometric, normal and orthometric height systems is provided in Filmer et al. (2010). Since the tidal corrections were not applied to the levelling observations in Argentina and Brazil, the normal-orthometric heights were considered to refer to the mean tide system in this particular study.

2 Methodology and Dataset

2.1 Levelling

We considered four levelling lines along Uruguay River (Fig. 1). Doing so, we connected the Argentine (along the west bank of the river) with the Brazilian (east bank) levelling lines at three border points. In this regard, two circuits (northern and southern circuits) of about 150 km length were formed. We established six BMs that materialize the connection points (CPs) along the international border of Argentina and Brazil. They are Santo Tomé/São Borja (CP A), Alvear/Itaquí (CP B) and Paso de los Libres/Uruguaiana (CP C) (Fig. 1). The distances between CPs are 4.6 km, 0.6 km and 2.3 km, respectively. Due to the distance and characteristics of the study region, the levelling surveys were conducted by using spirit levelling and trigonometric levelling. The accuracy of these observations is in agreement with the levelling specifications of $4\,\mathrm{mm}\sqrt{k}$, where k is the length of the levelled line in km.

2.2 Earth Gravitational Model 2008 (EGM2008)

The geopotential model EGM2008 (Pavlis et al. 2012) was included in the present work in order to analyse the offset and to connect both NVNs. EGM2008 is given as series of spherical harmonic coefficients up to degree and order (d/o) 2159 with additional coefficients up to d/o 2190. According to Yi and Rummel (2014), EGM2008 is the most comprehensive representation and the highest resolution of the Earth's gravitational field currently available. The particular choice of EGM2008 was mainly due to its high resolution.

2.3 GPS-Levelling Dataset

GPS observations were carried out at 14 BMs over the Argentine side and 22 over the Brazilian side to obtain "geoid heights" (the quotation marks here are because we considered the normal-orthometric heights to be an approximation of the orthometric heights). The ellipsoidal coordinates (φ, λ, h) refer to the SIRGAS reference frame SIR10P01, through MECO GPS station, located in Argentina. The measurements were performed by means of Leica and Trimble double frequency receivers. Static mode was applied and each session lasted from three to six hours. This GPS-levelling dataset was used to check the stability of the benchmarks in the study region. Additionally, another set of GPS-levelling data was used; there were 612 points over Argentina and 654 over Brazil (related to the 2011 realization), after the removal of outliers.

The information about the uncertainties of GPS-derived ellipsoidal heights and the normal-orthometric heights were not considered here. Additionally, the ellipsoidal heights are in a tide-free system (Poutanen et al. 1996), while the normal-orthometric heights are in a mean-tide system. To guarantee the consistency of the comparisons, we reduced the orthometric heights to a tide-free system (Ekman 1989). Although the International Association of Geodesy's (IAG) resolution No. 16 of 1983 recommends the zero-tide convention, we adopted the tide-free system in our comparisons due to its widespread use among the GPS community; the comparisons are not influenced by this particular choice due to differencing.

2.4 Treatment of Systematic Data Errors

The difference between the geoid heights from GPS-levelling (N_{GPS}) and those computed by using EGM2008 (N_{EGM}) is given as:

$$\Delta N_i = N_{GPS_i} - N_{EGM_i}, \quad (1)$$

where the subscript index i indicates the considered point. N_{GPS} represents the height of the national height reference frame above a reference ellipsoid, here the Geodetic Reference System 1980 (GRS80). However, following Rülke et al. (2012) and Kotsakis et al. (2012) significant systematic effects may remain in the pure offset estimation if Eq. (1) is considered. To remove the systematic effects in height simultaneously with the estimation of the offsets (δH), the observation Eq. (1) for ΔN_i can be written as (Kotsakis et al. 2012):

$$\Delta N_i = \delta H_i + x_1(\varphi_i - \varphi_0) + x_2(\lambda_i - \lambda_0)\cos\varphi_i + v_i, \quad (2)$$

where the unknowns δH_i, x_1 and x_2 represent the offset (cm), a north-south and west-east tilt (cm/degree) related to the centroid of the network (φ_0, λ_0), respectively, and the term v_i represents the random residual.

3 Results

The results and analysis of the determined offsets were derived in two ways: first, the closures of the circuits by considering the geodetic levelling approach and, second, the comparison of GPS-levelling against a global geoid model (EGM2008) by considering the gravity field approach.

3.1 The Geodetic Levelling Approach

The evaluation of closures of the two circuits presented at Fig. 1 indicates −0.0001 m in the southern loop and 0.0995 m in the northern one. The almost 10 cm misclosure obtained for the northern circuit is an unexpected result and suggests an inconsistency within it. It is important to mention that this misclosure error of 10 cm is related to heights estimated in the 1993 adjustment of the Brazilian NVN. Surprisingly, if the heights associated with the current realization of the Brazilian height system are considered (i.e. the 2011 adjustment) the misclosure error reaches the magnitude of 40 cm in the northern circuit. This indicates a single error in a particular BM that could not be identified because this study did not include all the points used in the 2011 adjustment. Indeed, this is not the first time that such problem has been identified with the Brazilian levelling lines. Hernández et al. (2002) reported a height difference between Brazilian and Venezuelan levelling networks of 3.45 m.

Table 1 Level offset between the Argentine and Brazilian NVNs at the connection points A, B and C (Fig. 1)

	$\delta H_{(AR)(BR)}$ (m)	
Connection points	1993	2011
Santo Tomé/São Borja (A)	−0.8195	−0.9802
Alvear/Itaquí (B)	−0.7008	−0.5457
Passo de los Libres/Uruguaiana (C)	−0.7210	−0.5280

The negative values indicate that the Brazilian vertical reference frame is below the Argentine vertical reference frame

The observed offset between the Argentine and Brazilian levelling networks at the CPs (Fig. 1) are shown in Table 1. The magnitude of the observed values is rather inhomogeneous, especially at CP A (São Borja/Santo Tomé) and even worst when considering the Brazilian heights related to the 2011 realization. This value reaches ∼82 cm while B (Itaquí/Alvear) and C (Uruguaiana/Paso de Los Libres) ∼71 cm and ∼72 cm, respectively considering the Brazilian heights related to 1993 realization. As we also can see from Table 1, the situation is even worse when conserving the 2011 realization.

3.2 Gravity Field Approach

In this particular comparison, the errors of the ellipsoidal heights, orthometric heights and geoid heights from EGM2008 were neglected. The statistics of the evaluation in terms of minimum, maximum, mean, standard deviation (SD) and root mean square error (RMSE) are summarized in Fig. 2 for both NVNs. The EGM2008-derived geoid heights fit marginally better with the Argentine GPS-levelling network than with the Brazilian in terms of SD as Fig. 2 shows. It is well known that the gravity anomaly values used for the EGM2008 project were of a proprietary nature or unavailable (e.g. Amazon region) over Brazilian territory (Pavlis et al. 2012). In such cases, the EGM2008 incorporated the gravity data up to a d/o 900 (Pavlis et al. 2013). Beyond d/o 900 "fill-in" gravity anomalies were applied, which implies that over Brazil EGM2008-derived geoid heights would have less accuracy in comparison with Argentina.

We examined the systematic effects and their impact on the estimated discrepancy between the Argentine and Brazilian vertical reference frames. The geoid height differences computed through Eq. (1) are presented in Fig. 2 in order to emphasize the systematic spatial tilt present in the GPS-levelling networks. It is clear that there is a significant east-west tilt, whereas the north-south tilt appears to be less important over the Argentine NVN. Over the Brazilian NVN the situation seems to be quite a lot better than over the Argentine one. The residuals for both countries are characterized by a strong bias in the Andean region (Argentina) and

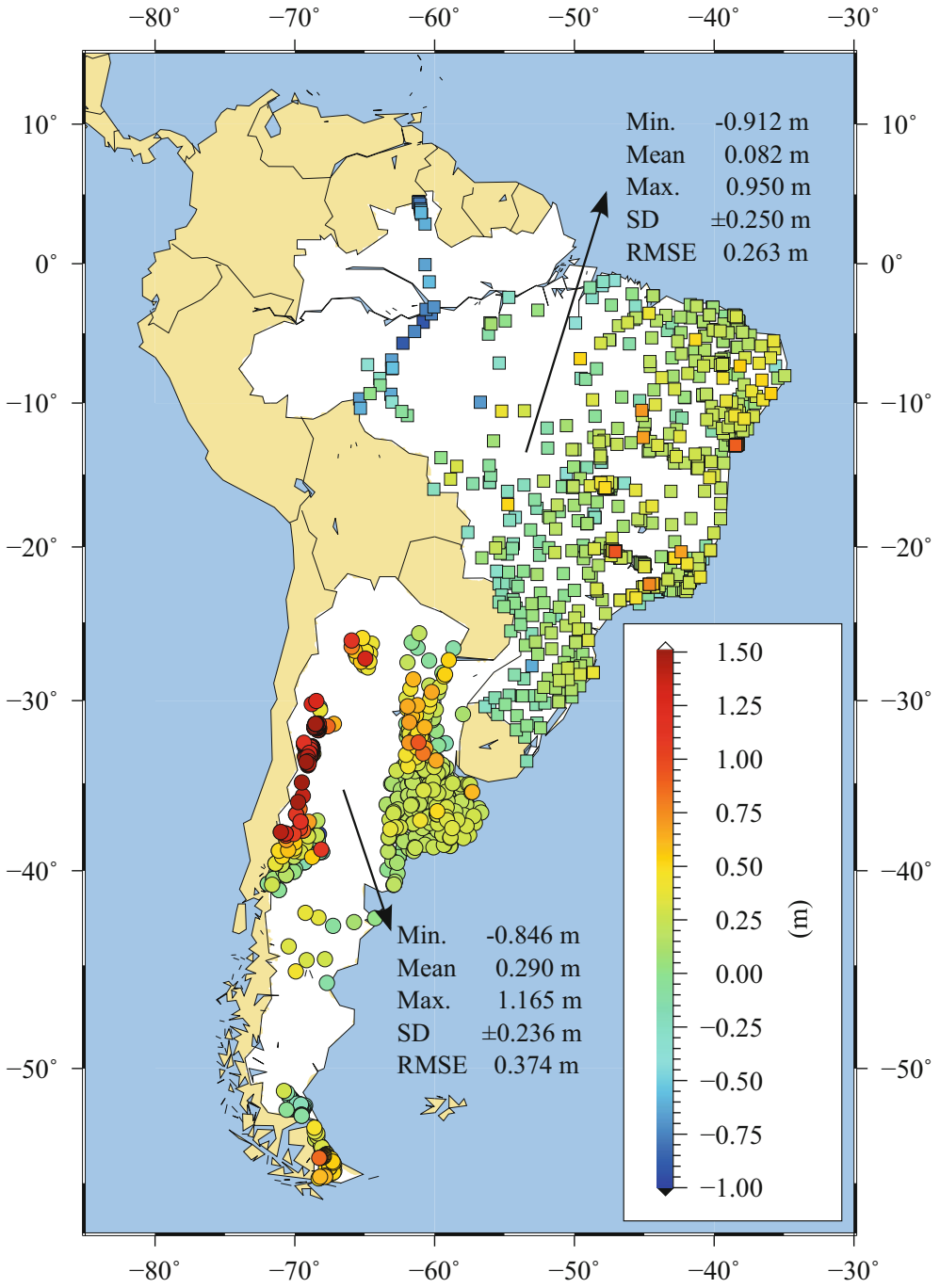

Fig. 2 Statistics and spatial distribution of the differences between GPS-levelling and EGM2008-derived geoid heights

Table 2 Estimated offsets and parameters for Argentina and Brazilian GPS-levelling corresponding to the bias corrector model in Eq. (2) and their respective RMSEs of the adjusted residuals (goodness of model fit)

Network	# of Points	$\varphi(^\circ)$	$\lambda(^\circ)$	δH (cm)	Tilt (cm/degree)		RMSE (cm)
					x_1	x_2	
Argentine	612	−36.202	−62.272	29.4±0.8	1.5±0.1	−3.4±0.4	20.8
Brazilian	654	−15.469	−46.314	8.1±0.8	−0.8±0.1	2.5±0.1	19.9

Amazon region (Brazil). Improvement in gravity coverage in those regions will play a central role in reducing the omission error of global geopotential models and in increasing the reliability of local geoid models of high-resolution.

In order to estimate the offsets for each NVN with respect to the EGM2008 geoid level, the apparent systematic bias shown in Fig. 2 was removed using Eq. (2). The resulting offsets δH and the parameters x_1 and x_2 are presented in Table 2. The RMSE values were calculated by using the adjusted residuals from the least-squares estimation. Because the GPS-levelling and the EGM2008-derived geoid heights come from independent methods, it is assumed that the RMSE of the residuals shows which network is stronger affected by systematic errors in the levelling.

Considering the GPS-levelling distribution over Argentina, the north-south and the west-east tilts estimated by means of Eq. (2) are 1.5 cm/degree and −3.4 cm/degree, respectively. In the case of Brazil, they are −0.8 cm/degree and 2.5 cm/degree, respectively. Although the tilt estimates of the spirit levelling approach and the gravity field approach refer to different reference surfaces, this provides a quite good agreement between the two surfaces. The east-west tilt of −3.4 cm/degree related to the centroid of the GPS-levelling distribution over Argentina is equal to the levelling specification of 4 mm $\sqrt{k}$ (∼3.4 cm/degree at φ_0). Despite this, the RMSE of the residuals presented in Table 2 shows that both GPS-levelling networks have the same quality.

4 Discussion

In order to check the quality of the both approaches adopted here, we compared the levelling results (geodetic levelling approach) with those coming from comparing the GPS-levelling data with the EGM2008 model. According to Fig. 1, the level differences between the two NVN were directly determined at the CPs A, B and C. The value obtained at the CP A (Santo Tomé/São Borja) presents a large discrepancy with respect to the other two CPs B and C and deserves further investigation. To explain the large value (of about 10 cm) of the misclosure of the northern circuit, the first suspicion is an unidentified error in the levelling height of the point A. This could be supported by the fact that the geoid gradient between this point A and the previous Brazilian BM is 10 cm/km and this value is reduced to 0.1 cm/km when using geometric levelling and EGM2008-derived geoid heights (excluding the closest Brazilian BM). A second levelling campaign confirmed the physical height adopted for the connection BM. Because of this uncertainty about CP A, we considered only CPs B and C, which provided a mean value of 0.7109 m and 0.5368 m related to the realization of 1993 and 2011, respectively.

The offset value obtained by considering the gravity field approach provided a mean value of approximately −21.3 ± 1.1 cm related to the 2011 realization. Unfortunately, we do not have the GPS-levelling data related to the 1993 realization. Sánchez (2007) provided an estimated offset between the Argentine and Brazilian vertical reference frames of approximately −26 cm based on EIGEN-CG03C model up to d/o 360 evaluated at each tide gauge collocated with SIRGAS stations, namely, Imbituba (−20 cm), Brazil and Mar del Plata (+6 cm), Argentina. In Ihde and Sánchez (2005), it is possible to infer two values of approximately −35 cm and +11 cm by considering the connection through Uruguay and Paraguay, respectively obtained from spirit levelling.

The mean estimated offset obtained by the gravity field approach is somewhat different to that of the geodetic levelling approach, which provided a mean value of −53.68 ± 2.3 cm related to the 2011 realization. It must be remarked that the gravity field approach is realized over a broad area while the levelling approach was conducted in a single small region. To account for this, the estimated offsets, tilts and the coordinates of the centroids (φ_0, λ_0) of Argentina and Brazil (Table 2) were used to calculate ΔN_{AR} and ΔN_{BR} for the connection points (cf. Rülke et al. (2012) for details). We found the values of +18.48 cm and −38.98 cm for ΔN_{AR} and ΔN_{BR}, respectively, which implies an offset of −57.46 cm at the connection points.

5 Summary and Outlook

The relative offsets between the Argentine and Brazilian vertical networks have been determined by using geodetic levelling and gravity field approaches. Our findings show that the estimated offset obtained by considering the geodetic levelling approach is approximately −72 cm if the Brazilian height system realization of 1993 is used, and −54 cm if

the realization of 2011 (official) is used at two of the three CPs. We excluded CP A (Fig. 1) that indicated an offset of −82 cm and −98 cm for the 1993 and 2011 realization, respectively. This shows inconsistencies between the two realizations of the Brazilian height system. For the gravity field approach, the offset between both NVNs is −57 cm, which implies a difference of approximately 3 cm between the two approaches, that is, between geodetic levelling and gravity field. The negative values indicate that the Brazilian vertical reference frame is below the Argentine vertical reference frame. Since Brazil and Argentina represent a significant part of South America, the solution of the datum problem between both countries could point towards a common vertical reference frame for the Atlantic side. Future work should benefit greatly by using data from the new adjustment of the Argentine NVN, which is based on geopotential numbers. Additionally, investigation of the eventual deformations of the Brazilian 2011 realization should be carried out.

Acknowledgements The authors thank CNPq (Brazilian National Council for Scientific and Technological Development) and CONICET (Argentine National Council for Scientific and Technical Research) for their financial support. We also thank the IBGE and IGN for providing the GPS-levelling data over Brazil and Argentina, respectively. We are grateful to the Associate Editor and the three reviewers for their remarks, which improved the manuscript.

References

Ekman M (1989) Impacts of geodynamic phenomena on systems for height and gravity. Bull Géod 63(3):281–296. Doi: 10.1007/BF02520477

Ferreira VG, de Freitas SRC (2011) Geopotential numbers from GPS satellite surveying and disturbing potential model: a case study of Parana, Brazil. J Appl Geod 5(3–4):155–162. Doi: 10.1515/JAG.2011.016

Filmer MS, Featherstone WE, Kuhn M (2010) The effect of EGM2008-based normal, normal-orthometric and Helmert orthometric height systems on the Australian levelling network. J Geod 84(8):501–513. Doi: 10.1007/s00190-010-0388-0

Fortes LPS (1998) An overview of the SIRGAS project. In: Advances in Positioning and Reference Frames, IAG Symposia, vol 118, pp 167–167. Doi: 10.1007/978-3-662-03714-0_26

Heck B, Rummel R (1990) Strategies for solving the vertical datum problem using terrestrial and satellite geodetic data. In: Sea Surface Topography and the Geoid, IAG Symposia, vol 104, pp 116–128. Doi:10.1007/978-1-4684-7098-7_14

Hernández JN, Blitzkow D, Luz R, Sánchez L, Sandoval P, Drewes H (2002) Connection of the vertical control networks of Venezuela, Brazil and Colombia. In: Vertical Reference Systems, IAG Symposia, vol 124, pp 324–327. Doi: 10.1007/978-3-662-04683-8_60

Ihde J, Sánchez L (2005) A unified global height reference system as a basis for IGGOS. J Geod 40(4–5):400–413. Doi: 10.1016/j.jog.2005.06.015

Kotsakis C, Katsambalos K, Ampatzidis D (2012) Estimation of the zero-height geopotential level W_o^{LVD} in a local vertical datum from inversion of co-located GPS, leveling and geoid heights: a case study in the Hellenic islands. J Geod 86(6):423–439. Doi: 10.1007/s00190-011-0530-7

Montecino HD, de Freitas SRC (2014) Strategies for connecting Imbituba and Santana Brazilian datums based on satellite gravimetry and residual terrain model. In: Earth on the Edge: Sci Sustain Planet, IAG Symposia, vol 139, pp 543–549. Doi: 10.1007/978-3-642-37222-3_72

Pavlis NK, Holmes SA, Kenyon SC, Factor JK (2012) The development and evaluation of the earth gravitational model 2008 (EGM2008). J Geophys Res Solid Earth 117:B04406. Doi: 10.1029/2011JB008916

Pavlis NK, Holmes SA, Kenyon SC, Factor JK (2013) Correction to the development and evaluation of the earth gravitational model 2008 (EGM2008). J Geophys Res 118(5):2633–2633. Doi: 10.1002/jgrb.50167

Poutanen M, Vermeer M, Mäkinen J (1996) The permanent tide in GPS positioning. J Geod 70(8):499–504. Doi: 10.1007/s001900050038

Rülke A, Liebsch G, Sacher M, Schäfer U, Schirme U, Ihde J (2012) Unification of European height system realizations. J Geod Sci 2(4):343–354. Doi: 10.2478/v10156-011-0048-1

Sánchez L (2007) Definition and realization of the SIRGAS vertical reference system within a globally unified height system. IAG Symposia 130:638–645. Doi: 10.1007/978-3-540-49350-1_9

Yi W, Rummel R (2014) A comparison of GOCE gravitational models with EGM2008. J Geod 73:14–22. Doi: 10.1016/j.jog.2013.10.004

Validation of GOCE/GRACE Satellite Only and Combined Global Geopotential Models Over Greece in the Frame of the GOCESeaComb Project

I.N. Tziavos, G.S. Vergos, V.N. Grigoriadis, E.A. Tzanou, and D.A. Natsiopoulos

Abstract

The GOCESeaComb project, funded by ESA in the frame of the PRODEX program, aims to utilize GOCE data within combination schemes in order to achieve high-quality and accuracy predictions related to Earth's gravity field, sea level and dynamic ocean topography. In this work the results from the detailed validation of the latest GOCE, GOCE/GRACE and combined global geopotential models are presented referring to the fourth release of the models and the various strategies (TIM, DIR, GOCO, EIGEN-S/c) employed for their determination. The validation is performed following two approaches. The first one refers to the evaluation of the GGMs signal and error in the form of the provided degree and error variances. The second refers to an external evaluation of the GGMs against local gravity, GPS/Leveling data and deflections of the vertical. In this validation step we follow a spectral enhancement approach of GOCE GGMs, where EGM08 is used to fill-in the medium and high-frequency content along with RTM effects for the high and ultra high part. From the evaluation with GPS/Levelling benchmarks, it is concluded that the GOCE/GRACE GGMs provide improved accuracies compared to EGM2008 by about 2 cm in the spectral range between d/o 120–230. Finally, GOCE/GRACE GGMs manage to provide the same, as EGM2008, level of reduction to the local gravity anomalies, with a standard deviation at the 6.1–6.2 mGal level and marginally better residuals, at the sub-arcsec level in the reduction of deflections of the vertical.

Keywords

Deflections of the vertical • Global geopotential models • GOCE • GPS/Levelling BMs • Gravity • Validation

1 Introduction

With GOCE entering the Earth's atmosphere in November 11, 2013, the contribution and new insights that have been brought to many fields in the geosciences are significant. GOCE managed to provide improved representations in the medium wavelengths of the gravity field spectrum to degree and order 210–240, resulting in advances in gravity field determination, dynamic ocean topography (DOT) modelling, new outlooks in the Earth's interior, etc. There have been many studies during the recent years investigating the performance of GOCE Global Geopotential Models (GGMs). In terms of the GOCE GGM external validation with GPS/Levelling and gravity data as well as deflections of the vertical (DoVs) it was found that its main impact is up to d/o 180–190 and 195–220 for the Release 2 and Release 3 GGMs, respectively (Gruber et al. 2011; Hirt et al. 2011; Šprlák et al. 2012; Vergos et al. 2014). GOCE contribution to height system unification has also gained

I.N. Tziavos (✉) • G.S. Vergos • V.N. Grigoriadis • E.A. Tzanou • D.A. Natsiopoulos
Department of Geodesy and Surveying, Aristotle University of Thessaloniki, University Box 440, 54124 Thessaloniki, Greece
e-mail: tziavos@topo.auth.gr

© Springer International Publishing Switzerland 2015

C. Rizos, P. Willis (eds.), *IAG 150 Years*, International Association of Geodesy Symposia 143,
DOI 10.1007/1345_2015_160

increased importance since the results show that especially in areas of small geoid variability, GOCE omission error is at the 1–2 cm range, as far as the determination of the vertical datum level offsets are concerned (Gruber et al. 2012; Hayden et al. 2012). Finally, GOCE has contributed significantly to DOT modelling since it has brought new insights in the geodetic determination of ocean circulation (Albertella et al. 2012; Knudsen et al. 2011; Tziavos et al. 2013). The focus of this work refers to the evaluation over Greece of the available Release 4 GGMs from GOCE, GOCE/GRACE and combined ones. Special attention is paid to the improvements they aforementioned GGMs bring to gravity field and geoid modelling.

2 Methodology, GGMs and Local Data

2.1 GOCE GGM Validation Methodology

For the validation of GOCE/GRACE GGMs, two methodologies have been followed, one internal and an external one. On a first stage their spectra have been evaluated in terms of their signal and error degree variances (both by-degree and cumulatively), the signal-to-noise ratio (SNR) and gain relative to EGM2008 (Pavlis et al. 2012). The signal and error degree variances reveal the spectral content of the GGMs for the various d/o investigated as well as the cumulative signal spectrum and signal error. The SNR provides useful information for the relative signal strength given the signal error, while the gain, relative to EGM2008, provides an indicative measure of the improvement brought by the GOCE/GRACE GGMs w.r.t. the reference GGM used. The GGMs are provided as sets of dimensionless spherical harmonic coefficients $\delta\overline{C}^{*}_{nm}$, $\delta\overline{S}_{nm}$ with their errors $\varepsilon_{\delta\overline{C}^{*}_{nm}}$, $\varepsilon_{\delta\overline{S}_{nm}}$. The asterix implies that the spherical harmonic coefficients are fully normalized and the δ that the normal potential has been subtracted. Given that the coefficients and errors of various geopotential models need to be compared, and some of them use different values for the geocentric gravitational constant GM and equatorial radius a, it is necessary to scale their harmonic coefficients. In that way, the computed harmonic coefficients can be comparable (Sneeuw 2000). Within the present validation and in the external one to follow, the Earth's geocentric gravitational constant GM and the gravity potential at the geoid Wo have been set to $GM = 398600.4418\ 10^9\,\mathrm{m}^3\ \mathrm{s}^{-2}$ and $Wo = 62636856.00\,\mathrm{m}^2\ \mathrm{s}^{-2}$. The mean Earth's radius R has been taken equal to 6378136.3 m and the normal gravity γ at the surface of the ellipsoid has been computed by the closed formula of Somigliana (Heiskanen and Moritz 1967). Moreover, the GRS80 ellipsoid, along with its defining and derived quantities, has been used as reference. Given the availability of unified spherical harmonic coefficients and their errors, the by-degree and cumulative signal and errors can be evaluated (here we will focus on geoid signal and error for the investigated GGMs), which can be determined as outlined in Vergos et al. (2006; 2014). As far as the SNR and gain are concerned, these can be evaluated either for each specific degree and order (2D case) or per-degree (1D case). In the latter, they are determined as (Sneeuw 2000):

$$SNR_n = \frac{\sigma_n}{\varepsilon_{\sigma_n}}, \tag{1}$$

$$GAIN_n = \frac{\varepsilon_{\sigma_n^{EGM2008}}}{\varepsilon_{\sigma_n^i}}. \tag{2}$$

In Eq. (1) σ_n denotes the geoid degree variances of the model under study and ε_{σ_n} its error degree variances. In the case of the GGM 1D gain, this is evaluated as the ratio between the EGM2008 error degree variances, $\varepsilon_{\sigma_n^{EGM2008}}$, and those of the GGM under study, $\varepsilon_{\sigma_n^i}$. The SNR represents the ratio between the GGM signal and its error spectrum per degree, i.e., indicating spectral bands that are solvable with power larger than the model error. The gain expresses the ratio between the errors of the "nominal" GGM, EGM2008 in our case, for a specific degree, and the GOCE-based ones. Both quantities are evaluated with their base 10 logarithm, so that the results that will be presented herein refer to the number significant digits either for the SNR or gain. Regarding the SNR we are looking for values larger than zero (0) since this is the threshold under which the GGM error is smaller than the signal. Accordingly, for the 1D gain, values larger than zero (0) indicate that the GOCE/GRACE GGM degree error is smaller than that of EGM2008.

For the external evaluation of the GOCE/GRACE GGMs, comparisons with collocated GPS/Levelling benchmarks (BMs), point free-air gravity anomalies and DoVs, which cover the entire part of continental Greece, are performed. As far as geoid heights are concerned, the differences between the GOCE/GRACE GGMs with the local data have been performed as:

$$\Delta N = N^{GPS/Lev} - N^i\big|_2^{n_1} - N^{EGM2008}\big|_{n_1+1}^{2160} - N^{RTM} - N_o, \tag{3}$$

where ΔN denotes the geoid heights differences at the GPS/Leveling BMs between the GPS-derived geoid heights ($N^{GPS/Lev}$) and those derived by the GGM ($N^i\big|_2^{n_1}$) under investigation. In Eq. (3) the evaluation is carried out with the GOCE/GRACE GGMs to some maximum degree of expansion (n_1), while the rest of the geoid signal is represented by EGM2008, from degree $n_1 + 1$ to degree 2160

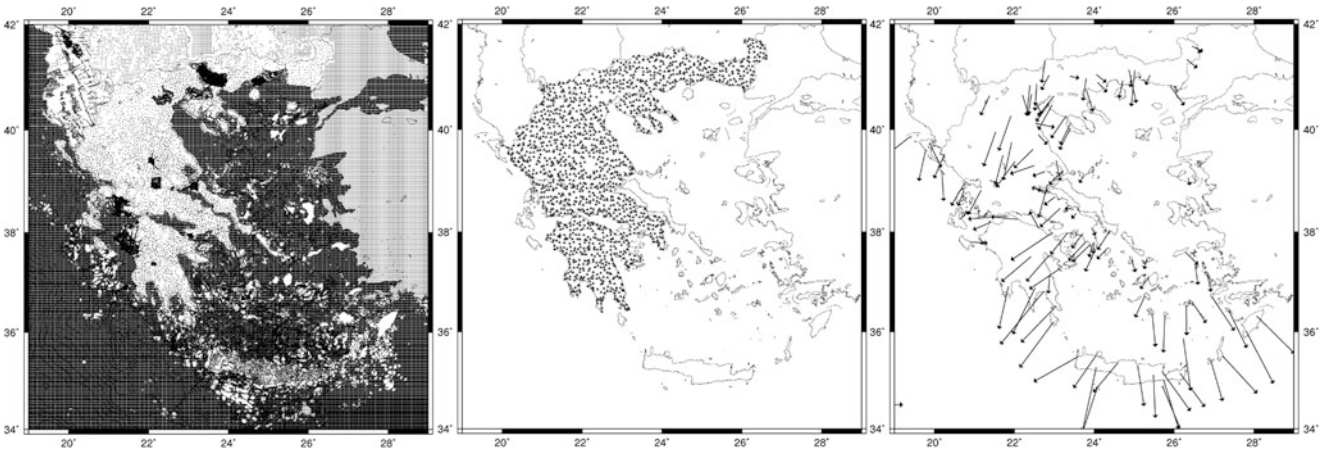

Fig. 1 Distribution of local gravity (*left*), GPS/Levelling (*centre*) and deflections of the vertical (*right*) data in Greece for GOCE GGM validation

along with RTM effects on geoid heights (N^{RTM}). The RTM effects on geoid heights are estimated on the BMs from a 3 arcsec resolution digital terrain and bathymetry model (Tziavos et al. 2010). The, smooth but varying, reference surface needed for the RTM effect is constructed by averaging the fine resolution topography grid and then low-pass filtering the average grid generated by taking moving averages of an appropriate number of adjacent blocks (Tziavos et al. 2010). The contribution of the zero-degree geoid term (N_o) is evaluated with respect to the GRS80 reference ellipsoid as in Heiskanen and Moritz (1967, Eq. 2.182). All computations were carried out in the Tide Free (TF) system, while any necessary transformations from the Zero-Tide (ZT) to the TF system were done following Ekman (1989). The aforementioned geoid height differences on BMs are first evaluated by the GOCE/GRACE GGM contribution, to their n_{max}, alone, i.e., without the fill-in information from EGM2008 and RTM effects, and then with all parameters outlined in Eq. (3). The latter is evaluated for every degree starting from $n_1 = 2$ up to the n_{max} of the GGM under investigation. Finally, it should be noted that the computed RTM effects correspond to a maximum harmonic degree of 216,000, so that the remaining omission error is negligible. In all geoid height evaluations a local LSC-based gravimetric geoid model (N^{LSC}) is used as ground-truth (Tziavos et al. 2013).

The same methodology has been followed for the evaluation of the reduction that the GOCE/GRACE GGMs provide to the available local point free-air gravity anomalies and DoVs, i.e., the contribution of the recent GGMs is filled-in by EGM2008 and RTM effects in order to derive the final residual fields. The evaluation in this case is performed from $n_1 = 2$ up to the n_{max} of the GGM under investigation, with an interval of 10 d/o, mainly due to the large number of gravity data. In any case the evaluation step does not alter the conclusions drawn.

2.2 GOCE/GRACE GGMs and Local Data

As far as the GOCE/GRACE GGMs are concerned, we will focus on the latest, Release 4, versions as well as to the latest combined models. Release 4 models are based on an effective data volume of 26.5 months of GOCE observations compared to 12 months for the Release 3 ones. Depending on the processing strategy three classes of models can be distinguished as (a) the TIM models using the time-wise approach (Pail et al. 2011), (b) the DIR models using the direct approach (Bruinsma et al. 2013), and c) the GOCO combined models where both GOCE and GRACE data are used (Pail et al. 2010). For GOCO, we have included in the validation its Release 3 version (GOCO03s) given that a Release 4 version is not available. The GO-DIR-R4 model is a combined GRACE/GOCE/SLR model, while GO-DIR-R3 was used as an a-priori gravity field up to d/o 240. Apart from the aforementioned GGMs, EGM2008 (Pavlis et al. 2012) and the latest EIGEN-6S, EIGEN-6C and EIGEN-6C2 models (Förste et al 2012) have been used as well.

The local data used for the GGM external validation refer to GPS/Levelling observations (1542 BMs) covering the entire part of continental Greece (cf. Vergos et al. 2014). This set of collocated GPS and Levelling data (see Fig. 1) is based on historical orthometric heights from the HMGS (Hellenic Military Geographic Service) and ellipsoidal heights collected within the HEPOS (Hellenic Positioning System) project. The orthometric heights refer to the tide-gauge station located at the Piraeus harbor, where MSL measurements were performed over the period 1933–1978. The true accuracy though of the HVD's leveling network is largely unknown. The ellipsoidal heights were determined in ITRF00 (epoch t = 2007.236) with their horizontal and vertical accuracy being estimated from the analysis of the original GPS observations to 1–4 cm (1σ) and 2–5 cm (1σ),

respectively. Moreover, point free-air gravity anomalies and DoVs have been used (see Fig. 1) from the latest database that has been compiled in the frame of the determination of a new Greek geoid model (Tziavos et al. 2010, 2013). The gravity dataset comprise a number of 294777 irregular point gravity observations (cf. Tziavos et al. 2013) with an accuracy (estimated through least-squares prediction) at the ±2.25 mGal level. The DoV dataset (99 values) consists of two basic sub-sets, one (the main with 89 DoVs) collected from dedicated astrogeodetic observations (Tziavos 1987) and a second (10 DoVs) collected during dedicated astro-geodetic observations with the ETH digital Zenith Camera DIADEM. The old DoV dataset was original determined in ED50 and properly transformed to GRS80 and a DoV accuracy varying between 0.1 to 0.3 arcsec (Tziavos 1987). The DIADEM DoV dataset has a horizontal position accuracy of 10 cm and the deflections have an accuracy of ±0.15 arcsec (Somieski 2008).

3 GGM Spectral Evaluation and External Validation

3.1 GOCE GGM Spectral Evaluation

As already mentioned, the spectral evaluation of the GOCE GGMs is based on their signal and error degree variances, the SNR and the gain relative to EGM2008. From this analysis, an improved representation of the geoid height error spectrum is evident as more GOCE data are included (TIM-R4 and DIR-R4 compared to GOCO03S), along with the improved error spectrum due to the use of GRACE data (DIR-R4 compared to TIM-R4). The DIR-R4 error spectrum is below that of EGM2008 up to d/o 214, while GOCO03s provides smaller errors up to degree 175. Among DIR-R4 and GOCO03s, the latter provides smaller errors up to d/o 98 due to the fact that in DIR-R4 GRACE and GOCE normal equations are blended for the entire spectrum, so that the influence of GOCE is visible in the low-degree harmonics. TIM-R4, which is based solely on GOCE observations gives smaller errors compared to EGM2008 from d/o 48 up to d/o 179, while it is better than GOCO03s from d/o 144 onwards. EIGEN6C and EIGEN6C2 have smaller errors compared to EGM2008 up to d/o 185 and then from d/o 319 onwards, signaling that in the intermediate band (d/o 185–318) EGM2008 was probably modeled in a more elaborate or enhanced way (given that this is the range that the satellite and terrestrial data are both used). In terms of the cumulative geoid errors, GOCO03s reaches the 1 cm geoid error to d/o 152, TIM-R4 to d/o 184 and DIR-R4 to d/o 192, while their total errors are at the 15.5, 11.3 and 4.27 cm, respectively. The DIR-R4 errors are significantly better than those of TIM-R4, where the lack of GRACE observations in the latter is evident, especially in the low degree harmonics. Even though TIM-R4 uses only GOCE data, its error spectrum is better than that of GOCO03S after d/0 180, hence signaling the improvements brought by adding more GOCE observations. On the other hand, DIR-R4 provides the overall best error spectrum with the smallest cumulative geoid errors to all d/o of investigation, showing the benefits of combined satellite-only (GOCE and GRACE) GGMs. EIGEN6C and EIGEN6C2 reach the 1 cm error at d/o 153 and 162 (EGM2008 reaches the 1 cm error at d/o 71), while their cumulative error is at the 9.5 cm and 8.5 cm (EGM2008 has a cumulative geoid error of 8.2 cm), respectively. Especially for the cumulative and by-degree geoid errors it should be bear in mind that the GGM errors are formal/calibrated ones resulting from different weight schemes for each GGM. Hence, they may be biased since they can be optimistic.

Figure 2 depicts the SNR and gain for the evaluated GOCE/GRACE GGMs. As it can be seen DIR-R4 retains better, compared to EGM2008, SNR for the entire spectrum up to d/o 211, while GOCO03S up to d/o 169. The SNR of TIM-R4 is worse than that of EGM2008 up to d/o 47 and better from d/o 48 to 181. EIGEN6S, incorporating all available GRACE and GOCE data, retains an SNR better than EGM2008 up to d/o 166, while for the two latest EIGEN combined models, their SNR is better than that of EGM2008 in the spectral bands between d/o 2–189 and 320–1420 for EIGEN6C and in the spectral bands between d/o 2–187 and 322–1949 for EIGEN6C2. As for the gain (see Fig. 2) the useful spectral band offered by the latest GOCE/GRACE models becomes apparent in terms of significant digits of the model gain w.r.t. EGM2008. This band is between d/o 47 to 180 for TIM-R4, and for the entire spectrum up to d/o 169 for GOCO03s and 214 for DIR-R4.

3.2 GOCE GGM Evaluation with GPS/Levelling Data

As far as the evaluation with the GPS/Levelling data is concerned, Table 1 summarizes the differences between the available GPS/Levelling and GGM geoid heights. Both the national gravimetric geoid model and EGM2008 provide a standard deviation (std) at the 14 cm, so they will provide the basis for the evaluation of the GOCE/GRACE and combined GGMs. When satellite only models are evaluated to their n_{max} without any spectral enhancement from EGM2008 and RTM effects, then, as expected, their differences are quite large (47–51 cm) due to the omission error. On the other hand, when fill-in information from EGM2008 along with the computed RTM effects are taken into account, then their performance is comparable and better than that of both EGM2008 and the local model. Figure 3 depicts the

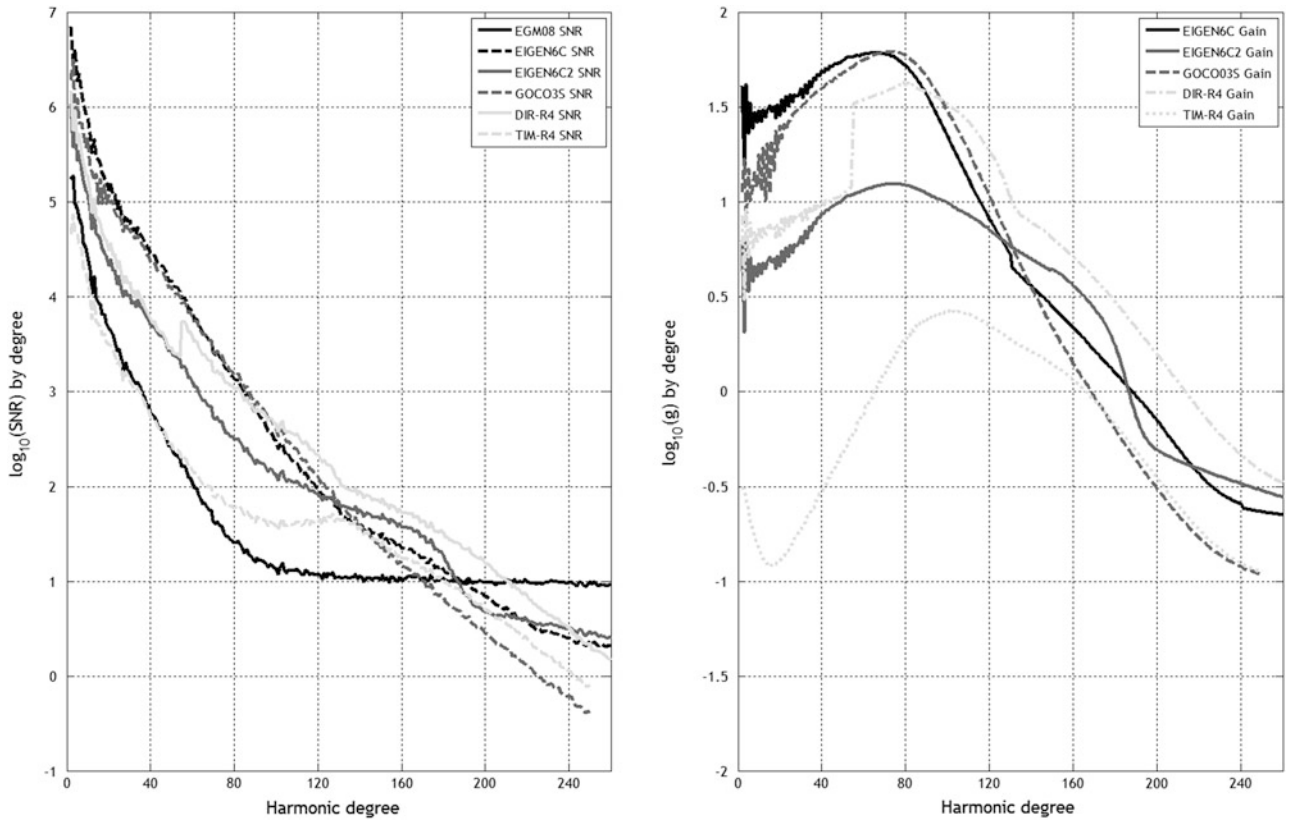

Fig. 2 GOCE GGM SNR and gain relative to EGM2008

Table 1 Statistics of the differences between GPS/levelling and geoid heights from the GGMs to their n_{max}, before (normal font) and after combination with EGM2008 and RTM effects (italics)

	n_1	Max	Min	Mean	Std
EGM2008	–	0.168	−0.810	−0.374	0.141
EIGEN6S	–	1.400	−1.837	−0.358	0.512
EIGEN6S	*165*	*0.049*	*−0.885*	*−0.394*	*0.124*
EIGEN6c	–	0.357	−0.867	−0.394	0.161
EIGEN6c	*165*	*0.072*	*−0.884*	*−0.392*	*0.129*
EIGEN6c2	–	0.193	−0.929	−0.388	0.137
EIGEN6c2	*165*	*0.061*	*−0.860*	*−0.389*	*0.123*
GOCO03S	–	1.415	−1.795	−0.353	0.496
GOCO03S	*163*	*0.076*	*−0.866*	*−0.393*	*0.123*
DIR-R4	–	1.379	−1.607	−0.361	0.476
DIR-R4	*165*	*0.054*	*−0.856*	*−0.391*	*0.123*
TIM-R4	–	1.260	−1.628	−0.352	0.484
TIM-R4	*166*	*0.060*	*−0.849*	*−0.395*	*0.123*
N^{LSC}	–	0.119	−1.033	−0.392	0.140

The first column (n_1) represents the maximum d/o after which EGM2008 is used. Unit: (m)

variation of the std of the geoid height differences between the enhanced GOCE/GRACE GGMs and GPS/Levelling.

The useful spectral range, i.e., with errors smaller than EGM2008 is up to d/o 215 for DIR-R4, while the smallest std at 12.3 cm is achieved at d/o 165. For TIM-R4 this spectral band is extended to d/o 225, while in the band between d/o 215 and 225 it provides better std compared to DIR-R4. The overall smallest std for TIM-R4 is reached at d/o 166 being at the 12.3 cm level. GOCO03S, given that it contains only 12 months of GOCE data, manages to provide better std than EGM2008 up to d/o 185, while in the range between d/o 110 to 125 it provides std's close to EGM2008. The overall best std is reached at d/o 163 being at the 12.4 cm level. It is interesting to notice that for both DIR-R4 and TIM-R4, the std are oscillating close to that of EGM2008 in the band between d/o 110 and 130. This consistent behavior is a matter of further research and can be probably attributed to EGM2008 and its development strategy. EIGEN6S has a similar behavior with the other satellite only models, while regarding EIGEN6c and EIGEN6c2 it was noticing that the latter provides smaller std for the entire spectrum compared to EGM2008, with the exception of d/o 108–111 where its std is 0.2–0.4 cm worse than that of EGM2008. This signals the fact that EIGEN6C2 is indeed a more robust GGM compared to EGM2008, due to the use of GOCE observations in its development.

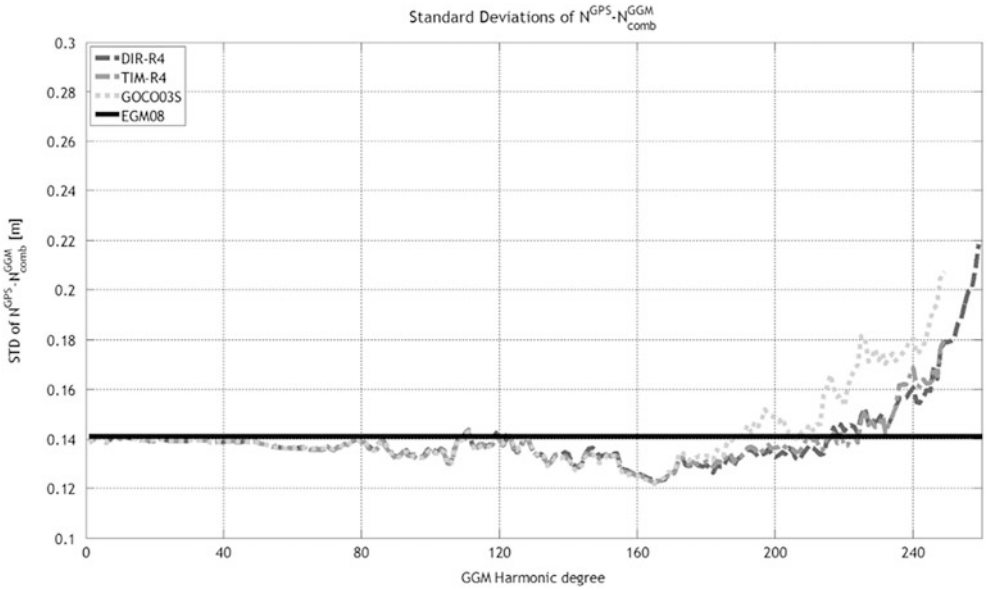

Fig. 3 Standard deviation of the differences between DIR-R4, TIM-R4 and GOCO03S with the GPS/Levelling geoid heights for various degrees of expansion

3.3 GOCE GGM Evaluation with Gravity and DoV Data

The same analysis has been performed for the reduction of the available point gravity anomalies and DoVs, with the results being summarized in Tables 2 and 3, respectively. From the evaluation of the gravity anomaly data set it was concluded that the residual fields of the GOCE/GRACE models provide the same level of reduction, in terms of the std, as EGM2008. It should be noted that as in the evaluation with the GPS/Levelling data, the contribution of GOCE/GRACE GGMs is filled with EGM2008 and RTM in order to reduce the omission error. TIM-R4 provides the same std for the residuals as EGM2008 up to d/o 120 (6.19 mGal), while after that it starts to increase and reaches 7.86 mGal at d/o 250 (filled with EGM2008 and RTM effects above that d/o). DIR-R4 reaches d/o 125 with a std similar to that of EGM2008 and at d/o 260 it increases to 8.91 mGal. Finally, GOCO03S reaches d/o 121 with a std similar to that of EGM2008 and at d/o 250 it increases to 9.19 mGal. The same behaviour is found for the combined models as well, with EIGEN6c2 providing a std of 6.52 mGal to its n_{max} of 1949, while it retains the same level of reduction as EGM2008 up to d/o ∼220. From Table 2 it can be concluded that the improvement offered by GOCE/GRACE GGMs, if any, can be found in the reduction of the mean value to the 0 mGal level. But this is marginal, since EGM2008 provides a mean value for the residual field of only 0.2 mGal. It should be noted though that most of the gravity anomalies that were used in the comparisons have also been used in the development of EGM08. Therefore, the comparisons with EGM08 are indicative, although an improvement at least in terms of the mean value would be expected.

Table 2 Statistics of the original free-air gravity anomalies over Greece, reduced (normal lettering) and residual fields (italics) from the various GGMs

	n_1	Max	Min	Mean	Std
Δg_f(original)	–	269.93	−236.10	−22.73	74.11
Δg_{res}(EGM2008)	–	*101.01*	*−96.45*	*−0.16*	*6.15*
Δg_{red}(EIGEN6S)	–	219.29	*−134.89*	*−4.07*	*27.97*
Δg_{res}(EIGEN6S)	*120*	*101.31*	*−96.08*	*−0.05*	*6.19*
Δg_{red}(EIGEN6c)	–	118.96	*−137.87*	*−0.57*	*9.34*
Δg_{res}(EIGEN6c)	*124*	*101.33*	*−96.06*	*−0.05*	*6.19*
Δg_{red}(EIGEN6c2)	–	94.97	*−149.20*	*−0.22*	*6.73*
Δg_{res}(EIGEN6c2)	*125*	*101.33*	*−96.13*	*−0.06*	*6.19*
Δg_{red}(GOCO03S)	–	*224.65*	*−132.06*	*−4.42*	*27.43*
Δg_{res}(GOCO03S)	*121*	*101.74*	*−96.56*	*−0.05*	*6.19*
Δg_{red}(GO-DIR-R4)	–	*223.69*	*−129.92*	*−4.34*	*27.76*
Δg_{res}(GO-DIR-R4)	*125*	*101.59*	*−95.86*	*−0.05*	*6.19*
Δg_{red}(GO-TIM-R4)	–	*223.57*	*−133.43*	*−4.35*	*27.34*
Δg_{res}(GO-TIM-R4)	*120*	*101.71*	*−95.67*	*−0.04*	*6.19*

The first column (n_1) represents the maximum d/o after which EGM2008 is used. Unit: (mGal)

A slightly better performance is found for the evaluation with the DoV dataset, where the GOCE/GRACE GGMs improve not only the mean value but the std as well. Again the contribution of GOCE/GRACE GGMs is filled with EGM2008 and RTM in order to reduce the omission error. For ξ (see Table 3), EIGEN6c and EIGEN6C2 reach a std of 2.07 and 2.11 arcsec at d/o 840 and 910, respectively, which

Table 3 Statistics of the original north-south (ξ) and west-east (η) deflections of the vertical over Greece and residual fields from the GGMs

	n_1	Max	Min	Mean	Std
ξ/η(original)	–	10.88/14.77	−27.77/−25.84	−6.89/−2.56	7.36/7.65
ξ_{res}/η_{res}(EGM2008)	–	5.44/5.96	−5.21/−4.41	−0.34/0.58	2.18/2.28
ξ_{res}/η_{res}(EIGEN6S)	225	4.70/5.93	−5.01/−4.01	−0.23/0.61	2.03/2.28
ξ_{res}/η_{res}(EIGEN6c)	840	5.19/5.97	−5.22/−4.53	−0.29/0.59	2.07/2.29
ξ_{res}/η_{res}(EIGEN6c2)	910	5.45/5.97	−5.34/−4.54	−0.30/0.59	2.10/2.29
ξ_{res}/η_{res}(GOCO03S)	220	4.97/4.85	−5.35/−5.07	−0.23/0.52	2.05/2.24
ξ_{res}/η_{res}(GO-DIR-R4)	220	5.41/5.61	−5.48/−4.97	−0.23/0.52	2.09/2.26
ξ_{res}/η_{res}(GO-TIM-R4)	220	5.24/5.29	−4.92/−5.59	−0.27/0.55	2.10/2.19

The first column (n_1) represents the maximum d/o after which EGM2008 is used. Unit: (arcsec)

are slightly better that the std of 2.18 arcsec for EGM2008. It is noticing that EIGEN6S manages to provide a std at the 2 arcsec level, the overall best, at d/o 225, along with the smallest mean at −0.23 arcsec. GOCO03S, TIM-R4 and DIR-R4 all reach at d/o 220 a std of 2.05, 2.10 and 2.09 arcsec, respectively with mean values below that of EGM2008. For DIR-R4, it is interesting to notice that its Release 3 version provides a std of 2.03 arcsec. The η component of the DoV presents slightly worst statistics, probably due to its higher variability over Greece (see Table 3). The combined GGMs are similar to EGM2008 with a std at the 2.3 arcsec level, while only TIM-T4 provides a std at the 2.19 arcsec. Finally, the mean value is smaller for the GOCE/GRACE GGMs by 0.05 arcsec the most, compared to EGM2008. It can be concluded therefore that for the DoVs, which are mapped in the high and ultra-high frequencies of the gravity field spectrum, GGMs, even combined ones, do not manage to depict their entire content, so that local data, with high spatial sampling are needed as well along with information about density variations.

4 Conclusions

An evaluation of the latest GOCE, GOCE/GRACE and combined GGMs has been presented, focusing on their spectral comparison and validation with local data. From the results acquired it becomes clear that the useful spectral band is between d/o 47 to 180 for TIM-R4, while it spans the entire spectrum up to d/o 169 for GOCO03s and 214 for DIR-R4. These spectral bands are confirmed from the evaluation with the GPS/Leveling data over Greece, since in terms of the std of the geoid height differences DIR-R4, TIM-R4 and GOCO provide smaller values up to d/o 215, 225 and 185, respectively. Moreover, d/o 163–165 seem to be the ones that the GOCE/GRACE models perform the best, since they improve the std, compared to EGM2008, by 2 cm. Finally, for the free-air gravity anomalies the evaluated GGMs perform similar to EGM2008, without any significant improvement, while the same is concluded for the DoV dataset as well, where the improvement is marginal.

Acknowledgements The authors wish to acknowledge the funding provided for this work by the European Space Agency in the frame of the ESA-PRODEX GOCESeaComb project (C4000106380).

References

Albertella A, Savcenko R, Janjić T, Rummel R, Bosch W, Schröter J (2012) High resolution dynamic ocean topography in the Southern Ocean from GOCE. Geophys J Int 190:922–930

Bruinsma SL, Förste C, Abrikosov O, Marty J-C, Rio M-H, Mulet S, Bonvalot S (2013) The new ESA satellite-only gravity field model via the direct approach. Geophys Res Lett 40:3607–3612. doi:10.1002/grl.50716

Ekman M (1989) Impacts of geodynamic phenomena on systems for height and gravity. Bull Geod 63(3):281–296

Förste C et al. (2012) A preliminary update of the Direct approach GOCE Processing and a new release of EIGEN-6C. Presented at the AGU Fall Meeting 3–7 Dec 2012 San Francisco, Abstract No. G31B-0923

Gruber T, Visser PNAM, Ackermann C, Hosse M (2011) Validation of GOCE gravity field models by means of orbit residuals and geoid comparisons. J Geod 85(11):845–860

Gruber T, Gerlach C, Haagmans R (2012) Intercontinental height datum connection with GOCE and GPS-levelling data. J Geod Sci 2(4):270–280. doi:10.2478/v10156-012-0001-y

Hayden T, Amjadiparvar B, Rangelova E, Sideris MG (2012) Evaluation of W0 in Canada using tide gauges and GOCE gravity field models. J Geod Sci 2(4):257–269. doi:10.2478/v10156-012-0008-4

Heiskanen WA, Moritz H (1967) Physical Geodesy. W.H. Freeman and Company, San Francisco

Hirt C, Gruber T, Featherstone WE (2011) Evaluation of the first GOCE static gravity field models using terrestrial gravity, vertical deflections and EGM2008 quasigeoid heights. J Geod 85(10):723–740

Knudsen P, Bingham R, Andersen OB, Rio M-H (2011) A global mean dynamic topography and ocean circulation estimation using a preliminary GOCE gravity model. J Geod 85(11):861–879

Pail R et al (2010) Combined satellite gravity field model GOCO01S derived from GOCE and GRACE. Geophys Res Lett 37:L20314. doi:10.1029/2010GL044906

Pail R et al (2011) First GOCE gravity field models derived by three different approaches. J Geod 85(11):819–843

Pavlis NK, Holmes SA, Kenyon SC, Factor JK (2012) The Development and Evaluation of the Earth Gravitational Model

2008 (EGM2008). J Geophys Res 117:B04406. doi:10.1029/2011JB008916

Sneeuw N (2000) A semi-analytical approach to gravity field analysis from satellite observations. Deutsche Geodätische Kommission Reihe C (Heft 527). Verlag der Bayerischen Akademie der Wissenschaften, München, p 117 ISBN (Print) 3-7696-9566-6, ISSN 0065-5325

Somieski A-E (2008) Astrogeodetic geoid and isostatic consideration in the North Aegean Sea, Greece. Dissertation for the Degree of Doctor of Philosophy, ETHZ, Dissert ETH No 17790. doi:10.3929/ethz-a-005710420

Šprlák M, Gerlach C, Pettersen PR (2012) Validation of GOCE global gravity field models using terrestrial gravity data in Norway. J Geod Sci 22:134–143

Tziavos IN (1987) Determination of geoidal heights and deflections of the vertical for the Hellenic area using heterogeneous data. Bul Géod 61:177–197

Tziavos IN, Vergos GS, Grigoriadis VN (2010) Investigation of topographic reductions and aliasing effects to gravity and the geoid over Greece based on various digital terrain models. Surv Geophys 31(3):23–67. doi:10.1007/s10712-009-9085-z

Tziavos IN, Vergos GS, Mertikas SP, Daskalakis A, Grigoriadis VN, Tripolitsiotis A (2013) The contribution of local gravimetric geoid models to the calibration of satellite altimetry data and an outlook of the latest GOCE GGM performance in GAVDOS. Adv Space Res 51(8):1502–1522. doi:10.1016/j.asr.2012.06.013

Vergos GS, Tziavos IN, Sideris MG (2006) On the validation of CHAMP- and GRACE-type EGMs and the construction of a combined model. Geod Cartogr 55(3):115–131

Vergos GS, Grigoriadis VN, Tziavos IN, Kotsakis C (2014) Evaluation of GOCE/GRACE Global Geopotential Models over Greece with collocated GPS/Levelling observations and local gravity data. In: Marti U (ed) Gravity, geoid and height systems, International Association of Geodesy Symposia, Vol 141. Springer, Switzerland, pp. 85–92. doi:10.1007/978-3-319-10837-7_11

Height System Unification Based on the Fixed GBVP Approach

Thomas Grombein, Kurt Seitz, and Bernhard Heck

Abstract

In general, any national or regional height reference system is related to an individual vertical datum, defined by one or several tide gauges. The discrepancies of these local vertical datums cause height datum offsets in a range of about ±1–2 m at a global scale. For the purpose of height system unification, global geopotential models derived from homogeneous satellite data provide an important contribution. However, to achieve a unification of high precision, the use of local terrestrial gravity data in the framework of a Geodetic Boundary Value Problem (GBVP) is required. By solving the GBVP at GNSS/leveling benchmarks, the unknown height datum offsets can be estimated in a least squares adjustment. In contrast to previous studies, related to the scalar free GBVP based on gravity anomalies, this paper discusses the alternative use and benefit of the fixed GBVP. This modern formulation of the GBVP is related to gravity disturbances, using the surface of the Earth as boundary surface. In contrast to gravity anomalies, gravity disturbances are not affected by the discrepancies of the local height datum. Therefore, in comparison to a scalar free GBVP approach, the proposed method is not affected by indirect bias terms, which will simplify a height system unification. In this paper, the theory of the fixed GBVP approach is developed and formulas in spherical approximation are derived. Moreover, the method is validated using a closed loop simulation based on the global geopotential model EGM2008, showing mm-accuracy of the estimated height datum offsets.

Keywords

Height system unification • Geodetic boundary value problem (GBVP) • Hotine's integral formula

1 Introduction

In geodesy, there are two different types of height systems: geometrical and physical. In the former, geometrically defined ellipsoidal heights are used, related to the orthogonal distance to a reference ellipsoid. In the latter, physical heights are utilized that refer to a physically defined reference surface linked to the Earth's gravity potential W.

The ellipsoidal height $h(P)$ of a point P on the Earth's surface can directly be measured using methods of GNSS positioning (Global Navigation Satellite Systems). By combining GNSS observations with other space techniques, global three-dimensional terrestrial reference frames have been established that provide sub-cm consistency in the vertical component, e.g., ITRF2008 (Altamimi et al. 2011).

For physical (or national) height systems the situation is quite different. Physical heights are determined by a combination of spirit leveling and gravimetry with respect to a fixed datum point P_0. These observations are then used

T. Grombein (✉) • K. Seitz • B. Heck
Geodetic Institute, Karlsruhe Institute of Technology (KIT), Englerstr. 7, Karlsruhe, 76128 Germany
e-mail: grombein@kit.edu

© Springer International Publishing Switzerland 2015

C. Rizos, P. Willis (eds.), *IAG 150 Years*, International Association of Geodesy Symposia 143,
DOI 10.1007/1345_2015_104

to derive geopotential numbers

$$C(P) := W_0 - W(P), \tag{1}$$

representing the difference of the gravity potential value between a leveling point P and the datum point P_0, i.e., $W_0 := W(P_0)$. In that way, the equipotential surface passing through P_0 is chosen as the reference level of the height system. Dividing Eq. (1) by the mean normal gravity value $\overline{\gamma}$ along the normal plumb line, the geopotential number $C(P)$ is transformed to the (metric) normal height $H(P)$ (Heiskanen and Moritz 1967, p. 170 f.).

For the practical realization of a physical height system, the height reference level is conventionally linked to the mean sea level (MSL), observed at one or several tide gauges, i.e., the datum point P_0 is selected such that the zero level is fixed to the local MSL. As the leveling networks of different national surveys mostly refer to individual tide gauges, hundreds of different national height systems exist worldwide that are realized by their own local vertical datum. Due to the sea surface topography, different tide gauges do not refer to the same equipotential surface. Therefore, the reference levels of different physical height systems are inconsistent by about ±1–2 m at a global scale (Heck 1990; Gerlach and Rummel 2013).

On the other hand, many global and regional applications such as monitoring of sea level change, ice sheet melting, or post-glacial rebound require a high-precision and consistent global physical height system. Moreover, this is also relevant for establishing the Global Geodetic Observing System (Ihde and Sánchez 2005). In order to overcome the problem of height datum inconsistencies, different strategies and approaches for height system unification have been discussed and proposed in various publications (e.g., Colombo 1980; Rapp 1988; Heck and Rummel 1990; Sansò and Venuti 2002; Sánchez 2009).

Considering a local height datum zone σ^i that is linked to the gravity potential value W_0^i, the geopotential number in Eq. (1) analogously reads

$$C^i(P) = W_0^i - W(P). \tag{2}$$

Combining Eqs. (1) and (2), the relation between the local datum zone σ^i and a global datum specified by the gravity potential value W_0 is described by the height datum offset

$$\delta H^i := \frac{C(P) - C^i(P)}{\overline{\gamma}} = \frac{W_0 - W_0^i}{\overline{\gamma}}. \tag{3}$$

For the determination of δH^i, observation points that combine physical and geometrical height information are of particular interest, i.e., GNSS/leveling benchmarks. For these points, global geopotential models (GGM) can be used to determine approximated values $C(P) = W_0 - W_{\mathrm{GGM}}(P)$, which can be inserted in Eq. (3). In this context, GGM derived from recent gravity field satellite missions like GRACE and GOCE provide an important contribution, as they provide a homogeneous reference surface that is not affected by a height datum offset (Rummel 2002; Gatti et al. 2013). Due to the limited resolution of the used GGM, such an approach suffers from an omission error. Although this error can be reduced, representing shorter wavelengths by the high-resolution EGM2008 (Pavlis et al. 2012) or regional geoid models, the expected accuracy for δH^i is limited to cm–dm level (Gruber et al. 2012; Rülke et al. 2012).

To achieve a unification at sub-cm level, the use of terrestrial gravity data in a Geodetic Boundary Value Problem is indispensable (GBVP, Heiskanen and Moritz 1967, p. 36 f.). For this purpose, the solution of the GBVP is used to estimate height datum offsets in a least squares approach (e.g., Heck and Rummel 1990). In contrast to previous publications, mostly related to the scalar free GBVP approach (Rummel and Teunissen 1988; Xu 1992; Gerlach and Rummel 2013), this paper discusses perspectives and benefits of the alternative use of a fixed GBVP approach for height system unification. In order to reduce systematic errors, a combination with a GGM and topographic information in a remove-compute-restore approach is advisable, as frequently used in gravimetric (quasi-)geoid determination (Forsberg and Tscherning 1997). However, such a combination is beyond the scope of this article. Therefore, the presented formulas will be restricted to the use of terrestrial gravity data.

The paper is organized as follows: in Sect. 2 the proposed fixed GBVP approach is presented and formulas in spherical approximation are derived. In order to validate the method and analyze its accuracy, a closed loop simulation based on EGM2008 is presented in Sect. 3. Finally, in Sect. 4, a summary and an outlook to ongoing research are provided.

2 Fixed GBVP Approach

Let the Earth's surface S be partitioned into n disjoint local height datum zones σ^i, $i = 1, \ldots, n$, i.e., $S = \bigcup_{i=1}^{n} \sigma^i$ with $\sigma^i \bigcap \sigma^k = \emptyset$ for $i \neq k$. Each datum zone is assumed to be linked to an individual equipotential surface defined by the gravity potential value W_0^i. Furthermore, let each datum zone σ^i contain m_i GNSS/leveling benchmarks P_j^i, $j = 1, \ldots, m_i$, where the (unbiased) ellipsoidal height h and the (biased) normal height H^i are known. For these benchmarks, the (biased) height anomaly $\zeta^i = h - H^i$ can be calculated, which is linked to the disturbing potential T by the generalized Bruns' formula (Heiskanen and Moritz 1967, p. 100):

$$\zeta^i(P_j^i) = \frac{T(P_j^i) - \left(W_0^i - U_0\right)}{\gamma} = \frac{T(P_j^i) - \Delta W_0}{\gamma} + \delta H^i, \tag{4}$$

where U_0 denotes the constant normal gravity potential value of the used reference ellipsoid, γ is the normal gravity value at the Earth's surface, and

$$\Delta W_0 := W_0 - U_0. \tag{5}$$

To determine the disturbing potential T, the fixed GBVP will be used that is based on gravity disturbances

$$\delta g := g(P) - \gamma(P) \approx -\frac{\partial T}{\partial r}\bigg|_S \tag{6}$$

resulting from the difference between the measured gravity $g(P)$ and the normal gravity $\gamma(P)$, both defined at the Earth's surface point $P \in S$. Here, $\partial/\partial r$ denotes the partial derivative with respect to the geocentric radius r. Considering the normal gravity formula (Heiskanen and Moritz 1967, p. 79), the ellipsoidal height $h(P)$ of the gravity measurement benchmark is required to obtain $\gamma(P)$. Thus, in the case of the fixed GBVP, the geometry of the Earth's surface S is assumed to be known, e.g, by GNSS positioning.

Utilizing the analytical solution of the fixed GBVP, the disturbing potential T can be obtained in constant radius approximation by Hotine's spherical integral formula (Hotine 1969, p. 311 ff.; Heck 2011):

$$T(\varphi, \lambda) = \frac{R}{4\pi} \iint_\sigma \delta g(\varphi', \lambda') \cdot \mathrm{H}(\psi)\, \mathrm{d}\sigma, \tag{7}$$

where

$$\mathrm{H}(\psi) = \frac{1}{\sin(\psi/2)} - \ln\left(1 + \frac{1}{\sin(\psi/2)}\right) \tag{8}$$

and ψ is the spherical distance between the position vectors of the computation point $P\,(r = R, \varphi, \lambda)$ and the running integration point $P'\,(\varphi', \lambda')$, both located on the sphere with radius R. The surface of the unit sphere is denoted by σ with the corresponding surface element $\mathrm{d}\sigma = \cos\varphi' \mathrm{d}\varphi' \mathrm{d}\lambda'$.

Applying Eq. (7) to Eq. (4) leads to

$$\zeta^i(P_j^i) = \frac{R}{4\pi\gamma} \iint_\sigma \delta g \cdot \mathrm{H}(\psi)\, \mathrm{d}\sigma - \frac{\Delta W_0}{\gamma} + \delta H^i, \tag{9}$$

which is the basic equation of the fixed GBVP approach that can already be used for the estimation of the unknown height datum offsets δH^i at GNSS/leveling benchmarks P_j^i.

However, the lacking availability of globally distributed gravity disturbances δg complicates the practical evaluation of Eq. (9). Since for most (historical) gravity measurement benchmarks of the pre-GNSS era the ellipsoidal height h has not been determined, gravity disturbances δg according to Eq. (6) could not be compiled. Instead, gravity measurements g have frequently been used to derive gravity anomalies Δg that serve as boundary values for the traditional scalar free GBVP. Taking into account the present situation, Eq. (9) will be extended by considering the transformation of gravity anomalies Δg to gravity disturbances δg.

2.1 Extension to Gravity Anomalies

Following the theory of Molodensky (Heiskanen and Moritz 1967, p. 291 ff.), gravity anomalies

$$\Delta g := g(P) - \gamma(Q) \approx \left(-\frac{\partial T}{\partial r} - \frac{2\gamma}{r}\zeta\right)\bigg|_\Sigma \tag{10}$$

differ from gravity disturbances δg in the normal gravity $\gamma(Q)$, evaluated at the telluroid $\Sigma \ni Q$ instead of the Earth's surface S. Considering that $h(Q) = H^i(P)$ (Heiskanen and Moritz 1967, p. 293), the normal gravity value $\gamma(Q)$ depends on the (biased) normal height. Thus, in contrast to gravity disturbances, gravity anomalies are affected by the height datum offset δH^i of the local datum zone σ^i (Heck 1990). This becomes clear when inserting Eq. (4) into Eq. (10):

$$\Delta g^i = \left(-\frac{\partial T}{\partial r} - \frac{2}{r}T + \frac{2}{r}\Delta W_0 - \frac{2\gamma}{r}\delta H^i\right)\bigg|_\Sigma. \tag{11}$$

Combining the boundary conditions of Eqs. (6) and (11), the (unbiased) gravity disturbance δg can be expressed as a function of the (biased) gravity anomaly Δg^i and the height datum offset δH^i using the linear approximation

$$\delta g = \Delta g^i + \left(\frac{2}{r}T - \frac{2}{r}\Delta W_0 + \frac{2\gamma}{r}\delta H^i\right)\bigg|_S + \delta_{\mathrm{BS}}, \tag{12}$$

where δ_{BS} denotes the error induced by the different boundary surfaces (S and Σ), which is neglected in the following.

Splitting Eq. (12) into three components

$$\delta g_0 := \Delta g^i + \frac{2}{r}T, \quad \delta g_1 := -\frac{2}{r}\Delta W_0, \quad \delta g_2 := \frac{2\gamma}{r}\delta H^i, \tag{13}$$

and inserting them separately into Eq. (9) results in

$$\zeta^i(P_j^i) = \zeta_0 + \zeta_1 + \zeta_2 - \frac{\Delta W_0}{\gamma} + \delta H^i, \tag{14}$$

where

$$\zeta_m := \frac{R}{4\pi\gamma} \iint_\sigma \delta g_m \cdot \mathrm{H}(\psi)\, \mathrm{d}\sigma, \quad m = 0, 1, 2. \tag{15}$$

Applying constant radius approximation, i.e., $r = R$, the evaluation of Eq. (15) leads to

$$\zeta_0 = \frac{R}{4\pi\gamma} \iint_{\sigma} \left(\Delta g^i + \frac{2}{R} T \right) \cdot \mathrm{H}(\psi)\, \mathrm{d}\sigma, \tag{16}$$

$$\begin{aligned} \zeta_1 &= -\frac{\Delta W_0}{2\pi\gamma} \iint_{\sigma} \mathrm{H}(\psi)\, \mathrm{d}\sigma = -\frac{\Delta W_0}{2\pi\gamma} \cdot 4\pi \\ &= -\frac{2\Delta W_0}{\gamma}, \end{aligned} \tag{17}$$

$$\zeta_2 = \sum_{i=1}^{n} \frac{\delta H^i}{2\pi} \iint_{\sigma^i} \mathrm{H}(\psi)\, \mathrm{d}\sigma, \tag{18}$$

where in the case of ζ_2, the (global) integral domain σ is decomposed into the disjoint height datum zones σ^i.

Finally, inserting Eqs. (16) – (18) into Eq. (14) results in

$$\zeta^i(P_j^i) = \zeta_0(\Delta g^i, T) + \delta H^0 + \delta H^i + \sum_{k=1}^{n} \delta H^k \cdot \mathrm{G}_j^{i,k}, \tag{19}$$

where

$$\delta H^0 := -\frac{3\Delta W_0}{\gamma}, \quad \text{and} \quad \mathrm{G}_j^{i,k} := \frac{1}{2\pi} \iint_{\sigma^k} \mathrm{H}(\psi)\, \mathrm{d}\sigma \Big|_{P_j^i}. \tag{20}$$

In Eq. (19) different kinds of height datum offsets occur. The height datum offset δH^i represents the direct influence of the datum zone σ^i containing P_j^i. This offset, also occurring in the basic Eq. (9), is frequently called direct bias term.

Moreover, Eq. (19) also comprises the height datum offsets δH^k $(k = 1, \ldots, n)$ of all datum zones, i.e., $\delta H^1, \ldots, \delta H^n$. These offsets are a consequence of the global integration of biased gravity anomalies Δg^i and are named indirect bias terms (Gerlach and Rummel 2013). Particularly, the evaluation of the corresponding factors $\mathrm{G}_j^{i,k}$ in Eq. (20) is complicated, as the separate integration requires the coordinates of the bounding polygon for each datum zone. While the indirect bias terms amount to about ±1–2 m, simulation studies for the scalar free GBVP approach presented by Gerlach and Rummel (2013) demonstrate that their influence can be reduced to a level below 1 cm, when a satellite-derived GGM is employed for representing the long-wavelength parts of ζ_0. However, it is worthwhile mentioning that the basic approach in Eq. (9) is not affected by the indirect bias terms. Therefore, if gravity disturbances δg become globally available, the indirect bias terms can be avoided, demonstrating the advantage of the fixed GBVP approach in future applications.

The parameter δH^0 in Eq. (19) comprises ΔW_0, defining the reference level of the global datum. As this global offset cannot be uniquely estimated within this approach, W_0 is assumed to be equal to U_0, i.e., ΔW_0 in Eq. (5) and δH^0 in Eq. (20) are set to zero. By this procedure, an "absolute" vertical datum is defined by convention (e.g., Heck 2004).

2.2 Least Squares Adjustment

Using Eq. (19) with $\delta H^0 = 0$, the observation equation for least squares adjustment (LSA) is provided by

$$L_j^i = \zeta^i - \zeta_0(\Delta g^i, T)\Big|_{P_j^i} = \delta H^i + \sum_{k=1}^{n} \delta H^k \cdot \mathrm{G}_j^{i,k}, \tag{21}$$

where Δg^i are the observed (biased) gravity anomalies and T the (unbiased) disturbing potential values, derived from an a priori model (e.g., EGM2008). The quantities on the left hand side of Eq. (21) are the known observations and those on the right hand side contain the unknowns to be estimated. The functional model according to Eq. (21) is specified by

$$\underbrace{\begin{pmatrix} l_1^1 + v_1^1 \\ l_2^1 + v_2^1 \\ \vdots \\ l_1^2 + v_1^2 \\ \vdots \\ l_{m_n}^n + v_{m_n}^n \end{pmatrix}}_{\mathbf{l}+\mathbf{v}} = \underbrace{\begin{pmatrix} 1 + \mathrm{G}_1^{1,1} & \mathrm{G}_1^{1,2} & \cdots & \mathrm{G}_1^{1,n} \\ 1 + \mathrm{G}_2^{1,1} & \mathrm{G}_2^{1,2} & \cdots & \mathrm{G}_2^{1,n} \\ \vdots & & & \\ \mathrm{G}_1^{2,1} & 1 + \mathrm{G}_1^{2,2} & \cdots & \mathrm{G}_1^{2,n} \\ \vdots & & & \\ \mathrm{G}_{m_n}^{n,1} & \mathrm{G}_{m_n}^{n,2} & \cdots & 1 + \mathrm{G}_{m_n}^{n,n} \end{pmatrix}}_{\mathbf{A}} \cdot \underbrace{\begin{pmatrix} \delta H^1 \\ \delta H^2 \\ \delta H^3 \\ \vdots \\ \delta H^n \end{pmatrix}}_{\mathbf{x}},$$

where $\mathbf{l}$ is the observation vector, $\mathbf{v}$ the inconsistency vector, and $\mathbf{x}$ the vector of unknowns. The design matrix $\mathbf{A}$ contains the partial derivatives of the observations with respect to the unknowns. Using a standard LSA, the unknown height datum offsets are estimated by

$$\hat{\mathbf{x}} = \mathbf{N}^{-1} \cdot \mathbf{A}^{\mathrm{T}} \mathbf{P} \cdot \mathbf{l}, \tag{22}$$

where $\mathbf{N} = \mathbf{A}^{\mathrm{T}}\mathbf{P}\mathbf{A}$ is the normal matrix and $\mathbf{P}$ is the weight matrix of the observations, which can be specified by an additional stochastic model.

3 Closed Loop Simulation

Using the presented fixed GBVP approach, a closed loop simulation is performed following a four-step sequence:

1. Definition of eight height datum zones σ^i with individual height datum offsets δH^i $(i = 1, \ldots, 8)$.
2. Addition of δH^i to EGM2008-derived observations.

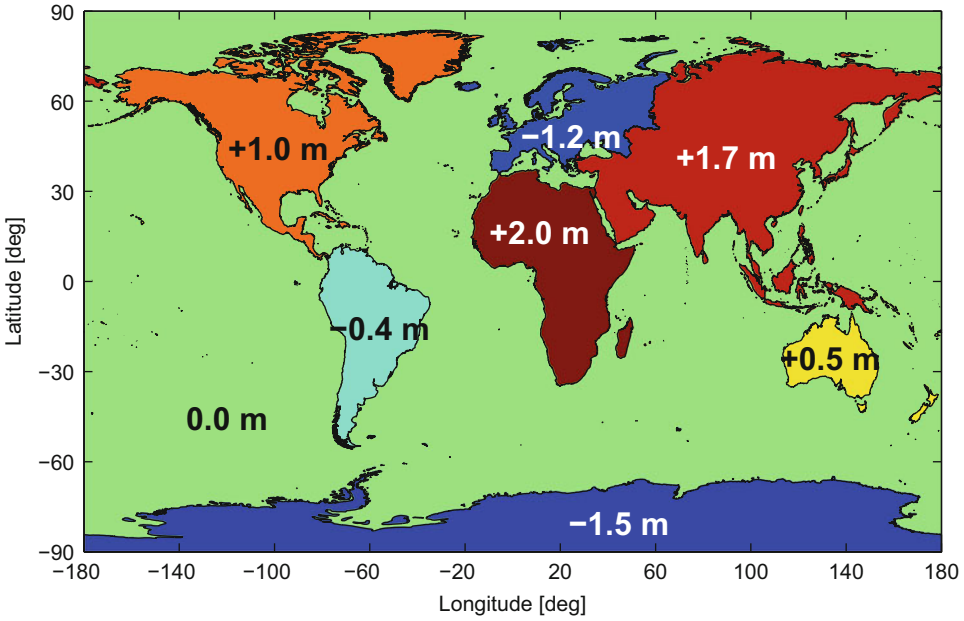

Fig. 1 Visualization of the height datum zones σ^i and their assumed height datum offsets δH^i used for the closed loop simulation

Table 1 Specification of the height datum zones σ^i, their assumed height datum offsets δH^i, and the error values ε^i according to Eq. (24) for the scenarios (a) – (d)

			Error values ε^i [mm]			
i	Datum zone σ^i	δH^i [m]	(a)	(b)	(c)	(d)
1	Asia	1.7	−0.2	1.3	−19.9	−0.6
2	North America	1.0	−0.4	1.5	−177.8	−4.1
3	Europe	−1.2	0.3	1.7	22.0	2.1
4	Africa	2.0	0.3	1.7	−24.4	2.2
5	South America	−0.4	−2.7	−0.9	10.6	−0.7
6	Australia	0.5	−0.5	2.2	10.1	2.2
7	Antarctica	−1.5	2.4	4.5	−25.7	3.8
8	Ocean	0.0	0.0	−2.7	−2.1	−2.5

3. Estimation of $\hat{\mathbf{x}}$ by Eq. (22) with $\mathbf{P} = \mathbf{I}$ (identity matrix).
4. Comparison of estimated and reference values.

As illustrated in Fig. 1 and specified by Table 1, the Earth's continents and oceans are utilized as height datum zones σ^i, where height datum offsets δH^i are assumed that cover the range of ± 1–2 m. Using EGM2008 to degree and order 2190, global grids of consistent height anomalies ζ_{EGM} ($5° \times 5°$), gravity anomalies Δg_{EGM} ($5' \times 5'$) and disturbing potential values T_{EGM} ($5' \times 5'$) are generated on a sphere with radius $R = 6,371$ km and normal gravity $\overline{\gamma} = \gamma = 9.81\ \mathrm{m\,s^{-2}}$. Applying the height datum offsets δH^i, simulated observations according to Eq. (21) are calculated by

$$L_j^i = \underbrace{\zeta_{\mathrm{EGM}} + \delta H^i}_{\zeta^i} - \zeta_0 \Big(\underbrace{\Delta g_{\mathrm{EGM}} - \frac{2\gamma}{R}\delta H^i}_{\Delta g^i}, \underbrace{T_{\mathrm{EGM}}}_{T} \Big) \Big|_{P_j^i}, \tag{23}$$

where the integration is performed by Gauss–Legendre quadrature (e.g., Schwarz 1989, p. 361 ff.).

To analyze the impact of the global distribution of the used benchmarks P_j^i, four different scenarios (a) – (d) are considered as displayed in Fig. 2. In scenario (a), all 2,592 observations L_j^i of the $5° \times 5°$ global grid are used in the LSA. In scenario (b), observations are restricted to continental areas (879 benchmarks), while in scenario (c) only observations in Europe, South America, and Australia are included (161 benchmarks). Scenario (d) is similar to (c), but additionally at least one benchmark is included in each datum zone (166 benchmarks). In each scenario, the height datum offsets of all datum zones are estimated.

In Table 1 the numerical results for the scenarios (a) – (d) are presented in terms of error values

$$\varepsilon^i = \delta H^i - \hat{x}^i, \tag{24}$$

where the estimated height datum offsets are denoted by $\hat{x}^i$, i.e., the components of $\hat{\mathbf{x}}$. Moreover, to quantify the stability of the LSA, Table 2 specifies the spectral condition number κ_2 of the normal matrix $\mathbf{N}$, i.e., the ratio of the largest to the smallest eigenvalue of the matrix (Schwarz 1989, p. 24f.).

In the ideal scenario (a), the error values attain a sub-mm level, only in South America and Antarctica slightly larger values occur. Excluding the observations of the oceans, scenario (b) produces error values at lower mm level. Going a step further towards a realistic scenario, case (c) demonstrates that the error values are increased to cm level or even dm level in North America. In contrast to the other scenarios, the large condition number of (c) indicates the instability of

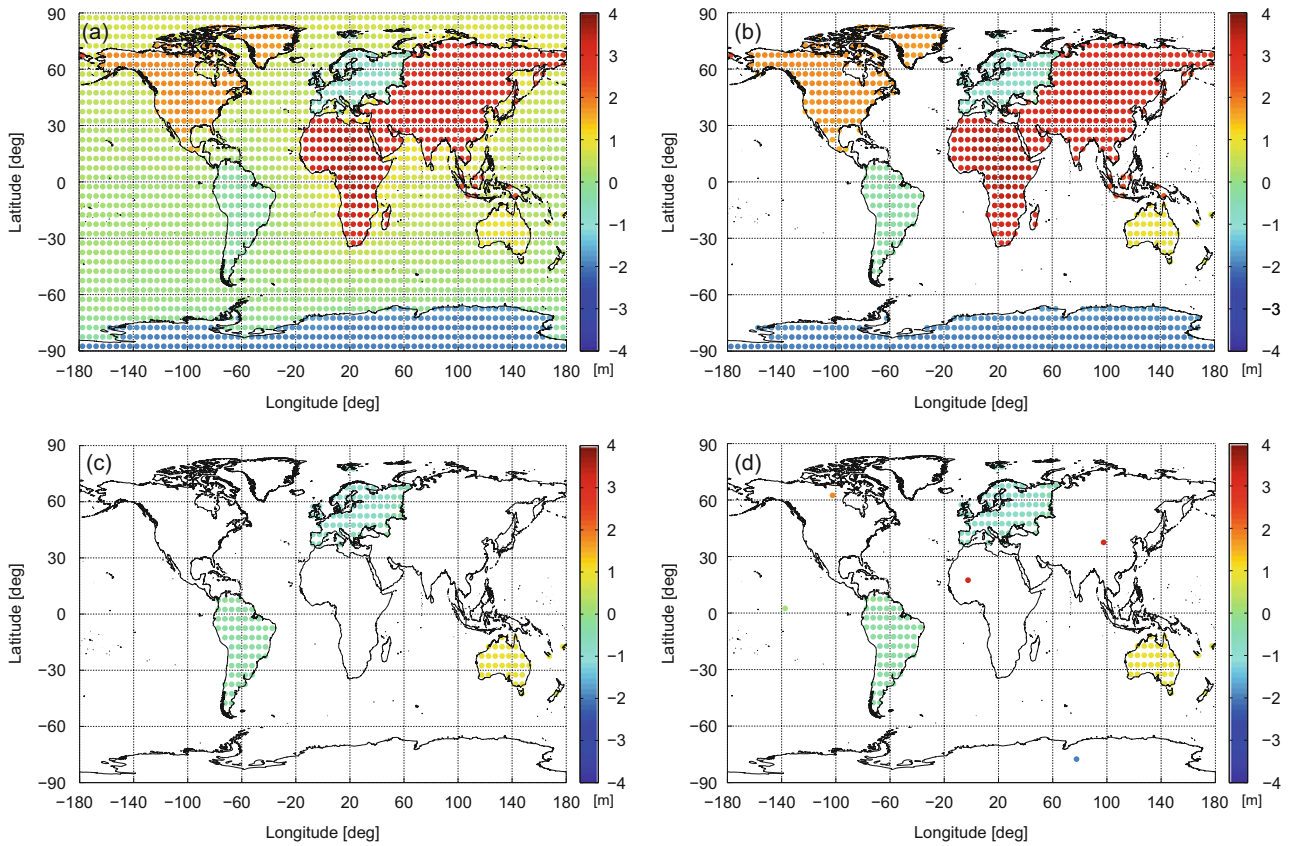

Fig. 2 Visualization of the global distribution of benchmarks P_j^i used in the scenarios (**a**) – (**d**). *Each dot* represents the value of an observation equation L_j^i according to Eq. (23)

Table 2 Spectral condition number κ_2 of the normal matrix **N**, quantifying the stability of the LSA for the scenarios (a) – (d)

Scenario	(a)	(b)	(c)	(d)
Condition number $\kappa_2(\mathbf{N})$	221	404	118480	246

the LSA. Concerning scenario (d), it is demonstrated that if at least one observation is added in each datum zone, this instability can be mitigated. Thus, scenario (d) provides an error level comparable to (b), showing that mm-accuracy can be achieved in principle. However, these accuracy values are quite optimistic and must be seen in the context of the assumed error-free observation data of the closed loop simulation. To obtain realistic values for practical applications, a formal error propagation procedure would have to be taken into account.

4 Summary and Outlook

In contrast to geometrically defined global terrestrial reference systems, physical height systems suffer from discrepancies of about ± 1–2 m due to the individual definition of their local vertical datum. In order to realize a comparison of physical heights, a height system unification is required.

In this paper, a method based on the solution of a fixed GBVP has been presented, where height datum offsets are estimated in a least squares adjustment. In contrast to previous approaches using the traditional scalar free GBVP, the formulation of the proposed method is based on (unbiased) gravity disturbances that do not cause indirect bias terms. Therefore, the fixed GBVP approach simplifies the estimation of height datum offsets, when gravity disturbances become globally available in the future. However, considering the current situation of the global gravity data base, the approach is extended by a transformation of gravity anomalies to gravity disturbances also comprising indirect bias terms. By conducting a closed loop simulation based on eight height datum zones and EGM2008-derived observations, the fixed GBVP approach has been validated, showing a mm-accuracy of the estimated height datum offsets. Furthermore, the stability of the adjustment has been analyzed showing a dependency on the global distribution of the observations; at least one observation should be located in each datum zone.

As future work, the impact of approximation errors on the presented spherical solution will be analyzed and taken

into account by suitable reductions. First results concerning the fixed GBVP are presented by Müßle et al. (2014). In addition, the combination of terrestrial gravity data with a GGM and topographic information will be investigated as well as a modification of Hotine's integral kernel to restrict the global integration area (Featherstone 2013).

Acknowledgements The authors acknowledge the financial support provided by the German Research Foundation (DFG) under grant number HE1433/20-1. Furthermore, we would like to thank three anonymous reviewers as well as the associated editor and the Editor-in-Chief for their valuable comments, which helped to improve the manuscript.

References

Altamimi Z, Collilieux X, Métivier L (2011) ITRF2008: an improved solution of the international terrestrial reference frame. J Geod 85(8):457–473. doi:10.1007/s00190-011-0444-4

Colombo OL (1980) A world vertical network. Rep 296, Dep. of Geodetic Science, Ohio State University, Columbus, USA

Featherstone WE (2013) Deterministic, stochastic, hybrid and band-limited modifications of Hotine's integral. J Geod 87(5):487–500. doi:10.1007/s00190-013-0612-9

Forsberg R, Tscherning CC (1997) Topographic effects in gravity field modelling for BVP. In: IAG symposia, vol 65, pp 239–272. doi:10.1007/BFb0011707

Gatti A, Reguzzoni M, Venuti G (2013) The height datum problem and the role of satellite gravity models. J Geod 87(1):15–22. doi:10.1007/s00190-012-0574-3

Gerlach C, Rummel R (2013) Global height system unification with GOCE: a simulation study on the indirect bias term in the GBVP approach. J Geod 87(1):57–67. doi:10.1007/s00190-012-0579-y

Gruber T, Gerlach C, Haagmans R (2012) Intercontinental height datum connection with GOCE and GPS-levelling data. J Geod Sci 2(4):270–280. doi:10.2478/v10156-012-0001-y

Heck B (1990) An evaluation of some systematic error sources affecting terrestrial gravity anomalies. Bull Géod 64(1):88–108. doi:10.1007/BF02530617

Heck B (2004) Problems in the definition of vertical reference frames. In: IAG symposia, vol 127, pp 164–173. doi:10.1007/978-3-662-10735-5_22

Heck B (2011) A Brovar-type solution of the fixed geodetic boundary-value problem. Stud Geophys Geod 55(3):441–454. doi:10.1007/s11200-011-0025-2

Heck B, Rummel R (1990) Strategies for solving the vertical datum problem using terrestrial and satellite geodetic data. In: IAG symposia, vol 104, pp 116–128. doi:10.1007/978-1-4684-7098-7_14

Heiskanen WA, Moritz H (1967) Physical geodesy. WH Freeman, San Francisco, USA

Hotine M (1969) Mathematical geodesy. ESSA Monograph 2, US Dep. of Commerce, Washington, USA

Ihde J, Sánchez L (2005) A unified global height reference system as a basis for IGGOS. J Geodyn 40(4–5):400–413. doi:10.1016/j.jog.2005.06.015

Müßle M, Heck B, Seitz K, Grombein T (2014) On the effect of planar approximation in the geodetic boundary value problem. Stud Geophys Geod 58(4):536–555. doi:10.1007/s11200-013-0249-4

Pavlis NK, Holmes SA, Kenyon SC, Factor JK (2012) The development and evaluation of the Earth Gravitational Model 2008. J Geophys Res 117, B04406. doi:10.1029/2011JB008916

Rapp RH (1988) The need and prospects for a world vertical datum. In: IAG symposia, vol 2, pp 432–445

Rülke A, Liebsch G, Sacher M, Schäfer U, Schirmer U, Ihde J (2012) Unification of European height system realizations. J Geod Sci 2(4):343–354. doi:10.2478/v10156-011-0048-1

Rummel R (2002) Global unification of height systems and GOCE. In: IAG symposia, vol 123, pp 13–20. doi:10.1007/978-3-662-04827-6_3

Rummel R, Teunissen P (1988) Height datum definition, height datum connection and the role of the geodetic boundary value problem. Bull Géod 62(4):477–498. doi:10.1007/BF02520239

Sánchez L (2009) Strategy to establish a global vertical reference system. In: IAG symposia, vol 134, pp 273–278. doi:10.1007/978-3-642-00860-3_42

Sansò F, Venuti G (2002) The height datum/geodetic datum problem. Geophys J Int 149(3):768–775. doi:10.1046/j.1365-246X.2002.01680.x

Schwarz HR (1989) Numerical analysis: a comprehensive introduction. Wiley, Chichester, UK

Xu P (1992) A quality investigation of global vertical datum connection. Geophys J Int 110(2):361–370. doi:10.1111/j.1365-246X.1992.tb00880.x

Airborne and Shipborne Gravimetry at GFZ with Emphasis on the GEOHALO Project

Svetozar Petrovic, Franz Barthelmes, and Hartmut Pflug

Abstract

In 2011 the German Research Centre for Geosciences (GFZ) purchased a new mobile gravimeter Chekan-AM. To be prepared for the GEOHALO mission the performance of the new instrument was tested in two shipborne campaigns. The achieved high repeatability of gravity measurements (within 1 mgal) completely met the expectations.

In the first half of June 2012 the multidisciplinary geoscientific airborne mission GEOHALO took place, airborne gravity measurements with our new equipment being the main part of it. The project covered the Italian Peninsula and surroundings and was accomplished by an international group of scientific and exploration institutions. The mission was flown on the new German High Altitude and LOng Range Research Aircraft (HALO). In contrast to applications in geophysical exploration, our idea was not to achieve the maximum resolution at the lowest flight speed and altitude possible, but to cover a relatively wide region in realistic time span using a jet aircraft. The experiment resulted in resolution and accuracy suitable for establishing links between satellite and terrestrial gravity measurements. In particular, it can be concluded that the equipment is very well suited for improving global combined (satellite-terrestrial) gravity field models in regions with sparse terrestrial data coverage.

Keywords

Airborne gravimetry • CHEKAN gravimeter • GEOHALO project • Shipborne gravimetry

1 Introduction

In 2011 the German Research Centre for Geosciences (GFZ) replaced its Air-Sea-Gravimeter S124 (L&R) which did not work reliably by a new equipment for airborne and shipborne gravimetry (Fig. 1). The central part of the system is a mobile gravimeter Chekan-AM (Krasnov et al. 2011a,b; Stelkens-Kobsch 2005). Other components of the equipment (like GNSS receivers) were updated as well.

S. Petrovic • F. Barthelmes (✉) • H. Pflug
GFZ German Research Centre For Geosciences, Section 1.2,
Telegrafenberg, 14473 Potsdam, Germany
e-mail: franz.barthelmes@gfz-potsdam.de

Successful application of this type of gravimeter (Chekan-AM) both in shipborne and airborne gravity campaigns was already reported in literature (Krasnov et al. 2011b; Zheleznyak 2010). We present briefly some results from our campaigns, especially from the airborne campaign GEOHALO. Additionally, this new equipment was used in three shipborne campaigns (see Sect. 2) to test the performance of the new instrument (campaigns on Lake Müritz and Lake Constance), and to improve parts of the German geoid (campaigns on Lake Constance and on the Baltic Sea).

The main purpose is to use the equipment in challenging airborne campaigns like GEOHALO (see Sect. 3) and in possible future missions in Antarctica (Scheinert 2010). In the focus are the conclusions relevant for forthcoming applications of our airborne instrumentation and methodology

© Springer International Publishing Switzerland 2015

C. Rizos, P. Willis (eds.), *IAG 150 Years*, International Association of Geodesy Symposia 143,
DOI 10.1007/1345_2015_17

Fig. 1 The equipment mounted inside the HALO aircraft: gravimeter Chekan-AM (*left*) and the operator rack (*right*)

in gravity field determination, in particular for geodetic purposes.

2 Shipborne Gravimetric Campaigns

We participated in three shipborne campaigns:

- October 2011: Lake Müritz (Germany), Figs. 2 and 3.
- October 2012: Bodensee (Lake Constance), cooperation with the German Federal Agency for Cartography and Geodesy (BKG), Figs. 2 and 4.
- June 2013: Oderhaff (Szczecin Lagoon) and an Ostsee (Baltic Sea) area adjacent to Poland – cooperation with BKG.

The 2 days mission on Lake Müritz was the first performance test of the new gravimeter. One profile (see Fig. 2) was measured seven times. Figure 3 shows the achieved high repeatability of the gravity measurements (within 1 mgal) at a resolution of ca. 400 m. The main purpose of the other two campaigns (accomplished in cooperation with BKG) was refining the existing gravity data and improving the geoid modeling in these border regions between Germany and neighboring countries (Schäfer et al. 2013). Very good performance of the gravimeter was confirmed again (Fig. 4). High quality results obtained with this type of instrument in shipborne gravimetry are already known from the literature (Zheleznyak 2010). Nevertheless, since gravimeters are no mass products, it is advisable to test the performance of every individual specimen.

3 Airborne Gravimetry in the Frame of GEOHALO Mission

In the first half of June 2012 our first airborne gravity campaign using Chekan-AM took place as part of the multidisciplinary geoscientific airborne mission GEOHALO. The project covered the Italian Peninsula and surroundings and

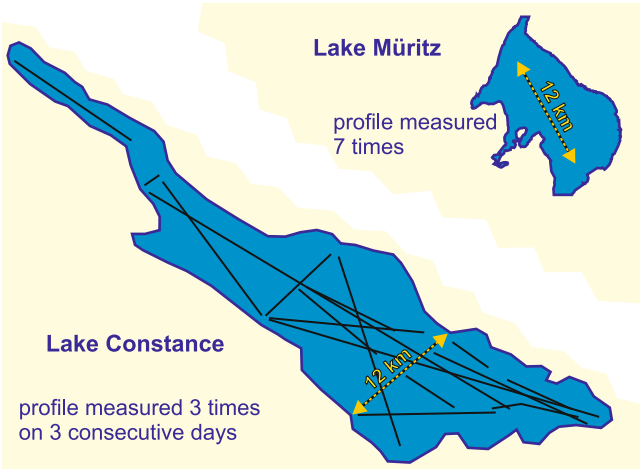

Fig. 2 Contours of the lakes Müritz and Constance, and the measured profiles

was accomplished by an international group of scientific and exploration institutions, see Scheinert et al. (2013) and Fig. 5. The mission was flown on the German High Altitude and LOng Range Research Aircraft (HALO), which is a modification of the business jet G550 (Gulfstream Aerospace Corporation). Hence, a jet aircraft was used flying at a higher altitude and with higher speed than it is usual for exploration purposes. In contrast to geophysical exploration (maximum resolution at the lowest flight speed and altitude possible) the leading idea was to demonstrate the possibility to cover a wide region in a realistic time span achieving the resolution needed to refine a global satellite-only gravity model in areas with sparse terrestrial data or to close the so-called "polar gap" (due to the satellites' inclinations) of dedicated satellite gravity field missions.

The parameters of the mission were: total length of all profiles of about 16,150 km, effective measurement time of circa 33 h, mostly at an altitude of approximately 3,500 m, and an average speed of 425 km/h.

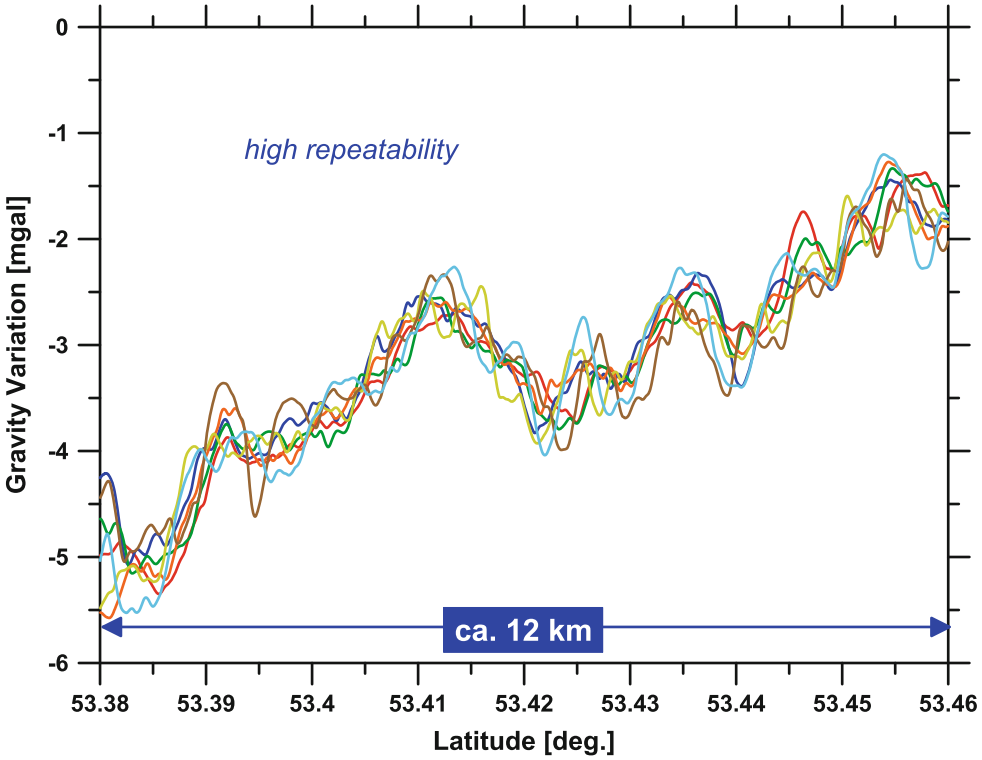

Fig. 3 Gravity variations (including the normal gravity) measured seven times along the same profile (see Fig. 2) on lake Müritz

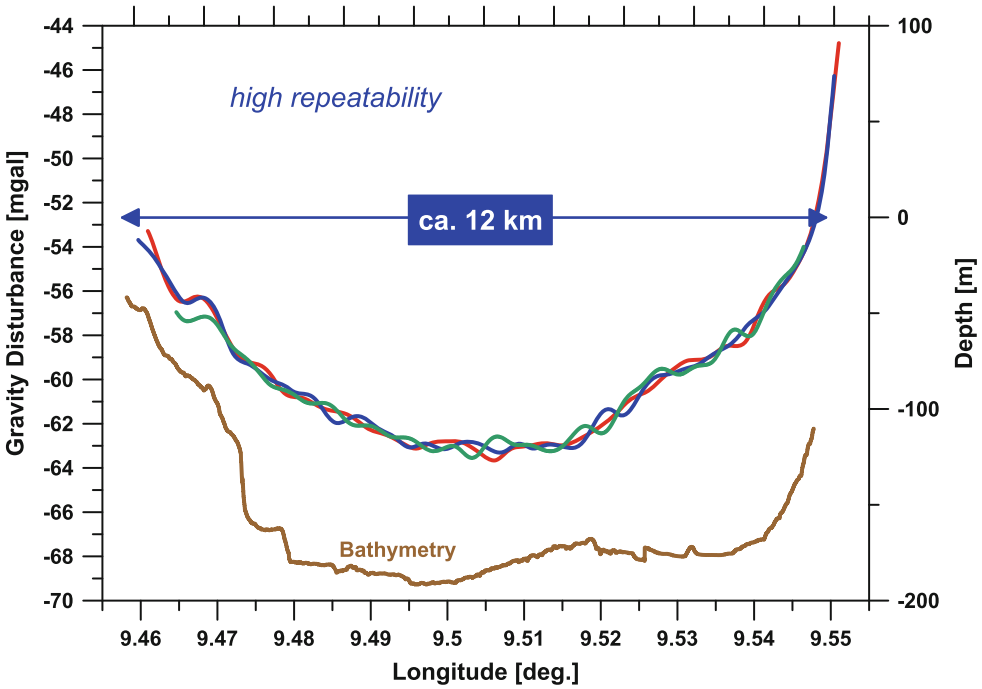

Fig. 4 Gravity disturbances measured three times along the same profile (see Fig. 2) on lake Constance

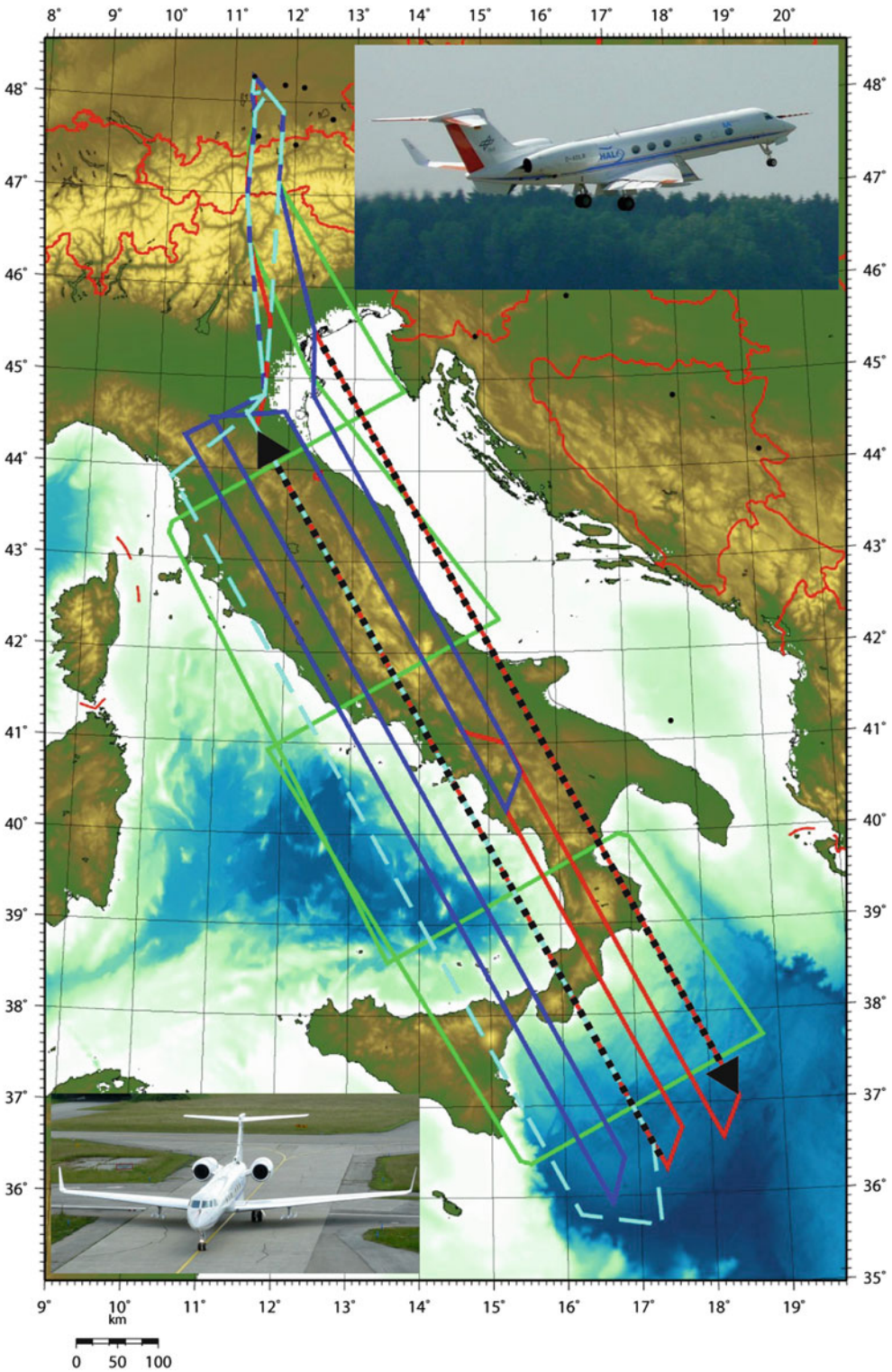

Fig. 5 Flight tracks of the 4 day mission, the results for two tracks (*black dotted lines*) are presented as example (Fig. 8)

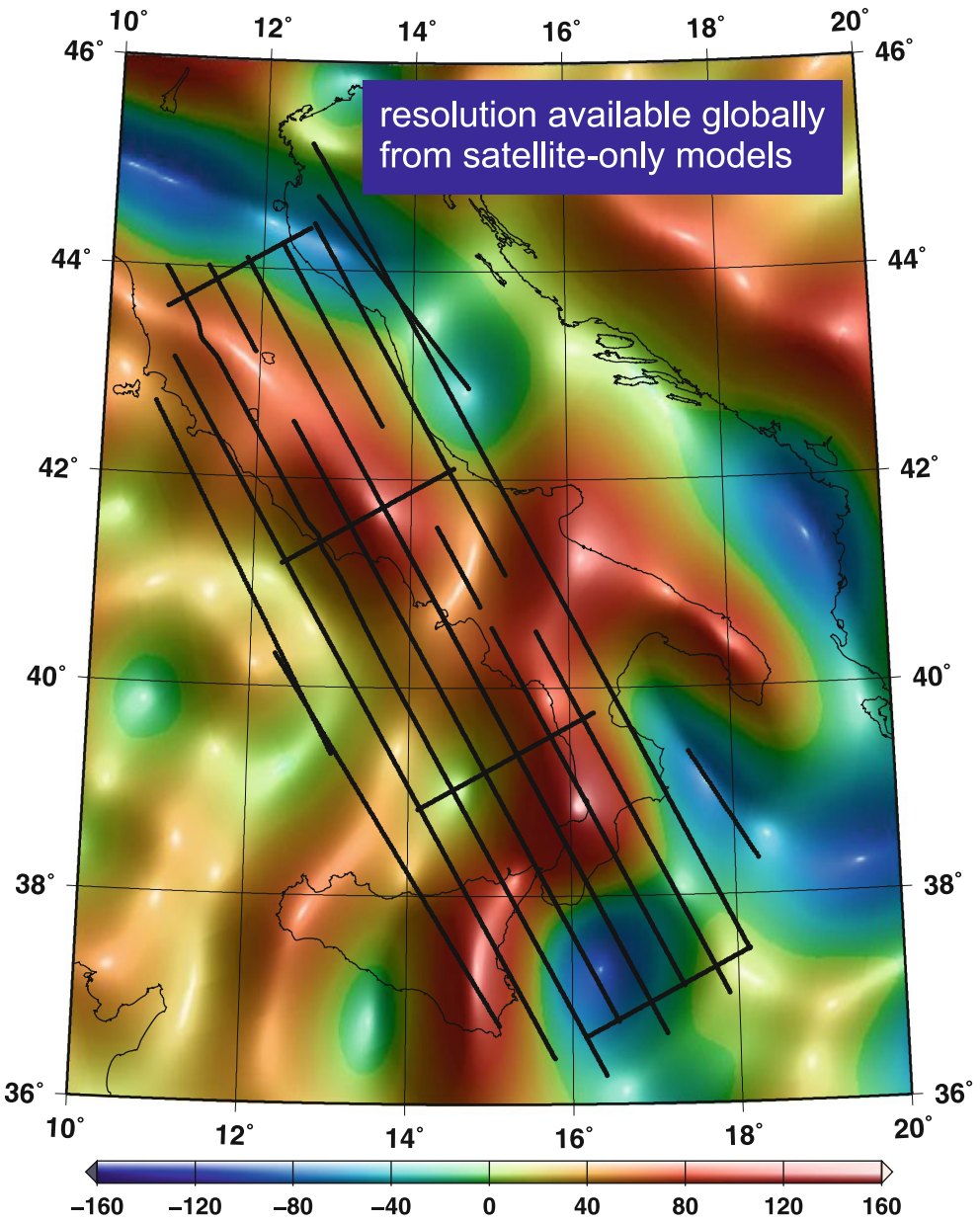

Fig. 6 Gravity disturbances on the ellipsoid of the satellite-only model EIGEN-6S and the locations of usable data of the GEOHALO mission

3.1 Data Processing Along Individual Profiles

The principles of airborne gravimetry can be found for instance in Forsberg and Olesen (2010). We applied the processing scheme presented by Krasnov et al. (2011b).

The recovery of gravimeter readings along the trajectory of the aircraft is based on the mathematical model and calibration constants provided by the manufacturer of the instrument. In order to calculate the gravity values (at flight altitude) the Eötvös correction (Jekeli 2001, eq. 10.95, p. 334) and the vertical component of the kinematic acceleration have to be subtracted. The last mentioned component is usually computed by numerical double differentiation of the position from GNSS. Due to the higher speed of the HALO aircraft, this procedure did not give satisfactory results and the inclusion of Doppler observations into the GNSS processing seems necessary.

Since all mentioned acceleration components contain high-frequency noise they have to be low-pass filtered, applying the same filter characteristics. A 100 s low-pass filter, used in data processing, corresponds at the aircraft speed of about 120 m/s to a spatial resolution of about 12 km (half wave length).

The gravimeter recordings taken before and after the flights always at approximately the same position were used to eliminate the drift of the gravimeter. After correcting the drift, the relative gravity values along the trajectories can be transformed into absolute gravity values using an appropriate gravity datum. For this, a local relative gravity survey was

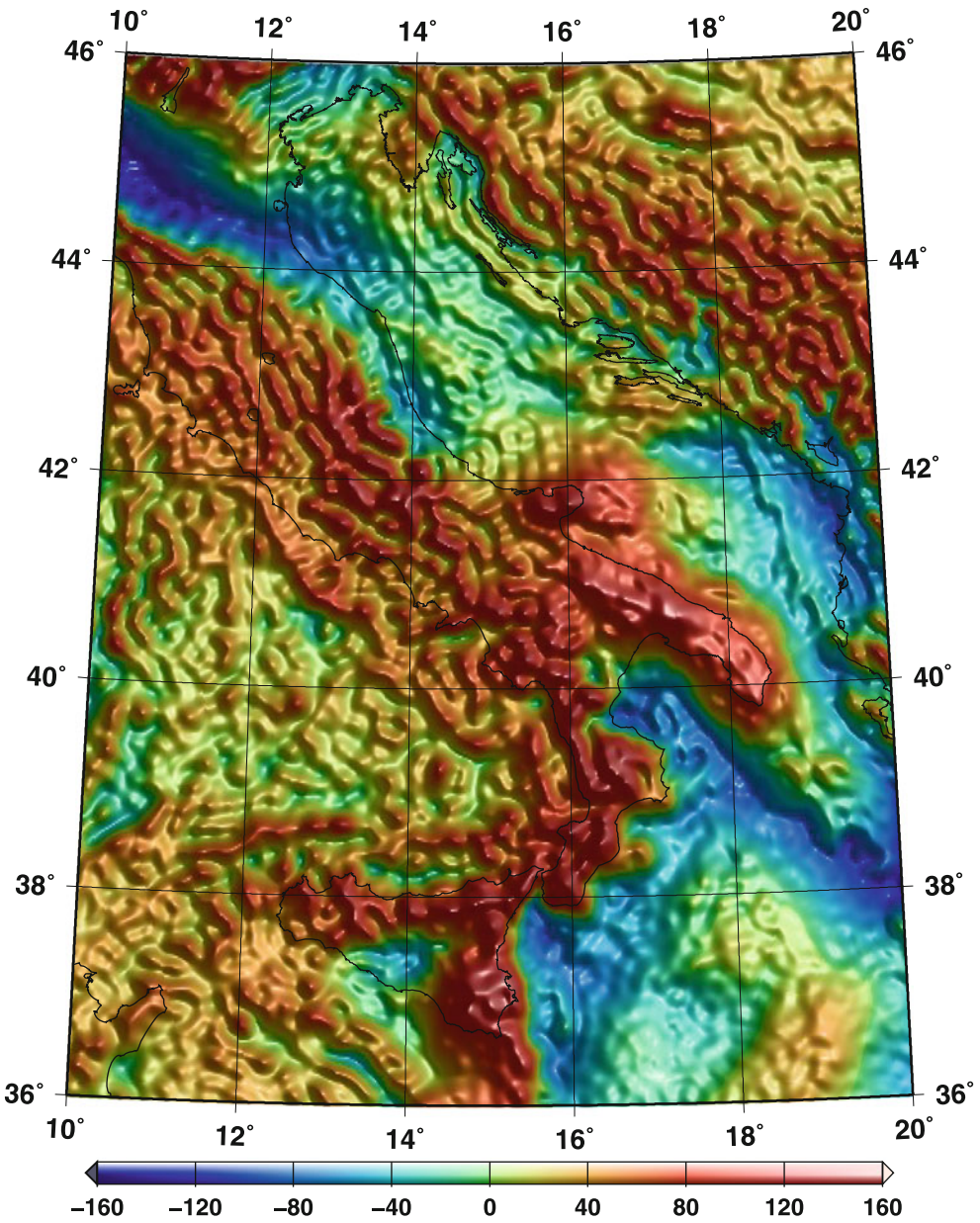

Fig. 7 Gravity disturbances on the ellipsoid of the model EIGEN-6C2

conducted during the time of the GEOHALO mission to link a local marker at the apron with gravity reference points in the vicinity of the airfield.

The investigations of several aspects, including the influence of the chosen way of GNSS processing, different low-pass filters, etc., are still going on and the outcome presented here has to be regarded as a first preliminary result.

3.2 Possibilities to Check the Collected Data

First, we eliminated approximately (only) 5% of the recordings which are definitively not usable (recordings immediately after the change of track, some short periods of too strong turbulences, and similar). The waste in airborne gravimetry is usually larger. We retained for the moment all data (Fig. 6) which might be usable at the end or should be analyzed for the reasons of mismatches.

After this, 19 cross-over points are obtained; 4 of them are obviously outliers, and will be analyzed in more details in future. The remaining 15 are obviously too few for any serious statistics (holds also for 19), and especially for any cross-over adjustment. Nevertheless, let us mention that the mean cross-over difference is 0.5 mgal, the mean of the absolute values of differences 2.9 mgal, and their RMS-difference 3.4 mgal. As explained, these values should not be over-interpreted.

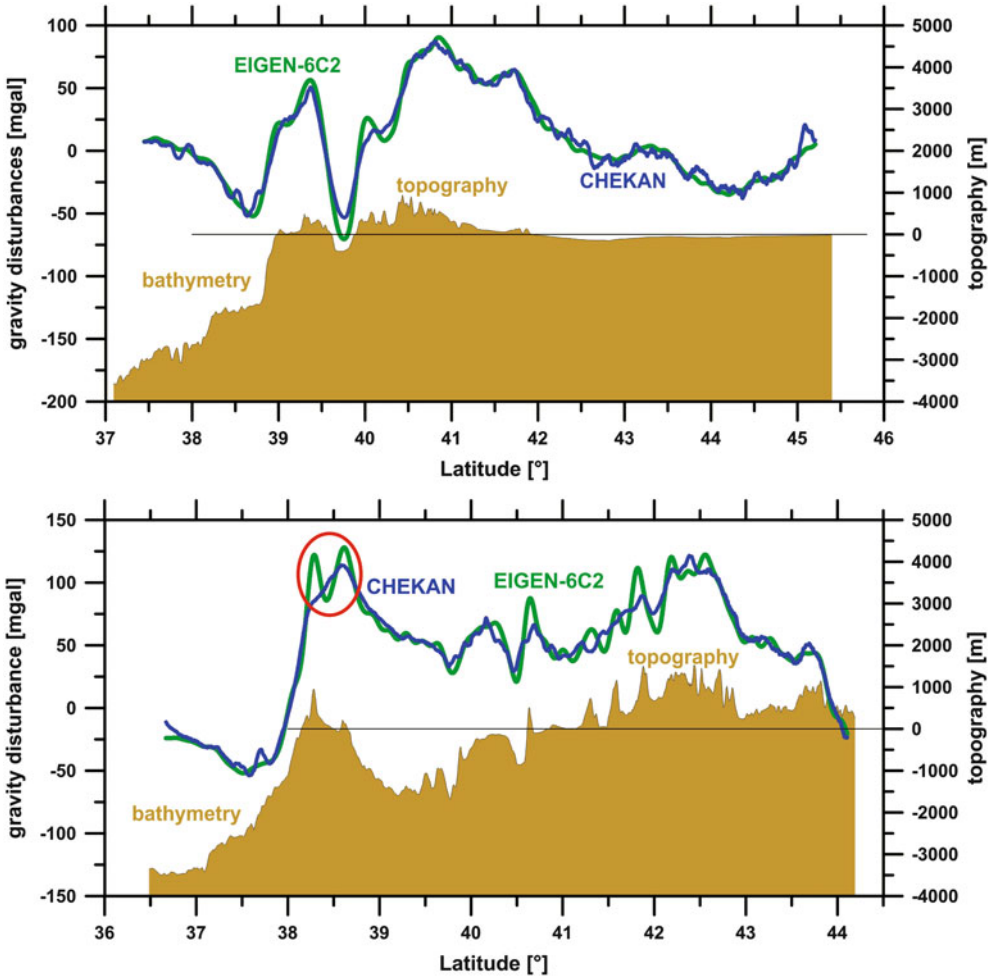

Fig. 8 Gravity disturbances measured along the two profiles displayed in Fig. 5 (eastern track: *top*, western track: *bottom*) and computed from the model EIGEN-6C2, both at flight altitude. Topography and bathymetry are also shown

Because there are only so few cross-over points, a detailed error analysis can only be done by comparisons with accurate ground data which is planed for future work in cooperation with Italian colleagues.

However, if airborne gravimetry is used not only to measure the gravity field along some special profiles but over a given region, as it was in our case, it has to be taken into account that the spatial resolutions along-track and cross-track are two different issues.

For this mission the along track resolution is about 12 km (see Sect. 3.1). The cross-track resolution is directly given by the track distance. For the GEOHALO mission the track distance of 40 km was a good balance between the different objectives of the participating multidisciplinary teams and the budget.

In areas where no or only sparse (or bad) terrestrial data are available the only gravity field information comes from the global satellite-only gravity field models. These models are represented mathematically in terms of spherical harmonics and recent models have maximum degrees and orders from $N_{max} = 230$ to $N_{max} = 260$ which corresponds to a best possible spatial resolution, i.e. smallest representable bumps and dales, of ca. 80–100 km (see e.g. Barthelmes 2013, table 1). Figure 6 shows the gravity disturbances of the model EIGEN-6S (Förste et al. 2013) ($N_{max} = 240$, data from LAGEOS, GRACE AND GOCE) for the Italian region. Additionally, the positions of the usable data of the mission are drawn.

The most recent global gravity field model which, additionally to satellite data, contains data from altimetry over the oceans, and terrestrial gravity measurements over the continents, is the model EIGEN-6C2 (Förste et al. 2013). The maximum degree and order of this spherical harmonic model is $N_{max} = 1949$ which corresponds to a best possible resolution of ca. 10–12 km. However, this resolution is only realized in regions where good and dense data are integrated into the model. Fortunately, this is the case for the Italian region and we can use this model for a first rough evaluation of the airborne gravity data. Figure 7 shows the gravity disturbances of this model for the area of interest.

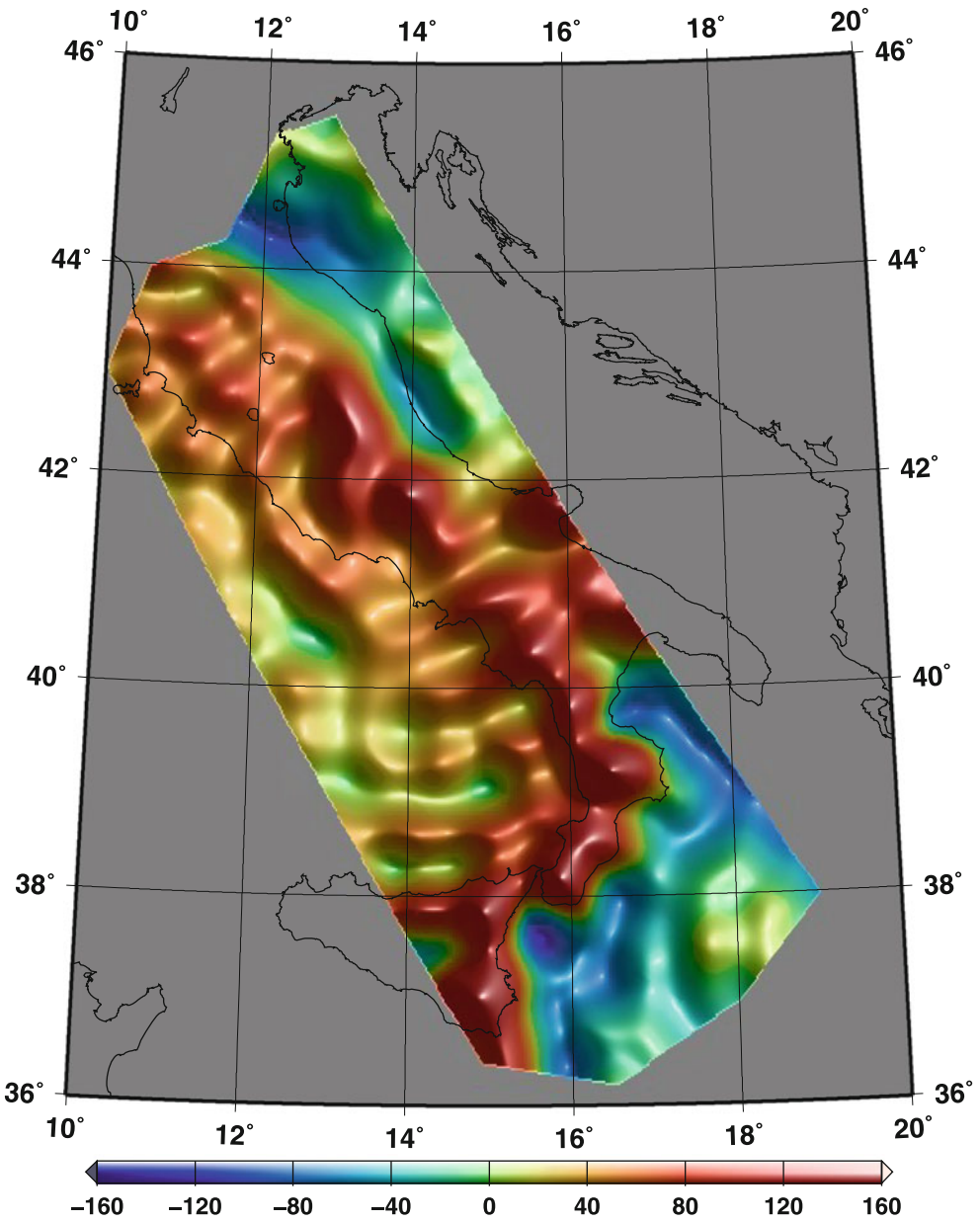

Fig. 9 Gravity disturbances on the ellipsoid of the model EIGEN-6C2 up to $N_{max} = 600$. This is the resolution expected due to the 40 km track distance

3.3 Comparison with the Global Model EIGEN-6C2

As a first step, the measurements along the tracks can be directly compared to the values computed from the model EIGEN-6C2 at the same points. Figure 8 shows these comparisons for the two tracks marked in Fig. 5. The normal gravity at the points has been subtracted; thus, the values are gravity disturbances at flight height. The curves show the expected resolution of about 10–12 km and the good match between the model and the measurements. The difference between our measurements and the global model EIGEN-6C2, marked with a red ellipse in Fig. 8, might be a result of the well-known oscillating behavior of a truncated spherical harmonic series at locations where structures with sharp edges should be approximated. Analogous comparisons with the model EIGEN-6C2 have been done for all tracks and show similar concordance. Although the final interpretation of the differences between the model and the measurements should be done in more detail after the final data processing, the quick visual comparison with EIGEN-6C2 gives an impression of the reliability of the airborne gravity measurements.

To use airborne gravity measurements for geodetic purposes in particular, if we want to compute geoid undulations from these data, and the measurements should be compared or combined with ground data and satellite derived models, the best way seems to be to compute a harmonic

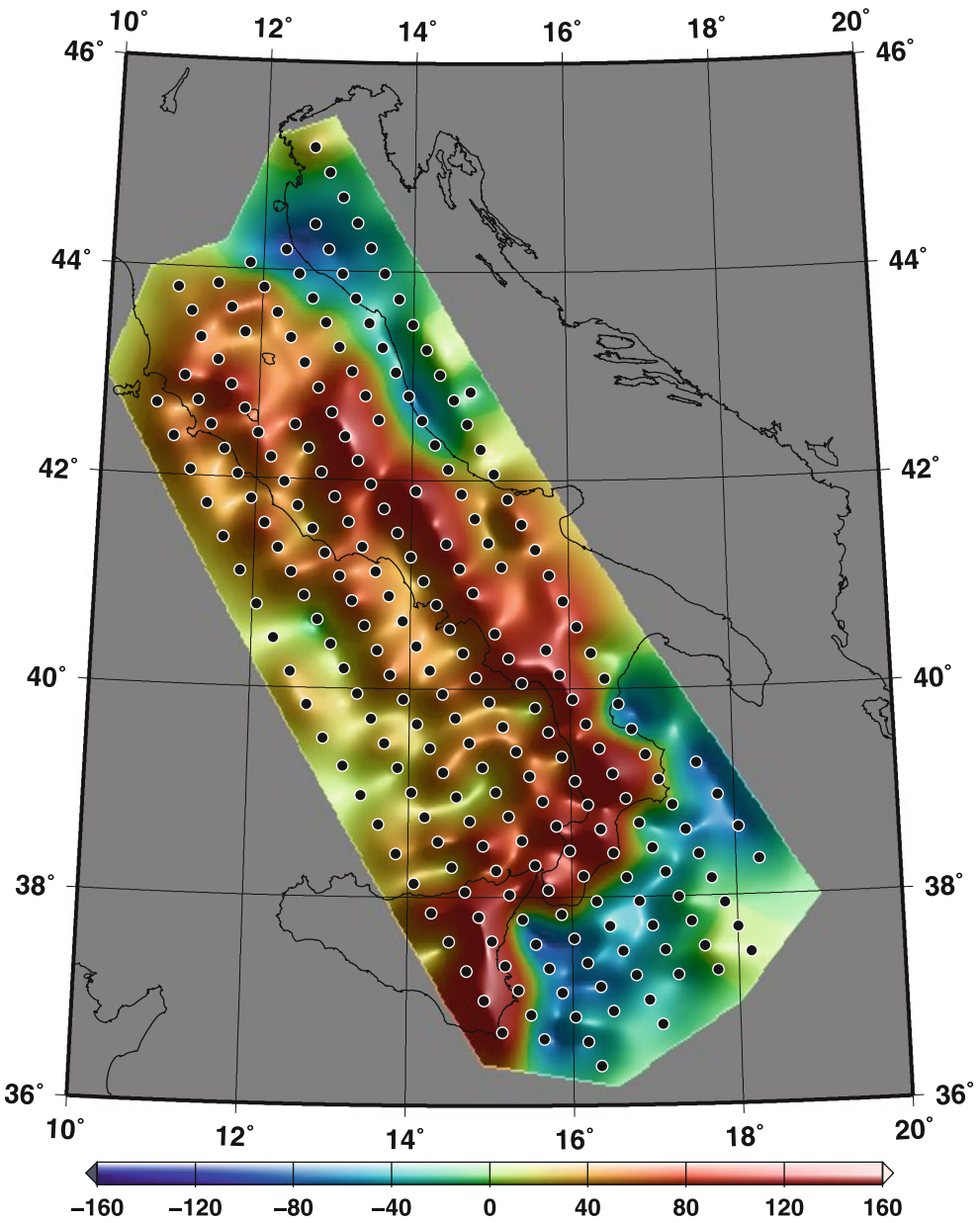

Fig. 10 Gravity disturbances on the ellipsoid of the point mass model (236 masses) computed alone from the airborne gravity values at flight height

function approximation which fits the data. The limit for the resolution of such a function is the 40 km track distance because we don't want to have a non-isotropic spatial resolution. This corresponds to a spherical harmonic representation with maximum degree and order of approximately $N_{max} = 600$. Figure 9 shows the gravity disturbances of the model EIGEN-6C2 truncated at degree $N = N_{max} = 600$, which gives an impression what can be expected by modeling the gravity measurements of the GEOHALO mission. This means that airborne gravity campaigns such as the GEOHALO-mission should be able to improve the globally available resolution of 80–100 km of the satellite-only models (Fig. 6) to a resolution of about 40 km shown in Fig. 9.

To demonstrate this in a first simple test we computed a point mass model with fixed positions and a fixed uniform depth by least squares fitting the masses to the measured gravity values. For this, the masses were distributed along the tracks at a distance and depth corresponding to the expected resolution limited by the 40 km track spacing. Thus, 40 km has been chosen for the depth and for the mean distance of the masses along the tracks, but no masses were placed under data gaps. From the gravity measurements at flight height the normal gravity has been subtracted and these data has been used to compute the magnitudes of the 236 masses by a least squares fit. The method of approximating the gravity field by point masses has been described in the past in many publications. Overviews are given e.g. by Barthelmes (1986, 1989), Barthelmes and Dietrich (1991), Claessens et al. (2001), and Klees et al. (2008). The resulting gravity disturbances of this point mass model on the

ellipsoid are shown together with the positions of the masses in Fig. 10. The Figs. 9 and 10 show very good agreement in all details, which confirms the quality of the airborne measurements.

For geoid computations from data of such a mission a satellite-only model should be subtracted prior to the fit of the harmonic function (and has to be added afterwards) to minimize the (long-wavelength) influence of the areas without measurements outside the region. If high resolution topography information is available, it should be used too. In areas where good ground data are available (like in our case) such airborne missions with long tracks can be used to homogenize the ground data. These topics as well as a detailed error analysis of the measurements are tasks for the future.

4 Conclusions and Outlook

Shipborne gravity campaigns confirmed the high repeatability of the measurements performed by the gravimeter CHEKAN-AM.

The GEOHALO experiment confirmed reasonable agreement with a high resolution global gravity field model (which is based on good terrestrial data in this region). Furthermore, this experiment resulted in resolution and accuracy suitable for establishing links between satellite and terrestrial gravity measurements. In particular, it can be concluded that the equipment is very well suited for improving global combined (satellite-terrestrial) gravity field models in regions with sparse terrestrial data coverage.

Acknowledgements The financial contribution of the German Research Foundation (DFG) in the frame of SPP 1294 ("High Altitude and LOng Range Research Aircraft") is gratefully acknowledged. The realization of the described mission was made possible by the efforts of all members of the GEOHALO team, especially of its coordinator Mirko Scheinert. We are also grateful to the Federal Agency for Cartography and Geodesy (BKG) for pleasant cooperation in two shipborne campaigns and especially for the big engagement in solving all logistic and organizational problems. Last but not least, we thank Anton Krasnov from the manufacturer of our gravimeter Chekan-AM, Concern CSRI Elektropribor (Saint Petersburg, Russia) for his helpfulness in solving questions connected with the functioning of the instrument.

References

Barthelmes F (1986) Untersuchungen zur Approximation des äußeren Gravitationsfeldes der Erde durch Punktmassen mit optimierten Positionen. Veröffentlichungen des Zentralinstituts für Physik der Erde 92, Zentralinstitut für Physik der Erde, Potsdam. http://www.gfz-potsdam.de/bib/pub/digi/barthelmes_diss1986.pdf

Barthelmes F (1989) Local gravity field approximation by point masses with optimized positions. In: 6th international symposium "geodesy and physics of the earth". Veröffentlichungen des Zentralinstituts für Physik der Erde, vol 102, Part 2, pp 157–167. ftp://ftp.gfz-potsdam.de/pub/home/sf/bar/publications/pm-local_89.pdf

Barthelmes F (2013) Definition of functionals of the geopotential and their calculation from spherical harmonic models: theory and formulas used by the calculation service of the international centre for global Earth models (ICGEM); http://icgem.gfz-potsdam.de/ICGEM/. Scientific Technical report STR09/02, Revised edition, January 2013, GeoForschungZentrum Potsdam. doi:10.2312/GFZ.b103-0902-26. http://gfzpublic.gfz-potsdam.de/pubman/item/escidoc:104132

Barthelmes F, Dietrich R (1991) Use of point masses on optimized positions for the approximation of the gravity field. In: Rapp R, Sansò F (eds) Determination of the geoid: present and future. International association of geodesy symposia. Springer, New York, pp 484–493

Claessens S, Featherstone W, Barthelmes F (2001) Experiences with point-mass modelling in the Perth region, Western Australia. Geo Res Aust 75:53–86

Forsberg R, Olesen AV (2010) Airborne gravity field determination. In: Xu G (ed) Sciences of geodesy - I. Springer, Berlin, pp 83–104. doi:10.1007/978-3-642-11741-1_3. http://dx.doi.org/10.1007/978-3-642-11741-1_3

Förste C, Bruinsma S, Flechtner F, Marty JC, Dahle C, Abrikosov O, Lemoine JM, Neumayer KH, Barthelmes F, Biancale R, König R (2013) A new combined global gravity field model including GOCE data up to degree and order 1949 of GFZ Potsdam and GRGS Toulouse. Paper presented at the general assembly European geosciences union, Vienna, 3–7 December 2013

Jekeli C (2001) Inertial navigation systems with geodetic applications. De Gruyter, Berlin [u.a.]. http://books.google.de/books?id=9OLlnQEACAAJ

Klees R, Tenzer R, Prutkin I, Wittwer TF (2008) A data-driven approach to local gravity field modelling using spherical radial basis functions. J Geod 82(1):457–471

Krasnov A, Nesenyuk L, Peshekhonov V, Sokolov A, Elinson L (2011a) Integrated marine gravimetric system. Development and operation results. Gyroscopy Navig 2(2):75–81. doi:10.1134/S2075108711020052. http://dx.doi.org/10.1134/S2075108711020052

Krasnov A, Sokolov A, Usov S (2011b) Modern equipment and methods for gravity investigation in hard-to-reach regions. Gyroscopy Navig 2(3):178–183. doi:10.1134/S2075108711030072. http://dx.doi.org/10.1134/S2075108711030072

Schäfer U, Liebsch G, Rülke A, Schirmer U, Barthelmes F, Petrovic S, Pflug H (2013) Recent ship-borne gravity campaigns in Germany—motivation, design and first results. Paper presented at the IAG Scientific Assembly, Potsdam, 1–6 September 2013

Scheinert M (2010) Progress in the regional determination of the Antarctic geoid. Poster presented at the SCAR open science conference, Buenos Aires, 3–6 August 2010

Scheinert M, Petrovic S, Heyde I, Barthelmes F, The GEOHALO Group (2013) The geodetic-geophysical flight mission GEOHALO: results of airborne gravimetry and further geodetic products. Paper presented at the IAG scientific assembly, Potsdam, 1–6 September 2013

Stelkens-Kobsch T (2005) The airborne gravimeter Chekan-A at the institute of flight guidance (IFF). In: Jekeli C, Bastos L, Fernandes J (eds) Gravity, geoid and space missions. International association of geodesy symposia, vol 129. Springer, Berlin, pp 113–118. doi:10.1007/3-540-26932-0_20. http://dx.doi.org/10.1007/3-540-26932-0_20

Zheleznyak L (2010) The accuracy of measurements by the CHEKAN-AM gravity system at sea. Izv Phys Solid Earth 46(11):1000–1003. doi:10.1134/S106935131011008X. http://dx.doi.org/10.1134/S106935131011008X

A Comparison of the Performance of Medium- and High-Quality Inertial Systems Grades for Strapdown Airborne Gravimetry

Richard Deurloo, Wenlin Yan, Machiel Bos, Diogo Ayres-Sampaio, Américo Magalhães, Matthias Becker, David Becker, and Luisa Bastos

Abstract

In 2010 and 2011 airborne field campaigns were carried out with the goal to assess and compare the performance of various GNSS/IMU systems for airborne gravimetry. These so-called strapdown gravimetry systems are less expensive, more compact and less power consuming, while being easier to install and operate, than spring gravimeters. Besides the quality of the IMU, the performance of a strapdown system depends on a number of factors, such as flight speed and flight altitude, as well as flight stability, among others. The results achieved showed that it is possible, with a simple set up based on only one GNSS antenna/receiver, and a medium cost IMU, to reach accuracies of a few miligal. This confirms the possibility to use medium cost strapdown systems for regional geoid improvement, in particular in areas lacking any other gravimetric data. The navigation grade IMUs, as expected, delivered better results. Comparison with the EGM2008 model showed an agreement better than 1 mGal over land and worst, of the order of a few mGal, in coastal areas. The paper also shows that with proper modelling and adequate filtering, good results can still be obatined even in more difficult/turbulent flight conditions.

Keywords

Airborne • GNSS • Gravity • IMU • Strapdown

R. Deurloo • W. Yan • D. Ayres-Sampaio • A. Magalhães • L. Bastos
Astronomical Observatory, University of Porto, Monte da Virgem, 4430-146 V.N. Gaia, Portugal
e-mail: richarddeurloo@gmail.com; williamtown.yan@gmail.com; dsampaio@fc.up.pt; americo.magalhaes@fc.up.pt; lcbastos@fc.up.pt

M. Bos
Space & Earth Geodetic Analysis Laboratory (UBI/IDL), Universidade da Beira Interior, Rua Marquês d'Ávila e Bolama, 6201-001 Covilhã, Portugal
e-mail: machielbos@gmail.com

M. Becker • D. Becker
Physical and Satellite Geodesy, Department of Civil and Environmental Engineering, Technische Universitaet Darmstadt, Franziska-Braun-Str. 7, 64287 Darmstadt, Germany
e-mail: becker@psg.tu-darmstadt.de; dbecker@psg.tu-darmstadt.de

L. Bastos (✉)
Interdisciplinary Centre of Marine and Environmental Research (CIIMAR/CIMAR), University of Porto, Rua dos Bragas 289, 4050-123 Porto, Portugal
e-mail: lcbastos@fc.up.pt

1 Introduction

Strapdown gravimetry systems are based on a combination of one or more Global Navigation Satellite System (GNSS) receivers and a (strapdown) Inertial Measurement Unit (IMU) or Inertial Navigation System (INS). Inertial systems are typically composed of a triad of accelerometers and a triad of angular rate sensors (e.g., Fiber-Optic Gyros (FOGs) or Ring-Laser Gyros (RLG)) which provide acceleration and angular velocities output along three orthogonal instrument axes. Because an IMU or INS provides measurements along three axes, strapdown GNSS/IMU gravimetry systems may be able to determine not just the vertical component of the gravity (i.e., scalar gravimetry), but also the horizontal components. In other words, it opens the possibility of determining the full gravity vector (i.e., vector gravimetry).

Typical strapdown gravimetry systems use navigation grade inertial systems. Although this provides excellent per-

© Springer International Publishing Switzerland 2015

C. Rizos, P. Willis (eds.), *IAG 150 Years*, International Association of Geodesy Symposia 143,
DOI 10.1007/1345_2015_18

formance, these systems are still quite expensive. Early results with navigation grade systems showed that accuracies were similar to those obtained with spring gravimeters. Spring gravimeters can provide accuracies of 2 mGal for spatial resolutions down to 4–5 km (Forsberg and Olesen 2010), while strapdown gravimetry systems have been reported to provide accuracies in the range of 1.5–2 mGal for a spatial resolution of 5–6 km or better for scalar gravimetry (Bruton et al. 1999; Kwon and Jekeli 2001).

However, the limited quality of the gyros of the medium-quality inertial systems does not allow the horizontal components of the gravity vector to be determined. Furthermore, in airborne applications, the gyro sensors are affected by air turbulence, engine vibration, temperature variation, among others, which contribute to degrade the attitude solutions. In airborne gravimetry precise attitude information is required. In a system with limited gyro performance, estimating heading with an error below 0.06° may not be possible. Hence acceleration errors of the order of 1 mgal can appear. The proper specification of the IMUs sensor errors contributes to improve the overall parameter estimation.

In the scope of two research projects developed at the University of Porto airborne surveys were performed in 2010 and 2011 over the Madeira archipelago and in the southern area of mainland Portugal using different types of aircrafts. One of the goals of these surveys was to acquire data to assess the performance of different GNSS/IMU systems, and associated processing approaches, to determine the gravity field. Among the systems tested were a medium-quality (tactical grade) IMU with FOG, a Litton LN-200, and two different high-quality (navigation grade) IMUs, an iXSea AIRINS with high performance FOG gyros and an iMAR RHQ-1003, with RLG.

In this work we describe the setup used for our airborne tests and we present results of the evaluation of the performance of the medium- and high-quality inertial systems. This includes an analysis of the results of overlapping flight lines obtained with the IMUs, a comparison with a global gravity field model, and a comparison with local terrestrial gravity data. A medium-quality inertial system is limited to determining the vertical component of the gravity vector, therefore the analysis and comparison presented here is limited to scalar gravimetry.

2 Campaigns and Processing

2.1 Campaigns and Sensors

To evaluate the performance of the different GNSS/IMU systems available, two field campaigns with different aircrafts and sensors were undertaken. The campaigns were realized in the scope of two research projects:

- GEOMAD (GEOid over MADeira) an EURFAR (European Facility For Airborne Research) project;
- PITVANT (Projecto de Investigação e Tecnologia em Veículos Aéreos Não-Tripulados) a project funded by the Portuguese Ministry of Defence.

The GEOMAD campaign (Fig. 1a) was performed in August/September of 2010 over the island of Madeira with an ATR42 aircraft. A Litton LN-200 and an iXsea AIRINS were used together with a GNSS receiver. GNSS data was acquired at a rate of 1Hz and IMU data at 200Hz and 100Hz respectively.

Two flights were completed covering the island with 6 east–west and 8 north–south flight tracks. The flight lines were spaced less than 10 km apart and had a combined length of around 1,700 km. The east–west lines were flown on 27 August at a constant height of 3,000 m; the north–south lines were flown on 31 August at a height of 2,600 m. The minimum height of these flights was limited by the topography of Madeira island, which has its highest point at around 1,860 m. The flights were flown on autopilot at a mean velocity of 110 m/s. These flights were smooth and without turbulence.

The PITVANT campaign (Fig. 1b) was flown in September of 2011 over mainland Portugal with a Casa C-212 Aviocar from the Portuguese Air Force. A Litton LN-200 and an iMar RQH were used, sampling at 200Hz and 300Hz respectively, together with one GNSS receiver sampling at 1Hz. The flight altitude ranged between 300 and 950 m. This flight was flown without autopilot (not available on this particular aircraft) at a mean velocity of 70 m/s. This test flight was done in the early to mid afternoon on a very hot day and there was a significant amount of turbulence.

For computing the position and velocity of the aircraft dual-frequency GNSS receivers were used on the aircraft and reference stations on the ground for precise relative positioning. For the GEOMAD campaign the reference station was set up in the island of Porto Santo, from where the plane took off.

2.2 Processing

As stated in the introduction, the limited quality of the gyros of the medium-quality inertial systems does not allow the horizontal components of the gravity vector to be determined. Therefore the estimation process was limited to the scalar gravimetry.

There are various approaches to estimate the gravity disturbance from the integration of GNSS and inertial sensors data. Again, because of its limited performance not all processing approaches are applicable to tactical grade systems.

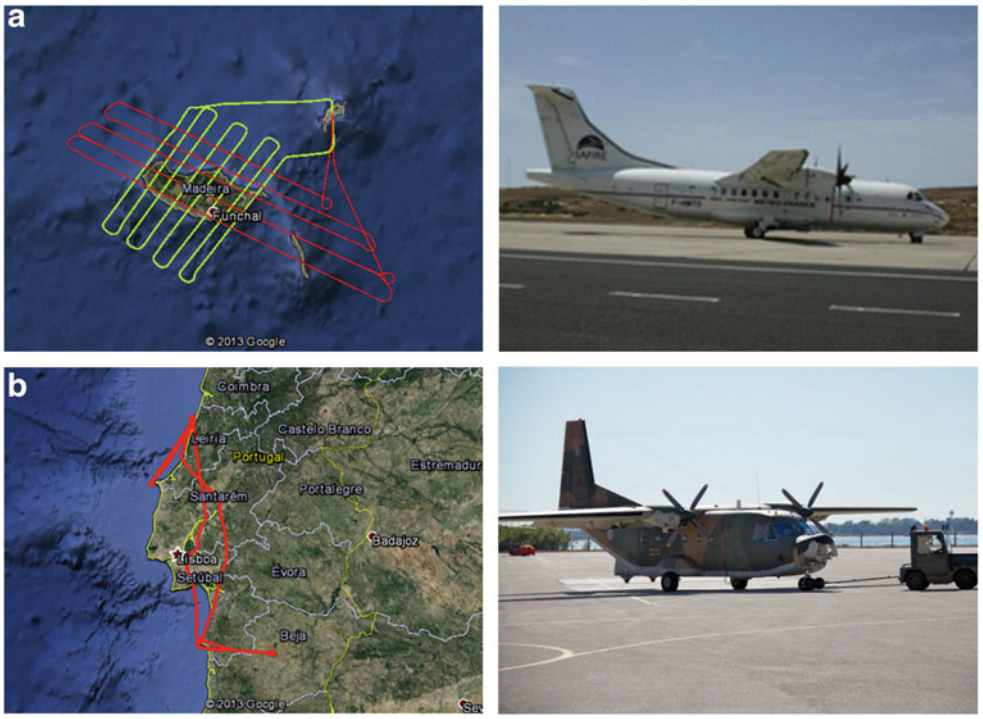

Fig. 1 Flight trajectories: (**a**) Flight profiles for part of the GEOMAD campaign (**b**) Trajectory during the PITVANT campaign

Here the so-called inertial navigation approach was used, in which the gravity disturbance (the difference between the actual gravity and the normal gravity) is estimated as an error state in the inertial navigation equations (Deurloo 2011).

A 16-state Extended Kalman Filter (EKF) is used for the estimation of the navigation errors (position, velocity, and attitude), sensor errors (accelerometer and gyro biases) and the gravity disturbance. The system error dynamics model for the EKF follows the typical inertial navigation equations (Jekeli 2001) and can then be written in the form of:

$$\delta\dot{\mathbf{x}} = \mathbf{F}\delta\mathbf{x} + \mathbf{G}\mathbf{w} \tag{1}$$

with the error state vector $\delta\mathbf{x}$ defined as:

$$\delta\mathbf{x} = \left[\, \delta\mathbf{r}_e^l \;\; \delta\mathbf{v}_e^l \;\; \boldsymbol{\Psi}_b^l \;\; \mathbf{b}_a \;\; \mathbf{b}_\omega \;\; \delta\mathbf{g}^i \,\right]^T \tag{2}$$

The position error vector $\delta\mathbf{r}_e^l$, velocity error vector $\delta\mathbf{v}_e^l$, orientation error vector $\boldsymbol{\Psi}_b^l$, have been augmented with the gravity disturbance vector and systematic inertial sensor errors. The vectors $\mathbf{b}_a$ and $\mathbf{b}_\omega$ are the sensor biases, and $\delta\mathbf{g}^i$ is the gravity disturbance. Note that all error vectors have three components with the exception of the gravity disturbance. For scalar gravimetry this has only one component. The inertial sensor errors are all modeled as random constant biases. The gravity disturbance is modeled as a random walk process. The (augmented) process noise $\mathbf{w}$ in Equation (1) is then:

$$\mathbf{w} = \left[\, \mathbf{w}_a \;\; \mathbf{w}_\omega \;\; \mathbf{w}_{\delta g} \,\right]^T \tag{3}$$

where the vectors $\mathbf{w}_a$ and $\mathbf{w}_\omega$ are the sensor white noise processes, and $\mathbf{w}_{\delta g}$ is the white noise process driving the random walk process of the gravity disturbance.

The observation model for the update of the EKF can be written in the form of:

$$\delta\mathbf{z} = \mathbf{H}\delta\mathbf{x} + \mathbf{v} \tag{4}$$

where $\delta\mathbf{z}$ contains the difference between the observed position and velocity (from GNSS) and the predicted position and velocity from the system dynamics:

$$\delta\mathbf{z} = \left[\, \delta\mathbf{z}_r \;\; \delta\mathbf{z}_v \,\right]^T \tag{5}$$

The vector $\mathbf{v}$ contains the observation noise:

$$\mathbf{v} = \left[\, \mathbf{v}_r \;\; \mathbf{v}_v \,\right]^T \tag{6}$$

3 Results and Discussion

The gravity estimation results from the two project campaigns are presented here. Figure 2 shows the results of one of the GEOMAD flight profiles over time (part of which was flown twice) and Figs. 3 and 4 show the results for sections of the PITVANT flight. The PITVANT results are shown for 2 sections where relatively smooth flight was possible: Ocean (oceanic coastal zone of Portugal) and Land (terrestrial zone southern Portugal).

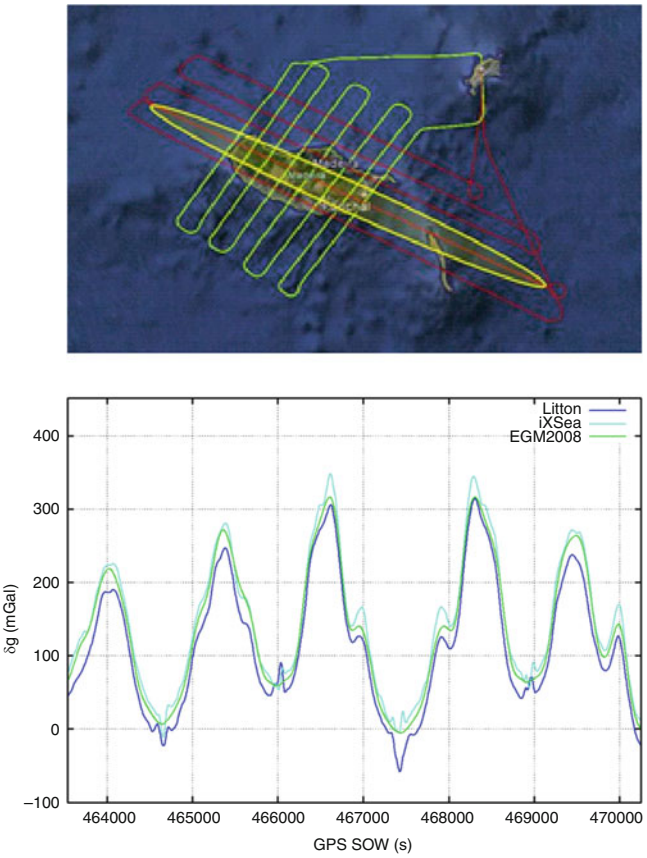

Fig. 2 GEOMAD: comparison of the results from the IMUs with the EGM2008 gravity model

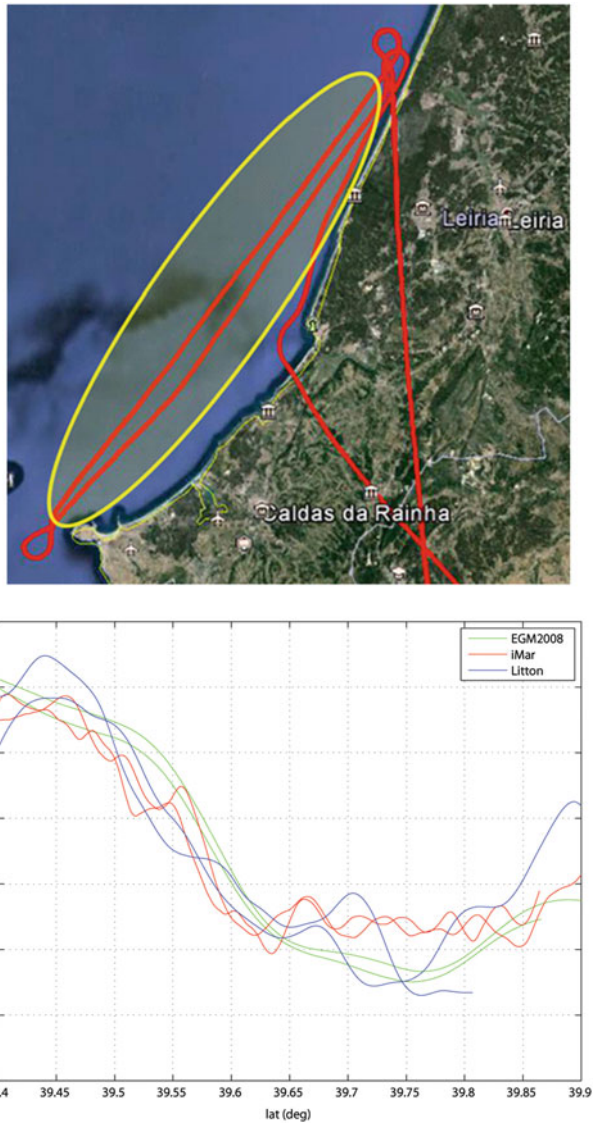

Fig. 3 PITVANT: comparison of the results from the IMUs with the EGM2008 model (Ocean)

All figures also show our observed gravity disturbances and those computed using the Earth Gravitational Model 2008 (EGM2008) global gravity model (Pavlis et al. 2012). In addition, Fig. 4 shows the gravity disturbances derived from the IGP (Instituto Geográfico Português) national gravity point network and the gravity disturbances derived from a number of specifically collected terrestrial control points (labelled as Mertola in Fig. 4). These ground observations were first converted to a fixed height of 300 m using the gravity gradient in free air, −0.3086 mGal/m, and spatially interpolated to form a grid. Next, at the location of the flight track these grid values were converted into gravity values at flight height using again the same gravity gradient.

The EGM2008 model was used as the baseline for the comparison. The mean and standard deviation are computed from the difference between the gravity disturbance results obtained from the Kalman filter algorithm and the gravity disturbance computed from the EGM2008 model for the selected sections shown in the figures. Table 1 shows the comparison of the results from the two IMUs with EGM2008 for the GEOMAD campaign.

Note that the Kalman filter contains an inherent low-pass filtering effect and the estimated gravity disturbance results from the Kalman filter are therefore already smooth. However to match the spatial resolution of the EGM2008 model (18 km full wavelength) an additional low-pass filtering was applied to the results for comparison. For the GEOMAD results a 164 s filter was applied to match the 110 m/s average ground speed.

During the GEOMAD campaign one of the flight lines was flown twice (in opposite direction). This line is highlighted in the map overview of Fig. 2. A comparison of the overlapping flight lines provides an indication of the pass-to-pass accuracy of the different IMUs. The results are shown in Table 2.

Figures 3 and 4 show the results for the two sections of the PITVANT campaign. Note that the graphs have been corrected for the mean between the estimated values and the EGM2008 derived gravity disturbances. This is done

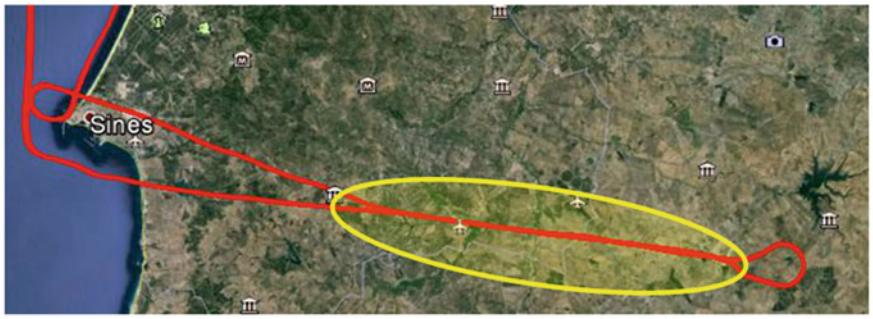

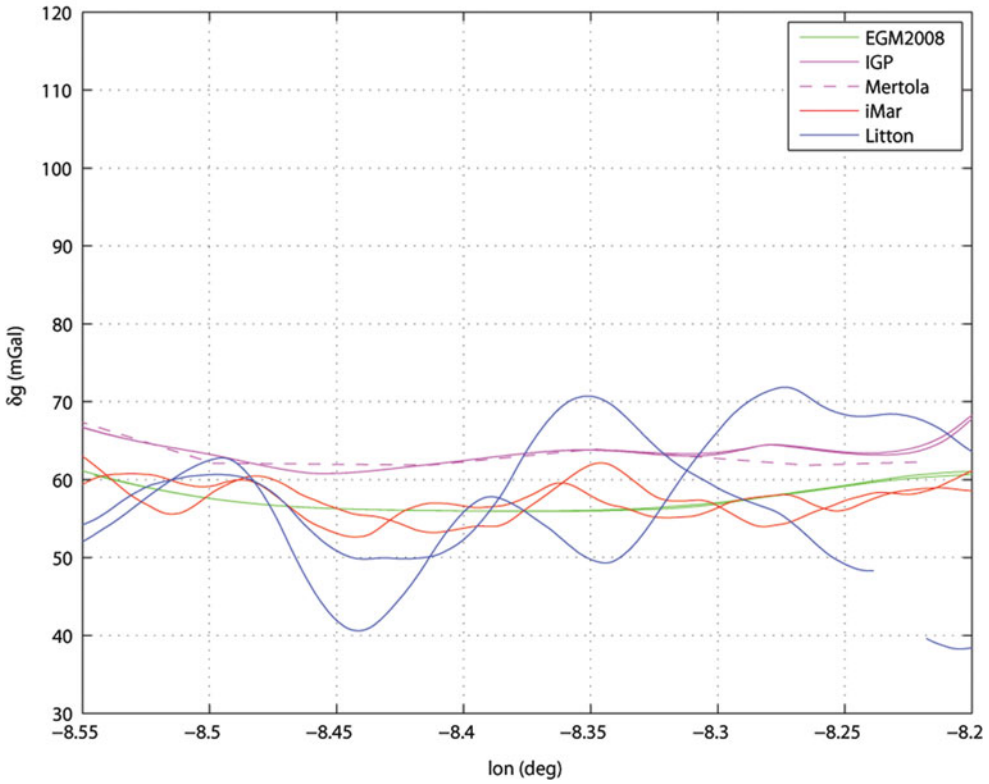

Fig. 4 PITVANT: comparison of the results from the IMUs with the EGM2008 model (Land)

Table 1 GEOMAD: comparison of the results from the IMUs with the EGM2008 gravity model (with 164 s low-pass filtering)

	iXsea (mGal)	Litton (mGal)
Mean	0.16	3.01
Std	6.51	8.62
Min	−21.11	−26.74
Max	17.67	33.06

Table 2 GEOMAD: comparison of the results from two overlapping flight lines (with 164 s low-pass filtering)

	iXsea (mGal)	Litton (mGal)
Mean	1.44	3.50
Std	2.09	6.51
Min	−6.87	−10.22
Max	1.26	14.49

to highlight the short-wavelength differences between the different IMUs. Tables 3 and 4 show the statistics for the PITVANT. Again these were obtained by first applying a 257 s low-pass filter to the Kalman filter results to match the EGM2008 spatial resolution at an average ground speed of 70 m/s.

In the PITVANT project, the gravity disturbance was estimated by iMar with an accuracy ranging from 0.76 to 0.92 mGal (considering both EGM2008 and terrestrial gravity data comparisons), over land, and from 4.15 to 5.15 mGal, over ocean. When compared with EGM2008, the performance of iMar was significantly better over land. This could be a consequence of the fact that EGM2008 is more accurate over land than over water because terrestrial gravity observations have been used to construct the model. That this difference with EGM2008 is real can also be deduced from

Table 3 PITVANT: comparison of the results from the IMUs with the EGM2008 gravity model (Ocean) (with 257 s low-pass filtering)

		iMar (mGal)	Litton (mGal)
Line a	Mean	−34.87	−100.00
	Std	4.13	5.00
	Min	−41.81	−110.80
	Max	−28.68	−90.30
Line b	Mean	−37.62	−109.17
	Std	5.15	6.61
	Min	−45.23	−128.71
	Max	−29.09	−100.91

Table 4 PITVANT: comparison of the results from the IMUs with the EGM2008 gravity model (Land) (with 257 s low-pass filtering)

		iMar (mGal)	Litton (mGal)
Line a	Mean	−27.87	−8.25
	Std	0.81	3.30
	Min	−29.82	−14.39
	Max	−26.59	−2.34
Line b	Mean	−28.10	−57.80
	Std	0.76	5.69
	Min	−29.70	−65.02
	Max	−27.23	−48.93

Table 5 PITVANT: comparison of the results from the IMUs with the terrestrial gravity data (Land) (also with 257 s low-pass filtering)

		iMar (mGal)	Litton (mGal)
Line a	Mean	−33.84	−14.22
	Std	0.87	2.47
	Min	−35.53	−19.97
	Max	−32.13	−9.87
Line b	Mean	−33.90	−64.05
	Std	0.92	5.99
	Min	−35.52	−70.38
	Max	−32.49	−52.80

the fact that both lines, flown in opposite directions, observed the same misfits (Table 5).

To obtain an indication of the accuracy of EGM2008, we also computed the gravity using the EIGEN-6C2 global geopotential model (Förste et al. 2013) along the flight path. We found that the difference between the two models has a mean of −1.8 mGal and a standard deviation of 1.7 mGal over the coastal area while these values are 0.7 and 1.2 mGal respectively over southern Portugal. However, the main difference between EGM2008 and EIGEN-6C2 is for wavelengths between 100 and 300 km and therefore these shorter wavelength errors will be the same in both models.

Moreover, the turbulence experienced during the flight may have also influenced the levels of accuracy achieved. As expected, the performance of the Litton (accuracy ranging from 3.30 to 5.99 mGal, over land, and from 5.0 to 6.61, over ocean) was slightly worse than that of the iMar, since it is a tactical grade IMU. Nonetheless, these are interesting results for the estimation of gravity disturbances with a low-cost IMU.

Concerning the GEOMAD's region, Catalão and Sevilla (2008) showed that, due to lack of accurate gravity data, there existed for Madeira an uncertainty of around 13–14 cm between their computed geoid and a set of local benchmarks on this island. Hence, the comparison results with EGM2008 are most likely affected by the model's low accuracy around Madeira. Also for this area we computed the gravity disturbances along the flight lines using the models EGM2008 and EIGEN-6C2. We found that the difference between the two models has a mean difference of 4.6 mGal and a standard deviation of 3.4 mGal.

The assumption of lower accuracy of EGM2008 over Madeira is supported by the increase of Litton's internal accuracy, computed from the overlapping flight lines (6.51 mGal). Note that this also applies to iXsea, which achieved an internal accuracy (2.09 mGal) less than half the standard deviation of the comparison with EGM2008. In addition, the navigation grade iXSea, with FOG, shows a performance similar to the iMar, with RLG, used in the PITVANT project. However, this performance must be analyzed with care since a direct comparison between the two IMUs was not possible, because the data were acquired in different campaigns with quite diverse observation conditions.

4 Conclusions

In strapdown gravimetry, with proper modeling of the sensor errors, high quality gravity information can be estimated in good flight conditions (smooth flight and no turbulence) from different types of inertial systems. With a navigation grade IMU, even in a more turbulent environment it is still possible to derive useful results through an adequate noise characterization and filtering.

As expected, the navigation grade IMUs (iXSea and iMar) delivered better results. Comparison with the EGM2008 model (for wavelength down to 18 km) shows accuracies as low as 0.8 mGal over land. In coastal areas the agreement with EGM2008 is less, showing accuracies of 4.2–6.5 mGal. This may in part be due to discrepancies in the EGM2008 model. Comparison of EGM2008 with the EIGEN-6C2 model shows accuracies between 1.7 and 3.4 mGal. This assumption is strengthened by the fact that the iXSea FOG IMU shows an internal accuracy (from an overlapping flight

line) of 2.1 mGal. The iMar RLG IMU delivered good results even in difficult observation conditions such as those that occurred during the PITVANT campaign.

A tactical grade sensor, like the Litton LN-200, can perform quite well in comparison with the much more expensive (5 to 8 times more) high-quality inertial systems. It provided an accuracy as low as 3.3 mGal for land and accuracies of 5.0–8.6 mGal for coastal areas for the comparison with EGM2008. For the overlapping flight line an accuracy of 6.5 mGal is obtained. The information derived with this type of system can be useful for regional geoid augmentation (Bos et al. 2011) and particularly in the land-ocean transition zones where global models show discrepancies.

Driving this research work is also a further aim of the University of Porto team to evaluate the feasibility to use medium to low cost sensors installed in Unmanned Aerial Vehicles (UAVs) for less demanding airborne gravimetry surveys such as coverage of remote areas where no other gravity data is available. This can provide new, less expensive, airborne survey options.

Acknowledgments The PITVANT project is funded by the Portuguese Ministry of Defence. The GEOMAD project was funded by EUFAR (European Facility for Airborne Research). We would like to thank Direcção Regional de Informação Geográfica e Ordenamento do Território for providing the GNSS data from stations on Madeira and Porto-Santo. During the write-up of this research, Machiel Bos was funded by national funds through FCT in the scope of the Project SFRH/BPD/89923/2012.

References

Bos MS, Deurloo RA, Magalhães A, Bastos L (2011) A new local geoid for Madeira. In: Proceedings of the "VII Conferência Nacional de Cartografia e Geodesia" (CNCG 2011), 5–6 May, 2011, Porto, Portugal

Bruton AM, Glennie C, Schwarz KP (1999) Differentiation for high-precision GPS velocity and acceleration determination. GPS Solutions 2(4):7–21

Catalao J, Sevilla M (2008) The use of ICAGM07 geoid model for vertical datum unification on Iberia and Macaronesian islands. American Geophysical Union, Fall Meeting 2008, abstract #G51B-0612

Deurloo RA (2011) Development of a Kalman filter integrating system and measurement models for a low-cost strapdown airborne gravimetry system. PhD dissertation. Department of Geosciences, Environment and Spatial Planning, Faculty of Sciences, University of Porto, Porto

Forsberg R, Olesen AV (2010) Airborne gravity field determination. In: Xu G (ed) Sciences of geodesy – I: advances and future directions. Springer-Verlag, New York, pp 83–104

Förste C, Bruinsma S, Flechtner F, Marty JC, Dahle C, Abrykosov O, Lemoine JM, Neumayer H, Barthelmes F, Biancale R, König R (2013) EIGEN-6C2 - a new combined global gravity field model including GOCE data up to degree and order 1949 of GFZ Potsdam and GRGS Toulouse. In: EGU General Assembly Conference Abstracts, EGU General Assembly Conference Abstracts, vol 15, p 4077

Jekeli C (2001) Inertial navigation systems with geodetic applications. Walter de Gruyter, Berlin/New York

Kwon JH, Jekeli C (2001) A new approach for airborne vector gravimetry using GPS/INS. J Geod 74(10):690–700

Pavlis NK, Holmes SA, Kenyon SC, Factor JK (2012) The development and evaluation of the Earth Gravitational Model 2008 (EGM2008). J Geophys Res 117:B04,406. doi:10.1029/2011JB008916

Assessment of the Recently Released GOCE-Based Models in Terms of Spectral and Spatial Resolution

Konstantinos Patlakis and Dimitrios Tsoulis

Abstract

Recently, many global geopotential models (GGMs) were computed and released based on data collected by the Gravity field and steady-state Ocean Circulation Explorer (GOCE) mission. Based on different computational approaches and different observations in terms of quantity and quality, the final product is a set of spherical harmonic coefficients representing the series expansion of the gravitational potential up to a certain maximum degree and order. In order to quantify and assess the features of these global gravity models, we perform a quality assessment both in an absolute and relative sense with respect to other similar models or some reference Earth gravity models. In this comparative analysis the so-called topographic/isostatic gravity models, which represent the contribution of global digital elevation maps for topography and ocean bathymetry to the gravity spectrum, have been included as well. Applying a range of available spatial and spectral accuracy and assessment measures, it becomes obvious that GOCE data contribute to the medium wavelength from degree and order 100 up to degree and order 200. The difference variances of the new released GOCE-based models with respect to the state-of-the-art model EGM2008 at the spectral bandwidth 100 to 200 and the spectral correlation among GOCE-models and EGM2008 up to degree and order 200 lead to the conclusion of an improvement in gravity field representation from the new GOCE models. This conclusion is enhanced with a statistical spatial analysis in regions, such as South America, Antarctica, Central Asia and Africa, where the differences among GOCE models and EGM2008 are large due to the lack of terrestrial data for the computation of the latter.

Keywords

EGM2008 • GOCE gravity models • Spatial assessment • Spectral assessment • Topographic/isostatic gravity model

1 Introduction

Based on the gradiometry and tracking observations and the detected orbit perturbations the analysis of GOCE (Rummel et al. 2011) data leads to the computation of new Earth gravity models. With the GOCE mission concluding its final phase we have entered the computation of gravity models which employ larger data sets and thus achieve the best possible accuracy. Recently many GOCE-based models have been released based on different computational techniques. Seven of them, released by different institutes, have been selected for the present study. In spite of the different computational techniques, the different parameterisation and of course the different time spanning of the considered data it is interesting to investigate the existence of similar spectral behaviour among the respective coefficient sets, and if such

K. Patlakis • D. Tsoulis (✉)
Department of Geodesy and Surveying, Aristotle University of Thessaloniki, Thessaloniki, Greece
e-mail: tsoulis@auth.gr; http://users.auth.gr/tsoulis

© Springer International Publishing Switzerland 2015

C. Rizos, P. Willis (eds.), *IAG 150 Years*, International Association of Geodesy Symposia 143,
DOI 10.1007/1345_2015_33

a correlation exists, to define the specific spectral bandwidth where it occurs. In addition, it is interesting to observe the correlation of the GOCE-based models with the compensated and uncompensated topography spectrum because of the nature of gradiometry observations and the link of second order gravitational derivatives with the upper crustal and topographic signal.

2 Data Sets

In the present study we investigate the spectral and spatial behaviour of seven recently released GOCE-based satellite gravity models which have been released publically via the International Centre for Global Earth Models (ICGEM, GFZ Potsdam). The selected models are representative of the various computational approaches that are used in global gravity field determination.

As most of the GOCE-based models have been computed using GRACE-based satellite or combined models as a priori information, our analysis includes not only the so-called GOCE-only models but also those satellite models which are based on the combination of GOCE data with data from other satellite missions.

The European Space Agency (ESA) released GOCE geopotential models are based on three different processing algorithms: the direct approach, the time-wise approach and the space-wise approach (Pail et al. 2011). For our assessment analysis we used the latest available releases, namely the fourth generation time-wise and direct models and the second generation space-wise model.

The GOCE-TIM-r4 (GO_CONS_GCF_2_TIM_R4) model (Pail et al. 2011), which is available up to spherical harmonic degree 250, was computed using the least squares solution for the adjustment of GOCE Satellite Gravity Gradiometry (SGG) and Satellite-to-Satellite Tracking (SST) observations from the period of November 2009 through June 2012. The SST part of the normal equations was estimated up to degree 130 using the short-arc integral approach (Mayer-Gürr 2008) applied to the GOCE kinematic orbits, while the SGG part was estimated up to the maximum solvable degree. Furthermore, a Kaula regularization was applied to the near-zonal coefficients in order to deal with the polar gap problem and to coefficients above degree 180 for improving the signal-to-noise ratio.

The GOCE-DIR-r4 (GO_CONS_GCF_2_DIR_R4) model (Bruinsma et al. 2013), available up to degree 260, was computed by combining GOCE gradiometry observations from November 2009 through August 2012, 25 years of SLR LAGEOS observations and almost 10 years of GRACE observations. Two GRACE models were used as a priori information, one up to harmonic degree 54 and one from degree 55 up to degree 180. In addition, a spherical cap regularization (Metzler and Pail 2005) was implemented up to degree 260 and a Kaula regularization was applied to all coefficients above degree 200.

The GOCE-SPW-r2 (GO_CONS_GCF_2_SPW_R2, Migliaccio et al. 2011) model, complete to degree 240, was evaluated directly by spherical harmonic analysis of the GOCE observations, which have been previously gridded at satellite altitude using global collocation. The second generation space-wise model uses no a priori information and has been computed from pure GOCE SGG and SST observations obtained for the time span between 31 October 2009 and 5 July 2010.

The ITG-Goce02 model (Schall et al. 2014), released by the Institut für Theoretische Geodäsie, University of Bonn (ITG) and available to degree 240, was calculated from GOCE gradiometry and GPS-orbit data obtained in the period between November 2009 and June 2010. The SST part of the normal equations was estimated using the short-arc integral approach (Mayer-Gürr 2008) applied to the GOCE kinematic orbits. A Kaula-type regularization has been applied to all coefficients above degree 5.

The JYY-GOCE02S model (Yi et al. 2013), released by the Institut für Astronomische und Physikalische Geodäsie, Technische Universität München, is a model complete to degree 230, that has been computed from GOCE SGG and SST data from November 2009 through August 2012. The SST part of the normal equations was estimated up to degree 120 using the short-arc integral approach applied to the GOCE kinematic orbits and the SGG part was estimated up to degree 230. For the polar gap stabilization due to the lack of GOCE observations discrete values from EGM2008 (Pavlis et al. 2012) up to degree 215 were used as pseudo-observations.

The GOCO03s model (Mayer-Gürr et al. 2012), released by the Gravity Observation Combination (GOCO) Consortium (http://www.goco.eu/), available to degree 250, was computed through a combination of GOCE SGG and SST observations from the period November 2009 through April 2011, 7 years of GRACE data, 5 years of SLR data obtained from five different satellites and 8 years of CHAMP data. A Kaula regularization has been applied to all coefficients above degree 180.

The EIGEN-6S model (Förste et al. 2011), released by the GFZ German Research Centre for Geosciences, Helmholtz Centre Potsdam, and derived from GRACE (January 2003 through June 2009), 6.5 years of LAGEOS data and GOCE gradiometric data from the time span 1 November 2009 till

30 June 2010, is a model which is complete up to degree and order 240. The SGG data contribute to degrees above 100 through an adapted filtering in the GOCE observation equations. Additionally, spherical cap regularization has been applied for the stabilization of the polar gap effects.

The Earth gravity model EGM2008 is the result of combining the ITG-Grace03s (Mayer-Gürr et al. 2010) gravitational model with a global 5 arc-minute equiangular grid of free air gravity anomalies, which is formed by merging terrestrial, altimetric, and airborne gravity data. Thus, EGM2008 expresses currently the best knowledge of the actual field in terms of direct gravity observations and high-frequency contributions due to the topography. Moreover, EGM2008 is independent of GOCE data, which makes it the best choice for the assessment of the GOCE-based models proving GOCE superiority at medium wavelength (e.g., Gruber et al. 2011; Hirt et al. 2011; Tsoulis and Patlakis 2013). For this reason, it is selected as the reference model for all performed comparisons.

For further comparisons and assessment of the geopotential models we used a gravity model which we define here as Topographic model and expresses the implied gravitational potential of the uncompensated topography for the Digital Terrain Model 2002 (DTM2002) (Saleh and Pavlis 2003) and a Topographic/Isostatic model which was obtained from an Airy/Heiskanen isostatic mechanism applied to the same terrain data.

3 Assessment of Gravity Models

3.1 Assessment Tools

The assessment and evaluation of a global geopotential model can be performed using various statistical quantities either in an absolute or a relative sense. One can compare the behaviour of the released spherical harmonic coefficients of these models in the entire spectrum range with quantities such as degree variances, error degree variances and cumulative errors per degree. More efficient is the comparison of spectral behaviour of GGMs with respect to a state-of-the-art model, e.g., EGM2008, or a model that represents a different kind of information, such as a Topographic/Isostatic model. The aforementioned comparison can be performed with relative statistic tools such as RMS differences by degree, correlation, smoothing and percentage difference by degree, gain, or signal-to-noise ratio. All these quantities have been used in many assessment studies and their definitions can be found in standard geodetic literature, e.g., Tscherning (1985), Rapp (1986), while they appear in more recent interpretation studies as well (e.g., Sneeuw 2000; Tsoulis and Patlakis 2013).

Due to the non-isotropy of the spherical harmonic error coefficients spectrum, i.e., the fact that the error spectrum depends on the spherical order m as well, all the aforementioned quantities can be computed as order-wise quantities giving a complete image of the spectral behaviour of GGMs (Tsoulis and Patlakis 2013).

For the sake of compactness only the definitions of correlation coefficients per degree and per order are given in the sequel. A newly adapted spectral definition is introduced, attempting to combine the correlation and smoothing coefficients in one quantity, assuring that no correlation artefacts due to an existing dominant scale factor in the two compared models are present. Thus, the correlation per degree and per order are defined respectively as

$$cor_l = 1 - \frac{\sum_{m=0}^{l} \left(\Delta \overline{C}_{lm}^2 + \Delta \overline{S}_{lm}^2 \right)}{\sigma^2 \left(\overline{C}_{lm}^B, \overline{S}_{lm}^B \right)} \tag{1}$$

and

$$cor_m = 1 - \frac{\sum_{l=m}^{l_{max}} \left(\Delta \overline{C}_{lm}^2 + \Delta \overline{S}_{lm}^2 \right)}{\sigma_m^2 \left(\overline{C}_{lm}^B, \overline{S}_{lm}^B \right)} \tag{2}$$

where $\left(\Delta \overline{C}_{lm}, \Delta \overline{S}_{lm} \right)$ denotes the difference of the fully normalized spherical harmonic coefficients of two expansions, symbolically denoted here as models A (new model, e.g., GOCE-based model) and B (reference model, e.g., EGM2008), $\left(\overline{C}_{lm}^B, \overline{S}_{lm}^B \right)$ are the spherical harmonic coefficients of model B, and $\sigma_l^2 \left(\overline{C}_{lm}^B, \overline{S}_{lm}^B \right)$ and $\sigma_m^2 \left(\overline{C}_{lm}^B, \overline{S}_{lm}^B \right)$ are respectively the degree and order variances of the second model. All these relative spectral assessment quantities permit the identification of characteristic spectral bandwidths of the evaluated models. Using this rough estimate of spectral bandwidths for which a characteristic correlation is present, a band-limited analysis in the spatial domain in terms of second order radial derivatives has been performed.

3.2 Results and Discussion

The current section includes results that present selected quantities which attempt to validate the aforementioned GOCE-based models with respect to EGM2008, T/I and the Topographic model, as these were defined in the previous

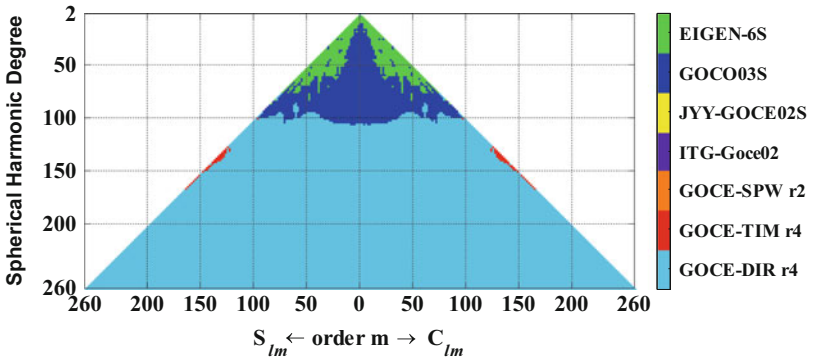

Fig. 1 Representation of spectral regions where the formal errors of a gravitational model are smaller than the formal errors of the other considered models

section. First, a comparison among the two dimensional error representation of all GOCE-based models has been performed, in order to identify in which part of the spectrum each model shows a better accuracy in terms of their formal errors. Then, the quantities of degree and order variances, error variances and differences variances have been computed giving an insight of the gravitational models behaviour over the entire spectrum. In addition, the relative spectral assessment quantities of correlation per degree and correlation per order have been evaluated in order to identify characteristic spectral bandwidths of the assessed models. In addition, a regional quantitative analysis in terms of R.M.S. differences among GOCE and EGM2008 has been performed in areas where large differences among the models are present.

In Fig. 1 a superiority in terms of formal errors of GOCE-DIR (r4) model from degree 100 to its maximum solvable degree with respect to the other considered models can be observed. For the spectrum up to degree 100, GOCO03S and EIGEN-6S models appear better error behaviour due to the inclusion of GRACE and LAGEOS data that have been elaborated in order to produce the potential coefficients in this particular spectral bandwidth. At the same time, one can observe that the sectorial coefficients' formal errors of GOCE-TIM (r4) in the degree range 120 to 170 are smaller compared with the coefficients' errors of all other considered models. A comparison of the GOCE-TIM (r4) model with the GOCE-DIR (r4) model in the above spectral range leads to the conclusion that this pattern may be due to the use of GRACE data for the DIR model up to degree 180 in contrast to the GOCE orbit data that have been used for the development of the TIM model. As the formal errors are obtained from the main diagonal of the covariance matrix that accompany the coefficients' estimation after the common adjustment of various satellite and/or terrestrial data, it is important to note that these errors do not reflect the actual accuracy of the estimated coefficients but an indication of the

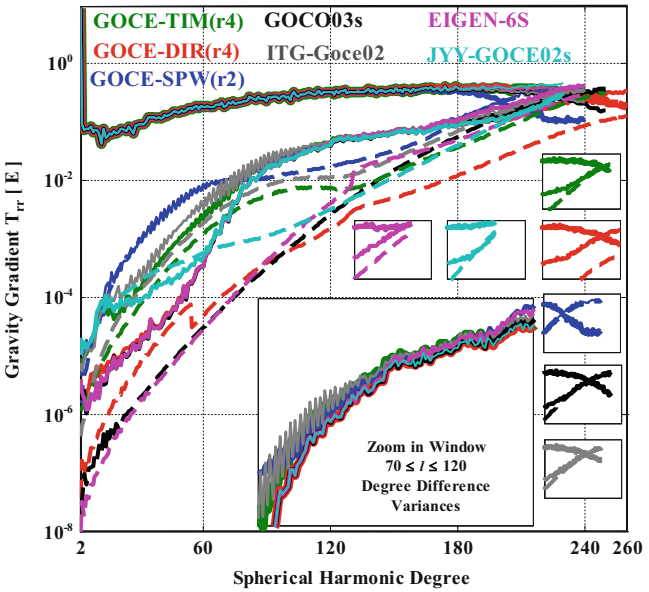

Fig. 2 Degree variances (*upper solid lines*), error variances (*dashed lines*) and differences with respect to EGM2008 (*lower solid lines*) in terms of second radial derivative T_{rr}. *Unit*: Eötvös. Small windows inside the figure show the three curves at the very last part of the computed spectrum

accuracy influenced mostly by the scaling and weighting of the covariance matrix.

In Fig. 2 a loss of signal for the GOCE-SPW (r2) model above degree 200 is apparent. Furthermore, one can observe that the difference variances curves with respect to EGM2008 are almost identical from degree 100 to degree 200 and far above the error variances curves, implying probably that GOCE measurements offer new information in the medium part of the gravity spectrum.

From Fig. 3 it becomes obvious that the models present a quite different spectral behaviour with respect to the order spectrum. The GOCE-only models, GOCE-SPW (r2), ITG-Goce02 and GOCE-TIM (r4) appear with great values of

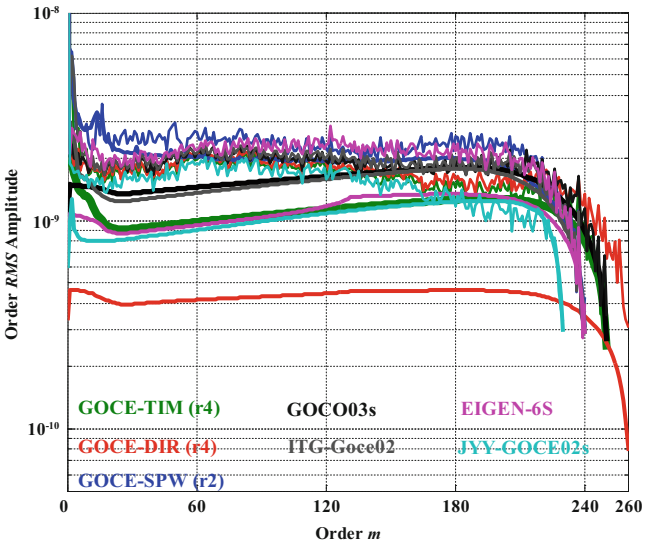

Fig. 3 Order error variances (*thick lines*) and differences with respect to EGM2008 (*thin lines*)

error variances in the first orders ($0 \leq m \leq 30$), probably due to the polar gap problem, with the GOCE-SPW (r2) model curve expressing greater variance values than the other models in this spectral range, revealing a probably less efficient polar gap parameterisation. Also, comparing the difference order variances curves with respect to EGM2008 with the order error variance curves of the GOCE-based models, a superiority of GOCE models up to order 200 can be observed. The usage of EGM2008 to the development of GOCE-SPW (r2) model is obvious as the difference and the error curves are really close to the whole spectral range. Furthermore it becomes obvious in this figure, that the formal errors of GOCE-DIR (r4) model are probably overoptimistic. This becomes evident by the fact that the order error variances of GOCE-DIR (r4) are much smaller than the differences to EGM2008 even in the very high degrees, where terrestrial data already dominate due to the attenuation with altitude.

Figure 4 presents the correlation coefficients per degree and order for the recently released GOCE-based models with respect to EGM2008, T/I model and the Topographic model. The correlation with respect to EGM2008 model starts to decline above degree 100 and becomes zero for degrees above 220. The not exact correlation in the aforementioned bandwidth might imply that GOCE models offer new information in this bandwidth which is missing from EGM2008 due to the lack of global coverage of the available terrestrial data included in its development.

The GOCE-based models display a quite high degree of correlation with T/I for the bandwidth degree range between 20 and 200. The upper bound of this degree bandwidth varies between the different GOCE models, reaching up to degree 240. The correlation patterns of the different GOCE models with respect to T/I are very similar. In addition, it should be observed that the JYY-GOCE02S model is the only model correlated with T/I up to its maximum solvable degree.

The link of the gradiometry observations to the uncompensated topography is nicely demonstrated in the correlation of the GOCE-based models with the Topographic model. The aforementioned correlation occurs in the spectral bandwidth defined between degrees 120 and 200, thus indicating the short-wavelength sensitivity of the GOCE models.

For a better understanding of the above spectral observations a regional spatial analysis has been performed and presented in Fig. 5. A forward computation of global grids of second order radial derivatives of the disturbing potential has been performed and a statistical comparison in terms of RMS (Root Mean Square) of differences between GOCE models and EGM2008 has been applied. The comparison has been restricted to areas where large differences of all GOCE models with respect to EGM2008 have been observed. These are areas with lack of terrestrial data coverage (so-called "fill-in" areas, Pavlis et al. 2012), such as South America, Africa, Central Asia, South–East Asia and Antarctica. For the sake of completeness, Europe enters the above comparison to show the good agreement between GOCE models and EGM2008 in areas with good terrestrial data coverage. In all of the above areas except Europe the RMS differences of radial gravity gradients are rather high. Figure 5 presents the RMS differences of radial gravity gradients of the disturbing potential computed for the aforementioned areas for all seven GOCE-based models that have been selected for the present study. All models show a similar behaviour almost up to degree 200 for every specific region apart from Antarctica. Antarctica is the only region for which the development of EGM2008 is based solely on GRACE information. The GOCE only models, SPW2, TIM4 and ITG, show a different behaviour up to degree 150 than the other GOCE-based models, probably due to the polar gap problem. In Africa, South America, Central and South–East Asia the RMS differences start to increase from degree 80, whereas the differences curves above degree 200 start to diverge and show a different behaviour for each model. In Europe, where adequate terrestrial data were utilized for the computation of EGM2008, the RMS differences are rather small up to degree 200.

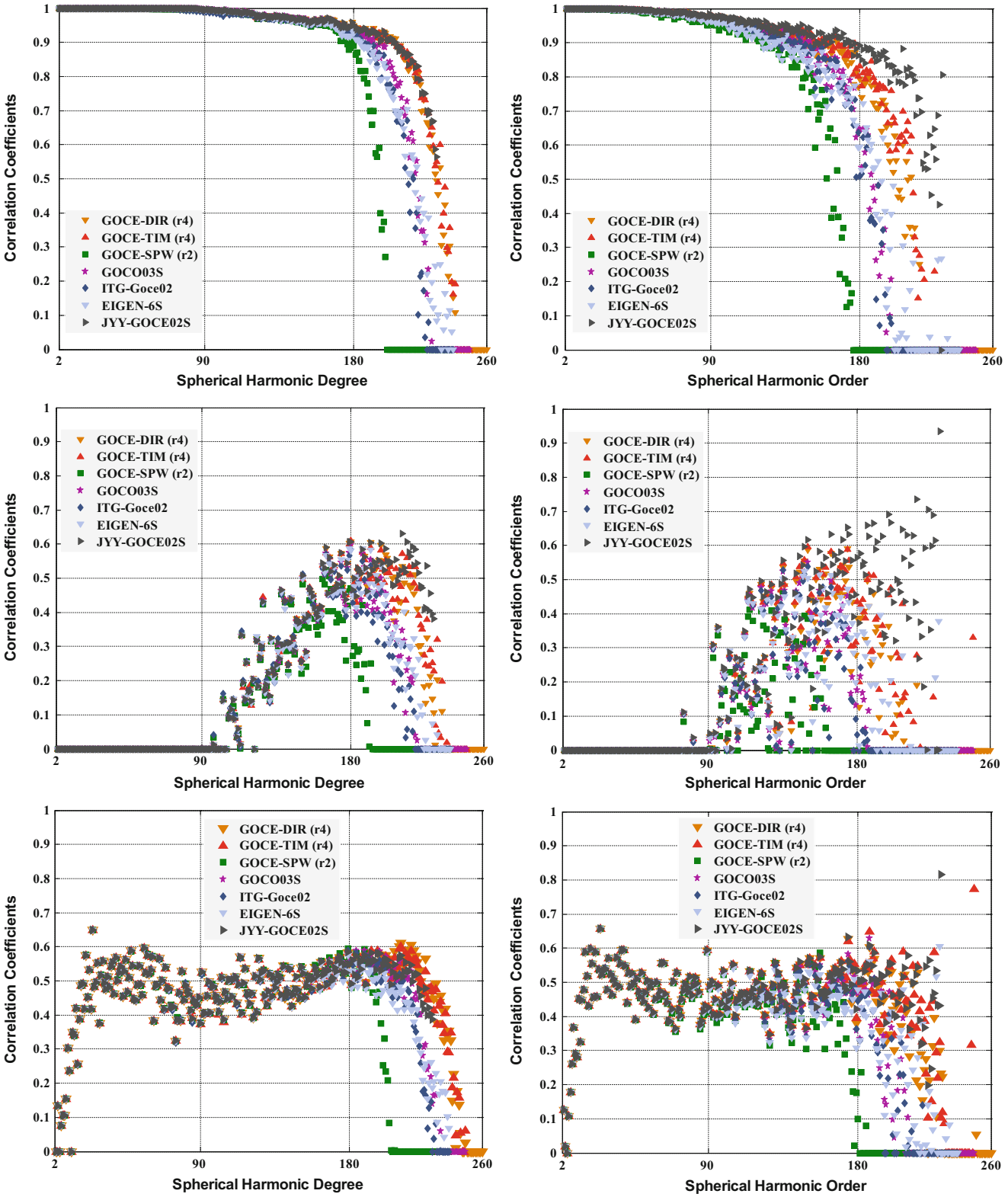

Fig. 4 Correlation Coefficients per degree (*left column*) and per order (*right column*) of the recently released GOCE-based models with respect to EGM2008 (*top row*), Topographic model (*middle row*) and T/I model (*bottom row*)

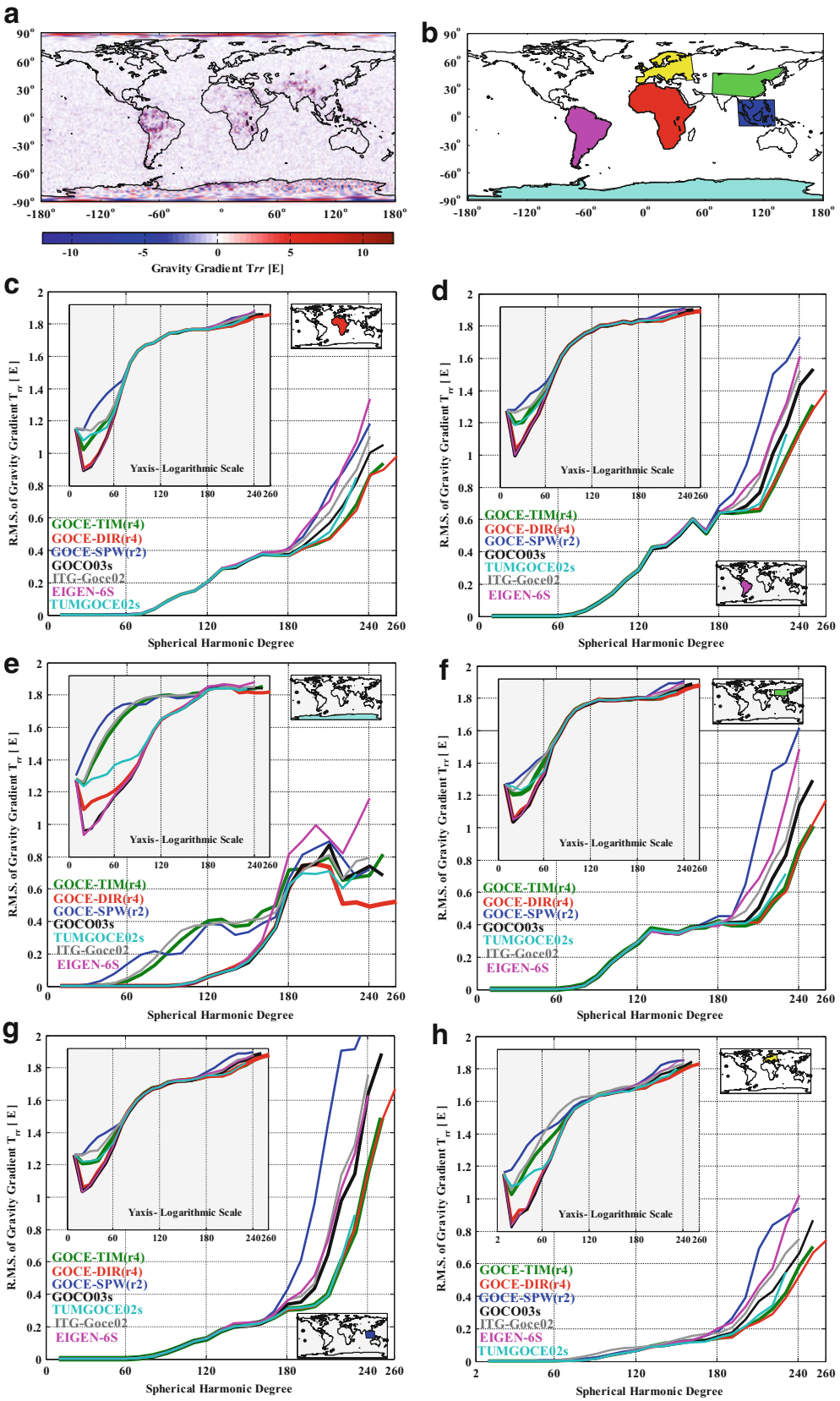

Fig. 5 (**a**) Differences of ITG-Goce02 w.r.t. EGM2008 up to degree and order 200, (**b**) areas where differences from (**a**) are larger, RMS differences of gravity gradient T*rr* in Africa (**c**), South America (**d**), Antarctica (**e**), Central Asia (**f**), South–East Asia (**g**) and Europe (**h**)

4 Concluding Remarks

We presented certain spectral and spatial comparisons using a selection of the most recently released GOCE-based models. The first remarks that can be drawn from these computations refer to the behaviour of the GOCE models with respect to EGM2008 within the degree bandwidth of roughly $100 < l < 200$. This specific bandwidth relates with the sensitivity of GOCE models in the medium and short wavelengths. The second major comment should include a reference to the spectral behaviour of all GOCE models with respect to T/I and Topographic model. A correlation of all GOCE models with the gravity model implied by an uncompensated topography within the degree bandwidth of $120 < l < 200$ and a quite large correlation with the model defined by an isostatically compensated topography within the degree bandwidth of $20 < l < 200$ can be observed. These remarks should be directly linked to the characteristics of the GOCE mission, which orbits at a low altitude and is sensitive to the upper crustal and topographic signal. The performed regional spatial analysis demonstrates nicely the improvement of the gravity field information, which is offered by GOCE in the degree range 100–200, over areas lacking terrestrial data such as Africa or South America.

References

Bruinsma SL, Förste C, Abrikosov O, Marty J-C, Rio M-H, Mulet S, Bonvalot S (2013) The new ESA satellite-only gravity field model via the direct approach. Geophys Res Lett 40(14):3607–3612. doi:10.1002/grl.50716

Förste C, Bruinsma S, Shako R, Marty J-C, Flechtner F, Abrikosov O, Dahle C, Lemoine J-M, Neumayer KH, Biancale R, Barthelmes F, König R, Balmino G (2011) EIGEN-6 – a new combined global gravity field model including GOCE data from the collaboration of GFZ-Potsdam and GRGS-Toulouse. Geophys Res Abst 13:EGU2011-3242-2

Gruber T, Visser PNAM, Ackermann CH, Hosse M (2011) Validation of GOCE gravity field models by means of orbit residuals and geoid comparisons. J Geod 85(11):845–860. doi:10.1007/s00190-011-0486-7

Hirt C, Gruber T, Featherstone W (2011) Evaluation of the first GOCE static gravity field models using terrestrial gravity, vertical deflections and EGM2008 quasi-geoid heights. J Geod 85(10):723–740. doi:10.1007/s00190-011-0482-y

Mayer-Gürr T (2008) Gravitationsfeldbestimmung aus der Analyse kurzer Bahnbögen am Beispiel der Satellitenmissionen CHAMP und GRACE. Dissertation, Schriftenreihe des Instituts für Geodäsie und Geoinformation, Heft 9. Institut für Geodäsie und Geoinformation, Rheinischen Friedrich-Wilhelms University. Bonn, Bonn, Germany, p 113, ISSN 1864–1133

Mayer-Gürr T, Eicker A, Kurtenbach E, Ilk KH (2010) ITG-GRACE: global static and temporal gravity field models from GRACE data. In: Flechtner F et al (eds) System earth via geodetic-geophysical space techniques, Advanced technologies in earth sciences. Springer, Berlin, pp 159–168. doi:10.1007/978-3-642-10228-8_13

Mayer-Gürr T, Rieser D, Höck E, Brockmann JM, Schuh W-D, Krasbutter I, Kusche J, Maier A, Krauss S, Hausleitner W, Baur O, Jäggi A, Meyer U, Prange L, Pail R, Fecher T, Gruber T (2012) The new combined satellite only model GOCO03s. Presented at International Symposium on Gravity, Geoid and Height Systems, 9–12 October 2012, Venice, Italy. Available at www.bernese.unibe.ch

Metzler B, Pail R (2005) GOCE data processing: the spherical cap regularization approach. Stud Geophys Geod 49(4):441–462. doi:10.1007/s11200-005-0021-5

Migliaccio F, Reguzzoni M, Gatti A, Sansò F, Herceg M (2011) A GOCE-only global gravity field model by the space-wise approach. In: Ouwehand L (ed) Proceedings of the 4th international GOCE user workshop, ESA Publ SP-696, ESA/ESTEC, Noordwijk, The Netherlands, ISBN: 978-92-9092-260-5, ISSN: 1609-042X

Pail R, Bruinsma S, Migliaccio F, Förste C, Goiginger H, Schuh W-D, Höck E, Reguzzoni M, Brockmann JM, Abrikosov O, Veicherts M, Fecher T, Mayrhofer R, Krasbutter I, Sansò F, Tscherning CC (2011) First GOCE gravity field models derived by three different approaches. J Geod 85(11):819–843. doi:10.1007/s00190-011-0467-x

Pavlis NK, Holmes SA, Kenyon SC, Factor JK (2012) The development and evaluation of the Earth Gravitational Model 2008 (EGM2008). J Geophys Res 117(B4):B04406. doi:10.1029/2011JB008916

Rapp RH (1986) Global geopotential solutions. In: Sünkel H (ed) Mathematical and numerical techniques in physical geodesy, vol 7, Lecture notes in earth sciences. Springer, Berlin-Heidelberg, pp 365–416. doi:10.1007/BFb0010136

Rummel R, Yi W, Stummer C (2011) GOCE gravitational gradiometry. J Geod 85(11):777–790. doi:10.1007/s00190-011-0500-0

Saleh J, Pavlis NK (2003) The development and evaluation of the global digital terrain model DTM2002. In: Tziavos IN (ed) Gravity and Geoid 2002, Proceedings of the 3rd Meeting of the IGGC,, Zitis Publ, Thessaloniki, Greece, pp 207–212

Schall J, Eicker A, Kusche J (2014) The ITG-Goce02 gravity field model from GOCE orbit and gradiometer data based on the short arc approach. J Geod. doi:10.1007/s00190-014-0691-2

Sneeuw N (2000) A semi-analytical approach to gravity field analysis from satellite observations. PhD Dissertation, Deutsche Geodätische Kommission, Reihe C, Heft Nr 527, München

Tscherning CC (1985) On the long-wavelength correlation between gravity and topography. In: Kautzleben H (ed) Proceedings of 5th International Symposium "Geodesy and Physics of the Earth", G.D.R. Magdeburg, 23–29 September 1984, Veröffentlichungen des Zentralinstituts für Physik der Erde 81(2), Akademie der Wissenschaften der DDR, Potsdam, pp 134–142

Tsoulis D, Patlakis K (2013) A spectral assessment review of current satellite-only and combined Earth gravity models. Rev Geophys 51:186–243. doi:10.1002/rog.20012

Yi W, Rummel R, Gruber T (2013) Gravity field contribution analysis of GOCE gravitational gradient components. Stud Geophys Geod 57(2):174–202. doi:10.1007/s11200-011-1178-8

Assessment of GOCE Models Over Mexico and Canada and Impact of Omission Errors

M.C. Santos, D. Avalos, T. Peet, M. Sheng, D. Kim, and J. Huang

Abstract

This paper reports a series of comparisons of geoidal heights derived from several GOCE models with (1) geoidal heights derived from GPS on benchmarks (referred to as geometric geoidal heights) over Mexico and Canada, and with (2) geoidal heights derived from the latest geoidal maps of Mexico (GGM2010) and Canada (PCGG2013) (referred to as gravimetric geoidal heights). The paper also looks quantitatively into omission errors. Comparison (1) and (2) were carried out not including and including omission errors. The GOCE models used in comparison (1) disregarding omission errors are the direct solution model (first, second and third generations), the time-wise solution model (first, second and third generations), GOCO02S model and GIF48 model, all evaluated up to their maximum degree/order. Only GOCE direct third generation model was used in comparison (1) considering omission errors, and in comparison (2) disregarding omission errors, the latter with respect to GGM2010. The GOCE models used in comparison (2) including correction for omission errors are the GOCE direct third generation, GOCO01S, GOCO03S and DGM-1S models, evaluated up to degree/order 180. This makes GOCE direct third generation as the only model common in all comparisons. Omission errors were evaluated based on the extra-high degree harmonics of EGM2008. The omission errors in Mexico and in Canada show a similar behaviour, with a near zero mean and a standard deviation at the order of ± 50 cm in Mexico and ± 45 cm in Canada. In both cases, maximum differences reach more than 4 m. The effect of omission errors can be better appreciated by looking at performance of the only GOCE model used in all comparisons, the direct third generation model. Comparing it with Mexican geometric geoidal heights: without correcting for omission errors, mean and standard deviation of -5.1 and ± 45.7 cm; including correction for omission errors,

M.C. Santos (✉) • T. Peet • M. Sheng • D. Kim
Department of Geodesy and Geomatics Engineering, University of New Brunswick, Fredericton, NB, Canada E3B 5A3
e-mail: msantos@unb.ca; t.peet@unb.ca; m.sheng@unb.ca; d.kim@unb.ca

D. Avalos
Instituto Nacional de Estadística y Geografía (INEGI), Aguascalientes, Mexico
e-mail: david.avalos@inegi.org.mx

J. Huang
Natural Resources Canada, Ottawa, ON, Canada
e-mail: Jianliang.Huang@NRCan-RNCan.gc.ca

© Springer International Publishing Switzerland 2015

C. Rizos, P. Willis (eds.), *IAG 150 Years*, International Association of Geodesy Symposia 143,
DOI 10.1007/1345_2015_28

mean and standard deviation of -1.6 ± 30.6 cm. Comparing it with GGM2010: without correcting for omission errors, mean and standard deviation of -17.4 and ± 51.3 cm; including correction for omission errors, mean and standard deviation of -2.8 ± 34.8 cm.

Keywords
Earth gravity model • EGM2008 • GGM2010 • GOCE • PCGG2013

1 Introduction

GOCE (Visser et al. 2002), the Gravity Field and Steady-State Ocean Circulation Explorer, is a satellite gradiometry mission that maps the Earth's gravity field in a homogenous way over most of the globe. ESA (1999) states as the mission goals "the determination of the stationary gravity field – geoid and gravity anomalies – to high accuracy and spatial resolution." The expectation is that it will provide a geoid model within one centimeter accuracy and gravity anomalies to an accuracy of a few mGal; all within a spatial resolution of 100 km. GOCE offers as its main product global gravity field models.

A major task is to validate these models by using external sources of information, of terrestrial and/or space origin, all of them with their own limitations. For example, terrestrial sources of information rely on GPS on benchmarks, and both techniques (GPS and geodetic leveling) have uncertainties associated with them. Regional gravimetric geoids, which can also be used to evaluate GOCE models, are based on both space (low degree terms of a geopotential model) and terrestrial data (gravity anomalies), all with uncertainties. Finally, GOCE models can be compared to other geopotential models built solely on space information. Several authors have discussed the limitations of the different data sources, such as Featherstone (2011).

There is already a huge family of GOCE models, computed using a variety of methods and either using just GOCE data or combining data from other satellite missions or terrestrial data with GOCE data. They also use data which cover different periods of time (ICGEM 2013).

Efforts in evaluating GOCE models are under way. For example, the IAG sponsored GGHS Meeting, held in Venice, in 2012, had a session dedicated to just that. By the time this paper is published, the proceedings of the GGHS Meeting will have been published already.

2 Comparisons Without Accounting for Omission Errors

2.1 Comparison of GOCE Geoidal Heights with Geometric Geoidal Heights

This paper builds on an earlier and unpublished work by Peet et al. (2012), which compared recently (at that time) developed GOCE gravity models and tested their applicability across the topography, in Canada and Mexico, by means of comparing Global Positioning System (GPS) observations taken on first-order orthometric benchmarks in both countries. Table 1 shows the models used in this evaluation.

This comparison used data provided by the Geodetic Survey Division (GSD) of Natural Resources Canada (NRCan): GPS-derived geodetic heights on first order benchmarks of the Canadian first-order levelling network – realization NOV07 (a total of 2,579 benchmarks – located mostly in the southern portion of the country); and, data from the Instituto Nacional de Estadística y Geografía (INEGI): GPS-derived geodetic heights on first order benchmarks of the North American Vertical Datum (NAVD88) (a total of 1,487 benchmarks – spread throughout Mexico). Differently from Canada, where the levelling lines go through rough terrain only in the West, the Mexican levelling lines go through rough terrain throughout the country, and it is expected to contain distortions reaching several decimeters in amplitude of medium wavelength.

A set of geoidal heights (from now on referred to as 'geometric') were derived from these data sets. GOCE geoidal heights were calculated over these benchmarks using the Fortran code developed by Rapp (1982) and expanded by others (Pavlis 1996). These were called as the 'gravimetric' undulations. Omission errors were not taken into account and geoidal heights were evaluated up to their maximum degrees.

Table 1 List of gravity models (after ICGEM 2013)

Model	Year	Degree	Solution	Data used (months)
GOCE TIM Gen1	2010	224	Time-wise	GOCE (2)
GOCE DIR Gen1	2010	240	Direct	GOCE (2)
GOCE TIM Gen2	2011	250	Time-wise	GOCE (6)
GOCE DIR Gen2	2011	240	Direct	GOCE (6)
GOCE TIM Gen3	2011	250	Time-wise	GOCE (18)
GOCE DIR Gen3	2011	240	Direct	GOCE (18), GRACE (6)
GOCO02S	2011	250		GOCE (2), GRACE (7)
GIF48	2011	360		GRACE, terrestrial observation

Table 2 Comparison of geometric geoidal height differences

	Mexico results (m)				Canada results (m)			
Model	Max	Min	Mean	Std. Dev.	Max	Min	Mean	Std. Dev.
TIM1	1.903	−2.286	−0.066	0.479	1.295	−1.529	−0.006	0.411
DIR1	1.985	−2.559	−0.063	0.440	1.228	−1.144	0.027	0.334
TIM2	1.788	−2.275	−0.069	0.448	1.302	−1.243	0.023	0.362
DIR2	1.740	−2.288	−0.075	0.457	1.290	−1.261	0.020	0.381
TIM3	1.816	−2.195	−0.057	0.441	1.276	−1.156	0.028	0.343
DIR3	1.844	−2.298	−0.051	0.457	1.377	−1.197	0.016	0.359
GOCO02S	1.852	−2.310	−0.077	0.480	1.271	−1.481	0.001	0.404
GIF48	1.844	−2.298	−0.051	0.457	1.366	−1.227	0.013	0.364

Table 2 presents statistics of comparison between GOCE and the geometric geoidal heights (in the sense of GOCE geoidal height minus geometric geoidal height). Mean differences are at the cm-level with 1-sigma standard deviation at the dm-level. The latter may be partially due to the commission and omission errors, which were not accounted for during the comparison. The third generation product yields the smallest mean values of geoidal heights differences except in Canada, where the smallest difference was obtained using the first generation time-wise.

2.2 Comparison of GOCE Geoidal Heights with GGM2010 Gravimetric Geoidal Heights

Still in Peet et al. (2012) there was a comparison between geoidal heights derived from the Geoide Gravimétrico Mexicano GGM2010 (Muoz-Abundes 2011) and from GOCE direct third generation, which yielded the best results over Mexico. Again, omission errors were disregarded. Figure 1 shows the differences computed along a grid (2.5′ by 2.5′). Statistics for only mainland Mexico include a mean of −0.174 m with a spread of 0.513 m and maximum and minimum values of 3.215 and −2.354 m respectively. There are larger variations in the regions of Baja California and southern Mexico. These regions show large amplitudes with a short wavelength (around 120 km, beyond degree 60). This feature may be due to disagreement between the GOCE dir 3 and the terrestrial data used to feed the GGM2010: GGM2010 uses a reference field up to degree 40 from the model EIGEN-GRACE_03S (Reigber et al. 2005) and terrestrial data for all higher degrees. Pavlis (1996) routine was also used here.

3 Omission Errors

Omission errors were evaluated by computing the contribution of EGM2008 (Pavlis et al. 2012, 2013) coefficients from degree 181 up to 2190. Figures 2 and 3 show the distribution and variation of omission errors over Mexico and Canada. Table 3 summarizes the statistics. Program Harmonic_Synth_v.02 was used for this evaluation. This program still uses the same approach as described in Pavlis (1996).

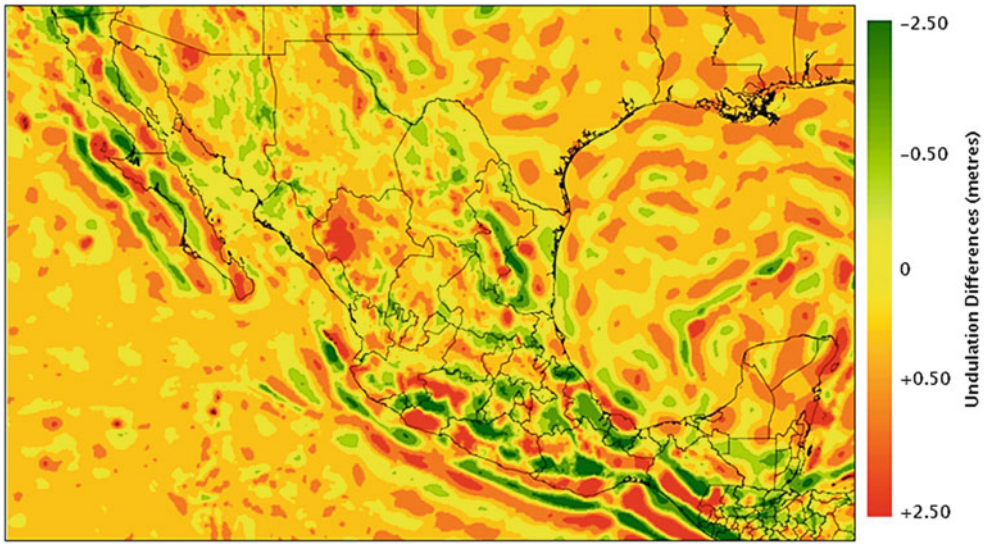

Fig. 1 GGM2010 vs. GOCE direct third generation

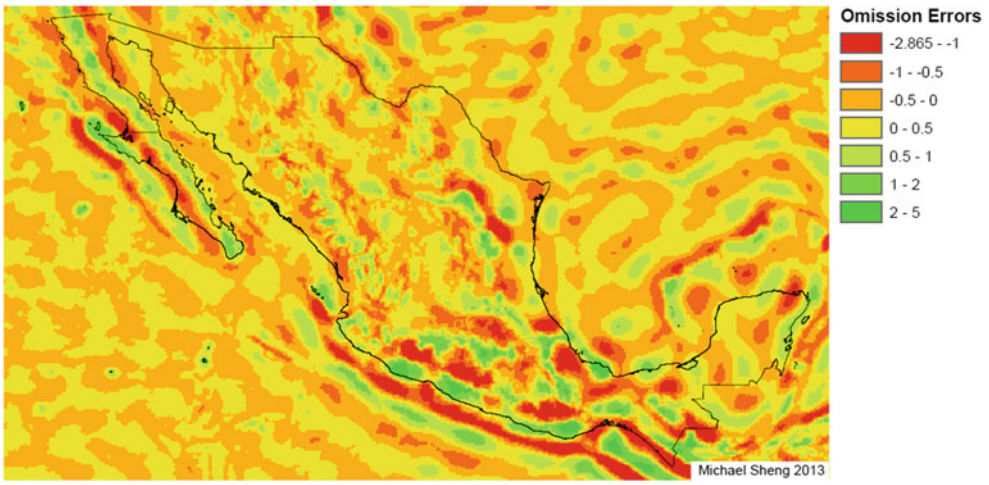

Fig. 2 Omission errors over Mexico (in metres)

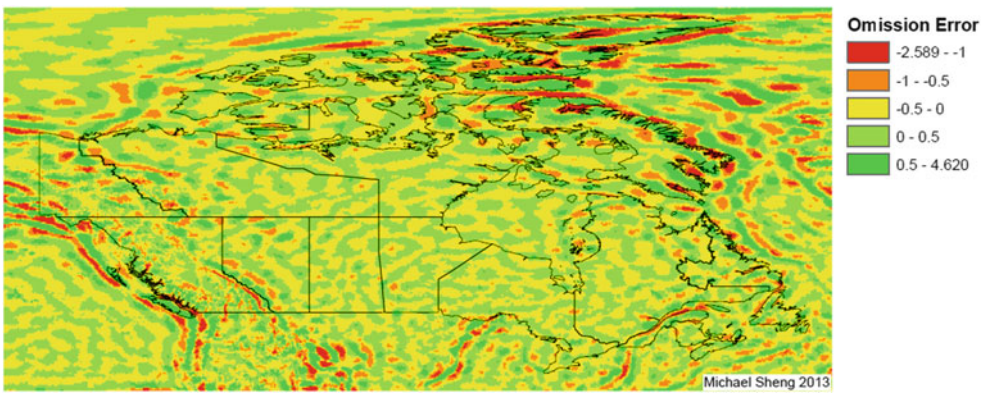

Fig. 3 Omission errors over Canada (in metres)

Table 3 Statistics about omission errors (values in m)

	Mexico	Canada
Mean	−0.001	0.001
Standard deviation	0.498	0.447
Maximum value	4.772	4.260
Minimum value	−2.880	−2.589

Table 4 List of Gravity models (after ICGEM 2013)

Model	Year	Degree	Solution
DGM-1S	2012	250	GOCE, Grace
GOCO03S	2012	250	GOCE, Grace
GOCE dir3	2011	240	GOCE, Grace, Lageos
GOCO01S	2010	224	GOCE, Grace

4 Comparisons Including Omission Errors

Model assessment considering omission errors was carried out by simply comparing geometric and gravimetric geoidal heights with those computed from the GOCE models, according to the following relationship:

$$\Delta N = (N_G - \delta N_{EGM2008}) - N_{GOCE}, \quad (1)$$

where N_G is the geoidal height as given by the geometric or gravimetric model, N_{GOCE} is the geoidal height as computed using a GOCE model, and $\delta N_{EGM2008}$ represents the omission errors.

4.1 Comparison Against Mexican Geometric Height

The comparisons considering omission errors using GOCE direct third generation model were carried out with respect to Mexican geometric geoidals heights. Statistics related to this comparison resulted in a mean of −0.016 m with a spread of 0.306 m; maximum and minimum values at the range of 2 m.

4.2 Comparison Against Gravimetric Height

The comparisons considering omission errors were also done with respect to the gravimetric geoid GGM2010 of Mexico and PCGG2013 (in a 2′ by 2′ grid) of Canada (Huang and Véronneau 2013). The four GOCE models used in this comparison are shown in Table 4, being evaluated by the Harmonic_Synth_v.02program. Note that only GOCE direct third generation is common to all comparisons. The other models were used because they are more recent. All models were evaluated up to degree 180. The use of degree 180 as a limit was a recommendation by Rummel (2012).

In this evaluation, we applied a zero degree term (sum of the mass and potential terms so that the geoidal heights are referred to the GRS80 ellipsoid) of −0.53 m in the evaluation involving the GGM2010 and −0.44 m for the evaluation involving the PCGG2013. Figures 4 and 5 show the results for the comparison done with respect to DGM-1S, for Mexico and Canada, respectively. Statistics summarized in Tables 5 and 6.

5 Concluding Remarks

We have performed a series of comparisons of geoidal heights derived from several GOCE models with the ones derived from GPS on benchmarks over Mexico and Canada and with the latest geoidal maps of Mexico (GGM2010) and Canada (PCGG2013). Some of the comparisons did not take omission errors into account, whereas some others did. The results indicate unequivocally the benefits of taking omission errors into account, as in doing so it results in a reduction in the spread of the differences. The limitation in the approach of using EGM2008 to evaluate omission error is that EGM2008 truncates at degree 2190. Therefore, it does not model all omission error (i.e., those beyond degree 2190). The omission errors that remain unaccounted for may be contributing to the remaining spread.

There are other important features in the study that need to be stressed in order to properly understand the results. In this study, in the comparison of GOCE models against geometric geoidal heights, the GOCE models were evaluated up to their maximum degree; whereas when omission errors were accounted for the GOCE models were evaluated up to degree 180. Other point is that not all models were the same in both comparisons: only GOCE direct 3rd generation was common to all comparisons. Nevertheless, the conclusion (about the benefits of taking omission errors into account) holds exactly due to the solution obtained with the latter model.

Results can be summarized as follows. Let us first call the comparisons of geoidal heights derived from several GOCE models with geoidal heights derived from GPS on benchmarks (referred to as geometric geoidal heights) over Mexico and Canada as comparison (1), and call the comparisons of geoidal heights derived from several GOCE models with geoidal heights derived from the latest geoidal maps of Mexico and Canada (referred to as gravimetric geoidal heights) as comparison (2). Comparison (1) disregarding omission errors, presented in Sect. 2.1, resulted in a mean difference in the order of -6 ± 46 cm in Mexico (best result

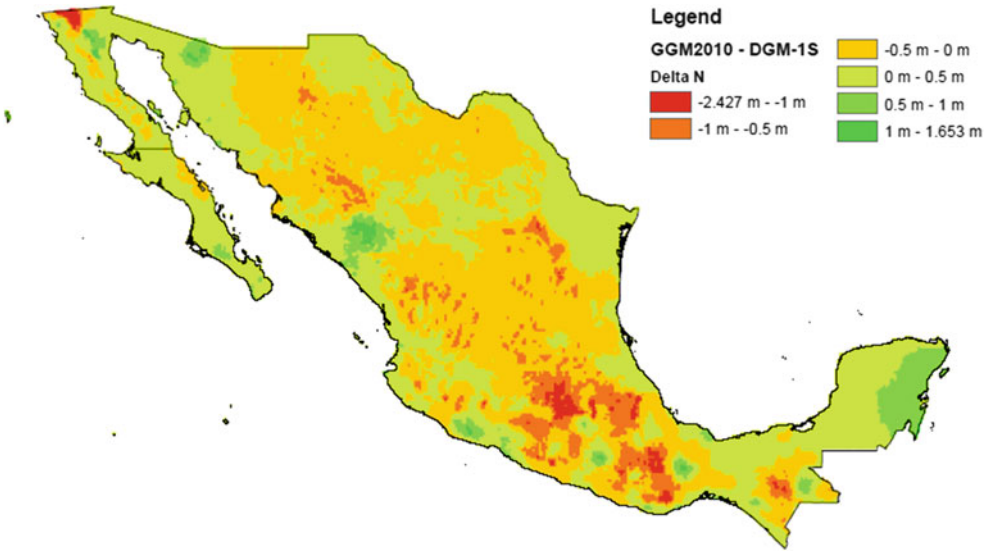

Fig. 4 Comparing GGM2010 with DGM-1S

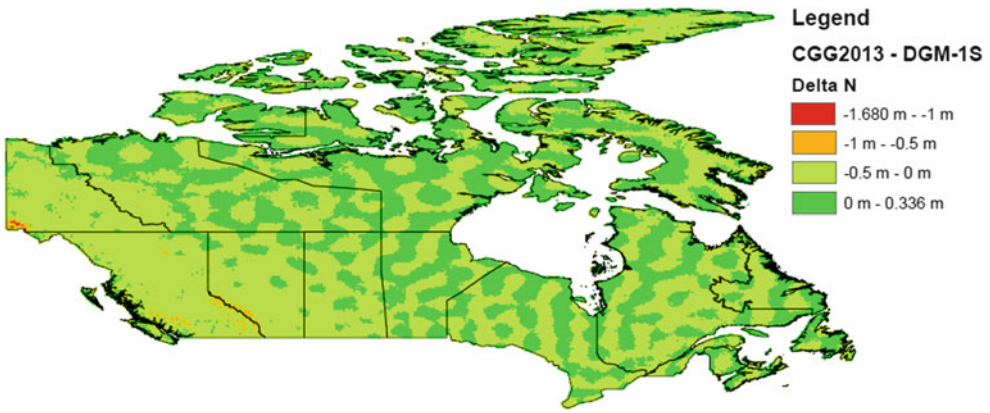

Fig. 5 Comparing PCGG2013 (same as CGG2013 in the legend) with DGM-1S

GOCE direct third generation), whereas in Canada most comparisons resulted in -2 ± 37 cm, being that the ones involving GOCE time-wise first generation and GOCO02S gave millimetre-level mean difference (which seems difficult to justify); maximum differences are slightly larger than 2 m. Comparison (1) taking omission errors into account, presented in Sect. 4.1, resulted in -1.6 ± 30.6 cm. Comparison (2) without taking into account omission errors, presented in Sect. 2.2, resulted in -17.4 and ± 51.3 mm. Comparison (2) taking the omission errors into account, presented in Sect. 4.2, seem to have resulted in a reduction in all parameters, being the mean difference in the order of -3 ± 35 cm in Mexico and -3 ± 9 cm in Canada. Maximum values are 2.5 m and 1.7 m, respectively.

The omission errors in Mexico and in Canada show a similar behaviour, with a near zero mean and a standard

Table 5 Summary of comparisons, only landmass considered, values in m

Mexico	DGM-1S	GOCO03S	GOCE dir3	GOCO01S
Mean	−0.030	−0.030	−0.028	−0.031
Standard deviation	0.348	0.348	0.348	0.349
Maximum	1.657	1.686	1.674	1.694
Minimum	−2.427	−2.489	−2.443	−2.515

Table 6 Summary of comparisons, only landmass considered, values in m

Canada	DGM-1S	GOCO03S	GOCE dir3	GOCO01S
Mean	−0.030	−0.030	−0.028	−0.030
Standard deviation	0.093	0.091	0.093	0.101
Maximum	0.336	0.334	0.342	0.338
Minimum	−1.680	−1.704	−1.691	−1.708

deviation at the order of ±50 cm in Mexico and ±45 cm in Canada. In both cases, maximum differences reach more than 4 m.

The effect of omission errors can be better appreciated by looking at performance of the only GOCE model used in all comparisons, the direct third generation model. Comparing it with Mexican geometric geoidal heights: without omission errors, mean and standard deviation of −5.1 and ±45.7 cm; including correction for omission errors, mean and standard deviation of -1.6 ± 30.6 cm. Comparing it with GGM2010: without omission errors, mean and standard deviation of −17.4 and ±51.3 cm; including correction for omission errors, mean and standard deviation of -2.8 ± 34.8 cm.

Acknowledgements Thanks to Natural Resources Canada and to Instituto Nacional de Estadística y Geografía for the provision of the geoid models PCGG2013 and GGM2010. GOCE models were obtained through ICGEM's website, also cordially acknowledged.

References

ESA (1999) Gravity field and steady-state ocean circulation mission. Reports for Mission Selection, the Four Candidate Earth Explorer Core Missions, ESA SP-1233(1)

Featherstone W (2011) Absolute and relative testing of gravimetric geoid models using global positioning system and orthometric height data. Comput Geosci 27:807–814

Huang J, Véronneau M (2013) Canadian gravimetric geoid model 2010. J Geod. doi:10.1007/s00190-013-0645-0

ICGEM (2013) Global gravity models – table of models. [On-line] http://icgem.gfz-potsam.de/ICGEM/. Accessed Aug 2013

Muoz-Abundes R (2011) Geoide Gravimetrico Mexicano 2010 (GGM10). Technical Report of the Instituto Nacional de Estadistica y Geografia, Aguascalientes, Mexico

Pavlis N (1996) A modification to the program f477. Department of Geodetic Science and Surveying Technical Report, Ohio State University, Columbus, Ohio

Pavlis NK, Holmes SA, Kenyon SC, Factor JK (2012) The development and evaluation of the earth gravitational model 2008 (EGM2008). J Geophys Res 117(B4):2156–2202. doi:10.1029/2011JB008916

Pavlis NK, Holmes SA, Kenyon SC, J. K. Factor (2013) Correction to the development and evaluation of the earth gravitational model 2008 (EGM2008). J Geophys Res 118(5):2633. doi:10.1002/jgrb.50167

Peet T, Santos MC, Avalos D, Vaníček P, Huang J (2012) Assessment of GOCE models over Canada and Mexico. Book of Abstracts, 2012 CWRA-CGU National Conference, Banff, AB, 5–8 June, 31

Rapp RH (1982) A FORTRAN program for the computation of gravimetric quantities from high degree spherical harmonic expansions. Department of Geodetic Science and Surveying Technical Report No. 334, Ohio State University, Columbus, Ohio

Reigber CH, Schmidt R, Flechtner F, Konig R, Meyer U (2005) An earth gravity field model complete to degree and order 150 from GRACE: Eigen-Grace02S. J Geod 39:1–10

Rummel R (2012) Personal communication. TU Munich

Visser P, Rummel R, Balmino G, Sünkel H, Johannensen J, Aguirre M, Woodworth PL, le Provost C, Tsherning CC, Sabadini R (2002) The European earth explorer mission GOCE: impact for the geosciences. Ice Sheets, Sea Level and the Dynamic Earth, Geodynamics Series. Am Geophys Union 29:95–107. doi 10.1029/029GD06

Verifying the Accuracy of Recent Global Geopotential Models in North-West Mozambique

M.S. Bos, R.M.S. Fernandes, P.G. Almeida, M. Cordeiro, and W. Coetzee

Abstract

Several high resolution global geopotential models have been published in recent years. Two of them are EGM2008 and EIGEN-6C2, which have accuracies on the order of 3–20 cm in Europe and Australia. However, part of this accuracy is related to the high number of gravity observations available in these areas. In Africa there are still many regions without terrestrial gravity observations such as north Mozambique. Using the results of a recent terrestrial gravity campaign in north-west Mozambique we conclude that the error of the EGM2008 and EIGEN-6C2 here is still on the order of ±60 cm, which strongly limits their use for many scientific and technical applications.

Keywords

EGM2008 • EIGEN-6C2 • Gravity model verification • Mozambique

1 Introduction

The geoid is used in many countries to define the reference surface of the national vertical height system. The shape of the geoid can be determined accurately by spirit levelling and gravity observations but this geodetic technique has the disadvantage that it is very labour intensive. Another option is to compute the geoid from gravity observations only. However, in the north of Mozambique both levelling data and gravity data are very sparse and as a result, the geoid is poorly defined.

With the recent publication of high resolution Global Geopotential Models (GGM's) such as EGM2008 (Pavlis et al. 2012) and EIGEN-6C2 (Förste et al. 2013), with wavelengths of 18 and 20 km respectively, one might wonder if these GGM's could be used to represent the geoid in this area. Claessens et al. (2009) compared EGM2008 with GPS/levelling data in Australia and found a standard deviation of 17.3 cm, lower than that of the Australian geoid AUGeoid98. Strykowski and Forsberg (2010) performed a similar test for Scandinavia and Greenland and obtained standard deviations between 3 and 11 cm, comparable to the accuracy of the national geoid models.

No such comparisons yet exists for the more recent model EIGEN-6C2 but Förste et al. (2013) compared this model up to degree 360 with GPS/levelling points in Europe, North America and Australia and found similar accuracy as that of EGM2008. They also compared EGM2008 with EIGEN-6C2 globally which clearly showed regions where their difference reach the metre level, such as in the north of Mozambique. The main reason for this is the availability and inclusion of GOCE data in EIGEN-6C2, which were

M.S. Bos • M. Cordeiro
University of Beira Interior, Instituto D. Luis, R. Marquês d'Ávila e Boloma, 6201-001 Covilhã, Portugal

R.M.S. Fernandes (✉)
University of Beira Interior, Instituto D. Luis, R. Marquês d'Ávila e Boloma, 6201-001 Covilhã, Portugal

Delft University of Technology, Kluyverweg 1, 2629HS Delft, The Netherlands
e-mail: rmanuel@di.ubi.pt

P.G. Almeida
University of Beira Interior, GEOBIOTEC, R. Marquês d'Ávila e Boloma, 6201-001 Covilhã, Portugal

W. Coetzee
Rio Tinto Coal Mozambique, Bairro Comunal de Matundo Parcela No 1049, Estrada Nacional No 103, Tete, Mozambique

© Springer International Publishing Switzerland 2015

C. Rizos, P. Willis (eds.), *IAG 150 Years*, International Association of Geodesy Symposia 143,
DOI 10.1007/1345_2015_102

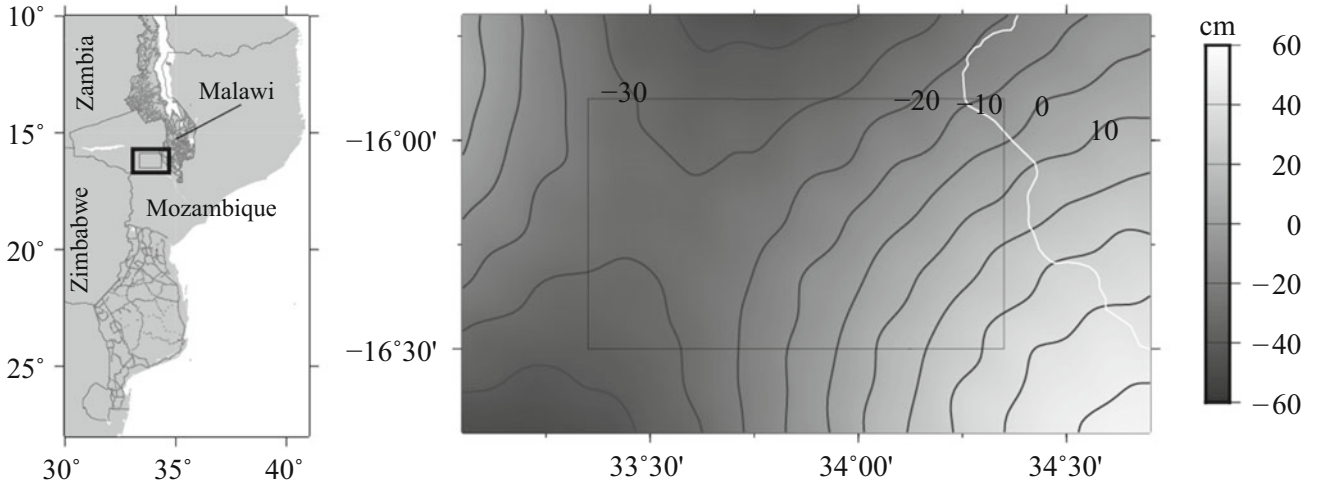

Fig. 1 The *left panel* shows Mozambique and the terrestrial gravity data that is available in the database of BGI (*dark gray dots*). The area where new gravity measurements were made is shown by the *rectangle with the thick black outline* which is shown in the *right panel*. The *inner rectangle* represents the area for which a new local quasi-geoid has been computed. The *right panel* shows the difference in height anomalies between EGM2008 ($N_{max} = 2{,}190$) and EIGEN-6C2 ($N_{max} = 1{,}949$)

not available for inclusion in EGM2008. The height anomaly difference between complete EGM2008 minus EIGEN-6C2 is shown in the right panel of Fig. 1 and varies between ±30 cm. The medium wavelength nature of these differences was investigated further by splitting them up into contributions from degrees 0–90, 91–200 and 201–1,949. The first group with the very long wavelength shows an east west variation from −3 to +3 cm. The second group with degrees 91–200 corresponds very closely to what is shown in Fig. 1 and can be interpreted as the effect of inclusion of GOCE data in EIGEN-6C2. Finally, the third group with the short wavelengths, degrees 201–1,949, shows differences smaller than ±2.5 cm because the short wavelength data in EIGEN-6C2 are based on those used in EGM2008.

This ±30 cm difference between the two GGM's can be taken as an indication of their accuracy and it is not enough to support technical applications (like aerial photogrammetric surveys) that are being required in the north-west of Mozambique due to mining activities. Furthermore, the area suffers from a lack of gravimetric data as can be seen from the left panel in Fig. 1 which shows the gravity data available in the database of Bureau Gravimétrique International (BGI). Thus, the short wavelength geoid contributions in EGM2008 and EIGEN-6C2 in this region are not based on real gravity data. To provide a better geoid model for the area, a gravity campaign was carried out in August and September 2012 in the north-west of Mozambique, see Fig. 1.

It must be noted that GGM's cannot be used to compute a geoid surface that lies underneath the surface, as is the case in north-west Mozambique. Therefore, we compute height anomalies which afterwards can be converted into geoid undulations using the digital terrain model derived from the Shuttle Radar Topography Mission (Farr et al. 2007) using the method of Rapp (1997). The magnitude of this conversion is less than 3 cm and since this correction is the same for all GGM's and our local geoid, we restrict ourselves to only discuss height anomalies. Furthermore, we use pseudo-height anomalies (Barthelmes 2013) which are evaluated on the ellipsoid since they only differ up to 1 cm from the correct height anomalies over our area of interest. Next, the results are given in the tide-free system and with respect to the WGS-84 ellipsoid.

The objective of this study is to quantify the accuracy of EGM2008 and EIGEN-6C2 over the area of north-west Mozambique, using our new local quasi-geoid as reference.

2 Gravity and GPS Observations

The gravity observations were made with two instruments. The first was a LaCoste & Romberg-G gravimeter, serial number 1019, of the Science Faculty of the University of Lisbon, Portugal. This instrument has no electrostatic feedback system although it has an electronic readout of the position of the beam. The second instrument was a Scintrex CG3M gravimeter of the Faculty of Civil Engineering and Geosciences of the Technical University of Delft, The Netherlands.

These are relative gravimeters and to obtain absolute gravity values, they need to be linked to at least one absolute gravity station. However, no such station exists in north Mozambique and we therefore used two absolute reference gravity stations in Malawi: at Chileka airport in Blantyre and

Table 1 Statistics of the 308 observed gravity disturbances and of the residual gravity values after subtracting the complete EGM2008 and EIGEN-6C2 model

Parameter	Mean	Std	Min	Max
$g_{obs} - \gamma$	−30.1	23.8	−81.1	24.9
$g_{obs} - g_{egm}$	0.8	19.1	−41.8	53.2
$g_{obs} - g_{eig}$	−0.6	18.0	−41.7	54.6

Unit is mGal

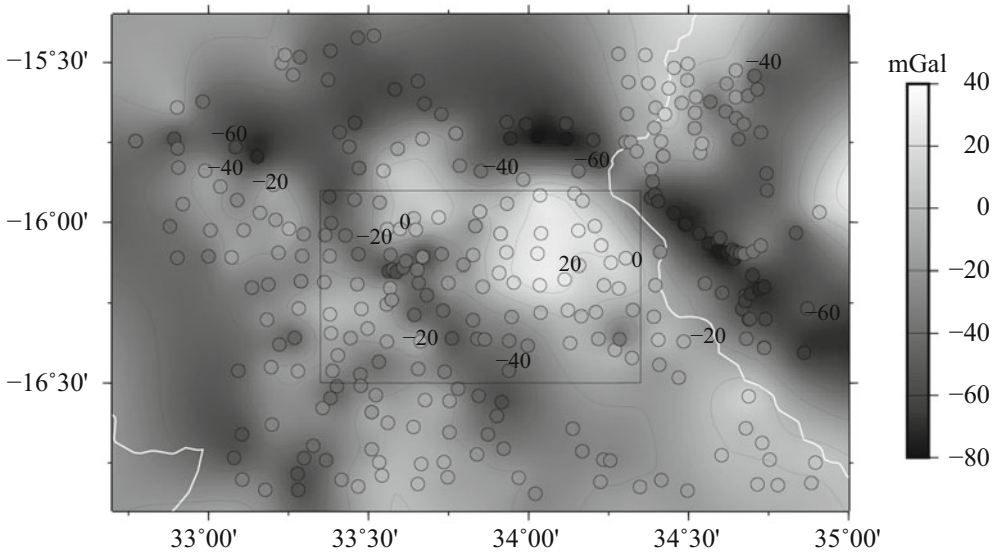

Fig. 2 The location of the 308 gravity observations used in this research. The observations in Malawi were taken from BGI. The *gray scale* represents the observed gravity disturbance which have been interpolated to facilitate interpretation

at the military airport at Zomba. From these two observations we concluded that the scale of our Scintrex gravimeter is good to 0.3%. GPS observations with a vertical accuracy of about 2 cm (r.m.s.) were made in parallel to the gravity observations which allows us to work with gravity disturbances (i.e., the observed gravity minus normal gravity γ).

At six locations the two instruments made observations in parallel. The difference at those points has a standard deviation of 0.185 mGal. In Malawi we also reobserved at nine gravity points listed by BGI. Here the standard deviation of the agreement was 0.848 mGal which is very satisfactory.

Statistics of the observations are given in Table 1 and the locations of the gravity observations are shown in Fig. 2. The observations in Malawi are taken from the BGI database. The grayscale represents the observed gravity disturbance and the most notable features are the low values in the Malawi rift system and the high values of +20 mGal just right of the center of Fig. 2. This was observed with the LaCoste & Romberg gravimeter but also a few observations made with the Scintrex in the area show high values. This area of positive gravity disturbances is not present in EGM2008 nor EIGEN-6C2 and creates a quasi-geoid undulation of around 80 cm as shown in Sect. 6.

Table 2 The variance of the observed gravity after subtracting the long wavelengths from the GGM from degree 0 to N_0

Degree N_0	EGM2008 (mGal^2)	EIGEN-6C2 (mGal^2)
90	548	550
180	668	626
360	624	574
720	494	447
1,440	389	345
1,949	381	337

3 Local Quasi-Geoid Computation Methodology

The local quasi-geoid was computed using Least-Squares Collocation (LSC) in combination with the Remove-Restore technique (Sansò and Sideris 2013, Chap. 7). The long wavelengths were subtracted using alternatively EIGEN-6C2 and EGM2008 to investigate their influence on the final result. Ideally we want to remove as much signal as possible in the remove step. In Table 2 we list the variance of the observed gravity values after subtracting the GGM for various values of the maximum degree N_0 and one

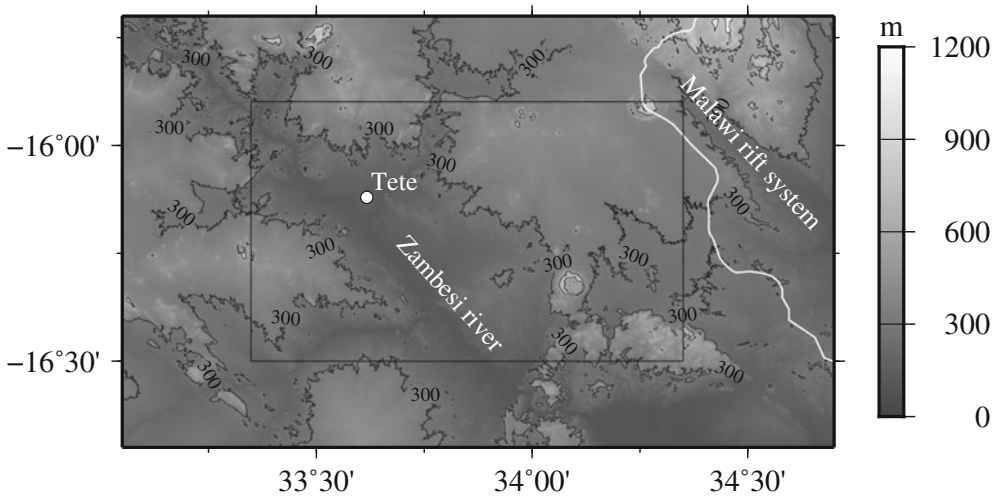

Fig. 3 The topography derived from Shuttle Radar Topography Mission. Major topographic features are named

can see that EIGEN-6C2 produces smaller residuals than EGM2008 and that for degrees higher than 1,440 further reduction is minimal. Nevertheless, we used in the remove step GGM's up to degree 1,949 to produce the smallest residual.

Terrain corrections were omitted since the area is not very mountainous with hills not higher than 400 m, as was shown in Fig. 3, and there is not a significant smoothing effect of the residual gravity field. Afterwards, the residual gravity disturbances were used to estimate a local covariance function using the standard spherical approximation. The covariance function was the conventional model 4 of Tscherning and Rapp (1974) with $B = 4$. The low degrees are replaced by the error degree variances of the GGM, scaled by a constant α. The covariance of the disturbing potential T at two points P and Q, can be computed by, see Eq. (7.14) of Sansò and Sideris (2013):

$$\mathrm{Cov}(T_P, T_Q) = \alpha \sum_{n=2}^{N_0} (\sigma_n^{err})^2 \left(\frac{R^2}{r_P r_Q}\right)^{n+1} P_n(t) + \sum_{n=N_0+1}^{\infty} \frac{A\, R_B^2}{(n-1)(n-2)(n+B)} \left(\frac{R_B^2}{r_P r_Q}\right)^{n+1} P_n(t) \quad (1)$$

where R is the mean radius of the Earth, σ_n^{err} the error degree standard deviations for the potential of a GGM, P_n the Legendre polynomial of degree n and t the cosine of the angular distance between the two points. The radii of points P and Q are given by r_P and r_Q, respectively. The covariance of the gravity disturbance between the two points can be derived from Eq. (1):

$$\mathrm{Cov}(\delta g_P, \delta g_Q) = \frac{d}{dr_P}\left(\frac{d\ \mathrm{Cov}(T_P, T_Q)}{dr_Q}\right) \quad (2)$$

The three parameters of the covariance function, represented by the vector $\boldsymbol{\theta}$, are amplitude A, radius of the Bjerhammer sphere R_B and scaling factor α of the error degree variances of the GGM. Their values are normally estimated using a least squares inversion procedure (Knudsen 1987) using the sample covariance as the data to which the empirical covariance function must be fitted. The sample covariance function is defined as:

$$\mathrm{Cov}(k) = \frac{\sum S_i x_i S_j x_j}{\sum S_i S_j} \quad (3)$$

where x_i and x_j are two gravity observations, each representative for a small area S_i and S_j, separated by an angular distance ψ_{ij}. Furthermore, we have $\psi_{k-1} < \psi_{ij} < \psi_k$ and the sums are taken over each observation pair that fulfills this angular distance requirement.

We found that the values of the scale factor α vary between 1 and 5. We also noted that a better agreement between our empirical covariance function, Eq. (1), and the sample covariance function, Eq. (3), was obtained when we used a lower value for N_0 than we used in the remove step. That is, the error degree variances given by the GGM's are not representative for our local region. A possible explanation for this is that the large gravity variations in our area are very different from their globally averaged counterparts.

4 Fitting of the Empirical Covariance Function

There are no definite rules on how to define the area S around each observation in Eq. (3), especially when the observations are irregularly spaced. Normally the observations are binned onto a regular grid. For increasing number of observations the influence of this problem diminishes but in our situation

it could have an effect and therefore we investigated also an alternative method. To explain our method, we recall that our model of the gravity field is (Moritz 1972, 1978):

$$\mathbf{x} = \mathbf{A}\mathbf{X} + \mathbf{s} + \mathbf{n} \tag{4}$$

where vector $\mathbf{x}$ of size q contains the gravity observations. The $q \times m$ design matrix $\mathbf{A}$ describes the systematic effects. If the only systematic effect is a mean of the gravity disturbances, then matrix $\mathbf{A}$, reduces to a column vector filled with ones and m equals 1. In the case that also a linear east-west and north-south trend is included, m equals 3 and matrix $\mathbf{A}$ becomes:

$$\mathbf{A} = \begin{pmatrix} 1 & \lambda_1 - \bar{\lambda} & \phi_1 - \bar{\phi} \\ 1 & \lambda_2 - \bar{\lambda} & \phi_2 - \bar{\phi} \\ \vdots & \vdots & \vdots \\ 1 & \lambda_q - \bar{\lambda} & \phi_q - \bar{\phi} \end{pmatrix} \tag{5}$$

where λ and ϕ denote the longitude and latitude values of the observations. $\bar{\lambda}$ and $\bar{\phi}$ are the average longitude and latitude values. The vector $\mathbf{X}$ of size m with unknown fixed parameters describes the scaling of the design matrix and needs to be estimated from the observations.

Vector $\mathbf{s}$ represents our medium to short wavelength gravity field at the observation points and has zero mean and a covariance $\mathbf{C}_{ss}$. Since we are using the spherical approximation, we have the relation:

$$\delta g = -\frac{\partial T}{\partial r} \tag{6}$$

Equation (6) can be used in combination with Eq. (1) to compute matrix $\mathbf{C}_{ss}$. Vector $\mathbf{n}$, of size q, represent the instrument noise, assumed to be random and with zero mean and covariance $\mathbf{C}_{nn}$. Following Forsberg (1993), we use a diagonal matrix with a standard deviation of 0.5 mGal. It is assumed that there is no correlation between the instrument noise $\mathbf{n}$ and the gravity signal $\mathbf{s}$. Furthermore, $\mathbf{C}_{xx} = \mathbf{C}_{ss} + \mathbf{C}_{nn}$. The auxiliary vector $\mathbf{z} = \mathbf{x} - \mathbf{A}\mathbf{X}$ is centred, i.e. it has zero mean value.

The vector $\mathbf{X}$ can be estimated using weighted least-squares:

$$\hat{\mathbf{X}} = \left(\mathbf{A}^T \mathbf{C}_{xx}^{-1} \mathbf{A}\right)^{-1} \mathbf{A}^T \mathbf{C}_{xx}^{-1} \mathbf{x} \tag{7}$$

Moritz (1978) explains that the gravity signal can be viewed as a random signal. To be precise, it can be described by a multivariate Gaussian probability distribution.

$$p(\mathbf{X}|\mathbf{x}) = \frac{1}{(2\pi)^{q/2} \det \mathbf{C}_{xx}{}^{1/2}} e^{-\mathbf{z}^T \mathbf{C}_{xx}^{-1} \mathbf{z}/2} \tag{8}$$

Taking the natural logarithm of Eq. (8) gives us the log-likelihood function:

$$\ln(p(\mathbf{X}|\mathbf{x})) = -\frac{1}{2}\left[q \ln(2\pi) + \ln \det \mathbf{C}_{xx} + \mathbf{z}^T \mathbf{C}_{xx}^{-1} \mathbf{z}\right] \tag{9}$$

Equation (9) is a Maximum Likelihood Estimation (MLE) problem that is solved using the Nelder–Mead method (Press et al. 1992) which varies the value of the parameters of vector $\boldsymbol{\theta}$ until the most likely value of Eq. (9) has been found. For each variation of the three parameters, Eq. (7) needs to be applied to update the values of $\hat{\mathbf{X}}$, used in the construction of vector $\mathbf{z}$. A stopping criterion must be provided and in our computations this was when the three parameters α, A (in mGal^2) and R_B (in km) were accurate to three digits. This maximisation algorithm cannot guarantee that the global maximum is found, instead of only a local one, but our experience so far has shown that Eq. (9) is well behaved and that there are no local maxima.

5 Simulations

To compare the MLE and sample covariance method, we have performed simulations. Synthetic gravity observations were computed using EGM2008 for our area of interest. The number of randomly distributed observations were 50, 100 and 200 with square areas of 70×70, 100×100 and $140 \times 140\,\text{km}^2$ respectively. For each case 100 runs were performed. The area sizes were chosen to obtain a mean separation of about 10 km between the observations. EIGEN-6C2 was used in the remove step but only up to degree 180 and 270 to keep sufficient gravity signal in the Least-Squares Collocation step. Equation (1) was used to model the covariance function, with parameters estimated using MLE and the sample covariance, and the degree N_0 up to which the error degree variances of EIGEN-6C2 were used was set to 270.

In Table 3 the results are shown and one can see that when EIGEN-6C2 up to degree 270 was used in the remove step both methods perform equally well while for degree 180 they both perform worse. The reason is that, for this particular situation, the gravity field of the latter shows more long wave-length signal that cannot be represented by the empirical covariance function. This effect depends on the size of the area. Nevertheless, we can conclude that binning of the observations mentioned in Sect. 4 to compute the sample covariance has no noticeable influence on the result.

Table 3 Difference between estimated quasi-geoid using EGM2008 gravity observations and EGM2008 itself

		MLE			Sample Cov		
N_0	Obs	Std	Min	Max	Std	Min	Max
180	50	14.9	8.8	25.5	17.6	6.9	26.8
	100	16.9	11.1	24.8	13.2	5.4	24.1
	200	14.3	7.1	20.9	13.4	8.2	17.2
270	50	8.0	5.1	12.6	8.3	5.3	15.1
	100	11.9	8.2	17.7	11.9	8.3	15.0
	200	11.2	8.2	14.6	11.8	6.5	16.8

The empirical covariance function was estimated using MLE and using the sample covariance. EIGEN-6C2 was used in the remove step up to degree 180 and 270 respectively. Units are cm

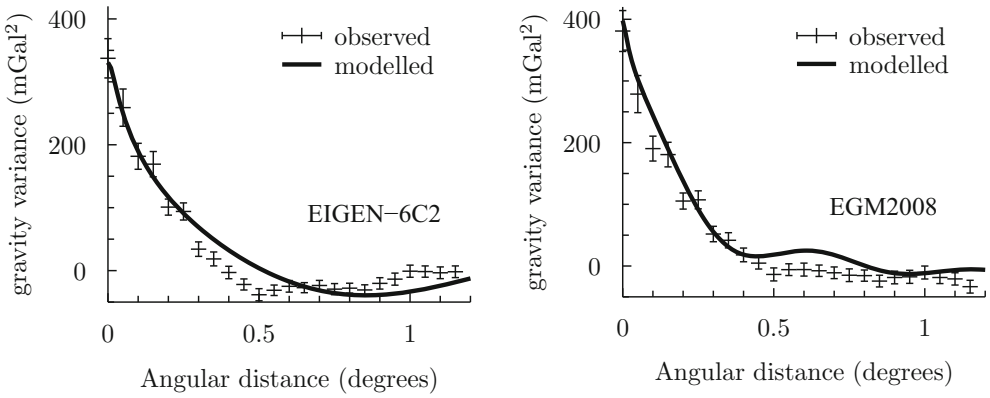

Fig. 4 The sample and modelled covariance after subtracting EIGEN-6C2 and EGM2008 up to degree 1,949 from the observed gravity values

6 Local Quasi-Geoid Results and Validation

As it was mentioned in Sect. 3, using the error degree variances of the GGM's to high degree did not produce an empirical covariance function that fitted well to the sample covariance. Using the log-likelihood value as criteria, we found that the best results were obtained when the error degree variances of the GGM, the σ_n^{err}'s, were used up to degree $N_0 = 270$ and higher degrees by the model of Tscherning and Rapp (1974), see Eq. (1). The sample covariance and the modelled covariance using the MLE estimated parameter values for EIGEN-6C2 and EGM2008 are shown in Fig. 4. For larger distances there are less pairs used in the sample covariance, resulting in a larger uncertainty. The standard deviation of the estimated sample variance is given by the error bar in Fig. 4.

To investigate the accuracy of the quasi-geoid we repeated these computations with the gravity observations replaced by values based on EGM2008. When EIGEN-6C2 was used to remove the long wavelengths of the gravity field the difference between the computed quasi-geoid and the EGM2008 quasi-geoid was around 5 cm.

The shape of the covariance function determines the accuracy estimation of the predicted quasi-geoid. When the error degree variances of EIGEN-6C2 are used for our covariance function, the scaling factor α in Eq. (1) is smaller than that when the error degree variances of EGM2008 are used. This is an indication that EIGEN-6C2 removes more of the long wavelength part of the gravity field in the remove step than EGM2008. The predicted accuracy of the computed quasi-geoid using EIGEN-6C2 in the remove step is around 7 cm for our area of interest, which is similar to the 5 cm accuracy we obtained when we used EGM2008 gravity observations as described earlier. When EGM2008 is used in the remove step a predicted quasi-geoid error is around 15 cm. For this case we also tried fitting a North-East and South-West trend in the LSC, using the design matrix of Eq. (5), but this gave slightly larger predicted error values. For these reasons, our quasi-geoid is computed with EIGEN-6C2 in the remove step.

To remove the bias between our local quasi-geoid and the existing national vertical datum, we computed the differences using 8 levelling benchmarks with known orthometric height for which we also observed their ellipsoidal height, as shown in Table 4. These observations could also be included in the LSC computation of our local quasi-geoid, called RTCM, but this has not been done since their uncertainty is very high. The differences between our local quasi-geoid and the quasi-geoids of EIGEN-6C2 and EGM2008 are plotted in Figs. 5 and 6. From Table 4 one can see that our new local quasi-geoid RTCM has a better fit with the GPS/levelling points than EGM2008 and EIGEN-6C2. This

Table 4 Comparison of geoid models with eight levelling/GPS points

Model	Mean	Std	Min	Max
EGM2008	59	19	40	96
EIGEN-6C2	29	23	4	73
RTCM	9	8	4	20

Units are cm

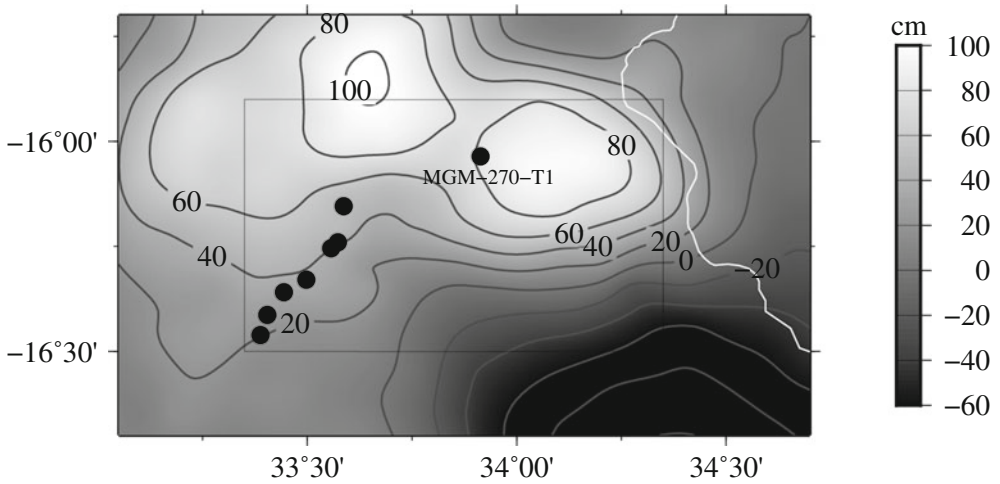

Fig. 5 The difference between our new local quasi-geoid, RTCM, minus EGM2008. Also plotted are the locations of the eight levelling/GPS points used in the comparison

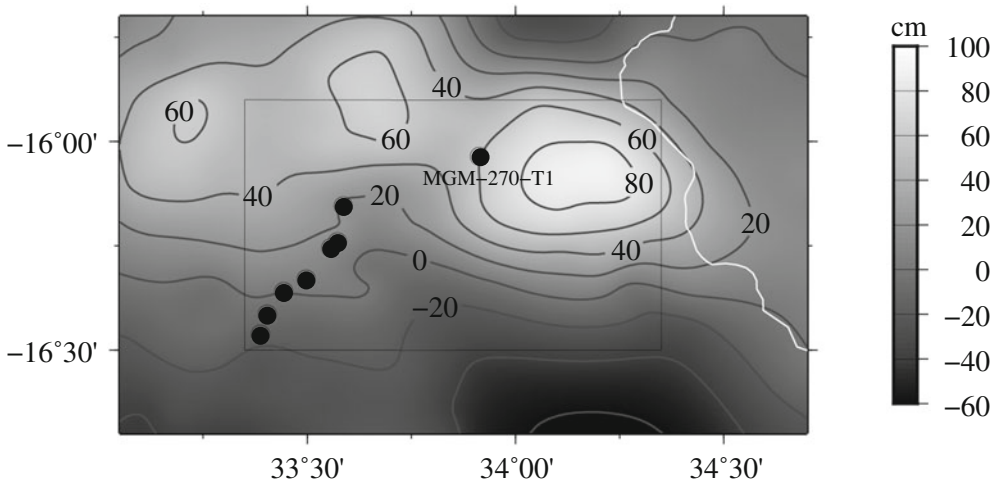

Fig. 6 The same as Fig. 5 but for EIGEN-6C2

is mostly caused by the difference with benchmark MGM-270-T1 which has a much better fit with our RTCM quasi-geoid, giving assurance that our 80 cm hill in the quasi-geoid caused by large positive free air gravity anomalies shown in Fig. 2 is correct. If we assume that this anomaly is caused by a spherical mass then it must lie somewhere at a depth of 35 km to create the observed 60 km diameter of the hill. Using trial and error, we found that a sphere with varying contrast density between 100 and 1,000 kg/m^3 and a diameter varying inversely between 21.0 and 9.8 km, respectively, would cause the observed anomaly of 20 mGal and the quasi-geoid undulation of 80 cm.

7 Conclusion and Discussion

Using results from a gravity campaign in August and September 2012 in north-west Mozambique a new local quasi-geoid was computed using 308 gravity observations. Although the amount of observations is relatively small,

we have verified, using an alternative Maximum Likelihood scheme, that accurate empirical covariance functions can be constructed from the sample covariance when EIGEN-6C2 was used to remove the long wavelength part of the observed gravity field.

This local quasi-geoid model was used as reference to assess the accuracy of the EGM2008 and EIGEN-6C2 global geopotential models in this area. We found differences of the order of ± 60 cm, twice the amount that one obtains by looking at the differences between EGM2008 and EIGEN-6C2 and four times the EGM2008 propagated error estimates.

Acknowledgements This work was only possible with the support (financial and logistic) of Rio Tinto Coal Mozambique (RTCM). We are grateful to Dr. Mikael Mzunzu of Dep. Surveys, Malawi for his help to get access to the absolute gravity points in Malawi and to Eng. Manuel F.G. Ferrão and Eng. José Quembo of Centro Nacional de Cartografia e Teledetecção, Mozambique, for providing us the orthometric heights of the levelling points used in this study. In addition, we would like to thank Prof. Roland Klees for lending us their Scintrex gravimeter. This research benefitted greatly from the supportive comments of three anonymous reviewers. It was reviewer 1 who suggested that the difference between EGM2008 and EIGEN-6C2 was concentrated in the spectral range of degrees 91 to 250. This work was financially supported by the Portuguese Foundation for Science and Technology through grants PEst-OE/CTE/UI4035/2014 and SFRH/BPD/89923/2012.

References

Barthelmes F (2013) Definition of functionals of the geopotential and their calculation from spherical harmonic models. Technical Report 09/02, Deutsches GeoForschungs Zentrum GFZ, Potsdam

Claessens S, Featherstone W, Anjasmara I, Filmer M (2009) Is Australian data really validating EGM2008, or is EGM2008 just in/validating Australia data? Newton's Bull 4:207–251

Farr TG, Rosen PA, Caro E, Crippen R, Duren R, Hensley S, Kobrick M, Paller M, Rodriguez E, Roth L, Seal D, Shaffer S, Shimada J, Umland J, Werner M, Oskin M, Burbank D, Alsdorf D (2007) The shuttle radar topography mission. Rev Geophys 45:2004. doi:10.1029/2005RG000183

Forsberg R (1993) Modelling the fine-structure of the geoid: methods, data requirements and some results. Surv Geophys 14:403–418. doi:10.1007/BF00690568

Förste C, Bruinsma S, Flechtner F, Marty JC, Dahle C, Abrykosov O, Lemoine JM, Neumayer H, Barthelmes F, Biancale R, König R (2013) EIGEN-6C2—a new combined global gravity field model including GOCE data up to degree and order 1949 of GFZ Potsdam and GRGS Toulouse. In: EGU general assembly conference abstracts, vol 15, p 4077

Knudsen P (1987) Estimation and modelling of the local empirical covariance function using gravity and satellite altimeter data. Bull Geod 61:145–160. doi:10.1007/BF02521264

Moritz H (1972) Advanced least-squares methods. Technical Report 175, Ohio State University, Columbus

Moritz H (1978) Least-squares collocation. Rev Geophys Space Phys 16:421–430. doi:10.1029/RG016i003p00421

Pavlis NK, Holmes SA, Kenyon SC, Factor JK (2012) The development and evaluation of the Earth Gravitational Model 2008 (EGM2008). J Geophys Res 117:B04406. doi:10.1029/2011JB008916

Press WH, Teukolsky SA, Vetterling WT, Flannery BP (1992) Numerical recipes in C: the art of scientific computing, 2nd edn. Cambridge University Press, New York. ISBN:0-521-43108-5

Rapp RH (1997) Use of potential coefficient models for geoid undulation determinations using a spherical harmonic representation of the height anomaly/geoid undulation difference. J Geodesy 71:282–289. doi:10.1007/s001900050096

Sansò F, Sideris MG (eds) (2013) Geoid determination, theory and methods. Springer, Berlin/Heidelberg

Strykowski G, Forsberg R (2010) Testing EGM2008 on leveling data from Scandinavia, adjacent Baltic areas, and Greenland. Int Assoc Geod Symp 135(6):505–509

Tscherning CC, Rapp RH (1974) Closed covariance expressions for gravity anomalies, geoid undulations, and deflections of the vertical implied by anomaly degree variance models. Technical Report 208, Ohio State University, Columbus

Impact of Numerical Weather Models on Gravity Field Analysis

Maria Karbon, Johannes Böhm, Elisa Fagiolini, Frank Flechtner, and Harald Schuh

Abstract

Atmospheric pressure variations are one of the major sources of gravity perturbations. Due to the high variability of the atmospheric masses and the sparse sampling of these by GRACE the signals alias into the observations taken by the satellites. The determination of accurate atmospheric gravity field coefficients (AGC) is indispensable for the elimination of these signals. For the determination of AGC it is state of the art to use high resolution Numerical Weather Prediction (NWP) models which take into account the time-variable three-dimensional distribution of the atmospheric mass. By subtracting the gravity spherical harmonics of a long term atmospheric mean field from the ones of the instantaneous atmosphere, the residual gravity spherical harmonic series is obtained. It describes the deviation of the actual gravity field from the mean gravity field due to atmospheric mass variations. NWP models are not perfect as they can show significant differences to in situ measurements. Further these models evolve and change throughout time, which can lead to changes in the pressure data and therefore in the AGC. In this study several aspects of NWP models are investigated, and the influence they have on the determination of the AGC is discussed. We present a strategy that was developed for dealing with changes in the NWP models, and compare our products to those of the GRACE Atmosphere and Ocean Dealiasing level-1B products and those provided by the Groupe de Recherche de Géodésie Spatiale (GRGS).

Keywords

Atmospheric de-aliasing • GRACE • Gravity • Numerical weather models

M. Karbon (✉) • H. Schuh
Deutsches GeoForschungsZentrum Potsdam, 1.1, GPS/Galileo Earth Observation, Telegrafenberg, 14473 Potsdam, Germany
e-mail: karbon@gfz-potsdam.de

J. Böhm
Technische Universiät Wien, GEO, Gußhausstraße 27-29, 1040 Wien, Austria

E. Fagiolini
Deutsches GeoForschungsZentrum Potsdam, 1.2 Global, Geomonitoring and Gravity Field, Münchner Str. 20, 82234 Weßling, Germany

F. Flechtner
Deutsches GeoForschungsZentrum Potsdam, 1.2 Global, Geomonitoring and Gravity Field, Telegrafenberg, 14473 Potsdam, Germany

1 Introduction

For more than a decade GRACE (Gravity Recovery and Climate Experiment) (Tapley et al. 2004) has been monitoring the time-variable Earth gravity field giving an insight into various mass redistribution processes. GRACE measures a combined gravity signal from all the processes that can perturb the satellites orbit. To obtain any individual contribution, independent knowledge in form of background models is required to separate these signals. Further short-term variations that are not resolvable by the GRACE sampling, cause aliasing artifacts in the monthly mean solution, the primary GRACE product (Tapley et al. 2004). Therefore a care-

© Springer International Publishing Switzerland 2015

C. Rizos, P. Willis (eds.), *IAG 150 Years*, International Association of Geodesy Symposia 143,
DOI 10.1007/1345_2015_88

ful reduction of the short-term (e.g. sub-daily to monthly) signals induced by the atmosphere and oceans is required (Han et al. 2004). In recent years many processing centers have experimented with deriving sub monthly solutions from GRACE data, e.g. Rowlands et al. (2005) or Kurtenbach et al. (2009), where the high frequency sub-monthly signals play an even more important role. This pushes further the development of the de-aliasing products, either by means of background models (Dobslaw et al. 2013) or by taking these signals into account within the parameter estimation. All these products rely on modern Numerical Weather Prediction (NWP) models. The dynamic atmospheric circulation is the most rapidly changing and currently the best measured fluid within the Earth's subsystems. Several agencies such as the European Center for Medium-Range Weather Forecast (ECMWF) provide NWP models to reconstruct the current state of the atmosphere and to project it into the future. From such models the atmospheric pressure change can be obtained and introduced into the GRACE analysis as a background model for the tidal and non-tidal contribution. NWP models allow a comprehensive approach by taking into account the vertical and horizontal expansion and permitting the separation of the direct effect, i.e. the Newtonian attraction, and the indirect effect, induced by the deformation due to loading (Neumeyer et al. 2004). Several methods were developed for using NWP models for de-aliasing the measurements of satellite gravity missions (Reigber et al. 2005; Flechtner and Dobslaw 2013) allowing the global computation of residual gravity spherical harmonics series. Within the project "GGOS (Global Geodetic Observing System, (Plag et al. 2009)) Atmosphere" at the Department of

Geodesy and Geoinformation (GEO) of Vienna University of Technology a service was established providing among other products also atmospheric gravity coefficients (AGC) in form of spherical harmonics coefficients currently up to degree and order 100 using pressure level data provided by ECMWF, Version 1 (Karbon et al. 2013). We also developed a strategy to deal with changes of the operational NWP models and to minimize their impact on the final product.

2 Numerical Weather Prediction Models

2.1 Data Description

The ECMWF operational analysis is one prime product for medium-range and seasonal forecasting applications (Stockdale et al. 1998; Rabier et al. 2000). For our operational products we use operational analysis pressure level data, where the vertical discretization is implemented through 25 levels, following continuous surfaces of equal pressure from 1,000 to 1 hPa. At each level, among other parameters, the temperature, the specic humidity, and the geopotential height on global equidistant grids with a horizontal resolution of 1×1 and a temporal resolution of 6 h (00, 06, 12, 18 UTC) are available. The ECMWF operational analysis data are downloaded daily from ECMWF to the GGOS server at GEO, TU Vienna (http://ggosatm.hg.tuwien.ac.at). For this study additional ECMWF data were used, i.e. operational analysis model level data, including the surface pressure and the geopotential at the surface. Global equidistant grids with a horizontal resolution of $1° \times 1°$ and $0.25° \times 0.25°$ were downloaded. Details about the vertical and horizontal discretization can be found at the ECMWF website (http://www.ecmwf.int/products/data/technical/).

2.2 Characteristics of NWP Models

Usually the terrain in numerical weather models does not follow the 'real' topography but the so called model orography which can generally be described as an envelope of the topography (Phillips 1960). The orography is derived by averaging and small-scale filtering the GTOPO30 terrain elevation data set. The resulting mean topography is realistic over most land areas but is insufficient in high mountain areas (Gegout et al. 2011). Several fundamental properties of atmospheric models depend on orography, i.e. on the average elevation of land over a model area. The higher the resolution of the model, the more the details of orography directly influence the simulated atmospheric processes (Miller et al. 1989; Rutt et al. 2006). Most NWP models use spherical harmonics in their internal computation as they are very efficient and can handle spherical geometry in a very natural way. But they are not able to describe discontinuities or steep gradients which occur e.g. in mountainous regions or along coast lines. This leads to spurious oscillations forming unwanted ripples. This so called Gibb's phenomenon as well as the influence of the representation of the topography within NWP models is frequently discussed in climate sciences and related fields, e.g. Navarra et al. (1994) and Dash and Mohandas (2005), but only allusively in the process of the determination of AGC. Also the meteorological community is aware about the problem of the inaccurate pressure values over land due to the input surface topography (Trenberth and Smith 2005). But the updates of the NWP models and the resulting jumps in the parameters have heightened the awareness of issues related to NWP models. The ECMWF NWP model is upgraded periodically to incorporate improvements in the physical model, the numerics, and the data assimilation

scheme, and to accommodate new observing technologies. Thus, inconsistencies in the time-series of model states arise (the history of the changes can be followed at: http://www.ecmwf.int/products/changes/). Such changes often involve the orography and thus are affecting many of the physical parameters. Most easily this can be seen in the atmospheric surface pressure at high altitudes in mountainous regions where jumps can be detected (http://www-app2.gfz-potsdam.de/pb1/op/grace/aod_issues/issues_aod1b_rl05.html). Duan et al. (2012) claim that such jumps in the atmospheric data are responsible for jumps up to 7 cm of equivalent water thickness which they detected in the GRACE de-aliasing product AOD1B (Flechtner and Dobslaw 2013). One way to avoid all the issues related to the model and its possible changes in time, is to use homogeneously reprocessed data such as ERA-Interim covering the years 1979 onwards. The big drawback of these products is that they are usually not available in near real time. ERA-Interim has now reached a latency of approximately 2 months. We decided to follow another strategy with implementing our own background models. The procedure will be described in detail in Sect. 3.2.

3 Methodology for AGC Determination

3.1 Fundamental Formulae

Traditionally atmospheric dealiasing products are provided as a set of gravity spherical harmonic coefficients $\triangle C_{nm}$ and $\triangle S_{\mathrm{nm}}$ computed up to degree n and order m, in our case $n = m = 100$, which represent the temporal and spatial variations of the atmospheric masses at a specific time epoch. Since Boy and Chao (2005) and others have shown the importance of including the vertical extension of the atmosphere in the dealiasing process of satellite gravity data, the basic formulae for the three-dimensional approach, as shown by Boy et al. (2001), Zenner et al. (2010), and Flechtner and Dobslaw (2013) are given here. The gravity spherical harmonics coefficients C_{nm} and S_{nm} can be calculated as follows:

$$\left\{ \begin{matrix} C_{nm} \\ S_{nm} \end{matrix} \right\} = -\frac{1}{(2n+1)\,Ma^n} \iint\limits_{Earth} \left[\int\limits_{r_s}^{0} r^{n+2} \rho \, dr \right] \times P_{nm}(\cos\theta) \left\{ \begin{matrix} \cos m\lambda \\ \sin m\lambda \end{matrix} \right\} \sin\theta d\theta d\lambda. \tag{1}$$

where r_s is the surface radius and M the mass of the Earth, a the radius of the spherical Earth, P_{nm} are the normalized Legendre polynomials, n and m stand for the degree and order of the spherical harmonic expansion.

Adopting the hydrostatic equation,

$$dp = -\rho g_r \, dr, \tag{2}$$

where g_r is the gravity acceleration at each level, we get:

$$\left\{ \begin{matrix} C_{nm} \\ S_{nm} \end{matrix} \right\} = -\frac{1}{(2n+1)\,Ma^n} \iint\limits_{Earth} \left[\int\limits_{p_s}^{0} \frac{r^{n+2}}{g_r} dp \right] \times P_{nm}(\cos\theta) \left\{ \begin{matrix} \cos m\lambda \\ \sin m\lambda \end{matrix} \right\} \sin\theta d\theta d\lambda \tag{3}$$

To analyze gravity field variations caused by atmospheric effects, i.e. to retrieve $\triangle C_{nm}$ and $\triangle S_{\mathrm{nm}}$, a quantity p_{VI} representing the mean state of the atmosphere, has to be subtracted from the inner integral. As a further simplification the gravity acceleration at each level g_r is replaced by a theoretical value g_0.

$$\left\{ \begin{matrix} \Delta C_{nm} \\ \Delta S_{nm} \end{matrix} \right\} = -\frac{1}{(2n+1)\,Ma^{n+2} g_0} \iint\limits_{Earth} \times \left(\left[\int\limits_{Ps}^{0} r^{n+4} dp \right] - p_{VI} \right) \times P_{nm}(\cos\theta) \left\{ \begin{matrix} \cos m\lambda \\ \sin m\lambda \end{matrix} \right\} \sin\theta d\theta d\lambda. \tag{4}$$

The indirect effect of the atmosphere on the gravity field can be included quite easily following Farrell (1972), using the load Love numbers representing the deformational behavior based on the rheology of the Earth, shown here exemplarily for the C_{nm} coefficients:

$$\Delta C_{nm}^{tot} = \Delta C_{nm} + k_n \Delta C_{nm} = (1 + k_n)\, \Delta C_{nm}. \tag{5}$$

Direct measurements of the density term ρdr or the correct metric of the radial coordinate r are not available within NWP models. Thus, it is common methodology to approximate the radius r using the geopotential height Φ given by the NWP model and ξ, describing the mean height above the mean sphere with the mean radius a of the spherical Earth (Zenner et al. 2010; Forootan et al. 2013; Flechtner

and Dobslaw 2013). One formulation is:

$$r = a + z + \xi = a + \frac{\Phi}{1 - \frac{\Phi}{a}} + \xi, \tag{6}$$

$$\Phi = \frac{1}{g}\int_0^z g_r dz = a\frac{z}{a+z}. \tag{7}$$

NWP models usually do not provide the geopotential height throughout all levels, but have to be derived using the geopotential at the surface and the temperature and specific humidity on levels or half levels. Several computation schemes for that procedure can be found in the literature, e.g. White (2000), Forootan et al. (2013), and Flechtner and Dobslaw (2013). As can be seen in Eq. (6) the values of Φ are only altitude dependent as they depend the mean radius a only. Further for the gravity acceleration in Eq. (7) usually a theoretical value g_0 is used. Also in Eq. (4) the constants g_0 and a appear. In the new AOD1B release (Flechtner and Dobslaw 2013) these parameters where replaced with more realistic values by considering the geometrical and physical shape of the Earth. Our processing allows us further to avoid the approximations made with Eqs. (6) and (7).

3.2 Improved Processing Strategy for NWP Data

One important point in processing the NWP data is to know where the Earth surface is, as many quantities are somehow related to it or dependent on it, for example the surface pressure or the limit of the downward integration of the gravitational force acting on a column of air in Eq. (4). But as mentioned earlier, NWP models usually follow an orography which can be subjected to changes. For this reason we decided to refer our NWP model data not any longer to the spherical Earth and the orography provided by ECMWF but to the WGS84 ellipsoid and to implement ETOPO5 as topography. To get the physical component of the Earth we introduced the low degree and order coefficients of the EGM96 gravity model. Doing this we can retrieve the gravity acceleration at all points and at all levels with the correct corresponding radii, all referred to the topography ETOPO5.

- In the first step the data points given in a three-dimensional grid are transformed to a set of geocentric coordinates (r_{84}, θ, λ) with respect to the WGS84 ellipsoid.
- To convert the geopotential height Z (geopotential given by ECMWF divided by the gravity constant of 9.80665 m/s^2 defined by the World Meteorological Organization) into an orthometric height H_o and to determine the geocentric radius $r_{el}(\theta, \lambda)$ for a point on a certain level and its corresponding gravity acceleration, a gravity model with its geoid undulation N is introduced (Fig. 1). We used the fully normalized coefficients of the tide-free EGM96 up to degree and order 2 for the gravity acceleration and the full set up to degree and order 360 for the geoid undulation as needed for the topography determination.

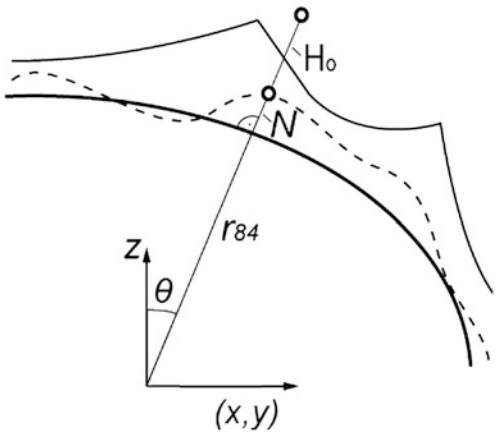

Fig. 1 The determination of the ellipsoidal height, with the *bold solid line* depicting the ellipsoid, the *dashed* one the geoid, and the *narrow line* the topography (Karbon 2013)

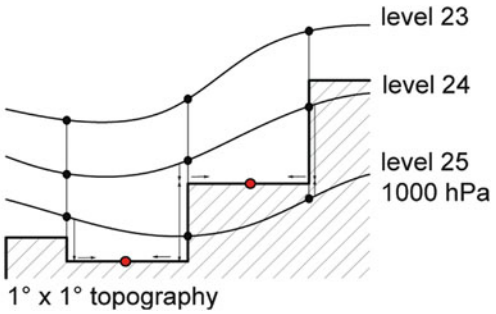

Fig. 2 The inter- and extrapolation scheme to the topography and calculation of the corresponding block mean values (Karbon 2013)

$$\begin{aligned} r_{el}(\theta,\lambda) &= r_{84}(\theta,\lambda) + H_{el}(\theta,\lambda) \\ &= r_{84}(\theta,\lambda) + H_o(\theta,\lambda) + N. \end{aligned} \tag{8}$$

In order to get realistic values for temperature and pressure at the Earth's surface, the virtual temperature T_v (calculated from the temperature and the specific humidity at each level of the NWP model) and P from the pressure levels are interpolated onto the digital elevation model ETOPO5. For this task the two enclosing pressure levels are identified (Fig. 2) for each surface point. The virtual temperature

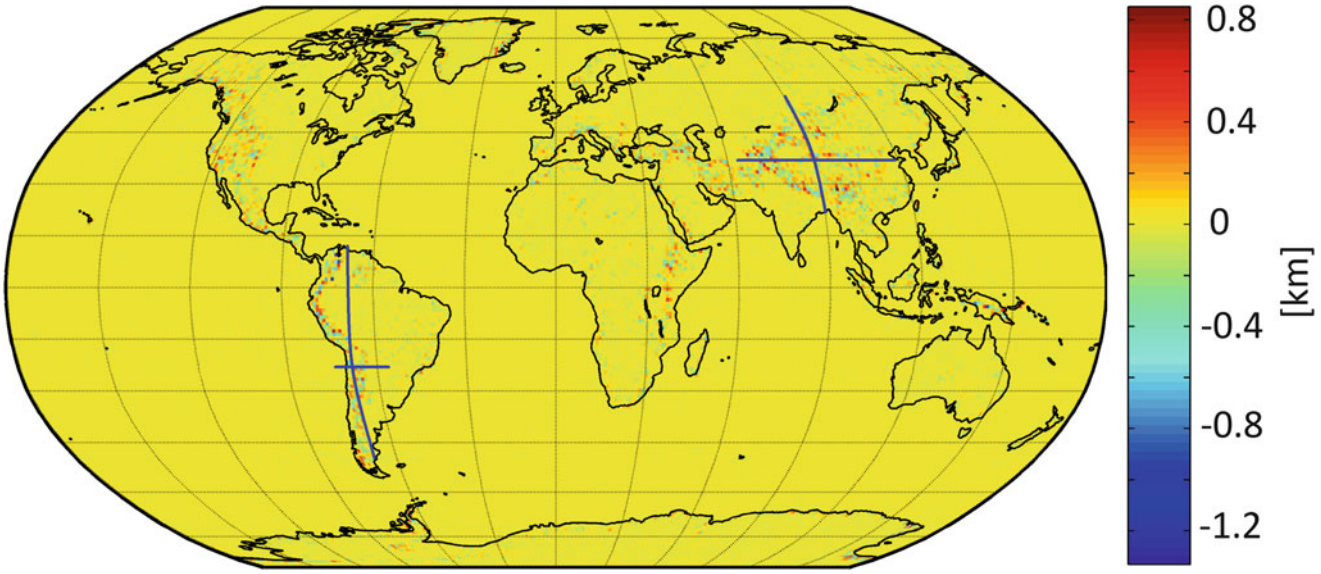

Fig. 3 Difference between the ECMWF orography ($1° \times 1°$) from January 1st, 2003 and 2013

is interpolated linearly and the pressure P is obtained by applying the exponential function Eq. (9):

$$P_s = P_i e^{(-c\Delta H)}, \quad \text{where} \quad \Delta H = H_s - H_i, \qquad (9)$$

and the coefficient c

$$c = \frac{\ln(P_i) - \ln(P_{i+1})}{H_{i+1} - H_i}. \qquad (10)$$

The subscript s stands for 'surface', the subscript i denotes the index for the level above 'surface' s and the subscript $i+1$ denotes the index for the level below s.

From the resulting fields block mean values with a spatial resolution of $1° \times 1°$ were determined, see Fig. 2. This ensures the mathematical correctness for the calculation of spherical harmonics and it was shown by Fagiolini et al. (2007) that this strategy allows an efficient numerical derivation of the spherical harmonics and the introduction of error estimations by weighted mean. For the AGC determination basically Eq. (4) is used, but with the gravity acceleration g_r at all points at all levels with the correct corresponding radii r instead of the constants g_0 and a. The mean field p_{VI} is determined in a similar way using data from the years 2008 and 2009. The coefficients are developed up to degree and order $m = n = 100$ and are written to ASCII-files in the same format as the AOD1B products. They are available at http://ggosatm.hg.tuwien.ac.at/GRAVITY/.

4 Numerical Results and Comparisons

4.1 Some Thoughts on the Orography

As mentioned before, NWP models are updated periodically causing changes to the orography. When comparing orographies used by ECMWF from different epochs and with different resolutions one can find differences in the kilometer range. Figure 3 shows the difference between the orographies provided at January 1st, 2003 and 2013. Large linear features arise, mainly in the Himalaya and the Andes, some extending over 1,000 km and more.

Table 1 summarizes some statistical properties of maps similar to the one in Fig. 3. For this purpose orographies provided January 1st, 2003, 2008, and 2013 are used, with a spatial resolution of $1° \times 1°$ and $0.25° \times 0.25°$. Each row shows the minimum, maximum, and rms of the difference between the data of January, 1st 2008, or 2013 w.r.t. the one of 2003. Two different resolutions, i.e. $1° \times 1°$ and $0.25° \times 0.25°$ are listed separately. The first value shows the difference in meter, and the second corresponds to the resulting difference in hPa considering the standard atmosphere following DIN 5450 (Schulz 1954) and thus can give a general idea of the effect of the difference in height.

To illustrate the discrepancies between the orographies better, several profiles along the blue lines through the Andes and the Himalaya in North–south and East–west direction

Table 1 Statistical properties of the orography maps, the first value is the height difference, the second the impact on the pressure

m/hPa	Resolution (degree)	Min	Max	rms
2003–2008	1	−774/90	587/69	69/8
	0.25	−946/108	839/96	37/4
2003–2013	1	−1,332/150	853/98	91/11
	0.25	−1,332/150	1,174/133	55/7

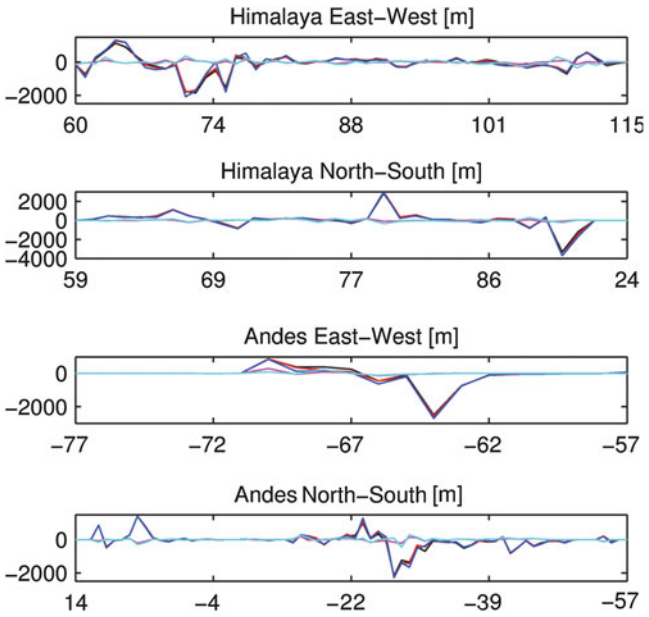

Fig. 4 Difference of the orography profiles through the Himalaya and the Andes w.r.t. the profile with $0.25° \times 0.25°$ resolution from ECMWF operational analysis data on January 1st with $1° \times 1°$ resolution (*black*: 2003, *red*: 2008, *blue*: 2013) and $0.25° \times 0.25°$ resolution (*magenta*: 2008, *cyan*: 2013)

where extracted and plotted in Fig. 4. The profile from January, 1st 2003 with a $0.25° \times 0.25°$ resolution is used as a reference to make the differences clearer, t. It can be noted, that the profiles taken from maps with the same resolution show a similar behavior and are adjacent to each other, whereas the profiles from different resolutions differ up to 2–4 km at their maxima.

As it can be seen in Figs. 3 and 4 as well as from the numbers in Table 1 the orography changes dramatically (hundreds of meters to a few kilometers) on areas that extend up to hundreds of square kilometers, although with a lot of scatter. But one has to keep in mind that these changes also affect other physical parameters within the model, such as the pressure. This has to be taken into consideration especially since several studies showed that the pressure error should not exceed 1 hPa over few hundreds of kilometers to make a reliable recovery of the continental hydrological signal possible and to avoid misinterpretation (Velicogna et al. 2001; Shengjie 2006).

It shall be mentioned, that these implications also apply to other providers of NWP models, e.g. the National Centers for Environmental Prediction (NCEP).

Products from other providers also show differences in other aspects, not just concerning the implementation of the Earth surface. These disagreements can lead to differences of several centimeters in geoid height when computing AGC (Karbon 2013). But unfortunately a simple comparison of two data sets does not reveal the inaccuracies that may be common to both.

4.2 Impact of the Processing Strategy

One of the most significant specialties in our processing scheme is the introduction of ETOPO5 to replace the orography given by ECMWF. Figure 5 shows the difference between the two orographies at the corresponding $1° \times 1°$ nodes. As can be seen, the plot shows some similarities to Fig. 3 as again the biggest discrepancies are in mountainous regions where the differences are in the kilometer range.

A main motivation for developing our processing for the NWP model data was to be independent of changes within the NWP models themselves. To test this assumption we compared our reprocessed NWP model data to ECMWF operational analysis data at selected points where it is known that the ECMWF surface pressure shows jumps in the time series. The upper plot in Fig. 6 shows surface pressure data for a point in Chile ($\varphi = -27.24$, $\lambda = 291.6$), the blue line is the raw ECMWF operational analysis data with jumps due to the periodical updates of the NWP model, the red line depicts our processed data where no jumps are visible. It can also be noted, that our reprocessed data show a smaller amplitude concerning the seasonal signal; as we have no in situ data available for this site an interpretation is difficult. But in a comparison with ERA-Interim the ECMWF operational analysis data show a smaller variation too. Fortunately we could compare our data-set to in situ pressure values gathered at the Conrad Observatory in Austria. It must be mentioned that this station is situated in a mountainous region with a very varied topography. This comparison is shown in the lower plot in Fig. 6, where the black line depicts the in situ measurement, the blue line the difference to the surface

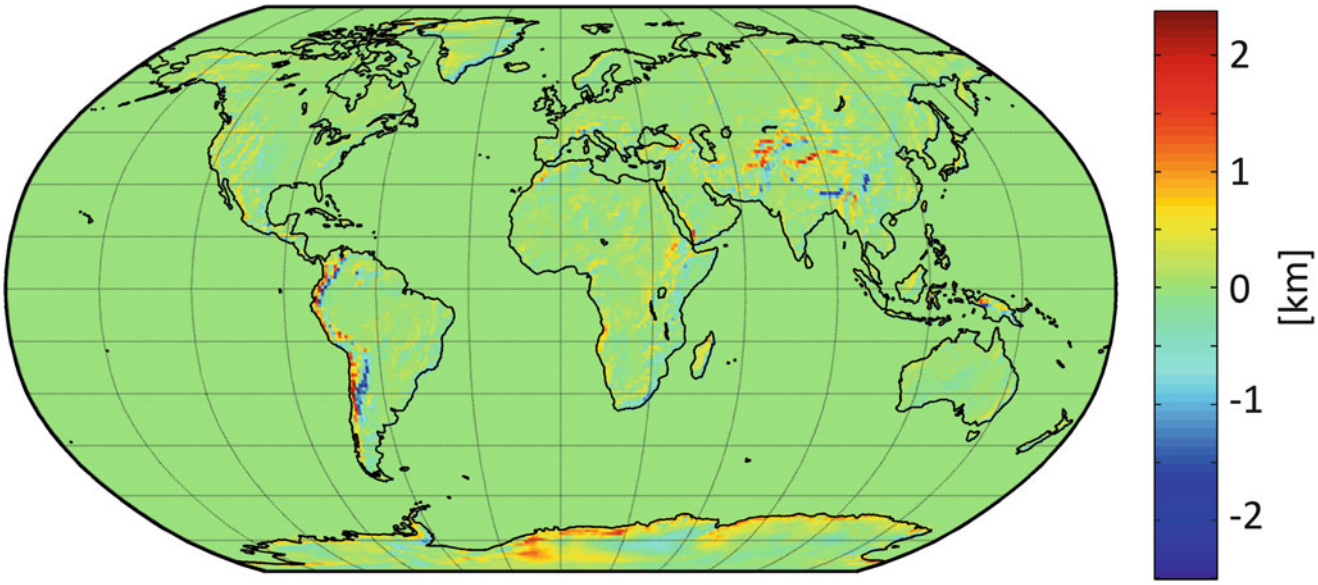

Fig. 5 Difference between the ECMWF orography (1° × 1°) and ETOPO5 at the corresponding nodes in kilometers

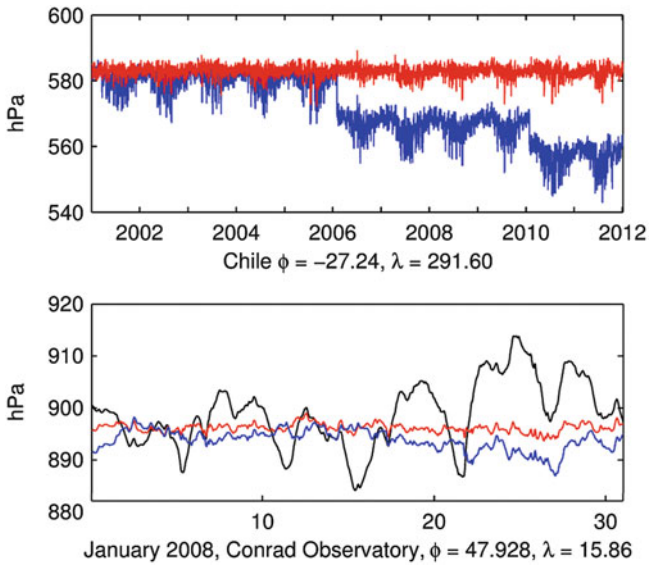

Fig. 6 *Upper plot*: Surface pressure in Chile ($\varphi = -27.24$, $\lambda = 291.6$) for 2001–2011, in *blue* for ECMWF operational analysis data, and in *red* for our processed data. *Red graph* shifted to *blue* one for easier comparison. *Lower plot*: Surface pressure at Conrad Observatory, Austria ($\varphi = 47.928$, $\lambda = 15.86$), in *black* in situ data, *blue* the difference to ECMWF operational analysis data, *red* the difference to our reprocessed data, graphs shifted

pressure data from ECMWF operational analysis data, and red the difference to our processed data. For a better comparison the graphs were shifted.

Comparisons with our data and ECMWF operational analysis data show a comparable performance with correlation coefficients of 0.99 and 0.97, although when looking at the rms our data set shows a much smaller deviation with 13.9 hPa compared to 46.18 hPa of the ECMWF. This confirms the findings by van Dam et al. (2010) who showed that a model resampled with ETOPO5 in most cases outperforms the original weather model data when it comes to distinct stations, although further comparisons are needed. It was shown with this procedure that we are independent from changes in the NWP models as no jumps nor other changes due to updates done at ECMWF can be found in our data.

4.3 Comparison Between AOD1B, GRGS and AGC

Several centers are generating de-aliasing products for GRACE processing. The most prominent is the AOD1B product provided by German Research Centre for Geosciences (GFZ) (Flechtner and Dobslaw 2013); here only the atmospheric part (atm) is of interest. $\text{AOD1B}_{\text{atm}}$ is based on 6 hourly ECMWF analysis model level data on a Gaussian n160 grid which corresponds to 0.5_ resolution. The main difference between our approach and the one used for $\text{AOD1B}_{\text{atm}}$, besides the model level data and its implied problematics concerning orography and internal model changes, can be found in the calculation of the inner integral as mentioned before. A tidal correction for the solar atmospheric tides S1 and S2 is applied for AOD1B, whereas we additionally consider S3 derived from ECMWF 3-hourly delayed Cut-off Analysis data (DCDA). A second center providing de-aliasing products is Groupe de Recherche de Géodésie Spatiale (GRGS) (Gegout 2009). The ECMWF model level data is based on operational analysis in form of spherical harmonics, truncated at T799 which corresponds

to 0.225° resolution, for the time period used here, i.e. January 2008. In contrast to the approach used for the calculation of the AOD1B and AGC product, here an up- and downward-continuation is implemented. S1, S2 and S3 are considered. When looking at the degree standard deviation calculated over 1 month (Fig. 7), all solutions show a very good agreement, i.e. the differences for most coefficients lie below the theoretical error line, except for degree 2 for both solutions, and up to degree 8 for $AOD1B_{atm}$. But when looking at singular epochs, e.g. January 1, 2008, 00 UTC (similar behavior confirmed for other epochs), the picture changes significantly, Fig. 8). Here the results of both centers differ on a substantial level, as it can be seen in Fig. 8a for $AOD1B_{atm}$, and in Fig. 8b for GRGS. In case of AOD1Batm it is hard to say where the differences visible here arise from. The most plausible explanation is the different calculation of the inner integral in Eq. (4).

Here of course also our processing strategy for the meteorological data adds its part to the discrepancies, but these two possible sources cannot be separated nor be quantified accurately. The different definition of the mean field (we use a mean over 2008–2009 whereas for AOD1B a mean over 2001–2002 was used) plays an inferior role as we could not find any significant signal in the pressure data that could explain the signal visible in Fig. 8a. Comparing again Fig. 3 with Fig. 5 one could conclude, that similar signals may be possible to be detected within the AOD1B product from different epochs. Although Duan et al. (2012) claim to have found such jumps in the AOD1B product, we cannot confirm their findings yet and as the differences between the various ECMWF operational analysis orographies are smaller than the ones between ECMWF and ETOPO5 also any effect deriving from them might be smaller, i.e. in the sub-millimeter range, and thus hard to detect.

The differences between AGC and GRGS are a factorf3–4 larger and of a large scale nature. No topographical signals, which are expected to be much smaller, are therefore visible. The signal shows a similar behavior for all epochs, strongly connected to the degree one spherical harmonics, which are associated with the center of the Earth and the degree 1 loading coefficients. A different definition in AGC and GRGS concerning this point might be a possible explanation. Looking at the temporal variation of the C20 coefficient in Fig. 9, the smoothness of the AGC series (blue) in contrast to the other de-aliasing products sticks out, meaning that in the AGC series the sub-daily variations are much smaller. But when comparing the AGC solution without tidal correction (black) to the $AOD1B_{atm}$ (cyan) and GRGS (red), the correlation is much better. The largest contribution to the sub-daily variation in the AGC C20 comes from the S2 tide, leading to the conclusion, that our applied tidal correction derived from ECMWF 3-hourly delayed Cut-off Analysis data (DCDA) (Karbon 2013) works fairly well.

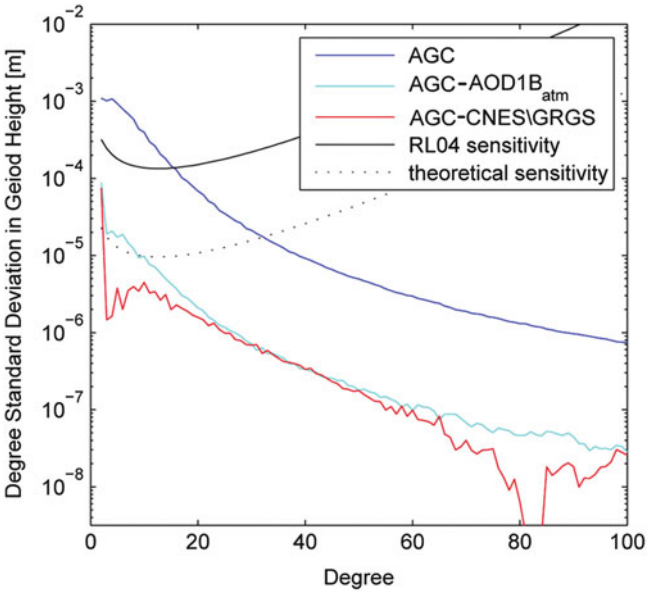

Fig. 7 Degree standard deviation in terms of geoid height for January 2008, in *blue* for AGC, in *cyan* the difference of AGC and AOD1Batm and in *red* AGC and GRGS. The *black line* marks the RL04 error level of GRACE, the *dashed* one the theoretical error as obtained by pre-launch simulations

5 Conclusions

NWP models are an indispensable tool for calculating the effect of the atmosphere on the Earth gravity field. But at the same time they are one of the weakest links in the processing, as no real errors of the NWP models are available; thus the accuracy of such models is not well determined. Also the evolution of the models has to be taken into account, as it can lead to jumps in the data. Even the spatial resolution of the data has an impact on the orography and thus on related physical parameters. As an alternative to using consistently reprocessed data sets like ERA-Interim provided by ECMWF, we presented a processing strategy for NWP model data which enables us to be independent from changes within the models used for operational analysis and thus keeps our meteorological data consistent through time. We compared our AGC to other providers of GRACE de-aliasing products and find with AOD1Batm a better agreement than with the GRGS product for single epochs, but for monthly solutions our product agrees better with the one from GRGS. A difference in the definition of the center of the Earth and related quantities might explain the discrepancies with GRGS. The differences to AOD1Batm can be traced back to our processing of the meteorological data as well the different calculation of the

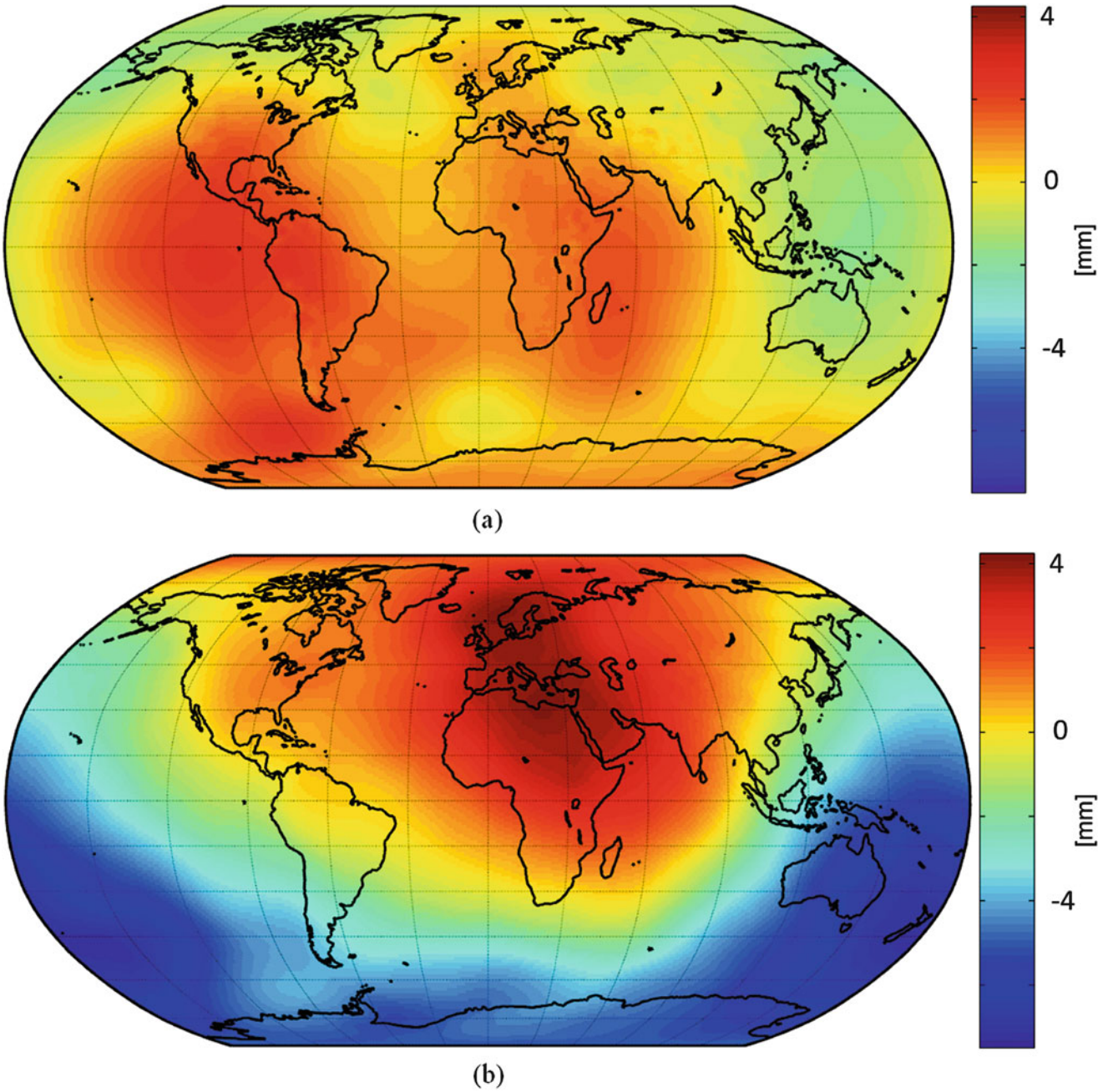

Fig. 8 (**a**) Difference of AGC and AOD1Batm and (**b**) AGC and GRGS in terms of geoid height for the epoch January 1, 2008, 00 UTC

vertical integration. We found signals which arise from the definition of the topography showing an amplitude of ± 0.5 to 0.8 mm with a wavelength of approximately 400–800 km and which can be found wherever the difference between the used topography/orography shows large gradients. This might be an indication that such signals may also be found within the AOD1B whenever a change in the ECMWF orography happened. But we could not yet confirm this assumption and if such signals are present, we expect them to be smaller than what we found here. Although such signals are small in amplitude as well as in spatial extent and might thus have a minor impact on the GRACE gravity field determination, this issue could become more important when temporal as well spatial resolution increase. Also for more local applications of NWP model data, e.g. correction of ground based gravity measurements or prediction of atmospheric loading effects at GNSS stations our approach can be a valuable alternative to the operational or reprocessed data sets.

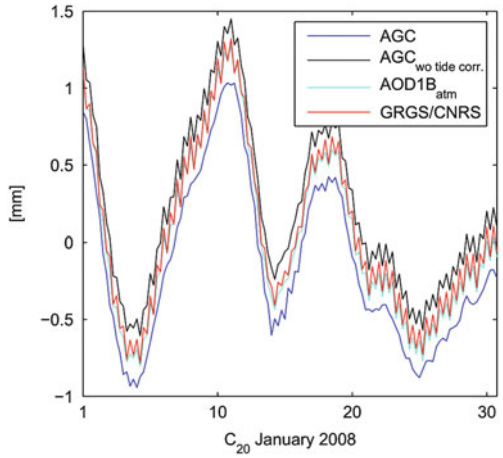

Fig. 9 C20 coefficient for January 2008, in *blue* AGC, in *black* AGC without tidal correction, *cyan* AOD1Batm and *red* GRGS

Acknowledgements We would like to thank the Austrian Science Fund (FWF) for supporting the project GGOS Atmosphere (P20902), and the ECMWF for providing the meteorological data. Special thanks go to Bruno Meurers from the University of Vienna for providing the in situ data at Conrad Observatory and to Pascal Gegout from the Géosciences Environnement Toulouse for providing the de-aliasing data. We also want to acknowledge the reviewers who helped to improve the manuscript.

References

Boy JP, Chao BF (2005) Precise evaluation of atmospheric loading effects on earths time-variable gravity field. J Geophys Res 110:B08412. doi:10.1029/2002JB002333

Boy JP, Gegout P, Hinderer J (2001) Reduction of surface gravity data from global atmospheric pressure loading. Geophys J Int 149:534–545

Dash SK, Mohandas S (2005) Comparative study of different orographic representations with respect to the Indian summer monsoon simulation. Acta Geophys Polon 53(3):325

Dobslaw H, Flechtner F, Bergmann-Wolf I, Dahle C, Dill R, Esselborn S, Sasgen I, Thomas M (2013) Simulating high-frequency atmosphere-ocean mass variability for dealiasing of satellite gravity observations: AOD1B rl05. J Geophys Res Ocean 118(7):3704–3711. doi:10.1002/jgrc.20271

Duan J, Shum CK, Guo J, Huang Z (2012) Uncovered spurious jumps in the grace atmospheric de-aliasing data: potential contamination of grace observed mass change. Geophys J Int 191(1):83–87. doi:10.1111/j.1365-246X.2012.05640.x

Fagiolini E, Zenner L, Flechtner F, Gruber T, Schwarz G, Trautmann T, Wickert J (2007) The sensitivity of satellite gravity field determination to uncertainites in atmospheric models. Joint GSTM/SPP Kolloquium, Potsdam. http://www.massentransporte.de/fileadmin/20071015?17?Potsdam/di180002fiagolini.pdf

Farrell WE (1972) Deformation of the earth by surface loads. Rev Geophys Space Phys 10(3):761–797

Flechtner F, Dobslaw H (2013) AOD1B product description document for product release 05 (Rev. 4.0, Sept 9, 2013). Tech Rep

Forootan E, Didova O, Kusche J, Locher A (2013) Comparisons of atmospheric data and reduction methods for the analysis of satellite gravimetry observations. J Geophys Res Solid Earth

Gegout P (2009) Background models used in geodetic data processing

Gegout P, Biancale R, Soudarin L (2011) Adaptive mapping functions to the azimuthal anisotropy of the neutral atmosphere. J Geod 85(10):661–677. doi:10.1007/s00190-011-0474-y

Han SC, Jekeli C, Shum C (2004) Time-variable aliasing effects of ocean tides, atmosphere, and continental water mass on monthly mean grace gravity field. J Geophys Res Solid Earth (1978–2012) 109(B4)

Karbon M (2013) Atmospheric effects on gravity space missions. Geowissenschaftliche Mitteilungen, vol 94/2013, Department of Geodesy and Geoinformation of the Vienna University of Technology

Karbon M, Böhm J, Wijaya D, Schuh H (2013) Atmospheric effects on gravity space missions, Atmospheric effects in space geodesy. Springer, Berlin/Heidelberg, pp 159–180. doi:10.1007/978-3-642-36932-2_5

Kurtenbach E, Mayer-Gürr T, Eicker A (2009) Deriving daily snapshots of the Earth's gravity field from GRACE data using Kalman filtering. Geophys Res Lett 36(17). doi: 10.1029/2009GL039564

Miller M, Palmer T, Swinbank R (1989) Parameterization and influence of subgridscale orography in general circulation and numerical weather prediction models. Meteorol Atmos Phys 40(1-3):84–109. doi:10.1007/BF01027469

Navarra A, Stern W, Miyakoda K (1994) Reduction of the Gibbs oscillation in spectral model simulations. J Climate 7(8):1169–1183

Neumeyer J, Hagedorn J, Leitloff J, Schmidt T (2004) Gravity reduction with three-dimensional atmospheric pressure data for precise ground gravity measurements. J Geodyn 38:437–450

Phillips NA (1960) Numerical weather prediction. Advances in computers, vol 1. Elsevier, pp 43–90. doi:10.1016/S0065-2458(08)60606-3

Plag H, Gross R, Rothacher M (2009) Global geodetic observing system for geohazards and global change. Geosciences 9:96–103

Rabier F, Jrvinen H, Klinker E, Mahfouf JF, Simmons A (2000) The ECMWF operational implementation of four-dimensional variational assimilation. I: experimental results with simplified physics. Q J Roy Meteorol Soc 126(564):1143–1170. doi:10.1002/qj.49712656415

Reigber C, Schmidt R, Flechtner F, König R, Meyer U, Neumayer K, Schwintzer P, Zhu SY (2005) An earth gravity field model complete to degree and order 150 from grace: eigen-grace02s. J Geodyn 39(1):1–10

Rowlands D, Luthcke S, Klosko S, Lemoine F, Chinn D, McCarthy J, Cox C, Anderson O (2005) Resolving mass flux at high spatial and temporal resolution using grace intersatellite measurements. Geophys Res Lett 32(4):L04,310

Rutt IC, Thuburn J, Staniforth A (2006) A variational method for orographic filtering in NWP and climate models. Q J Roy Meteorol Soc 132(619):1795. doi:10.1256/qj.05.133

Schulz W (1954) Tabellen für die Normatmosphäre nach DIN 5450 bis 20 km Höhe. Braunschweig [Flughafen] Dt. Forschungsanstalt f. Luftfahrt e.V

Shengjie G (2006) GPS radio occultation and the role of atmospheric pressure on spaceborne gravity estimation over Antarctica. PhD thesis, Ohio State University

Stockdale TN, Anderson DLT, Alves JOS, Balmaseda MA (1998) Global seasonal rainfall forecasts using a coupled ocean-atmosphere model. Nature 392:370–373. doi:10.1038/32861

Tapley B, Bettadpur S, Watkins M, Reigber C (2004) The gravity recovery and climate experiment: mission overview and early results. Geophys Res Lett 31(L09607):4–9

Trenberth KE, Smith L (2005) The mass of the atmosphere: a constraint on global analyses. J Climate 18(6)

van Dam T, Altamimi Z, Collilieux X, Ray J (2010)Topographically induced height errors in predicted atmospheric loading effects. J Geophys Res Solid Earth (1978–2012) 115(B7)

Velicogna I, Wahr J, Van den Dool H (2001) Can surface pressure be used to remove atmospheric contributions from GRACE data with sufficient accuracy to recover hydrological signals? J Geophys Res 106(B8):16415–16434

White P (2000) IFS Documentation Part III: Dynamics and Numerical Procedures (CY21R4). Meteorol Bull M1.6/4

Zenner L, Gruber T, Jäggi A, Beutler G (2010) Propagation of atmospheric model errors to gravity potential harmonics – impact on GRACE De-aliasing. Geophys J Int 182(2):797–807

Practical Aspects of the Unification of Height System Realizations in Europe

Axel Rülke, Gunter Liebsch, Martina Sacher, Uwe Schäfer, Johannes Ihde, and Philip L. Woodworth

Abstract

Three different approaches for the unification of height reference frames have been used to compute datum offsets between national vertical reference frames in Europe: the oceanographic approach, the spirit leveling approach and the gravity field approach. All three methods are discussed and advantages and drawbacks are evaluated. A set of tide gauge locations is used to compute height datum offsets between national height reference frames in Europe based on all three approaches. The results agree on a level of 5–10 cm. In summary, the gravity field approach is the most flexible approach. The ESA satellite gravity mission GOCE ensures a uniform global level in the range of 1–2 cm. Hence, the gravity field approach is a suitable approach for future realizations of the European Vertical Reference Frame as well as for the establishment of a World Height System.

Keywords

Height system unification • Tide gauges • Vertical datum • Vertical reference systems

1 Introduction

The unification of height systems (Ardalan and Safari 2005; Gatti et al. 2012; Rummel and Teunissen 1988; Xu 1992) and the establishment of a World Height System (Burša et al. 2004, 2001; Ihde and Sánchez 2005; Rapp 1995; Rummel and Teunissen 1988; Sánchez 2009) have been discussed for a long time within the geodetic community.

A. Rülke (✉)
Federal Agency for Cartography and Geodesy, Richard-Strauss-Allee 11, 60598, Frankfurt/Main, Germany
e-mail: axel.ruelke@bkg.bund.de

G. Liebsch • M. Sacher • U. Schäfer
Federal Agency for Cartography and Geodesy, Leipzig, Germany

J. Ihde
Federal Agency for Cartography and Geodesy, Frankfurt/Main, Germany

P.L. Woodworth
National Oceanography Centre, Liverpool, UK

In practice, the zero level of height reference systems is defined conventionally. Usually, this reference level is realized by connecting the height reference level to the sea level by tide gauge observations over a specific time span. Different states of the sea level can be used, such as the mean sea level, the mean high water or the tide gauge zero point itself. In Europe the definitions of the height system reference levels are based on different tide gauge locations, different sea level states and different observation periods. This leads to relative offsets between the reference levels of different national height systems.

In general, the unification of national height reference frames corresponds to the solution of a simple datum problem. In this case, the requirements for the connection of two separate vertical reference frames are simple: at least one representative of each height reference frame and a physical height difference between these representatives. The representatives can be benchmarks of the national height reference frame or tide gauges, which are connected to them. The physical height difference can be determined by different observations and models: (1) spirit levelings, (2) oceanographic models and (3) ellipsoidal heights obtained e.g. by

© Springer International Publishing Switzerland 2015

C. Rizos, P. Willis (eds.), *IAG 150 Years*, International Association of Geodesy Symposia 143,
DOI 10.1007/1345_2015_168

Table 1 Overview of the national vertical reference systems

	Height system realization			Analyzed points	
Country	Name	Type	Tidal system	Tide gauges	GNSS/leveling
Denmark		Orthometric	Non	1	42
France	NGF-IGN69	Normal	Mean	1	164
Germany	DHHN92	Normal	Mean	2	85
Great Britain	ODN	Orthometric[a]	mean	12	182
Netherlands	NAP	Uncorrected	Non	3	15
Norway	NN2000	Normal	Zero	1	64
Spain	REDNAP	Orthometric	Mean	4	173
Europe	EVRF2007	Normal	Zero	24	725

In addition, the number of points used for this investigation is given

[a]The orthometric correction used by the Ordnance Survey in its 2nd and 3rd geodetic levelling is based on a normal gravity correction calculated on a latitude and height basis (Fane, 2006, personal communication). This means, that in practice the Great Britain national heights are normal-orthometric heights

GNSS or satellite altimetry in combination with gravity field or geoid models. In detail, the unification of vertical reference frames is more complicated. Different conventions, such as solid earth tides (especially permanent tides), types of physical heights (orthometric heights, normal heights etc.), and the definition of the normal potential need to be taken into account (Table 1). More details on the fundamental concepts can be found in physical geodesy textbooks (e.g. Hofmann-Wellenhof and Moritz 2006). In addition, observations, such as leveling observations over large distances, may be influenced by systematic effects. According to the different observations and models we distinguish three different approaches for the connection of independent height reference frames (Rummel et al. 2002): (1) the geodetic leveling approach, (2) the gravity field approach and (3) the ocean leveling approach. A detailed description of an application based on the gravity field approach and the geodetic leveling approach is presented in Rülke et al. (2012).

The zero-tide convention is recommended by IAG resolution No. 16 adopted at the General Assembly in Hamburg, 1983. In this work we follow this recommendation although it has not been applied to most national, vertical reference systems and has some drawbacks in the practical use of vertical reference systems.

2 Height Reference Frame Unification Approaches

2.1 Spirit Leveling Approach

Within this approach a multi-national network solution is computed from observed potential differences of the first order leveling networks and additional cross-border connections. An example is the European Vertical Reference Frame (EVRF) 2007 (Sacher et al. 2009), which is used in this investigation. The datum offset of a national reference frame i corresponds to the difference of its heights H_i to the heights in the unified height reference frame H_{EVRF}. Therefore, the datum offset m is related to the datum convention of EVRF2007, which is Normaal Amsterdams Peil (NAP):

$$H^z_{EVRF} - (H^a_i + \delta^H_{a\to z}) = m + sys - e \qquad (1)$$

Systematic variations of the datum offset and residuals are indicated by sys and e. Assuming that the national heights are expressed in the tidal system a, the tidal correction $\delta^H_{a\to z}$ converts them into the zero-tide system z. Heights of the EVRF2007 are already realized in this tidal system and need no additional correction. Here, the number and quality of the border-crossing leveling lines are key elements and inhomogeneous within the European leveling network. Due to individual national standards, this is also true for the quality and the accuracy of the leveling networks themselves. Precise leveling observations over long distances are costly in terms of labor and time. This partly leads to very long observation periods which can hardly be assigned to a specific observation epoch. In addition, there are no available information about height changes with time for large parts of the European leveling network. This degrades the ability to connect national leveling networks over large distances with high precision. On short distances the accuracy of height transfers by leveling networks is very high and will be also in the future the best choice. However, leveling networks have a low redundancy and therefore they are susceptible to systematic errors, especially over long distances. Geographical obstacles, such as channels and sea water bodies complicate spirit leveling observations and weaken the connections between continental Europe and Fennoscandia or the British Isles.

2.2 Oceanographic Approach

The oceanographic approach estimates the height differences of the tide gauge zero points by means of an oceanographic model. If the tide gauges are connected to their national height reference frames, which means the height of the tide gauge zero point above the reference level of the national height system is known, these differences can easily be converted to differences of the corresponding national height reference frames. The observation equation compares the height of the oceanographic model for a certain sea level, e.g. the mean sea level, at the tide gauge location over a certain period H_{SST} with the corresponding height above the national reference level obtained by tide gauge observations H_{MSL}. It is assumed, that the national height system is given in the tidal system a and the oceanographic model in the mean-tide system. $\delta^H_{m\to z}$ converts the oceanographic model from the mean-tide into the zero-tide system:

$$(H_{SST} + \delta^H_{m\to z}) - (H^a_{MSL} + \delta^H_{a\to z}) = m - e \qquad (2)$$

In this case, the height offsets m will be estimated with respect to the reference level of the oceanographic model, which is usually an arbitrary choice.

It is evident from Eqs. (1) and (2) that both approaches are independent of any gravity field model. Thus, it can be also used as a validation tool for gravity field models or vice versa. The oceanographic approach can be applied globally, but naturally it is limited to coastal areas. In addition, the number of tide gauges is rather small and is further decreased by the fact, that many tide gauges are not well surveyed with respect to the national height reference frame or at least this information is not publicly available. The oceanographic models have limited spatial resolutions and the results may be influenced by local effects, such as complicated coast lines, local bathymetry or tide gauge locations in estuaries.

2.3 Gravity Field Approach

The gravity field approach combines ellipsoidal heights h^b_i e.g. from GNSS observations, national physical height H^a_i and a gravity field model $\zeta^z_{i_{Mod}}$ in the zero-tide system z:

$$(h^b_i + \delta^h_{b\to z}) - \zeta^z_{i_{Mod}} - (H^a_i + \delta^H_{a\to z}) = m + sys - e \qquad (3)$$

The tidal systems are a for the physical heights and b for the ellipsoidal heights. Commonly, ellipsoidal heights are computed in the non-tidal system within the GNSS community. In contrast, gravity field models are often given in the zero-tide system, indicated by the subscript z.

The gravity field approach is a true global approach and does not require direct observations between neighboring national height reference frames. The offsets m are related to a certain conventional equipotential surface of the Earth gravity field W_0, the geoid. The ellipsoidal heights and the gravity field model are independent of leveling observations used for the determination of the national vertical reference frame. This makes an independent validation of vertical reference frames possible. At present, the spatial resolution of satellite-only gravity field models is limited to about 100 km. The shorter wavelengths of the gravity field which is covered by the satellite-only models induce the omission error of about 30 cm in the mean. It can reach 1 m in a point-wise comparison and reach extreme values of about 3 m at some islands (Gruber et al. 2012). The satellite-only gravity field models need to be densified to overcome this problem. This can be done by the incorporation of terrestrial observations (see e.g. EIGEN-6C models Förste et al. 2012) or a combination of the satellite-only model and regional high resolution gravity field models (e.g. Rülke et al. 2012).

3 Data Sets

We used data sets of 24 tide gauges located in seven European countries from the Permanent Service for Mean Sea Level (PSMSL). There is only one suitable tide gauge available for Denmark, France and Norway respectively which limits the reliability of the estimated datum offsets for those countries. There are 12 tide gauges for Great Britain well distributed over the whole coast of the country. Spain has four tide gauges, which are placed in two locations (Fig. 1, Table 1).

For comparisons a European data set of GNSS/leveling points originated from the European EUVN_DA data set could be used (Kenyeres et al. 2010). The distribution of the points is shown in Fig. 1 and Table 1.

Two oceanographic models have been used: The POLCOMS model (Holt and James 2001) has a spatial resolution of $1/9°$ by $1/6°$ and 20 levels in the vertical. It is forced by 3 hourly air pressure, winds and head fluxes as well as fresh water input from 36 rivers. Exchanges with the Baltic sea is modeled. The Liv/MIT model is the implementation by Liverpool University of the MIT model (Marshall et al. 1997). Its spatial resolution is $1/6°$ by $1/5°$ and 23 levels in the vertical. The model is forced by monthly wind stresses from the NCEP model and constrained by observed temperature and salinity values. Both models are completely independent of geodetic observations.

The computations of the gravity field approach are based on the combined satellite-only global gravity field model

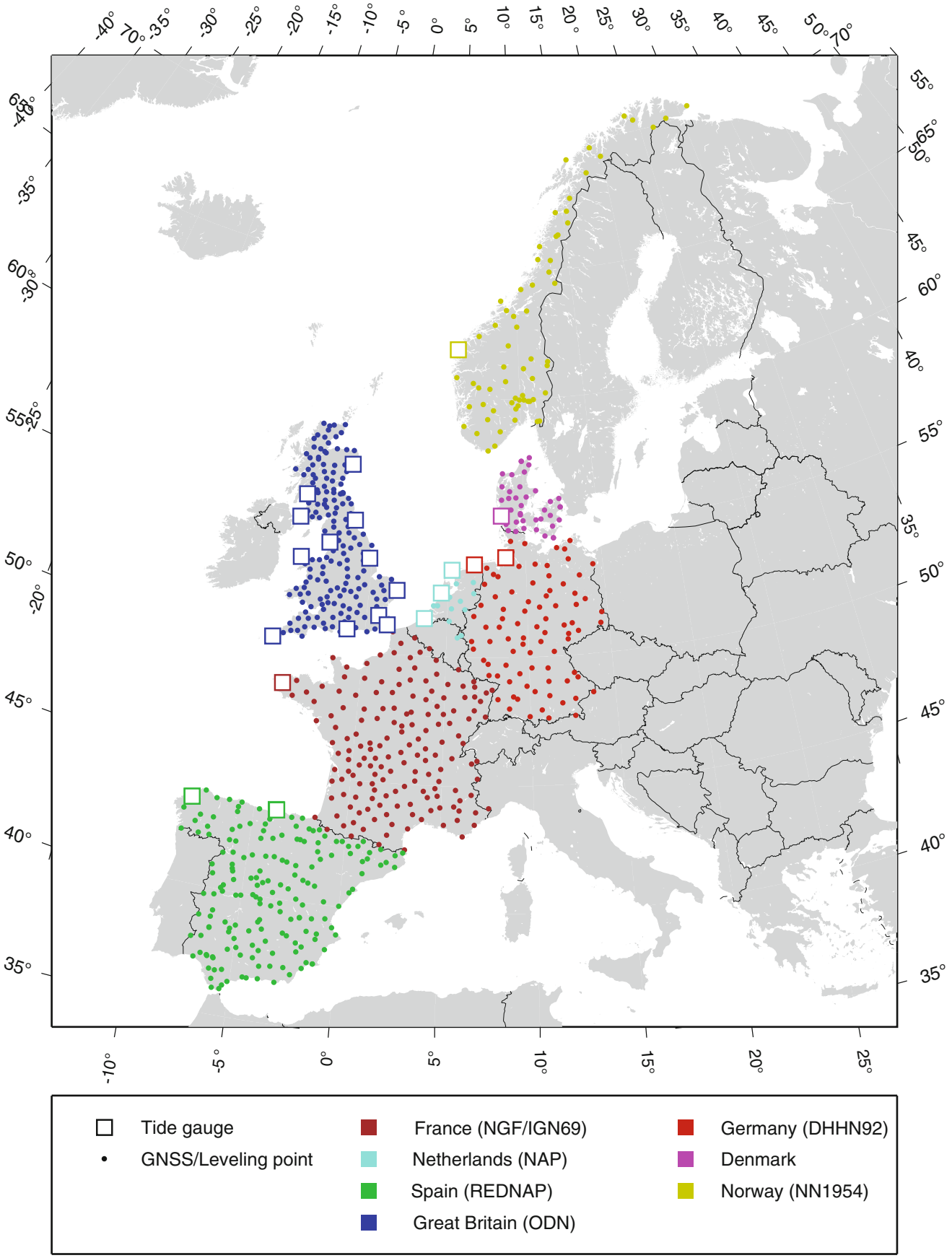

Fig. 1 Geographical distribution of the tide gauges and GNSS/leveling points in Europe

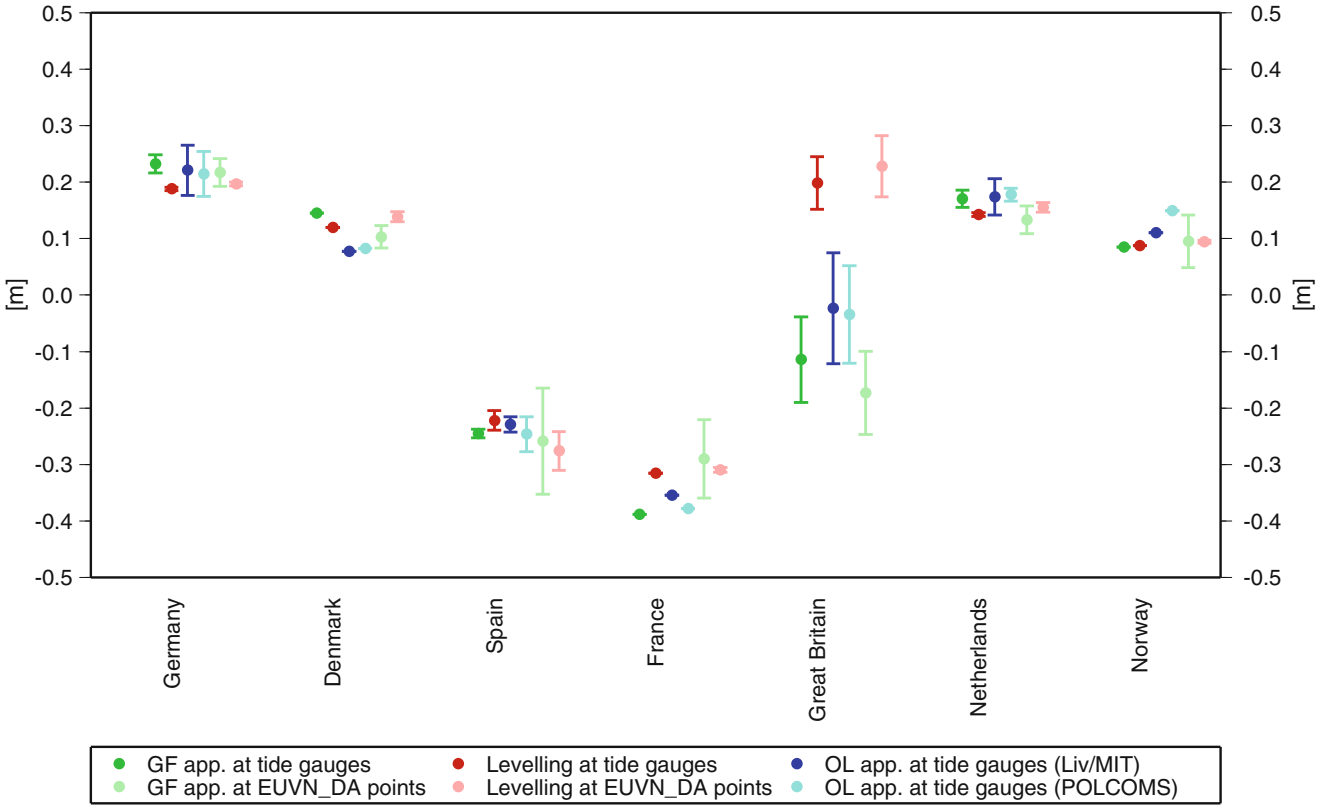

Fig. 2 Estimated height system datum offsets and their standard deviations computed from gravity field approach (*green*, first estimate from left to right of each country), spirit leveling approach (*red*, second) and oceanographic approach (*blue*, third and fourth). The *dark green*, the *dark red* and the *blue points* are the results computed at tide gauge locations. The *light green* (fifth) and *light red points* (sixth) are results based on GNSS/leveling points

GOCO03s (Mayer-Gürr 2012) and the high resolution European Gravimetric Geoid (EGG) 2008 (Denker 2013). The combination method based on a filtering approach is described in Rülke et al. (2012).

4 Results and Interpretation

As discussed above, all three methods provide datum offsets with respect to different reference levels. In order to make all three methods comparable to each other, a mean offset needs to be determined for each approach individually using all observation points. The Great Britain values have been skipped for the estimation of the mean offset for the spirit leveling approach. This is due to the fact, that the British national heights of the ODN have been computed from a leveling network which has been aligned to the heights of the previous realization (Christie 1994; Penna et al. 2013) while the European adjustment of the EVRF is free of these constraints. This yields to a disagreement between the estimated offsets for the spirit leveling approach and the other two approaches for Great Britain.

Figure 2 summarizes the estimated offsets for each approach. The results of the oceanographic approach (light and dark blue points) based on two different ocean models agree on a level of about 5 cm. In many cases the two other approaches (dark red and dark green points for the spirit leveling and the gravity field approach respectively) also agree on a level of 5 cm and reach about 10 cm in some cases. For comparisons the spirit leveling and gravity field approach has been applied to a set of well distributed GNSS/leveling data points in the various countries (Kenyeres et al. 2010, Table 1). Although there is only a small number of tide gauges available, the agreement between them and the GNSS/leveling points is on the 5–10 cm level. This means, that the tide gauges are a good representative of the national vertical datums.

5 Summary and Conclusions

Three different approaches for the unification of height systems have been introduced and applied to European tide gauges. All methods give reasonable results and agree at a

level of about 5 cm in the most cases and do not exceed 10 cm.

Apart from this fact, the gravity field approach has the most potential for the unification of heights system realizations as well as for the realization of a global height reference system. It is the only really global applicable approach and probably the most precise and reliable method.

At present all national height reference frames in Europe are based on spirit leveling. For a large number of networks an overall error estimate, including geoid, leveling and GNSS errors of less than 3 cm indicates a state-of-the-art accuracy for the national networks (Rülke et al. 2012). Currently, there are still some activities in the European countries to re-observe their first-order leveling networks, such as Germany.

In this sense, the present situation is different compared to large countries like Australia, Canada or the United States. In these countries, the transition from a leveling based to a GNSS and gravity field based height system realization is in progress (Featherstone et al. 2012; Hains et al. 2013; Smith 2013). Canada has decided to migrate to a gravity field based vertical datum in 2013 (Hains et al. 2013).

For the future it can be expected that the importance of continental leveling networks is decreasing. Also future pan-European height reference frames should be realized based on the gravity field approach. The satellite gravity mission GOCE has provided a homogeneous global gravity field with an accuracy of a view cm up to a spatial resolution of about 100 km for this purpose (Pail et al. 2011). The combination of the global models with regional data reduce the omission error and make the method also applicable for small countries. In larger countries the omission error of satellite-only gravity field models may cancel out to a certain degree in the datum offset estimation. In detail this depends on the coverage with GNSS/Leveling points and the roughness of the residual gravity field (Rülke et al. 2012).

A joint course of action on the unification of height systems, the realization of future national height systems and the establishment of a World Height System needs an appointed decision of their conventions (cf. Sánchez 2012). As a first step for practical applications it is suggested to establish a data center for the collection of up to date GNSS/leveling data sets as a basis for height system unification as well as for the verification of gravity field models.

Acknowledgements This investigation has been performed within the Support to Science Element GOCE+ Height System Unification of the European Space Agency. We acknowledge the associate editor and the three reviewers for their comments to improve the manuscript.

References

Ardalan A, Safari A (2005) Global height datum unification: a new approach in gravity potential space. J Geodesy 79:512–523. doi:10.1007/s00190-005-0001-0

Burša M, Kouba J, Müller A, Raděj K, True SA, Vatrt V, Vojtíšková M (2001) Determination of geopotential differences between local vertical datums and realization of a world height system. Stud Geophys Geod 45:127–132. doi:10.1023/A:1021860126850

Burša M, Kenyon S, Kouba J, Šíma Z, Vatrt V, Vojtíšková M (2004) A global vertical reference frame based on four regional vertical datums. Stud Geophys Geod 48:493–502. doi:10.1023/B:SGEG.0000037468.48585.e6

Christie RR (1994) A new geodetic heighting strategy for Great Britain. Surv Rev 32(252):328–343

Denker H (2013) Regional gravity field modeling: theory and practical results, chap. 5. In: Xu G (ed) Sciences of geodesy - II. Springer, Berlin, pp 185–291. doi:10.1007/978-3-642-28000-9_5

Featherstone WE, Filmer MS, Claessens SJ, Kuhn M, Hirt C, Kirby JF (2012) Regional geoid-model-based vertical datums – some Australian perspectives. J Geod Sci 2(4):370–376. doi:10.2478/v10156-012-0006-6

Förste C, Bruinsma S, Flechtner F, Marty JC, Lemoine JM, Dahle C, Abrikosov O, Neumayer KH, Biancale R, Barthelmes F, Balmino G (2012) A preliminary update of the direct approach GOCE processing and a new release of EIGEN-6C. Presented at AGU fall meeting 2012, Abstract No. G31B-0923, San Francisco, 3–7 December 2012

Gatti A, Reguzzoni M, Venuti G (2012) The height datum problem and the role of satellite gravity models. J Geodesy, pp 1–8. doi:10.1007/s00190-012-0574-3

Gruber T, Gerlach C, Haagmans R (2012) Intercontinental height datum connection with GOCE and GPS-levelling data. J Geodetic Sci 2(4):270–280. doi:10.2478/v10156-012-0001-y

Hains D, Véronneau M, Huang J (2013) Modernization of Canada's geodetic vertical datum. Paper read at IAG general assembly, Potsdam, 1–6 September 2013

Hofmann-Wellenhof B, Moritz H (2006) Physical geodesy, 2nd edn. Springer, Vienna. ISBN:978-3-211-33545-1

Holt JT, James ID (2001) An s coordinate density evolving model of the northwest European continental shelf: 1. Model description and density structure. J Geophys Res Oceans 106(C7):14015–14034. doi:10.1029/2000JC000304

Ihde J, Sánchez L (2005) A unified global height reference system as a basis for IGGOS. J Geodyn 40(4–5):400–413. doi:10.1016/j.jog.2005.06.015

Kenyeres A, Sacher M, Ihde J, Denker H, Marti U (2010) EUVN_DA: realization of the European continental GPS/leveling network. In: IAG symposia, vol. 135. Springer, Berlin/Heidelberg, pp 315–320. doi:10.1007/978-3-642-10634-7_41

Marshall J, Hill C, Perelman L, Adcroft A (1997) Hydrostatic, quasi-hydrostatic, and nonhydrostatic ocean modeling. J Geophys Res Oceans 102(C3):5733–5752. doi:10.1029/96JC02776

Mayer-Gürr T (2012) The new combined satellite only model GOCO03s. www.goco.eu

Pail R, Bruinsma S, Migliaccio F, Förste C, Goiginger H, Schuh WD, Höck E, Reguzzoni M, Brockmann J, Abrikosov O, Veicherts M, Fecher T, Mayrhofer R, Krasbutter I, Sansó F, Tscherning C (2011) First GOCE gravity field models

derived by three different approaches. J Geodesy 85:819–843. doi:10.1007/s00190-011-0467-x

Penna NT, Featherstone WE, Gazeaux J, Bingham RJ (2013) The apparent British sea slope is caused by systematic errors in the levelling-based vertical datum. Geophys J Int 194:772–786. doi:10.1093/gji/ggt161

Rapp RH (1995) A world vertical datum proposal. AVN 102(8–9): 297–304

Rülke A, Liebsch G, Sacher M, Schäfer U, Schirmer U, Ihde J (2012) Unification of European height system realizations. J Geodetic Sci 2(4):343–354. doi:10.2478/v10156-011-0048-1

Rummel R, Teunissen P (1988) Height datum definition, height datum connection and the role of the geodetic boundary value problem. Bull Geod 62:477–498

Rummel R, Balmino G, Johannessen J, Visser P, Woodworth P (2002) Dedicated gravity field missions – principles and aims. J Geodyn 33(1–2):3–20

Sacher M, Ihde J, Liebsch G, Mäkinen J (2009) EVRF2007 as realization of the European vertical reference system. B Geod Sci Aff 68(1):35–50

Sánchez L (2009) Strategy to establish a global vertical reference system. In: IAG symposia, vol. 134. Springer, Berlin, pp 273–278

Sánchez L (2012) Towards a vertical datum standardisation under the umbrella of global geodetic observing system. J Geod Sci 2(4):325–342. doi:10.2478/v10156-012-0002-x

Smith DA, Véronneau M, Roman DR, Huang J, Wang YM, Sideris MG (2013) Towards the unification of the vertical datum over the North American continent. In: IAG Symposia, vol 138. doi:10.1007/978-3-642-32998-2_36

Xu P (1992) A quality investigation of global vertical datum connection. Geophys J Int 110:361–370

Towards a Consistent Estimation of the Earth's Gravity Field by Combining Normal Equation Matrices from GRACE and SLR

Christoph Haberkorn, Mathis Bloßfeld, Johannes Bouman, Martin Fuchs, and Michael Schmidt

Abstract

Since 2002, the satellite mission GRACE observes the Earth's static gravity field and its natural changes. The estimation of degree 1 and 2 coefficients is difficult, especially the accuracy of the flattening coefficient $C_{2,0}$ is weak. In temporal GRACE gravity field models, $C_{2,0}$ is therefore often replaced by a value based on Satellite Laser Ranging measurements. In this study, we combine both techniques to get a consistent normal equation matrix, which allows us to study correlations between spherical harmonic coefficients. Unlike common practice, we use 8 SLR satellites and set-up normal equations up to degree 20. The combination is done using different weighting factors to investigate the influence of both techniques on the combined normal equation matrix. Our results show that especially the coefficient $C_{2,0}$ benefits from SLR data, but also (near-) sectorial coefficients and coefficients which correspond to resonance frequencies of SLR satellites. Moreover, we find that high correlations in the SLR normal equation between zonal coefficients are reduced by the combination.

Keywords

Combination of NEQ matrices • GRACE • Gravity field • Integral equation approach • SLR

1 Introduction

The main goal of the Gravity Recovery And Climate Experiment (GRACE) is the determination of the Earth's static gravity field and its temporal variations to detect mass displacements (Tapley et al. 2004). The mission consists of two identical satellites, providing the range (ρ), range-rate ($\dot{\rho}$) and the range-acceleration ($\ddot{\rho}$) along the line of sight between the two satellites. Additional data, such as accelerometer and GPS data, are needed to compute accurate satellite orbits. Based on GRACE measurements, global gravity field models in terms of spherical harmonic coefficients are derived (Barthelmes and Köhler 2012). Maximum degree and order of these models depend on the time span of the data. For the RL05 monthly fields, e.g., the maximum degree is either 60 or 90, depending on the processing strategy (Barthelmes and Köhler 2012). Examples for such models are the time series of Geoforschungszentrum (GFZ) Potsdam (Dahle et al. 2012) and the time series of Jet Propulsion Laboratory (JPL) (Watkins and Yuan 2012). The values of the lowest degrees ($C_{0,0}, C_{1,m}, S_{1,1}, C_{2,m}, S_{2,m}$) are usually kept fixed or are replaced by values from other techniques. This is due to the limited sensitivity of GRACE at these explicit degrees (Cheng et al. 2011).

Satellite Laser Ranging (SLR) is a method to determine highly accurate orbits of satellites that are equipped with Retro Reflector Arrays (RRA). Based on these observations, it is possible to estimate the low degree coefficients of the Earth's gravity field as well as other parameters such as station coordinates and Earth Orientation Parameters

C. Haberkorn (✉) • M. Bloßfeld • J. Bouman • M. Fuchs • M. Schmidt
Deutsches Geodätisches Forschungsinstitut (DGFI),
Alfons-Goppel-Straße 11, 80539 München, Germany
e-mail: haberkorn@dgfi.badw.de

© Springer International Publishing Switzerland 2015

C. Rizos, P. Willis (eds.), *IAG 150 Years*, International Association of Geodesy Symposia 143,
DOI 10.1007/1345_2015_76

(EOPs). Due to the spherical shape of the satellites used in this study, non-gravitational orbit perturbations can be modeled very accurately. This means that after correcting for these non-gravitational and other gravitational effects, the remaining orbit perturbations are solely caused by variations in the Earth's gravity field. A consequence is, that spherical satellites with high altitude are less sensitive to non-gravitational forces.

Most recent models for the static gravity field, like GOCO03s (Mayer-Gürr et al. 2012), combine data from GRACE, SLR and other satellites. The SLR part is derived from 5 satellites and contributes to coefficients up to degree 5 (Mayer-Gürr et al. 2011, 2012). Monthly SLR gravity fields are based on measurements to five satellites and contain coefficients up to degree 5. Commonly, SLR $C_{2,0}$ is used to replace this value in GRACE monthly gravity fields (Cheng et al. 2011; Flechtner et al. 2013). In our study we consistently combine GRACE and SLR normal equation (NEQ) matrices, where 8 SLR satellites contribute to one SLR NEQ matrix, which is set up to degree and order 20.

We present first results of the SLR and GRACE combination for January 2007. We combine the single technique NEQs to study the implications for the combination of both techniques which does not rely on data processing strategies since common variance-covariance information is analyzed. The processing of the GRACE and SLR NEQ matrices is shown in Sects. 2 and 3, respectively. In Sect. 4, the combination process is described. The results of our study are analyzed in Sect. 5. Section 6 summarizes the results and gives an outlook on future work.

2 GRACE

Different approaches have been developed to compute gravity fields based on GRACE data, e.g. the energy balance approach (Bjerhammar 1967) and the integral equation approach (IEA) (Mayer-Gürr 2008). The IEA has the advantage that less accurate GPS measurements are not combined with the more accurate range measurements of the microwave ranging instrument (KBR) as observable (Mayer-Gürr 2008). GPS data provide only additional information on orbit positions, needed for linearization purposes. The differentiation of the range measurements with respect to time yields range-rates and range-accelerations, where the former are used in this study.

The IEA (Mayer-Gürr 2008) is based on the equation of motion. To compute a satellite position $\mathbf{r}(\tau_i)$ at time τ_i, the GRACE orbit is divided into short arcs with a length of, e.g., 30 min. The position depends on the motion of the satellite which itself is depending on all accelerations $\mathbf{a}$, acting on the satellite:

$$\mathbf{r}(\tau_i) = (1-\tau_i)\mathbf{r}_A + \tau_i \mathbf{r}_B - T^2 \int_0^1 K(\tau_i, \tau')\mathbf{a}(\tau')\mathrm{d}\tau'. \quad (1)$$

Here, $\mathbf{r}_A$ and $\mathbf{r}_B$ denote the beginning and ending 3D position of the arc, τ is the normalized time of the arc and T denotes the time span (30 min). All three components of the acceleration vector $\mathbf{a}$ have to be integrated along the arc using the integration kernel K:

$$K(\tau_i, \tau') = \begin{cases} \tau'(1-\tau_i) & \text{for } \tau' \le \tau_i \\ \tau_i(1-\tau') & \text{for } \tau' > \tau_i \end{cases}$$

Using matrix formulation, Eq. (1) can be rewritten for a complete arc of N discrete positions as

$$\mathbf{r} = \begin{pmatrix} 1-\tau_1 \\ \vdots \\ 1-\tau_N \end{pmatrix} \otimes \mathbf{I}_3 \cdot \mathbf{r}_A + \begin{pmatrix} \tau_1 \\ \vdots \\ \tau_N \end{pmatrix} \otimes \mathbf{I}_3 \cdot \mathbf{r}_B - T^2 \cdot (\mathbf{K} \otimes \mathbf{I}_3) \cdot \mathbf{a} \quad (2)$$

with

$$\mathbf{r}^T = \left(\mathbf{r}(\tau_1)^T, \ldots, \mathbf{r}(\tau_N)^T\right), \quad \mathbf{a}^T = \left(\mathbf{a}(\tau_1)^T, \ldots, \mathbf{a}(\tau_N)^T\right)$$

and in which $\mathbf{I}_3$ denotes the 3×3 identity matrix and $\otimes$ denotes the Kronecker product. The Kronecker product is needed to write the equation for all three components of the position. To link the accelerations $\mathbf{a}$ with the gravity field, a representation of the gravity potential V is needed. Here we use spherical harmonic coefficients $C_{n,m}$ and $S_{n,m}$, which describe V as a function of the position $\mathbf{r}$:

$$V(\mathbf{r}) = \frac{GM_\oplus}{a_\oplus} \sum_{n=0}^{N_{\max}} \left(\frac{a_\oplus}{\|\mathbf{r}\|}\right)^{n+1} \sum_{m=0}^{n} (A_{n,m} + B_{n,m}) P_{n,m}(\sin\phi), \quad (3)$$

with

$$A_{n,m} = C_{n,m} \cdot \cos m\lambda, \qquad B_{n,m} = S_{n,m} \cdot \sin m\lambda$$

and in which

$GM_\oplus$	geocentric gravitational constant,
$a_\oplus$	equatorial radius of the Earth,
$P_{n,m}(\sin\phi)$	associated Legendre polynomials and
$\|\mathbf{r}\|, \phi, \lambda$	position of the satellite in spherical coordinates.

Based on Eq. (3) we get an expression for the accelerations $\mathbf{a} = \operatorname{grad} V$:

$$\mathbf{a} = \mathbf{G} \cdot \boldsymbol{\beta} \quad (4)$$

with

$$(\mathbf{G})_{k,j} = \frac{\partial(\text{grad } V)_k}{\partial \beta_j}, \quad \boldsymbol{\beta} = \left(C_{0,0},\, C_{1,0},\, C_{1,1},\, S_{1,1},\, \ldots\right)^T$$
$$j = 1, \ldots, J \qquad J = \text{number of model parameters.}$$

Here, $\boldsymbol{\beta}$ contains the coefficients starting from degree 0, as the satellite's motion is affected by all coefficients.

The derivative of $\mathbf{r}$ with respect to time yields the equation for the velocity vector $\dot{\mathbf{r}}$:

$$\dot{\mathbf{r}} = \frac{1}{T} \cdot \left(\begin{pmatrix} -1 \\ \vdots \\ -1 \end{pmatrix} \otimes \mathbf{I}_3, \begin{pmatrix} 1 \\ \vdots \\ 1 \end{pmatrix} \otimes \mathbf{I}_3 \right) \cdot \boldsymbol{\gamma} - T \cdot (\dot{\mathbf{K}} \otimes \mathbf{I}_3) \cdot \mathbf{G} \cdot \boldsymbol{\beta}. \quad (5)$$

with $\boldsymbol{\gamma}^T = \left(\mathbf{r}_A^T,\ \mathbf{r}_B^T\right)$.

After applying Eqs. (2) and (5) to both GRACE satellites 1 and 2, the differences between both position vectors and between both velocity vectors are computed. Based on the position differences, the unit vector $\mathbf{e}^{12}$ in line of sight is calculated and further the range-rate $\dot{\rho}$:

$$\dot{\rho}(\tau_i) = \mathbf{e}^{12}(\tau_i)^T \cdot \dot{\mathbf{r}}^{12}(\tau_i). \quad (6)$$

By linearizing of Eq. (6), we obtain the design matrix $\mathbf{A}_{GRACE}$ and the NEQ matrix for the GRACE observations:

$$\mathbf{N}_{GRACE} = \mathbf{A}_{GRACE}^T \mathbf{P}_{GRACE} \mathbf{A}_{GRACE} \quad (7)$$

in which

$\mathbf{P}_{GRACE}$ weighting matrix, here: $\mathbf{P}_{GRACE} = \mathbf{I}$.

The design matrix is built up in a way that it contains only the set of coefficients for which corrections have to be estimated. I.e. coefficients with degree $n < 2$ are not included, because they are kept fixed.

3 SLR

The SLR analysis at DGFI is done using the 'DGFI Orbit and Geodetic parameter estimation Software' (DOGS) (Gerstl 1997). This software fulfills the most recent requirements of the International Laser Ranging Service (ILRS) (Pearlman et al. 2002) where DGFI is appointed as an official analysis center. In the Orbit Computation library DOGS-OC, the SLR observation equation is modeled as the one-way range measurement ρ:

$$\begin{aligned} \rho + \epsilon = {} & \|\mathbf{r}_{\mathbf{sat}}(t_M + \delta t) - \mathbf{r}_{\mathbf{sta}}(t_M + \delta t)\| + \delta\rho \\ & + c_{trop}(1 + \delta r) + c_{rel} + c_{sta} + c_{masc} + c_{mesc}, \end{aligned} \quad (8)$$

in which

ϵ measurement error,
$\mathbf{r}_{\mathbf{sat}}(t_M)$ position of satellite in the Celestial Reference System (CRS) at epoch t_M [m],
$\mathbf{r}_{\mathbf{sta}}(t_M)$ position of the station in the CRS at epoch t_M [m],
t_M approximated epoch of reflection of the signal at the satellite [s],
δt time bias of measurement [s],
$\delta\rho$ range bias of measurement [m],
δr bias of tropospheric refraction [-],
c_{trop} tropospheric range correction [m],
c_{rel} relativistic range correction [m],
c_{sta} station-dependent SLR correction [m],
c_{masc} satellite-specific center of mass correction (difference between reflector and center of mass of the satellite) [m] and
c_{mesc} SLR array-dependent correction [m].

In addition to the above listed corrections of ρ, $\mathbf{r}_{\mathbf{sta}}(t_M)$ is corrected in advance for various effects such as solid Earth tides and ocean tides. The position vector $\mathbf{r}_{\mathbf{sat}}(t_M)$ of the satellite is affected by numerous gravitational and non-gravitational perturbation accelerations. The total acceleration of a near-Earth satellite can be described as

$$\ddot{\mathbf{r}}_{\mathbf{sat}} = \mathbf{a} = \mathbf{a}_{\mathbf{KEP}} + \mathbf{a}_{\mathbf{GE}} + \mathbf{a}_{\mathbf{GM}} + \mathbf{a}_{\mathbf{GP}} + \mathbf{a}_{\mathbf{GT}} + \mathbf{a}_{\mathbf{NG}}, \quad (9)$$

with

$\mathbf{a}_{\mathbf{KEP}}$ gravitational acceleration caused by the point-concentrated mass of the Earth ($C_{0,0}$),
$\mathbf{a}_{\mathbf{GE}}$ gravitational acceleration caused by the Earth ($C_{n,m}$, $S_{n,m}$ with $n, m \in \mathbb{N}^+$ and $m \leq n$),
$\mathbf{a}_{\mathbf{GM}}$ gravitational acceleration caused by the Moon,
$\mathbf{a}_{\mathbf{GP}}$ gravitational acceleration caused by the Sun and other planets,
$\mathbf{a}_{\mathbf{GT}}$ gravitational acceleration caused by mass variations of solid Earth and ocean tides and
$\mathbf{a}_{\mathbf{NG}}$ non-gravitational accelerations caused by atmospheric and solar drag, Earth albedo and infrared, relativistic accelerations, empirical accelerations, non-gravitational tides and attitude control of the satellite.

Due to the spherical shape of the used satellites, $\mathbf{a}_{\mathbf{NG}}$ can be modeled very accurately. To compute the acceleration $\mathbf{a}_{\mathbf{KEP}} + \mathbf{a}_{\mathbf{GE}}$, we use the potential from Eq. (3), where the factor $(a_\oplus / \|\mathbf{r}\|)^{(n+1)}$ describes the upward continuation of the gravitational potential. In this study, we use SLR observations to 8 different satellites Ajisai, Etalon 1,2, LAser GEOdynamics Satellite 1,2 (LAGEOS1,2), Larets, Starlette and Stella. The variety of orbit parameters such as altitude, inclination and revolution period (Table 1) allows to improve the estimation of parts of the gravity field coefficients (GFCs)

Table 1 Specific parameters of the eight used spherical SLR satellites

Satellite	Diameter [m]	Altitude [km]	Inclination [Degree]	Revolution Period [h]
Ajisai	2.15	1,494	50.0	1.93
Etalon1	1.29	19,135	65.5	11.26
Etalon2	1.29	19,130	64.3	11.26
LAGEOS1	0.60	5,903	109.8	3.74
LAGEOS2	0.60	5,791	52.7	3.64
Larets	0.21	696	98.0	1.64
Starlette	0.24	963	49.8	1.69
Stella	0.24	813	98.3	1.68

The orbit parameters are the mean values of the GPS weeks 1,408 until 1,411 (Jan 2007)

since satellites with lower orbit altitude are more sensitive to the Earth's gravity field due to a smaller damping of the signal (Bloßfeld et al. 2014). Furthermore, they have different resonance frequencies, depending on their orbit. The different inclinations allow to de-correlate the Earth's flattening (mainly $C_{2,0}$) and the precession of the orbital planes (Bloßfeld et al. 2011).

For each of the satellites, weekly NEQs which contain orbit parameters, empirical accelerations, weekly station coordinates, daily EOP offsets and weekly GFCs up to degree and order 20 are set up. In order to de-correlate the different parameter groups (Bloßfeld et al. 2011), we eliminated all parameters except the GFCs from the NEQs. The combination of the satellite-specific NEQs to a weekly multi-satellite NEQ is done using variance component estimation (Koch and Kusche 2002). In this study, the SLR combination is done for January 2007 (GPS weeks 1408 until 1411). We approximated this month with four multi-satellite weekly NEQs which are combined on NEQ level to the monthly NEQ: $\mathbf{N}_{SLR}$. Other monthly solutions might require a combination of 4–5 weeks and a down-weighting of weeks at the beginning and end of a month. In the combination, common parameters of the weekly NEQs such as monthly GFCs up to degree and order 20 are stacked. A more detailed description of the used data and the combination strategy of the different SLR satellites can be found in Bloßfeld et al. (2014).

4 Combination

As mentioned above, we use data of January 2007 for our studies. For GRACE, $\mathbf{N}_{GRACE}$ is set up for the estimation of $u_1 = 3717$ coefficients, corresponding to the spectral range from degree 2 up to 60. For SLR, a set of $u_2 = 437$ coefficients is estimated, reaching from degree and order 2 to degree and order 20.

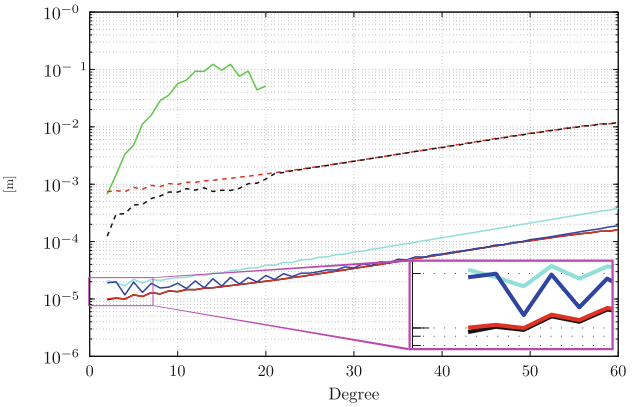

Fig. 1 Error degree variances from $\mathbf{N}_{GRACE}$ ($\hat{\sigma}^2_{GRACE} = 8.8 \cdot 10^{-11}$) (*red, dashed*); $\mathbf{N}_{GRACE}$ ($\hat{\sigma}^2_{GRACE} = 1.6 \cdot 10^{-14}$) (*red, solid*); $\mathbf{N}_{SLR}$ ($\hat{\sigma}^2_{SLR} = 7.9 \cdot 10^{-1}$) (*green*); combined solution ($\hat{\sigma}^2_{GRACE} = 8.8 \cdot 10^{-11}$) (*black, dashed*); combined solution ($\hat{\sigma}^2_{GRACE} = 1.6 \cdot 10^{-14}$) (*black, solid*); JPL monthly solution RL05 (*cyan*); GFZ monthly solution RL05a (*blue*)

The combination of GRACE and SLR is done at the normal equation level. Before combining, the NEQ matrix $\mathbf{N}_{SLR}$ of dimension $u_2 \times u_2$ (containing the coefficients up to degree and order 20) has to be extended to the size of $\mathbf{N}_{GRACE}$: $u_1 \times u_1$. This is done by filling the parts of higher degree and order coefficients with zeros. The combined NEQ matrix $\mathbf{N}_c$ is:

$$\mathbf{N}_c = \frac{1}{\hat{\sigma}^2_{SLR}} \mathbf{N}_{SLR} + \frac{1}{\hat{\sigma}^2_{GRACE}} \mathbf{N}_{GRACE}. \tag{10}$$

For the combination, the weighting factors $1/\hat{\sigma}_i^2$ determine the impacts of the single techniques on the resulting NEQ matrix. Normally, the a posteriori variance factors are used. For SLR, the value $\hat{\sigma}^2_{SLR} = 7.9 \cdot 10^{-1}$ results from the least squares adjustment of the SLR single-technique solution. For GRACE, as we primarily focus on the use of the NEQ matrix and did not compute the NEQ vector, we use several values from existing GRACE solutions, ranging from $\hat{\sigma}^2_{GRACE} = 8.8 \cdot 10^{-11}$ to $\hat{\sigma}^2_{GRACE} = 1.6 \cdot 10^{-14}$. The larger value is chosen to show a test case for a high SLR influence (see Fig. 1, dashed lines). In this way, the influence of SLR can be studied. The smaller one is chosen in such a way, that the error degree variances with degree $n > 20$ (which are not influenced by SLR) are equal to the GFZ monthly solution (Barthelmes and Köhler 2012) (see Fig. 1, solid lines).

The matrix $\mathbf{N}_c^{-1}$ contains the full variance-covariance information and is therefore used in the analysis. The standard deviation (STD) of each parameter $\boldsymbol{\beta}_j$ is:

$$\sigma_{\boldsymbol{\beta}_j} = \sqrt{\left(\mathbf{N}_{c_{(j,j)}}\right)^{-1}}, \qquad j = 1, \ldots, u_1 \tag{11}$$

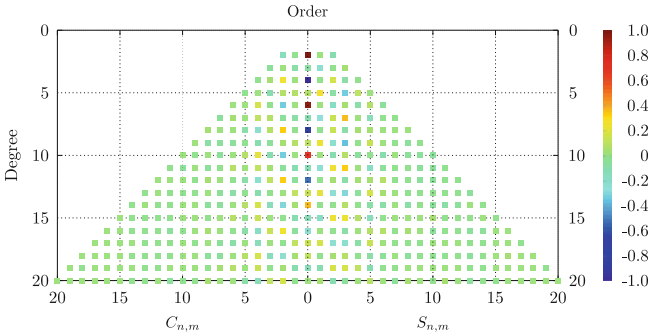

Fig. 2 Correlations between coefficient $C_{2,0}$ and other coefficients computed using $\mathbf{N}_{SLR}$

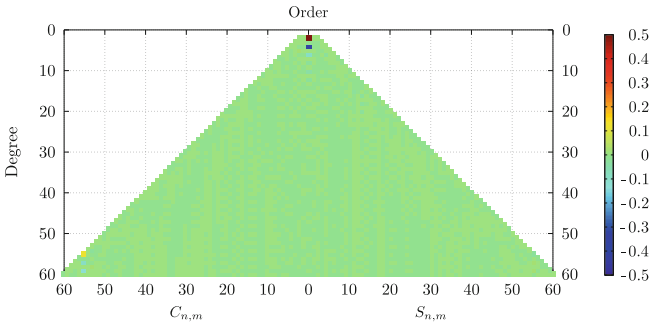

Fig. 3 Correlations between coefficient $C_{2,0}$ and other coefficients computed using $\mathbf{N}_{GRACE}$. Please note the different color axis

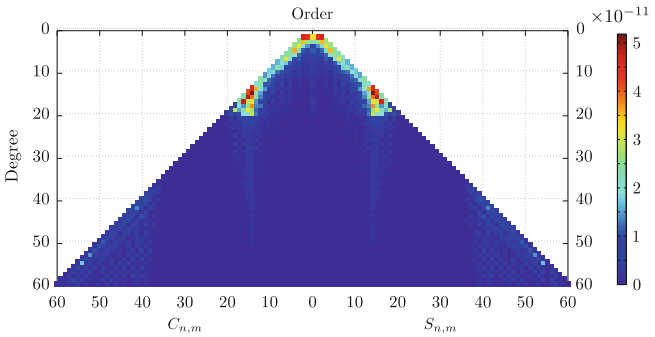

Fig. 4 STDs of the GRACE-only solution minus STDs of the combined solution. $\hat{\sigma}^2_{GRACE} = 8.8 \cdot 10^{-11}$ and $\hat{\sigma}^2_{SLR} = 7.9 \cdot 10^{-1}$

5 Results

The result of the combination depends on the weights, which are defined by the variance factors. We show the results for two test cases, one with a lower weight for GRACE which emphasizes the implications of SLR w.r.t. the combined solution and one with a weight according to GRACE formal errors derived from the GFZ/JPL solution to show the minimum (maybe realistic) influence of SLR.

Figure 1 reveals, that for a small GRACE weighting factor, the error degree variances up to degree 20 of the combined solution show the pattern of SLR (black, dashed line). Although GRACE has the smaller degree variances, they are improved by a factor of 50 at maximum by combining $\mathbf{N}_{GRACE}$ with $\mathbf{N}_{SLR}$. Giving GRACE a high weight, the influence of SLR is much smaller and visible in the combined NEQ only up to degree 3 (see zoomed part of Fig. 1).

The NEQ matrices contain the full variance-covariance information, which is needed to investigate correlations between coefficients. Due to these correlations, coefficients are not separated correctly from each other. Figure 2 shows the correlations between $C_{2,0}$ and other coefficients for $\mathbf{N}^{-1}_{SLR}$. $C_{2,0}$ shows high positive correlations with $C_{6,0}$ and $C_{10,0}$, high negative correlations with $C_{4,0}$, $C_{8,0}$ and $C_{12,0}$. Replacing $C_{2,0}$ in GRACE gravity fields with an SLR derived value neglects these correlations and effects of other coefficients on $C_{2,0}$.

Figure 3 shows that $\mathbf{N}_{GRACE}$ contains much less correlations than $\mathbf{N}_{SLR}$. Larger ones exist only between $C_{2,0}$ and $C_{4,0}$, which reaches only about 30% of the SLR value. By combining $\mathbf{N}_{SLR}$ and $\mathbf{N}_{GRACE}$ the correlations resemble the SLR or the GRACE solution, depending on the weighting factors, but GRACE has a positive effect to decorrelate the zonal SLR coefficients.

The effect of the combination on the STDs of the coefficients are plotted in Fig. 4 for $\hat{\sigma}^2_{GRACE} = 8.8 \cdot 10^{-11}$ and Fig. 5 for $\hat{\sigma}^2_{GRACE} = 1.6 \cdot 10^{-14}$, respectively. They show the difference in STDs from the GRACE-only NEQ matrix minus the STDs from the combined NEQ matrix. For the combined STDs, Eq. (11) is used, for the GRACE-only values they have to be scaled with the variance factor. In both plots, only positive values occur, meaning that the STD of each parameter has a smaller value in the combined solution than in the single-technique solution. Figure 4 reveals the pattern of the SLR impact, as SLR has a high weight. Large improvements are achieved for coefficients of degree 2. Further enhancements are attained for the sectorial and near-sectorial coefficients. This is due to the various inclinations of the SLR satellites between 50° and 110°, whereas GRACE has a nearly polar orbit. Furthermore, resonance frequencies of SLR satellites improve the estimation of coefficients with an order of 14 to 16. Although SLR contributes only up to degree 20, artefacts are visible in the coefficients of resonance frequencies with degree higher than 20 and in coefficients with degree and order higher than 40. This effect might be due to the truncation of $\mathbf{N}_{SLR}$ to highest degree 20. For further investigations, we will set up $\mathbf{N}_{SLR}$ with highest degree 60 to study correlations between the coefficients without any aliasing effects. When GRACE gets a higher weight compared to SLR, these effects are reduced but still are present, especially in coefficients with degree 2 and 4, as well as the zonal coefficients and coefficients of resonance frequencies (see Fig. 5).

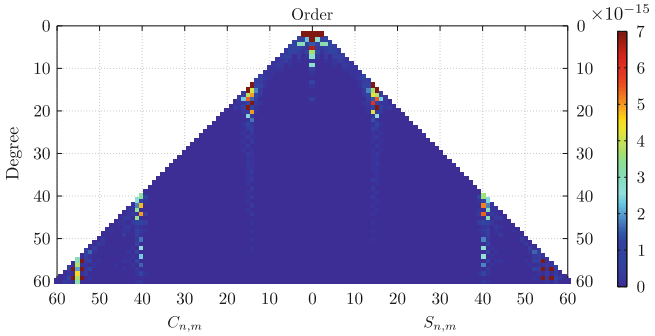

Fig. 5 STDs of the GRACE-only solution minus STDs of the combined solution. $\hat{\sigma}^2_{GRACE} = 1.6 \cdot 10^{-14}$ and $\hat{\sigma}^2_{SLR} = 7.9 \cdot 10^{-1}$

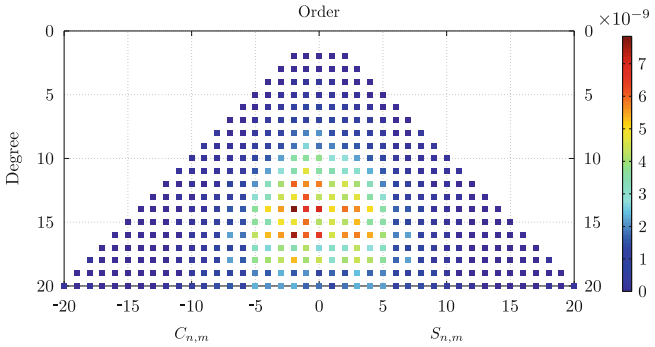

Fig. 6 STDs of the SLR-only solution minus STDs of the combined solution. The differences show more or less the formal errors of the SLR solution, as they are at least up to two orders of magnitudes larger than the GRACE-only solution and the combined solution

On the other hand, GRACE shows small formal errors in the zonal and near-zonal coefficients, as for GRACE the correlations between zonal coefficients are much smaller. The difference between the SLR-only and the combined solution shows the highest values for these coefficients, starting around degree 6 (see Fig. 6). The structure here is complementary to those in Figs. 4 and 5. These values do not change significantly when choosing different weighting factors. As it is shown in Fig. 1, SLR has in general a higher STD than the GRACE or the combined solution. So the differences resemble more or less the formal errors of the SLR solution and independent of $\hat{\sigma}^2_{GRACE}$. The smaller STDs for coefficients with degree 19 and 20 compared to coefficients with $n < 19$ might be caused by aliasing effects.

6 Summary and Outlook

The work presented here is a first assessment of a consistent monthly combination of SLR and GRACE, where for the former more satellites than common were taken and the NEQs were set up to a higher degree than usually done. Our correlation studies indicate positive effects of the combination process. The limitations of GRACE for gravity field determination are mainly caused by its inability to estimate the coefficient $C_{2,0}$ accurately, as well as the (near-)sectorial coefficients. In contrast, the multi-satellite SLR solution allows to obtain these coefficients up to degree 20 with higher accuracy than a GRACE-only solution. Combining both techniques leads to a more accurate dataset of spherical harmonic coefficients.

The combination was done for two test cases, one with a very low weight for $\mathbf{N}_{GRACE}$, one with a quasi-realistic weight for $\mathbf{N}_{GRACE}$. This allows to study the minimum and maximum influence of $\mathbf{N}_{SLR}$. Improvements for $\mathbf{N}_{GRACE}$ occur in the very low-degree, sectorial and near-sectorial, as well as in resonance-order coefficients. The impact of the SLR contribution to the combined NEQ matrix is controlled by the weighting factors. A high weight for SLR increases the influence clearly, but choosing an optimistic value for $\hat{\sigma}^2_{GRACE}$, SLR still has a minor, but positive, impact. Looking at $\mathbf{N}^{-1}_{SLR}$, SLR coefficient $C_{2,0}$ shows large correlations with the other zonal coefficients. By combining $\mathbf{N}_{SLR}$ with $\mathbf{N}_{GRACE}$, these correlations can be reduced and therefore the coefficients can be separated better in the estimation process.

Future work will be to analyse the estimated set of coefficients and compare them to existing gravity field models. To do this, the NEQ vector for GRACE has to be set up. Second, an appropriate weighting strategy has to be chosen to obtain the full information of both techniques. This and correlations between consecutive observations have to be considered, which leads to the need of an appropriate stochastical model, introduced by the weighting matrices $\mathbf{P}_{GRACE}$ (see Eq. (7)) and $\mathbf{P}_{SLR}$. The matrix $\mathbf{N}_{SLR}$ is truncated to maximum degree 20, which can cause aliasing effects. We will set up $\mathbf{N}_{SLR}$ up to degree 60 to study these effects. Up to now, the NEQ matrices $\mathbf{N}_{GRACE}$ and $\mathbf{N}_{SLR}$ are computed once and then put together in the combination step. Linearization errors are therefore not reduced, as no iteration is done. Here, updated NEQ matrices of GRACE and SLR after the combination can improve the estimation. To receive a time series of temporal gravity fields for further studies on the benefits of a combination, data of more months have to be processed.

Acknowledgements The authors like to thank the editors and the anonymous reviewers for their helpful comments and discussion.

References

Barthelmes F, Köhler W (2012) International Centre for global Earth Models (ICGEM). J Geodesy Geodesist Handbook 86(10):932–934

Bjerhammar A (1967) On the energy integral for satellites. Report of the Royal Institute of Technology

Bloßfeld M, Müller H, Angermann D (2011) Adjustment of EOP and gravity field parameters from SLR observations. In: Proceedings of the 17th ILRS Workshop, pp 292–296, ISBN: 978-3-89888-999-5

Bloßfeld M, Stefka V, Müller H, Gerstl M (2014) Satellite Laser Ranging. A tool to realize GGOS? In: Rizos C (ed) Proceedings of the 2013 IAG Scientific Assembly, Potsdam, Germany, September 1–6, 2013

Cheng M, Tapley BD, Ries JC (2011) Variations of the Earth's figure axis from satellite laser ranging and GRACE. J Geophys Res 116:B01409. Doi: 10.1029/2010JB000850

Dahle C, Flechtner F, Gruber C, König D, König R, Michalak G, Neumayer K (2012) GFZ GRACE Level-2 Processing Standards Document for Level-2 Product Release 0005, (Scientific Technical Report STR12/02- Data, Revised Edition, January 2013), Potsdam, p 21. Doi: 10.2312/GFZ.b103-1202-25

Flechnter F et al (2013) Status GFZ RL05 and RL05a GRACE L2 Products. GRACE Science Team Meeting, Austin, TX, October 23–25, 2013

Gerstl M (1997) Parameterschätzung in DOGS-OC. DGFI Int. Bericht Nr. MG/01/1996/DGFI, 2nd edn

Koch KR, Kusche J (2002) Regularization of geopotential determination from satellite data by variance components. J Geodesy 76:259–286. Doi: 10.1007/s00190-002-0245-x

Mayer-Gürr T (2008) Gravitationsfeldbestimmung aus der Analyse kurzer Bahnbögen am Beispiel der Satellitenmissionen CHAMP und GRACE. Schriftenreihe des Instituts für Geodäsie und Geoinformation der Rheinischen Friedrich-Wilhelms-Universität Bonn, Heft 9

Mayer-Gürr T et al (2011) The satellite-only global gravity field model GOCO02S. Presentation at the EGU General Assembly 2011, Vienna, Austria

Mayer-Gürr T et al (2012) The new combined satellite only model GOCO03s. Presentation at the International Symposium on Gravity, Geoid and Height Systems 2012, Venice, Italy

Pearlman MR, Degnan JJ, Bosworth JM (2002) The international laser ranging service. Adv Space Res 30(2):135–143. Doi: 10.1016/S0273-1177(02)00277-6

Tapley BD, Bettadpur S, Watkins M, Reigber C (2004) The gravity recovery and climate experiment: mission overview and early results. Geophys Res Lett 31(9):L09607

Watkins M, Yuan D (2012) JPL Level-2 Processing Standards Document For Level-2 Product Release 05

Tailored Reference Geopotential Model for Africa

Hussein A. Abd-Elmotaal, Kurt Seitz, Mostafa Abd-Elbaky, and Bernhard Heck

Abstract

In the framework of the African Geoid Project, the currently available gravity data set contains many significant gaps allover the continent. A possible way to fill in these gaps before the geoid computation process, is to use a global geopotential model which best fits the African gravity field. Hence, the aim of this paper is to create a tailored reference geopotential model for Africa to be used to fill the gravity data gaps with reasonable values. With the ongoing improvement of the data base, this tailored model will also be updated iteratively. The remove-restore technique has been applied using a newly compiled $30'' \times 30''$ Digital Height Model for Africa based on SRTM. As global geopotential reference model serves EGM2008 which shows similar behaviour for Africa like GRACE/GOCE derived models. The local and global data sets, in terms of topographically-isostatically reduced gravity anomalies, are merged and used to estimate by three different techniques the potential coefficients of the tailored reference models for Africa. The used harmonic analysis techniques are the FFT technique, the least-squares technique and the Gauss-Legendre numerical integration technique. The results show that the tailored models computed within this investigation provide significantly smaller reduced anomalies (about 50 %) than those of EGM2008 or models derived from the GRACE and GOCE satellite missions for the African continent.

Keywords

Africa • Geoid determination • Harmonic analysis • Tailored geopotential models

1 Introduction

The quality of the reference geopotential model used in the framework of the remove-restore technique plays an important role in estimating the accuracy of the interpolated gravity anomalies and hence the computed geoid. In other words, if the residual field is biased and has a high variance, then using such a biased/high variance field in the geoid computation process gives less accurate interpolated quantities, and hence worse geoid fitting to the GNSS/levelling derived geoid. Practical studies so far have proved that none of the existing reference geopotential models fits the African gravity field better than ± 30 mgal standard deviation as listed in Table 3 (cf. Abd-Elmotaal 2015).

Thus, the aim of this investigation is to develop a high-degree reference geopotential model tailored to the African gravity field. This can be done in several equivalent ways (see, e.g., Pavlis et al. 2007). The used approach is explained in Sects. 2 and 5. Such a tailored geopotential model is then

H.A. Abd-Elmotaal (✉) • M. Abd-Elbaky
Faculty of Engineering, Civil Engineering Department, Minia University, Minia, Egypt
e-mail: abdelmotaal@lycos.com

K. Seitz • B. Heck
Geodetic Institute, Karlsruhe Institute of Technology, Englerstrasse 7, 76128 Karlsruhe, Germany
e-mail: kurt.seitz@kit.edu

© Springer International Publishing Switzerland 2015

C. Rizos, P. Willis (eds.), *IAG 150 Years*, International Association of Geodesy Symposia 143,
DOI 10.1007/1345_2015_84

used to fill the existing large gaps of the current gravity data set over Africa.

The used data sets are described. The methodology to create the tailored geopotential model is explained. The local gravity anomalies for the African data window are gridded, after removing the effect of the topographic-isostatic (topo-iso) masses, in a $30' \times 30'$ grid using the Kriging interpolation technique. The local gridded data are merged with the global $30' \times 30'$ gravity anomalies, computed using EGM2008 (Pavlis et al. 2012) till degree and order $N = 360$ after removing the effect of the global topographic-isostatic masses using the coarse digital height model (DHM) TBASE $30' \times 30'$, to establish the data set for computing the tailored geopotential models. When using one of the recent GRACE/GOCE geopotential models (Tapley et al. 2007; Förste et al. 2008; Pail et al. 2011) the residuals are even larger (Abd-Elmotaal 2015). Therefore EGM2008 is used throughout this investigation as reference model.

The merged $30' \times 30'$ global field is then used to estimate the harmonic coefficients of the tailored reference model by three different harmonic analysis techniques. These techniques are the FFT technique, the least-squares technique and the Gauss-Legendre numerical integration technique. A detailed comparison among the computed tailored geopotential models in both frequency and space domain is carried out.

It should be noted that many researchers have computed tailored geopotential models to best suit their specific areas of interest. The reader may refer, e.g., to Weber and Zomorrodian (1988), Wenzel (1998), Abd-Elmotaal (2007).

2 Basic Idea and Methodology

Within the remove-restore technique (Forsberg 1984), the effect of the topographic-isostatic masses is removed from the source gravity data and then restored to the resulting gravity potential coefficients. The reduced gravity anomalies Δg_{red} in the framework of the remove-restore technique are computed by

$$\Delta g_{red} = \Delta g_F - \Delta g_{TI} - \Delta g_{GM} \,, \tag{1}$$

where Δg_F stands for the free-air anomalies, Δg_{TI} is the reduction due to the topographic-isostatic masses, and Δg_{GM} is the effect of the global geopotential model (reference field) on the gravity anomalies. This relation is used to validate the derived tailored geopotential models (cf. Fig. 8 and Table 3) and the used reference GPMs (EGM2008, EIGEN-5C, GGM03C, GOCE = GO_CONS_GCF_2_TIM_R3).

If we aim to have, theoretically, zero reduced anomalies by tailoring the geopotential model, then the left hand-side of Eq. (1) is put to zero. Thus we can compute the gravity anomalies Δg_{GM_T} referring to the tailored geopotential model as:

$$\Delta g_{GM_T} = \Delta g_F - \Delta g_{TI} \,. \tag{2}$$

This relation is used to compute point-wise the topo-iso reduced residual gravity anomalies within the African window.

For the global field, reducing the gravity anomalies due to the topo-iso masses is performed by removing the harmonic coefficients of the global topo-iso masses $\bar{T}_{nm}$, as outlined in Sect. 3 computed by Eq. (6), (from degree 2 to degree and order 360) from the EGM2008 global geopotential model yielding a model which corresponds to the so-called "isostatic field":

$$\left(\bar{C}_{nm}\right)_{GM,TI} = \left(\bar{C}_{nm}\right)_{EGM2008} - \bar{T}_{nm} \,, \tag{3}$$

where $2 \le n \le 360$ and $-n \le m \le n$.

Accordingly, we are going to reduce both our global and local gravity anomalies by the effect of the topographic-isostatic masses (cf., e.g., Rummel et al. 1988). For the local field, reducing the gravity anomalies due to the topographic-isostatic masses is performed by removing the effect of the topo-iso masses Δg_{TI} (using the TC-program, written originally by Forsberg (1984) after major improvements by Abd-Elmotaal and Kühtreiber (2003), within a radius of 167 km around each computation point) from the free-air anomalies according to Eq. (2).

To finally apply the harmonic analysis techniques to compute the potential coefficients of the tailored model, the point-wise given smoothed gravity anomalies from Eq. (2) have to be interpolated on a regular grid within the African window. The Kriging interpolation technique is used to interpolate a $30' \times 30'$ grid. This regional grid (African window) is a sub-grid of the global grid. The global grid contains the synthesized values of the "isostatic field", which is defined in Eq. (3). The tailoring of the global field to the African window is carried out by replacing the grid values from the global field by the interpolated values within the African window.

3 Harmonic Analysis of the Topographic-Isostatic Potential

The harmonic coefficients of the topography and its isostatic compensation as well as the harmonic series expansion of the topographic-isostatic potential can be expressed by

Abd-Elmotaal and Kühtreiber (2003, pp. 78–79):

$$T_{TI}(P) = \frac{GM}{r_P} \sum_{n=0}^{\infty} \left(\frac{R}{r_P}\right)^n \sum_{m=-n}^{n} \bar{T}_{nm} \bar{R}_{nm}(P)\,, \quad (4)$$

where the Laplace surface spherical harmonics $\bar{R}_{nm}(P)$ are defined by Hofmann-Wellenhof and Moritz (2006)

$$\bar{R}_{nm}(P) = \bar{P}_{n|m|}(\cos\theta_P) \begin{cases} \cos m\lambda_P & \text{for } m \geq 0 \\ \sin |m|\lambda_P & \text{for } m < 0 \end{cases} \quad (5)$$

and $\bar{P}_{n|m|}(\cos\theta)$ are the fully normalized Legendre functions, GM is the geocentric gravitational constant, r_P is the radius vector, θ_P is the co-latitude, λ_P is the geographical longitude of the computation point P. The fully normalized dimensionless potential coefficients $\bar{T}_{nm}$ are given by

$$\bar{T}_{nm} = \frac{R^3}{M(2n+1)(n+3)} \iint_{\sigma} \left\{ \rho_Q \left[\left(1 + \frac{H_Q}{R}\right)^{n+3} - 1 \right] + \Delta\rho_Q \left(1 - \frac{T_\circ}{R}\right)^{n+3} \cdot \left[\left(1 - \frac{t_Q}{R - T_\circ}\right)^{n+3} - 1 \right] \right\} \bar{R}_{nm}(Q)\, d\sigma, \quad (6)$$

where $\rho_Q = 2670$ kg m^{-3} denotes the topographic density, $\Delta\rho_Q = 400$ kg m^{-3} denotes the density anomaly, $T_\circ = 30$ km is the normal crustal thickness, H is the topographic height, t is the compensating root/antiroot and M denotes the mass of the earth (Sünkel 1985).

Equation (6) is given with practical aspects in Abd-Elmotaal and Kühtreiber (2003) and is a specification of the rigorous formula developed in Pavlis and Rapp (1990).

4 The Data

4.1 Local African Free-Air Gravity Anomalies

All currently available sea and land free-air gravity anomalies for Africa has been collected by the first author, the chair of the IAG African Geoid Project (AGP). Unfortunately some gravity information from former databases, of, e.g., Merry (2003) and Merry et al. (2005), are not currently available for the AGP, which is a project of the IAG. Ongoing efforts will be done to enhance the distribution and quality of the gravity data necessary for the African Geoid Project. An automated smart technique for gross-error detection has been successfully applied (Abd-Elmotaal and Kühtreiber 2014).

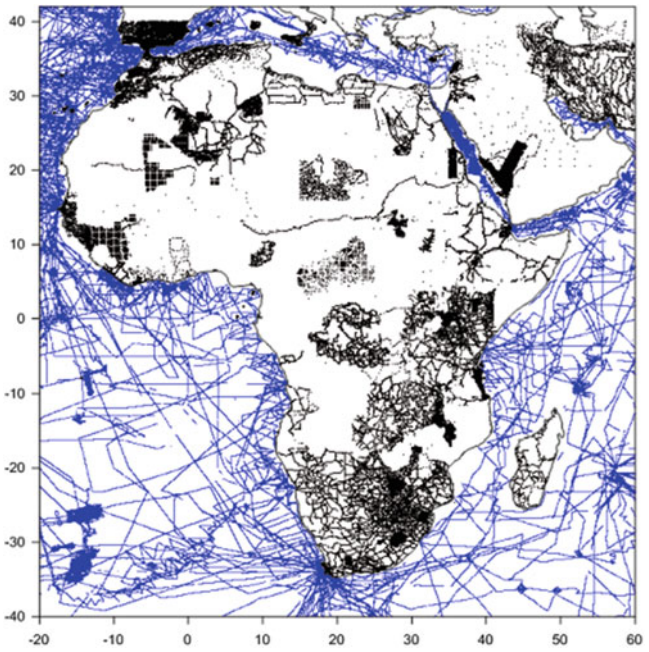

Fig. 1 Distribution of the local African free-air gravity anomalies. *Black*: land-based; *blue*: shipborne

Figure 1 shows the distribution of the free-air gravity anomalies within the Africa window used for the current investigation. The distribution of the free-air gravity anomaly stations on land is very poor. Many areas are empty. The distribution of the data points on sea is slightly better than that on land, however, also many areas are still empty. A first attempt incorporating altimetry derived gravity anomalies gave very bad results. They seem to be too smooth and do not match the shipborne data (Abd-Elmotaal and Makhloof 2013). Therefore altimetry derived gravity anomalies are not currently used in the African Geoid Project. It needs further investigations in using altimetry data in combination with the shipborne data. The statistics of the used free-air gravity anomalies are given in Table 3.

4.2 Digital Height Models

For the terrain reduction computation, a set of fine and coarse Digital Height Models (DHM's) is needed. The SRTM30+ ($30'' \times 30''$) (Farr et al. 2007) is used as fine DHM to compute the topo-iso effects at the gravity points which are located inside the African window $-42° \leq \phi \leq 44°$, $-22° \leq \lambda \leq 62°$ (see Fig. 2). To compute the coefficients of the topographic-isostatic effects according to Eq. (6), the TBASE (Row et al. 1995) global DHM ($30' \times 30'$) is used as coarse DHM. These coefficients are subtracted from the

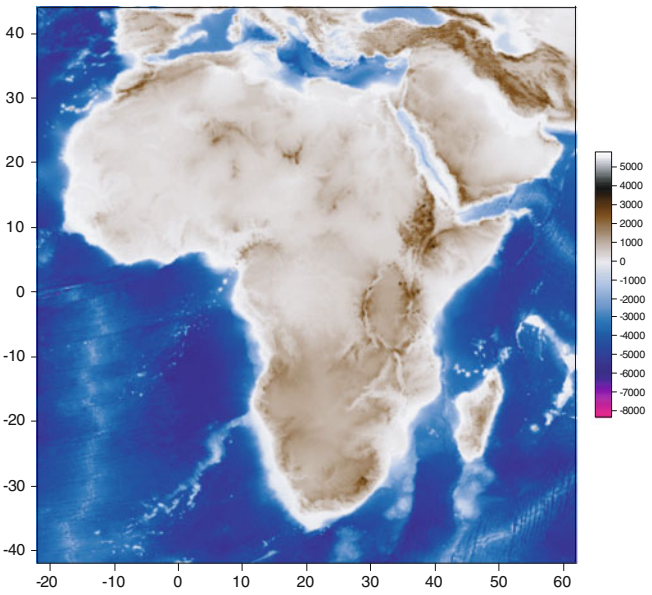

Fig. 2 The fine DHM SRTM30+. Units in [m]

EGM2008 coefficients, as defined in Eq. (3), which leads to the topographic-isostatic reduced global $30' \times 30'$ grid of gravity anomalies.

5 Preparing the Gravity Anomalies

The TBASE $30' \times 30'$ global topographic-bathymetric DHM (Row et al. 1995) has been used to compute the harmonic coefficients of the global topographic-isostatic masses T_{TI} using Eq. (6) till degree and order $N = 360$.

Figure 3 shows the TBASE $30' \times 30'$ global DHM. The heights range between $-8,789$ m and 6,088 m with an average of about -1897 m and standard deviation of 2,649 m.

The harmonic coefficients of the topo-iso reduced field are created according to Eq. (3) by subtracting the harmonic coefficients of the global topo-iso masses T_{TI} from those of the EGM2008 model (Pavlis et al. 2012). These reduced global topo-iso potential coefficients, till d/o $N = 360$, are used to generate a global $30' \times 30'$ field of topo-iso reduced gravity anomalies.

The effect of the topo-iso masses within a radius of 167 km around the computational point is subtracted from the local African free-air gravity anomaly Δg_F available for this investigation. The topo-iso reduction is done in order to smooth the data before the interpolation is carried out. These topo-iso anomalies have been interpolated in a $30' \times 30'$ grid using the Kriging interpolation technique. Figure 4 shows the local grid of $30' \times 30'$ interpolated anomalies Δg_{GM_T} computed from Eq. (2) for the African window. The local $30' \times 30'$ interpolated topo-iso reduced gravity anomalies for Africa have been merged with the created topo-iso reduced

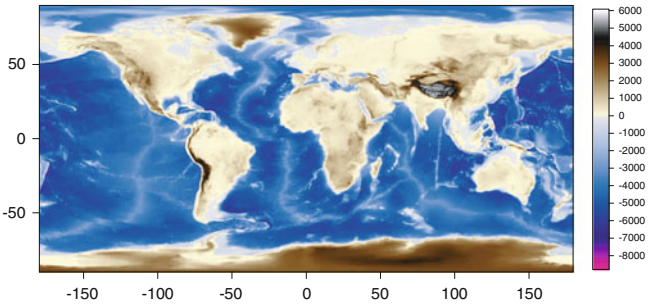

Fig. 3 TBASE $30' \times 30'$ global DHM. Units in [m]

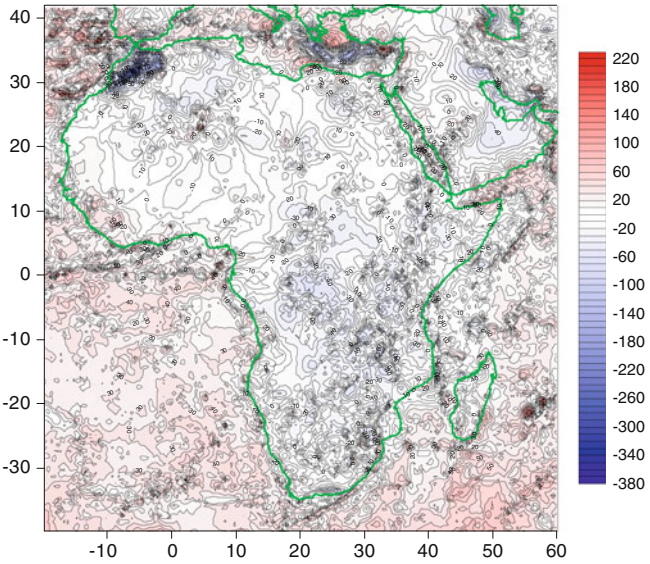

Fig. 4 The local African $30' \times 30'$ interpolated gravity anomalies. Units in [mgal]

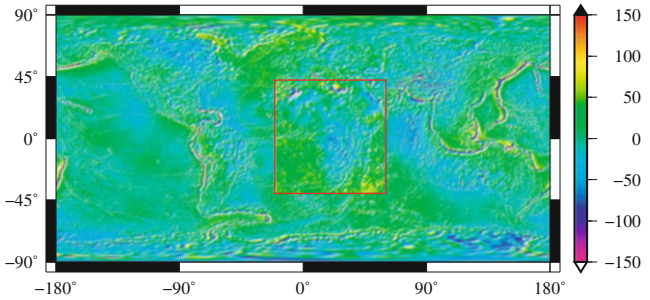

Fig. 5 The global $30' \times 30'$ merged field including the gravity anomalies for Africa (*solid rectangle*). Units in [mgal]

$30' \times 30'$ global gravity anomalies forming the data set for computing the tailored geopotential model for Africa. Figure 5 shows that merged field, where the boundaries of the African window (local field) are indicated by a solid rectangle. Table 1 illustrates the statistics of the used three gravity anomaly fields. The standard deviation of the reduced gravity anomalies become 1 mgal smaller when merging the local

Table 1 Statistics of the used three topographic-isostatic reduced gravity anomaly grid fields

Covered area	Statistical parameters [mgal]				
	# Cells	Min.	Max.	Mean	Std
Global	259,200	−334.7	276.4	−0.8	27.4
Local	26,240	−376.2	203.8	8.5	29.6
Merged	259,200	−376.2	276.4	−0.2	28.3

gravity anomaly data for Africa (10 % of the whole global data set). The mean value has been affected by 0.6 mgal.

The described approach of creating the global gridded isostatic gravity anomalies, which includes the merged African window, is based on arbitrarily distributed point values. The disadvantage of this procedure is that possibly the interpolation has to be applied over larger distances. We approve this, because the aim is to generate a tailored model to fill in the data gaps with reasonable values based on the actual available point data.

Several other methods are applicable (Pavlis et al. 2007) to generate the global grid that serves as input data for the harmonic analysis. For example, alternatively block mean values can be generated by averaging the available terrestrial gravity data within the cells of geographic extent. Of course, these area-mean values should be computed only over those cells, if sufficient point data are available, to compute a representative area-mean value for the respective cell. For those blocks where no such area-mean values can be computed in absence of sufficient point values, mean values from a recent satellite-only model from GRACE and GOCE (Bruinsma et al. 2013) may be synthesized.

6 Tailored Geopotential Models for Africa

The merged $30' \times 30'$ global field, which is given on the surface of the reference ellipsoid GRS80, has been used to estimate the potential coefficients of the tailored reference model in the basis of spherical harmonics by three harmonic analysis techniques (cf. Colombo 1981), namely:

1. FFT technique (Abd-Elmotaal 2004).
2. Least-squares technique (Heck and Seitz 1991).
3. Gauss-Legendre numerical integration technique (Abd-Elmotaal et al. 2013).

Figure 6 show in the upper right panel the modulus of the coefficients $\left(\bar{C}_{nm}\right)_{FFT}$ and $\left(\bar{S}_{nm}\right)_{FFT}$ of the tailored geopotential model for Africa computed using the FFT analysis technique, with comparison to the global GPM EGM2008 coefficients (upper left panel). Their absolute differences are plotted in the lower left panel and show, that mainly the coefficients up to d/o $n = 180$ are changed their absolute value. In addition, the absolute relative difference between the EGM2008 and the $\mathrm{FFT}_{Tailored}$ coefficients are defined as follow:

$$\delta\bar{C}_{nm} = \frac{|(\bar{C}_{nm})_{EGM2008} - (\bar{C}_{nm})_{Tailored}|}{|(\bar{C}_{nm})_{EGM2008}|}, \qquad \delta\bar{S}_{nm} = \frac{|(\bar{S}_{nm})_{EGM2008} - (\bar{S}_{nm})_{Tailored}|}{|(\bar{S}_{nm})_{EGM2008}|}. \tag{7}$$

They are graphically presented in the lower right panel of Fig. 6. From this relative plot it is obvious that many of the potential coefficients are changed due to the tailoring. The scaling to their absolute values shows that for most of the coefficients the magnitude is unchanged, because $\delta\bar{C}_{nm} < 1$ and $\delta\bar{S}_{nm} < 1$ holds. The respective plots for the coefficients computed from LST and Gauss look very similar and are not given here.

7 Validation of the Tailored Reference Models for Africa

The gridded $30' \times 30'$ gravity anomaly data for the African window are compared with those estimated from using the tailored models. This gives an assessment of the quality in terms of mean, range and standard deviation (std) of the computed tailored models. Figure 8 show the differences at the grid points between the African $30' \times 30'$ interpolated gravity anomalies and the estimated gravity anomalies using the FFT tailored geopotential model for Africa. The white areas indicate absolute differences less than 5 mgal. The figure show good matching over the African window. The Gauss technique give identical result to FFT as can be seen from the statistics in Tables 2 and 3.

The tailored model derived from LST is slightly different from the FFT model. The statistical values are very similar. From the degree variances can be seen in Fig. 7 that LST has less energy in the coefficients of higher degree starting from $n = 180$. Table 2 illustrates the statistics of the residuals at the grid points of the African gravity anomalies using the three tailored reference models as well as using the EGM2008 geopotential model. It confirms that using the tailored geopotential models gives smaller residuals at the grid points, as can be expected (Pavlis 1988), especially for FFT and Gauss tailored models. The LST results give also rather small residuals compared to EGM2008. For the sake of a more detailed comparison and checking of the computed tailored geopotential models, these have been used to compute the gravity anomalies at the 1,190,289 data points. Table 3 illustrates the statistics of the reduced gravity anomalies for Africa. Here Δg_{red} is computed according to Eq. (1). The three tailored geopotential models (FFT, LST, Gauss) created in this investigation give better residual gravity anomalies (unbiased and have much less variance and range) as listed in Table 3. Again the FFT

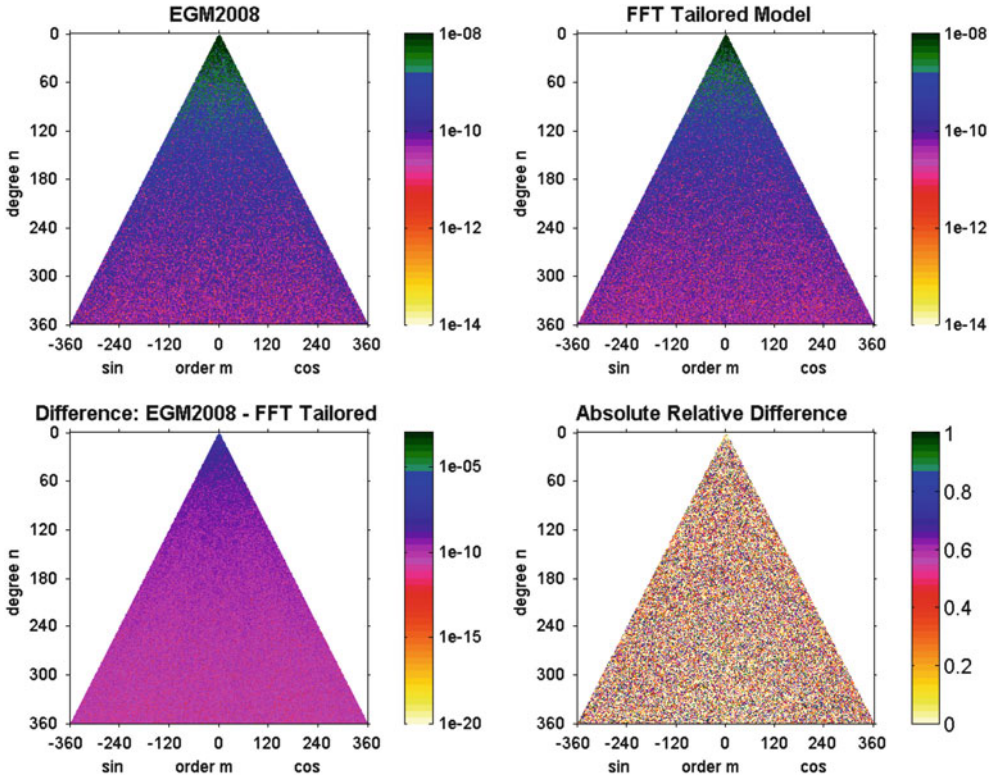

Fig. 6 The tailored geopotential model for Africa computed using the FFT harmonic analysis technique

Table 2 Statistics of the residuals of the African gravity anomalies at the grid points using different reference models

Geopotential	Statistical parameters [mgal]				
model	Min.	Max.	Mean	Range	Std
EGM2008	−525.9	122.4	5.7	648.3	32.8
FFT tailored	− 57.8	66.6	1.4	124.4	3.8
LST tailored	− 92.7	108.8	3.3	201.5	7.8
Gauss tailored	− 56.5	67.2	2.3	123.7	3.8

Table 3 Statistics of the reduced gravity anomalies Δg_{red} for Africa at the 1,190,289 data points using different reference models and free air anomalies Δg_F

Anomalies	Statistical parameters [mgal]					
type	N	Min.	Max.	Mean	Range	Std
Δg_F	–	−624.5	452.9	−4.4	1, 107.3	41.9
EGM2008	360	−598.9	197.6	22.4	796.5	29.4
GOCE	250	−579.7	238.2	21.9	817.9	30.0
EIGEN-5C	360	−594.7	192.0	22.3	786.6	29.3
GGM03C	360	−590.4	209.7	22.3	800.1	29.3
FFT	360	−192.0	210.0	4.1	402.0	20.8
LST	360	−207.5	222.7	5.9	430.2	22.0
Gauss	360	−191.5	210.8	5.0	402.2	20.9

and the Gauss geopotential tailored models give best results. For these two tailored geopotential models, the variance and the range were reduced by 50% compared to their values in case of using EGM2008 or the satellite based models GO_CONS_GCF_2_TIM_R3 (Pail et al. 2011, GOCE), EIGEN-5C (Förste et al. 2008, GRACE combined) and GGM03C (Tapley et al. 2007, GRACE combined). The statistical values confirm the results of Abd-Elmotaal 2015, which have shown that GOCE and GRACE models give comparably bad results like EGM2008—at least in Africa. Therefore, e.g. EGM2008 was chosen as a start model of the tailored geopotential model for Africa.

The absolute relative difference $\delta\bar{C}_{nm}$ and $\delta\bar{S}_{nm}$ (see Eq. (7)) in the coefficients of the tailored models with respect to EGM2008 is plotted in the lower right panel of Fig. 6 for the FFT results. It can be seen that the relative change to the coefficients of the tailored model concerns all coefficients. No systematic behaviour is visible. From the lower left panel (Fig. 6) it can be seen that mainly the potential coefficients up to degree and order $n = 180$ alter their values. This is in accordance to what can be observed in the degree variances shown in Fig. 7.

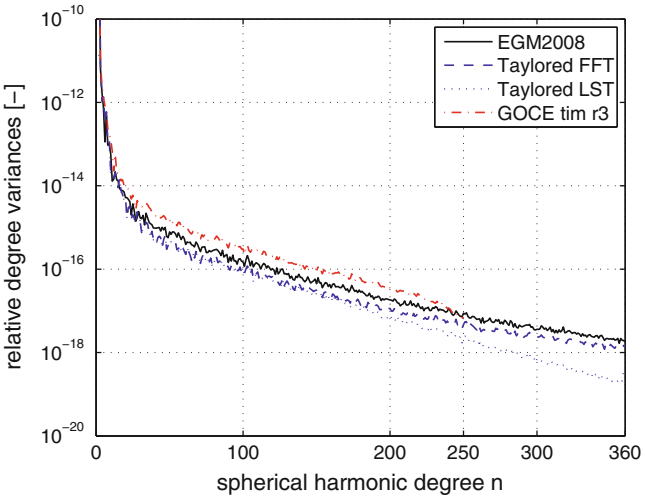

Fig. 7 Relative degree variances for the tailored geopotential models FFT and LST for Africa, EGM2008 and GOCE

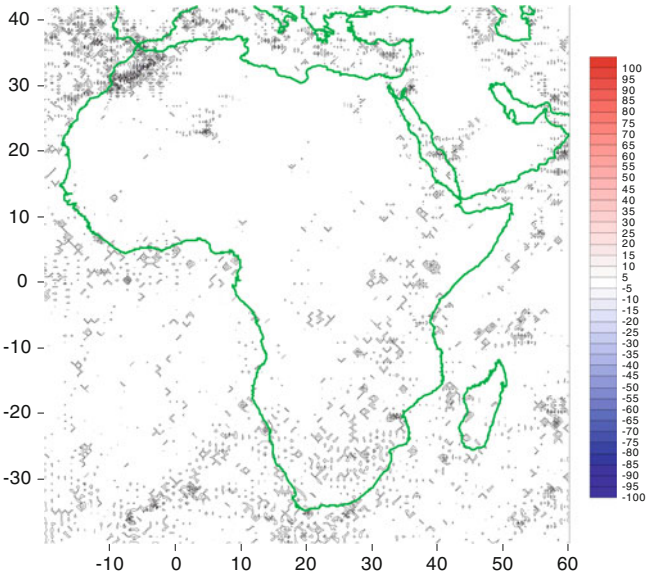

Fig. 8 Differences between the African $30' \times 30'$ interpolated gravity anomalies and the synthesized gravity anomalies using the FFT tailored geopotential model. Units in [mgal]

8 Conclusion

High-degree tailored reference geopotential models for Africa, complete to degree and order 360, have been developed in this investigation. They will be used to fill in the large data gaps which are present in the database of the African Geoid Project. It is expected that this will strongly improve the quality of the next geoid generation over the African continent.

The gravity anomalies (topo-iso) for Africa have been compiled and interpolated to a local data-grid of $30' \times 30'$ resolution. This grid has been merged with a global grid of EGM2008-based topographically-isostatically reduced gravity anomalies. Three different harmonic analysis techniques have been successfully applied to estimate the harmonic coefficients of the tailored models. They are the FFT, the least-squares and the Gauss numerical integration techniques. The tailored geopotential models created in this investigation give smaller residual gravity anomalies for Africa (unbiased and have much less variance and range). The variance and the range decreased by about 50 % compared to the original free air anomalies. The FFT and the Gauss harmonic analysis techniques give quite similar results, which are very close to the LST derived potential coefficients. The tailored geopotential models created within this investigation are more suitable than EGM2008 or recent GRACE/GOCE derived geopotential models for gravity interpolation considering the large data gaps appearing in the African gravity data base.

Acknowledgements The authors would like to thank four anonymous reviewers, as well as the Editor-in-Chief, for their valuable comments, which helped to improve the manuscript. Financial support of the STDF/ DAAD is kindly acknowledged.

References

Abd-Elmotaal H (2004) An efficient technique for harmonic analysis on a spheroid (ellipsoid and sphere). VGI 3(4):126–135

Abd-Elmotaal H (2007) Reference geopotential models tailored to the Egyptian gravity field. Boll Geod Sci Affini 66(3):129–144

Abd-Elmotaal H, Kühtreiber N (2003) Geoid determination using adapted reference field, seismic Moho depths and variable density contrast. J Geod 77(1–2):77–85

Abd-Elmotaal H, Kühtreiber N (2014) Automated gross error detection technique applied to the gravity database of Africa. General Assembly of the European Geosciences Union, Vienna, Austria, 27 April–2 May 2014

Abd-Elmotaal H, Makhloof A (2013) Gross-errors detection in the shipborne gravity data set for Africa. Geodetic Week, Essen, 8–10 Oct 2013

Abd-Elmotaal H (2015) Validation of GOCE models in Africa. Newton's Bull 5 (in press)

Abd-Elmotaal H, Seitz K, Abd-Elbaky M, Heck B (2013) Comparison among three harmonic analysis techniques on the sphere and the ellipsoid. J Appl Geod 1–18. Doi:10.1515/jag-2013-0008.

Bruinsma S, Förste C, Abrikosov O, Marty JC, Rio MH, Mulet S, Bonvalot S (2013) The new ESA satellite-only gravity field model via the direct approach. Geophys Res Lett 40(14):3607–3612. Doi:10.1002/grl.50716.

Colombo O (1981) Numerical methods for harmonic analysis on the sphere. Ohio State University, Department of Geodetic Science and Surveying, Report 310

Farr T, Rosen P, Caro E, Crippen R, Duren R, Hensley S, Kobrick M, Paller M, Rodriguez E, Roth L, Seal D, Shaffer S, Shimada J, Umland J, Werner M, Oskin M, Burbank D, Alsdorf D (2007) The shuttle radar topography mission. Rev Geophys 45:RG2004. Doi:110.1029/2005RG000183.

Forsberg R (1984) A study of terrain reductions, density anomalies and geophysical inversion methods in gravity field modelling. Ohio State University, Department of Geodetic Science and Surveying, Report 355

Förste C, Flechtner F, Schmidt R, Stubenvoll R, Rothacher M, Kusche J, Neumayer KH, Biancale R, Lemoine JM, Barthelmes F, Bruinsma J, König R, Meyer U (2008) EIGEN-GL05C – A new global combined high-resolution GRACE-based gravity field model of the GFZ-GRGS cooperation. General Assembly of the European Geosciences Union, Vienna, Austria, 13–18 April 2008

Heck B, Seitz K (1991) Harmonische Analyse. Technical Report, Geodetic Institute, University of Karlsruhe

Hofmann-Wellenhof B, Moritz H (2006) Physical geodesy. Springer, NewYork

Merry C (2003) The African geoid project and its relevance to the unification of African vertical reference frames. 2nd FIG Regional Conference Marrakech, Morocco, 2–5 Dec 2003

Merry C, Blitzkow D, Abd-Elmotaal H, Fashir H, John S, Podmore F, Fairhead J (2005) A preliminary geoid model for Africa. A window on the future of geodesy. Springer, Berlin, pp 374–379

Pail R, Bruinsma S, Migliaccio F, Förste C, Goiginger H, Schuh W, Höck E, Reguzzoni M, Brockmann J, Abrikosov O, Veicherts M, Fecher T, Mayrhofer R, Krasbutter I, Sansò F, Tscherning C (2011) First GOCE gravity field models derived by three different approaches. J Geod 85(11):819–843. Doi:10.1007/s00190-011-0467-x

Pavlis N (1988) Modeling and estimation of a low degree geopotential model from terrestrial gravity data. Ohio State University, Department of Geodetic Science and Surveying, Report 386

Pavlis N, Rapp R (1990) The development of an isostatic gravitational model to degree 360 and its use in global gravity modeling. Geophys J Int 100:369–378

Pavlis N, Factor J, Holmes S (2007) Terrain-related gravimetric quantities computed for the next EGM. In: Kiliçoğlu A, Forsberg R (eds) Proceedings of the 1st international symposium IGFS: gravity field of the Earth, Istanbul, Turkey, 2006, Harita Dergisi, Special Issue 18, pp 318–323

Pavlis N, Holmes S, Kenyon S, Factor J (2012) The development and evaluation of the earth gravitational model 2008 (EGM2008). J Geophys Res 117:B04406. Doi:10.1029/2011JB008916.

Row L, III, Hastings D (1995) Terrain base global terrain model. National Geophysical Data Center and World Data Center-A for Solid Earth Geophysics, Boulder, Colorado URL ftp://ftp.ngdc.noaa.gov/Solid_Earth/Topography/tbase_5min/tbase.txt.

Rummel R, Rapp R, Sünkel H, Tscherning C (1988) Comparisons of global topographic/isostatic models to the earth's observed gravity field. Ohio State University, Department of Geodetic Science and Surveying, Report 388

Sünkel H (1985) An isostatic earth model. Ohio State University, Department of Geodetic Science and Surveying, Report 367

Tapley B, Ries J, Bettadpur S, Chambers D, Cheng M, Condi F, Poole S (2007) The GGM03 mean earth gravity model from GRACE. American Geophysical Union, Fall Meeting, San Francisco, 10–14 Dec 2007

Weber G, Zomorrodian H (1988) Regional geopotential model improvement for the Iranian geoid determination. Bull Geod 62:125–141

Wenzel H (1998) Ultra high degree geopotential models GPM98A, B and C to degree 1800 tailored to Europe. Rep Finnish Geodetic Institute 98(4):71–80

Towards an Alternative Geoid Fitting Technique

Norbert Kühtreiber and Hussein Abd-Elmotaal

Abstract

In this paper an alternative geoid fitting technique is proposed. Within the fitting process the transformation between a physically determined geoid and a GPS/levelling derived geoid is modeled on the basis of least squares collocation. The basic idea behind the proposed technique is to select a minimal amount of GPS benchmarks which fit the geoid within the area under consideration based on minimum range and standard deviation criteria. While the selected GPS benchmarks are used for the fitting, the residuals at the remaining GPS benchmarks represent an external check of the relative GPS/geoid accuracy. In order to ensure the quality of the transformation surface gross errors in the GPS benchmarks need to be detected. The proposed technique is thus formulated as a three step procedure: detection of gross errors among the GPS benchmarks, determination of the minimum amount of GPS benchmarks and a final external check of the relative GPS/geoid accuracy.

A first practical test of the technique is done for fitting the geoid of Austria to the GPS/levelling derived geoid.

Keywords

Blunder detection • Geoid fitting • Least squares prediction

1 Introduction

The determination of a geoid can be done based on different well known approaches (Heiskanen and Moritz 1967). If, e.g., gravity anomalies are given, Stokes' formula can be used. From a theoretical point of view the resulting gravimetric geoid is an absolute geoid if several conditions are fulfilled e.g. the value of W_0 needs to be chosen adequately. For details on the conditions needed see e.g. Smith (1998). On the other hand also GPS/levelling geoids provide absolute values only if the local vertical datum is connected to a tide gauge on the geoid and GPS heights are given in an ITRF. For details refer to e.g. Gatti et al. (2012) and Jekeli (2000).

If the measurements used for the geoid computation are deflections of the vertical, they will be transformed via Helmert's formula to relative geoid heights. In this case obviously the knowledge of absolute geoid undulations (e.g. geoidal heights derived by GPS/levelling) is a must.

The process of fitting the geoid solutions to GPS/levelling heights enables the transformation from GPS-heights to a national height system as well as the assessment of the geoid solutions. Many papers are existing on that topic, e.g. Featherstone (2001), Fotopoulos et al. (2003), Iliffe et al. (2003), Featherstone and Sproule (2006), Krynski and Łyszkowicz (2006), Voigt et al. (2008) or Wang et al. (2012). In the sequel the expression transformation surface will be

N. Kühtreiber (✉)
Institute of Navigation, Graz University of Technology, Steyrergasse 30, 8010 Graz, Austria
e-mail: norbert.kuehtreiber@tugraz.at

H. Abd-Elmotaal
Faculty of Engineering, Civil Engineering Department, Minia University, Minia 61111, Egypt
e-mail: abdelmotaal@lycos.com

© Springer International Publishing Switzerland 2015

C. Rizos, P. Willis (eds.), *IAG 150 Years*, International Association of Geodesy Symposia 143,
DOI 10.1007/1345_2015_94

used, for the fitted geoid as it performs the above mentioned transformation of GPS-heights to a national height system.

In the above mentioned concepts the fitting is performed as a separate step after the geoid computation has been done. If collocation (Moritz 1980; Kühtreiber 2003; Kühtreiber et al. 2011) is used, different gravity field data (gravity anomalies, deflections of the vertical, GPS/levelling heights, etc.) can be combined in one computational step, assumed that a reasonable covariance function of the disturbing potential is known.

In the following a new strategy for the fitting will be discussed.

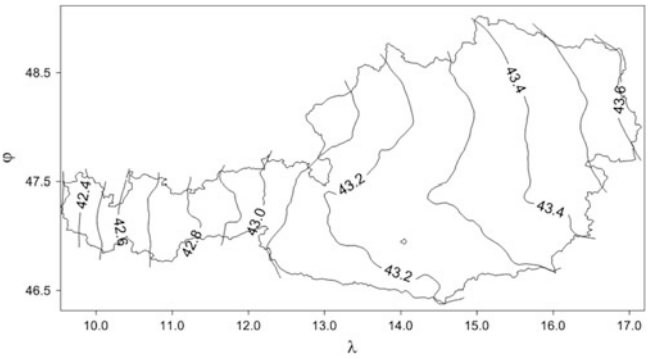

Fig. 1 Transformation surface of the astrogravimetric geoid of Austria used for the current investigation. Contour interval: 10 cm

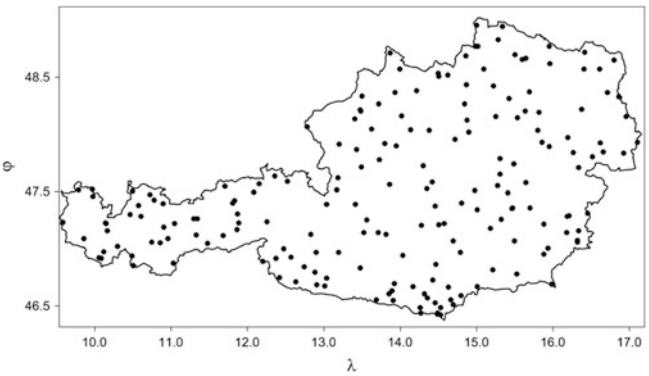

Fig. 2 Basic 192 GPS/Levelling for Austria

2 Basic Idea

The proposed fitting technique comprises the following tasks. In a first step gross errors among the GPS/levelling data are detected and deleted by a robust technique. It should be mentioned that the following steps will only give reasonable results if one can assure that there is no blunder in the GPS/levelling points used in the fitting process. In a second step the transformation surface between the GPS/levelling geoid and a gravimetric (astrogeodetic) geoid is derived. Also the minimum amount of fitting data points which are needed to model the transformation surface with a certain precision is identified in this step. In the third and final step the quality of the solution is checked independently by the GPS points not used to determine the transformation surface.

The GPS/levelling geoid heights N_{GPS} are given by $N_{GPS} = h_{GPS} - H_{lvl}$. Using data at several benchmarks the transformation surface between ellipsoidal heights h_{GPS} and a national height system H_{lvl} can be determined. Most important to all fitting techniques is the quality of N_{GPS} values, see, e.g. Featherstone and Sproule (2006), Fotopoulos et al. (2003), Iliffe et al. (2003) or Krynski and Łyszkowicz (2006). Possible sources for the falsification of N_{GPS} are:

Gross errors of h_{GPS} through wrong manual antenna height measurements or instabilities in the monumentation.

Systematic errors through assumptions and theoretical approximations, e.g. GPS model errors (tropospheric and ionospheric effects), the use of wrong model parameters in the evaluation of GPS heights, wrong or inexact orthometric height reduction, influences of geodynamic effects (uplift, land subsidence). Datum inconsistencies among the heights or long wavelength distortions in the levelling network due to historic reasons.

Random errors of the measurements used to compute h_{GPS} and H_{lvl}.

3 Test Environment

3.1 Geoid Computation

As testbed, the astrogravimetric geoid computation of Austria which was presented at the International Symposium on Gravity, Geoid and Height Systems in Venice 2012 was used. In brief the computation of this astrogravimetric geoid was done as follows. In a first step a dense grid of deflections of the vertical was predicted using the classical Vening Meinesz formula (Heiskanen and Moritz 1967). Afterwards the predicted deflections have been transformed to geoid differences by Helmert's formula. As the problem is overdetermined we have applied a least squares adjustment process where the geoid height of one single point is set to zero. This results in a mean offset of the astrogravimetric geoid of about 43 m which is apparent in the transformation surface given in Fig. 1.

Finally the geoid surface is fitted to GPS/levelling heights. For Austria a number of 192 GPS/levelling points is available; see Fig. 2. For all points, the orthometric height and the GPS height are given. This data set has been used for

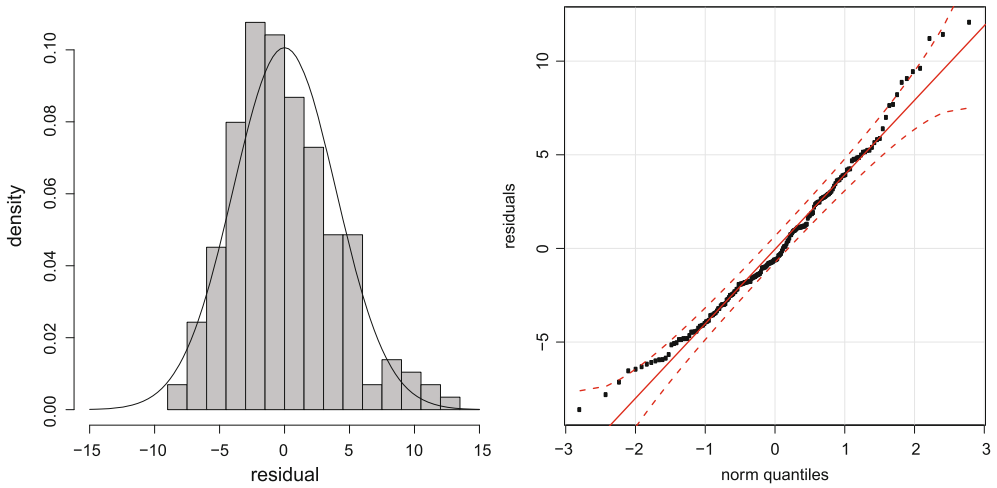

Fig. 3 Statistics of the remaining residuals if the transformation surface is modeled by a second order polynomial. The histogram on the *left hand side* is based on the residuals for the 192 GPS/levelling points. The *right hand side* shows the qq-plot of the residuals and the limits of a 95% probability of the normal distribution is existing (*dashed line*)

the recent geoid solution of Austria (Kühtreiber et al. 2011). The distribution of the data is more or less homogeneous, although in a few cases the distance between neighboring points is much less than the average point distance. This data set has been improved and checked several times through the last years. Therefore the assumption that no systematic or gross errors exist in the data set is justified for the moment.

3.2 Transformation Surface

In the following the transformation surface will be split into a trend part which is determined by least squares adjustment of a second order polynomial function and a residual part.

Figure 3 shows the statistics of the residuals reduced by the trend part. The histogram and the qq-plot of the residuals prove that besides some outliers the residuals are normally distributed. The standard deviation of the residuals is 4.0 cm and thus 68.8%, 95.3% and 99.5% of the residuals are within the limits of 1σ, 2σ and 3σ.

This is an additional indication that the values of the residuals are random and therefore least squares prediction can be applied (Kraiger 1988). The basic procedure takes advantage of the well-known formulas of collocation (Moritz 1980). For the estimation $\hat{l}_P$

$$\hat{l}_P = \mathbf{C}_P^T \bar{\mathbf{C}}^{-1} \mathbf{l} \tag{1}$$

with the corresponding prediction error σ_P^2

$$\sigma_P^2 = C_0 - \mathbf{C}_P^T \bar{\mathbf{C}}^{-1} \mathbf{C}_P \tag{2}$$

holds. Herein $\mathbf{C}_P$ is the vector of the covariances between $\mathbf{l}$ and l_P and $\bar{\mathbf{C}} = \mathbf{C} + \mathbf{D}$ is the sum of the covariance matrix of the l_i quantities and the noise variance-covariance matrix of the error of l_i. The covariances of the matrices $\mathbf{C}_P^T$ and $\mathbf{C}^{-1}$ are computed using the generalized covariance model of Hirvonen

$$C(s) = \frac{C_0}{(1 + A^2 s^2)^p} \tag{3}$$

which is an expansion of Hirvonen's function found in Heiskanen and Moritz (1967). The parameter A can be determined by

$$A = \frac{1}{\xi}(2^{1/p} - 1)^{1/2} \tag{4}$$

using the correlation length ξ which fulfills

$$C(\xi) = \frac{1}{2} C_0 \quad . \tag{5}$$

The second parameter of the generalized Hirvonen covariance model is p, which is closely related to the curvature parameter χ by

$$\chi = 2p(2^{1/p} - 1) \quad . \tag{6}$$

For details refer to Moritz (1976) and Kraiger (1988). The approximation error

$$\varepsilon_P = l_P - \hat{l}_P \quad , \tag{7}$$

the difference between the observed value l_P and the predicted value $\hat{l}_P$ may be used to define

$$\sigma_{\hat{l}} = \left(\frac{\sum \varepsilon_P^2}{N} \right)^{1/2} \tag{8}$$

the mean approximation error $\sigma_{\hat{l}}$.

4 Alternative Fitting Technique

As already mentioned in Sect. 2 the new proposed fitting technique consists of three steps. In the following the steps of the fitting process will be described in detail and illustrated by a practical example.

4.1 STEP 1: Bad Point Detection

The detection of bad GPS/levelling points needs the application of robust techniques. There are several techniques existing. For instance least squares collocation may be used as tool to detect gross errors (Tscherning 1991; Abd-Elmotaal and El-Tokhey 1997). The most important point is that the used technique has to be robust, as blunder values might be hidden. That means a data point which apparently shows a big difference between predicted and observed value may be correct but is falsified by a blunder in the neighborhood. Therefore, although the differences between predicted values and observed values are normally distributed, the simple empirical $3\,\sigma$ test, will not rigorously be applicable. Consider the example of fitting the astrogeodetic geoid solution (Sect. 3) to the GPS/levelling points shown in Fig. 2.

First of all, predictions are done for all measurements using the generalized Hirvonen covariance function given by Eq. (3). The optimal number of measurements needed for the prediction was determined empirically. The number of about 10–15 points around the prediction point proved to be a reasonable amount to speed up the computation time without losing precision (see also Kraiger 1988). For p a value of 0.25 was used. The predicted values are compared to the measurements (of course the observation at the predicted point has not been used for the prediction). Table 1 shows the part of a list which is sorted according to the absolute difference between the prediction value $\hat{l}_i$ and the measurement l_i starting from the biggest absolute difference. Considering Table 1, the first point in the list 143111 seems to be a gross error. We notice a difference of 37.9 cm which compared to the rms of the differences, which is 1.6 cm, is 20 times larger. If only this criterion is used to judge whether point 143111 is a blunder or not, we get a wrong result, as the measurement in 143111 is ok.

Consider therefore the information given in Table 2. We analyze all measurements which are used for the prediction in point 143111, but now we are interested in the impact of each measurement to the prediction result. The first row of Table 2 shows the predicted value $\hat{l}_{143111}$ if the 14 nearest points are used for the prediction. As result we get −34.0 cm. Row 2 gives the prediction value $\hat{l}_{143111}$ using the same measurements, but this time the value at point 143115 has not been used for the prediction. The corresponding value

Table 1 Comparison between predicted values ($\hat{l}_i$) and observations (l_i)

Line no.	i	l_i	$\hat{l}_i$	$l_i - \hat{l}_i$
1	143111	3.9	−34.0	37.9
2	133347	−0.6	−18.0	17.4
...				
14	112320	−3.0	4.7	−7.7
15	143115	−4.7	2.7	−7.3

All values are given in [cm]

Table 2 Prediction value $\hat{l}_{143111}$ using different observations

Points used for the prediction	$\hat{l}_{143111}$ [cm]	s [km]
All points (14)	−34.0	
All except 143115	2.1	6.9
All except 143184	−3.5	7.7
All except 143132	−35.2	18.3
All except 170089	−34.2	20.7
...	...	...

The measurement in point 143111 is $l = 3.9$ cm. s refers to the distance between the reference point and the omitted point

of 2.1 cm means that if the measurement at point 143115, which is nearest to 143111, is not used for the interpolation, the predicted value is close to the measurement! Row 3 shows the case if the information of 143184 is omitted. The prediction result of −3.5 cm is bad. If 143132 is not used (while 143115 and 143184 are used) to predict $\hat{l}_{143111}$, the result is totally off. This effect is similar for the rest of all points. The interpretation of Table 2 is, that the big discrepancy between measurement and prediction noticed in Table 1 is the result of a gross error in 143115 but not in 143111.

That means situations exist where the biggest differences between prediction and measurement occur for correct data points, while points with gross errors are not detected. Or in other words good points may be deleted if only the criterion based on Table 1 is used.

After thoroughly checking the GPS/levelling data set, two bad points could be detected and were eliminated from the reference data set. In the following a data set of 190 GPS/levelling points was used.

4.2 STEP 2: Selection of Fitting Points

If we disregard errors in the data (modeling errors as well as random errors) for the moment, then the difference between the computed geoid and the GPS/levelling data should be smooth. That means not all points need to be used for the fitting and can alternatively be used for an quasi-external and independent check of the accuracy of the geoid computation.

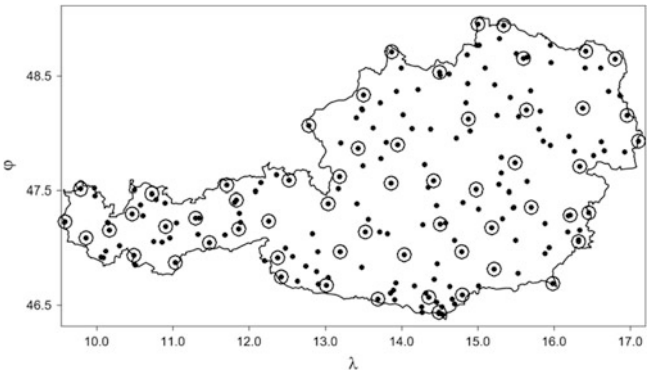

Fig. 4 The 58 Points used for fitting the geoid (*dots surrounded by circles*) and the 132 points used for external checking (*dots*)

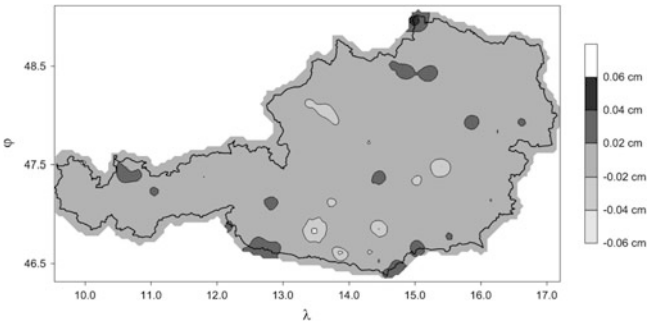

Fig. 5 Difference between the fitting surface based on all fitting points (190) and the fitting surface using a minimum amount of 58 fitting points

Figure 1 shows the transformation surface for our test case. The contour plot is based on a grid with a resolution of $0.03° \times 0.05°$ in the latitude and longitude directions, respectively. The grid was interpolated using all 190 fitting points in a least squares prediction process. As a reference for evaluating the effect of reducing the fitting points, the above mentioned transformation surface (based on all GPS/levelling points) was chosen. Consider our example. The challenge is to detect the minimum amount of fitting points needed, while the difference to the reference is kept within a predefined limit. Figure 4 shows the final reduced data set of 58 fitting points. If this reduced set of points is used to predict the transformation surface, the standard deviation of the difference to the reference is 1.1 cm, while the maximum and minimum difference are −4.5 and 5 cm respectively (see Fig. 5). The reduced data set is the result of a semiautomated process. First of all points along the border have been fixed. Afterwards the reduction of the points was done in an iteration. In each step the fitting points have been reduced depending on the information we get from Table 2, which has been computed for all points. These tables show whether a point has a huge impact on the prediction of the neighboring points or not. After the points with the small

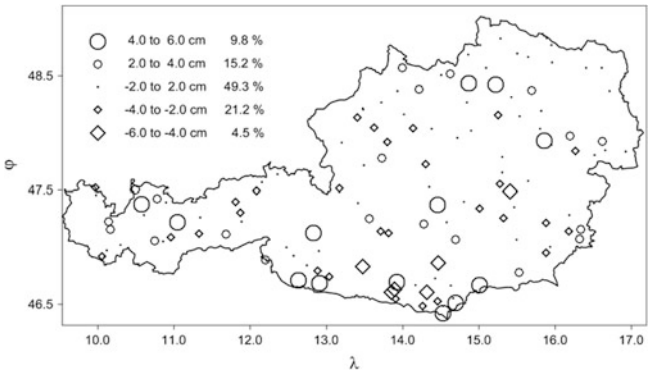

Fig. 6 External check of the geoid's accuracy resulting in a standard deviation of 2.8 cm

impacts are eliminated from the fitting points, the grid of the transformation surface is recomputed on the basis of the remaining fitting points. If the difference to the reference solution for the transformation surface (all GPS/levelling points are used) is bigger than a defined amount the reduction process is stopped. Of course STEP 2 will be developed to a fully automated process, in order to make the method applicable and time efficient.

4.3 STEP 3: Quality Assessment

Finally we can do a quality assessment by checking the interpolated geoid height with the known GPS/levelling height for all GPS/levelling points which have not been used in the geoid fitting process to describe the transformations surface. That means an external check can be done.

Figure 6 shows the result of the external check for our test. The differences are grouped in several classes. As a result we see that about 50% of the differences are between ±2 cm. The standard deviation of the differences is 2.8 cm. The minimum and the maximum difference are −6.1 and 5.7 cm. For nearly the whole area no correlation of the differences and the height or position of the corresponding GPS/levelling point is evident. On the other hand a cluster of high negative or positive differences is existing near the border in the most southern part of Austria. This area is a high mountainous area and part of the Eastern Alps in Europe. The reason for this evidence needs to be investigated in more detail when the proposed technique works in a fully automated mode.

5 Conclusion

The new fitting technique combines a gross error detection for the GPS/levelling points with the determination of the minimum amount of GPS/levelling points needed to describe

the transformation surface (difference between the national levelling height system and GPS derived heights). As additional advantage the residual GPS/levelling data can be used as external check. The proposed method has been applied in a case study for Austria. The proposed fitting technique performed very well. Two gross errors among the checked data set of GPS/levelling points could be detected. It was possible to describe the transformation surface by about one third of all existing benchmarks with a standard deviation of 1.1 cm and thereby allowing to estimate the precision of the fitting with 2.8 cm (external check).

In future the strength of the proposed technique will be shown by applying it to geoid surfaces computed by different techniques. Improvements are possible in the implementation of a fully automated process for the detection of bad points (STEP 1) and the selection of the minimum number of fitting points (STEP 2). As the selection of the fitting points is a time consuming optimization process, investigations on the effectiveness of this step are needed.

References

Abd-Elmotaal H, El-Tokhey M (1997) Detection of gross-errors in the gravity net in Egypt. Surv Rev 266:223–228

Featherstone WE (2001) Absolute and relative testing of gravimetric geoid models using Global Positioning System and orthometric height data. Comput Geosci 27:807–814

Featherstone WE, Sproule DM (2006) Fitting AUSGeoid98 to the Australien height datum using GPS/Levelling and least squares collocation: application of a cross-validation technique. Surv Rev 38:573–582

Fotopoulos G, Featherstone WE, Sideris, MG (2003) Fitting a gravimetric geoid model to the Australian height datum via GPS data. In: Tziavos IN (ed) Gravity and geoid 2002. Department of Surveying and Geodesy, Aristotle University of Thessaloniki, Thessaloniki, pp 173–178

Gatti A, Reguzzoni M, Venuti G (2012) The height datum problem and the role of satellite gravity models. J Geod 87:15–22

Heiskanen WA, Moritz H (1967) Physical geodesy. W.H. Freeman and Company, San Francisco and London

Iliffe JC, Ziebart M, Cross PA, Forsberg R, Strykowski G, Tscherning CC (2003) OSGM02: A new model for converting GPS-derived heights to local height datums in Great Britain and Ireland. Surv Rev 37: 276–293

Jekeli C (2000) Heights, the geopotential, and vertical datums. Technical Report 459, Department of Civil and Environmental Engineering and Geodetic Science, Ohio State University, Ohio

Kraiger G (1988) Influence of the curvature parameter on least-squares prediction. Manuscr Geodaet 13:164–171

Krynski J, Łyszkowicz, A (2006) Fitting gravimetric quasigeoid model to GPS/levelling data in Poland. In: Proceedings of the 1st international symposium of the international gravity field service (IGFS). Istanbul, pp 231–237

Kühtreiber N (2003) High precision geoid determination of Austria using heterogeneous data. In: Tziavos IN (ed) Gravity and geoid 2002. Department of Surveying and Geodesy, Aristotle University of Thessaloniki, Thessaloniki, pp 144–149

Kühtreiber N, Pail R, Wasle B, Pock C, Wirnsberger H, Hofmann-Wellenhof B, Of G, Steinbach O, Hoeggerl N, Imrek E, Ruess D, Ullrich C (2011) Improved Austrian geoid solution combining terrestrial and satellite gravity data (GEOID+). ASAP Phase VI Project - Final Report, Graz

Moritz H (1976) Covariance functions in least-squares collocation, OSU Rep 240

Moritz H (1980) Advanced physical geodesy. Wichmann, Karlsruhe

Smith DA (1998) There is no such thing as "The" EGM96 geoid: Subtle points on the use of a global geopotential model. IGeS Bull 8:17–28

Tscherning CC (1991) The use of optimal estimation for gross-error detection in databases of spatially correlated data. BGI Bull d'Inf 68:79–89

Voigt C, Denker H, Hirt C (2008) Regional astrogeodetic validation of GPS/levelling data and quasigeoid models. In: Observing our changing earth. Springer, Berlin, pp 413–420

Wang YM, Saleh J, Roman DR (2012) The US gravimetric geoid of 2009 (USGG2009): model development and evaluation. J Geod 86:165–180

Part IV

Observing, Understanding and Assessing Earth Hazards

Geodetic Imaging by Airborne LiDAR: A Golden Age in Geodesy – A Bonanza for Related Sciences

William E. Carter, Craig L. Glennie, and Ramesh L. Shrestha

Abstract

One and a half centuries after the founding of the IAG, geodetic imaging (GI) represents a golden age in geodesy, and a bonanza of never-before-available quantitative information for research in related fields of science. Airborne LiDAR (light detection and ranging) observations, and such derived products as 'bare earth' digital elevation models, are being used to study: earthquake deformation fields, fault slip rates, folding mechanisms, landslide dynamics, channel network evolution, soil mantle development, bedrock surface cracking, landscape response to tectonics, lava flow fluxes, marsh evolution, salmon habitat, beach erosion, forestry, and archaeological sites. LiDAR technology is still developing rapidly, with high priority being given to multi-color systems, and miniaturization that will enable the deployment of LiDAR in remotely piloted aircraft, a.k.a., drones. As such technological improvements become operational new scientific problems will be brought within reach of an increasingly diverse community of researchers.

Keywords

Geodetic Imaging • LiDAR • Unmanned Aerial Vehicle

1 Introduction

A 'golden age' in a specified art, skill, or activity is a period of historically high productivity, and in science is often associated with the introduction of new theory/technology, enabling the collection of greatly improved or completely new observations. One and a half centuries after the founding of the IAG, geodesy is enjoying a golden age, enabled by Einstein's theories of special and general relativity, and several new observing techniques developed during the past half century, including very long baseline Interferometry (VLBI), satellite (SLR) and lunar laser ranging (LLR), and global navigation satellite systems (GNSS). These space age observing systems have enabled geodesists to develop a global infrastructure, which in turn supports the operation of yet other observing techniques including airborne light detection and ranging (LIDAR), a.k.a, airborne laser scanning (ALS). Using ALS, geodesists are able to map hundreds, or even thousands, of square kilometers of terrain, including areas covered in dense vegetation or shallow water (up to several meters deep) and create 'bare earth' geodetic images (images of the surface of the earth in which the three-dimensional coordinates of all points are known relative to a well-defined geodetic reference frame, such as the international terrestrial reference frame (ITRF), at the time of the mapping), at resolutions of 5–10 points/m^2 and with 5–10 cm absolute vertical accuracy. High resolution (decimeter scale) geodetic 'bare earth' images, especially of areas hidden beneath dense vegetation, enable researchers to study terrain on landscape scales, at spatial and temporal resolutions never before possible, revolutionizing the study of phenomena as diverse as earthquake deformation fields, fault

Article Presented at IAG Scientific Assembly 2013

W.E. Carter (✉) • C.L. Glennie • R.L. Shrestha
University of Houston, Houston, TX, USA
e-mail: wecarter@UH.edu

© Springer International Publishing Switzerland 2015

C. Rizos, P. Willis (eds.), *IAG 150 Years*, International Association of Geodesy Symposia 143,
DOI 10.1007/1345_2015_121

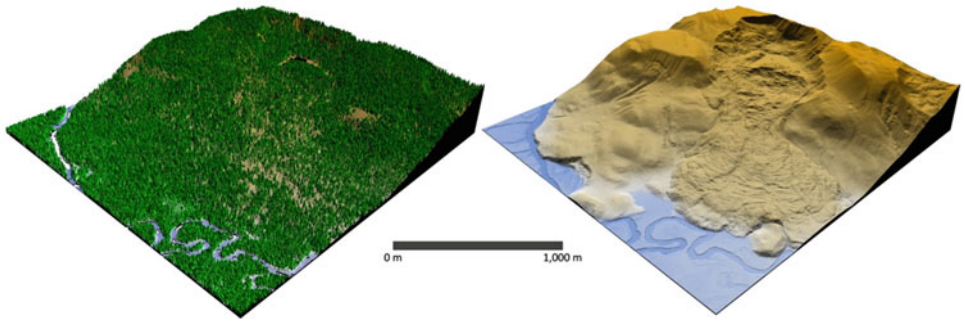

Fig. 1 False color geodetic images of an area near the Flathead River, Montana, created with ALS data collected by NCALM, revealing a large landslide hidden beneath a forest

slip rates, folding mechanisms, landslide dynamics, channel network evolution, soil mantle development, bedrock surface cracking, landscape response to tectonics, lava flow fluxes, marsh evolution, salmon habitat, beach erosion, forestry, and archaeological sites (Glennie et al. 2013).

2 The National Center for Airborne Laser Mapping (NCALM)

The initial cost of purchasing an ALS system is substantial: roughly a million dollars. Maintaining and operating the system, and processing the observations to extract high resolution geodetic images, can run into the hundreds of thousands dollars per year, depending on the locations and extents of the areas mapped. In addition to the fixed costs there is also a steep learning curve involved in mastering the collection and processing of the observations. Significant errors can be easily introduced into the data set by improper survey operations, data processing or interpretation of the geodetic imaging products. Consideration of these factors led the National Science Foundation (NSF), in 2003, to approve a proposal by researchers at the University of Florida (now at the University of Houston) and the University of California, Berkeley, to establish and operate the National Center for Airborne Laser Mapping (NCALM), to provide ALS observations and derived products to NSF PIs (Principal Investigators). During the first decade of operation NCALM has done some 130 projects for 40 PIs and 70 graduate students, covering approximately 25,000 km^2. These projects have resulted in an ever increasing number of theses and dissertations, and more than 180 papers published in refereed journals, including *Nature*, *Science*, *Proceedings of the National Academy of Sciences*, and *Physics Today*. In 2012, one refereed paper, utilizing ALS observations collected by NCALM, was published, on average, every 9.7 days. NSF recently approved a proposal to extend the operation of NCALM for an additional 5 years, beginning August 1, 2013. The data for all of these projects are also made freely available to interested researchers, through NCALM's partnership with Open Topography (Crosby et al. 2011), through the web portal at www.opentopography.org.

3 Scientific Findings Derived from ALS Observations

There are far too many projects and scientific findings to provide a comprehensive overview of the impact that the ALS observations collected by NCALM during the past decade have had on various branches of science, in the limited space available here. A more in-depth overview, with an extensive list of references, is presented in (Glennie et al. 2013), and a few select scientific findings that have come from NCALM supported projects are presented below.

3.1 Landslides

In mountainous areas landslides are generally the dominant form of erosion, but the terrain is often covered with forest, making it difficult to locate and accurately map the extent of past or pending landslides. Monitoring areas subject to landslides using ground survey or aerial photographic techniques is too time consuming and costly to be practical. As a result, in populated areas, landslides (including so called mud slides) often result in loss of life and extensive property damage. Figure 1 is an example of how landslides, even in areas covered with pine forests, can be mapped with ALS. Because the 3D coordinates of all points in the geodetic images are known, the perimeter, area, and volume of such landslides can be calculated with better accuracy than ever before. Recently, extensive mapping of the Eel River, in California, led to the discovery of the site of a landslide that temporarily blocked the Eel River some 2,500 years ago, resulting in a genetic mixing of native anadromous fish (Mackey et al. 2011).

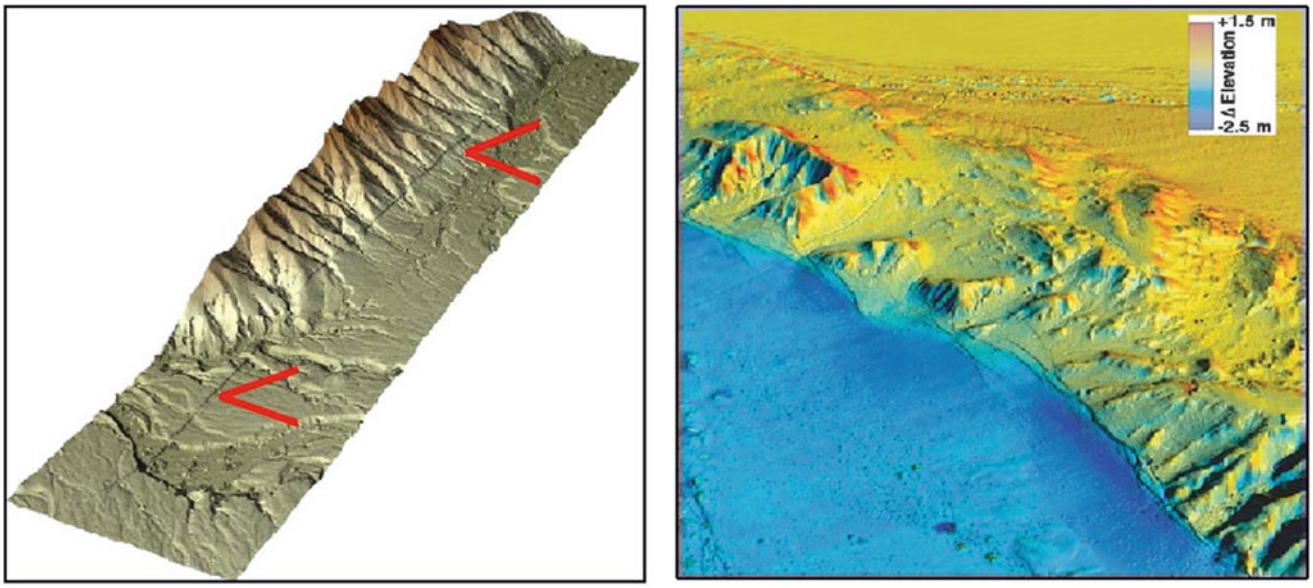

Fig. 2 On the *left* is a shaded relief geodetic image created from ALS observations showing the scarp created by the El Mayor-Cucupah earthquake; the *red hash marks* point to the approximate scarp location. On a *right* is a false color image (credit P. Gold, A. Elliot, and M. Oskin, keckcaves.org) of the difference between DEMs of ALS mappings before and after the earthquake

3.2 Active Tectonics

Another natural event that can result in loss of life and property damage is an earthquake. Many earthquakes are located along, or very near, existing fault lines. During the past decade NCALM has mapped a majority of the major fault lines in California, including sections that are covered with vegetation varying from desert scrub, to brush, to redwood forests. When future earthquakes occur along those faults it will be possible to re-map the vicinity of the affected fault line and quickly determine the magnitude and pattern of the surface ruptures. As luck would have it, the first area in western North America to be hit by a sizable earthquake since NCALM became operational did not occur in California, but in Mexico, on April 4, 2010. The earthquake is referred to as the El Mayor-Cucupah Earthquake, and it took a number of months for the funding and permits to be obtained before NCALM could map the area (see Fig. 2). Fortuitously, the area surrounding the El Mayor-Cucupah earthquake had been included in an ALS survey conducted some years earlier, collected by the Instituto Nacional de Estadística y Geografía (INEGI). The initial survey had much lower point density and precision than that done by NCALM, but nonetheless it provided an opportunity to use differential ALS (difference the digital elevation models (DEMs) created from the two ALS mappings) to estimate surface motions between the two mappings of 1–2 m in elevation along the scarp, which were presumably mostly directly associated with the recent earthquake (Fig. 2). Initial results from this analysis are presented in Oskin et al. (2012).

3.3 Bathymetry

It was mentioned above that some ALS systems can now map the surface of the earth in areas covered with shallow water, such as lakes, streams, and coastal waters. NCALM has a bathymetric sensor that utilizes a green laser that can penetrate water to depths of several meters, depending on the clarity of the water. The goal in developing this sensor was to be able to make seamless DEMs and geodetic images of areas of interest containing a mix of dry terrain and terrain covered by streams, lakes or coastal waters, such as those shown in Fig. 3, covering the inlet between the Gulf of Mexico and the Intracoastal Waterway, near Destin, in the panhandle of Florida. The ALS data captured the complex of buildings immediately next to the inlet, the break water, the sandy beaches and sand dunes surrounding the inlet, the water surface, and the terrain beneath the water, including waves in the sand on the bottom of the inlet, as well as areas covered with sea grass (Fernandez-Diaz et al. 2013).

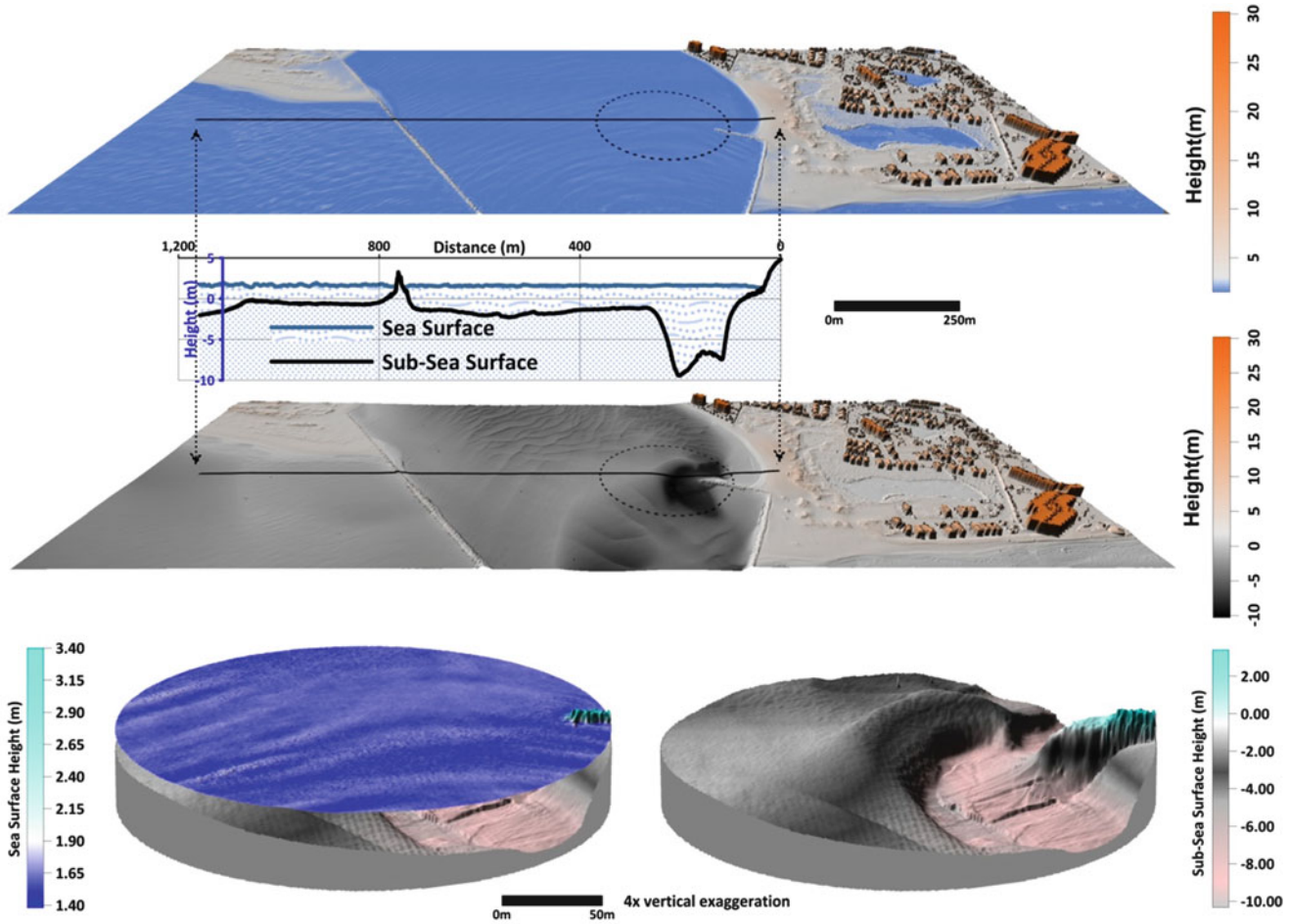

Fig. 3 From *top* to *bottom*, are: a false color geodetic image of the inlet, adjoining beaches and sand dunes, and residential area; a cross section of the inlet showing the depth of the water derived from the ALS observations; a shaded relief image of the area with the water removed; enlargements of the deep section of the inlet with and without the water

3.4 Archaelogy

ALS mapping is currently revolutionizing archaeological studies in Mesoamerica, especially in areas covered with heavy vegetation. For the first time it is possible for archaeologists to see landscapes hidden beneath rain forests, and the results have been compared to the introduction of radio carbon dating decades ago. Even at sites where archaeologists have been working for decades, ALS observations have revealed hundreds of previously undetected ruins of buildings, ancient roadways, extensive agricultural terracing, and openings to more than 60 previously undiscovered caves (Chase et al. 2011; Weishampel et al. 2011). In 2012 NCALM mapped a region in Honduras that explorers and archaeologists have been trying to penetrate since the conquistadors first arrived in the sixteenth century (Carter et al. 2012). Hidden below a triple canopy rain forest, NCALM used ALS observations to identify and precisely locate the ruins of two cities, as well as the remains of buildings and modifications to the landscape, scattered through the region (see Fig. 4).

3.5 Disaster Response

NCALM has mapped several areas with ALS for disaster preparation and response including: beaches before and after major storms and hurricanes; areas hit by forest fires; areas before, during, and after floods; crustal motions along major fault lines to estimate past motions, and to use with post-earthquake maps to quantity motion; and ground zero after the 911 terrorist attack to document event and help repair work (Fernandez-Diaz et al. 2012). Much more could be done, but the current use of ALS for disaster response is

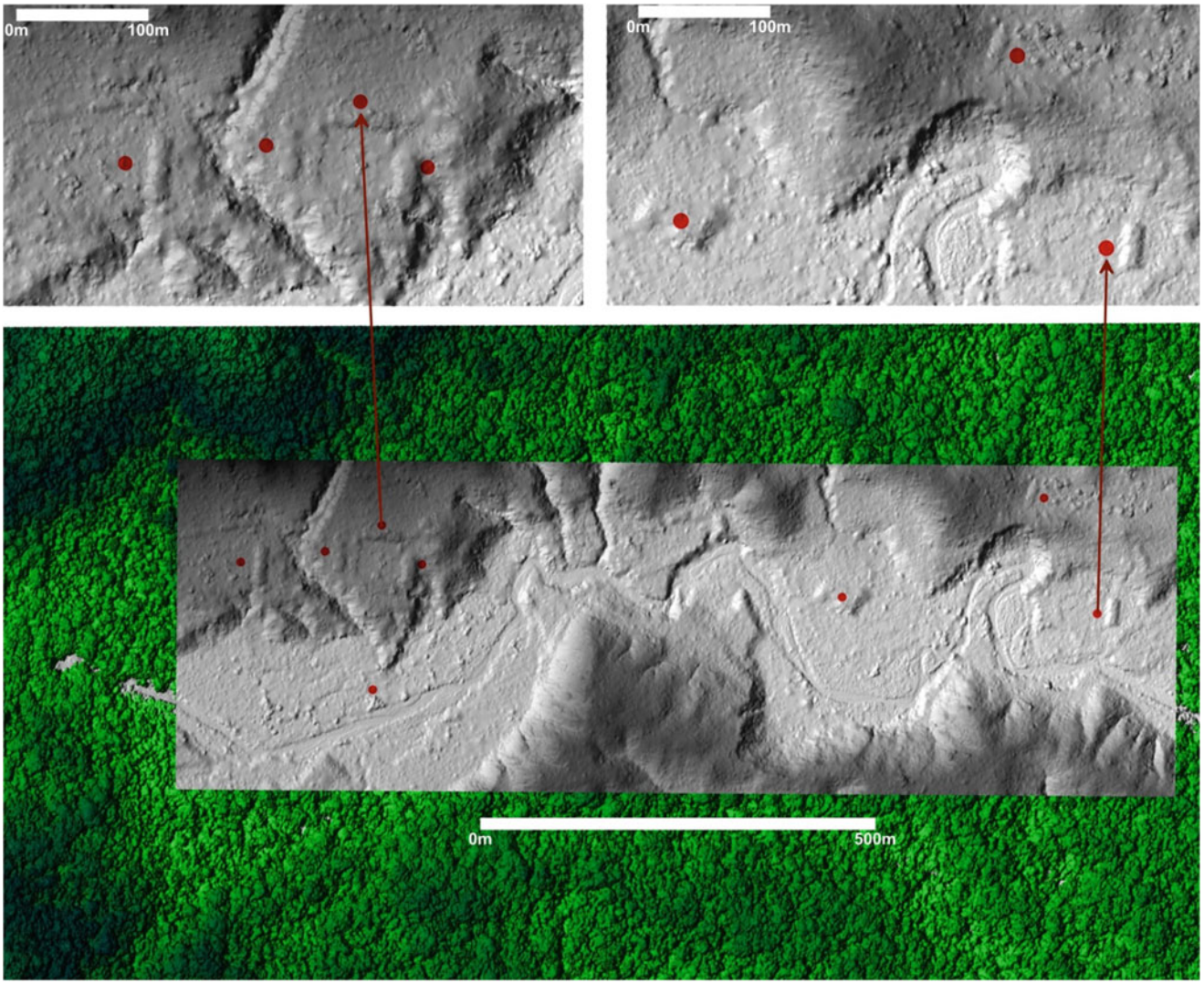

Fig. 4 This geodetic image shows an area in the Mosquitia region of Honduras where previously undiscovered archaeological ruins have been located beneath the dense fain forest. *Red dots mark* archaeological features

limited by: the cost of keeping aircraft, ALS equipment and personnel on standby for immediate deployment; receiving clearance to enter air space in disaster areas; and the limited flight times of piloted aircraft, which require local logistical support. Unmanned Aerial Vehicle (UAV) ALS currently under development will: reduce stand-by and mission costs; enable immediate response to disasters locally, regionally (Fig. 5) and, eventually, globally (Fig. 6); enable continuous monitoring of evolving disasters for periods of several days to weeks.

4 Concluding Remarks

One of the most striking changes in the practice of geodesy since the founding of the IAG 150 years ago is the quantity of observational data collected. One century after the founding of IAG geodesists worked with regional geodetic networks containing 'thousands and thousands' of ground stations,

Fig. 5 Photo shows and example of a moderate wingspan UAV that could immediately be used for local and regional ALS data collection

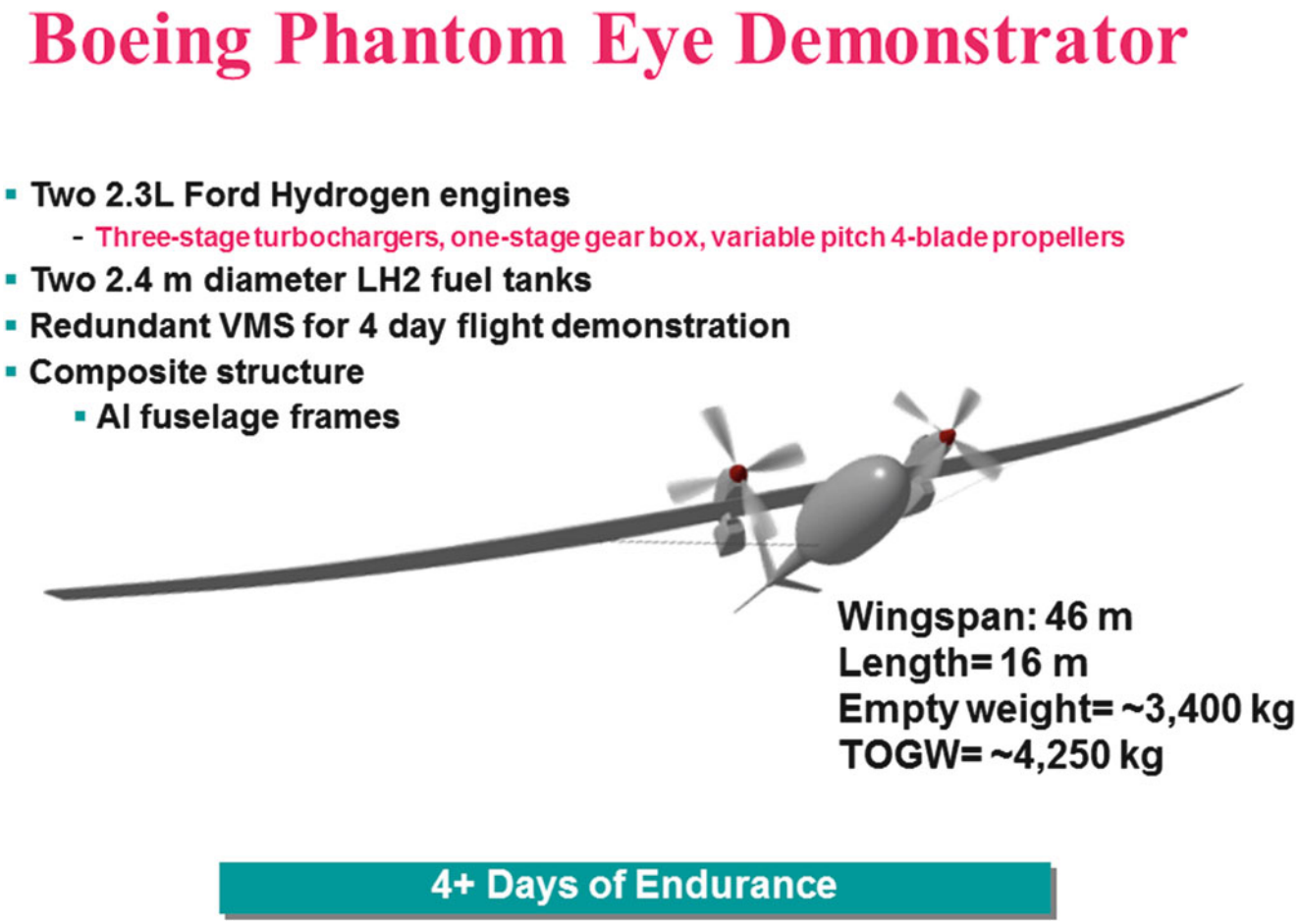

Fig. 6 Artist sketch shows an example of a large wing UAV being developed to operate at altitudes of 20 km or more, and eventually be able to stay aloft continuously for weeks (Credit: Boeing Aircraft Inc.)

derived from observations collected by ground survey teams. Today, one and a half centuries after the founding of IAG, geodesists work with 3-dimensional point clouds containing 'billions and billions' of points, collected by satellites, piloted aircraft and ground survey teams. One decade from now, 160 years after the founding of the IAG geodesists will likely be working with points clouds containing trillions and trillions of points, many, if not most, of which will be collected from UAVs.

References

Carter WE, Shrestha RL, Fisher C, Leisz S (2012) Geodetic imaging: a new tool for Mesoamerican archaeology. Eos Trans Am Geophys Union 93(42):413–415. doi:10.1029/2012EO420002

Chase A, Chase D, Weishampel J, Drake J, Shrestha R, Slatton K, Awe J, Carter W (2011) Airborne LiDAR, archaeology, and the ancient Maya landscape at Caracol, Belize. J Archaeol Sci 38(2):387–398. doi:10.1016/j.jas.2010.09.018

Crosby CJ, Arrowsmith JR, Nandigam V, Baru C (2011) Online access and processing of Lidar topography data. In: Keller R, Baru C (eds) Geoinformatics: cyberinfrastructure for the solid earth sciences. Cambridge University Press, Cambridge

Fernandez-Diaz JC, Shrestha RL, Carter WE, Glennie CL, Sartori MP, Singhania A (2012) NCALM's lessons learned and insights into the future from ten + years of providing geodetic images for the monitoring of hazards and the response to disasters. In: American Geophysical Union Fall Meeting, San Francisco, pp G53A–1128

Fernandez-Diaz JC, Glennie CL, Carter WE, Shrestha RL, Sartori MP, Singhania A, Legleiter CJ, Overstreet BT (2013) Early results of simultaneous terrain and shallow water bathymetry mapping using a single-wavelength airborne LiDAR sensor. IEEE J Selected Topics Appl Earth Obs Remote Sens (99):1–13. doi:10.1109/JSTARS.2013.2265255

Glennie CL, Carter WE, Shrestha RL, Dietrich WE (2013) Geodetic imaging with airborne LiDAR: the Earth's surface revealed. Rep Prog Phys 76(8):086801

Mackey BH, Roering JJ, Lamb MP (2011) Landslide-dammed paleolake perturbs marine sedimentation and drives genetic change in anadromous fish. Proc Natl Acad Sci. doi:10.1073/pnas.1110445108

Oskin M, Arrowsmith J, Corona A, Elliott A, Fletcher J, Fielding E, Gold P, Garcia J, Hudnut K, Liu-Zeng J, Teran O (2012) Near-field deformation from the el mayor-Cucapah earthquake revealed by differential LIDAR. Science 335(6069):702–705. doi:10.1126/science.1213778

Weishampel J, Hightower J, Chase A, Chase D, Patrick R (2011) Detection and morphologic analysis of potential below-Canopy cave openings in the Karst landscape around the Maya polity of Caracol, using airborne LiDAR. J Cave Karst Stud 73(3):187–196.10.4311/2010EX0179R1

Analysis of Precipitable Water Estimates Using Permanent GPS Station Data During the Athens Heavy Rainfall on February 22th 2013

Symeon Katsougiannopoulos, Christos Pikridas, Nicholas Zinas, Miltiadis Chatzinikos, and Stylianos Bitharis

Abstract

The Global Positioning System (GPS) has been used in the remote sensing of the atmosphere. A significant component of the atmosphere that affects the GPS signals is the zenith tropospheric delay (ZTD). The computation of ZTD estimates can directly or indirectly reflect weather variations. Through the analysis of ZTD values the hydrostatic and wet component of the total delay can be determined. For example, the wet tropospheric delay could be derived by subtracting the hydrostatic from the total delay. Hydrostatic delay can be estimated from surface or other meteorological data. The wet tropospheric delay can then be used in the derivation of the amount of precipitable water. Precipitable water plays a significant role in the physical and chemical processes of the atmosphere. It also greatly contributes to studies of weather forecasting and climate change. In this study GPS data from 12 permanent stations covering the broader area of the city of Athens, between February 18th and 24th, were used. This period was selected because of a heavy rainfall event on February 22nd. Data were processed using the GAMIT software and precipitable water (PW) estimates with 1 h time interval were derived. The PW values were analyzed in combination with meteorological data such as cloudiness, wind direction and precipitation obtained from the Hellenic Center for Marine Research and the Hydrological Observatory of Athens. The results indicate consistency between the estimated PW values and the related meteorological observations. This study suggests that a continuous record of PW estimates and meteorological variables is highly recommended for further studies on the behavior of the atmospheric water vapor and its contribution to the climate monitoring.

Keywords

Permanent GPS data • Precipitable water estimation • Weather front • Image analysis

1 Introduction

Atmospheric water vapor is extremely variable in both space and time and it's a key variable for weather and climate modeling and prediction. The radio signals transmitted from GPS satellites are delayed by the atmosphere before they are received on the Earth's surface. The delay caused by the neutral atmosphere is named the tropospheric delay. This delay can be converted to zenith tropospheric delay (ZTD) using an appropriate mapping function and can be separated into two components: the zenith hydrostatic delay (ZHD)

S. Katsougiannopoulos (✉) • C. Pikridas • M. Chatzinikos • S. Bitharis
Department of Geodesy and Surveying, AUTh, Thessaloniki, Greece
e-mail: sikatsou@gmail.com; cpik@topo.auth.gr; mchatzin@topo.auth.gr; stylbith@gmail.com

N. Zinas
Tekmon Geomatics LLP, Ioannina, Greece
e-mail: nzinas@tekmon.gr

© Springer International Publishing Switzerland 2015

C. Rizos, P. Willis (eds.), *IAG 150 Years*, International Association of Geodesy Symposia 143,
DOI 10.1007/1345_2015_16

which depends on the dry air gases and accounts for the biggest part of the tropospheric delay, and the zenith wet delay (ZWD) which depends upon the moisture content of the atmosphere (Schüler 2001; Hofmann-Wellenhof et al. 2008; Fotiou and Pikridas 2012). This "wet" delay, caused by atmopsheric water vapor, can be detected using GPS processing techniques once a model for the dry delay is removed. Precipitable water (PW) is the depth of water that would result if all atmospheric water vapor in a vertical column of air condensed to liquid. For that reason, estimated zenith wet delays by GPS can be converted to PW values (Hofmann-Wellenhof et al. 2008). A relative approach has been proposed by Bevis et al. (1992) and the amount of precipitable water (PW) contained in the neutral atmosphere can be derived with an accuracy of 1–2 mm (Rocken et al. 1995) using ground-based GPS stations (Karabatic et al. 2011).

On February 22th of 2013 a heavy rainfall event occurred in Athens resulting to big floods and damage to property and the environment. In this paper PW values were analyzed for few days before and after the rainfall event. These estimated values were combined with meteorological data such as cloudiness, wind direction and precipitation obtained from the Hellenic Center for Marine Research and the Hydrological Observatory of Athens.

2 GPS Data Analysis

For the estimation of PW values a GPS network consisting of 21 permanent stations was utilized. Twelve of those stations are located in Greece in the broader area of Athens. These stations are mapped in Fig. 1. The remaining nine stations are IGS stations (Dow et al. 2009) that contribute to EUREF network (Bruyninx 2004), forming long baseline distances. This choice was mandatory in order to retrieve absolute tropospheric delays. More specifically, for this kind of GPS network with interstation distances of several hundred kilometers (more than 500 Km) the GPS receivers at each end of a baseline observe common satellites at different elevation angles and as a consequence their signals are not affected from highly correlated errors (Duan et al. 1996).

We analyzed the GPS phase observations using the GAMIT software (Herring et al. 2010). A satellite elevation cutoff of 10° was used in the data processing. IGS final precise orbit information was retrieved from IGS directory referred to the IGS08 reference frame and the new IGS_08.atx model with absolute antenna calibration values was applied (Schmid 2013). The tropospheric delay was modeled using a priori values from the Saastamoinen model (Saastamoinen 1972) together with a standard atmosphere model for extrapolation. The estimated tropospheric delays were mapped to the zenith direction using the dry and wet GMF mapping function (Boehm et al. 2006). The derived Zenith Wet Delays are calculated according to relation $\mathrm{ZWD} = \mathrm{ZTD} - \mathrm{ZHD}$.

Estimated zenith wet delays (ZWD) by GPS can be converted to PW using the formula (Bevis et al. 1992; Schüler 2001):

$$PW = \frac{ZWD}{Q}. \tag{1}$$

The Q factor is expressed as:

$$Q = 10^{-6}\rho\frac{R_0}{M_W}\left(k_2' + \frac{k_3}{T_m}\right), \tag{2}$$

where ρ is the density of liquid water, R_0 is the universal gas constant, M_W is the molar mass of water vapor and T_m is the weighted mean temperature of the atmosphere in [K]. The physical constants k_2' and k_3 are taken from Davis et al. (1985).where, $k_2' = 17\ Kmb^{-1}$, $\quad k_3 = 3.776 \times 10^5\ Kmb^{-1}$

Finally the Q factor is given by,

$$Q = 0.10200 + \frac{1708.08}{T_m} \tag{3}$$

Concerning the parameter T_m, Bevis et al. (1992) suggested that it can be estimated from the surface temperature T_s because of the strong correlation between the two variables. In our study the parameter T_m was estimated according to the formula by Mendes et al. (2000) which holds for mid-latitudes.

$$T_m = 50.4 + 0.789 \cdot T_s \tag{4}$$

where, T_s: surface temperature in [Kelvin] and T_m: mean temperature of the atmosphere in [Kelvin]. Introducing the Eq. (4) into Eq. (3) then we get that:

$$Q = 0.10200 + \frac{1708.08}{50.4 + 0.789 \cdot T_s} \tag{5}$$

Combine the Eqs. (1) and (5), we have that PW equals to:

$$PW = ZWD \cdot \frac{50.4 + 0.789 \cdot T_s}{1713.221 + 0.0800478 \cdot T_s} \tag{6}$$

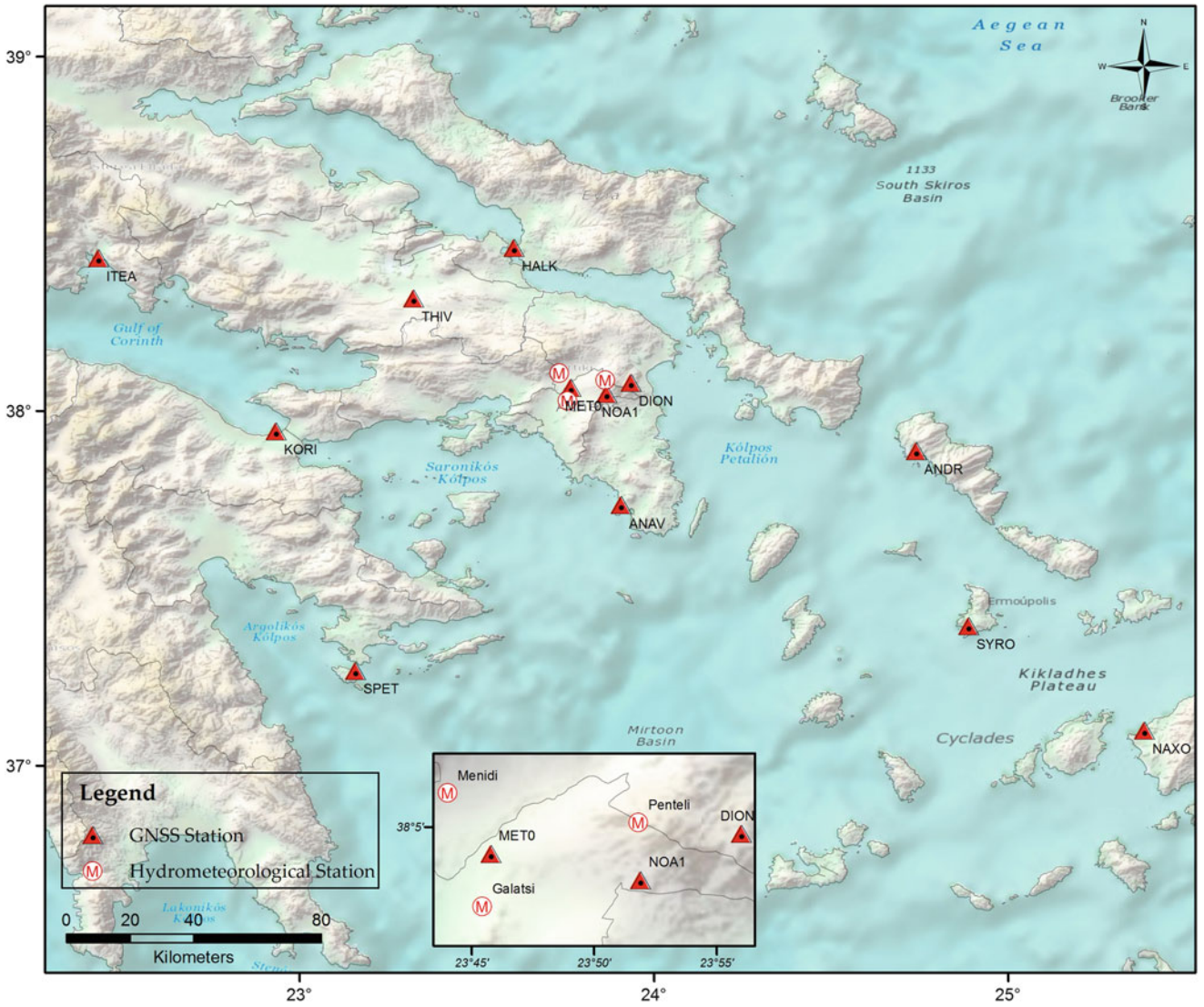

Fig. 1 The distribution of meteostations and GPS permanent stations within and over the broader area of Athens

Both, the numerator and the denominator of the above Eq. (6) are polynomial expressions. Dividing (between them) the two polynomials, we finally get the equivalent formula (Eq. 7), which was used in our study (Katsougiannopoulos 2008).

$$PW = ZWD \cdot \left[9.80392157 - \frac{16746.0706}{0.080478 \cdot T_s + 1713.24} \right] \tag{7}$$

The ZWD is given in [mm] and the surface temperature T_s in [K]. This equation is a useful formula to calculate the PW (in mm) from ZWD values, introducing only the surface temperature T_s. This formula is suitable for mid-latitudes.

3 Results

In our study, T_s values were used from surface observations provided by the Hydrological Observatory of Athens (http://hoa.ntua.gr). The estimated hourly PW values for the test period are illustrated in Fig. 2. Focusing on Fig. 2, two cases appeared which are related to different volumes of rainfall events. The first case refers to a light event that occurred on 19th February (DOY 50) and the second one depicts the heavy rainfall of February 22th (DOY 53).

As shown from Fig. 2 the computed PW values from GPS data processing reflect the cloudiness which existed

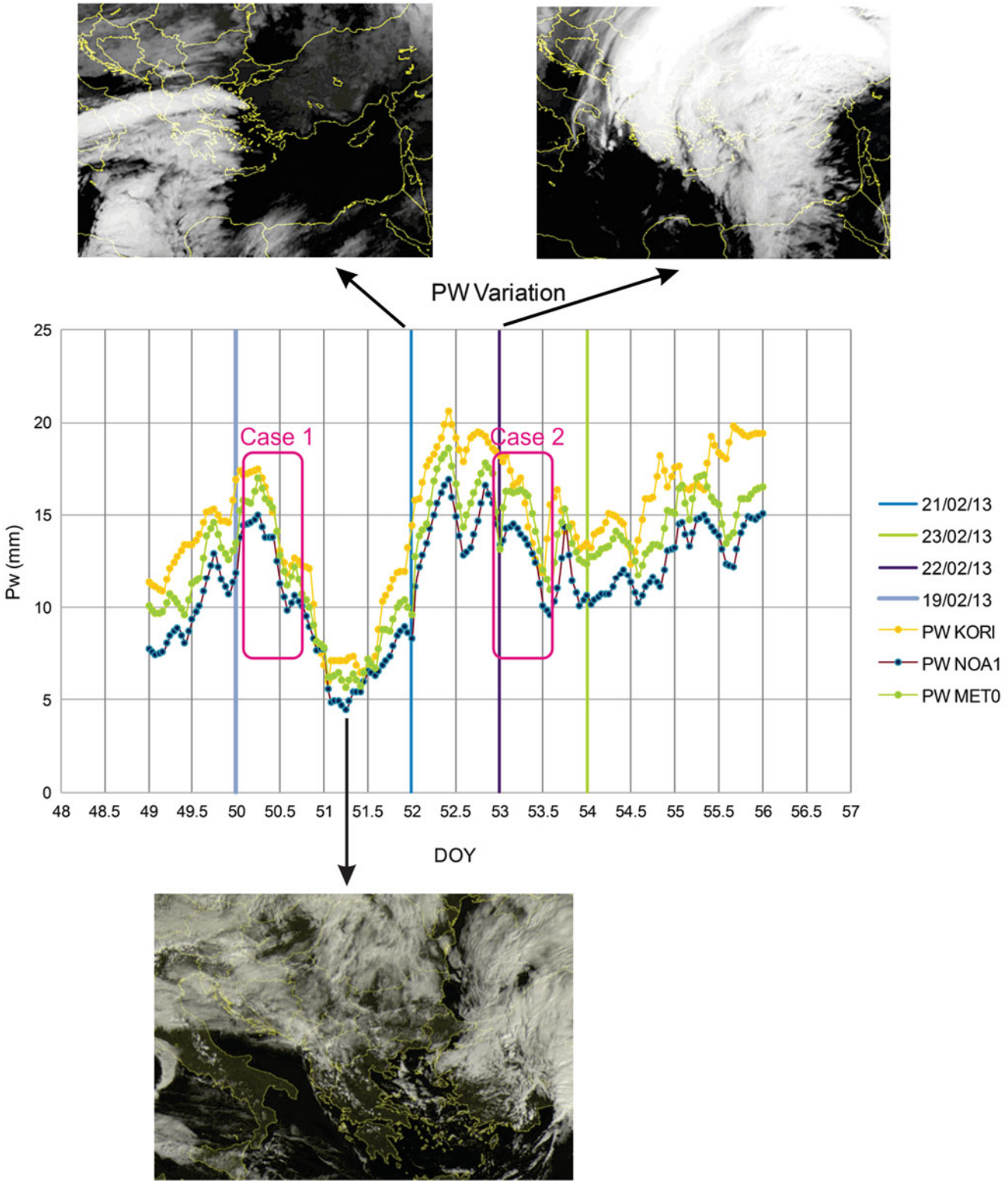

Fig. 2 Precipitable water variation values for GPS stations KORI, NOA1 and MET0 and the corresponding cloud aggregations

at that time in the atmosphere over the test area. Namely, high PW values correspond to high cloudiness while lower values correspond to sparsely cloud aggregations. This fact provides important information for the rainfall event and suggests that GPS tropospheric products are good indicators for such purposes. On this point we would like to address that

Table 1 ZWD and PW values for MET0 GPS station

DOY	ZWD (mm)	PW (mm)	f_{mean}	
			Greek area	Study area
51.2500	35.8	5.64	45.542	51.531
52.0000	60.7	9.56	132.303	169.256
52.4167	118	18.59	219.417	254.400
52.5833	91	14.34	228.243	250.886
52.8333	113	17.81	211.117	239.583
53.0417	97.7	15.40	171.795	242.923
53.2083	103.55	16.32	150.470	239.374
53.5833	69.3	10.92	125.340	212.336

high PW values do not necessarily mean that a high rainfall event will occur. This also depends on additional meteorological parameters like air temperature, relative humidity, wind direction etc. Cooling the air reduces its ability to hold water vapour, and triggers the formation of water droplets.

Further analysis of the three grayscale meteo images of Fig. 2 (using the ImageMagick v6.0 software) shown that cloud formation over the study area changed from 20.2 to 99.7% during the test period. The grayscale pixel average embodies the overall gray level of images. The image with more clouds percentage always has a larger gray-scale pixel average value (Changhui et al. 2013). The expression of calculating the average value (f_{mean}) is written as follows:

$$f_{\text{mean}} = \sum_{i=0}^{m-1} \sum_{j=0}^{n-1} \frac{f\,(i,j)}{m \times n} f\,(i,j)$$

$$f\,(i,j) = \text{gray-scale pixel value (0–255)}$$

$$m \times n = \text{Image size}$$

$$i,j = \text{Image coordinates}$$

Table 1 summarizes the related result values for station MET0 which is located inside of the Athens urban area.

Moreover, the correlation values between the term f_{mean} with ZWD and PW for the study area (Athens territory) reached at the level of 0.80 for both and for the Greek Area at the level of 0.76.

PW relaxation occurred for each event after the rainfall. Table 2 summarizes the correlation values, for the day with the heavy rainfall event, between PW and precipitation values (absolute values of PW, not the change of PW with precipitation values) of two permanent GPS stations located inside the urban area of the city of Athens and three nearby meteorological stations (Menidi, Galatsi, Penteli) provide the relevant rainfall values. Negative correlation values depict the fact that when a rainfall event occurs, then an associated PW value decreases. This shows that the rainfall correlates only with short-period drops in PW. In addition, a critical point which arises and has to be clarified is that a correlation coefficient which based (only) on a limited amount of data is not a robust promising technique. It is obvious that much more data samples and investigation is needed. As a consequence, in this study, this test comparison can be considered as a first approach, which in general can helps for further combination analysis of meteo-parameters and GPS related products.

Table 2 Correlation factors between total hourly rainfall and precipitable water values per stations

		Precipitation sensor stations		
		Menidi	Galatsi	Penteli
GNSS stations	MET0	−0.692	−0.893	−0.856
	NOA1	−0.724	−0.882	−0.852

In order to relate the PW amount with the precipitation values additional meteorological data such as temperature, wind direction as well as surface topography need to be considered. In case 2, the strength of PW relaxation is smaller than in case 1 but the precipitation is much higher. This is clearly shown for the same stations (Table 2) in Fig. 3 where in blue and red colors are the 19th and 22th rainfall values respectively. This issue is of important interest and will be discussed next.

Until now we have basically analyzed the amount of PW over the main urban area of the Athens, with rainfall data. But, this analysis may suffer from cloud formation status.

From Figs. 2 and 3 it becomes clear that PW values alone cannot show the precipitation amount because in both cases described above we get high PW estimates but with different rainfall height values. In a more detailed analysis it is considered necessary to take into account the contribution of the weather front motion. For this reason the case of the 22th of February is studied in detail. A weather front is often called a frontal zone. This zone is subject to rather strong turbulence and cloud formation which finally results to precipitation, because of the differences in wind patterns, temperature and humidity.

Figure 4 depicts the frontal motion for Friday 22th of February 2013. It's a satellite image where we can identify

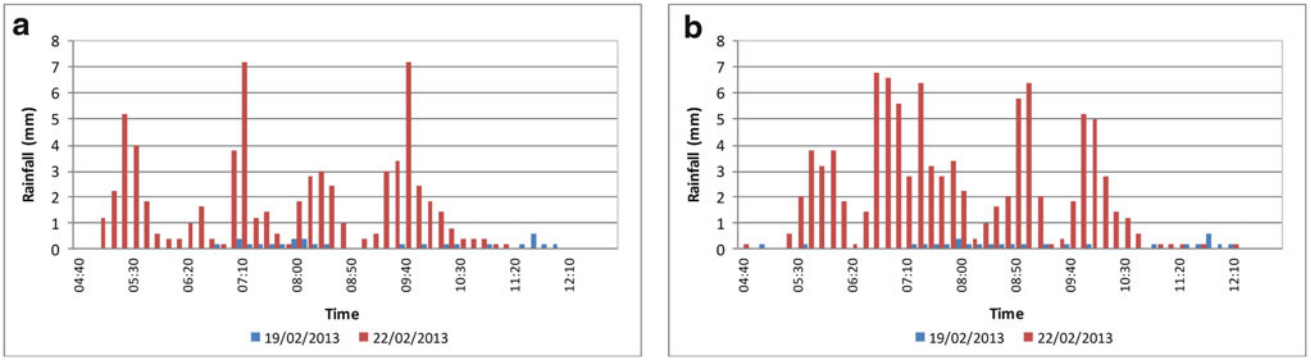

Fig. 3 Rainfall evolution for stations (**a**) Galatsi, (**b**) Penteli

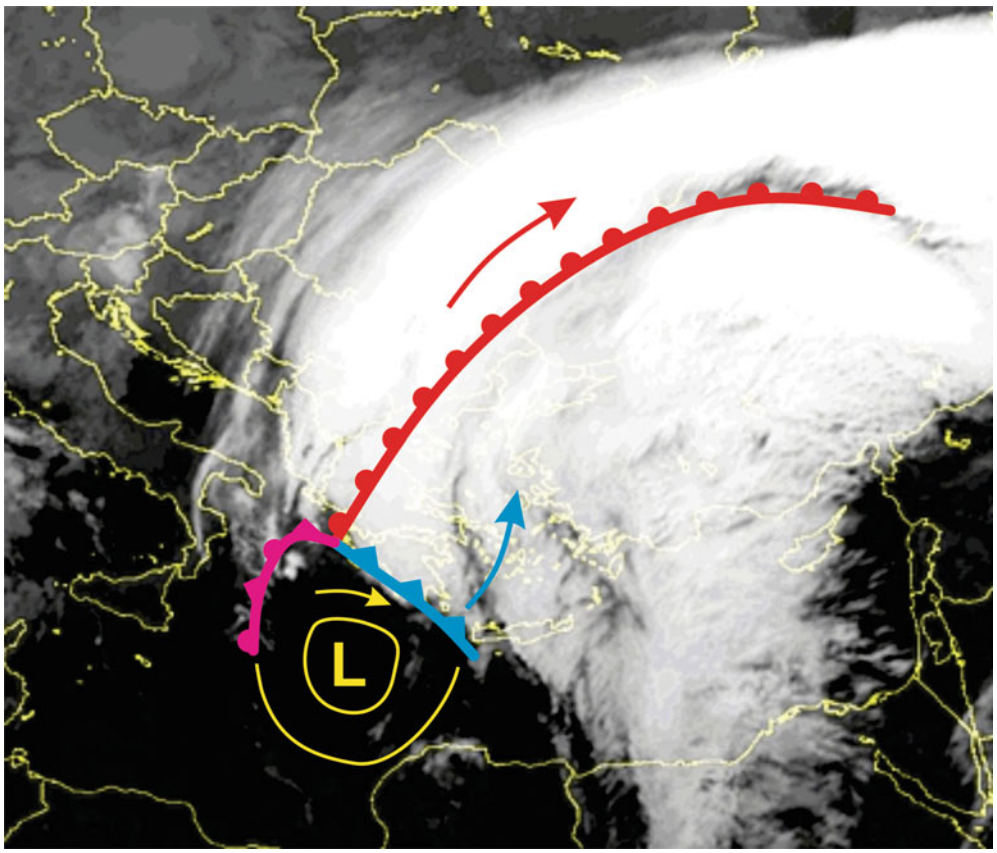

Fig. 4 Frontal system motions on Friday 22 of February 2013 (0:00 UTC)

fronts by the long, narrow bands of cloud that accompany them. The cold front has a southwest direction while at the same time (as shown in Fig. 5), strong south wind fields exist over the Aegean sea. In Greece, the cold fronts often have southwest direction and the same direction wind fields accompany them (Sachsamanoglou and Makrogiannis 1998). During the passage of a cold front, temperature falls rapidly, the wind veers, humidity stays high and pressure may undergo a sudden jump (Gregorius and Blewitt 1998).

Furthermore, we would like to note that the authors are currently working on a software development which will have the capability to correlate the wind and temperature field using grid data from ECMWF and PW values from GPS networks.

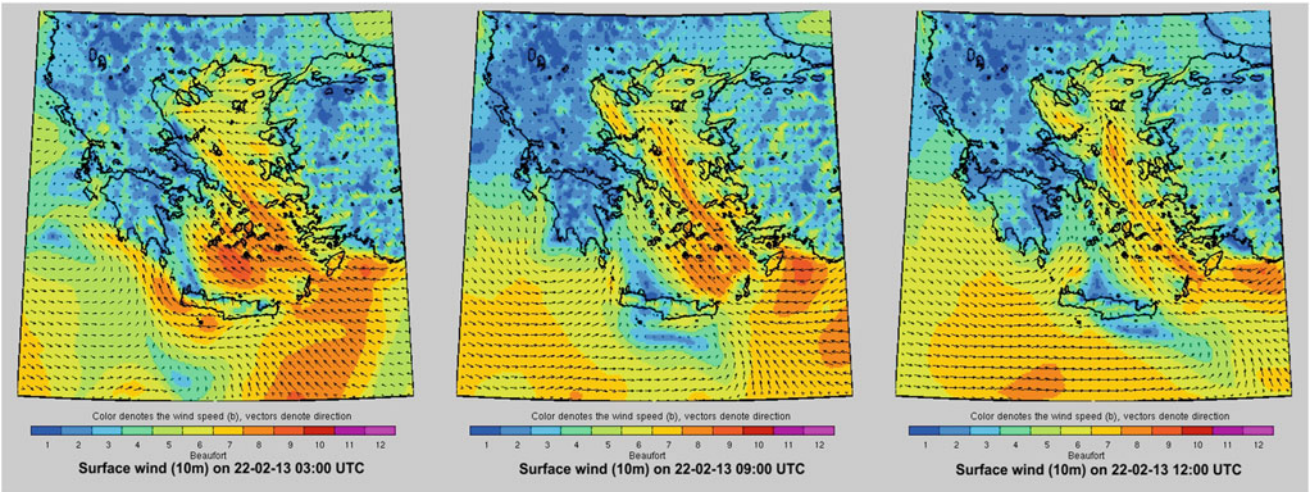

Fig. 5 Surface wind (Beaufort scale) on Friday 22 of February 2013 (*source*: Poseidon.hcmr.gr)

4 Conclusions

In this study, precipitable water values were calculated at 1 h time intervals for twelve permanent GPS stations. The geographical station distribution fully covers the city of Athens and its broader area. The study period covers 6 days within February 2013 when a heavy rainfall event occurred. For that reason PW values were analyzed with rainfall data for the same period. The analysis shows that, for all stations, after the rainfall the PW values decreased which reflects the relaxation phenomenon. This is also confirmed through the correlation analysis between total hourly rainfall per station and PW station values. In addition, the higher PW values over some GPS stations among the others, does not always reflect the rainfall status. Furthermore, the (long period) GPS tropospheric products (ZTD or PW values) are good indicators and can help to improve the physics of a weather model (Moll et al 2008).

References

Bevis M, Businger S, Herring TA, Rocken C, Anthes RA, Ware RH (1992) GPS meteorology: remote sensing of atmospheric water vapor using the global positioning system. J Geophys Res 97:15784–15801

Boehm J, Niell A, Tregoning P, Schuh H (2006) Global mapping function (GMF): a new empirical mapping function. Geophys Res Lett 33:L07304. doi:10.1029/2005GL025546

Bruyninx C (2004) The EUREF permanent network: a multi-disciplinary network serving surveyors as well as scientists. Geoinformatics 7:32–35

Changhui Y, Yuan Y, Minjing M, Menglu Z (2013) Cloud detection method based on feature extraction in remote sensing images. Int Arch Photogramm Remote Sens Spat Inf Sci XL-2-W1:173–177. doi:10.5194/isprsarchives-XL-2-W1-173-2013

Davis JL, Herring TA, Shapiro II, Rogers AE, Elgered G (1985) Geodesy by radio interferometry. Effects of atmospheric modeling errors on estimates of baseline length. Radio Sci 20:1593–1607

Dow JM, Neilan RE, Rizos C (2009) The international GNSS service in a changing landscape of global navigation satellite systems. J Geod 83:191–198. doi:10.1007/s00190-008-0300-3

Duan J, Bevis M, Fang P, Bock Y, Chiswell ST, Businger ST (1996) GPS meteorology: direct estimation of the absolute value of precipitable water. J Appl Meteorol 35:830–838

Fotiou A, Pikridas C (2012) GPS and geodetic applications, 2nd edn. Editions Ziti, Thessaloniki

Gregorius T, Blewitt G (1998) The effect of weather fronts on GPS measurements. GPS World 9(5):52–60

Herring TA, King RW, McClusky SC (2010) GAMIT reference manual: GPS analysis at MIT. Department of Earth Atmospheric and Planetary Science, Massachusetts Institute of Technology, Cambridge

Hofmann-Wellenhof H, Lichtenegger B, Wasle H (2008) GNSS – global navigation satellite systems. Springer, New York

Karabatic A, Weber R, Haiden T (2011) Near real-time estimation of tropospheric water vapour content from ground based GNSS data and its potential contribution to weather now-casting in Austria. Adv Space Res 47:1691–1703

Katsougiannopoulos S (2008) Study of tropospheric effect on GNSS signals. Application to the European area, PhD thesis, Department of Geodesy and Surveying, Aristotle University of Thessaloniki, Greece

Mendes VB, Prates G, Santos L, Langley RB (2000) An evaluation of the accuracy of models of the determination of the weighted mean temperature of the atmosphere. In: Proceedings of ION, 2000 National Technical Meeting, January 26–28, Pacific Hotel Disneyland, Anaheim, CA

Moll P, Poli P, Ducrocq V (2008) Assimilation of ground based GNSS data at Meteo France. Presentation at EGVAP workshop, November, Denmark

Rocken C, van Hove T, Johnson J, Solheim F, Ware R, Bevis M, Businger S, Chiswell S (1995) GPS Storm-GPS sensing of atmospheric water vapor for meteorology. J Atmos Oceanic Tech 12:468–478

Saastamoinen J (1972) Atmospheric correction for the troposphere and stratosphere in radio ranging of satellites. In: Henriksen SW, Mancini A, Chovitz BH (eds) The use of artificial satellites for

geodesy, vol 15, Geophysical monograph series. AGU, Washington DC, pp 247–251
Sachsamanoglou C, Makrogiannis T (1998) General meteorology. Editions Ziti, Thessaloniki
Schmid R (2013) IGS Antenna working group. In: Dach R, Jean Y (eds) IGS technical report 2012, pp 141–147
Schüler T (2001) On ground-based gps tropospheric delay estimation. PhD thesis, Institute of Geodesy and Navigation University FAF Munich, Germany

Airborne LiDAR Data as a Base for the Open Space 3D Model Construction

Eimuntas Paršeliūnas and Dominykas Šlikas

Abstract

Digital elevation models (DEM) provide basic information on heights of the Earth's surface and objects upon it. The specific terms Digital Terrain Model (DTM) and Digital Surface Model (DSM) are often used to specify the surface objects described by an elevation model. A DTM usually refers the physical surface of the Earth, when a DSM describes the upper surface of the landscape. In any case, a digital elevation model is the interface between the Earth's surface and the air. When modelling the interface to the air, we would like to introduce a kind of DSM – Open Space 3D Model, which is restricted by a surface generated over the physical Earth's surface, natural and artificial objects, and in which the distances between the rough elements of this surface are not less than a given critical tolerance. In other words we have in mind the moving objects of the certain dimensions, which could freely move in such open space. The open space surface is similar to a digital surface model, therefore in general it is more smoother.

The technological peculiarities of an open space 3D model generation are analysed. The two main sources of data were suggested to apply: the raw airborne LiDAR data and the orthophotomaps. The method for generation of an open space surface is presented too.

An open space 3D model on experimental territory was generated. The data of single orthophotomap at a scale of 1:10,000 (5×5 km) was applied. The comparisons against digital terrain model and digital surface model are given.

Keywords

Airborne LiDAR • Digital surface model • Digital terrain model • Open space 3D model

1 Introduction

The number of applications of the LiDAR (Light Detection and Ranging) data is growing up. One of the main motive for its usage is the high speed of data acquisition (Antanavičiūtė et al. 2013; Schickler and Thorpe 2001; Stankevičius and Kalantaitė 2009; Žalnierukas and Čypas 2006). One of the main fields of the LiDAR data usage in the geodesy and remote sensing is construction of the digital elevation models (Arrowsmith 2006; El-Sheimy et al. 2005; Meng et al. 2010; Sulaiman et al. 2010; Susaki 2012; Yan et al. 2012; Zhang and Whitman 2005). But the raw LiDAR data are not only geodetic heights, but also the information about other natural and artificial objects on Earth's surface (for example, vegetation, buildings, etc.) (Fowler 2001; Stankevičius and Kalantaitė 2009). We would like to propose the algorithm for generation of the open space surface model, which supplements the Earth's surface (digital surface model – DSM) and the relief surface (Digital Terrain Model – DTM) models group. The specific terms Digital Terrain Model (DTM) and Digital Surface Model (DSM) are often used to specify the surface objects described by an elevation model (Maune et al.

E. Paršeliūnas (✉) • D. Šlikas
Vilnius Gediminas Technical University, Geodetic Institute, Vilnius, Lithuania
e-mail: eimis@vgtu.lt; dominykas.slikas@vgtu.lt

© Springer International Publishing Switzerland 2015

C. Rizos, P. Willis (eds.), *IAG 150 Years*, International Association of Geodesy Symposia 143,
DOI 10.1007/1345_2015_27

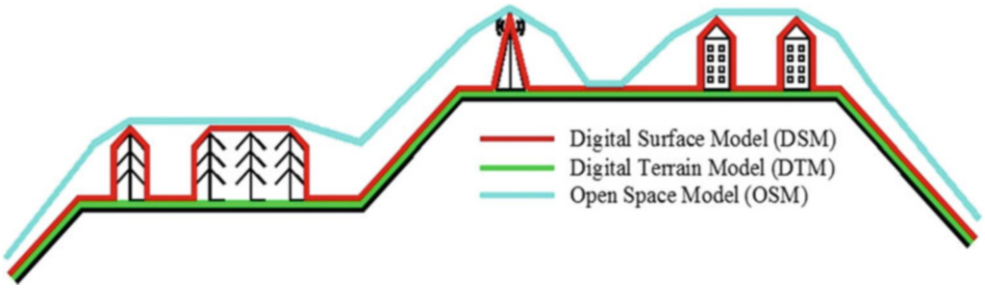

Fig. 1 Surfaces represented by a Digital Surface Model, Digital Terrain Model and Open Space Model

2001; Minnesota 2014). A DTM usually refers the physical surface of the Earth, when a DSM describes the upper surface of the landscape. In any case, a digital elevation model is the interface between the Earth's surface and the air. When modelling the interface to the air, we would like to introduce a kind of DSM – Open Space 3D Model.

An open space could be defined as a space, which is restricted by a surface, which is generated over the physical Earth's surface, natural and artificial objects, and in which the distances between its objects are not less than given critical tolerance (Kalantaitė et al. 2012). In non-urbanised territories and in the woodless areas the surface of the open space model coincides with the digital terrain surface and in the forests it will pass over the trees, in towns it will pass over the roofs of the buildings. In other words we have in mind the moving objects of the certain dimensions which could freely fly (move) in such open space. We intend to apply only 2D restrictions to moving objects, for example, airplane could move over the bridge, but not under it because there is no sufficient free space. The open space surface will be very close to the digital relief model surface in the agriculture areas and grasslands, but it will pass above trees in the forests, or over building's roofs in the cities (Fig. 1).

In some sense the open space 3D model is similar, for example, to the Digital Surface Model (DSM) or to the obstacles limitation map of the airport area (Eurocontrol 2011). However, the developers of such maps and models do not take into account the moving objects dimensions, so their final results are DSM's.

2 Experimental Data

In 2008–2010 the airborne LiDAR data were captured for all territory of Lithuania. According to the technical requirements, the density of the points approximately is four points per 1 m^2. This results to the acquisition of a very high resolution data set with a good spatial distribution. The accuracy of any airborne LiDAR data point is not worse than 15 cm in height component, and not worse than 30 cm in plane position (Žalnierukas et al. 2009). At the same time the colour orthophotomaps were produced also.

The raw airborne LiDAR data were classified into three groups: Earth's surface data, buildings data and vegetation data. Therefore for the purpose of development of the open space 3D model the data were divided into two sets: filtered data set – Earth's surface data, and non-filtered data set – all airborne LiDAR data. The research territory of 1 km^2 was chosen with a total amount of the airborne LiDAR data points – about 1.5 million (Fig. 2).

From the Fig. 2a it is obvious, that the density of the points in the area of the water body is fewer, than in the other places of a territory. It is even less than it should be according to the technical requirements. Therefore the surfaces of the water bodies are flat, and the lack of data points do not have significant influence on the quality of the open space 3D model.

3 Method of the Open Space 3D Model Construction

In the first step the 3D models based on the both data sets (Fig. 2) were generated. They were expressed by the Triangle Irregular Networks (TIN). In the second step the 3D model based on the non-filtered data set is combined with the orthophotomap to visualise the territory. This combination of the 3D model and the orthophotomap will be used for the control of the open space 3D model. In the third step we suggest to apply the local interpolation algorithm (Arrowsmith 2006; El-Sheimy et al. 2005; Meng et al. 2010; Sulaiman et al. 2010; Susaki 2012; Tang et al. 2013; Yan et al. 2012; Zhang and Whitman 2005) the result of which will lead to the generation of the open space 3D model. First of all the critical dimension X of the moving object should be defined. This dimension will be the cell size of the grid network of the open space 3D model. For example, let it be 10 m. Later the airborne LiDAR points are grouped according to the network cells, and in each cell the maximal value of the point's height is retrieved. These maximal height values are assigned to the

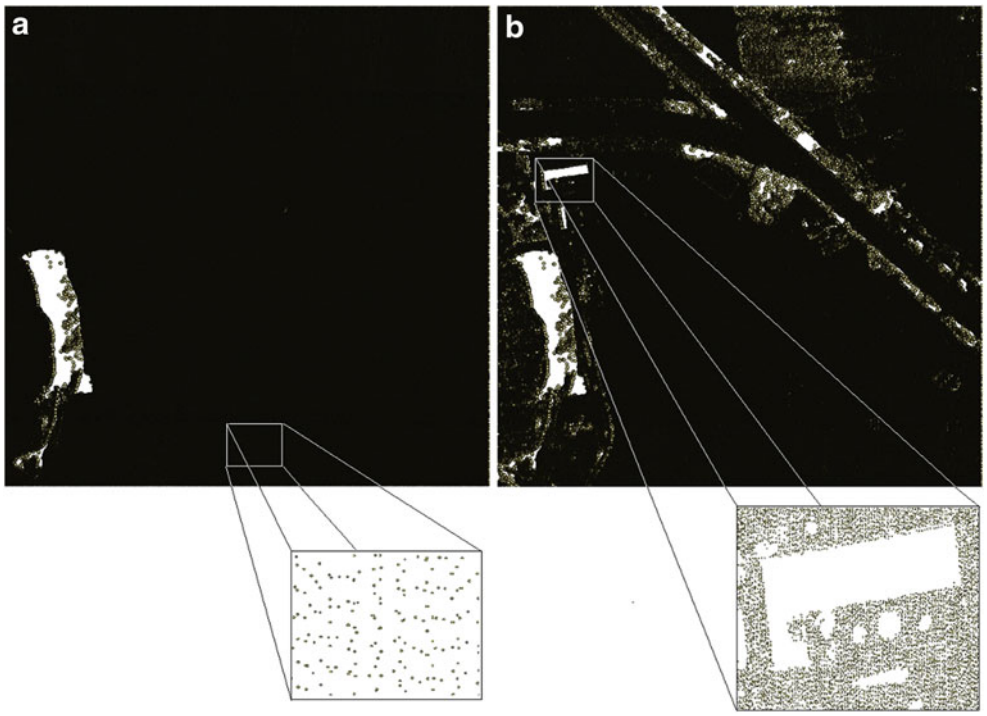

Fig. 2 Graphical views based on airborne LiDAR data sets (**a** – all points, **b** – Earth's surface data set)

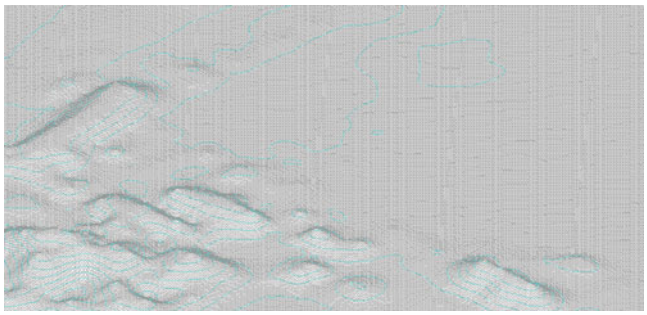

Fig. 3 Isometric view of the open space 3D model surface

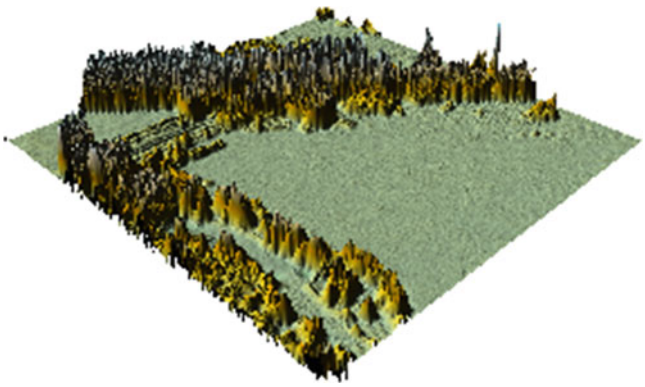

Fig. 4 Isometric view of the differences surface

central point of each cell. Graphical representation of the created open space 3D model surface is shown in the Fig. 3.

To test the open space 3D model we could create the surface based on all airborne LiDAR points (LiDAR surface), and later on to subtract from the LiDAR surface the open space 3D model surface to obtain the surface of two models differences (Fig. 4).

These differences should be with sign "+". Otherwise the open space 3D model will contain obstacles, that do not correspond to space 3D model definition.

To analyse more details of the quality of the open space 3D model we could create profiles along the created surfaces. For example, in the Fig. 5 the two profiles are shown: over the building and over the railroad.

It is seen, that in some places (for example, between points 11 and 12 of the profile to the left of the figure) the obstacles still remain in the open space 3D model. That's means, that an algorithm of the open space 3D model construction should be improved. It could be done by adding points with the maximal height values in the middle between the central points of the grid network cells. The number of the points in the open space 3D model will increase four times. Therefore the open space 3D model will be free from any obstacles. Also should be noted, that data of some obstacles like poles, antennas, towers should be included in the airborne LiDAR data set additionally and manually,

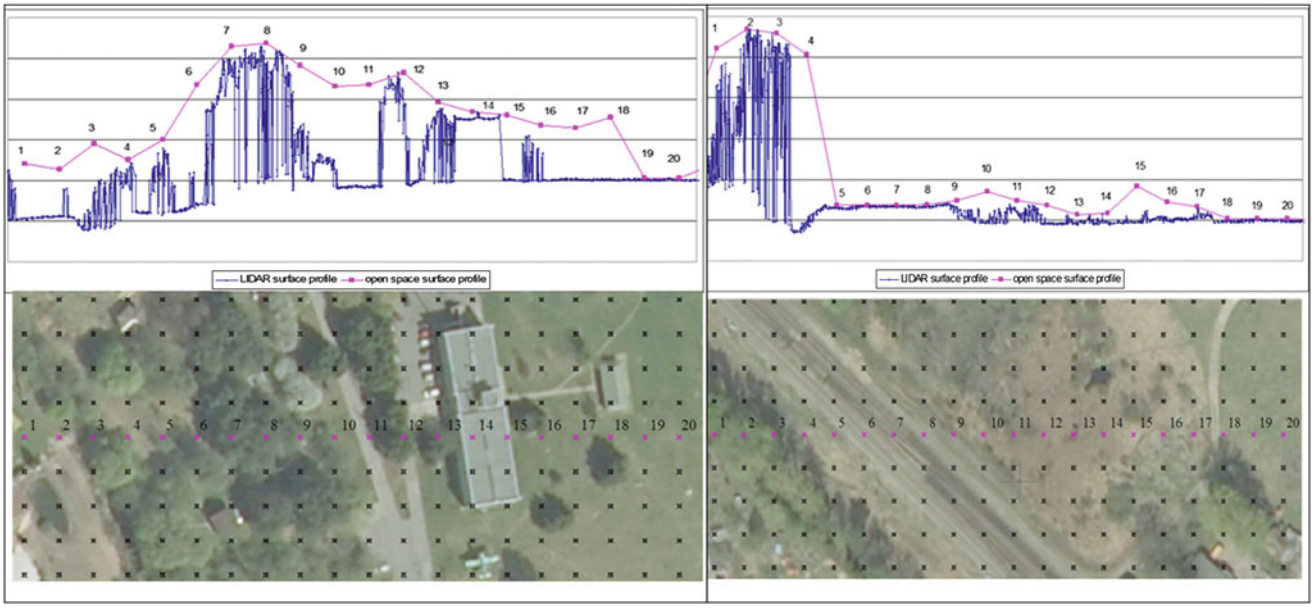

Fig. 5 Graphical view of the profile over the building and over the railroad

because these obstacles could not be detected by the LiDAR scanning process.

4 Conclusions

1. The concept of open space 3D model has been proposed, thus complimenting the group of the available digital models of the Earth's surface – Digital Surface Model (DSM) and Digital Terrain Model (DTM). The airborne LiDAR full data set was suggested to use for the construction of the open space 3D model.
2. The method for the development of the open space 3D model was presented. The method uses the local interpolation algorithm and the critical dimensions of the moving objects in the open space to create the grid network of the open space 3D model surface.

References

Antanavičiūtė U, Obuchovski R, Paršeliūnas EK, Popovas D, Šlikas D (2013) Some issues of the calibration of the Terrestrial Laser Scanner Leica Scanstation C10. Geod Cartogr 39(3):138–143. doi:10.3846/20296991.2013.840356

Arrowsmith JR (2006) Notes on LiDAR interpolation, p 12 (draft)

El-Sheimy N, Valeo C, Habib A (2005) Digital terrain modeling: acquisition, manipulation, and applications. Artech House, Boston, p 257

Eurocontrol (2011) Terrain and obstacle data manual, Edition 2.0, p 247

Fowler R (2001) Topographic LiDAR. In: Maune D (ed) Digital elevation model technologies and applications. American Society for Photogrammetry and Remote Sensing, Maryland, pp 207–236

Kalantaitė A, Paršeliūnas EK, Romanovas D, Šlikas D (2012) Generating the open space 3D model based on LiDAR data. Geod Cartogr 38(4):152–156. doi:10.3846/20296991.2012.758438

Maune DF, Kopp SM, Crawford CA, Zervas CE (2001) Introduction. In: David F, Maune (eds) Digital elevation model technologies and applications: the DEM users manual. ASPRS, Chapter 1, pp 1–31

Meng X, Currit N, Zhao K (2010) Ground filtering algorithms for airborne LiDAR data: a review of critical issues. Remote Sens 2:833–860. doi:10.3390/rs2030833

Minnesota LiDAR Research and Education Subcommittee (2014) Glossary of LiDAR-related terms. http://www.mngeo.state.mn.us/committee/elevation/research_education /MnLiDARGlossary.pdf, p16

Schickler W, Thorpe A (2001) Surface estimations based on LiDAR. In: Proceeding of the ASPRS annual conference, St. Louis, Missouri, p 11

Stankevičius Ž, Kalantaitė A (2009) Simplification algorithms of selection parameters of LiDAR ground surface points cloud. Geod Cartogr 35(2):44–49. doi:10.3846/1392-1541.2009.35.44-49

Sulaiman NS, Majid Z, Setan H (2010) DTM generation from LiDAR data by using different filters in open – source software. Geoinf Sci J 10(2):89–109

Susaki J (2012) Adaptive slope filtering of airborne LiDAR data in urban areas for digital terrain model (DTM) generation. Remote Sens 4:1804–1819. doi:10.3390/rs4061804

Tang J, Pilesjö P, Persson A (2013) Estimating slope from raster data – a test of eight algorithms at different resolutions in flat and steep terrain. Geod Cartogr 39(2):41–53. doi:10.3846/20296991.2013.806702

Yan M, Blaschke T, Liu Y, Wu L (2012) An object-based analysis filtering algorithm for airborne laser scanning. Int J Remote Sens 33(22):7099–7116

Žalnierukas A, Čypas K (2006) Airborne laser scanning technological analysis. Geod Cartogr 32(4):101–105

Žalnierukas A, Ruzgienė B, Kalantaitė A, Valaitienė R (2009) Analysis of accuracy of Lithuania city scanning by applying LiDAR method. Geod Cartogr 35(2):55–60. doi:10.3846/1392-1541.2009.35.55-59

Zhang K, Whitman D (2005) Comparison of three algorithms for filtering airborne LiDAR data. Photogram Eng Rem Sens 71(3):313–324

An Inventory of Surface Movements in the Upper Rhine Graben Area, Southwest Germany, from SAR-Interferometry, GNSS and Precise Levelling

Thomas Fuhrmann, Andreas Knöpfler, Michael Mayer, Andreas Schenk, Malte Westerhaus, Karl Zippelt, and Bernhard Heck

Abstract

Recent surface movements in the Upper Rhine Graben (URG) area are investigated with geodetic techniques. Line of sight (LOS) displacement rates from SAR interferometry (InSAR), horizontal and vertical rates from coordinate time series of permanent GNSS sites and vertical rates from precise levelling measurements are estimated with high accuracy. We show that the data sets are capable of providing detailed insight into the current movements in the URG area, which is required for a better understanding of geodynamic processes as well as for a reasonable exploitation of geopotentials in the URG. This paper focusses on a comparison of results from InSAR and levelling on a regional and on a local scale. A case study highlights temporal differences in the deformation characteristics of an oil extraction area detected from ERS-1/2 and Envisat data as well as from levelling measurements in multiple epochs. In order to benefit from the advantages of each technique, our work aims on a proper combination to consistently link the different observation methods in a rigorous multi-technique approach.

Keywords

GNSS • InSAR • Levelling • Surface movements • Upper Rhine Graben

1 Introduction

The Upper Rhine Graben (URG) is located in the border triangle between Germany, France and Switzerland and is considered to be the most seismically active region of NW Europe (Ziegler 1992; Lemeille et al. 1999) with a significant probability for the occurrence of destructive earthquakes (Meghraoui et al. 2001). In recent years, the URG is characterised by small tectonic movements, but an extensive use of its geopotentials, e.g., geothermal energy, raw oil and groundwater. Therefore, researchers and decision makers require precise information on the current displacements in the URG area. We use the data sets from InSAR, GNSS and precise levelling presented in Fig. 1 to estimate surface displacements.

The paper reviews the characteristics of the geodetic networks existing in the URG area (Sect. 2) and presents the currently available results of single method analyses for a region in the northern part of the URG (Sect. 3.1). A case study in an area partly affected by oil extraction provides insight into temporal characteristics of a man-induced displacement phenomenon (Sect. 3.2).

2 Database and Processing Strategy

The spatial distribution of stations and data sets used for the determination of displacements is shown in Fig. 1. SAR acquisitions from ESA's Earth observation satellites ERS-1/2 and Envisat are used from one descending and two ascending

T. Fuhrmann • A. Knöpfler • M. Mayer • A. Schenk • M. Westerhaus (✉) • K. Zippelt • B. Heck
Geodetic Institute, Karlsruhe Institute of Technology, Englerstr. 7, 76131 Karlsruhe, Germany
e-mail: malte.westerhaus@kit.edu

© Springer International Publishing Switzerland 2015

C. Rizos, P. Willis (eds.), *IAG 150 Years*, International Association of Geodesy Symposia 143,
DOI 10.1007/1345_2015_116

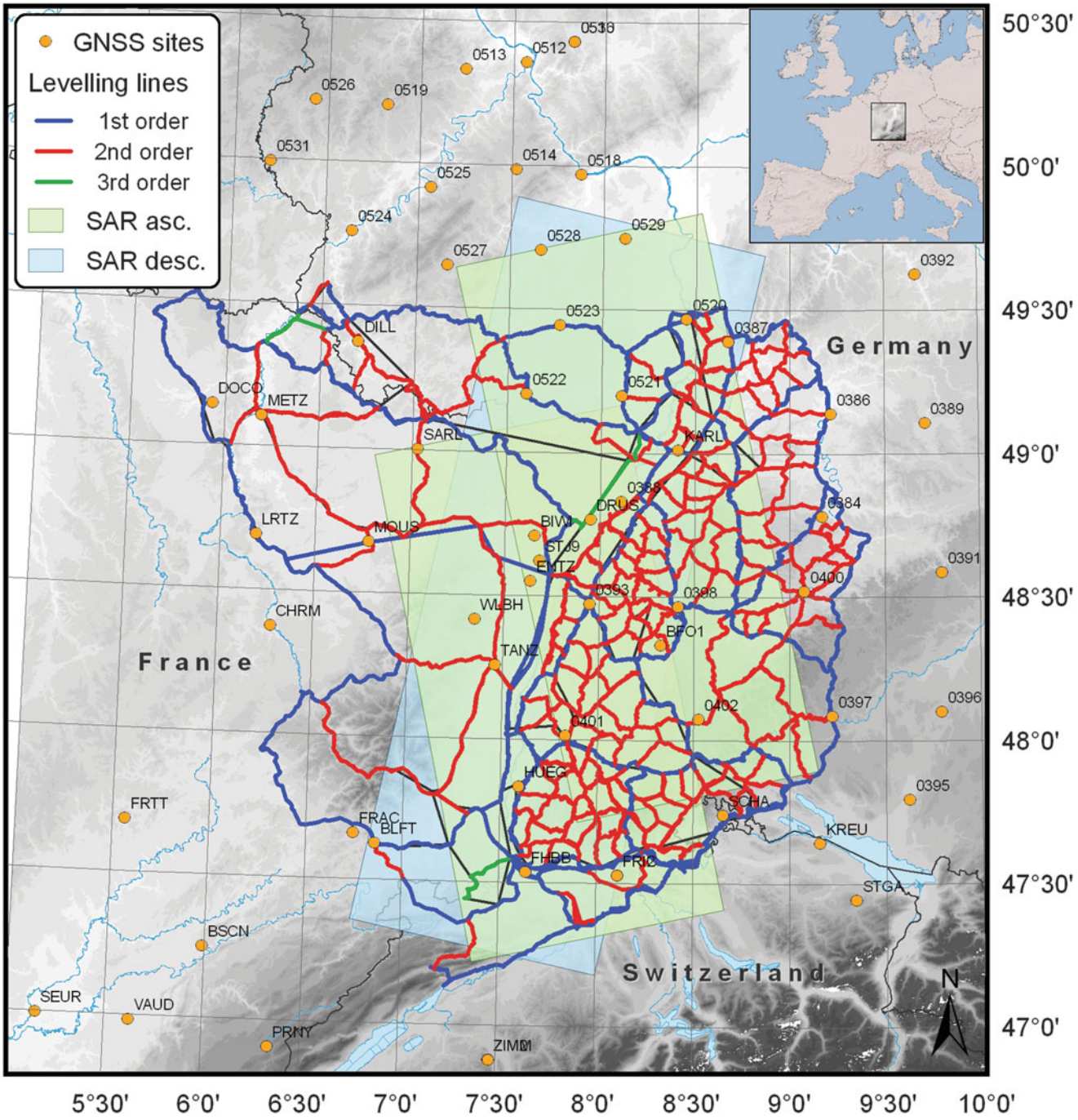

Fig. 1 Study area and spatial distribution of geodetic data sets: GNSS sites of the Upper Rhine Graben network GURN, ERS-1/2 and Envisat data of track 258, 487 (ascending) and track 294 (descending), and levelling lines of French, German and Swiss surveying agencies. In the French part, the last complete 1st order levelling was carried out in 1964. In 2001, a traverse from Strasbourg (STJ9) to Nancy (LRTZ) was measured comprising only few former benchmarks. *Black straight lines* mark historical data measured before the year 1900. The course of the historical lines sometimes differs from later measurements, e.g., north of Strasbourg and west of Basel (FHBB). The levelling benchmarks in these parts cannot be used for displacement estimation

tracks. Data of permanently operating GNSS sites are made available from different surveying agencies and companies in Germany, France and Switzerland within the transnational project GURN (GNSS Upper Rhine Graben network). Levelling campaigns are carried out by German, French and Swiss surveying agencies between fixed benchmarks following lines of different order. The characteristics of each data set and the processing strategies for the calculation of displacements from each technique are presented in the following subsections.

2.1 InSAR

To obtain a high accuracy for line of sight (LOS) displacement rates, ERS-1/2 and Envisat data from ascending and descending orbits covering a period from 1992 to 2000 and 2002 to 2010, resp., are being processed using the StaMPS (Stanford Method for Persistent Scatterers) software package (Hooper et al. 2007). As whole stripes of data along the URG are ordered from ESA's archives instead of standard frames, unfocussed raw data is used. The following steps are applied on the raw data for the determination of LOS displacements:

1. Focussing of raw data to create single look complex images using ROI_PAC (Rosen et al. 2004),
2. Coregistration and interferogram formation using DORIS (Kampes et al. 2003),
3. Persistent scatterer (PS) analysis using StaMPS (Hooper et al. 2007).

In contrast to the ascending tracks 258 and 487 displayed in Fig. 1, the descending track 294 has a similar orientation as the URG itself and appropriately covers our area of interest. Therefore, we started the InSAR processing with this track. The temporal distribution of SAR acquisitions used for the determination of LOS velocities in the Northern URG is shown in Fig. 2. Unfortunately, only 18 Envisat scenes are available at track 294 in the Northern URG. The ERS-1 and ERS-2 data are consistently processed in a common analysis, leading to a total number of 56 scenes.

As the expected displacements in the URG area are small and the analysed SAR data cover a large area, the separation of atmospheric effects and orbit errors plays an important role in the PS-InSAR processing chain. To reduce the influence of orbit errors, phase ramps are estimated for all slave images and subtracted from the deformation signal. In addition, to diminish atmospheric signals, spatially correlated noise is estimated for all slave images and subtracted from the interferometric signal using spatial filtering as described in Hooper et al. (2007). The result of the PS processing are LOS velocities at PS points mainly located in urban areas.

2.2 GNSS

The GNSS Upper Rhine Graben network has been formed in a research cooperation between the Institut de Physique du Globe de Strasbourg, Ecole et Observatoire des Sciences de la Terre, France and the Geodetic Institute, Karlsruhe Institute of Technology, Germany. GURN was established in September 2008 as a long-term project in order to derive displacement rates from time series of daily estimated site coordinates based on a highly precise and highly sensitive

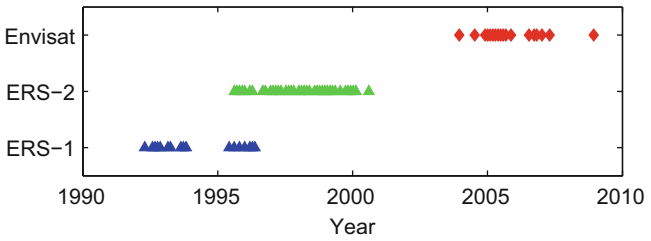

Fig. 2 Temporal distribution of SAR acquisitions from ERS-1, ERS-2 and Envisat at track 294, Northern URG area

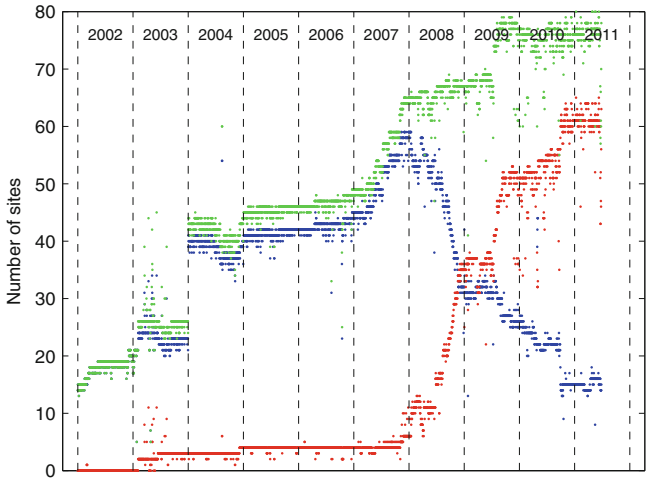

Fig. 3 Number of available GURN sites, from 2002 until 2011. *Blue*: GPS-only tracking sites, *red*: GPS+GLONASS tracking sites, *green*: total number of sites

network of permanently operating GNSS sites (Knöpfler et al. 2009). Figure 3 shows the evolution of the network sites. Since 2010 GURN consists of approx. 80 sites, most of them capable of tracking GPS and GLONASS signals.

In order to derive daily coordinate estimates at GURN sites, GNSS data are processed using the Bernese GNSS Software (Dach et al, 2007). Based on the ITRF2005 network solution and according to Nocquet and Calais (2003), residual velocities are calculated with respect to an European plate Euler pole estimated purely from the geodetic data set for each site using local topocentric coordinates (Northing, Easting, Up). To avoid a contamination with artificial jumps due to hardware changes at the GNSS sites, the estimation of linear velocities is restricted to periods of more than 2 years between known antenna changes using a robust linear regression approach, which is non-sensitive to outliers (Dumouchel and O'Brien 1989). Further details on the database and the processing strategy are given in Fuhrmann et al. (2013). The GNSS analysis provides 3D displacement rates at GNSS sites mostly located on buildings with typical distances of 50–60 km. As a matter of fact, the precision of the vertical

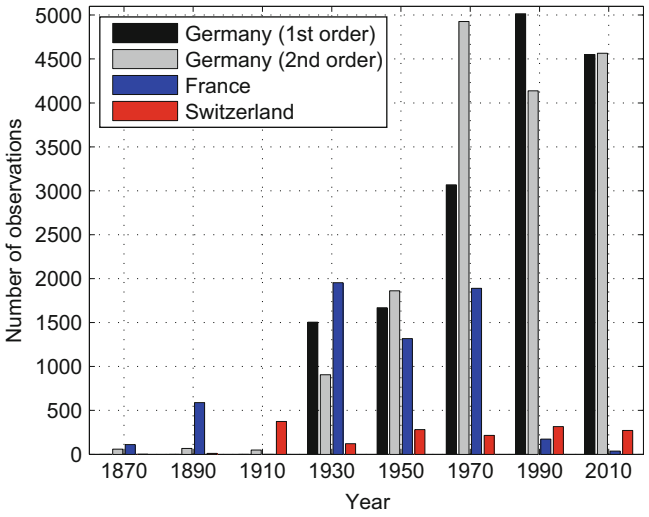

Fig. 4 Temporal distribution of levelling observations at repeatedly measured benchmarks for different groups of data

displacement component is worse by a factor of about two in comparison with the precision of the horizontal components.

2.3 Levelling

In contrast to InSAR and GNSS data, levelling data are available over a much longer time span in the URG area. Our analysis uses data from the end of the nineteenth century until today offering the possibility to detect small movements with high accuracy. The data have been recorded by the national surveying agencies of Germany, France and Switzerland along lines building closed loops of several 100 km length. The lines of the national networks are divided into different orders depicting the hierarchy of the measurements w.r.t. accuracy and repetition. As the data are measured by different surveying agencies, they are inhomogeneous in space and time (see Figs. 1 and 4, resp.). Only repeatedly measured levelling benchmarks are used for the calculation of displacements.

Due to the temporal inhomogeneities of the levelling network we apply a kinematic adjustment approach on the data directly yielding vertical displacement rates. The kinematic adjustment models a benchmark height using its elevation at a reference epoch plus the height change over time represented by a polynomial of low degree yielding coefficients for linear, accelerated and higher order terms (Zippelt 1988). We estimate linear and optionally accelerated motions by an adjustment procedure using a Gauss-Markov model with the measured height differences as observations. Further details on the kinematic adjustment approach including a quality check of levelling data using loop misclosures are provided in Fuhrmann et al. (2013).

Focussing on the local behaviour, a direct comparison of benchmark heights is performed in addition to the kinematic analysis. Fixing the height of a stable starting point of a line, heights are calculated for every benchmark along the line for every measurement epoch. A comparison of the heights at repeatedly measured benchmarks yields vertical displacements w.r.t. the starting point and the reference epoch. In contrast to the kinematic approach which yields average displacement rates, this method resolves for the temporal characteristics of a displacement. It is applied to data in the northern part of the URG for an investigation of increased deformation rates possibly caused by oil extraction. Both analysis strategies provide accurate vertical displacements at benchmarks with a high spatial resolution along a levelling line, but with large spatial gaps between the lines.

3 Results

First results from the three geodetic techniques are presented in this section. In a regional comparison (Sect. 3.1), vertical displacement rates estimated from levelling data are compared to LOS velocities at PS points estimated from a PS analysis of ERS-1/2 scenes of the descending track 294. A local case study (Sect. 3.2) compares results from levelling, InSAR and one GNSS site in an oil extraction area.

3.1 Regional Comparison

Figure 5 shows the vertical displacement rates in the Northern URG area from kinematic network adjustment of levelling measurements. Results for the region east of the River Rhine are presented in Fuhrmann et al. (2013). In total, more than 40,000 height differences have been used as observations yielding vertical rates at more than 15,000 benchmarks with an accuracy better than 0.3 mm/a for 90% of the rates. About 10% of the vertical rates have been classified as outliers since their value significantly differs from estimates at adjacent benchmarks. The reference point is located in a presumed stable region of the Black Forest (basement rocks) and has been measured in five epochs.

Additionally, the LOS velocities at approx. 256,000 PS points from a combined processing of 56 ERS-1/2 acquisitions are shown in Fig. 5. LOS velocities are estimated using time series of PS displacements in 55 interferograms w.r.t. a master scene (1997-08-18). Only velocities with a standard deviation less than 0.5 mm/a are displayed (>95% of all analysed PS points, mean value: 0.3 mm/a). The LOS velocities refer to a reference area located in a part of Karlsruhe, where the results from levelling reveal displacement rates within $\pm$ 0.1 mm/a.

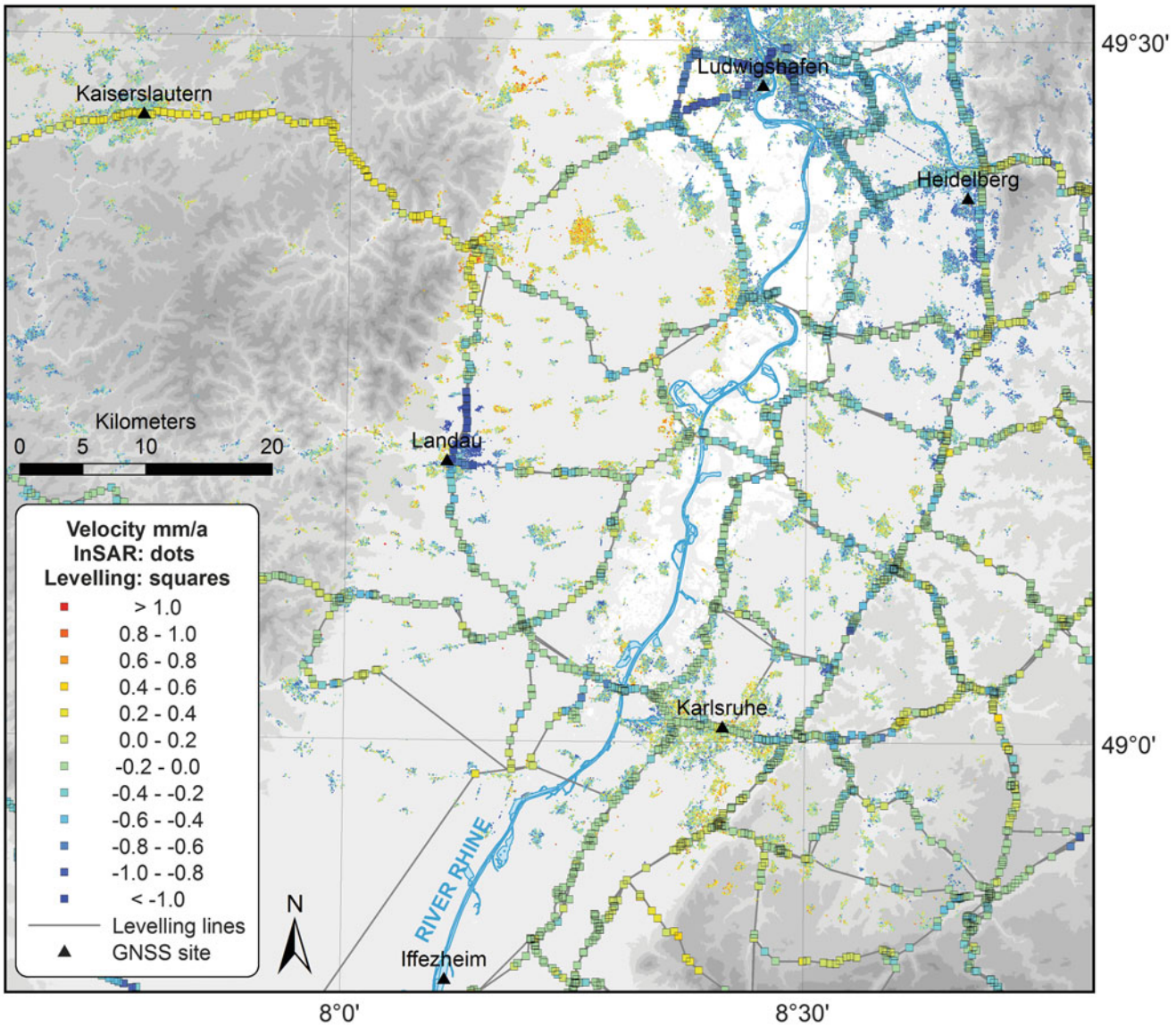

Fig. 5 Velocity estimates from PS analysis of ERS descending track 294 (LOS) and from kinematic adjustment of levelling data (*vertical*). The PS points are mostly located in urban areas, as the rural areas suffer from temporal decorrelation

Figure 5 gives a first impression of the spatial distribution of the available geodetic data in the URG region. The density of PS points is high in urban areas with significant gaps in forested and rural areas. Many of the urban PS clusters are connected via levelling lines that run along the main roads. The three data sets are linked in cities where GNSS data are available. Since only SAR data from the descending orbit has been processed so far, a comparison of the single method results is restricted to a few general conclusions. One has to keep in mind that (a) the rates from levelling are estimated using a longer time span of data than for the PS processing and (b) the rates from levelling are purely vertical whereas the LOS velocities from InSAR contain horizontal information as well. Nevertheless, we can conclude that tectonic displacement rates in the area are small since both techniques concurrently provide displacement rates that are mostly in the range of -0.5 to $+0.5$ mm/a. These results are in accordance with geological considerations. Analysing the levelling data a small uplift tendency is evident on the shoulders of the URG, particularly in the NW part ($+0.3$ mm/a), which is not fully supported by the SAR data. Two regions of increased subsidence rates presumably due to non-tectonic processes are clearly visible in both data sets: (a) Mannheim/Ludwigshafen possibly caused by groundwater usage, and (b) North of Landau possibly due to oil extraction. The latter is investigated in detail in the following section.

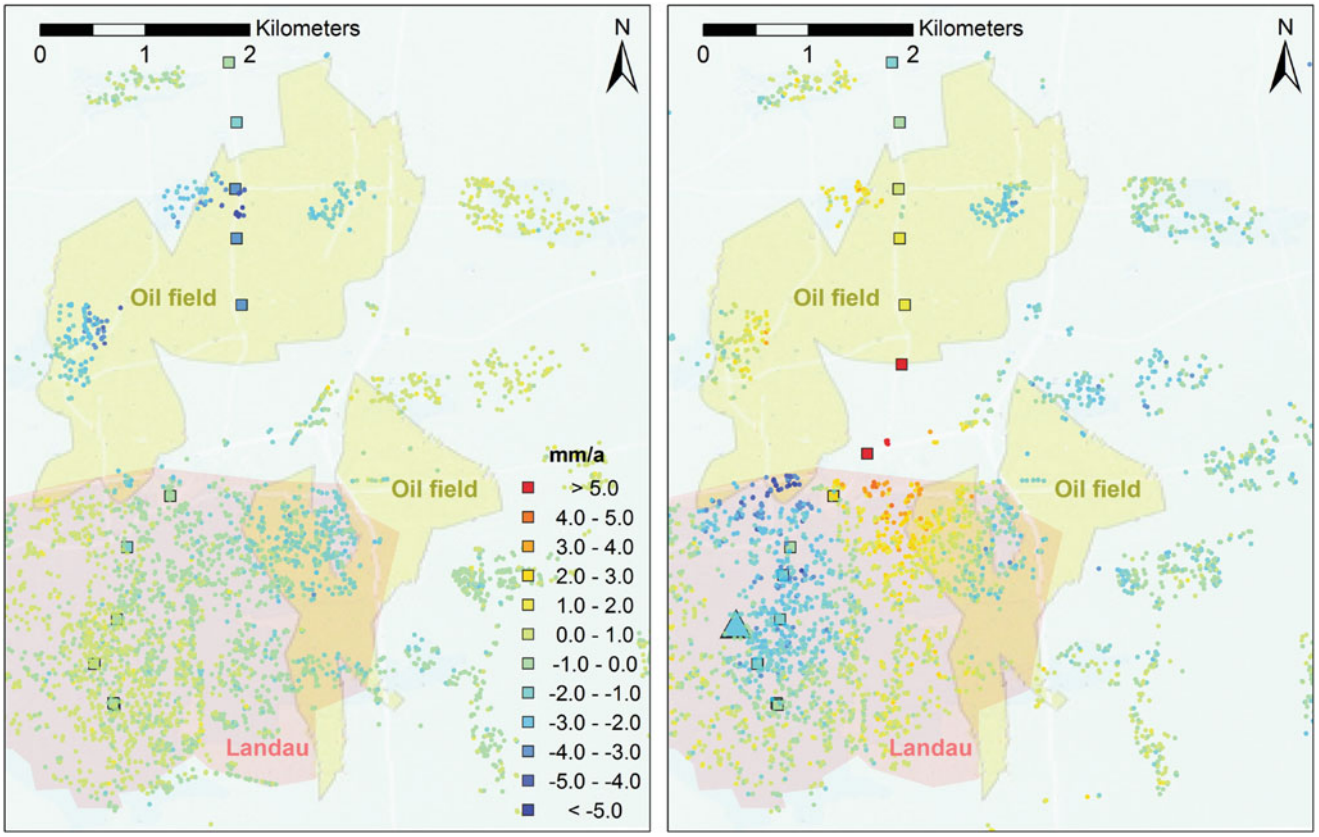

Fig. 6 Oil fields close to Landau and deformation measured by InSAR, GPS and levelling: LOS velocities at PS points (*circles*) with standard deviations <0.5 mm/a estimated from ERS-1/2 data (1992–2000, *left*) and standard deviations <1.5 mm/a estimated from Envisat data (2003–2008, *right*), *vertical* displacement rates at levelling benchmarks (*squares*) from two epochs (*left*: 1994 and 2003, *right*: 2003 and 2009) and linear trend of up component for GNSS site Landau from 2004 to 2009 (*triangle*)

3.2 Case Study: Oil Extraction Area

The oil field Landau is chosen as a test site for an intercomparison of the three geodetic techniques since (a) the displacement rates are significantly larger than in most other parts of the URG, (b) the LOS velocities are expected to be only marginally influenced by horizontal movements, assuming a point-like pressure source in the ground, and (c) additional levelling campaigns have been carried out. Two periods with temporally overlapping data sets are available: 1992–2003 (levelling, InSAR (ERS-1/2)) and 2003–2009 (levelling, InSAR (ENVISAT), GPS). Figure 6, left, shows the results from ERS-1/2 and two levelling epochs before 2003. The LOS velocities and the vertical displacement rates from levelling fit well together at places where both data sets overlap, indicating that the major deformation is vertical. The LOS velocities are converted into vertical by multiplication with $1/cos(23°) = 1.09$ (e.g., 5 mm/a LOS $\widehat{=}$ 5.4 mm/a vertical). Assuming a continuous deformation field, it can be stated that both techniques complement each other reasonably well in adjacent areas where only one data set is available. Within the oil fields North and East of Landau significant subsidence is visible (−1 to −5 mm/a), whereas the city of Landau is more or less stable. After 2003 (Fig. 6, right), the centre of the subsidence of the oil field North of Landau is shifted southwards showing magnitudes from −1 to −6 mm/a. In the area between the two oil fields a reverse movement with uplift rates of up to +7 mm/a is obvious. The GPS time series (Up component) from 2004 to 2009 delivers a linear rate of −2.6 mm/a in Landau city, overestimating the vertical displacement compared to adjacent levelling and PS points (−1.5 mm/a for both techniques). We attribute this to known inaccuracies of the vertical GPS component as presented in Fuhrmann et al. (2013). The case study demonstrates that InSAR and levelling are both capable to resolve displacement rates at the mm/a level under the prevailing conditions in the URG, and that improved information can be drawn from a combination of both techniques.

4 Conclusions and Outlook

Within this paper, we presented our database, processing strategies and first results of a comprehensive analysis of cross-border geodetic data sets in the URG and surrounding regions. A regional comparison of displacement rates from levelling and InSAR as well as a local case study in an oil extraction area have proven the potentials of the data sets available in the URG area. The resulting velocity estimates reach accuracies on the mm/a to sub-mm/a level. The results from a kinematic adjustment of levelling data are most accurate because of (a) the inherent accuracy of the method, and (b) the large temporal baseline of available data, while the additional value of GNSS has to be further checked.

In order to obtain the best possible solution for 3D displacements over a large area we aim to combine the results of the three techniques. A joint interpretation however is challenging since each method relies on its own characteristics. Problems are inherent especially due to major differences in the temporal and spatial resolution and different time-dependent reference frames of the results. Thus, for a rigorous combination of the three techniques a proper interpolation of the data on a common grid is indispensable (Cuenca et al. 2012), along with weighting algorithms and outlier detection. The velocity components will be obtained from the different data sets by an adjustment approach along with analytical optimisation (Hu et al. 2011). The resulting 3D velocity field will contribute to an improved understanding of intraplate deformation processes and will deliver important boundary conditions for numerical geomechanical models. However, the geodetically observed surface displacements will always reflect a mixture of processes acting on different spatial and temporal scales (mining, groundwater withdrawal, natural hydrologic changes, glacial isostatic rebound, regional geochemical processes, tectonics) and have to be analysed appropriately.

Acknowledgements We thank the national surveying authorities for supplying GNSS and levelling data, as well as ESA for providing SAR data under the project ID 14193. The project is funded through the German Science Foundation (DFG) under grant HE 1433/17-2.

References

Cuenca MC, Hanssen R, Hooper A, Arikan M (2012) Surface deformation of the whole Netherlands after PSI analysis. In: Proceedings Fringe 2011 Workshop, Frascati, Italy, 19–23 September 2011

Dach R, Hugentobler U, Fridez P, Meindl M (2007) User manual of the Bernese GPS Software Version 5.0. Astronomical Institute, University of Bern

Dumouchel W, O'Brien F (1989) Integrating a robust option into a multiple regression computing environment. In: Computer Science and Statistics: Proceedings of the 21st Symposium on the Interface, American Statistical Association, Alexandria, VA, pp 297–301

Fuhrmann T, Heck B, Knöpfler A, Masson F, Mayer M, Ulrich P, Westerhaus M, Zippelt K (2013) Recent surface displacements in the Upper Rhine Graben – preliminary results from geodetic networks. Tectonophysics 602(0):300–315. doi:10.1016/j.tecto.2012.10.012

Hooper A, Segall P, Zebker H (2007) Persistent scatterer interferometric synthetic aperture radar for crustal deformation analysis, with application to Volcán Alcedo, Galápagos. J Geophys Res 112(B7). doi:10.1029/2006JB004763

Hu J, Zhu J, Li Z, Ding X, Wang C, Sun Q (2011) Robust estimating three-dimensional ground motions from fusion of InSAR and GPS measurements. In: International Symposium on Image and Data Fusion (ISIDF), 2011, pp 1–4. doi:10.1109/ISIDF.2011.6024238

Kampes BM, Hanssen RF, Perski Z (2003) Radar interferometry with public domain tools. In: Third International Workshop on ERS SAR Interferometry, FRINGE03, Frascati, Italy

Knöpfler A, Masson F, Mayer M, Ulrich P, Heck B (2009) GURN (GNSS Upper Rhine Graben Network) Status and first results. 95th Journées Luxembourgeoises de Géodynamique, Echternach, Luxemburg, extended abstracts

Lemeille F, Cushing M, Cotton F, Grellet B, Audru FMJC, Flehoc FRC (1999) Evidence for Middle to Late Pleistocene faulting within the northern Upper Rhine Graben (Alsace Plain, France). Comptes Rendus de l'Academie des Sciences Series IIA Earth and Planetary Science 328(12):839–846. doi:10.1016/S1251-8050(99)80200-6

Meghraoui M, Delouis B, Ferry M, Giardini D, Huggenberger P, Spottke I, Granet M (2001) Active Normal Faulting in the Upper Rhine Graben and Paleoseismic Identification of the 1356 Basel Earthquake. Science 293(5537):2070–2073. doi:10.1126/science.1010618

Nocquet JM, Calais E (2003) Crustal velocity field of western Europe from permanent GPS array solutions, 1996–2001. Geophys J Int 154(1):72–88. doi:10.1046/j.1365-246X.2003.01935.x

Rosen PA, Hensley S, Peltzer G, Simons M (2004) Updated repeat orbit interferometry package released. Eos, Transactions American Geophysical Union 85(5):47. doi:10.1029/2004EO050004

Ziegler PA (1992) European Cenozoic rift system. Tectonophysics 208:91–111. doi:10.1016/0040-1951(92)90338-7

Zippelt K (1988) Modellbildung, Berechnungsstrategie und Beurteilung von Vertikalbewegungen unter Verwendung von Präzisionsnivellements, vol C 343. Bavarian Academy of Sciences and Humanities, Munich

On the Use of Bistatic TanDEM-X Images to Quantify Volumetric Changes of Active Lava Domes

Julia Kubanek, Malte Westerhaus, and Bernhard Heck

Abstract

TanDEM-X is a recent SAR mission, consisting of two almost identical spacecraft flying in close formation. The small distance between the two radar satellites allows two images to be acquired at the same time (bistatic images), strongly reducing the influence of temporal decorrelation, which is one of the major sources of error in repeat-pass interferometric analyses. For the first time, we successfully apply TanDEM-X data to observe topographic changes at active volcanoes by using the image pairs to generate high-resolution digital surface models (DSMs) for each transit of the satellites. Taking the difference between two bistatic DSMs allows us to assess substantial topographic changes and/or sudden ground displacements above the 1 m level. As the first test case, we used bistatic TanDEM-X data to assess topographic change due to the major Merapi 2010 eruption. The preliminary estimated volumetric loss of $19 \times 10^6\,m^3$ is reasonable; however, strong phase noise due to geometrical decorrelation and resulting unwrapping errors affect the result. To demonstrate that much smaller topographic changes are observable with TanDEM-X, we further analyzed data acquired before and after a small explosion at Volcán de Colima in June 2011. The estimated volume loss of $2 \times 10^5\,m^3$ fits well to ground truth data.

Keywords

Double differential DSMs • InSAR • Lava domes • Merapi • TanDEM-X • Volcán de Colima • Volume estimates

1 Introduction

Synthetic aperture radar interferometry (InSAR) uses the phase difference between two radar images of the same target area to determine surface deformation on a centimeter to millimeter scale. Several studies have shown that radar data acquired in repeated satellite passes can successfully be employed to monitor ground displacements at active volcanoes using InSAR (Lu et al. 2005; Massonnet et al. 1995; Stevens and Wadge 2004; Zebker et al. 2000). InSAR can also be used to generate DSMs with meter-level accuracy. There have been attempts to quantify topographic changes at volcano edifices from the difference of two or more DSMs generated using InSAR (Wadge 2003). The main problem for both approaches results from the repeat-pass intervals of common radar satellite missions. Although COSMO-SkyMed has the potential for 1-day repeats and TerraSAR-X has an 11-day repeat, repeat times are, under normal conditions, one to several weeks. As long as the backscattering conditions of the ground remain stable, repeat-pass InSAR has proven its applicability in volcano monitoring (Lu et al. 2005; Wadge et al. 2011). However, major surface changes, which commonly occur during volcanic crises due to ash fall, lava flows, lava dome collapse, or explosions, lead to coherence loss, thus preventing interferometric analysis (Lu and Freymueller 1998; Stevens and Wadge 2004; Stevens et al. 2001; Wadge 2003).

J. Kubanek (✉) • M. Westerhaus • B. Heck
Geodetic Institute, Karlsruhe Institute of Technology, Englerstraße 7, 76131 Karlsruhe, Germany
e-mail: julia.kubanek@kit.edu

© Springer International Publishing Switzerland 2015

C. Rizos, P. Willis (eds.), *IAG 150 Years*, International Association of Geodesy Symposia 143,
DOI 10.1007/1345_2015_172

To overcome some of the problems of the repeat-pass interferometric approach, we employ data from the innovative German TanDEM-X (TerraSAR-X add-on for Digital Elevation Measurement) mission in volcano research. Our focus is on monitoring large changes at the summits of dome-building volcanoes. The TanDEM-X mission consists of two almost-identical radar satellites, TerraSAR-X and TanDEM-X, which fly in close formation. In bistatic acquisition mode, one satellite emits the radar pulse and both satellites receive the reflected signal, thus acquiring images of the same place on the Earth's surface at the same time from slightly different positions (Krieger et al. 2007). The simultaneous acquisition of two images considerably increases the coherence compared to data acquired in repeat-pass mode (Martone et al. 2012) and thus enables generating a DSM during every pass of the satellite pair. Differencing two or more DSMs obtained from bistatic image pairs of the same region reveals topographic changes without the necessity of maintaining coherence between temporally separated passes of the satellite pair.

We generated DSMs of Merapi in Indonesia and Volcán de Colima in Mexico using bistatic TanDEM-X data. The data were recorded before and after phases of increased volcanic activity that led to topographic changes in the summit area of each volcano. We performed differential analysis of the DSMs from image pairs recorded at different times to assess the volume changes in the summit areas of both volcanoes. As the TanDEM-X mission is a new radar satellite mission, we discuss possible error sources using Merapi as a test site.

2 Test Sites: Lava Domes of Stratovolcanoes

The focus of the present study is on dome-building volcanoes. Lava domes are a significant volcanic hazard, as their collapse can trigger pyroclastic flows and surges, thus leading to death and severe destruction (Calder et al. 2002). The rate of lava-dome growth can reach up to several cubic meters per second (Sparks et al. 1998). The damage potential of the pyroclastic flows correlates with the volume of collapsing material and thus with the magma extrusion rate. The rate of magma ascent is difficult to determine at lava-dome volcanoes for the reason that the ascending material does not reach the surface directly, but is stored in a growing lava dome. Geometric changes of the lava dome can, however, be tracked.

To assess whether bistatic TanDEM-X data can be successfully used to observe lava-dome changes, we employed bistatic TanDEM-X data recorded during active phases at two stratovolcanoes. Our test sites, Merapi in Indonesia and Volcán de Colima in Mexico, are both dome-building volcanoes with frequent but varying levels of activity.

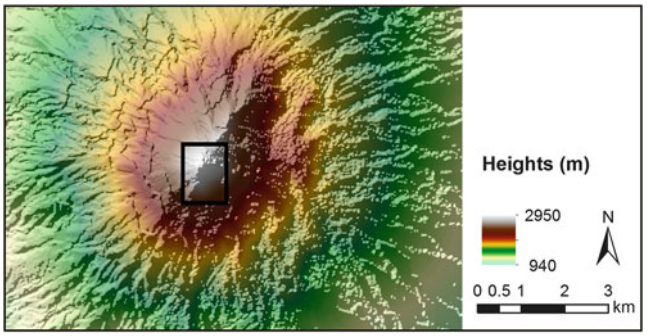

Fig. 1 Relief map of Merapi generated using bistatic TanDEM-X data. The *rectangle* highlights the area used for analyzing topographic changes in the summit area due to the 2010 eruption

2.1 Merapi

Merapi (7.542°S, 110.442°E, pre-2010 eruption summit 2,968 m above sea level), is one of the most active volcanoes in Indonesia, and one of the most hazardous volcanoes in the world (Fig. 1). Since 1786, activity has mainly involved lava-dome growth and destruction. Major eruptions have occurred every 30–60 years, with small eruptions every 2–6 years during the last several decades (Newhall et al. 2000; Voight et al. 2000). The last severe Merapi eruption, which occurred in October/November 2010, also involved dome growth and collapse and had a volcanic explosivity index (VEI) of ~4. The 2010 eruption, which was much more explosive than previous ones of the twentieth century, started with an explosion that destroyed the 2006 lava dome; a new dome was built up and destroyed again during the course of the eruption (Pallister et al. 2013). The increased activity lasted for about 12 days and led to a complex topographic change in the summit area of Merapi (Pallister et al. 2013).

2.2 Volcán de Colima

Volcán de Colima (19.513°N, 103.587°W, 3,860 m above sea level) is located close to the city of Colima in western Mexico (Hutchinson et al. 2013) (Fig. 2). Over the last five centuries, the volcano has experienced a variety of volcanic processes culminating in explosive events with a VEI of ~4 (Gonzáles et al. 2002). The recent activity of Volcán de Colima included four phases of dome growth during 1998–1999, 2001–2003, 2004, and 2007–2011. On June 26, 2011, a small explosion occurred on the western crater rim, signaling the end of magma ascent to the summit and the end of the most recent eruptive period (James and Varley 2012). Subsequently, the

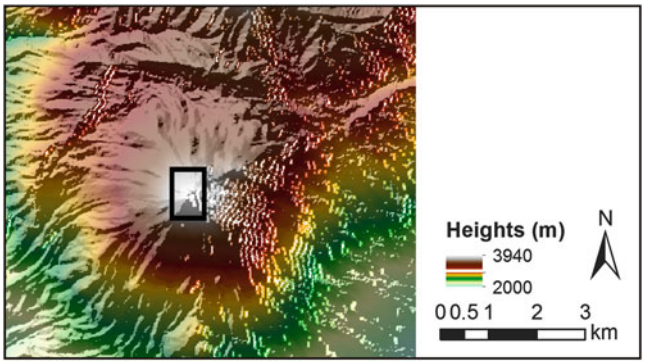

Fig. 2 Relief map of Volcán de Colima generated using bistatic TanDEM-X data. The *rectangle* highlights the area used for analyzing topographic changes in the summit area due to the 2011 activity

volcano was quiet until a new episode of activity started in January 2013.

3 Topographic Change Estimation Using TanDEM-X

Our first case study is the 2010 Merapi eruption. As the eruption was the largest and most explosive in more than a century (Surono et al. 2012), we expected a considerable volume change in the summit area. To test whether the presented method is also feasible for observing much smaller changes, we analyzed a phase of minor activity at Volcán de Colima in June 2011 as a second case study.

We used the Delft object-oriented radar interferometric software (DORIS) (Kampes et al. 2003) to process the TanDEM-X data and built DSMs of both volcanoes. As the TanDEM-X mission is a new satellite mission we had to adapt DORIS to process this novel kind of SAR data.

The interferometric phase ϕ_{InSAR} for monostatic data is, according to Hanssen (2001),

$$\phi_{InSAR} = \frac{4\pi}{\lambda}\Delta r, \tag{1}$$

where the factor 4π results from the fact that the signal is transmitted and received by the same satellite, λ is the wavelength, and Δr is the path-length difference from antenna to ground between the first and the second overflight. In the bistatic acquisition, only one satellite emits the radar signal while both satellites receive it. We changed the formula accordingly to:

$$\phi_{InSAR} = \frac{2\pi}{\lambda}\Delta r. \tag{2}$$

Table 1 TanDEM-X observation times of Merapi including acquisition parameters (pre = pre-eruption, post = post-eruption)

Acquisition date	Effective baseline (m)	Altitude of ambiguity (m)
10/15/2010, pre	162	36
10/24/2011, post	76	79
11/04/2011, post	65	94

Due to the bistatic acquisition geometry of the satellites, we use the term "effective baseline" for the TanDEM-X products, which is half the length of the perpendicular baseline (Krieger et al. 2007). As the two bistatic radar images provided by the German Aerospace Center (DLR) are already coregistered, we started the processing with generating interferograms from each bistatic data pair. A simple comparison of the resulting DSMs enabled assessment of the topographic changes due to volcanic activity. The theoretical relative horizontal accuracy of the TanDEM-X DSMs is 3 m, and the theoretical vertical accuracy is 4 m for slopes >20%; the spatial resolution is 12 m (Krieger et al. 2007). Weigt et al. (2012) confirmed that the requirements for the absolute height accuracy of 10 m and the relative height error of 2 m can be reached or, in certain areas, even exceeded. The authors predicted height errors of 1.7 m and 2.5 m for altitudes of ambiguity of 30 m and 45 m, respectively.

We generated three DSMs for Merapi, one of which was from data recorded on 10/15/2010, shortly before the eruption (hereafter referred to as pre-eruption DSM); the other two data pairs were recorded about 1 year after the eruption, on 10/24/2011 and 11/04/2011 (hereafter referred to as post-eruption DSMs) (Table 1). All data pairs were recorded in stripmap mode from the descending orbit with an incidence angle of 37° and effective baselines ranging from 65 to 162 m. We only used data from the descending orbit, as no ascending orbit data were acquired before the eruption started in 2010.

We used the two post-eruption DSMs to generate a mean post-eruption DSM and compared it with the pre-eruption DSM to analyze the topographic changes. As the post-eruptive, fissured topography of Merapi leads to extended shadow areas, we combined the resulting difference image with a shadow map (Fig. 3). The comparison of the DSMs recorded before and after the eruption revealed a maximum height decrease of up to 200 m in the summit area (Fig. 3c). The summit area was heavily eroded and deepened by the several explosions and pyroclastic flows generated during the eruption. One major erosion feature, together with the large crater formation, is the deepening of the Gendol gorge in the southeastern part of the summit area (Pallister et al. 2013),

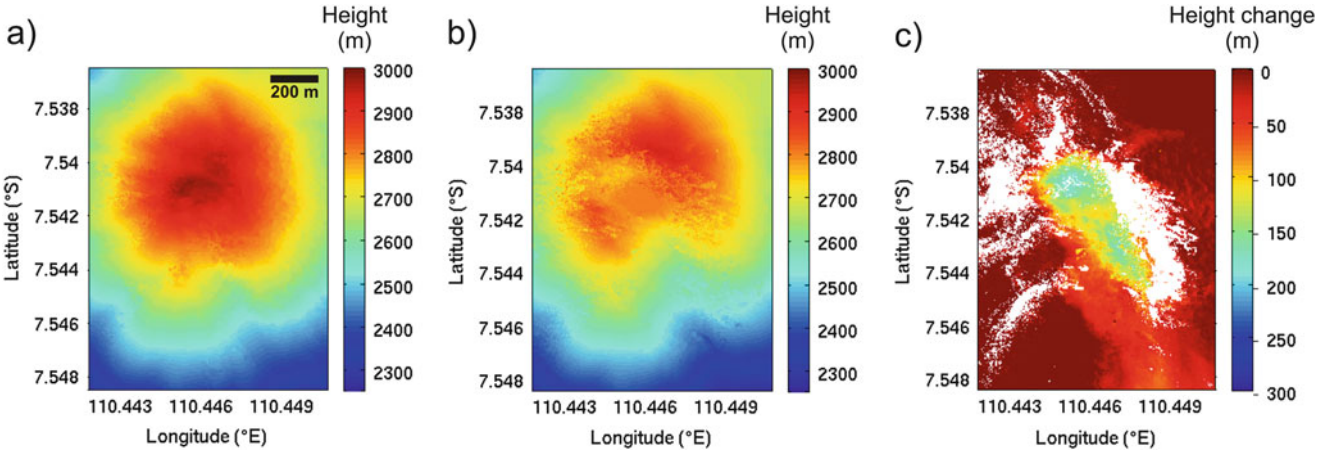

Fig. 3 Height change in the summit area of Merapi due to the 2010 eruption. (**a**) Map view of the pre-eruption DSM recorded on 10/15/2010, (**b**) map view of the mean post-eruption DSM, (**c**) difference image of the pre-eruption DSM and the mean post-eruption DSM overlaid by a shadow mask

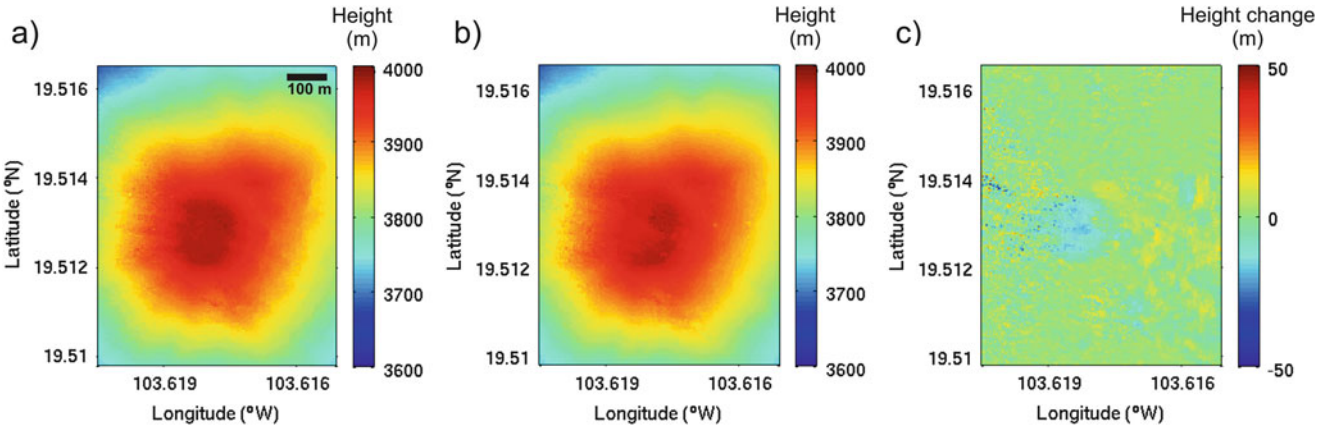

Fig. 4 Height change in the summit area of Volcán de Colima due to the explosion in June 2011. (**a**) Map view of the mean DSM of the two pre-explosion DSMs, (**b**) map view of the mean post-explosion DSM, (**c**) difference image of the mean pre-explosion DSM and the mean post-explosion DSM

where we observed a major height change (Fig. 3c). We used trapezoidal integration to calculate a volume decrease in the summit area of $19 \times 10^6\,m^3$. Pallister et al. (2013) calculated a volumetric loss of $6 \times 10^6\,m^3$ due to the eruption of 26th October 2010, and an additional portion of crater wall material of $10 \times 10^6\,m^3$ that was removed during the dome destruction of 4th to 5th November. We further had to subtract the new lava dome which was produced on 6th November ($1.5 \times 10^6\,m^3$), resulting in a total volumetric loss of ~$14.5 \times 10^6\,m^3$. We assume that Pallister et al. (2013) only included the area around the lava dome, whereas our volume estimates additionally include the deepening of the Gendol gorge, which explains the larger values derived from the TanDEM-X data. Furthermore, we cannot exclude errors, especially due to unwrapping (see Sect. 4), in our volume estimates.

To test whether meter-scale topographic changes are also observable with TanDEM-X, we analyzed the topographic loss due to the June 2011 explosion at Volcán de Colima. As the explosion occurred at the western crater rim, the height change is visible only in data recorded by the descending orbit. We therefore analyzed six bistatic data pairs recorded from this orbit, two of which were recorded before the explosion on 06/08/2011 and on 06/19/2011 (hereafter referred to as pre-explosion DSMs), and four data pairs recorded in July and August (after the explosion, hereafter referred to as post-explosion DSMs) (Table 2). All data pairs were recorded in stripmap mode, and the effective baselines of the data pairs vary from 65 to 88 m (Table 2).

We used the two pre-explosion DSMs to generate a mean pre-explosion DSM and compared it with a mean post-explosion DSM generated using the four post-explosion DSMs.

Table 2 TanDEM-X observation times of Volcán de Colima including acquisition parameters (pre = pre-explosion, post = post-explosion)

Acquisition date	Effective baseline (m)	Altitude of ambiguity (m)
06/08/2011, pre	88	57
06/19/2011, pre	86	57
06/30/2011, post	79	63
07/11/2011, post	78	64
07/22/2011, post	74	67
08/24/2011, post	65	76

The analysis of DSMs of Volcán de Colima before and after the minor explosive activity of June 2011 revealed topographic changes of up to 20 m (Fig. 4), with a mean volume change of 2×10^5 m^3. We can compare this result to a study conducted by James and Varley (2012), who used 3D photogrammetric reconstructions of surface topography based on visual imagery to derive high-resolution DSMs to investigate lava-dome changes at Volcán de Colima in June 2011. The authors report a volumetric loss due to the June 2011 explosion of 1.9×10^5 m^3.

4 Discussion of Potential Errors in the DSMs

One of the major sources of error is geometrical decorrelation caused by the side-looking geometry of slant-range SAR systems. As geometrical decorrelation is particularly problematic in areas characterized by complex topography, we identified this as the most severe error source in the Merapi case study. Whereas the summit of Merapi had a conical shape before the 2010 eruption started (Fig. 5a), post-eruption topography consists of a deep crater and gorge toward the southeast (Fig. 5b). Steep walls in the east and west result in shadow and layover areas, respectively, and grazing incidence angles along the flanks tilted away from the SAR sensor (Fig. 5b). We assume that unwrapping is especially error-prone in regions where shadow merges with layover, which can be seen at the western and the eastern end of the cross sections of the two post-eruption DSMs (Fig. 6). We excluded these regions in the volume estimate using a shadow mask as the first step to address unwrapping errors (Fig. 3c).

It is apparent that whereas the pre-eruption DSM has a smooth shape, the post-eruption DSMs show a higher noise level. As all other acquisition parameters (e.g., orbit, incidence angle) remained constant during the different satellite passes, we ascribe this effect partially to the varying cross-track baseline between the satellites in the different

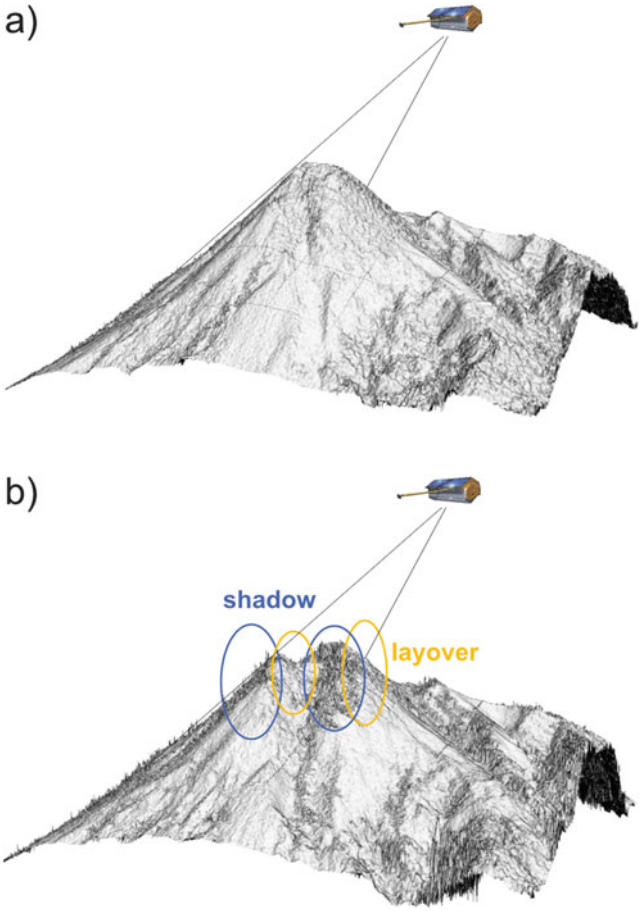

Fig. 5 (**a**) 3-D view of the pre-eruption DSM of Merapi recorded on 10/15/2010 seen from the south. (**b**) 3-D view of the post-eruption DSM recorded on 10/24/2011 seen from the south. Layover areas are marked with *yellow ellipses*, shadow areas and areas with a lower resolution due to grazing incidence angles are marked with *blue ellipses*. The smooth shape of the pre-eruption DSM versus the noisy shape of the post-eruption DSM becomes obvious

acquisitions. Whereas the effective baseline corresponding to the pre-eruption DSM is 162 m, the effective baselines related to the two post-eruption DSMs are 76 and 65 m – only half the length of the pre-eruption DSM (Table 1). The altitude of ambiguity, which is defined as the height difference due to an interferometric phase shift of 2π, is inversely proportional to the effective baseline. We thus expect an increase of noise in the post-eruption DSMs by a factor of 2.5 according to the decreased baselines of the post-eruption DSMs. However, the increase in noise in the post-eruption DSMs is too large to be explained only by the baseline length. We ascribe the additional noise contribution to unwrapping errors. Altogether, the geometrical effects cause the quality of the DSMs to deteriorate. We did not try to assess the accuracy of the DSMs of Merapi and

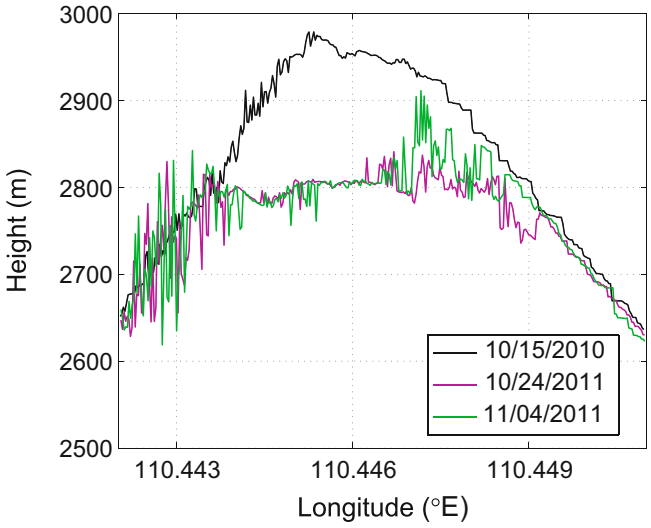

Fig. 6 West-to-east cross section of the Merapi DSMs, passing over the center of the volcano along 7.541°S

Volcán de Colima, but we assume that a quantification at Volcán de Colima would be more promising, as the smoother topography simplifies unwrapping.

5 Conclusion and Outlook

We show for the first time that bistatic TanDEM-X data can successfully be employed in volcano research to monitor topographic changes at active lava domes. The Merapi case study demonstrates that surface changes of up to 200 m are clearly detectable. The second case study at Volcán de Colima illustrates that much smaller changes of up to 20 m are also observable. These results indicate that it is possible to observe topographic changes and calculate volume change in the summit areas of dome-building volcanoes. As broad-scale, up-to-date observations of a changing lava dome are often impossible from ground- or airborne-based observations, we conclude that TanDEM-X provides a valuable source of information about changes at active lava domes.

Further research will focus on quantifying the DSM accuracy and validating the present preliminary volume estimates. We further plan to include ascending data sets in the analysis, since the location of shadow and layover areas is complementary to the images acquired from the descending orbit. The fusion of both acquisition geometries will result in more accurate DSMs and thus better volume estimates.

Acknowledgements The TanDEM-X data were provided by DLR. We thank DLR for funding the study under contract no. 50 EE0957, with funds from the German Federal Ministry for Economic Affairs and Energy (BMWi) due to a decision of the German Bundestag. We thank Sylvain Charbonnier and two anonymous reviewers for their careful comments, which helped to improve the manuscript.

References

Calder E, Luckett R, Sparks R, Voight B (2002) Mechanisms of lava dome instability and generation of rockfalls and pyroclastic flows at Soufriere Hills Volcano, Montserrat. In: Druitt T, Kokelaar B (eds) The eruption of Soufriere Hills Volcano, Montserrat, from 1995 to 1999, memoirs 21. Geological Society, London, pp 173–190

Gonzáles MB, Ramírez J, Navarro C (2002) Summary of the historical eruptive activity of Volcán de Colima, Mexico 1519–2000. J Volcanol Geotherm Res 117:21–46. doi:10.1016/S0377-0273(02)00233-0

Hanssen RF (2001) Radar interferometry. Data interpretation and error analysis. Kluwer Academic Publishers, New York

Hutchinson W, Varley N, Pyle DM, Mather TA, Stevenson JA (2013) Airborne thermal remote sensing of the Volcán de Colima (Mexico) lava dome from 2007 to 2010. In: Pyle DM, Mather TA, Biggs J (eds) Remote-sensing of volcanoes and volcanic processes: integrating observation and modelling, vol 380. Geological Society Special Publication, pp 203–228. doi:10.1144/SP380.8

James MR, Varley N (2012) Identification of structural controls in an active lava dome with high resolution DEMs: Volcán de Colima, Mexico. Geophys Res Lett 39:L22303. doi:10.1029/2012GL054245

Kampes B, Hanssen R, Zbigniew P (2003) Radar interferometry with public domain tools. In: Proceedings of Fringe 2003 workshop, Frascati, 1–5 December 2003

Krieger G, Moreira A, Fiedler H, Hajnsek I, Werner M, Younis M, Zink M (2007) TanDEM-X: a satellite formation for high resolution SAR interferometry. IEEE Trans Geosci Remote Sens 45:3317–3341. doi:10.1109/TGRS.2007.900693

Lu Z, Freymueller J (1998) Synthetic aperture radar interferometry coherence analysis over Katmai volcano group, Alaska. J Geophys Res 103:29887–29894. doi:10.1029/98JB02410

Lu Z, Masterlark T, Dzurisin D (2005) Interferometric synthetic aperture radar study of Okmok volcano, Alaska, 1992–2003: magma supply dynamics and postemplacement lava flow deformation. J Geophys Res 110:1–18. doi:10.1029/2004JB003148

Martone M, Bräutigam B, Rizzoli P, Gonzales C, Bachmann M, Krieger G (2012) Coherence evaluation of TanDEM-X interferometric data. ISPRS J Photogramm Remote Sens 73:21–29. doi:10.1016/j.isprsjprs.2012.06.006

Massonnet D, Briole P, Arnaud A (1995) Deflation of Mount Etna monitored by spaceborne radar interferometry. Nature 375:567–570. doi:10.1038/375567a0

Newhall CG et al (2000) 10,000 years of explosive eruptions of Merapi Volcano, Central Java: archaeological and modern implications. J Volcanol Geotherm Res 100:9–50. doi:10.1016/S0377-0273(00)00132-3

Pallister J, Schneider D, Griswold J, Keeler R, Burton W, Noyles C, Newhall C, Ratdomopurbo A (2013) Merapi 2010 eruption – chronology and extrusion rates monitored with satellite radar used in eruption forecasting. J Volcanol Geotherm Res 261:144–152. doi:10.1016/j.jvolgeores.2012.07.012

Sparks RSJ et al (1998) Magma production and growth of the lava dome of the Soufrière Hills Volcano, Montserrat, West Indies: November 1995 to December 1997. Geophys Res Lett 25:3421–3424. doi:10.1029/98GL00639

Stevens N, Wadge G (2004) Towards operational repeat-pass SAR interferometry at active volcanoes. Nat Hazards 33:47–76. doi:10.1023/B:NHAZ.0000035005.45346.2b

Stevens NF, Wadge G, Williams CA (2001) Post-emplacement lava subsidence and the accuracy of ERS InSAR digital ele-

vation models of volcanoes. Int J Remote Sens 22:819–828. doi:10.1080/01431160051060246

Surono et al (2012) The 2010 explosive eruption of Java's Merapi volcano - a '100-year' event. J Volcanol Geotherm Res 241–242:121–135. doi:10.1016/j.jvolgeores.2012.06.018

Voight B, Constantine E, Siswowidjoyo S, Torley R (2000) Historical eruptions of Merapi Volcano, Central Java, Indonesia, 1768–1998. J Volcanol Geotherm Res 100:69–138. doi:10.1016/S0377-0273(00)00134-7

Wadge G (2003) Measuring the rate of lava effusion by InSAR. In: Proceedings of Fringe 2003 workshop, Frascati 1–5 December 2003

Wadge G, Cole P, Stinton A, Komorowski JC, Stewart R, Toombs A, Legendre Y (2011) Rapid topographic change measuredby high-resolution satellite radar at Soufrière Hills Volcano, Montserrat, 2008–2010. J Volcanol Geotherm Res 199:142–152. doi:10.1016/j.jvolgeores.2010.10.011

Weigt M, Rizzoli P, Bachmann M, Bräutigam B, Schulze D (2012) TanDEM-X mission - interferometric performance and global DEM acquisition status. In: Radar 2012, IET international conference on radar systems, Glasgow, 22–25 October 2012

Zebker HA, Amelung F, Jonsson S (2000) Remote sensing of volcano surface and internal processes using radar interferometry. In: Mouginis-Mark PJ, Crisp JA, Fink JH (eds) Remote sensing of active volcanism. Geophysical monograph series, vol 116. AGU, pp 179–205. doi:35400009795346.0100

On Integration of Geodetic Observation Results for Assessment of Land Subsidence Hazard Risk in Urban Areas of Indonesia

Hasanuddin Z. Abidin, Heri Andreas, Irwan Gumilar, Bambang D. Yuwono, Dodid Murdohardono, and S. Supriyadi

Abstract

Several large urban areas in Indonesia, i.e. Jakarta, Bandung and Semarang, have experienced land subsidence. These urban land subsidences are mainly caused by the combination of excessive groundwater extraction, natural consolidation of alluvium soil, and load of constructions (i.e. settlement of high compressibility soil). The impact of land subsidence can be already seen in several forms, such as cracking of buildings and infrastructure, the wider expansion of (coastal) flooding areas, and increased inland sea water intrusion. It also badly influence the quality of living environment and life in the affected areas. Land subsidence in Jakarta has been studied using leveling surveys, GPS surveys, and InSAR techniques. The results obtained from these technique over the period between 1982 and 2011 show that observed subsidence rates in Jakarta are about 1–15 cm/year, and can reach up to 20–28 cm/year at certain location and certain period. In Bandung basin, land subsidence phenomenon has been studied using GPS surveys and InSAR methods. Based on these methods, it was found that during the period between 2000 and 2011, several locations in the Bandung basin have experienced subsidence, with an average rate of about 8 cm/year and can reach up to about 23 cm/year. In Semarang, land subsidence has been studied using Levelling surveys, GPS surveys, Microgravity surveys and InSAR technique. Based on the estimation from those measurement methods, land subsidence with rates of up to about 19 cm/year were observed during the period of 1999 up to 2011. The observed land subsidence rates in Jakarta, Bandung and Semarang in general have spatial and temporal variations. Results from various geodetic observation methods can give a better picture on the magnitudes and rates of land subsidence, and its variation both in spatial and temporal domain. Integration of those results however, can not always be performed in an ideal manner, since each geodetic method has its own operational strengths and weaknesses in large urban environment.

Keywords

Bandung • GPS • InSAR • Jakarta • Land subsidence • Leveling • Microgravity • Semarang

H.Z. Abidin (✉) • H. Andreas • I. Gumilar
Geodesy Research Group, Faculty of Earth Science and Technology, Institute of Technology Bandung, Jl. Ganesha 10, Bandung, Indonesia
e-mail: hzabidin@gd.itb.ac.id

B.D. Yuwono
Department of Geodetic Engineering, Diponegoro University, Semarang, Indonesia

D. Murdohardono
Centre for Groundwater Resources and Environmental Geology, Geological Agency of Indonesia, Bandung, Indonesia

S. Supriyadi
Department of Physics, Semarang State University, Semarang, Indonesia

© Springer International Publishing Switzerland 2015

C. Rizos, P. Willis (eds.), *IAG 150 Years*, International Association of Geodesy Symposia 143,
DOI 10.1007/1345_2015_82

Fig. 1 Large cities of Indonesia affected by land subsidence phenomena, i.e. Jakarta, Bandung and Semarang, all located in Java island

1 Introduction

Land subsidence is natural-anthropogenic hazard affecting quite many large urban areas (cities) in the world, such as Houston (Buckley et al. 2003), Mexico City (Cabral-Cano et al. 2008), Osaka (Murayama 1970), Tokyo (Ishii et al. 1970), Shanghai (Chai et al. 2004), Taipei (Chen et al. 2007) and Bangkok (Phien-wej et al. 2006). In urban areas of Indonesia, this silent-type hazard have occurred in Jakarta (Abidin et al. 2001, 2008a, 2010a, 2011), Bandung (Abidin et al. 2008b, 2009, 2012a, 2013), and Semarang (Abidin et al. 2010b, 2012b). Location of these three Indonesian cities are shown in Fig. 1. These urban land subsidences maybe caused by the combination of excessive groundwater extraction, natural consolidation of alluvium soil, load of constructions (i.e. settlement of high compressibility soil), and sometimes tectonic activities.

In general, the impacts of land subsidence in urban areas can be seen in the forms of cracking of permanent constructions and roads, 'sinking' of houses and buildings, changes in river canal and drain flow systems, wider expansion of coastal and/or inland flooding areas, and increased inland sea water intrusion. In the case of coastal cities such as Jakarta and Semarang, where their coastal areas have relatively higher subsidence rates (Abidin et al. 2010a, 2012b), the collateral impact in the form of coastal flooding even more damaging. In this coastal areas, frequent and severe coastal flooding not just deteriorates the function of building and infrastructures, but also badly influences the quality of living environment and life (e.g. health and sanitation condition). In urban areas, comprehensive information on the characteristics of land subsidence is important for several planning and risk assessment efforts, such as spatial-based groundwater extraction regulation, effective control of (inland and coastal) flood and seawater intrusion, conservation of environment, design and construction of infrastructures, sub-surface utility planning, sewerage and drainage system design, and spatial development planning in general. Therefore, systematic and continuous monitoring of land subsidence is obviously needed and critical to the welfare of the peoples.

Land subsidence in urban areas can be observed using several geodetic methods, such as leveling, GPS survey, InSAR, microgravity, and geometric-historic. Each method has its own strength and limitation, and its integration is usually needed to give a better picture on the magnitudes and rates of land subsidence, and its variation both in spatial and temporal domain. This paper presents and discusses the integration of several geodetic observation results for risk assessment of land subsidence in three large cities of Indonesia, namely Jakarta, Bandung and Semarang.

2 Geodetic Methods and Results of Land Subsidence Estimation

Land subidence in Jakarta, Bandung and Semarang have been studied using several geodetic methods as shown in Table 1. Systematic land subsidence study in Jakarta, Semarang and Bandung was conducted since 1982, 1999, and 2000 respectively.

From all of those geodetic methods, the geometric-historic method is actually the newest method introduced in estimating land subsidence in Jakarta, Semarang and Bandung. This method is based on field measurement, historical (documented) and interview data of subsidence affected object observed in the field. In estimating subsidence (average) rate, linear rate assumption is used in this method. Figure 2 shows the implementation of this geometric-historic method in the case of house affected by land subsidence. In

Table 1 Implementation of geodetic methods for studying land subsidence characteristics in Jakarta, Bandung and Semarang

City	Leveling	GPS survey	InSAR	Microgravity	Geometric-Historic
Jakarta	Since 1982	Since 1997	Since 2005	Since 2008	Since 2010
Bandung	Limited	Since 2000	Since 2007	Since 2008	Since 2010
Semarang	Since 1999	Since 2008	Since 2007	Since 2002	Since 2011

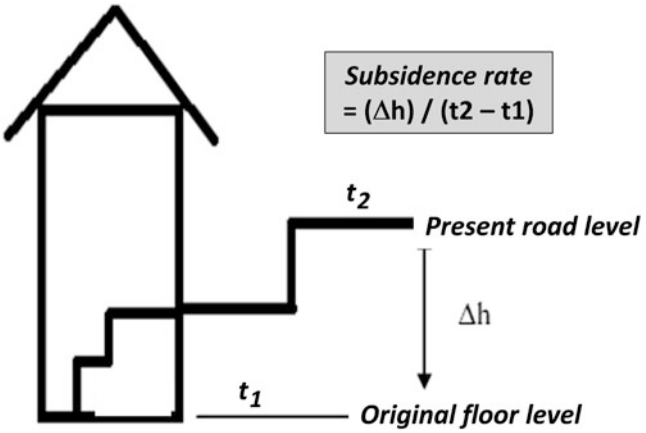

Fig. 2 Principle of geometric-historic method for land subsidence estimation. This method is based on field measurement, historical (documented) and interview data, and uses linear rate assumption

the beginning (epoch t_1), the house floor and road surface is at the same level. Due to land subsidence, both surfaces were lowering down at certain rate. For convenience, the subsidence affected road should has the same level with other connected part of the road; and therefore people will usually patched that subsiding road surface whenever required. Therefore, after sometimes the vertical separation (Δh) between the original floor level and present road surface becomes apparent. If this vertical separation is measured at epoch t_2, then the average subsidence rate in that location can be estimated as shown in Fig. 2.

In general it was found that subsidence phenomena in Jakarta, Semarang and Bandung have spatial and temporal variations, with typical subsidence rates of about 5–10 cm/year in average, although it can have higher subsidence rates at certain locations and times. More detail results from these studies can be seen in Abidin et al. (2001, 2008a, b, 2009, 2010a, b, 2011, 2012a, b, 2013), Chaussard et al. (2013), Fukuda et al. (2008), Ng et al. (2012), Kuehn et al. (2009), Lubis et al. (2011), Supriyadi (2008), and Sumantyo et al. (2012).

3 Integration of Geodetic Observation Results

In principle, each geodetic method has its own strengths and limitations in revealing characteristics of land subsidence phenomena in urban areas (see Table 2). In their implementation, usually the methods do not always have the same spatial and temporal domains of observation. Due to the nature of urban environment and its dynamics, location of GPS station, leveling benchmarks, and geometric-historic observation sites, cannot be easily collocated. Their epochs of observations are usually also different. Even with InSAR techniques, sometimes due to the characteristics of land coverage and land use dynamics in urban areas, good coherences or stable permanent scatterers in the images, sometimes cannot be fully obtained in certain part of the urban areas. Therefore in order to have real, correct and comprehensive information on land subsidence phenomena, results from various geodetic observations results should be integrated. Besides having complementary function, the integration will also allow the comparison and validation of results from various methods, which can then lead to more reliable land subsidence information.

In this paper, the integration mechanism is studied by using the observed land subsidence in Jakarta, Bandung and Semarang, which their summarized rates are shown in Tables 3, 4, and 5. It should be emphasized here that the subsidence rates shown in these Tables, are related to certain spatial coverage and observation period. Moreover, each geodetic method also has different accuracy of derived subsidence rates. Therefore the observed subsidence rates derived by different techniques, can have different ranges (min and max), as shown in the Tables. However, in general the typical rates of land subsidence estimated by various techniques Jakarta, Bandung and Semarang are more or less in agreement, as shown in Tables 3, 4, and 5.

In spatial representation, land subsidence characteristics derived from various geodetic methods are usually not exactly similar, as shown by illustration in Fig. 3. Certain spatial frequency of subsidence can be observed by certain geodetic method, and not by the other method. Therefore integration of results from various geodetic methods can be useful in recovering the whole spatial frequencies of land subsidence phenomena. The fact that land subsidence phenomena in urban areas have usually both spatial and temporal variations also makes this integration more favorable.

Integration of various geodetic observation results of land subsidence can performed in several ways. If each method has different observation period, then the easiest way is to combine spatially all subsidence rates given by all methods without applying any weighting schemes, as illustrated by Fig. 4. In this case, subsidence rates from various methods

Table 2 Typical strength and limitation of geodetic method for land subsidence (LS) study in urban areas

	Leveling surveys	GPS surveys	InSAR	Microgravity	Geometric-Historic
LS information	Point-wise	Point-wise	Continuous	Point-wise	Point-wise
Spatial coverage	Local	Local to regional	Local to regional	Local	Local
Temporal coverage	User dependent	User dependent	Images availability dependent	User dependent	User dependent
Ground benchmark	Required	Required	Not required	Required	Not required
Data acquisition (survey)	Day time and weather dependent	Day and night, weather independent	Dependent on satellite passes in the region	Day and night, weather dependent	Day time and weather dependent
Typical limitation	Laborious and time consuming	Signal obstruction by buildings, infrastructures and trees	Poor image coherence due to land use and land cover dynamics	Requires stringent observation strategy and quite costly	Based on historical and interview data which not always accurate
Typical accuracy level of LS	mm (relative)	mm-cm (relative)	mm-cm (relative)	mm-cm (relative)	cm-dm (relative)

Table 3 Observed land subsidence rates in Jakarta; after Abidin et al. (2001, 2011)

No.	Method	Subsidence rates (cm/year) Min–Max	Typical	Observation period
1	Leveling Surveys	1–9	3–7	1982–1991
		1–25	3–10	1991–1997
2	GPS Surveys	1–28	4–10	1997–2011
3	InSAR	1–12	3–10	2006–2010

Table 4 Observed land subsidence rates in Bandung; after Abidin et al. (2012a), Chaussard et al. (2013), Chatterjee et al. (2013), Ng et al. (2012)

No.	Method	Subsidence Rates (cm/year) Min–Max	Typical	Observation period
1	GPS Surveys	1–23	4–11	2000–2010
3	InSAR	1–19	5–12	1999–2010

Table 5 Observed land subsidence rates in Semarang; after Abidin et al. (2012b), Kuehn et al. (2009), Murdohardono et al. (2007, 2009), Supriyadi (2008)

No.	Method	Subsidence rates (cm/year) Min–Max	Typical	Observation period
1	Leveling Surveys	1–17	2–10	1999–2003
2	GPS Surveys	1–19	3–10	2008–2011
3	PS InSAR	1–10	3–8	2002–2006
4	Microgravity	1–15	2–10	2002–2005

are assumed to be homogeneous and linear in times. Before being integrated, subsidence rates from each method are compared against each other if the observation points are closed together. Statistically outlier rates are discarded and not used for the integration.

The second approach that can be used is to give different weights for subsidence or subsidence rates derived from different methods. Many weighting schemes can actually be implemented. In this case, we use the weighting scheme proposed by Karabatic (2011), and investigates its performance in integrating GPS and InSAR derived land subsidence in Bandung basin in the period of 1999 to 2010 (Abidin et al. 2008b, 2009, 2012a, 2013). In this case, the integrated (GPS and InSAR) subsidence magnitudes ($dh^{GPS/InSAR}$) at each InSAR sampling points i (φ_i,λ_i) are computed using following relation (Gumilar 2013):

$$dh(\varphi_i,\lambda_i)^{GPS/InSAR} = f\,(\varphi_i,\lambda_i)\,.\,dh(\varphi_i,\lambda_i)^{InSAR}. \quad (1)$$

The weighting factors at each sampling points (φ_i,λ_i) are computed by considering also the GPS derived subsidence magnitudes at several stations (Φ_k ,Λ_k) inside a 15 km radius from the sampling point, using the following relation:

$$f\,(\varphi_i,\lambda_i) = \sum_{k=1}^{N} W^k\,(\varphi_i,\lambda_i)\,.f\,(\Phi_k,\Lambda_k)\,, \quad (2)$$

where:

$$W^k\,(\varphi_i,\lambda_i) = \begin{cases} \dfrac{\left(r_{ik}^{-2}\right)}{\sum_k \left(r_{ik}^{-2}\right)} & for\ r_{ik} < 15\ km \\ 0 & for\ r_{ik} > 15\ km \end{cases},$$

$$f\,(\Phi_k,\Lambda_k) = \frac{dh(\Phi_k,\Lambda_k)^{GPS}}{dh(\Phi_k,\Lambda_k)^{InSAR}},$$

N = number of involved GPS stations, which is about 40 stations in case of Bandung, and

r_{ik} = distance from the InSAR sampling point i (φ_i,λ_i) to GPS station k (Φ_k ,Λ_k).

The integration result using this weighting scheme is shown in Fig. 5 (right side). If it is compared with the result of using no weighting scheme (left side) it can be

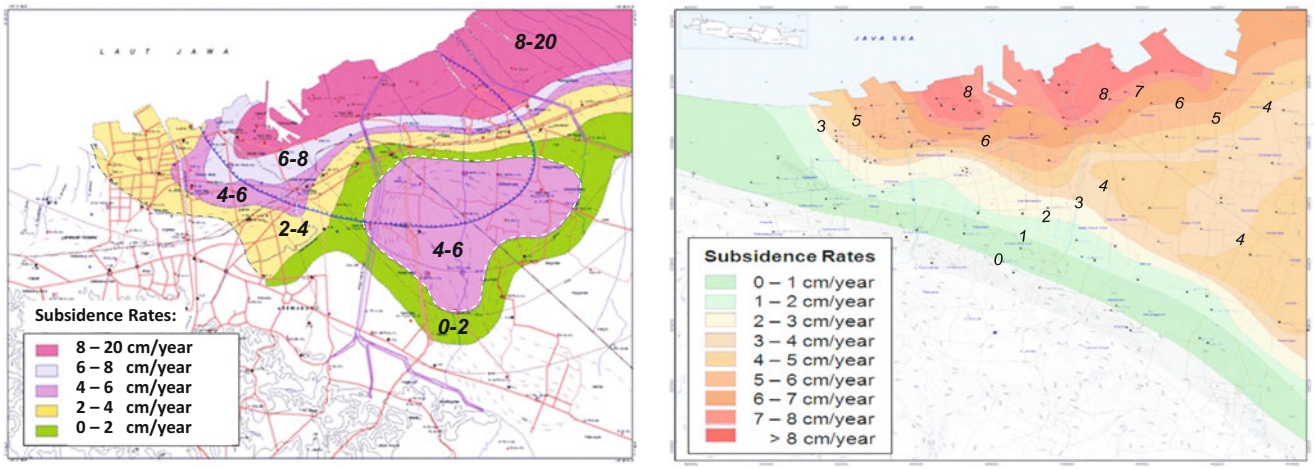

Fig. 3 Example of different spatial characteristic of land subsidence in Semarang: (*left*) Levelling derived subsidence rates in the period of 2000 to 2001, after Murdohardono et al. (2007); (*right*) PS InSAR derived subsidence rates in the period of 2002 and 2006; after Murdohardono et al. (2009) and Kuehn et al. (2009)

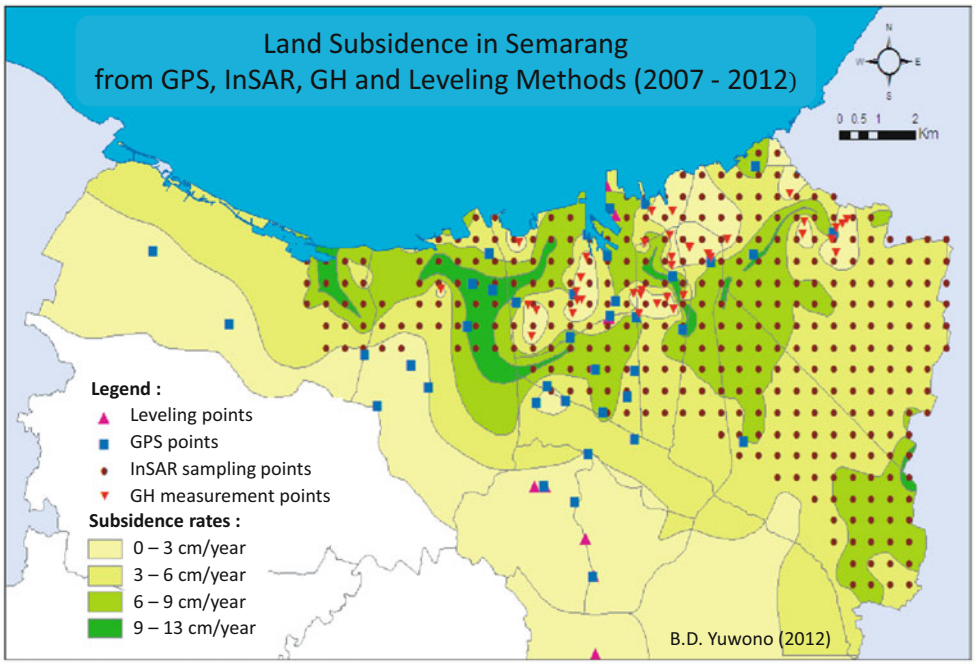

Fig. 4 Characteristics of land subsidence rates in Semarang derived from integration of Leveling, GPS, InSAR and Geometric-Historic observation results; after Yuwono (2013)

seen that although general spatial pattern of subsidence is relatively similar, however land subsidence magnitudes in a few locations are slightly different.

Validation on the quality of integrated land subsidence result is not an easy task to accomplish. For example in Fig. 5 above, how we can judge that the weighted result is better than the unweighted one. One method is to compare the integration result with the modeling result. However proper modeling of land subsidence itself is not an easy task to perform, since land subsidence in Bandung basin can be caused by combination of several factors (Abidin et al. 2013). This validation method is therefore cannot yet be performed at this times. The other method of validation is to compare the integration result with the observed impact of land subsidence in the field.

Impact of land subsidence in Bandung basin is shown by Fig. 6. Based on the observed subsidence impacts in Ketapang area (see Fig. 5), then by comparing it with the average GPS-derived subsidence rates from 2000 to 2010 (see Fig. 6), it can be concluded that the integrated

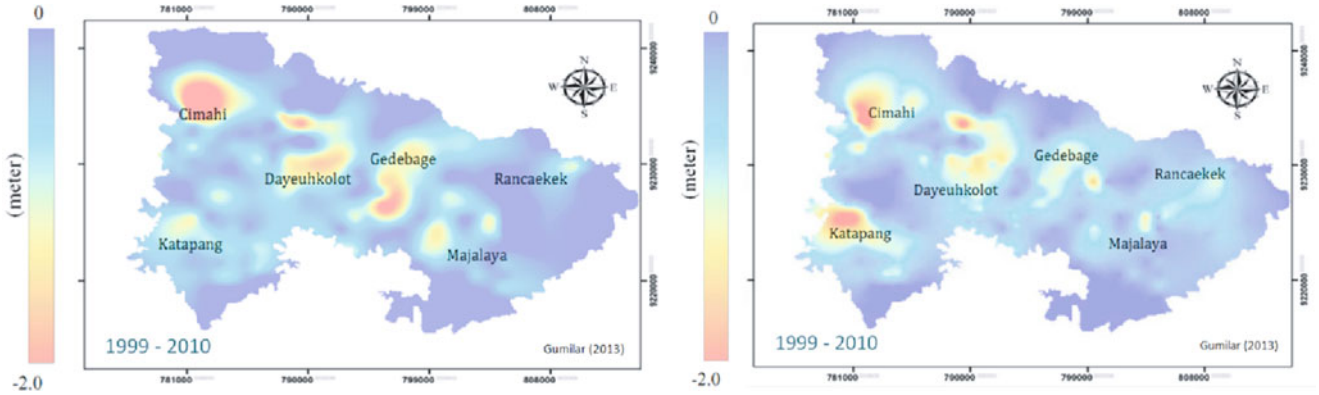

Fig. 5 Characteristics of land subsidence in Bandung basin from 1991 to 2010 as derived from integration of GPS surveys and InSAR results, withouth (*left side*) and with (*right side*) weighting schemes

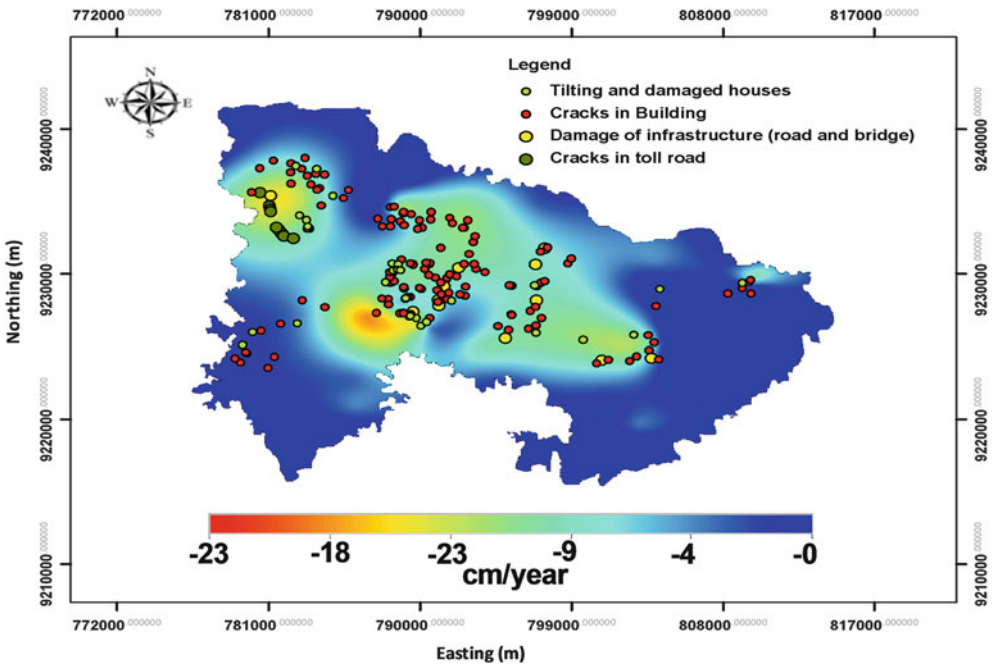

Fig. 6 Example of distribution of land subsidence impacts in Bandung, overlapped with the average GPS-derived subsidence rates from 2000 to 2010; after Abidin et al. (2013)

GPS-InSAR subsidence is in better agreement with the observed subsidence impacts compared to those GPS derived subsidence only. However, if we compare these observed subsidence impacts with the weighted and unweighted subsidence results of GPS and InSAR integration, there is no strong indication which one is better. Although, the weighted result seems to be in better agreement in Ketapang area, but the agreement in other areas are relatively similar for these two approaches. In this case, there is a possibility that not all impacts of subsidence in Bandung basin have been found and positioned. More subsidence impact survey should be performed to validate which one is better between the unweighted and weighted integration scheme of GPS and InSAR results.

4 Closing Remarks

Several large urban areas of Indonesia are prone toward land subsidence phenomena, such as Jakarta, Bandung, Semarang, Medan and Surabaya. Since land subsidence information is important to be considered for various urban development activities, then systematic and continuous monitoring of land subsidence is obviously important to be conducted.

Since all geodetic methods have their own strentghs and limitations in observing and estimating land subsidence in urban areas, then integration of various geodetic observation results is necessary and should be done for better assessment of subsidence hazard risk. Integrated land subsidence information will have better spatial and temporal characteristics of land subsidence phenomena; and this will lead to better understanding about its causes and impacts. Proper mitigation and adaption toward land subsidence phenomena can then be performed in effective and efficient manner.

However, integrating various geodetic observation results for obtaining the real and complete characteristics of land subsidence phenomena is quite a challenging task. These geodetic results have their own spatial and temporal resolution, and also their own accuracy and precision of estimated subsidence. Therefore the integration mechanism being adopted should take into account these different natures of subsidence results. Proper validation mechanism of the integration result should also be established. Moreover, the assumption of homogeneity and linearity of subsidence rates used in this integration study is not always true, and further research should be performed to take properly into account this non-homogeneity and non-linearity problem.

References

Abidin HZ, Djaja R, Darmawan D, Hadi S, Akbar A, Rajiyowiryono H, Sudibyo Y, Meilano I, Kusuma MA, Kahar J, Subarya C (2001) Land Subsidence of Jakarta (Indonesia) and its geodetic-based monitoring system. Nat Hazards 23(2/3)365–387

Abidin HZ, Andreas H, Djaja R, Darmawan D, Gamal M (2008a) Land subsidence characteristics of Jakarta between 1997 and 2005, as estimated using GPS surveys. GPS Solut Springer Berlin/Heidelberg 12(1):23–32

Abidin HZ, Andreas H, Gamal M, Wirakusumah AD, Darmawan D, Deguchi T, Maruyama Y (2008b) Land subsidence characteristics of the Bandung Basin, Indonesia, as estimated from GPS and InSAR. J Appl Geodesy 2(3):167–177. doi:10.1515/JAG.2008.019

Abidin HZ, Andreas H, Gumilar I, Wangsaatmaja I, Fukuda Y, Deguchi T (2009) Land subsidence and groundwater extraction in Bandung Basin (Indonesia). In: Trends and sustainability of groundwater in highly stressed aquifers, IAHS Publication no. 329, ISSN: 0144-7815, pp 145–156

Abidin HZ, Andreas H, Gamal M, Gumilar I, Napitupulu M, Fukuda Y, Deguchi T, Maruyama Y, Riawan E (2010a). Land subsidence characteristics of the Jakarta Basin (Indonesia) and its relation with groundwater extraction and sea level rise. In: Taniguchi M, Holman IP (eds) Groundwater response to changing climate, IAH Selected Papers on Hydrogeology No. 16, CRC, London, ISBN:978-0-415-54493-1, Chap 10, pp113–130

Abidin HZ, Andreas H, Gumilar I, Sidiq TP, Gamal M, Murdohardono D, Supriyadi, Fukuda Y (2010b) Studying land subsidence in semarang (Indonesia) using geodetic methods. In: Proceedings of the FIG Congress 2010, FS 4D – landslide and subsidence monitoring II, Sydney, Australia, 11–16 April 2010

Abidin HZ, Andreas H, Gumilar I, Fukuda Y, Pohan YE, Deguchi T (2011) Land subsidence of Jakarta (Indonesia) and its relation with urban development. Nat Hazards 59(3):1753–1771

Abidin HZ, Gumilar I, Andreas H, Murdohardono D, Fukuda Y (2012a) On causes and impacts of land subsidence in Bandung Basin, Indonesia. Environ Earth Sci. doi:10.1007/s12665-012-1848-z

Abidin HZ, Andreas H, Gumilar I, Sidiq TP, Fukuda Y (2012b) Land subsidence in coastal city of Semarang (Indonesia): characteristics, impacts and causes. J Geomatics Nat Hazards Risk. doi:10.1080/19475705.2012.692336

Abidin HZ, Gumilar I, Andreas H, Murdohardono D, Fukuda Y (2013) On causes and impacts of land subsidence in Bandung Basin, Indonesia. Environ Earth Sci 68(6):1545–1553

Buckley SM, Rosen PA, Hensley S, Tapley BD (2003) Land subsidence in Houston, Texas, measured by radar interferometry and constrained by extensometers". J Geophys Res 108(B11):2542. doi:10.1029/2002JB001848

Cabral-Cano E, Dixon TH, Miralles-Wilhelm F, Díaz-Molina O, Sánchez-Zamora O, Carande RE (2008) Space geodetic imaging of rapid ground subsidence in Mexico City. Geol Soc Am Bull 120:1556–1566

Chai JC, Shen SL, Zhu HH, Zhang XL (2004) Land subsidence due to groundwater drawdown in Shanghai. Geotechnique 54(2):143–147

Chatterjee RS, Syafiudin MF, Abidin HZ (2013) Land subsidence characteristics in Bandung City, Indonesia as Revealed by spaceborne geodetic techniques and hydrogeological observations. Photogram Eng Remote Sensing 79(7):639–652

Chaussard E, Amelung F, Abidin HZ, Hong S-H (2013) Sinking cities in Indonesia: ALOS PALSAR detects rapid subsidence due to groundwater and gas extraction. Remote Sens Environ, Elsevier 128:150–161

Chen CT, Hu JC, Lu CY, Lee JC, Chan YC (2007) Thirty-year land elevation change from subsidence to uplift following the termination of groundwater pumping and its geological implications in the Metropolitan Taipei Basin, Northern Taiwan. Eng Geol 95:30–47

Fukuda Y, Higashi T, Miyazaki S, Hasegawa T, Yoshii S, Fukushima Y, Nishijima J, Tanigushi M, Abidin HZ, Delinom RM (2008) Groundwater and land subsidence monitoring in 3 Mega-Cities, Indonesia, by means of integrated geodetic methods. Paper presented at the AGU Fall Meeting 2008, San Fransisco, 15–19 December

Gumilar I (2013) Mapping land subsidence characteristics based on the integration of GPS and InSAR, and estimation of economic losses due to land subsidence (Case Study: Bandung Basin). PhD Dissertation, in Indonesian, Department of Geodesy and Geomatics Engineering, Institute of Technology Bandung, October, 265 pp

Ishii M, Kuramochi F, Endo T (1970) Recent tendencies of the land subsidence in Tokyo. Publication No. 121 of the Internationa] Association of Hydrological Sciences. Proc Anaheim Symp Dec:25–34

Karabatic A (2011) Precise Point Positioning (Ppp) – an alternative technique for ground based Gnss troposphere monitoring. PhD Dissertation, Vienna University of Technology, Faculty of Mathematics and Geoinformation, February, 252 pp

Kuehn F, Albiol D, Cooksley G, Duro J, Granda J, Haas S, Hoffmann-Rothe A, Murdohardono D (2009) Detection of land subsidence in Semarang, Indonesia, using stable points network (SPN) technique. Environ Earth Sci. doi:10.1007/s12665-009-0227-x

Lubis AM, Sato T, Tomiyama N, Isezaki N, Yamanokuchi T (2011) Ground subsidence in Semarang-Indonesia investigated by ALOS–PALSAR satellite SAR interferometry. J Asian Earth Sci 40(5):1079–1088

Murayama S (1970) Land subsidence in Osaka. In: Proceedings of the Tokyo symposium on land subsidence, vol 1, International Association of Scientific Hydrology and UNESCO, September 1969, Tokyo, pp 105–130

Murdohardono D, Tobing TMHL, Sayekti A (2007) Over Pumping ff Ground Water as one of Causes of Sea Water Inundation in Semarang City. Paper presented at the international symposium and workshop on current problems in groundwater management and related water reosurces issues, Kuta, Bali, 3-8 December

Murdohardono D, Sudradjat GM, Wirakusumah AD, Kühn F, Mulyasari F (2009) Land subsidence analysis through remote sensing and implementation on municipality level; case study: semarang municipality, Central Java Province, Indonesia. Paper presented at the BGR-GAI-CCOP Workshop on Management of Georisks, 23–25 June, Yogyakarta

Ng AH-M, Ge L, Li X, Abidin HZ, Andreas H, Zhang K (2012) Mapping land subsidence in Jakarta, Indonesia using persistent scatterer interferometry (PSI) technique with ALOS PALSAR. Int J Appl Earth Obs Geoinf 18:232–242

Phien-wej N, Giao PH, Nutalaya P (2006) Land subsidence in Bangkok, Thailand. Eng Geol 82(4)187–201

Sumantyo JTS, Shimada M, Mathieu PP, Abidin HZ (2012) Long-term consecutive DInSAR for volume change estimation of land deformation. IEEE Trans Geosci Remote Sensing 50(1):259–270

Supriyadi (2008) Separation of gravity anomaly caused subsidence and ground water level lowering of time lapse microgravity data using model based filter: case study semarang Aluvial Plain (in Indonesian). PhD Dissertation, Institute of Technology Bandung, September, 146 pp

Yuwono BD (2013) Geospatial analysis of cause and impacts of land subsidence in Semarang. MSc Thesis, in Indonesian, Department of Geodesy and Geomatics Engineering, Institute of Technology Bandung, 184 pp

Observation of Triggering Factors and Development of Landslides by Borehole Tiltmeters on the High Bank of the River Danube in Dunaszekcső, Hungary: A Case Study

Gyula Mentes

Abstract

In Hungary the high loess banks along the west side of the River Danube are prone to landslides that cause a lot of damage. Several landslides have occurred in Dunaszekcső. In August 2007 the commencement of a slow sliding process was visually observed here and two borehole tiltmeters were installed in the dangerous area. One instrument was placed on the stable part and the other on the unstable part of the high loess wall. A large landslide occurred here on 12 February 2008, so the whole sliding process was recorded by the tiltmeters. The instrument on the sliding part of the high bank was reinstalled one year after the slump because of the large movements. The tiltmeter on the stable part was working continuously and so the processes by which the high bank tried to keep its balance were recorded. However, the high bank did not come to an equilibrium state and in 2010 a new crack appeared about 8–10 m from the 2008 slide headwall. The recorded tilt is similar to the tilt process before the first slump. Besides tilt measurements, the water level of the River Danube, the ground water table, and the ground and air temperature were also monitored. The potential evapotranspiration of the area was also determined to study the effect of the vegetation. This paper presents the tilt processes and the relationships between tilt and hydrological and meteorological parameters.

Keywords

Ground water • High bank • Landslide • Landslide prediction • River Danube • Tiltmeter

1 Introduction

Landslides of the high loess banks along the west side of the River Danube cause a lot of damage. In most cases the large slides are preceded by very small movements which cannot be detected by the usual geodetic methods as GPS, EDM measurements, precise levelling and PInSAR technique. Highly sensitive borehole tiltmeters can be used for monitoring these small movements (see e.g. Fabian and Kümpel 2003; García et al. 2010). In Dunaszekcső after the onset of a landslide in August 2007 a geodetic network was established and two borehole tiltmeters were installed for monitoring the movements. Besides geodetic (Újvári et al. 2009) and tilt measurements, the water level of the River Danube, ground water table variations, the ground and air temperatures, and precipitation values were measured. The evapotranspiration of the area was also calculated to study the effect of vegetation on the high bank movements. In this study the tilt processes of the sliding are demonstrated and the meteorological and hydrological parameters are compared with the tilt data and their effect on the high bank tilts is investigated in detail.

Poster presentation at the conference IAG 2013: 150 YEARS IAG, International Association of Geodesy, Scientific Assembly Potsdam, Germany, from 1 to 6 September, 2013.

G. Mentes (✉)
Geodetic and Geophysical Institute, Research Centre for Astronomy and Earth Sciences, Hungarian Academy of Sciences, Csatkai E. u. 6-8, 9400 Sopron, Hungary
e-mail: mentes@ggki.hu

© Springer International Publishing Switzerland 2015

C. Rizos, P. Willis (eds.), *IAG 150 Years*, International Association of Geodesy Symposia 143,
DOI 10.1007/1345_2015_81

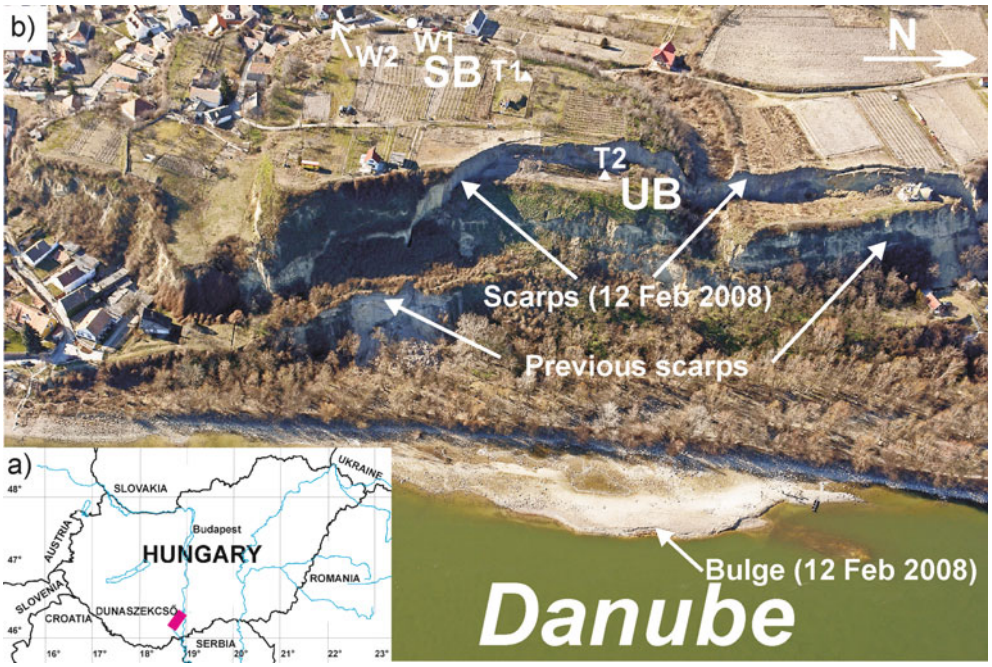

Fig. 1 The location of Dunaszekcső in Hungary (**a**) and the oblique aerial photo (**b**) of the test site (photo was taken by László Körmendy on 17 February after the large landslide on 12 February 2008). T1, T2 and W1, W2 show the location of the borehole tiltmeters and the ground water level gauges, respectively

2 Test Site

The high loess walls along the right side of the River Danube are prone to landslides. One of the dangerous landslides occurred at Dunaszekcső on 12 February 2008. Dunaszekcső is situated about 20 km north of the southern border of Hungary. Figure 1 shows the location (left lower corner) and an oblique aerial photo of the study area taken after the large landslide on 12 February 2008. The photo shows also the scarps of previous landslides.

The basement formations of the high bank at Dunaszekcső are Triassic–Jurassic limestones located at 200–250 m below the surface. These basement rocks are covered by clayey and sandy sediments formed in the Upper Miocene and the Pliocene. The upper 70 m thick loess layer (about 50 m above the average water level of the River Danube) has brown to red fossil soils accumulated during the Pleistocene (Kraft 2005; Újvári et al. 2009). The landslide process is influenced by the interaction between the ground water and the water of the River Danube. The ground water transfers the loess at the basement to the Danube and the river ablates it. A tight brown stripe of loess sediment can be often seen in the current of the river which proves the above mentioned assumption (Újvári et al. 2009; Karbon et al. 2011).

3 Measurement Methods

The tilt of the loess wall was measured by highly stable Model 722A borehole tiltmeters produced by Applied Geomechanics Inc. This instrument has a dual-axis tilt sensor and a built-in temperature sensor which is used for the measurement of the borehole temperature. The resolution of the tilt and temperature sensors is 0.1 μrad and 0.1°C, respectively (Applied Geomechanics Inc. 1991). One tiltmeter (T1) was installed on the stable (SB) and the other instrument (T2) on the unstable (UB) part of the high wall (see Fig. 1a). The instruments are oriented so that their +x axes point to the east and their +y axes to the north. The installation of the tiltmeters is described by Mentes et al. (2012) in detail. Tilt measurements are carried out since October 2007. Two water level gauges were installed at locations W1 (in October 2009) and W2 (in March 2010). W1 is located ca. 100 m west of the sliding block (UB), while W2 is situated approximately 200 m south of W1 at a slightly lower height (see Fig. 1b). Tilt, borehole, air temperature and ground water level data were sampled hourly while water level data of the River Danube and precipitation data were available daily. The data were downloaded from the data loggers when the batteries were changed every 40–50 days. Daily water level data of

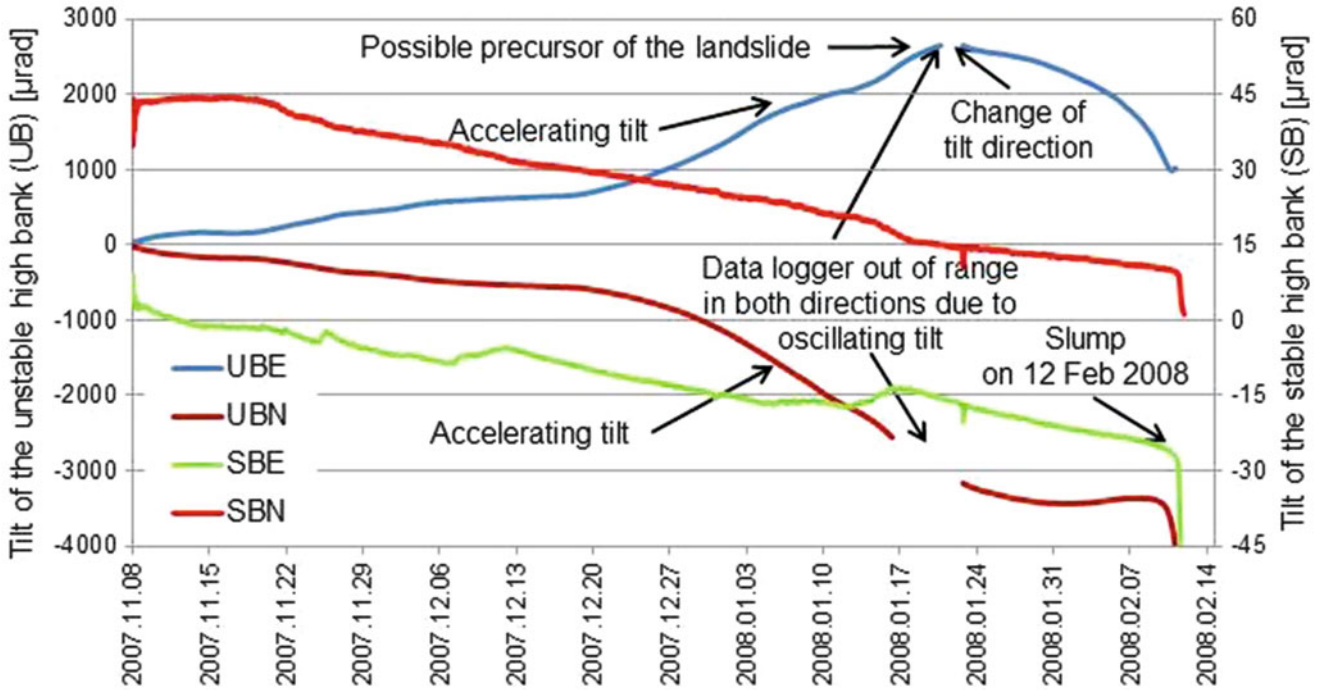

Fig. 2 Tilts of the high loess wall before and during the large landslide on 12 February 2008. SBE and SBN indicate the eastern and northern components of tilts measured on the stable part of the high bank (T1), UBE and UBN denote the eastern and northern components of tilts measured on the (unstable) slumped block (T2). Increasing positive values of UBE and SBE mean eastward tilt, while negative values indicate tilt towards the west. Increasing northern components (UBN and SBN) mean tilt towards the north, while decreasing values indicate southward tilt

the River Danube is measured relative to the zero point of the water gauge, which has a height of 79.92 m above the Baltic Sea. This data has been downloaded from the publicly available website of the Directorate of Water Management (www.vizugy.hu, last accessed: 10 May 2013).

4 Results

4.1 Tilt Processes Before the Large Slump (12 Febuary 2008)

Figure 2 shows the tilt records between 8 November 2007 and 12 February 2008 covering a time period before the landslide event. The tiltmeter T1 (see Fig. 1b) on the stable bank (SB) recorded a continuous tilt toward the west (SBE component) and south (SBN component) directions with small direction changes while tiltmeter T2 on the unstable bank section (UB) measured tilts to the east, toward the River Danube (UBE) and south (UBN) directions till 21 January 2008. Large tilt direction changes occurred during the gaps in the tilt records. The east-west sensor of the tiltmeter T2 returned to its original position after some direction changes, but the tilt direction turned (rotational slide) and a strong tilt (UBE) in the west direction was recorded till the large slump in February. The north-south sensor of the tiltmeter T2 went out of range several times both in the north and south directions and after some changes it tilted strongly to the south (UBN) and went out of the measuring range. These parts of the tilt record were not drawn in Fig. 2. This tilt component of the instrument was readjusted into its zero position during the battery change, so the amount of the tilt during the gap is not known. The tilt curve following the gap had to be shifted to obtain a continuous tilt record. These large tilt changes were due to a rotation and a subsidence of the unstable part of about 30 cm (Újvári et al. 2009). The large tilt changes of the unstable part of the high bank between 17 and 21 January 2008 can be assumed to be a precursor of the large slump. The photo in Fig. 1b shows the study area after the large landslide on 12th February 2008 (ca. 300,000 m^3 earth slid down on this day).

4.2 Tilt Processes After the Large Slump Till 31 August 2010

During the slump of the unstable part of the high bank, tiltmeter T2 went out of its measuring range since the borehole was tilted by 18.9° toward the west by the rotating phase of the landslide. The instrument was re-installed after the slump but the tilts of the slumped part of the loess wall

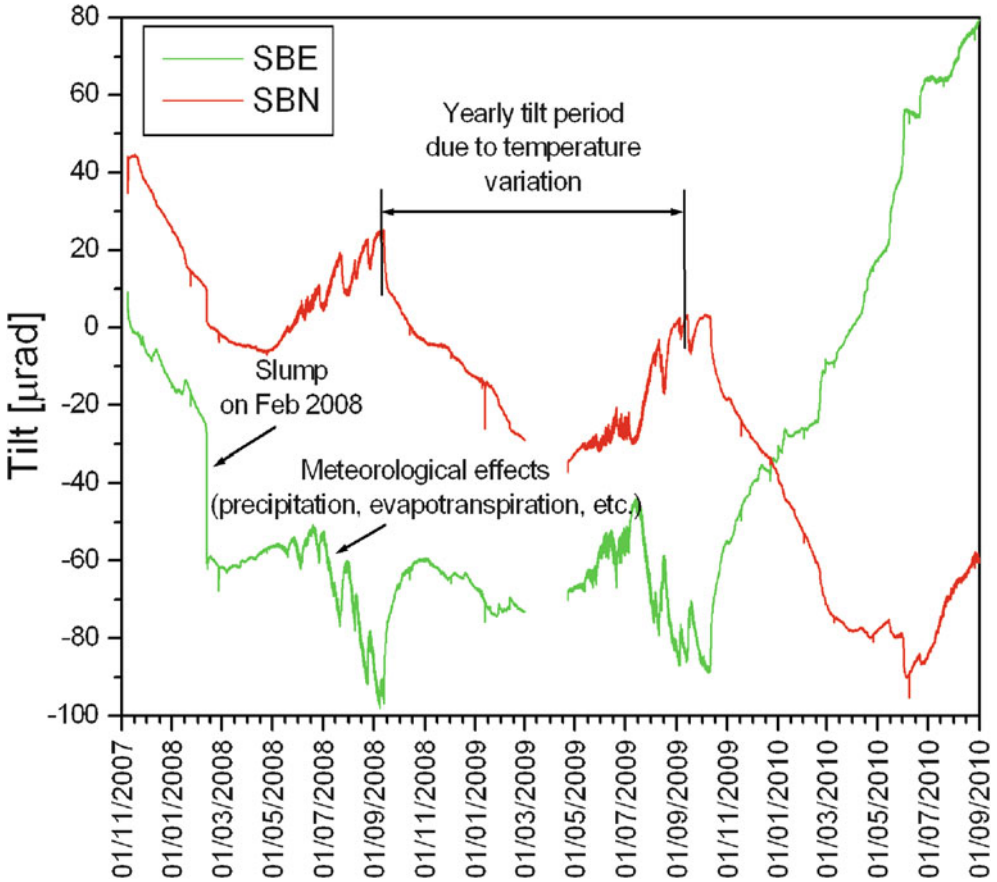

Fig. 3 Tilt of the stable part (tiltmeter T1) of the high loess wall between 1 November 2007 and 31 August 2010. SBE and SBN indicate the eastern and northern tilt components Tilt curves going in positive direction mean tilts toward to east and north

were larger than the measuring range of the tiltmeter. Usable tilt data was obtained only from 1 September 2010. During this time tiltmeter T1 recorded the tilt of the stable part of the loess wall. The tilt record is shown in Fig. 3. The short period tilts during summers are due to meteorological effects. The tilts have also a seasonal variation which is caused by the annual temperature variation. The tilts variations with a period of longer than some weeks are due to the fact that the high bank is not yet in equilibrium state after the slump.

4.3 Tilt Processes After the Large Slump from 1 September 2010 to 28 February 2013

Figure 4 shows the tilt data measured on the stable (T1) and unstable part of the high bank (re-installed T2) together with the W1 and W2 ground water levels (see Fig. 1b) and the Danube's water level (DWL). The hourly measured tilt data is corrected for the surface temperature because the temperature variations caused tilts of 5–15 μrad C^{-1}. The hourly measured tilt and ground water level data were daily averaged to be comparable with the daily measured water level of the River Danube. Correlation and multiple variable regression analyses were applied between the tilt components and the hydrologic data to get an insight how the tilt values depend on the water level variations. Table 1 shows the results calculated from data between 1 September 2010 and 28 February 2013. The regression coefficients (admittances) between the tilt components and water levels show the tilt values caused by a water level change of 1 m. The highest regression coefficients were obtained in the case of the unstable part of the loess bank between UBE and W1 (1,028 μrad m^{-1}) and UBN and W1 (676 μrad m^{-1}). These values are about one or two orders of magnitude higher than the tilts caused by the loading from the water level variations of the River Danube. This and the small correlation coefficients between the water level of the Danube and tilt components mean that the movements of the high bank are mainly governed by the ground water level variations. The alternating tilt directions are in connection with the see-saw of the high bank during the subsidence sequences caused by the mass loss at the base of the high bank (Újvári et al. 2009; Karbon et al. 2011; Kraft 2011).

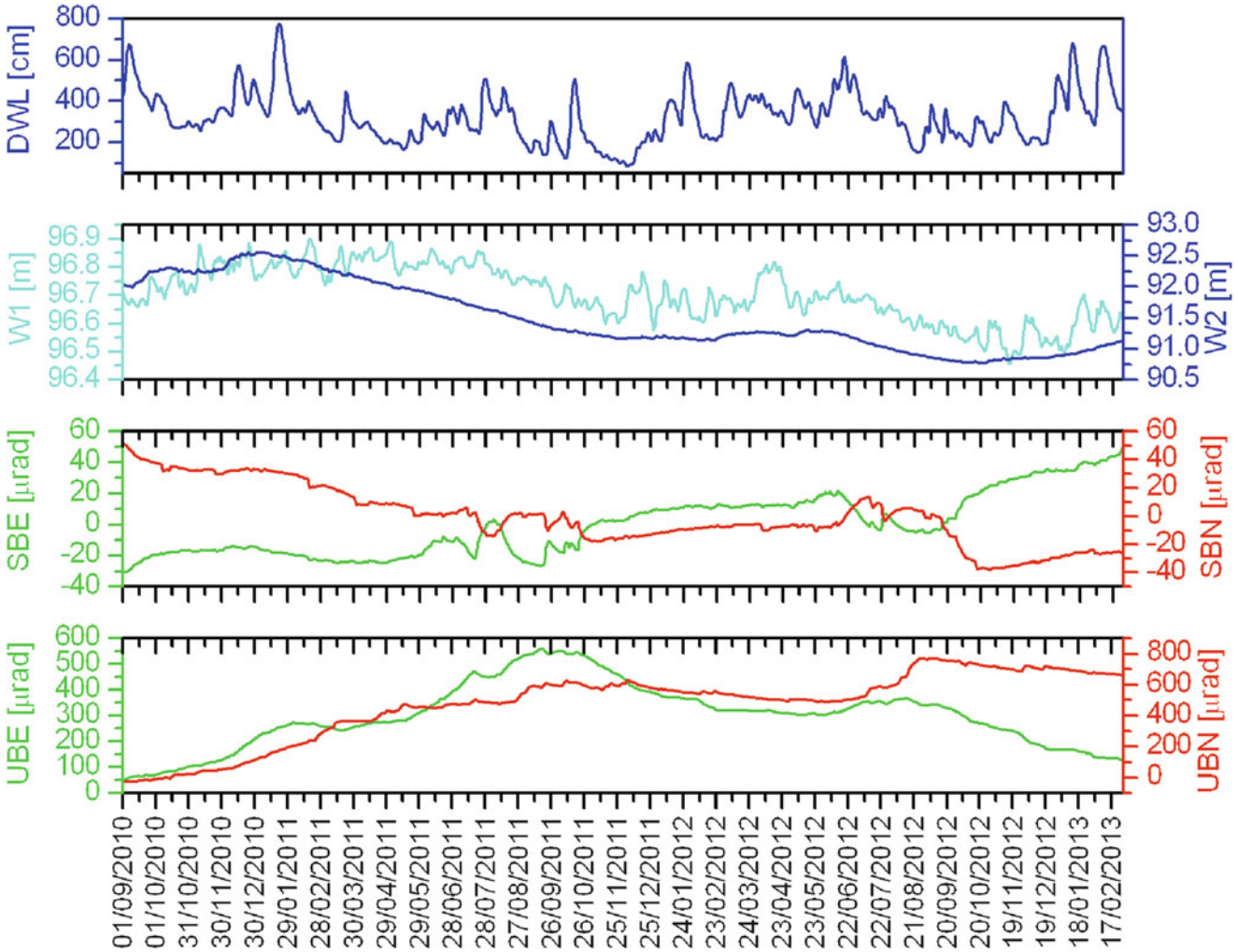

Fig. 4 Water level variations of the River Danube (DWL), ground water level (W1 and W2) relative to the Baltic Sea level and tilt recordings for the period of 1 Sept 2010 to 27 Feb 2013. SBE and SBN indicate the eastern and northern tilt components measured on the stable part of the high bank (T1), while UBE and UBN denote the eastern and northern tilt components measured on the unstable slumped block (T2). Increasing positive values of UBE and SBE mean eastward tilt, while negative values indicate tilt towards the west. Increasing northern components (UBN and SBN) mean tilt towards the north, while decreasing values indicate southward tilt

Table 1 Results of the correlation and multiple regression analyses between tilts and water levels calculated from data between 1 September 2010 and 28 February 2013. SBE and SBN are the east and north components of the tilt data measured on the stable part of the bank, UBE and UBN are the east and north components of the tilt data measured on the unstable (sliding) part of the bank, W1 and W2 are the ground water levels measured relative to Baltic Sea level and DWL is the water level of the River Danube

	Correlation coefficients			Regression coefficients (admittances)		
Tilt components	W1	W2	DWL	W1 (µrad m^{-1})	W2 (µrad m^{-1})	DWL (µrad m^{-1})
SBE	−0.704	−0.773	0.135	−36	−24	4
SBN	0.639	0.859	0.228	−25	35	1
UBE	0.044	−0.336	−0.396	1,028	−209	−28
UBN	−0.623	−0.904	−0.298	576	−434	−20

4.4 Effect of Precipitation and Evapotranspiration on the High Bank Tilts

Small daily tilt variations with exponential rising and falling edges are superimposed on the tilt curves (Fig. 5). These tilts are due to the pore pressure variations of the ground (Kümpel et al. 1996) which are caused by ground water level variations, precipitation and by the variation of the evapotranspiration (evaporation of the soil and transpiration of the plants) of the test site. The potential evapotranspiration (PET) was calculated by the Thornthwaite method

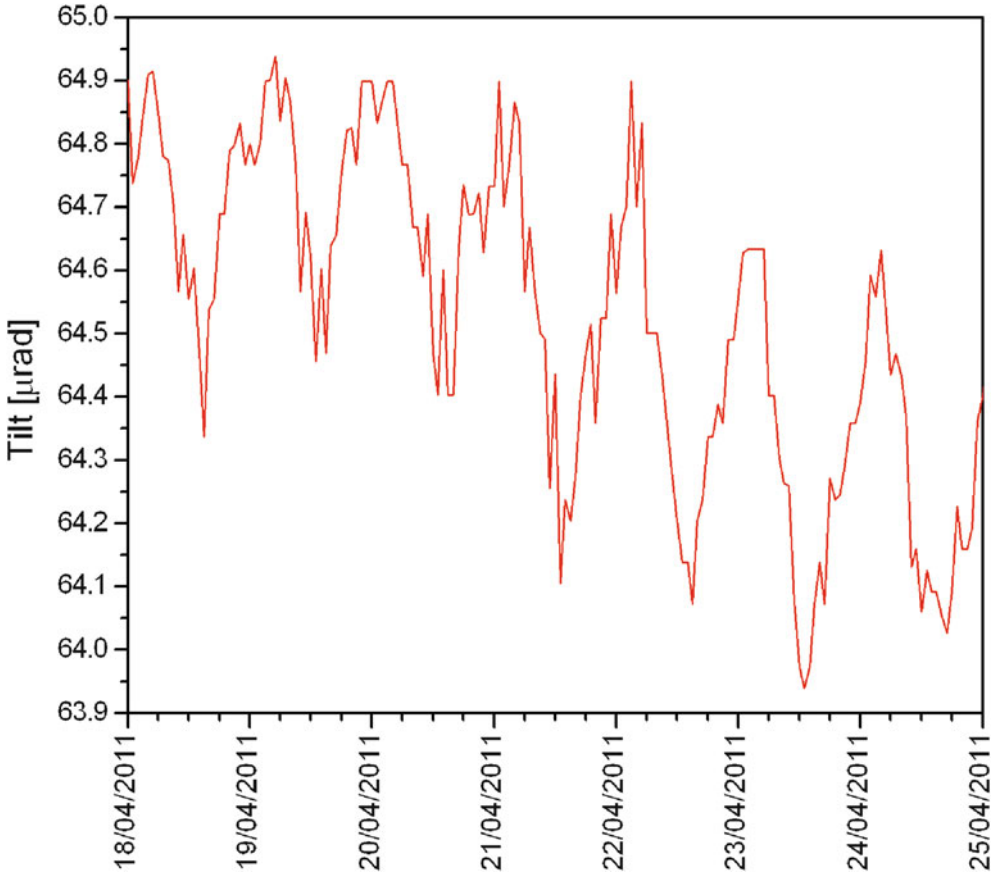

Fig. 5 Daily tilt variations

(Thornthwaite 1948; Rey 1999) on the basis of the vegetation map of the test area (Bódis and Mentes 2012; Mentes and Bódis 2012). Since the Thornthwaite formula gives the monthly PET values, monthly precipitation and monthly averages of the small tilt amplitudes – obtained by high-pass filtering of the tilt data – were calculated for the sake of comparison. Figure 6 shows the calculated values. It can be seen that the PET values and the tilt amplitudes are the highest in the growing period of the plants (see also Fig. 3). Precipitation on the test site does not play a considerable role in the tilt processes of the high bank (see also Újvári et al. 2009).

5 Discussion and Conclusions

Újvári et al. (2009) and Karbon et al. (2011) proposed a rotational slider block model for this slide on the basis of geodetic measurements. However, the sliding is always preceded by subsidence series of the unstable part of the high bank caused by the mass loss at the basement due to removal (ablation) of the high bank material by the ground water flow into the Danube. Table 1 shows that the ground water has the largest effect on the high bank stability. After a subsidence event both (stable and unstable) parts of the high bank get into a new equilibrium state by alternating small tilts (movements), according to the tilt measurements. It can be inferred from the continuous tilt measurements that the decreasing support of the unstable part and the decreasing cohesion between the stable and unstable parts lead to the abrupt slump of the unstable part in the last phase of the high bank movements. The mass loss before the slump causes a large eastward (towards the River Danube) tilt of the unstable part of the high bank (see Fig. 2) which turns into a westward tilt about one month before the slump. The observation of this change of tilt direction could be used for forecasting of the main slump in the case of on-line tilt measurements. The alternating tilt direction (see Figs. 2, 3, and 4) after the slump and the visual observation of the water of the River Danube prove that the mass loss is continuing with changing speed and a new growing crack appeared about 8 m behind the slump front wall in 2009 which could lead to a new slump in the next years. Recording similar tilting process during a second slump which was recorded in 2008 would confirm that borehole tiltmeters could play an important role in early warning systems.

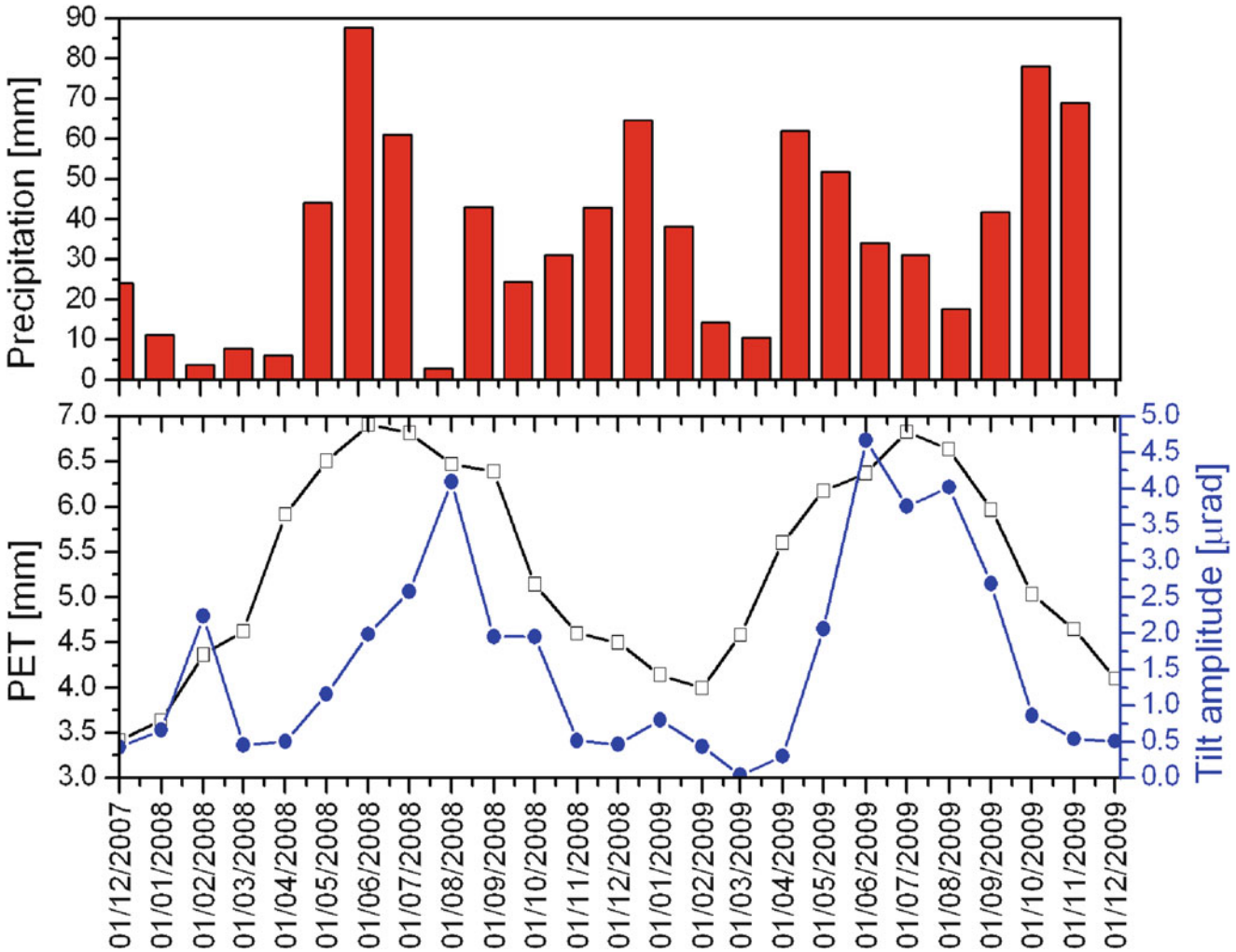

Fig. 6 Relationships between potential evapotranspiration (PET), monthly averages of the precipitation and tilt amplitudes (circles)

The effect of local precipitation on the high bank movements can be neglected and can further be decreased by planting suitable vegetation, which hinders the infiltration of the water into the soil due to intensive transpiration. Precipitation plays the main role in increasing the ground water level in the watershed area of the high bank. Between 1980 and 2005 the ground water level increased about 2 m (Kraft 2011) behind the high wall. This is the main reason for the present landslide processes in this area.

The study of the character and causes of the small tilts by highly sensitive borehole tiltmeters can contribute to more accurate understanding of landslide processes.

Acknowledgements This work was funded by the Hungarian National Research Fund (OTKA) under project K 81295. Special thanks to Tibor Molnár for his careful maintenance of the instruments, and to Ágnes Gimesiné Németh, Ferenc Schlaffer and Frigyes Bánfi for their help in the fieldwork: drilling boreholes, battery changes and reading the data out.

References

Applied Geomechanics Inc. (1991) User's Manual No. B-91-1004: Model722 Borehole Tiltmeter. Santa Cruz

Bódis VB, Mentes Gy (2012) The role of vegetation in the daily and yearly small tilt variations of the Danube's high bank. Hungary Zeitschrift für Geomorphologie 56(Suppl 2):133–141. doi:10.1127/0372-8854/2012/S-00095

Fabian M, Kümpel H-J (2003) Poroelasticity: observations of anomalous near surface tilt induced by ground water pumping. J Hydrol 281:187–205

García A, Hördt A, Fabian M (2010) Landslide monitoring with high resolution tilt measurements at the Dollendorfer Hardt landslide, Germany. Geomorphology 120:16–25

Karbon M, Brückl E, Hegedűs E, Preh A (2011) Kinematics of a mass movement constrained by sparse and inhomogeneous data. Nat Hazards Earth Syst Sci 11:1609–1618

Kraft J (2005) A dunaszekcsői Töröklyuk kialakulása és fennmaradása (Evolution and survival of the Töröklyuk cave at Dunaszekcső). Mecsek Egyesület Évkönyve a 2004-es egyesületi évről. Új Évfolyam 8:133–153 (in Hungarian)

Kraft J (2011) Dunai magaspart dunaszekcsői részletének rogyásos suvadásai (Slumping of Danube's high bank at Dunaszekcső). In: Török Á, Vásárhelyi B (eds) Mérnökgeológia-Kőzetmechanika, pp 1–12 (in Hungarian)

Kümpel H-J, Varga P, Lehmann K, Mentes Gy (1996) Ground tilt induced by pumping – preliminary results from the Nagycenk Test Site, Hungary. Acta Geod Geoph Hung 31(1-2):67–79

Mentes Gy, Bódis VB (2012) Relationships between short periodic slope tilt variations and vital processes of the vegetation. J Appl Geodesy 6(2):83–88

Mentes Gy, Bányai L, Újvári G, Papp G, Gribovszki K, Bódis VB (2012) Recurring mass movements on the Danube's bank at Dunaszekcső (Hungary) observed by geodetic methods. J Appl Geodesy 6(3-4):203–208

Rey JM (1999) Modelling potential evapotranspiration of potential vegetation. Ecol Model 123:141–159

Thornthwaite CW (1948) An approach toward a rational classification of climate. Geogr Rev 38(1):55–94

Újvári G, Mentes Gy, Bányai L, Kraft J, Gyimóthy A, Kovács J (2009) Evolution of a bank failure along the River Danube at Dunaszekcső, Hungary. Geomorphology 109:197–209

Coastal Sea Level Monitoring in Indonesia: Connecting the Tide Gauge Zero to Leveling Benchmarks

Julia Illigner, Ibnu Sofian, Hasanuddin Z. Abidin, M. Arief Syafi'i, and Tilo Schöne

Abstract

After the tsunami in 2004, Badan Informasi Geospasial (BIG), Indonesia, and its international partners established a large network of coastal tide gauge stations for the Indonesian Tsunami Early Warning System (InaTEWS). In the frame of the German Indonesian Tsunami Early Warning System (GITEWS), Germany donated ten tide gauge stations equipped with geodetic GNSS receivers and recently three more stations for subsidence monitoring. This network establishes a backbone for dedicated sea level research projects, for tsunami warnings, for subsidence monitoring and for the unification of the national height reference system. The radar sensors of the tide gauges establish long-term control points to connect the tide gauge zero to the leveling benchmarks and thus to the local height system. This paper evaluates the individual station offsets of the radar gauge zero, which is essential to connect the measured sea level to the vertical control network (VCN).

Keywords

Dipping • GNSS-controlled tide gauges • Indonesian height reference system • Radar gauge reference offset • Radar tide gauges

1 Introduction

Indonesia with more than 17,000 islands is the fourth most populous nation in the world. Its welfare and economic growth are strongly linked with a viable marine infrastructure and safety. But natural hazards, like excessive sea level rise, earthquakes, tsunamis, volcano eruptions, land subsidence of coastal communities and others hazards pose a permanent threat to society. Badan Informasi Geospasial (BIG, formerly BAKOSURTANAL) operates large networks of GNSS stations and tide gauges. These networks are used for monitoring environmental threats and changes (e.g., Ningsih et al. 2011; Fenoglio-Marc et al. 2012), harbor safety, tsunami early warning and also to monitor land subsidence (Abidin et al. 2012). Especially the network of GNSS-controlled tide gauges installed as part of the GITEWS project (Schöne et al. 2011) (Fig. 1) and by University of Hawaii Sea Level Center (UHSLC) (M. Merrifield pers. comm.) delivers a wider range of data in support of long-term stable sea level records, the establishment of an Indonesian unified height system (vertical control network, VCN) and of the IGS TIGA project (Schöne et al. 2009).

The VCN in Indonesia was established using precise leveling surveys regularly carried out by BIG. The first VCN sub-network was already established in the western and central parts of Java Island in the period of 1925 to 1930. At present, there are more than 5,900 VCN benchmarks distributed along national or provincial roads across several

J. Illigner (✉) • T. Schöne
Helmholtz Zentrum Potsdam, GeoForschungsZentrum GFZ, Potsdam, Germany
e-mail: julia@gfz-potsdam.de; tschoene@gfz-potsdam.de

I. Sofian • M.A. Syafi'i
Badan Informasi Geospasial (BIG), Cibinong, Indonesia
e-mail: ibnu.sofian@big.go.id; arief.syafii@big.go.id

H.Z. Abidin
Geodesy Research Group, Institute of Technology Bandung, Bandung, Indonesia
e-mail: hzabidin@gd.itb.ac.id

© Springer International Publishing Switzerland 2015

C. Rizos, P. Willis (eds.), *IAG 150 Years*, International Association of Geodesy Symposia 143,
DOI 10.1007/1345_2015_23

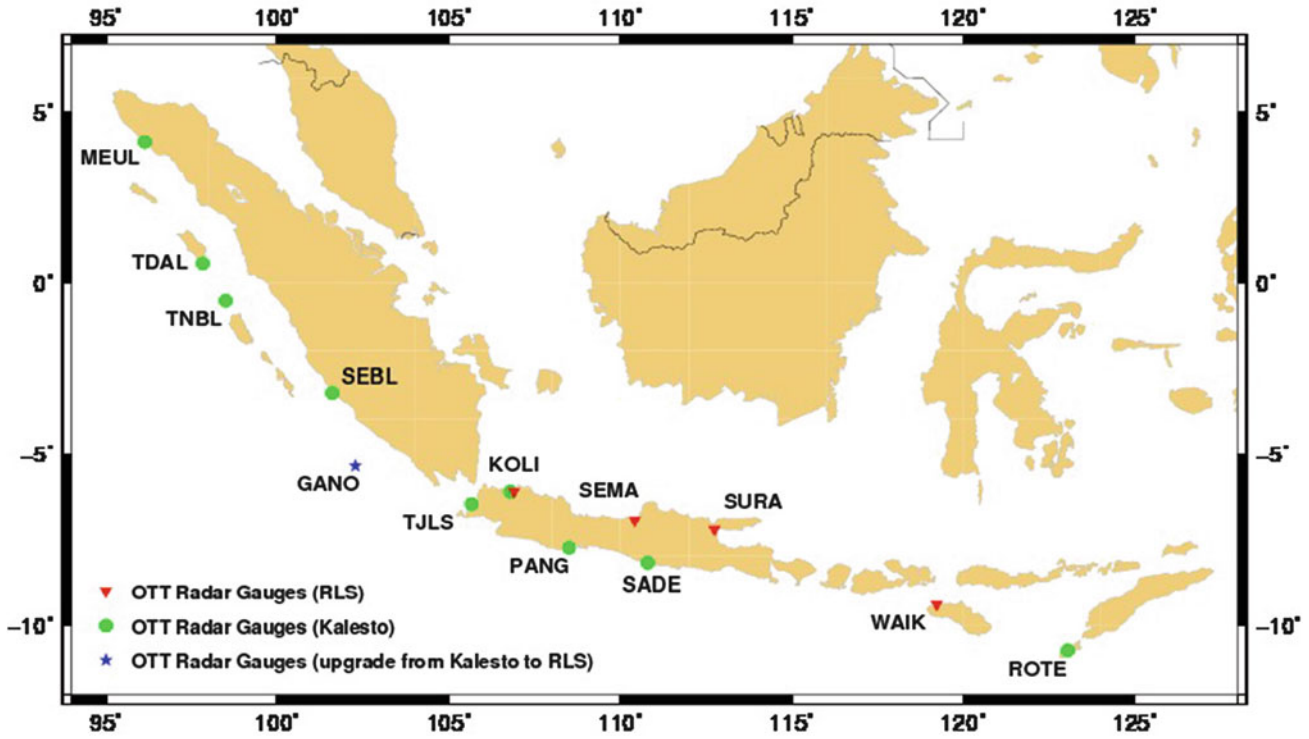

Fig. 1 Indonesia's GNSS-controlled Tide Gauge Network. Radar gauges in these installations are either OTT Kalesto or OTT RLS. Some stations have been upgraded from Kalesto to RLS (GNSS-controlled stations installed by UHSLC are not shown)

main islands, i.e., Java, Sumatra, Bali, Lombok, some parts of Sulawesi, Kalimantan and Maluku islands (BIG 2012). In general, the VCN network on each island is connected to their respective vertical datum based on Mean Sea Level (MSL) derived from tide gauge observations. Therefore, the realization of a unified vertical datum for the VCN, as it can be supported by GNSS-controlled tide gauges, is indeed an important issue for Indonesia.

2 GNSS-Controlled Tide Gauge Stations

BIG operates and oversees a network of more than 120 tide gauge stations. Over the past 9 years, a network of GNSS-controlled stations has been installed to support various applications. Installations (Fig. 1) as part of the GITEWS project (Schöne et al. 2011) sample tide gauge data every 20 s to 1 min. Each station is equipped with a radar gauge manufactured by OTT Hydrometry (Kempten, Germany) of the type OTT Kalesto or OTT RLS, a pressure gauge (OTT ODS4-K) and, additionally, with either a second pressure gauge or a float gauge (OTT OWK). Meteorological data is acquired every minute to support the data analysis. For most of these installations, the GNSS antenna is located directly on top of the tide gauge hut (Fig. 2). The GNSS-controlled tide gauge sub-network concentrates on sites located in tsunami-prone areas. This network was recently extended to areas with large subsidence rates (Jakarta (KOLI), Semarang (SEMA), and Surabaya (SURA)) to assess coastal vulnerability. With their GNSS control, the derived sea level values are in a geocentric reference frame and thus can be corrected for vertical land motion. Each tide gauge station has a leveling control network to ensure long-term stability and to establish the connection between the tide gauge reference height and the VCN. The local control networks include up to five benchmarks, the GNSS antenna reference point, a reference point at the radar gauge housing (Fig. 3), and if possible also the reference point of the pressure sensor.

3 Establishing the Local Height Reference for Tide Gauges

Beside the basic requirement of a long-term drift-free stability of tidal records, an increasing number of sea level related studies require the connection of tide gauge records to the local (e.g., chart datum) and/or national height system (for applications, see the discussions in Merrifield et al. 2012). In the past, the tidal readings have been regularly either taken or supported by manual readings from a pole staff. Thus, all readings were referenced to this leveled tide pole. Recently an increasing number of autonomous stations were installed

Fig. 2 Tide Gauge at Pangandaran (PANG, Indonesia). The antenna of the GNSS, which monitors the height and vertical motion of the tide gauge, is located on the roof of the tide gauge hut

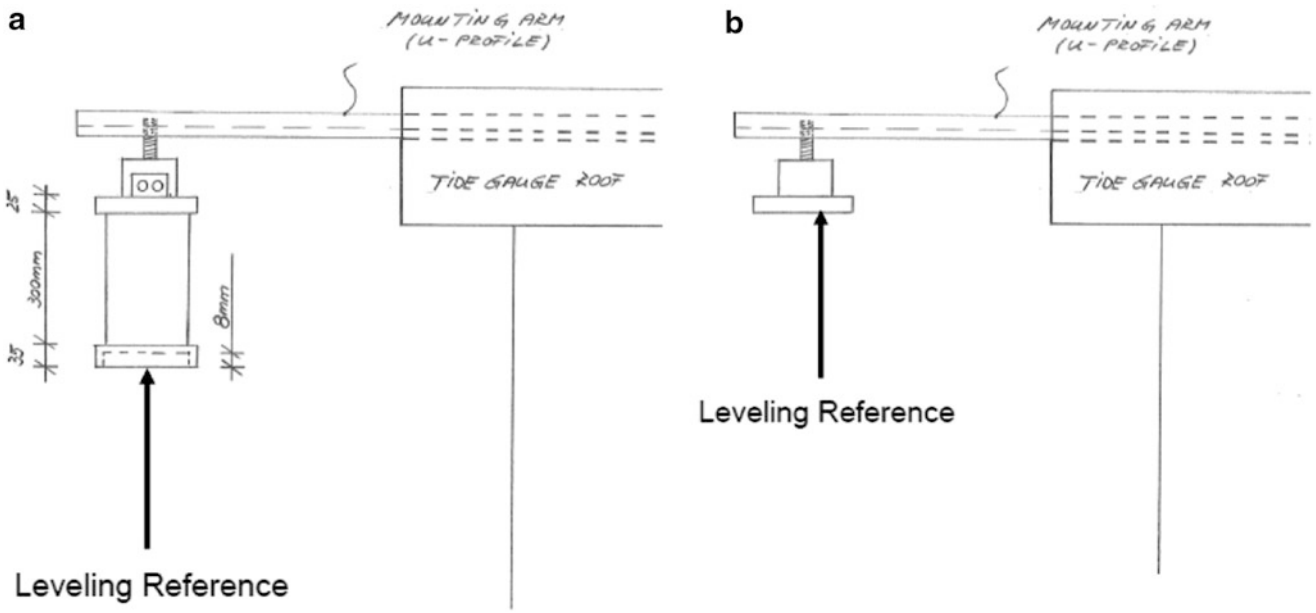

Fig. 3 OTT Kalesto (**a**) and OTT RLS (**b**) radar gauge leveling reference

in remote areas and thus they are unattended and unsupported by local operators. This affects the ability to cross-check the tide gauge readings and to ensure the correct maintenance of the tide gauge zero (TGZ).

Technologies for the datum determination and datum control of tide gauges have been developed and are applied in standard installations (IOC 1985). These are for example readings of the pole staff or simultaneous readings of the water level by a tide gauge and a measuring tape to a leveled contact point. Other technologies have been developed, e.g., the half-tide method (Woodworth et al. 1996) which is used to connect pressure probes to the local height datum.

In recent years radar gauges have been increasingly introduced into tide gauge installations (e.g., Boon et al. 2009), since they allow contact-free measurements less vulnerable to bio-fouling. Many of the radar sensors have a "reference" for leveling (antenna phase center, zero point (ZP)) or provide calibrated offsets for their ZP (Heitsenrether et al. 2011). This allows a direct connection of the radar readings to the TGZ.

In all GITEWS installations, as well as in a large number of BIG installations, the OTT Kalesto is used. Unfortunately this type of gauge does not have a defined ZP. Thus the sensor's ZP has no physical relation to the housing and, moreover, may vary between instruments by up to 15 cm (OTT Hydrometry, pers. comm.). This missing definition prevents using leveling to establish the local reference. Woodworth and Smith (2003) suggested lab calibrations; however, this method is not employed in most installations in Indonesia.

For the successor instrument, the OTT RLS, the leveling reference (ZP) is the sensor's Teflon ground plate with a specified offset of -7 ± 6 mm (OTT Hydrometry, personal communication).

3.1 Dipper Measurements

Dipper measurements to a leveled contact point (CP) are one of the suggested methods for datum determination and control (IOC 1985). Several readings during a high-to-low tide cycle are compared with the radar gauge measurements. If the radar gauge reference mark is also leveled, the dipper measurements can be used to determine and monitor the ZP offset of the radar gauge. The dipper approach with regularly repetitions is sufficient for locations with well trained personnel; installations in Indonesia are often very remote and without trained local observers. Thus for all GITEWS installations, only a limited number of dipper measurements could be performed during short maintenance visits. The low number slightly limits the accuracy of the local reference.

Dipper measurements are also carried out for the Ocean Data and Information Network for Africa (ODINAFRICA) project, where Woodworth (2006) suggested weekly repetitions. All ODINAFRICA installations use OTT Kalesto gauges. To allow an independent view on the achievable precision (how closely individual measurements agree with each other) and accuracy (how closely individual measurement agree with the correct value) of dipper measurements in general, the dipper measurements for Chabahar (Iran), Aden (Yemen), Karachi (Pakistan), and Takoradi (Ghana) have been analyzed. Each weekly campaign has approximately 15 readings. The tabulated values are collected by the Permanent Service for Mean Sea Level (PSMSL, www.psmsl.org/data/calibrations). The radar measurements have been acquired from the IOC Sea Level Monitoring Facility (www.ioc-sealevelmonitoring.org) maintained by the Flanders Marine Institute (Oostende, Belgium) and time series of common readings have been constructed.

For each weekly dipper campaign the median and standard deviation (SD) is calculated. The SD is a good measure of the observational precision under varying sea state conditions and for individual 'observer errors'. The variability of the dipper medians allows an assessment of the stability of the radar ZP estimation. In conclusion from the four analyzed data sets, this method is reliable enough to establish a height reference to better than 5 cm repeatability with an SD of ± 2 cm. For three stations, the majority of the weekly dipper measurements are within a 3 cm band. The SD of the weekly median is ± 1.5 cm (Aden), ± 1.9 cm (Chabahar), ± 2.2 cm (Karachi), and ± 3.1 cm (Takoradi) respectively. The time series of dipper measurements for these four gauges neither indicate an instrumental drift nor a height dependency, although Karachi reveals a small positive sensor shift after 10/2009.

In another study, Martín Míguez et al. (2012) analyzed the performance of the Kerguelen radar gauge with dipper, ocean bottom pressure, and GPS buoy data. Comparisons of dipper readings with the radar gauge also show a SD of ± 2 cm for the weekly repetitions, a value similar to their comparisons with ocean bottom pressure data and a GPS-equipped buoy time series and similar to the analysis of the ODINAFRICA dipper campaigns.

3.2 Establishing the Height Reference for GITEWS Tide Gauge Installations

Several GNSS-controlled tide gauges with OTT Kalesto radar gauge (Enggano/GANO, Kolinamil/KOLI, Meulaboh/MEUL, Pangandaran/PANG, Rote/ROTE, Sadeng/SADE, Tanahbala/TNBL, and Telukdalam/TDAL) and OTT RLS radar gauges (Enggano/GANO, Kolinamil/KOLI, Semarang/SEMA, Surabaya/SURA, and Waikelo/WAIK) have been analyzed (Fig. 1). At Enggano/GANO the OTT Kalesto was replaced by an OTT RLS, while in Kolinamil/KOLI both types of radar gauges have been operated in parallel for comparison. On these stations, dipper measurements for both kinds of sensors have been performed. To further evaluate the variability of OTT Kalesto instrumental offsets, other installations outside Indonesia (Aden (Yemen)/ADEN, Jask (Iran)/JASK, and Mtwara (Tanzania)/MTWA) are analyzed. As outlined above, all GITEWS installations have a leveling control network. The reference marks at the radar gauge housing (Fig. 3a, b), the GPS antenna reference point (ARP), the CP for the dipper measurements, and, where technically possible, the pressure

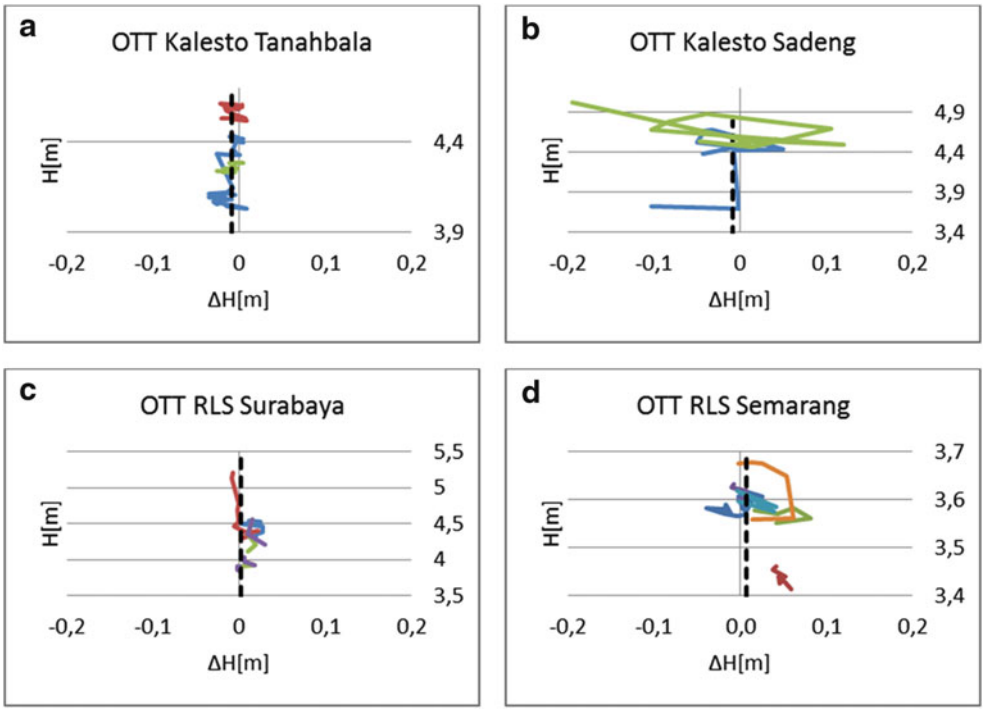

Fig. 4 Examples of dipper analyses for the OTT KALESTO (**a**, **b**) and the OTT RLS (**c**, **d**). *Different lines* indicate different dipper campaigns. The *black dotted line* indicates the derived offset. The values are displayed as Van de Casteele diagrams. The Y-Axis shows the radar gauge distance to the water surface, the X-axis the ZP offset

sensor depth are regularly leveled. Thus, not only the height reference can be established but possible radar gauge ZP offsets can be estimated.

For all stations, the ZP offset is calculated as the median of the differences between the sea surface heights derived from OTT Kalesto/RLS readings and from dipper measurements (for examples see Fig. 4). The number of dipper campaigns vary from one in Enggano (Kalesto) and Rote to five in Semarang. In Mtwara, Jask, Kolinamil and Aden, a pressure sensor has been installed and leveled according to the half-tide method (Woodworth et al. 1996). This allows the usage of pressure readings instead of dippings to determine the ZP offset of the radar gauge. Pressure readings have been corrected for a mean salinity, but may still contain small errors like salinity changes and stratification. The performance and stability of the pressure gauges have been tested with the Van de Casteele Test (Martín Míguez et al. 2008).

The analysis confirms the variability of the ZP between different OTT Kalesto gauges (Table 1). All evaluated OTT Kalesto gauges (Fig. 5, left side) have negative ZP offsets between −0.1 and −10.5 cm, except ROTE with +2 cm The SD is estimated from the dipper measurements and is between ±1 and ±5 cm. This varying SD reflects the local sea state conditions and also the experience of the observer (Table 1). For stations where the leveled half-tide pressure sensor is used as a complement for dipping (Mtwara and

Table 1 ZP offsets of the analyzed OTT Kalesto (above) and the RLS (below) with their standard deviations (SD)

		ZP Offset (m)	SD (m)	GPS (ARP)-Radar (LR) (m)
OTT Kalesto	KOLI	−0.027	±0.017	1.440
	GANO	−0.086	±0.034	−0.431
	MEUL	−0.029	±0.049	1.038
	PANG	−0.022	±0.048	1.632
	SADE	−0.033	±0.040	0.615
	TDAL	−0.042	±0.049	1.464
	TNBL	−0.009	±0.011	1.660
	ROTE	0.026	±0.033	1.481
	ADEN	−0.095	±0.022	No GPS
	JASK	−0.089	±0.010	1.910
	MTWA	−0.067	±0.014	2.023
OTT RLS	SEMA	0.007	±0.028	1.039
	KOLI	0.088	±0.028	1.031
	GANO	0.012	±0.035	−0.737
	SURA	0.002	±0.010	1.119
	WAIK	−0.020	±0.025	0.931

The height difference between the leveling reference (LR) of the radar gauge added to the ZP offset and the leveled GPS Antenna Reference Point (ARP) can now be used to connect the sea level to the Indonesian height system and to the results of the IGS TIGA (Schöne et al. 2009). The offsets are visualized in Fig. 5.

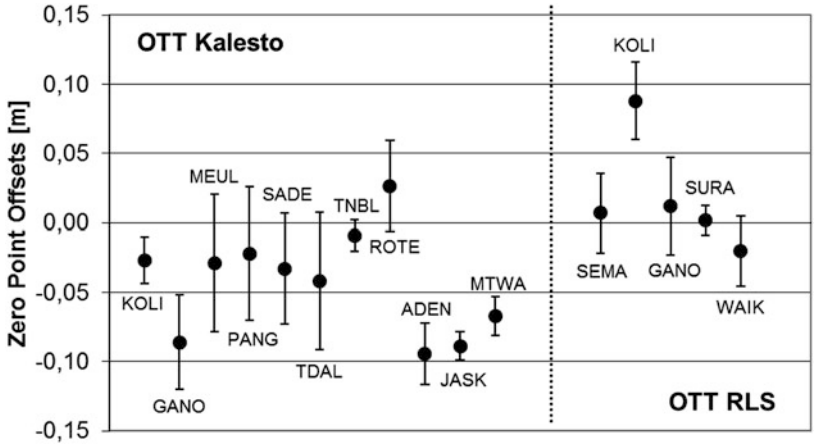

Fig. 5 Radar gauge ZP offsets for OTT Kalesto and OTT RLS installed in the Indonesian Tide Gauge network. The OTT RLS values are corrected for the −7 mm factory offset

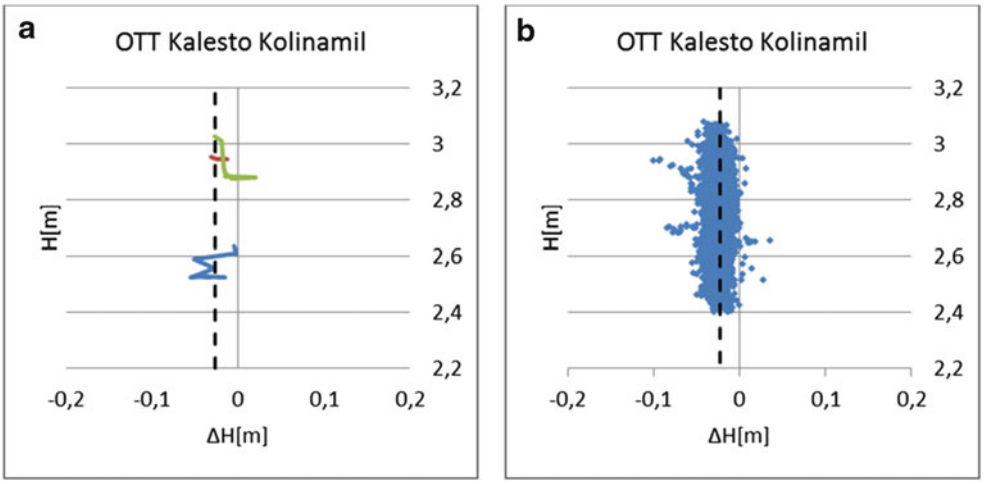

Fig. 6 Comparison of offset determination derived from dipper measurements (a) and from the comparison with a geodetically leveled pressure sensor (b). The offsets ΔH are shown versus the OTT KALESTO radar distance to the sea level. The colors in (a) are for the different dipper campaigns. The black dotted line indicates the resulting offset

Jask), the SD is calculated from the differences between the pressure and radar readings.

The spread of ZP biases for the OTT RLS (Fig. 5, right side) is 11 cm, while most ZP offsets are grouped near zero (Table 1). Since there are fewer sensors evaluated, no final statement can be made whether the ZP as given by OTT Hydrometry is valid and stable. Currently there is no explanation for the large ZP offset for the RLS at KOLI.

To further evaluate the accuracy of dipper measurements, the ZP offsets for the OTT Kalesto in KOLI and ADEN have been estimated by both, the dipper measurements and by comparison with the readings from a geodetically leveled pressure gauge (half-tide gauge). For comparison a data set of one week with a sampling interval of 1 min has been used. The selected data period is directly after the installation of the calibrated pressure sensors.

The resulting ZP offset for the OTT Kalesto in KOLI derived from dipper measurements is -2.7 ± 2.0 cm (Fig. 6a), while it is -2.3 ± 0.7 cm derived from the pressure sensor comparison (Fig. 6b). For the OTT Kalesto in ADEN the ZP offset is -10.5 ± 2.2 cm derived from dipper measurements and -11.0 ± 1.1 cm derived from the pressure sensor comparison. This confirms that even a limited number of dipper measurements taken during calm sea state conditions can provide a sufficient stable estimation of the ZP offset.

From this study it can be concluded, that the height reference of radar gauges can be estimated to better than ±2.5 cm repeatability even with a limited number of dipper readings.

4 Summary

In Indonesia, a growing network of GNSS-controlled tide gauge stations exist, which can be used for multi-purpose applications. One research focus is the unification of the Indonesian height reference system. To connect the sea level readings to the height system and to maintain the long-term stability of the tide gauge records, the tide gauge zero for each station has to be measured and is maintained. The OTT Kalesto which is extensively used in Indonesia, have no defined zero reference, and for the OTT RLS the ZP offset also has to be controlled. For a number of GNSS-controlled stations, the ZP bias is estimated and the tide gauge records now can be referenced to the local leveling network as well

as to GNSS analyses (Table 1). Currently the international IGS TIGA Working Group is processing GNSS data which is supported by this work. The combination of this study and TIGA results will allow connecting the sea level at selected stations to the Indonesian height system.

Acknowledgement The authors wish to acknowledge the work of their colleagues at BIG and GFZ doing the field work, the local tide gauge operators, and also the observers on other stations performing the dipper measurements, in particular Sayed Nourbakhsh (Iran), Mustafa Esmail (Yemen) and the operators of Karachi and Takoradi. Also the work of PSMSL in preparing and storing the dipper sheets is acknowledged. Tide Gauge data have been downloaded from the IOC Sea Level Monitoring Facility. Also the work of ODINAFRICA is highly appreciated. The author would also like to thank the Pakistan Navy and the Gwadar Port Authority. The stations Kolinamil (Jakarta) and Semarang are operated by BIG and GFZ under the Geodetic Hazard Monitoring program of GFZ. Mtwara (Tanzania), Jask (Iran) and Chabahar (Iran) are operated by GFZ with the support of NCC (Iran) and the Tanzania Ports Authority. The work has been carried out under the German Ministry of Research and Education grant 03TSU07. We also thank the three anonymous reviewers for the helpful comments.

References

Abidin HZ, Andreas H, Gumilar I, Sidiq TP, Fukuda Y (2012) Land subsidence in coastal city of Semarang (Indonesia): characteristics, impacts and causes. J Geomat Nat Haz Risk. doi:10.1080/19475705.2012.692336

BIG (2012) Geospatial information in Indonesia, country report to the 19th United Nations regional cartographic conference for Asia and the Pacific and 18th permanent committee on GIS infrastructure for Asia and the Pacific meeting, Bangkok, Thailand, 28 October – 1 November 2012. http://unstats.un.org/unsd/geoinfo/RCC/docs/rccap19/crp/E_Conf.102_CRP8_COUNTRY%20REPORT%20Indonesia%20fin.pdf. Accessed 14 Oct 2013

Boon JD, Heitsenrether RM, Bushneil M (2009) Microwave-acoustic water level sensor comparisons: sensor response to change in oceanographic and meteorological parameters. OCEANS 2009, MTS/IEEE Biloxi - marine technology for our future: global and local challenges 1(10):26–29

Fenoglio-Marc L, Schöne T, Illigner I, Becker M, Manurung P, Khafid (2012) Sea level change and vertical motion from satellite altimetry, tide gauges and GPS in the Indonesian region. Mar Geod 35(Supplement 1):137–150. doi:10.1080/01490419.2012.718682

Heitsenrether RM, Hensley WM, Boon JD (2011) Results from NOAA's test and evaluation of microwave radar water level sensors and plans for a transition to operational applications. Oceans 1(10):19–22

IOC (1985) Manual on sea level measurement and interpretation, vol 4, No. 14, IOC/UNESCO

Martín Míguez B, Testut L, Wöppelmann G (2008) The Van de Casteele test revisited: an efficient approach to tide gauge error characterization. J Atmos Oceanic Tech 25:1238–1244

Martín Míguez B, Testut L, Wöppelmann G (2012) Performance of modern tide gauges: towards mm-level accuracy. Sci Mar 76(S1). doi:10.3989/scimar.03618.18A

Merrifield M, Holgate S, Mitchum G, Pérez B, Rickards L, Schöne T, Woodworth P, Wöppelmann G, Aarup T (2012) Global sea level observing system (GLOSS) implementation plan – 2012. IOC technical series No. 100. http://www.unesco.org/ulis/cgi-bin/ulis.pl?catno=217832&set=50929BE4_3_465&gp=1&lin=1&ll=1. Accessed 04 Oct 2013

Ningsih NS, Suryo W, Anugrah SD (2011) Study on characteristics of residual water level in Jakarta, Semarang, and Surabaya Waters – Indonesia and its relation to storm events in November 2007. Int J Basic Appl Sci 11(5):116205–117474

Schöne T, Schön N, Thaller D (2009) IGS tide gauge benchmark monitoring pilot project (TIGA) - scientific benefits. J Geod 83(3–4):249–261. doi:10.1007/s00190-008-0269-y

Schöne T, Illigner J, Manurung P, Subarya C, Khafid, Zech C, Galas R (2011) GPS-controlled tide gauges in Indonesia – a German contribution to Indonesia's tsunami early warning system. Nat Haz Earth Syst Sci 11:731–740. doi:10.5194/nhess-11-731-2011

Woodworth PL (2006) Suggested method for datum determination for the radar gauges provided for ODINAFRICA and GLOSS-Africa. http://www.psmsl.org/train_and_info/training/presentations/oostende/kalesto_calibration_plw.ppt. Accessed 04 Oct 2013

Woodworth PL, Smith DE (2003) A one-year comparison of radar and bubbler tide gauges at Liverpool. Int Hydrogr Rev 4:2–9

Woodworth PL, Vassie JM, Spencer R, Smith DE (1996) Precise datum control for pressure tide gauges. Mar Geod 19(1):1–20. doi:10.1080/01490419609388068

Investigation on the Postseismic Deformation Associated with the 2011 Tohoku Earthquake Based on Terrestrial and Seafloor Geodetic Observations: To Evaluate the Further Seismic Hazard Potential on the Plate Interface Beneath the Northeastern Japanese Islands

Takeshi Iinuma, Ryota Hino, Motoyuki Kido, Yukihito Osada, Daisuke Inazu, Yoshihiro Ito, Syuichi Suzuki, Yusaku Ohta, and Hiromi Fujimoto

Abstract

The 2011 Tohoku Earthquake (M9.0), which occurred on the plate boundary between the subducting Pacific plate and continental plate has been associated with postseismic deformation, including aseismic slip at the plate interface (postseismic slip). In order to evaluate the potential for further seismic activity, we investigated the spatial and temporal evolution of the postseismic slip based not only on terrestrial GPS data but also on seafloor geodetic data. We estimated the displacements due to the postseismic slip by subtracting the displacements due to large aftershocks and viscoelastic relaxation from the original displacement time series data and used a time-dependent inversion method to estimate the postseismic slip distributions. The resultant postseismic slip distributions depend strongly on the assumed value of the viscosity. However, the following two features are independent of the viscosity assumption: (1) large postseismic slip has been occurring at a very shallow ($\leq$20 km in depth) portion of the plate interface south of the area of huge coseismic slip and (2) significant postseismic slip has occurred at a deep (approximately 50 km in depth) portion of the plate interface. The results suggest that the elastic strain and the stress concentrated at the plate interface at a depth of approximately 30 km in the segment off the Boso Peninsula have not yet been released and continue to generate large aftershocks.

Keywords

GPS • Interplate coupling • Postseismic slip • Postseismic deformation • Seafloor geodesy • Viscoelastic relaxation

T. Iinuma (✉)
International Research Institute of Disaster Science, Tohoku University, 468-1, Aza-Aoba, Aramaki, Aoba-ku, Sendai 980-0845, Japan
e-mail: iinuma@jamastec.go.jp

Present Address: Research and Development Center for Earthquake and Tsunami, Japan Agency for Marine-Earth Science and Technology, 3173-25, Showa-machi, Kanazawa-ku, Yokohama 236-0001, Japan

R. Hino • M. Kido • Y. Osada • H. Fujimoto
International Research Institute of Disaster Science, Tohoku University, Sendai, Japan

present address (R. Hino): Graduate School of Science, Tohoku University, Sendai, Japan

present address (Y. Osada): GNSS Technologies Inc., Tokyo, Japan

present address (H. Fujimoto): National Research Institute for Earth Science and Disaster Prevention, Tsukuba, Japan

D. Inazu
National Research Institute for Earth Science and Disaster Prevention, Tsukuba, Japan

present address: UTokyo Ocean Alliance, the University of Tokyo, Tokyo, Japan

S. Suzuki • Y. Ohta
Graduate School of Science, Tohoku University, Sendai, Japan

Y. Ito
Disaster Prevention Research Institute, Kyoto University, Uji, Japan

© Springer International Publishing Switzerland 2015

C. Rizos, P. Willis (eds.), *IAG 150 Years*, International Association of Geodesy Symposia 143,
DOI 10.1007/1345_2015_162

1 Introduction

A M 9.0 earthquake, the 2011 Tohoku Earthquake, occurred on 11 March 2011, and a huge tsunami associated with the earthquake killed approximately 20,000 people. Many studies have investigated the source process and coseismic slip distribution of this huge earthquake based on seismological and geodetic data, and these studies have revealed that the M9 earthquake ruptured not only the deep (depth: 40–50 km) portion of the plate interface but also the shallow ($\leq$30 km in depth) plate interface with a very large ($\geq$50 m) amount of slip (e.g., Ide et al. 2011; Ito et al. 2011; Koper et al. 2011; Pollitz et al. 2011; Simons et al. 2011; Iinuma et al. 2012). The latitudinal range of the area of very large slip did not exceed 200 km, which is small for a M 9.0 earthquake.

This huge earthquake has been associated with postseismic deformations as well as past large earthquakes that occurred around the Japanese Islands associated with postseismic deformations. In particular, the postseismic slip events that were associated with recent interplate earthquakes in the northeastern Japan subduction zone, such as the 1993 Sanriku-Haruka-Oki (Mw 7.6) and 2005 Miyagi-Oki (Mw 7.2) earthquakes, released moments as large as the seismic moments that were released by their main shocks (e.g., Heki et al. 1997; Miura et al. 2006). Ozawa et al. (2011) have reported the postseismic slip associated with the 2011 Tohoku Earthquake based on terrestrial continuous GPS observation. However, we cannot precisely estimate the postseismic slip at the very shallow portion of the plate interface based only on terrestrial GPS data, because such offshore areas are too far from the coast of northeastern Japan.

Therefore, the problem as to whether postseismic slip has been occurring at the plate interface in the very shallow portion north and south of and adjacent to the area of very large coseismic slip remains unsolved. Solving this problem is very important in order to evaluate further seismic risks in and around the rupture area of the 2011 Tohoku Earthquake, because postseismic slip can aseismically release strain energy that has accumulated due to interplate coupling during the interseismic period and may reduce the size of the earthquakes that may occur in the near future.

Therefore, we investigated the spatial and temporal evolution of the postseismic slip at the plate interface based not only on the terrestrial GPS data but also on the seafloor geodetic data, such as crustal movements measured by means of GPS/Acoustic ranging and vertical displacements observed using Ocean Bottom Pressure gauges.

2 Data and Analysis

2.1 Displacement Time Series

We used a displacement time series obtained from terrestrial continuous GPS observations from 23 April 2011 to 10 December 2011, seafloor crustal deformation measurements obtained by means of GPS/Acoustic ranging (GPS/A), and changes in the Ocean Bottom Pressure (OBP) recorded using a free-fall/pop-up system to estimate the spatio-temporal evolution of the postseismic slip associated with the 2011 Tohoku Earthquake. Figure 1 shows the distribution of the observation points.

GPS data observed at stations that have been managed by the Geospatial Information Authority of Japan (GSI), Tohoku University, the Japan Nuclear Energy Safety Organization (JNES), and the National Astronomical Observatory (NAO) are analyzed to obtain daily station coordinates by applying Precise Point Positioning (PPP) (Zumberge et al. 1997) with GIPSY-OASIS II software. A total of 383 GPS sites are used in the inversion analysis.

A total of seven GPS/A stations in and around the rupture area of the 2011 Tohoku Earthquake have been in operation by the Japan Coast Guard (JCG) and Tohoku University since the occurrence of the earthquake. In the inversion analysis, we used five GPS/A stations managed by the JCG at which more than two observation data have been collected. We have performed observation at GJT3, which is one of Tohoku University's sites, three times, but some problems with data processing still remains. With respect to another site, we have no data in the analysis period. Therefore, we have not included Tohoku University's sites in the inversion analysis.

The 1-Hz-sampled OBP records of six sites are available for the analysis period. We estimated and eliminated the ocean tide by applying harmonic analyses (Tamura et al. 1991), the motion of the seawater layer by a global barotropic ocean model forced by applying synoptic atmospheric disturbances (Inazu et al. 2012), and long-term instrumental drift caused by the characteristics of the quartz pressure sensors (e.g., Watts and Kontoyiannis 1990). Since these pressure gauges were installed before the 2011 Tohoku Earthquake, the secular change in the OBP due to the sensor's drift is able to be excluded by linear and exponential curve fitting. Thus, we are able to obtain vertical displacement time series due to the postseismic deformation associated with the 2011 Tohoku Earthquake from pressure records. These OBP records are shorter than the entire analysis period. Thus, we

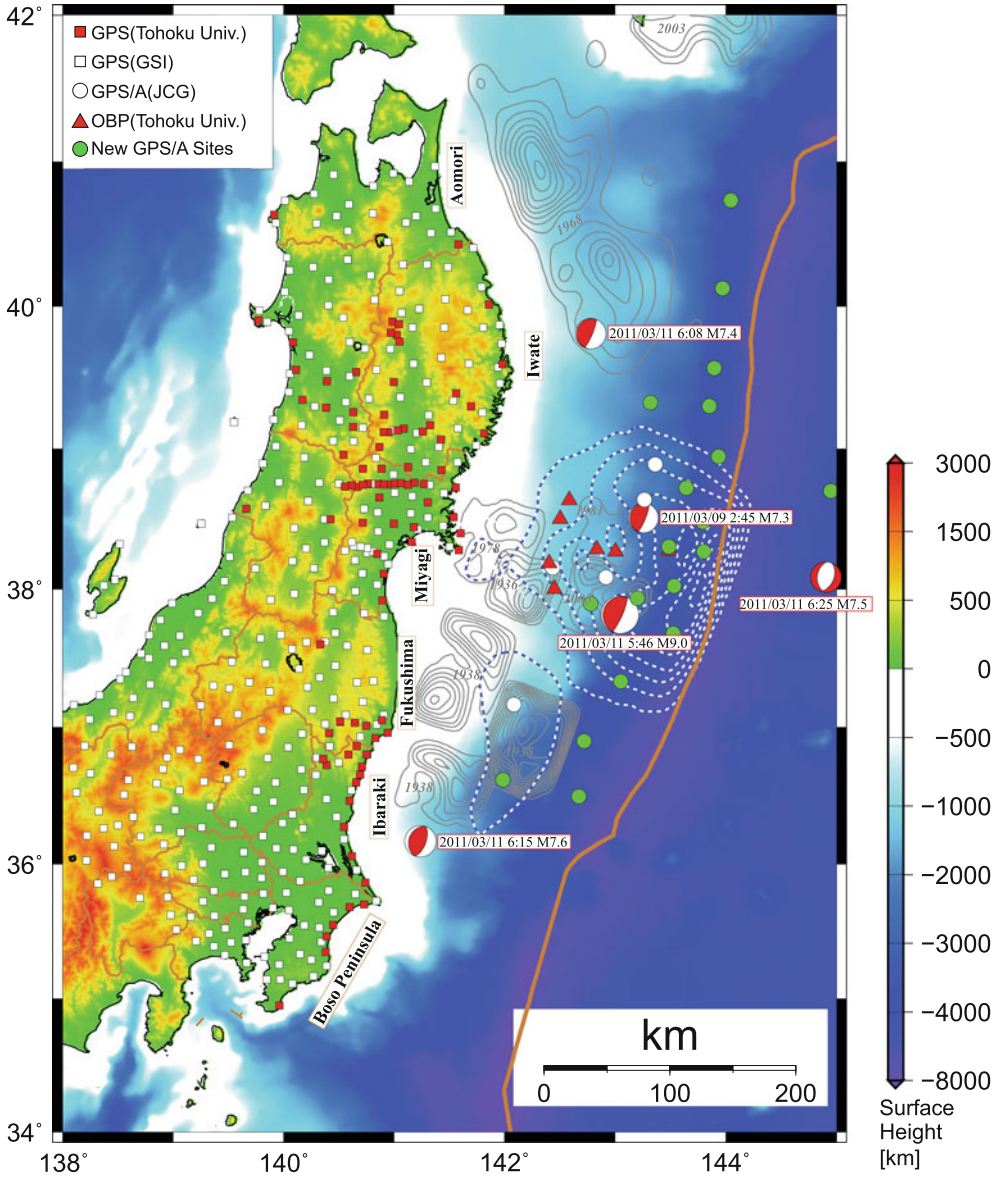

Fig. 1 Map of the study area. *Squares*, *circles*, and *triangles* indicate the terrestrial GPS, seafloor GPS/A, and OBP sites, respectively. The *red symbols* correspond to the sites of Tohoku University, and the *white symbols* represent the sites of other organizations (terrestrial GPS sites of GSI and seafloor GPS/A sites of JCG). The *green circles* represent new GPS/A stations installed in 2012 (Kido et al. 2012). The locations of the centroids of the mainshock, the largest foreshock (9 March 2011, M7.3), and three large aftershocks that occurred on 11 March 2011 (M7.4 off Iwate Prefecture, M7.5 far off Miyagi Prefecture and M7.6 off Ibaraki Prefecture) are indicated along with their focal mechanisms determined by JMA (Hirose et al. 2011). The hypocenter of the mainshock is indicated by a *yellow star*. The *gray* contours denote the slip areas for recent major earthquakes at Tokachi-oki in 2003 (M8.0) and 1968 (M7.9), Miyagi-oki in 1978 (M7.4), 1981 (M7.0) and 1936 (M7.4), and Fukushima-oki in 2003 (M7.1) and 1938 (M7.3, M7.4 and M7.5) (Murotani 2003; Yamanaka 2003; Yamanaka and Kikuchi 2003, 2004). The *brown lines* denote the prefectural borders and the trench axis. The names of prefectures along the Pacific coast (Aomori, Iwate, Miyagi, Fukushima, and Ibaraki) are presented along their coasts

extrapolated the time series by fitting a logarithmic function to the available postseismic displacement time series, because if we regard that there is totally no data at the OBP sites after their recover, the up-down motion on the seafloor becomes too unstable.

2.2 Displacement Due to Postseismic Slip

We estimated displacements due to the postseismic slip by subtracting those due to the plate motion, large aftershocks, and viscoelastic relaxation from the original displacement

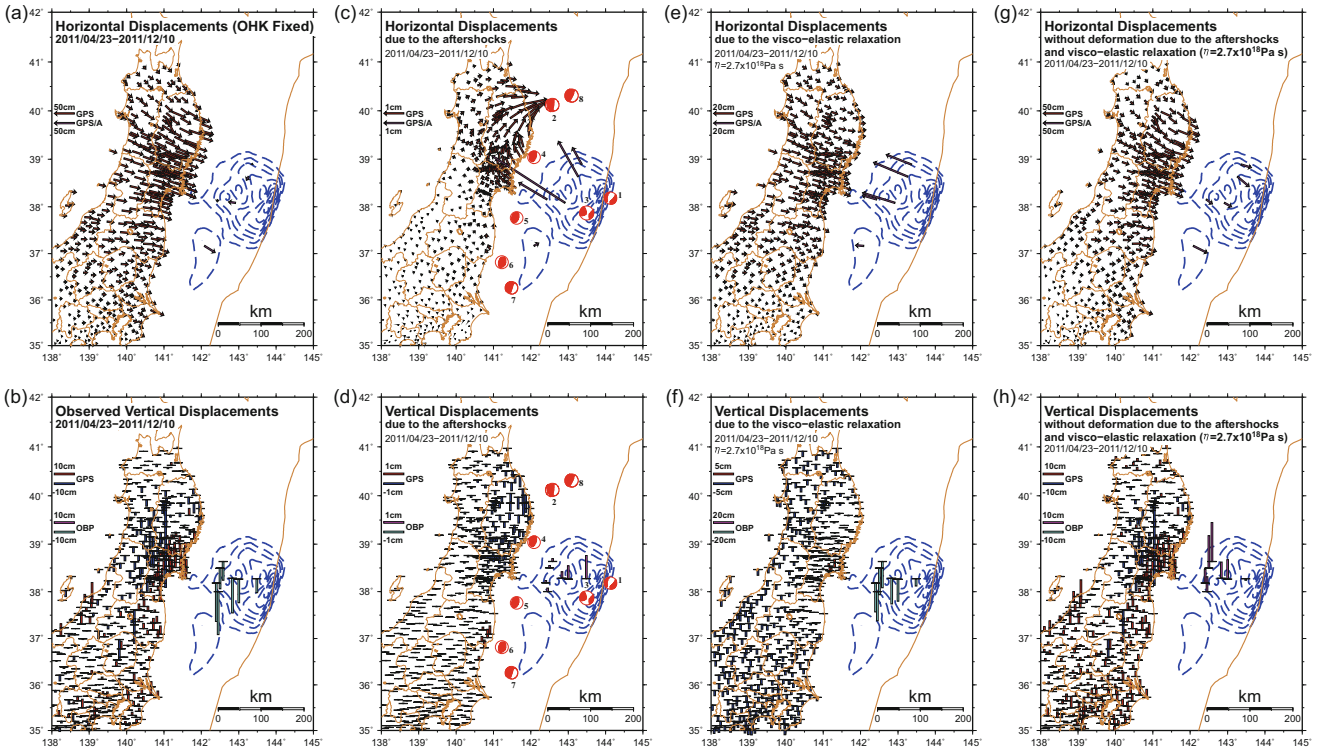

Fig. 2 (**a**) Horizontal and (**b**) vertical observed displacements in the post-Tohoku earthquake period of from 23 April 2011 to 10 December 2011. Horizontal vectors are in the Okhotsk plate fixed reference frame. The *blue dashed* contours represent the coseismic slip distribution estimated by Iinuma et al. (2012). (**c**) Horizontal and (**d**) vertical displacements due to the aftershocks that occurred in the analysis period. Eight aftershocks produce significant displacements, and the sum of the displacements due to each earthquake is plotted. Numbers of aftershocks are corresponding with the numbers of events in Table 1. (**e**) Horizontal and (**f**) vertical displacements due to the viscoelastic relaxation when we assume the viscosity in the viscoelastic layer to be 2.7×10^{18} Pa s. (**g**) Horizontal and (**h**) vertical displacements regarded as being due to the postseismic slip that are obtained by subtracting displacements due to the aftershocks and viscoelastic relaxation from observed displacement for each site. Note that the scales of the displacements in this figure differ among panels

time series data. First, displacements were transformed into the Okhotsk plate fixed reference frame by applying the plate motion model of the ITRF2005 (Altamimi et al. 2007) from ITRF2005 (GPS) and the Eurasia plate fixed reference frame (GPS/A). Figure 2a, b show the displacement field in the Okhotsk plate fixed reference frame.

Several earthquakes (aftershocks) occurred during the analysis period. We estimated and excluded the displacement due to the earthquakes that did not occur at the plate interface in order to extract the displacements due to deformation at the plate interface, including seismic and aseismic slip. Calculating the displacements at observation stations based on the CMT solutions of the Japan Meteorological Agency during the analysis period, we concluded that eight earthquakes that occurred in the subducting slab and the continental plate may produce significant displacements at the observation points (Fig. 2c, d). The parameters of these earthquakes are listed in the Table 1.

The displacement field due to the viscoelastic relaxation is predicted by assuming a spherical layered structure with a 50-km-thick elastic surface layer and a Maxwell body beneath the elastic layer. We used VISCO1D (Pollitz 1997) to calculate the viscoelastic response for the coseismic slip model based on the terrestrial and seafloor geodetic data (Iinuma et al. 2012). Several different values of the viscosity in the viscoelastic layer were examined, namely, 1.0×10^{18}, 2.7×10^{18}, and 1.0×10^{19} Pa s. The intermediate value, 2.7×10^{18} Pa s, was estimated by Ohzono et al. (2012) for the Tohoku district based on 1.5 years of postseismic deformation following the 2008 Iwate-Miyagi Nairiku earthquake (Mw 6.8). We adopted this value as an optimum value based on the examination of the resultant postseismic slip distribution. Figure 2e, f present this displacement field due to the visco-elastic relaxation process.

3 Postseismic Slip Distribution

A time-dependent inversion method devised by Yagi and Kikuchi (2003) is applied to estimate the postseismic slip distributions associated with the 2011 Tohoku earthquake after eliminating contributions other than the postseismic slip

Table 1 Source parameters of earthquakes (aftershocks) included the analysis of this study

No.	Date	Time	Longitude [°E]	Latitude [°N]	Depth [km]	Strike [°]	Dip [°]	Rake [°]	Mw
1	2011/05/05	23:58:19	144.13	38.18	12	50	60	−52	6.1
2	2011/06/23	06:50:50	142.57	40.12	47	12	70	110	6.7
3	2011/07/10	09:57:07	143.49	37.87	21	67	74	7	7.0
4	2011/07/23	13:34:23	142.09	38.87	54	23	67	103	6.3
5	2011/07/25	03:51:25	141.63	37.71	53	22	68	91	6.3
6	2011/07/31	03:53:50	143.22	36.81	59	21	39	93	6.4
7	2011/09/15	17:00:08	141.48	36.26	17	18	80	87	6.2
8	2011/09/17	04:26:35	143.09	40.26	22	26	76	99	6.6

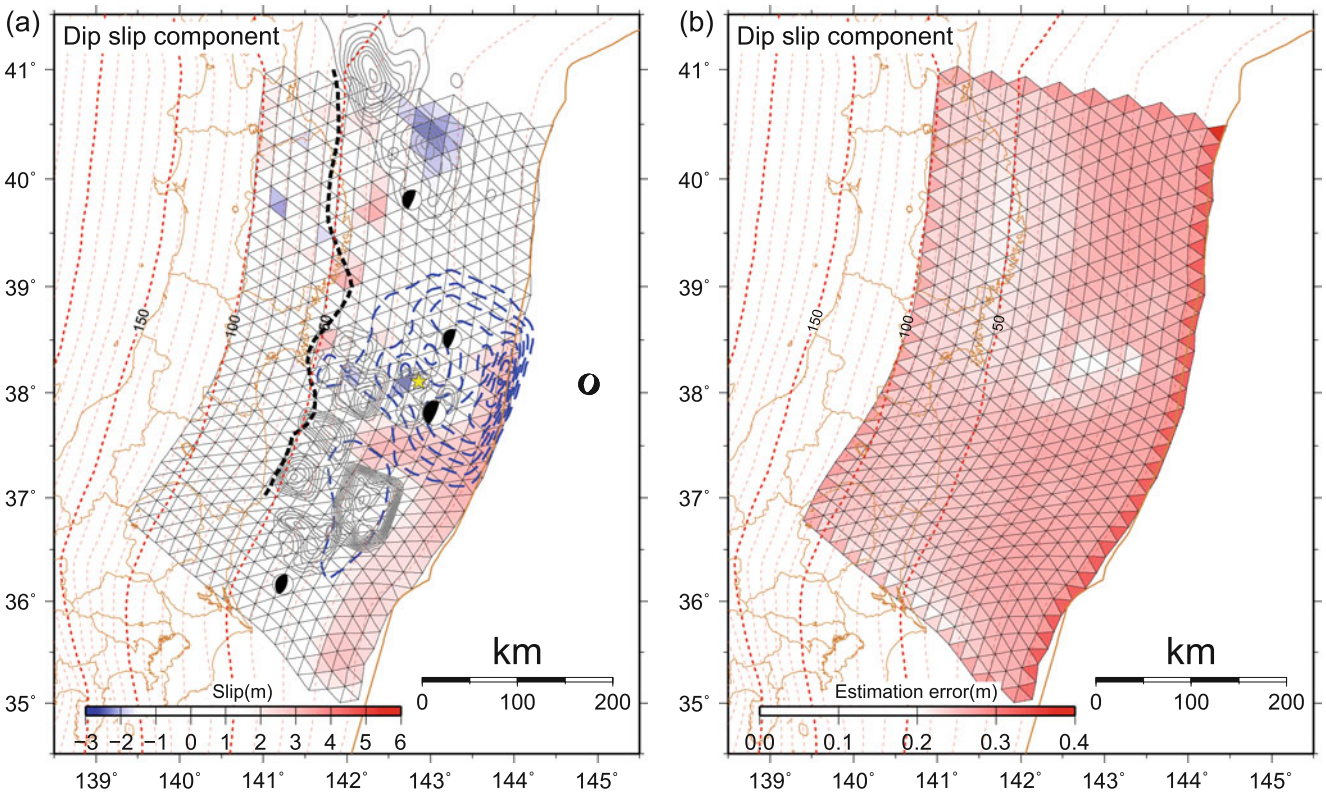

Fig. 3 (**a**) Cumulative distribution of the estimated postseismic slip. Each triangular fault is colored by its dip-slip component of the postseismic slip. The *black dashed line* denotes the down-dip limit of interplate earthquakes determined by Igarashi et al. (2001). The *broken red lines* show the depth of the subducting plate interface (Nakajima and Hasegawa 2006)

at the plate interface from the displacement time series data (Fig. 2g, h). The postseismic slip distribution is expressed by only the dip-slip on the triangulated tessellation of the plate interface geometry determined by Nakajima and Hasegawa (2006) in a homogeneous elastic half-space (Meade 2007). Strike-slip components are ignored in order to reduce the computation time. We virtually enshallowed the depth of the plate interface for the calculation of the green function for the seafloor sites by their water depth in order to adjust the closeness to the plate boundary fault of such sites. For example, with respect to seafloor site MYGW, which is located on the seafloor at a water depth of 1.7 km, we subtracted 1.7 km from the original depth of each subfault at the plate interface in order to reposition the free surface of the homogeneous elastic half-space from the sea surface to the seafloor. The weights of the constraint condition with respect to the spatial and temporal smoothness of the slip distribution, and the Dirichlet type boundary condition are optimized by minimizing Akaike's Bayesian Information Criterion (ABIC) (Akaike 1977, 1980).

Figure 3a shows the cumulative postseismic slip distribution computed for the analysis period of approximately 8 months along with its estimation error (Fig. 3b). Comparisons between the observed and calculated (predicted) displacements for the preferred model are shown in Fig. 4a, c, whereas Fig. 4b, d present the residuals between

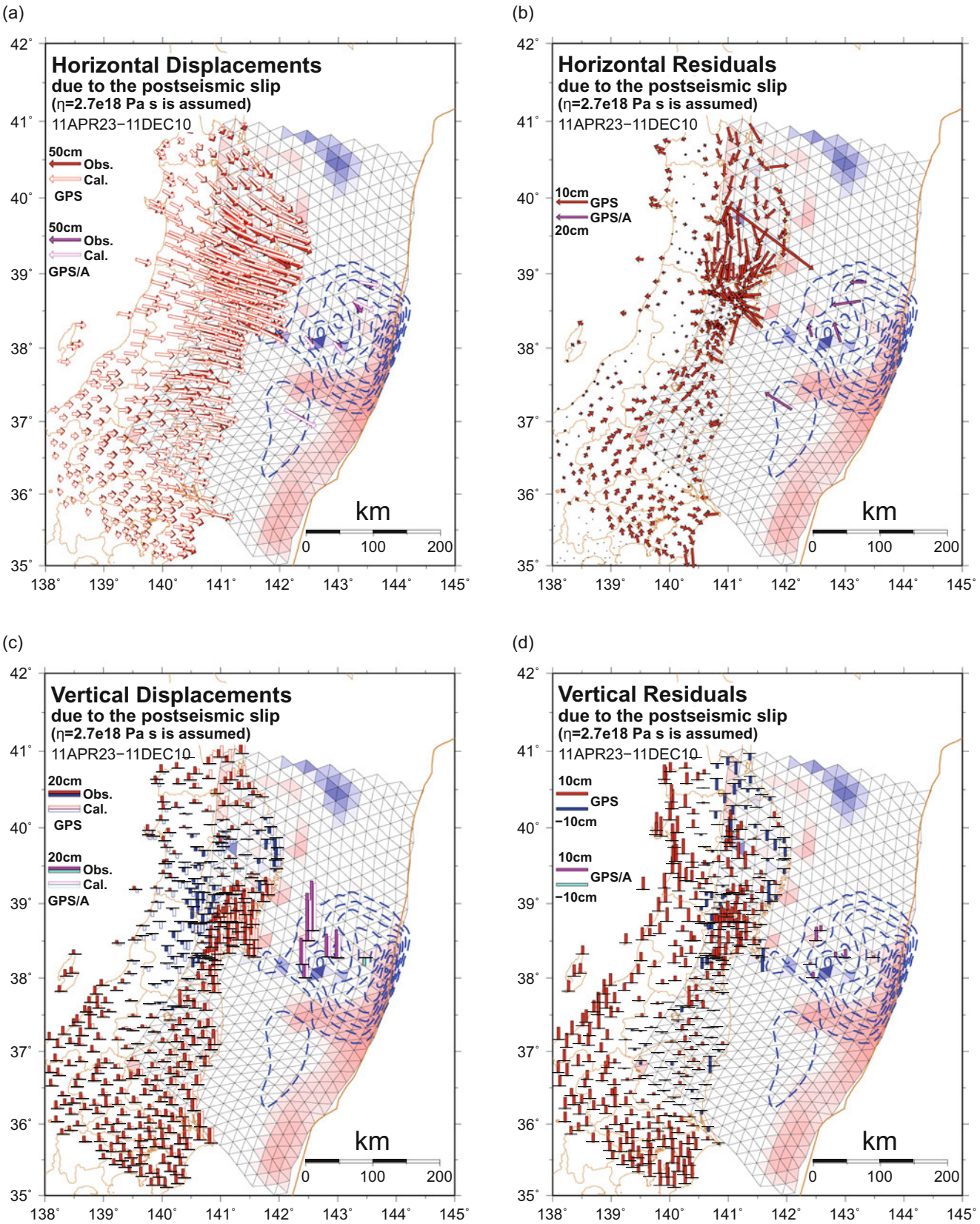

Fig. 4 (**a**) A comparison of the calculated and observed (after subtraction with respect to the aftershocks and viscoelastic relaxation) corrected horizontal displacement and (**b**) their residuals (observation–calculation). (**c**) A comparison of the calculated and observed (after subtraction with respect to the aftershocks and viscoelastic relaxation) vertical displacement and (**d**) their residuals (observation–calculation)

the calculated and observed displacements. The results revel the following: (1) large postseismic slip has been occurring at the very shallow (depth: $\leq$20 km) portion of the plate interface off Ibaraki and Fukushima prefectures, (2) the slip corresponding to the normal fault motion is dominant at the intermediate portion (depth: 20–50 km) off Aomori prefecture, and (3) not large, but significant, slip occurred at the deep portion (depth: $\geq$50 km) of the plate interface, above the coastline of NE Japan.

These results suggest that the elastic strain and stress concentrated due to the mainshock at the plate interface at a depth of approximately 30 km at the segments off Boso Peninsula where the subducting Pacific plate contacts overriding continental plate and not Philippine Sea plate have not yet been released and are still able to generate large interplate earthquakes. However, because the strain energy in the shallowest portions of such segments are being released by the postseismic slip, tsunamis as large as that generated by the 2011 event are unlikely to occur, even if such large aftershocks occur.

The above results and discussion are still tentative because the spatial resolution of the inversion analysis is not sufficient to reveal the detailed distribution of the postseismic slip on the very shallow portion of the plate interface. We have been performing seafloor geodetic observations with an enhanced observation network that is composed of 20 new seafloor stations constructed since 2012 (Kido et al. 2012). Further investigation of the postseismic slip distribution using the crustal deformation data obtained from the new network in the near future is necessary in order to obtain a comprehensive understanding of the postseismic slip distribution of the 2011 Tohoku earthquake.

Acknowledgements The authors would like to thank JCG for providing GPS/A data. GPS data were provided by JNES, GSI, and NAO. The present study was supported through the MEXT project, "Evaluation and disaster prevention research for the coming Tokai, Tonankai and Nankai earthquakes" and by JSPS KAKENHI (20244070). Figures were created using GMT software (Wessel and Smith 1998).

References

Akaike H (1977) On entropy maximization principle. In: Krishnaiah PR (ed) Application of statistics. North-Holland Publishing Company, Amsterdam, pp 27–41

Akaike H (1980) Likelihood and the Bayes procedure. In: Bernardo JM, DeGroot MH, Lindley DV, Smith AFM (eds) Bayesian statistics. University Press, Valencia, pp 143–166

Altamimi Z, Collilieux X, Legrand J, Garayt B, Boucher C (2007) ITRF2005: a new release of the international terrestrial reference frame based on time series of station positions and Earth orientation parameters. J Geophys Res 112:B09401. doi:10.1029/2007JB004949

Heki K, Miyazaki S, Tsuji H (1997) Silent fault slip following an interplate thrust earthquake at the Japan trench. Nature 386:595–598

Hirose F, Miyaoka K, Hayashimoto N, Yamazaki T, Nakamura M (2011) Outline of the 2011 off the Pacific coast of Tohoku earthquake (Mw 9.0) – Seismicity: foreshocks, mainshock, aftershocks, and induced activity. Earth Planets Space 63:513–518

Ide S, Baltay A, Beroza GC (2011) Shallow dynamic overshoot and energetic deep rupture in the 2011 Mw 9.0 Tohoku-Oki earthquake. Science 332:1426–1429

Igarashi T, Matsuzawa T, Umino N, Hasegawa A (2001) Spatial distribution of focal mechanisms for interplate and intraplate earthquake associated with the subducting Pacific plate beneath the northeastern Japan arc: a triple-planed deep seismic zone. J Geophys Res 106:2177–2191

Iinuma T et al (2012) Coseismic slip distribution of the 2011 off the Pacific coast of Tohoku earthquake (M9.0) refined by means of seafloor geodetic data. J Geophys Res 117:B07409

Inazu D, Hino R, Fujimoto H (2012) A global barotropic ocean model driven by synoptic atmospheric disturbances for detecting seafloor vertical displacements from in situ ocean bottom pressure measurements. Mar Geophys Res 33:127–148

Ito T, Ozawa K, Watanabe T, Sagiya T (2011) Slip distribution of the 2011 off the Pacific coast of Tohoku earthquake inferred from geodetic data. Earth Planets Space 63:627–630

Kido M, Fujimoto H, Osada Y, Ohta Y, Yamamoto J, Tadokoro K, Okuda T, Watanabe T, Nagai S, Yasuda K (2012) Development of GPS/A seafloor geodetic network along Japan trench and onset of its operation, Abstract T13F-2697 presented at 2012 fall meeting, AGU, San Francisco 3–7 December 2012

Koper KD, Hutko AR, Lay T, Ammon CJ, Kanamori H (2011) Frequency-dependent rupture process of the 2011 Mw 9.0 Tohoku earthquake: comparison of short-period P wave backprojection images and broadband seismic rupture models. Earth Planets Space 63:599–602

Meade BJ (2007) Algorithms for the calculation of exact displacements, strains, and stresses for triangular dislocation elements in a uniform elastic half space. Comput Geosci 33:1064–1075

Miura S, Iinuma T, Yui S, Uchida N, Sato T, Tachibana K, Hasegawa A (2006) Co- and post-seismic slip associated with the 2005 Miyagi-oki earthquake (M7.2) as inferred from GPS data. Earth Planets Space 58:1567–1572

Murotani S (2003) Rupture processes of large Fukushima-Oki earthquakes in 1938. Master's thesis, The University of Tokyo

Nakajima J, Hasegawa A (2006) Anomalous low-velocity zone and linear alignment of seismicity along it in the subducted Pacific slab beneath Kanto, Japan: reactivation of subducted fracture zone? Geophys Res Lett 33:L16309

Ohzono M, Ohta Y, Iinuma T, Miura S, Muto J (2012) Geodetic evidence of viscoelastic relaxation after the 2008 Iwate-Miyagi Nairiku earthquake. Earth Planets Space 64:759–764

Ozawa S, Nishimura T, Suito H, Kobayashi T, Tobita M, Imakiire T (2011) Coseismic and postseismic slip of the 2011 magnitude-9 Tohoku-Oki earthquake. Nature 475:373–376

Pollitz FF (1997) Gravitational-viscoelastic postseismic relaxation on a layered spherical Earth. J Geophys Res 102:17921–17941

Pollitz FF, Burgmann R, Banerjee P (2011) Geodetic slip model of the 2011 M9.0 Tohoku earthquake. Geophys Res Lett 38:L00G08

Simons M et al (2011) The 2011 magnitude 9.0 Tohoku-Oki earthquake: mosaicking the megathrust from seconds to centuries. Science 332:1421–1425

Tamura Y, Sato T, Ooe M, Ishiguro M (1991) A procedure for tidal analysis with a Bayesian information criterion. Geophys J Int 104:507–516

Watts DR, Kontoyiannis H (1990) Deep-ocean bottom pressure measurements: drift removal and performance. J Atmos Oceanic Technol 7:296–306

Wessel P, Smith W (1998) New, improved version of generic mapping tools released. Trans Am Geophys Union (EOS) 79:579

Yagi Y, Kikuchi M (2003) Partitioning between seismogenic and aseismic slip as highlighted from slow slip events in Hyuga-nada, Japan. Geophys Res Lett 30:1087

Yamanaka Y (2003) Off Fukushima-ken earthquake, 31 October 2003 (M6.8) (in Japanese). http://www.eri.u-tokyo.ac.jp/sanchu/Seismo_Note/EIC_News/031031.html

Yamanaka Y, Kikuchi M (2003) Source process of the recurrent Tokachi-oki earthquake on September 26, 2003, inferred from teleseismic body waves. Earth Planets Space 55:e21–e24

Yamanaka Y, Kikuchi M (2004) Asperity map along the subduction zone in northeastern Japan inferred from regional seismic data. J Geophys Res 109:B07307

Zumberge JF, He MB, Jefferson DC, Watkins MM, Webb FH (1997) Precise point positioning for the efficient and robust analysis of GPS data from large networks. J Geophys Res 102:5005–5017

Rapid Coseismic Fault Determination of Consecutive Large Interplate Earthquakes: The 2011 Tohoku-Oki Sequence

Yusaku Ohta, Tatsuya Kobayashi, Ryota Hino, Tomotsugu Demachi, and Satoshi Miura

Abstract

Real-time monitoring of crustal deformation is important in achieving rapid understanding of earthquake magnitude and fault model. Recently, an algorithm called Real-time Automatic detection method for Permanent Displacement ("*RAPiD*") has been developed to detect/estimate static ground displacements due to earthquake faulting from real-time kinematic (RTK)-GPS time series. We applied this algorithm to the 2011 off Ibaraki earthquake (M_w 7.7), which occurred only 30 min after the 2011 Tohoku-Oki earthquake (M_w 9.0). The *RAPiD* algorithm worked well with the long baseline RTK-GPS time series for quasi real-time coseismic displacement detection and estimation. A quasi real-time fault determination was also attempted with an automatic detection/estimation displacement field. We found that the estimated moment release reached M_w 7.7 60 s after the origin time, almost the same as the actual seismic moment for this earthquake. We also assessed the long-term stability of the RTK-GPS time series under a 200-km baseline condition. We found the time series precision degraded slightly in summer compared with winter. However, the total stability is good for monitoring crustal deformation. These results suggest clearly that using real-time GPS data in conjunction with the *RAPiD* algorithm can provide rapid coseismic fault determination, even for consecutive large earthquakes.

Keywords

Rapid coseismic fault determination • RTK-GNSS (GPS) • The 2011 Tohoku earthquake • Tsunami early warning

1 Introduction

Real-time monitoring of crustal deformation is extremely important in achieving rapid understanding of earthquake magnitude and fault model. This is because the measured permanent displacement gives a direct indication of the true earthquake size (seismic moment magnitude, M_w), which in turn provides information for tsunami forecasting. Blewitt et al. (2006, 2009) proposed a potential key design for a Global Navigation Satellite System (GNSS)-based approach that could contribute to real-time earthquake source determination and tsunami warning. Sobolev et al. (2007) also proposed a near-field GPS array concept ("GPS-Shield") for the issuance of early tsunami warnings within 10 min after an earthquake. After these pioneering works, the 2011 off the Pacific coast of Tohoku earthquake (M_w 9.0) (hereafter, 2011 Tohoku earthquake) occurred, following which many efforts for rapid earthquake size determination based on real-time GNSS data have progressed. Melgar et al. (2012) proposed an algorithm (named "*fastCMT*") for the rapid determination of the moment tensor and centroid location for large earthquakes based on real-time high-rate GPS data. Wright et al. (2012) applied the precise point positioning strategy to the processing of GPS data for the 2011

Y. Ohta (✉) • T. Kobayashi • R. Hino • T. Demachi • S. Miura
Research Center for Prediction of Earthquakes and Volcanic Eruptions, Graduate School of Science, Tohoku University, Miyagi, Japan
e-mail: ohta@aob.gp.tohoku.ac.jp

© Springer International Publishing Switzerland 2015

C. Rizos, P. Willis (eds.), *IAG 150 Years*, International Association of Geodesy Symposia 143,
DOI 10.1007/1345_2015_109

Tohoku earthquake for rapid coseismic fault slip determination. Hoechner et al. (2013) applied the "GPS shield" concept proposed by Sobolev et al. (2007) to the 2011 Tohoku earthquake. They also estimated tsunami height along the coastline of Japan based on the estimated slip distribution on the plate interface. Their estimate was that the tsunami height exceeded 10 m around the central part of the Tohoku area. Colombelli et al. (2013) also developed an algorithm to invert for the slip distribution on the fault plane. Their "self-adapting" strategy does not require restrictive a priori assumptions about the ongoing earthquake. The initial fault plane used for the slip inversion is built based on quick preliminary magnitude estimation and the model is then upgraded as new values of the magnitude are established. Tsushima and Ohta (2014) reviewed near field tsunami forecasting based on the offshore tsunami data and onshore real-time GNSS data.

We also have developed an algorithm, called the Real-time Automatic detection method for Permanent Displacement (*RAPiD*), to detect/estimate static ground displacements due to earthquake faulting from real-time kinematic (RTK)-GPS time series (Ohta et al. 2012). The algorithm identifies permanent displacements by monitoring the difference between a short-term average (STA) and a long-term average (LTA) of the GPS time series, for which the characteristic function D is defined as follows:

$$D = |STA(t) - LTA(t)| - SD\,(LTA(t)) \tag{1}$$

where $LTA(t)$ and $STA(t)$ are the long- and short-term averages of the time series as functions of time t, respectively and $SD(LTA(t))$ represents the standard deviation of $LTA(t)$. $STA(t)$ and $LTA(t)$ are defined as follows:

$$STA(t) = \frac{\sum_{i=t-\alpha+1}^{t} p_i x_i}{\sum_{i=t-\alpha+1}^{t} p_i}, LTA(t) = \frac{\sum_{i=t-\beta+1}^{t} p_i x_i}{\sum_{i=t-\beta+1}^{t} p_i} \tag{2}$$

where x_i is the norm of the horizontal components at $t = i$. And, α and β are the proper time-window lengths. In the work by Ohta et al. (2012), they used 60 and 600 s for the values of α and β, respectively. This selection of time-window length is based mainly on the source time length of the tsunamigenic earthquake. The p_i is a weighting parameter based on the quality of the RTK-GPS time series. For the detection of the displacement, Ohta et al. (2012) define a threshold value K before the monitoring. When $D > K$, the occurrence of displacement is recognized. Please refer to Ohta et al. (2012) for more detailed information on the *RAPiD* algorithm. Ohta et al. (2012) applied the algorithm to data pertaining to the 2011 Tohoku earthquake (M_w 9.0) to test the possibility of coseismic displacement detection based on the GNSS Earth Observation Network System (GEONET) 1-Hz data. Furthermore, the obtained displacement fields were inverted for a fault model. The inversion estimated a fault model with Mw 8.7, which is close to the actual M_w value of 9.0, within 5 min from the origin time (Ohta et al. 2012).

The 2011 Tohoku earthquake not only caused the mainshock, but also large aftershocks. One of the large aftershocks occurred only 30 min after the mainshock; this was the earthquake off Ibaraki, which was an interplate earthquake with magnitude M_w 7.7 (estimated by the JMA). Monitoring consecutive large earthquakes such as these is important for the prevention of secondary damage caused by tsunamis. For the M_w 7.7 aftershock in the off Ibaraki case, the earthquake early warning system (EEW) of the JMA did not work because of high background noise from the coda waves of the mainshock and other active aftershocks, and because of power failures and wiring disconnections (Hoshiba et al. 2011). Over the past 1,000 years, large earthquakes (around M_w 8.0) have occurred repeatedly every 100–200 years along the Nankai Trough in southwestern Japan, where the Philippine Sea plate is being subducted beneath the Amurian plate. The most recent large events were the 1944 Tonankai earthquake and the 1946 Nankai earthquake and furthermore, we expect the next large interplate earthquakes to occur along the Nankai Trough. Some past events have occurred consecutively, for example, the 1854 Ansei earthquake first ruptured the Tonankai and Tokai segment, and then 32 h later the Nankai segment was ruptured. Based on these past cases of huge interplate earthquakes, a robust earthquake and tsunami early warning system based on various seismic and geodetic sensors is required. In this short report, we perform an a posteriori analysis of the 2011 off Ibraki earthquake, which was one of the large aftershocks of the 2011 Tohoku earthquake, to test our quasi real-time approach to crustal displacement detection/estimation. We also discuss briefly the long-term stability of the RTK-GPS time series based on Japan's nationwide GEONET data.

2 Data and Analysis

2.1 RTK-GPS Analysis and Its Assessment for Long-Term Precision Stability

We used GEONET data for this short report. For the RTK-GPS analysis, we used RTKLIB v. 2.4.1. (RTKLIB; an open source program for GNSS positioning, http://www.rtklib.com), which features the long baseline RTK-GNSS technique for detecting deformation caused by earthquakes

for baselines over several hundreds of kilometers. In this analysis, we only used the GPS satellite system for the monitoring large-scale crustal deformation.

The precision of the RTK-GPS time series depends strongly on the baseline length. Thus, Ohta et al. (2012) showed that the baseline-length-dependent precisions of RTK-GPS time series, if ultra-rapid orbit information from the International GNSS Service (IGS) (Dow et al. 2009) is used, are within the ranges of 1.2–3.3 mm/100 km and 3.3–8.6 mm/100 km of standard deviation for the horizontal and vertical components, respectively. These results indicate that the precisions of baseline estimation are 12–33 mm for the horizontal and 33–86 mm for the vertical components, respectively, for a baseline length of 1,000 km. It was suggested that this is sufficiently precise for fault model estimation of large earthquakes, because 1,000 km is a sufficient distance, given that the base station for the RTK-GPS is set at this distance from the epicenter to avoid coseismic steps, even for huge earthquakes. For monitoring purposes, long-term stability, such as monthly to yearly, is also an important factor because false alarms must be avoided for a reliable warning system. Thus, we also assess the long-term stability of the RTK-GPS time series.

For the assessment of the long-term stability of RTK-GPS time series, we chose sites 0036 and 0585 as the reference and rover sites, respectively (Fig. 1), for which the baseline length is 200 km. For real-time orbit information, we used the ultra-rapid orbit products provided by the IGS and broadcast orbit information (e.g., Boyd 2009). The precise orbit information provides us exact GPS satellite positions relative to the WGS-84 reference frame. The precise ephemeris consists of two parts: an observed part and predicted part (predicted part of IGS ultra-rapid orbit, hence IGUP), which is estimated by extrapolation from past GPS satellite positions and can be obtained in real time. In contrast, the broadcast orbit (hereafter BRDC) is transmitted directly from GPS satellites to receivers using the Keplerian factors format. We processed the 30-second-interval raw data for the entire year of 2009 based on the BRDC and IGUP orbit information, and Fig. 2 shows the results. The calculated standard deviations (SDs) of the entire yearly time series are also summarized in Fig. 2. It is clear that the calculated SDs with IGUP are less than 20 and 50 mm in the horizontal and vertical components, respectively, and even for the BRDC result, the SDs are less than 30 and 60 mm in each component. In Fig. 2, a diagonal pattern in the time series can be seen clearly. This is caused by multipath errors, which are highly repeatable from day to day with a sidereal period (23 h 56 m 4 s) (e.g., Bock 1991; Choi et al. 2004; Larson et al. 2007). Choi et al. (2004) suggested that "orbit repeat filtering" (repeating time: 23 h 55 m 55 s) is better than pure sidereal filtering. In Fig. 2, we also found that the precision of the time series degrades in summer compared with winter. The degradation in summer may be caused by difficulties involving time-dependent tropospheric effects and estimations of its component's gradients. Interestingly, the SDs in the horizontal components are less than 30 mm, even through the summer. This suggests that the RTK-GPS time series is largely stable throughout the year, despite the small annual pattern detected. Based on this example, we conclude that the RTK-GPS time series is stable enough for the monitoring of large-scale crustal deformation.

2.2 A Posteriori Analysis of the 2011 Off Ibaraki Earthquake

For the a posteriori processing of the 2011 off Ibaraki earthquake, we used station 0065 as the reference site (Fig. 1). For the assessment of the detection of the occurrence of consecutive earthquakes by our *RAPiD* algorithm, we used GPS data from the occurrence of the M9 Tohoku earthquake until the end of the off Ibaraki earthquake. The other detailed settings of the RTK-GPS processing strategies are the same as those detailed in Ohta et al. (2012). To simplify crustal deformation monitoring, we did not apply sidereal filtering to the RTK-GPS time series in this study.

3 Application to the Aftershock of the 2011 Tohoku Earthquake

3.1 Example of Displacement Detection/Estimation Process

Figure 3 shows an example of the time series of the RTK-GPS data and the characteristic function D values (see Eq. 1) defined by the *RAPiD* algorithm at GEONET station 3009 on March 11, 2011, when the M_w 9.0 Tohoku earthquake and its aftershock occurred. Owing to the coseismic displacement of the mainshock, the D value based on the horizontal components started increasing and exceeded the threshold level (red line) for event detection. Figure 3 also shows the off Ibaraki earthquake as the M9 aftershock. For this station, the coseismic displacement of this aftershock is clearly larger than that of the mainshock. Figure 3 indicates clearly that the *RAPiD* algorithm works under the circumstance of consecutive earthquake occurrence. On the other hand, the D value based on the horizontal components clearly shows a negative value after the M9 mainshock (Fig. 3). For the *RAPiD* algorithm, the $SD(LTA(t))$ is introduced to avoid false alarms caused by strong ground shaking. This means avoiding false alarms when there is no permanent displacement with strong ground shaking; thus, the $SD(LTA(t))$ must be large after the mainshock. The result found was that the value of D decreased within the window length of the LTA. Therefore,

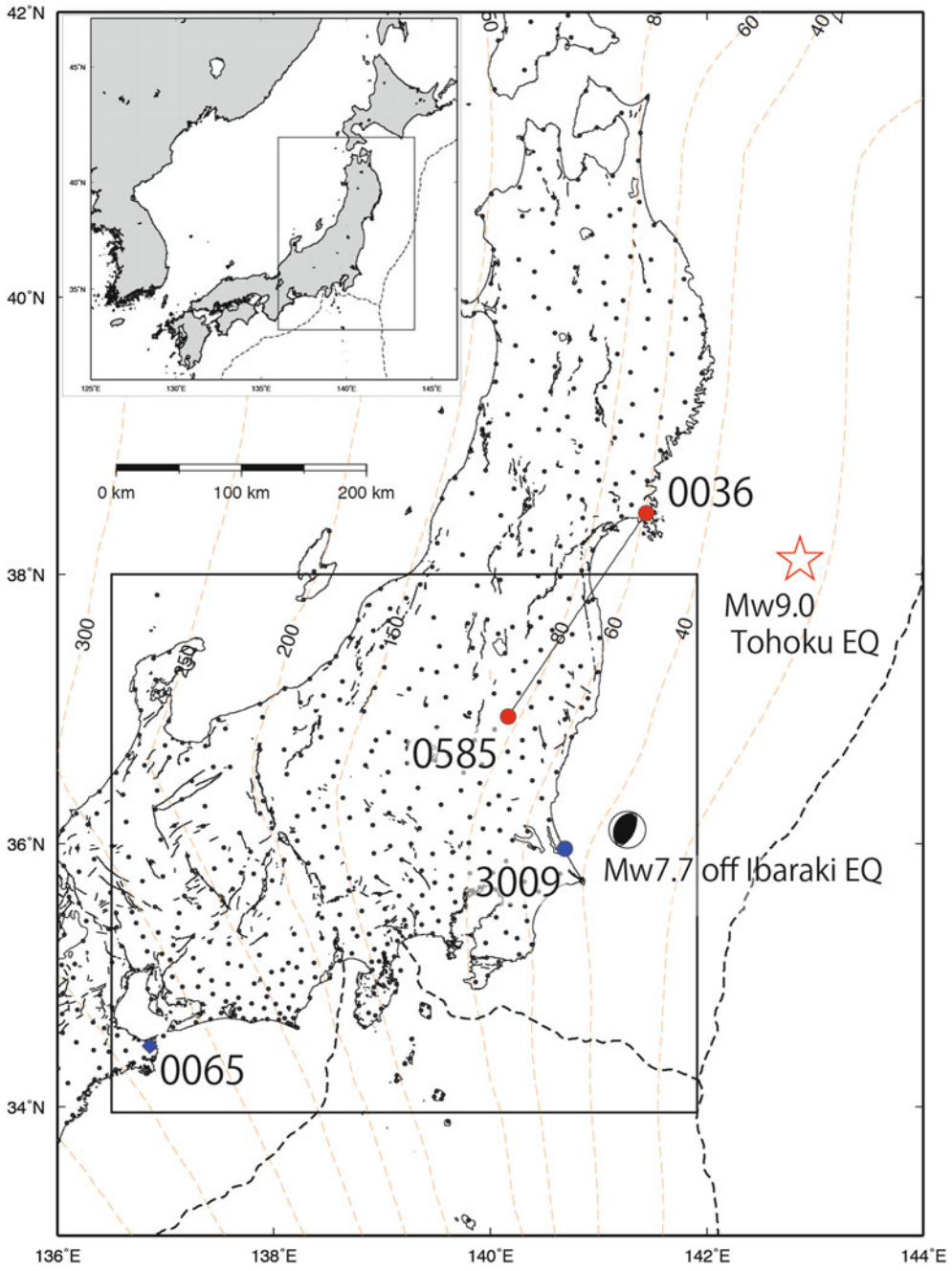

Fig. 1 GPS site distribution for this study. *Black circles* denote GEONET sites. The *red circles* denote the GEONET stations for the assessment of long-term stability in Sect. 2.1. The *blue diamond* denote the reference station for the posteriori processing for the M_w 9.0 Tohoku earthquake and its aftershock. The blue circle denote the location of example station for figure 3. The *black rectangular region* denotes the study area for the a posteriori coseismic fault determination for the 2011 off Ibaraki earthquake. The *open red star* represents the hypocenter of the 2011 Tohoku earthquake determined by the JMA. The mechanism solution represents the 2011 off Ibaraki earthquake determined by the National Research Institution for Earth Science and Disaster Prevention. The *orange dashed contours* denote the subducting Pacific plate compiled by Nakajima and Hasegawa (2006)

the permanent displacement detection ability of the *RAPiD* algorithm will decrease just after the large earthquake. The length of this low performance window is strongly dependent on the LTA window length and duration of ground shaking during the preceding earthquake. In the example case, the low performance time is around 10 min after the mainshock, which is almost the same as with the LTA window length (600 s). We believe this short time period (∼10 min) is an acceptable range for the detection of consecutive large earthquakes. One idea for avoiding the low performance time

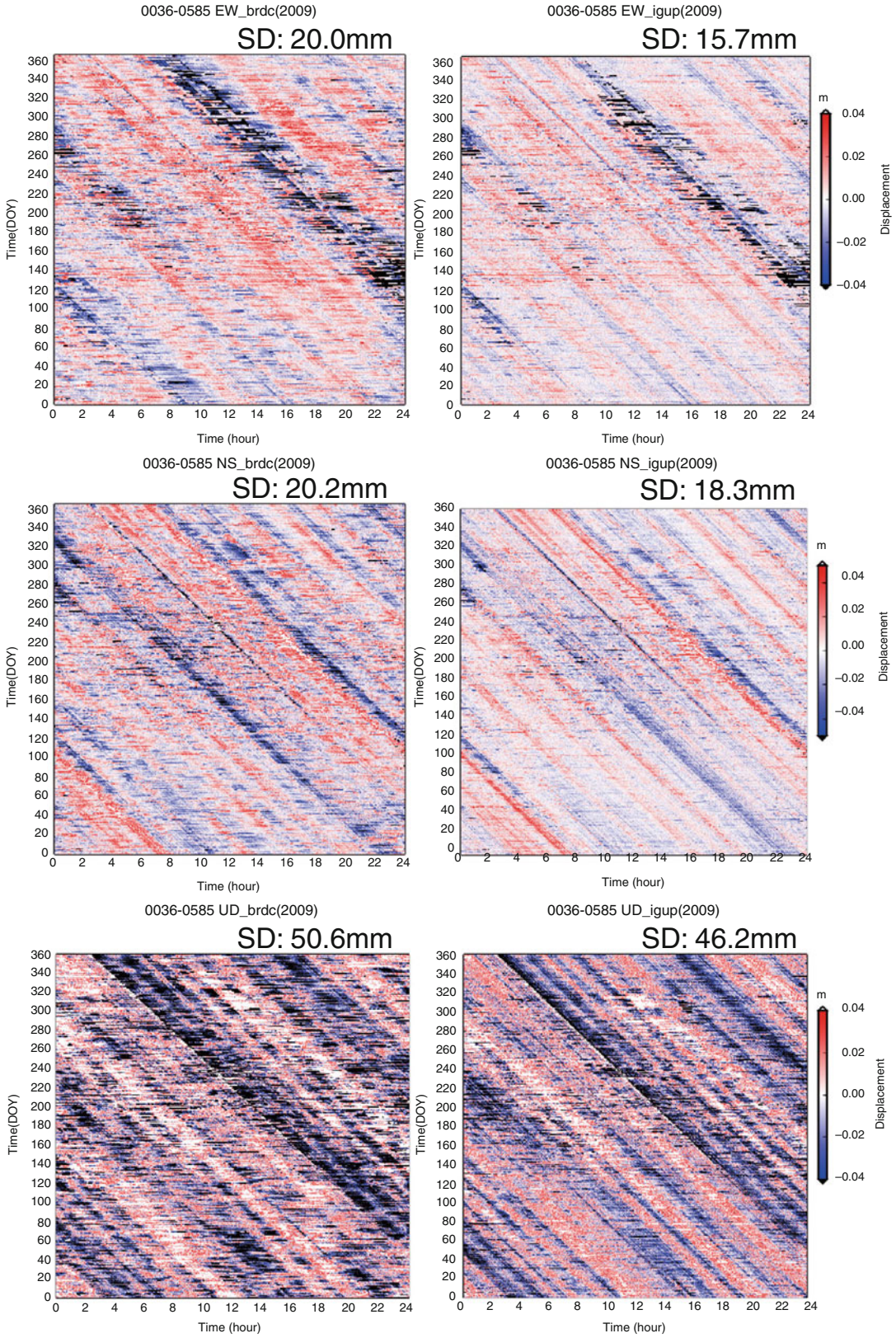

Fig. 2 Three-component RTK-GPS time series during DOY1-365, 2009 at station 0585 referred to station 0036 using broadcast orbit (left row, EW, NS, and UD) and IGS ultra-rapid orbit information (right row, EW, NS, and UD). The *vertical axis denotes* the DOY in 2009 and the *horizontal axis* denotes the hours in the day. The *color* indicates the perturbation of the coordinates from the averaged daily position: *red color* positive perturbation and *blue color* negative perturbation. The SD of the time series is presented in each figure

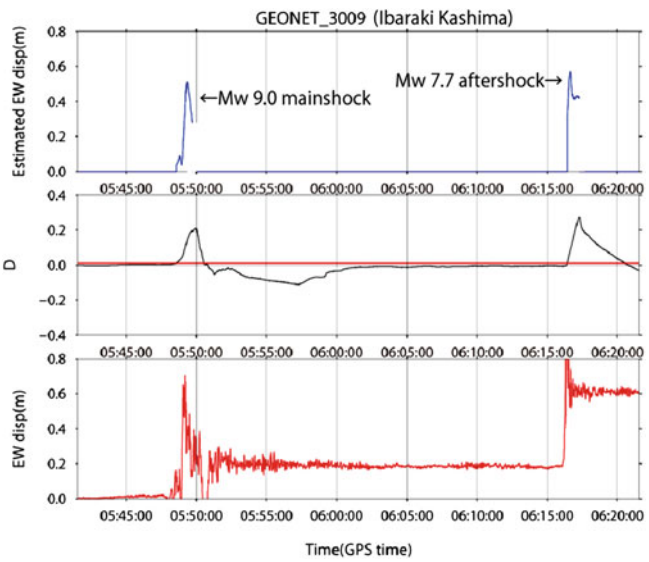

Fig. 3 Time series example of the 2011 Tohoku earthquake and its aftershock at GEONET site 3009 referred to the station 0065. *Top*, *middle*, and *bottom row* represent the norm of the horizontal component time series, the *D* value, and the raw EW component time series, respectively. The *red line* in the middle time series represents the threshold value *K*, determined previously based on each baseline's noise level

just after the large event is a flexible LTA value. In the *RAPiD* algorithm, the event detection restarts when the *D* value is lower than the threshold value *K*. If we make the LTA time-window length shorter than the original in this timing for the consecutive large events, then the low performance time will also become shorter. It is to be noted that even though the low performance time window exists, the *RAPiD* algorithm might still detect sufficiently large coseismic displacements.

Next, we show quasi real-time fault determination based on the *RAPiD* algorithm for this aftershock.

3.2 Quasi Real-Time Fault Determination for the 2011 Off Ibaraki Earthquake

Figure 4 shows several snapshots of the three-component coseismic displacement fields based on the *RAPiD* algorithm. It is clear that the large displacement is evident mainly in the horizontal component. We also estimated the coseismic fault plane based on the estimated permanent displacement. The estimated coseismic displacement fields were inverted repeatedly for a rectangular fault model at a time interval of 15 s using a nonlinear inversion method with a priori information (Matsu'ura and Hasegawa 1987). In the inversion, Green's function was used, which relates fault motion to surface displacement in an elastic half-space (Okada 1992). The estimated parameters occasionally depend on the initial values assumed in the recursive procedure. To estimate all the fault parameters (location, depth, length, width, strike, dip, rake, and slip amount), we assumed initial values for the fault location. We used the first coseismic displacement detection GPS site information for the initial fault location. In this analysis, *RAPiD* algorithm detected coseismic displacement 35 s after the origin time in station 3022 (Fig. 4). We used the coordinate of this station for initial fault location. When the initial horizontal fault location determined, the initial fault depth could also determine based on the model of the subducting plate interface (e.g. Nakajima and Hasegawa 2006). We also assumed the fault length, width, and slip amount with very large uncertainty. We gave uncertainty for these initial fault parameters for the inversion analysis: fault location (3.5° in latitude and longitude), depth (20 km), fault length (50 km), width (50 km), and slip amount (7 m). We gave the relatively strong constraint to the other parameters (strike, dip and rake angle) with interplate earthquake into consideration. For the actual operation, the EEW by JMA based on the seismic data will be useful for the determination of initial fault parameters. Even if the EEW does not work, we can assume the initial fault location based on the coseismic displacement information by GPS data.

The estimated simple rectangular fault model explains the displacement data basically well (Fig. 4). The temporal change in the coseismic fault shows the rupture expansion. At 45 s after the earthquake, the estimated coseismic fault model did not explain the coseismic displacement field. It may be caused by the ongoing rupture process along the fault plane. At 60 s after the earthquake, the estimated moment magnitude had already reached M_w 7.7 (assumed rigidity: 40GPa). At this point, the coseismic fault rupture was almost complete, based on the GPS displacement fields. Furthermore, 180 s after the earthquake, all of the GPS sites completed the displacement estimations, and we assigned this length of time to the final coseismic fault model for this earthquake. The estimated moment magnitude finally reached M_w 7.7, which slightly smaller than the seismological results. The Global CMT (centroid moment tensor) Project estimated a value of M_w 7.9 from the CMT inversion for this earthquake. Kubo et al. (2013) also estimated the coseismic slip distribution based on the strong-motion and post-processing

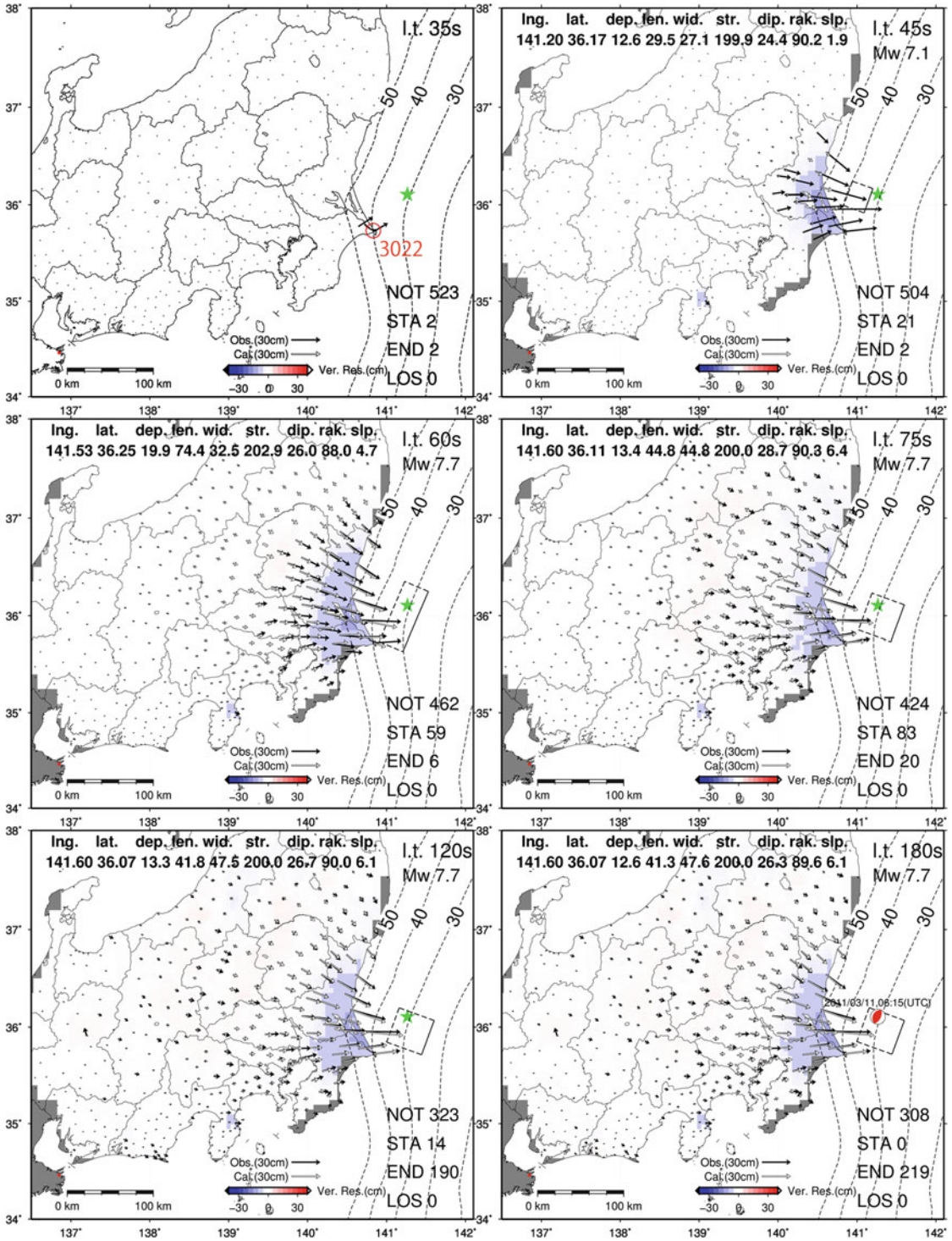

Fig. 4 Several snapshots at 15-second intervals of the three-component GPS displacement and automatically estimated fault model for the 2011 off Ibaraki earthquake using the data up to the lapse time (l.t. measured from the origin – shown in the *upper right* of each respective snapshot). Snapshot of 35 s after the earthquake is consistent with the first coseismic displacement detection timing in the GEONET 3022 site (*red circle*). *Black rectangular areas* denote the fault model estimated at each lapse time. Details of the estimated fault model parameters are shown above each snapshot. Longitude, latitude, and depth denote the location of the upper-left corner of rectangular fault plane, looking down from the hanging wall side. *Black vectors* represent observed horizontal displacements. The *open vectors* indicate calculated horizontal displacements based on the estimated fault model. The *colors* indicate residual between observed and calculated (O–C) value of the vertical component. NOT, STA, END, and LOS in the lower right of each snapshot represent the numbers of stations judged before signal arrival, during displacement increase, after final displacement, and troubled, respectively. The mechanism solution in 180 s after the origin time represents the F-net solution for the 2011 off Ibaraki earthquake determined by NIED

kinematic GPS analysis. Their results showed the estimated moment magnitude and the maximum slip were M_w 7.9 and 6.3 m, respectively. This underestimation might be mainly caused by errors in the estimation of the fault depth during our inversion.

The estimated coseismic fault model was located clearly (around 10–15 km) shallower than the actual subducting plate interface (Fig. 4). For the inversion, we considered an interplate earthquake by the initial fault parameter assumption. The estimated fault parameters, however, have strong trade off between each other. For example, the fault depth and slip amount on the fault had large correlation. Thus, our estimated fault plane was not forced to be on the subducting plate interface.

For the actual monitoring, we should pay attention not only interplate earthquake, but also other types of the earthquake mechanism. In fact, the large intraslab earthquake (M7.1) occurred in April 7 2011 at the Miyagi-Oki region, which is located within the rupture area of the 2011 Tohoku earthquake (e.g. Ohta et al. 2011). For such case, the initial fault parameters are very important for the rapid fault model estimation. As described in the Introduction, Melgar et al. (2012) developed "*fastCMT*" algorithm for the rapid determination of the moment tensor and centroid location. Such approach may be important for the initial focal mechanism determination.

An M7–8 class earthquake is expected to exhibit a source-time function duration of several tens of seconds to a few minutes. Our *RAPiD* algorithm can define the "final" solution (180 s) based on the number of GPS sites with completed displacement. On the other hand, after 60 s from the onset of the earthquake, our estimation result (M_w 7.7) had already reached agreement with the actual one (M_w 7.9 by GCMT solution). This suggests that the use of our algorithm would make it possible to raise an alert before the "final" solution, which would be useful for a timelier earthquake and/or tsunami early warning system. Furthermore, the source time function is not only a factor for effective tsunami excitation, but also for the rupture velocity and its expansion. Thus, the real-time onshore GPS data are useful not only for estimation of the magnitude, but also for the fault expansion and time dependence of the fault rupture. Of course, the estimated point source deduced from seismological/geodetical data can be translated to the finite fault model experimentally by applying the scaling law between fault dimension and magnitude. In the case of large earthquakes, however, the relationships between coseismic fault expansion and its aspect ratio are diverse. This is because the width and length of the seismogenic zone differ between each subduction zone. Based on the above, it can be stated that onshore GPS data have an advantage in the robust estimation of coseismic fault dimension, location, and its slip amount.

4 Conclusion

We applied the *RAPiD* algorithm to the 2011 off Ibaraki earthquake, which was one of the large aftershocks following the 2011 Tohoku earthquake. The *RAPiD* algorithm worked well with the long baseline RTK-GPS time series for quasi real-time coseismic displacement detection/estimation. A quasi real-time fault determination was also attempted with an automatic detection/estimation displacement field. We found that the estimated moment release 60 s after the origin time reached M_w 7.7, which was almost similar to the actual moment magnitude for this earthquake. Furthermore, we established the length of the low performance time window of the *RAPiD* algorithm just after the large earthquake. For the 2011 Tohoku sequence, the low performance time was around 10 min after the mainshock. This period might be an acceptable length for the detection of consecutive large earthquakes. We also assessed the stability of the RTK-GPS time series for the entire year and found that it demonstrated a highly repeatable day-to-day pattern with a sidereal period caused by the multipath effect. We found that the time series disturbance in summer was slightly larger than in winter. Based on this analysis, it is concluded that the RTK-GPS time series is basically stable enough for the monitoring of crustal deformation. These results suggest that the RTK-GPS data and our algorithm are useful for rapid coseismic fault determination, even for consecutive large earthquakes.

Acknowledgements The authors would like to thank Prof. Manabu Hashimoto and Prof. Jeffrey T. Freymueller for their invitation to the International Association of Geodesy Scientific Assembly in Potsdam. The paper benefited from careful reviews by Dr. Ronni Grapenthin, Prof. Jeffrey T. Freymueller and two anonymous reviewers. We thank the GSI for providing GPS data. We are also very grateful to IGS for providing high-quality precise ephemerides as well as real-time observation data from their tracking stations. This study was supported partly by a grant-in-aid for young scientists (start-up 19840006) from the Research of Japan Society for the Promotion of Science. This study was also supported by the project of the Ministry of Education, Culture, Sports, Science and Technology, Japan, titled "Observation and Research Program for the Prediction of Earthquakes".

References

Blewitt G, Kreemer C, Hammond WC, Plag H-P, Stein S, Okal E (2006) Rapid determination of earthquake magnitude using GPS for tsunami warning systems. Geophys Res Lett 33:L11309. doi:10.1029/2006GL026145

Blewitt G, Hammond WC, Kreemer C, Plag H-P, Stein S, Okal E (2009) GPS for real-time earthquake source determination and tsunami warning systems. J Geod 83:335–343. doi:10.1007/s00190-008-0262-5

Bock Y (1991) Continuous monitoring of crustal deformation. GPS World 2(6):40–47

Boyd D (2009) GPS constellation status and performance. Paper presented at 49th Meeting, Civ. GPS Serv. Interface Comm., Savannah, Ga

Choi K, Bilich A, Larson K, Axelrad P (2004) Modified sidereal filtering: implications for high-rate GPS positioning. Geophys Res Lett 31:L22608. doi:10.1029/2004GL021621

Colombelli S, Allen RM, Zollo A (2013) Application of real-time GPS to earthquake early warning in subduction and strike-slip environments. J Geophys Res 118(7):3448–3461. doi:10.1002/jgrb.50242

Dow JM, Neilan RE, Rizos C (2009) The international GNSS service in a changing landscape of global navigation satellite systems. J Geod 83:191–198. doi:10.1007/s00190-008-0300-3

Hoechner A, Ge M, Babeyko AY, Sobolev SV (2013) Instant tsunami early warning based on real-time GPS - Tohoku 2011 case study. Nat Hazards Earth Syst Sci 13(5):1285–1292. doi:10.5194/nhess-13-1285-2013

Hoshiba M, Iwakiri K, Hayashimoto N, Shimoyama T (2011) Outline of the 2011 off the pacific coast of Tohoku earthquake (Mw 9.0)—earthquake early warning and observed seismic intensity. Earth Planets Space 63(7):547–551. doi:10.5047/eps.2011.05.031

Kubo H, Asano K, Iwata T (2013) Source-rupture process of the 2011 Ibaraki-oki, Japan, earthquake (M w 7.9) estimated from the joint inversion of strong-motion and GPS Data: relationship with seamount and Philippine Sea Plate. Geophys Res Lett 40(12):3003–3007. doi:10.1002/grl.50558

Larson KM, Bilich A, Axelrad P (2007) Improving the precision of high-rate GPS. J Geophys Res 112:B05422. doi:10.1029/2006JB004367

Matsu'ura M, Hasegawa Y (1987) A maximum likelihood approach to nonlinear inversion under constraints. Phys Earth Planet Int 47:179–187. doi:10.1016/0031-9201(87)90076-8

Melgar D, Bock Y, Crowell BW (2012) Real-time centroid moment tensor determination for large earthquakes from local and regional displacement records. Geophys J Int 188:703–718. doi:10.1111/j.1365-246X.2011.05297.x

Nakajima J, Hasegawa A (2006) Anomalous low-velocity zone and linear alignment of seismicity along it in the subducted Pacific slab beneath Kanto, Japan: reactivation of subducted fracture zone? Geophys Res Lett 33:L16309. doi:10.1029/2006GL026773

Ohta Y, Miura S, Ohzono M, Kita S, Iinuma T, Demachi T, Tachibana K, Nakayama T, Hirahara S, Suzuki S, Sato T, Uchida N, Hasegawa A, Umino N (2011) Large intraslab earthquake (2011) after the 2011 off the Pacific coast of Tohoku earthquake (M9.0): coseismic fault model based on the dense GPS network data. Earth Planets Space 63(12):1207–1211. doi:10.5047/eps.2011.07.016

Ohta Y, Kobayashi T, Tsushima H, Miura S, Hino R, Takasu T, Fujimoto H, Iinuma T, Tachibana K, Demachi T, Sato T, Ohzono M, Umino N (2012) Quasi real-time fault model estimation for near-field tsunami forecasting based on RTK-GPS analysis: application to the 2011 Tohoku-Oki Earthquake (Mw 9.0). J Geophys Res 117:B0231116. doi:10.1029/2011JB008750

Okada Y (1992) Internal deformation due to shear and tensile faults in a half-space. Bull Seismol Soc Am 82:1018–1040

Sobolev SV, Babeyko AY, Wang R, Hoechner A, Galas R, Rothacher M, Sein DV, Schröter J, Lauterjung J, Subarya C (2007) Tsunami early warning using GPS-Shield arrays. J Geophys Res 112(B8):1–18. doi:10.1029/2006JB004640

Tsushima H, Ohta Y (2014) Review on near-field tsunami forecasting from offshore tsunami data and onshore GNSS data for tsunami early warning. J Disaster Res 9(3):339–357

Wright TJ, Houlié N, Hildyard M, Iwabuchi T (2012) Real-time, reliable magnitudes for large earthquakes from 1 Hz GPS precise point positioning: the 2011 Tohoku-Oki (Japan) earthquake. Geophys Res Lett 39:1–5. doi:10.1029/2012GL051894

GRACE Gravity Data to Enhance the Modeling of Coseismic Slip Distribution for the 2011 Tohoku-Oki Earthquake

M.J. Fuchs, T. Broerse, A. Hooper, J. Pietrzak, and J. Bouman

Abstract

The 2011 Tohoku-Oki earthquake with 9.0 Mw led to an enormous mass redistribution originated from large deformation due to faulting and had a massive impact on the coastal area of eastern Japan. While the satellite gravity mission GRACE (Gravity Recovery and Climate Experiment) can detect the gravitational change caused by this tremendous event, slip distributions are usually derived from GPS, seismic and (in the more particular case) tsunami data. We evaluate the differences between measured and modeled coseismic gravity changes for three fault slip models derived from either GPS and tsunami data, GRACE data, or a combination of all three data types. The data are weighted according to their measurement accuracy in a Bayesian joint inversion approach. We perform a long term average of GRACE data, which increases sensitivity and reduces artefacts, and find that the postseismic gravity change leaks into the derived mean gravity field. We try to reduce this problem by averaging only 6 months of postseismic GRACE data, where the postseismic gravity signal, which superimposes onto the coseismic signal of ≈ 6 μGal (for a geometric based model) peaks approximately 3 months after earthquake occurrence. Consequently fault slip models merely derived from GPS (10 days avg.) and tsunami data ($<$ 5h time span) show deviations of ≈ 2 μGal to a GRACE 6 monthly averaged combined solution which indicates the difference accumulated from the geometric and gravimetric modelling and the postseismic gravity signal in the GRACE data.

Keywords

Fault-slip distribution • GRACE • Gravity change • GPS data • Japan Tohoku-Oki earthquake • Joint inversion • Tsunami data

1 Introduction

The 2011 Tohoku-Oki earthquake occurred on March 11 at 05:46:24 UTC and had a devastating impact on the coastal area of Japan. The mainshock and numerous aftershocks took place in the vicinity of the subduction zone between the Pacific and North American plate. The earthquake released strain accumulated over several hundreds of years (Ozawa

M.J. Fuchs (✉)
Alfons-Goppel-Straße 11, München, Germany
e-mail: fuchs@dgfi.badw.de

T. Broerse
Department of Geosciences and Remote Sensing, Delft University of Technology, Delft, The Netherlands

A. Hooper
School of Earth and Environment, University Leeds, Leeds, UK

J. Pietrzak
TU Delft, Delft, The Netherlands

J. Bouman
German Geodetic Research Institute, Technical University Munich (TUM), Munich, Germany

© Springer International Publishing Switzerland 2015

C. Rizos, P. Willis (eds.), *IAG 150 Years*, International Association of Geodesy Symposia 143,
DOI 10.1007/1345_2015_90

et al. 2012), and with an estimated magnitude of 9.0 Mw the 2011 Tohoku-Oki earthquake was the largest megathrust earthquake recorded in the area of Japan in modern history.

The fault rupture mechanism has been controversially discussed, where it is claimed that the shallow part of the plate interface slips either aseismically or seismically (Kodaira et al. 2012). Fujita et al. (2006) reported a large interseismic landward movement of a sea-floor benchmark (observation period 2002 to 2005) and suggested a strong interplate coupling of the shallow part of the plate interface which suggests the shallow portion of the fault can slip seismically. GPS stations located on the mainland of Japan indicate a maximum site displacement of 5 m horizontally and 1 m vertically (Nishimura et al. 2011; Ozawa et al. 2011). Sea floor markers, located even closer to the focal regions, indicate a much larger site displacement of up to 31 m (Kido et al. 2011). A combination of GPS and tsunami data in the fault slip inversion shows that there is strong evidence that the majority of slip occurred close to the trench (Hooper et al. 2012), where the observed slip patterns differ between GPS based fault slip models and models that include tsunami data (Lay et al. 2011; Hooper et al. 2012).

Various studies have shown that the detected gravitational change in the Earth's gravity, using GRACE data only, can be used to constrain earthquake source parameters (Cambiotti et al. 2011; Wang et al. 2012a; Han et al. 2011, 2013). Recent studies show that GOCE spaceborne gradiometric measurements can be used to measure a coseismic induced gravity gradient change (Fuchs et al. 2013; Bouman et al. 2014; Broerse et al. 2011b), To our knowledge, no distributed slip model is available for the Japan-Tohoku-Oki earthquake that incorporates GRACE and/or GOCE data next to land-based geodetic data such as GPS.

A drawback of satellite gravity data is that long integration intervals of weeks to months are needed and that the spatial resolution is typically limited to 400 km (Tapley et al. 2004). In addition the total mass change is measured which may make it difficult to differentiate between coseismic or postseismic gravity change and hydrology or ocean induced gravity signals. A disadvantage of GPS is that it observes the rupture asymmetrically as there are only data available on land. GRACE, in contrast, observes gravity signals over continental and as oceanic areas. An advantage of including spaceborne gravity data in a joint inversion approach is that these data are sensitive to the total deformation of Earth's interior and direct mass effect, whereas GPS and tsunami data are sensitive to surface deformation only. Thus this data have different sensitivities and this study identifies possible combination issues and addresses the preliminary version of a combined fault slip model using GPS, tsunami and satellite gravity data to obtain a more accurate mapping in terms of total-mass displacement and surface displacement for the fault slip inversion of the 2011 Tohoku-Oki earthquake

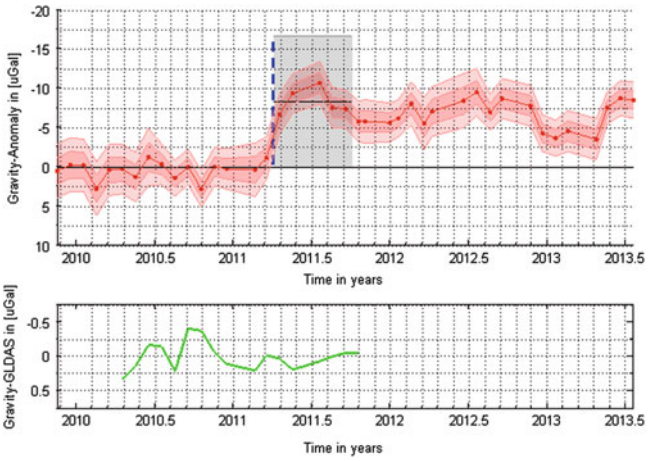

Fig. 1 Temporal gravity change derived from GRACE CSR monthly solutions (Gaussian filtered 300 km) in *red* at the position of the maximum gravity drop (39.0° N,139.5° E). The 1 and 2 sigma errors were derived from the GFZ solutions. *Note*: The scale of the y-axis has been reversed. The *gray* indicated area represents the averaging period with mean value. *Blue dashed line* indicates March 2011. Lower plot shows GLDAS derived gravity correction (*green line*)

The gravity change, due to the 2011 Tohoku-Oki earthquake, derived from GRACE data is discussed in Sect. 2. Section 3 discusses our combined model approach for the slip inversion. Section 4 evaluates the obtained slip distribution and the gravity data fits. Section 5 concludes our work.

2 Gravity Change Derived from the GRACE Mission

The GRACE mission, launched 2002, provides range differences, measured with μm accuracy between two satellites at an orbital height of approximately 500 km, which are used to derive the mean Earth's gravity field and temporal variations in Earth's natural system (Tapley et al. 2004). The spatio-temporal resolution at which the temporal gravity field can be sensed is typically limited to one month at ≈ 400 km resolution (Tapley et al. 2004). We subtract two average fields of 12 and 6 months GRACE CSR release 5 global gravity field solutions (Bettadpur et al. 2012) before (March 2010 to March 2011) and after the 2011 Tohoku-Oki earthquake (March 2011 to Aug. 2011). Temporal corrections, such as solid earth tides, indirect tides, and ocean tides, have been applied to these solutions. We apply in addition a hydrological correction derived from the GLDAS monthly solutions (Rodell et al. 2004), which however has only a minor influence on the temporal gravity signal for the region of Japan (Fig. 1).

Figure 2 shows a half yearly gravity change (to 12 months before earthquake occurrence) derived from the GRACE CSR-series at the reference sphere, applying a Gaussian-

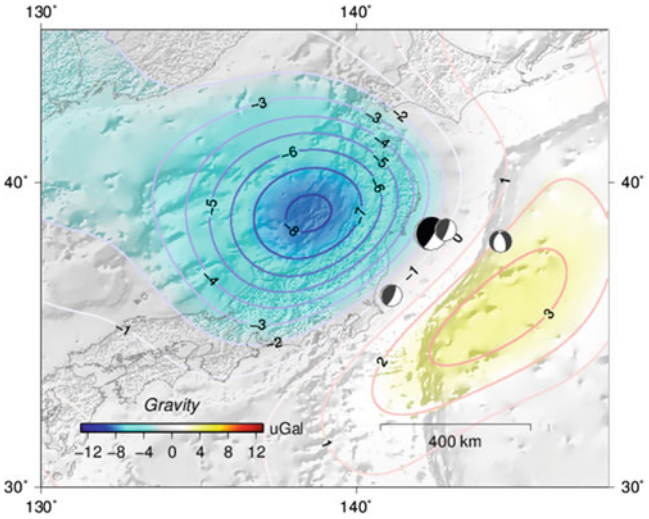

Fig. 2 GRACE gravity difference of 12 months before and 6 months after earthquake occurrence in [μGal].The *beach-balls* indicate the location of the mainshock (epicentre) and three major aftershocks

filter of 300 km. The filter width of 300 km minimizes the omission error that is introduced because the GRACE monthly fields are truncated at spherical harmonic degree 60. Later on we apply a consistent filtering to the untruncated Green functions for gravity (introduced in Sect. 3). Instead using solutions provided from GFZ and JPL, which show up with a slightly lower performance, we stick here to the CSR-solution because in a first test this solution represents the earthquake modeled gravity signal best in terms of maximum amplitude and error behavior. A similar result has been obtained by Sakumura et al. (2014) who analysed the quality performance of GRACE release 5 ensembles where also slight differences between the solutions have been indicated. The gravitational change derived from the monthly stacked CSR-solutions (Fig. 2) results in a maximum gravity change of ≈ 8 μGal ($1\,\mu\text{Gal} = 10^{-8}$ m/s^2) which is in agreement with Matsuo and Heki (2011) and Han et al. (2011).

3 Joint Inversion Approach for Geometric and Gravimetric Measurements

For the combination of different observation types a joint-inversion approach has been set up based on the fault slip inversion of Hooper et al. (2012). The model geometry covers 261 subfaults estimating a strike-slip and a dip-slip component, where a fixed orientation of each subfault patch is established with a strike angle of 194.43°. The single patch size for a subfault element is 25 km along strike and 20 km downdip, resulting in a model area of approximately 260 × 500 km. To model the trench geometry optimally we use sub-fault patches located close to the trench (see Fig. 3). Between the Japan trench and 80 km off the trench region we use a dip angle of 5°, beyond that we use 15° dip angle. This configuration represents the fault plane as reconstructed by the seismic reflection study of Fujie et al. (2006). In comparison to Hooper et al. (2012) we apply a modified regularization scheme and apply a downweighting for GPS stations that show high residuals at the coastal area of Japan. The near and far field displacements for a half-space Earth model are computed according to Okada (1992). The gravitational change is computed from a compressible semi-analytical normal mode model (Sabadini and Vermeersen 2004) including sea water correction where realistic coast lines and self-gravitation are being applied (Broerse et al. 2011a). We use the same elastic properties for the spherical Earth model and the half-space model (e.g. shear modulus and Poisson's ratio) for seismogenic depths. Furthermore the gravity modeling assumes a stratification for the crust (0–24.4 km) and the lithospheric mantle (24.4–60 km). Differences in our model approach (flat Earth versus spherical Earth) should not exceed 10% in terms of gravity within the angular distances of 10 degrees according to Sun and Okubo (1993).

All observation types are incorporated, using the derived Green's functions, in a Bayesian inversion approach (Hooper et al. 2012). The Green's functions for gravity change are derived in a set of spherical harmonic coefficients (truncated at degree and order 375) and are weighted with the correspondent Gaussian-filter coefficients to derive the gravity change for each patch for unit slip in strike and dip slip direction. Since the GRACE-CSR series do not provide covariance or variance information, we derive from error propagation the a priori gravity errors using the GFZ variance information and introduce this information in the inversion process.

4 Estimation of a Geometric, Gravimetric and a Combined Fault Slip Distribution

First, we compute the slip-distribution for a solution merely based on tsunami and GPS data (1040 land and 5 seafloor GNSS stations). The GPS/tsunami solution (Fig. 3) has a residual amplitude to the GRACE observations with maximum of $\approx 6\,\mu$Gal, which indicates that there is a significant signal difference present due to unmodeled slip by the pure geometric solution, gravity model imperfections or due to ancillary signal present in the GRACE data. Secondly, a GRACE-only solution is computed (see Fig. 4). Because of the limited spatial resolution neighboring fault slip patches are highly correlated and a relatively strong regularization has to be applied, which is estimated by the Bayesian inversion algorithm. The regularization minimizes the second

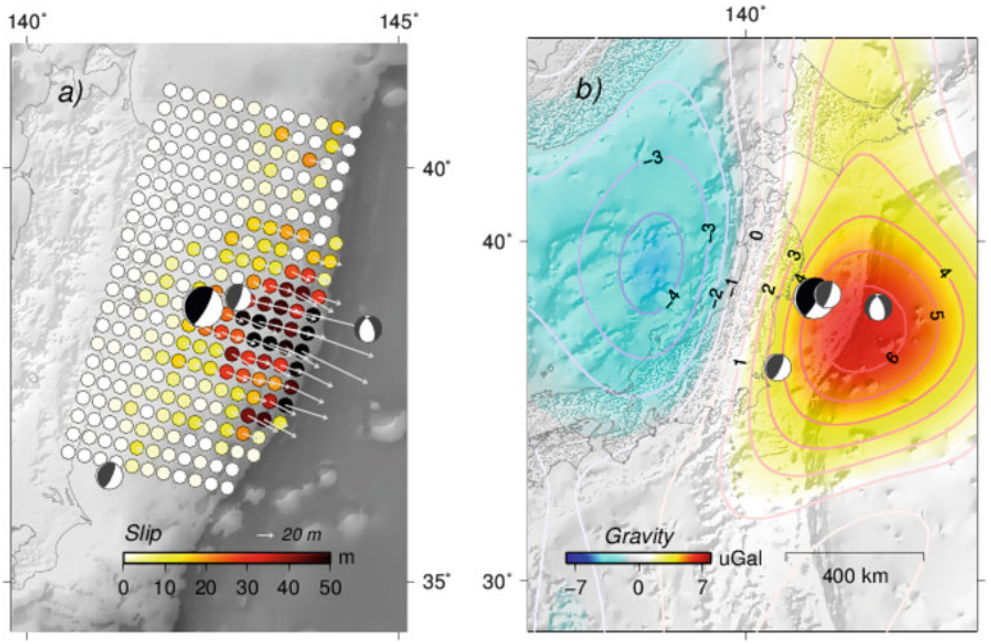

Fig. 3 (**a**) Slip distribution derived from GPS and tsunami data. *Gray arrows* indicate the slip distribution (rake angle) for each fault slip patch. The absolute slip for each patch is given by the colour scheme. (**b**) Gravity model residual to the GRACE observation (modeled minus observed gravity)

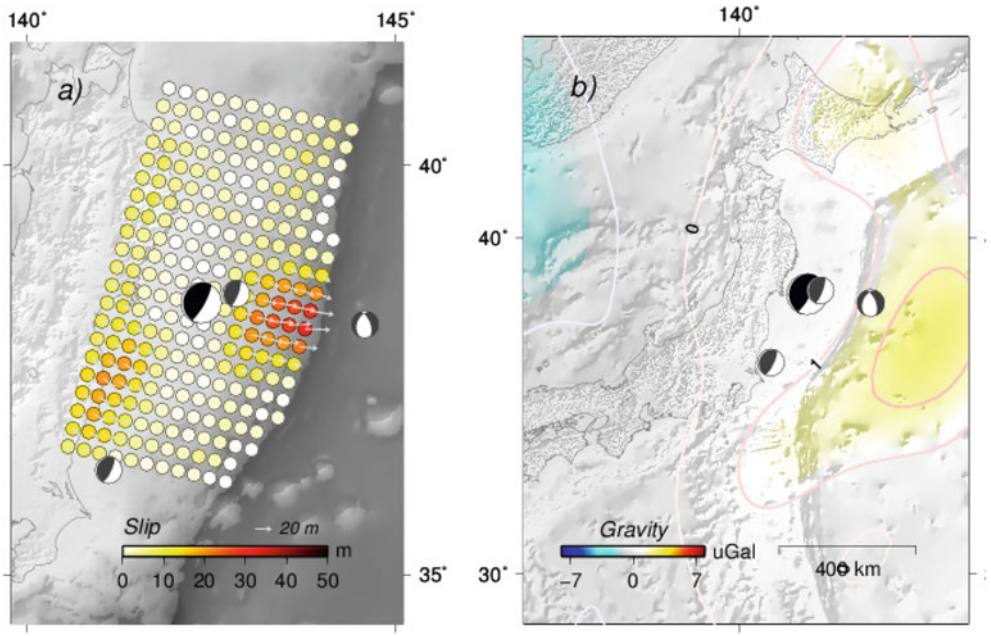

Fig. 4 (**a**) Slip distribution derived from GRACE-only data. *Gray arrows* indicate the slip distribution for each fault slip patch (rake angle). The absolute slip for each patch is given by the colour scheme. (**b**) Gravity model residual to the GRACE observation (modeled minus observed gravity)

derivative of the spatial fault slip distribution, resulting in a smooth slip pattern. In contrast, a GPS and tsunami-based solution needs less regularization because the problem is better conditioned and therefore shows a distinct slip pattern close to the trench, where for a GRACE only solution the slip pattern is more smooth. The amplitude for the model fit of the GRACE-only solution to GRACE measurements is in the area with the largest gravity change $\approx 1.5\,\mu$Gal (see Fig. 4), which is below the estimated $2\,\sigma$ error of $1.52\,\mu$Gal.

Compared with the GPS/tsunami model we see that the GRACE-derived slip distribution is smoother and shows elongated deep slip (most western patches) that is not resolved by the GPS/tsunami data. As the gravity change in strike slip direction (north-south) is much smaller than

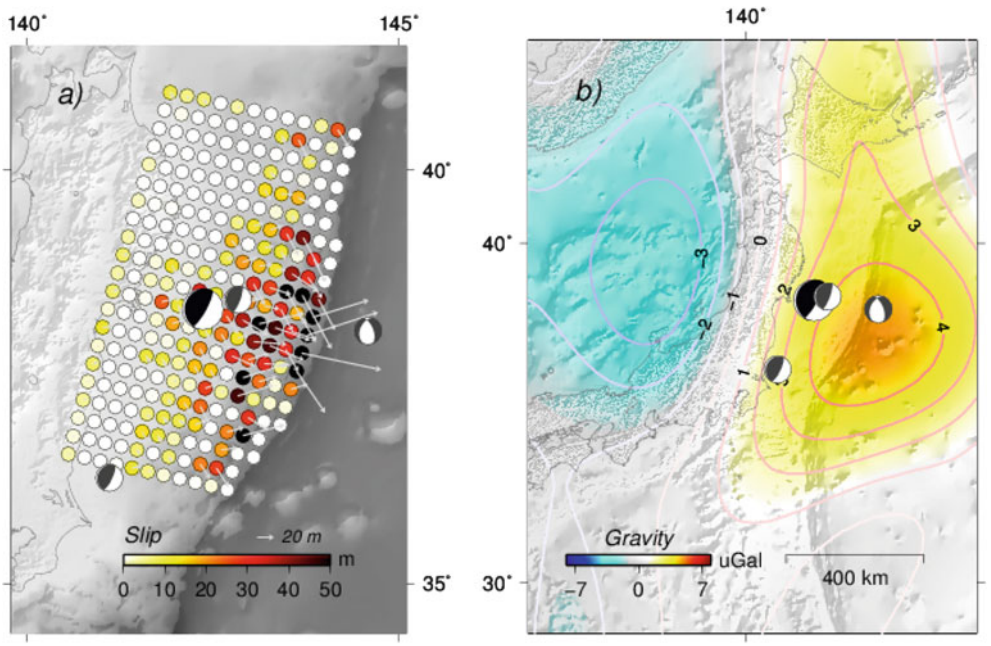

Fig. 5 (**a**) Slip distribution derived from GPS, tsunami and GRACE data. *Gray arrows* indicate the slip distribution (rake angle) for each fault slip patch. The absolute slip for each patch is given by the colour scheme. (**b**) Gravity model residual to the GRACE observation (modeled minus observed gravity)

in dip slip direction (east-west) we expect GRACE to be less sensitive to the strike slip, which possibly explains the elongated profile. Moreover the lack of surface deformation information may affect the spatial constraint of the GRACE only fault slip solution. Finally, we compute a combined model using GPS, tsunami and GRACE measurements. In Fig. 5 the model that incorporates all three measurement techniques and the corresponding gravity fit is shown. The gravity residuals of the combined solution become lower compared with the GPS and tsunami only model but deviations of $\approx$ 4.5 μGal are still present, which are well above the estimated 2 σ error and therefore significant.

Figure 5 shows a heterogeneous slip pattern compared with the purely geometric derived solution which might be attributed to a lower estimated regularization parameter and distortions caused by contrary sensitivities of GRACE (sensitive to deep slip) and tsunami data.

To specify the contribution of postseismic onto the coseismic change we integrated GRACE monthly gravity changes and GPS displacement rates for monthly intervals, after the occurrence of the 2011 Tohoku-Oki earthquake, in a combined GPS/GRACE fault slip model. Figure 6 shows a postseismic change for May 2011, which has been estimated as linear trend using consecutive months. The derived gravity change has similarity with the residual gravity pattern shown in Fig. 3. This suggests that the coseismic gravity misfit of the combined model is due to postseismic signal that is included in the 6 monthly average. The derived gravity change signals (on a monthly basis) are in the same order as the derived two sigma error estimates for gravity (Fig. 1) and therefore omit a clear statement. Looking at Fig. 6 the integrated GPS and GRACE data claim a distinct deep slip pattern as main cause of afterslip. This pattern extends to the south and shows there a higher amount of shallow slip, which might be an explanation for supplementary gravity changes south of the focal region. In the area, where most of the coseismic slip took place, our model claims a low amount of afterslip.

5 Discussion and Conclusion

For the first time GPS, tsunami and gravity data have been combined for a joint inversion of seismic slip. The main contribution of gravity change in a half yearly GRACE average has been identified as coseismic contribution but we conclude that significant gravity differences (modeled minus observed) are present with a negative amplitude of −3 μGal and a positive amplitude of 4.5 μGal. Responsible for this difference might be a short-term postseismic gravity peak around 3 months after earthquake occurrence with a subsequent accumulation of postseismic gravity signal. This has been indicated looking at monthly GRACE solutions and a GPS/GRACE combined fault slip model (May 2011) where a postseismic gravity signal after earthquake occurrence has

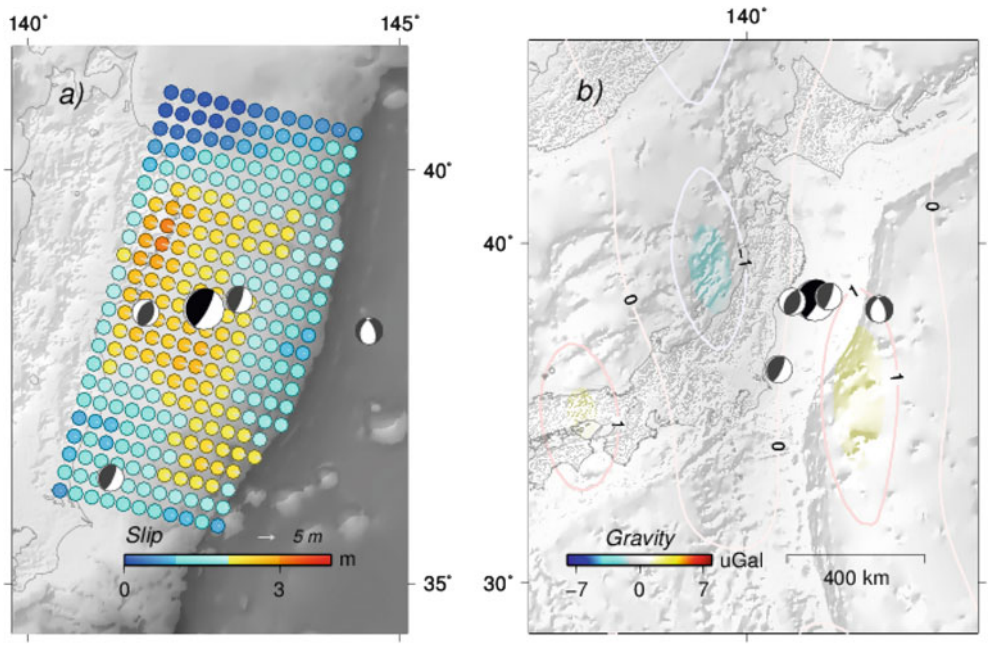

Fig. 6 Postseismic change for May 2011. (**a**) Postseismic slip inversion. (**b**) Postseismic gravity change derived from GRACE monthly solution

been found. However the low signal-to-noise ratio of the GRACE time series (Fig. 1) does not allow a clear description of the postseismic signal.

This circumstance makes it difficult to include GRACE data in the coseismic source model for the 2011 Tohoku-Oki earthquake when a clear separation of coseismic and postseismic changes is not trivial due to the noise level and limited time resolution. Moreover an estimate of the postseismic gravity change should be considered, which together with a combination of postseismic GPS observations may identify the main mechanisms behind the postseismic relaxation.

Taking into account the fast initial velocities, as measured by GPS (Ozawa et al. 2011), and its subsequent decay after only a few months, we expect the effect of afterslip to be dominant in the first months after earthquake occurrence. Based on time series of GRACE gravity changes at the location where the maximum gravity drop (Fig. 1) is found after the Tohoku earthquake, the gravity changes show different stages. This has been previous shown by Ogawa and Heki (2007), who pointed out the reversal of polarity between co- and postseismic gravity change. The higher amplitude of the GRACE observed gravity changes, compared with the forward model, might be explained by substantial afterslip. However one year of postseismic GRACE gravity changes still indicate a net amplitude decrease of gravity at the location of the largest gravity change.

After the 2004 Sumatra-Andaman earthquake viscoelastic mantle relaxation (with a transient creep component) has been put forward as a dominant cause for postseismic gravity changes by a number of authors such as e.g. Han et al. (2008); Panet et al. (2010); Hoechner et al. (2011). Depending on the magnitude of the earthquake, viscoelastic relaxation of coseismically induced stresses is thought to be the main deformation mechanism from years to decades around a ruptured fault as pointed out by Wang et al. (2012b). It has yet to be determined what are the contributions of both (afterslip and mantle relaxation) after the 2011 Tohoku-Oki earthquake using a combined inversion approach.

References

Bettadpur S, and the CSR Level-2 Team (2012) Insights into the Earth System mass variability from CSR-RL05 GRACE gravity fields. Geophysical research abstracts, vol 14. EGU2012-6409, EGU General Assembly

Bouman J, Fuchs M, Broerse T, Vermeersen B, Visser P, Schrama E, Schmidt M (2014) Modelling and observing the Mw 8.8 Chile 2010 and Mw 9.0 Japan 2011 Earthquakes using GOCE. In: Chris R, Pascal W (eds) Earth on the edge: science for a sustainable planet. IAG Symposium 139, ISBN 978-3-642-37221-6. Springer, Berlin

Broerse DBT, Vermeersen LLA, Riva REM, van der Wal W (2011a) Ocean contribution to co-seismic crustal deformation and geoid anomalies: application to the 2004 December 26 Sumatra-Andaman earthquake. Earth Planet Sci Lett 305:341–349. Doi:10.1016/j.epsl.2011.03.011

Broerse DBT, Visser PNAM, Bouman J, Fuchs M, Vermeersen LLA, Schmidt M (2011b) Modelling and observing the 8.8 Chile and 9.0 Japan earthquakes using GOCE. In: Proceedings of the 4th international GOCE user workshop, ESA Publication SP-696

Cambiotti G, Bordoni A, Sabadini R, Colli L (2011) GRACE gravity data help constraining seismic models of the 2004 Sumatran earthquake. J Geophys Res 116:B10403

Fuchs M, Bouman J, Broerse T, Visser P, Vermeersen B (2013) Observing coseismic gravity change from the Japan Tohoku-Oki

2011 earthquake with GOCE gravity gradiometry. J Geophys Res Solid Earth. Doi:10.002/jgrb.50381

Fujie G, Ito A, Kodaira S, Takahashi N, Kaneda Y (2006) Confirming sharp bending of the Pacific plate in the northern Japan trench subduction zone by applying a travel time mapping method. Phys Earth Planet Inter 157:72–85

Fujita M, Ishikawa T, Mochizuki M, Sato M, Toyama S, Katayama M, Kawai K, Matsumoto Y, Yabuki T, Asada A, Colombo O (2006) GPS/Acoustic seafloor geodetic observation: method of data analysis and its application. Earth Planets Space 58:265–275

Han S, Sauber J, Luthcke S, Ji C, Pollitz F (2008) Implications of post-seismic gravity change following the great 2004 Sumatra-Andaman earthquake from the regional harmonic analysis of GRACE inter-satellite tracking data. J Geophys Res 113(B11):B11413

Han SC, Sauber J, Riva R (2011) Contribution of satellite gravimetry to understanding seismic source processes of the 2011 Tohoku-Oki earthquake. Geophy Res Lett 38:L24312. Doi: 10.1029/2011GL049975

Han SC, Sauber J, Riva R, Okal E (2013) Source parameter inversion for recent great earthquakes from decade-long observation of global gravity fields. J Geophys Res. Doi: 10.1002/jgrb.50116

Hoechner A, Sobolev S, Einarsson I, Wang R (2011) Investigation on after- slip and steady state and transient rheology based on postseismic deformation and geoid change caused by the Sumatra 2004 earthquake. Geochem Geophys Geosyst 12:Q07010

Hooper A, Pietrzak J, Simons W, Cui H, Riva R, Naeije M, Terwisscha van Scheltinga A, Schrama E, Stelling G, Socquet A (2012) Importance of horizontal seafloor motion on tsunami height for the Mw=9.0 Tohoku-Oki earthquake. Earth Planet Sci Lett 361:469–479. Doi: 10.1016/j.epsl.2012.11.013

Kido M, Osada Y, Fujimoto H, Hino R, Ito Y (2011) Trench-normal variation in observed seafloor displacements associated with the 2011 Tohoku-Oki earthquake. Geophys Res Lett 38:L24303. Doi:10.1029/2011GL050057

Kodaira S, No T, Nakamura Y, Fujiwara T, Kaiho Y, Miura S, Takahashi N, Kaneda Y, Taira A (2012) Coseismic fault rupture at the trench axis during the 2011 Tohoku-oki earthquake. Nature Geosci 5:646–650. Doi:10.1038/ngeo1547

Lay T, Yamazaki Y, Ammon CJ, Cheung KF, Kanamori H (2011) The 2011 Mw 9.0 off the Pacific coast of Tohoku earthquake: Comparison of deep-water tsunami signals with finite-fault rupture model predictions. Earth Planets Space 63:797–801. Doi:10.5047/eps.2011.05.030

Matsuo K, Heki K (2011) Coseismic gravity changes of the 2011 Tohoku-Oki earthquake from satellite gravimetry. Geophys Res Lett 38:L00G12. Doi:10.1029/2011GL049018, 2011

Nishimura T, Munekane H, Yarai H (2011) The 2011 off the Pacific coast of Tohoku earthquake and its aftershocks observed by GEONET. Earth Planets Space 63:631–636. Doi:10.5047/eps.2011.06.025

Ogawa R, Heki K (2007) Earthquake-induced gravity field changes slowly recover to initial conditions. Geophys Res Lett (GRL) paper. Doi:10.1029/2007GL029340

Okada Y (1992) Surface deformation due to shear and tensile faults in a halfspace. Bull Seismol Soc Am 75:1135–1154

Ozawa S, Nishimura T, Suito H, Kobayashi T, Tobita M, Imakiire T (2011) Coseismic and postseismic slip of the 2011 magnitude-9 Tohoku-Oki earthquake. Nature 475:373–376. Doi:10.1038/nature10227

Ozawa S, Nishimura T, Munekane H, Suito H, Kobayashi T, Tobita M, Imakiire T (2012) Preceding, coseismic, and postseismic slips of the 2011 Tohoku earthquake, Japan. J Geophys Res 117:B07404. Doi:10.1029/2011JB009120

Panet I, Pollitz F, Mikhailov V, Diament M, Banerjee P, Grijalva K (2010) Upper mantle rheology from GRACE and GPS postseismic deformation after the 2004 Sumatra-Andaman earthquake. Geochem Geophys Geosyst 11(6):Q06008

Rodell M, Houser PR, Jambor UEA, Gottschalck J, Mitchell K, Meng CJ, Toll D (2004) The global land data assimilation system. Bull Am Meteorol Soc 85:381–394. Doi: http://dx.doi.org/10.1175/BAMS-85-3-381

Sabadini R, Vermeersen B (2004) Global dynamics of the earth: applications of normal mode relaxation theory to solid-earth geophysics. Kluwer Academic, Dordrecht

Sakumura C, Bettadpur S Bruinsma S (2014) Ensemble prediction and intercomparison analysis of GRACE time-variable gravity field models. Geophys Res Lett. Doi:10.1002/2013GL058632

Sun W, Okubo S (1993) Surface potential and gravity changes due to internal dislocations in a spherical Earth. II. Application to a finite fault. Geophys J Int 132:79–88

Tapley BD, Bettadpur S, Ries JC, Thompson PF, Watkins MM (2004) GRACE Measurements of mass variability in the earth system. Science 305(5683):503–505

Wang L, Shum CK, Simons FJ, Tapley B, Dai C(2012a) Coseismic and postseismic deformation of the 2011 Tohoku-Oki earthquake constrained by GRACE gravimetry. Geophys Res Lett 39:L07301. Doi: 10.1029/2012GL051104

Wang K, Hu Y, He J (2012b) Deformation cycles of subduction earthquakes in a viscoelastic earth. Nature 484:327–332

Local-Scale Precipitable Water Vapor Retrieval from High-Elevation Slant Tropospheric Delays Using a Dense Network of GNSS Receivers

Eugenio Realini, Kazutoshi Sato, Toshitaka Tsuda, Masanori Oigawa, Yuya Iwaki, Yoshinori Shoji, and Hiromu Seko

Abstract

Local-scale monitoring of the temporal and spatial variability of precipitable water vapor (PWV) is crucial to improve the nowcasting and forecasting of localized meteorological hazards. While GPS is now routinely employed to retrieve PWV from estimated tropospheric delays (GPS meteorology), even the densest GPS networks available have a spatial resolution of the order of tens of kilometers, which is too coarse for detecting local fluctuations of water vapor. A densification of existing networks, at least in urban areas, is necessary to provide reliable and continuous water vapor monitoring with sufficiently high horizontal resolution. Densifying existing networks down to few kilometers of inter-station distances, however, introduces at least two issues: first, a horizontal smoothing effect occurs, induced by the significant overlapping of the inverse cones above low elevation angles typically used for GPS observation processing; second, an issue of economic nature might arise if geodetic receivers are used for large-scale densifications (e.g. for early warning systems serving large cities). We tackle the first issue by using only high-elevation slant delays for PWV retrieval, and in particular by exploiting the Japanese Quasi-Zenith Satellite System (QZSS), and the second issue by investigating the use of low-cost single-frequency receivers with local ionosphere delay models. In this work we describe the results obtained in PWV retrieval from high-elevation GPS and QZSS slant delays, estimated using a dense network of receivers installed near Kyoto, Japan.

Keywords

GNSS meteorology • GPS • Low-cost receivers • Meteorological hazard • QZSS • Water vapor

E. Realini (✉)
Research Institute for Sustainable Humanosphere (RISH), Kyoto University, Uji, Kyoto, Japan
Present Address:
Geomatics Research & Development (GReD) srl, Lomazzo, Como, Italy
e-mail: eugenio.realini@g-red.eu

K. Sato
RISH, Kyoto University, Uji, Kyoto, Japan
Present Address:
Satellite Navigation Office, Satellite Applications Mission Directorate I, Japan Aerospace Exploration Agency (JAXA), Tokyo, Japan
e-mail: satoh.kazutoshi@jaxa.jp

T. Tsuda • M. Oigawa • Y. Iwaki
RISH, Kyoto University, Uji, Kyoto, Japan
e-mail: tsuda@rish.kyoto-u.ac.jp; masanori_ohigawa@rish.kyoto-u.ac.jp; yuya_iwaki@rish.kyoto-u.ac.jp

Y. Shoji • H. Seko
Meteorological Research Institute (MRI), Japan Meteorological Agency (JMA), Tokyo, Japan
e-mail: yshoji@mri-jma.go.jp; hseko@mri-jma.go.jp

© Springer International Publishing Switzerland 2015

C. Rizos, P. Willis (eds.), *IAG 150 Years*, International Association of Geodesy Symposia 143,
DOI 10.1007/1345_2015_167

1 Introduction

Monitoring the temporal and spatial variability of precipitable water vapor (PWV) at a local scale is crucial to improve the nowcasting and forecasting of localized sudden storms and heavy rain, that can have spatial scales down to few kilometers. Local fluctuations of PWV, in fact, may be associated with increases of water vapor in the lower troposphere, which cause deep convection that may result in heavy rainfall (Shoji 2013). Water vapor plays an important role in the generation of intense moist convection because it releases significant quantities of latent heat by condensation. Before the initiation of convection, convergence of water vapor near the ground surface occurs. Seko et al. (2004) reported that the local-scale amount of water vapor at a height of 1 km increased about 20 min before the formation of rain drops because of the ground surface convergence process. This local-scale signal can be a precursor of rainfall, thus it is deemed important to detect it by high-resolution PWV measurements.

Global Navigation Satellite Systems (GNSS) provide a PWV monitoring method that is continuous in time with high observation rates (contrary to radiosondes), and not adversely affected by meteorological conditions, nor requiring calibration (contrary to microwave radiometers). However, even the densest regional GNSS networks available, such as GEONET in Japan, have inter-station distances of the order of tens of kilometers, which is not sufficient for the accurate detection of local fluctuations of water vapor. A densification of existing networks, at least in urban areas, is necessary for providing reliable and continuous water vapor monitoring with sufficiently high horizontal resolution.

PWV is typically retrieved from zenith tropospheric delays that are estimated from several slant delays above low elevation angles. When using a receiver network with inter-station distances of few kilometers, however, this causes a significant horizontal smoothing effect in the retrieved water vapor field. We thus proposed the use of high-elevation slant delays in order to retrieve high-resolution PWV maps from dense networks without losing information about local-scale fluctuations (Sato et al. 2013). Using only GPS would not always provide at least one satellite at a sufficiently high elevation, therefore we investigate the use of QZSS. This system, once completed, will in fact provide at least one satellite continuously close to the zenith over Japan, providing a means to monitor high-resolution PWV using its high-elevation slant delays.

Heavy rain early warning systems based on GNSS monitoring networks would be particularly useful if installed in densely populated places; however, several urban areas cover hundreds of square kilometers, and the densification of currently existing networks over such extended areas by using dual-frequency receivers would be impractical in terms of cost. Therefore we are carrying out experiments using low-cost single-frequency receivers, and evaluating their performance for water vapor monitoring. When dealing with single-frequency observations one has to take into account the ionospheric delay, which has to be effectively modeled and removed. To this purpose, we have tested two models: the High-Resolution Ionospheric Model (HiRIM—Rocken et al. 2000), as implemented in the GNSS processing software RTNet,[1] and the Satellite-specific Epoch-differenced Ionospheric Delay (SEID) model, developed at the German Research Centre for Geosciences (GFZ) (Deng et al. 2009, 2011), comparing their performance.

The paper is organized as follows: Sect. 2 briefly describes the dense GNSS network used in this work, the PWV retrieval procedure and its validation; Sect. 3 illustrates the estimation of the spatial distribution of PWV over the network and discusses how it is affected by using high-elevation slant delays; Sect. 4 is about the comparison between the RTNet and SEID local ionospheric delay models and it includes results of PWV retrieval from single-frequency observations from both geodetic and low-cost instruments.

2 PWV Retrieval from Uji Dense GNSS Network

We have installed a total of 17 dual-frequency GNSS stations with a horizontal spacing of 1–2 km near the Uji campus of Kyoto University, Japan (Fig. 1). The stations can receive both GPS and QZSS signals. The stations are distributed over an area of about 10×6 km^2. Meteorological stations are installed close to 10 GNSS stations for monitoring pressure and temperature, which are needed for accurate PWV estimation. Meteorological observations are spatially interpolated by inverse distance weighting on the location of the remaining 7 GNSS stations, by taking into account their different heights. The results discussed in this article were obtained by post-processing dual-frequency code and phase measurements (using the iono-free observable) with RTNet software by Kalman-filtered precise point positioning (PPP), with float phase ambiguities. Each station was processed independently. Antenna coordinates were estimated, together with the receiver clock error and the ZTD. Processing settings include an observation rate of 30 s, final orbits and 30-s satellite clocks provided by IGS, and an elevation cutoff of 10°. The dry part of the Saastamoinen model (Saastamoinen 1973) is used for computing the a priori ZTD; the dry and wet formulations of the Global Mapping Function (GMF) (Böhm et al. 2006) are used respectively

[1] http://www.gps-solutions.com/.

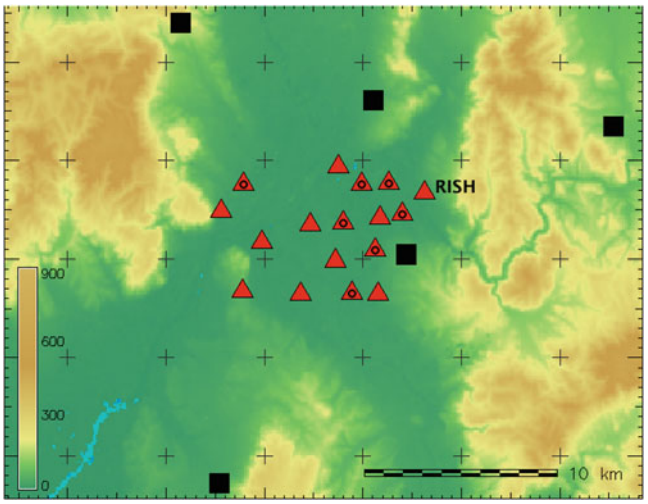

Fig. 1 The dense GNSS network installed near Uji (Kyoto, Japan); *triangles* indicate Uji network GNSS stations; triangles containing a *circle* indicate Uji network GNSS stations without a co-located meteorological station; *squares* indicate the closest GEONET stations; the grid nodes (*crosses*) have a spacing of 5 km; the relief map was computed using Shuttle Radar Topography Mission (SRTM3) altimetry data (the height is orthometric and expressed in meters)

for the a priori and the estimated ZTDs. The estimated ZTD is then reduced to its wet part (i.e. the zenith wet delay, ZWD) by removing the dry component (i.e. the zenith hydrostatic delay, ZHD), which is estimated by means of the Saastamoinen model, applied using the ground pressure observed by the meteorological stations within the network. The ZWD is then converted to PWV using the conversion coefficient proposed by Askne and Nordius (1987). The weighted mean temperature of the atmosphere, needed for calculating the conversion coefficient, is estimated from the observed ground temperature using the equations derived by Shoji (2010), obtained from radiosonde measurements over Japan.

The PWV retrieved from the dense network has been validated in two intensive observation campaigns, during July-August 2011 and 2012, with respect to radiosondes (Vaisala RS92, 31 launches in total) and a microwave radiometer (Radiometrics MP-3000A, about 20000 epochs in total). The comparison was carried out using GPS observations of the RISH station (see Fig. 1), which was co-located with the radiosondes launch site and the microwave radiometer. The results of the first campaign are detailed in Sato et al. (2013), and they were confirmed in the second campaign: both the GPS-radiosondes and GPS-radiometer comparisons yielded a difference of about 2 mm RMSE. The difference with respect to both instruments was reduced to about 1 mm when specific GPS slant delays were used, close to the radiosondes/radiometer measuring directions.

3 PWV Spatial Distribution Results Using High-Elevation Slant Delays

The spatial distribution of PWV detected by the Uji network is estimated by stochastic prediction using kriging (Matheron 1963). We apply kriging on the PWV residuals, i.e. the residuals obtained after removing a time-dependent component (epoch-wise mean among all stations) and a station-dependent component (station-wise mean over all epochs). The station-dependent component contains any height-dependent component as well as possible station-specific errors. After applying the kriging, the time-dependent component and the station-dependent component are added back in order to retrieve an absolute PWV value for the predicted field. It should be noted that adding back the time-dependent component is straightforward, since it is common among all the stations, while adding back the station-dependent component is more delicate, because it varies over the prediction area; in our tests it was deemed sufficient to approximate it with a bilinear surface, but more complex approaches might be considered (e.g. interpolating by inverse distance weighting). The stochastic prediction by kriging can be applied only when PWV residuals exhibit spatial dependency (i.e. if the spatial variogram is not flat). This is true only when there are significant PWV fluctuations over the dense network, i.e. with magnitude larger than the observation error; otherwise, the residuals are disregarded and the PWV field is produced simply by adding back the time and station-dependent terms. When using high-elevation slant delays, these are selected by an elevation angle threshold (for GPS) or by selecting a specific satellite (for QZSS); the slant delays are then mapped to the zenith direction by the same mapping function used for the processing (i.e. the GMF), averaged if multiple slants are used, and converted to PWV. It is worth pointing out that this high elevation angle threshold is only applied to select slant delays for PWV retrieval; the observation processing always uses a 10° elevation cutoff.

Figure 2 shows examples of the predicted PWV field (left) and its prediction error standard deviation (right) on 2012/07/08 at 18:00:00 (GPS time), obtained by using GPS slant delays higher than 10° (top), higher than 60° (middle), and using only QZSS slant delays (bottom). At this epoch, the QZSS satellite had an elevation angle of 77.2°. The detected PWV field is smoother when using large inverse cones (i.e. using slant delays above 10°), as expected because of the significant overlapping of the observation cones, while it shows stronger fluctuations in the other two cases. When using only QZSS slant delays the retrieved PWV field appears more detailed and with higher spatial variability. The prediction error standard deviation increases as the retrieved

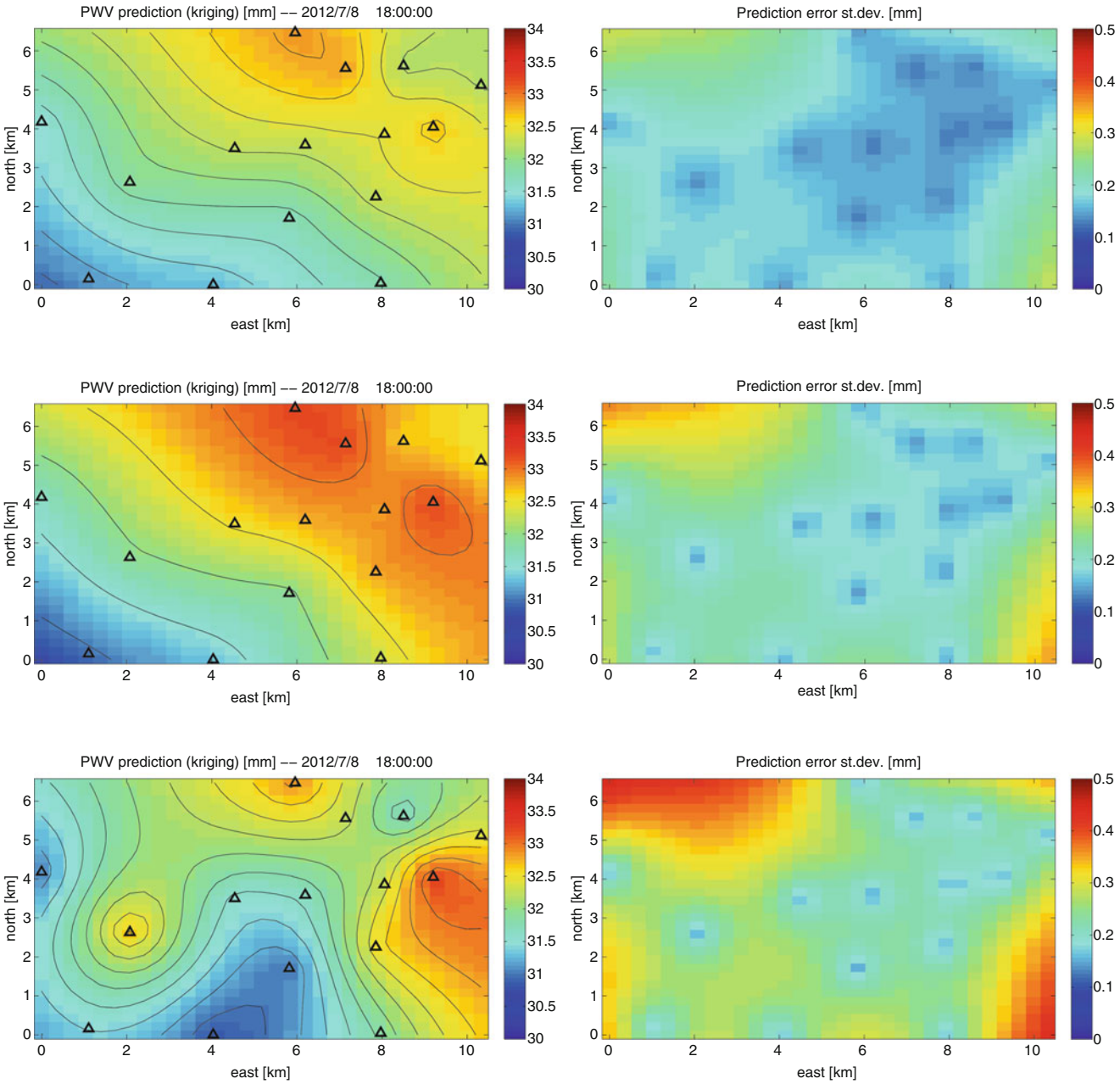

Fig. 2 Kriged PWV map (*left*) and prediction error standard deviation (*right*) by using GPS slant delays higher than 10° (*top*), GPS slant delays higher than 60° (*middle*) and only QZSS slant delays (*bottom*; elevation= 77.2°), on 2012/07/08 at 18:00:00 GPS time

PWV field gets less smooth; this is also expected, because higher variability in the estimated PWV for stations with the same horizontal geometry yields higher values for the variogram; we use the same model for approximating the empirical variogram (i.e. a linear function), therefore the prediction error increases; this might be improved by using a more complex function for approximating the variogram. In general, the smoother the field, the easier it is to perform the prediction. Nevertheless, even in the QZSS-only case the standard deviation stays below 0.2–0.3 mm within the network, which is acceptable since the PWV fluctuations detected over the area of interest are in the range of 2–3 mm. Further tests were carried out to verify that the detected PWV fluctuations were not due to ground temperature fluctuations. The stochastic prediction procedure was thus applied to the estimated ZWD values, which do not depend on ground temperature: the resulting spatial distributions of the ZWD field confirmed the results represented in Fig. 2.

4 Testing Low-Cost Single-Frequency Receivers and Local Ionospheric Delay Models for PWV Retrieval

Single-frequency observations need to be corrected for the ionospheric delay, which has to be effectively modeled and removed. We have tested the HiRIM model, as implemented in RTNet, Rocken et al. (2000) and the SEID model (Deng et al. 2009, 2011). Both models use a thin shell model for the ionosphere and generate satellite-specific ionosphere corrections, by employing dual-frequency receivers surrounding the single-frequency ones. The satellite-specific ionospheric correction is retrieved for each dual-frequency receiver, fitted by first- or second-order polynomial and evaluated at the ionospheric piercing points defined by the location of the single-frequency receivers. The main difference between the two models lies in the fact that the RTNet implementation of the HiRIM model estimates the ionospheric delay model parameters by Kalman filtering, based on a network solution,[2] while the SEID model fits the epoch-differenced ionospheric delays obtained by means of the geometry-free observable L4 (i.e. the difference between the two phase observations L1 and L2) at each epoch. The HiRIM approach employs double-differences in order to be able to resolve integer phase ambiguities for the ionospheric model estimation, thus removing correlations between ambiguity parameters and the estimated ionosphere (Rocken et al. 2000); on the other hand, the SEID model removes the ambiguity parameters by epoch-differencing, deeming the time variation of the ionospheric delay sufficient for ZTD estimation (Deng et al. 2009). It has to be noted that the SEID model reconstructs L2 observations from the L1 observations of the single-frequency receivers, by cumulating in time the interpolated epoch-differenced L4; thus the integer nature of the reconstructed ambiguities is lost, forcing the ZTD estimation process to use float ambiguities. This is not a problem in our case, since we are using Kalman-filtered PPP with float phase ambiguities for PWV retrieval (see Sect. 2).

The performance of the HiRIM and SEID models with the Uji network was evaluated by comparing the PWV retrieved by single-frequency observations (and a local ionospheric delay model) with respect to the reference PWV retrieved from dual-frequency observations. Both geodetic and low-cost instruments were used as the target single-frequency receivers. While we used the HiRIM implementation already available in RTNet, the code to apply the SEID model was developed by us in MATLAB, using existing open source software such as goGPS[3] (Realini and Reguzzoni 2013) and GpsTools[4] for implementing basic functions (e.g. RINEX file reading and writing, observation discontinuities fixing, etc.). The tests carried out to evaluate the accuracy degradation caused by the usage of low-cost hardware instead of geodetic-level hardware and by the error introduced by the two local ionospheric delay models are detailed in the next two sub-sections.

Table 1 Statistics on the difference between the iono-free PWV solution (JAVAD receiver) and the single-frequency PWV solutions with the three receivers; all values in mm

	JAVAD	FURUNO	u-blox
Mean	1.0	1.1	0.8
St. dev.	2.2	2.3	3.1
RMSE	2.5	2.6	3.3

4.1 Impact of Low-Cost Hardware on PWV Retrieval

The accuracy degradation due to the use of low-cost receivers and antennas instead of geodetic ones was evaluated by comparing the PWV retrieved by L1 observations and a local ionospheric delay model (here only HiRIM was used). The L1 observations were logged by three receivers: a geodetic-grade dual-frequency JAVAD receiver, a survey-grade single-frequency FURUNO receiver and a low-cost single-frequency u-blox receiver. Their respective antennas were located less than 3 m from each other. The ionospheric model was generated by using the eight closest GEONET stations, located less than 10 km from the test location; the same model was applied to all three receivers. Table 1 shows the RMS error (RMSE) between the PWV obtained by iono-free processing of dual-frequency observations by the JAVAD receiver and the PWV obtained from single-frequency observations by the three receivers, with the ionospheric model, over a timespan of about 22 h (2686 epochs at 30-s rate) on 11–12 July 2012.

The accuracy degradation, in terms of RMSE, was 0.1 mm when using FURUNO hardware and 0.8 mm when using u-blox hardware. The degradation associated to u-blox hardware might be attributed mostly to the use of a low-cost patch antenna rather than the use of the low-cost receiver itself (Takasu and Yasuda 2008). Low-cost antennas are in fact more sensitive to multipath compared to geodetic ones, and their calibration parameters are generally not available. It is also worth pointing out that the 2.5 mm of RMSE between

[2] While the original HiRIM model converted double-differenced delays to zero-differenced delays, currently RTNet estimates the ionospheric delays at the zero-difference level.

[3] http://www.gogps-project.org/.

[4] http://gpspp.sakura.ne.jp/gpstools/gt_release.htm.

Table 2 Statistics on the difference between the iono-free PWV solution and the single-frequency PWV solutions with the two ionospheric models; all values in mm

	HiRIM (as in RTNet)	SEID (custom implementation)
Mean	−2.8	−0.1
St. dev.	3.4	1.6
RMSE	4.4	1.6

the iono-free solution and the L1 solution using the same JAVAD receiver are to be attributed to the error introduced by the HiRIM model. This large error was the original motivation that led us to investigate alternative approaches to local ionospheric delay modeling, which resulted in the comparison between HiRIM and SEID described in the next sub-section.

4.2 Impact of Local Ionospheric Delay Models on PWV Retrieval (Preliminary Results)

The comparison between the HiRIM and SEID models was carried out by processing about 5 days of 30-s observations (13,967 epochs) from one of the stations in the dense network, on 6–10 July 2012. Both models were generated by using the 4 closest GEONET stations, and a first-order polynomial to fit the corrections. The RMSE introduced by the two local ionospheric delay models is 4.4 mm for the HiRIM model (as implemented in RTNet), and 1.6 mm for the SEID model (see Table 2).

5 Conclusions

Local-scale PWV fluctuations were detected by a dense network of GNSS receivers, and the feasibility of using only high-elevation slant delays for PWV retrieval was tested. Using high-elevation QZSS slant delays resulted in spatial distributions with higher variability compared to using GPS slant delays higher than 60°, while standard PWV retrieval from GPS slant delays higher than 10° confirmed the expected horizontal smoothing effect. Tests involving low-cost single-frequency receivers and local ionospheric delay models were carried out; preliminary results are promising, suggesting that existing networks of geodetic receivers could be densified by lower cost single-frequency instruments for PWV retrieval. Preliminary results of the comparison between the HiRIM model (RTNet implementation) and SEID model (custom implementation) show better performance of the latter; further comparison tests are needed to confirm the results.

References

Askne J, Nordius H (1987) Estimation of tropospheric delay for microwaves from surface weather data. Radio Sci 22(3):379–386

Böhm J, Niell A, Tregoning P, Schuh H (2006) Global mapping function (GMF): a new empirical mapping function based on numerical weather model data. Geophys Res Lett 33(7):L07,304

Deng Z, Bender M, Dick G, Ge M, Wickert J, Ramatschi M, Zou X (2009) Retrieving tropospheric delays from GPS networks densified with single frequency receivers. Geophys Res Lett 36(19):L19802

Deng Z, Bender M, Zus F, Ge M, Dick G, Ramatschi M, Wickert J, Löhnert U, Schön S (2011) Validation of tropospheric slant path delays derived from single and dual frequency GPS receivers. Radio Sci 46(6):RS6007

Matheron G (1963) Principles of geostatistics. Econ Geol 58(8):1246–1266

Realini E, Reguzzoni M (2013) goGPS: open source software for enhancing the accuracy of low-cost receivers by single-frequency relative kinematic positioning. Meas Sci Technol 24(11):115,010

Rocken C, Johnson JM, Braun JJ, Kawawa H, Hatanaka Y, Imakiire T (2000) Improving GPS surveying with modeled ionospheric corrections. Geophys Res Lett 27(23):3821–3824

Saastamoinen J (1973) Contributions to the theory of atmospheric refraction. Bull Géod (1946–1975) 107(1):13–34

Sato K, Realini E, Tsuda T, Oigawa M, Iwaki Y, Shoji Y, Seko H (2013) A high-resolution, precipitable water vapor monitoring system using a dense network of GNSS receivers. J Disaster Res 8(1):37–47

Seko H, Nakamura H, Shoji Y, Iwabuchi T (2004) The meso-γ scale water vapor distribution associated with a thunderstorm calculated from a dense network of GPS receivers. J Meteorol Soc Jpn 82(1B):569–586

Shoji Y (2010) Accurate estimation of precipitable water vapor using ground-based GPS observation network and its data assimilation into a mesoscale numerical weather prediction model. Ph.D. thesis, Kyoto University

Shoji Y (2013) Retrieval of water vapor inhomogeneity using the japanese nationwide GPS array and its potential for prediction of convective precipitation. J Meteorol Soc Jpn 91(1):43–62

Takasu T, Yasuda A (2008) Evaluation of RTK-GPS performance with low-cost single-frequency GPS receivers. In: Proceedings of international symposium on GPS/GNSS, pp 852–861

Observing and Modelling the High Water Level from Satellite Radar Altimetry During Tropical Cyclones

Xiaoli Deng, Zahra Gharineiat, Ole B. Andersen, and Mark G. Stewart

Abstract

This paper investigates the capability of observing tropical cyclones using satellite radar altimetry. Two representative cyclones Yasi (February 2011) and Larry (March 2006) in the northeast Australian coastal area are selected based also on available tide gauge sea level measurements. It is shown that altimetry data can capture high water levels induced by Larry and Yasi through a careful re-processing and re-editing of the data. About 18 years of data from multi-satellite altimetry missions including TOPEX/Poseidon, Jason-1 and Jason-2, and seven tide gauges around the northern Australian coast are integrated using a multivariate regression approach. The results reveal that the multi-regression model can, in general, explain >60 % of sea level variances in the study area. The model is then validated using independent data from tide gauge in Townsville. The comparison results indicate that the high sea levels predicted by the model taken into account of both altimetry and tide-gauge data agree well with those observed at Townsville during cyclone Larry.

Keywords

Coastal sea level • Multivariate regression • Satellite radar altimetry • Tropical cyclone

1 Introduction

Much of the northern Australian coastline being close to the equator is a region where tropical cyclones tend to form, thus being more frequently affected by these cyclones. Every November to April, northern Australia endures its annual cyclone season. It is normally attributed to air pressure changes and local wind stress on the water near the coast and often associated with extreme water level events. In addition, rising sea levels in the region has been found to be up to 2.5 times of the globally averaged sea-level rise (Church et al. 2009; Deng et al. 2011). Therefore, information about extreme sea levels associated with severe tropical cyclones due to rising sea levels is sought after by coastal management and planning agencies now and into the future.

Exceptionally high sea levels have claimed many victims throughout the history of northern Australia (Power and Pearce 2006). For examples, on 20 March 2006, severe tropical cyclone Larry made landfall south of Innisfail in north Queensland, while severe tropical cyclone Yasi in early February 2011 was the most intense cyclone to hit this region since 1918. Both cyclones incurred enormous economic, social and ecological damage to the region.

With regards to measuring sea levels, tide gauge and satellite radar altimetry have vastly different spatial and temporal samplings. Tide gauges have been fundamentally and traditionally measuring in situ relative sea level accurately at selected coastal locations. Radar altimeters on board satellites measure geocentric sea level from a distance of ~1,000 km above the ocean surface, as well as wind speed and wave height over a 2–5 km radius (Fu and Haines 2013).

X. Deng (✉) • Z. Gharineiat • M.G. Stewart
School of Engineering, The University of Newcastle, University Drive, Callaghan NSW 2308, Australia
e-mail: Xiaoli.Deng@newcastle.edu.au

O.B. Andersen
DTU Space, Technical University of Denmark, Elektrovej, Lyngby, Denmark

© Springer International Publishing Switzerland 2015

C. Rizos, P. Willis (eds.), *IAG 150 Years*, International Association of Geodesy Symposia 143,
DOI 10.1007/1345_2015_108

The altimetry 6-km sampling sea-level measurements are confined along the specific repeat ground tracks of a particular satellite altimeter satellite because of its repeat patterns. However, satellite altimetry can still provide important sea level measurements along several ground tracks during a cyclone period, which can be used for monitoring of extreme events (Deng et al. 2011; Scharroo et al. 2005; Lillibridge et al. 2013; Han et al. 2012). This is because the cyclone usually takes several days of propagation over oceans before it hits the land (Power and Pearce 2006).

The data observed by altimetry and tide gauges can be integrated to take advantage of the high temporal sampling of the tide gauges and the high spatial sampling of the satellite (e.g., Høyer and Andersen 2003; Cheng et al. 2012). In this paper by combining the data through a multivariate regression method (Emery and Thomson 2001), we investigate and intend to show the detection of storm induced high water signals in the northern Australia coastal region prone to tropical cyclones. The paper also illustrates that satellite altimeter can capture high water level variations associated with cyclones even hours to days in advance of their landfall. We also show that including the altimeter observation in a multi-regression model of the region leads to significantly improved sea level forecasting at the tide gauge in Townville (146.8°E, 19.3°S).

2 Data and Area of Study

The data used are sea level measurements (1992–2010) from both satellite altimetry and tide gauges in the northern Australian coastal area (latitudes 24°S–2°S and longitudes 108°E–162°E). The sea surface heights (SSHs) from multi-satellite altimeter missions TOPEX/Poseidon, Jason-1 and Jason-2 (http://www.aviso.oceanobs.com/en/missions.html) are obtained from the Radar Altimeter Database System (RADS), which are available from the web site: http://rads.tudelft.nl/rads/rads.shtml. Instead of grid data with low resolution, the along-track SSHs with sample spacing ~6 km (1-hz data) are used in this paper to ensure the short-lifetime high frequency sea levels can be measured.

The standard geophysical and environmental corrections from RADS are applied to altimeter data, which include the modelled dry and wet tropospheric corrections derived from the European Centre for Medium-Range Weather Forecasts (ECMWF, http://www.ecmwf.int/), ionospheric range delay, geocentric ocean tide model, solid Earth and pole tide models, and sea state bias correction. The dynamic atmospheric correction (DAC, Pascual et al. 2008) and inverse barometric correction are not applied to altimeter or tide-gauge data, because the tide-gauge data are not corrected for these effects. This enables the high frequency sea level signal

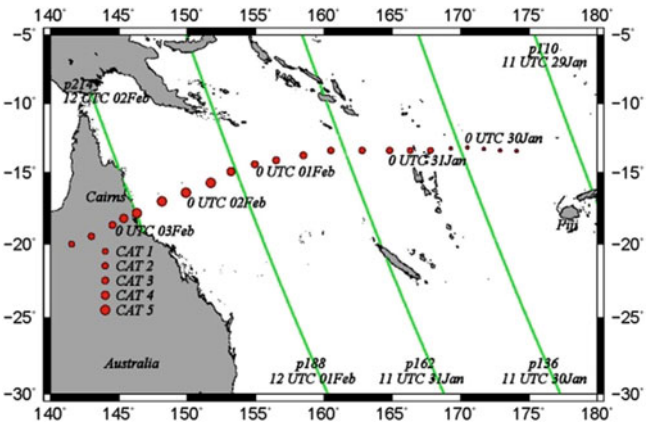

Fig. 1 Distribution of selected altimeter Jason-1 ground tracks (in *green*) passed the oceanic regions offshore of northeast Queensland, Australia, during the period of Yasi from 29 January to 2 February 2011 (corresponding to cycles 334 and 335). The westward tracks and intensity information about cyclone Yasi are shown in *red dots*

relation to extreme sea levels to be maintained. A mean sea surface DTU10 model (Cheng and Andersen 2010) has been removed from altimetry SSHs to retrieve along-track sea level anomalies (SLAs).

As is true in any extreme storm, while large waves and currents were expected, altimeter data from standard data products (e.g., RADS) are found to be flagged out and unavailable during cyclones. However, Fig. 1 shows available trackers from altimeter Jason-1 across the region during cyclone Yasi period between 29 January and 2 February 2011 (corresponding to cycles 334 and 335). As can be seen, there are a number of small islands in the area, where altimeter data can be contaminated by the land (Deng and Featherstone 2006). In addition, waveforms were affected by heavy rains accompanying cyclone Yasi, resulting in erroneous sea level measurements. Thus, instead of directly using standard altimeter sea level data, Ku-band raw waveform measurements from Jason-1 are used. The waveforms are retracked to retrieve sea level measurements. The retracked SLAs are then computed and analysed.

The hourly tide-gauge sea level records are obtained from the Australian National Tidal Centre (http://www.bom.gov.au/oceanography/) and the University of Hawaii Sea Level Centre (http://uhslc.soest.hawaii.edu/home) at eight stations (Fig. 5). Tide-gauge data are resampled to generate the time series that are compatible to altimeter along-track data. At each tide station, the mean sea level is estimated and removed; and the local ocean-tide correction estimated using the response method (details in next paragraph) is applied. The tide-gauge data are then resampled by averaging tide-gauge data within 3 h around the time of altimeter along-track measurements.

A number of global tidal models developed from and for satellite altimetry have been analysed in the study area. The

results show that applying these global models cannot fully remove tides due to complicated tidal dynamics in the region, as evidenced by considerable residual ocean-tide signals in the sea-level measurements (Idris et al. 2014). Therefore, tides are removed in this study based on the response method (Munk and Cartwright 1996) that models the tide correction pointwisely. The response method has been found to achieve precise estimates of major tidal constituents in the diurnal and semi-diurnal bands, as well as the largest shallow water constituent, M_4, after some modifications by Andersen (1999). As such, the tidal correction pointwisely modelled based on the response method is applied to both altimetric and tide-gauge sea level measurements, which provides the compatible data sets for this study.

3 Capturing Cyclone-Induced High Water from Satellite Altimetry

3.1 Tropical Cyclone Larry

Severe Tropical Cyclone Larry made landfall at the tropical north Queensland coast near Innisfail (146.0°E, 17.5°S) on Monday 20 March 2006. Top panel in Fig. 2 shows the track of Larry during 15–18 March 2006, as well as an overlaid altimetry pass 149 from Jason-1 cycle 154 on March 18 2006, while bottom panel shows altimeter SLAs and their means and standard deviations along Jason-1 pass 149.

The tropical cyclone low developed over the eastern Coral Sea and reached cyclone intensity during the early hours of 18 March and continued on a general westerly course towards the Queensland coast. Larry rapidly strengthened in the following 48 h reaching intensity of Australian cyclone category 3 at 12:00 UTC 18 March and brought to the region destructive winds (224–280 km/h) at 12:00 UTC 19 March as it marched gradually westwards towards the coast as also illustrated in Fig. 2. Most observed altimeter along-track SLAs are higher than 2 times the standard deviations when satellite crossed the cyclone near longitude 158°E on 18 March (Fig. 2 bottom panel), indicating that Jason-1 altimeter successfully captured high water levels induced by Larry.

3.2 Tropical Cyclone Yasi

Severe Tropical Cyclone Yasi in early February 2011 was one of the most powerful cyclones to hit Queensland, Australia, since records commenced. Yasi began developing as a tropical low northwest of Fiji on 29 January and quickly intensified to a cyclone category. It maintained its west-southwest movement, and rapidly intensified to a category 3 by 4 pm on 31 January. Yasi further intensified in next 3 days and took a more west-southwestward movement and began to accelerate towards the tropical Queensland coast. It reached category 5 with wind speeds >280 km/h when making landfall on the north Queensland coast near Mission Beach early on 3 February (Fig. 1).

In this study, wind speed, wave height, and SLAs are retrieved from a waveform retracking procedure using both fitting and threshold algorithms (c.f. Deng and Featherstone 2006) and analysed along altimeter ground passes in Fig. 1. An example of the profiles of altimeter-derived wave height, wind speed and sea level along tracks passing through Yasi, as well as the captured infrared image (http:/www.bom.gov.au), are show in Fig. 3.

It is found that the intensification of wave height and wind speed increases with the growth of the wind driven cyclone approaching the north Queensland coast (not shown). Both wave heights and wind speeds reach the maximum at a point where each altimeter track is at its closest distance to the centre or eye of the cyclone. They change symmetrically with respect to the eye (Fig. 3a). The peak values of wave height (∼14 m) and wind speed (∼29 m/s) are observed along altimeter Jason-1 pass p188 around 11:50 UTC on 1 February, when Yasi increases its intensity to cyclone category 5. Here we note that there is a difference between the altimeter-observed and categorized cyclone wind speeds. This is because altimeter measures the wind at 10 m above the mean sea surface within the satellite footprint, which differs from those measured by other means (Zieger et al. 2009; Griffin and Middleton 1991).

The sea level measured by Jason-1 altimeter (Fig. 3b) is noisy compared to wave heights and wind speeds (Fig. 3a). However, it still can be seen that the storm induced SLAs change with respect to the cyclone eye with the maximum of ∼80 cm. The similar feature of noisy SLAs was also observed by Scharroo et al. (2005) during Hurricane Katina in August 2005. As such, the results suggest that retrieved wave heights and wind speed are more important measurements than storm induced SLAs. This may also indicates that the waveform retracking strategy used does not suit the waveforms that are distorted by heavy rains associated with the storm, thus producing erroneous sea level measurements. This presents a challenge of how to infer accurate altimeter sea level measurements during severe cyclones, for which further investigation is continuing.

4 Modelling Sea Levels from Satellite Altimetry and Tide Gauges for Cyclone Warning

The data from multi-satellite altimetry missions and tide gauges are integrated into a consistent map of coastal sea

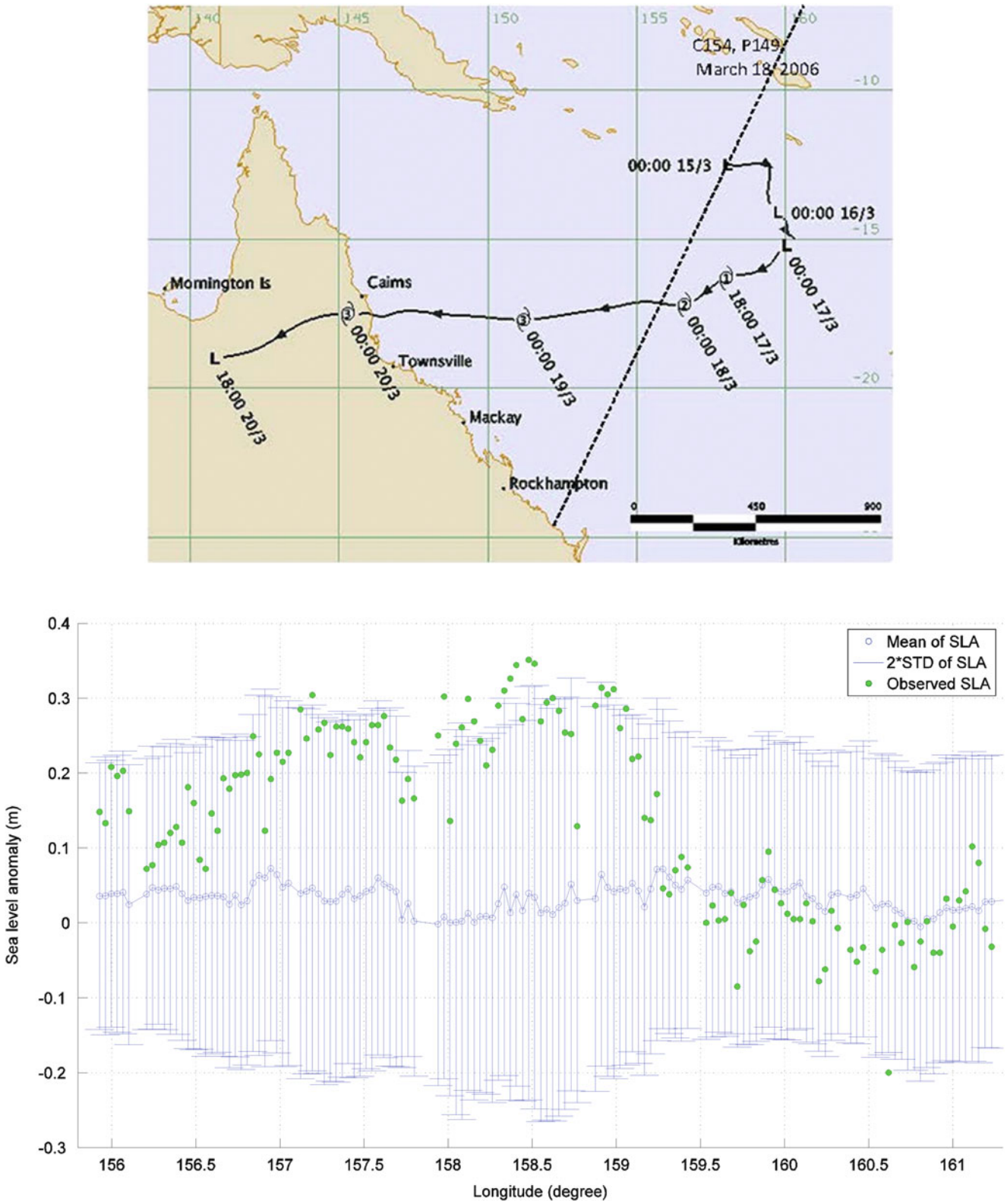

Fig. 2 Tropical cyclone Larry hitting the Queensland coast in March 2006. *Top panel* shows the path, category of Larry and the dates of the cyclone, as well as altimeter Jason-1 pass 149 (*dash line*) from cycle 154 on 18 March 2006. *Bottom panel* presents the altimeter along-track mean sea level anomalies (SLAs) around zero (*blue circles*), their 2 times of standard deviations (*blue bars*), and observed SLAs when the cyclone Larry started on 18 March 2006, showing that observed along-track SLAs (*green circles*) are near or more than 2 times of standard deviations between longitudes 156°E–159°E

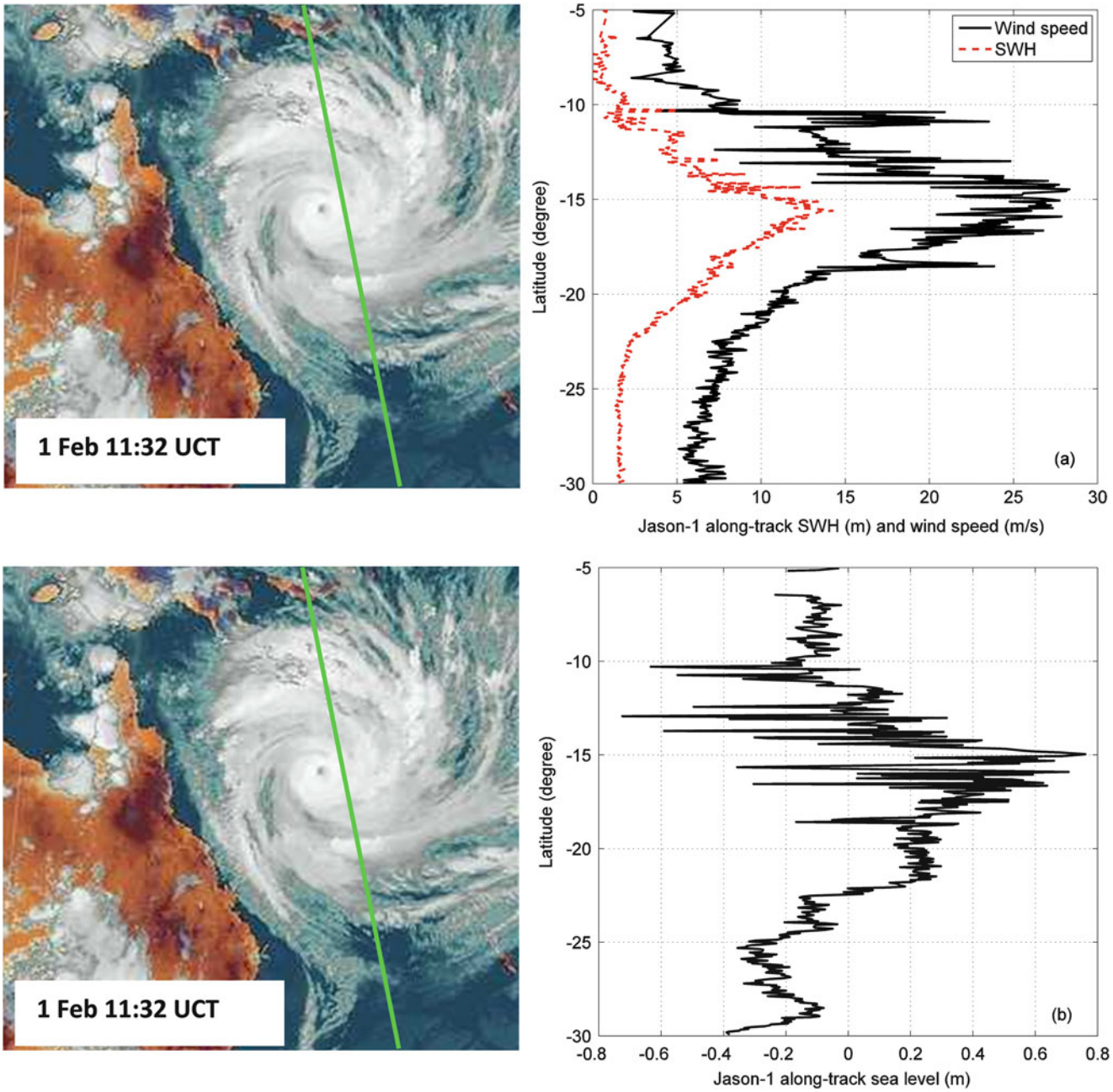

Fig. 3 Tropical cyclone Yasi hitting the Queensland coast in early February 2011. *Left panel* shows the satellite-captured infrared image (at 11:32 UTC) of Cyclone Yasi track and overlaid Jason-1 altimeter pass 188 (11:50–11:55 UTC) on 1 February 2011. The satellite image was taken ∼20 min before Jason-1 pass 188 measurements. The *right panels* show the altimeter measurements of (**a**) wind speeds (in m/s, *black curve*) at 10 m above the mean sea surface, (**a**) wave heights (in m, *red curve*), and (**b**) along-track SLAs (in m) with respect to DTU10 mean sea surface, respectively. The Y-axis in *left panel* represents the along-track latitude (in *degree*), which has the same length scale as *right panel*

level for monitoring of extreme sea levels around northern Australia in this section. To achieve this the along-track altimeter-derived sea level is described as a function of sea level measurements from all tide gauges. The function is built using a multivariate regression method (Høyer and Andersen 2003; Cheng et al. 2012; Deng et al. 2011).

4.1 Multivariate Regression

The nearly real-time sea level observed by altimetry can be modelled by a multivariate regression method using tide-gauge data sets as (Høyer and Andersen 2003)

$$\underset{n\times 1}{\mathbf{y}} = \underset{n\times m}{\mathbf{X}}\ \underset{m\times 1}{\mathbf{b}} + \underset{n\times 1}{\boldsymbol{\varepsilon}} \tag{1}$$

where **y** is a (n × 1) vector of the time series of altimeter sea levels at a point, **X** is a (n × m) matrix with tide-gauge sea level measurements at all gauges, **b** is a (m × 1) unknown parameter vector, and **ε** is a (n × 1) error vector. The unknown parameters **b** can be estimated using least squares adjustment. The solution of the multivariate regression model provides predictions at the time of interests, which can be used to monitor sea level variations.

The performance of the regression model (Eq. 1) is assessed using two measures in this study: the root mean square (RMS) error of regression and the hintcast skill (or the square of the coefficient of multiple correlation). The hintcast skill, R^2, is defined as (Emery and Thomson 2001)

$$R^2 = \frac{\sum (y_i - \overline{y})^2 - \sum (y_i - \hat{y}_i)^2}{\sum (y_i - \overline{y})^2} \qquad (2)$$

where $\hat{y}_i$ ($i = 1, 2, \ldots, n$) is the estimated altimeter SLA time series through the multivariate regression. The numerator of R^2 summarises the variation in altimeter SLAs explained by the multiple regression. The skill cast, R^2, ranges from 0 to 1, with the value near 1 indicating strong correlation between estimated altimeter SLAs and tide-gauge sea level measurements.

Theoretically, good performance of the model means that the multi-variables (i.e. tide-gauge sea level data) have strong correlations with altimeter SSHs. Therefore, a pointwise correlation analysis is necessary to determine whether a tide gauge should be included in the multivariate regression procedure.

4.2 Results and Discussion

The temporal correlation (1992–2010) between multi-altimeter SLAs and tide-gauge data at each individual tide station is calculated before the multiple regression. Correlation coefficients >0.9 are observed around all tide gauges. Figure 4 shows an example of the distribution of temporal correlations as a representative of general correlation around all other tide gauges. It can be seen that strong correlations (>0.6) appear in most of the study area.

The multivariate regression model (Eq. 1) is used to map predictive sea level variations using data from both altimetry and seven tide gauges. The regression is conducted on the time series at every altimeter along-track point. Quality measures of the RMS of multiple regression and hintcast skill, R^2, are also computed at each along-track point. Figures 5 and 6 show the spatial distribution of hintcast skills and RMS errors, respectively. It can be seen that the model can explain >60% of variances along the coastline. Moreover, near tide gauge Milner Bay in the Gulf of Carpentaria the RMS errors

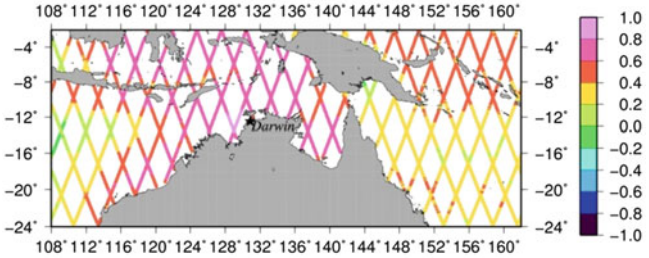

Fig. 4 Spatial distribution of temporal correlation coefficients between coastal and offshore SLAs for tide gauge Darwin between 1992–2010

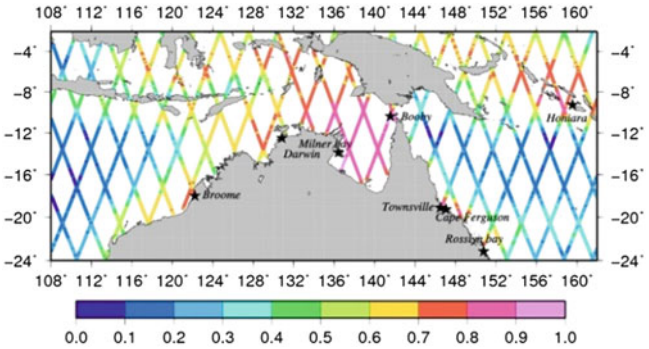

Fig. 5 The hintcast skill distribution off the northern coast of Australia

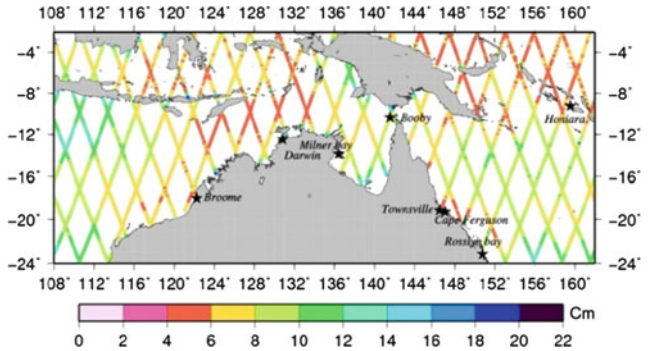

Fig. 6 The RMS error distribution off the northern coast of Australia

(∼6 cm) are small and hincast skills (>0.9) are close to its max value. These suggest that the sea level variability in the Gulf of Carpentaria and along the coastline in the area is dominated by high-frequency fluctuations, which can be well explained by the multi-regression model.

The tide gauge Townsville (Fig. 6), north of tide gauge Cape Ferguson (Fig. 6) ∼26 km, is located near Innisfail (146.0°E, 17.5°S), where cyclone Larry made landfall in March 2006. Data from Townsville has not been used in multi-regression modelling, as the observed sea level there is to be used to validate that the model from combined altimetry and tide gauges can predict sea levels at the time of interest. For this purpose, two multi-regression models are considered. One is to predict sea levels taking into account both satellite altimetry and tide gauges at the nearest position

Table 1 The results of the two-tail student's *t*-test at the significance level $\alpha = 0.05$ for the tide-gauge only multivariate regression at Cape Ferguson

Variable (tide gauge)	*t-test* statistic	p-value	Reject or accept H_0
Booby	2.20	0.03	Reject
Broome	**0.45**	**0.65**	**Accept**
Darwin	2.28	0.02	Reject
Honiara	2.48	0.01	Reject
Milner Bay	**0.31**	**0.76**	**Accept**
Rosslyn Bay	11.64	0.00	Reject

to Townsville along altimeter track 175, while the other is to predict sea levels using only tide gauges at Cape Ferguson the nearest tide gauge to Townsville.

In order to determine which tide gauges should be included in the multi-regression model in relation to selected locations, the two-tail student's *t*-test was also performed. This is because the hintcast skill (Fig. 5) tells how altimeter-observed sea levels respond to those observed by the entire set of independent tide gauges, but it does not indicate how significant a tide gauge can contribute to the predicted sea level. For the *t*-test, the null hypothesis H_0 is regression coefficient $b_i = 0$ for $i = 1, 2, \ldots, 6$ (cf. Eq. 2), meaning that the predicted sea level is not related to the *i*-th tide gauge. The alternative hypothesis H_1 is $b_i \neq 0$.

Table 1 lists the *t*-test results at the significance level $\alpha = 0.05$ for the tide-gauge only regression model at Cape Ferguson. The results suggest that tide gauges located at the north–west Australian coast, such as Broome and Milner Bay, have their model coefficients $b_i = 0$ at the significance level $\alpha = 0.05$. Tide gauge Darwin is rejected ($b_i \neq 0$) by the *t*-test at $\alpha = 0.05$, but is accepted ($b_i = 0$) at $\alpha = 0.01$. Similar results were also obtained from the test performed for the model using both altimeter and tide-gauge data at the nearest along-altimeter-track point to Townsville. The *t*-test results could be related to the regional sea level variability that differs for east and north–west Australian coastal oceans, where there is local thermal expansion in the ocean from changes in ocean currents and positions of frontal regimes, driven by changes in regional wind forcing and atmospheric fluxes. Therefore, tide gauges Darwin, Broome and Milner Bay are not included in the multi-regression model.

The predicted sea levels around cyclone Larry (15–25 March 2006) are compared with those observed at tide gauge in Townsville (Fig. 7). Figure 7 illustrates that the multi-regression model from combined satellite altimetry and tide gauges at the nearest along-altimeter-track point to Townsville (red curve) predicts well high sea levels induced by cyclone Larry, showing a good agreement with tide gauge records at Townsville (blue curve).

The multi-regression model was applied to predict water levels at Cape Ferguson, the nearest tide gauge to Townsville, by using the tide gauge data at Booby and Roselyn Bay only. From Fig. 7 it shows that the model (black curve) cannot predict the high water levels associated with cyclone Larry at Cape Ferguson though these were captured there (Fig. 8c). For a further investigation of the regression model efficiency, the de-tided hourly sea level records a few days before and after Larry are plotted at tide gauges Booby, Townsville, Cape Ferguson and Rosslyn Bay (Fig. 8). The anomalous high water level (~0.75 m) induced by Larry is observed at

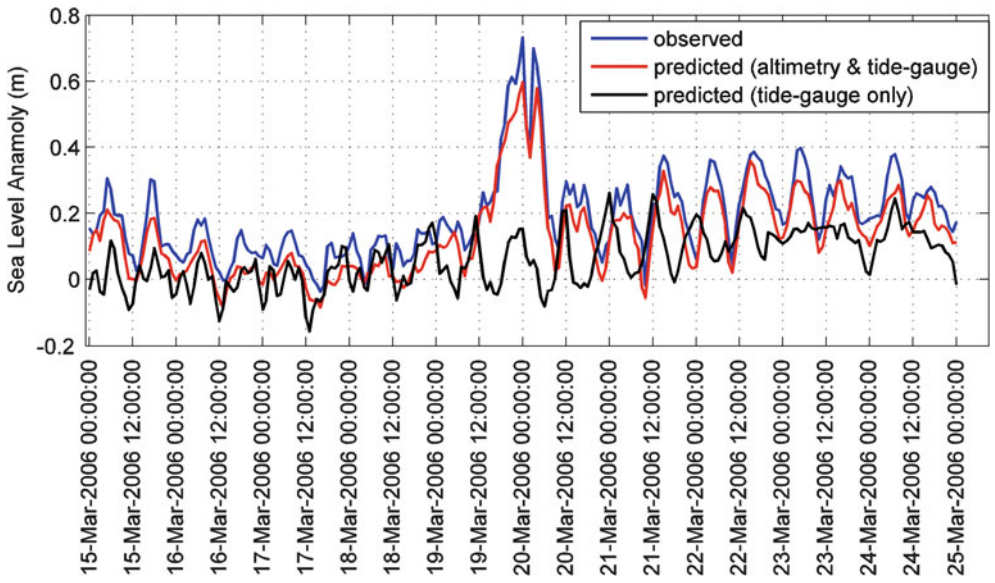

Fig. 7 Comparison between modelled and observed sea level variations at Townsville around cyclone Larry (15–25 March 2006). Sea levels observed at Townsville are shown in blue. The multi-regression modelled sea levels are shown in *red* for using both altimetry and 4-tide-gauge data, and in *black* for only using tide-gauge data

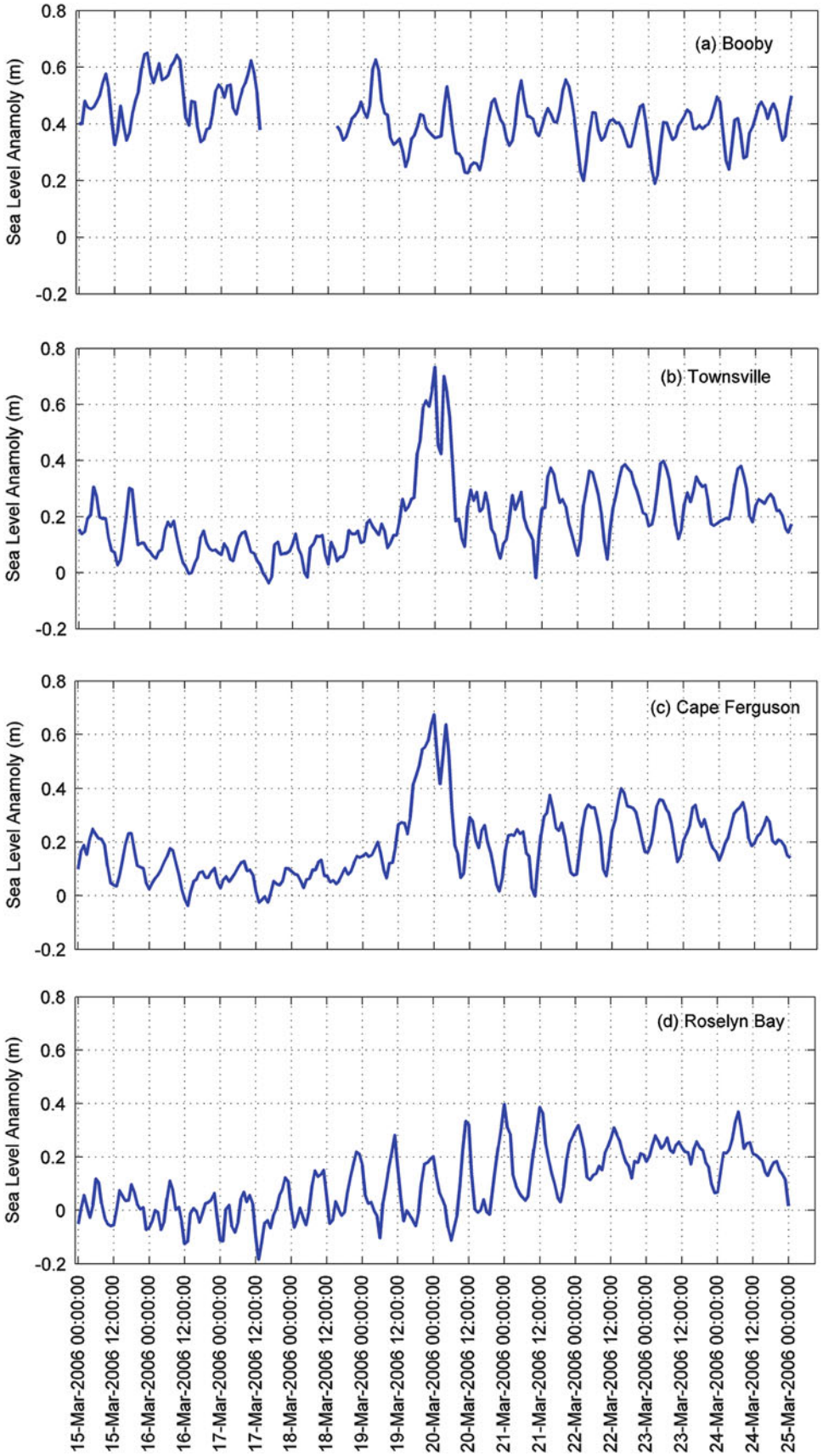

Fig. 8 De-tided hourly sea level records (15–25 March 2006) around cyclone Larry at tide gauges (**a**) Booby, (**b**) Townsville, (**c**) Cape Ferguson and (**d**) Roselyn Bay. The anomalous high water level ∼0.75 m induced by Larry is observed at (**b**) Townsville and (**c**) Cape Ferguson around 00:00:00 on 20 March 2006 when Larry made landfall

validating gauge Townsville (Fig. 8b) and model-predicted site Cape Ferguson (Fig. 8c) around 00:00:00 on 20 March 2006 when Larry made landfall, while it was not recorded at tide gauges Booby (Fig. 8a) and Roselyn Bay (Fig. 8d), both having distance >600 km to Townsville. This distant spacing may explain why high water signals could not be captured at Booby and Roselyn Bay, and then cannot be modelled for Townsville using sea levels observed at both tide gauges (Fig. 7).

From the above analysis and in the case of cyclone Larry, the importance of including satellite altimetry in modelling extreme sea levels, especially in coasts with sparse tide gauges, becomes very clear as it significantly increases the correlation between observed and modelled sea levels.

5 Conclusions

We have illustrated the altimeter's capability of capturing high water levels induced by cyclones through analysis of two selected tropical cyclones Larry and Yasi in the northeast Queensland coast. The results also reveal the importance of combining the coarse temporal sampling by the satellite altimeter in the deep ocean with the high temporal sampling at tide gauges in sparse coastal locations using a multi-regression model.

Examining the data delivered by the standard data products from space agencies illustrated that most of the altimeter data within and close to the cyclone were rejected as they were flagged as invalid mainly due to effects of heavy rain and waves associated with cyclones. However careful re-processing and re-editing of the data reveals that the data could be used to capture high water levels induced by Larry and Yasi, and to perform a multi-regression model to forecast sea level at the northern coast of Australia.

The results of this study indicate that for the northern coast of Australia sea-level variations from both altimetry and tide gauges have high coherence (>60%). In comparison with sea levels observed at Townville tide gauge demonstrates the importance of including satellite altimetry in the multi-regression model. Such a model could be of great benefit for further research into monitoring of extreme sea level events in the relatively vulnerable region due to effects of climate change.

Acknowledgments We would like to thank Dr Yongchun Cheng (Technical University of Denmark), the reviewers and editor for their constructive comments on this article.

References

Andersen OB (1999) Shallow water tides in the northwest European shelf region from Topex/Poseidon altimetry. J Geophys Res 104(C4):7729–7741

Cheng Y, Andersen OB (2010) Improvement in global ocean tide model in shallow water regions. Poster, SV.1-68 45, OSTST, Lisbon, 18–22 Oct

Cheng YC, Andersen OB, Knudsen P (2012) Integrating non-tidal sea level data from altimetry and tide gauges for coastal sea level prediction. Adv Space Res 50:1099–1106

Church JA, White NJ, Hunter JR, McInnes KL, Mitchell WM, O'Farrell SP, Griffin DA (2009) Sea level. In: Poloczanska ES, Hobday AJ, Richardson AJ (eds) A marine climate change impacts and adaptation report card for Australia 2009. NCCARF Publication 05/09, ISBN 978-1-921609-03-9

Deng X, Featherstone WE (2006) A coastal retracking system for satellite radar altimeter waveforms: application to ERS-2 around Australia. J Geophys Res 111:C06012. doi:10.1029/2005JC003039

Deng X, Griffin DA, Ridgway K, Church JA, Featherstone WE, White N, Cahill M (2011) Satellite radar altimetry for geodetic, oceanographic and climate change studies in Australian coasts. In: Vignudelli SKA, Cipollini P (eds) Coastal altimetry. Springer, Berlin. doi:10.1007/978-3-642-12796-0_18

Emery WJ, Thomson RE (2001) Data analysis methods in physical oceanography, 2nd edn. Elsevier, New York, p 638

Fu LL, Haines BJ (2013) The challenges in long-term altimetry calibration for addressing the problem of global sea level change. Adv Space Res 51(8):1284–1300

Griffin DA, Middleton JH (1991) Local and remote wind forcing of New South Wales inner shelf currents and sea level. J Phys Oceanogr 21:304–322

Han G, Ma Z, Chen D, deYoung B, Chen N (2012) Observing storm surges from space: hurricane Igor off Newfoundland. Sci Rep 2:1010. doi:10.1038/srep01010

Høyer JL, Andersen OB (2003) Improved description of sea level in the North Sea. J Geophys Res. doi:10.1029/2002JC001601

Idris NH, Deng X, Andersen OB (2014) The Importance of coastal altimetry retracking and detiding: a case study around the Great Barrier Reef, Australia. Int J Remote Sens. doi:10.1080/01431161.2014.882032

Lillibridge J, Lin M, Shum CK (2013) Hurricane Sandy storm surge measured by satellite altimetry. Oceanography 26(2):8–9. doi:10.5670/oceanog.2013.18

Munk WH, Cartwright DE (1996) Tidal spectroscopy and prediction. Philos Trans R Soc Lond A 259:533–583

Pascual A, Marcos M, Gomis D (2008) Comparing the sea level response to pressure and wind forcing of two barotropic models: validation with tide gauge and altimetry data. J Geophys Res 113:C07011. doi:10.1029/2007JC004459

Power SB, Pearce KB (2006) Climate change research in the Bureau of Meteorology: abstracts of presentations at a workshop held on 10 February 2006, Melbourne, Australia

Scharroo R, Smith WHF, Lillibridge JL (2005) Satellite altimetry and the intensification of Hurricane Katrina. EOS 80:366

Zieger S, Vinoth J, Young IR (2009) Joint Calibration of multiplatform altimeter measurements of wind speed and wave height over the past 20 years. J Atmos Ocean Technol. doi:10.1175/2009JTECHA1301.1

Part V

Science and Applications of Earth Rotation and Dynamics

Outline of the Chronology of the Developments of Geodynamic Investigations Connected with Earth Rotation Studies in the Twentieth Century: Authors' Perspective

Barbara Kolaczek and Jolanta Nastula

Abstract

In this paper, important scientific milestones are mentioned and information about developments and organizations of research in the considered field is given. The chronology was worked out in order to enable quick and easy comparisons of events from all centuries. The chronology is presented in the form of six tables containing successive periods: Table 1 1840–1910, Table 2 1910–1960, Table 3 1960–1980, Tables 4 and 5 1980–1999, Table 6 2000–2010. A table devoted to the most important earlier discoveries and theories is added as an annex. The list of references is given at the end of the paper.

Keywords

Chronology of developments of: • Polar motion • Terrestrial and celestial reference frames • Models of geophysical fluids and theories • Fundamental physical constants

1 Introduction

There were big developments in geodynamic investigations in the twentieth century. In this paper the scope of the chronology of developments of geodynamic investigations from the end of the nineteenth century until the beginning of the twenty-first century is presented in the following seven areas, chosen by us:

1. Theories
2. Establishment of definitions, astronomical constants and geophysical models
3. Instruments
4. Analyses of observations
5. Organizations of observations and investigations
6. Celestial reference frames
7. Terrestrial reference frames

Tables 1 and 2 show that in the first half of the twentieth century developments were achieved through the optical astrometry technique. The number of observations increased. Observational instruments and clocks were improved and more accurate star catalogues were created. The annual and Chandler (427 days) oscillations of polar motion were determined by Chandler (1891a, b, 1892a, b). The International Latitude Service (ILS) was organized in 1899 (Helmert and Albrecht 1899). Ephemeris time – ET – was defined in 1954.

The slow development of the theory of Earth's rotation continued. Secular polar motion, seasonal oscillations of UT and the retardation of Earth's rate were discovered (Wanach 1916). Table 3 shows that in the middle of the twentieth century more accurate systems of fundamental astronomical and geodetic constants were adopted and atomic time was defined.

Throughout the twentieth century, new more accurate theories of nutation and precession and polar motion were developed. The chronology of the adoption of more accurate new systems of fundamental astronomical constants, of geophysical standards (MERIT, IERS) and of introducing new more accurate star catalogs (GC, FK3 – FK5, Hipparcos) are given in Tables 2 and 4. The new celestial reference frame (ICRF/ICRS) (Table 4) and new time scales (Ephemeris Time – ET and Atomic Time – AT) connected with introducing new atomic clocks in 1955 (Table 2) are given.

B. Kolaczek • J. Nastula (✉)
Space Research Centre of the PAS, Bartycka 18a, Warsaw, Poland
e-mail: nastula@cbk.waw.pl

© Springer International Publishing Switzerland 2015

C. Rizos, P. Willis (eds.), *IAG 150 Years*, International Association of Geodesy Symposia 143,
DOI 10.1007/1345_2015_86

Table 1 1840–1910

THEORIES	**Ueber die Grösse und Figur der ERDE Baeyer (1861)**	**Ellipsoids Bessel, Clarke, Krasowsky, Hayford 1841 1866 1909/1940 1909/1924 (IUGG) Non rigid Earth theory and effects of the fluid core, elastic deformations Hough (1895), Darwin (1887), Sloudsky (1895), Liouville (1858), Poincare (1910), Love (1909) Linear Liouville, Liouville (1858)**		
DEFINITIONS ASTRONOMICAL CONSTANTS AND GEOPHYSICAL MODELS	**Adoption of the first system of fundamental astronomical constants (10 constants) 1896**			
ANALYSES OF OBSERVATIONS	**First determinations of annual (360 d) and Chandler (427d) oscillations of polar motion 1891/1892, Chandler (1891a, b, 1892a, b)**		**Explanation of the lengthening of the CW period by the elastic yielding of the Earth, Newcomb (1982)**	**Determination of astronomical nutation constant 9.210, Newcomb (1892)**
	Determinations of latitude variations with opposite phases in Berlin and Honolulu 1891/1892 , Przybyllok (1915)			
ORGANIZATIONS		**International Latitude Service - ILS - with 6 stations on the parallel of 39^0 0.8' in 1899, Helmert and Albrecht (1899)**		
CELESTIAL REFERENCE FRAMES				
TERRESTIAL REFERENCE FRAMES				
	1840			**1910**

New observational services of BIH, IPMS and BIH Service of Earth Rotation were organized. Project MERIT – Monitoring of Earth Rotation and Intercomparison of Techniques – was accepted in 1979 by the IAU and IUGG (Table 3).

The Observational Campaign MERIT was organized in 1983–1984 (Tables 4 and 5). The result of this was the organization of Earth rotation services: IERS – International Earth Rotation Service, IGS, ILRS, DORIS and IVS (Table 5). MERIT Standards and IERS Standards were determined and accepted (Table 4).

In the years 1970–1980 new observational techniques using observations of artificial satellites and VLBI were introduced to determine Earth's rotation, causing a big development in this research (Table 3). The global gravity field models were determined (Table 3).

Introducing new observational techniques using satellite and VLBI methods in the seventies of the twentieth century caused a quick development of geodynamics investigations, especially of Earth Orientation Parameters (EOP), of the global gravity field (Standard Earth), and of celestial and terrestrial reference systems (ICRS, ITRS) (Tables 3, 4, 5, and 6).

The higher accuracy of observations and determined data allowed deep studies of excitations of the Chandler wobble, of geophysical excitations of seasonal polar motion and of UT and Free Core Nutation to be conducted (Malkin and Terentev 2003; Brzeziński and Kosek 2004), as well as seasonal variations of the geocenter (Table 5) to be determined and analyzed.

The IERS Geophysical Global Fluid Center – GGFC – with the Bureaus: Mantle, Core, Gravity, Geocenter, Oceans, Hydrology, Tides and Atmosphere was organized in 1997 (Table 5).

In the period 1980–1999 extensive analysis of the impact of geophysical surficial fluids (Atmospheric Angular Momentum – AAM, Oceanic Angular Momentum – OAM, Hydrological Angular Momentum – HAM) on Earth rotation and polar motion excitation was conducted (Table 4) (Barnes et al. 1983; Hide et al. 1980; Gross 2003). Studies of the excitation of the Chandler wobble and analysis of its parameters were conducted (Table 4) (Smith and Dahlen 1981).

Short oscillations of polar motion were detected and studied. Determinations of new celestial and terrestrial reference frames with much higher accuracy took place.

Table 2 1910–1960

THEORIES	**Development of the theory of the nutation of an elastic Earth with a liquid core, Jeffreys (1916, 1949), Jeffreys and R.O. Vicente (1957), Molodensky (1961)**		**Woolard's theory of nutation with 69 terms and 0.05" accuracy (1953)**	
		Hydro-atmospheric variation of latitude, Jeffreys (1916)		
		Motion term excitation, Munk and Groves (1952) Atmospheric excitation of the wobble, Munk and Hassan (1961)		
DEFINITIONS, ASTRONOMICAL CONSTANTS AND GEOPHYSICAL MODELS	**General star catalogue GC: 33342 stars with accuracy of 1", Boss (1937)**	**Fundamental star catalogues FK3, FK4, FK5 containing: 873, 1535, 1535 stars with accuracy 0.02" (1937 - 1988)**		
		Definition of Ephemeris Time – ET 1s=1/31556925.9747 of the tropical year 1900 accepted in 1954		
INSTRUMENTS	**Photographic Zenith Tube – PZT 1913**	**Quartz Clock (accuracy 1×10^{-4}) 1940**	**Atomic Clock (accuracy 1×10^{-6}) 1955**	**Danjon Astrolabe 1958**
ANALYSES OF OBSERVATIONS	**First evidence for secular polar motion 0.003"/year, Wanach (1916)**	**Discovery of seasonal oscillation of UT Stoyko (1937)**	**Detection of retardation of the rate of Earth's rotation De Sitter (1927), Spencer Jones (1939)**	
CELESTIAL REFERENCE FRAMES		**General star catalogue GC: 33342 stars with accuracy of 1", Boss (1937)**	**Fundamental star catalogues FK3, FK4, FK5 containing: 873, 1535, 1535 stars with accuracy 0.02" 1937-1988, Fricke et al. (1988)**	
TERRESTIAL REFERENCE FRAMES				
	1910			**1960**

Observation of the Hipparcos Astrometric Satellite, 1990–1993, made it possible to determine the Hipparcos Star Catalogue with accuracy of 1mas and work out the International Celestial Reference Frame – ICRS (0.1 mas) (Tables 4 and 5).

The new observational technique GPS was introduced to determine Earth's rotation (Table 4).

The development of theory in the years 2000–2010 was dominated by the adoption of new theories of nutation (Mathews et al. 2002) and precession Capitaine et al. (2003) (Table 6). The launches of two satellite missions: GRACE – Gravity Recovery and Climate Experiment, 2002 (Balmino et al. 2001; Tapley et al. 2004) and GOCE – Gravity Field Steady – State Ocean Circulation Explorer, 2009 (Balmino et al. 2001; Drinkwater et al. 2003; GOCE 2010), were the big turning point in the research field of the gravitational field of Earth, climate change and ocean topography (Table 6). Since its launch in 2002, GRACE has been a source of data of temporal changes in Earth's gravitational field. This gravitational field has been used to estimate excitations of polar motion and LOD variations (Chen and Wilson 2005; Nastula et al. 2007). The GOCE mission was the first of satellites intended to map in unprecedented detail Earth's gravitational gravity field (Förste et al. 2008, 2012).

The IERS Conventions were developed (IERS 2003, 2010). The IAU 2009 system of astronomical constants, the second realization of the International Celestial Reference Frames (ICRF 2) and International Celestial Reference System (ICRS) were adopted (Table 6).

In the first decade of the twenty-first century, the mystery of the Chandler oscillation excitation sources was explained by the total impact of the atmosphere and ocean (Gross 2000; Brzeziński and Nastula 2002) (Table 6). During this period there were many advances in polar motion and LOD interpretation because of the improvement of AAM, OAM and HAM data (Chen and Wilson 2005; Nastula et al. 2007; Jin et al. 2010). The impact of Hydrological Angular Momentum (HAM) has been difficult to estimate from conventional hydrologic models and data.

Table 3 1960–1980

THEORIES	New theory of precession, Lieske et al. (1977)		New theory of nutation, Wahr (1981) Anelastic and viscoelastic rotational models, mantle rheology, Farrell (1972), Peltier (1974) The normal mode approach to Earth rotation, Smith (1977)
DEFINITIONS, ASTRONOMICAL CONSTANTS AND GEOPHYSICAL MODELS	Adoption of the second system of fundamental astronomical constants (36) 1964	Adoption of the third system of fundamental astronomical constants (28) 1976	Definition of the Atomic Time - TAI (192631770 oscillations of cesium 153 atom) 1971
	Adoption of the Geodetic reference system 1967	Definition of the Conventional International Origin of the Terrestrial Coordinate System-CIO 1967	The Earth's Model 1066A, 1066B, Gilbert and Dziewoński (1975), PREM Dziewoński and Anderson (1981)
INSTRUMENTS	Application of the observation of Earth's geodetic artificial satellites, Lageos-1, 1976; Lageos-2 , 1992; Seasat, 1978; Starlette, 1975; Ajisai, 1986; Stella, 1993; TOPEX –POSEIDON, 1992 for determining Earth's rotation.		
	Introduction of new observational techniques to determine Earth's rotation: Doppler, 1973; SLR , 1978; VLBI, 1978; GPS, 1983		
ANALYSES OF OBSERVATIONS	Determinations of the Markowitz wobble (0.02"-0.03"), Markowitz (1960,1967), Dickman (1981)		Determinations of global gravity field models described by harmonics from 8 – 1420 from observations of Earth's artificial satellites in the period 1966-2013, Gaposchkin (1973), Förste et al. (2008, 2012)
ORGANIZATIONS	Burreau International de l'heure - BIH, Rapid Service 1955-1967	International Polar Motion Services - IPMS 1962-1988	BIH Service of Earth's rotation 1968-1988
	Project Monitoring of Earth Rotation and Intercomparison of Techniques - MERIT was accepted in 1979 by the IAU and IUGG		
TERRESTIAL REFERENCE FRAMES	Determinations of the BIH Terrestrial Reference System in 1968 and 1984 and improving it to BIH TRS 1988 (IERS Conventions, 2010)		
	1960		1980

In 2003 the IAG undertook a new initiative – the organization of the GGOS (Global Geodetic Observing System) of the IAG (Table 6). Many scientific conferences including the IAU Symposia and Colloquia, the IAG Symposia and others presenting scientific achievements in this field were organized in the twenty-first century.

The IAU Colloquium 178 Polar Motion: Historical and Scientific Problems, S. Dick, D. McCarthy, B. Luzum was organized in 1999 in Cagliari, Italy on the 100th anniversary of the organization of the ILS.

Some selected major references discussing the history of Earth rotation studies are those of Smith and Turcotte (1993), Lambeck (1980, 1988), Munk and MacDonald (1975), Dick et al. (2000) and Gross (2007).

Acknowledgements The research reported here was supported by the Polish National Science Centre, through project No. 2012/05/B/ST10/02132. The authors would like to thank Pascal Willis, Richard Gross, Steve Dickman and anonymous reviewers for valuable comments.

A.1 Annex The most important earlier discoveries and theories

In the second century B.C. Hipparchus discovered Earth's precession with a constant of the annual precession of the equinoxes, $p = 46''$.

In 1687 Newton, in his book "Philosophiae naturalis principia mathematica", defined the first bases of dynamics, the law of gravitation and the theory of Earth rotation.

In 1748 Bradley discovered astronomical nutation from observation analyses.

In 1758 Euler foresaw the free nutation of solid Earth within a period of 305 days in "De movement de rotation des Corps Solides autour d'un axe variable".

Table 4 1980–1999

THEORIES	**Anelastic and viscoelastic rotational models, mantle rheology, Yuen et al. (1982)**		
	The normal mode approach to Earth rotation, Smith and Dahlen (1981)		
DEFINITIONS, ASTRONOMICAL CONSTANTS AND GEOPHYSICAL MODELS	**MERIT Standards Numerical constants and models 1983-1984**	**IERS Standards Numerical constants and models 1989-1996**	**Adoption of the International Celestial Reference System – ICRS (0.1 mas-pole, 10 mas-equator) – and Frames – ICRF (608 radiosources with 212 defining ones), IAU 1997/1998**
	Hipparcos Star Catalogue with accuracy of 1 mas (118218 stars), ESA (1997)		**Accurate model of tectonic plate motion – Nuvel 1, NNR Nuvel, 1992**
INSTRUMENTS	**Hipparcos Astrometric Satellite, 1990-1993, Introduction of new observational techniques to determine Earth's rotation, GPS, 1983**		**Ring laser, Stedman (1997)**
ANALYSES OF OBSERVATIONS	**Determination and interpretation of secular polar motion, Dickman (1981), Wilson and Vicente (1980), Chao (1983), Zhao and Dong (1988)**		
	Studies of excitations of the Chandler wobble, determinations and analyses of parameters of the Chandler wobble (period 434 days, damping coefficient Q = 40-170) , Anderson and Minster (1979), Smith and Dahlen (1981)		
	Detection of the high correlation of seasonal oscillation of Atmospheric Angular Momentum (AAM) and LOD, Hide et al. (1980), Merriam (1980, 1982, 1984)		
	Introduction of the definition of the Effective Angular Momentum Function, widely used in practice, Barnes et al. (1983)		
	1980		**1999**

In 1828 Gauss introduced and defined the idea of a geoid.

XVIII–XIX – Investigations of the free nutation of the Earth with a liquid core D'Alambert, Lagrange, Laplace, Poinsot

References

Altamimi Z, Collilieux X, Métivier L (2008) Analysis and results of ITRF2008, IERS Technical Note No. 37

Anderson DL, Minster JB (1979) Geophys J Roy Astron Soc 58(2):431–440. doi:10.1111/j.1365246X.1979.tb01033.x

Babcock A, Wilkins GA (1986) Proceedings of the 128th symposium of the international astronomical union, held in Coolfont, West Virginia, USA, 20–24 October 1986

Baeyer JJ (1861) Ueber die Gröse and Figur der Erde, Eine Denkschrift zur Begründung einer mittel-europäischen. Gradmessung, Berlin

Balmino G, Perosanz F, Rummel R, Sneeuw N, Suenkel H (2001) CHAMP, GRACE and GOCE: mission concepts and simulations. Bull Geofis Teori Appl 40(3–4):309–320

Barnes RTH, Hide R, White AA, Wilson CA (1983) Atmospheric angular momentum fluctuations, length-of-day changes and polar motion. Proc R Soc Lond A 38731–38773. doi:10.1098/rspa.1983.0050

Barthelmes F, Esselborn S (2008) The GeoForschungsZentrum Potsdam / Groupe de Recherche de Géodésie Spatiale satellite-only and combinedgravity field models: EIGEN - GL04S1 and EIGEN - GL04C. J Geod 82(6):331–346. doi:10.1007/s00190-007-0183-8

Boss B (1937) General catalogue of 33342 stars for the epoch 1950, GC. Publications of the Carnegie Institution of Washington, 468, Reissued by Johnson Reprint Co., New York

Bradley J (1748) A letter to the Right honorable George Earl of Maccles field concerning on apparent motion observed in some of the fixed stars. Phil Trans R Soc Lond 45

Brzeziński A (2012) Private communication

Brzeziński A, Kosek W (2004) Free core nutation: stochastic modelling versus predictibility. In: Finkelstein A, Capitaine N (eds) Proceedings Journes Systemes de Reference Spatio-Temporels 2003. Astrometry, geodynamics and Solar system dynamics: from milliarcseconds to microarcseconds. Institute of Applied Astronomy of the Russian Academy of Science, St. Petersburg, pp 99–106

Brzeziński A, Nastula J (2002) Oceanic excitation of the Chandler wobble. Adv Space Res 30(2):381–386

Brzeziński A, Nastula J, Kolaczek B, Ponte RM (2003) Oceanic excitation of polar motion from intraseasonal to decadal periods, vol 128. Proceedings of the IAG General Assembly, Sapporo, Japan, June 30–July 11, 2003. Springer, Berlin, pp 591–596

Capitaine N, Wallace PT, Chapront J (2003) Expressions for IAU 2000 precession quantities. Astron Astrophys 412:567–586

Chandler S (1891a) On the variation of latitude I. Astron J 11:83

Chandler S (1891b) On the variation of latitude I. Astron J 249:65–70

Chandler S (1892a) On the supposed secular variations of latitudes. Astron J 255:113–116

Table 5 1980–1999cd

ANALYSES OF OBSERVATIONS	Intensive investigations of the geophysical excitations of LOD and polar motion by AAM (Atmospheric Angular Momentum), OAM (Oceanic Angular Momentum) and HAM (Hydrological Angular Momentum) 1980-2010 Detection and investigations of short and rapid periodical variation of Earth rotation with sub-seasonal periods, fortnightly periods , diurnal, semi-diurnal and sub-diurnal periods 1980-2010 Determinations and analyses of the Free Core Nutation (0.2 mas) 1980-1984, McCarthy (2005), Malkin and Terentev (2003), Brzeziński and Kosek (2004) Determinations and analyses of seasonal variations of the geocenter (~ 1cm /year), Gross (2003)	
ORGANIZATIONS	Observational Campaign MERIT - Monitoring of Earth Rotation and Intercomparison of Techniques 1983-1984 MERIT Workshops were organized in 1981, 1983, 1985 New International Earth Rotation Services – IERS, 1988 recommended by the MERIT/COTES Joint Working Group IERS Geophysical Global Fluid Center – GGFC – with the Bureaus: Mantle, Core, Gravity Geocenter, Oceans, Hydrology, Tides, Atmosphere, 1997	
	New Services of Earth Rotation IGS 1993 ILRS 1998 DORIS 1999 IVS 2000	IAU Colloquium 178, Polar Motion: Historical and Scientific Problems, Cagliari, 1999 S. Dick, D.D. McCarthy, B. Luzum (2000)
CELESTIAL REFERENCE FRAMES	Hipparcos Star Catalogue with accuracy of 1 mas (118218 stars), ESA (1997)	Adoption of the International Celestial Reference System – ICRS (0.1 mas-pole, 10 mas equator) – and Frames – ICRF (608 radiosources with 212 defining ones), IAU 1997/1999
TERRESTIAL REFERENCE FRAMES	First International Terrestrial Reference System – ITRS – and Frames – ITRF, 1988	
	1980	1999

Chandler S (1892b) On the variation of latitude II. Astron J 277:97–101

Chao BF (1983) Autoregressiv harmonic analysis of the earth's polar motion using homogeneous international lattitude service data. J Geophys Res 88(10299–10307):1983

Chen JL, Wilson CR (2005) Hydrological excitation of polar motion (1993–2002). Geophys J Int 160(3):833–839. doi:10.1111/j.1365-246X.2005.02522.x

Darwin G (1887) On the influence of geological changes on the earth's axis of rotation. Phil Trans R Soc A 167:272

de Sitter W (1927) On the secular accelerations and the fluctuations of the longitudes of the moon, the sun, Mercury and Venus. Bull Astron Inst Netherlands 4:21

Dick S, McCarthy DD, Luzum B (eds) (2000) Proceedings of IAU Colloquium 178 Polar motion: historical and scientific problems, 27–30 September, 1999, Cagliari, Italy. ASP, Sheridan Books Inc

Dickman SR (1981) Investigation of controversial polar motion of features using homogeneous International Latitude Service data. J Geophys Res 86:4904–4912

Drinkwater MR, Floberghagen R, Haagmans R, Muzi D, Popescu A (2003) GOCE: ESA's first earth explorer core mission. In: Beutler GB, Drinkwater MR, Rummel R, von Steiger R (eds) Earth gravity field from space – from sensors to earth sciences, vol 18, In the space sciences series of ISSI. Kluwer, Dordrecht, pp 419–432. ISBN 1-4020-1408-2

Dziewoński AM, Anderson DL (1981) Preliminary reference earth model (PREM). Phys Earth Planet Int 25:297–356

Dziewoński AM, Gilbert F (1971) Solidity of the inner core of the earth inferred from normal mode observations. Nature 234:465–466

ESA (1997) The Hipparcos and Tycho Catalogues, ESA SP–1200

Eubanks TM (1993) Variations in the orientation of the earth. In: Smith DE, Turcotte DI (eds) Contributions of space geodesy to geodynamics-earth dynamics, vol 24, Geodynamic series. AGU, Washington DC, pp 1–54

Eubanks TM, Steppe JA, Dickey JO, Rosen RD, Salstein DA (1988) Causes of rapid motions of the earth's pole. Nature 334:115–119

Euler L (1758) De movement de rotation des Corps Solides autour d'un axe variable. Histoire de l'Académie Royale des Sciences et Belles Lettres, Berlin

Farrell WE (1972) Deformation of the earth by surface loads. Rev Geophys 10:761–797

Förste C, Schmidt R, Stubenvoll R, Flechtner F, Meyer U, König R, Neumayer H, Biancale R, Lemoine J-M, Bruinsma S, Loyer S, Barthelmes F, Esselborn S (2008) The GeoForschungsZentrum Potsdam / Groupe de Recherche de Geodesie Spatiale stellite-only and combined gravity field models: EI GEN-GL04S1 and EIGEN-GL04C. J Geod 82(6):331–346. doi:10.1007/s00190-007-0183-8

Förste C, Bruinsma SL, Shako R, Abrikosov O, Flechtner F, Marty J-C, Lemoine J-M, Dahle C, Neumeyer H, Barthelmes F, Biancale R,

Table 6 2000–2010

THEORIES	Adoption of the new theory of precession and nutation IAU 2000A (0.2 mas), IAU 2000B (1 mas) by the IAU XXIV IAU General Assembly Resolutions 2003 Mathews, Herring, Buffet (2002)		PO 3 precession theory (Capitaine et al. 2003) Adopted by XXVII IAU GA Resolution 2006
DEFINITIONS, ASTRONOMICAL CONSTANTS AND GEOPHYSICAL MODELS	IERS Conventions numerical constants and geophysical models, IERS (2003, 2010)	Adoption of the second realization of the International Celestial Reference Frames (ICRF 2) and International Celestial Reference System (ICRS) XXVII IAU GA Resolution, 2009	Adoption of the IAU 2009 System of Astronomical Constants XXVII IAU GA Resolution, 2009
INSTRUMENTS	Gravity satellite GRACE - Gravity Recovery and Climate Experiment, 2002, Tapley et al. (2004)		Gravity satellite GOCE – Gravity Field Steady – State Ocean Circulation Explorer, 2009, GOCE (2010)
ANALYSES OF OBSERVATIONS	Explanation of CW excitation by combination of the atmospheric and oceanic angular momentum, Gross (2000), Brzeziński and Nastula (2002). Improvement of HAM estimation. Many advances in PM and LOD interpretation took place because of the improvement in OAM and HAM data, Chen and Wilson (2005), Nastula et al. (2007), Jin et al., (2010)		
ORGANIZATIONS	IAU Colloquium 178 Polar Motion: Historical and Scientific Problems, Cagliari, 1999 S. Dick, D. McCarthy, B. Luzum (2000)		GGOS – Global Geodetic Observing System – of the IAG – International Association of Geodesy – 2003
CELESTIAL REFERENCE FRAMES		International Celestial Reference System (ICRS) XXVII IAU GA Resolution, 2009	
TERRESTIAL REFERENCE FRAMES		New ITRF 2008 (934 stations at 580 sites) 2010, Altamimi et al. (2008)	
2000			2010

Balmino G, König R (2012) A new release of EIGEN-6: The latest combined global gravity field model including LAGEOS, GRACE and GOCE data from the collaboration of GFZ Potsdam and GRGS Toulouse, Geophysical Research Abstracts, vol 14. EGU2012-2821-2, EGU General Assembly 2012

Fricke W, Schwan W, Lederle T (1988) Fifth fundamental catalogue (FK5), Veroffen-tlichungen, Astronomisches Rechen – Institut Heidelberg, No. 32., Verlag G. Braun

Gambis D, Biancale R (2006) Contribution of SLR and LLR to earth orientation and terrestrial reference frame monitoring. Proceedings of 15th international laser workshop, Canberra, 16–20 October, 2006, p 99. http://cddis.gsfc.nasa.gov/lw15/index.html

Gaposchkin EM (1973) 1973 Smithsonian standard earth (III), Smithsonian Institution Astrophysical Observatory, Cambridge, Mass

Gauss CF (1828) Disquisitiones generales circa superficies curvas, Typis Dieterichianis, Gottingae

Gilbert F, Dziewoński AM (1975) An application of normal mode theory to the retrieval of structural parameters and source mechanisms from seismic spectra. Phil Trans R Soc Lond A278: 187–269

GOCE High Level Processing Facility GOCE Level 2 Product Data Handbook Doc. No.: GO-MA-HPF-GS-0110 Issue: 4 Revision: 2 Date: 23/06/2010

Gross RS (2000) The excitation of the Chandler wobble. Geophys Res Lett 27:2329–2332

Gross RS (2003) The IAG/IAPSO joint working group on geodetic effects of nontidal oceanic processes, XXIII General Assembly of the IUGG, Sapporo, Japan

Gross RS (2007) Earth rotation variations: long period. In: Herring TA (ed) Physical geodesy, vol 3, Treatise on geophysics. Elsevier, Oxford, pp 239–294

Helmert FR, Albrecht T (1899) Den internationalen Polhöhendiendt. Astron Nachr 148(3532):4–56

Hide R, Birch RT, Morrison LV, Shea DJ, White AA (1980) Atmospheric angular momentum fluctuations and changes in the length of the day. Nature 286:114–117

Hough S (1895) The oscillations of a rotating ellipsoïdal shell containing fluid. Phil Trans R Soc Lond 186:469–506

IERS CONVENTIONS (2003). In: McCarthy DD, Petit G (eds) IERS Convention Centre, IERS Technical Note No. 32. http://www.iers.org/IERS/EN/Publications/TechnicalNotes/tn32.html

IERS CONVENTIONS (2010). In: Petit G, Luzum B (eds) IERS Convention Centre, IERS Technical Note No. 36. http://www.iers.org/IERS/EN/Publications/TechnicalNotes/tn36.html

Jeffreys H (1916) Causes contributory to the annual variation of latitude. Mon Not R Astron Soc 76(6):499–525

Jeffreys H (1949) Dynamic effects of a liquid core. Mon Not R Astron Soc 109:670–687; 110:162–173

Jeffreys H, Vincente R (1957) The theory of nutation and the variation of latitude. Mon Not R Astron Soc 117:556–575

Jin SG, Chambers DP, Tapley BD (2010) Hydrological and oceanic effects on polar motion from GRACE and models. J Geophys Res 115, B02403. doi:10.1029/2009JB006635

Kolaczek B (2004) Landmarks of the history of investigations of polar motion, nutation and time, artificial satellites. J Planet Geod (ISSN 0208–841X) 39(1):7–38

Kołaczek B, Nastula J (2001) Seasonal oscillations of the polar motion in the last fifty years, Kinematics and Physics of Celestial Bodeies. Suppl. Ser., 2000, N3. In: Yatskiv YS (ed) Astronomy in Ukraine – 2000 and Beyond, pp 51–54

Kolaczek B, Kosek W, Schuh H (2000) Short – period oscillations of earth rotation. Proceedings of IAU colloquium 178 polar motion:

historical and scientific problems, 27–30 September, 1999, Cagliari, Italy. ASP, USA, pp 533–544
Kryński J (ed) (2004) Nowe Obowiązujące Systemy Współrzędnych Ziemskich i Niebieskich oraz ich Wzajemne Relacje, Monographic series of the Institute of Geodesy and Cartography, Nr 10, Warsaw
Lagrange JL (1788) Mécanique Analitique, Pris
Lambeck K (1980) The earth's variable rotation: geophysical causes and consequences. Cambridge University Press, Cambridge
Lambeck K (1988) Geophysical geodesy. The slow deformations of the earth. Clarendon, Oxford
Lambeck K, Cazenave A (1973) The earth's rotation and atmospheric circulation-I Seasonal variations. J Roy Astron Soc 32:79–93
Lambeck K, Cazenave A (1974) The earth's rotation and atmospheric circulation-I The continuum. J Roy Astron Soc 38:49–61
Lieske JH, Lederle T, Fricke W (1977) Expression for the precessions quantities based upon the IAU (1976) system of astronomical constants. Astron Astrophys 58:1–16
Liouville J (1858) Développements sur un chapitre de la Mécanique de Poisson, J Math Pures Appl Deuxième Sér Tome 3:1–25
Love AEH (1909) The yielding of the earth to disturbing forces. Proc Roy Soc A 82:73–88
Malkin Z, Terentev D (2003) Investigation of the parameters of the free core nutation from VLBI data, Comm. IAA RAS, No. 149, pp 1–24
Markowitz W (1960) Latitude and longitude, and the secular motion of the pole. In: Runcorn SK (ed) Methods and techniques in geophysics. Wiley-Interscience, Hoboken, pp 325–361
Markowitz W (1961) International determination of the total motion of the pole. Bull Geod 59:29–41
Markowitz W (1967) Current astronomical observations for studying continental drift, polar motion and the rotation of the Earth. In: Markowitz W, Guinot B (eds) Continental drift, secular motion of the pole and rotation of the earth. D. Redel Publishing Co, Dordrecht
Mathews PM, Herring TA, Buffet BA (2002) Modelling of nutation-precession: new nutation series for non-rigid earth, and insights into earth's interior. J Geophys Res 107:B4. doi:10.1029/2001JB000390
McCarthy DD (2005) The free core nutation. Proceedings Journees Systemes de Reference Spatio Temporels, Paris (2004), pp 101–105
Merriam JB (1980) Zonal tides and changes in the length of day. Geophys J Roy Astron Soc 62:551–556
Merriam JB (1982) A comparison of recent theoretical results on the short-period terms in the length of day. Geophys J Roy Astron Soc 69:837–840
Merriam JB (1984) Tidal terms in universal time: effects of zonal winds and mantle Q. J Geophys Res 89
Molodensky MS (1961) The theory of nutation and diurnal tides. Commun Obs R Belg 288:25–56
Mueller II (1985) Proceedings of the international conference on "earth rotation and the terrestrial reference frame", Columbus, Ohio, July 31-August 2, 1985. Department of Geodetic Science, Ohio State University, Columbus, Ohio, USA
Mueller II (2000) The first decade of the IERS. In: Dick S, McCarthy D, Luzum B (eds) Proceedings of IAU colloquium 178 Polar motion: historical and scientific problems, 27–30 September, 1999, Cagliari, Italy. ASP, Sheridan Books Inc
Muller I, Zerbini S (1988) Lecture notes in earth sciences, vol 22. Proceedings of an international workshop "the interdisciplinary role of space geodesy", Erice, Sicily, Italy, July 23–29, 1988
Munk WH, Groves G (1952) The effect of winds and ocean currents on the annual variation in latitude. J Meteorol 9:385–396
Munk WH, Hassan EM (1961) Atmospheric excitation of the earth's wobble. Geophys J R Astron Soc 4:339–358
Munk WH, Macdonald GJF (1975). In: Batchelor GK, Miles JW (eds) The rotation of the earth. A geophysical discussion. Cambridge University Press, Cambridge
NASA (1999) Space interferometry mission – SIM
Nastula J, Ponte RM, Salstein DA (2007) Comparison of polar motion excitation series derived from GRACE and from analyses of geophysical fluids. Geophys Res Lett 34, L11306. doi:10.1029/2006GL028983
Newcomb S (1892) On the dynamics of the earth's rotation, with respect to the periodic variations of latitude. Mon Not R Astron Soc Lond 52:336–341
Newton I (1687) Philosophiae naturalis principia mathematica
Pavlis NK, Holmes SA, Kenyon SC, Factor JK (2012) The development and evaluation of the Earth Gravitational Model 2008 (EGM2008). J Geophys Res 117(B4). doi:10.1029/2011JB008916
Peltier WR (1974) The impulse response of a Maxwell Earth. Rev Geophys 12:649–669
Peltier WR (1976) Global isostatic adjustment, II. The inverse problem. Geophys J Roy Astron Soc 62:49–58
Poincaré H (1910) Sur la précession des corps déformables. Bull Astron XXVII:321–356
Poinsot L (1834) Théorie Novelle de la Rotation des Corps, L'Institut. J. Général des Sociétés et Travaux Scientifiques, 2. Paris
Przybyllok E (1915) Űber des Verhalten des Schraubenwertes auf den sechs Stationen des Internationalen Breitendienstes. Astron Nachr 200(4800):405–410
Richards EG (1998) MAPPING TIME-the calendar and its history. Oxford University Press, Oxford
Sabadini R, Peltier WR (1981) Pleistocene Deglaciation and the earth's rotation: implications for mantle viscosity. Geophys J Roy Astron Soc 66:553–578
Sloudsky TH (1895) De la rotation de la Terre supposée fluide en son intérieur. Bull Soc Impériale des Naturalistes, Moscou IX(2):285–318; suite: X:162–170 (1896)
Smith ML (1977) Wobble and nutation of the earth. Geophys J 50:103–140
Smith ML, Dahlen FH (1981) The period of Q of the Chandler wobble. Geophys J 64:223–281
Smith DE, Turcotte DI (1993). In: Smith DE, Turcotte DI (eds) Contributions of space geodesy to geodynamics-earth dynamics. Geodynamic Series, vol 24. AGU, Washington DC
Spencer Jones H (1939) The rotation of the earth and the secular acceleration of the Sun, Moon and planets. Mon Not R Astron Soc 99:541–558
Stedman GE (1997) Ring-laser tests of fundamental physics and geophysics. Rep Prog Phys 60:615–688
Stoyko N (1937) Sur la periodicite dans l'irregularite de la rotation de la Terre, Comptes rendus des Seances de l'Academie des Sciences, Paris, vol 205, p 79
Tapley BD, Bettadpur S, Ries JC et al (2004) GRACE measurements of mass variability in the earth system. Science 3055683:503–505. doi:10.1126/science.1099192
Vermeersen LLA, Fournier A, Sabadini R (1997) Changes in rotation induced by Pleistocene ice masses with stratified analytical earth models. J Geophys Res 102:27689–27702
Von H. Geheimen Rath, Bessel R (1842), Ueber einen Fehler in der Berechnung der französischen Gradmessung und seinen Einfluß auf die Bestimmung der Figur der Erde. Astron Nachr Band 19(438):97–116
Vondrak J, Weber R, Ron C (2005) Free core nutation direct observations and resonance effect. Astron Astrophys 444:297–303
Wahr JM (1981) The forced nutations of an elliptical, rotating, elastic and oceanless earth. Geophys J Roy Astron Soc 64:705–727
Wanach B (1916) Resultate des Internationalen Breitendienstes. Bd. V. Z. B. Internat. Erdmessung, N. F. Veröff. Nr. 30. Berlin
Wilson CR, Gabay S (1981) Excitation of the earth's polar motion: a reassessment the new data. Geophys Res Lett 8:745–748

Wilson CR, Vicente RO (1980) An analysis of the homogeneous ILS polar motion series. Geophys J Roy Astron Soc 62:605–616

Woolard EW (1953) Theory of the rotation of the earth around its center of mass. Astron Paper Am Ephem 15:1

Yuen DA, Sabadini R, Boschi EV (1982) Viscosity of the lower mantle as inferred from rotational data. J Geophys Res 87:10745–10762

Zhao M, Dong D (1988) A new research for the secular polar motion in this century. In: Babcock AK, Wilkins GA (eds) The earth's rotation and reference frames geodesy and geodynamics. Reidel, Dordrecht Holland, pp 385–392

Hydrological Excitations of Polar Motion from GRACE Gravity Field Solutions

J. Nastula, D.A. Salstein, and W. Popiński

Abstract

We use the latest time-variable Earth gravity field harmonics from the GRACE satellite mission (Release 5 – RL05) to determine seasonal and nonseasonal scales of polar motion excitation functions from global geophysical fluids, and particularly from the portion from land-based hydrology. Hydrological excitation functions of polar motion from the mass of equivalent water thicknesses (EWT) derived gravimetrically from the solutions of three GRACE processing centers, the Center for Space Research (CSR), the Jet Propulsion Laboratory (JPL) and the GeoforschungsZentrum (GFZ), are intercompared. Additionally, we estimate the hydrological signal as well in a different manner, as a residual from geodetically observed polar motion, by subtracting atmospheric (pressure + wind) and oceanic (bottom pressure + currents) contributions. Among the gravimetric excitation functions based on RL05 there are still significant differences between center results which we attribute mainly to residual signals over ocean areas. It appears that the CSR processing may lead to stronger agreement between the hydrological signal and residual values, surely due to details in the processing, like resolutions to different degree and order used in the static background gravity model.

Keywords

Earth rotation variations • Geodesy and gravity

1 Introduction

Knowledge of continental hydrological mass variations caused by land water, snow, and ice, is strongly needed for a full understanding of the excitation of polar motion. This impact, calculated as Hydrological Angular Momentum (HAM), has been difficult to estimate from conventional hydrologic models and data, and it is not as well known as Atmospheric (AAM) and Oceanic Angular Momentum (OAM). The use of measurements from global gravimetry, whose values indicate mass distribution, offers an alternative method to determine this needed signal. Since its launch in 2002, the Gravity Recovery and Climate Experiment (GRACE) has been a source of data of temporal changes in Earth's gravity field. These gravity field series have been used to estimate excitations of polar motion, though with varying degree of confidence (Chen and Wilson 2005, 2008; Nastula et al. 2007). The so-called Level 2 gravity field products are available in the form of changes in the GSM coefficients: ΔC_{nm}, ΔS_{nm} (Tapley et al. 2004).

There have been a series of releases of GRACE data. Here we use the most recently updated solution of Release 5 (RL05) processed by three centers: the Center for Space Research (CSR), the Jet Propulsion Laboratory (JPL) and the

J. Nastula (✉)
Space Research Centre of the PAS, Bartycka 18a, Warsaw, Poland
e-mail: nastula@cbk.waw.pl

D.A. Salstein
Atmospheric and Environmental Research, Lexington, MA, USA

W. Popiński
Department of Methodology and Standards, Central Statistical Office, Warsaw, Poland

© Springer International Publishing Switzerland 2015

C. Rizos, P. Willis (eds.), *IAG 150 Years*, International Association of Geodesy Symposia 143,
DOI 10.1007/1345_2015_85

GeoforschungsZentrum (GFZ). GSM coefficients of Level 2 gravity field products are used here to compute the equivalent water thickness (EWT) distribution, which reflects mainly variability in the hydrosphere over land masses, and to a lesser extent changes in ice mass, and from seismic events. It should be emphasized that the GRACE data processing requires the removal of short-term mass variations in the atmosphere and in the oceans because these mass changes cause time variant gravity field forces that act on the orbiting satellites. High frequency variations in the gravitational field can result from a number of sources including tides (improved tide models are necessary for all missions), and mass redistribution of atmosphere, oceans, and continental water (snow, ice, hydrology) (Flechtner 2004). Therefore, to ensure that high frequency variations are not aliased into the monthly estimates of the gravity field, background models of mass variations in the ocean and atmosphere are removed from the GRACE gravity data before processing. Any errors in these background models will result in errors in the GRACE data. Clearly, the EWT distributions are also affected by errors of atmospheric and oceanic modeling approaches. For example Quinn and Ponte (2008) show that errors increase near some continental regions with large land hydrology signals and also near Greenland and Alaska, where there are large mass trends. For estimations after the annual and semi-annual signals have been removed, data errors near regions with large land hydrology signals tend to be reduced.

Global gravimetric polar motion excitation functions are estimated from time-variable EWT distributions, which we separate into contributions from the land-based hydrosphere and from a residual signal over the ocean.

We first explore the extent of agreement among the three RL05 by computing these gravimetric excitation functions. Secondly, we estimate how well polar motion is explained with their use, focusing on non-seasonal time scales. Lastly, we estimate ocean-based residual signals in gravimetric polar motion, unassigned to the land.

2 Method

The GRACE satellite mission produces data of temporal changes in Earth's gravity field. The Level 2 gravity field products, available as changes in the ΔC_{nm} and ΔS_{nm} geopotential coefficients (GC) (Tapley et al. 2004), include GSM (Static Field GC) coefficients, so-called GAB (Non-tidal Ocean GC averaged over certain time periods), GAC (temporally averaged Non-tidal Atmosphere and Ocean GC) and GAD (temporally averaged Ocean Bottom Pressure GC) coefficients from atmosphere, atmosphere plus ocean, and ocean bottom pressure GC, respectively, derived from atmosphere and ocean models.

The GSM coefficients reflect mainly the influence of the land-based hydrosphere, and to a lesser extent, ice mass and seismic events, but do not include atmospheric and oceanic signals. To obtain information about the impact of all three geophysical fluids – land-based hydrosphere, atmosphere and oceans, the GAC coefficients should be added back to the GSM ones. Errors in this process are derived from atmospheric and oceanic model errors, as well as several initial assumptions needed to generate the de-aliasing coefficients, such as the choice of a simplified 2-year mean.

Using the coefficients ΔC_{nm}, ΔS_{nm}, the effective measures of the EWTs, the hypothetical mass change of a layer of water necessary to explain the observed changes in the gravitational field (Chambers 2006), are computed:

$$\Delta\sigma = \frac{a_E \rho_E}{3\rho_W} \sum_{n=0}^{n=l} \sum_{m=0}^{n} \frac{(2n+1)}{(1+k_n)} W_n P_{nm}(\sin\phi) \cdot \{\Delta C_{nm}(t)\cos m\lambda + \Delta S_{nm}(t)\sin m\lambda\}, \quad (1)$$

$\Delta\sigma$ – thickness of the equivalent water layer,
P_{nm} – normalized associated Legendre polynomials degree n order m,
ρ_E – average density of the Earth (5,517 kg/m^3),
ρ_W – average density of water (1,000 kg/m^3),
k_n – Love load numbers of degree n,
l – the upper summation limit,
a_E – average equatorial radius of the Earth,
ϕ,λ – latitude and longitude,
W_n – Gauss filter function necessary to remove characteristic disorders of the EWT (stripes). Here we use 300 km radius for the Gauss filter
ΔC_{nm} ΔS_{nm} – coefficients.

The equatorial components of the polar motion excitation functions available for transfer of fluid angular momentum to the solid Earth have been formalized as the χ_1 and χ_2 components, towards longitudes 0° and 90° E, respectively (Barnes et al. 1983).

There are two different methods to estimate polar motion excitation from the GRACE observations. Gravimetric polar motion excitation (χ_1 and χ_2) can be simply estimated directly from GRACE degree-2 and order-1 coefficients (ΔC_{21},ΔS_{21}) (Chen et al. 2004, 2012; Nastula et al. 2007; Seoane et al. 2009, 2012). However, these coefficients contain signals from hydrological variations over land and also from residual signals over oceans. A second approach is to directly employ the EWT maps, based on a full set of expansion coefficients, to compute contributions over land areas and to estimate the related over-ocean residual signal (Seoane et al. 2011, 2012; Chen et al. 2012; Jin et al. 2010, 2012).

With EWT data, $\Delta\sigma$, one can determine either global or regional polar motion excitation functions with appropriate

integration limits (Barnes et al. 1983; Eubanks 1993; Chen and Wilson 2008) using the following formulas:

$$\chi_1 = -\frac{1.098a_E^2}{(C-A)}\iint \Delta\sigma\,(\phi,\lambda,t)\sin(\phi)\cos(\phi)\cos(\lambda)\,ds$$
$$\chi_2 = -\frac{1.098a_E^2}{(C-A)}\iint \Delta\sigma\,(\phi,\lambda,t)\sin(\phi)\cos(\phi)\sin(\lambda)\,ds, \quad (2)$$

$\Delta\sigma$ – thickness of the equivalent water layer,
a_E – average equatorial radius of the Earth,
ϕ,λ – latitude and longitude,
C,A – Earth's principal moments of inertia.

3 Data

We use the following data: GSM – coefficients: ΔC_{nm}, ΔS_{nm} from RL05 GRACE solutions developed by CSR, JPL, and GFZ. They are used to compute EWT distributions on a global grid with spatial resolution $1^\circ \times 1^\circ$, and do not include the effects of the atmosphere and ocean. The gravity models are determined by the JPL and GFZ solutions to degree and order 90 while the model obtained by CSR is estimated to degree and order 60 (http://icgem.gfz-potsdam.de/ICGEM/).The GAC dealiasing coefficients: ΔC_{nm},ΔS_{nm} of the gravitational field from atmospheric pressure (using ECMWF data) results and from ocean bottom pressure (using OMCT model results) are prepared by all three GRACE data centers.(http://icgem.gfz-potsdam.de/ICGEM/). Next three AAM + OAM merged nontidal atmospheric and oceanic polar motion excitation functions were computed from each of the three GAC sets using formulas (1) and (2). GEOD geodetic polar motion excitation χ_1 and χ_2 functions, were computed from the x, y pole coordinates from the IERS C04 combined solution (Gambis 2004). Additionally, the motion terms, consisting of atmospheric winds (from NCEP) and oceanic currents (from ECCO) are removed from the series by the IERS. GEOD–AAM–OAM three sets of geodetic residuals containing the hydrological part of polar motion excitation were obtained by removing each of the three merged GAC atmospheric and oceanic excitation from the geodetic excitation functions are computed. For consistency with the GSM data, we calculated GEOD–AAM–OAM, using each of the JPL, CSR, and GFZ series.All data series cover the period from the beginning of 2003 to the first half of 2013 and are averaged into monthly intervals.

4 Analyses and Results

Examples of patterns of the EWT based on the CSR data for merged atmosphere plus ocean, from GAC (Fig. 1a) and for land hydrology from the GSM coefficients (Fig. 1b), show considerable variability; moreover, values for these two geophysical fluids are quite different from other.

Atmospheric and oceanic mass variability occurs largely in the high and midlatitudes of Europe, Asia and North America. Strong changes occur as well over Greenland, Antarctica, the Pacific midlatitudes, and the Southern ocean. For the hydrological maps, however, we note that the most prominent signals occur in monsoonal regions (Fan and van den Dool 2004), in latitudes equatorward of 30°N and S, primarily in the Amazon, Central Africa, South Africa, North Australia, and India. Strong variations are also seen over ice-covered Greenland and Antarctica. It should be noted that results over the ocean, representing changes in residual mass after removal of atmospheric and oceanic signals ideally should not show significant change; in many studies results in these regions are just masked out accordingly (Chambers 2006; Nastula et al. 2009; Nastula and Salstein 2011; Seoane et al. 2011).

Figures 2a–f compare the variability of the χ_1 and χ_2 components of the gravimetric excitation function of polar motion, computed from the GSM coefficients. Results are separated into contributions over the whole globe, over land, and over ocean areas. Figures 2g–l show similar comparisons after removal of trends and seasonal oscillations from the χ_1 and χ_2 components; these are estimated with a least-squares fitting model, comprised of a 1st order polynomial and a sum of sinusoids with periods 1,1/2 and 1/3 years.

First, we should emphasize that significant differences occur in the solutions from the three data centers, even though they are all based on similar procedures applied to the same original RL05 GRACE data (Figs. 2a, b, g, h). Thus, interpreting polar motion with GRACE is difficult. Table 1 is a summary of processing characteristics of the models; perhaps the most significant difference here is the resolution of the background static model (Dahle et al. 2013; Watkins and Yuan 2012; Bettadpur 2012). The biggest difference can be seen in the excitation functions computed from the GFZ and the JPL coefficients. The series obtained from GFZ are clearly smoothed, while the series received from JPL shows the largest variation (Fig. 2g–l, Table 2).

The gravimetric excitation functions separated into contributions from land and over-ocean areas are shown in Fig. 2c–f, i–l. It should be noted that if atmospheric (ECMWF) and oceanic (OMCT) models used by the data centers to estimate the GAC coefficients would describe perfectly the global mass changes, then over-ocean signals would be close to zero. Errors in these models, however, preclude such a state. The resulting residual signal is clearly visible over the ocean area on Fig. 1b. Similarly, a strong signal can be seen in excitation functions computed from the over-ocean area (Fig. 2e, f, k, l). It is interesting that changes over land, which represent the real signal from

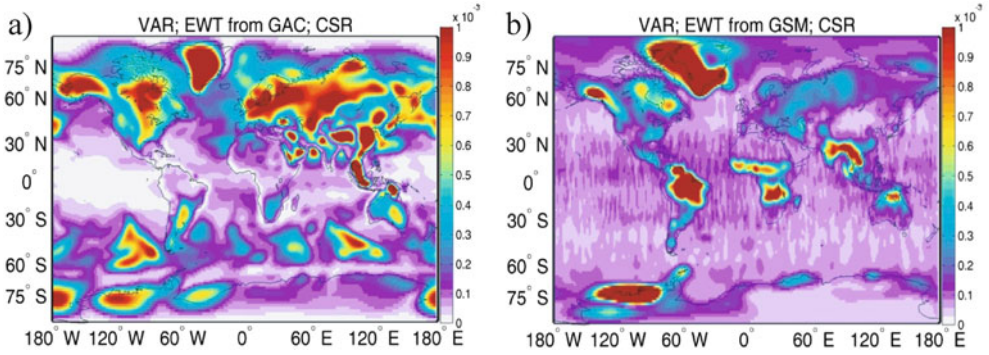

Fig. 1 Equivalent water thickness variance maps computed from GAC (*left panel*) and from GSM (*right panel*) dealiasing coefficients from the CSR data. (Variance maps from the other processing centers are similar). Map on the *left* reflects merged atmospheric and oceanic mass variability, while that on the *right* reflects land-based hydrosphere mass variability (units m^2/grid area, spatial resolution $1° \times 1°$)

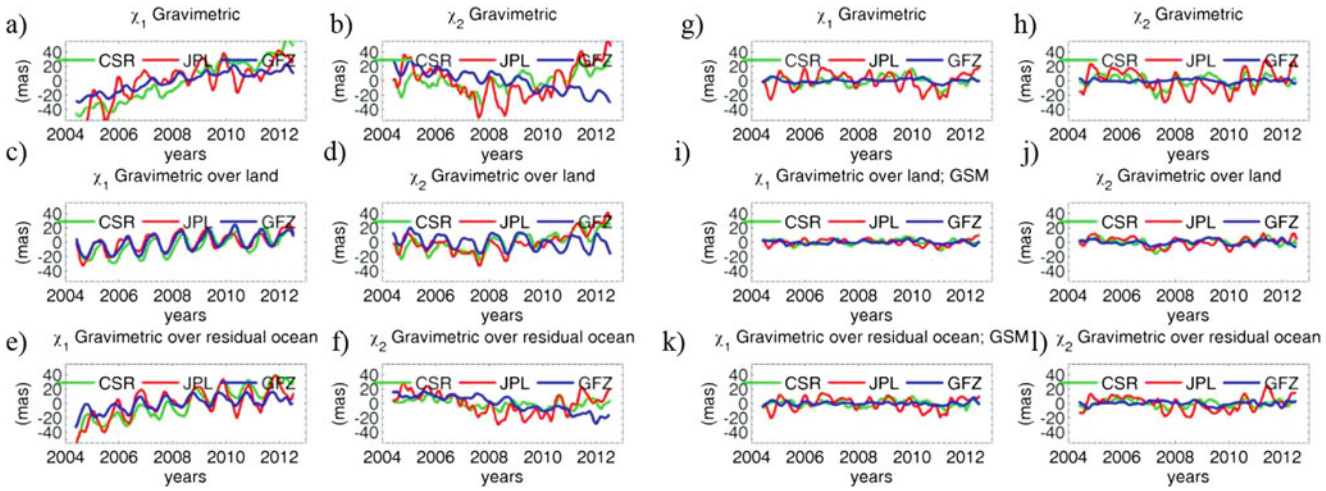

Fig. 2 Comparison of gravimetric polar motion excitation functions computed from EWT maps estimated from the GSM coefficients from the three centers CSR, JPL, and GFZ. The GSM-based series reflect hydrological excitation and are separated into contributions over the whole globe (*top panels*), land area (*middle panels*) and residual ocean area (*bottom panels*). Figures (**g–l**) show the series with trend and seasonal oscillations (annual, semi-annual, 120 days) removed

land-based hydrology, have variations comparable to those computed from over-ocean area and representing the residual signal, especially in case of nonseasonal variations (Table 2). Nonseasonal over-land signals have variances even smaller than variances of the nonseasonal over-ocean signals.

Comparison of the variance values from Table 2 shows that the signals designated for the over-ocean area, rather than the land areas, are, to a greater extent, the source of the spread in results obtained by the data centers. It might be assumed that significant over-ocean area signals are due to leakage effects from the continents. In order to verify this hypothesis we estimated separately the impact of the extension of the land mask further into the ocean shelf areas. Although the magnitude of over-ocean signals in the gravimetric excitation has changed slightly, it remains significant nevertheless.

To check which of these differing gravimetric-based hydrological excitation series is most compatible with the geodetic excitation, we compared them with residuals after the atmospheric and oceanic series are subtracted from the geodetic series (GEOD–AAM–OAM). Fig. 3 shows comparisons of these residuals for two cases: global gravimetric series only, and after trends and seasonal signals are removed. Table 3 shows the resulting correlation coefficients and variances of differences between geodetic residuals and gravimetric excitations for the HAM contributions; these are separated into global, over-land, and over-ocean domains. For one thing, the JPL series has strongest variance of the difference between HAM and the residuals. The CSR series has generally higher correlation coefficients of the χ_2 term. Interestingly though, as can be seen from Fig. 3, all gravimetric functions calculated from gravity data show a trend that is not present in the geodetic residuals. Figure 3 reveals though that relatively good agreement between hydrological excitation and geodetic residuals is obtained from the CSR data, especially for χ_2.

Table 1 Selected attributes of processing methods by the three processing centers CSR, GFZ, JPL

	CSR	GFZ	JPL
Orbit Software	MSODP	MSODP	MIRAGE
Linear Solver Software	AESoP	AESoP	MIRAGE
Indirect J2 Effect	Sun and Moon	Moon only	Moon only
Frame-CTRS	IGS2008	ITRF2008(IGS08)	ITRF-2000
Background static model	GIF48 to degree and order 360	EIGEN-6C to degree and order 200.	GIF48 to degree and order 180
	The normalization conventions are as defined in IERS-2010	The normalization conventions are as defined in IERS-2010	The normalization conventions are as defined in IERS96
Planetary Ephemeris	DE-405	DE 421	DE-405
Ocean Tides Diurnal/Semidiurnal	GOT4.8	EOT11a	GOT4.7
Ocean Tides Long period	FES2004	EOT11a	GOT4.4 and SCEQ (semi-annual and annual)
Rotational Deformation Model	Elastic Model	Elastic Model	Elastic Model
	Contribution to C_{21} & S_{21}	Contribution to C_{21} & S_{21}	Contribution to C_{21} & S_{21}
Precession and Nutation	IAU200A	IAU2006/2000	IAU 1976 Precession
			IAU 1980 Nutation
Sidereal Rotation	$R = R_3(-GST)$	$R = R_3(-ERA)$	$R = R_3(-GST)$

Table 2 Comparison of variances of gravimetric excitation (HAM), computed over the whole globe, land area, and residual ocean area, for detrended and non-seasonal variations (mas^2)

Detrended series							Non-seasonal					
Area	Global		Over land		Over ocean		Global		Over land		Over ocean	
Center	χ_1	χ_2	χ_1	χ_2	χ_1	χ_2	χ_1	χ_2	χ_1	χ_2	χ_1	χ_2
JPL	276.8	546.6	112.2	143.5	225.3	194.4	140.1	234.9	17.0	41.3	73.0	104.0
GFZ	31.2	41.9	94.6	85.6	58.8	20.7	6.2	5.3	5.9	10.9	5	8.2
CSR	49.8	120.0	104.0	88.0	95.2	32.3	46.4	64.9	14.6	26.7	21.9	21.9

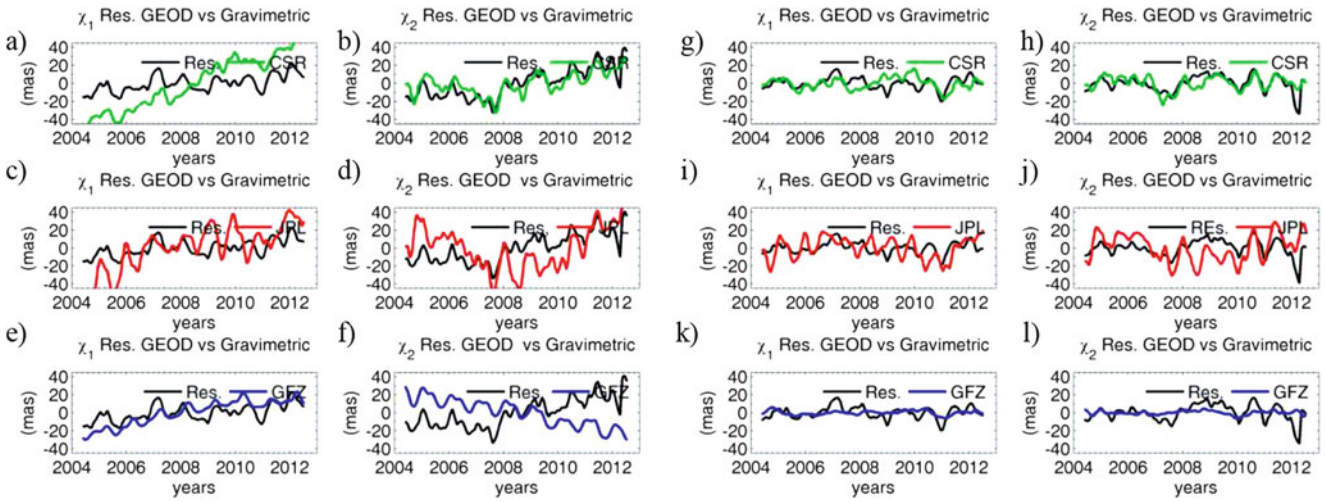

Fig. 3 Comparison of gravimetric excitation functions computed from EWT maps estimated from GSM coefficients from the three centers CSR, JPL, GFZ with geodetic residuals GEOD–AAM–OAM. Each of the series of residuals was determined based on the GAC series from the corresponding center. Figures (**g–l**) show the series with trend and seasonal oscillations (annual, semi-annual, 120 days) removed

This conclusion is confirmed by results shown in both parts of Table 3. The table shows another interesting fact, that excitation functions computed by integration over the land area only are better correlated with the geodetic residuals than are global functions. It is thus clear that the excitation functions obtained from integration

Table 3 Comparison of detrended and non seasonal variations of gravimetric excitation (HAM), computed over the whole globe, land area and residual ocean area with non seasonal variations of geodetic residuals in terms of correlation coefficients and variances of differences

Correlation Coefficients HAM vs. Geodetic residuals							Variance of the difference HAM – Geodetic residuals (mas^2)					
	Global		Over land		Over ocean		Global		Over land		Over ocean	
	χ_1	χ_2	χ_1	χ_2	χ_1	χ_2	χ_1	χ_2	χ_1	χ_2	χ_1	χ_2
Center	Detrended											
JPL	0.31	0.53	0.5	0.57	−0.01	0.39	256	398.2	88.3	108.6	281.6	166.1
GFZ	0.22	0.32	0.44	0.43	−0.26	−0.47	56.3	103.8	86.5	106.9	190.1	184.4
CSR	0.36	0.71	0.4	0.7	−0.22	0.27	82.6	65.1	104	64.7	144.4	102.6
Center	Non-seasonal											
JPL	0.32	0.23	0.32	0.33	0.28	0.14	62.7	256.7	42.2	89.6	84.4	165.8
GFZ	0.3	0.2	0.2	0.37	0.12	−0.03	134.2	84.6	43.5	75.9	45.1	110.6
CSR	0.18	0.58	0.34	0.56	0.27	0.37	40	62.7	40.1	56.6	67.8	72.2

over ocean areas are not correlated with the geodetic residuals.

5 Conclusions

GRACE is a powerful tool to determine time-variable geophysical mass fields, and in particular that of the changing land-based hydrology, which can be estimated otherwise only with complex hydrological models. We found though that these gravimetric-hydrological excitation functions, based on the recent GRACE RL05 release, obtained by the three processing centers, JPL, GFZ, CSR, still differ significantly. One difference noted was that a greater degree of smoothness is exhibited by the GFZ than the JPL and CSR products. Analyses show that the use of these new data to compare with geodetic residuals does not bring significant new results from previous studies (Seoane et al. 2009, 2011; Jin et al. 2010, 2011, 2012; Chen et al. 2012; Nastula et al. 2011), though confirms the current extent of the differences among the series. Overall, though, the best agreement between gravimetric-hydrological excitation functions and geodetic residuals was obtained for the χ_2 component of gravimetric excitation function computed from the CSR data series, and this may be due to some positive attributes in the processing, like different degree and order used in the background static model. It is interesting because the gravity model obtained by CSR is estimated to degree and order 60 only. On the other hand using the gravity model up to degree and order 90 should reduce significantly the expected leakage effect.

By using the EWT to determine gravimetric functions we can estimate the separate contributions of the land and the residual over-ocean area to the global changes. We found that residual changes computed from the over-ocean area make an important contribution to the gravimetric-hydrological excitation. However these somewhat unrealistic signals are much less correlated with the geodetic residuals than are the gravimetric functions computed over land. In addition, the over-ocean functions differ from each other more than do the functions calculated from land area. Some of the distinctions may occur because the resolution of land-based hydrology may be spilling over into the bordering areas of the oceans, as we note. Documenting the current level of uncertainty will be important in attributing the origin of geophysical polar motion excitation for now and future solutions.

Acknowledgements The research reported here was supported by the Polish National Science Centre, through the project No 2012/05/B/ST10/02132, and by the U.S. National Science Foundation under project ATM-0913780. Authors thank the anonymous reviewers for their helpful comments.

References

Barnes RTH, Hide R, White AA, Wilson CA (1983) Atmospheric angular momentum fluctuations, length-of-day changes and polar motion. Proc R Soc Lond A 38731–38773. doi:10.1098/rspa.1983.0050

Bettadpur S (2012) CSR level-2 processing standards document for product release 05 GRACE 327–742. http://podaac.jpl.nasa.gov/gravity/grace-documentation

Chambers DP (2006) Evaluation of new GRACE time-variable gravity data over the ocean. Geophys Res Lett 33(17), LI7603

Chen JL, Wilson CR (2005) Hydrological excitation of polar motion, 1993–2002. Geophys J Int 160:833–839. doi:10.1111/j.1365-246X.2005.02522

Chen JL, Wilson CR (2008) Low degree gravity changes from GRACE, earth rotation, geophysical models, and satellite laser ranging. J Geophys Res 113:B06402. doi:10.1029/2007JB005397

Chen JL, Wilson CR, Tapley BD, Ries JC (2004) Low degree gravitational changes from GRACE: validation and interpretation. Geophys Res Lett 31(22), L22607

Chen JL, Wilson CR, Zhou YH (2012) Seasonal excitation of polar motion. J Geodyn 62:8–15. doi:10.1016/j.jog.2011.12.002

Dahle C, Flechtner F, Gruber C, König D, König R, Michalak G, Neumayer KH (2013) GFZ level-2 processing standards document for product release 05 GRACE 327–743. http://podaac.jpl.nasa.gov/gravity

Eubanks TM (1993) Variations in the orientation of the earth. In: Smith DE, Turcotte DI (eds) Contributions of space geodesy to geodynamics-earth dynamics, Geodynamic Series, vol 24. AGU, Washington DC, 1–54

Fan Y, van den Dool H (2004) Climate prediction center global monthly soil moisture data set at 0.5 resolution for 1948 to present. J Geophys Res 109, D10102. doi:10.1029/2003JD004345

Flechtner F (2004) GRACE AOD1B product description document, GRACE 327–750 (GR-GFZ-AOD-0001)

Gambis D (2004) Monitoring earth orientation at the IERS using space-geodetic observations. J Geod 78:295-3-2

Jin SG, Chambers DP, Tapley BD (2010) Hydrological and oceanic effects on polar motion from GRACE and models. J Geophys Res 115, B02403. doi:10.1029/2009JB006635

Jin SG, Zhang LJ, Tapley BD (2011) The understanding of length-of-day variations from satellite gravity and laser ranging measurements. Geophys J Int 184(2):651–660. doi:10.1111/j.1365-246X.2010.04869.x

Jin SG, Hassan AA, Feng GP (2012) Assessment of terrestrial water contributions to polar motion from GRACE and hydrological models. J Geodyn 62:40–48. doi:10.1016/j.jog.2012.01.009

Nastula J, Salstein DA (2011) Regional geophysical excitation functions of polar motion over land areas. In: Geodesy for planet earth: Proceedings of the 2009 IAG symposium, Buenos Aires, Argentina, 31 August–4 September 2009 (IAG Symposia), vol 136. 491–497

Nastula J, Ponte RM, Salstein DA (2007) Comparison of polar motion excitation series derived from GRACE and from analyses of geophysical fluids. Geophys Res Lett 34, L11306. doi:10.1029/2006GL028983

Nastula J, Salstein DA, Kolaczek B (2009) Patterns of atmospheric excitation functions of polar motion from high-resolution regional sectors. J Geophys Res 114, B04407. doi:10.1029/2008JB005605

Nastula J, Pasnicka M, Kolaczek B (2011) Comparison of the geophysical excitations of polar motion from the period: 1980.0–2009.0. Acta Geophys 59(3):561–577

Quinn K, Ponte RM (2008) Estimating weights for the use of time-dependent gravity recovery and climate experiment data in constraining ocean models. J Geophys Res 113, C12013. doi:10.1029/2008JC004903

Seoane L, Nastula J, Bizouard C, Gambis D (2009) The use of gravimetric data from GRACE mission in the understanding of polar motion variations. Geophys J Int 178:614–622

Seoane L, Nastula J, Bizouard C, Gambis D (2011) Hydrological excitation of polar motion derived from GRACE gravity field solutions. Int J Geophys. doi:10.1155/2011/174396

Seoane L, Biancale R, Gambis D (2012) Agreement between earth's rotation and mass displacement as detected by GRACE. J Geodyn 62:49–55

Tapley BD, Bettadpur S, Ries JC et al (2004) GRACE measurements of mass variability in the earth system. Science 3055683:503–505. doi:10.1126/science.1099192

Watkins M, Yuan D (2012) JPL level-2 processing standards document for product release 05 GRACE 327–744. http://podaac.jpl.nasa.gov/gravity

Rapid UT1 Estimation by Combining VLBI Intensives with GNSS

Tobias Nilsson, Maria Karbon, Benedikt Soja, Virginia Raposo-Pulido, Robert Heinkelmann, Julian Mora Diaz, Cuixian Lu, Li Liu, and Harald Schuh

Abstract

We present a Kalman filter for combining dUT1 from the VLBI Intensive sessions with GNSS results for rapid estimation of dUT1. In order to be able to also combine polar motion, pre-reduced normal equations for the Intensive sessions are used in the Kalman filter. We validate our results by comparing with dUT1 estimates from standard global 24-h VLBI sessions. It is found that the Kalman filter is able to use the polar motion measured by GNSS to properly correct the errors in dUT1 caused by inaccurate a priori polar motion. Furthermore, we investigate how the coordinates of the Tsukuba VLBI station can be handled in the analysis after the Tōhoku (Japan) Earthquake in 2011.

Keywords

Combination • Earth rotation • Intensives • Kalman filtering • VLBI

1 Introduction

Very Long Baseline Interferometry (VLBI) is the only space geodetic technique able to measure Universal Time (dUT1=UT1-UTC). Satellite techniques – such as Global Navigation Satellite Systems (GNSS) – are only capable of estimating the length of day (LOD), i.e. the negative time derivative of dUT1. Normally two to three 24 h long global geodetic VLBI sessions are performed every week with the purpose of determining dUT1 and the other Earth Orientation Parameters (EOP). Typically the results from these sessions are available after 1 or 2 weeks, sometimes even later.

In order to provide dUT1 estimates with lower latency and higher temporal resolution, special 1 h long VLBI sessions are performed every day with the goal of estimating dUT1: the so-called Intensive VLBI sessions (Robertson et al. 1985). These sessions normally include only two (sometimes three) stations on a long East-West baseline. The results from these sessions are typically available within 1 or 2 days, however it has been demonstrated that it is possible to have the results within a few minutes if the observations are transferred electronically to the correlator in real-time (Sekido et al. 2008). On weekdays the observations are normally made with the baseline Wettzell (Germany) – Kokee Park (Hawaii, USA), and on weekends with the baseline Wettzell – Tsukuba (Japan). Additionally, since August 2007 there is an Intensive session on Monday mornings including three stations: Wettzell, Tsukuba, and Ny-Ålesund (Spitsbergen, Norway). Occasionally, e.g. when one of the stations is down for repair, other stations are also participating. The stations which have contributed to the Intensives 2008–2012 are shown in Fig. 1.

Due to their low latency and high resolution, the Intensives are very important for the estimation of dUT1. Thus it is important to achieve the highest possible accuracy of the dUT1 values estimated from these sessions (e.g. the IERS retreat 2013[1] identified the improvement of the dUT1

T. Nilsson (✉) • M. Karbon • B. Soja • V. Raposo-Pulido • R. Heinkelmann • J. Mora Diaz • C. Lu • L. Liu • H. Schuh
Department 1: Geodesy and Remote Sensing, Helmholtz Centre Potsdam, GFZ German Research Centre for Geosciences, 14473 Potsdam, Germany
e-mail: nilsson@gfz-potsdam.de

[1] http://www.iers.org/nn_10902/IERS/EN/Organization/Workshops/Retreat2013.html.

© Springer International Publishing Switzerland 2015

C. Rizos, P. Willis (eds.), *IAG 150 Years*, International Association of Geodesy Symposia 143,
DOI 10.1007/1345_2015_105

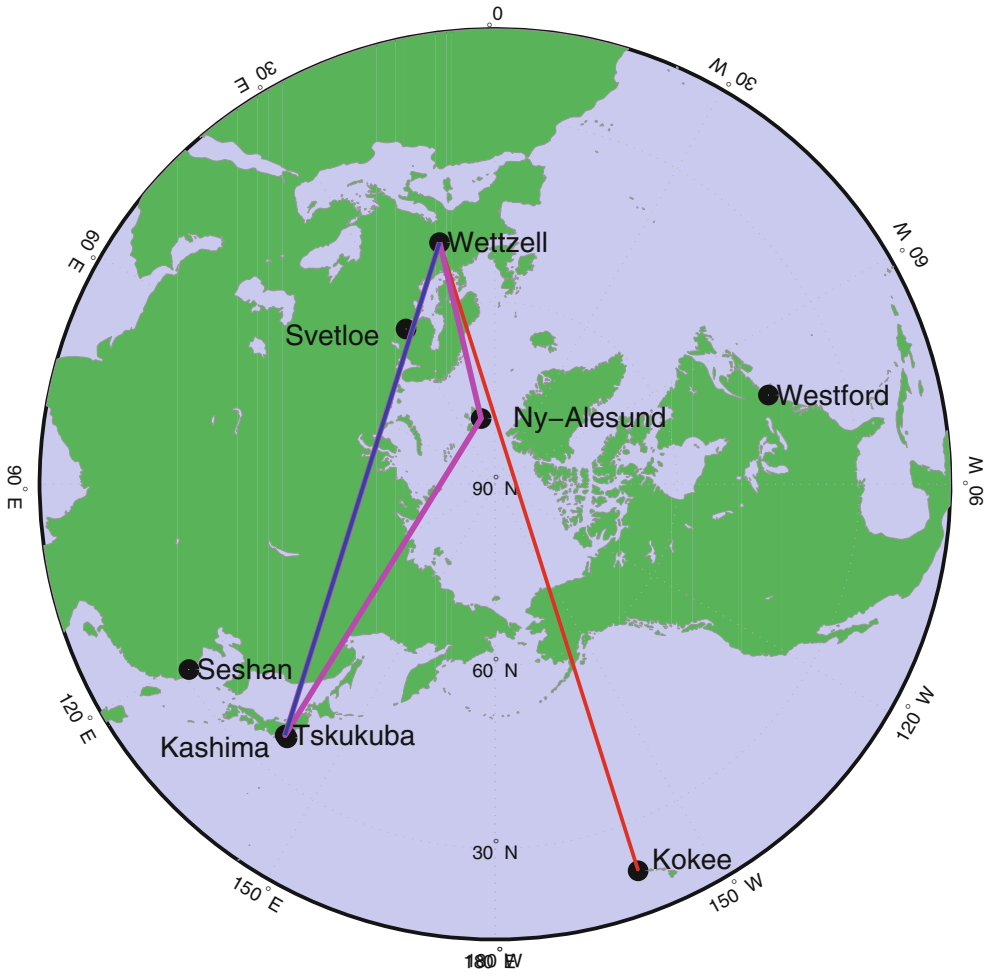

Fig. 1 The stations contributing to the VLBI Intensives 2008–2012. The *red*, *blue*, and *magenta lines* show the baselines used in the INT1 (Wettzell–Kokee), INT2 (Wettzell–Tsukuba), and INT3 (Wettzell, Tsukuba, Ny-Ålesund) sessions, respectively

estimation from the Intensives as a major topic for the future). The accuracy of the Intensive sessions are however limited due to several reasons. Since the Intensive sessions are only 1 h long they typically include only 20–40 observations. This makes the solution relatively weak, since apart from dUT1 other parameters, like clocks and zenith wet delays, also need to be estimated. Furthermore, the sky distribution of the celestial radio sources is relatively poor since normally only one baseline is used and a source needs to be simultaneously visible from both stations of the baseline. Thus, it is not possible to estimate nuisance parameters like the tropospheric delay accurately. Furthermore, since typically only one baseline is used it is impossible to estimate the full set of EOP. Normally only dUT1 is estimated, while polar motion and precession/nutation are fixed to a priori values. Errors in these a priori values will cause errors in the dUT1 estimates (Nothnagel and Schnell 2008). It is also not possible to estimate the station coordinates, hence these are also fixed to a priori values. This is normally not a big problem as the coordinates are well known since the stations in use have a long history of observations. However, if this is not the case, like for Tsukuba after the 2011 Tōhoku Earthquake, it could cause systematic effects and deteriorate the results.

External information about polar motion can be obtained from other techniques, like GNSS, with about the same latency as the data from the Intensives. GNSS also provides measurements of the LOD, which can be used for constraining the dUT1 variations for short periods of a few days. Thus, one way to improve the accuracy of the Intensives would be to combine with GNSS results. There have been a few studies on this topic, for example Thaller et al. (2008) combined the two techniques at the normal equation level and found a benefit of including polar motion from GNSS.

In this work we make such a combination by applying a Kalman filter. This filter is designed to produce rapid results, i.e. as soon as the data from an Intensive are available, these could be fed into the filter to produce a new dUT1 estimate.

The design of the Kalman filter is presented in Sect. 2. We test the filter using data from the period 2008–2012. The data analysis and results are presented in Sects. 3 and 4, respectively. Finally, the conclusions are given in Sect. 5.

2 The Kalman Filter

In a Kalman filter the estimation of the unknown parameters, $\mathbf{x}$, are done sequentially, epoch by epoch (Brown and Hwang 1997). It is assumed that the temporal variation of $\mathbf{x}$ is described by:

$$\mathbf{x}_k = F_k \mathbf{x}_{k-1} + \mathbf{w}_k \tag{1}$$

where $\mathbf{x}_{k-1}$ and $\mathbf{x}_k$ are the values of $\mathbf{x}$ at epochs t_{k-1} and t_k, respectively, F_k is the state transition matrix, and $\mathbf{w}_k$ is the process noise. Knowing F_k, we can calculate the predicted value of $\mathbf{x}_k$, $\tilde{\mathbf{x}}_k$, based on $\mathbf{x}_{k-1}$:

$$\tilde{\mathbf{x}}_k = F_k \mathbf{x}_{k-1} \tag{2}$$

$$\tilde{P}_k = F_k \, P_{k-1} \, F_k^T + Q_k \tag{3}$$

where $\tilde{P}_k$, P_{k-1}, and Q_k are the variance-covariance matrices of $\tilde{\mathbf{x}}_k$, $\mathbf{x}_{k-1}$, and $\mathbf{w}_k$, respectively.

At epoch t_k we have the measurements $\mathbf{z}_k$, which are related to $\mathbf{x}_k$ by:

$$\mathbf{z}_k = H_k \mathbf{x}_k + \mathbf{v}_k \tag{4}$$

where H_k is the observation matrix and $\mathbf{v}_k$ the observation noise. The Kalman filter combines $\tilde{\mathbf{x}}_k$ and $\mathbf{z}_k$ in an optimum way to estimate $\mathbf{x}_k$ and its variance-covariance matrix P_k:

$$P_k = \left(H_k^T \, R_k^{-1} \, H_k + \tilde{P}_k\right)^{-1} \tag{5}$$

$$\mathbf{x}_k = \tilde{\mathbf{x}}_k + P_k \, H_k^T \, R_k^{-1} \, (z_k - H_k \tilde{\mathbf{x}}_k) \tag{6}$$

Here, R_k denotes the variance-covariance matrix of $\mathbf{v}_k$.

In this work we estimate polar motion, $p = x_p - i\, y_p$, and dUT1, U, in the Kalman filter. Thus we need models for the temporal variations of these parameters in order to obtain F_k. As commonly done when estimating EOP in a Kalman filter, we apply the Euler-Liouville equation for this purpose (Morabito et al. 1988):

$$\frac{\partial U}{\partial t} = -\frac{\delta \Lambda}{\Lambda_0} \tag{7}$$

$$\frac{\partial p}{\partial t} = i\, \sigma_{ch} (p - \chi) \tag{8}$$

where $\delta\Lambda$, Λ_0 is the excess and nominal LOD, respectively, σ_{ch} the frequency of the Chandler wobble, and $\chi = \chi_x + i\,\chi_y$ is the polar motion excitation function. In the Kalman filter we thus estimate six parameters: U, x_p, y_p, $\delta\Lambda$, χ_x, and χ_y. For the temporal variations of $\delta\Lambda$ and χ we assume random walk processes with power spectral densities of $0.0036\,\mathrm{ms}^2/\mathrm{day}^3$ and $246.6\,\mathrm{mas}^2/\mathrm{day}$, respectively (Morabito et al. 1988).

3 Data Analysis

We have tested the Kalman filter by combining data from the Intensives with GNSS data for the period 2008–2012. We analysed all good quality Intensive sessions from this period (in total 1680 sessions) with the Vienna VLBI Software (VieVS, Böhm et al. 2012). The a priori polar motion and dUT1 values were obtained from the latest IERS Bulletin A prediction, while the celestial pole offsets were obtained by extrapolating the values from the IERS C04 series (Bizouard and Gambis 2009) from the period up to 1 month before the Intensive session. The extrapolation was made assuming that the celestial pole offsets varies periodically with the free core nutation frequency. Thus, the a priori EOP correspond to what typically is available in real time. The other a priori parameters also correspond to what can be available within 1 to 2 days.

In the analysis we set up the normal equations for estimation of a clock offset, clock drift, tropospheric zenith wet delays (one estimate per station), dUT1, and polar motion. For a single-baseline session it is impossible to estimate both polar motion and dUT1 since the equation system will be singular. Thus we included the normal equations directly in the Kalman filter. This is possible by identifying the terms $H_k^T R_k^{-1} H_k$ and $H_k^T R_k^{-1} z_k$ as the normal equation matrix and the right hand side vector, respectively (after pre-reducing the tropospheric delays and clocks).

For the GNSS data, we used the IGS rapid product (Dow et al. 2009). This provides polar motion and LOD estimates with daily resolution (estimation epoch is at noon). The estimates are available with a delay of less than 1 day, i.e. similar to or faster than the Intensives.

In order to check the results from the Kalman filter, we made a reference solution by analysing all good-quality global 24 h VLBI sessions from the period 2008–2012 with VieVS (in total 523 sessions). For these sessions we estimated all five EOP with daily resolution, tropospheric zenith wet delays and clocks with 1 h resolution, tropospheric gradients with 6 h resolution, and daily station coordinate offsets.

4 Results

Figure 2 shows differences between the dUT1 estimates and the results from the global 24 h VLBI sessions. The differences were calculated at the mean epochs of the 24 h VLBI sessions (these are typically about 11 h after the last Intensive session). Here the data of 168 Intensive sessions

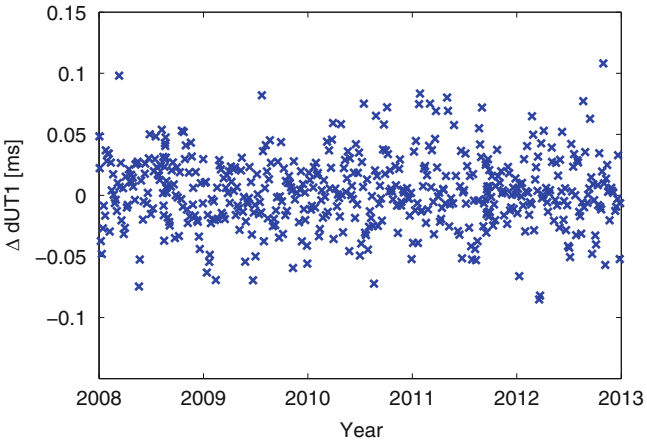

Fig. 2 Differences between the Kalman filter dUT1 estimates and the results from the analysis of the 24 h global VLBI sessions

Table 1 Weighted mean (WM) and weighted RMS (WRMS) differences between dUT1 estimates from the Kalman filter and the 24 h global VLBI sessions

Solution	WM (μs)	WRMS (μs)
Intensives	2.3	57.7
Intensives + GNSS LOD	2.0	40.1
Intensives + GNSS PM	0.9	36.0
Intensives + GNSS LOD & PM	3.1	26.4

from the period after the 11 March 2011 Tōhoku Earthquake containing the station Tsukuba were excluded. The reason is that the coordinates of Tsukuba are not very well known after the Earthquake. For a discussion on how these sessions could be included in the Kalman filter, see Sect. 4.1.

Table 1 shows the weighted mean (WM) and Weighted Root Mean Square (WRMS) differences between dUT1 estimates from the Kalman filter and the global 24 h VLBI sessions. The results for four different Kalman filter solutions are shown, including different amounts of GNSS data. The worst results (highest WRMS) are obtained when using no GNSS data at all (in this case the polar motion is fixed to the a priori values in the Kalman filter). When including LOD or polar motion from GNSS the results are improved, and consequently the best results are obtained when including both LOD and polar motion in the Kalman filter.

The improvement in the WRMS differences seen when including LOD from GNSS is mainly because these values are the mean epochs of the 24 h VLBI sessions, and these are different from the epochs of the Intensive sessions. Thus, the Kalman filter has to extrapolate the dUT1 from the Intensive epoch to the epoch of the 24 h VLBI session, and for this, accurate LOD is beneficial. If we instead compare the results at the epochs of the Intensive sessions that are inside a 24 h VLBI session, we do not see such a significant improvement when including GNSS LOD (WRMS difference decreases from 22.1 to 20.2 μs). The improvement seen when including polar motion from GNSS is because the a priori polar motion being used in the Intensives data analysis is inaccurate. The IERS Bulletin A predictions have an accuracy of about 2 mas (4 days prediction); using the results of Nothnagel and Schnell (2008) this would cause dUT1 errors of about 33 μs for INT1 sessions and 62 μs for INT2 sessions. The Kalman filter is able to correct these errors with the more accurate polar motion from GNSS.

4.1 The 2011 Tōhoku Earthquake

On 11 March 2011, a magnitude 9.0 Earthquake occurred near the Pacific coast of Tōhoku, Japan. As a consequence of this Earthquake the Tsukuba VLBI station was moved about 70 cm towards the East, followed by a further 20 cm post-seismic motion to the East over the next 1.5 years. This caused a big problem for the Intensive sessions including Tsukuba since the station position needs to be very accurately known in the data analysis; from geometrical considerations we would expect that an error of 1 cm in the East component of one station's coordinates will result in a dUT1 error of about 10 μs.

One possibility to obtain the post-Earthquake coordinates of Tsukuba is to estimate them in the Kalman filter. Normally, it is impossible to estimate both the coordinates of one station and dUT1 in the data analysis of a single-baseline VLBI session. However, with the Kalman filter it is possible since it combines the measurements of an Intensive session with the predictions of the unknown parameters (e.g. dUT1) from the previous epochs. Thus, just after the Earthquake the filter will tend to trust the predictions of dUT1 and use the Intensive data to correct the Tsukuba station position. As time goes on, the accuracy of the Tsukuba station position will increase, then this station will again contribute to the dUT1 estimation. In the Kalman filter we modelled the post-Earthquake position of Tsukuba as an offset to its original position plus a varying velocity. The velocity was modelled as a random walk process with power spectral density of 50 $cm^2/year^3$. To further enhance the estimation of the Tsukuba displacement, the positions observed by GNSS can be included as additional observations in the Kalman filter.

Since the Intensives with Tsukuba are normally performed on weekends, it is not feasible to check the accuracy of this method using the normal 24 h sessions since these are normally not observed on weekends. However, on some weekends after the 2011 Tōhoku Earthquake extra Intensive sessions with the Wettzell–Kokee Park baseline were observed, just before the Wettzell–Tsukuba Intensive (in total 49 sessions). Thus we can use the results from these extra Intensives to check the results of the regular Intensives including Tsukuba. We made a reference Kalman filter

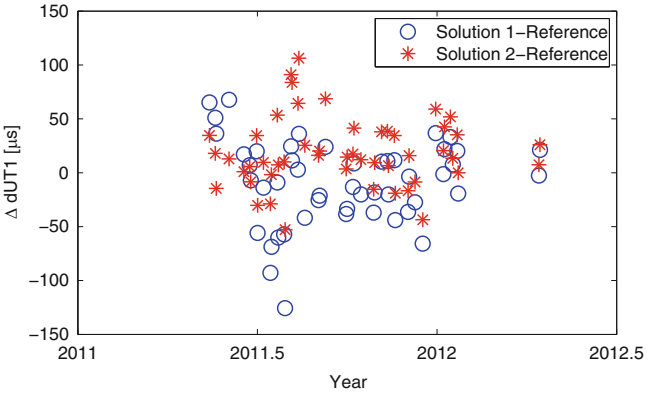

Fig. 3 Differences in dUT1 between Kalman filter solution including the post-Earthquake Intensives with Tsukuba, and a reference solution where these sessions were excluded (see text). In solution 1 the post-Earthquake position of Tsukuba was estimated only from the Intensive data, in solution 2 also the displacement measured by GNSS was used

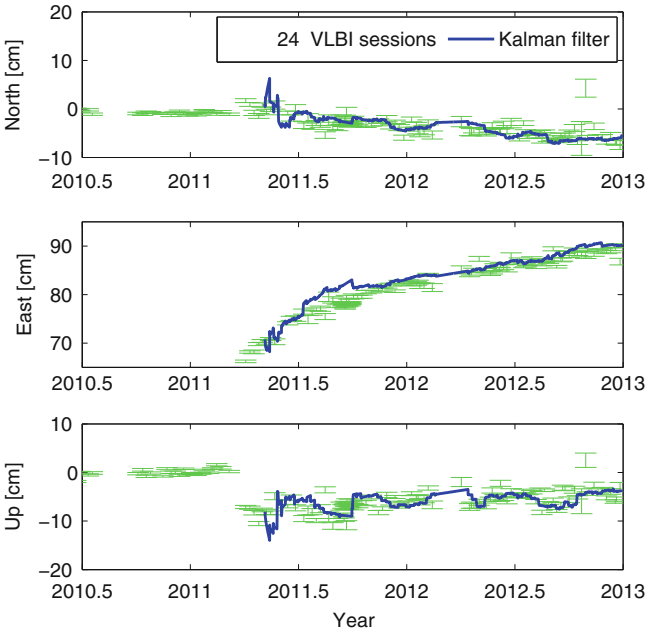

Fig. 4 The displacement of the Tsukuba VLBI station after the 2011 Tōhoku Earthquake, estimated from the 24 h VLBI sessions (*green*) and from the Kalman filter using data from the Intensives (*blue*)

solution where the post-Earthquake Intensives with Tsukuba were excluded. Then two solutions including these sessions but excluding the extra Wettzell-Kokee Park Intensives. In the first solution the coordinates of Tsukuba were estimated only using the Intensive data, in the second solution the position changes obtained by GNSS were also included, i.e. we assumed that the displacements of the GNSS station and the VLBI antenna were identical. We then calculated the differences between the two solutions and the reference solution at the days of the extra Wettzell–Kokee Park Intensives. These differences are shown in Fig. 3. If the coordinates of Tsukuba would be accurately corrected, we would expect all three solutions to have the same accuracies at these time epochs, hence the differences should be small. The WRMS differences were 37.7 and 33.6 μs for the first and second solution, respectively. The second solution is slightly better than the first one for the months just after the Earthquake, while at later epochs the two solutions produce similar results. The reason for the worse results by the fist solution in the months following the Earthquake is that it takes time for the estimated Tsukuba position to converge to an accurate value. This convergence is faster if GNSS data is included.

Another way to check the accuracy is to investigate the coordinates estimated by the Kalman filter. The post-Earthquake coordinates obtained when only estimating them from the Intensive data are shown in Fig. 4. For comparison, the coordinates obtained from the analysis of the global 24 h VLBI sessions are shown. Just after the Earthquake the Kalman filter needs some time to converge to the correct position. Thus, there is an overestimation of the East displacement in the beginning by about 5 cm. After a few months, however, the coordinates agree within the error bars (1-σ formal errors) of those from the 24 h VLBI sessions. If the coordinates form GNSS are also included in the Kalman filter, the estimated coordinates convergence much faster; thus the agreement with the 24 h VLBI sessions is good for all post-Earthquake epochs.

5 Conclusions and Outlook

The Kalman filter presented in this work is able to combine the data from the VLBI Intensives with GNSS results to provide accurate dUT1 estimates. In case inaccurate a priori polar motion is used in the data analysis of the Intensives, the Kalman filter is able to correct the errors caused by these using the more accurate GNSS polar motion estimates. Furthermore, the LOD from GNSS helps constraining the short period dUT1 variations and are important for interpolation/extrapolation of the dUT1 estimates from the epochs of the Intensives to other epochs. The Kalman filter is also able to estimate non-linear station motions, occurring e.g. after an Earthquake. Hence, we recommended to use the method presented in this paper (or a similar one) when combining data from the Intensives with the results from other techniques, like GNSS. Many IVS Analysis Centers already provide normal equations for the Intensives including polar motion and station coordinates.

Alternatively, a simpler approach for correcting the polar motion would be to include the GNSS polar motion directly as a priori polar motion in the data analysis of the Intensives. The advantage of doing the correction in the Kalman filter is that the filter automatically extrapolates the polar motion estimates from the GNSS to the Intensive epochs. In case no

recent GNSS data are available, the filter will use the older information it has. The formal errors of dUT1 provided by the filter will appropriately take into account the uncertainties in the polar motion, i.e. if the polar motion estimates are very uncertain the formal error of dUT1 will increase. Furthermore, the Intensives may also contribute slightly for improving the polar motion estimates, at least those Intensives which include three (or more) stations (although the impact is probably very small).

The Kalman filter could easily be extended to include more parameters and/or more advanced modelling options. One possibility is to include tropospheric delays in the filter. The troposphere is a major error source for the Intensives (Nilsson et al. 2011), hence including external information about these from e.g. GNSS could improve the dUT1 accuracy. Initial tests have shown that the improvement is relatively small, however more investigations are needed. It is also possible to take into account possible systematic errors, etc. in the GNSS or VLBI measurements, e.g. include modelling of a GNSS LOD bias (Senior et al. 2010). Furthermore, additional data could be included in the Kalman filter, for example atmospheric excitations from numerical weather prediction models (Freedman et al. 1994) or observations from ring laser gyroscopes (Nilsson et al. 2012).

Acknowledgements We are grateful to the VLBI stations contribution to the Intensives and to the International VLBI Service for Geodesy and Astrometry (Schuh and Behrend 2012) for providing the data. This work was supported by the Austrian science fund (FWF), project number P24187-N21.

References

Bizouard C, Gambis D (2009) The combined solution C04 for Earth orientation parameters consistent with international terrestrial reference frame 2005. In: Geodetic reference frames, IAG symposium, vol 134. Springer, Munich, pp 265–270. doi:10.1007/978-3-642-00860-3_41

Böhm J, Böhm S, Nilsson T, Pany A, Plank L, Spicakova H, Teke K, Schuh H (2012) The new Vienna VLBI software. In: Kenyon S, Pacino MC, Marti U (eds) IAG scientific assembly 2009 (no. 136 in international association of geodesy symposia). Springer, Buenos Aires, pp 1007–1011. doi:10.1007/978-3-642-20338-1_126

Brown RG, Hwang PYC (1997) Introduction to random signals and applied Kalman filtering, 3rd edn. Wiley, London

Dow JM, Neilan RE, Rizos C (2009) The international GNSS service in a changing landscape of global navigation satellite systems. J Geodesy 83:191–198. doi:10.1007/s00190-008-0300-3

Freedman AP, Steppe JA, Dickey JO, Eubanks TM, Sung LY (1994) The short-term prediction of universal time and length of day using atmospheric angular momentum. J Geophys Res 99(B4):6981–6996. doi:10.1029/93JB02976

Morabito DD, Eubanks TM, Steppe JA (1988) Kalman filtering of earth orientation changes. In: Babcock A, Wilkins GA (eds) The Earth's rotation and reference frames for geodesy and geodynamics. Reidel, Dordrecht/Holland, pp 257–267

Nilsson T, Böhm J, Schuh H (2011) Universal time from VLBI single-baseline observations during CONT08. J Geodesy 85(7):415–423. doi:10.1007/s00190-010-0436-9

Nilsson T, Böhm J, Schuh H, Schreiber U, Gebauer A, Klügel T (2012) Combining VLBI and ring laser observations for determination of high frequency Earth rotation variation. J Geodyn 62:69–73. doi:10.1016/j.jog.2012.02.002

Nothnagel A, Schnell D (2008) The impact of errors in polar motion and nutation on UT1 determinations from VLBI intensive observations. J Geodesy 82:863–869. doi:10.1007/s00190-008-0212-2

Robertson DS, Carter WE, Campbell J, Schuh H (1985) Daily Earth rotation determinations from IRIS very long baseline interferometry. Nature 316:424–427

Schuh H, Behrend D (2012) VLBI: A fascinating technique for geodesy and astrometry. J Geodyn 61:68–80. doi:10.1016/j.jog.2012.07.007

Sekido M, Takiguchi H, Koyama Y, Kondo T, Haas R, Wagner J, Ritakari J, Kurihara S, Kokado K (2008) Ultra-rapid UT1 measurement by e-VLBI. Earth Planets Space 60:865–870

Senior K, Kouba J, Ray J (2010) Status and prospects for combined GPS LOD and VLBI UT1 measurements. Artif Satell 45(2):57–73. doi:10.2478/v10018-010-0006-7

Thaller D, Tesmer V, Dach R, Krügel M, Rothacher M, Steigenberger P (2008) Combining VLBI intensive with GPS rapid solutions for deriving a stable UT time series. In: Finkelstein A, Behrend D (eds) Proceedings of the fifth IVS general meeting: measuring the future, pp 8–13. http://ivscc.gsfc.nasa.gov/publications/gm2008/

Reference Frame-Induced Errors in VLBI Earth Orientation Determinations

Robert Heinkelmann, Maria Karbon, Tobias Nilsson, Virginia Raposo-Pulido, Benedikt Soja, and Harald Schuh

Abstract

This paper presents how Very Long Baseline Interferometry (VLBI) realizes the Earth Orientation Parameters (EOP) and which accuracy can be theoretically reached depending on the involved reference frames. The definition of EOP is based on the transformation between the Geocentric Celestial Reference System (GCRS) and the International Terrestrial Reference System (ITRS). The ITRS part is in common for all the space geodetic techniques. The method applied here utilizes the uncertainty of the orientation of the actual set of radio sources of a VLBI observing session related to GCRS and the uncertainty of the orientation of the set of terrestrial network stations related to ITRS for the assessment of the uncertainty of the EOP. The uncertainty of the initial orientation of the GCRS is about 35 μas and the uncertainty of the orientation stability is about 0.7 μas/year. In addition small systematics are present due to the aberration caused by the rotation of our galaxy at the level of 5 μas/year. The uncertainty of the initial orientation of the ITRS of about 800 μas is about 20 times larger, while the uncertainty of the orientation rate of about 80 μas/year is about 100 times larger compared to the corresponding celestial values. The initial orientation and the orientation stability of ITRS could be much more precisely defined by constraining it to the GCRS via the EOP.

Keywords

Earth orientation parameters • Reference frames • Reference systems • VLBI

1 Introduction

With the Global Geodetic Observing System (GGOS) the International Association of Geodesy (IAG) has defined its main project in the field of space geodesy. Requirements for the future global terrestrial reference frame are specified to be 1 mm position accuracy and 0.1 mm/year velocity accuracy (Plag and Pearlman 2009). An angle of 32 μas projected onto the Earth's equator is approximately equal to 1 mm. This ambitious goal can only be reached employing a new generation of space geodetic observing systems. The geodetic Very Long Baseline Interferometry (VLBI) community, namely the International VLBI Service for Geodesy and Astrometry (IVS), has therefore launched developments towards a new VLBI system: VLBI2010 (Behrend et al. 2008). In the future this new equipment will form a new network of VLBI2010 antennas, called VGOS (VLBI2010 Geodetic Observing System). The progress of this observing system is definitely an important step towards the realization of the GGOS goals. Besides, it has to be assessed whether the involved datum definitions and analysis procedures hold for the aforementioned accuracy requirements as well. In this paper we investigate to what extent the Earth orientation parameters (EOP) determined by VLBI are affected by the

R. Heinkelmann (✉) • M. Karbon • T. Nilsson • V. Raposo-Pulido • B. Soja • H. Schuh
Department 1: Geodesy and Remote Sensing, Helmholtz Centre Potsdam, GFZ German Research Centre for Geosciences, 14473 Potsdam, Germany
e-mail: heinkelmann@gfz-potsdam.de

© Springer International Publishing Switzerland 2015

C. Rizos, P. Willis (eds.), *IAG 150 Years*, International Association of Geodesy Symposia 143,
DOI 10.1007/1345_2015_158

uncertainty of the initial orientation and orientation stability of the involved reference systems and frames.

The EOP, by definition, are the transformation parameters between the Geocentric Celestial Reference System (GCRS) and the International Terrestrial Reference System (ITRS). This can be symbolically written as (IERS Conventions 2010)

$$[GCRS] = Q\,(X, Y, \ldots)\; R\,(ERA)\; W\,\left(x_p, y_p, \ldots\right)\,[ITRS] \tag{1}$$

where the time dependent rotation matrices are depending on the EOP, the celestial pole coordinates, the Earth rotation angle, which is linear proportional to the time scale realized by Earth rotation $UT1$, and the terrestrial pole offsets. In general, in three dimensional space a transformation possibly includes in addition three translations and a factor or tensor which relates the metrics of the systems to each other. In the case of VLBI, the translation and metric are separately treated in the theoretical VLBI model by a Lorentz transformation (cf. IERS Conventions 2010). Consequently, GCRS and ITRS have the same origin and thus the same metric and differ only in terms of the orientation. This difference in orientation is defined as Earth orientation. Earth orientation is modelled by three consecutive rotation matrices as shown above. The IERS Conventions (2010) say about the above equation that '[...] it should be clear that the numerical implementation of those formulas involves the IAU/IUGG adopted realization of those reference systems, i.e. the International Terrestrial Reference Frame (ITRF) and the International Celestial Reference Frame (ICRF) [...]'. In the following sections we will outline the realization of the systems (GCRS, ITRS) by VLBI assessing the uncertainties of the initial orientation and of the orientation rate of the involved frames, which are the basis for the accuracy of the EOP.

2 The Realization of the GCRS Orientation by VLBI

The complete chain of systems/frames from the definition (GCRS) to the actual realization (VLBI session CRF) is treated in this section, and the uncertainties of involved models, rotations, and other relations w.r.t. the original orientation are assessed. The orientation of the GCRS and the Barycentric Celestial Reference System (BCRS) are specified by International Astronomical Union (IAU) resolutions: IAU Res. A4 (1991) recommends the usage of the two fundamental systems GCRS and BCRS and defines their respective metrics, which were effectively updated by IAU Res. B1.3 (2000). While BCRS is resting in the Solar System Barycenter, GCRS moves along the Earth's orbit in the curved space time of the Solar System. This motion implies a slight difference of the respective orientations due to the de Sitter precession denoted as geodesic precession and nutation by Fukushima (1991). The currently adopted precession/nutation models (IAU 2006/2000) account for these effects. If those are correctly applied, the orientations can be considered identical. Fukushima (1991) specifies the uncertainty of the geodesic precession model to be 0.7 μas/year, and the uncertainty of the geodesic nutation model being better than 1 μas. Since the orientation does not play a role for the definition of GCRS and BCRS, which deals with the involved metrics only, their orientations were later defined to equal the orientation of the International Celestial Reference System (ICRS) through IAU Res. B2 (2006). According to IAU Res. B2 (1997) the default orientation of the ICRS is given through the IERS celestial reference frame solution of the year 1995 (IERS95) as described by the ICRS Product Center of IERS (Arias et al. 1995). The current definition of the ICRS neglects the aberration due to the rotation of our galaxy, the Milky Way. Most recent results by Malkin (2013) show that this effect is at the level of about 5 μas/year.

After the IAU adopted the ICRS being materialized by VLBI, the first International Celestial Reference Frame (ICRF) was created. This frame was based on the solution of the Working Group on Reference Frames (WGRF) and its orientation was realized by a rotation onto IERS95. The determination of the three rotation angles additionally involved three deformation parameters, which were, however, not applied for the transformation. Ma et al. (1998) describe that 117 IERS95 defining sources – those sources used for the NNR condition and thus for the axes definition – and an additional set of 16 southern sources available in both frames were used for the computation of the rotations, which were about 6 μas with an uncertainty of about 20 μas. ICRF then was extended twice: ICRF-Ext.1, ICRF-Ext.2 (Fey et al. 2004). Nevertheless, both extensions left the positions of the defining sources unchanged to consistently add the new sources to the existing frame, while preserving the orientation. Eleven years later, the second realization of the ICRS (ICRF2) was produced by an IERS/IVS Working Group (Fey et al. 2009). This Working Group selected the VLBI radio source catalogue of the NASA Goddard Space Flight Centre (GSFC) as the basis for the new ICRF2 due to its superior quality and completeness. The orientation of ICRF2 was again aligned to its predecessor (ICRF-Ext.2) by rigid rotation, this time based on a four parameter transformation, since two of the deformation parameters were found to be insignificant (Fey et al. 2009). The determination of the rotation angles was based on 97 ICRF-Ext.2 defining sources and additional 41 southern sources. The angles were in the range of about 8–34 μas and were determined with an uncertainty of about 20 μas. ICRF2 is the state-of-the-art celestial frame; a priori source

Table 1 EOP differences (μas or μs) when using ICRF-Ext.2 instead of ICRF2 as fixed a priori values for radio source coordinates

EOP	Shift	Drift (year^{-1})	WRMS
Δx_p	−4.1±0.7	−9.1±0.1	43.4
Δy_p	1.7±0.5	1.4±0.1	28.1
$\Delta dUT1$	−1.7±0.03	−0.5±0.01	1.8
ΔX	0.1±0.5	−1.4±0.1	32.1
ΔY	8.3±0.5	−1.3±0.1	27.6

Only the positions of special handling radio sources have been adjusted. Values are taken from Gordon et al. (2013)

Table 2 EOP differences (μas or μs) when using ICRF-Ext.2 instead of ICRF2 as a priori values and adjusting radio source coordinates applying NNR

EOP	Shift	Drift (year^{-1})	WRMS
Δx_p	11.1±0.8	−1.8±0.2	47.5
Δy_p	−4.0±0.7	3.3±0.1	40.5
$\Delta dUT1$	−0.5±0.1	0.07±0.01	2.8
ΔX	37.6±0.8	−0.4±0.1	47.3
ΔY	20.8±0.8	0.1±0.1	45.5

Values are taken from Gordon et al. (2013)

positions for the analysis of VLBI sessions should be taken from this catalogue. The individual VLBI sessions include only a subset of the radio sources of ICRF2. In the analysis of the VLBI sessions the defining radio source coordinates were estimated by applying no net rotation (NNR) conditions. The other sets of radio sources, other and special handling sources were estimated but not included in the NNR condition. Both characteristics, the subset as well as the adjustments due to parameter estimation, slightly alter the orientation of the individual VLBI session network ('VLBI session CRF') w.r.t. the a priori catalogue ICRF2.

For numerical assessment, Tables 1 and 2 show the differences in EOP between two global VLBI solutions using the ICRF-Ext.2 or the ICRF2 for a priori source coordinates. For the first comparison (Table 1) the radio source positions were not adjusted, while for the second comparison (Table 2) the radio source coordinates were estimated applying NNR. For both cases the coordinates of special handling sources were estimated. The values are taken from Gordon et al. (2013). The comparison shows that there are small systematics in the EOP depending on the CRF. However, the size of most of the effects is below the level of the axes stability of ICRF-Ext.2 (20 μas). The largest shifts can be found for the celestial pole coordinates ($\Delta X = 37.6\,\mu\text{as}$ and $\Delta Y = 20.8\,\mu\text{as}$) when applying ICRF-Ext.2 instead of ICRF2 with the NNR approach, which are much smaller or even vanish for the fixed coordinate approach. This shows that the NNR condition applied on the various subsets of radio sources given by the VLBI session does not exactly preserve the orientation. Most of the drifts of the EOP obtained with the fixed approach are larger than those obtained with the NNR approach. In particular the Δx_p drift of $-9.1\,\mu\text{as/year}$ shows that there are small apparent proper motions of radio sources which are leading to small drifts between ICRF-Ext.2 and ICRF2 if radio source positions are not adjusted. Besides the systematic effects, it is obvious that the repeatabilities (WRMS) of the EOP are better, if the radio source coordinates are not estimated.

Summing up, the uncertainty of the orientation of the GCRS can be obtained forming the square root of the sum of the squares of the various individual uncertainties identified from the definition (GCRS) to the actual realization ('VLBI session CRF'). This uncertainty is about 35 μas with a respective stability of 0.7 μas/year (uncertainty of the geodesic precession model) and a small systematic drift of 5 μas/year (neglected galactic aberration). By comparison it was found that the approach with fixed celestial coordinates provides better repeatabilities (WRMS) of the EOP. Since the approach with fixed coordinates provides smaller 'VLBI session CRF' differences, it can be concluded that the EOP without estimation of radio source coordinates (only estimating those of special handling radio sources) are more consistent with respect to each other and thus more accurate in the sense of that they are closer to the definition [Eq. (1)].

3 The Realization of the ITRS Orientation by VLBI

In this chapter we assess the uncertainty and stability of the terrestrial orientation realized by VLBI. A detailed historical overview on how the International Latitude Service (ILS) started on determining the Conventional International Origin (CIO) has been published by Höpfner (2000). For example in Potsdam there is a more than a century long history of latitude determinations (Meinig 1992). On the terrestrial side we start with the ITRS, which was adopted by the International Union of Geodesy and Geophysics (IUGG) Res. 2 (2007): *[...] the orientation is operationally maintained in continuity with past international agreements (BIH orientation); [...].* Practically this means that the default orientation of the ITRS is the orientation given by the Bureau International de l'Heure (BIH) Terrestrial System (BTS84), the BIH orientation at 1984.0. Guinot (2000): '*The orientation of the BTS84 was fixed by the condition that the ERP be continuous at the changeover from the old to the new techniques*'. With 'old techniques' Guinot (2000) meant optical astrometric observations and with 'new techniques' the space geodetic techniques. Note that at this time (1984) the orientation of the ITRS was attached to the celestial frame via the EOP, while today vice versa, a new IERS EOP series is provided for each new release of the ITRF. The BTS84 orientation was realized by the BIH frame of the year 1984. Until the foundation of the IERS the BIH released three

more frames: BTS85, BTS86, BTS87. According to Boucher and Altamimi (1989) the orientations between those and the first IERS Terrestrial Reference Frame (ITRF88) were ensured by '*[...] putting an alignment constraint on ERP parameters, using BIH values [...]*'. The rotations between BTS84 and ITRF88 as reported by Boucher and Altamimi (1990) were up to 7.5 mas with a maximal uncertainty of 0.8 mas. The uncertainty of the rotations between BTS84 and BTS85 slightly differs between this publication (0.8 mas) and Boucher and Altamimi (1988), who before reported an uncertainty of 0.7 mas, an effect which is probably due to various subsets of stations forming the basis for the computation of the transformation parameters.

In the years after ITRF88 until today the IERS released a series of 11 ITRS realizations. The rotation between the latest realization, ITRF2008, and ITRF88 is specified to be maximal 100 µas (see Table 4.1 of IERS Conventions 2010). If a VLBI-only TRF is used for the VLBI session analysis, e.g. VTRF2008, additional uncertainties are to be considered due to rotations of up to 100 µas between the multi-technique combined frame (ITRF2008) and the VLBI-only frame (VTRF2008), which reach 20 µas. To determine EOP from recent VLBI sessions these catalogues have to be revised continuously for example considering new stations and station displacements due to major Earthquakes, such as the 8.8 M_W Maule, 2010, or the 9.0 M_W Tōhoku, 2011, events. Since the VLBI datum stations TIGOCONC and TSUKUB32 were affected by these Earthquakes, the set of datum stations for defining the NNR condition had to be revised leading to small rotations of about 20 µas assessed by determining two solutions one with the two sites and another one without the two sites in the terrestrial NNR/NNT datum. The last step from the definition (ITRS) to the realization is the 'VLBI session TRF', formed by the subset of the observing VLBI stations. In analogy to the 'VLBI session CRF', it is only possible to apply NNR on the specific subset of ITRF2008 (or VTRF2008, see above) stations, which participated in the observations. On the terrestrial side, the relatively small number of VLBI stations involved in a VLBI session, currently about seven to eleven sites, puts a considerable limit to the effectiveness of the NNR constraint. The EOP from different station networks (Malkin 2009; Lambert and Gontier 2006) can differ by up to 100 µas.

Besides the definition, realization, and maintenance of the initial orientation, it is necessary to ensure the stability of the orientation over time, the orientation rate. In the beginning, the time evolution of the first BTS frames (BTS84, BTS85) was unspecified. Due to the short duration of availability of space geodetic techniques' results, it was not yet possible to estimate reliable site velocities and thus for the later BTS frames (BTS86, BTS87) and the early ITRFs (ITRF88, ITRF89, and ITRF90) the time evolution was constrained to the geophysical plate kinematic model AMO-2 (Minster and Jordan 1978). With ITRF91 velocities were estimated for the first time from space geodetic techniques constrained to a plate kinematic model, NNR-NUVEL-1 (Argus and Gordon 1991) and later (ITRF92) NNR-NUVEL-1A (DeMets et al. 1994). With the exception of ITRF93, which was again aligned to the IERS EOP, the succeeding ITRFs were all aligned to the NNR-NUVEL-1A model up to ITRF2000 (Altamimi et al. 2002). The most recent realizations ITRF2005 (Altamimi et al. 2007) and ITRF2008 (Altamimi et al. 2011) were then constrained to the preceding frames. Ignoring the ITRF93, the maximal orientation rates can be found between ITRF2008 and ITRF88 being 20 µas/year.

For numerical assessment, we compare three IERS EOP C04 series (Bizouard and Gambis 2009); two of them were consistently determined together with the two latest ITRF releases (Fig. 1). In y_p there is a shift of −270 µas and a drift of −14 µas/year between ITRF2000 and ITRF2008, which is even larger between ITRF2000 and ITRF2005. Between ITRF2005 and ITRF2008 there is still a y_p shift of 56 µas and a drift of 7 µas/year, what does not agree with the assumption that the rotations being equal to zero between the two frames as specified in the IERS Conventions (2010), but lies within the specified uncertainties of 80 µas and 80 µas/year (Altamimi et al. 2011).

Summing up, the uncertainty of the orientation of the ITRS can be obtained forming the square root of the sum of the squares of the various individual uncertainties identified between the definition (ITRS) and the actual realization (VLBI session TRF). This uncertainty is about 813 µas and the uncertainty of the orientation rate is about 82 µas/year. Due to unmodelled geophysical signals in regularized station coordinates reported in the ITRFs it is not recommended to fix station coordinates to their a priori values. It can be concluded that the estimation of EOP together with station coordinates provides consistent EOP and station coordinates, which, however, might be slightly inconsistent with respect to each other due to the NNR condition on the rather small number of stations and might be significantly misaligned to the definition, the ITRS, due to the long history of ITRS realizations.

4 Conclusions

The current procedure of inheritage of orientation from the preceding realization to the current realization applying the NNR constraint based on various subsets of network stations or radio sources works insufficiently because each new frame inherits the orientation uncertainty of all its predecessors and adds its own orientational uncertainty. Thus, since the definition of the terrestrial initial orientation in 1984 with an uncertainty of 0.8 mas and the 16 realizations from BTS84

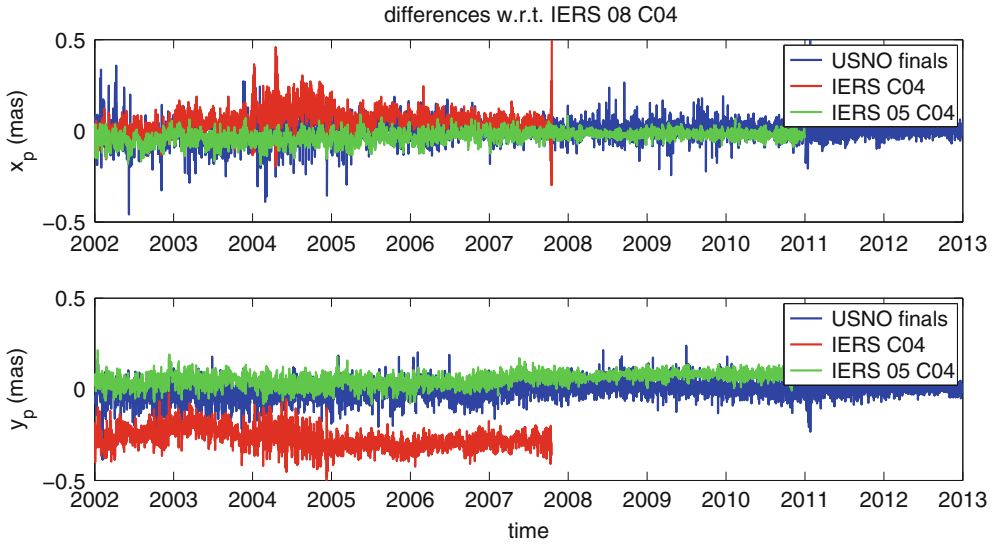

Fig. 1 Difference of pole coordinates prior to ITRF2005 ('IERS C04') and consistent to ITRF2005 ('IERS 05 C04') with those consistent to ITRF2008. The difference to the United States Naval Observatory (USNO) finals is included as well for an estimate of the effect of a different combination procedure on EOP

until ITRF2008, the uncertainty of the orientation has been continuously increasing. To stop this possibly increasing misalignment it would be necessary to redefine the ITRS orientation. The fact that the BIH orientation of 1984.0 was based on optical astrometric observations, which are not maintained in the same way today, also underpins this idea. Since 1984 the network stations used for the initial definition of the orientation have significantly drifted away due to plate motion and other geophysical effects.

At the celestial site the inheritage of the uncertainty of the orientation is in principle the same. However, here the uncertainties are, in general, much smaller and so far there have only been two frames released since the definition of the ICRS in 1995. In addition, there are significantly more celestial objects (radio sources) which are more homogeneously distributed compared to the station distribution on Earth. Apart from the aberration due to galactic rotation, which should be considered by an ICRS redefinition in near future, the apparent proper motions of radio sources are also very small or even negligible.

Alternatively, it should be possible to ignore the chain of preceding frames and to directly refer the orientation of the current frame to the definition. However, a drawback of this approach would be that the low number of common network stations or celestial objects of the old systems and the current frames would probably degrade the accuracy of this approach. Nevertheless, such a datum realization would unequivocally refer to the initial orientation specified by the definition and not continuously increase from one realization to the next.

Since ITRF2005 the EOP have been adjusted together with the station coordinates. Starting with ITRF2005 the IERS EOP can thus be considered being attached to the corresponding ITRF. Since the rotations between ITRF2000 and ITRF2005 were constrained to be zero but significant differences between IERS C04 prior to ITRF2005 and those adjusted with ITRF2005 exist (see Fig. 1), one can conclude that the IERS EOP prior to ITRF2005 were not consistent with the ITRFs prior to ITRF2005. Reconsidering the fact that the terrestrial initial orientation was defined by constraining it to the EOP, it becomes evident that between the BIH orientation of 1984.0 (BTS84) and the orientation of the current realizations (ITRF2005, ITRF2008) the initial orientation is inconsistent to a significant extent. This becomes obvious when looking at the large rotations w.r.t. ITRF93, the largest rotation is -1.71 mas and the largest rotation rate is $-190\,\mu$as/year, because this frame was in contrast to the other ITRFs aligned to the EOP and not to the orientation of the preceding frame. Between ITRF2005 and ITRF2008 the orientation was again realized by NNR condition and the corresponding rotations between the frames are specified to be zero with an uncertainty of $80\,\mu$as (Altamimi et al. 2011). Figure 1 clearly shows that there are shifts of up to $56\,\mu$as between y_p consistent with ITRF2005 and ITRF2008, and thus we can conclude that the application of the terrestrial NNR condition does not precisely guarantee no net rotation. Therefore, we consider an initial terrestrial orientation to be more than one order of magnitude more precisely realized by constraining it to the EOP consistent with the state-of-the-art ICRF in the manner it was achieved for the early BIH frames.

The EOP accuracy is a matter of consistency. For the ultimate consistency, the ITRF, the EOP, and the ICRF have to be determined in one monolithic adjustment. Thus, beyond IUGG Res. 3 (2011), for the future of more accurate

products, we conclude that '*[...] highest consistency between the ICRF, the ITRF, and the EOP as observed and realized by the IAG and its components such as the IERS should be a primary goal in all future realizations [...]*' not only of the ICRS, but also of the ITRS, and the linking EOP.

Acknowledgements We are grateful to the International Earth Rotation and Reference Systems Service (IERS) for providing the data. We thank three unknown reviewers for the constructive comments.

References

Altamimi Z, Sillard P, Boucher C (2002) ITRF2000: a new release of the international terrestrial reference frame for Earth science applications. J Geophys Res 107(B10):2214. doi:10.1029/2001JB000561

Altamimi Z, Collilieux X, Legrand J, Garayt B, Boucher C (2007) ITRF2005: a new release of the international terrestrial reference frame based on time series of station positions and Earth orientation parameters. J Geophys Res 112(B9):401. doi:10.1029/2007JB004949

Altamimi Z, Collilieux X, Métivier L (2011) ITRF2008: an improved solution of the international terrestrial reference frame. J Geodesy 85:457–473

Argus DF, Gordon RG (1991) No-net-rotation model of current plate velocities incorporating plate motion model NUVEL-1. Geophys Res Lett 18(11):2039–2042

Arias EF, Charlot P, Feissel M, Lestrade J-F (1995) The extragalactic reference system of the international Earth rotation service, ICRS. Astron Astrophys 303:604–608

Behrend D, Böhm J, Charlot P, Clark T, Corey B, Gipson J, Haas R, Koyama Y, MacMillan DS, Malkin Z, Niell A, Nilsson T, Petrachenko B, Rogers A, Tuccari G, Wresnik J (2008) Recent progress in the VLBI2010 development. In: Sideris M (ed) Observing our changing Earth. Springer, Berlin, pp 833–840

Bizouard C, Gambis D (2009) The combined solution C04 for Earth orientation parameters consistent with international terrestrial reference frame ITRF2005. In: Drewes H (ed) Geodetic reference frames. Springer, Berlin, pp 265–270

Boucher C, Altamimi Z (1988) Status of the realization of the BIH Terrestrial System. In: Babcock AK, Wilkins GA (eds) The Earth's rotation and reference frames for geodesy and geodynamics, International Astronomical Union, symposium no. 128. Kluwer Academic, Dordrecht, pp 107–114

Boucher C, Altamimi Z (1989) The initial IERS terrestrial reference frame. IERS Technical Note 1, 102, Central Bureau of IERS - Observatoire de Paris, Paris

Boucher C, Altamimi Z (1990) Evolution of the realizations of the terrestrial reference system done by the BIH and IERS (1984–1988). IERS Technical Note 4, 113, Central Bureau of IERS - Observatoire de Paris, Paris

DeMets C, Gordon RG, Argus DF, Stein S (1994) Effect of recent revisions to the geomagnetic reversal time scale on estimates of current plate motions. Geophys Res Lett 21(20):2191–2194

Fey AL, Ma C, Arias EF, Charlot P, Feissel-Vernier M, Gontier A-M, Jacobs CS, Li J, MacMillan DS (2004) The second extension of the international celestial reference frame. Astron J 127:3587–3608

Fey AL, Gordon D, Jacobs CS (eds) (2009) The second realization of the international celestial reference frame by very long baseline interferometry. IERS Technical Note 35, Verlag des Bundesamts für Kartographie und Geodäsie, Frankfurt am Main, p 204

Fukushima T (1991) Geodesic nutation. Astron Astrophys 244:L11–L12

Gordon D, Ma C, MacMillan DS, Bolotin S, Le Bail K, Gipson J (2013) Effects of ICRF2 on the TRF, CRF, and EOP. In: Altamimi Z, Collilieux X (eds) Reference frames for application in geosciences. International association of geodesy symposia, vol 138. Springer, Berlin, pp 175–179

Guinot B (2000) History of the Bureau International de l'Heure. In: Dick S, McCarthy D, Luzum B (eds) Polar motion: historical and scientific problems. ASP conference series, vol 208, pp 175–184

Höpfner J (2000) The international latitude service - a historical review, from the beginning to its foundation in 1899 and the period until 1922. Surv Geophys 21(5–6):521–566

IERS Conventions 2010 (2010). In: Petit G, Luzum B (eds) IERS technical note no. 36, Verlag des Bundesamts für Kartographie und Geodäsie, Frankfurt am Main. http://www.iers.org/IERS/EN/Publications/TechnicalNotes/tn36.html

Lambert SB, Gontier A-M (2006) A Comparison of R1 and R4 IVS networks. In: Behrend D, Baver K (eds) IVS 2006 general meeting proceedings, NASA/CP-2006-214140, pp 264–268

Ma C, Arias EF, Eubanks TM, Fey AL, Gontier A-M, Jacobs CS, Sovers OJ, Archinal BA, Charlot P (1998) The international celestial reference frame as realized by very long baseline interferometry. Astron J 116:516–546

Malkin ZM (2009) On comparison of the Earth orientation parameters obtained from different VLBI networks and observing programs. J Geodesy 83:547–556

Malkin ZM (2013) On the Galactic aberration constant, Journees 2013. http://arxiv.org/abs/1309.5298

Meinig M (1992) One century latitude determinations at Potsdam. In: Montag H, Reigber Ch (eds) Geodesy and physics of the Earth. International association of geodesy symposia, vol 112. Springer, Berlin, pp 427–429

Minster JB, Jordan TH (1978) Present-day plate motions. J Geophys Res 83(B11):5331–5354

Plag H-P, Pearlman M (eds) (2009) The global geodetic observing system: meeting the requirements of a global society on a changing planet in 2020, vol 332. Springer, Berlin/Heidelberg. ISBN:978-3-642-02686-7

The New IAU/IAG Joint Working Group on Theory of Earth Rotation

José M. Ferrándiz and Richard S. Gross

Abstract

The Earth's rotation is considered to be one of the three pillars of modern Geodesy. In 2012 the International Association of Geodesy (IAG) and the International Astronomical Union (IAU) initiated a process to establish a Joint Working Group (JWG) on the Theory of Earth Rotation with the purpose of promoting the development of improved theories of Earth rotation which reach the accuracy required to meet the needs of the near future as recommended by, e.g., GGOS, the Global Geodetic Observing System of the IAG. The JWG was approved by both organizations in April 2013 with the chairs being the two authors of this paper. Its structure comprises three Sub Working Groups (SWGs) addressing Precession/Nutation, Polar Motion and UT1, and Numerical Solutions and Validation, respectively. The SWGs should work in parallel for the sake of efficiency, but should keep consistency as an overall goal. This paper offers a view of the objectives and scope of the JWG and reports about its initial activities and plans.

Keywords

Earth rotation • Geodesy • Geodynamics

1 Introduction

The International Association of Geodesy (IAG) and the International Astronomical Union (IAU) established a new Joint Working Group on the Theory of Earth Rotation recently in 2013. A draft of a proposal to establish the JWG was initiated around the time of the IAU General Assembly held in Beijing in August 2012 where a business meeting of IAU Commission 19 took place. The draft was opened to suggestions and discussions at the beginning of the next year and circulated among members of IAU C19 and IAG. Afterwards the IAU C19 Organizing Committee, the IAU Division A Steering Committee, and the IAG Executive Committee approved the final JWG proposal in April 2013.

1.1 Purpose

According to the proposal, the purpose of the new JWG is to *"promote the development of theories of Earth rotation that are fully consistent and that agree with observations and provide predictions of the Earth Rotation Parameters (ERP) with the accuracy required to meet the needs of the near future as recommended by, e.g., GGOS, the Global Geodetic Observing System of the IAG"*.

J.M. Ferrándiz (✉)
Department of Applied Mathematics, University of Alicante, Alicante, Spain
e-mail: jm.ferrandiz@ua.es

R.S. Gross
Jet Propulsion Laboratory, California Institute of Technology, Pasadena, CA, USA
e-mail: richard.s.gross@jpl.nasa.gov

© Springer International Publishing Switzerland 2015

C. Rizos, P. Willis (eds.), *IAG 150 Years*, International Association of Geodesy Symposia 143,
DOI 10.1007/1345_2015_166

1.2 Context

Let us recall that GGOS 2020 demands accuracy of the order of 1 mm to the frames of reference, besides stability in time of 0.1 mm/year (Plag and Pearlman 2009). The former accuracy in position, measured on the Earth surface, corresponds roughly to an angle of 30 μas.

From the observational side, the accuracy and performance of the major techniques are increasing. A good example is provided by the new generation of VLBI systems. A number of stations compliant with the VLBI2010 specifications are already in operation, in addition to those being deployed or that have been approved by their respective funding institutions. Besides, the various IAG services are committed to reach GGOS goals. Therefore, in the next few years it is expected that there will be new series of more accurate Earth Orientation Parameters (EOPs). Moreover, following the experience of the continuous VLBI campaigns (Nilsson et al. 2010; Böhm et al. 2012), the whole set of EOPs will be produced at sub-daily intervals.

Currently, series of Earth Orientation Parameters (EOPs) are provided by several Analysis Centers and by the International Earth Rotation and Reference Systems Service (IERS), the international body in charge of both Earth rotation monitoring and prediction and of the realization and maintenance of the International Celestial Reference Frame and the International Terrestrial Reference Frame (ICRF and ITRF, respectively). Recent analyses of the main features of EOP, ICRF and ITRF appear in articles like Bizouard and Gambis (2009), Fey et al. (2004) and Altamimi et al. (2011), respectively. Additional information can be found in various IERS Technical Reports.

The set of EOPs currently in use was agreed upon following the recommendation of an IAU Working Group on Nutation (Seidelmann 1982) and was modified by Resolutions B1.7 and B1.8 adopted at the IAU XXVI General Assembly in 2000, which entered in force in 2003.

Let us recall that the transformation of the coordinates referred to ICRF and ITRF is specified by five EOPs instead of the minimum of three parameters (which is the number of independent angles needed to specify the transformation from a given frame to another) because an intermediate system is used, the Celestial Intermediate Reference System, with the Celestial Intermediate Pole and Origin (CIP and CIO, respectively). Note the CIP replaced the formerly used Celestial Ephemeris Pole (CEP).

The five EOPs are:

- Precession/nutation (dX, dY in the CIO-based paradigm or $d\varepsilon$, $d\psi$ in the equinox-based system)
- Earth rotation angle (ERA, or in the equinox-based paradigm GMST or GAST - Greenwich Mean Sidereal Time or Greenwich Apparent Sidereal Time)
- Polar motion (x, y)

Precise definitions of the main and auxiliary parameters and frames can be found in the IERS Conventions 2010 (Petit and Luzum 2010), The Explanatory Supplement to the Astronomical Almanac (Urban and Seidelmann 2013) or SOFA (Standards of Fundamental Astronomy) documentation (Hohenkerk and the IAU SOFA Board 2010), for instance.

Other interesting properties (Seidelmann 1982) that favored the adoption of five EOPs were that both sets of nutation angles and polar motion (PM) were free from diurnal components either in the "inertial" or the "body-fixed" reference systems, respectively. Besides, nutations are caused by mainly astronomically driven, predictable effects, while PM are caused by mainly geophysical, difficult to predict effects.

On time scales shorter than a day, polar motion consists largely of ocean tidally driven variations having amplitudes as large as about 0.3 milliarseconds (mas). On time scales longer than a day, polar motion consists largely of: (1) an annual wobble having a nearly constant amplitude of about 100 mas, (2) the Chandler wobble having a variable amplitude ranging between about 100 and 200 mas, (3) quasi-periodic variations on decadal time scales having an amplitude of about 30 mas (known as the Markowtiz wobble), and (4) a trend of about 3.5 mas/year. The variations longer than a day are caused largely by changes in the mass distribution of the Earth's mantle and global surface geophysical fluids (see, e.g., Gross 2007 for a review of polar motion).

On time scales shorter than a day, length-of-day (LOD) variations consist largely of ocean tidally driven variations having amplitudes as large as about 0.2 milliseconds (ms). On time scales longer than a day, LOD consists largely of: (1) solid body and ocean tidally driven variations having amplitudes as large as about 0.4 ms, (2) intraseasonal variations having excursions as large as about 0.4 ms caused largely by intraseasonal variations in the zonal winds, (3) a semiannual variation having a nearly constant amplitude of about 0.3 ms caused largely by semiannual variations in the zonal winds, (4) an annual variation having a nearly constant amplitude of about 0.4 ms caused largely by annual variations in the zonal winds, (5) interannual variations having excursions as large as about 0.4 ms caused largely by interannual variations in the zonal winds, (6) decadal-scale variations having excursions as large as about 4 ms caused largely by core-mantle interactions, and (7) a trend of about 1.8 ms/century caused largely by both tidal dissipation in the Earth-Moon system and by glacial isostatic adjustment (see, e.g., Gross 2007 for a review of LOD variations).

Concerning nutations, let us recall that IAU adopted a new nutation theory in 2000, based on MHB2000 (Mathews et al. 2002) as well as a new precession model in 2006 (Hilton et al. 2006), based on P03 by Capitaine et al. (2003). They are

known as IAU 2000 nutation model and IAU 2006 precession model, or shortened names as IAU2000/2006.

The real accuracy of the various series of EOP is difficult to assess. Recent estimates of the precision of individual solutions corresponding to different techniques and analysis centers, when compared to combined solutions, can be found in the IERS Annual Report 2011 (Dick 2011), especially Sects. 3.5.1 and 3.5.2. To provide some reference values extracted from that source, uncertainty of VLBI estimations of the celestial pole is about 80–90 μas in average. In the case of the terrestrial pole, VLBI uncertainty goes up to about 170 μas, whereas GPS estimations are about 50–70 μas in average. The real accuracy of the various series of EOP is likely to be worse than this because of the presence of errors that the series have in common.

The situation is worse for the predictions of EOP values. For instance, tables 3 and 4 of Sect. 3.5.2 of the IERS AR 2011 show that the wrms (weighted root mean square) of the differences between EOP predictions produced by the daily solutions and the 05/08 C04 combination series are always larger than 150 μas for each EOP.

As for the current IAU2000/2006 precession/nutation models, the most predictable component of Earth rotation, a reference value can be settled about 140–150 μas, in terms of wrms of the observation-model differences (Capitaine et al. 2009, 2012). Let us notice that the remarkable efforts made in the last years to improve the models have not been accompanied by a significant reduction of the residual wrms. Given the values of those uncertainties/inaccuracies, we must conclude that the goal of the new JWG is really quite challenging.

2 Terms of Reference

The terms of reference (ToR) of the JWG are:

1. A main objective of the Joint Working Group (JWG) is to assess and ensure the level of consistency of Earth Orientation Parameter (EOP) predictions derived from theories with the corresponding EOPs determined from analyses of the observational data provided by the various geodetic techniques. Consistency must be understood in its broader meaning, referring to models, processing standards, conventions etc.
2. Clearer definitions of polar motion and nutation are needed for both their separation in observational data analysis and for use in theoretical modeling.
3. Theoretical approaches must be consistent with IAU and IAG Resolutions concerning reference systems, frames and time scales.
4. Searching for potential sources of systematic differences between theory and observations is encouraged, including potential effects of differences in reference frame realization.
5. The derivation of comprehensive theories accounting for all relevant astronomical and geophysical effects and able to predict all EOPs is sought. In case more than one theory is needed to accomplish this, their consistency should be ensured.
6. There are no a priori preferred approaches or methods of solution, although solutions must be suitable for operational use and the simplicity of their adaptation to future improvements or changes in background models should be considered.
7. The incorporation into current models of corrections stemming from newly studied effects or improvements of existing models may be recommended by the JWG when they lead to significant accuracy enhancements.

3 Desired Outcomes

It is desired that the JWG:

1. Contribute to improving the accuracy of precession-nutation and EOP theoretical models by proposing both new models and additional corrections to existing models.
2. Clarify the issue of consistency among conventional EOPs, their definitions in various theoretical approaches, and their practical determination.
3. Establish guidelines or requirements for future theoretical developments with improved accuracy.

It is clear that the overall goals of the JWG cannot be achieved within only two years of activity, but the first term (until the next General Assembly of both IAU and IAG, i.e., mid 2015) should be used to develop a solid concept of how to reach its aims.

4 Structure and Operation

The structure of the JWG is more complex than usual because its subject is quite broad and requires the participation of several fields of specialization covering the characteristics of the full set of current EOPs. On the other hand, the establishment of independent JWGs for the different sub-fields would imply a serious risk of obtaining results that would not be consistent with each other. Therefore, the JWG was structured as a whole JWG containing three Sub Working Groups (SWG).

The whole JWG has the following people in charge:

Chair: Jose M. Ferrándiz (representing IAU)

Vice-Chair: Richard Gross (representing IAG)

Table 1 Members by sub working groups

SWG	1 Precession/nutation	2 Polar motion and UT1	3 Numerical solutions and validation
Chair	**J Getino**, Spain	**A Brzezinski**, Poland	**R Heinkelmann**, Germany
Members	Y Barkin, Russia	**BF Chao**, Taipei	**BF Chao**, Taipei
	N Capitaine, France	W Chen, China	W Chen, China
	V Dehant, Belgium	**J Ferrándiz**, Spain	**V Dehant**, Belgium
	A Escapa, Spain	**R Gross**, USA	**J Ferrándiz**, Spain
	J Ferrándiz, Spain	**CL Huang**, China	D Gambis, France
	M Folgueira, Spain	SG Jin, China	E Gerlach, Germany
	A Gusev, Russia	W Kosek, Poland	**R Gross**, USA
	R Gross, USA	J Nastula, Poland	**CL Huang**, China
	T Herring, USA	**J Ray**, USA	B Luzum, USA
	CL Huang, China	D Salstein, USA	Z Malkin, Russia
	J Mueller, Germany	**H Schuh**, Germany	JF Navarro, Spain
	Y Rogister, France	**F Seitz**, Germany	**J Ray**, USA
	H Schuh, Germany	WB Shen, China	**Y Rogister**, France
	J Souchay, France	D Thaller Germany	ME Sansaturio, Spain
	V Zharov, Russia	**QJ Wang** , China	**H Schuh**, Germany
		YH Zhou, China	**F Seitz**, Germany
			M Thomas, Germany
			QJ Wang, China

Members of more than one SWG are in bold

In their turn, the three SWGs forming the JWG are:

1. **Precession/Nutation** (Chair: Juan Getino)
2. **Polar Motion and UT1** (Chair: Aleksander Brzezinski)
3. **Numerical Solutions and Validation** (Chair: Robert Heinkelmann)

SWG 3 will be dedicated to numerical theories and solutions, relativity and new concepts and validation by comparisons among theories and observational series. The subjects of SWG 1 and 2 are self-explanatory.

These three SWGs should work in parallel for the sake of efficiency. To guarantee that the SWGs are linked together as closely as the needs of consistency demand, the Chair and Vice-chair of the JWG, Ferrándiz and Gross, will be involved in all SWGs as will the President of C19, Cheng-li Huang.

In order to further improve the interaction of the SWGs, a number of people are members of more than one SWG as indicated in Table 1, containing the membership list, by typing their names in bold.

5 Additional Information

A dedicated web site of the JWG is hosted by the institution of the Chair, the University of Alicante, Spain. It can be accessed directly at http://web.ua.es/en/wgther/

Acknowledgements The authors thank the editor, P. Willis, and three anonymous referees for their useful comments. JMF acknowledges partial support of the Spanish government under grant AYA2010-22039-C02-01 from Ministerio de Economía y Competitividad (MINECO). The work of RSG described in this paper was performed at the Jet Propulsion Laboratory, California Institute of Technology, under contract with the National Aeronautics and Space Administration. Support for that work was provided by the Earth Surface and Interior Focus Area of NASA's Science Mission Directorate.

References

Altamimi Z, Collilieux X, Metivier L (2011) ITRF2008, an improved solution of the International Terrestrial Reference Frame. J Geod 85(8):457–473

Bizouard C, Gambis D (2009) The combined solution C04 for Earth orientation parameters consistent with international terrestrial reference frame 2005. IAG Symp 134:265–270

Böhm S, Brzezinski A, Schuh H (2012) Complex demodulation in VLBI estimation of high frequency Earth rotation components. J Geodyn 62:56–58

Capitaine N, Wallace PT, Chapront J (2003) Expressions for IAU2000 precession quantities. Astron Astrophys 412(2):567–586. doi:10.1051/0004-6361:20031539

Capitaine N, Mathews PM, Dehant V, Wallace PT, Lambert SB (2009) On the IAU 2000/2006 precession–nutation and comparison with other models and VLBI observations. Celest Mech Dyn Astron 103:179–190

Capitaine N, Lambert S, Yao K, Liu J (2012) Evaluation of the accuracy of the IAU 2006/2000 precession-nutation. Presentation given at JD7 Space-time reference systems for future research, 28th IAU GA, Beijing, China. http://www.referencesystems.info/uploads/3/0/3/0/3030024/capitaine_6.07.pdf

Dick WR (ed) (2011) IERS Annual Report 2011. Verlag des Bundesamts für Kartographie und Geodäsie, Frankfurt AM, http://www.iers.org/AR2011/

Fey AL, Ma C, Arias EF, Charlot P, Feissel-Vernier M, Gontier AM, Jacobs CS, Li J, Macmillan DS (2004) The second extension of the International Celestial Reference Frame: ICRF-EXT.1. Astron J 127:3587–3608

Gross RS (2007) Earth rotation variations — long period. In: Herring TA (ed) Physical geodesy. Treatise on geophysics, vol 3, Elsevier, Oxford, pp 239–294

Hilton JL, Capitaine N, Chapront J, Ferrándiz JM, Fienga A, Fukushima T, Getino J, Mathews P, Simon JL, Soffel M, Vondrak J, Wallace P, Williams J (2006) Report of the International Astronomical Union Division I Working Group on Precession and the Ecliptic. Celest Mech Dyn Astron 94(3):351–367. doi:10.1007/s10569-006-0001-2

Hohenkerk C, the IAU SOFA Board (2010) SOFA tools for Earth attitude. IAU. http://www.iausofa.org

Mathews PM, Herring TA, Buffett BA (2002) Modeling of nutation and precession: New nutation series for nonrigid Earth, and insights into the Earth's Interior. J Geophys Res 107(B4):2068–2094

Nilsson T, Böhm J, Schuh H (2010) Sub-diurnal Earth rotation variations observed by VLBI. Artif Satellites 45. doi:10.2478/v10018-010-0005-8

Petit G, Luzum B (eds) (2010) IERS Conventions 2010. IERS TN 36, Verlag des Bundesamts für Kartographie und Geodäsie, Frankfurt AM. http://www.iers.org/TN36/

Plag HP, Pearlman M (eds) (2009) Global geodetic observing system: meeting the requirements of a global society on a changing planet in 2020. Springer-Verlag, Berlin-Heidelberg

Seidelmann PK (1982) 1980 IAU theory of nutation – the final report of the IAU Working Group on Nutation. Celest Mech 27:79–106

Urban SE, Seidelmann PK (eds) (2013) The Explanatory Supplement to the Astronomical Almanac, 3rd edn. University Science Books, Mill Valley

Part VI

Observation Systems and Services

Satellite Laser Ranging

A Tool to Realize GGOS?

Mathis Bloßfeld, Vojtěch Štefka, Horst Müller, and Michael Gerstl

Abstract

Satellite Laser Ranging (SLR) is currently the unique technique to determine station coordinates, Earth Orientation Parameters (EOPs) and Stokes coefficients of the Earth's gravity field from one observation equation with a high accuracy. These parameters form the so-called 'three pillars' (Plag and Pearlman, 2009) of the Global Geodetic Observing System (GGOS). In its function as an official analysis center of the International Laser Ranging Service (ILRS) (Pearlman et al., 2002), DGFI is developing and maintaining software to process SLR observations called 'DGFI Orbit and Geodetic parameter estimation Software' (DOGS). The software is used to analyze SLR observations and to compute multi-satellite solutions. In this study, up to 10 satellites (ETALON1/2, LAGEOS1/2, STELLA, STARLETTE, AJISAI, LARETS, LARES and BLITS) with different orbit characteristics (e.g., inclination and altitude) are combined. The relative weighting of the satellites is done using a variance component estimation. The diverse orbits allow to decrease the correlation of parameters such as gravity field coefficients (GFCs) and EOPs. Beside the Earth's gravity field (weekly GFCs with degree and order ≤ 6 and monthly GFCs with degree and order ≤ 20) and rotation (terrestrial pole coordinates, UT1-UTC extrapolated with LOD), 3-D station coordinates are estimated weekly or monthly. Different combined solutions are compared to LAGEOS-only solutions. If LARES is combined with LAGEOS1/2, a significant improvement in the GFCs, the EOP and the TRF can be achieved. If more satellites are combined, the variation of the pole coordinates w.r.t. the IERS 08 C04 time series can be reduced up to 56%. Furthermore, systematics in LOD are nearly completely eliminated. The variation of the station coordinates w.r.t. SLRF2008 (http://www.ilrs.gsfc.nasa.gov/science/awg/SLRF2008.html, 2013) can be reduced by about 30%.

Keywords

Earth gravity field • EOP • GGOS • SLR • TRF

1 Introduction

According to Plag and Pearlman (2009), the aims of the Global Geodetic Observing System (GGOS) are expressed in terms of the 'three pillars' of geodesy. Observations of the Earth gravity field, the Earth rotation and the Earth geometry rely on Earth-fixed terrestrial reference frames which provide the basis for Earth system observations. One major goal of GGOS is to adjust the parameters of the

M. Bloßfeld (✉) • H. Müller • M. Gerstl
Deutsches Geodätisches Forschungsinstitut der Technischen Universität München (DGFI-TUM), Munich, Bavaria, Germany
e-mail: mathis.blossfeld@tum.de

V. Štefka
Astronomical Institute, Academy of Sciences of the Czech Republic, Prague, Czech Republic

© Springer International Publishing Switzerland 2015

C. Rizos, P. Willis (eds.), *IAG 150 Years*, International Association of Geodesy Symposia 143,
DOI 10.1007/1345_2015_202

three pillars in one common adjustment. Satellite Laser Ranging (SLR) is a tool to do even more than this since its observation equation integrates, beside others, all three parameter groups. Therefore, no external conditions such as, e.g., local ties are necessary to connect the observation equations. Nevertheless, both realizations (common adjustment and integral observation equation) possess the problem of correlated parameters. Figure 1 emphasizes the correlations between the satellite-dependent orbit parameters like the nodal precession, the even degree zonal Stokes coefficients of the Earth gravity field, the Earth Orientation Parameters (EOPs) and the orientation of the TRF. To decrease the correlations between the parameters, one has in principle two different possibilities:

- **Inter-technique combination**. Combination of different techniques (e.g., GNSS (Global Navigation Satellite Systems), SLR, VLBI (Very Long Baseline Interferometry), DORIS (Doppler Orbitography and Radiopositioning Integrated on Satellites), SST (Satellite-to-Satellite Tracking) using GRACE (Gravity Recovery And Climate Experiment), gradiometry using GOCE (Gravity field and steady-state Ocean Circulation Explorer), ...)
- **Intra-technique combination**. Combination of, e.g., SLR observations to satellites with different orbit characteristics.

In this paper, we focus on the intra-technique SLR combination and discuss the ability of SLR to realize the GGOS vision by estimating the parameters of the three pillars in one common adjustment. Therefore, we combine the observations to 10 spherical passive satellites, each of them equipped with a retro-reflector array and tracked by globally distributed SLR stations. The data used and the method of weighting the normal equations (NEQs) is discussed in Sects. 2 and 3. In the Sects. 4–6, the estimated parameters are analyzed and validated. Section 7 summarizes the results and answer the question if SLR is a valuable tool to realize GGOS.

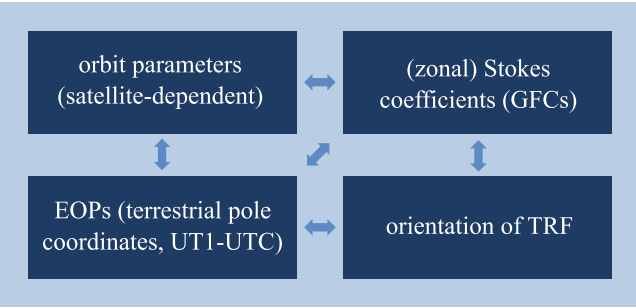

Fig. 1 Interactions between the 'three pillars' of the GGOS and the satellite orbits

2 Data

The data are provided by the International Laser Ranging Service (ILRS) (Pearlman et al. 2002). Figure 2 shows the mission durations of the 10 satellites used in this study. The longest observation time spans are obtained for the STARLETTE and the LAGEOS1 satellites which have been launched both before 1977 and are continuously observed until now. The most recently launched satellite is LARES. The combined solution covers a time interval of 13.5 years from 2000.0 until 2013.5. For a short period between February 2012 and January 2013, 10 satellites were observed in parallel. On January 22nd, 2013, BLITS was hit by space debris (Kelso 2013) and is therefore excluded from the solution since that day. Table 1 summarizes the orbit and technical characteristics of the used satellites. In order to decorrelate the nodal precession $\dot{\Omega}$ of the satellite orbit from the Length-Of-Day (LOD), it is important to combine satellites with prograde (inclination $i < 90°$) and retrograde ($i > 90°$) nodal precession (Bloßfeld et al. 2011). In the combined solution of this study, the ratio of pro- to retrograde satellites is 6/4.

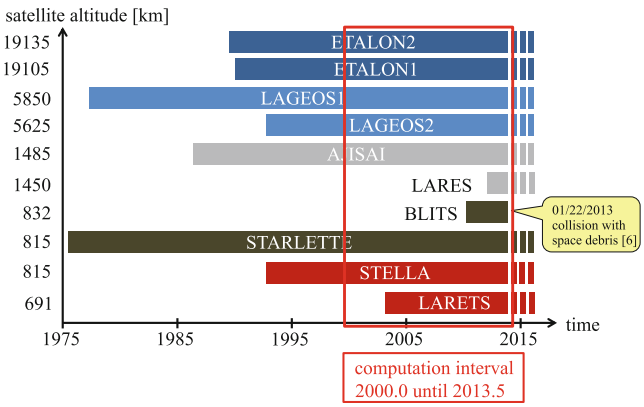

Fig. 2 Mission duration of used satellites

Table 1 Satellite and orbit characteristics of the used satellites

Satellite	Altitude (km)	Inclination (deg)	AMR (mm^2/kg)
LAGEOS1 (LA1)	5,850	109.9	694.7
LAGEOS2 (LA2)	5,625	52.7	697.5
ETALON1 (ET1)	19,105	65.0	929.4
ETALON2 (ET2)	19,135	64.4	929.4
STARLETTE (STA)	815	49.8	956.4
AJISAI (AJI)	1,485	50.0	5,300.0
LARES (LRS)	1,450	69.5	269.0
STELLA (STE)	815	98.6	962.5
LARETS (LTS)	691	98.2	1,488.0
BLITS (BTS)	832	98.8	3,014.0

AMR means area-to-mass ratio

3 Combination of Satellites

The NEQs of the 10 satellites are combined as:

$$N_c = \lambda_1 N_1 + \lambda_2 N_2 + \ldots + \lambda_{10} N_{10} \quad (1)$$

with $\lambda_i = 1/\sigma_i^2$ and σ_i being the a posteriori variance factor of the single satellite NEQ. The σ_i are obtained from a variance component estimation (Bloßfeld and Seitz 2012; Böckmann and Tesmer 2010), which is performed for three different weekly solution setups: **(T)** only station coordinates are estimated, **(T+E)** station coordinates and EOPs (terrestrial pole coordinates and UT1-UTC) are estimated and **(T+E+G)** station coordinates, EOPs and gravity field coefficients (GFCs) with degree and order ≤ 6 are estimated. The weights are summarized in Table 2. In the **(T)** and **(T+E)** solution, the smallest σ_i^2 are obtained for the LA1/2 NEQs which means that they have the highest impact on the estimated parameters. The ETALON satellites have got a lower weight since they have fewer observations than the LAGEOS satellites and they are orbiting the Earth at an altitude of about 20,000 km (Table 1). The other six satellites are down-weighted in the combination, since their altitudes are below 1,500 km and the drag of the high atmosphere acting on the satellites cannot be modeled very accurately. Since the VCE depends on the weighted sum of the residuals squared (Bloßfeld and Seitz 2012; Böckmann and Tesmer 2010), model deficiencies affect directly the obtained variance component σ_i. From the six satellites, LRS has the largest weight since this satellite has the largest AMR and is therefore less sensitive to the atmospheric drag. Nevertheless, its altitude is very small and other non-modeled perturbations due to, e.g., high degree and order GFCs (C_{nm}, S_{nm} with $n, m > 20$ are fixed to a priori) are not modeled accurately.

The high weights of the LAGEOS and ETALON satellites in the solution **(T+E+G)** can be explained by the fact that the EOPs and TRF parameters are dominating the weekly solution (ratio TRF+EOPs versus GFCs: 3/1). The weights of the satellites with an altitude lower than 1,500 km (Low Earth Orbiters; LEOs) increase, if GFCs are estimated. This fact is caused by the low altitude of the LEOs. The lower the satellite altitude is, the more sensitive they are to the Earth gravity field. More sensitive means that their orbits are influenced by the shorter wavelengths of the gravity field (higher degree and order of the GFCs). The STE, LTS and BTS satellites are down-weighted in the combination for several reasons:

- STE is orbiting the Earth at an altitude of 815 km on a sun-synchronous orbit (Tapley et al. 1996). This means that solar radiation pressure causes systematics in the orbit which are difficult to model. As a consequence, the NEQ is down-weighted in the combination.
- The LTS satellite has a very inappropriate Area-to-Mass Ratio (AMR) (0.21 m diameter and a mass of 23.28 kg). Since the satellite has an altitude of only 691 km, the air drag is very difficult to model and the NEQ is down-weighted.
- BTS is also light (7.53 kg) and has a diameter of 0.17 m (large AMR). Therefore, its altitude of 832 km causes difficulties in air drag modeling.

Table 2 Estimated variance components for three solution setups

Satellite	σ_i^2(T)	σ_i^2(T+E)	σ_i^2(T+E+G)
LAGEOS 1 (LA1)	6.1	6.7	6.1
LAGEOS 2 (LA2)	4.2	3.9	3.9
ETALON 1 (ET1)	22.0	22.2	22.1
ETALON 2 (ET2)	16.9	17.0	16.8
STARLETTE (STA)	46.1	43.3	20.7
AJISAI (AJI)	21.9	20.0	13.1
LARES (LRS)	23.4	21.6	12.5
STELLA (STE)	101.0	102.3	59.3
LARETS (LTS)	359.8	361.3	329.5
BLITS (BTS)	187.9	193.5	162.7

Setup **(T)** contains station coordinates, setup **(T+E)** contains station coordinates and EOPs and setup **(T+E+G)** contains GFCs with degree and order ≤ 6, in addition

4 Earth Gravity Field

In order to study the sensitivity of the satellites to the Earth gravity field, we computed four different test solutions of a monthly gravity field of maximal degree and order 20 in January 2007 (see Fig. 3). The LA1/2 solution shows a sensitivity to GFCs with degree and order ≤ 5. Especially the C_{nm}, S_{nm} with $n = 5$ show a small standard deviation since these coefficients are in resonance with the LAGEOS orbits.

Although the weight for the LTS NEQ w.r.t. the LA1/2 NEQ is very small, the combination shows a higher sensitivity up to degree six and especially the sectoral GFCs (C_{nm}, S_{nm} with $n = m \leq 20$) benefit from the combination. The resonance degree and order for LTS is 15. If the LA1/2 NEQ is combined with the STA NEQ (weight: 1/8), especially the tesseral GFCs (C_{nm}, S_{nm} with $n \neq m \leq 20$) benefit. The lower right plot in Fig. 3 shows the standard deviations for the GFCs up to degree and order 20 for an eight satellite combination. LRS and BTS are not included in this solution since they have been launched after 2007 (see Fig. 2). In this solution, only the zonal GFCs with degree and order 10–18 show a higher standard deviation. This is caused by the lack of resonance frequencies in the GFCs of degree < 5 and order $\in [10, 20]$. The satellites which could fill up this lack must have a resonance frequency smaller than 5° but with order between 10 and 20. At the moment, only the ETALON

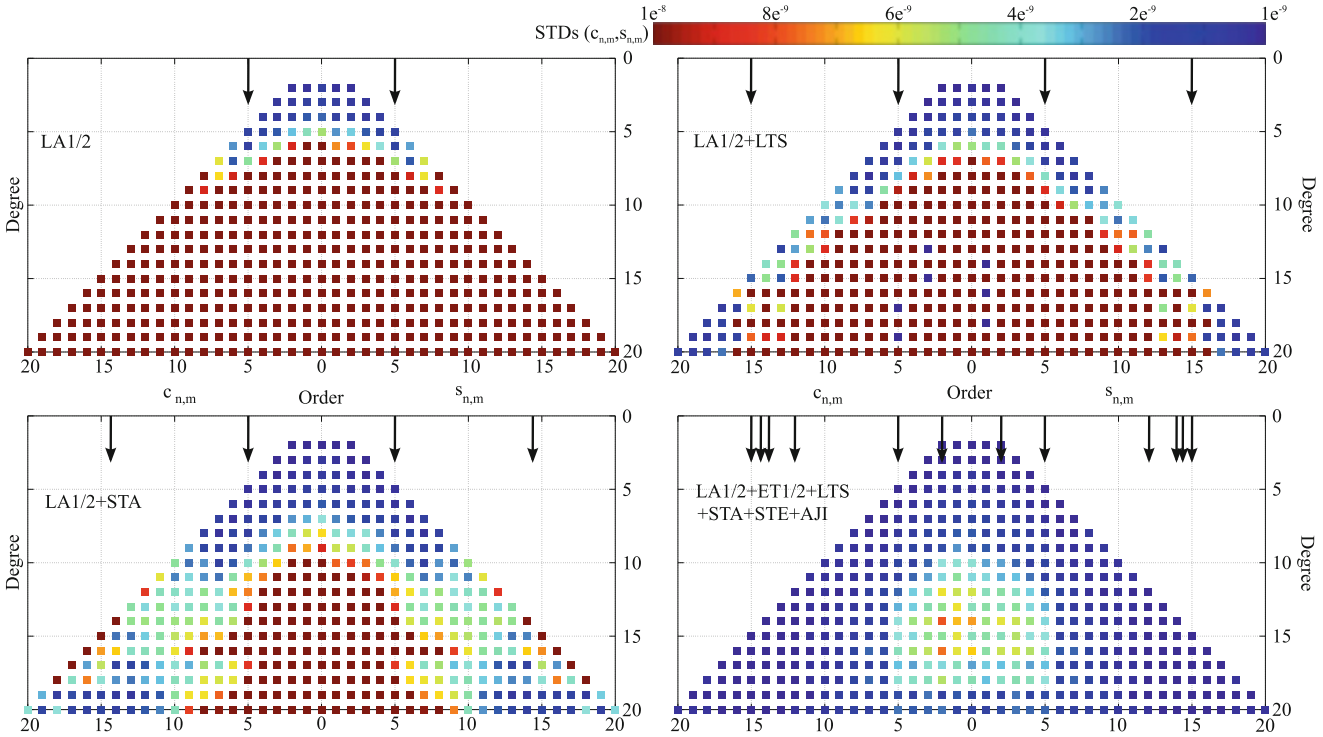

Fig. 3 Standard deviations of four different solutions of GFCs with degree and order $\leq$ 20 in January 2007. The panels show the LAGEOS1/2 (*upper left*), the LAGEOS1/2+LARETS (*upper right*), the LAGEOS1/2+STARLETTE (*lower left*) and the eight satellite (*lower right*) solution. The *black arrows* indicate the resonance frequencies of the satellites used in the solutions

satellites have a resonance frequency of two but are poorly observed. Due to their high altitude, they are not sensitive to such high orders of the gravity field. Nevertheless, to take more benefit of their resonance frequency, a suggestion to the ILRS is to ask the stations for a more frequent observation.

5 Earth Orientation Parameter

Together with weekly GFCs of degree and order $\leq$ 6, the EOPs are estimated in one common adjustment. Since the GFCs and the EOPs are highly correlated via the orbital elements ($\dot{\Omega}$) (Bloßfeld et al. 2011), at least two satellites with precessing orbital planes in prograde and retrograde directions have to be combined. In the 'DGFI Orbit and Geodetic parameter estimation Software' (DOGS), the LOD information is used to extrapolate a polygon of daily (every 0 h) UT1-UTC values. To remove the rank deficiency of the solution, the UT1-UTC value at the mid-arc epoch is fixed to IERS 08 C04. A systematic deviation of an obtained solution is equal to an offset in LOD. This parametrization has the advantage that (1) less parameters are needed to describe the time dependency within an n-day time interval than it is the case for the UT1-UTC and LOD (offset and drift) representation and (2) that the offsets can be determined more stable than the rates (Thaller 2008; Seitz 2009).

Figure 4 shows the differences of the estimated UT1-UTC values w.r.t. the IERS 08 C04 time series (ftp://hpiers.obspm.fr/iers/eop/eopc04) which is assumed to be error-free. In the topmost panel, the systematic deviations of the LA1 solution are the dominating time series. Since the solution contains only one orbital plane, $\dot{\Omega}$ of that plane envolves in the same direction as LOD. Therefore, the parameters are highly correlated and no reasonable solution can be obtained. In each of the lower panels, the time series with the largest systematic errors is neglected. The smallest systematic deviations are obtained for the 10-satellite solution. They are about 100 times smaller than the deviations of the LA1 solution. This fact is caused by the mix of different inclinations and the resulting de-correlation of GFCs, $\dot{\Omega}$ and LOD. In Table 3, the weighted Root-Mean-Square (WRMS) values for the difference time series of the pole coordinates are summarized. Especially in the y-pole, the combination of 10 satellites improves the solution significantly. For the 10-satellite solution, 15.9 µ as for the x-pole and 16.4 µ as for the y-pole are obtained.

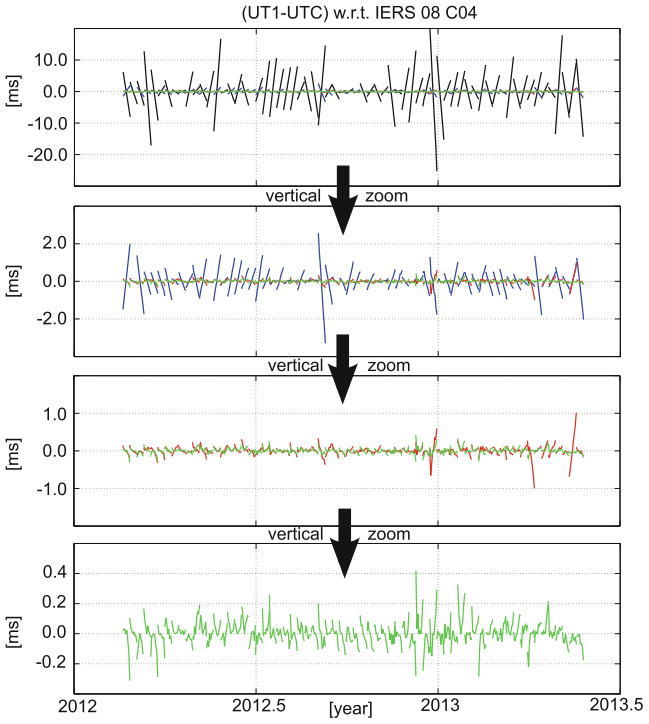

Fig. 4 Weekly UT1-UTC polygons w.r.t. IERS 08 C04 for four different solution types: LA1 (*black*), LA1/2 (*blue*), LA1/2 + LRS (*red*), 10 satellites (*green*)

Table 3 WRMS values of the pole coordinate time series w.r.t. IERS 08 C04 for the solution types of Fig. 4

WRMS [μ as]	LA1	LA1/2	LA1/2+LRS	10 sat.
Δ x-pole	39.2	16.5	15.9	15.9
Δ y-pole	50.0	37.2	26.5	16.4

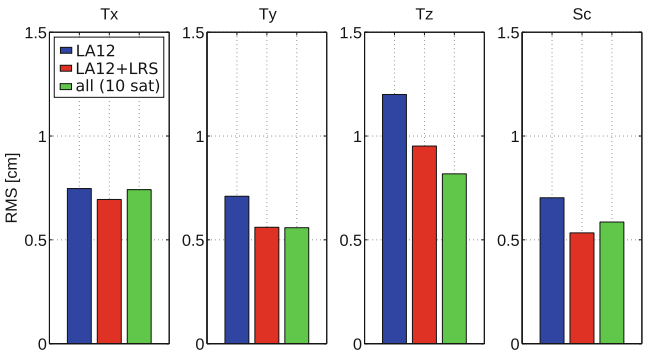

Fig. 5 Mean RMS of translation and scale parameters of the three solutions (LA1/2: *blue*, LA1/2+LRS: *red*, 10 sat.: *green*) w.r.t. SLRF2008. The mean RMS values are obtained from the parameter time series of a weekly seven-parameter similarity transformation

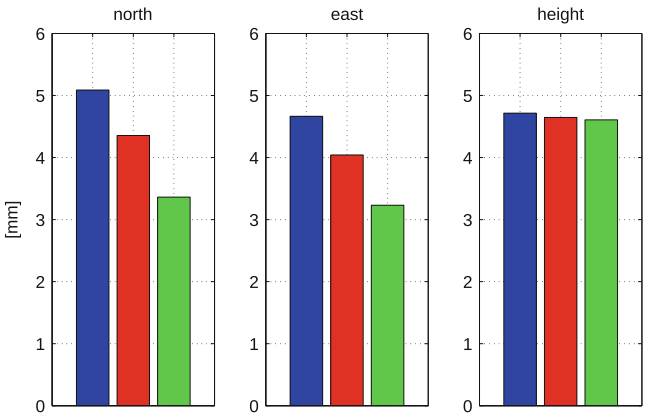

Fig. 6 Mean WRMS values of all station coordinates separated in North, East and height component of the three solutions (LA1/2: *blue*, LA1/2+LRS: *red*, 10 sat.: *green*)

6 Terrestrial Reference Frame

Together with the GFCs and the EOPs, also weekly 3-D station coordinates are estimated. The orientation of the TRFs is realized by No-Net-Rotation (NNR) conditions applied over a subset of stable stations (Angermann et al. 2004; Bloßfeld et al. 2014). Stations are assumed to be stable if they have a long, nearly continuous observation history and a low scatter in the weekly station coordinates. The selection is a highly intuitive process. To avoid non-interpretable results and to be comparable to official ILRS products, we stuck to a list of 'core stations' which is provided by the ILRS. Nevertheless, it is sometimes necessary to extend this list in order to achieve a solution. To validate the obtained TRFs, a weekly seven-parameter similarity transformation w.r.t. SLRF2008 (SLRF2008 2013) is computed. Thereby, the SLRF2008 is assumed to be error-free. The mean RMS values of those datum parameters which are determined by SLR without external conditions are shown in Fig. 5. The LA1/2 solution shows the largest mean RMS values. They are between 0.5 and 0.7 mm for the x- and y-translation and the scale and between 0.8 and 1.2 mm for the z-translation. If LARES is combined to LA1/2, the mean RMS values of the datum parameters decrease by between 14% and 22%. If all 10 satellites are combined, the mean RMS values in the x-translation and the scale increase. The increase of the mean RMS might be explained with the perturbed orbits of some LEOs. If model deficiencies affect the TRF estimates of a LEO, this effect would partly propagate into the LA1/2 TRF estimates although the LEO is down-weighted in the combination. Only the z-translation benefits from a combination of all satellites.

Figure 6 shows the mean WRMS values of all station coordinate residuals after the transformation. The reduction for a LA1/2+LRS solution w.r.t. a LAGEOS-only solution is about 14% for the horizontal components (north, east) and only 1% for the height. If more satellites are combined, the WRMS further decrease by about 20% in north and east and again only 1% in the height. The large reduc-

tion in north and east is mainly caused by the fact that the sky coverage of observations above a station improves with more satellites taken into account. The height component of the stations benefits only very slightly from a combination, since the vertical observation geometry does nearly not improve with more observations to different satellites.

In addition to the improvement of the station repeatability, also the weekly or monthly network coverage improves. Stations which did not observe LA1/2 within a week or month would not contribute to an LA1/2 TRF. If observations to more satellites are included and a station observes at least one of the satellites, it will contribute to the obtained TRF. Therefore, the network will be more dense.

7 Conclusions

One possibility to realize the common estimation of the 'three pillars' of GGOS (Earth geometric shape, rotation and gravity field) is the combination of SLR observations to satellites with different orbit characteristics.

SLR has the advantage that all parameters of the pillars are included in its observation equation. Therefore, no external conditions such as, e.g., local ties are necessary to connect different observation techniques. When we combine weekly NEQs of up to 10 satellites using a VCE, the results can be summarized as follows:

- The mix of different satellite heights and orbit resonances allows a stable estimation of GFCs together with orbit parameters, TRF and EOPs.
- The longer the arc length is (at maximum, 28-days are used in this study), the smaller are the standard deviations of the estimated GFCs. We obtained well-determined GFCs up to degree and order 20 with monthly solutions (monthly solutions are derived from four stacked weekly solutions).
- The mix of different satellite inclinations allows to reduce the UT1-UTC systematics due to a decrease of the correlations of GFCs, $\dot{\Omega}$ and LOD.
- The more satellites are combined, the smaller is the variation of the pole coordinates w.r.t. IERS 08 C04.
- LARES helps to reduce the scatter of the weekly translation and scale parameters w.r.t. SLRF2008 up to 22% w.r.t. the LAGEOS-only solution. Additionally, the mean WRMS of all residual station coordinates is reduced (mainly in the horizontal components).
- With 10 satellites, the mean WRMS is reduced by about 34% w.r.t. the LAGEOS-only solution.
- During some weeks, some of the stations do not observe LA1/2, so for the TRF derived purely from LA1/2, those stations do not contribute during those weeks. If the observation to 10 satellites are used and these stations observed at least one of them, the station network is more dense.

In the case of the monthly gravity fields obtained from the 10 satellite solution, the GFCs with degree $\in [0, 5]$ and order $\in [10, 20]$ show a higher standard deviation than the other. To reduce this lack of information, a suggestion to the ILRS is be to ask the stations to enforce the observation of the ETALON satellites. Since their orbit has a resonance frequency of 2, their observations possibly help to strengthen the estimation of the near-zonal GFCs, although the sensitivity of the ETALON orbits will not reach orders $\in [10, 20]$.

To conclude, we want to focus again on the combination of the LAGEOS satellites with LARES. When GFCs are estimated together with EOPs and TRF parameters, the error in LOD/UT1-UTC and the variation in the pole coordinates of the LA1/2+LRS solution is significantly reduced and comparable to the 10 satellite solution. Also the station coordinates benefit strongly in the horizontal components by the combination. In comparison to LA1/2 and ET1/2, LRS is down-weighted. Nevertheless, the relative weight of LRS is the largest relative weight of the satellites with altitudes below 1,500 km since LRS has the smallest AMR of all satellites. This study supports the intention of the ILRS to include LARES observations in the standard processing. If doing so, also the GFCs must be included in the standard solutions.

Acknowledgements The authors want to thank the ILRS for providing the observational data. This work contributes to the research group 'Space-time reference systems for monitoring global change and for precise navigation' (FOR1503) of the German Research Foundation (DFG). The authors also want to thank the editor and the three anonymous reviewers for proof-reading the manuscript.

References

Angermann D, Drewes H, Krügel M, Meisel B, Gerstl M, Kelm R, Müller H, Seemüller W, Tesmer V (2004) ITRS combination center at DGFI: a terrestrial reference frame realization 2003, Reihe B. Verlag der Bayerischen Akademie der Wissenschaften, München

Bloßfeld M, Seitz M (2012) The role of VLBI in the weekly inter-technique combination. In: Behrend D, Baver KD (eds) IVS 2012 general meeting proceedings, NASA/CP-2012-217504

Bloßfeld M, Müller H, Angermann D (2011) Adjustment of EOP and gravity field parameters from SLR observations. Proceedings of the 17th ILRS workshop, pp 292–296. ISBN:978-3-89888-999-5

Bloßfeld M, Seitz M, Angermann D (2014) Non-linear station motions in epoch and multi-year reference frames. J Geod 88(1):45–63. doi:10.1007/s00190-013-0668-6

Böckmann S, Tesmer V (2010) VLBI terrestrial reference frame contributions to ITRF2008. J Geod 84(3):201–219. doi:10.1007/s00190-009-0357-7

Kelso TS (2013) Chinese space debris may have hit Russian satellite. http://www.blogs.agi.com/agi/2013/03/08/chinese-space-debris-hits-russian-satellite/. Accessed 25 Sept 2013

Pearlman MR, Degnan JJ, Bosworth JM (2002) The international laser ranging service. Adv Space Res 30(2):135–143. doi:10.1016/S0273-1177(02)00277-6

Plag HP, Pearlman MR (2009) In: Plag HP, Pearlman MR (eds) Global geodetic observing system - meeting the requirements of a global society on a changing planet in 2020. Springer, Berlin, Heidelberg, New York. doi:10.1007/978-3-642-02686-7

Seitz M (2009) Kombination geodätischer Raumbeobachtungsverfahren zur Realisierung eines terrestrischen Referenzsystems. Dissertation, Reihe C, 630, Verlag der Bayerischen Akademie der Wissenschaften

SLRF2008 (2013) http://www.ilrs.gsfc.nasa.gov/science/awg/SLRF2008.html. Accessed 25 Sept 2013

Tapley BD, Watkins MM, Ries JC, Davis GW, Eanes RJ, Poole SR, Rim HJ, Schutz BE, Shum CK, Nerem RS, Lerch FJ, Marshall JA, Klosko SM, Pavlis NK, Williamson RG (1996) The joint gravity model 3. J Geophys Res 101(B12):28029–28049. doi:10.1029/96JB01645

Thaller D (2008) Inter-technique combination based on homogeneous equation systems including station coordinates, earth orientation and troposphere parameters. Scientific technical report STR 08/15, Deutsches GeoForschungsZentrum (GFZ). doi:10.2312/GFZ.b103-08153

PositioNZ-PP: An Online GPS Processing Application for New Zealand

Chris Pearson, Chris Crook, Aaron Jordan, and Paul Denys

Abstract

PositioNZ-PP is an on-line GPS processing utility for New Zealand that is currently being developed by Land Information New Zealand (LINZ). The system was developed to process user supplied static GPS data using New Zealand's PositioNZ CORS network as reference stations. There are already many services like this around the world; however LINZ decided to create its own system to utilize the PositioNZ CORS network and to allow the calculation of coordinates in terms of the NZGD2000 datum. The GPS processing engine incorporates components that check the input RINEX file, identify and acquire RINEX data for the three best PositioNZ stations to act as control, acquire appropriate International GNSS Service (IGS) orbit files and initiate GPS processing. This step generates a set of International Terrestrial Reference Frame (ITRF) coordinates at the epoch of observation, which still must be transformed to the reference epoch of NZGD2000. Because of New Zealand's location on the Pacific Australian plate boundary, current day models of tectonic deformation are necessary to correct coordinates for tectonic motion that has occurred between the epoch of observation and the reference epoch (2000.0). The PositioNZ-PP system makes use of two subroutines for this purpose. The first (the Station Coordinate Prediction Model) uses parameters determined from a least square analysis of the time series from PositioNZ CORS network to correct coordinates for changes associated with the secular velocity, seasonal (annual and semi-annual) cycles, offsets caused by equipment changes and co-seismic displacements, decaying post-seismic signals and slow-slip events. This subroutine estimates accurate coordinates for the PositioNZ CORS network at the epoch of observation. The second subroutine (the New Zealand Deformation Model) uses a gridded model of the secular velocity field and the co-seismic displacement associated with any relevant earthquakes to transform the coordinates associated with the user data to NZGD2000 at epoch 2000.0.

Keywords

Australia • CORS • GNSS • Infrastructure • New Zealand • Positioning

C. Pearson (✉) • P. Denys
School of Surveying, University of Otago, Box 56, Dunedin, New Zealand
e-mail: Chris.pearson@otago.ac.nz

C. Crook • A. Jordan
Land Information New Zealand, PO Box 5501, Wellington, New Zealand

1 Introduction

Over the last 10 years, a number of on-line positioning services have been developed to allow the public to submit GPS data from user stations and receive coordinates usually by email (Ghoddousi-Fard and Dare 2006). These include the OPUS service operated by the US National Geodetic Survey

© Springer International Publishing Switzerland 2015

C. Rizos, P. Willis (eds.), *IAG 150 Years*, International Association of Geodesy Symposia 143,
DOI 10.1007/1345_2015_159

(Snay and Soler 2008) using NGS's PAGES software[1] and the CRS-PPP operated by Natural Resources Canada using Precise Point Positioning technique.[2] Currently AUSPOS[3] run by Geoscience Australia is the only Southern Hemisphere service. AUSPOS has limitations for New Zealand users as it produces coordinates at the epoch of observation in the ITRF2008 reference frame and not in NZGD2000, New Zealand's national datum, and does not incorporate all of the PositioNZ CORS network.

This paper describes progress in the development of a GPS processing engine for New Zealand (NZ) using the PositioNZ CORS network. PositioNZ-PP is under development by LINZ (Palmer 2010). It is an on-line GPS processing application that processes NZ user supplied GPS data observed in 'static' mode using reference stations of the PositioNZ CORS network (Collett 2010). While PositioNZ stations record both GPS and GLONASS, PositioNZ-PP currently only uses the GPS. We hope to incorporate other GNSS data later. When fully deployed, the data will be processed automatically using Bernese GPS software (Dach et al 2007) and the coordinates will be transformed into NZGD2000 datum. Development of the GPS processing engine is basically complete, the user interface is under development and the Station Coordinate Prediction Model and the New Zealand Deformation Model (each of which corrects coordinates for crustal deformation) are currently being upgraded to incorporate recent earthquakes in New Zealand. It is planned that the system will be ready for deployment during 2014.

2 Description of the GPS Processing Procedure

The process starts with a RINEX file submitted by a user through the LINZ web page. The antenna type and height are taken initially from the RINEX file header but the web interface allows users to check the values and ensure that these are accurate. The program then performs some quality assurance tests on the data, determines rough initial coordinates for the stations and identifies three suitable PositioNZ reference stations to use as control stations. It then uses a mathematical model to predict ITRF coordinates for the reference stations at the time the user submitted RINEX file was observed. These coordinates are used as a priori coordinates for the GPS processing and as control for the ITRF coordinates for the user station that are determined in a network adjustment. Once the processing is complete, the final ITRF coordinates are converted to NZGD 2000. Key steps in this process are described in more detail below.

3 Pre-processing User File

The user file is checked by the UNAVCO supported GPS RINEXing and quality assurance program TEQC[4] (Estey and Meertens 1999). During this step the program determines the time interval spanned by the observations and performs some quality assurance tests to confirm that the observation ratio is at least 95% and the maximum multipath index is less than 2. In addition this step confirms that the file contains at least 120 epochs (i.e. at least 1 h of data at a 30-s rate) of observations and that the maximum duration of the file is less than 48 h. If any of these requirements are not met, the file is rejected. The approximate position is also extracted from the RINEX file at this stage and is used for the PositioNZ reference station ranking procedure discussed below. The next step is to identify and acquire the best available precise orbit files. The program will use the final, rapid or ultra-rapid orbit depending on file availability when the job is processed.

4 Selection of Reference Stations

The next step in the PositioNZ-PP workflow is to identify three reference stations among the 38 PositioNZ sites (see Fig. 1 for a map showing the location of the sites). Normally GPS on-line positioning services select reference stations based on minimizing the distance to the user's station (Ghoddousi-Fard and Dare 2006). PositioNZ-PP uses two parameters. The first, and most important, is the length of the baseline between the user's station (the coordinate associated from the submitted RINEX file) and the candidate reference station. The length is the distance between the two positions calculated from the difference in their geocentric coordinates; however, the parameter that goes into the weighting is a percentage value (Dfactor) depending on the interval within which the calculated length falls. The second ranking function is one minus the dot product of the user station (us)-reference station baseline for the candidate reference station (cs) baseline ($\mathbf{X}_{cs}$-$\mathbf{X}_{us}$) and the previously selected reference station (ps) baseline ($\mathbf{X}_{ps}$-$\mathbf{X}_{us}$) divided by the product of the baseline lengths for the previously selected and candidate stations. This function (Eq. 1) is designed to identify a group of candidate reference stations that (as much as possible) surround the user station.

[1] www.ngs.noaa.gov/GRD/GPS/DOC/

[2] http://webapp.geod.nrcan.gc.ca/geod/tools-outils/ppp.php

[3] http://www.ga.gov.au/earth-monitoring/geodesy/auspos-online-gps-processing-service.html

[4] http://facility.unavco.org/software/teqc

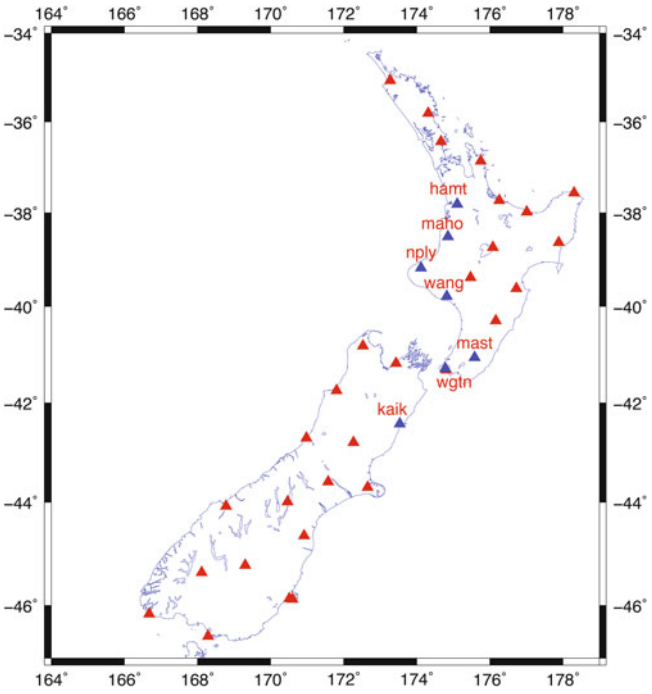

Fig. 1 New Zealand PositioNZ network. The stations in the LINZ PositioNZ network that were used to provide test data sets are ploted as *blue triangles* while all others are plotted as *red*

$$dot = 1 - \frac{(\mathbf{X}_{ps} - \mathbf{X}_{us}) \bullet (\mathbf{X}_{cs} - \mathbf{X}_{us})}{BaselineLength_{ps} BaselineLength_{cs}} \quad (1)$$

The final ranking involves the Dfactor and dot criterion combined, with the former and later having 65% and 35% respective weighting. Our experience shows that the number of intervals in the Dfactor table was the key step in optimizing reference station selection. Currently the Dfactor table has 50 intervals with a 1 km distance step for the first interval, followed by 10 km for the next 40 intervals beyond which steps become increasingly course until a maximum of 5,000 km is reached. The Dfactor table extends to very large distances to support users in New Zealand's remote Sub-Antarctic and Kermadec Islands.

Modelling studies show that the PositioNZ stations are well configured to act as base stations within mainland New Zealand. Figure 2 shows contour plots of baseline distance averaged over the top three reference station choices. The figure shows that the average baseline distance for the three base stations selected using the algorithm discussed above is nearly always less than 100 km and always less than 150 km except for a limited area in the far north of North Island and the southern end of Stewart Island where the average distance increases to nearly 200 km. The effect of Eq. (1) on the reference station selections is shown in Fig. 3. Figure 3a shows a contour plot of the minimum azimuth difference of baselines to the top three reference stations for our preferred reference station ranking while Fig. 3b shows a similar plot where the ranking is just based on distance. A comparison of these two plots demonstrates our preferred algorithm selects reference stations with a greater diversity of azimuths than can simple distance based ranking.

Once a candidate reference station is identified the program attempts to acquire the RINEX data. If the file is not available or the time coverage between the user station and the reference station is not at least 95%, PositioNZ-PP will go to the next station on the list.

5 Station Coordinate Prediction Model

Before a GPS processing session is started, the code develops accurate a priori coordinates of the reference stations at the epoch of observation using LINZ's Station Coordinate Prediction Model. While a priori coordinates are always required by GPS processing, this step is particularly important because the GPS processing algorithm used by PositioNZ-PP determines the final coordinates using the network adjustment step in Bernese, which holds the a priori coordinates fixed. As a result, the a priori coordinates must be highly accurate because they in effect are the control for the final NZGD2000 coordinates that are given to the users. This model incorporates the measured velocity for each station and the effect of annual seasonal variation in the coordinates, any offsets caused by equipment changes or earthquakes events. The model also includes a function for decaying exponential post-seismic signals, which are caused by major earthquakes and slow-slip events. Slow slip events, which are common in central New Zealand (Wallace and Beavan 2010; Wallace et al. 2012), are important in modeling the time series for PositioNZ stations along the east coast of North Island and the northern end of South Island. This model, which is based on a prototype developed by GNS Science (Beavan 2008), was recently updated to include the effects of the 2009 Dusky Sound Earthquake (Beavan et al. 2010) and 2010–2011 Christchurch earthquake sequence (Beavan et al. 2012) along with all slow slip events that have occurred since 27 June 2008 (Pearson 2013). The model needs to be continuously monitored and maintained to respond to new slow slip events, as well as other influences such as GNSS equipment changes.

6 GPS Processing Engine

The next step is to initiate GPS processing using a Bernese Processing Engine (BPE) script. This first imports reference station RINEX files and performs some checks to identify

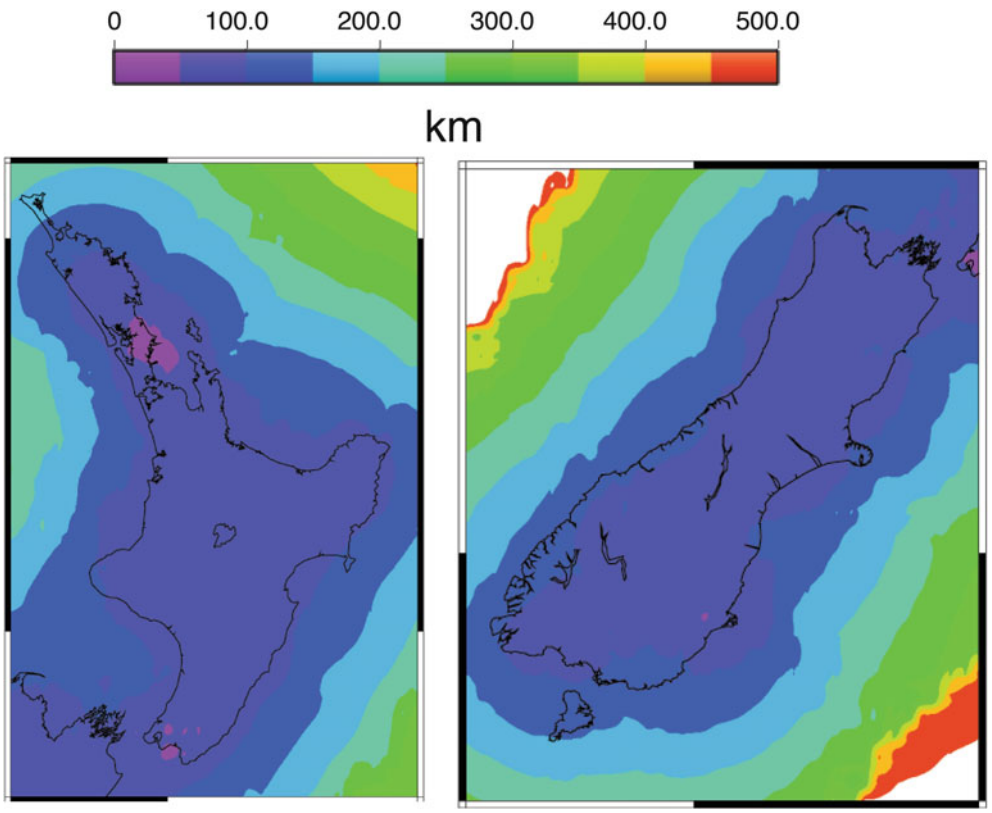

Fig. 2 Contour plot showing average distances using the top three PositioNZ stations identified by the reference station ranking algorithm

and remove any bad data. Next the process forms baselines between the reference and user stations in a star pattern centered on the user station. Each baseline is checked to identify and fix cycle slips as well as outlier observations. The next step is to resolve the carrier phase ambiguities for each baseline using the quasi-ionosphere-free (QIF) strategy (Dach et al. 2007). This stratagem, which is only available using high end GPS processing software such as the Bernese suite, is optimized for longer baselines (up to approximately 2,000 km) and fairly long observing sessions. While most users will not require such long baselines, users in New Zealand's remote offshore islands and the Ross Dependency probably will because the average distance to reference stations increases rapidly away from the main islands of New Zealand (see Fig. 2). The last step is the network solution where the carrier phase ambiguities are fixed at their values from the QIF step and the reference station coordinates are held fixed at the observation epoch which are determined by the Station Coordinate Prediction Model discussed above. During this step the final coordinates are determined in the ITRF datum and at the epoch of observation.

7 Determination of NZGD2000 Coordinates

The GPS processing discussed above produces ITRF2008 coordinates at the epoch of observation. To convert them to NZGD2000, the coordinates are first transformed to ITRF96 coordinates at the epoch of observation using the ITRF2008 and ITRF96 transformation (Pearson 2013). These ITRF96 coordinates are then transformed between the epoch of observation and epoch 2000.0 using the New Zealand deformation model. The model is currently being updated by Crook et al. (2013) to include models of the 2009 Dusky Sound earthquake (Beavan et al. 2010) and the 2010–2011 Christchurch earthquake sequence (Beavan et al. 2012). This model has grids specifying the horizontal velocities and displacements associated with the Dusky Sound earthquake and Christchurch earthquakes. Using these grids, the total displacement between the epoch of observation and 2000.0 can be calculated by multiplying the velocities by the time interval between the observation and reference epochs and

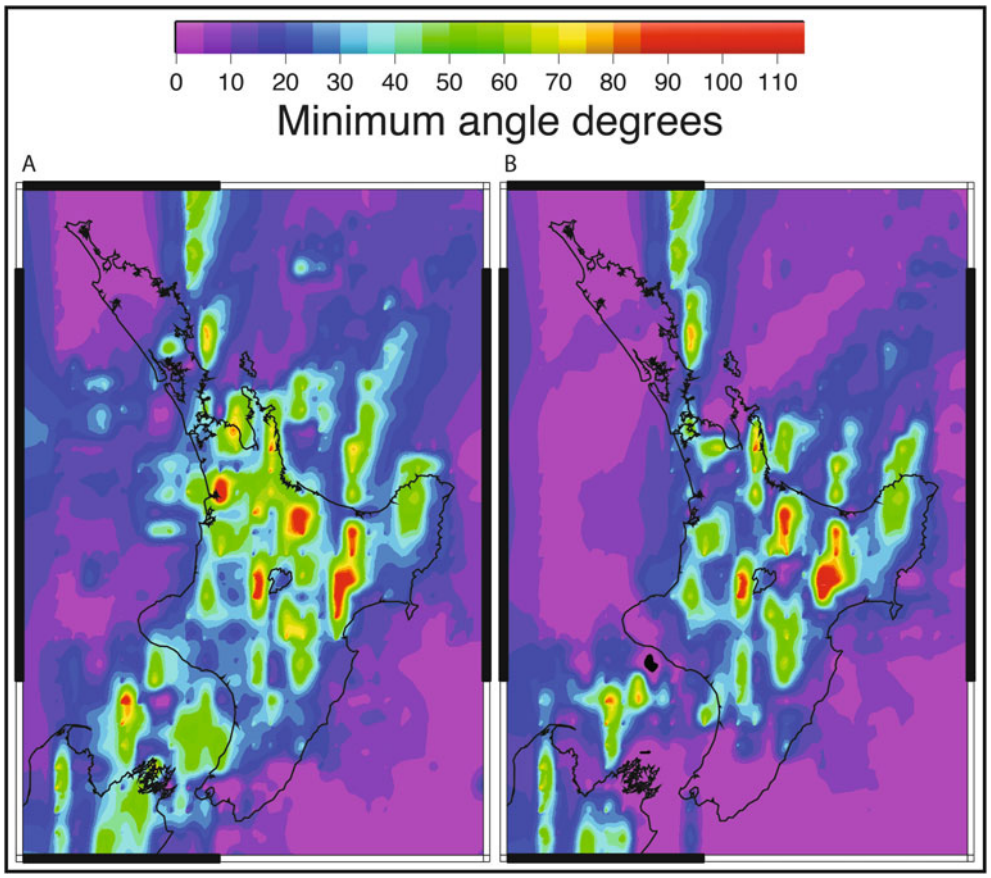

Fig. 3 Contour plot showing minimum angles formed between the three reference station- user station baselines as a function of the rover location for the North Island of New Zealand. (**a**) Is calculated using both the distance ranking function and the dot function in Eq. (1) with a 65% and 35% weighting respectively while (**b**) just uses the distance ranking function

adding any seismic displacements. The NZGD2000 coordinates are calculated by applying the displacement vector to the ITRF96 coordinates at the epoch of observation (Blick and Grant 2010).

8 Preliminary Estimate of Accuracy Achievable by PositioNZ-PP Processing Engine

We use seven PositioNZ sites as test stations. These were selected to avoid areas affected by recent earthquakes in New Zealand. The location of the test stations are shown in Fig. 1. Since PositioNZ-PP will reject reference stations whose name is the same as that of the user station and the distance is less than 10 m, the test station will not also be used as a reference station.

9 Method

All tests were conducted between day of year (DOY) 348 and 365 in 2011 (19 days) and DOY 027 to 029 in 2012 (3 days). The standard 24 h RINEX files were acquired for each of the 21 days and processed using the PositionNZ-PP algorithm. In addition, we took 47 non-overlapping 4 h samples and 130 non-overlapping 2 h samples for each station using the windowing capability of TEQC to divide the 24 h RINEX files into shorter sessions. In order to average out the effect of changes in the satellite constellation, the 2 and 4 h samples were selected so that the sampled time intervals are spread evenly over the day. Each data set was processed using a slightly modified PositioNZ-PP processing algorithm that saved the geocentric Cartesian coordinates at the epoch of observation for each test station. The epoch

Table 1 Summary test data

	RMS E (mm)	Max E (mm)	Min E (mm)	RMS N (mm)	Max N (mm)	Min N (mm)	RMS Up (mm)	Max Up (mm)	Min Up (mm)
24 h	2	4	−5	2	6	−9	6	24	−27
4 h	6	13	−4	6	12	−15	16	43	70
2 h	11	106	−60	8	35	−40	19	46	−62
2 h[a]	17	81	−46	8	38	−17	26	42	−75

RMS residuals and maximum and minimum residuals for 24, 4 and 2 h tests. The test involves a combination of data sets from 10 individual PositioNZ sites

[a]2 h tests that include data from 2 GMT days

of observation was used since the models used to convert coordinates to (or from) epoch 2000.0 have not yet been updated for the combined effects of the co-seismic and post seismic displacements from the Christchurch earthquake sequence and Dusky Sound earthquake of 2009. This means that the projected coordinates for the reference stations may be slightly displaced from their true positions but all of the test stations were selected so that they were located outside of the regions undergoing significant co-seismic displacements. All of the test data sets ran normally. In total, at each of the seven test stations the number of test solutions included:

- twenty-one × 24 h solutions;
- forty-seven × 4 h solutions, and;
- one hundred and thirty × 2 h.

Because the updated Station Coordinate Prediction Model was not available for these tests, our best estimate of the position of each station is to average the twenty-one 24 h test solutions so we used this as a point of comparison for the coordinates produced by the individual solutions. This procedure assumes that the lack of information on crustal deformation has a minimal effect on the results of the test because the measurements and final coordinates refer to very similar epoch times. As a result the reduction of the coordinates to NZGD2000 is unnecessary. The results for all of the test stations were then combined into a single estimate of the RMS. The results (summarized in Table 1) suggest that the PositioNZ-PP processing engine can produce standard deviations of ±11 mm in the East direction, ±8 mm in the North direction and ±19 mm in the up direction for 2 h observing sessions. These results are comparable to those achieved by the National Geodetic Surveys OPUS service (Soler et al. 2006). Analysis of the 2 h tests suggests that small, but significant changes in accuracy can be expected as a function of the time of the day due to the combined effect of changes in satellite geometry and atmospheric conditions.

All of our tests used final IGS orbits, however many users will submit datasets to PositioNZ-PP before the about 2 weeks latency period for the final orbits has elapsed. In this case PositioNZ-PP will default to use the best available orbit (which will usually be the IGS Rapid orbit). To quantify the effect that rapid orbits might have on the precision of the estimated coordinate, we repeated the analysis described above for two sites using the same datasets used in the original test and version of the GPS engine modified to use only rapid orbits. The maximum difference between coordinates developed using rapid and final orbits was less than 0.1 mm suggesting that the use of rapid orbits is unlikely to have any significant effect on the accuracy of PositioNZ-PP coordinates. To quantify the effect of sessions incorporating more than one GMT day, we tested a total of forty 2 h sessions that started 1 h before GMT midnight. These sessions were spread over 7 days and used six PositioNZ sites. The resulting accuracies (shown on the bottom row of Table 1) are comparable to the results for sessions that do not include more than one GMT day.

10 Conclusions

The GPS processing part of PositioNZ-PP online GPS processing tool is almost complete. It is hoped that the system will be ready for deployment during 2014. Results of preliminary testing using the IGS final orbits suggest that the PositioNZ-PP processing engine can produce standard deviations of ±11 mm in the East component, ±8 mm in the North component and ±19 mm in the up component for 2 h samples. These results are comparable to those achieved by the National Geodetic Surveys OPUS service (Soler et al. 2006). The standard deviations improve to ±6 mm in the East and North and ±16 mm in the up component for the 4 h samples. For the 24 h data sets, the RMS values were ±2 mm in the North and East and ±6 mm in the up components respectively. The results were not significantly degraded using the IGS rapid orbits rather than the final orbits.

Acknowledgements Jeremy Palmer made significant contributions to the development of the PositioNZ-PP program. The work described in this paper was funded by a research grant from Land LINZ to the University of Otago. This paper benefited from a review by Bjorn Johns.

References

Beavan RJ (2008) Consultancy services for coordinates for PositioNZonLine, Phase 2 (PONL-02). Consultancy Report for Land Information New Zealand. GNS Science, Lower Hutt

Beavan J, Samsonov S, Denys P, Sutherland R, Palmer N, Denham M (2010) Oblique slip on the Puysegur subduction interface in the 2009 July MW 7.8 Dusky Sound earthquake from GPS and InSAR observations: implications for the tectonics of southwestern New Zealand. Geophys J Int 183(3):1265–1286. doi:10.1111/j.1365-246X.2010.04798.x

Beavan J, Motagh M, Fielding E, Donnelly N, Collett D (2012) Fault slip models of the 2010–2011 Canterbury, New Zealand, earthquakes from geodetic data, and observations of post-seismic ground deformation. N Z J Geol Geophys 55(3):207–221

Blick G, Grant D (2010) The implementation of a semi-dynamic datum in New Zealand –ten years on. In: XXIV FIG Congress 2010, Sydney, Australia, 2010. International Federation of Surveyors pp 1–14

Collett DE (2010) Developing a national real-time CORS Network in New Zealand. In: Online proceedings of the XXIV FIG Congress 2010, Sydney, Australia, 2010 2012 International Federation of Surveyors pp 1–9. https://www.fig.net/pub/fig2010/techprog.htm. Accessed 13 Apr 2012

Crook C, Donnelly N (2013) Updating the NZGD2000 deformation model. In Denys, P., Strack, M., Moore, A.B. and Wigham, P. (eds). Joint Proceedings of the NZIS conference: Celebrating the Past, Redefining the Future and SIRC NZ 2013 Conference, 29th-31st August, Dunedin

Dach R, Hugentobler U, Fridez P, Meindl M (2007). Bernese GPS software version 5.0. Astron. Inst., University of Bern, Bern, 612 pp

Estey LH, Meertens CM (1999) TEQC: The Multi-Purpose Toolkit for GPS/GLONASS Data. GPS Solut 3(1):42–49. doi:10.1007/pl00012778

Ghoddousi-Fard R, Dare P (2006) Online GPS processing services: an initial study. GPS Solut 10(1):12–20. doi:10.1007/s10291-005-0147-5

Palmer J (2010) PositioNZ-PP – A GPS post-processing service New Zealand In: In: Online proceedings of the XXIV FIG Congress 2010, Sydney, Australia, 2010. International Federation of Surveyors. pp 1–14 https://www.fig.net/pub/fig2010/techprog.htm. Accessed 13 Apr 2012

Pearson C (2013) Investigations in support of PositioNZonLine interim report. Consultancy Report School of Surveying. University of Otago, Dunedin

Snay R, Soler T (2008) Continuously operating reference station (CORS): history, applications, and future enhancements. J Surv Eng 134:95–104. doi:10.1061/(ASCE)0733-9453(2008)134:4(95)

Soler T, Michalak P, Weston ND, Snay RA, Foote RH (2006) Accuracy of OPUS solutions for 1- to 4-h observing sessions. GPS Solut 10(1):45–55. doi:10.1007/s10291-005-0007-3

Wallace LM, Beavan J (2010) Diverse slow slip behavior at the Hikurangi subduction margin, New Zealand. J Geophys Res 115(B12), B12402. doi:10.1029/2010jb007717

Wallace LM, Beavan J, Bannister S, Williams C (2012) Simultaneous long-term and short-term slow slip events at the Hikurangi subduction margin, New Zealand: Implications for processes that control slow slip event occurrence, duration, and migration. J Geophys Res 117(B11), B11402. doi:10.1029/2012jb

Geodetic Monitoring Networks: GNSS-Derived Glacier Surface Velocities at the Global Change Observatory Inylchek (Kyrgyzstan)

Cornelia Zech, Tilo Schöne, Julia Neelmeijer, Alexander Zubovich, and Roman Galas

Abstract

The German Research Centre for Geosciences (GFZ, Potsdam, Germany) and the Central-Asian Institute for Applied Geosciences (CAIAG, Bishkek, Kyrgyzstan) jointly established the Global Change Observatory "Gottfried Merzbacher" at the Inylchek Glacier in eastern Kyrgyzstan which is one of the largest non-polar glaciers of the world and consists of two glacier streams. The flow of melt-water from the northern tributary forms a lake (Lake Merzbacher) that is dammed by the calving ice front of the southern Inylchek Glacier. At least once a year a glacial lake outburst flood (GLOF) occurs and the complete water of the Lake Merzbacher drains through sub-glacial channels. To monitor the glacier dynamics including the post-drainage ice dam response, a small network of remotely operated multi-parameter stations (ROMPS) was installed at different locations at the glacier. Directly located near the ice dam, a continuously measuring kinematic GNSS station provides precise long-term data of variations in the dynamics of the ice dam for the years 2010, 2011 and 2012. While the station reflects the horizontal motion of the ice dam towards the Lake Merzbacher, the vertical component shows a clear loss of elevation as a "long-term" response after the GLOF lasting for several weeks instead of only a few days. In correspondence to the elevation decrease, the surface velocity has a higher variability due to a relaxing process of the ice dam but changes significantly to a nearly constant velocity during the winter time.

Keywords

Global Change Observatory Central Asia • Inylchek Glacier • Kinematic GNSS glacier monitoring station • Lake Merzbacher

1 Introduction

Freshwater is one of the most important natural resources and plays a key role for living, economic development and agricultural production. Especially in Central Asia (Fig. 1), where water is non-uniformly distributed over the entire region and summer precipitation is rare (Sorg et al. 2012), the availability and direct access is often a reason for disputes between various countries. The melt-water, coming from the glaciers and snow covered hills in the Tian Shan, Pamir, Alai and Hindukush Mountains, contributes significantly to the natural water supply. While the countries Kyrgyzstan,

C. Zech (✉) • T. Schöne • J. Neelmeijer
Helmholtz Centre Potsdam, GFZ German Research Centre for Geosciences, Potsdam, Germany
e-mail: czech@gfz-potsdam.de

A. Zubovich
Central-Asian Institute for Applied Geosciences (CAIAG), Bishkek, Kyrgyz Republic

R. Galas
Technical University of Berlin (TU Berlin), Berlin, Germany

© Springer International Publishing Switzerland 2015

C. Rizos, P. Willis (eds.), *IAG 150 Years*, International Association of Geodesy Symposia 143,
DOI 10.1007/1345_2015_38

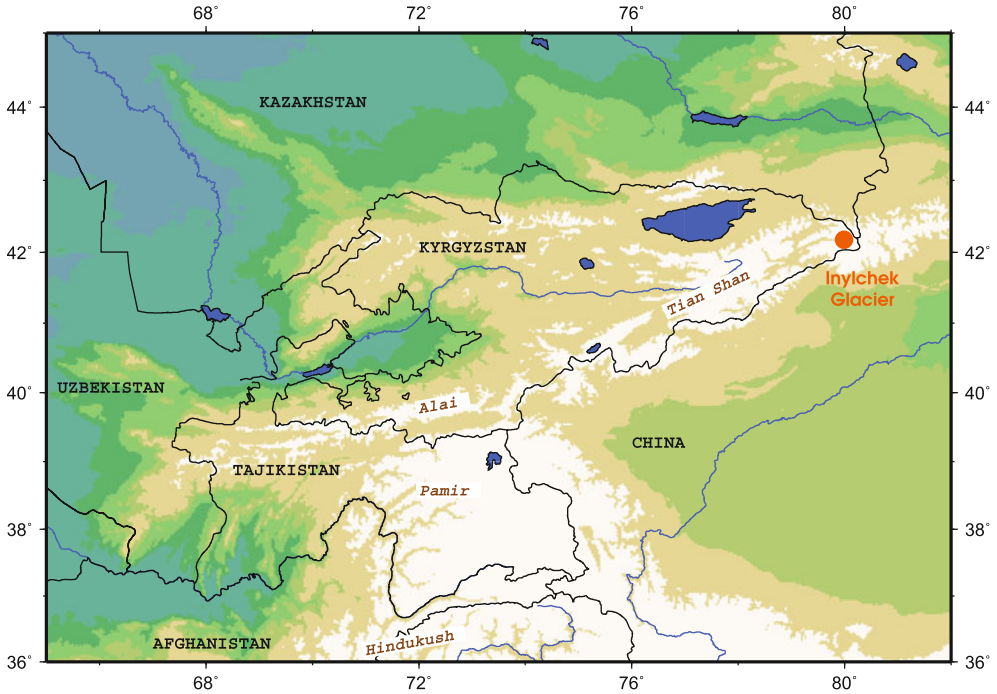

Fig. 1 Map of Central Asia with the Tian Shan Mountains in eastern Kyrgyzstan showing the location of the Inylchek Glacier at the border to China and Kazakhstan

Tajikistan, northern Afghanistan and northwest China have direct access to this freshwater source, the downstream countries Uzbekistan, Kazakhstan and Turkmenistan depend on the river discharge coming from the upper mountain regions and large glacier systems (UNISDR et al. 2009).

1.1 ROMPS Monitoring Networks

In Central Asia, the knowledge about changes in the Earth System including information about current climate and water availability is still incomplete also due to the scarcity of reliable and appropriate hydrometeorological data sets (Unger-Shayesteh et al. 2013). The sustainable water management between Central Asian countries requires dedicated highly specialized monitoring networks that especially cover remote areas in high altitudes. Based on the concepts for tsunami early warning systems (Schöne et al. 2011), the German Research Centre for Geosciences (GFZ, Potsdam, Germany) developed remotely operated multi-parameter stations (ROMPS) (Schöne et al. 2013). These stations allow a wide range of applications and are suitable for the operation in different environments. Currently, a hydrometeorological network of ROMPS is continuously operated in Central Asia distributed primarily along river systems that drain towards the Lake Aral or eastwards to the Tarim Basin. All stations integrate a geodetic Global Navigation Satellite System (GNSS) receiver and a basic set of WMO-conform meteorological sensors (WMO 2008). As they are designed for the operation in remote areas, the stations are running on solar power only and transmit their data via a satellite communication system to a data centre in Potsdam (www.cawa-project.net, Germany).

1.2 Inylchek Glacier

In 2009, the GFZ and the Central-Asian Institute for Applied Geosciences (CAIAG, Bishkek, Kyrgyzstan) jointly installed the Global Change Observatory "Gottfried Merzbacher" (GCO) at the Inylchek Glacier. The Inylchek Glacier is located at the central Tian Shan Mountains in the northeastern region of Kyrgyzstan close to the border of China and Kazakhstan (Fig. 1). It is one of the largest non-polar glaciers of the world comprising a northern and southern valley glacier stream, both stretching from east to west (Fig. 2). Several non-uniformly behaving inflows join the southern glacier stream and separate again close to the junction of the northern and southern valley. Whereas parts of the ice stream follow the main flow direction to the glacier snout, other parts turn into the valley of the northern tributary and terminate there as an ice dam. The accumulation of melt-water from the northern tributary is dammed by the ice dam and forms a glacial lake. This lake is named Lake Merzbacher after Gottfried Merzbacher who visited the area in 1903 (Merzbacher 1905). As the ice dam prevents continuous discharge, the lake is filled by melt-water in late spring until it suddenly outbursts and completely drains

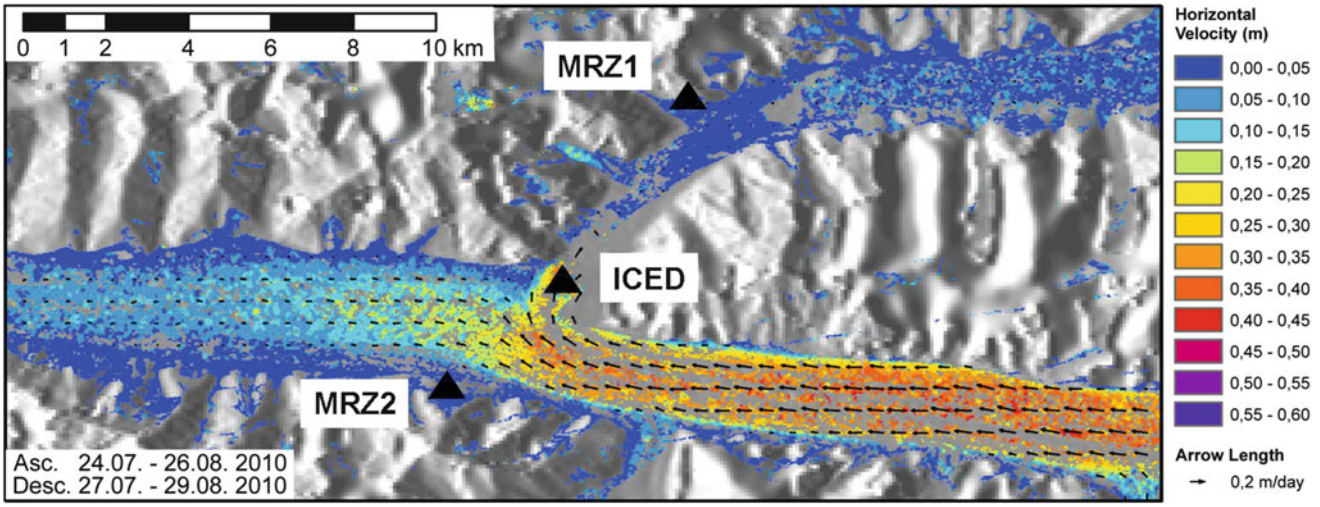

Fig. 2 Northern and southern tributary of the Inylchek Glacier showing surface velocities with *black arrows* and the locations of the GNSS monitoring stations marked with *black triangles* (modified after Neelmeijer et al. 2014)

through sub-glacial channels. These glacier lake outburst floods (GLOFs) occur regularly at least once a year during summer time (Glazirin 2010).

Various studies have been carried out regarding the GLOF and glacier kinematics at the Inylchek Glacier. Wortmann et al. (2013) used water gauge data to model and estimate the outburst flood volumes and Xie et al. (2013) extracted details from satellite images to model and forecast the GLOF. On the contrary, Hagg et al. (2008) and Mayer et al. (2008) studied the glacier's movement and surface melt rates with in situ glaciological measurements. In this paper we study the motion of the ice dam from precise GNSS measurements for several months in 2010, 2011 and 2012. Although the processed data does not include the direct pre- and post-drainage reaction of the ice dam with regard to the GLOF, the data shows a significant behaviour of the ice dam as a "long-term" response lasting for some weeks after the water of the lake has drained. We will show that the relaxation process of the ice dam as a result of the GLOF continues over several weeks instead of only a few days.

1.3 The Inylchek GNSS Array

The Global Change Observatory at the Inylchek Glacier comprises a GNSS array for the observation of the glacier's kinematics. The array (Fig. 2) consists two installations on a stable ground and one kinematic station on the ice stream close to the calving ice wall of Lake Merzbacher. The main station (code MRZ1) was installed in 2009 as a ROMPS station and is located at the western rim of the northern Inylchek Glacier stream. In 2010, the network was expanded by a second ROMPS station (code MRZ2) at the southern rim and a kinematic GNSS station (code ICED) located directly on the moving ice dam (Fig. 3). The station network integrates several hydrometeorological sensors, a broadband seismometer, two automated cameras for glacier observations and Topcon GB1000 geodetic GNSS receivers at each station with 1 Hz data sampling. Due to the limitation of sun exposure in winter time, when the sun does not come over the southern mountain crests, the automated solar powered system ICED stopped data collection around winter solstice. In summer 2013, a failover system was added to allow automatic restarts towards spring time.

2 GNSS Results of the Inylchek Ice Dam Monitoring

The GNSS data collected in 2010, 2011 and 2012 from all three GNSS stations (ICED (kinematic), MRZ1, MRZ2) were processed with the kinematic positioning software TRACK (Herring et al. 2009). MRZ1, located on a stable rock, was held fixed as the reference station and ICED and MRZ2 as kinematic stations with loose constraints on the MRZ2 initial positions. As the distances between the stations are not small enough to neglect the ionospheric disturbances (baselines vary from 7.5 km for MRZ1-MRZ2 and 4.8 km for MRZ1-ICED), the ionospheric delay corrected phase (LC) was used for position estimation and integer bias fixing. Furthermore, the atmospheric delay was parameterized and estimated during the processing. To account for unresolved bias parameters, a Kalman filter was applied to smooth the results. Although 1 Hz data are processed, only the mean daily positions have been used in the analysis. For times of spurious results, the 1 Hz data have been analyzed in more detail. To further examine the movement of the station ICED, horizontal surface velocities were calculated by using the daily mean positions.

Fig. 3 Kinematic ice dam station (ICED) with a Topcon GNSS receiver, a Vaisala WXT520 weather sensor, power supply and HF radio antennas

2.1 Horizontal Motion of the Station ICED

As ICED moves with the glacier system towards crevasses near the calving ice wall at the Lake Merzbacher, the station was moved back annually close (but not exactly) to its initial position to avoid damages and the loss of equipment. For all campaigns from 2010 to 2012, the ICED station performs a horizontal motion to north–east reflecting the movement of the glacier towards the northern tributary (Lake Merzbacher). Due to sub-debris melting of the glacier, the station suddenly changes its position (horizontal and vertical component) a few times every campaign. Especially, on August 1st 2012, the station experienced a horizontal displacement of 1 m towards the north–east direction but only 15 cm in the vertical component. These sudden displacements in a very short time interval with no influence to the further motion indicate a stick–slip motion (Sergienko et al. 2009) caused by a variation of the ice/till interface either by changes in the presence of melt-water in the sub-glacial channels or a sticky spot in the ice stream. Although this distinction from causes in the sub-glacial topography is challenging, the change in melt-water deposits and displacement of cavities seems more realistic in the period of post-drainage response. Changes in the sub-glacial topography would lock or displace the ice stream causing a reduced velocity but the opposite (surface velocity is 5 times higher than before) is reflected in the measurements (Fig. 5).

2.2 Vertical Motion of the Station ICED

Throughout the year, the change in elevation of the ice dam is dominated by the sub-glacial topography but during the melting season, it is influenced by the formation of the Lake Merzbacher. While the lake level raises and consequently the water pressure against the ice wall increases, parts of the water penetrate underneath the ice dam in sub-glacial channels (Nye 1976). This temporally stored water separates the ice from its bed, forcing the ice dam to elevate. Mayer et al. (2008) described that in 2005 almost the region within 1.6 km apart from the ice dam was affected by this effect and became afloat during the filling of the Lake Merzbacher. Figure 4 shows the rapid loss in elevation until late October in response to the discharge after the GLOF. Bormudoi et al. (2012) calculated relative warm lake water temperatures with MODIS data of slightly more than 10°C around the GLOF which additionally supports the rapid ice melt and, therefore, an expansion of sub-glacial channels (Isenko and Mavlyudov 2002). These sub-glacial channels as well as basal crevasses and englacial fractures that were formed during the rise of the ice dam before the GLOF (Sugiyama et al. 2008), derogate after the lake's water has drained and thus support the loss in elevation. In late October, the elevation of the ice dam starts again to increase slightly. This elevation trend is less dominant in 2011 compared to the years 2010 and 2012. On the contrary, the horizontal component is not influenced and

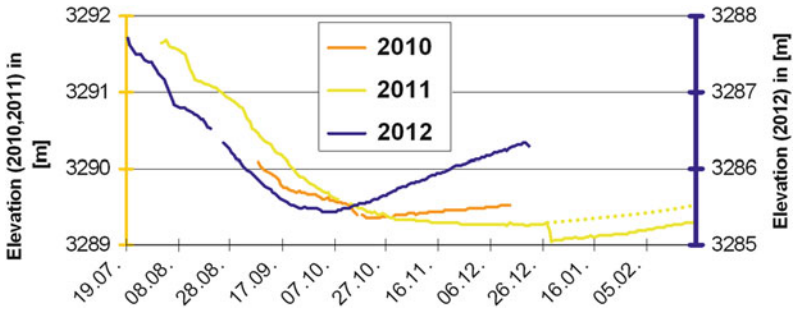

Fig. 4 Elevation differences for the years 2010, 2011, and 2012. Elevations in 2010 and 2011 belong to the left-hand side axis, while 2012 corresponds to the right-hand side axis. The *dotted yellow line* indicates a continuation without stick–slip motion. The different elevations result from the varying initial positions of the ICED station, which is installed on safe rather than identical positions

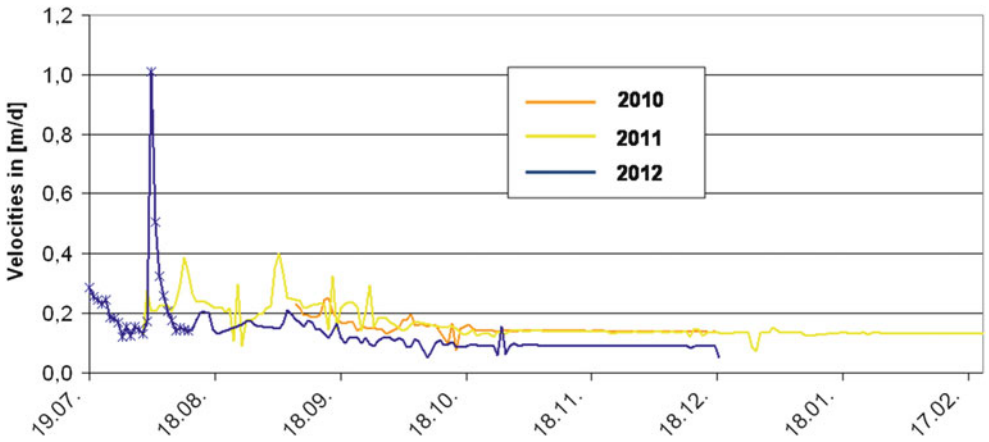

Fig. 5 Calculated horizontal surface velocities for the years 2010, 2011, and 2012. Differences of velocities in the later period of the year are due to varying initial positions of the ICED station

shows a constant motion. Therefore, the individual increase in elevation of each year is the result of a varying sub-glacial topography due to different initial positions of the station ICED.

The general vertical motion trend is disturbed by short-term jumps. At December 27th 2011, an event with a horizontal displacement of 50 cm towards north–west and a 25 cm loss in elevation occurred. A characterization as a slip event due to sub-debris melting seems implausible as the presence of melt-water is negligible during the cold winter time with temperatures far below 0°C (measured day time temperatures are between −10 and −20°C). An induced local stress caused by the different behaviour of varying cohesive components (debris and ice) in the glacier stream, resulting in a sudden release and thus displacement seems more realistic (Jansen and Hergarten 2006).

2.3 Horizontal Surface Velocities of the ICED Station

The daily horizontal surface velocities (Fig. 5) can be separated into higher and more volatile velocities as a post-drainage response of the ice dam and the lower nearly constant velocities during the winter period starting in late October every year. The decrease in discontinuous velocities after the GLOF indicates the presence of remaining water-filled cavities in the drainage system. These water-filled cavities support the ice flow resulting in higher velocities due to a reduced friction of the ice (Fischer and Clarke 1997). Additionally, a relaxing process of the glacier ice towards the ice dam is a result of the loss of water pressure against the ice wall from the discharged Lake Merzbacher. Furthermore, the loss of ice mass during the summer time due to melting

Table 1 Horizontal and vertical movement of the station ICED derived from the GNSS processing with TRACK and calculated mean horizontal surface velocities

	2010	2011	2012
GLOF date	15–16 July 2010	18–19 July 2011	16–18 June 2012
Available data	6 September 2010 to 18 December 2010 (103 days)	31 July 2011 to 21 Feburary 2012 (204 days)	17 July 2012 to 18 December 2012 (154 days)
Covered distance	19.5 m	41.9 m	25.2 m
Total vertical displacements	0.69 m	2.63 m	2,18 m
Mean horizontal surface velocities	0.15 m/day	0.16 m/day	0.13 m/day

The GLOF dates are according to CAIAG (Shabunin and Dudashvili, personal communication)

processes especially in sub-glacial channels and intensive calving into the Lake Merzbacher supports replenishment of ice, thus resulting in higher velocities.

The peak at August 1st 2012 corresponds to the abrupt change in the horizontal position of 1 m towards the north–east direction. Nevertheless, the distinction between variable sliding velocities and significant changes in the till is difficult without a detailed knowledge of the underlying topography. In contrast, during winter time, when the air temperatures fall far below 0°C, the velocities decrease and become nearly constant indicating a slower motion of the glacier due to refreezing of pore water and, therefore, a reduced amount of water in the ice bed (Kellerer-Pirklbauer and Kaufmann 2012). The suddenly reduced velocity at December 27th 2011 event (horizontal displacement of 50 cm) reflects a locally induced stress and subsequently abrupt release of the moving ice. But this short-time interruption does not alter the consistent winter velocities. Although the surface velocity in 2012 is slightly lower compared to the years before as a result of the different initial position of the station ICED, the averaged horizontal surface velocities for the analysed periods do not significantly vary within the 3 years and range from 0.13 to 0.16 m/day. Table 1 compares the horizontal and vertical motion as well as the derived mean surface velocities in 2010, 2011 and 2012. These values only reflect the behaviour of the glacier flow measured by the station ICED after the outburst of the lake.

3 Remote Sensing

For validation purposes of the post-GLOF velocities the GNSS results from the ICED station are compared to surface velocities derived from TerraSAR-X StripMap data. The latter surface velocities were calculated over 8 images taken between July 24th and August 26th 2010 by applying the Amplitude Tracking Method. Details for the TerraSAR-X processing and accuracy assessments are given in Neelmeijer et al. (2014). The resolution of the strip map data of 25 m allows the extraction of only one collocated motion value of 0.34 m/day (average of four TerraSAR-X data pairs). Unfortunately, no ICED data is available for the given period in 2010. However, the velocities of the ICED station have a similar pattern every year, thus similar velocities patterns are assumed for the radar data, too. Therefore, we compare the TerraSAR-X radar data from 2010 with the GNSS ICED data from 2011 and 2012. The mean velocities of the ICED data calculated from the beginning of the GNSS time series (Table 1) until August 26th 2011 and 2012 are 0.23 m/day and 0.22 m/day respectively. These mean velocities are slightly lower than the radar data velocity. Possible reasons are inconsistencies in the radar data processing due to incorrect co-registration of the images (errors in the detection and correlation of stable features in the images) as well as the coarse resolution of 25 m. Changes inside the 25×25 m compartment are not reflected in the averaged velocity. But in general, the velocities from two distinct different methods agree in the same range and differ only marginally.

4 Conclusion and Outlook

The movement of the ice dam of the Inylchek Glacier and the Lake Merzbacher considerable interact with each other. The processed GNSS data from 2010 to 2012 demonstrate a similar motion pattern from year to year and prove that the post-drainage reaction of the ice dam does not last only for a few days but rather extend over several weeks. The temporally stored lake water in sub-glacial channels causes an uplift of the ice dam from the crest. After the discharge of the Lake Merzbacher, the elevation of the ice dam decreases until late October and is then dominated by the sub-glacial topography. This change in elevation temporally corresponds with the change of the surface velocities. The higher but decreasing post-GLOF surface velocities are the result of a relaxing process of the ice dam and a replenishment of ice. During the winter time, the velocities become nearly constant.

The comparison of GNSS derived velocities with velocities from remote sensing data is feasible. Remote sensing provides data with a high spatial coverage but lower resolution, accordingly, significant short-term changes cannot be

observed. On the contrary, continuously operated field stations offer the possibility of precisely monitoring significant changes in the glacier's kinematics (e.g., changes in elevation and changes in velocities) for longer time spans and have the potential of forecasting important events (e.g., the GLOF) as a future prospective. Based on the experience on operating kinematic GNSS stations in remote areas, the station concept has been improved to allow a year-around record.

Acknowledgements The installation and operation of the monitoring network at Lake Merzbacher is funded by the German Research Centre for Geosciences (GFZ, Potsdam) and supported by the Central Asian Institute for Applied Geosciences (CAIAG, Bishkek) as part of the Global Change Observatory Central Asia of GFZ. This work is also supported by the CAWa project (www.cawa-project.net) which is funded by the German Federal Foreign Office as part of the "German Water Initiative for Central Asia" (the so-called "Berlin Process", grant AA7090002). Further funding is provided by the German Federal Ministry of Education and Research in the frame of PROGRESS, the Potsdam Research Cluster for Georisk Analysis, Environmental Change and Sustainability (www.earth-in-progress.de). The authors thank their colleagues at GFZ and CAIAG for preparing, installing and maintaining the monitoring stations. In particular the work of T. Queisser, N. Stolarczuk, M. Köppl, A. Shakirov, A. Sharshebaev, F. Yunusov, S. Barkalov, B. Aliev, A. Serenkov, and A. Dudashvili is gratefully acknowledged.

References

Bormudoi A, Shabunin A, Hazarika MK, Zaginaev V, Samarakoon L (2012) Studying the outburst of the Merzbacher lake of Inylchek Glacier, Kyrgyzstan with remote sensing and field data, Proceedings 33rd Asian Conference on Remote Sensing 2012, 26–30 November 2012, Pattaya, Thailand

Fischer UH, Clarke UH (1997) Stick-slip sliding behaviour at the base of a glacier. Ann Glaciol 24:390–396

Glazirin GE (2010) A century of investigations on outburst of the ice-dammed lake Merzbacher (Central Tien Shan). Aust J Earth Sci 103(2):171–179

Hagg W, Mayer C, Lambrecht A, Helm A (2008) Sub-debris melt rates on southern Inylchek Glacier, Central Tian Shan. Geogr Ann A 90(1):55–63

Herring TA, King RW, McClusky SC (2009) Documentation for the GAMIT/GLOBK GPS processing software release 10.3, Massachusetts Institute of Technology, Cambridge

Isenko E, Mavlyudov B (2002) On the intensity of ice melting in supraglacial and englacial channels. Bull Glaciol Res 19:93–99

Jansen F, Hergarten S (2006) Rock glacier dynamics: stick-slip motion coupled to hydrology. Geophys Res Lett 33, L10502. doi:10.1029/2006GL026134

Kellerer-Pirklbauer A, Kaufmann V (2012) About the relationship between rock glacier velocity and climate parameters in central Austria. Aust J Earth Sci 105(2):94–102

Mayer C, Lambrecht A, Hagg W, Helm A, Scharrer K (2008) Post-drainage ice dam response at Lake Merzbacher, Inylchek Glacier, Kyrgyzstan. Geogr Ann A 90(1):87–96

Merzbacher G (1905) The Central Tian-Shan mountains (1902–1903), London, Murray, 1905, 1st UK edn, p 294

Neelmeijer J, Motagh M, Wetzel HU (2014) Estimating spatial and temporal variability in surface kinematics of the Inylchek Glacier, Central Asia, using TerraSAR-X Data. Remote Sens 6(10):9239–9289

Nye JF (1976) Water flow in glaciers: Jökulhlaups, tunnels, and veins. J Glaciol 17(76):181–207

Schöne T, Illigner J, Manurung P, Subarya C, Khafid ZC, Galas R (2011) GPS-controlled tide gauges in Indonesia – a German contribution to Indonesia's tsunami early warning system. Nat Haz Earth Syst Sci 11:731–740. doi:10.5194/nhess-11-731-2011

Schöne T, Zech C, Unger-Shayesteh K, Rudenko V, Thoss H, Wetzel HU, Gafurov A, Illigner J, Zubovich A (2013) A new permanent multi-parameter monitoring network in Central Asian high mountains – from measurements to data bases. Geosci Instrum Method Data Syst 2:97–111. doi:10.5194/gi-2-97-2013, www.geosci-instrum-method-data-syst.net/2/97/2013/

Sergienko OV, Macayeal DR, Bindschadler RA (2009) Stick-slip behavior of ice streams: modeling investigations. Ann Glaciol 50(52):87–94(8)

Sorg A, Bolch T, Stoffel M, Solomina O, Beniston M (2012) Climate change impacts on glaciers and runoff in Tien Shan (Central Asia). Nat Climate Change 2:725–731. doi:10.1038/NCLIMATE1592

Sugiyama S, Bauder A, Huss M, Riesen P, Funk M (2008) Triggering and drainage mechanisms of the 2004 glacier-dammed lake outburst in Gornergletscher, Switzerland. J Geophys Res 113:F04019. doi:10.1029/2007JF000920

Unger-Shayesteh K, Vorogushyn S, Farinotti D, Gafurov A, Duethmann D, Mandychev A, Merz B (2013) What do we know about past changes in the water cycle of Central Asian headwaters? A review. Global Planet Change. doi:10.1016/j.gloplacha.2013.02.004

UNISDR, World Bank, and World Meteorological Organization (2009) Central Asia and Caucasus disaster risk management initiative (CAC DRMI), Risk assessment for Central Asia and Caucasus – Desk study review. http://www.preventionweb.net/files/11641_CentralAsiaCaucasusDRManagementInit.pdf. Accessed 20 Dec 2012

WMO (2008) Guide to Meteorological Instruments and Methods of Observation, WMO-No. 8. http://www.wmo.int/pages/prog/gcos/documents/gruanmanuals/CIMO/CIMO_Guide-7th_Edition-2008.pdf. Accessed 20 Dec 2012

Wortmann M, Krysanova V, Kundzewicz ZW, Su B, Li X (2013) Assessing the influence of the Merzbacher Lake outburst floods on discharge using the hydrological model SWIM in the Aksu headwaters, Kyrgyzstan/NW China, Hydrol Proces. doi:10.1002/hyp.10118

Xie Z, ShangGuan D, Zhang S, Ding Y, Liu S (2013) Index for hazard of Glacier lake outburst flood of lake Merzbacher by satellite-based monitoring of lake area and ice cover. Global Planet Change 107:229–237

Scheduling Scenarios for VLBI Observations of Satellites

Thomas Artz, Judith Leek, Laura La Porta, and Axel Nothnagel

Abstract

In this paper, a methodology for automatic scheduling of Very Long Baseline Interferometry (VLBI) observations of satellites is presented and first scheduling approaches are investigated. For this investigation the orbit of a geostationary satellite has been chosen, but, the methodology has also been successfully applied to an orbit of a Global Navigation Satellite Systems satellite. A scheduling procedure based on covariance optimization is developed and observations are simulated. In contrast to other simulation studies for a dedicated VLBI satellite mission, we are performing a scheduling process where observations of quasars and satellites are considered being equally important. Thus, the satellites are consistently included into a VLBI experiment. To validate the individual schedules, simplistic daily constant orbit shifts are estimated and analyzed. In this way, the necessary time between two subsequent satellite observations and the geometry of the observing network are investigated. Taking into account all circumstances, large global networks are the best option for estimating orbit shifts. Such a configuration leads to a large number of observations and a good observing geometry for the orbit. For a geostationary satellite, it is sufficient to carry out only one observation per hour or even longer. However, the presented results are only valid for the estimation of orbit shifts. Various improvements of these initial investigations are imaginable, e.g., considering orbit parameters within the scheduling process or estimating realistic orbit parameters.

Keywords

Satellites • Scheduling • Simulation • VLBI

1 Introduction

In the first decade of the twenty-first century, the space geodetic techniques namely the Global Navigation Satellite Systems (GNSS), Satellite Laser Ranging (SLR), Doppler Orbitography and Radiopositioning Integrated by Satellite (DORIS) and Very Long Baseline Interferometry (VLBI) have been co-existing and forming the foundation of the International Terrestrial Reference Frame (ITRF; Altamimi et al. 2011). However, there are only a few connections among these techniques realized by terrestrial local ties between the instruments of different techniques at so-called fundamental stations. Besides, there are SLR observations of GNSS satellites (e.g., Thaller et al. 2011) and first approaches have been done to observe GNSS satellites with VLBI radio telescopes (e.g., Tornatore et al. 2011). However, for the calculation of the ITRF, which is a fundamental product of space geodesy, the terrestrial local ties are considered to connect the individual terrestrial reference frames (TRFs) of the different techniques. Furthermore, the Earth Orientation Parameters (EOPs) are used to align these

T. Artz (✉) • J. Leek • L. La Porta • A. Nothnagel
Institute of Geodesy and Geoinformation, University of Bonn, Nußallee 17, 53113 Bonn, Germany
e-mail: artz@igg.uni-bonn.de; leek@igg.uni-bonn.de; laporta@mpifr-bonn.mpg.de; nothnagel@igg.uni-bonn.de

© Springer International Publishing Switzerland 2015

C. Rizos, P. Willis (eds.), *IAG 150 Years*, International Association of Geodesy Symposia 143,
DOI 10.1007/1345_2015_111

TRFs. Concerning the International Celestial Reference Frame (ICRF), we have to deal with a product which is determined on the basis of a TRF and EOPs solely from VLBI. Thus, the ICRF and the ITRF are not consistent, which is not in alignment with the concept of a Global Geodetic Observing System (GGOS; Plag and Pearlman 2009).

One of the prospects to improve GGOS would be to implement so-called space ties. These might be realized via satellites which are equipped with payloads for all techniques mentioned above. The local vectors between the reference points on the space vehicle must then be precisely known by the constructional properties. Thus, all space geodetic techniques would have a common target in space. As a consequence, the ICRF could be connected to the ITRF, and also a link of the dynamical reference frames of GNSS, SLR, and DORIS satellites to the ICRF could be realized. For such an improvement of GGOS, VLBI observations are indispensable.

The observation of radio signals emitted from satellites with VLBI is no new method. First tracking approaches were performed in the 1970s (e.g., Preston et al. 1972). However, almost all VLBI observations of satellites were performed only to determine orbit parameters. In contrast, a dedicated mission that aims to introduce space-ties needs a sophisticated design. We assume a signal which is similar to the radiation of quasars. Thus, the satellite observations can be handled in the same way as traditional quasar observations within the analysis. However, there are still issues to be solved which are not considered within this paper. These are, e.g., antenna tracking or the correlation with an appropriate a priori model to derive the group delay observables.

The purpose of this publication is to schedule satellite and quasar observations together. This approach is different to other simulation studies concerning VLBI observations of satellites. Plank et al. (2013), e.g., simply scheduled via visibilities. Our schedules differ in terms of network size and observation repeat cycle of the satellite observations. In this initial study, no real orbit parameters are determined. In contrast, daily orbit shifts are used to compare various session designs. Thus, various results are not representative for realistic dynamical orbit parameters. However, it is presented how different scheduling approaches affect the estimation of satellite parameters. As satellite and quasar observations are having equal rights, both are used to determine also other geodetic as wells as nuisance parameters which improves the stability of the parameter estimation process.

2 Scheduling of VLBI Observations

The scheduling of quasar and satellite observations is performed having equal rights. This can be done as the signal characteristics of the satellite is considered to be designed in relation to the characteristics of the recorded quasar observations (see Artz et al. 2013).

For scheduling the observations, an approach has been developed, which aims at optimizing the observing geometry. This approach was also used for investigating the opportunities of Twin-Telescopes (Leek et al. 2012) and is part of parallel investigations to this study. However, until now no real VLBI sessions have been scheduled with this procedure. In the scheduling process, the observations are chosen stepwise by analyzing the Jacobian matrix, which consists of the partial derivatives of the VLBI observables with respect to clock polynomials, zenith wet delays, UT1, and polar motion. Orbit shifts are not used for the optimization, as no difference between quasars and satellite should be introduced. However, the procedure theoretically allows to use orbit parameters for the scheduling. As the Jacobian matrix $\mathbf{X}$ characterizes the geometry of a VLBI session, a geometric improvement can be determined by indicators derived from the Hat matrix $\mathbf{H}$, which is computed with $\mathbf{X}$ and the covariance matrix $\mathbf{\Sigma}_{\mathbf{yy}}$ of the observations $\mathbf{y}$

$$\mathbf{H} = \mathbf{X}\left(\mathbf{X}^T\mathbf{\Sigma}_{\mathbf{yy}}^{-1}\mathbf{X}\right)^{-1}\mathbf{X}^T\mathbf{\Sigma}_{\mathbf{yy}}^{-1} \tag{1}$$

(e.g., Förstner 1987). Since the elements of the Hat matrix indicate how much weight each observation has on the adjusted observations (e.g., Menke 1984), the main-diagonal elements of $\mathbf{H}$ are called impact factors $\mathbf{h}_{ii} = diag(\mathbf{H})$. Observations with large impact factors are so-called high leverage points. These observations are important for the geometrical stability of a least-squares solution, they affect the accuracy of the estimated parameters significantly, and are necessary to avoid a defect of the configuration (Vennebusch et al. 2009). On this account, the impact factors are qualified to serve as selection criteria in an automatic scheduling procedure.

At each step of the scheduling process, the Jacobian matrix is extended by the rows of a new feasible scan and the corresponding impact factors are computed. As the geometry should be optimized, the following observations should be those with the greatest impact. Thus, the impact factors of all feasible new scans are compared to each other.

The duration of the observations is calculated individually depending on various characteristics like signal strengths, antenna specifications and slewing times. The procedure equals the one implemented within the NASA program SKED.[1] Thus, the observation length are about 1 min on average for the regional network and 4 min for the global one.

To be able to use a satellite in the schedule, the representation of the satellite position has to be identical to the representation of quasars. As quasar positions are typically described by right ascension and declination, this representation has also been calculated for the satellite for each relevant

[1] http://lupus.gsfc.nasa.gov/files_user_manuals/sked/sked.pdf.

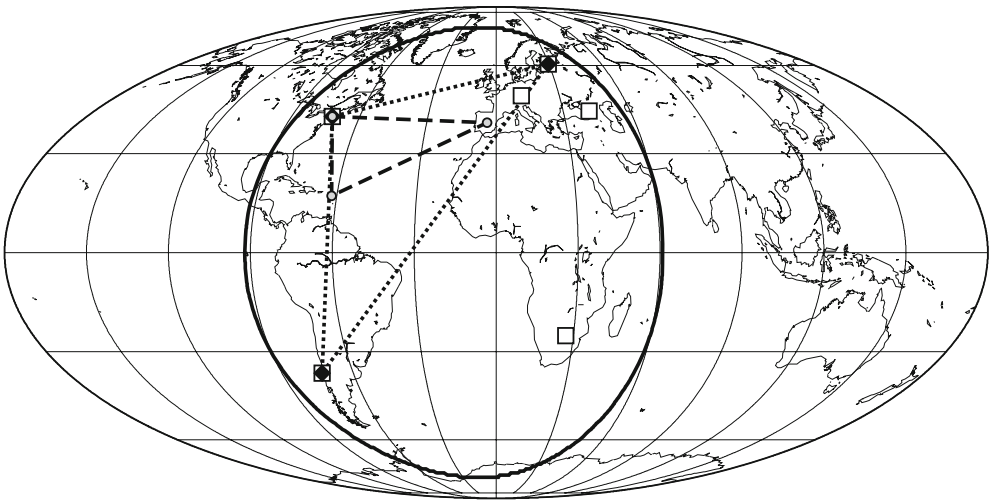

Fig. 1 Observing networks used for the schedules: global network with six stations by *squares*; global network with three stations by *diamonds* connected by *dotted lines*; regional network by *circles* connected by *dashed lines*

epoch. For this purpose, the simplified perturbation model SDP4 (Hoots and Roehrich 1980) has been implemented to calculate the actual position of the satellite which is then transformed to apparent right ascension and declination. As the satellite is at finite distance from the Earth, a curved wave front has to be assumed which is different from quasar observations where an approximation of a plane wave front is valid. As a consequence, right ascension and declination depend on the epoch as well as the observers position on the Earth. Thus, the calculation of the satellite position is performed independently for each station at each time step. Furthermore, the satellite is considered within the scheduling as a strong source with an equivalent flux density of 3 Jy.

With the procedure described above, various schedules have been created where only one geostationary satellite (GEO) besides the quasars is used, which is located at a longitude of 15.5° west. The main advantage of a GEO is that the footprint of the signal on the Earth's surface does not change. Thus, the satellite is constantly visible for a specific set of stations during a 24 h long VLBI session. The procedure could directly be applied to a satellite with the orbit of a GNSS satellite. This satellite moves with respect to the Earth and is, thus, not always observable from any point on the Earth. First schedules for a GNSS-like orbit have been created. However, they are not shown here due to the sake of clarity.

To derive different schedules, two global networks, one with three and one with six observing telescopes, were used. Furthermore, a regional network with three sites was tested as well (cf. Fig. 1). Additionally, network characteristics like baseline length as well as baseline orientation could have effects on the schedules. However, these parameters have not been considered in our investigation. Furthermore, the minimum time difference between two subsequent satellite observations was set to 5 min. For additional investigations concerning the time difference between successive satellite observations, the global network with three stations was used, and the minimum time difference was set to 60 and 120 min. This resulted in schedules, where the mean actual differences between two subsequent satellite observations are then 24, 72, and 141 min, respectively, with quasar observations in between.

3 Simulation of VLBI Observations

For the various scheduling scenarios, simulated observations have been generated in the same way as described by Artz et al. (2013). The simulation is based on a rough estimate of the VLBI error budget with a root sum squared error of 38 ps. There are three types of simulated stochastic components: clock behavior, atmospheric variations and baseline dependent white noise with a standard deviation of 10 ps. The clock variations have been modeled by a power-law process (Kasdin and Walter 1992) that has been adjusted to reach an Allan standard deviation of $1 \cdot 10^{-14}$@50 min. The atmospheric variations are modeled as equivalent zenith wet delays and mapped to the actual elevation of an observation as presented by Nilsson and Haas (2010). For the simulation, a refractive index structure constant of ${C_n}^2 = 1 \cdot 10^{-14}\,\mathrm{m}^{-\frac{2}{3}}$ and constant wind speeds of 2 m/s in north-south as well as 8 m/s in east-west direction have been used. Furthermore, a deterministic part of the observable is considered which is made up of state of the art modeling as well as of the observing geometry. For this purpose, the VTD library[2] is

[2] http://astrogeo.org/vtd/.

used, which provides consistent delay models for far and near zone objects in the Solar System Barycenter Frame.

For each schedule, 25 Monte-Carlo-style simulation runs have been performed. This enables to calculate repeatabilities as precision measure besides the standard deviations.

It has to be mentioned that no errors of the a priori satellite orbits are simulated. As only orbit shifts are estimated (cf. Sect. 4), this would only increase the residuals of the satellite observations and, thus, the a posteriori variance factor. In turn, the standard deviations of all parameters would slightly increase. The repeatabilities would not be affected.

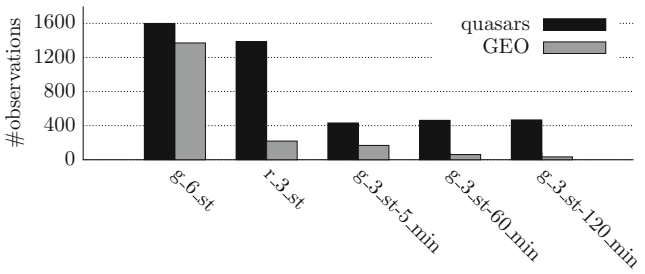

Fig. 2 Number of observations for the GEO schedules. The solution names are abbreviations that represent the network (global or regional), as well as the number of stations and the minimum time between two subsequent satellite observations

4 Parameter Estimation

To determine orbit parameters from the simulated VLBI observations, a least squares adjustment has been performed, where a typical VLBI parameterization has been chosen: station positions, EOPs, second degree polynomial clocks plus hourly continuous piece-wise linear function (CPWLF), hourly CPWLF for zenith wet delays, and CPWLF for troposphere gradients with a temporal resolution of 12 h. For the orbit, a constant translation in the Earth fixed reference frame, i.e., X-,Y- and Z-shifts, for a single 24 h session have been estimated, which correspond to the estimate of the apparent geocenter.

The orbit paramterization seems somewhat out-dated as sophisticated parameterizations with dynamic orbits and stochastical pulses could be used. However, the estimates are only used to judge the different schedules, which would be complicated by a complex parameterization. For a realistic orbit parameterization (i.e., with orbital elements) a distribution of the observations along the orbit is required, e.g., to determine the eccentricity. As we do not expect that VLBI observations alone can provide stable orbit parameters, we use simplistic orbit shifts to validate our schedules. Most likely, a combination of VLBI and other techniques should be performed to estimate dynamic orbits.

5 Results

5.1 Characteristics of the Schedules

The five schedules differ from each other in the number of the observing sites (3–6 antennas used) and in their distribution (global or regional), as well as in the observation repeat cycles of the satellite (cf. Fig. 2). Hence, we have to distinguish between the observations of quasars and of the satellites. As expected, concerning the quasar observations, the global approach with six stations yields the most observations. Theoretically, a three station network should yield only one fifth of the observations in comparison to a six station network. This is almost the case for the global network with three stations. However, for the regional network, this assumption is not valid. Due to a limited common visibility of stations in the northern and in the southern hemisphere of the Earth, several baselines of the global networks are not observable. In contrast, the stations of the regional network can observe identical quasars always all the time. Thus, there is a comparably high number of observations for the regional network.

The number of observations is also represented in the local observing geometries. In Fig. 3, a skyplot for the North American station is shown. Obviously, the best sampling of the local hemisphere above the telescope is yielded in the regional network with three stations. In contrast, the global networks are not that well sampled, indicating that observations on several baselines are not possible.

The situation is different for GEO observations, as all stations are always able to observe the GEO as the networks and the position of the GEO are chosen to match this criterion. Thus, the theoretical considerations concerning the number of observations were validated (cf. Fig. 2). Furthermore, the time periods between the GEO observations of the individual telescopes for the different schedules are comparable. Obviously, the situation for the GEO is better the more stations are used, and the smaller the observation repeat cycle is.

5.2 Orbit Shift Estimates

The accuracy of the estimated orbit shifts in terms of standard deviations are at the mm-level for the global network with six stations. For the global network with three stations, they are at the cm-level, while for the regional network at the dm-level (cf. Table 1). It should be noted that the differences among the standard deviations are not only due to the different number of observations, given that a larger improvement than $\sqrt{n}$ can be seen when increasing the number of stations.

There are several reasons for the variations in the results listed in Table 1. If we compare the two networks with

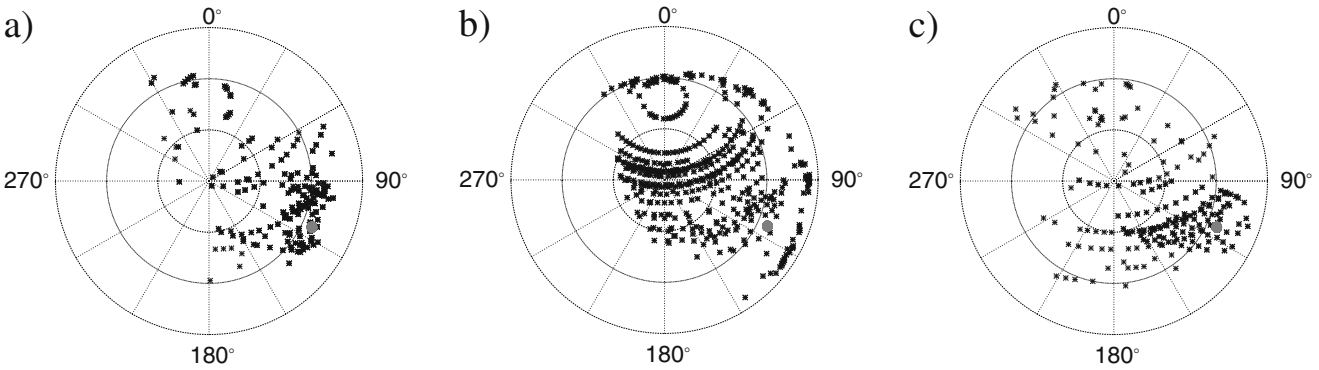

Fig. 3 Skyplots of the station Westford (USA) for the schedules: (**a**) global six station network with GEO, (**b**) regional three station network with GEO, (**c**) global three station network with GEO. The quasar observations are indicated by *stars* while the satellite observations are indicated by *gray dots*

three stations (g-3st-5 min and r-3st-5 min) the supremacy of a global network becomes clear. The global approach leads to more stable orbit estimates, although the number of GEO observations is at the same level and the r-3st-5 min schedule provides more quasar observations. Furthermore, the Z-component in the regional approach is worse, as the extension of the observing polyhedron in North-South direction is significantly larger for the g-3st-5 min schedule.

Comparing the two global networks (g-6st-5 min and g-3st-5 min), the standard deviations are smaller for the six station network by a factor of five for the X- and Y-components and by a factor three for the Z-component. This is due to the number of observations and, more importantly, there is an improvement due to a better observing geometry which can be seen in Fig. 3. Especially, the troposphere parameters and the EOPs are estimated more stably which leads to more precise orbit shifts. Furthermore, these 3D orbit shifts are less correlated to the other parameters. The high precision for the Z-estimates in comparison to the equatorial shifts for the g-3st-5 min schedule can be explained by the location of the stations: the three station network has two distinct large North-South baselines, while there is only one East-West baseline. Especially the deselection of the station in South Africa degrades the East-West expansion of the network, and thus, leads to weaker equatorial orbit components.

The same conclusions can be drawn from the repeatabilities of the 25 Monte-Carlo realizations for each schedule. The repeatabilities can be expressed by root mean squared (RMS) estimates which are shown in Fig. 4 for the X-component. The respective RMS estimates are listed in Table 1. However, these are smaller than the standard deviations, an unexpected result, which has to be investigated in the future.

For the observation repeat cycle of the satellite, the standard deviations increase for schedules with bigger gaps between satellite observations. This has been expected due to the smaller number of satellite observations. The repeatabilities of the estimates (cf. Fig. 4b) are at the same level for g-3st-5 min and g-3st-60 min with RMS estimates on the mm-level for X and Y and around 15 mm for the

Table 1 Average standard deviations and repeatabilities (RMS) of the orbit estimates for different scheduling approaches (abbreviations, cf. Fig. 2, units: mm)

	Standard deviations			Repeatabilities		
Schedule	σ_X	σ_Y	σ_Z	X	Y	Z
g-6st-5 min	5.3	5.3	5.0	2.4	3.3	12.2
g-3st-5 min	23.3	21.7	13.1	2.6	2.8	11.3
r-3st-5 min	75.9	75.5	142.2	19.3	34.5	124.8
g-3st-60 min	46.7	47.8	25.9	6.2	4.6	15.3
g-3st-120 min	60.3	57.4	31.8	10.5	16.8	24.8

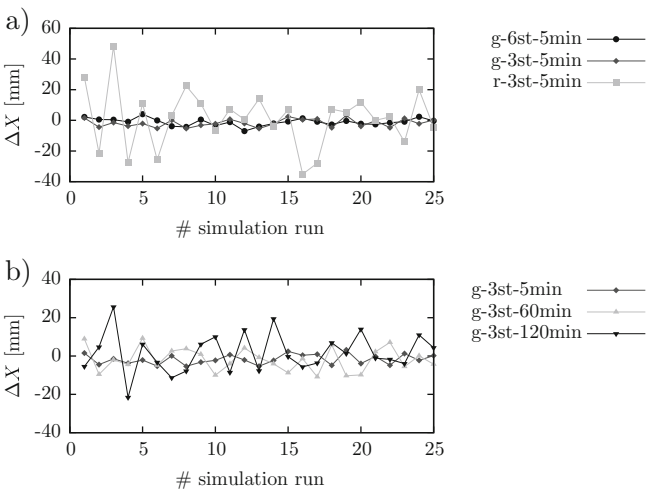

Fig. 4 Estimates of the X-component of the orbit for 25 simulation runs. The *upper panel* shows the results for the network tests and the *lower panel* the results for the different observation repeat cycles of the satellite (abbreviations, cf. Fig. 2)

Z-component. The g-3st-120 min solution only leads to a slightly worse repeatability (cf. Table 1). We conclude, that a good temporal coverage is not that important for stable orbit parameters, at least not for estimating orbit shifts in the TRF. A re-assessment will be necessary if a realistic orbit parameterization with orbital elements will be applied, as a distribution of the observations along the orbit would be required (e.g., to determine the eccentricity).

6 Conclusions and Outlook

Taking a satellite which is emitting a radio signal in the geodetic VLBI frequency regime, observations to this satellite can be embedded in a typical VLBI session. Thus, having solved several practical issues as the tracking of satellites, a VLBI experiment can be performed where satellites as well as quasars are observed.

The automatic procedure is able to schedule quasars as well as satellites. The aim of the scheduling is to prepare a session with an optimal observing geometry in the sense of the least squares adjustment. Here, five test schedules have been created with a geostationary satellite. From these schedules, observations have been simulated, and a typical VLBI parameter estimation has been performed with standard VLBI and simplistic orbit parameters, i.e., daily 3D shifts in the TRF.

By analyzing the standard deviations of the orbit shifts and the repeatabilities of the orbit estimates from 25 Monte-Carlo simulation runs for each schedule, the superiority of a global network with a large number of stations has been demonstrated. The reason is twofold: on the one hand, better geometry and more observations are available, and on the other hand, especially the Z-component of the orbit is significantly less correlated to the other parameters. Furthermore, it has been shown that a repeat cycle of the satellite observations of more than 1 h is sufficient for a GEO to gain good simplistic orbit shifts.

Improvements of our first steps can be achieved in several ways. Adding orbit parameters directly to the scheduling process will improve the scheduling. Especially when satellites which move with respect to the Earth are scheduled, the algorithm will automatically choose stations that are able to observe the satellite. By improving the orbit parameterization, a better validation of the schedules might be obtained. Whether the VLBI technique alone can provide stable orbit parameters or not remains an open issue. Most likely, a combination of VLBI and other space techniques should be performed. Finally, improving the software implementation or processing environment will greatly enhance the progress of this investigation as it currently suffers from the computational load that is needed for scheduling large networks.

References

Altamimi Z, Collilieux X, Métivier L (2011) ITRF2008: an improved solution of the international reference frame. J Geodesy 85(8):457–473. doi:10.1007/s00190-011-0444-4

Artz T, Nothnagel A, La Porta L (2013) VLBI observations of geostationary satellites. In: Zubko N, Poutanen M (eds) Proceedings of the 21th EVGA working meeting, reports of the finnish geodetic institute, pp 217–221. ISBN: 978-951-711-296-3

Förstner W (1987) Reliability analysis of parameter estimation in linear models with applications to mensuration problems in computer vision. Comput Vis Graph Image Process 40(3):273–310

Hoots FR, Roehrich RL (1980) Spacetrack report no. 3: models for propagation of NORAD element sets. Technical Report, Aerospace Defense Center, Peterson Air Force Base

Kasdin N, Walter T (1992) Discrete simulation of power law noise. In: Proceedings of the 1992 IEEE frequency control symposium, pp 274–283

Leek J, Artz T, Nothnagel A (2012) Prospects of IVS-intensive sessions with twin-telescopes. In: Behnrend D, Baver KA (eds) IVS 2012 general meeting proceedings, launching the next-generation IVS network, NASA/CP-2012-217504. pp 33–37

Menke W (1984) Geophysical data analysis: discrete inverse theory. Academic, San Diego

Nilsson T, Haas R (2010) Impact of atmospheric turbulence on geodetic very long baseline interferometry. J Geophys Res 115:B03,407. doi:10.1029/2009JB006579

Plag HP, PearlmanM (2009) Global geodetic observing system meeting the requirements of a global society on a changing planet in 2020. Springer, Berlin/Heidelberg. ISBN: 978-3-642-02686-7. doi:10.1007/978-3-642-02687-4

Plank L, Böhm J, Krasna H, Schuh H (2013) VLBI satellite tracking for precise coordinate determination – a simulation study. In: Zubko N, Poutanen M (eds) Proceedings of the 21th EVGA working meeting, reports of the finnish geodetic institute, pp 105–101. ISBN: 978-951-711-296-3

Preston RA, Ergas R, Hinteregger HF, Knight CA, Robertson DS, Shapiro II, Whitney AR, Rogers AEE, Clark TA (1972) Interferometric observations of an artificial satellite. Science 178:407–409. doi:10.1126/science.178.4059.407

Thaller D, Dach R, Seitz M, Beutler G, Mareyen M, Richter B (2011) Combination of GNSS and SLR observations using satellite co-locations. J Geodesy 85(5):257–272. doi:10.1007/s00190-010-0433-z

Tornatore V, Haas R, Pogrebenko D, Casey S, Calves GM, Keimpema A (2011) Single baseline GLONASS observations with VLBI: data processing and first results. In: Alef W, Bernhart S, Nothnagel A (eds) Proceedings of the 20th EVGA working meeting, schriftenreihe des instituts für Geodäsie und geoinformation der Rheinischen-Friedrich-Wilhelms Universität Bonn, no. 22. ISSN 1864-1113, pp 162–165

Vennebusch M, Nothnagel A, Kutterer H (2009) Singular value decomposition and cluster analysis as regression diagnostics tools for geodetic applications. J Geodesy 83:877–891. doi:10.1007/s00190-009-0306-5

GGOS Bureau of Products and Standards Inventory of Standards and Conventions for Geodesy

D. Angermann, M. Gerstl, L. Sánchez, T. Gruber, U. Hugentobler, P. Steigenberger, and R. Heinkelmann

Abstract

The Bureau of Products and Standards (BPS), the former Bureau for Standards and Conventions supports IAG's Global Geodetic Observing System (GGOS) in its goals to integrate the *three pillars* of geodesy: geometry, rotation and gravity field of the Earth and to obtain geodetic products of highest accuracy and consistency. The key objective of the BPS is to ensure the adoption and implementation of common standards and conventions by all IAG components as a fundamental prerequisite for a consistent processing of the different geometric and gravimetric observations. This paper provides the charter of the BPS and gives an overview about the present activities. A major focus of the work is on the compilation of an inventory based on the evaluation of the standards and conventions currently in use by the IAG Services and their contributing analysis centres for the data processing and for the generation of geometric and gravimetric products, such as geodetic reference frames, Earth orientation parameters, gravity field models and satellite orbits. The paper presents some results of this evaluation regarding numerical standards, including time and tide systems and it addresses various aspects related to the geopotential value W_0 and to the datum definition of the International Terrestrial Reference System (ITRS).

Keywords

Geodesy • Geopotential W_0 • GGOS • ITRS datum definition • Standards and conventions

1 Introduction

The Global Geodetic Observing System (GGOS) was originally created as an IAG project in 2003 and in 2007 it became the status of a full component of IAG (Rummel 2000; Plag and Pearlman 2009; Kutterer et al. 2012). The IAG Services and Commissions provide the geodetic infrastructure and products as well as the expertise and support for scientific developments, which are the basis for monitoring the Earth system and for global change research. GGOS relies on the observing systems and analysis capabilities already in place in the IAG Services and envisions the continued development of innovative technologies, methods and models to improve our understanding of global change processes. GGOS provides a framework that ranges from the acquisition, transfer and processing of a tremendous amount of observational data

D. Angermann (✉) • M. Gerstl • L. Sánchez
Deutsches Geodätisches Forschungsinstitut der Technischen Universität München (DGFI-TUM), Arcisstraße 21, 80333 Munich, Germany
e-mail: deflef.angermann@tum.de

T. Gruber • U. Hugentobler • P. Steigenberger
Institute for Astronomical and Physical Geodesy, Technische Universität München, Arcisstraße 21, 80333 Munich, Germany

R. Heinkelmann
Helmholtz-Zentrum Potsdam, Deutsches GeoForschungsZentrum Potsdam, Telegrafenberg, 14473 Potsdam, Germany

P. Steigenberger
Deutsches Zentrum für Luft- und Raumfahrt (DLR), Germany

© Springer International Publishing Switzerland 2015

C. Rizos, P. Willis (eds.), *IAG 150 Years*, International Association of Geodesy Symposia 143,
DOI 10.1007/1345_2015_165

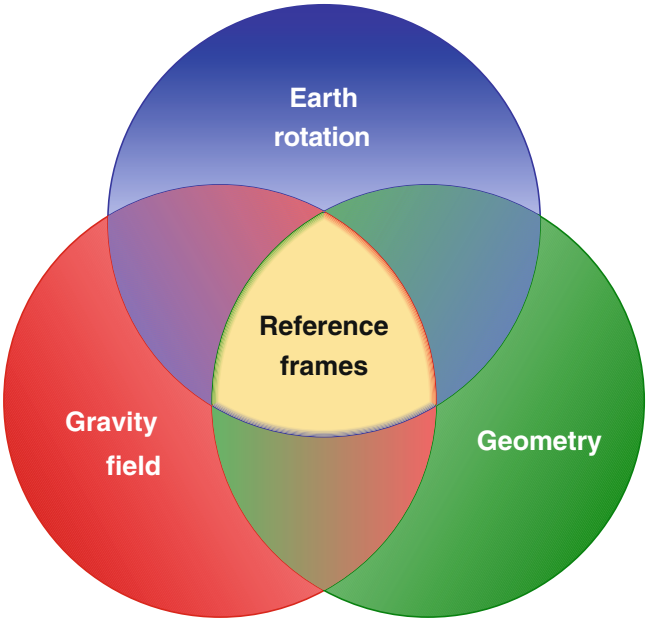

Fig. 1 Integration of the three pillars geometry, Earth rotation and gravity field (Rummel 2000, modified by Plag and Pearlman 2009)

to its proper integration. Consistency among the data sets from the different (geometric and gravimetric) observation techniques is of crucial importance for the generation of highly accurate GGOS products and for the integration of geometry, Earth rotation and the gravity field (Fig. 1), which is a key goal of GGOS.

The BPS was established as a GGOS component in 2009. Its tasks include keeping track of the strict observance of adopted geodetic standards and conventions applied by different IAG components and assuring consistency of data sets and products released by the services. It is essential that the analyses of all the different geodetic observations are based on the same standards and conventions to be applied across all IAG components. It is equally important that users of geodetic products are aware of the standards and conventions these products are based on, to fully exploit their accuracy and to allow for a coherent interpretation.

This paper presents in the first part the GGOS Bureau of Products and Standards its mission and goals and the people involved as well as the interactions with the IAG and other entities involved in the generation and maintenance of geodesy-related standards and conventions. The second part addresses present activities of this Bureau, which focus on the compilation on an inventory of standards and conventions used for the generation of IAG/GGOS products.

2 GGOS Bureau of Products and Standards

The Bureau of Products and Standards (BPS), the former Bureau for Standards and Conventions, is hosted and supported by the Deutsches Geodätisches Forschungsinstitut (DGFI) and the Institut für Astronomische und Physikalische Geodäsie (IAPG) of Technische Universität München, under the umbrella of the Forschungsgruppe Satellitengeodäsie (FGS). Initially, U. Hugentobler acted as director of the Bureau. In April 2011, D. Angermann was selected as his successor. The present members of the BPS are D. Angermann (director), T. Gruber (deputy director), M. Gerstl, U. Hugentobler, L. Sánchez, R. Heinkelmann and P. Steigenberger (Angermann 2012; Hugentobler et al. 2012).

2.1 Mission and Objectives

The work of the BPS is primarily built on the IAG Services and the products they derive on an operational basis for Earth monitoring making use of various space geodetic observation techniques such as VLBI, SLR/LLR, GNSS, DORIS, altimetry, gravity satellite missions, gravimetry, etc. The purpose and major goal of the BPS is to ensure that common standards and conventions are adopted and implemented by the IAG components as a fundamental basis for the analysis of the different geodetic observations to ensure consistent results for the geometry, rotation and gravity field of the Earth along with its variations in time. The BPS supports GGOS in its goal to obtain products of highest accuracy, consistency, and temporal and spatial resolution, which refer to a unique reference frame, stable over decades in time.

According to the Terms of Reference the objectives of the BPS are:

- To keep track of the strict consideration of adopted geodetic standards, standardized units, fundamental physical constants, resolutions and conventions in the generation of IAG/GGOS products.
- To review, examine and evaluate all standards, constants, resolutions and conventions adopted by IAG or its components and recommend their use or propose the necessary updates.
- To identify gaps, inconsistencies and deficiencies in standards and conventions and to initiate steps to remove them.
- To propose the adoption of new standards where necessary.

Table 1 Representatives of IAG services, IAU and other entities in the BPS (status: Dec. 2014)

G. Petit, France, T. Herring (USA)	International Earth Rotation and Reference Systems Service (IERS)
U. Hugentobler, Germany	International GNSS Service (IGS)
E. Pavlis, USA	International Laser Ranging Service (ILRS)
J. Gipson, USA	International VLBI Service for Geodesy and Astrometry (IVS)
F. Lemoine, J. Ries, both USA	International DORIS Service (IDS)
R. Barzaghi, Italy	International Gravity Field Service (IGFS)
F. Barthelmes, Germany	International Center for Global Gravity Field Models (ICGEM)
S. Bonvalot, France	International Gravimetric Bureau (BGI)
R. Heinkelmann, Germany	International Astronomical Union (IAU), Working Group "Numerical Standards for Fundamental Astronomy"
M. Craymer, Canada	Chair of Control Body for the ISO Geodetic Registry Network
J. Ádám, Hungary	Chair of the IAG Communication and Outreach Branch
J. Ihde, Germany	IAG representative to ISO/TC211
J. Kusche, Germany	Representative of gravity community

– To propagate standards and conventions to the wider scientific community and promote their use.

2.2 Representation of IAG Components and Other Entities in the BPS

A close interaction with the IAG Services is essential to accomplish the tasks of the BPS, including the evaluation of the standards and conventions currently adopted by all IAG components and other entities involved. This has been achieved by selecting representatives from the IAG Services, the International Astronomical Union (IAU) and other entities (summarized in Table 1) as Associate Members of the BPS.

3 Major Activities of the BPS

The present activities of the BPS focus on the compilation of an inventory of standards and conventions currently applied for the analysis of geometric and gravimetric observations and for the generation of IAG/GGOS products.

The numerical standards currently in use by the geodetic community are officially defined by the Geodetic Reference System 1980 (GRS80, Moritz 2000). Well established and also in common use are the IERS Conventions, which are regularly updated. The latest version, the IERS Conventions 2010 (Petit and Luzum 2010), serves as the basis for the analysis of geometric observations as well as for the definition and realization of geodetic reference systems and for the generation of IERS products. For the analysis of gravimetric observations different standards and conventions are currently in use, e.g., EIGEN (Förste et al. 2012), GOCE (European GOCE Gravity Consortium 2012), EGM2008 (Pavlis et al. 2012).

Relevant are also resolutions adopted by the International Union of Geodesy and Geophysics (IUGG), the IAU and IAG as well as standards and fundamental physical constants adopted by external bodies, e.g., the International Organisation for Standardisation (ISO), the International Bureau of weights and measures (BIPM) and the Committee on Data for Science and Technology (CODATA).

A major activity of the BPS is to review the standards and conventions used for the generation of the IAG/GGOS products in order to compile a so-called *product-based* inventory. It should be noted that an official definition of GGOS products is still outstanding. However, the declaration of the GGOS Meeting held on 02/03 November, 2009 at the Bundesamt für Kartographie und Geodäsie (BKG, Frankfurt a. M.) recommends that IAG Services and products be recognized as GGOS Services and products. According to this declaration, products, addressing the celestial reference systems and frames, terrestrial reference systems and frames, Earth orientation parameters, GNSS satellite orbits, gravity field models, height systems and their realizations should be considered as IAG/GGOS products. This list can be extended by adding other geodesy-related products that may be defined within GGOS.

These activities and the compilation of such an inventory requires the participation of the Measurement Services and interaction between the BPS and IAG, IAU and the other entities involved in standards and conventions. These links have been established by including representatives from these entities as Associated Members of the BPS (Table 1).

4 Selected Examples of This Inventory

As a first example, we look at the present status of numerical standards, including the definition of time and tide systems. A second example focuses on W_0, the geopotential value as the reference for gravimetric quantities and for the

Table 2 Comparison of numerical standards

Quantity	GRS80 (Moritz 2000)	Fundamental Parameters (Groten 2004)	IERS2010 (Petit and Luzum 2010)	EGM2008 Pavlis et al. (2012)	Unit
Gravit. constant (GM)					
– TCG-value	398.6005	398.6004418	398.6004418		$[10^{12}\ m^3\ s^{-2}]$
– TT-value			398.6004415	398.6004415	
Equatorial radius (a)					
– Zero-tide value			6,378,136.6		
– Mean-tide value		6,378,136.7			[m]
– Tide free value	6,378,137.0			6,378,136.3	
Dyn. form factor (J_2)					
– Zero-tide value	1,082.63	1,082.6359	1,082.6359	1,082.6361	$[10^{-6}]$
Ang. Rot. velocity (ω)	7.292115	7.292115	7.292115	7.292115	$[rad\ s^{-1}]$

The IERS conventions 2010 provide the TCG-value for the gravitational constant (GM) in Table 1.1, in addition the TT-compatible value is given in that document in Sect. 1.2

unification of height systems. The latter addresses a key IAG/GGOS product, the International Terrestrial Reference Frame (ITRF), and in particular the ITRS datum definition vs. its realization.

4.1 Numerical Standards, Time and Tide Systems

The IUGG resolution No. 7 (1979) and the IAG resolution No. 1 (1980) recommended that we use the Geodetic Reference System 1980 (Moritz 2000) as the official reference for geodetic work. The GRS80 is defined by four conventional constants [GM, a, J_2, ω], which are given with their numerical values in Table 2. However, some of the adopted GRS80 values may change with time, so we would be better to speak about *fundamental parameters* instead of *constants* (Groten 2004). In the last few years, substantial progress has been achieved in the estimation of these parameters and their temporal changes. Consequently, the introduction of a new Geodetic Reference System (i.e., GRS2000) was a key topic within the geodetic community, in particular in Special Commission 3 "Fundamental Constants" (Groten 2004) of the IAG (in its old structure). However, after lengthy discussion and consideration, it was decided not to propose any change of the existing GRS80 at that time. Nevertheless, some progress was made and a consistent set of fundamental parameters and current (2004) best estimates have been compiled (Groten 2004). These values are also shown in Table 2, together with the numerical standards of the IERS Conventions 2010 (Petit and Luzum 2010) and those of the Earth Gravitational Model 2008 (EGM 2008, Pavlis et al. 2012).

As we can see from Table 2 the numerical standards given in the different sources are quite different for some parameters. It can be recognized that different values, such as the equatorial radius of the Earth [a] and for the dynamical form factor [J_2], are expressed in different tide systems and that GM depends on the definition of the time system. Confusion may also be caused within the IERS Conventions itself, since the GRS80 ellipsoid parameters are recommended for the transformation of cartesian to geographical coordinates, while other values are given for the numerical standards in the IERS Conventions 2010 (Table 2).

The time and tide systems as used by the different geodetic communities is a potential source of confusion and inconsistency. The IUGG resolutions from 1991 require units to be consistent with the Geocentric Coordinate Time (TCG) scale. In practice, however, Terrestrial Time (TT) scale is commonly used since all geodetic measurements are time tagged with a time scale consistent with TT.

As mentioned, another source of inconsistency is the use of different tidal systems for geodetic applications and purposes. While the gravimetric services provide products mostly in the zero tide system, in agreement with IAG resolution 16 of the 18th General Assembly 1983, the geometric services provide their products, e.g., the ITRF, in the tide free system. In applications involving satellite altimetry, the mean tide system is commonly used.

All the geodetic products should be expressed in the same time and tide system before combining them. Using different numerical standards, time and tide systems is a potential source for inconsistencies and even errors of geodetic products. In particular users not specialized in geodesy may have difficulties in using geodetic products correctly due to their lack of knowledge about the properties of the products.

4.2 Geopotential Value W_0

The W_0 value defines which of the infinite equipotential surfaces of Earth's gravity field serves as the reference level (i.e. zero-height surface) for the height determination. In

Table 3 Examples of global W_0 estimations

W_0 [m^2/s^2]	Comments	References
62,636,860.850	GRS80 ($W_0 = U_0$)	Moritz (2000)
62,636,856.16	Mean sea surface T/P, EGM96	Burša et al. (2002)
62,636,856.0	A rounded value was adopted based on best estimates	Groten (2004)
62,636,856.0	IERS Conventions 2010 (from Groten 2004)	Petit and Luzum (2010)
62,636,854.6	Mean sea surface T/P, EGM96	Burša et al. (2007)
62,636,853.4	Mean sea surface T/P, EIGEN-GC03C, epoch 2000.0	Sánchez (2007)
62,636,854.38	Mean sea surface CLS01, EIGEN-GL04S, epoch 2000.0	Sánchez (2009)
62,636,854.2	Mean sea surface DNSC08, ECCO2, EGM2008	Dayoub et al. (2012)

The values are extracted from Table 3 of Sánchez (2012)

principle, any W_0 reference value can be adopted for the determination of vertical coordinates. However, to achieve worldwide consistency within a global vertical reference system, the geopotential value W_0 should be conventionally defined and the value must be realizable and reproducible with high precision at any time and location around the world (Sánchez 2012).

The definition of a world height system and W_0, which is a common initiative of GGOS Theme 1 "Global Unified Height Systems", IAG Commissions 1 and 2, and the International Gravity Field Service (IGFS), have been addressed for many years, e.g., by the Inter-Commission Project 1.2 "Vertical Reference Frames" (Ihde 2009) and since 2009 by the Working Group "Vertical Datum Standardization" (Sánchez 2012).

A major goal of this Working Group is to provide a reliable W_0 value to be introduced as the conventional reference level for the realization of a global vertical reference system. Towards this aim, a summary of different global W_0 computations has been compiled (Sánchez 2012). Some selected examples from this compilation are shown in Table 3. Recent empirical estimations of W_0 differ by about $2\,m^2\,s^{-2}$ from the W_0 value ($62{,}636{,}856.0\,m^2\,s^{-2}$) adopted in the IERS Conventions 2010 (Petit and Luzum 2010) and thus, the conventionally adopted value corresponds to an equipotential surface located about 20 cm below the sea surface presently mapped by satellite altimetry (Sánchez 2012). The IERS value has also been adopted by IAU as the reference value (see IAU report of numerical constants, Luzum et al. 2011), and it is directly related to the corresponding scale factor L_G, which is used for the transformation between TT and TCG time scales [see Eq. (2)]. The relation between L_G and W_0 is given by

$$L_G = W_0/c^2 \tag{1}$$

A possible change of the currently adopted W_0 to a more realistic value (as obtained from recent computations) would then have some impact on the IAU.

Another issue is, that the geoid cannot be considered as a static surface, as sea level change and mass redistribution affects the geoid with associated time variations in W_0. Dayoub et al. (2012) have estimated the value $W_0 = 62{,}636{,}854.2 \pm 0.2\,m^2\,s^{-2}$ at the epoch 2005.0 with a secular variation $dW_0/dt = -0.027 \pm 0.0005\,m^2\,s^{-2}\,year^{-1}$ from a detailed analysis and examination of altimetric sea surfaces. Here, a question is whether the W_0 value should change with the mean sea level or should be defined as quasi-stationary.

4.3 ITRS Definition vs. Its Realization

According to the IERS Conventions (Petit and Luzum 2010) the ITRS definition fulfills the following conditions:

- It is geocentric, the center of mass being defined for the whole Earth, including oceans and atmosphere;
- The unit length is the meter (SI). This scale is consistent with the TCG time coordinate for a geocentric local frame, in agreement with IAU and IUGG (1991) resolutions;
- Its orientation was initially given by the Bureau International de l'Heure (BIH) orientation of the BIH Terrestrial System (BTS) at epoch 1984.0;
- The time evolution of the orientation is ensured by using a no-net-rotation (NNR) condition with regard to horizontal tectonic motions over the whole Earth.

In the following we compare the ITRS definition with its realization.

- Origin: The ITRF origin is realized by SLR observations. Through orbit dynamics, SLR is sensitive to determine the centre of mass (CM), if the first degree harmonics of the Earth gravity field are fixed to zero. In the current ITRS realizations with a linear station motion model, SLR coordinates and velocities are mean geocentric positions, averaged over the SLR observation time span (Bloßfeld et al. 2014). However, observed from the crust (i.e. *crust-based frame*), the origin is realized as a mean CM (Blewitt 2003; Dong et al. 2003). In the IERS Conventions 2010 (Petit and Luzum 2010) the differences between the instantaneous geocentric position and the mean CM are called geocenter motions in the ITRF (i.e., *vector from the ITRF origin to the instantaneous center of mass*). Furthermore, the SLR results may be affected by the relatively sparse network distribution (Collilieux et al. 2009).

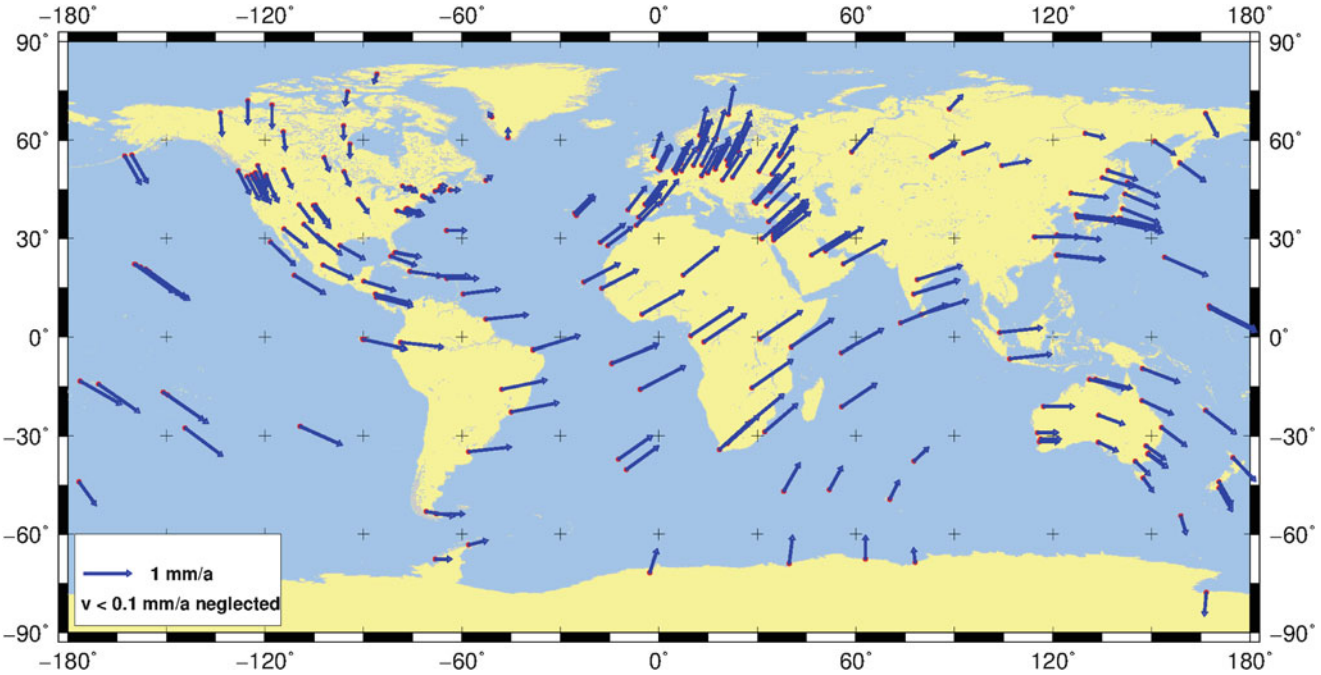

Fig. 2 Differences of horizontal station velocities between APKIM2005 and NNR-NUVEL-1A model

– Scale: The scale is consistent with the TCG time coordinate (IAU and IUGG resolutions, 1991), whereas its realization utilizes terrestrial time (TT). The relation between both time scales is given by the equation:

$$L_G = 1 - d(TT)/d(TCG) = 6.969290134 \cdot 10^{-10} \quad (2)$$

Thus, the difference between both time scales is about $0.7 \cdot 10^{-9}$, equivalent to a height difference of 4.5 mm at the surface of the Earth.

– Orientation: The orientation is realized by successive transformations with respect to the previous ITRF realization. Thus, its realization depends on the network geometries and the stations used for the transformations, including the weighting.

– Time evolution of the orientation: The orientation rate of the ITRF2000 (Altamimi et al. 2002) was aligned to that of the geological model NNR-NUVEL-1A (Argus and Gordon 1991; DeMets et al. 1990, 1994), which is also the reference for the succeeding realizations, i.e., the ITRF2008 (Altamimi et al. 2011; Seitz et al. 2012), and it is accomplished by successive transformations (similar to the orientation). The problem with this type of realization is that the geological model does not fulfill the NNR-condition of the ITRS definition, because deformation zones are neglected and this model reflects plate motions averaged over millions of years, which differ from present-day motion. Studies have been performed to quantify this discrepancy (see next paragraph).

A series of Actual Plate KINematic Models (APKIM) have been developed at DGFI (Drewes 2009). Figure 2 shows the discrepancies between the latest APKIM model and the geophysical NNR-NUVEL-1A model. The station velocities differ significantly with a rate of 1.1 mm/year around a rotation pole with a latitude of about −60° and a longitude of about 120° (Drewes 2012). Thus, it is proposed that the kinematic datum should be given by a present-day crustal motion and deformation models to fulfill the ITRS definition.

5 Conclusions

Common standards and conventions are of crucial importance for the generation of consistent IAG/GGOS products that shall be homogeneously applied for processing geometric and gravimetric observations. The product-based inventory compiled by the BPS presents the current status regarding standards and conventions, indicating that there are several inconsistencies. The fact that the numerical standards are partly given in different time and tide systems needs to be considered by the users and respective transformations have to be performed. For a correct interpretation and use of geodetic products the applied standards and conventions must be clearly documented. As a major outcome of this inventory, the BPS will also provide recommendations on how to resolve inconsistencies and gaps.

References

Altamimi Z, Sillard P, Boucher C (2002) ITRF2000: a new release of the international terrestrial reference frame for Earth science applications. J Geophys Res 107(B10). doi:10.1029/2001JB000561

Altamimi Z, Collilieux X, Metivier L (2011) ITRF2008: an improved solution of the international terrestrial reference frame. J Geodesy 85(8):457–473. doi:10.1007/s00190-011-0444-4

Angermann D (2012) Standards and conventions for geodesy. In: Drewes H, Hornik H, Adam J, Rozsa S (eds) The geodesists handbook 2012. J Geod 86(10):961–964. doi:10.1007/s00190-012-0584-1

Argus DF, Gordon R (1991) No-net-rotation model of current plate velocities incorporation plate motion model NUVEL-1. Geophys Res Lett 18:2038–2042. doi:10.1029/91GL01532

Blewitt G (2003) Self-consistency in reference frames, geocenter definition, and surface loading of the solid Earth. J Geophys Res 108(B2). doi:10.1029/2002JB008082

Bloßfeld M, Seitz M, Angermann D (2014) Non-linear station motions in epoch and multi-year reference frames. J Geodesy 88(1):45–63. doi:10.1007/s00190-013-0668-6

Burša M, Groten E, Kenyon S, Kouba J, Radej K, Vatrt V, Vojtíšková M (2002) Earth's dimension specified by geoidal geopotential. Studia geoph et geod 46:1–8

Burša M, Šíma Z, Kenyon S, Kouba J, Vatrt V, Vojtíšková M (2007) Twelve years of developments: geoidal geopotential W_0 for the establishment of a world height system - present and future. In: Proceedings of the 1st international symposium of the international gravity field service, Istanbul, pp 121–123

Collilieux X, Altamimi Z, Ray J, van Dam T, Wu X (2009) Effect of the satellite laser ranging network distribution on geocenter motion estimates. J Geophys Res 114(B4). doi:10.1029/2008.JB005727

Dayoub N, Edwards SJ, Moore P (2012) The Gauss-Listing potential value W_0 and its rate from altimetric mean sea level and GRACE. J Geodesy 86:681–694. doi:10.1007/s00190-012-1547-6

DeMets C, Gordon RG, Argus DF, Stein S (1990) Current plate motions. Geophys J Int 101:425–478

DeMets C, Gordon RG, Argus DF, Stein S (1994) Effect of recent revisions of the geomagnetic reversal timescale on estimates of current plate motions. Geophys Res Lett 21(20):2191–2194. doi:10.1029/94GL02118

Dong D, Yunck T, Heflin M (2003) Origin of the international terrestrial reference frame. J Geophys Res 108(B4). doi:10/1029/2002JB0022035

Drewes H (2009) The actual plate kinematic and crustal deformation model APKIM2005 as basis for a non-rotating ITRF. In: Drewes H (ed) Geodetic reference frames. IAG symposia, vol 134. Springer, Berlin, pp 95–99. doi:10.1007/978-3-642-00860-3

Drewes H (2012) How to fix the geodetic datum for reference frames in geosciences applications? In: Kenyon S, Pacino MC, Marti U (eds) Geodesy for planet Earth. IAG symposia, vol 136. Springer, Berlin, pp 67–76. doi:10.1007/978-3-642-20338-1

European GOCE Gravity Consortium (2012) GOCE high level processing facility GOCE standards. In: Gruber T, Abrikosov O, Hugentobler U (eds) Document GO-TN-HPF-GS-011

Förste C, Bruisma SL, Shako R et al (2012) A new release of EIGEN-6, the latest combined gravity field model including LAGEOS, GRACE and GOCE data from the colloboration of GFZ Potsdam and GRGS Toulouse, EGU general assembly. Geophs Res Abstr 14:EGU2012-2821-2

Groten E (2004) Fundamental parameters and current (2004) best estimates of the parameters of common relevance to astronomy, geodesy, and geodynamics. J Geodesy 77:724–731. doi:10.1007/s00190-003-0373-y

Hugentobler U, Gruber T, Steigenberger P, Angermann D, Bouman J, Gerstl M, Richter B (2012) GGOS bureau for standards and conventions: integrated standards and conventions for geodesy. In: Kenyon S, Pacino MC, Marti U (eds) Geodesy for planet Earth. IAG symposia, vol 136. Springer, Berlin, pp 995–998. doi:10.1007/978-3-642-20338-1

Ihde J (2009) Inter-commission project 1.2: vertical reference frames. In: Drewes H, Hornik H (eds) International Association of Geodesy, Report 2007–2009, Travaux, p 36

Kutterer H, Neilan R, Bianco G (2012) Global geodetic observing system (GGOS). In: Drewes H, Hornik H, Adam J, Rozsa S (eds) The geodesists handbook 2012. J Geodesy 86(10):915–926. doi:10.1007/s00190-012-0584-1

Luzum B, Capitaine N, Fienga A et al (2011) The IAU 2009 system of astronomical constants: report of the IAU working group on numerical standards for fundamental astronomy. Celest Mech Dyn Astron 110(4):293

Moritz H (2000) Geodetic reference system 1980. J Geodesy 74:128–162. doi:10.1007/s001900050278

Pavlis NK, Holmes SA, Kenyon SC, Factor JK (2012) The development of the Earth gravitational model 2008 (EGM2008). J Geophys Res 117(B04406). doi:10.1029/2011JB008916

Petit G, Luzum B (2010) IERS conventions 2010. IERS Technical Note No. 36, Frankfurt am Main

Plag HP, Pearlman M (2009) Global geodetic observing system. Meeting the requirements of a global society on a changing planet in 2020. Springer, Berlin. doi:10.1007/978-3-642-02687-4

Rummel R (2000) Global integrated geodetic and geodynamic observing system (GIGGOS). In: Rummel R, Drewes H, Bosch W, Hornik H (eds) Towards an integrated global geodetic observing system (IGGOS). IAG symposia, vol 120. Springer, Berlin, pp 253–260. doi:10.1007/978-3-642-59745-9

Sánchez L (2007) Definition and realization of the SIRGAS vertical reference system within a globally unified height system. In: Tregoning P, Ch Rizos (eds) Dynamic planet. IAG symposia, vol 130. Springer, Berlin, pp 638–645. doi:10.1007/978-3-540-49350-1-92

Sánchez L (2009) Strategy to establish a global vertical reference system. In: Drewes H (ed) Geodetic reference frames. IAG symposia, vol 134. Springer, Berlin, pp 273–278. doi:10.1007/978-642-3-00860-3-42

Sánchez L (2012) Towards a vertical datum standardisation under the umbrella of global geodetic observing system. J Geodetic Sci 2(4):325–342. doi:10.2478/v10156-012-0002-x

Seitz M, Angermann D, Bloßfeld M, Drewes H Gerstl M (2012) The DGFI realization of ITRS: DTRF2008. J Geodesy 86(12):1097–1123. doi:10.1007/s00190-012-0567-2

Monitoring of Antenna Changes at IGS Stations in Iceland

Peter Steigenberger, Urs Hugentobler, Uwe Hessels, Klaus Röttcher, Simon Lutz, and Rolf Dach

Abstract

GNSS antenna changes are in particular critical for the long-term stability of the coordinate time series and the reference systems realized with these stations. Depending on the antenna types and the available antenna calibrations, discontinuities of up to several centimeters can be introduced. Therefore, a monitoring of the antenna changes is important to verify the continuity of the time series.

In order to add Galileo tracking capability the GNSS equipment at the Icelandic IGS stations Reykjavik and Hoefn had to be replaced. Temporary GNSS sites were set up in the vicinity of both sites. These short baselines are analyzed with different observables. In addition, the temporary sites were included in the routine processing of the Center for Orbit Determination in Europe analysis center of the IGS. The equipment changes introduced discontinuities of up to 1.5 cm in the coordinates derived from the global solution. Depending on the analysis strategy and observables used, the results of the short baselines differ by up to 2.5 cm.

Keywords

Equipment upgrade • Global positioning system • GNSS • Permanent station

1 Introduction

Since the establishment of the International Global Navigation Satellite Systems (GNSS) Service (IGS, Dow et al. 2009) in 1994, the IGS tracking network has continuously grown to a number of currently 427 stations. Changes of the GNSS equipment are inevitable in order to replace faulty hardware or to add additional tracking capabilities. Due to updates of the operational GNSS GPS and GLONASS and the emerging GNSS BeiDou and Galileo, a transition from legacy GPS or GPS/GLONASS hardware to multi-GNSS antennas and receivers is mandatory. However, antenna changes can introduce discontinuities of up to several centimeters, in particular in the height component (e.g., Steigenberger 2009). Potential reasons for discontinuities introduced by equipment changes are:

P. Steigenberger (✉)
Institut für Astronomische und Physikalische Geodäsie, Technische Universität München, Arcisstraße 21, 80333 München, Germany

Present address: Deutsches Zentrum für Luft- und Raumfahrt, German Space Operations Center, Münchener Straße 20, 82234 Weßling, Germany
e-mail: peter.steigenberger@dlr.de

U. Hugentobler
Institut für Astronomische und Physikalische Geodäsie, Technische Universität München, Arcisstraße 21, 80333 München, Germany

U. Hessels • K. Röttcher
Bundesamt für Kartographie und Geodäsie, Geodätisches Observatorium Wettzell, Sackenrieder Straße 25, 93444 Bad Kötzting, Germany

S. Lutz • R. Dach
Astronomisches Institut, Universität Bern, Sidlerstraße 5, 3012 Bern, Switzerland

© Springer International Publishing Switzerland 2015

C. Rizos, P. Willis (eds.), *IAG 150 Years*, International Association of Geodesy Symposia 143,
DOI 10.1007/1345_2015_115

– increased number of observations in particular at low elevations due to replacement of degraded or outdate equipment
– better observation quality due to improved tracking techniques, including multipath mitigation
– change in the antenna-monument-environment coupling due to a different antenna being introduced
– change in the elevation of the antenna phase center resulting in different multipath effects
– different tracking of different frequencies/signals meaning stronger tracking of the weaker L2 signal
– error in the antenna height determination.

The IGS network plays an important role in the realization of the International Terrestrial Reference System, e.g., its latest version ITRF2008 (Altamimi et al. 2011). But, discontinuities in the station coordinate time series degrade the stability and accuracy of the reference frame. Rebischung et al. (2012) report 23 discontinuities due to equipment changes for the reference frame stations of IGS08, the IGS implementation of ITRF2008, in a time period of 2 years.

In order to monitor the equipment upgrades of the two Icelandic IGS stations Reykjavik and Hoefn, GNSS observations were collected at two adjacent sites. Previous studies of Steigenberger et al. (2013) have shown that the numerical values of discontinuities obtained from different observables, i.e., L1, L2, and the ionosphere-free linear combination LC can differ significantly due to site-specific effects. Whereas single-frequency solutions provide a better precision because of the smaller noise, solutions obtained with LC agree better with global solutions also relying on this linear combination. Therefore, different setups for the analysis of the short baselines are compared with results obtained from global and regional solutions of the Center for Orbit Determination in Europe (CODE, Dach et al. 2009).

Different strategies for monitoring antenna changes are presented in Sect. 2. The upgrades of the two IGS stations and the processing of their GNSS observations are described in Sects. 3 and 4, respectively. Finally, Sect. 5 discusses the results obtained from global and local GNSS analysis.

2 Strategies for Monitoring Antenna Changes

The IGS site guidelines[1] (IGS Infrastructure Committee 2013) offer several recommendations regarding equipment changes:

– Of particular importance to the IGS is the stable, long-term operation of the network. Therefore, changes to any stations configuration or immediate surroundings should be carefully planned to minimize discontinuities in the station's position time-series.

[1] http://igscb.jpl.nasa.gov/network/guidelines/guidelines.html.

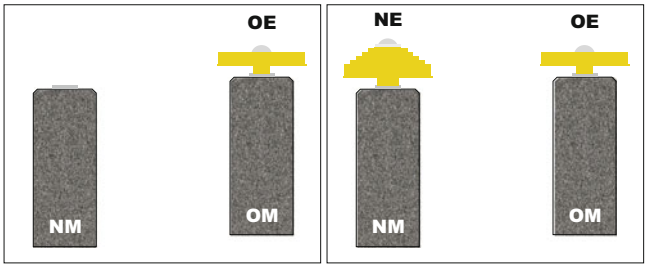

Fig. 1 Ideal case: the new equipment (NE) is installed on a new monument (NM) and the old equipment (OE) is operated in its original environment (OM) until failure

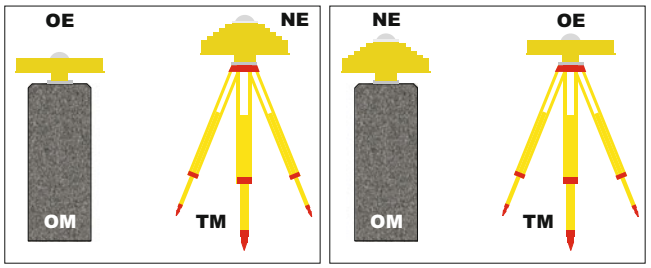

Fig. 2 Operating the new equipment on a temporary marker (TM, *left*) and swap of the equipment (*right*)

– New equipment to be installed should be first installed on one of the additional monuments at the station site (...), or on a semi-permanent location at the site set up for this purpose. Data from the additional monument should be recorded for as long as possible with the new equipment (at least 1 month) in parallel to the original station (barring substitution after catastrophic failure).
– When upgrading a Co-located or a Reference Frame station, the parallel observation period should be 2 months or more.

In the following, three different scenarios for monitoring GNSS antenna changes are discussed.

2.1 New Monument

The first scenario is the ideal case: the new equipment is installed on a new permanent monument close to the legacy GNSS site, see Fig. 1. The legacy equipment is operated as long as possible, i.e., until failure of one of its components. This setup allows for an optimal tieing of the old and the new site. However, for many stations it is difficult or even impossible to permanently install a second antenna close to the original site and additional efforts are necessary for the long-term operation and the analysis of the second site.

2.2 Equipment Swap

According to the IGS site guidelines a semi-permanent location is also possible and indicated by a tripod in Fig. 2.

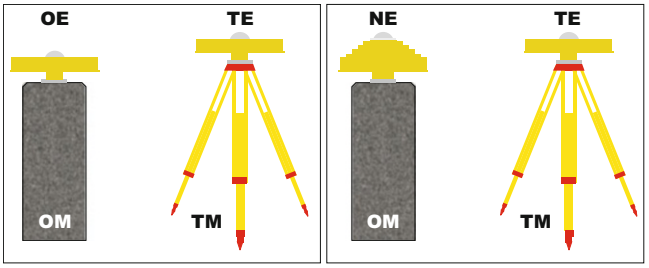

Fig. 3 Monitoring of the equipment change with a temporary site. TE stands for temporary equipment

The advantage of this approach is that the new equipment can be tested in-situ. In case of an unexpected malfunction, it can be replaced without having touched the original equipment. As both antennas are removed for the equipment change it is quite easy to measure the height difference between the permanent and the temporary maker with local surveys. Based on the GNSS-derived height differences before and after the equipment change and this "ground truth", empirical corrections can be derived.

2.3 Monitoring with Temporary Site

The third scenario is a temporary site that is used to monitor the antenna change (Fig. 3). This approach is not fully consistent with the IGS site guidelines but it allows to apply the correction method of Wanninger (2009) to correct for site- and antenna-specific effects. As the temporary site does not change, discontinuities can be determined from the analysis of the short baseline between the permanent site before and after the equipment change and the temporary site.

3 Antenna Changes at Reykjavik and Hoefn

The German Federal Agency for Cartography and Geodesy (Bundesamt für Kartographie und Geodäsie, BKG) operates 21 globally distributed permanent stations contributing to the IGS tracking network. Two of these stations are located in Iceland, namely Reykjavik (REYK) on the North American Plate and Hoefn (HOFN) on the Eurasian Plate (see Fig. 4). GPS receivers were installed in 1995 and 1997, respectively. In 2007 both sites were upgraded to GPS+GLONASS capable receivers. HOFN is an IGS reference frame site contributing to IGS08 (Rebischung et al. 2012).

At Reykjavik the temporary site REY2 was installed about one meter separated from REYK (see Fig. 5). For Hoefn the situation was even more comfortable: a second GNSS permanent site (HOFS) is operated by the Norwegian Mapping

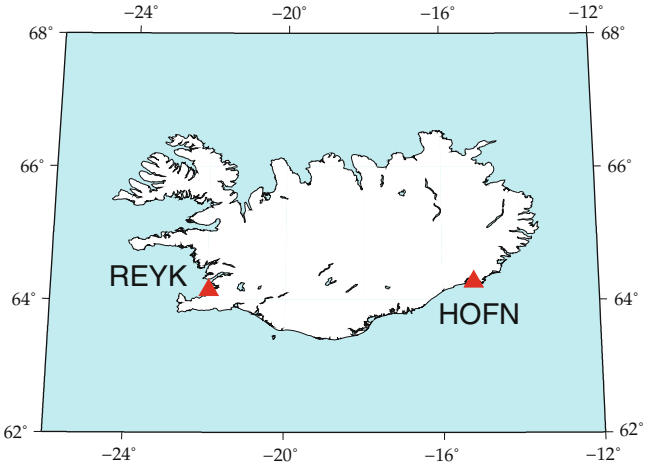

Fig. 4 Location of the Icelandic IGS stations Reykjavik (REYK) and Hoefn (HOFN)

Fig. 5 Temporary Trimble antenna (REY2) installed at the IGS station Reykjavik (REYK, Leica antenna)

Authority less than 10 m away from HOFN. Observation data as well as site logs of the four sites are available at the BKG GNSS Data Center (http://igs.bkg.bund.de/). The antennas and receivers before and after the equipment changes as well as the time intervals considered in this study are listed in Table 1. The changes to Leica AR25.R4 antennas with LEIT radome took place in early May 2013. The newly installed Leica GR25 receivers are 120 channel multi-GNSS receivers capable of tracking GPS (L1, L2, L5), GLONASS (L1, L2), Galileo (E1, E5a, E5b, E5), and SBAS (L1). For all involved antennas except for HOFS, individual antenna calibrations are available: robot calibrations (Menge et al. 1998) done by Geo++ or Senatsverwaltung Berlin and anechoic chamber calibrations (Görres et al. 2006) performed by University of Bonn. A quality check with the teqc software (Estey and

Table 1 GNSS equipment employed at the IGS permanent as well as temporary sites

Station	Site	Type	Start	End	Receiver	Antenna		Cal.
Hoefn	HOFN	IGS	16 Sep 2012	05 May 2013	TPS E_GGD	TPSCR3_GGD	CONE	Geo++
			05 May 2013	06 Jul 2013	LEICA GR25	LEIAR25.R4	LEIT	Bonn
	HOFS	Permanent	16 Sep 2012	06 Jul 2013	TRIMBLE NETR9	TRM41249.00	NONE	n/a
Reykjavik	REYK	IGS	20 Feb 2013	02 May 2013	TPS E_GGD	TPSCR.G3	TPSH	Geo++
			02 May 2013	06 Jul 2013	LEICA GR25	LEIAR25.R4	LEIT	Bonn
	REY2	Temporary	20 Feb 2013	06 Jul 2013	LEICA GRX1200+GNSS	TRM29659.00	NONE	Berlin

The column *Cal.* refers to the method of antenna calibration: robot calibrations by *Geo++* or Senatsverwaltung *Berlin*, anechoic chamber calibrations by University of *Bonn*

Meertens 1999) reveals a multipath reduction on L1 and L2 of about 30–50% with the new equipment for both sites. Since this update, both stations contribute Galileo and SBAS observations to the Multi-GNSS Experiment (MGEX, Rizos et al. 2013) of the IGS.

4 GNSS Processing

The latest development version 5.3 of the Bernese GNSS Software (Dach et al. 2007) is used to process double difference GPS carrier phase observations of the short baselines between the IGS and the temporary sites. Satellite orbits and Earth rotation parameters from CODE are used. In order to determine the discontinuities due to the equipment changes, the coordinates of the temporary sites HOFS and REY2 are fixed and daily coordinates are estimated for HOFN and REYK. A 3° elevation cut-off angle and elevation-dependent weighting with $w = \cos^2 z$ is applied where z stands for the zenith angle. L1 and L2 ambiguities are fixed to integers with the Sigma method (Dach et al. 2007) but no ambiguity fixing is done for observations affected by the so-called quarter-cycle issue (i.e., IIR-M and IIF satellites, Leica receivers, Wübbena et al. 2009). The ambiguity resolution rate is 100% for the baseline HOFN/HOFS before the antenna change and about 85% for the other baselines (HOFN/HOFS after the equipment change and REYK/REY2 before and after the change).

Due to the vicinity of the sites, estimating troposphere zenith delays does not make sense from a physical point of view. Therefore, hydrostatic zenith delays from the ECMWF are used for all sites for the first solution type. They are mapped to the observation direction with the Vienna Mapping Function 1 (VMF1, Boehm et al. 2006). However, earlier studies of Dilßner et al. (2008) have shown, that the estimation of troposphere parameters significantly affects the height discontinuities introduced by antenna changes. Therefore, a second solution type was computed including the estimation of troposphere zenith delays for HOFN and REYK with 2-h parameter spacing. The troposphere zenith delays of HOFS and REY2 were fixed to the model mentioned above.

Table 2 Setup for the different local, regional, and global GNSS solutions

ID	Type	Freq.	Troposph.	Ant. cal.
B1	Local	L1	No	igs08.atx
B2	Local	L2	No	igs08.atx
B3	Local	LC	No	igs08.atx
B1I	Local	L1	No	Individual
B2I	Local	L2	No	Individual
B3I	Local	LC	No	Individual
T1	Local	L1	Yes	igs08.atx
T2	Local	L2	Yes	igs08.atx
T3	Local	LC	Yes	igs08.atx
T1I	Local	L1	Yes	Individual
T2I	Local	L2	Yes	Individual
T3I	Local	LC	Yes	Individual
COE	Regional	LC	Yes	epnc_08.atx
COD	Global	LC	Yes	igs08.atx

LC stands for the ionosphere-free linear combination of L1 and L2. The column *Troposphere* indicates the estimation of troposphere zenith delays

In general type-mean receiver antenna calibrations from the IGS antenna model igs08.atx[2] (Rebischung et al. 2012) are used. However, as individual antenna calibrations are available for 5 out of 6 antennas (see Table 1), special solutions with these calibrations are computed. For the EUREF (Bruyninx et al. 2012) solution the individual antenna calibrations provided in epnc_08.atx[3] are used for HOFN and REYK, type-mean calibrations from igs08.atx for HOFS and REY2.

For comparison purposes, the temporary sites were added to the operational solutions of CODE for the IGS (COD) and EUREF (COE). In contrast to the solutions discussed so far, these two solutions are based on a rigorous combination of GPS and GLONASS. They are based on the ionosphere-free linear combination and include the estimation of troposphere parameters for all stations. An overview of the solutions discussed in the next section is given in Table 2.

[2] Available at http://igscb.jpl.nasa.gov/igscb/station/general/igs08.atx.

[3] Available at http://www.epncb.oma.be/ftp/station/general/epnc_08.atx.

Table 3 Station coordinate discontinuities due to equipment changes at the IGS stations Hoefn and Reykjavik and their formal errors based on the assumption of white noise

	Hoefn			Reykjavik		
Solution	ΔNorth (mm)	ΔEast (mm)	ΔUp (mm)	ΔNorth (mm)	ΔEast (mm)	ΔUp (mm)
B1	0.4 ± 0.03	−2.4 ± 0.03	1.8 ± 0.06	0.9 ± 0.08	2.4 ± 0.09	1.9 ± 0.42
B2	1.5 ± 0.03	−0.4 ± 0.03	2.6 ± 0.06	1.2 ± 0.09	1.7 ± 0.09	5.0 ± 0.40
B3	−1.4 ± 0.05	−5.4 ± 0.03	0.6 ± 0.13	0.4 ± 0.09	3.3 ± 0.10	−3.4 ± 0.46
B1I	0.6 ± 0.03	−2.7 ± 0.03	1.9 ± 0.06	0.6 ± 0.08	1.3 ± 0.09	2.1 ± 0.43
B2I	0.9 ± 0.03	−1.1 ± 0.03	2.2 ± 0.06	1.0 ± 0.09	1.8 ± 0.09	5.2 ± 0.40
B3I	0.2 ± 0.05	−5.1 ± 0.03	1.4 ± 0.13	−0.2 ± 0.09	**0.3 ± 0.10**	−3.5 ± 0.47
T1	0.4 ± 0.03	−2.4 ± 0.03	1.3 ± 0.07	1.0 ± 0.08	2.3 ± 0.07	1.5 ± 0.54
T2	1.5 ± 0.03	−0.4 ± 0.03	4.3 ± 0.07	1.2 ± 0.09	1.7 ± 0.07	7.7 ± 0.50
T3	−1.2 ± 0.04	−5.4 ± 0.03	−3.3 ± 0.16	0.7 ± 0.09	3.2 ± 0.08	−9.0 ± 0.62
T1I	0.6 ± 0.03	−2.7 ± 0.03	2.1 ± 0.07	0.7 ± 0.08	1.2 ± 0.07	**1.4 ± 0.54**
T2I	0.8 ± 0.03	−1.1 ± 0.03	5.1 ± 0.07	0.9 ± 0.09	1.8 ± 0.07	10.2 ± 0.50
T3I	0.3 ± 0.04	−5.0 ± 0.03	−2.4 ± 0.16	0.3 ± 0.09	0.3 ± 0.08	−13.2 ± 0.62
COD	**0.2 ± 0.07**	−6.2 ± 0.05	−1.1 ± 0.21	0.6 ± 0.10	1.9 ± 0.11	−14.1 ± 0.43
COE	**0.1 ± 0.08**	−6.3 ± 0.06	−1.6 ± 0.26	0.7 ± 0.10	2.1 ± 0.10	−13.0 ± 0.42

Values smaller than the threefold formal errors are given in bold

5 Results

Offsets due to the equipment change were determined in a least squares adjustment by estimating separate mean coordinates in a local frame before and after the change. The numerical values as well as their formal errors are listed in Table 3. As an example, the time series of Reykjavik obtained from the CODE IGS solution is shown in Fig. 6. Discontinuities are visible in all three coordinate components but are in particular pronounced in the height component.

The formal errors for Hoefn are smaller compared to Reykjavik due to the longer observation time before the equipment change: 218 days with GNSS observations for Hoefn vs. 59 days for Reykjavik. The formal errors of the horizontal discontinuities are very similar for the local solutions. For the height component, they are larger by a factor of two, or even more if troposphere parameters are estimated. The increased noise of the ionosphere-free linear combination is in particular visible in the height component and is even more pronounced for the discontinuity estimates from the global and regional solutions COD and COE.

Based on the threefold formal errors, almost all estimated discontinuities are significant. The few insignificant discontinuities are given in bold in Table 3. However, one has to be aware that the formal errors in Table 3 are based on white noise. As GPS time series usually include flicker noise, they are too optimistic by a factor of about 2–3. The largest horizontal discontinuities of more than 5 mm occur for the East component of Hoefn for solutions based on the ionosphere-free linear combination. In general, the local and the global/regional solutions agree within 1–2 mm. For the height component of Hoefn the agreement is also quite good when applying the same analysis options in the global and the local solution, i.e., including the estimation of

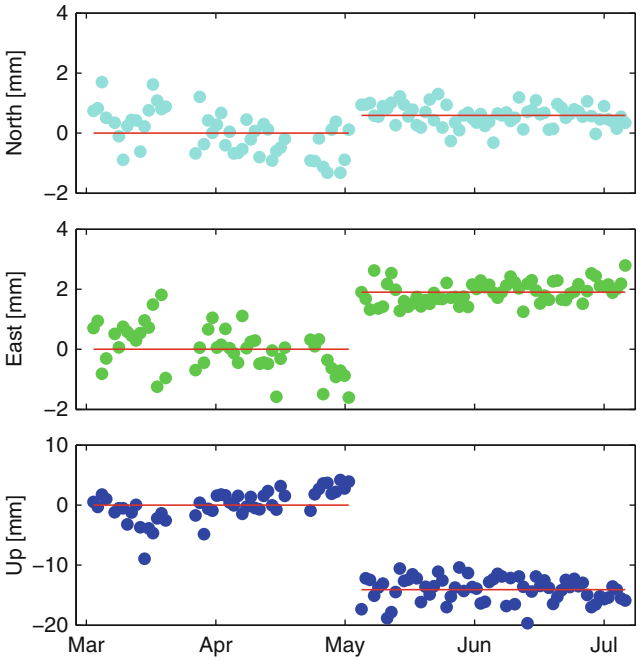

Fig. 6 Station coordinate time series of REYK obtained from the CODE global solution (COD). The *red lines* indicate the mean coordinates before and after the equipment change. The mean values of the time series before the antenna change were aligned to zero

troposphere zenith delays also in the local solutions (T3 and T3I). Enabling this option changes the height discontinuities by up to 4 mm for Hoefn and almost 1 cm for Reykjavik. It is interesting to note that the L2 height discontinuities are larger compared to L1 for all different setups of the local solutions.

The largest discontinuity as well as the largest differences between global and local solutions are visible for the height component at Reykjavik. On the one hand, analysis of the CODE IGS solution gives a discontinuity of −14.1 mm, the EUREF solution differs only by 1.1 mm from that value. On

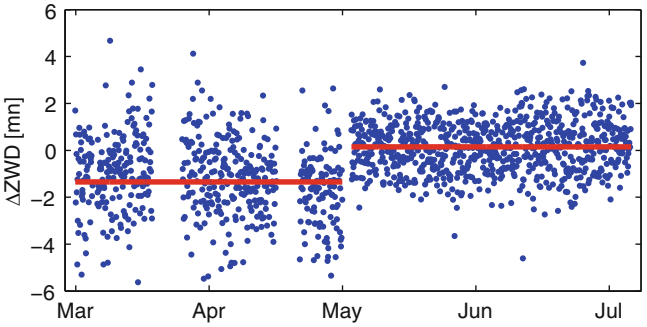

Fig. 7 Troposphere zenith wet delay differences between REYK and REY2 obtained from the CODE global solution (COD). The *red lines* indicate the mean ZWD values before and after the equipment change

the other hand, the discontinuities obtained from the local solutions range from −3.5 to +5.2 mm if no troposphere parameters are estimated. Solution T3I including troposphere estimation and considering individual antenna calibrations provides the best agreement between the global and local solutions. However, as the global solution was computed with type-mean antenna calibrations, this seems to be a coincidence.

With a few tens of a millimeter up to about one millimeter, the differences between solutions with individual antenna calibrations and type-mean values from igs08.atx are small. The maximum differences of up to 4 mm occur for the height component at Reykjavik when using L2 or LC (T2 vs. T2I and T3 vs. T3I).

Due to the large height discontinuity, the equipment change at Reykjavik can also be seen in the difference of the troposphere zenith wet delay (ZWD) estimates of REYK and REY2 in the global and regional solutions. Figure 7 shows these differences obtained from the CODE global solution where a discontinuity of 1.5 mm is clearly visible. The scatter of the ZWD differences is significantly smaller after the equipment change: the standard deviation decreases from 1.8 to 1.1 mm indicating a better performance of the new equipment.

6 Summary and Conclusions

The equipment changes at the two IGS stations HOFN and REYK caused remarkable discontinuities of 6 mm in the East component of Hoefn and even 14 mm in the height component of Reykjavik in the global analysis. Pronounced differences between solutions obtained from L1, L2, and ionosphere-free (LC) observables are an indicator for site-specific systematic effects like multipath (Dilßner et al. 2008; King and Watson 2010). Estimating troposphere zenith delays in the local solution improves the agreement of the height discontinuities obtained from the global and local analysis. However, as the sites are very close to each other, the troposphere estimation does not account for physical differences but it absorbs systematic effects in a similar way as in the global solution. Differences between global/regional and local solutions based on LC including the estimation of troposphere parameters could be explained by slightly different preprocessing options of both solution types.

If one wants to obtain the coordinate offset due to an antenna change from a local GNSS campaign, one has to use the ionosphere-free linear combination and estimate differential tropospheric corrections in order to get a good agreement with global solutions. Single-frequency solutions or solutions without estimating troposphere parameters significantly differ due to systematic errors although their precision is higher. We recommend the setup of the new equipment at a separate monument at least for co-location sites to provide the best possible tieing of the old and new site and stability for the terrestrial reference frame. However, both stations have to be processed by the analysis centers to benefit from this approach.

Acknowledgements HOFS GNSS data was kindly provided by the Norwegian Mapping Authority.

References

Altamimi Z, Collilieux X, Métivier L (2011) ITRF2008: an improved solution of the international terrestrial reference frame. J Geod 85(8):457–473. doi:http://doi.org/10.1007/s00190-011-0444-4

Boehm J, Werl B, Schuh H (2006) Troposphere mapping functions for GPS and very long baseline interferometry from European Centre for Medium-Range Weather Forecasts operational analysis data. J Geophys Res 111(B2):B02406. doi:http://doi.org/10.1029/2005JB003629

Bruyninx C, Habrich H, Söhne W, Kenyeres A, Stangl G, Völksen C (2012) Enhancement of the EUREF permanent network services and products. In: Geodesy for Planet Earth, International Association of Geodesy Symposia, vol 136, pp 27–34. doi:http://doi.org/10.1007/978-3-642-20338-1_4

Dach R, Hugentobler U, Fridez P, Meindl M (eds) (2007) Bernese GPS Software Version 5.0. Astronomical Institute, University of Bern, Bern, Switzerland

Dach R, Brockmann E, Schaer S, Beutler G, Meindl M, Prange L, Bock H, Jäggi A, Ostini L (2009) GNSS processing at CODE: status report. J Geod 83(3–4):353–365. doi:http://doi.org/10.1007/s00190-008-0281-2

Dilßner F, Seeber G, Wübbena G, Schmitz M (2008) Impact of Near-field effects on the GNSS position solution. In: Proceedings of ION GNSS 2008, Institute of Navigation, Savannah, USA, pp 612–624

Dow JM, Neilan RE, Rizos C (2009) The International GNSS Service in a changing landscape of Global Navigation Satellite Systems. J Geod 83(3–4):191–198. doi:http://doi.org/10.1007/s00190-008-0300-3

Estey LH, Meertens CM (1999) TEQC: The multi-purpose toolkit for GPS/GLONASS data. GPS Solutions 3(1):42–49. doi:http://doi.org/10.1007/s10291-002-0027-1

Görres B, Campbell J, Becker M, Siemes M (2006) Absolute calibration of GPS antennas: laboratory results and comparison with field and robot techniques. GPS Solutions 10(2):136–145. doi:http://doi.org/10.1007/s10291-005-0015-3

IGS Infrastructure Committee (2013) IGS Site Guidelines

King MA, Watson CS (2010) Long GPS coordinate time series: multipath and geometry effects. J Geophys Res 115:B04403. doi:http://doi.org/10.1029/2009JB006543

Menge F, Seeber G, Völksen C, Wübbena G, Schmitz M (1998) Results of absolute field calibration of GPS antenna PCV. In: Proceedings of ION GPS-98, Nashville, Tennessee, pp 31–38

Rebischung P, Griffiths J, Ray J, Schmid R, Collilieux X, Garayt B (2012) IGS08: the IGS realization of ITRF2008. GPS Solutions 16(4):483–494. doi:http://doi.org/10.1007/s10291-011-0248-2

Rizos C, Montenbruck O, Weber R, Weber G, Neilan R, Hugentobler U (2013) The IGS MGEX experiment as a milestone for a comprehensive multi-GNSS service. In: Proceedings of the ION 2013 Pacific PNT Meeting, pp 289–295

Steigenberger P (2009) Reprocessing of a global GPS network. Deutsche Geodätische Kommission, Reihe C (640), http://dgk.badw.de/fileadmin/docs/c-640.pdf

Steigenberger P, Hugentobler U, Schmid R, Hessels U, Klügel T, Seitz M (2013) GPS-specific local effects at the Geodetic Observatory Wettzell. In: Altamimi X Z; Collilieux (ed) Reference frames for applications in geosciences, Springer, IAG Symposia, vol 138, pp 125–130. doi:http://doi.org/10.1007/978-3-642-32998-2_20

Wanninger L (2009) Correction of apparent position shifts caused by GNSS antenna changes. GPS Solutions 13(2):133–139. doi:http://doi.org/10.1007/s10291-008-0106-z

Wübbena G, Schmitz M, Bagge A (2009) Some thoughts on satellite induced phase shifts aka “the L2C quarter cycle problem” and the impact on RINEX and RTCM. Technical Report, Geo++ Gesellschaft für satellitengestützte geodätische und navigatorische Technologien mbH, http://www.geopp.de/media/docs/pdf/geopp_phase_shift_l2c.pdf

The Status of GNSS Data Processing Systems to Estimate Integrated Water Vapour for Use in Numerical Weather Prediction Models

F. Ahmed, F.N. Teferle, R.M. Bingley, and D. Laurichesse

Abstract

Modern Numerical Weather Prediction (NWP) models make use of the GNSS-derived Zenith Total Delay (ZTD) or Integrated Water Vapour (IWV) estimates to enhance the quality of their forecasts. Usually, the ZTD is assimilated into the NWP models on 3-hourly to 6-hourly intervals but with the advancement of NWP models towards higher update rates e.g. 1-hourly cycling in the Rapid Update Cycle (RUC) NWP, it has become of high interest to estimate ZTD on sub-hourly intervals. In turn, this imposes requirements related to the timeliness and accuracy of the ZTD estimates and has lead to a development of various strategies to process GNSS observations to obtain ZTD with different latencies and accuracies. Using present GNSS products and tools, ZTD can be estimated in real-time (RT), near real-time (NRT) and post-processing (PP) modes. The aim of this study is to provide an overview and accuracy assessment of various RT, NRT, and PP IWV estimation systems and comparing their achieved accuracy with the user requirements for GNSS meteorology. The NRT systems are based on Bernese GPS Software 5.0 and use a double-differencing strategy whereas the PP system is based on the Bernese GNSS Software 5.2 using the precise point positioning (PPP) strategy. The RT systems are based on the BKG Ntrip Client 2.7 and the PPP-Wizard both using PPP. The PPP-Wizard allows integer ambiguity resolution at a single station and therefore the effect of fixing integer ambiguities on ZTD estimates will also be presented.

Keywords

Global Navigation Satellite Systems • Integrated water vapour • Near real-time • Numerical weather prediction • Post processing • Real-time • Troposphere • Zenith total delay

1 Introduction

Atmospheric water vapour is a primary greenhouse gas and plays an important role in the formation of weather systems and climate change. Global Navigation Satellite System (GNSS) signals experience a propagation delay, which, along with other factors, is also related to the amount of water vapour in the lower atmosphere. Hence GNSS observations can be processed to estimate this delay with millimetre-level accuracy and together with surface meteorological data

F. Ahmed (✉) • F.N. Teferle
Geophysics Laboratory, University of Luxembourg, L-1359 Luxembourg, Luxembourg
e-mail: furqan.ahmed@uni.lu

R.M. Bingley
Nottingham Geospatial Institute, University of Nottingham, Nottingham NG7 2TU, UK

D. Laurichesse
Centre National d′Etudes Spatiales, 31401 Toulouse, France

© Springer International Publishing Switzerland 2015

C. Rizos, P. Willis (eds.), *IAG 150 Years*, International Association of Geodesy Symposia 143,
DOI 10.1007/1345_2015_178

Table 1 General characteristics of GNSS processing systems at UL

System	Update cycle	Output sampling	Processing engine
PP	Post- processed	1 h	BSW5.2
NRT	Hourly	15 min	BSW5.0
RT-I	10 min	1 s	BNC2.7
RT-II	10 min	5 s	PPPW

BSW5.2 denotes the Bernese GNSS Software 5.2, BSW5.0, the Bernese GPS Software 5.0, BNC2.7 the BKG Ntrip Client 2.7, and PPPW the PPP-Wizard

Table 2 User requirements for GNSS Meteorology as outlined by COST Action 716 (Offiler 2010)

	Integrated water vapour (IWV)	
	Target	Threshold
Horizontal domain	Europe to National	
Repetition cycle	5 min	1 h
Integration time	MIN(5 min, rep cycle)	
Relative accuracy	1 kg/m^2 (6 mm in ZTD)	5 kg/m^2 (30 mm in ZTD)
Timeliness	5 min	30 min

can be used to compute the amount of atmospheric water vapour on various temporal and spatial scales (e.g. Bevis et al. 1994). The term "GNSS Meteorology" refers to the assimilation of GNSS-derived atmospheric information in NWP models as well as the combination of NWP model output and GNSS observations while issuing the forecasts. GNSS Meteorology has in general a positive impact on the quality of weather forecasts (e.g. Bennitt and Levick 2011; De Haan 2011; Gutman et al. 2004; Vedel et al. 2004). Long-term analysis of GNSS data is also being used for climatological studies (e.g. Nilsson and Elgered 2008; Stende 2006). The EUMETNET EIG GNSS water vapour programme (E-GVAP) is a programme for collection and distribution of NRT ground based GNSS data for operational meteorology since 2005 (http://egvap.dmi.dk). Analysis centres located all over Europe submit NRT GNSS-derived delay and IWV solutions to E-GVAP for validation, monitoring and research. The Troposphere Working Group of the International GNSS Service (IGS) (Dow et al. 2009) produces a high-precision GPS-based troposphere product, known as the IGS Final Troposphere product. The current version of this product is produced at the United States Naval Observatory (USNO) and contains ZTD estimates obtained using the precise point positioning (PPP) strategy (Zumberge et al. 1997) in form of 27-h long sessions with a sampling interval of 5 min (Byram et al. 2011). Beginning from 1997, the IGS Final Troposphere product was initially based on the network processing strategy but later in 2007, the PPP strategy was adopted for its production which had advantages over the older approach (Byun et al. 2009). In this paper we will refer to the current version of this product as IGFT. The Potential of Precipitable Water Vapour Measurements using Global Navigation Satellite Systems in Luxembourg (PWVLUX) is a research project which aims at studying the potential for the use of GNSS in operational meteorology and climatology in Luxembourg and its surrounding areas (the Greater Region). Under the framework of this project, various data processing systems have been established at the University of Luxembourg in collaboration with the University of Nottingham to estimate ZTD and IWV from GNSS observations in PP, NRT, and RT modes. Some characteristics of these systems are shown in Table 1.

The COST Action 716 (Elgered et al. 2005) developed various user requirements for GNSS meteorology which specify threshold and target values on timeliness, accuracy and resolution, etc, of ZTD and IWV estimates for use in NWP nowcasting (Table 2) (Offiler 2010). The accuracy requirements for IWV can be translated to their equivalent for ZTD (6 mm target and 30 mm threshold). If the RMS of the bias from IGFT is considered as a measure of relative accuracy, the obtained ZTD solutions can be compared to these requirements.

In this paper, we provide the current status of these systems along with their characteristics. Furthermore, we carry out a comparative analysis of these systems with IGFT and the accuracy requirements for GNSS meteorology. To read about the comparisons of GPS-derived ZTD estimates with those from other, non-GPS techniques, we refer the reader to Teke et al. (2011).

2 Processing Systems

Since 2011 the University of Luxembourg has established a number of GPS processing systems for the routine estimation of ZTD in collaboration with the University of Nottingham and the Centre National d'Etudes Spatiales. The hourly NRT system is based on Bernese GPS Software 5.0 (BSW5.0) (Dach et al. 2007, 2009) and uses double differencing to process a Europe-wide network (Fig. 1). A sub-hourly NRT system with an update cycle of 15 min is also based on BSW5.0 and is used to process 15 min RINEX files created from RT streams. It currently does not contribute to any meteorological activities and therefore it has not been considered for assessment in this study. The two RT systems use the PPP strategy and are based on the Federal Agency for Cartography and Geodesy (BKG) Ntrip Client (BNC) 2.7 (Weber and Mervart 2012) and the PPP-Wizard (Laurichesse 2011) software packages. The PP system has been implemented using the Bernese GNSS Software 5.2 (BSW5.2) (Dach 2013) and also uses PPP. Table 3 summarizes some specific characteristics of the various processing systems.

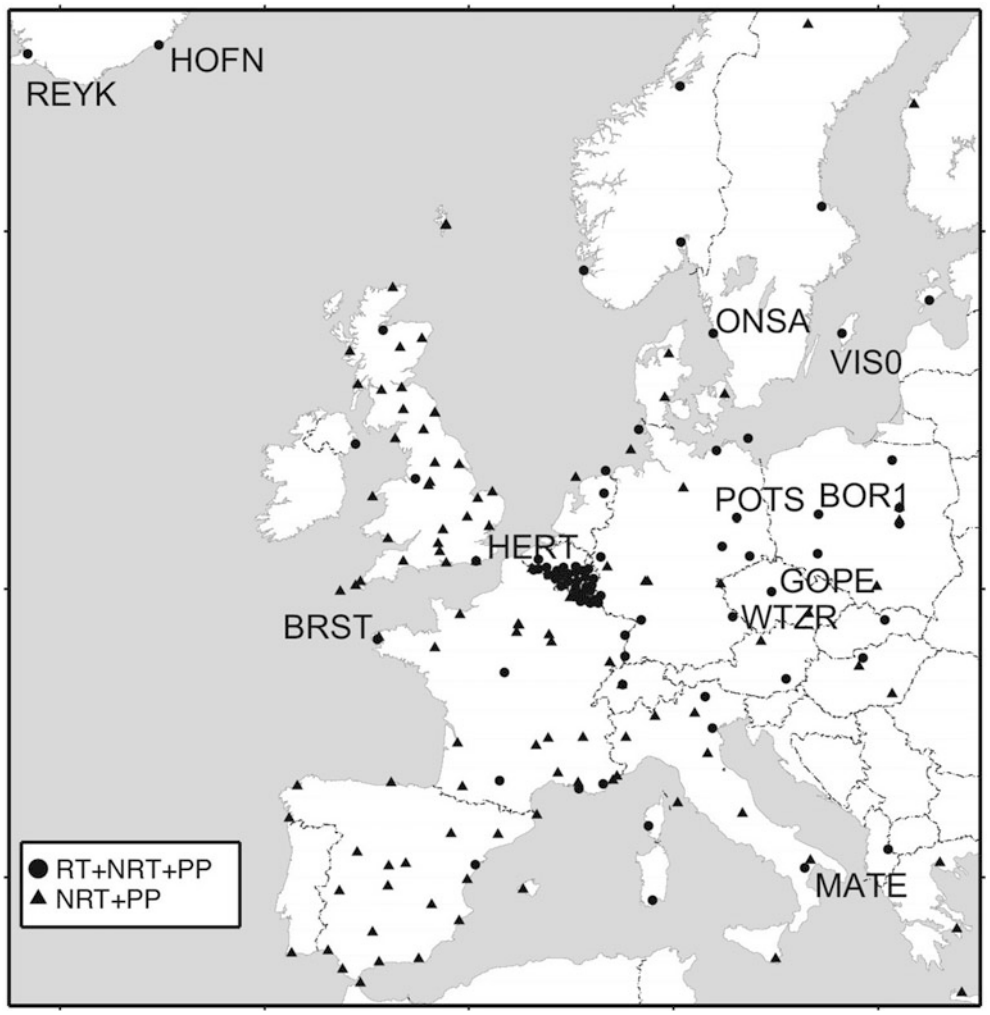

Fig. 1 Network of GNSS stations in Western Europe processed by the PP-, NRT-, and RT-systems at UL (global stations are not shown)

Table 3 Specific characteristics of GNSS processing systems at UL

System:	PP	NRT	RT-I	RT-II
GNSS used	GPS	GPS	GPS	GPS
Processing strategy	PPP	Double differencing	PPP	PPP
Receiver PCV correction	Yes	Yes	No	No
Receiver PCO correction	Yes	Yes	Yes	No
Satellite PCV correction	Yes	Yes	No	Yes
Satellite PCO correction	Yes	Yes	No[a]	No[a]
Coordinates computed	Yes	Yes	Yes	No
Input raw data format	Daily RINEX	Hourly RINEX	RTCM-3 streams	RTCM-3 streams
Input orbit/clock products	CODE final	IGS ultra-rapid	IGS02 (RTIGS)	CLK9B (CNES)
Ambiguity resolution	No	No	No	Yes

[a]In the RT correction streams used, the satellite's position refers to the ionosphere free phase center of its antenna and therefore the satellite antenna PCO correction is not necessary

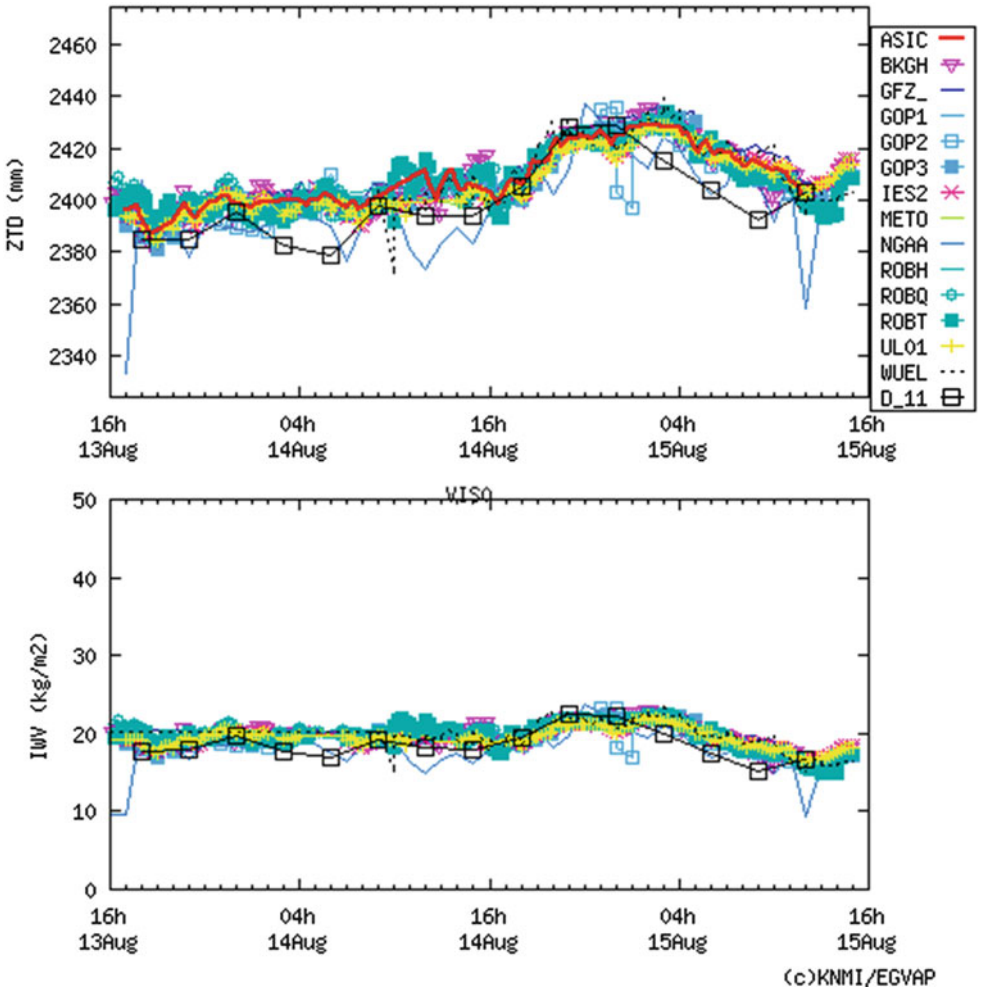

Fig. 2 E-GVAP ZTD (*top*) and IWV (*bottom*) time series comparison for station VIS0 from 2013-08-13 16:00UTC to 2013-08-15 16:00UTC. The UL01 solution is shown in *yellow* (http://www.egvap.dmi.dk)

3 Accuracy Assessment of the ZTD Estimates

The results from the hourly NRT system are submitted to E-GVAP as test solution UL01. E-GVAP allows a comparative analysis of the ZTD and IWV time series on a station-by-station basis and for an entire solution using the modelled values from the NWP model of the Royal Netherlands Meteorological Institute (KNMI) as a reference. A recent ZTD and IWV time series from the UL01 solution in comparison with other solutions for the GNSS station Visby (VIS0) are shown in Fig. 2. For this period and station, UL01 ZTD has a mean bias of -0.84 ± 14.81 mm with the ZTD from the KNMI NWP model. We note that for the stations used in this study (shown with 4-character ID in Fig. 1), ZTD from UL01 has a mean bias of 3.71 ± 11.90 mm with that from the KNMI NWP model. This compares well with the 3.42 ± 9.95 mm computed for all other E-GVAP analysis centers processing these stations.

Besides this comparison of the hourly NRT solution to other E-GVAP solutions we have also carried out an evaluation with regards to IGFT. In order to do so we extracted a 20-day long (April 20 to May 10, 2013) data set containing ZTD estimates from the solutions of the RT-I, RT-II, NRT and PP processing systems at UL. The selected GNSS stations belong to the IGS and the choice of stations was based on the availability of RT observation data and the maximum number of epochs common in all the solutions. Figure 1 shows the network of all GNSS stations in Europe included in the processing by the systems and identifies the 11 stations, with their 4-character ID, which were used in this analysis.

After the extraction of the data set, the ZTD time series were formed and compared. Figure 3 shows the example time series for BOR1, HOFN, POTS and VIS0 obtained by the four systems and IGFT. For clarity we have introduced artificial offsets in the figure. It is clearly visible that all five solutions generally follow the same pattern. Some data

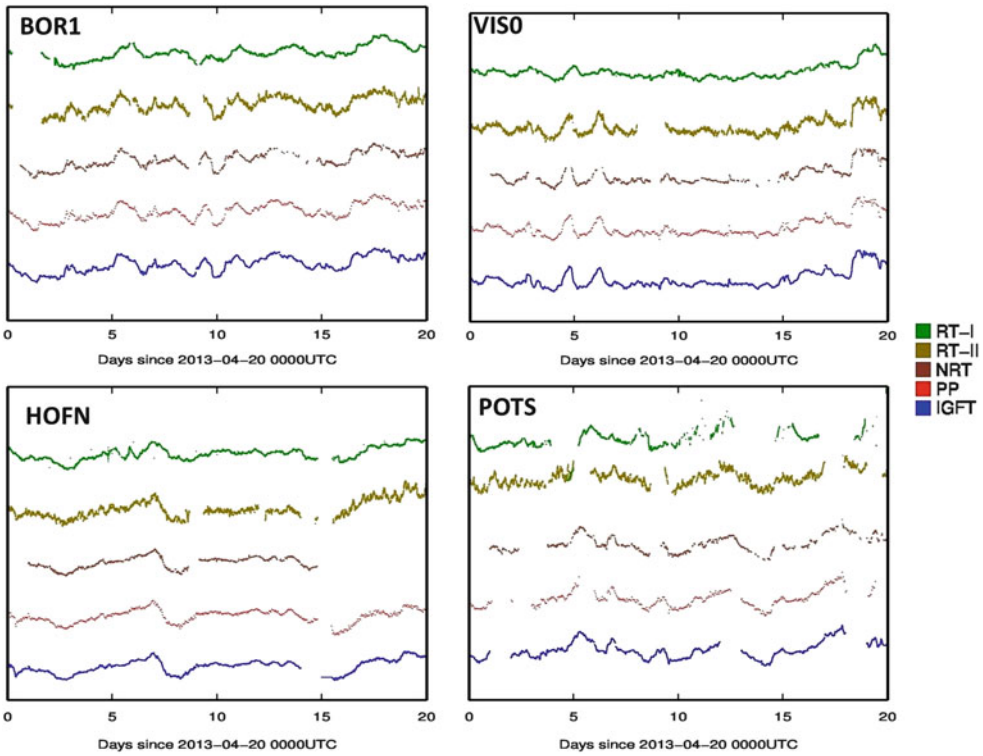

Fig. 3 ZTD time series for the stations BOR1, VIS0, HOFN and POTS obtained using the PP, NRT, RT-I and RT-II systems at UL compared to IGFT

gaps are visible in all solutions and not just in the RT-I, RT-II and NRT ones, which is an indication that also the delayed processes of the PP and IGFT solutions could not recover these data. It is also visible that the scatter of the solutions varies. This is most pronounced for RT-II, which shows many short-term variations. As these are not evident in the other solutions, these are an artifact of the PPP-Wizard software. It is also suggested that the ZTD variations, on temporal scales from a day to a few days, are fairly consistent between the RT-II, NRT, PP and IGFT solutions. Only for the RT-I solution the ZTD estimates are somewhat smoothened due to the constraints in the Kalman filter approach used by BNC2.7. This is apparent when rapid changes in the ZTD estimates occur, e.g. around day 7 for HOFN or days 5 and 6 for VIS0. The value of the troposphere white noise sigma (equal to 1e−5 m/s) used in BNC2.7 could be another possible reason for the delays or smoothness in the RT-I solution. On the other hand, there is no suggestion that the NRT, PP and IGFT solutions cannot track rapid variations as well as the RT-II solution.

Based on the 11 stations selected in this study we compute various statistics by taking the common epochs from the UL and IGFT reference data sets (Table 4). It can be seen that the PP and NRT systems show mean differences to the IGFT of -0.86 ± 4.44 mm and -0.27 ± 5.18 mm, respectively, whereas the mean differences of the RT-I and RT-II ZTD estimates to those from IGFT are 8.60 ± 27.97 mm and 60.40 ± 37.26 mm, respectively. The IGFT reference solution is based on BSW5.0 and thus the two solutions using the same software, i.e. PP and NRT, might have an advantage in this comparison. The large bias for RT-II is a consequence of the fact that the PPP-Wizard currently does not allow the application of antenna up eccentricity (height) and receiver antenna phase center models for offsets and variations, so resulting in a mismatch between the constrained coordinates of the survey marker and the ZTD estimation at the antenna phase center. This issue will need to be addressed. Furthermore, the lack of receiver antenna phase center variation corrections in RT solutions is believed to be one of the reasons for the larger short-term variations (scatter) in their ZTD estimates. Although a bias in the ZTD can be overcome during their assimilation into NWP models, these short-term variations and variations in the standard deviation (SD) would clearly be undesirable. Even though the RT-II solution has a large bias and variability, it can be seen that among the two RT solutions, it is more sensitive to rapid changes and tracks ZTD variations similarly well as the NRT, PP and IGFT solutions.

In favour of the RT-II system using the PPP-Wizard is the fact that it is capable of resolving the integer ambiguities in RT PPP. In order to study the effect of integer ambiguity resolution on the ZTD estimates, another RT solution for the same stations and time period has been obtained after disabling the ambiguity resolution feature in the PPP-Wizard. Using the same RT products a mean difference of 0.39 ± 5.47 mm has been observed between the ambiguity float and

Table 4 Accuracy of the ZTD estimation systems relative to IGFT and their comparison to the user requirements for NWP nowcasting

System	Mean (mm)	SD (mm)	RMS (mm)	Difference from required target (mm)	Difference from required threshold (mm)	Remarks
PP	−0.86	4.44	5.19	−0.81	−24.81	Meets the target
NRT	−0.27	5.18	5.43	−0.57	−24.57	Meets the target
RT-I	8.60	27.97	30.42	24.42	−0.42	Meets the threshold
RT-II	60.40	37.26	47.81	41.81	17.81	Exceeds the threshold

ambiguity fixed solutions. Although this is a small effect, the RT-II fixed solution was improved over the float solution.

Considering the averaged RMS difference between each solution and the IGFT as a measure of its absolute accuracy, the achieved accuracies have been compared to the GNSS meteorology user requirements for NWP nowcasting as outlined in COST Action 716. As a result of this comparison, it was found that the PP and NRT systems meet the target requirements, RT-I system meets the threshold requirements whereas the RT-II system currently exceeds the threshold requirements.

4 Conclusions

The four ZTD and IWV estimation systems at the University of Luxembourg have been introduced and their relative accuracy has been assessed by comparing them to solutions from E-GVAP and the IGS Final Troposphere (IGFT) product. We showed that the near real-time (NRT) systems show good agreement at the few millimetre level with estimates from E-GVAP, and that the post-processing (PP) and NRT systems show a sub-millimetre level agreement to IGFT. The agreement of the real-time (RT) estimation systems RT-I and RT-II to IGFT is on the order of tens of millimeters. For RT-II this is a consequence of the fact that the PPP-Wizard currently does not allow the application of antenna up eccentricity (height) and receiver antenna phase center models of offsets and variations, a circumstance which will need to be addressed urgently. Nevertheless, using the PPP-Wizard the integer ambiguities can be resolved for RT PPP, which provided a slight improvement to the ambiguity-fixed solution of RT-II. Finally, when comparing these results to the GNSS meteorology user requirements for NWP nowcasting as outlined in COST Action 716, we can conclude that the PP and NRT systems meet the target requirements, RT-I system meets the threshold requirements whereas the RT-II system currently exceeds the threshold requirements.

Acknowledgements This project is funded by the Fonds National de la Recherche, Luxembourg (Reference No. 1090247) and travel has been supported through the COST Action ES1206. We are thankful to the editor and the three anonymous reviewers for their constructive reviews. We also thank the Administration du Cadastre et de la Topographie (SPSLux), Service Public de la Wallonie (Walcors), British Isles continuous GNSS Facility (BIGF), EUREF, and the IGS for GNSS data and products.

References

Bennitt G, Levick T (2011) The impact of assimilating zenith total delay measurements from ground-based GNSS receivers in the Met Office numerical weather prediction UK model. Geophys Res Abstr 13:EGU2011-6705

Bevis M, Businger S, Chiswell S, Herring TA, Anthes RA, Rocken C, Ware RH (1994) GPS meteorology: Mapping zenith wet delays onto precipitable water. J Appl Meteorol 33:379–386. doi:10.1175/1520-0450(1994)033<0379:GMMZWD>2.0.CO;2

Byram S, Hackman C, Slabinski V, Tracey J (2011) Computation of a high-precision GPS-based troposphere product by the USNO. In: Proceedings of the 24th International Technical Meeting of the Satellite Division of the Institute of Navigation ION GNSS 2011, pp 572–578

Byun SH, Bar-Sever YE (2009) A new type of troposphere zenith path delay product of the International GNSS Service. J Geodesy 83(3–4):1–7

Dach R (2013) Bernese GNSS Software: new features in version 5.2. Astronomical Institute, University of Bern, Bern

Dach R, Brockmann E, Schaer S, Beutler G, Meindl M, Prange L, Bock H, Jäggi A, Ostini L (2009) GNSS processing at CODE: status report. J Geodesy 83(3–4):353–365

Dach R, Hugentobler U, Fridez P, Meindl M (2007) Bernese GPS Software Version 5.0. Astronomical Institute, University of Bern, Bern

De Haan S (2011) Impact of GPS ZTD on rainfall estimates in an hourly update cycle of a numerical weather prediction model. Geophys Res Abstr 13:EGU2011-4222

Dow John M, Neilan RE, Rizos C (2009) The International GNSS Service in a changing landscape of Global Navigation Satellite Systems. J Geodesy 83(3–4), 191–198

Elgered G, Plag H-P, Marel H, Barlag S, Nash J (eds) (2005) Exploitation of ground-based GPS for operational numerical weather prediction and climate applications, EUR 21639, Luxembourg, 2005 [ISBN 92-898-0012-7]

Gutman S, Sahm SR, Benjamin SG, Schwartz BE, Holub KL, Stewart JQ, Smith TL (2004) Rapid retrieval and assimilation of ground based GPS precipitable water observations at the NOAA forecast systems laboratory: impact on weather forecasts. J Meteorol Soc Jpn Ser II 82(1B):351–360

Laurichesse D (2011) The CNES real-time PPP with undifferenced integer ambiguity resolution demonstrator. In: Proceedings of the 24th International Technical Meeting of The Satellite Division of the Institute of Navigation ION GNSS 2011, pp 654–662

Nilsson T, Elgered G (2008) Long-term trends in the atmospheric water vapor content estimated from ground-based GPS data. J Geophys Res 113(D19). doi:10.1029/2008JD010110

Offiler D (2010) Product requirements document version 1.0 - 21 December 2010. EIG EUMETNET GNSS Water Vapour Programme (E-GVAP-II)

Stende M (2006) Monitoring climate variability and change by means of GNSS data. In: Foelsche U, Kirchengast G, Steiner A (eds) Atmosphere and climate, pp 275–285. Springer, Berlin/Heidelberg. doi:10.1007/3-540-34121-8_23

Teke K, Böhm J, Nilsson T, Schuh H, Steigenberger P, Dach R, Heinkelmann R, Willis P, Haas R, Garca-Espada S, Hobiger T, Ichikawa R, Shimizu S (2011) Multi-technique comparison of troposphere zenith delays and gradients during CONT08. J Geodesy 85(7):395–413

Vedel H, Huang XY, Haase J, Ge M, Calais E (2004) Impact of GPS zenith tropospheric delay data on precipitation forecasts in Mediterranean France and Spain. Geophys Res Lett 31(2). doi:10.1029/2003GL017715

Weber G, Mervart L (2012) BKG Ntrip Client (BNC) Version 2.7 Manual. Federal Agency for Cartography and Geodesy, Frankfurt, Germany

Zumberge JF, Heflin MB, Jefferson DC, Watkins MM, Webb FH (1997) Precise point positioning for the efficient and robust analysis of GPS data from large networks. J Geophys Res 102(B3):5005–5017. doi:10.1029/96JB03860

GOP-TropDB Developments for Tropospheric Product Evaluation and Monitoring: Design, Functionality and Initial Results

Gabriel Gyori and Jan Dousa

Abstract

The high-performance PostgreSQL database (GOP-TropDB) capable to deal with billions of data records has been developed at the Geodetic Observatory Pecný (GOP) for monitoring tropospheric parameters from various sources – space geodetic techniques (GNSS, VLBI, DORIS), observations (radio sounding, water vapour radiometers, in-situ measurements) and meteorological products from numerical weather models. This paper describes initial motivations and functionalities, basic database structure supporting various data sources and optimization for huge data sets. Initial database exploitations and outputs are demonstrated together with discussion on foreseen developments. Recently, we targeted implementations in support of a routine intra-technique tropospheric product evaluation and monitoring within the Tropospheric working group of the International GNSS Service (IGS). The inter-technique comparisons with tropospheric products available from the International DORIS Service and the International VLBI Service for Geodesy and Astrometry of the International Association of Geodesy were implemented too.

Keywords

DORIS • GNSS • Numerical weather model • Radiosonde • Troposphere • VLBI • Zenith path delays

1 Introduction

Since 2000, the Geodetic Observatory Pecný (GOP) analysis centre has contributed with near real-time tropospheric estimation to various projects – COST Action 716 (1999–2004), TOUGH (2003–2006), E-GVAP I–III (2006–2016) and, recently, GNSS4SWEC (COST ES1206, 2013–2017). For the period of 1996–2012, GOP also provided a homogeneous re-analysis of data from the Global Navigation Satellite System (GNSS) permanent network of the International Association of Geodesy Reference Frame Sub-Commission for Europe (EUREF). Homogeneous tropospheric parameters are then suitable for a regional climate study. A regular long-term evaluation of tropospheric parameters is an indispensable task for the assessment of all applied models (tropospheric as well as others), processing strategies (near real-time, etc.) and thus giving an important feedback for further improvements.

Initially, comparisons of GOP tropospheric products – zenith total delays (ZTD) from GNSS permanent stations – were done using scripts for data stored in a plain text format. Along with expanding period (more than 1–2 years) and number of stations (more than a few tens), original design was replaced by a simple and easy-to-use database system driven by the MySQL server. This system was in use for the monitoring of all GOP near real-time and post-processing operational tropospheric products during 2002–2010 as well as for other specific studies (Dousa 2003).

Recently, we initiated developing the third generation database system, which is enhanced in many aspects – driven

G. Gyori • J. Dousa (✉)
Research Institute of Geodesy, Topography and Cartography, Geodetic Observatory Pecny, Ústecká 98, 25066 Zdiby, Czech Republic
e-mail: jan.dousa@pecny.cz

© Springer International Publishing Switzerland 2015

C. Rizos, P. Willis (eds.), *IAG 150 Years*, International Association of Geodesy Symposia 143,
DOI 10.1007/1345_2015_193

by the powerful PostgreSQL database server (a free alternative to the enterprise solutions), flexible internal structure, fully automated comparisons, various data sources, huge data sets, auxiliary data for calculating corrections, parameter conversions, interpolations and many others. A flexible structure was requested for a fully automated tropospheric data comparisons (both intra- and inter-technique) including the searching of near points, data filtering, converting, interpolating, statistics and various extractions.

The database is referred to as GOP-TropDB herein. This paper describes the motivation for the database design and functionalities, basic data structure, data import and data preprocessing, comparison procedure including tropospheric ties, performance optimization and initial results from comparisons. The final section gives conclusion and outlook for future developments.

2 Aimed Applications and Functionalities

Motivations for the development of new and powerful GOP-TropDB consist in various applications:

1. intra-technique tropospheric parameter comparisons for the assessment of (a) (near) real-time processing strategy (GNSS), (b) new models applied in reprocessing (GNSS, VLBI, DORIS), (c) consistency among individual satellite constellation results (GNSS), (d) assessment of different parametrizations (ZTDs, tropospheric gradients),
2. inter-technique comparisons for evaluating quality of individual observations (space geodetic techniques, radio sounding, radiometers, numerical weather fields),
3. preservation of historical tropospheric products including the quality control with record flagging and a unique access to the data inventory and data extractions
4. feedback to data and product providers by monitoring the quality of new models and strategies, evaluating individual tropospheric products (GNSS, DORIS, VLBI), facilitates parameter corrections and conversions, monitoring radiosonde data, in-situ meteorological data etc.

All these applications operated in an automated mode requires the following functionalities of GOP-TropDB:

- accommodate different tropospheric data types,
- preserve meta data (position, instrumentation etc.),
- identify collocating points in a specified distance or area,
- compare various types of tropospheric data or products,
- estimate vertical corrections supported with auxiliary data,
- generate comparison differences and statistics,
- provide parameter conversion supported with auxiliary data, e.g. ZTD to integrated water vapour,
- interpolate grid data to a requested position and time,
- data quality checking and individual record flagging,
- extract specific data time series for a climate study (long-term trend estimates, temporal/spatial variations, etc.),
- web-based interface for user-friendly database inventory.

The last three functions have not been implemented yet and they will be completed in future in a close co-operation with the coordinator of the IGS Tropospheric working group.

The structure of the data organization in GOP-TropDB is one of the most important aspect defining database performance and flexibility for future extensions. For this reason, we paid particular attention to design the database structure in support of all the functionalities aforementioned. It includes efficient data representation in database tables and columns, readiness to steadily increasing data volume (e.g. new products, accumulation in time), data sorting for optimal and fast data access, duplicity data handling (e.g. identification of unique points, re-writing policy) and others. The GOP-TropDB structure is described in brief in next section.

3 Data Structure

The GOP-TropDB is designed as a relational database driven by the PostgreSQL server. The database accommodates different tropospheric and meteorological data types from space geodetic techniques (GNSS, VLBI, DORIS), direct observations (e.g. radiosondes, radiometers, in-situ or synoptic meteorological data) and other products (e.g. NWM extracted 2D horizontal grids). The GOP-TropDB supports additional auxiliary data sets – Earth Gravitational Model 2008 (Pavlis et al. 2012), ETOPO1 Global Relief Model (Amante and Eakins 2009), ERA-Interim global reanalysis (Dee et al. 2011) and Global Pressure and Temperature model – GPT2 (Lagler et al. 2013) and, optionally, others in future.

Specific database tables are defined for different data types containing different data columns, see Table 1. The same data types from different sources are stored within a single table distinguished by source identification only. The source is unique for each point and represents a specific solution, e.g. from EUREF, IGS, individual analysis etc. Since the GNSS data table is expected to be the largest one, we distinguished two tables using the same structure – *tGNSS* and *tUSER*. The former is designed to store final GNSS products for a wide community interests such as inter-technique comparisons, climate studies, reference tropospheric values for assessments of individual or specific tropospheric estimates. The latter represents GNSS solutions for evaluation of new models and strategies for near real-time processing, multi-GNSS constellations, tropospheric horizontal gradients or other individual user solutions.

Data tables are organized in a common scheme using epoch-wise records which differ in data columns only, see Table 1. The first column is usually the epoch represented

Table 1 Database tables for various data types (P – pressure; T – temperature; E – partial water vapour pressure; β, λ and γ – fitted parameters for vertical approximations of T, E and ZWD, respectively; H_g – orthometric grid height; H – precise station height at data epoch; N – geoid undulation; O – Orography; N-GRD and E-GRD – North and East horizontal tropospheric gradients, respectively; IWV – integrated water vapour)

Product/Data	DB table	Data columns
PointType	tPointType	Accuracy of horizontal and vertical position, Type description, Point group, Site/Grid identificaton
Instrument	tInstrument	EPOCH, Antenna, Receiver, N-eccentricity, E-eccentricity, U-eccentricity
Source	tSource	Source name, Source description
Point	tPoint	Name, Latitude, Longitude, Height, *Orography*, *Undulation*, <Source>, <PointType>, <Instrument>
GNSS	tGNSS	EPOCH,<Point>,ZTD,rms(ZTD),ZWD,N-GRD,rms(N-GRD),E-GRD,rms(E-GRD),H,*P*,*T*,β,γ,*IWV*,Flag
USER (GNSS)	tUSER	EPOCH,<Point>,ZTD,rms(ZTD),ZWD,N-GRD,rms(N-GRD),E-GRD,rms(E-GRD),H,*P*,*T*,β,γ,*IWV*,Flag
VLBI	tVLBI	EPOCH,<Point>,ZTD,rms(ZTD),ZWD,N-GRD,rms(N-GRD),E-GRD,rms(E-GRD),H,*P*,*T*,β,γ,*IWV*,Flag
DORIS	tDORIS	EPOCH,<Point>,ZTD,rms(ZTD),ZWD,N-GRD,rms(N-GRD),E-GRD,rms(E-GRD),H,*P*,*T*,β,γ,*IWV*,Flag
WVR	tWVR	EPOCH,<Point>,P,T,E,ZTD,ZWD,Flag
Meteo data	tMETEO	EPOCH,<Point>,P,T,E,Flag
Radiosondes	tRAOBS	EPOCH,<Point>,P,T,E,ZTD,ZWD,β,rms(β),λ,rms(λ),γ,rms(γ),Flag
NWM	tNWM	EPOCH,<Point>,P,T,E,ZTD,ZWD,β,rms(β),λ,rms(λ),γ,rms(γ),Flag
GPT2	tGPT2	<Point>, P, E, T, dT, N, H_g
EGM2008	tGEOID	<Point>, N
ETOPO1	tRELIEF	<Point>, O

Data columns not available from original sources and completed by interpolating auxiliary data, such as EGM2008, ETOPO1, GPT2, NWM, are marked in italics. Finally, <> represents reference to another table, e.g. <Point> refers to a line in table tPoint

with the PostgreSQL data type 'TIMESTAMP WITHOUT TIMEZONE'. The second column provides a reference to a *tPoint* table record, which stores unique information for each site's geo-references (latitude, longitude, height, orography, geoid undulation and point type), information about data source (identification name) and information about site and its instrumentation (site name, full description, antenna, receiver, eccentricities to the reference point). All data columns are table-specific represented by numerical values. Additionally, tables include a flag column for recording results of assessments which can be used in the record exclusions from future comparisons, extractions etc. The flags are not filled during the data import, but they could be updated applying additional quality checking procedures planned in future developments. Such flags could provide e.g. feedback to data providers, product extractions for other user comparisons, long-term trend studies and others. Every record in the *tPoint* table is uniquely identified by its name, source and position (latitude, longitude, height) taking into account horizontal and vertical accuracy specified in point types definition.

Any comparison strongly depends on the level of standardization used for individual data provision (e.g. processing models, parametrization). Usually, we distinguish two sources for data – operational and reanalysis. While the first is considered as evolving in time in terms of the configuration, models and methods, the latter is expected to be methodically homogeneous in time. The source description (*tSource*) is then ready to include any specific information about the source as provided in a documentation from the producer. The individual site instrumentations in any product is also kept in *tPoint* table records using references to *tInstrument* table records.

Some data variables are not available for certain products, e.g. meteorological data for GNSS products, geoid undulation, orography and others marked in italics in Table 1. Relevant columns are completed in a homogeneous way using auxiliary datasets as described above. When meteorological data are completed by bilinear interpolation in space and by linear interpolation in time from the ERA-Interim model, the integrated water vapour is calculated and filled simultaneously to keep the consistency with all parameters.

The following data tables and data types are currently supported in the GOP-TropDB – *tGNSS*, *tUSER*, *tVLBI*, *tDORIS*, *tRAOBS*, *tWVR*, *tNWM*, *tMETEO* and tables with auxiliary data like *tGEOID*, *tRELIEF* and *tGPT*, see Table 1. Additional data tables can be implemented in future, e.g. for slant tropospheric delays. More details about design and structure were also given in Dousa and Gyori (2013).

4 Data Import and Data Pre-processing

Data import to the database is done in three steps:

1. downloading and archiving data from variety of sources in original formats (usually compressed),
2. decoding and converting original data and preparing SQL insert command via specific database stored procedures,
3. executing SQL command in the PostgreSQL server.

Data are downloaded using Linux *cron* daemon which calls *rsync* and *wget* standard programs. Extraction, Transform and Load (ETL) procedures were implemented for data

Table 2 List of existing extract/transform/load (ETL) tools for data extracting, transforming and loading into the database

ETL procedure	Input format	Procedure	Remarks
tro-snx-gnss2DB.pl	GNSS Tropo-SINEX	fInsertGNSS	ZTDs, IGS/EUREF products
tro-snx-vlbi2DB.pl	VLBI Tropo-SINEX	fInsertVLBI	ZTDs, VLBI products
tro-snx-doris2DB.pl	DORIS Tropo-SINEX	fInsertDORIS	ZTDs, DORIS products
bsw-trp2DB.pl	Bernese TRP	fInsertGNSS	ZTDs, GOP products
cost-trp2DB.pl	COST-716	fInsertGNSS	ZTDs, E-GVAP
rt-flt2DB.pl	Tefnut output	fInsertGNSS	ZTDs, GOP real-time analysis
met-rnx2DB.pl	Meteo RINEX	fInsertMETEO	in-situ meteo data (GNSS)
cost-met2DB.pl	COST meteo data	fInsertMETEO	COST-716 meteorological data (synoptic sites)
raobs2DB.pl	BADC profiles	fInsertRAOBS	pre-processed data, radiosondes
wvr2DB.pl	Radiometrics	fInsertWVR	pre-processed data, radiometers
nwm2DB.pl	NWM data (GRIB)	fInsertNWM	pre-processed data, numerical weather models
gpt2DB.pl	GPT2 model	fInsertGPT	Global Pressure and Temperature model (grid)
geoid2DB.pl	EGM2008	fInsertGEOID	Global Geoid model (grid)
relief2DB.pl	ETOPO1	fInsertRELIEF	Global Relief model (grid)

decoding from various formats and different sources, see Table 2. Sources providing vertical profiles, such as radiosondes or numerical weather models, are processed according to Vedel et al. (2001) prior to their loading into the database. The processing consists of extracting surface values (meteorological data), calculating values integrated from the full profile (zenith wet delays, integrated water vapour) and fitting vertical approximation parameters. The data decoding and database filling is started regularly from the Linux *cron* scheduler.

The GOP-TropDB stored procedures for data loading utilize standard INSERT and UPDATE queries of the Structure Query Language (SQL). While the first command is used for a new inclusion, the second is applied for an update of existing records.

5 Comparison Procedure

Historically, the most important functionality of the GOP-TropDB was the comparison of various tropospheric data sets. The procedure currently implemented consists of the sequence of the following steps

- comparison configuration (manual),
- searching collocation points (pair definition),
- generation of data differences for selected pairs,
- statistics over differences for selected pairs,
- extraction and visualization.

The configuration is prepared in a specific database table *tPairConf* and via function arguments. Both includes the selection of data column to be compared (e.g. ZTD, ZHD, ZWD, IWV, tropospheric gradients, pressure, temperature), data sources and, optionally, site mask. Additional settings consists of the criteria defined for the searching of collocation points (vertical and horizontal distance), maximum sigma for data filtering and limits of the confidence interval applied for detecting outliers in differences. Pairs generated in the second step are stored in a specific table (*tPair*) as well as data differences (*tDiff*) calculated in the third step.

Data are represented in a different sampling rate and, generally, values do not refer to the same epochs. We thus apply a comparison resolution interval for calculating a mean over all values for a given data source. The interval is set to 60 min by default, but the resolution could be changed in the settings according to input product characteristics. Set up between 10 and 60 min is usually reasonable. The default value of 60 min is the trade-off between standard GNSS data product sampling rate and the temporal variability of tropospheric parameters. In future, the procedure can be easily enhanced by a functional fitting over values in a comparison interval rather than a simple averaging.

Vertical corrections are applied before calculating differences independently for the pressure, ZHD and ZWD. The first two are the same as described in Teke et al. (2013). A ZWD vertical correction is, however, calculated using the new pressure- or height-dependent formula developed at GOP and based on the reference ZWD value and its exponential decay parameter γ [–] (typically close to 2.5) defined by

$$\frac{ZWD}{ZWD_0} = \left(\frac{P}{P_0}\right)^{\gamma+1} \tag{1}$$

where index 0 represents a reference value and P, P_0 is pressure in Pa. The vertical ZWD correction is derived as

$$\begin{aligned} \Delta ZWD &= ZWD_0 \left[\left(\frac{P}{P_0}\right)^{\gamma+1} - 1\right] \\ &= ZWD_0 \left[\left(1 - \frac{\beta(h-h_0)}{T_0}\right)^{\frac{(\gamma+1)g_0}{R_d\beta}} - 1\right]. \end{aligned} \tag{2}$$

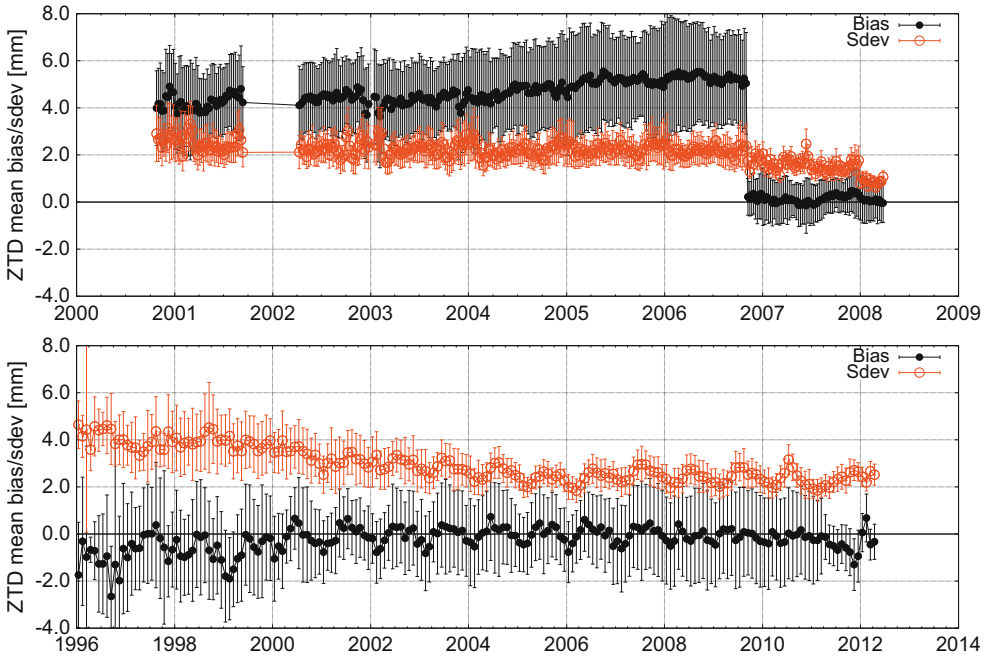

Fig. 1 Time series of mean biases and standard deviations calculated from all common stations between IGS original and IGS repro1 tropospheric products (*top*) and EUREF and IGS repro1 products (*bottom*)

where h, h_0 is height in meters, T_0 and β is temperature and its lapse rate in K and $\mathrm{K \cdot m^{-1}}$, respectively, $R_d = 287.058\,\mathrm{J \cdot kg^{-1} \cdot K^{-1}}$ is gas constant for dry air and $g_0 = 9.80665\,\mathrm{m \cdot s^{-2}}$ is standard gravity acceleration.

The procedure uses statistics over the specified pair differences via iterative estimates of systematic error, standard deviation and root mean square for each pair and interval individually. The outliers are rejected according to the configuration criteria (limits of confidence interval) using actually estimated mean and standard deviation. The statistics are thus provided applying an iterative approach within the statistical function. Five statistic modes are supported for the requested interval – all, yearly, monthly, weekly and hourly. The first calculates total statistics over specified period, while the last provides statistics on a hourly basis (i.e. data filtered by hour of day). Other modes calculate statistics individually for a sequence of specified intervals within requested period.

Since all differences are saved in a specific table, statistic modes can be repeated efficiently on a regular basis for generating long-time series as demonstrated in Fig. 1. The extractions, visualizations and interpretation of statistic results are the final step of the procedure for which initial examples are given in Sect. 7.

6 Database Optimization

The GOP-TropDB is currently running on a dedicated server with the GNU Linux operating system Debian 6.0.7, reserved 12GB memory and 8-thread 64-bit Intel(R) Xeon(R) CPU. Recently, the database achieved more than a billion of records (majority from GNSS sources). This amount of data already caused the lack of performance in executing some SQL queries. Along with optimizing the implementation of database stored procedures, we devoted particular effort in optimizing the database via assessing the impact of the following aspects

- PostgreSQL server configuration
- PostgreSQL release version
- file system for data storage
- data table partitioning

Table 3 displays the definition of testing clusters in which modifications were applied sequentially. Achieved performance was tested in two high-demanding operations – data import and data difference calculations. Three changes are interesting to discuss – the PostgreSQL configuration tuning up, table partitioning and interval for comparisons. The first change increased the performance by a factor of 2–4, in particular for all time-consuming procedures (e.g. inserting)

Table 3 Variant of GOP-TropDB optimization and resulting performance in data import (Import) and difference calculation (Diff)

File	Partitions		PostgreSQL		Compare	Import	Diff
sys	data	diff	vers	conf	interval (min)	(s)	(s)
ext3	–	–	8.4	–	60	4712	835
ext4	–	–	8.4	–	60	5050	864
ext4	–	–	8.4	yes	60	1348	660
ext4	year	–	8.4	yes	60	1663	1033
ext4	year	year	8.4	yes	60	1653	1079
ext4	year	year	8.4	yes	10	1637	7563
ext4	year	year	9.2	–	60	5759	1228
ext4	year	year	9.2	yes	60	1739	1207

Table 4 Statistics from the partitioning test via applying ANALYZE function for repeated SQL commands

Repeat run	Station	Source	Exec time partitions (ms)	Exec time single table (ms)
1st	GOPE	EUREF-repro1	1363	1300
2nd	GOPE	EUREF-repro1	13	48
3rd	GOPE	EUREF-repro1	13	48
1st	ALBH	IGS-repro1	47	125,576
2nd	ALBH	IGS-repro1	0.1	4422
3rd	ALBH	IGS-repro1	0.1	4422

if dedicated hardware features were exploited adequately. The second change showed slightly worse performance in terms of data insertion procedure since the table partitioning itself needs additional overheads.

The partitioning can be understood as a physical splitting of any large table into several child tables for keeping size-limited volumes of data (e.g. several millions of records for each child table) and still supporting all operations on them virtually aggregated in the parent table. The implementation is taking advantage of inherited features of parent tables by all child tables. All operations could be, however, performed on parent table virtualizing a common access. The partitioning was implemented on a yearly basis for all large datasets including data differences. The performance should not degrade with a significant growth of data volume in time. The third change showed that the processing time increased linearly for generation of differences when the comparison interval was shortened (six times longer run for 10 min resolution of comparison against 60 min).

Table 4 demonstrates a query repeated for an extraction of a single station tropospheric parameter time series from two sources – EUREF and IGS, where the second has more records by a factor of about 12. While any initial query is very time-consuming, the query repeated in a short time is much faster due to the PostgreSQL caching capability which strongly depends on memory reserved. A significant difference can be also observed by applying a query on a single table or a partitioned table for every year.

The current optimization using the table partitioning was aimed primarily for the growing data volume in time. With adding more products (e.g. individual GNSS analysis centre solutions, other numerical weather models) will also cause a huge growth of data, however, it will not be necessary to store all of them within a single database. The effort can be effectively distributed for specific focuses at individual database instances. Considering that the source code can be redistributed, all tasks can be handled consistently and selected datasets can be also replicated between database instances in future if necessary. The optimization was described in detail also in Dousa and Gyori (2013).

7 Examples of GOP-TropDB Use

In order to demonstrate the initial database functionality, we show several examples of routine evaluations for intra-technique (GNSS) and inter-technique comparisons of the tropospheric products. The following datasets were loaded into the database and used for the comparisons:

- International GNSS Service (IGS) operational (Byram et al. 2011) and reprocessed (Repro1) tropospheric products (Byun and Bar-Sever 2009),
- EUREF GPS combined tropospheric results based on reprocessed (Repro1) European GNSS network (Soehne et al. 2009),
- GOP DORIS tropospheric estimates (Stepanek et al. 2010),
- Radiosonde profiles from the UK Met Office database accessed via the British Atmospheric Data Centre (UK MetOffice Global Radiosonde Data 2006),

We will focus on individual dataset comparison and result interpretation in future. Now we aim at showing a usefulness of various GOP-TropDB outputs and functionalities using a few selected cases only.

Figure 1 displays time series of long-term comparisons calculated over all common station pairs. The top plot shows the original IGS final tropospheric product compared on a weekly basis with the first IGS homogeneously reprocessed product using all IGS stations (more than 250). This plot clearly shows a jump in the ZTD bias on 5 November 2006 which is due to the change in the GNSS antenna phase centre variation model in the IGS operational solution. The bottom plot shows a monthly comparison of IGS and EUREF Repro1 products all common European stations (approximately 90 over the while period). Similarly, new IGS and EUREF reprocessing (Repro2) solutions expected to be available in 2014 will be assessed in all statistical modes using all common stations.

Results of the statistical function are visualized in various ways – using histograms, time series or geographical plots. We applied database functionality for the evaluation of various GOP tropospheric products (near real-time, real-time, multi-GNSS constellation, global hourly) in a long-term study which is in detail described in Dousa and Vaclavovic (2013). Such comparisons provide important feedbacks on the quality of different strategy implementations and models applied. For example, we identified a systematic error between GPS and GLONASS (Dousa 2012) which was later described as the effect of inconsistent satellite antenna offsets for both systems (Dilssner et al. 2009).

In a similar way, through the comparison of ZTDs from the DORIS solution by GOP and the IGS final product, the effect of the South Atlantic Anomaly (SAA) on theSPOT-5

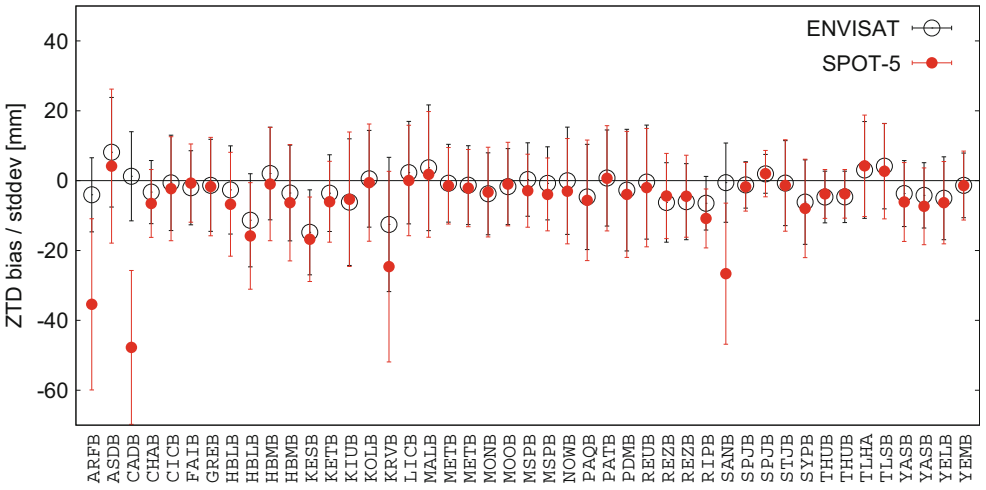

Fig. 2 Zenith total delay comparison in 2006–2008 between DORIS (Envisat, SPOT-5) and IGS GNSS estimates revealed large differences for SPOT-5 satellite at four stations in South America (AFRB, CADB, KRVB and SANB). Based on this comparison the SAA effect on SPOT-5 observations was first recognized

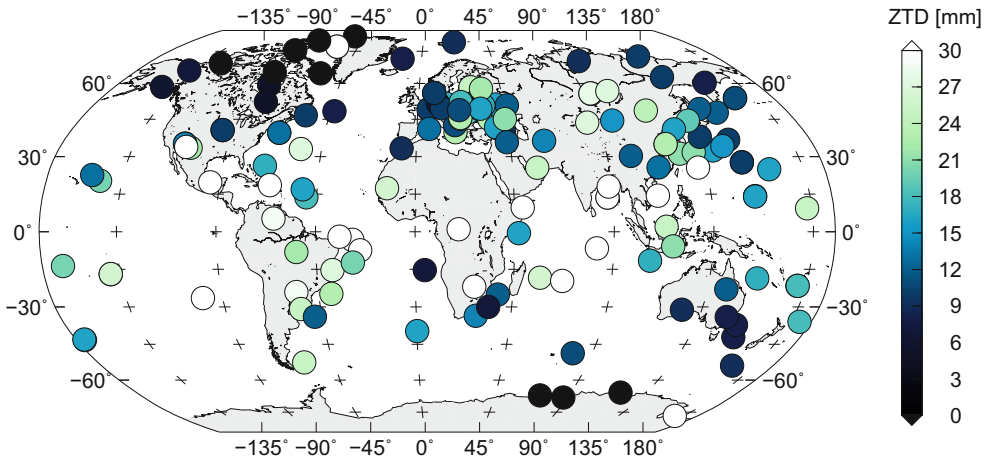

Fig. 3 Geographical representation of ZTD standard deviations from comparison of IGS reprocessing and global radiosonde dataset from UK Met Office (via BADC)

satellite oscillator was identified (Stepanek et al. 2010; Bock et al. 2010) and, later on, also successfully modelled (Stepanek et al. 2013). The effect revealed as large ZTD biases at four DORIS stations in South America for the SPOT-5 satellite – AFRB, CADB, KRVB and SANB in the period of 2006–2008, see Fig. 2. Such inter-technique comparison necessarily applied tropospheric corrections from a vertical difference between collocated station pairs.

Another inter-technique comparison is represented by GNSS ZTD estimates and ZTD values integrated from radiosonde observations. Some previous studies already revealed radiosonde humidity biases, e.g. Wang and Zhang (2008) and Bock and Nuret (2009), which are of high importance for any meteorology and climatology applications. Our procedure includes radiosonde data quality checking and profile processing, applying height corrections due to geoid undulations and ZHD and ZWD corrections due to vertical differences between radiosondes and GNSS stations. Geographical visualisation of standard deviations from such comparisons is showed in Fig. 3. The latitudinal dependence is mainly due to a significantly larger amount of water vapour within the tropical belt.

8 Summary and Outlook

The principal development of GOP-TropDB for the purpose of tropospheric data and products preservation, monitoring and evaluation was completed. Achieved functionality was demonstrated in several examples of inter-/intra-technique comparisons. The database is ready to perform similar inter-technique assessments as previously provided in Teke et al. (2013), but in a fully automated way. In particular, such operational comparisons will be exploited for evaluating large datasets from GNSS analyses (counting billions of records) – reprocessing campaigns (1996–2013), near real-time tropospheric estimates in support of numerical weather predictions and others. Current development is coordinated within the Tropospheric working group of the International GNSS Service, which includes inter-technique comparison with similar products from the International DORIS Service and International VLBI Service for Geodesy and Astrometry of the International Association of Geodesy.

The database is, however, expected to be a useful tool for data archiving for a long-term trend study (climatology)

supported with internal quality checking (data flagging), parameter conversions (ZTD to ZWD, ZWD to integrated water vapour, etc.), additional product comparisons (tropospheric gradients, slant delays) and inventory and dissemination functions (extraction of specific site tropospheric time series over a long period, etc.). The individual product quality checking for all the stations, i.e. independently of any reference product, is important in order to serve climatological community. Such procedure can be based on formal errors evaluation, discontinuities detections, outliers detection based on temporal correlation study or others. The ZTD to ZWD conversion is currently expected to be provided homogeneously using data from the ERA-Interim numerical weather model.

The database is considered to be linked to the internet with different access scenarios. These will be implemented in a close co-operation in the IGS Tropospheric Working Group and the GNSS4SWEC project in Europe. Considered scenarios are (a) a public view over static outputs of intra- and inter-technique comparisons, (b) a limited or restricted access to an active database inventory functions and selected data set queries, (c) database replication or partial data sharing with partners within the projects mentioned above.

Acknowledgements The principal database development was supported by the Czech Science Foundation (No. P209/12/2207). The work related to the use for climatology are being developed for the COST ES1206 project which is supported by national project GNSS4SWEC-CZ (LD14102). The contribution to the International GNSS Service (IGS) Tropospheric Working Group (WG) is being supported with Czech Ministry of Education, Youth and Sports (LH14089). In this context we thank Dr Christine Hackman from the United States Naval Observatory for coordinating the IGS TropoWG and all fruitful discussions related to the developments. We thank three anonymous reviewers and editors for all comments that improved the paper. Finally, we are thankful to all data and product providers used in the GOP database and referenced in the text.

References

Amante C, Eakins B (2009) ETOPO1 1 arc-minute global relief model: procedures, data sources and analysis. Tech. rep., NOAA

Bock O, Nuret M (2009) Verification of radiosonde humidity data and NWP model analyses and forecasts during AMMA with GPS precipitable water estimates. Weather Forecast 24:1085–1101

Bock O, Willis P, Lacarra M, Bosser P (2010) An inter-comparison of zenith tropospheric delays derived from DORIS and GPS data. Adv Space Res 46(12):1648–1660

Byram S, Hackman C, Tracey J (2011) Computation of a high-precision GPS-based troposphere product by the USNO. In: ION GNSS Proceedings

Byun S, Bar-Sever Y (2009) A new type of troposphere zenith path delay product of the international GNSS service. J Geod 83(3–4):367–373

Dee DP et al (2011) The ERA-interim reanalysis: configuration and performance of the data assimilation system. Q R Meteorol Soc 137(656):553–597

Dilssner F, Springer T, Flohrer C, Dow J (2009) Estimation of phase centre corrections for GLONASS-M satellite antennas. J Geod 84:467–480

Dousa J (2003) Evaluation of tropospheric parameters estimated in various routine analyses. Phys Chem Earth 29(2–3):167–175

Dousa J (2012) Developments of the GLONASS ultra-rapid orbit determination at Geodetic Observatory Pecny. In: Kenyon S, Pacino M, Marti U (eds) Geodesy of Planet Earth, IAG Symposia Series, vol 136. Springer, New York, pp 1029–1036

Dousa J, Gyori G (2013) Database for tropospheric product evaluation - implementation aspects. FCE Geoinformatics 10:27–40

Dousa J, Vaclavovic P (2013) Long-term evaluation of new ground-based GNSS tropospheric products. In: Rizos WC (ed) IAG Symposia Series. Springer (this volume)

Lagler K, Schindelegger M, Boehm J, Krasna H, Nilsson T (2013) GPT2: empirical slant delay model for radio space geodetic techniques. Geophys Res Lett 40:1069–1073

Pavlis N, Holmes S, Kenyon S, Factor J (2012) The development and evaluation of the Earth Gravitational Model 2008 (EGM2008). J Geophys Res: Solid Earth 117(B4):406

Soehne W, Figurski M, Szafranek K (2009) Homogeneous Zenith total delay parameter estimation from European permanent GNSS sites. In: Presented at EUREF 2009 symposium, Florence, May 27–30

Stepanek P, Dousa J, Filler V, Hugentobler U (2010) DORIS data analysis at Geodetic Observatory Pecny using single-satellite and multi-satellite geodetic solutions. In: Willis P (ed) DORIS special issue: precise orbit determination and applications to the earth sciences. Adv Space Res 46(12):1578–1592

Stepanek P, Dousa J, Filler V (2013) SPOT-5 DORIS oscillator instability due to South Atlantic Anomaly: mapping the effect and application of data corrective model. Adv Space Res 52:1355–1365

Teke K, Nilsson T, Boehm J, Hobiger T, Steigenberger P, García-Espada S, Haas R, Willis P (2013) Troposphere delays from space geodetic techniques, water vapour radiometers, and numerical weather models over a series of continuous VLBI campaigns. J Geod 87:981–1001

UK Meterorological Office (2006) Global Radiosonde Data, NCAS British Atmospheric Data Centre

Vedel H, Mogensen KS, Huang XY (2001) Calculation of zenith delays from meteorological data, comparison of NWP models, radiosonde and GPS delays. Chem Phys Earth Part A 26(6–8):497–502

Wang J, Zhang L (2008) Systematic errors in global radiosonde precipitable water data from comparisons with ground-based GPS measurements. J Climate 21:2218–2238

BCAL/UFPR: The GNSS Antenna Calibration Service of Latin America

S.C. Movio Huinca, C. Pereira Krueger, B. Heck, M. Mayer, and A. Knöpfler

Abstract

The usage of individual calibration values for GNSS (Global Navigation Satellite Systems) antennas is of fundamental importance for state-of-the-art GNSS positioning at millimeter accuracy level, especially concerning precise height determination. In Brazil, the awareness of the user community regarding this important error source has to be sharpened. In contrast to Europe, where manifold research is carried out focusing on antenna calibration and different agencies provide calibration services, in Latin America the users have to be sensitized with respect to receiver antenna handling. Therefore, the first Latin American GNSS antenna calibration basis BCAL/UFPR (Baseline Calibration Station for GNSS Antennas at UFPR) was established at the Federal University of Paraná (UFPR; Curitiba, Paraná, Brazil) in close cooperation with the Geodetic Institute of the Karlsruhe Institute of Technology (Karlsruhe, Germany). The BCAL/UFPR is actually equipped with three pillars and enables the determination of antenna parameters applying the relative field calibration approach. The antenna modeling parameters are derived at absolute level, because the reference antenna (3D choke ring antenna type) was calibrated absolutely by Geo++ (Garbsen, Germany). In this context, five antennas of the same model (Trimble Zephyr GNSS Geodetic II) were calibrated at BCAL/UFPR. The goal of the case study is to verify the difference between individual parameters determined at BCAL/UFPR and mean parameters published by the NGS (National Geodetic Service, USA). This article presents information related to BCAL/UFPR and discusses the results of recent calibration investigations.

Keywords

BCAL/UFPR • GNSS • NGS • Relative antenna calibration • Site-specific effects

1 Introduction

To meet the increased demands of the GNSS community related to both absolute and relative highly accurate point positioning, the highly precise individual antenna models were shoved into the center of attention. PCO (phase center offset) and PCV (phase center variations) define the electrical phase center of the antenna depending on the direction and

S.C.M. Huinca (✉)
Department of Rural Engineering, FAEM/UFPel Federal University of Pelotas, Pelotas, Rio Grande do Sul, Brazil
e-mail: suelen.huinca@gmail.com

C.P. Krueger
Department of Geomatics, Federal University of Paraná, Centro Politécnico, CP 19.001, CEP 81531-990 Curitiba, Paraná, Brazil
e-mail: ckrueger@ufpr.br

B. Heck • M. Mayer • A. Knöpfler
Geodetic Institute, Karlsruhe Institute of Technology (KIT), Englerstraße 7, D-76131 Karlsruhe, Germany
e-mail: bernhard.heck@kit.edu; michael.mayer@kit.edu; andreas.knoepfler@kit.edu

© Springer International Publishing Switzerland 2015

C. Rizos, P. Willis (eds.), *IAG 150 Years*, International Association of Geodesy Symposia 143,
DOI 10.1007/1345_2015_21

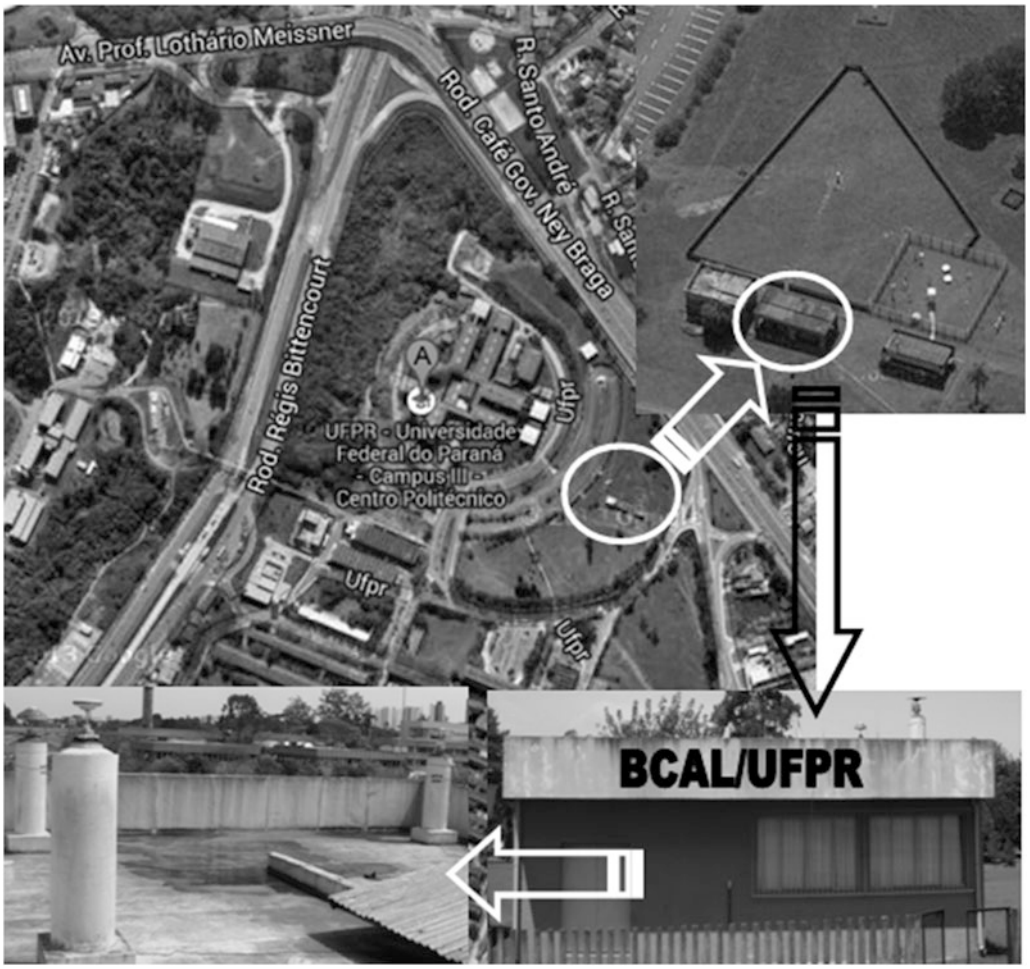

Fig. 1 Location at BCAL/UFPR

the frequency of the signal. The PCO is a 3d displacement vector between the frequency dependent average phase center and the antenna reference point. PCV are additional direction-dependent correction values and have to be taken into account at the observation level. It is well-known, that within highest-precision GNSS positioning antennas have to be treated and calibrated individually. Within the fundamental study of Schupler and Clark (1991) it was proven that GPS (Global Positioning System) antennas have different electronic properties, even if they are physically similar.

In Europe manifold research is carried out focusing on antenna calibration and different agencies provide calibration services. In contrast, the Latin American GNSS community has to be sensitized with respect to correct receiver antenna handling within GNSS data processing. Therefore, the first GNSS antenna calibration basis in Latin America was established in Brazil at the Federal University of Paraná (UFPR; Curitiba, Paraná) in close cooperation with the Geodetic Institute of the Karlsruhe Institute of Technology (GIK, Karlsruhe, Germany). This calibration basis is named BCAL/UFPR and makes use of the relative field calibration method (Huinca et al. 2012; Kouba 2009).

This paper will present information related to BCAL/UFPR and discuss the results of recent calibration investigations which document the importance of the correct modeling of GNSS receiver antennas within highly precise GNSS applications. Therefore, differences between individual antenna calibration values determined for five Trimble Zephyr GNSS Geodetic II antennas at BCAL/UFPR and with respect to parameters published by the National Geodetic Survey (NGS) are analyzed.

2 BCAL/UFPR

The BCAL/UFPR was established at the Centro Politécnico on the campus of Paraná Federal University in the city of Curitiba, on the rooftop of the astronomical observatory (Fig. 1) at the annex auditory alongside the LAGEH (Spatial Geodesy and Hydrography Laboratory). This location was chosen with respect to logistic aspects

(e.g., power supply, security) and expected signal quality (e.g., multipath effects). See Krueger et al. (2008) for a detailed verification of the multipath load of the calibration field.

Based on GIK's experiences related to the establishment and monumentation of geodetic network points three stable pillars could be constructed consisting of material with long-life expectancy. BCAL/UFPR is actually equipped with the pillars 1000, 2000, and 3000. The pillars are 1.3 m high and have a core of steel and concrete.

BCAL/UFPR makes use of the relative field calibration approach, where a short baseline (length: approx. 10 m) is applied to eliminate spatially correlated errors (e.g., atmospheric delay). As reference antenna a LEIAR25 choke ring antenna, calibrated absolutely by Geo++, (Garbsen, Germany) in combination with a Leica GPS1200 receiver is used. In contrast, the NGS recommends that choke ring antennas of the type AOAD/MT (Allen Osborne Associates Dorne Margolin T; Kouba 2009) should be chosen as reference antenna. The antennas to be calibrated are rotated with the so-called DRB device. The DRB was developed by the Geodetic Institute of the Technical University of Dresden (TU Dresden; Germany) to meet the needs of scientific experiments, especially in GNSS antenna calibration (Frevert et al. 2003). This automatic device rotates the GNSS antenna to be calibrated within 1 min from North to South to West to East direction. Therefore, the data sampling rate is chosen to 15 s. A tilting of the antennas is not performed. 24 h data sets are collected to provide repeated coverage of the full antenna horizon (Wanninger and May 2000).

In order to legitimize the calibration procedure (e.g., location, equipment, software) applied at BCAL/UFPR, it was necessary to perform validation experiments. This validation was carried out in 2011, where antennas of the types LEIAX1202GG and TRM22020.00+GP were calibrated repeatedly at BCAL/UFPR as well as at TU Dresden using the relative field calibration method and by Geo++ using the absolute robot field calibration procedure (Wübbena et al. 1997). Based on these analyses, the calibration procedure applied at BCAL/UFPR was confirmed (Huinca et al. 2012). Compared to these calibrations experiments, this paper focusses on a larger sample size.

3 Methods and Data

Five Zephyr GNSS Geodetic II antennas (TRM57971.00 NONE) were calibrated at BCAL/UFPR using the relative field calibration approach described above. The reference (calibration) antenna was established at pillar 1000 (2000), see Fig. 2.

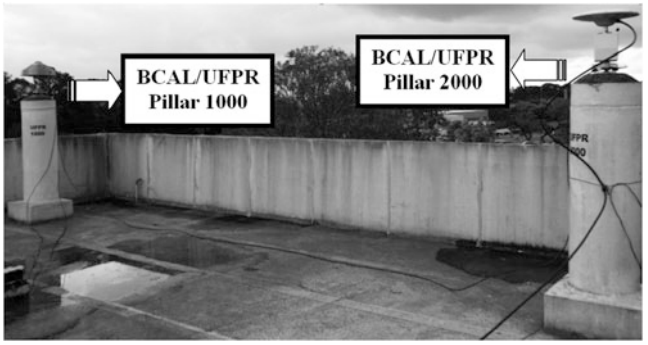

Fig. 2 Calibration at BCAL/UFPR

Table 1 Nomenclature used within this article

Serial number	Date	GPS day	Session	Nomenclature
1441107828	17/11/2012	322	S1	7828-S1
	20/11/2012	325	S2	7828-S2
			Mean	7828-M
1441112357	7/11/2012	312	S1	2357-S1
	16/11/2012	321	S2	2357-S2
			Mean	2357-M
1441053123	8/11/2012	313	S1	3123-S1
	14/11/2012	319	S2	3123-S2
			Mean	3123-M
1441053217	9/11/2012	314	S1	3217-S1
	19/11/2012	324	S2	3217-S2
			Mean	3217-M
1441112202	10/11/2012	315	S1	2202-S1
	13/11/2012	318	S2	2202-S2
			Mean	2202-M

To guarantee reliable results and to be able to estimate the quality of the calibration procedure two calibrations (S1 resp. S2) have been carried out per antenna. Table 1 provides the nomenclature used within this paper, where M refers to the mean value of S1 resp. S2.

The data processing was performed in post-processing using the software Wasoft/Kalib 2.0 (link: www.wasoft.de/e/kalib/index.html). The determined frequency-dependent GPS antenna parameters consist of individual PCO values (northing, easting, up) and direction-related PCV. These data are validated and compared to the values published by the NGS, which are identical for the GPS frequencies of the antenna type under research to values published by the International GNSS Service.

4 Analyses

The discussion of the analysis results is separated into two parts. Section 4.1 compares the calibration results type-related, while Sect. 4.2 focusses on comparisons related to NGS values.

4.1 Type-Related Comparison

Five GNSS antennas of the type TRM57971.00 NONE were calibrated twice. Figure 3 (Fig. 4) shows the resulting horizontal PCO values of L1 (L2).

Analyzing Figs. 3 and 4, it could be observed that the 2D differences between two individual calibrations of individual antennas are less than 1 mm for all calibrated antennas. This emphasizes the good reliability of the applied calibration procedure. In addition, the two calibrations of one specific antenna (S1, S2) fit nicely with respect to other antennas of the same type.

The PCO up component differences related to S1 and S2 of identical antennas fit in the range of 1 mm if the GPS data were collected with the same minimum elevation angle. The L1 and L2 PCO up components of all ten calibrations varies in the range of 2 mm. Due to the fact that the measurements of S2 of the antennas 7828 and 2357 were collected with a minimum elevation angle of 13° instead of 10°, the calculations described in Sect. 4.2 are carried out with an minimum elevation angle of 15°.

4.2 Comparison to NGS Values

In Sect. 4.1 analyses related to antenna parameters stemming from individual parameter estimations are carried out. In order to be able to compare these antenna parameters – consisting of PCO and PCV – with respect to published NGS parameters (NGS sample size: 8), we transformed all PCO–PCV-sets determined based on observations collected at BCAL/UPFR to the NGS PCO values. Hereby, the PCV values are constraint in order to derive a PCV mean value of zero within the elevation interval [25°; 75°].

Figure 5 (Fig. 6) shows the elevation-dependent PCV related to L1 (L2). The PCV derived based on measurements carried out at BCAL/UFPR fit for zenith distances $z > 10°$ in the range of 1 mm. For smaller zenith distances the differences increase. This behavior is especially due to the constraining within the transformation procedure. Nevertheless the Figs. 5 and 6 proof that BCAL/UFPR is able to

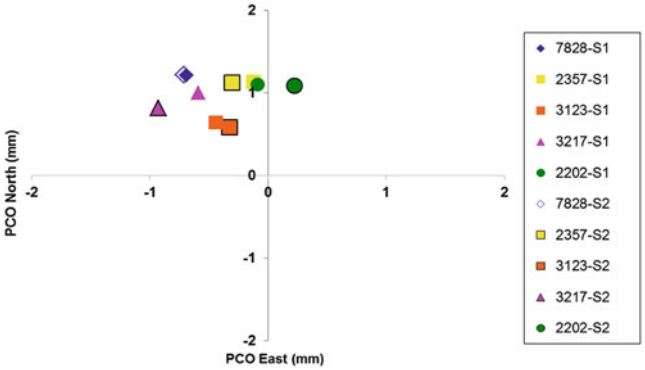

Fig. 3 Horizontal L1 PCO values

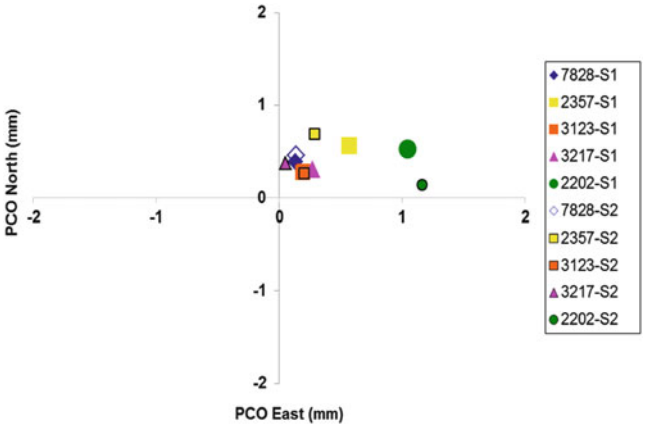

Fig. 4 Horizontal L2 PCO values

provide reliable calibration results. In addition, Figs. 5 and 6 depict the elevation-dependent NGS PCV values. It is clearly visible that the results gained at BCAL/UFPR differ significantly from the NGS values. Further investigations have to be carried out in order to check if these differences are due to site-specific effects.

In Figs. 3 and 4 it was shown, that two calibrations of one specific antenna (S1, S2) fit nicely with respect to other antennas of the same type. This finding is not confirmed analyzing elevation-dependent PCV values (Figs. 5 and 6). Analyzing azimuth- and elevation-dependent PCV of the antennas under research (Figs. 7, 8, and 9), this finding becomes prominent again.

The Figs. 7, 8, and 9 focus on azimuth- and elevation-dependent PCV-differences related to transformed NGS parameters. These figures are representative for the antennas under research and for both carrier frequencies. The PCV pattern – especially in zenith and southern direction – of antenna 7828 (Figs. 8 and 9) differ from the PCV pattern of antenna 3123 shown in Fig. 7.

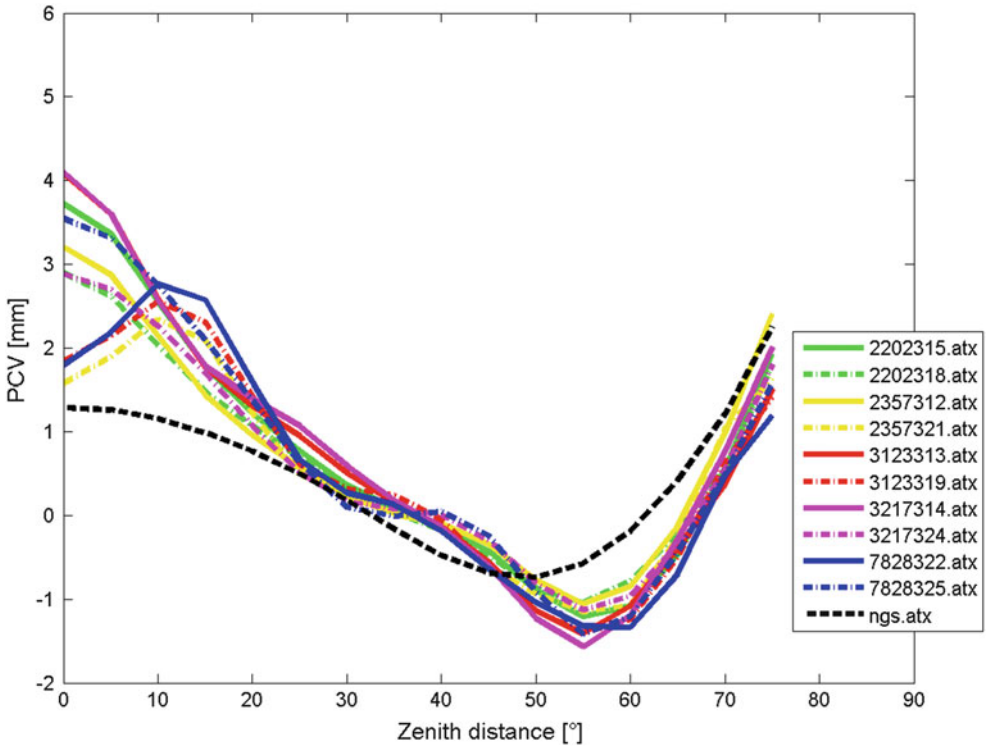

Fig. 5 L1 elevation-dependent PCV values

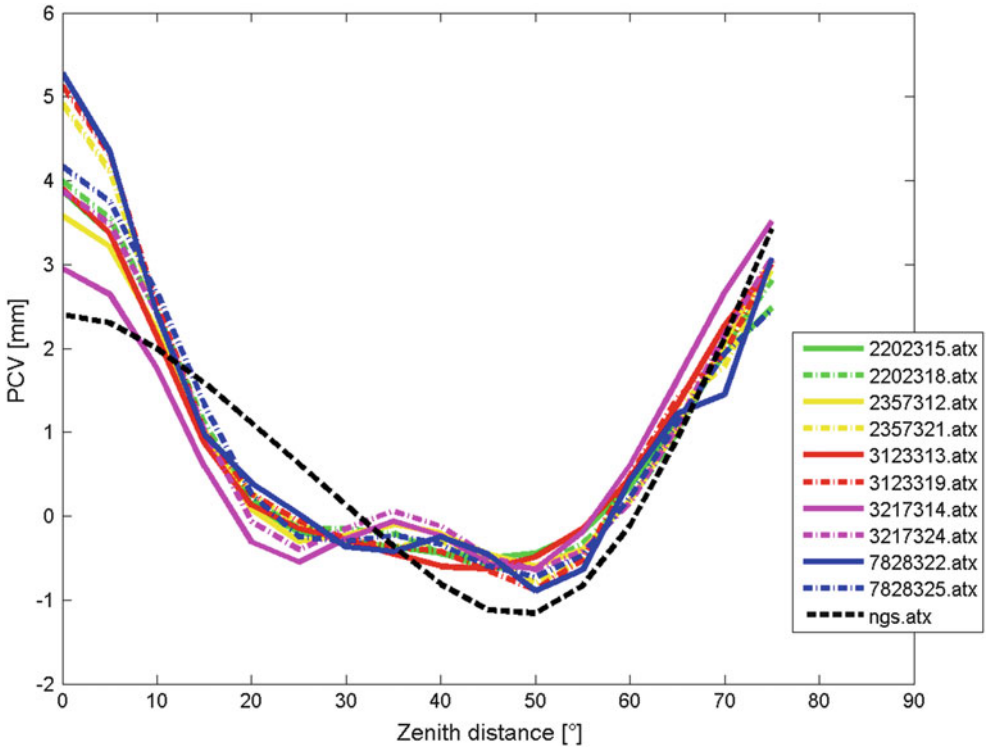

Fig. 6 L2 elevation-dependent PCV values

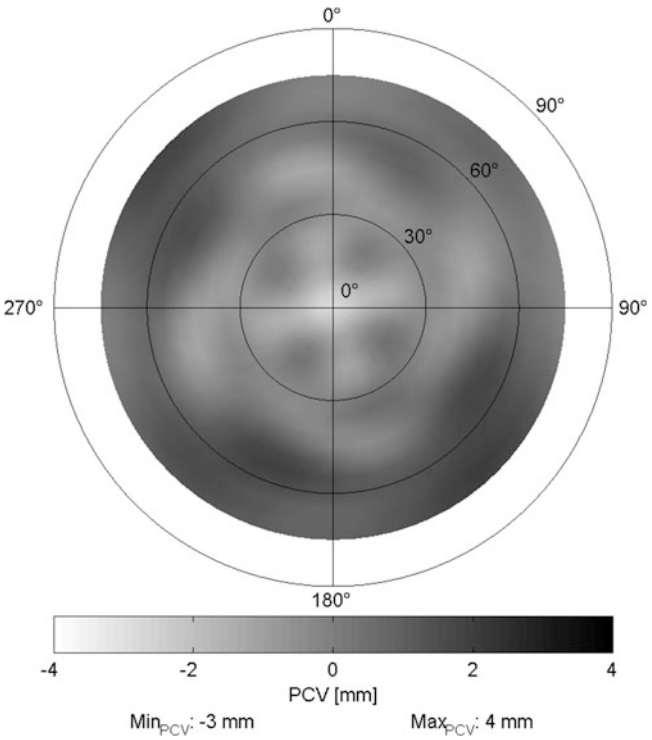

Fig. 7 L1 PCV values of antenna 3123 in S1

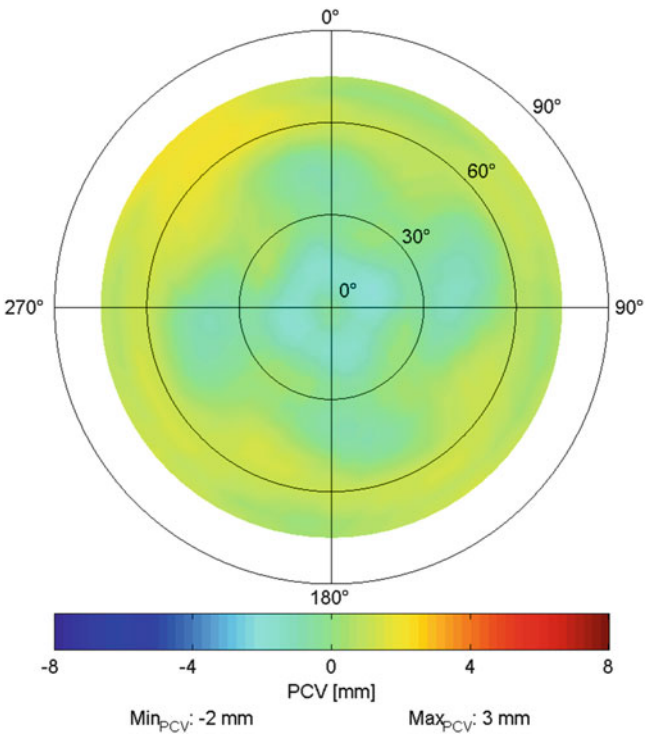

Fig. 8 L1 PCV values of antenna 7828 in S1

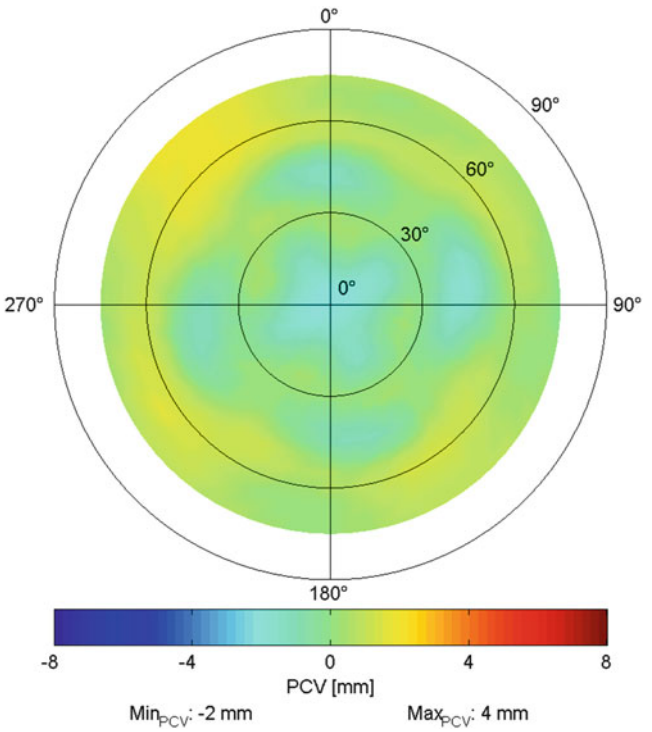

Fig. 9 L1 PCV values of antenna 7828 in S2

5 Conclusions

At the BCAL/UFPR five antennas of the same type have been calibrated. Each antenna was calibrated twice. Within this paper the data evaluation strategy as well as the analysis of the determined antenna models was presented. It could be proven that (1) BCAL/UFPR is able to provide reliable calibration results and (2) the determined antenna parameters of different antennas of the same type differ from each other as well as from the model published by the NGS.

Investigations – related to the determination of individual antenna calibration models – are important especially when highest-precision GNSS applications are under focus. Therefore, the establishment of the first basis for GNSS antennas in Latin America was of great importance.

Future investigations will focus on a more detailed analysis of low-elevation antenna parameters in combination with site-specific effects. A special focus will be on the documentation of the representativeness and the transferability of the antenna parameters determined at BCAL/UFPR to other measurement locations. In addition, the effects of individual calibration parameters with respect to estimated coordinates will be under research.

References

Frevert V, Nuckelt A, Stöcker D (2003) Beschleunigte Feldkalibrierung von GPS-Antennen. DGON-Symposium POSNAV 2003, Dresden, March 18–19 2003. Schriftenreihe des Geodätischen Instituts 3:353–359

Huinca SCM, Krueger CP, Mayer M, Knöpfler A, Heck B (2012) Installation of a baseline calibration station for GNSS antennas at UFPR/Brazil. In: Kenyon S, Pacino MC, Marti U (eds) Proceedings of IAG symposium 2009 scientific assembly "Geodesy for Planet Earth", 31. Springer Series International Association of Geodesy Symposia, vol 136, pp 739–744

Kouba J (2009) A guide to using international GNSS service (IGS) products. igscb.jpl.nasa.gov/igscb/resource/pubs/UsingIGSProductsVer21.pdf. Accessed 15 July 2013

Krueger CP, Freiberger Jr J, Heck B, Mayer M, Knöpfler A, Schäfer B (2008): Establishing a GNSS receiver antenna calibration field in the framework of PROBRAL. In: Sideris MG (ed) Observing our changing earth. Proceedings of the 2007 IAG General Assembly, Perugia, Italy, July 2–13, 2007. Springer Series: IAG Symposia, vol 133. Springer Verlag, Berlin/Heidelberg, pp 701–708

Schupler BR, Clark TA (1991) How different antennas affect the GPS observable. GPS World 2:32–36

Wanninger L, May M (2000) Carrier phase multipath calibration of GPS reference stations. In: Proceedings of the 13th international technical meeting of the satellite division of the Institute of Navigation, ION GPS 2000, Salt Lake City, UT, USA, 19–22 September 2000

Wübbena G, Schmitz M, Menge F, Seeber G, Völksen C (1997) A new approach for field calibration of absolute antenna phase center variations. J Inst Navig 44(2):247–256

Solar Corona Electron Densities from VLBI and GIM Data

Benedikt Soja, Robert Heinkelmann, and Harald Schuh

Abstract

The electron density of the solar corona can be determined by multi-frequency radio measurements, e.g. to spacecraft during superior solar conjunctions. Recently, also Very Long Baseline Interferometry (VLBI) has been successfully used to estimate coronal electron densities. The greatest challenge was to separate the dispersive effects of the solar corona and the Earth's ionosphere. Here, we developed and applied another approach including global ionospheric maps (GIM) to eliminate the effect of the ionosphere. By using such an external data set, an independent validation of the previous results is possible. The models of the electron density derived by these two approaches agree well: the electron density at the Sun's surface is calculated as $(1.24 \pm 0.42) \times 10^{12}\,\mathrm{m}^{-3}$ (VLBI only) and $(1.31 \pm 0.51) \times 10^{12}\,\mathrm{m}^{-3}$ (VLBI + GIM). The results are compared to external information about indicators of solar activity (e.g. Sunspot numbers), coronagraph images as well as to models of the electron density determined by measurements to spacecraft.

Keywords

Electron density • GIM • Ionosphere • Solar corona • VLBI

1 Introduction

The solar corona is a dispersive medium for electromagnetic waves. The effect depends on the electron density which can be determined by dual-frequency measurements, e.g. to spacecraft during superior solar conjunctions (Tyler et al. 1977; Pätzold et al. 2012). During the last 45 years, several models of the electron density have been obtained using this technique (Bird et al. 2012). Recently, also Very Long Baseline Interferometry (VLBI, Schuh and Böhm 2013) has been successfully used to estimate electron densities of the solar corona (Soja et al. 2014). VLBI observations closer than 15° to the Sun are sparse in the International VLBI Service for Geodesy and Astrometry (IVS) program since 2002. In 2011/2012 twelve so-called R&D sessions were dedicated to include such observations. By analyzing these observations, it was possible to separate the dispersive effects of the solar corona from those of Earth's ionosphere and to estimate the corona's electron density.

Another possibility for removing the effects of the ionosphere from the dispersive delays observed by VLBI is the use of the total electron content (TEC) information provided by global ionospheric maps (GIM). The resulting models can be used to validate the results from the approach using only VLBI data.

2 Methods

Considering VLBI observations close to the Sun, the dispersive delays, obtained from group delay measurements in S- and X-band, include the effects of the plasmas of the solar corona and Earth's ionosphere, as well as instrumental delays

B. Soja (✉) • R. Heinkelmann • H. Schuh
GFZ German Research Centre for Geosciences, Potsdam, Germany
e-mail: benedikt.soja@gfz-potsdam.de

© Springer International Publishing Switzerland 2015

C. Rizos, P. Willis (eds.), *IAG 150 Years*, International Association of Geodesy Symposia 143,
DOI 10.1007/1345_2015_155

Table 1 For each R&D session discussed in this work, the elongation of the source for which the ray paths passed closest to the Sun and the number of successful observations to sources within 15° elongation are given

Session	Date	Minimal elongation	No. of obs. within 15°	N_0 [10^{12} m^{-3}] VLBI only	VLBI+GIM
RD1106	Nov 29 2011	3.9°	33	0.02 ± 0.90	-1.96 ± 3.35
RD1107	Dec 06 2011	4.0°	59	4.62 ± 1.01	-3.49 ± 6.75
RD1201	Jan 24 2012	4.8°	31	8.03 ± 3.09	1.53 ± 3.54
RD1202	Apr 03 2012	5.8°	39	2.18 ± 1.09	-3.06 ± 1.23
RD1203	May 30 2012	10.5°	52	6.27 ± 5.26	3.83 ± 3.66
RD1204	Jun 19 2012	4.4°	32	2.78 ± 2.16	2.42 ± 1.53
RD1205	Jul 10 2012	6.1°	186	1.40 ± 0.75	4.57 ± 0.89
RD1206	Aug 28 2012	3.9°	193	0.70 ± 0.28	0.88 ± 0.33
RD1207	Sep 25 2012	6.1°	120	1.61 ± 2.24	3.54 ± 1.46
RD1208	Oct 02 2012	3.9°	103	2.98 ± 0.76	1.52 ± 1.61
RD1209	Nov 27 2012	4.2°	57	0.22 ± 0.59	5.23 ± 1.84
RD1210	Dec 11 2012	4.7°	80	6.18 ± 1.38	6.09 ± 5.56
Weighted mean from all R&D sessions				1.24 ± 0.42	1.31 ± 0.51

Furthermore, the estimated electron density models for $\beta = 2.3$ and their standard errors (68% confidence interval) are listed. For both approaches, an average model is computed by weighting the individual models with their inverse variances

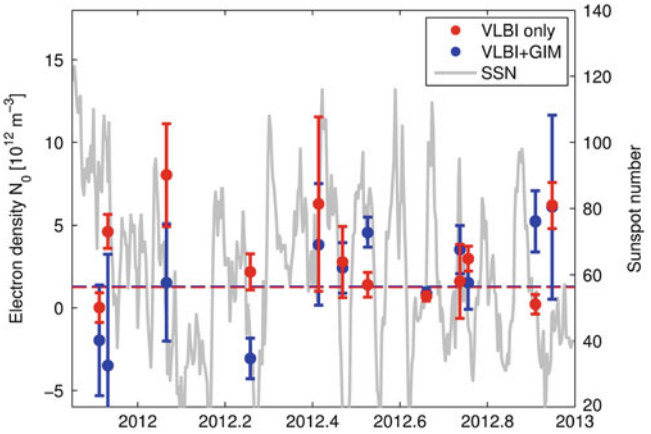

Fig. 1 For each of the 12 R&D sessions, the estimated power-law parameters N_0 are plotted for both approaches (1σ standard errors), compared to daily Sunspot numbers (SSN). The *dashed lines* represent the weighted mean of the N_0 values

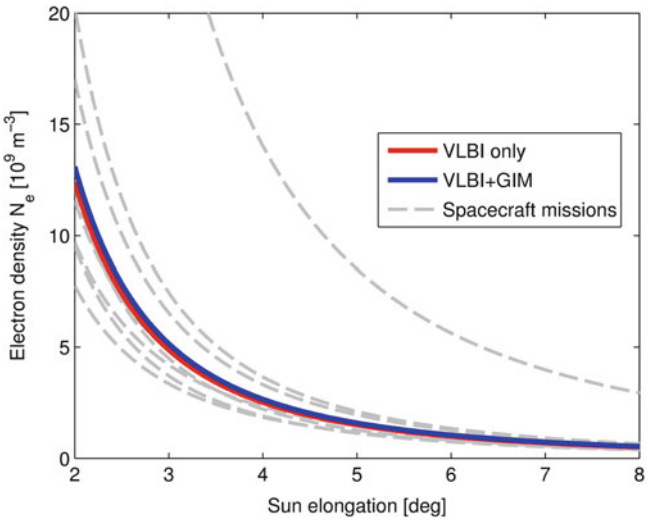

Fig. 2 The averaged electron density models from VLBI data (2011/2012) are compared to previous models obtained from measurements to spacecraft (1970–2008). The latter values are taken from Bird et al. (2012)

(Soja et al. 2013). The electron density N_e of the corona can be described using a radial power law (Verma et al. 2013):

$$N_e(r) = N_0 \cdot r^{-\beta} \tag{1}$$

with the heliocentric distance r in units of solar radii ($1\ R_\odot \approx 0.27°$ solar elongation), the theoretical electron density at the Sun's surface N_0 [corresponding to $N_e(1\ R_\odot)$] and the radial fall-off parameter β. For β, we used a value of 2.3, as recommended, e.g., by Berman (1977).

In the first approach ("VLBI only"), the unknown parameters of the corona, the power law parameter N_0, and of the ionosphere, the vertical total electron content (VTEC) time series for each VLBI station (cf. Hobiger et al. 2006), and the hardware delays, the session-wise constant offsets for each station, are estimated in a least-squares adjustment. This procedure is described in detail by Soja et al. (2014).

The second approach ("VLBI+GIM") uses the information provided by GIM data to compute the ionospheric delays for every VLBI observation (Ros et al. 2011) using the Vienna VLBI Software (VieVS, Böhm et al. 2012). By subtracting the ionospheric delays from the total dispersive delays, only the effects of the solar corona and station hardware remain and can be estimated in an adjustment (Soja et al. 2013).

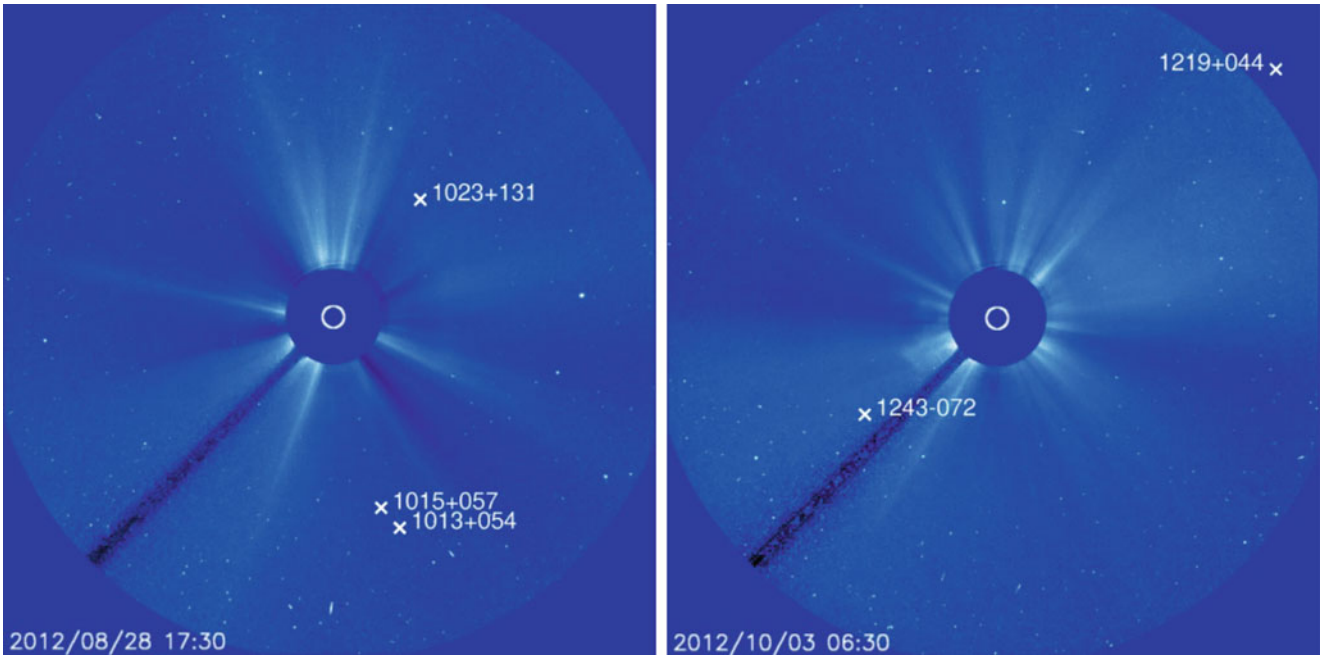

Fig. 3 LASCO coronagraph images (Brueckner et al. 1995) during two VLBI sessions indicating the regions of different coronal density within about 8.7° elongation. The *white circle* represents the position of the Sun. The *dark diagonal area* on the *lower left* in each image is due to a pylon holding the occultation disc. The positions of the observed radio sources are visualized by *white crosses*

3 Data

We analyzed VLBI data from the 12 R&D sessions between 11/2011 and 12/2012, scheduled by the International VLBI Service for Geodesy and Astrometry (IVS, Schuh and Behrend 2012). These are the only geodetic VLBI experiments since 2002 which include observations closer than 15° elongation to the Sun (Soja et al. 2012). The number of observations closer than 15° elongation to the Sun was between 30 and 200 for each of these sessions, the rest of the observations was scheduled applying other criteria like sky coverage. The closest successful observations were at 3.9° elongation (see Table 1). These 12 VLBI R&D sessions are discussed in greater detail by Soja et al. (2014).

For the second approach, the GIM provided by the International GNSS Service (IGS, Hernández-Pajares et al. 2009) were used. The IGS GIM are a combination of the GIM of four analysis centers (CODE, ESOC, JPL, and UPC). As only the CODE analysis center uses GLONASS data, the IGS GIM are based on GPS data mostly.[1] The VTEC values are provided on a grid with a spatial resolution of 5.0° × 2.5° and a temporal resolution of 2 h. The uncertainties are stated to be between 2 and 8 TECU (Ros et al. 2011). When compared to the estimation of VTEC from VLBI data with a precision of about 1 TECU and an average temporal resolution of up to 30 min (Hobiger 2006), the GIM might seem inferior. However, the actual accuracy of VLBI VTEC values might be lower than the precision (Dettmering et al. 2011). In any case, it is important to obtain independent validation of the results from using only VLBI data by incorporating external information.

Currently, only GNSS data is used to derive the IGS maps, but for the future, IGS might include other techniques like radio sounding with FORMOSAT-3/COSMIC (Krankowski et al. 2011). This could improve the accuracy and the spatio-temporal resolution of the GIM and lead to improved results when estimating the coronal electron density with this approach.

4 Results and Discussion

For each of the 12 VLBI R&D sessions, the electron density of the corona was estimated using both approaches. The results are listed in Table 1 and displayed in Fig. 1. For some of the sessions, differences between the approaches are reflected in the estimated electron densities. Using the VLBI+GIM approach, three of the models provide negative electron densities which are physically not possible. The VLBI only approach is more reliable in that respect. Larger differences between the approaches are found for sessions with less observations within 15° elongation or with radio sources at larger elongations. The electron densities

[1] http://igs.org/projects/iono/index.html.

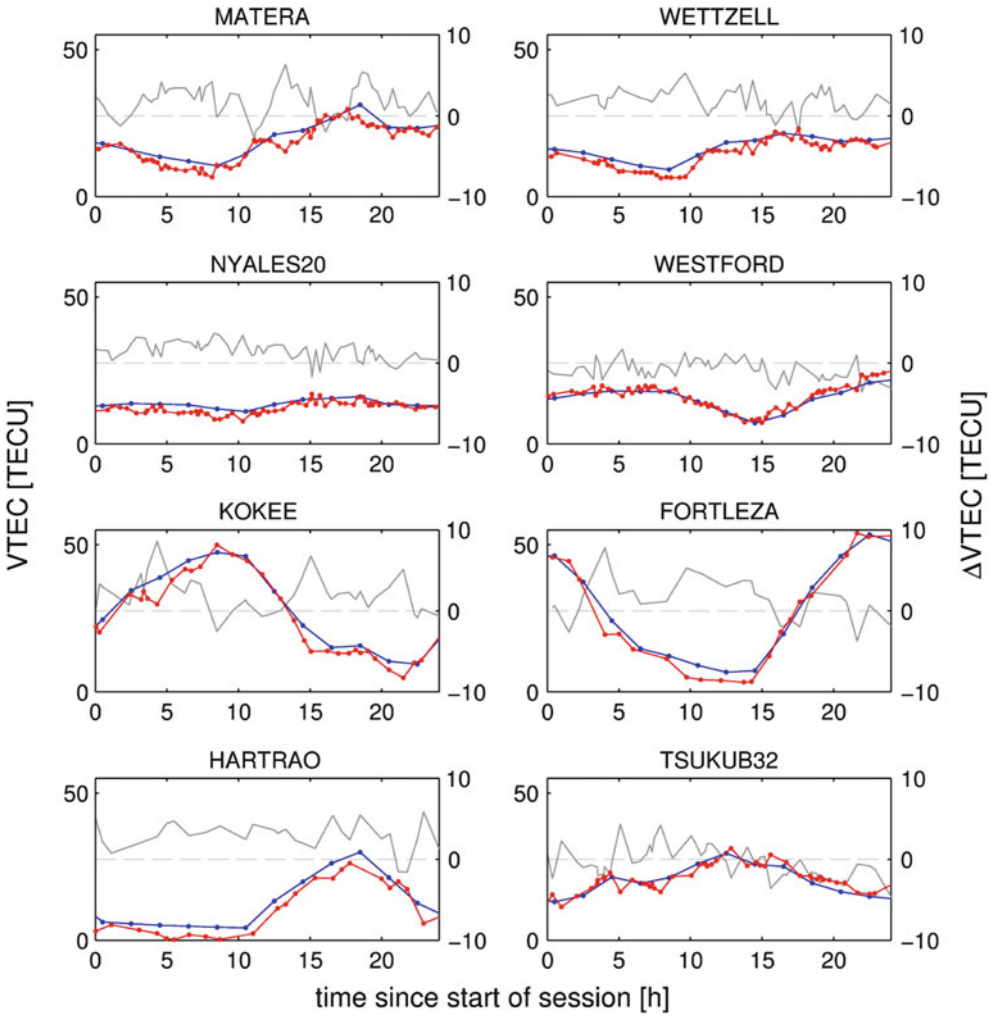

Fig. 4 For session RD1205, the station-wise ionospheric VTEC time series estimated from VLBI observations (*red*) using the methods developed by Hobiger et al. (2006) and interpolated from the IGS GIM product (*blue*, Hernández-Pajares et al. 2009). The difference ΔVTEC between the two time series is shown in *grey*

estimated for session RD1206 feature the best agreement and also the lowest standard errors. During this session the highest number of observations close to the Sun took place and the line-of-sights to radio source 1023+131 passed the Sun at an angular distance of only 3.9°.

The weighted averages of N_0 are $(1.24 \pm 0.42) \times 10^{12}\,\mathrm{m}^{-3}$ (VLBI only) and $(1.31 \pm 0.51) \times 10^{12}\,\mathrm{m}^{-3}$ (VLBI+GIM). The difference between these two models is only a small fraction of the uncertainties. In Fig. 2, the VLBI models are compared to previous models from measurements to spacecraft during superior solar conjunctions (Bird et al. 2012). There, the electron density is plotted as a function of the solar elongation for each model. The models from VLBI data agree well with the models from spacecraft tracking.

No significant correlations are found between the individual electron densities and indicators for overall solar activity like Sunspot numbers (SSN), see Fig. 1. The scatter of the individual N_0 values is, to a large extent, due to violations of the assumption of a radial-symmetric density distribution. This becomes evident by analyzing the geometry of the observed radio sources with respect to Large Angle and Spectrometric COronagraph (LASCO, Brueckner et al. 1995) images. The white-light brightness measured by the coronagraph can be used to distinguish regions of different density in the corona. Figure 3 shows, for example, the LASCO images for the sessions in August 2012 (observations in low density regions) and October 2012 (high density regions). The N_0 value is lower than average for the first session and higher for the second (0.7 vs. $3.0 \times 10^{12}\,\mathrm{m}^{-3}$, respectively). Similar agreement is found for all other sessions.

The two approaches discussed in this study only differ by incorporating different means to assess the ionospheric effects. Figures 4 and 5 illustrate the VTEC resulting from

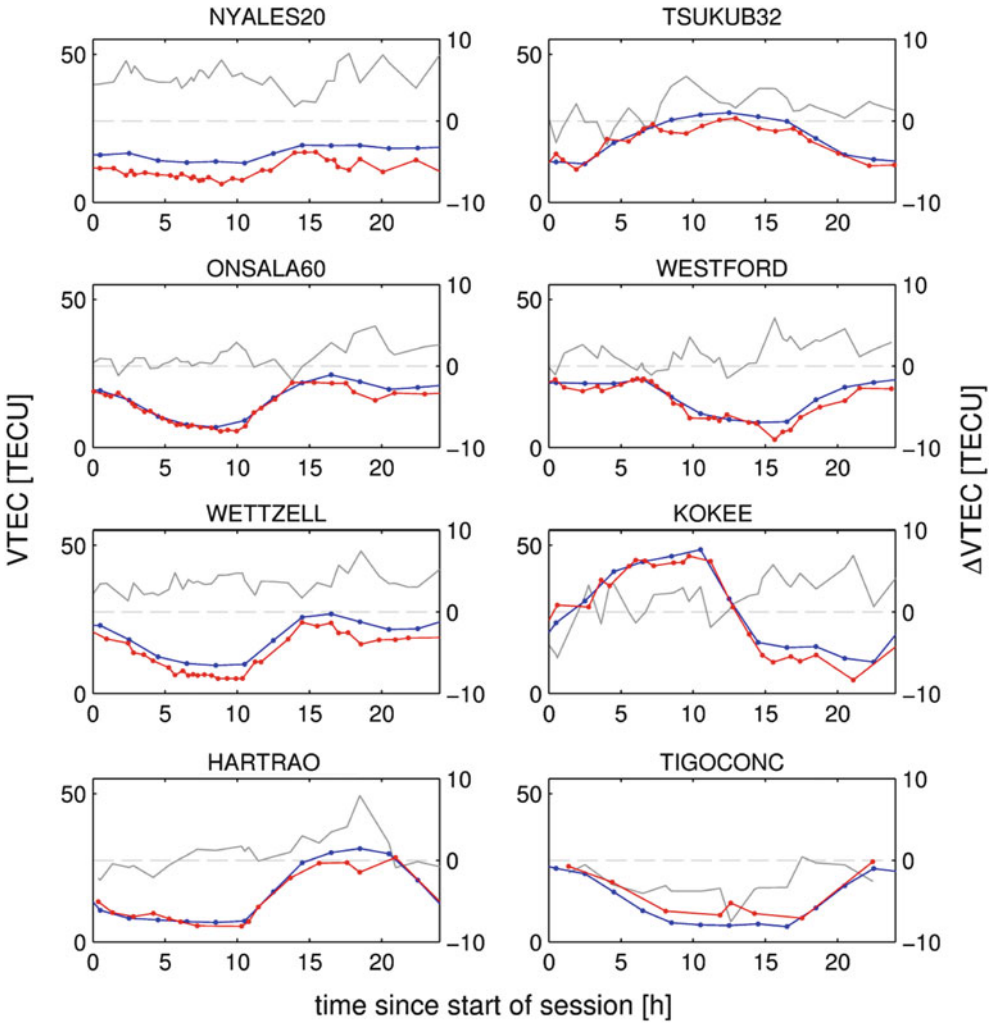

Fig. 5 For session RD1206, the station-wise ionospheric VTEC time series estimated from VLBI observations (*red*) using the methods developed by Hobiger et al. (2006) and interpolated from the IGS GIM product (*blue*, Hernández-Pajares et al. 2009). The difference ΔVTEC between the two time series is shown in *grey*

both approaches for two sessions. The estimation of VTEC from VLBI data allows for a higher temporal resolution and includes more short-term variations compared to the smoother GIM data. The VTEC differences are less than 8.6 TECU. Some stations have larger inter-technique biases than others (as also discussed by Dettmering et al. 2011; Hobiger 2006). The biases lead to differences in the estimated dispersive instrumental delays of the specific stations, similar to the correlation of the tropospheric zenith wet delays and clock parameters in the analysis of the non-dispersive effects (Schuh and Böhm 2013). In the case of the VLBI only approach, we determined the correlations between the estimated parameters of the corona and the ionosphere from the a posteriori variance-covariance matrix from the least-squares adjustment. For all R&D sessions, the correlations were found to be less than 5%. This means that the power-law parameter N_0 is not significantly affected by station-specific VTEC biases which are rather absorbed by the instrumental delays.

The temporally higher resolved ionosphere estimates in the VLBI only approach could be a reason that the corresponding coronal electron density values are more reliable. Also, inconsistencies introduced by mixing different techniques might explain the deficiencies in the VLBI+GIM approach. Generally, a model (even if based on real measurements) is not as accurate as dedicated measurements.

5 Conclusions

Our work shows that the inclusion of GIM data leads to a reasonable average electron density model of the corona (cf. Fig. 2). This can be seen as a validation of the results obtained using VLBI data only. Still, the precision (in terms

of standard errors, cf. Table 1) and reliability (with three negative estimates of electron density) are inferior to the VLBI only approach. This could be improved in the future with GIM including data from several space-geodetic techniques and featuring increased spatial and temporal resolutions.

The VLBI+GIM approach clearly separates the effects of the ionosphere from those of the corona. We found that also by applying the VLBI only approach, the parameters of the corona and the ionosphere can be estimated without being significantly correlated. Finally, we show that the VLBI observations are sensitive to regional density variations in the corona by comparison with coronagraph data.

Discussed in this paper are the 12 VLBI R&D sessions in 2011 and 2012 specifically dedicated to studies for which close observations to the Sun are necessary. At the end of 2013, the IVS decided to decrease the solar cut-off elongation angle from 15° to 4° for all geodetic sessions. This change means that in the future observations close to the Sun will take place several days per week. These observations will enable continuous solar corona investigations by VLBI in the following years which hopefully promotes VLBI to contribute to solar research and monitoring.

Acknowledgements The authors thank the IVS for observing, correlating and providing the VLBI data used in this work. The work of Jing Sun (scheduling of the R&D experiments) and Dirk Behrend (cross-checking the schedules) is much valued. The authors thank the IGS for providing GIM products. The SOHO/LASCO data used here are produced by a consortium of the Naval Research Laboratory (USA), Max-Planck-Institut fuer Aeronomie (Germany), Laboratoire d'Astronomie (France), and the University of Birmingham (UK). SOHO is a project of international cooperation between ESA and NASA.

References

Berman AL (1977) Electron density in the extended corona – two views. Deep Space Network Progress Report, 42-41. Jet Propulsion Laboratory, Pasadena

Bird M, Pätzold M, Häusler B, Asmar S, Tellmann S, Hahn M, Efimov A, Chashei I (2012) Coronal radio sounding experiments with the ESA spacecraft MEX, VEX, and Rosetta. In: 511th WE-Heraeus-seminar. Bad Honnef, January 31–February 3 2012

Böhm J, Böhm S, Nilsson T, Pany A, Plank L, Spicakova H, Teke K, Schuh H (2012) The new Vienna VLBI software VieVS. In: Kenyon S, Pacino MC, Marti U (eds) Proceedings of IAG scientific assembly, 2009, pp 1007–1011. doi:10.1007/978-3-642-20338-1_126

Brueckner GE, Howard RA, Koomen MJ, Korendyke CM, Michels DJ, Moses JD (1995) The large angle spectroscopic coronagraph (LASCO). Sol Phys 162:357–402

Dettmering D, Schmidt M, Heinkelmann R, Seitz M (2011) Combination of different space-geodetic observations for regional ionosphere modeling. J Geodesy 85:989–998

Hernández-Pajares M, Juan JM, Sanz J, Orus R, Garcia-Rigo A, Feltens J, Komjathy A, Schaer SC, Krankowski A (2009) The IGS VTEC maps: a reliable source of ionospheric information since 1998. J Geodesy 83:263–275. doi:10.1007/s00190-008-0266-1

Hobiger T (2006) VLBI as a tool to probe the ionosphere. Ph.D. thesis, Faculty of Mathematics and Geoinformation, Vienna University of Technology

Hobiger T, Kondo T, Schuh H (2006) Very long baseline interferometry as a tool to probe the ionosphere. Radio Sci 41:RS1006

Krankowski A, Zakharenkova I, Krypiak-Gregorczyk A, Shagimuratov I, Wielgosz P (2011) Ionospheric electron density observed by FORMOSAT-3/COSMIC over the European region and validated by ionosonde data. J Geodesy 85(12):949–964. doi:10.1007/s00190-011-0481-z

Pätzold M, Hahn M, Tellmann S, Häusler B, Bird MK, Tyler GL, Asmar SW, Tsurutani BT (2012) Coronal density structures and CMEs: superior solar conjunctions of Mars express, Venus express, and Rosetta: 2004, 2006, and 2008. Sol Phys 279(1):127–152. doi:10.1007/s11207-012-9991-y

Ros CT, Böhm J, Schuh H (2011) Use of GNSS-derived TEC maps for VLBI observations. In: Alef W, Bernhart S, Nothnagel A (eds) Proceedings of the 20th meeting of the European VLBI group for geodesy and astrometry, pp 114–117

Schuh H, Behrend D (2012) VLBI: A fascinating technique for geodesy and astrometry. J Geodyn 61:68–80. doi:10.1016/j.jog.2012.07.007

Schuh H, Böhm J (2013) Very long baseline interferometry for geodesy and astrometry. In: Xu G (ed) Sciences of geodesy II: innovations and future developments. Springer, Berlin/Heidelberg

Soja B, Plank L, Schuh H (2012) General relativistic delays in current and future VLBI. In: Schuh H, Böhm S, Nilsson T, Capitaine N (eds) Proceedings of the Journées 2011: Systèmes de référence spatio-temporels, pp 41–44

Soja B, Sun J, Heinkelmann R, Schuh H, Böhm J (2013) Sun corona electron densities derived from VLBI sessions in 2011/2012. In: Zubko N, Poutanen M (eds) Proceedings of the 21st meeting of the European VLBI group for geodesy and astrometry, pp 159–163

Soja B, Heinkelmann R, Schuh H (2014) Probing the solar corona with very long baseline interferometry. Nat Commun 5:4166. doi:10.1038/ncomms5166

Tyler GL, Brenkle JP, Komarek TA, Zygielbaum AI (1977) The Viking solar corona experiment. J Geophys Res 82(28):4335–4340. doi:10.1029/JS082i028p04335

Verma AK, Fienga A, Laskar J, Issautier K, Manche H, Gastineau M (2013) Electron density distribution and solar plasma correction of radio signals using MGS, MEX, and VEX spacecraft navigation data and its application to planetary ephemerides. Astron Astrophys 550:A124. doi:10.1051/0004-6361/201219883. eprint:1206.5667

Status of TIGA Activities at the British Isles Continuous GNSS Facility and the University of Luxembourg

A. Hunegnaw, F.N. Teferle, R.M. Bingley, and D.N. Hansen

Abstract

In 2013 the International GNSS Service (IGS) Tide Gauge Benchmark Monitoring (TIGA) Working Group started their reprocessing campaign which proposes to re-analyse all relevant GPS observations from 1995 to the end of 2012 in order to provide high quality estimates of vertical land motion for monitoring of sea level changes. The TIGA Working Group will also produce a combined solution from the individual TIGA Analysis Centres (TAC) contributions. The consortium of British Isles continuous GNSS Facility (BIGF) and the University of Luxembourg TAC (BLT) will contribute weekly minimally constrained SINEX solutions from its reprocessing using the Bernese GNSS Software (BSW) version 5.2 and the University of Luxembourg will also act as a TIGA Combination Centre (TCC). The BLT will generate two solutions, one based on BSW5.2 using a network double difference (DD) strategy and a second one based on BSW5.2 using a Precise Point Positioning (PPP) strategy. In the DD strategy we have included all IGb08 core stations in order to achieve a consistent reference frame implementation.

As an initial test for the TIGA combination, all TACs agreed to provide weekly SINEX solutions for a four-week period in December 2011. Taking these individual TAC solutions the TCC has computed a first combination using two independent combination software packages: CATREF and GLOBK. In this study we will present preliminary results from the BLT reprocessing and from the combination tests.

Keywords

Combination • GPS • Reprocessing • SINEX • TIGA

1 Introduction

Sea level change as a consequence of climate variations has a direct and significant impact for coastal areas around the world. Over the last two centuries sea level changes have been estimated from the analysis of tide gauge records. However, tide gauges measure sea level relative to benchmarks on land. It is well established that these records need to be decoupled from vertical land movements. Global Navigation Satellite System (GNSS) technology, in particular the Global Positioning System (GPS), has made it possible to obtain highly accurate measurements of vertical land movements close to or at tide gauges (Teferle et al. 2006; Wöppelmann et al. 2007; Rudenko et al. 2013).

Under the umbrella of the International GNSS Service (IGS), the Tide Gauge Benchmark Monitoring (TIGA) Working Group has been established to bring expertise of the GNSS community to the Global Sea-level Observing

A. Hunegnaw (✉) • F.N. Teferle
Faculté des Science, de la Technologie et de la Communication, University of Luxembourg, 6 rue Richard Coudenhove-Kalergi 1359, Luxembourg
e-mail: addisu.hunegnaw@uni.lu

R.M. Bingley • D.N. Hansen
Nottingham Geospatial Institute, University of Nottingham, Nottingham NG7 2TU, UK

© Springer International Publishing Switzerland 2015

C. Rizos, P. Willis (eds.), *IAG 150 Years*, International Association of Geodesy Symposia 143,
DOI 10.1007/1345_2015_77

System (GLOSS) community to solve issues related to the accuracy and reliability of the vertical component as measured by GPS and to provide time series of vertical land movement in a well-defined global reference frame (Schöne et al. 2009). In the past, to achieve this objective up to six TIGA Analysis Centres (TACs) were contributing individual solutions, employing different GPS processing software and analysis strategies. Some of the TACs have carried out their processing based on old IGS standards such as relative satellite and receiver antenna phase centre variation (PCV) models. In effect, interpreting GPS-derived vertical land movements will be difficult due to inconsistencies caused by model and strategy differences. This gave the motivation for the TIGA working group to start a reprocessing campaign which proposes to re-analyse all relevant GPS observations from 1995 to the end of 2012, conforming to the latest IGS standards.

The consortium of the British Isles continuous GNSS Facility (BIGF) and the University of Luxembourg TIGA Analysis Centres (BLT), as one of the TIGA Analysis Centres (TAC), has started a reprocessing of more or less the complete TIGA archive hosted at the University of La Rochelle (ULR). The BLT will generate SINEX format solutions based on the Bernese GNSS Software (BSW) version 5.2 (Dach et al. 2007), one using a network double difference (DD), and the second a Precise Point Positioning (PPP) strategy. Internally BLT will generate two network DD solutions, one at BIGF and one at the University of Luxembourg (UL), which only differ in their station selection. Only one internally combined SINEX file will be delivered to the TIGA working group.

In the past, the networks processed by the individual TACs differed significantly, some were regional and some were global with very few or none common stations between them (Schöne et al. 2009). The quality of a combined solution depends on the number of common stations in the contributing TAC solutions, which can be used during the combination. Currently, there are three global TAC solutions available with varying numbers of common stations between them.

In order to improve the redundancy in our preliminary combination test, we have included the solution from IGS Analysis Centre (AC) at the Massachusetts Institute of Technology (MIT). Table 1 lists the three TACs (BLT, GFZ, ULR) and one IGS AC (MIT) contributing to this combination test. All the three TACs include a core global network of sites from the IGb08 reference stations (Rebischung 2012). Taking these individual TAC solutions, the TCC has computed a first combination using two independent combination software packages: Combination and Analysis of Terrestrial Reference Frame (CATREF) (Altamimi et al. 2002) and Global Kalman filter VLBI and GPS analysis program (GLOBK) (Herring and King 2006).

Table 1 TIGA and IGS analysis centres used in this study

TAC(AC)	Description
ULR	Centre Littoral de Geophysique, University of La Rochelle (ULR), France
GFZ	GeoForschungsZentrum Potsdam (GFZ), Germany
BLT	British Isles continuous GNSS Facility and the University of Luxembourg TAC (BLT), UK and Luxembourg
MIT	Massachusetts Institute of Technology, USA

In this study we will present preliminary results from the BLT reprocessing, a comparison of two independent combinations using software packages CATREF and GLOBK, and a first TIGA combination for a test period in December 2011.

2 Processing and Combination Methodologies

The BLT reprocessing strategy follows closely that of (Steigenberger et al. 2006) while incorporating recent model developments and the latest International Earth Rotation and Reference Systems Service (IERS) 2010 conventions (Petit and Luzum 2010). We summarize our network DD processing in Table 2. The two BLT partners each process all IGb08 core stations. Additionally, BIGF includes the dense network of the British Isles while UL covers more or less the complete archive of TIGA[1] (see Fig. 1). Hence UL generates daily SINEX solutions from up to 450 GPS stations using the UL High Performance Computing (HPC) facility. The daily free normal equations from both BLT partners are combined for computing a minimum constrained solution (no-net rotation and no-net translation) conditions with respect to the IGb08 reference frame. Stations with large residuals exceeding ± 20 mm in the North and East components, and ± 30 mm in the Up component in the daily combination are reduced from the normal equations.

Independent of the BLT TIGA solution, UL has also produced a PPP solution from 1995 to the end of 2012. Firstly, this serves as an internal quality control of the TIGA archive held at the University of La Rochelle (ULR) and the information held by BLT. This highlighted a number of issues related to non-IGS station log files and respective RINEX header information. Secondly, PPP provides good quality a priori coordinate solutions for non-IGS stations.

The PPP strategy is made possible by fixing Centre for Orbit Determination in Europe (CODE) final satellite orbits,

[1] http://tiga.sonel.org/.

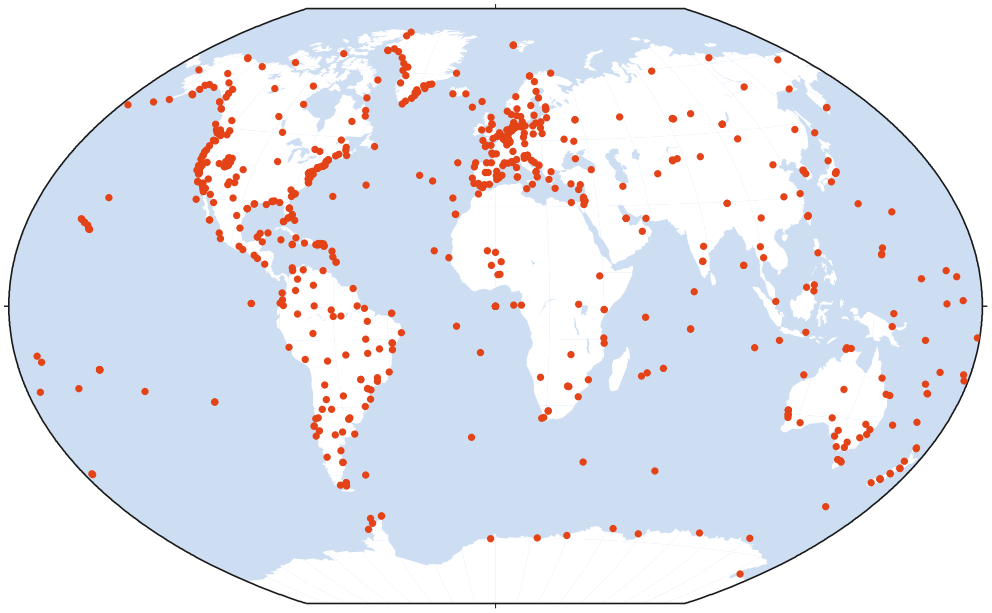

Fig. 1 GPS network processed at UL for TIGA

Table 2 Summary of the GPS data processing strategy at the UL

Parameters	Description
GPS software	Bernese version 5.2 (Dach et al. 2007)
Data	Double-differenced phase and code observations from up to 450 stations per day
Elevation cut-off angle	3° and elevation dependent weighting ($w = \cos^2 z$, zenith angle z)
Ionospheric refraction	Ionospheric-free linear combination (L3) together with the 2nd order correction
Tropospheric refraction	An a priori dry tropospheric delay (Saastamoinen) computed from standard atmosphere. For wet part continuous piecewise-linear troposphere parameters estimated in 2-hour interval, plus gradients in north-south and east-west directions at 24 h intervals. Vienna Mapping Function for hydrostatic and wet components are implemented
Earth orientation	C04 series IERS Bulletin B
Antenna PCV	IGS absolute elevation and azimuth dependent PCV igs08.atx file (http://igscb.jpl.nasa.gov/igscb/station/general/pcv_archive)
Earth and polar tide	IERS2010 (Petit and Luzum 2010)
Ocean loading	Computed using FES2004 ocean tide model (http://holt.oso.chalmers.se/loading/)
Datum	No-Net-Rotation (NNR) and No-Net-Translation (NNT) with respect to IGb08 (Rebischung 2012). However, any conditions such as NNT or No-Net-Scale (NNS) or a combination of them can be applied since we save the normal equations of our DD processing
Ambiguity resolution	Resolved to integers up to 6,000 km using different techniques depending on the baseline length
Meta data	Intensive meta data check

satellite clocks and Earth rotation parameters (ERP). This processing follows more or less the description in Table 2.

However, our final reprocessed solution will be based on the network DD strategy along with other TACs SINEX files to generate a combined SINEX file.

As part of the TIGA reprocessing, all TACs will provide minimally-constrained solutions in the form of SINEX files for the TIGA combination. It was agreed that all TACs would provide four weeks of SINEX solutions for the GPS weeks 1665–1668, i.e. December 2011. So far, only three TAC solutions have become available for the combination test (see Fig. 2) but at least one more is expected to be available for the final combination. The main purpose of the combination is to determine better coordinate estimates for all TIGA stations expressed in the current IGb08 reference frame. Prior to combination the TAC solutions are pre-processed and checked for completeness and conformity of their SINEX files and for station name inconsistencies. Then the constraints applied to the individual solutions are removed and the normal equations of the parameter set of interest are added together.

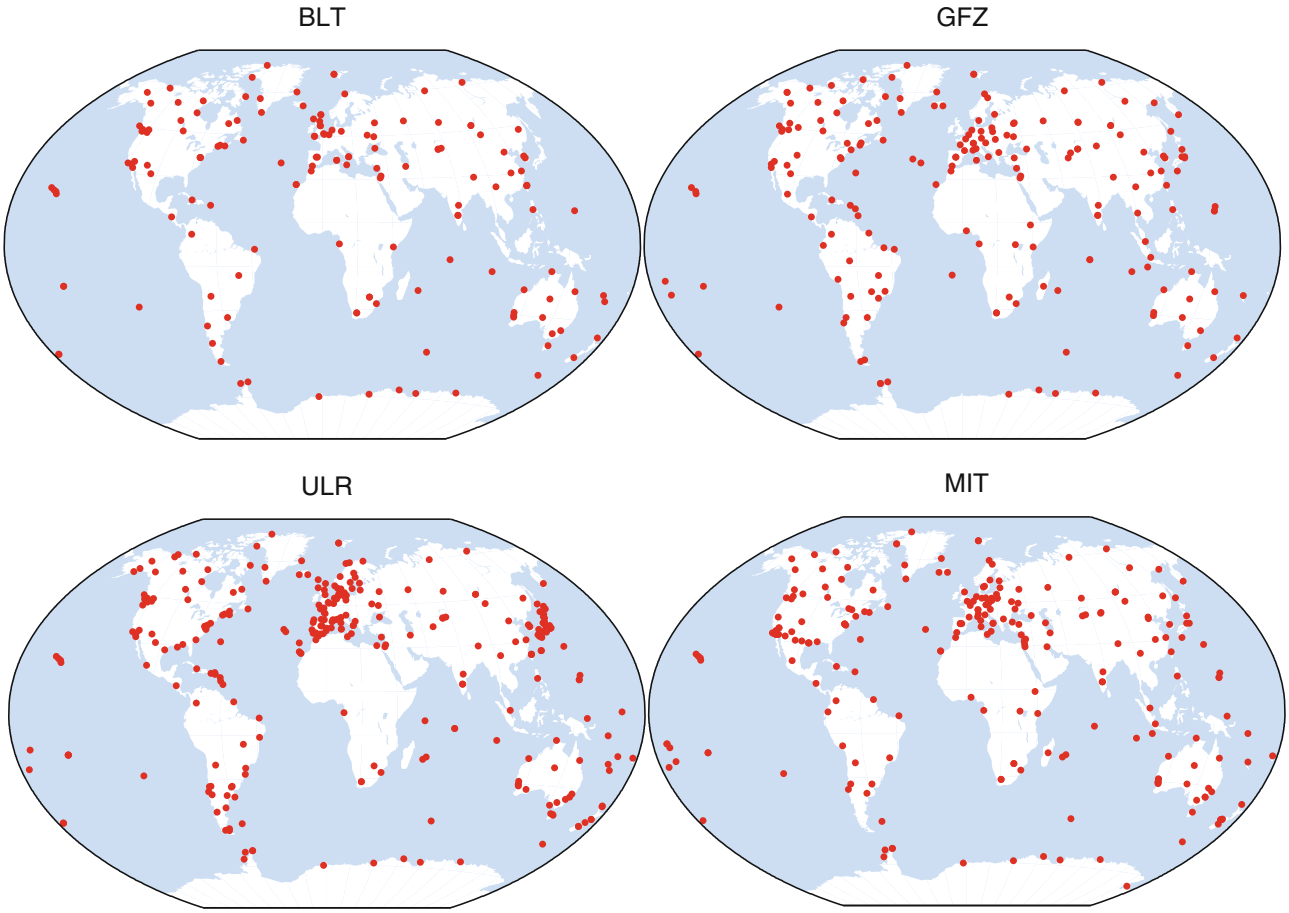

Fig. 2 TIGA (BLT, GFZ and ULR) and IGS (MIT) AC solutions used for the TIGA combination in this study

The reconstruction of the individual unconstrained normal equation system ($\mathbf{N}_i^{unc}$) provided by the TACs for consecutive weekly epoch t is done using Eq. (1):

$$\mathbf{N}_{i,t}^{unc} = \hat{\sigma}_{i,t}^2 \mathbf{C}_{\hat{\mathbf{x}}_{i,t}\hat{\mathbf{x}}_{i,t}}^{-1} - \hat{\sigma}_{i,t}^2 \mathbf{C}_{\mathbf{x}_{i,t}\mathbf{x}_{i,t}}^{-1} \quad (1)$$

where the variance-covariance matrix of the parameters ($\mathbf{C}_{\hat{\mathbf{x}}\hat{\mathbf{x}}}$) computed from the constraints applied are provided in the form of a SINEX file. $\hat{\sigma}$ is the a posteriori variance factor. The resulting loose normal equation matrix should be singular, resulting from the three degrees of freedom of the unobserved network orientation. To remedy the rank deficiency and to define a uniform reference frame, constraints are imposed to estimate the final solution through Least-Squares and Kalman Filter procedure, as implemented in the CATREF and GLOBK approaches, respectively. Readers are referred to (Altamimi et al. 2002) and (Dong et al. 1998) for the general mathematical combination models used in CATREF and GLOBK, respectively.

3 Results: BLT Processing and Assessment of Combinations Using CATREF and GLOBK

This section presents preliminary results of the BLT reprocessing, a comparison of CATREF and GLOBK combinations, and of the four-week TIGA combination test.

3.1 Reprocessing

Reprocessing following the final network DD strategy using BSW5.2 is well under way at both BLT consortium partners and the results will likely be available by the middle of 2014. Here we only show a set of daily PPP and DD solutions for 2011. Note, PPP only serves as a quality check and provides a priori coordinates for non-IGS stations. For example, Fig. 3 compares the daily PPP and DD North, East and Up component time series for ONSA. Overall the time

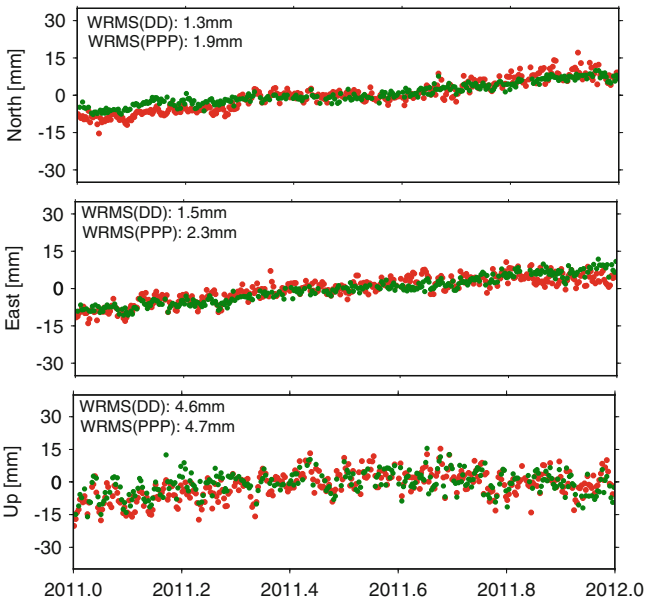

Fig. 3 Local topocentric components (East, North and Up) time series for station ONSA. *Red circles* represent the PPP, *green* the DD strategy. Also shown are the weighted root mean square (WRMS) statistics for PPP and DD solutions

series from both processing solution agree well. As expected the weighted root mean square (WRMS) shows a significant improvement for the DD over the PPP solution, especially for the horizontal components. The largest improvement (34 %) is seen for the East component and stems largely from the ability of the DD strategy to resolve carrier-phase ambiguities to integers (Blewitt 1989). This is not possible for PPP in BSW5.2, but it has been shown to result in a 30 % improvement of the East component (Ge et al. 2008), which is clearly in agreement with this study. Although the PPP solution agrees well with the network DD one in all three components, there are some systematic differences between them. For example, at ONSA both the horizontal components (North and East) show short-term deviations (Fig. 3). These may be a result of the satellite orbit and clock, as well as the Earth rotation products applied during processing or may stem from insufficient modelling of systematic biases which is of particular importance for PPP. Also the inconsistent use of these models during product generation and their application during processing by users has resulted in such (Fu et al. 2012). However, there is no discernible bias in the PPP solution in the Up component.

3.2 Assessment of Combinations Using CATREF and GLOBK

To assess the implementation of CATREF at TCC UL, we combined eight IGS AC solutions. Each of these included different numbers of stations, ranging from 189 to 450. A key

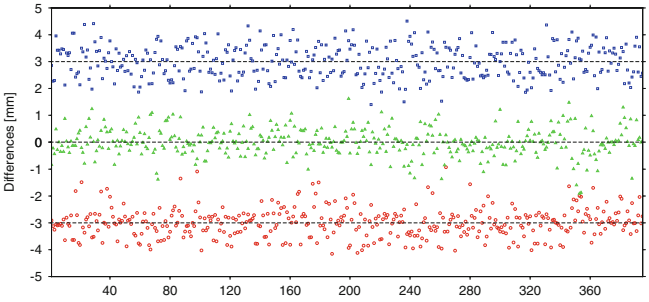

Fig. 4 Coordinate differences for 400 stations between CATREF/GLOBK combination of eight IGS AC solutions for December 2011. The differences are arranged *alphabetically* according to the IGS station four-character ID. *Green circles* represent the coordinate differences for the X, *red* for the Y and *blue* for the Z component. For clarity the Y and Z components are offset by 3 mm

aspect of the CATREF combination process is the selection of a realistic weight for each of the contributing ACs. For this, an a posteriori variance factor (scaling) is applied to all individual covariance matrices in an iterative way until both the individual and global variances are unity. Note that during this procedure outlier rejection is applied to those stations having a normalized position residual (raw residual divided by its observation a priori error) exceeding a threshold of five. In our case, three iterations were necessary to provide a refined estimation of variance factors free from the influence of outliers with respect to the threshold criteria.

We compare the individual transformation parameters of the eight IGS AC solutions that were used in our combination with the official IGS report section 5.3.1 for GPS week 1666.[2] The reported transformation parameters agree well, particularly in the translation parameters, not shown here.

Following our CATREF implementation, we have also generated an independent solution using the GLOBK software package by combining the same eight IGS AC solutions. The difference in the estimated Cartesian coordinates between the two packages is shown in Fig. 4. In this figure the differences are ordered *alphabetically* according to the IGS station four-character ID. There are neither systematic variations nor a bias visible in the figure. We calculated RMS values of 0.5 mm, 0.5 mm, and 0.6 mm for the X, Y and Z components, respectively.

After rearranging the coordinate differences *regionally* according to the station nine-character DOMES number, we plotted them again, see Fig. 5. We can now see clear systematic variations in the differences. Furthermore it is suggested that small biases between the combined solutions of the two software packages exist. For example, the coordinate differences between points 80 and 170 show those stations located in North America. If we only take their differences

[2] http://igscb.jpl.nasa.gov/pipermail/igsreport/.

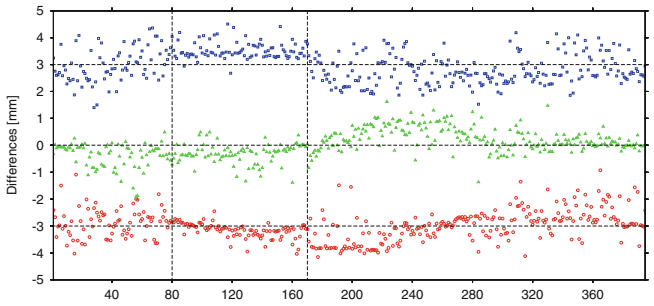

Fig. 5 Coordinate differences for 400 stations between CATREF/GLOBK combination of eight IGS AC solutions for December 2011. The differences are arranged *regionally* according to the station nine-character DOMES number. For example, the coordinate differences between points 80 and 170 (the two *vertical dotted lines*) show those stations located in North America. *Green circles* represent the coordinates differences for the X, *red* for the Y and *blue* for the Z component. For clarity the Y and Z components are offset by 3 mm

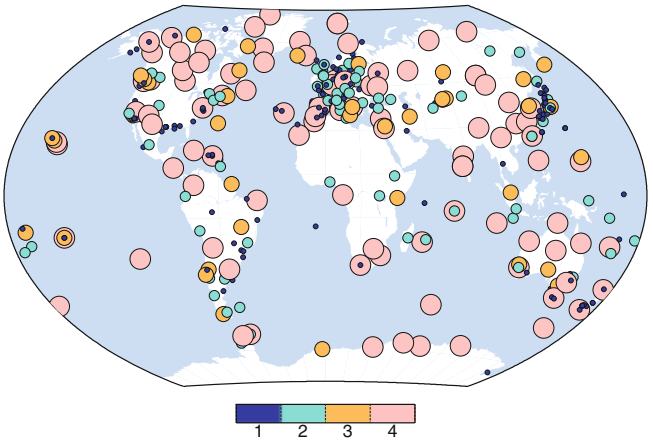

Fig. 6 The number of TACs per site for the GPS week 1,666 combination

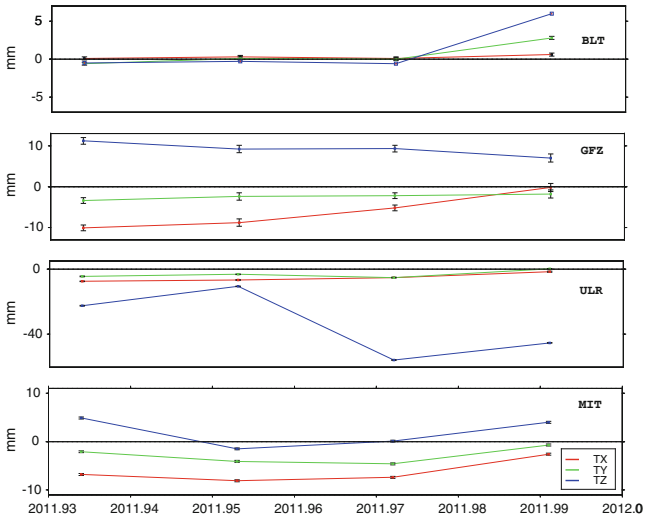

Fig. 7 Translation parameters time series between BLT, GFZ, ULR and MIT solutions and the combined solution for the test period in December 2011 with error bars. The X-axis is in decimal year that corresponds to the GPS week

we find RMS values of 0.3 mm in all three components and biases of 0.3 mm in both X and Y components, and 0.5 mm in the Z component. Although these sub-millimetre coordinate differences may be negligible, their impact should be further investigated based on multi-year combination results.

This study confirms that the two independent combinations as implemented by the TCC at UL agree at the one millimetre level and demonstrates that either of the two independent software packages may be used by the TCC. However, there is a significant advantage of GLOBK over CATREF in terms of processing time.

3.3 Results: TIGA Combination

We present the results of the TIGA combination using three TACs solution and the solution from the IGS AC at MIT for GPS Weeks 1665–1668. Figure 6 shows the number of common stations available for this test period in December 2011. This figure indicates that there are more overlapping stations between the TACs compared to previous TIGA solutions (Schöne et al. 2009). One of the requirements for TIGA reprocessing is that TACs include all IGb08 core stations.

Figure 7 depicts the Helmert transformation parameters between the individual TAC and the combined solutions. The error bars plotted in this figure are 1-sigma standard errors of the Helmert transformation parameters. The transformation parameters are indicative of the influence of each individual solution on the combined solution and thus traditionally are used as precision indicators for the combined solution. Except for the Z translation parameter from ULR, the results show consistency of the individual solution on a weekly basis. The inconsistency in ULR's Z translation parameter may stem from their dynamic station selection, which changes on a daily basis (Wöppelmann et al. 2009). However, it is difficult to draw any firm conclusions based on only a four-week test period.We note that the TIGA combination is particularly beneficial compared to the IGS combination for sea level studies. This is because the TAC SINEX files contain non-IGS GPS stations that are near or at tide gauges as well as more South American stations compared to the IGS AC SINEX files.

4 Conclusions

In this study we have presented preliminary results from the BLT reprocessing, a comparison of two independent combinations using software packages CATREF and GLOBK, and

a first TIGA combination for December 2011. Attempting to exploit the complete TIGA archive, an initial processing using PPP has identified a series of issues with non-IGS station log files that restricted recovering important components of station information. After resolving these and inconsistencies between station log files and RINEX header information, accurate a priori coordinates for non-IGS stations were estimated.

The comparison of the two combination software packages revealed millimetre-level agreement in the coordinates of 400 stations. However, the coordinate differences exhibit regionality, with regional variations in scatter and biases. An issue that requires further investigation for long-term combinations.

Our study has generated a preliminary TIGA combination from three TAC solutions for December 2011. To improve the number of overlapping stations, we have incorporated the IGS AC solution from MIT. Our implementations have shown that a weekly combined solutions can be carried out either with CATREF or GLOBK and confirm that the two independent packages agree to within ± 1 mm. However, in terms of computation time, GLOBK outperforms CATREF. A combined solution can provide results for a larger number of stations in a single consistent reference frame than any of the individual TACs may be able to. This holds true even for stations contributed by a single TAC but at a loss of reliability. As more TAC solutions become available, the TIGA combinations will also able to identify any inconsistencies between different individual solutions as evidenced from the well established IGS combination. This would deliver the full potential of a TIGA combination, i.e. to provide time series of vertical land movements at or close to tide gauges for sea level studies in a well defined global reference frame.

Acknowledgements The computational resources used in this study were provided by the High Performance Computing Facility at the University of Luxembourg, Luxembourg. The IGS and its ACs are highly appreciated for their data, products and solutions. We are especially thankful to the TIGA data providers and the SONEL archive, and acknowledge the contributions from three anonymous reviewers.

References

Altamimi Z, Sillard P, Boucher C (2002) A new release of International Terrestrial Reference Frame for Earth science applications. J Geophys Res 107(B10):2214. Doi:10.1029/2001JB000561

Blewitt (1989) Carrier phase ambiguity resolution for the global positioning system applied to geodetic baselines up to 2000 km. J Geophys Res 94(B8):10,187–10,203. Doi:10.1029/JB094iB08p10187

Dach R, Hugentobler U, Fridez P, Meindl M (2007) Bernese GPS Software Version 5.0. Technical Report, Astronomical Institute, University of Bern, Switzerland

Dong D, Herring T, King R (1998) Estimating regional deformation from a combination of space and terrestrial geodetic data. J Geod 72:200–214. Doi:10.1007/s001900050161

Fu Y, Freymueller J, van Dam T (2012) The effect of using inconsistent ocean tidal loading models on GPS coordinate solutions. J Geod 86:409–421. Doi:10.1007/s00190-011-0528-1

Ge M, Gendt G, Rothacher M, Shi C, Liu J (2008) Resolution of Gps carrier-phase ambiguities in Precise Point Positioning (PPP) with daily observations. J Geod 82:389–399. Doi:10.1007/s00190-007-0187-4

Herring T, King R (2006) GLOBK Reference Manual: Global Kalman filer VLBI and GPS analysis program release 10.3. Technical report, Department of Earth, Atmospheric, and Planetary Science, Massachusetts Institute of Technology, Cambridge

Petit G, Luzum B (2010) IERS Technical Note no 36., IERS Convention Centre. Technical report, Frankfurt am Main: Verlag des Bundesamts für Kartographie und Geodäsie

Rebischung P (2012) IGb08: an update on IGS08. http://igscb.jpl.nasa.gov/pipermail/igsmail/2012/006655.html

Rudenko S, Schön N, Uhlemann M, Gendt G (2013) Reprocessed height time series for GPS stations. Solid Earth 4:23–41. Doi:10.519/se-4-23-2013

Schöne T, Schön N, Thaller D (2009) IGS tide gauge benchmark monitoring pilot project (TIGA): Scientific benefits. J Geod 83:249–261. Doi:10.1007/s00190-008-0269-y

Steigenberger T, Rothacher M, Dietrich R, Fritsche M, Rülke A, Vey S (2006) Reprocessing of a global GPS network. J Geophys Res 111(B05):200–214. Doi:10.1029/2005JB003747

Teferle F, RM B, Williams S, Baker T, Dodson A (2006) Using continuous GPS and absolute gravity to separate vertical land movements and changes in sea level at tide gauges in the UK. Philos Trans Roy Soc 364:917–930. Doi:10.1098/rsta.2006.1746

Wöppelmann G, Martín Míguez B, Bouin M, Altamimi Z (2007) Geocentric sea-level trend estimates from GPS analyses at relevant tide gauges world-wide. Global Planet Change 57:396–406. Doi:10.1016/j.gloplacha.2007.02.002

Wöppelmann G, Letetrel C, Santamaria-Gómez A, Bouin M, Collilieux X, Altamimi Z, Williams S, Martín Míguez B (2009) Rates of sea-level change over the past century in a geocentric reference frame. Geophys Res Lett 36:L12607

The King Edward Point Geodetic Observatory, South Georgia, South Atlantic Ocean

A First Evaluation and Potential Contributions to Geosciences

F.N. Teferle, A. Hunegnaw, F. Ahmed, D. Sidorov, P.L. Woodworth, P.R. Foden, and S.D.P. Williams

Abstract

During February 2013 the King Edward Point (KEP) Geodetic Observatory was established in South Georgia, South Atlantic Ocean, through a University of Luxembourg funded research project and in collaboration with the United Kingdom National Oceanography Centre, British Antarctic Survey, and Unavco, Inc. Due to its remote location in the South Atlantic Ocean, as well as being one of few subaerial exposures of the Scotia tectonic plate, South Georgia Island has been a key location for a number of global monitoring networks, e.g. seismic, geomagnetic and oceanic. However, no permanent geodetic monitoring station has been established previously, despite the lack of observations from this region. In this study we will present an evaluation of the GNSS and meteorological observations from the KEP Geodetic Observatory for the period from 14 February to 31 December 2013. We calculate multipath and positioning statistics and compare these to those from IGS stations using equipment of the same type. The on-site meteorological data are compared to those from the nearby KEP meteorological station and the NCEP/NCAR reanalysis model, and the impact of these data sets on integrated water vapour estimates is evaluated. We discuss the installation in terms of its potential contributions to sea level observations using tide gauges and satellite altimetry, studies of tectonics, glacio-isostatic adjustment and atmospheric processes.

Keywords

Global Navigation Satellite Systems • King Edward Point Geodetic Observatory • South Atlantic Ocean • South Georgia Island

1 Introduction

During February 2013 the King Edward Point (KEP) Geodetic Observatory was established in South Georgia, South Atlantic Ocean, through a collaboration between the University of Luxembourg, National Oceanography Centre, and the British Antarctic Survey. Unavco, Inc supported the project by procuring and configuring the equipment. The primary objectives of the observatory are to measure crustal movements close to the tide gauge at KEP using a state-of-the-art autonomous, continuous Global Navigation Satellite System (GNSS) station and to establish a network of stable benchmarks to provide a long-term vertical datum at KEP research station.

With its remote location, South Georgia is one of few land areas in the ocean-dominated Southern Hemisphere, which can be employed to densify the global geodetic infrastructure and counteract the hemisphere imbalance in ground-based observations (Fig. 1a). Although KEP research station hosts

F.N. Teferle (✉) • A. Hunegnaw • F. Ahmed • D. Sidorov
Geophysics Laboratory, University of Luxembourg, Luxembourg L-1359, Luxembourg
e-mail: norman.teferle@uni.lu

P.L. Woodworth • P.R. Foden • S.D.P. Williams
National Oceanography Centre, Joseph Proudman Building, 6 Brownlow Street, Liverpool L3 5DA, UK

© Springer International Publishing Switzerland 2015

C. Rizos, P. Willis (eds.), *IAG 150 Years*, International Association of Geodesy Symposia 143,
DOI 10.1007/1345_2015_175

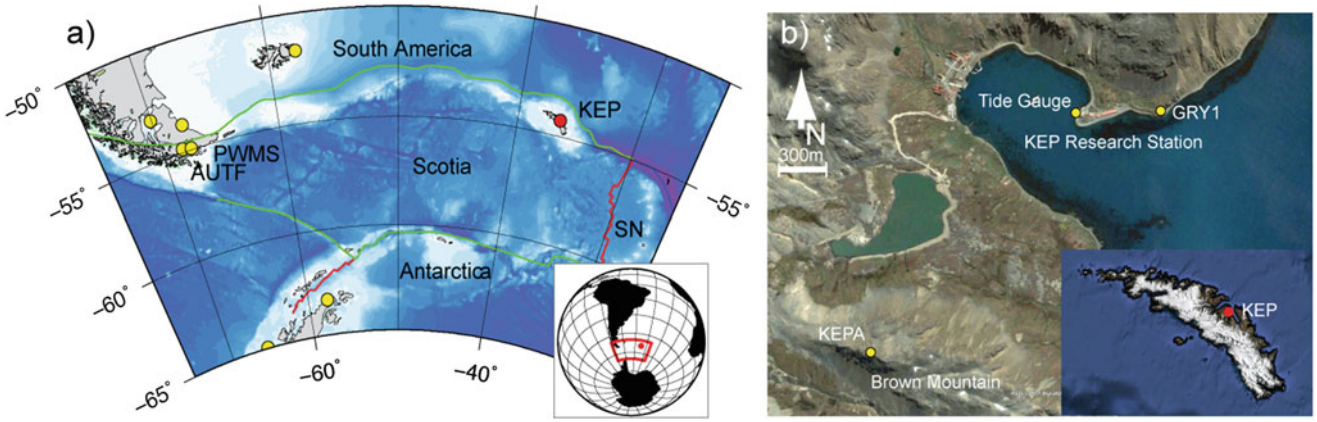

Fig. 1 (**a**) Location of King Edward Point (KEP – *red circle*), South Georgia and tectonic plates in the South Atlantic Ocean (SN denotes the South Sandwich Plate). The plate boundaries include transforms/fracture zones (*green*), ridges (*red*), and trenches (*blue*) according to Smalley et al. (2007). Existing continuous GNSS stations are shown as *yellow circles*. (**b**) Locations of KEPA continuous and GRY1 campaign GNSS stations, and of the tide gauge with respect to KEP research station. Imagery from Google Earth

instruments for a number of global monitoring networks, e.g. the seismic (IRIS 2011), geomagnetic (Harris et al. 2011) and oceanic (IOC 2012) networks, no permanent geodetic monitoring station has been established previously despite the lack of observations from this region. It is noteworthy that the Scientific Committee of Antarctic Research (SCAR) established the campaign Global Positioning System (GPS) station GRY1 near KEP research station (Fig. 1b) and observed it for 2 days during 1998 (Dietrich et al. 2001). However, no re-occupation has been carried out. Hence, with the large number of GNSS applications in the geosciences today, the importance of establishing and maintaining a continuous GNSS station on South Georgia Island, which follows the recommendations of the International GNSS Service (IGS) (Dow et al. 2009), cannot be underestimated.

Besides the application to sea level research the first crustal movement estimates from the KEP Geodetic Observatory (KEPGO) will provide valuable information on present-day geophysical processes. South Georgia Island is one of few subaerial exposures of the Scotia plate (Fig. 1a). The only two other continuous GNSS stations on this largely oceanic plate are those in Ushuaia, Argentina (AUTF) and Puerto Williams, Chile (PWMS) (Smalley et al. 2003). Although information from geology, geophysics, seismology and satellite altimetry has led to a reasonable understanding of the Scotia Sea tectonic evolution (Barker 2001), i.e. it is expected that the northern edge of the Scotia plate forms a left lateral transform with the South American plate, which has a transform rate of approximately 7 mm/year (Thomas et al. 2003), there is still an incomplete understanding of the tectonic history of South Georgia and its associated shelf areas (Smalley et al. 2007). Furthermore, the recent study by Graham et al. (2008) revealed that the entire shelf area has been glaciated to the edges during the Cenozoic. Although it is believed that the glaciation and deglaciation cycles may have occurred several times, it is not clear if the shelf was covered during the Last Glacial Maximum (Bentley et al. 2007; Gordon et al. 2008). Hence, both regional and global glacial isostatic adjustment models may benefit from additional constraints from GNSS observations on South Georgia Island.

Besides the GNSS station the observatory also operates a weather station, which records a number of atmospheric variables in order to derive accurate integrated water vapour (IWV) estimates (Bevis et al. 1992). These meteorological observations together with the IWV products will contribute an important record of atmospheric conditions for South Georgia, potentially helping to improve local weather forecasts (Shanklin et al. 2009). Of particular interest will be the GNSS observations for monitoring of the ionosphere over this region, improving both spatial and temporal density of observations useful for ionospheric models, such as the SIRGAS (Sistema de Referencia Geocéntrico para Las Américas) Ionospheric Model (Brunini et al. 2013).

This paper introduces the KEP Geodetic Observatory and its continuous GNSS station. This is followed by an evaluation of the GNSS and meteorological measurements collected over the first 10 months of its operation.

2 KEP Geodetic Observatory

The KEP Geodetic Observatory consists of an autonomous, continuous GNSS station (4-char ID: KEPA and DOMES number: 42701M001) with auxiliary equipment on Brown Mountain, as well as benchmarks on Brown Mountain and at KEP research station (Fig. 1b). It employs a Trimble NetR9 GNSS receiver, a Trimble choke ring GNSS antenna with

Fig. 2 GNSS antenna and radome on 1-m mast (*left*) and aluminium pipe frame with electronics and auxiliary equipment (*right*)

the Dorne Margolin element (TRM59800.00), and a SCIS radome. The receiver records GPS, GLONASS and Galileo observations in two sessions with recording intervals of 1 and 15 s. The antenna and radome have been absolutely calibrated by the National Geodetic Survey (NGS) prior to installation (Bilich et al. 2012). KEPA is located on the highest point of Brown Mountain, which lies southwest of the research station. The GNSS antenna and monument are bolted onto a rock outcrop with an aluminium pipe frame housing the auxiliary equipment and enclosures approximately 30 m away (Fig. 2). A Vaisala WXT-520 weather station is attached to the top of the frame and temperature, pressure, wind speed and wind direction are fed into the GNSS receiver. The GNSS receiver telemeters to KEP research station via an Intuicom EB-1 900 MHz Ethernet two-way radio bridge, which is connected to the existing VSAT communication link. Due to bandwidth limitations of this satellite link, the download of the GNSS data can, for the foreseeable future, only be performed on a daily basis. Further details on equipment and configuration can be found in the technical report of the installation (Teferle 2013).

3 Results

This section presents the first results for data quality, position estimates and meteorological measurements for 14 February to 31 December 2013.

3.1 Data Quality

The standard tool within the IGS for the analysis of GNSS data quality is Teqc (Estey and Meertens 1999). It allows the computation of a number of quality control metrics of which the most important ones include code-multipath on L1 and L2, denoted as MP1 and MP2, and the number of cycle slips per observations. The latter ratio can be expressed in terms of cycle-slips-per-observations in 1000, leading to a number close to zero for the optimal case. Estey and Meertens (1999) described the computation of the MP1 and MP2 metrics in detail and here we use the root-mean-square value after fitting a moving average to the absolute multipath values. The computed metrics only partly reflect the multipath environment at a particular site because they dependent on the receiver type and the receiver settings. Hence, for the KEPA data quality evaluation we compare the above metrics only for stations using receivers of the same type and assume that none of the observation data have been filtered. At the time of this study Trimble NetR9 receivers were operated at 27 stations within the global IGS tracking network. Furthermore, CON2 and PHIG, two sites installed and operated by Unavco Inc. in Antarctica, use the same receiver and the same 1-m antenna mast as KEPA. For this evaluation only the Global Positioning System (GPS) data with a 30 s recording interval have been used.

Figure 3 depicts the time series of the quality control metrics MP1, MP2 and cycle-slips-per-observations for KEPA, CON2 and PHIG, and 27 IGS stations. It can be seen that the data quality of KEPA varies with the MP1 level being fairly high and the levels for the other two metrics being amongst the lowest. This is also shown by the medians for these metrics in the right panels, which have been sorted according to magnitude. Although at different levels, all three time series remain fairly constant over the first 10 months of operation and show no spikes, which does not hold true for many of the IGS stations. The cycle-slips-per-observations metric remains consistently low, so that it is hardly visible in the figure and KEPA outperforms all other stations in this metric, which confirms its largely undisturbed environment on top of Brown Mountain.

The MP1 time series for KEPA shows clear variations from mid-May until mid-October. These are also visible in the MP2 time series but to a much smaller degree. As the

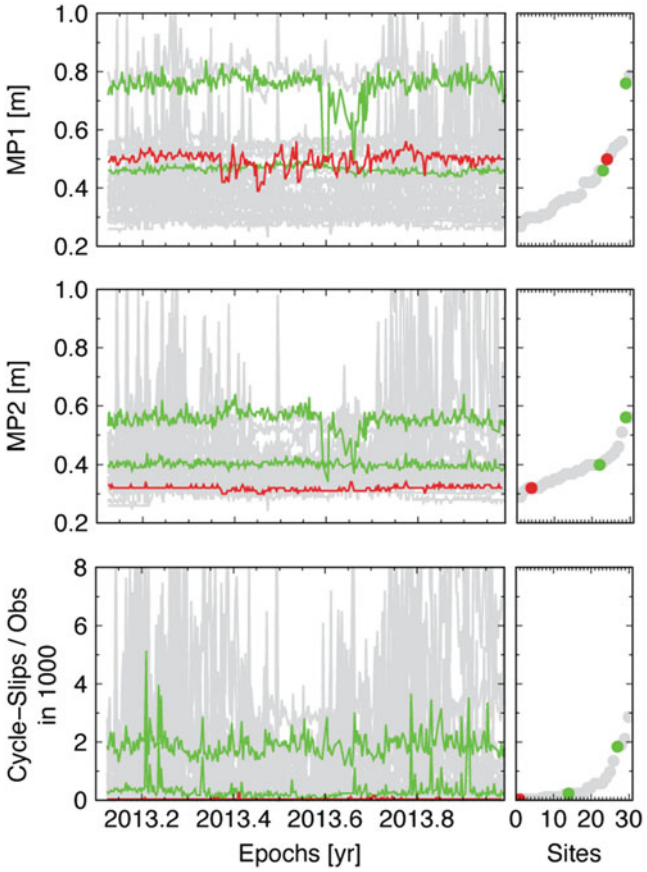

Fig. 3 Time series of quality control metrics MP1, MP2 and cycle-slips-per-observations in 1000 for 30 stations using a Trimble NetR9 receiver for 14 February to 31 December 2013. Shown are IGS stations (*grey*), CON2 (*bottom green*) and PHIG (*top green*) and KEPA (*red*). The panels on the *right* show the cumulative distribution of the medians for the quality control metrics for all stations

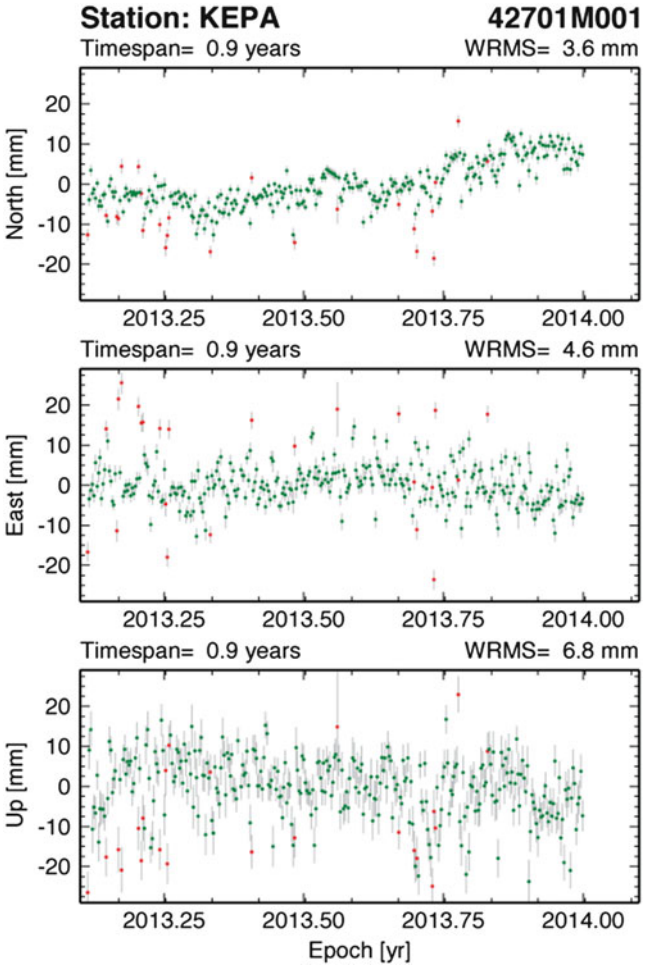

Fig. 4 Position time series for KEPA for 14 February to 31 December 2013. Position outliers are indicated by *red circles* and uncertainties are three times the daily standard error from the GPS processing

onset of these variations, i.e. the 16 May, coincides with the first snow cover during the 2013 Austral winter, it is believed that KEPA's multipath levels are susceptible to the local snow conditions, a circumstance which is already being exploited at other stations (Larson and Nievinski 2012). Unfortunately there are no official snow cover records for South Georgia to confirm this. In this study we inferred information on snow conditions from archived images taken by a webcam at KEP research station and as such, these only show the conditions at the research station and not on Brown Mountian.

Figure 3 also shows that KEPA's data quality metrics are nearly equivalent to CON2 and much better than PHIG. This suggests that not all of the apparent multipath effects at these stations are a consequence of the use of the 1-m mast, but that there is also be a strong station-specific environmental component.

3.2 Position Estimates

Using 27 IGS stations, CON2 and PHIG, and KEPA daily position estimates were obtained using the Bernese GNSS Software version 5.2 (Dach et al. 2007) in precise point positioning (PPP) mode for 14 February to 31 December 2013. We applied only GPS observations with an elevation cut-off angle of 10° and used the final satellite orbit and clock, as well as the Earth rotation products from the IGS analysis centre CODE (Centre for Orbit Determination in Europe). For more details on the processing strategy the reader is referred to Hunegnaw et al. (2014).

Figure 4 depicts the position time series for KEPA. The figure also indicates outlying (red) and accepted solutions (green) as well as the weighted root mean square (WRMS) as

computed from a linear trend fit. An outlier rejection criteria of three times the WRMS was applied and outlying solutions were removed in all three components. The WRMS statistics of 3.6 and 4.6 mm for the North and East components, respectively, are slightly larger than expected. However, the WRMS of the Up component is typical with a value of 6.8 mm. This is confirmed when comparing these to the mean WRMS and standard deviation computed for the other 29 stations: 2.1 ± 0.5 mm (North); 3.2 ± 0.9 mm (East); 6.1 ± 1.5 mm (Up). Furthermore, it is suggested that most outlying solutions can be associated with the North and East components.

Using azimuth and elevation information together with the MP1 metric, we found that the GNSS signals affected by multipath stem from satellites observed in an easterly to south-easterly direction with an elevation of less than 15°. Hence we identified the rocks shown in the right-hand foreground of Fig. 2 (left panel) as the source and attribute the larger scatter in the horizontal components to the apparent multipath. Although a preliminary double-difference solution seems to be less affected by the multipath, we will investigate ways to improve the data quality of the station.

Figure 4 does not show any station velocities as the timespan is too short to give any reliable values separated from potential seasonal signals. However, there is an indication of a positive velocity for the North and a negative one for the Up component. The East component does not indicate any long-term motion at this point.

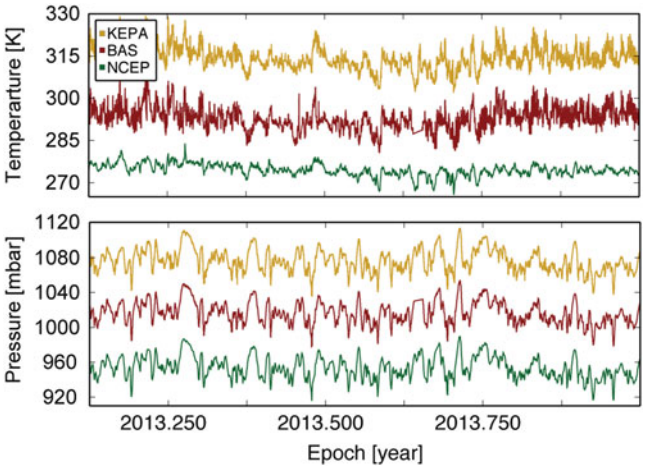

Fig. 5 Time series of temperature (*top*) and pressure (*bottom*) from KEPA and KEP research station (BAS) weather stations, and NCEP/NCAR reanalysis gridded data from 14 February to 31 December 2013. Time series are offset for clarity. The observations for KEPA are reported at 15 min and for BAS at hourly intervals. NCEP data are provided at 6-h intervals

Table 1 Median and RMS of differences in temperature and pressure computed for the meteorological observations from KEPA and KEP research station (BAS), and NCEP/NCAR reanalysis gridded data

	Temperature (K)		Pressure (hPa)	
	Median	RMS	Median	RMS
KEPA – BAS	−2.1	2.6	−0.2	0.9
KEPA – NCEP	−1.1	2.6	2.8	3.1
BAS – NCEP	0.6	3.4	3.0	3.3

3.3 Troposphere Estimates

We use the observations of the weather sensor of the KEP Geodetic Observatory and the automatic weather station at KEP research station, denoted as BAS, together with NCEP/NCAR reanalysis (Kalnay et al. 1996) gridded data to verify the meteorological observations (for briefness only temperature and pressure) and to evaluate the impact of these data sets on integrated water vapour (IWV) estimates. In order to do so we applied the standard barometric height correction to the observations from BAS to account for the height difference between the KEP research station and KEPA. Figure 5 shows the time series of air temperature and pressure for 14 February to 31 December 2013. Clearly visible are the excellent agreements between the observations themselves and the model values. Table 1 shows the median and root-mean-square (RMS) agreements for the differences in these meteorological data and the gridded information. Given the lower specifications of the KEPA weather sensor when compared to BAS, it can be argued that it performed well with median and RMS pressure differences of −0.2 and 0.9 hPa, respectively.

Accurate pressure information is critical for the conversion of GNSS-derived zenith tropospheric delay into IWV and an error in pressure of 1 hPa maps into an error in IWV of 0.36 kg/m^2. With the required accuracies for IWV estimates of 1–5 and 0.25–2.5 kg/m^2 for forecasting and climate monitoring applications (Barlag et al. 2004), respectively, the RMS statistics indicate, if the relative accuracies between these data sets are taken as absolute, that observations and gridded data agree fairly well, and that a IWV product computed using pressure values from KEPA would be within the ranges for the above meteorological applications.

4 Conclusions

The new King Edward Point (KEP) Geodetic Observatory and its KEPA GNSS station have been introduced and an initial evaluation has been performed. The data quality metrics for the first 10 months have been fairly stable and indicate that multipath effects are present with some sensibility to snow covering the ground. The number of cycle slips per observations are extremely low. The initial position estimates

from precise point positioning indicate a larger than average scatter in the daily solutions which has been attributed to the apparent multipath. Further tests will show to which extent more precise network solutions improve the position time series while ways to reduce the multipath are being investigated. The meteorological observations from the KEP Geodetic Observatory and KEP weather stations show excellent agreement, indicating that the former fulfills the GNSS meteorology requirements for forecasting and climate monitoring applications.

The KEP Geodetic Observatory is located in the geodetically under-sampled South Atlantic Ocean. Considering this and the general hemisphere imbalance in geodetic networks, the KEPA GNSS station has the potential to make an important contribution to a number of future studies besides its primary objectives of measuring crustal movements close to the KEP tide gauge and providing a long-term vertical datum for sea level studies.

Acknowledgements The authors would like to acknowledge numerous colleagues from the University of Luxembourg, National Oceanography Centre, British Antarctic Survey and the Government of South Georgia and the South Sandwich Islands for their support of the observatory. We are greatful to three anonymous referees whose constructive comments greatly improved the manuscript. The IGS and its analysis centers are thanked for providing GNSS data and products.

References

Barker PF (2001) Scotia Sea regional tectonic evolution: implications for mantle flow and palaeocirculation. Earth Sci Rev 55:1–39

Barlag S, De Haan S, Offiler D (2004) GPS meteorology user requirements version 1.0, Technical report, Targeting Optimal Use of GPS Humidity data in meteorology, COST-716

Bentley MJ, Evans DJA, Fogwill CJ, Hansom JD, Sugden DE, Kubik PW (2007) Glacial geomorphology and chronology of deglaciation, South Georgia, sub-Antarctic. Quatern Sci Rev 26(56):644–677

Bevis M, Businger S, Herring TA, Rocken C, Anthes RA, Ware R (1992) GPS meteorology: Remote sensing of atmospheric water vapour using the global positioning system. J Geophys Res 97:15787–15801

Bilich A, Schmitz M, Görres B, Zeimetz P, Mader G, Wübbena G (2012) Three-method absolute antenna calibration comparison. IGS Workshop 2012, Olsztyn, Poland, 23–27 July

Brunini C, Azpilicueta F, Gende M, Camilion E, Gularte E (2013) Improving SIRGAS ionospheric model. IAG Symposia 123:261–266

Dach R, Hugentobler U, Fridez P, Meindl M (eds) (2007) Bernese GPS Software Version 5.0, 612 pp. Astronomical Institute, University of Bern, Bern

Dietrich R, et al. (2001) ITRF coordinates and plate velocities from repeated GPS campaigns in Antarctica an analysis based on different individual solutions. J Geodesy 74(11–12):756–766. doi:10.1007/s001900000147

Dow JM, Neilan RE, Rizos C (2009) The International GNSS Service in a changing landscape of Global Navigation Satellite Systems. J Geodesy 83:191–198. doi:10.1007/s00190-008-0300-3

Estey L, Meertens C (1999) TEQC: The multi-purpose toolkit for GPS/GLONASS data. GPS Solutions 3(1):42–49

Gordon JE, Haynes VM, Hubbard A (2008) Recent glacier changes and climate trends on South Georgia. Global Planet Change 60(1–2):72–84

Graham AGC, Fretwell PT, Larter RD, Hodgson DA, Wilson CK, Tate AJ, Morris A (2008) A new bathymetric compilation highlighting extensive paleoice sheet drainage on the continental shelf, South Georgia, sub-Antarctica. Geochem Geophys Geosys 9(7):Q07011

Harris T, et al. (2011) South Georgia Magnetic Observatory. In: IUGG XXV General Assembly: Earth on the Edge: Science for a Sustainable Planet, Melbourne, Australia, 28 Juness–7 July 2011

Hunegnaw A, Teferle FN, Bingley RM, Hansen D (2014) Status of reprocessing and combinations at the British Isles continuous GNSS Facility and the University of Luxembourg TIGA Analysis Centre, IAG Symposia (this issue)

Incorporated Research Institutions for Seismology Consortium (2011) IRIS Annual Report, IRIS Consortium, Washington DC, 40 pp

IOC (2012) Global Sea-Level Observing System (GLOSS) Implementation Plan 2012, UNESCO/IOC, Intergovernmental Oceanographic Commission Technical Series No. 100, 41pp

Kalnay E, et al. (1996) The NCEP/NCAR 40-year reanalysis project. Bull Am Meteorol Soc 77:437–470

Larson K, Nievinski F (2012) GPS snow sensing: results from the EarthScope Plate Boundary Observatory. GPS Solutions 17:41–52. doi:10.1007/s10291-012-0259-7

Smalley R, et al. (2003) Geodetic determination of relative plate motion and crustal deformation across the Scotia-South America plate boundary in eastern Tierra del Fuego. Geochem Geophys Geosys 4(9):1070. doi:10.1029/2002GC000446

Smalley R, Jr, Dalziel IWD, Bevis MG, Kendrick E, Stamps DS, King EC, Taylor FW, Lauría E, Zakrajsek A, Parra H (2007) Scotia arc kinematics from GPS geodesy. Geophys Res Lett 34(21):L21308

Shanklin J, Moore C, Colwell S (2009) Meteorological observing and climate in the British Antarctic Territory and South Georgia: Part 1. Weather 64(5):127–134

Teferle, FN (2013) The King Edward Point Geodetic Observatory: Technical Report, pp 59, University of Luxembourg. Available at: http://hdl.handle.net/10993/5520

Thomas C, Livermore R, Pollitz F (2003) Motion of the Scotia Sea plates. Geophys J Int 155(3):789–804

The International DORIS Service (IDS): Recent Developments in Preparation for ITRF2013

Pascal Willis, Frank G. Lemoine, Guilhem Moreaux, Laurent Soudarin, Pascale Ferrage, John Ries, Michiel Otten, Jerome Saunier, Carey Noll, Richard Biancale, and Brian Luzum

Abstract

The International DORIS Service (IDS) was created in 2003 under the umbrella of the International Association of Geodesy (IAG) to foster scientific research related to the French DORIS tracking system and to deliver scientific products, mostly related to the International Earth rotation and Reference systems Service (IERS). We first present some general background related to the DORIS system (current and planned satellites, current tracking network and expected evolution) and to the general IDS organization (from Data Centers, Analysis Centers and Combination Center). Then, we discuss some of the steps recently taken to prepare the IDS submission to ITRF2013 (combined weekly time series based on individual solutions from several Analysis Centers). In particular, recent results obtained from the Analysis Centers and the Combination Center show that improvements can still be made when updating physical models of some DORIS satellites, such as Envisat, Cryosat-2 or Jason-2. The DORIS contribution to ITRF2013 should also benefit from the larger number of ground observations collected by the last generation of DGXX receivers (first instrument being onboard Jason-2 satellite). In particular for polar motion, sub-milliarcsecond accuracy seems now to be achievable. Weekly station positioning internal consistency also seems to be improved with a larger DORIS constellation.

Keywords

DORIS • International DORIS Service • Jason-2 • Polar Motion • Terrestrial Reference Frame

P. Willis (✉)
IGN, Direction de la Recherche et de l'Enseignement, Saint-Mandé, France

IPGP, UMR 7154, Gravimétrie et géodésie, Université Paris Diderot, Sorbonne Paris Cité, Paris, France
e-mail: pascal.willis@ign.fr; willis@ipgp.fr

F.G. Lemoine
GSFC, Greenbelt, MD, USA
e-mail: frank.g.lemoine@nasa.gov

G. Moreaux • L. Soudarin
CLS, Toulouse, France
e-mail: gmoreaux@cls.fr; lsoudarin@cls.fr

P. Ferrage
CNES, Toulouse, France
e-mail: pascale.ferrage@cnes.fr

J. Ries
U. Texas, Center for Space Research, Austin, TX, USA
e-mail: ries@csr.utexas.edu

M. Otten
ESA, Darmstaadt, Germany
e-mail: michiel.otten@esa.int

J. Saunier
IGN, Service de Geodesie et de Nivellement, Saint-Mande, France
e-mail: jerome.saunier@ign.fr

C. Noll
GSFC, CDDIS, Greenbelt, MD, USA
e-mail: carey.e.noll@nasa.gov

R. Biancale
CNES, Toulouse, France
e-mail: richard.biancale@cnes.fr

B. Luzum
USNO, Washington, DC, USA
e-mail: brian.luzum@usno.navy.mil

© Springer International Publishing Switzerland 2015

C. Rizos, P. Willis (eds.), *IAG 150 Years*, International Association of Geodesy Symposia 143,
DOI 10.1007/1345_2015_164

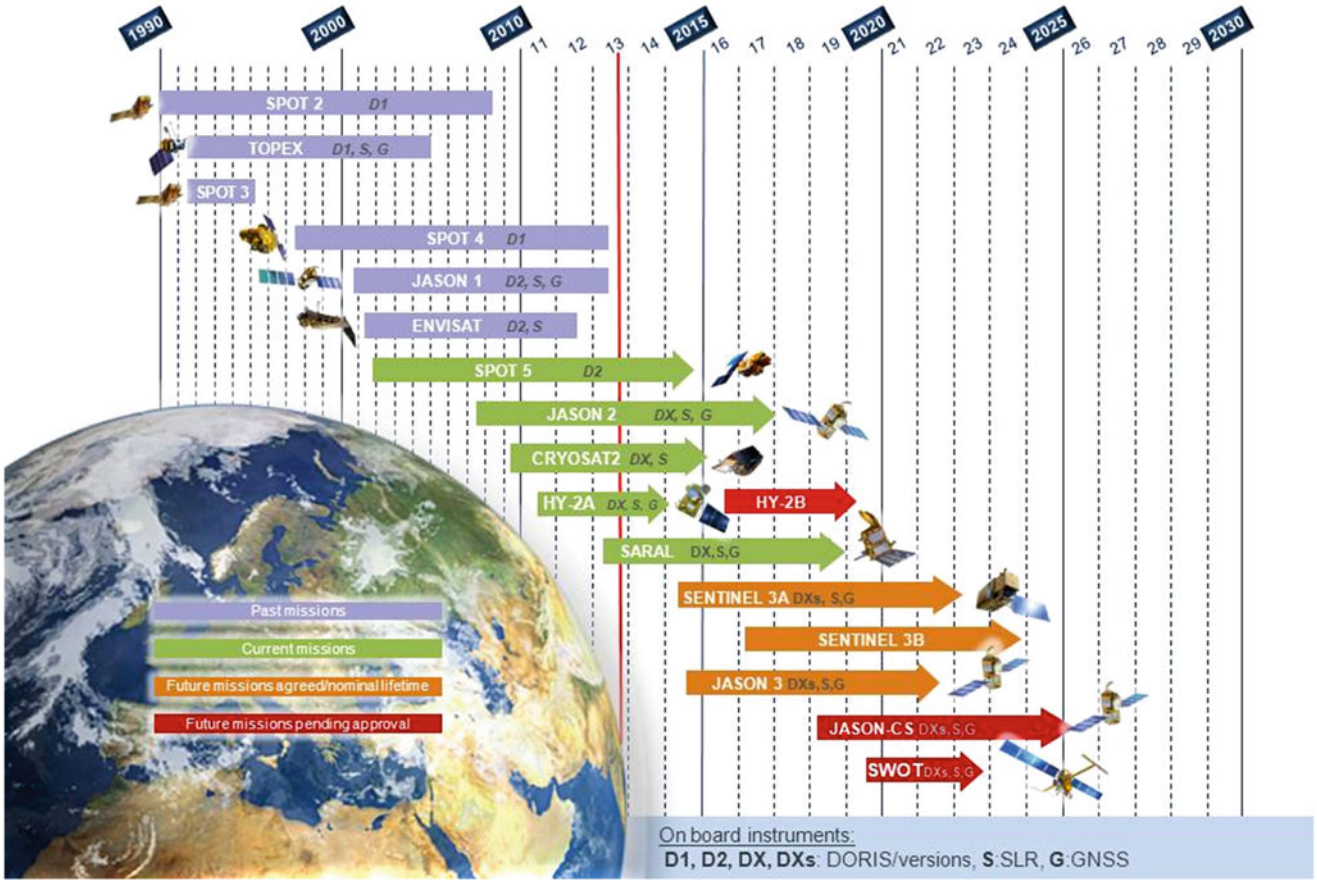

Fig. 1 Current DORIS satellite constellation (September 2013)

1 Introduction

Following a preliminary Pilot Project (Tavernier et al. 2002), an International DORIS Service (IDS) was created in 2003 to foster international scientific cooperation for geodesy and geophysics (Willis et al. 2010). DORIS is an acronym for Doppler Orbitography and Radiopositioning Integrated by Satellite. The goal of this paper is to present the first steps taken by the IDS groups in preparation for the next ITRF2013, to discuss new DORIS results, future improvements and possible limitations. We will present recent improvements related to the DORIS technique (evolution of the satellite constellation and ground infrastructure). Then, after a brief description of the current IDS organization, we will detail the current IDS plans in preparation for ITRF2013. Finally, we will provide a few examples showing areas where further improvements are still required.

2 DORIS Ground and Satellite Infrastructure

Unlike Global Navigation Satellite Systems (GNSS), the number of DORIS satellites changes with time as the main application of this system is Precise Orbit Determination (POD) for real-time (Jayles et al. 2010) or post-processing applications (Cerri et al. 2010; Lemoine et al. 2010) and not time and positioning on the Earth. As of September 2013, data from five DORIS satellites can be used for geodesy and geophysics through the IDS Data Centers, including the recent Chinese HY-2A satellite and the Indian Saral satellite, both launched for altimetry.

Figure 1 shows that more DORIS satellites should also be launched in the next few years. According to CNES, the DORIS system could maintain operations at least until 2026 (Ferrage, personal communication), if not 2030. It must also be noted that the most recent DORIS satellites now include

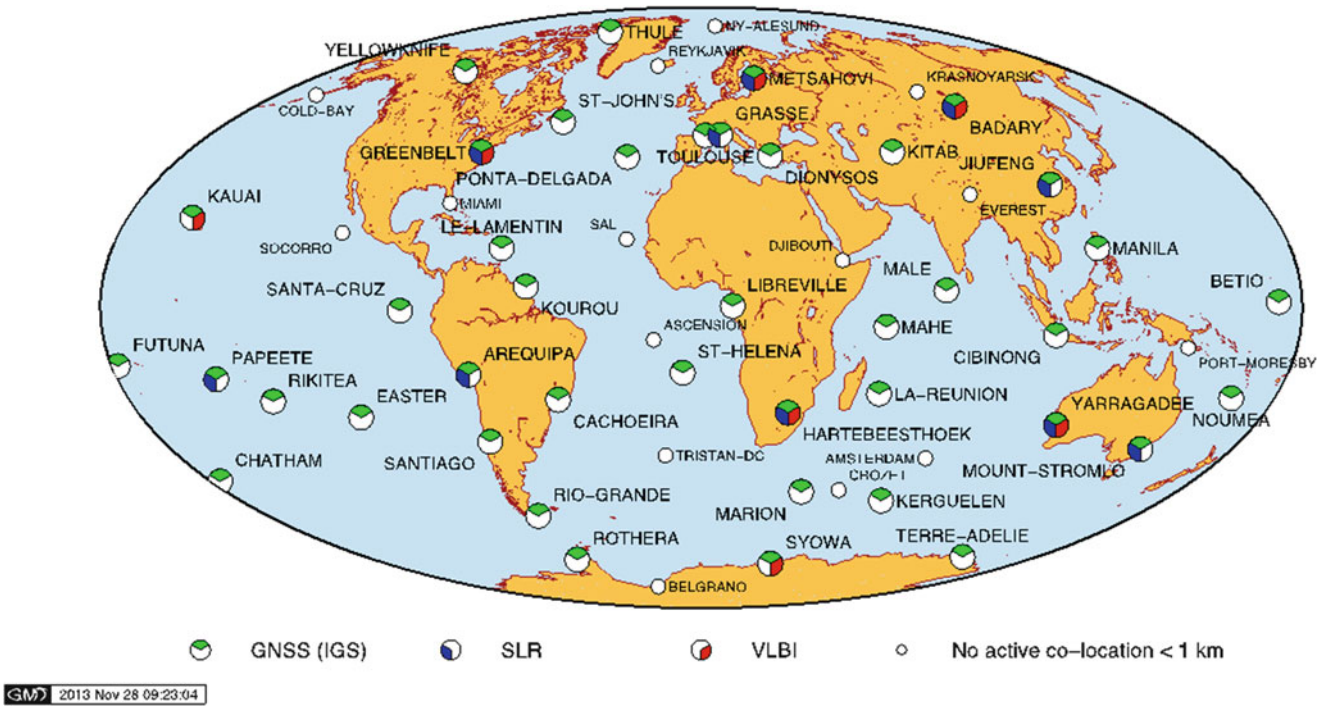

Fig. 2 Current DORIS tracking network and co-location with other geodetic space techniques (November 2013)

Table 1 Past and current IDS analysis centers

Analysis Center	Acronym	Country	Software package	Current status
ESA/ESOC	ESA	Germany	NAPEOS	Active
Geosciences Australia	GAU	Australia	GEODYN	Past
GeoForschungsZentrum	GFZ	Germany	EPOS	Proposed
NASA/GSFC	GSC	USA	GEODYN	Active
Geodetic Observatory of Pecny	GOP	Czech Rep.	Bernese	Active
IGN	IGN	France	GIPSY-OASIS	Active
INASAN	INA	Russia	GIPSY-OASIS	Active
CNES/CLS	LCA	France	GINS/DYNAMO	Active

onboard DGXX receivers, allowing a more robust tracking of the ground stations, thanks to their new multi-channel technology (Auriol and Tourain 2010). Up to seven DORIS ground tracking stations can be tracked simultaneously by each of the new satellites (instead of previously only one for SPOT-2,-3, -4 and TOPEX/Poseidon and later two for SPOT-5, Jason-1, and Envisat).

Since 1993, the DORIS ground tracking network has remained rather stable with time (Fagard 2006) with 50 to 60 operating stations. As displayed in Fig. 2, this network is geographically well distributed and also includes a large number of sites co-located with other space techniques such as Very Long Baseline Interferometry (VLBI), Satellite Laser Ranging (SLR) and GNSS, contributing and enhancing the development of the ITRF and its applications (Altamimi et al. 2005; Altamimi and Collilieux (2010)). For the ground equipment, only two types of DORIS antennae have been used. The Alcatel antennae, used initially, have now been all replaced with the Starec generation.

More information regarding these stations, such as the description of co-located instruments, for instance geodetic technique instruments but also absolute gravity and tide gauges, can be found in the electronic supplement of Willis et al. (2010) and also online through a GoogleEarth application developed by the IDS Central Bureau at http://ids-doris.org/network/googleearth.html).

3 International DORIS Service: Current Structure and Products

Like the other IAG Services, the IDS is organized as follows: several Analysis Centers (see Table 1) generating different scientific products, a Combination Center (at CLS)

Table 2 List of current IDS products (September 2013)

Product	Format	Frequency delivery	From Analysis Center	From Combination Center
Station coordinates	SINEX	Weekly	√	√
Earth Orientation Parameters	IDS	Weekly	√	√
Geocenter motion	IDS	Weekly	√	√
Orbits	sp3	Daily	√	
Reference frame	SINEX	Yearly	√	

combining these results, two Data Centers (at NASA/CDDIS and at IGN) archiving the different DORIS data and products (Noll 2010), a Central Bureau (CNES/CLS/IGN) providing day-to-day operations and in particular maintaining the IDS Web site (http://ids-doris.org), and a Governing Board giving long-term directions and ensuring regular contact with other entities such as the IAG, Global Geodetic Observing System (GGOS) and the IERS.

As of September 2013, six Analysis Centers (using 5 different software packages) plan to participate in the IDS combination, providing weekly time series of station positions with full covariance information in SINEX format with either normal equations or as loosely constrained solutions with full covariance information. These six individual contributions will be merged by the IDS Combination Center (Valette et al. (2010)), providing a unique DORIS time series, which would then be used by the ITRF Combination Centers (Altamimi et al. (2011); Seitz et al. 2012) to realize the future ITRF2013 solution, in conjunction with similar combinations provided by VLBI, SLR and GNSS.

Table 2 displays the different products generated for the IDS by the Analysis Centers (ACs) and/or by the Combination Center.

DORIS can also provide other types of scientific results such as precise orbit determination, as discussed before, as well as tropospheric Zenith Total Delays (ZTDs), as recently shown by Bock et al. (2010) and Stepanek et al. (2010).

4 Plans Towards ITRF2013

Almost all Analysis Centers plan to use the most recent EIGEN-6S2 gravity field (Förste et al. (2012); Rudenko et al. submitted), which augments a new static field with annual fits to time variable gravity coefficients derived from the GRACE mission (Tapley et al. (2004)) or from SLR data outside this period of time (Cerri et al. (2013)). As proposed for ITRF2008, solar radiation reflectivity scaling factors or improved macromodels will be used for all DORIS satellites when modeling the radiation pressure accelerations (Gobinddass et al. (2009); Le Bail et al. (2010)) and an atmospheric drag parameter will be estimated more frequently (every 30 min to 8 h, depending on the satellite altitude and on the daily values of the geomagnetic indices) (Gobinddass et al. (2010); Stepanek et al. (2010)). The implementation of the satellite attitude laws in POD software has been re-verified by some analysis centers. The periodic changes in the solar array pitch of the SPOT-5 satellite after 22 January 2008, as previously detected in Gobinddass et al. (2009) are also now explicitly accounted for, following new information available from CNES (ftp://ftp.ids-doris.org/pub/ids/satellites/DORISSatelliteModels.pdf). Problems related to some DORIS data sets were also recently corrected: timetagging for Envisat, South Atlantic Anomaly (SAA) effects on SPOT-5 oscillator (Stepanek et al. (2013)).

Some problems that were not previously detected and which affected the ITRF2008 solutions are now solved. As an example, Fig. 3 shows that some DORIS Analysis Centers did not handle properly the frequency offsets between the actual frequency of the transmitted signal at 2GHz by the beacons and its nominal value (2.03625 GHZ). The error, which resulted from using standard station frequency value, was corrected by modifying the partial derivatives for bias estimation. This error mostly affected the estimated station height, introducing discontinuities in some of the AC solutions, which were consequently propagated into the combined solution as well as in the ITRF2008.

As shown in Fig. 3, the new solutions do not display any discontinuity related to a change in ground oscillator frequency, while the previous solutions used in preparation of ITRF2008 were affected by a large discontinuity. This problem is now solved and consequently should not affect the IDS combination, nor the future ITRF2013 solution.

5 Early Results Towards ITRF2013

In preparation for ITRF2013, intensive comparisons were made by all Analysis Groups under the direction of the Analysis Coordinator (Frank Lemoine). Some of the orbit comparisons for all satellites were made and some of them demonstrated deficiencies for some of the Analysis Centers. In preparation for ITRF2013, more detailed tests were also performed for some of the DORIS orbit parameters, especially the once-per-revolution (OPR) empirical accelerations, usually estimated once per day for each satellite. The magnitude of the empirical accelerations reflects the quality of the non-conservative force modeling and can be

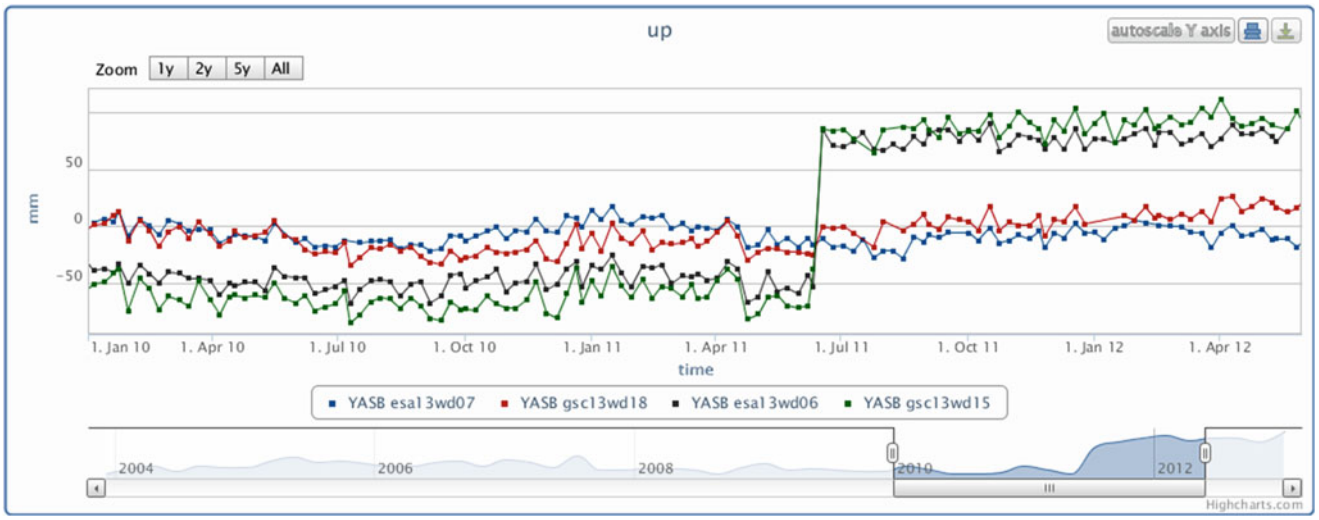

Fig. 3 Time series of weekly station height determination for Yarragadee station: two solutions used for ITRF2008 and their current preliminary solutions for ITRF2013 (using Plottool). Previous esawd08 (in *green*) and gscwd06 (in *black*) show a clear discontinuity, coming from a data processing artifact

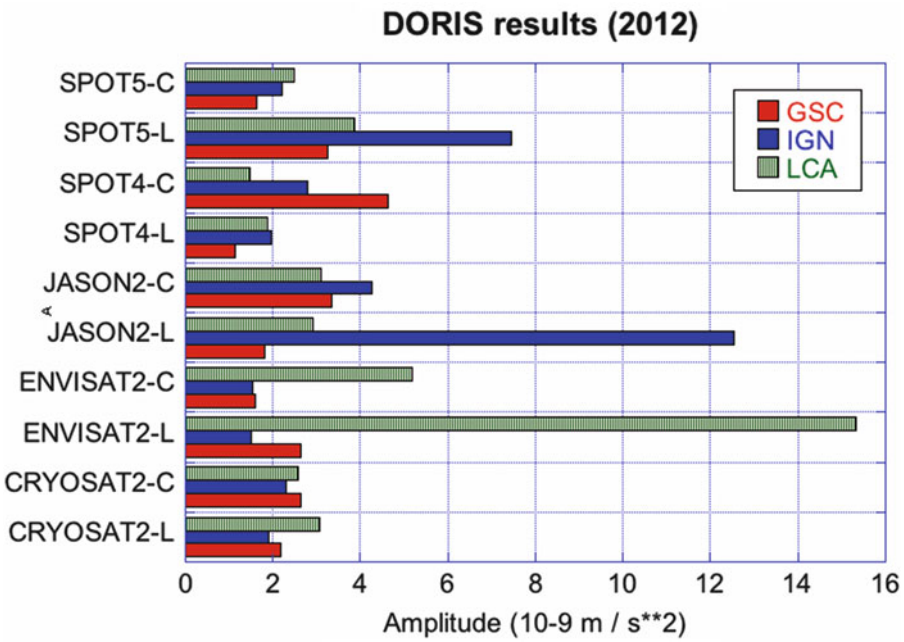

Fig. 4 RMS of DORIS empirical parameters (once-per-revolution) estimated by satellite (in 2012), cross-track (C), and along-track (L)

used to identify problems in the satellite force models used in the data processing. This is important for the quality of the DORIS results as previous studies demonstrated that errors in non-conservative force models can map into errors in the geodetic results such as TZ-geocenter or the height of high latitude stations. These errors can appear with strong signals at the satellite draconitic (solar beta-prime) periods, when large values of the OPR try to mitigate deficiencies in the solar radiation pressure modeling (Willis et al. (2006)). The estimation of a cross-track empirical once-per revolution (OPR) acceleration has been a standard practice in POD analysis for altimeter satellites or by DORIS analysis centers (e.g. Le Bail et al. (2010); Lemoine et al. (2010); Zelensky et al. (2010); Cerri et al. (2010)). However, this parameter is not always well-determined and appears to weaken the DORIS coordinate solutions in certain satellites. For this reason, some ACs decided to avoid estimating the cross-track OPR as was the practice for all previous ITRF solutions (including ITRF2008).

Figure 4 summarizes for 2012 the RMS daily amplitude of the along-track and cross-track accelerations for the DORIS satellites processed by the GSC, IGN, and LCA analysis

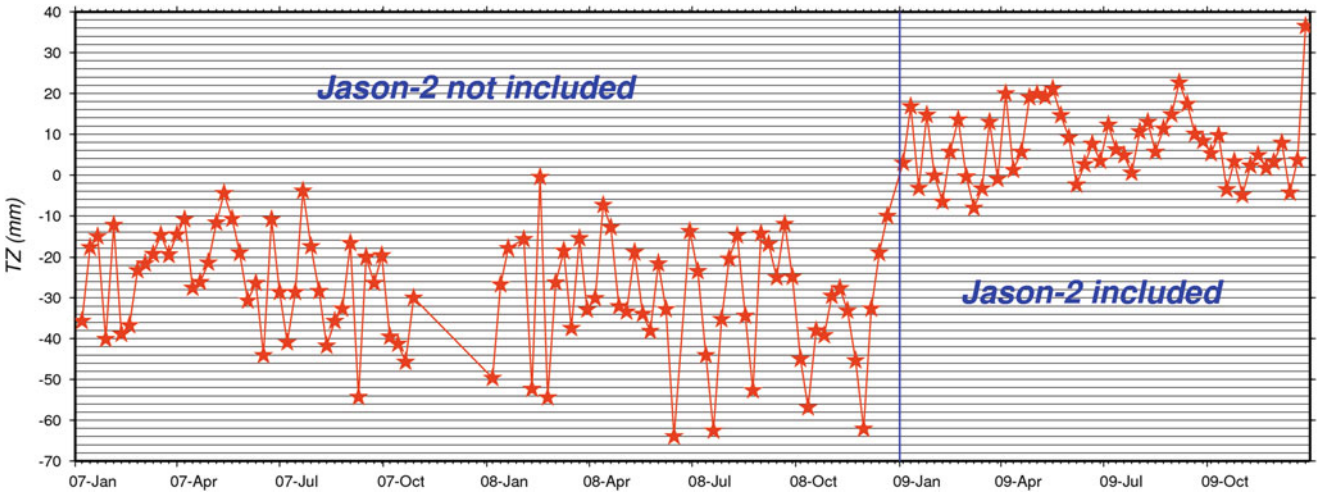

Fig. 5 TZ-geocenter weekly comparisons between the preliminary IDS combined weekly solution and the ITRF2008. *Vertical line* in *blue* corresponds to a change in the DORIS constellation

centers. Some modeling problems are still evident in these statistics: e.g., Envisat for LCA, Jason-2 and SPOT-5 for IGN. It can also be seen that the groups that perform better for these satellites may not perform as well for other satellites. Systematic inter-comparisons of results between groups and open discussions should help to resolve such disparities in performance, allowing all groups to provide the best possible results by the end of this verification phase. Early discussions already allowed some groups to identify and to resolve modeling issues for some satellites.

However, other problems are also common to all groups and may be more difficult to solve. For example, Fig. 5 shows that a significant jump can be seen in the DORIS results for Tz translation (from the combined solution) when the new Jason-2 data are introduced. A more detailed analysis showed that all groups observe this feature. This apparent discontinuity in Tz has two origins: (1) From the end of the availability of DORIS on TOPEX/Poseidon (in November 2004), as Jason-1 was not included in the weekly solutions due to the sensitivity of its Ultra Stable Oscillator (USO) to radiation in the SAA region, Jason-2 was the first satellite with a different orbit plane (66° of inclination compared to 98° for the rest of the DORIS constellation at that time); (2) Jason-2 is the first satellite with the so-called DORIS receiver on board that can track up to seven beacons simultaneously (compared to one for SPOT-2-4 and two for SPOT-5 and Envisat). We interpret this change – a better centering of the Tz parameter of the combination solution – as beneficial, and thus it motivated the DORIS ACs to consider the inclusion of Jason-1 from November 2004 to July 2008. The Jason-1 DORIS data will be processed with the SAA data correction provided by Lemoine and Capdeville (2006), where the Jason-1 station data most affected by the SAA will be down-weighted or excluded from the combination.

We also observe impacts on the Earth orientation parameters such as polar motion, when data from the new DORIS satellites (Jason-2, Cryosat-2, HY-2A) are added to the weekly solutions. We compare in Fig. 6 the differences in the computed EOP values with the IERS C04 series (Bizouard and Gambis 2009). The series was provided by the ESA analysis center and represents a step in the development of that analysis center's contribution to the IDS combination for ITRF2013. The largest EOP discrepancies occur prior to 2002 – before SPOT-5 and Envisat started providing data. A noticeable improvement occurs especially for the Xpole after the addition of Jason-2. The mean and standard deviation of the differences are given in Table 3 for the different time periods.

This improvement is due after 2008 to the large increase in the amount of data available with the new DGXX receiver onboard Jason-2 (typically 8,000 data points per day for SPOT-5 or Envisat but 17,000 for Jason-2). We note an improvement in the standard deviation of the differences with IERS C04 after the addition of each new satellite with a DGXX receiver.

The improvement in precision due the increase of DORIS data can also be seen when looking at geodetic station positioning. As shown in Fig. 7, DORIS station position consistency regularly improves with time, when considering the gscwd23 weekly soution, which is an improved GSFC weekly solution compared to the solution submitted before by this group in view of ITRF2008 (Le Bail et al. (2010)). In Fig. 7, vertical bars indicate epochs of changes in the DORIS constellation.

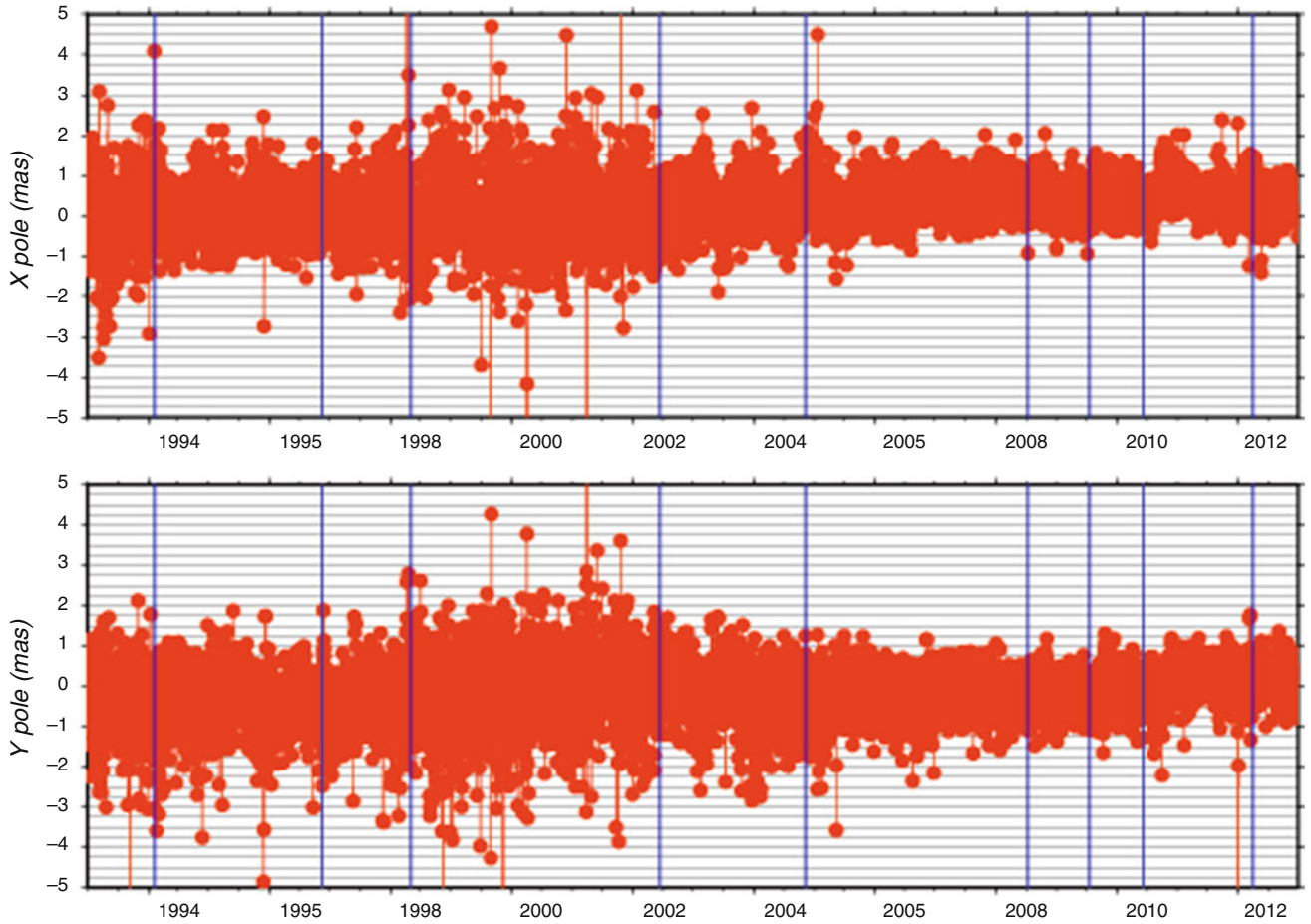

Fig. 6 Polar motion daily difference between the gscwd23 combined weekly solution and IERS C04 series. *Vertical lines* in *blue* correspond to changes in the DORIS constellation

Table 3 Time evolution of polar motion differences between the esawd08 weekly solution and IERS C04 series

Period	Number of DORIS satellites	X pole mean/std (in mas)	Y pole mean/std (in mas)
2000-001 to 2002-160	3	0.292/2.609	0.207/1.449
2002-167 to 2004-312	5 (+Envisat + SPOT-5)	0.270/2.111	−0.177/1.009
2004-319 to 2008-195	4 (-TOPEX/Poseidon)	0.197/1.958	0.106/0.902
2008-202 to 2010-150	5 (+Jason-2)	0.273/0.882	0.237/0.521
2010-157 to 2011-275	6 (+Cryosat-2)	0.283/0.545	0.202/0.374
2011-282 to 2012-152	7 (+HY-2A)	0.384/0.398	0.292/0.343

Some statistics are also provided for these results in Table 4, where the increasing number of available DORIS satellites continuously improves the geodetic results, as discussed before in Willis (2007). Major differences are due to the availability of the new Envisat and SPOT-5 data in mid-2002, the end of TOPEX data in 2004 (which surprisingly seems to improve results at that time) and the availability of the new Jason-2 data in late 2008.

Other improvements are also under consideration in preparation of ITRF2013, such as the use of antenna phase laws corrections for the Alcatel and Starec antennae, equivalent to the GPS phase center corrections, but only showing an elevation dependency due to the nature of the DORIS transmitting antennae. Possible use of the most recent DORIS data provided by the HY-2A and Saral satellites is also under consideration by different DORIS ACs.

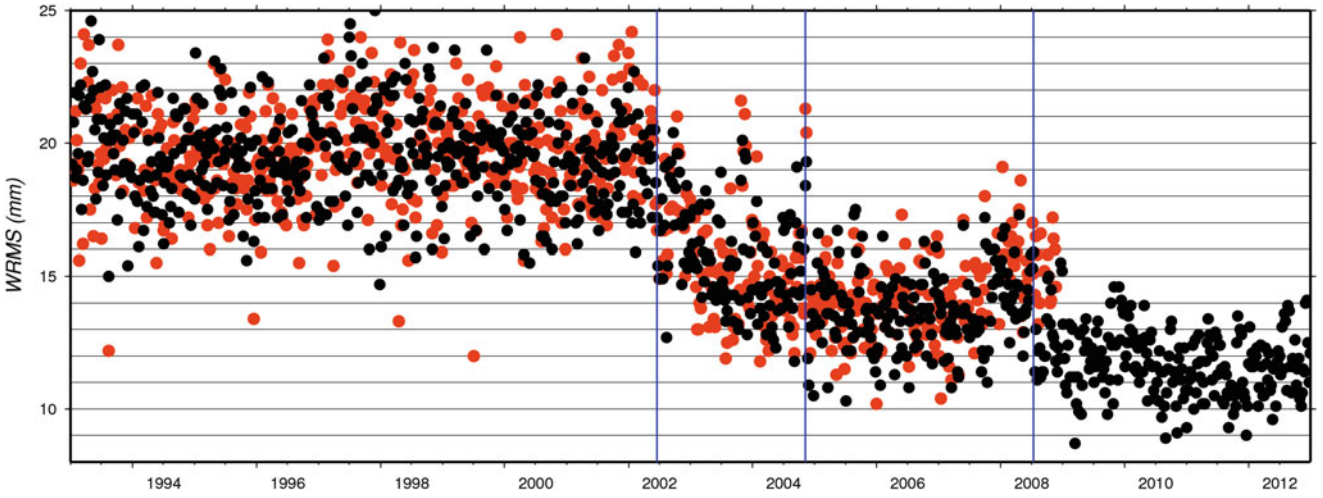

Fig. 7 Internal consistency of the gscwd10 (previous solution in *red*) and gscwd23 solution (new solution in *black*). 3D WRMS when comparing station positions in 3D with the previous week. *Vertical lines* in *blue* correspond to changes in the DORIS constellation

Table 4 Time evolution of DORIS geodetic precision (WRMS) as indicated by the internal consistency of the gscwd10 weekly solution (previous solution) and gscwd23 weekly solution (new solution). Comparison with similar results from previous week

Period	Number of DORIS satellites	WRMS of gscwd10 (in mm)	WRMS of gscwd23 series (in mm)
1993-001 to 2002-173	3	19.71	19.54
2002-174 to 2004-318	5	15.63	15.71
2004-319 to 2008-201	4	14.15	13.79
2008-202 to 2012-365	5		11.77

6 Conclusions

In conclusion, the DORIS system should remain operational until 2026, if not 2030. The IDS has started several validation studies in preparation for ITRF2013, involving the current six Analysis Centers and the Combination Center. Satellite-specific and DORIS-data related problems were identified and most of them are now resolved. Improvements in the accuracy of the DORIS-derived geodetic products are expected for the future combined solution, for both the polar motion determination and the station positioning. Such improvements are due to the large increase in DORIS data per station, thanks to the new DGXX receivers on-board the satellites, as well as improved data processing strategies: a new gravity field including time variable coefficients, satellite physical models or phase center corrections. At the time of writing, all IDS groups are working to refine their data processing scheme in order to be ready in time for the IDS submission to ITRF2013.

Acknowledgements Part of this work was supported by the Centre National d'Etudes Spatiales (CNES). It is based on observations with DORIS deployed on SPOTs, TOPEX/Poseidon, Envisat, Jason-2, Cryosat-2 and HY-2A satellites. This paper is IPGP contribution number 3477.

References

Altamimi Z, Collilieux X (2010) Quality assessment of the IDS contribution to ITRF2008. Adv Space Res 45(12):1500–1509. doi:10.1016/j.asr.2010.03.010

Altamimi Z, Boucher C, Willis P (2005) Terrestrial reference frame requirements within GGOS perspective. J Geodyn 40(4-5):363–374. doi:10.1016/j.jog.2005.06.002

Altamimi Z, Collilieux X, Metivier L (2011) ITRF2008, an improved solution of the International Terrestrial Reference Frame. J Geod 85(8):457–473. doi:10.1007/s00190-011-0444-4

Auriol A, Tourain C (2010) DORIS system, the new age. Adv Space Res 46(12):1484–1496. doi:10.1016/j.asr.2010.05.015

Bizouard C, Gambis D (2009) The combined solution C04 for Earth Orientation Parameters consistent with International Terrestrial Reference Frame 2005. IAG Symp 134:265–270. doi:10.1007/978-3-642-00860-3_41

Bock O, Willis P, Lacarra M, Bosser P (2010) An intercomparison of zenith tropospheric delays derived from DORIS and GPS data. Adv Space Res 46(12):1648–1660. doi:10.1016/j.asr.2010.05.018

Cerri L, Berthias JP, Bertiger WI, Haines BJ, Lemoine FG, Mercier F, Ries JC, Willis P, Zelensky NP, Ziebart M (2010) Precision orbit determination standards for the Jason series of altimeter missions. Marine Geod 33(S1):379–418. doi:10.1080/01490419.2010.488966

Cerri L, Lemoine JM, Mercier F, Zelensky NP, Lemoine FG (2013) DORIS-based point mascons for the long term stability of precise orbit solutions. Adv Space Res 52(3):466–476. doi:10.1016/j.asr.2013.03.023

Fagard H (2006) Twenty years of evolution of the DORIS permanent network, From its initial deployment to its renovation. J Geod 80(8-11):429–456

Förste C, Bruinsma SL, Shako R, Abrikosov O, Flechtner F, Marty JC, Lemoine JM, Dahle C, Neumeyer H, Barthelmes F, Biancale R, Balmino G, König R (2012) A new release of EIGEN-6, the latest combined gravity field model including LAGEOS, GRACE and GOCE data from the collaboration of GFZ Potsdam and GRGS Toulouse, EGU General Assembly, Geophys Res Abstracts 14, EGU2012-2821-2.

Gobinddass ML, Willis P, de Viron O, Sibthorpe A, Zelensly NP, Ries JC, Ferland R, Bar-Sever Y, Diament M, Lemoine FG (2009) Improving geocenter time series using an empirical rescaling of solar radiation pressure models. Adv Space Res 44(11):1279–1287. doi:10.1016/j.asr.2009.08.004

Gobinddass ML, Willis P, Menvielle M, Diament M (2010) Refining DORIS atmospheric drag estimation in preparation of ITRF2008. 45(12):1566 –1577. doi:10.1016/j.asr.2010.04.004

Jayles C, Chauveau JF, Rozo F (2010) DORIS/Jason2, Better than 10 cm on-board orbits available for near-real-time altimetry. Adv Space Res 46(12):1497–1512. doi: 10.1016/j.asr.2010.04.030

Le Bail K, Lemoine F, Chinn D (2010) GSFC DORIS contribution to ITRF2008. Adv Space Res 46(12):1471–1499. doi:10.1016/j.asr.2010.01.030

Lemoine JM, Capdeville H (2006) A corrective model for Jason-1 DORIS Doppler data in relation to the South Atlantic Anomaly. Adv Space Res 80(8-11):507–523. doi:10.1007/s00190-006-0068-2

Lemoine FG, Zelensky N, Chinn D, Pavlis D, Beckley B, Luthcke SB, Willis P, Ziebart M, Sibthorpe A, Boy JP, Luceri V (2010) Towards development of a consistent orbit determination, TOPEX/Poseidon, Jason-1 and Jason-2. Adv Space Res 46(12):1513–1540. doi:10.1016/j.asr.2010.05.007

Noll CE (2010) The Crustal Dynamics Data Information System, A resource to support scientific analysis using space geodesy. Adv Space Res 45(12):1421–1440. doi:10.1016/j.asr.2010.01.018

Rudenko S, Dettmering D, Eselborn S, Schöne T, Förste C, Lemoine JM, Ablain M, Alexandre D, Neumayer KH (2014) Influence of time variable geopotential models o precise orbits of altimetry satellites, global and regional mean sea level trends. Adv Space Res 54(1):92–118. doi:10.1016/j.asr.2014.03.010

Seitz M, Angermann D, Blossfeld M, Drewes M, Gerstl M (2012) The 2008 DGFI realization of the ITRS, DTRF2008. J Geod 86(12):1097–1123. doi:10.1007/s00190-012-0567-2

Stepanek P, Dousa J, Filler V, Hugentobler U (2010) DORIS data analysis at Geodetic Observatory Pecny using single-satellite and multi-satellite solutions. Adv Space Res 46(12):1578–1592. doi:10.1016/j.asr.2010.04.015

Stepanek P, Dousa J, Filler V (2013) SPOT-5 oscillator instability due to South Atlantic Anomaly, mapping the effect and application of data corrective model. Adv Space Res 52(7):1355–1365. doi:10.1016/j.asr.2013.07.010

Tapley BD, Bettadpur S, Ries JC, Thompson PF, Watkins MM (2004) GRACE measurements of mass variability in the Earth system. Science 305(5683):503–505. doi: 10.1126/science.1099192

Tavernier G, Soudarin L, Larson K, Noll C, Ries JC, Willis P (2002) Current status of the DORIS Pilot Experiment and the future international DORIS Service. Adv Space Res 30(2):151–155. doi:10.1016/S0273-1177(02)00279-X

Valette JJ, Lemoine FG, Ferrage P, Yaya P, Altamimi Z, Willis P, Soudarin L (2010) IDS contribution to ITRF2008. Adv Space Res 46(12):1614–1632. doi:10.1016/j.asr.2010.05.029

Willis P (2007) Analysis of a possible future degradation in the DORIS geodetic results related to changes in the satellite constellation. Adv Space Res 39(10):1582–1588. doi:10.1016/j.asr.2006.11.018

Willis P, Berthias JP, Bar-Sever YE (2006) Systematic errors in the Z-geocenter derived using satellite tracking data, a case study from SPOT-4 DORIS data in 1998. J Geod 79(10-11):567–572. doi:10.1007/s00190-005-0013-9

Willis P, Fagard H, Ferrage P, Lemoine FG, Noll CE, Noomen R, Otten M, Ries JC, Rothacher M, Soudarin L, Tavernier G, Valette JJ (2010) The International DORIS Service (IDS), toward maturity. Adv Space Res 45(12):1408–1420. doi:10.1016/j.asr.2009.11.018

Zelensky N, Lemoine FG, Chinn D, Rowlands D, Luthcke S, Beckley B, Pavlis D, Klosko S, Ziebart M, Sibthorpe AJ, Willis P, Luceri V (2010) DORIS/SLR POD modeling improvements for Jason-1 and Jason-2. Adv Space Res 46(12):1541–1558. doi:10.1016/j.asr.2010.05.008

Part VII

Imaging & Positioning Techniques and Applications

Combined GPS, BeiDou, Galileo, and QZSS Single-Epoch, Single-Frequency RTK Performance Analysis

Robert Odolinski, Peter J.G. Teunissen, and Dennis Odijk

Abstract

In this contribution we will focus on instantaneous (single-epoch) single-baseline Real-Time Kinematic (RTK) combining four CDMA satellite systems. We will combine the Chinese BeiDou, the European Galileo, the American GPS and the Japanese QZSS system. To further strengthen the underlying model and maximize the redundancy, attention will be given to overlapping frequencies between the systems. With calibrated Inter System Biases (ISBs), it enables one to use a common pivot satellite between the respective systems when parameterizing the double-differenced ambiguities. We make use of the LAMBDA method for ambiguity resolution, and the performance is evaluated by ambiguity success-rates and by comparing the estimated positions to very precise benchmark coordinates. This will be based on various elevation cut-off angles so as to mimic conditions with obstructed satellite visibility (such as in urban canyons). It will be shown by how much the increased strength of the combined models allow for improved ambiguity resolution performance and positioning robustness over the single-systems.

Keywords

BeiDou • Cut-off angle • Galileo • GPS • Multi-GNSS • QZSS • Real time kinematic

1 Introduction

The BeiDou Navigation Satellite System (BDS) attained Asia-Pacific regional operational status in the end of December 2011. The current (December 2013) BDS constellation consists of five Geostationary Earth Orbit (GEO), five Inclined Geo-Synchronous Orbit (IGSO) and four Medium Earth Orbit (MEO) satellites. BDS satellites currently transmit at three frequencies, B1, B2 and B3 in Quadrature phase-shift keying (QPSK) modulation, as is shown in Table 1 and given together with the L1, L2 and L5 GPS frequencies. Some first BDS positioning results based on real data can be found in e.g. Montenbruck et al. (2013).

Two Galileo In-Orbit Validation Element (GIOVE) satellites have been in orbit since 2005 and 2008 respectively. The four In-Orbit Validation (IOV) MEO satellites that since 2012 are currently (December 2013) available for positioning broadcast signals at E1, E5a, E5b, and E6 frequencies (Table 1). The E6 frequency will only be received as part of Galileo's Commercial Service. Initial results on combined single-frequency Galileo+GPS single-baseline RTK were presented in Odijk and Teunissen (2013). It was shown that with overlapping frequencies and a-priori corrected Inter System Biases (ISBs), one maximizes the redundancy and each additional Galileo satellite to GPS then contributes to the solution. The nature and variation of GIOVE-GPS ISBs were also investigated in Montenbruck et al. (2011).

R. Odolinski (✉) • D. Odijk
GNSS Research Centre, Curtin University of Technology, Bentley, WA 6102, Australia
e-mail: Robert.Odolinski@curtin.edu.au

P.J.G Teunissen
GNSS Research Centre, Curtin University of Technology, Bentley, WA 6102, Australia

Mathematical Geodesy and Positioning, Delft University of Technology, Delft, The Netherlands

© Springer International Publishing Switzerland 2015

C. Rizos, P. Willis (eds.), *IAG 150 Years*, International Association of Geodesy Symposia 143,
DOI 10.1007/1345_2015_123

Table 1 BDS, Galileo, QZSS and GPS signals

Sat. system	Band	Freq. (MHz)	Wavelength (cm)
BDS	**B1**	1561.098	19.20
BDS/Galileo	B2/E5b	1207.140	24.83
BDS	B3	1268.520	23.63
QZSS, GPS/Galileo	**L1/E1**	1575.42	19.03
QZSS, GPS	L2	1227.60	24.42
QZSS, GPS/Galileo	L5/E5a	1176.45	25.48

The Quasi-Zenith Satellite System (QZSS) uses the same orbital period as a traditional equatorial geostationary orbit, however, it has a large orbital inclination and therefore moves with respect to the Earth (JAXA 2013). The system is designed to enable users in the coverage area to receive QZSS signals from a high elevation angle at all times in East Asia and Japan. The QZSS L1, L2 and L5 signals all overlap the GPS signals (Table 1). Currently (December 2013) one satellite is in orbit named MICHIBIKI, or QZS-1, which was launched September 2010.

In this contribution we present four-system GPS+BDS+Galileo+QZSS instantaneous (single-epoch), single-frequency single-baseline RTK results. Special attention will be given to the overlapping frequencies between the systems. We will focus on the frequencies B1, E1 and L1 of GPS/QZSS (Table 1) in this contribution to maximize the number of available satellites as well as overlapping frequencies for single-frequency RTK.

We start with describing the between-receiver single-differenced (SD) GNSS observation equations in Sect. 2, and to make it brief we present them for a combination of Galileo and GPS. Results are then given for ambiguity success rates and RTK positioning in Sect. 3, and we conclude with a summary and discussion.

2 System of Single-Differenced GNSS Observation Equations

Let us consider the receivers $r = 1, 2$ tracking satellites $s_* = 1_*, \ldots, m_*$, where m_* is the number of satellites of one GNSS system $*$ (B for BDS, E for Europe/Galileo, Q for QZSS and G for GPS). When we have non-overlapping single-frequencies we define the frequency as 1_*, where 1_* is the frequency for system $*$, whereas for overlapping frequencies the symbol $*$ is omitted.

For the following single-baseline RTK model we use external products for satellite orbits, and between-receivers single-differences (SD) is subsequently performed on the system of observation equations with respect to the 'pivot' receiver 1. The satellite delays common to both receivers are then eliminated (satellite clocks, any remaining orbit errors, satellite hardware (HW) code and phase delays, and initial phase delays). For short baselines of a few km the relative atmospheric delays can be neglected as well.

We present the following dual-system combination of GPS (G) and Galileo (E) for notational convenience (combination of other satellite systems with overlapping frequencies goes along similar lines), where we share the receiver clock between the systems (the GPS-to-Galileo Time-Offset (GGTO) is eliminated by the SDs). The combined system can then be formulated in the following rank defect, (linearized) SD system of observation equations, in units of range and for *overlapping frequencies*, where we omit time stamps for brevity,

$$\begin{aligned} p_{12,1}^{s_G} &= c_1^{s_G T}\Delta x_1 - c_2^{s_G T}\Delta x_2 + dt_{12} + d_{12,1}^{G} \\ \phi_{12,1}^{s_G} &= c_1^{s_G T}\Delta x_1 - c_2^{s_G T}\Delta x_2 + dt_{12} + \delta_{12,1}^{G} + \lambda_1 M_{12,1}^{s_G} \\ p_{12,1}^{s_E} &= c_1^{s_E T}\Delta x_1 - c_2^{s_E T}\Delta x_2 + dt_{12} + d_{12,1}^{G} + d_{12,1}^{GE} \\ \phi_{12,1}^{s_E} &= c_1^{s_E T}\Delta x_1 - c_2^{s_E T}\Delta x_2 + dt_{12} + \delta_{12,1}^{G} + \delta_{12,1}^{GE} + \\ &+ \lambda_1 M_{12,1}^{s_E} \end{aligned} \tag{1}$$

where $(\cdot)_{12} = (\cdot)_2 - (\cdot)_1$ is the notation for between-receiver SDs, the SD code and phase observable is denoted $p_{12,1}^{s*}$ and $\phi_{12,1}^{s*}$ respectively, $c_r^{s*T} = \frac{(x^{s*} - x_r)^T}{||x^{s*} - x_r||}$ is the line-of-sight unit vector from the receiver r to the satellites obtained from linearizing the system of equations with respect to the receiver coordinates, and λ_1 is the wavelength corresponding to frequency 1. The unknowns read,

x_r	vector with receiver X, Y, Z coordinates
dt_{12}	SD receiver clock error
$d_{12,1}^{G}$	SD GPS receiver HW code delay
$\delta_{12,1}^{G}$	SD GPS receiver HW phase delay
$d_{12,1}^{GE} = d_{12,1}^{E} - d_{12,1}^{G}$	SD differential code ISB
$\delta_{12,1}^{GE} = \delta_{12,1}^{E} - \delta_{12,1}^{G}$	SD differential phase ISB
$M_{12,1}^{s*} = N_{12,1}^{s*} +$	SD non-integer ambiguity due
$+\varphi_{12,1}(t_0)$	to SD initial phase delay for the receiver $\varphi_{12,1}(t_0)$, where
$N_{12,1}^{s*}$	is the SD integer ambiguity

We refrain from carrying through SD random observation noise and un-modeled effects such as multipath for notational convenience.

Note that we in (1) made use of the reparameterization such that $d_{12,1}^{E} = d_{12,1}^{G} + d_{12,1}^{GE}$ and $\delta_{12,1}^{E} = \delta_{12,1}^{G} + \delta_{12,1}^{GE}$, since the receivers are tracking the satellites on the same overlapping frequency. Thus if the differential ISBs can be assumed zero/corrected all receiver-dependent parameters in (1) can be shared between the systems, which increases the redundancy of the resulting full-rank model (see Sect. 2.3).

Table 2 Single-epoch, single-frequency and single-baseline RTK S-basis choice and number of rank deficiencies

Model	S-basis choice	# of rank defects
Eq. (1)	$\Delta x_1, dt_1, d^G_{2,1}, M^{s*}_{1,1}, \delta^*_{1,1}, d^*_{1,1}, M^{1*}_{2,1}$	$11 + m_G + m_E$

2.1 Rank Deficiency Elimination by S-System Theory

The number of rank defects is the number of linear combinations of the column vectors of the design matrix that produces the zero vector, of which the combinations are said to span the null space of the design matrix. These rank defects can be eliminated through an application of S-system theory (Teunissen 1985; Teunissen et al. 2010), implying null-space identification, S-basis constraining and interpretation of the estimable parameters. The number of rank defects and S-basis choice for the model in (1) is given in Table 2.

2.2 Full-Rank RTK Functional Model: ISBs Unknown

The SD, and (linearized) full-rank observation equations for *overlapping frequencies* and a combined GPS+Galileo system is then expressed as,

$$\begin{aligned}
p^{s_G}_{12,1} &= -{c_2^{s_G}}^T \Delta x_{12} + d\tilde{t}_{12} \\
\phi^{s_G}_{12,1} &= -{c_2^{s_G}}^T \Delta x_{12} + d\tilde{t}_{12} + \tilde{\delta}^G_{12,1} + \lambda_1 \tilde{M}^{1_G s_G}_{12,1} \\
p^{s_E}_{12,1} &= -{c_2^{s_E}}^T \Delta x_{12} + d\tilde{t}_{12} + \tilde{d}^{GE}_{12,1} \\
\phi^{s_E}_{12,1} &= -{c_2^{s_E}}^T \Delta x_{12} + d\tilde{t}_{12} + \tilde{\delta}^G_{12,1} + \tilde{\delta}^{GE}_{12,1} + \lambda_1 \tilde{M}^{1_E s_E}_{12,1}
\end{aligned} \tag{2}$$

The estimable unknowns are expressed as follows,

$\Delta x_{12} = \Delta x_2 - \Delta x_1$ Relative receiver coordinates,
$d\tilde{t}_{12} = dt_{12} + d^G_{12,1}$ Relative receiver clock with code delay of GPS
$\tilde{\delta}^G_{12,1} = \delta^G_{12,1} - d^G_{12,1} + \lambda_1 M^{1_G}_{12,1}$ GPS receiver HW phase delay
$\tilde{d}^{GE}_{12,1} = d^E_{12,1} - d^G_{12,1}$ Galileo-GPS code ISB
$\tilde{\delta}^{GE}_{12,1} = \delta^E_{12,1} - \delta^G_{12,1} + \lambda_1 M^{1_G 1_E}_{12,1}$ Galileo-GPS phase ISB
$\tilde{M}^{1_* s_*}_{12,1} = M^{s_*}_{12,1} - M^{1_*}_{12,1}$ Double-differenced integer ambiguities

One can see that the phase ISB is biased by double-differenced (integer) ambiguities of the pivot satellites of both GPS (1_G) and Galileo (1_E). One can also reparameterize the differential phase ISB into a Galileo-specific HW phase delay relative to the GPS HW code delay on frequency 1, as follows (the code ISB is already relative to the GPS HW code delay),

$$\tilde{\delta}^E_{12,1} = \tilde{\delta}^G_{12,1} + \tilde{\delta}^{GE}_{12,1} = \delta^E_{12,1} - d^G_{12,1} + \lambda_1 M^{1_E}_{12,1} \tag{3}$$

In other words, the model in (2) is equivalent (in terms of redundancy) to the one taken when one does not have overlapping frequencies and wants to estimate system-specific HW delays for frequency 1_*.

Note also in (2) that the Galileo-GPS code ISB is estimable on the first frequency, whereas for GPS the Differential Code Bias (DCB) is not estimable. One can thus prove that the functional model (2) is equivalent, in terms of redundancy, to the model when one takes different receiver clocks for each system (see e.g. Odolinski et al. 2013). This since the code ISB then plays the role as the additional unknown. The number of observations, estimable unknowns and redundancy for the model (2) is shown in Table 3.

2.3 Full-Rank RTK Functional Model: ISBs Corrected

We can express the phase ISB correction as follows (Odijk and Teunissen 2013),

$$\begin{aligned}
\overline{\delta}^{GE}_{12,1} &= \delta^{GE}_{12,1} + \lambda_1 z_{12,1} = \\
&= \delta^{GE}_{12,1} + \lambda_1 M^{1_G 1_E}_{12,1} - \lambda_1 \left(M^{1_G 1_E}_{12,1} - z_{12,1} \right)
\end{aligned} \tag{4}$$

where $z_{12,1}$ is an integer ambiguity that originates from the observations that are used to determine the ISB corrections. This ambiguity is in principle different from $M^{1_G 1_E}_{12,1}$ in the observations (2) to be corrected.

Thus when we apply the correction in (4) to the Galileo phase observations in (2), the ambiguity difference part of the correction can be lumped into the ambiguities,

$$M^{1_E s_E}_{12,1} + \left(M^{1_G 1_E}_{12,1} - z_{12,1} \right) = M^{\mathbf{1_G} s_E}_{12,1} - z_{12,1} \tag{5}$$

i.e. the ambiguity becomes differenced with respect to the pivot satellite of GPS (1_G) minus the integer ambiguity that is lumped into the phase ISB correction (4). If we denote the code ISB correction as $\overline{d}^{GE}_{12,1} = d^{GE}_{12,1}$, we then have the following full-rank Galileo-part of the observation equations (the GPS part is equivalent to (2)),

$$\begin{aligned}
p^{s_G}_{12,1} &= -{c_2^{s_G}}^T \Delta x_{12} + d\tilde{t}_{12} \\
\phi^{s_G}_{12,1} &= -{c_2^{s_G}}^T \Delta x_{12} + d\tilde{t}_{12} + \tilde{\delta}^G_{12,1} + \lambda_1 \tilde{M}^{1_G s_G}_{12,1} \\
p^{s_E}_{12,1} - \overline{d}^{GE}_{12,1} &= -{c_2^{s_E}}^T \Delta x_{12} + d\tilde{t}_{12} \\
\phi^{s_E}_{12,1} - \overline{\delta}^{GE}_{12,1} &= -{c_2^{s_E}}^T \Delta x_{12} + d\tilde{t}_{12} + \tilde{\delta}^G_{12,1} + \lambda_1 \tilde{M}^{1_G s_E}_{12,1}
\end{aligned} \tag{6}$$

Table 3 Single-epoch, single-frequency, single-baseline RTK redundancy and solvability condition (overlapping frequencies)

Model	# of obs.	# of unknowns	Redundancy	Solvability condition
Single-system	$2m_*$	$4+m_*$	m_*-4	$m_* \geq 4$
GPS+Galileo (2) **ISBs unknown**	$2m_G+2m_E$	$5+m_G+m_E$	m_G+m_E-5	$m_G+m_E \geq 5$
GPS+Galileo (6) **ISBs corrected**	$2m_G+2m_E$	$4+m_G+m_E$	m_G+m_E-4	$\mathbf{m_G+m_E \geq 4}$
Four-system **ISBs unknown**	$2m_G+2m_E$ $+2m_B+2m_Q$	$7+m_G+m_E$ $+m_B+m_Q$	m_G+m_E $+m_B+m_Q-7$	m_G+m_E $+m_B+m_Q \geq 7$
Four-system **ISBs corrected**	$2m_G+2m_E$ $+2m_B+2m_Q$	$4+m_G+m_E$ $+m_B+m_Q$	m_G+m_E $+m_B+m_Q-4$	$\mathbf{m_G+m_E}$ $\mathbf{+m_B+m_Q \geq 4}$

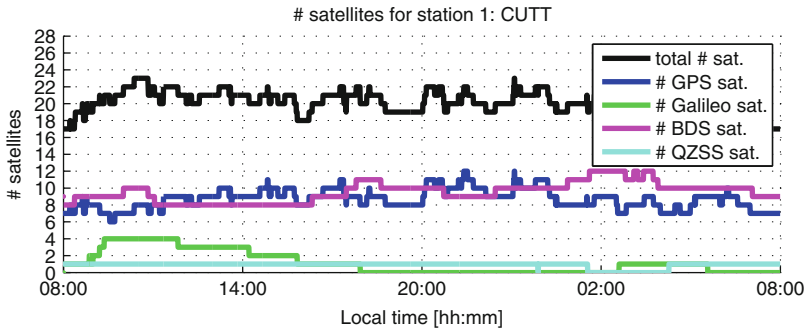

Fig. 1 Satellite visibility for CUTT April 29, 2013

where $\tilde{M}_{12,1}^{1_G s_E} = M_{12,1}^{1_G s_E} - z_{12,1}$ is the estimable ambiguity as defined in (5). Note that this ambiguity will also be estimable for $s_E = 1_E$ (one additional unknown as compared to (2)). In other words, with a-priori corrected values for the two differential code and phase ISBs, the redundancy of this model increases with one as compared to the model in (2), see Table 3.

2.4 Redundancy and Solvability

In Table 3 we give the number of observations, the number of estimable unknowns and the redundancy for the single-baseline RTK models (2) and (6), as well as for a four-system model assuming that all frequencies overlap between the systems. In the last column a *solvability condition* is defined, which is the number of satellites required to solve coordinate parameters. The single-system RTK model in the Table can be found in (2) for GPS, where BDS-/Galileo- or QZSS-only models will have a similar definition of the unknowns.

One can imply from Table 3 that with the ISBs corrected model (6) at least four satellites are needed for the combined systems for positioning, whereas if the ISBs are unknown (2) five satellites are required in case of a dual-system, and seven for the four-system model.

Table 4 Zenith-referenced code and phase STDs

	Frequency	Code $\sigma_{p,1*}$ (cm)	Phase $\sigma_{\phi,1*}$ (mm)
GPS	L1	37	3
BDS	B1	30	3
Galileo	E1	30	2
QZSS	L1	30	3

3 Results

Data from 29–30 April 2013 of CUTA and CUTT (both Trimble NetR9 receivers with an inter-distance of 1 km) at Curtin University, are evaluated, with a measurement interval of 30 seconds. The LAMBDA method is used for integer ambiguity resolution (Teunissen 1995), and the Detection, Identification and Adaptation (DIA) procedure to eliminate outliers (Teunissen 1990). The positioning results are evaluated by comparing the estimated positions to very precise benchmark coordinates. The number of satellites visible for CUTT for an elevation cut-off angle of 10° is given in Fig. 1.

We see similar number of satellites for BDS and GPS, and we have (December 2013) four Galileo satellites and one QZSS satellite visible. The stochastic RTK model settings are given in Table 4. This is based on the exponential

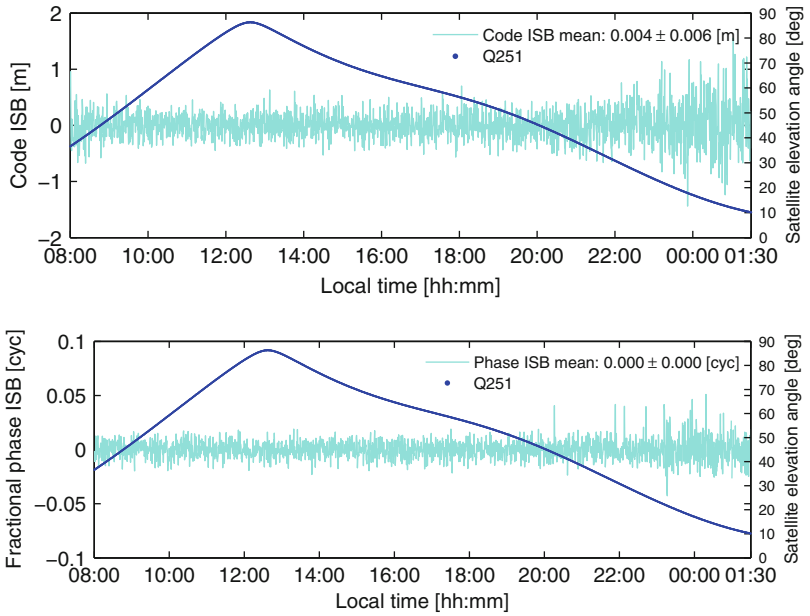

Fig. 2 L1-L1 QZSS-GPS code ISB (*top*), phase ISB (*bottom*) for a zero-baseline setup CUT0-CUT2 (both Trimble NetR9), 29 April 2013, and a cut-off angle of 10°

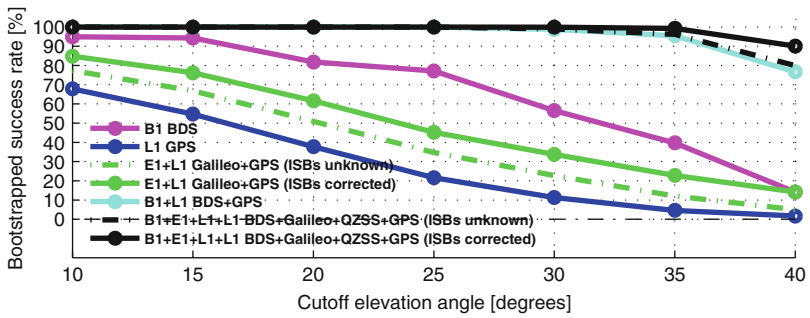

Fig. 3 Bootstrapped success rates for single-epoch, single-frequency RTK vs different elevation cut-off angles of 10–40°

elevation weighting function by Euler and Goad (1991), where $\sigma_{p,1*}$ and $\sigma_{\phi,1*}$ are the zenith-referenced a priori code and phase standard deviation (STD) respectively for undifferenced observations.

3.1 Inter System Biases

We focus on Trimble-Trimble receivers throughout this contribution. To investigate whether the QZSS-GPS ISBs are zero for similar receiver types, we depict in Fig. 2 the code and (fractional) phase differential ISBs for L1-L1 QZSS-GPS. This is based on single-epoch RTK for a zero baseline with fixed receiver positions of CUT0-CUT2 (at Curtin University), and an elevation cut-off angle of 10°. The STDs are computed assuming the ISBs to be *constant in time* during the time span to illustrate the ISBs repeatability.

We see noisier behavior of the ISBs when the QZSS satellite sets at a low elevation angle that causes less precise observations. The phase ISB mean value is however zero and the code ISB is also close to zero (mean value of 4 mm), and the code and phase STDs (6 mm and below 0.001 cycles respectively) also fall well within the code and phase measurement noise levels in Table 4, which makes it plausible to believe that they are time-constant. This was also concluded to be the case with the same data set for E1-L1 Galileo-GPS ISBs, with similar precision and close to zero mean values (not explicitly shown herein).

3.2 Bootstrapped Success Rates for Large Cut-Off Angles

The formal bootstrapped success rate (SR) is an accurate lower bound to the Integer Least-Squares (ILS) success rate (Teunissen 1998, 1999) and can thus be used to infer whether integer ambiguity resolution can be expected to be successful. To compute the bootstrapped success rate we only need the variance covariance matrix of the (decorrelated) float ambiguities and we follow equation (19) in Teunissen (1998).

The bootstrapped success rates for CUTA-CUTT and different elevation cut-off angles between 10° and 40° are given in Fig. 3 for B1 BDS in magenta, L1 GPS as blue, E1+L1 Galileo+GPS as green, B1+L1 BDS+GPS in cyan,

Table 5 Empirical ILS success rate for single-epoch, single-frequency RTK and *full* ambiguity resolution, CUTA-CUTT and an elevation cut-off angle of 10–40°. April 29–30, 2013

System/ freq. cut-off	Empirical Integer Least Squares SR P_{s_E} (%) (deg)					
	10	20	25	30	35	40
B1 BDS	97.5	88.2	84.8	64.5	48.6	19.1
L1 GPS	82.9	55.7	34.8	19.9	9.1	3.7
E1+L1	91.5	72.9	54.0	39.8	26.6	16.6
Galileo+GPS	(87.1)	(65.3)	(45.8)	(31.3)	(18.7)	(9.4)
B1+L1	98.4	**100**	**100**	99.6	98.0	84.3
BDS+GPS						
B1+E1+L1+L1	98.4	**100**	**100**	**100**	99.8	94.3
BDS+Galileo	(98.4)	(**100**)	(**100**)	(99.7)	(98.2)	(85.9)
+QZSS+GPS						

The success rates corresponds to ISBs corrected when applicable (in brackets SRs are given when ISBs are unknown for overlapping frequencies)

and a combined B1+E1+L1+L1 four-system RTK model in black (full lines for ISBs corrected, dotted lines for ISBs unknown).

We see in Fig. 3 a dramatic decrease of the success rates with respect to increasing cut-off angles for the single-systems, whereas the success rate remains at stable values close to 100% for cut-off angles up to 35° for the four-system with ISBs corrected. We also see the positive effect on the success rates when the differential ISBs are assumed zero/corrected.

3.3 Integer Least Squares Ambiguity Success Rates

We compute the empirical ILS success rate by comparing the single-epoch estimated integer ambiguities to reference ambiguities. These reference ambiguities were estimated by using a combined system with multiple-frequencies and a Kalman filter over the entire observation time-span, assuming the ambiguities time-constant. The empirical success rate is defined as,

$$P_{s_E} = \frac{\#\text{correctly fixed epochs}}{\text{total \# of epochs}} \tag{7}$$

The ILS success rates are presented in Table 5 for elevation cut-off angles of 10–40°, for different variations of satellite combinations.

In Table 5 we see that the ILS success rates are consistent with the values of the Bootstrapped success rates in Fig. 3, except for the 10° cut-off angle for B1+L1 and the four-system models with 98.4% ILS success rate (and 100% bootstrapped success rate). We investigated these instances and found that for both days (during the same short period of time) the ambiguities of two GPS satellites that were rising and setting were wrongly fixed, as a consequence of low elevation multipath. This thus illustrates one of the benefits of using larger cut-off angles for a combined system.

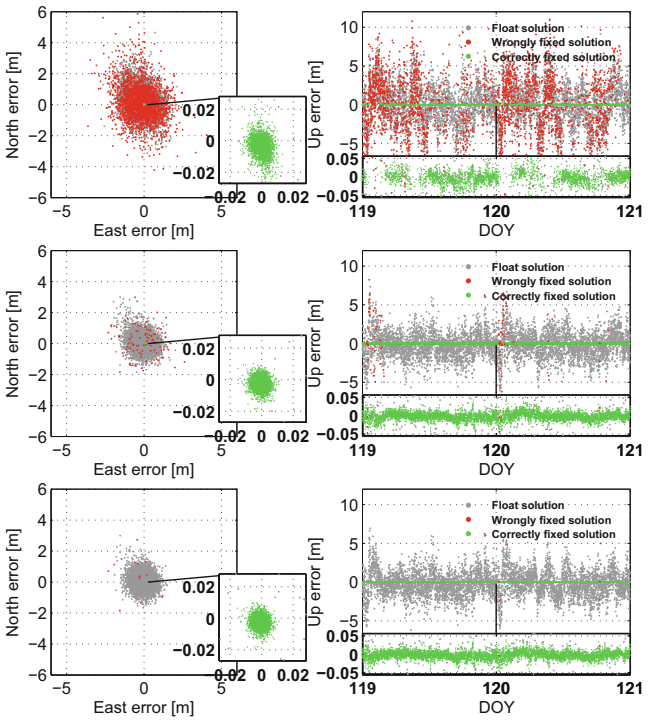

Fig. 4 B1 BDS (*first row*), B1+L1 BDS+GPS (*second row*), and B1+E1+L1+L1 ISBs corrected (*last row*). Float (*gray*), correctly fixed (*green*), wrongly fixed (*red*) solutions for 35° cut-off angle, single-epoch RTK, CUTA-CUTT

3.4 Positioning Results for Large Cut-Off Angles

In order to illustrate the positioning results for a large elevation cut-off angle of 35°, we give in Fig. 4 the single-frequency B1 BDS, B1+L1 BDS+GPS and a four-system B1+E1+L1+L1 (with ISBs corrected) positioning results. The correctly fixed solution (green) is given together with the float solution (gray), and the wrongly fixed solutions (red).

Figure 4 illustrates that the correctly fixed positioning errors are at the mm-cm level and about two-orders of magnitude more precise than the float solution at dm-meter-level. It also illustrates the need of integer validation techniques (Verhagen and Teunissen 2013) since wrong fixing can lead to worse positioning performance compared to the

float solution. Importantly an increase of availability of very precise positioning results can be seen in particular for the four-systems.

4 Conclusions

In this contribution we studied a four-system combination of B1 BDS, E1 Galileo, L1 QZSS and L1 GPS for instantaneous (single-epoch) single-frequency RTK positioning. We focused our attention on Inter System Biases (ISBs), on the integer ambiguity success rates as well as positioning for larger elevation cut-off angles.

The code and (fractional) phase differential ISB for L1-L1 QZSS-GPS were estimated with values close to zero mean and the standard deviations fall well within the code and phase measurement noise levels (Fig. 2), which makes it plausible to believe that they are time-constant. Similar values were also observed for E1-L1 Galileo-GPS ISBs (not explicitly shown), and thus we conclude that one can safely neglect the ISBs for similar receiver types. Future studies will involve different receiver types and other overlapping frequencies.

The Integer Least Squares (ILS) empirical success rates were given for several satellite elevation cut-off angles between 10–40° in Table 5, with larger angles suitable in e.g. urban canyons. We can conclude that the four-system model allows for *continuous* instantaneous RTK up to the 30° cut-off angle (100% success rate), which is not the case for the single-systems. Moreover the four-system model achieved larger success rates compared to Galileo+GPS and BDS+GPS, resulting in better precise positioning availability (Fig. 4).

Acknowledgements This work has been executed in the framework of the Positioning Program Project 1.01 "New carrier phase processing strategies for achieving precise and reliable multi-satellite, multi-frequency GNSS/RNSS positioning in Australia" of the Cooperative Research Centre for Spatial Information (CRC-SI). The second author is the recipient of an Australian Research Council (ARC) Federation Fellowship (project number FF0883188). All this support is gratefully acknowledged.

References

Euler HJ, Goad CG (1991) On optimal filtering of GPS dual frequency observations without using orbit information. Bull Geod 65:130–143

JAXA (2013) Japan Aerospace Exploration Agency (JAXA), Navigation Service Interface Specification for QZSS (IS-QZSS), V1.5. Technical report, 225 pp.

Montenbruck O, Hauschild A, Hessels U (2011) Characterization of GPS/GIOVE sensor stations in the CONGO network. GPS Solut 15(3):193–205

Montenbruck O, Hauschild A, Steigenberger P, Hugentobler U, Teunissen PJG, Nakamura S (2013) Initial assessment of the COMPASS/BeiDou-2 regional navigation satellite system. GPS Solut 17(2):211–222

Odijk D, Teunissen PJG (2013) Characterization of between-receiver GPS-Galileo inter-system biases and their effect on mixed ambiguity resolution. GPS Solut 17(4):521–533

Odolinski R, Teunissen PJG, Odijk D (2013) An analysis of combined COMPASS/BeiDou-2 and GPS single- and multiple-frequency RTK positioning. In: ION Pac PNT, Honolulu, pp 69–90

Teunissen PJG (1985) Generalized inverses, adjustment, the datum problem and S-transformations. Optimization of Geodetic Networks. ed E W Grafarend and F Sanso (Berlin: Springer) pp 11–55

Teunissen PJG (1990) An integrity and quality control procedure for use in multi sensor integration. In: Proceedings of ION GPS 1990, CO, pp 513–522. Also in: GPS red book series, vol VII. Integrated systems, ION Navigation, 2012

Teunissen PJG (1995) The least squares ambiguity decorrelation adjustment: a method for fast GPS integer estimation. J Geod 70:65–82

Teunissen PJG (1998) Success probability of integer GPS ambiguity rounding and bootstrapping. J Geod 72:606–612

Teunissen PJG (1999) An optimality property of the integer least-squares estimator. J Geod 73:587–593

Teunissen PJG, Odijk D, Zhang B (2010) PPP-RTK: results of CORS network-based PPP with integer ambiguity resolution. J Aeronaut Astronaut Aviat Ser A 42(4):223–230

Verhagen S, Teunissen PJG (2013) The ratio test for future GNSS ambiguity resolution. GPS Solut (17):535–548

Metrology for Long Distance Surveying: A Joint Attempt to Improve Traceability of Long Distance Measurements

F. Pollinger, M. Astrua, A. Bauch, S. Bergstrand, B. Görres, J. Jokela, U. Kallio, H. Koivula, H. Kuhlmann, V. Kupko, K. Meiners-Hagen, M. Merimaa, W. Niemeier, P. Neyezhmakov, M. Poutanen, F. Saraiva, S. Schön, S.A. van den Berg, J.-P. Wallerand, and M. Zucco

Abstract

Based on the current state of technology, distance measurements over a few hundred metres in air with relative uncertainties significantly better than 10^{-6} are still an almost impossible challenge. In the European Joint Research Project (JRP) "Metrology for long distance surveying" measurement uncertainties in GNSS-based and optical distance metrology are going to be thoroughly investigated, novel technologies and primary standards developed and guidelines to improve surveying practice in the field worked out. A better understanding and a decrease of measurement uncertainty is also targeted for the critical local tie measurement at geodetic fundamental stations.

Keywords

Calibration • EDM • GNSS • Local ties • Long distance • Reference baseline

1 Introduction

The art of precise distance measurement has always been the foundation of surveying and geodesy. Therefore, these disciplines have mastered and developed respective technologies and methods for centuries. Not to forget, the very first definition of the "metre" goes back to a masterpiece in triangulation work in the eighteenth century (Méchain and Delambre 1806). Modern state of the art distance meters achieve uncertainties of one part in 10^{-6} under favorable conditions. But there are applications where relative uncertain-

F. Pollinger (✉) • A. Bauch • K. Meiners-Hagen
Physikalisch-Technische Bundesanstalt (PTB), Bundesallee 100, 38116 Braunschweig, Germany
e-mail: florian.pollinger@ptb.de

M. Astrua • M. Zucco
Instituto Nazionale di Ricerca Metrologica (INRIM), Strada delle Cacce 91, 10135 Torino, Italy

S. Bergstrand
SP Technical Research Institute of Sweden, P.O. Box 857, 50115 Borås, Sweden

B. Görres • H. Kuhlmann
University of Bonn, Institute of Geodesy and Geoinformation, Nußallee 17, 53115 Bonn, Germany

J. Jokela • U. Kallio • H. Koivula • M. Poutanen
Finnish Geodetic Institute, PL 15, Geodeetinrinne 2, 02431 Masala, Finland

P. Neyezhmakov • V. Kupko
National Scientific Centre "Institute of Metrology" (NSC-IM), 42 Mironositskaya Street, 61002 Kharkov, Ukraine

M. Merimaa
Centre for Metrology and Accreditation (MIKES), Tekniikantie 1, 02151 Espoo, Finland

W. Niemeier
Technische Universität Braunschweig, Institut für Geodäsie und Photogrammetrie, Pockelstraße 3, 38106 Braunschweig, Germany

F. Saraiva
Instituto Português da Qualidad (IPQ), Rua António Gião 2, 2829-513 Caparica Institut, Portugal

S. Schön
Leibniz Universität Hannover, Institut für Erdmessung, Schneiderberg 50, 30167 Hannover, Germany

S.A. van den Berg
National Metrology Institute VSL, Thijsseweg 11, 2629 JA Delft, The Netherlands

J.-P. Wallerand
Conservatoire National des Arts et Métiers (CNAM), 292 rue Saint-Martin, 75141 Paris Cédex 03292, France

© Springer International Publishing Switzerland 2015

C. Rizos, P. Willis (eds.), *IAG 150 Years*, International Association of Geodesy Symposia 143,
DOI 10.1007/1345_2015_154

ties of 10^{-6} (or even better) are desirable (or in principle even necessary already today), independent from environmental conditions on site or from measurement devices.

One example for "challenging" environmental conditions is the transfer of positions and coordinates to sub surface levels where GNSS position sensors cannot be operated. One prominent example of the current limitations of such a task is the determination of the baseline distance for the time of flight neutrino experiment between CERN and the OPERA detector in the Gran Sasso underground laboratory. The overall uncertainty of 20 cm of this 730 km measurement was limited by the EDM measurement of the last kilometre which had to be performed in a tunnel (Colosimo et al. 2011).

Another example for ultimate requirements on measurement uncertainty are monitoring networks. Movements of 0.2 mm per year are a typical magnitude when monitoring, for example, crustal deformations in the vicinity of locations of nuclear power plants (Jokela et al. 2012). Similar requirements occur in the context of motion observations of micro-tectonic plates (Nocquet et al. 2011) or in studies of postglacial rebound phenomena (Milne et al. 2001). Besides the short term effects of the influence of environmental conditions, device independency of the measurement result is of utmost importance in order to ensure the correct interpretation of these observations. To achieve this, traceability to the sub millimetre level must be ensured.

In particular, local tie measurements at geodetic fundamental stations are most critical length measurements whose uncertainty is of utmost importance. As link between celestial and terrestrial reference frames they form a critical cornerstone for the traceability of GNSS-based distance measurements in general. Moreover, deduced reference frames are used for observations and conclusions in many disciplines in earth sciences (Plag and Pearlman 2009). Both, optical techniques, like EDM and levelling, and "short range" GPS are used to connect the respective reference point position on site. Already the current requirement of 1 mm uncertainty for slope distances in 3 D for the relative positions of the respective reference points is not achievable without a proper calibration of all instruments and a traceable scale in GNSS measurement. But particular scientific applications for positioning, e.g. in sea level monitoring for disaster prevention or climatologic studies demand an even lower uncertainty for positioning services in the near future (Gross et al. 2009, p. 211). To meet these demands, an uncertainty requirement for local tie measurements for geodetic fundamental stations of at least 1 mm, or even 0.1 mm is discussed (Rothacher et al. 2009, p. 242, p. 248).

There are two measurement principles which form the basis for current high-accuracy long distance measurements: electro-optical distance meters (EDM) or distance meters based on the analysis of GNSS signals (GNSS-based DM). Both approaches, however, are currently not capable of achieving traceability to the SI definition of the metre with 1 mm or even sub millimetre uncertainty over the respective long distances in air as needed. The accuracy of EDM predominantly suffers from the insufficient determination of the effective environmental conditions over the complete distance of hundreds of metres. Sophisticated approaches have been developed to circumvent this problem, like the "local scale parameter method" (Brunner and Rüeger 1992; Brunner and Lienhardt 2012). Additional information is required, however, like the exact knowledge of at least one distance involved in the network, limiting the applicability of these approaches. GNSS based distance measurements are influenced by various effects, such as propagation delays in the ionosphere and troposphere, signal reflections by the ground, and by obstacles in the antenna neighbourhood, as well as antenna phase centre variations. Hence substantial progress both in technology and in methodology is necessary to provide the measurement tools for current and future challenges in distance metrology in surveying and geodesy. To provide these, experts from two different scientific communities, geodesy and metrology, have united in the frame of the European Metrology Research Programme (EMRP) in a joint research programme (JRP) "Metrology for long distance surveying" (JRP Surveying) (JRP SIB60 Consortium 2013). In this JRP the uncertainty of the scale in long distance metrology for measurements up to 1 km shall be reduced and traceability to SI units shall be fostered. In the course of the JRP, which started in July 2013, novel technological and methodical solutions for calibration and long distance measurement will be developed. To achieve these ambitious goals, in total more than 25 person years will be invested in the course of the project. Most of these developments will be immediately available to improve traceability in surveying, geodesy and earth sciences. This paper intends to present the scientific ideas and approaches of the project with the aim to invite the geodetic community to provide guidance and feedback. The consortium can be contacted, e.g., by the project webpage (JRP SIB60 Consortium 2013).

2 On Traceability to the SI Definition

To ensure universality and long-term comparability, every length measurement has to be traceable to the SI-definition of the metre:

> The metre is the length of the path travelled by light in vacuum during a time interval of 1/299 792 458 of a second. (Giacomo 1984)

Neither GNSS-based DM nor EDMs are direct realisations of this definitions in case of long distance measurements. Although both principles are based on the propagation of electromagnetic waves, the propagation velocity is altered by the influence of the traversed medium. In the case

of GNSS-based distance metrology, the traceability chain includes also other contributions, e.g. the link of celestial to terrestrial reference system and their traceability. According to the "Guide to the Expression of Uncertainty in Measurement" (GUM) (JCGM 2008), all contributions which influence the measurement uncertainty of the measurand have to be characterised and estimated. Traceability to the SI-definition of the metre implies both, a traceability chain to a primary standard, and the knowledge of the total uncertainty amounted during this chain.

3 The Joint Research Project

The JRP Surveying intends to provide novel technologies and methods to characterise and to decrease measurement uncertainties in geodetic distance metrology. To achieve this overall goal, the following major scientific goals are targeted:

- measurement uncertainty contributions to GNSS-based DM will be thoroughly characterised. Goal is a knowledge of the uncertainty contributions to the sub-millimetre level
- the development of primary optical standards, EDMs, with an expanded relative measurement uncertainty of 10^{-7}
- the exploration of femtosecond-laser-based DM for geodetic length metrology
- the development of rigorous calibration procedures both for EDM, and GNSS-based DM
- the development of quasi-real time measurement systems to reduce the uncertainty of local tie measurement to 1 mm or below

3.1 Contributions to GNSS-Based Distance Metrology

The accuracy of GNSS-based DM is determined by a large set of influences, including the antenna parameters, but also propagation delays in troposphere and ionosphere, near field effects or the local surrounding (Seeber 2003), or the accuracy of the link of the terrestrial reference frame to the celestial one. Fortunately, the calibration of the electromagnetic properties of the "isolated" GNSS antennas [i.e. the calibration of the antenna phase centre offset (PCO) and phase centre variations (PCV)] has made considerable progress in the last years. Different approaches are being followed, characterised by different levels of effort and accuracy: field calibration based on manual rotation, field calibration controlled by robots and the fully automated antenna calibration in an anechoic chamber (Görres 2010). It should be noted, however, that the electromagnetic influence of the surrounding of the antenna, often referred to as "near-field" and "multipath effects", is not covered by this calibration. Other influences are even more difficult to study separately as laboratory simulation is not possible and the single influences are difficult to isolate. Previous studies demonstrated that "best repeatability" in GNSS distance observations was not necessarily equivalent to best compatibility with calibrated EDM distance (Koivula et al. 2012).

To develop a complete measurement uncertainty budget for GNSS-based DM, it is necessary to study the different sources of uncertainty as isolatedly as possible. Therefore, PCO- and PCV-calibrated antenna sets will be used, and the examined distances will be traceable by complementary methods. The consortium will run long-term measurement campaigns on baselines of lengths between several hundred metres up to 73 km referenced to the same atomic clock ("common-clock baseline") (Weinbach and Schön 2011). Using this data, the influence of short periodic tropospheric refraction, the choice of specific models, and multipath effects will be studied on single-difference level. Another focus of the research program is dedicated to near-field effects, investigating for example typical mounting scenarios. For applications in surveying, a quantification in terms of uncertainty of obstruction effects is also targeted. Both effects are studied with specially designed experiments and simulations. The results will be verified by measurement campaigns in comparison to calibrated EDMs, and will influence a proposition for a refined design of a GNSS test field for system calibration which will be set up at Metsähovi, Finland.

3.2 Contributions to Electro-Optical Distance Metrology

In case of EDMs, a device verification or characterisation is already a standard procedure for every serious surveying office and sophisticated field-procedures have been developed (Rüeger 1996; ISO 2012). Calibrations traceable to the SI definition of the metre with uncertainties below 10^{-6} are, however, non-trivial. Calibrations of the modulation frequency requires a secured knowledge of the measurement principle and of the sources of uncertainty associated with its implementation. As measurement principles get more and more sophisticated for commercial devices, those assumptions are highly difficult to fulfill for the end user and an independent calibration provider. Therefore, system calibration on reference baselines is preferable. But using (long-term stable) reference baselines as transfer standards, a traceable determination of the reference lengths is necessary – requiring a sufficiently accurate traceable primary standard.

In case of an optical distance measurement, the number density and composition of air molecules in the beam path determines in principle the index of refraction, thus the

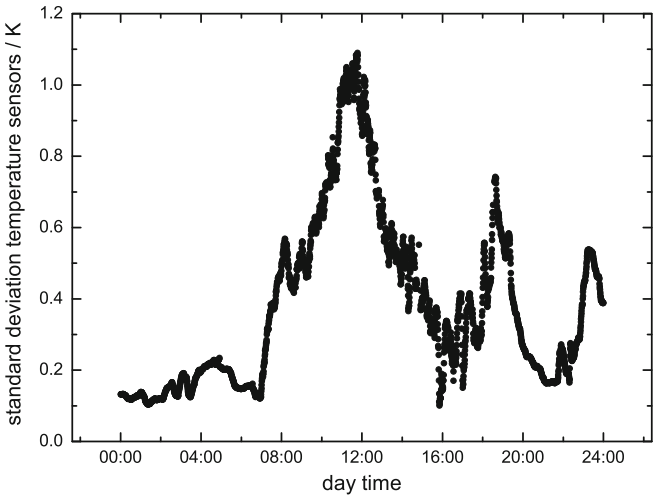

Fig. 1 Evolution of the standard deviation of 59 temperature sensors spaced by 10 m from the mean value at the PTB 600 m reference baseline on a sunny day (Pollinger et al. 2012)

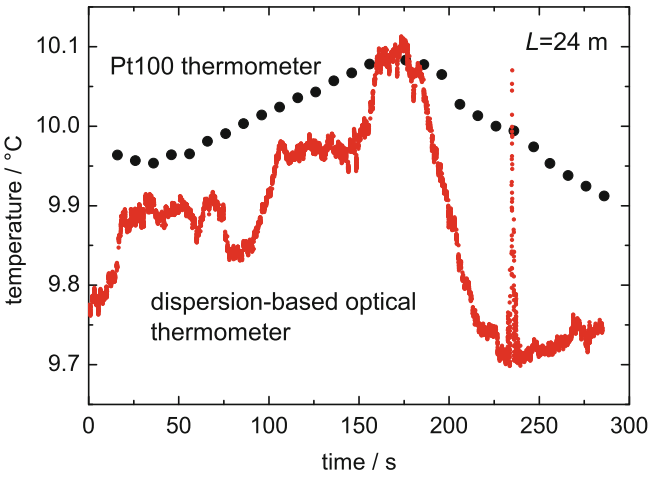

Fig. 2 An optical thermometer based on two-color interferometry reveals fast temperature fluctuations. For comparison, reference data from a Pt-100 sensor is given (compare Meiners-Hagen and Pollinger 2012)

relation between optical and geometrical path length. Using the approximation formulae recommended by IAG (Ciddor 1996; Ciddor and Hill 1999), the index of refraction can be determined by a measurement of the thermodynamic properties air pressure, air temperature, humidity, and carbon dioxide contents in the height of the beam. For high accuracy compensation, however, these parameters have to be determined with high accuracy as well: a relative uncertainty of 10^{-7} requires, for example, a knowledge of the effective temperature along the whole beam path of approximately 0.1 K. To map local gradients of these temperatures, a dense network of sensors is necessary. As can be seen in Fig. 1, such a network can be subject to standard deviations of up to 1 K and beyond on sunny days. Moreover, not only spatial, also temporal gradients pose a severe challenge for such a high-accuracy measurement. Classical temperature sensors, like Pt100 sensors or even mercury thermometers, are not capable to follow the fast local changes of temperature that can be observed in the field. As can be seen in Fig. 2 optical thermometer reveal the limited response of this type of sensors. Today, there are two complex approaches to resolve this problem: the use of a primary standard based on white light interferometry (e.g. the classical Väisälä interferometer Jokela and Häkli 2010), or the execution of an extensive round robin using several forefront commercial EDMs (Heunecke 2012). Both approaches, however, are extremely tedious and require a large effort.

In the course of the JRP Surveying, primary and transfer standards with low measurement uncertainties will be developed. Recent advance in the properties of laser sources and experience gathered in a previous European research project (Wallerand et al. 2008) make it possible to develop field-capable EDMs based on multi-wavelength interferometry and dispersion-based refractivity compensation. Thus, relative measurement uncertainties of 1×10^{-7} are targeted. Two different devices will be developed: a more complex one intended as a metrological primary standard, and a second more robust one as a suitable transfer standard. In addition to these devices, two different measurement principles will be developed to investigate the possibilities to exploit the fascinating spectral properties of femtosecond lasers for long distance metrology.

Moreover, the JRP also intends to contribute to a better understanding of the uncertainty contributions to the electro-optical distance measurement at the targeted level of uncertainty. For this purpose, spectroscopic thermometry will be performed over several hundred metres to improve the understanding of spatial and temporal gradients (Hieta et al. 2011). These results which are traceable via a different measurement principle can be compared to the dispersion-based observations.

Finally, besides the influence of refraction, also air turbulence with the resulting beam bending, phase fluctuations and beam wandering can strongly influence the uncertainty of the length measurement under uncontrolled conditions (Weiss et al. 2001). The magnitude of these effects will be studied with a particularly designed longterm experiment at INRIM, Torino, Italy in order to draw quantifiable conclusions on optimum and sub-optimum measurement conditions for the distance measurement in terms of measurement uncertainty.

3.3 Distance Metrology at Fundamental Geodetic Stations

A specific challenge for distance metrology is the determination of local ties at geodetic fundamental station. Compared to the pure 1D measurement, the complexity of the measurement problem of local ties increases due to unwanted geometrical variations on different time scales caused e.g. by elevation dependent deformations, temperature differences and ground instability. The goal of JRP Surveying is to contribute to the understanding of the local tie measurement and to reduce the uncertainty of this measurement significantly below 1 mm, ideally towards 0.1 mm. For this purpose, two calibrated (near) real-time observation systems will be developed, one based on optical, one on GNSS-based distance metrology. Both systems are planned to be installed at Onsala, Sweden and Metsähovi, Finland. Their limitations in uncertainty will be carefully studied and characterised. In particular, it is intended to compare the performance of both systems in a simultaneous baseline measurement during a dedicated campaign between Onsala and Metsähovi.

3.4 Contributions to Surveying Practice

The technical and fundamental scientific work performed in the JRP Surveying will hopefully lead to a better understanding of magnitudes of uncertainties for both distance measurement techniques, GNSS-based DM and EDM. The consortium will thoroughly collect these information and extract and publish guidelines for improved surveying practice. These are intended to be applicable for the end user in surveying. To ease the application, these guidelines will be implemented in software tools for calibration in the course of the project. As in the course of the project an intensive round robin with different devices will connect the reference baselines at Nummela, Munich and Braunschweig, a core for a future European network of primary reference baselines will be established. They can provide a traceable scale for other baselines, for example.

4 Conclusions

Long distance measurements with relative uncertainties better than 10^{-6} under uncontrolled environments is still an unresolved challenge in metrology. In the frame of the EMRP, geodesists, surveyors, and metrologists from nine European countries have united to face this challenge, tackling both GNSS-based, but also optical distance metrology. Several different approaches were introduced and discussed in this contribution. The internatinonal community of surveyors and geodesists is invited to accompany the project critically.

Acknowledgements The research project described in this paper is funded within the European Metrology Research Programme (EMRP) as JRP SIB60 Surveying. The EMRP is jointly funded by the EMRP participating countries within EURAMET and the European Union.

References

Brunner F, Lienhardt W (2012) Anwendung der "local scale parameter method (LSPM)" bei der vermessung von basislinien. AVN 119(08–09):363–368

Brunner F, Rüeger JM (1992) Theory of the local scale parameter method for EDM. Bull Geod 66:355–364

Ciddor PE (1996) Refractive index of air: new equations for the visible and near infrared. Appl Opt 35(9):1566–1573

Ciddor PE, Hill RJ (1999) Refractive index of air. 2. Group index. Appl Opt 38(9):1663–1667

Colosimo G, Crespi M, Mazzoni A, Jones M, Missiaen D (2011) Determination of the CNGS global geodesy. OPERA Public Note 132:1–7

Giacomo P (1984) News from the BIPM. Metrologia 20(1):25

Görres B (2010) Ist das GNSS–Antennenproblem gelöst? Zeitschrift für Vermessungswesen zfv 135(4):256–267

Gross R, Beutler G, Plag H (2009) Integrated scientific and societal user requirements and functional specifications for the GGOS. In: Plag HP, Pearlman M (eds) Global geodetic observing system meeting the requirements of a global society on a changing planet in 2020. Springer, Berlin/Heidelberg, pp 209–224

Heunecke O (2012) Auswertung des Ringversuchs auf der neuen Kalibrierbasis der UniBw München zur Bestimmung der Sollstrecken. AVN 2012(11–12):380–385

Hieta T, Merimaa M, Vainio M, Seppä J, Lassila A (2011) High-precision diode-laser-based temperature measurement for air refractive index compensation. Appl Opt 50(31):5990–5998

ISO (2012) Optics and optical instruments – field procedures for testing geodetic and surveying instruments – Part 4: electro-optical distance meters (EDM instruments to reflectors). http://www.iso.org/iso/home/store/catalogue_tc/catalogue_detail.htm?csnumber=54624

JCGM (2008) Evaluation of measurement data - guide to the expression of uncertainty in measurement, 1st edn. JCGM 100:2008. http://www.iso.org/sites/JCGM/GUM-introduction.htm

Jokela J, Häkli P (2010) Interference measurements of the Nummela standard baseline in 2005 and 2007. Publications of the Finnish Geodetic Institute, vol 144. Finnish Geodetic Institute, Kirkkonummi

Jokela J, Häkli P, Poutanen M, Kallio U, Ahola J (2012) Improving length and scale traceability in local geodynamical measurements. In: Kenyon S, Pacino MC, Marti U (eds) Geodesy for planet Earth, international association of geodesy symposia, vol 136. Springer, Berlin/Heidelberg, pp 59–66

JRP SIB60 Consortium (2013) JRP surveying project webpage. http://www.emrp-surveying.eu. Accessed 20 Dec 2013

Koivula H, Häkli P, Jokela J, Buga A, Putrimas R (2012) GPS metrology: bringing traceable scale to a local crustal deformation GPS network. In: Kenyon S, Pacino MC, Marti U (eds) Geodesy for planet Earth, international association of geodesy symposia, vol 136. Springer, Berlin/Heidelberg, pp 105–112

Méchain M, Delambre M (1806) Base de système métrique decimal ou mesure de l'arc du meridian compris entre les parallèles de Dunkerque et Barcelone, execute en 1792 et années suivantes. Suite des Mémoires de l'institute, Tome Premier

Meiners-Hagen K, Pollinger F (2012) Rückführbare Messung langer Distanzen in der PTB - Traceable measurements of long distances in the PTB. AVN 118(08–09):283–290

Milne GA, Davis JL, Mitrovica JX, Scherneck HG, Johansson JM, Vermeer M, Koivula H (2001) Space-geodetic constraints on glacial isostatic adjustment in Fennoscandia. Science 291(5512):2381–2385

Nocquet J, Walpersdorf A, Jouanne F, Masson F, Chéry J, Vernant P (2011) Slow deformation in the western alps from a decade of continuous GPS measurements. In: Proceedings of 3rd international colloquium - scientific and fundamental aspects of the Galileo programme, Copenhagen, 31 August–2 September 2011

Plag H, Pearlman M (eds) (2009) Global geodetic observing system meeting the requirements of a global society on a changing planet in 2020. Springer, Berlin/Heidelberg

Pollinger F, Meyer T, Beyer J, Doloca NR, Schellin W, Niemeier W, Jokela J, Häkli P, Abou-Zeid A, Meiners-Hagen K (2012) The upgraded PTB 600 m baseline: a high-accuracy reference for the calibration and the development of long distance measurement devices. Meas Sci Technol 23(9):094018

Rothacher M, Beutler G, Behrend D, Donellan A, Hinderer J, Ma C, Noll C, Oberst J, Pearlman M, Plag HP, Richter B, Schöne T, Tavernier G, Woodworth PL (2009) The future global geodeticobserving system. In: Plag HP, Pearlman M (eds) Global geodetic observing system meeting the requirements of a global society on a changing planet in 2020. Springer, Berlin/Heidelberg, pp 237–273

Rüeger JM (1996) Electronic distance measurement –an introduction, 4th edn. Springer, Berlin

Seeber G (2003) Satellite geodesy, 2nd edn. Walter de Gruyter, Berlin/New York

Wallerand JP, Abou-Zeid A, Badr T, Balling P, Jokela J, Kugler R, Matus M, Merimaa M, Poutanen M, Prieto E, van den Berg S, Zucco M (2008) Towards new absolute long distance measurement in air. In: NCSL International Workshop and Symposium, Orlando

Weinbach U, Schön S (2011) GNSS receiver clock modeling when using high-precision oscillators and its impact on PPP. Adv Space Res 47(2):229–238

Weiss A, Hennes M, Rotach M (2001) Derivation of the refractive index and temperature gradiens from optical scintillometry to correct atmospherically induced errors for highly precise geodetic measurements. Surv Geophys 22:589–596

On the Handling of Outliers in the GNSS Time Series by Means of the Noise and Probability Analysis

Anna Klos, Janusz Bogusz, Mariusz Figurski, and Wieslaw Kosek

Abstract

The data pre-analysis plays a significant role in the noise determination. The most important issue is to find an optimum criterion for outliers removal, since their existence can affect any further analysis. The noises in the GNSS time series are characterized by spectral index and amplitudes that can be determined with a few different methods. In this research, the Maximum Likelihood Estimation (MLE) was used. The noise amplitudes as well as spectral indices were obtained for the topocentric coordinates with daily changes from few selected EPN (EUREF Permanent Network) stations. The data were obtained within the EPN re-processing made by the Military University of Technology Local Analysis Centre (MUT LAC). The outliers were removed from the most noisy 12 EPN stations with the criteria of 3 and 5 times the standard deviations (3σ, 5σ) as well as Median Absolute Deviation (*MAD*) to investigate how they affect noise parameters. The results show that the removal of outliers is necessary before any further analysis, otherwise one may obtain quite odd and unrealistic values. The probability analysis with skewness and kurtosis was also performed beyond the noise analysis. The values of skewness and kurtosis show that assuming a wrong criterion of outliers removal leads to the wrong results in case of probability distribution. On the basis of the results, we propose to use the *MAD* method for the outliers removal in the GNSS time series.

Keywords

EPN • Kurtosis • MLE • Noises • Outliers • Skewness

1 Introduction

Commonly, the noises in most of geophysical time series are described as a power-law process (Agnew 1992) with the power spectrum equal to:

$$P_x(f) = P_0\left(\frac{f}{f_0}\right)^{\kappa} \tag{1}$$

where f is the spatial or temporal frequency, P_0 and f_0 are the normalising constants and κ is the spectral index of noise (Mandelbrot and Van Ness 1968). Agnew (1992) described that the spectral indices for the geophysical processes often fall between -3 and -1. The integer values of indices indicate special types of noises: "$\kappa = -2$" represents random-walk process which is related to the monument instability of the GPS antennae (Johnson and Agnew 1995; Williams et al. 2004; Klos et al. 2014); "$\kappa = -1$" stands for the flicker noise process (Mandelbrot 1983) that is recognized in most

A. Klos (✉) • J. Bogusz • M. Figurski
Faculty of Civil Engineering and Geodesy, Military University of Technology, Kaliskiego St. 2, 00-908 Warsaw, Poland
e-mail: aklos@wat.edu.pl

W. Kosek
University of Agriculture, Environmental Engineering and Land Surveying, Mickiewicza Av. 24/28, 30-059 Kraków, Poland

Polish Academy of Sciences, Space Research Centre, Bartycka St. 18A, 00-716 Warsaw, Poland

© Springer International Publishing Switzerland 2015

C. Rizos, P. Willis (eds.), *IAG 150 Years*, International Association of Geodesy Symposia 143,
DOI 10.1007/1345_2015_78

of GNSS time series (Mao et al. 1999; Williams et al. 2004; Bogusz and Kontny 2011); "$\kappa = 0$" corresponds to the white noise which is not correlated in time.

Any of the topocentric component is thought to follow the sum of:

$$x(t) = x_0 + v_x \cdot t + \sum_{i=1}^{n} [A_i \cdot \sin(\omega_i \cdot t + \varphi_i)] + O_x + \sum_{j=1}^{m} p_j \cdot x_j^{off} + \varepsilon_x(t) \quad (2)$$

where x_0 is the initial value, v_x is the velocity, A, ω, ϕ are the amplitude, angular velocity and phase shift of the i-th periodic component of a time series, O_x stands for any known outliers, x^{off} for offsets, p is the Heaviside step function, ε_x is the noise. The noises in geophysical time series are correlated in time. This correlation has a great impact on any linear parameters that are estimated from these time series (Williams 2003).

The outliers detection and their removal plays a significant role in the interpretation of the GNSS data. The disputable issue here is the criterion. The most common criteria that depend on the time series character are the removal of values greater than 3 or 5 times the standard deviation. Bergstrand et al. (2007) estimated the noises in the GPS time series after removal of the outliers with 5σ criterion what was stated to be more conservative approach than the 3σ one, used for instance by Johansson et al. (2002). Dong et al. (2006) used the method of discarding the residuals exceeding the constant values of 100, 100 and 300 mm for east, north and vertical components, respectively, to remove the outliers before performing the Principal Component Analysis (PCA). It is worth to note that sigma-based methods correspond strictly to the normal distribution of data. However, what about data that are not normally distributed? Having the above in mind, we decided to investigate the influence that the outliers removal method may have on the time series characteristic using skewness, kurtosis (derived from the moments of data probability density function – PDF) and noise analysis (with Maximum Likelihood Estimation). We took 12 extremely spread EPN time series and removed the outliers with three chosen criterions. At the beginning, the commonly used 3 and 5 times of standard deviations were applied that assume data normal distribution. Then, the Median Absolute Deviation criterion was used. Our main goal of this research was to show how the proper removal of outliers affects estimation of kurtosis and skewness and therefore our understanding of the nature of the data. As shown previously by Peinke et al. (2004) or Sura and Gille (2003), the geophysical phenomena are not necessarily Gaussian. The deviations from Gaussianity can have an impact on the real dynamics. On the other hand, Sura and Gille (2010) stated that the skewness is positive if the additive and multiplicative noises are positively correlated and the skewness is negative if the noise terms are negatively correlated.

2 Data Processing and Methods

The time series used in the following research were obtained within the reprocessing project ("repro-1") according to the EPN guidelines (Bruyninx et al. 1996) using Bernese 5.0 software (Dach et al. 2007). It was performed at the Military University of Technology in the Centre of Applied Geomatics that is one of the 16 independent Local Analysis Centres (MUT LAC). The coordinates in the ITRF2005 reference frame (Altamimi et al. 2007) were obtained as the result. The set of 12 stations with the greatest number of outliers was selected to the research. The white and power-law noise were assumed to be present in the time series before the Maximum Likelihood Estimation (MLE) with CATS software (Williams 2008). The MLE method follows the equation of:

$$lik(\widehat{v}, C) = \frac{1}{(2 \cdot \pi)^{N/2} \cdot (\det C)^{1/2}} \cdot \exp\left(-0.5 \cdot \widehat{v}^T \cdot C^{-1} \cdot \widehat{v}\right) \quad (3)$$

The power-law noise is characterized by spectral index κ and the amplitude A. The MLE method has been already successfully used to evaluate noises in many researches, described e.g. in the papers by Beavan (2005), Bergstrand et al. (2007), Teferle et al. (2008), Bos et al. (2008).

3 Outliers Removal in the Noise Analysis

Three methods of outliers removal were tested in this research. The first and the second one removed the outliers greater than 3 and 5 times the standard deviation of time series (referred to as: 3 sigma (3σ), 5 sigma (5σ)), respectively. The third one focused on the Median Absolute Deviation – *MAD* (Mosteller and Tukey 1977; Sachs 1984), of time series. No interpolation of removed data was performed. The advantage of *MAD* method is being much more robust for outliers than sigma-based methods. The 'robust' is being used throughout the paper when describing the *MAD* method. We mean here that the data median value makes *MAD* not to be as sensitive to outliers as the sigma-based criterions are. The *MAD* is calculated from:

$$MAD = median(|X_i - median(X)|) \quad (4)$$

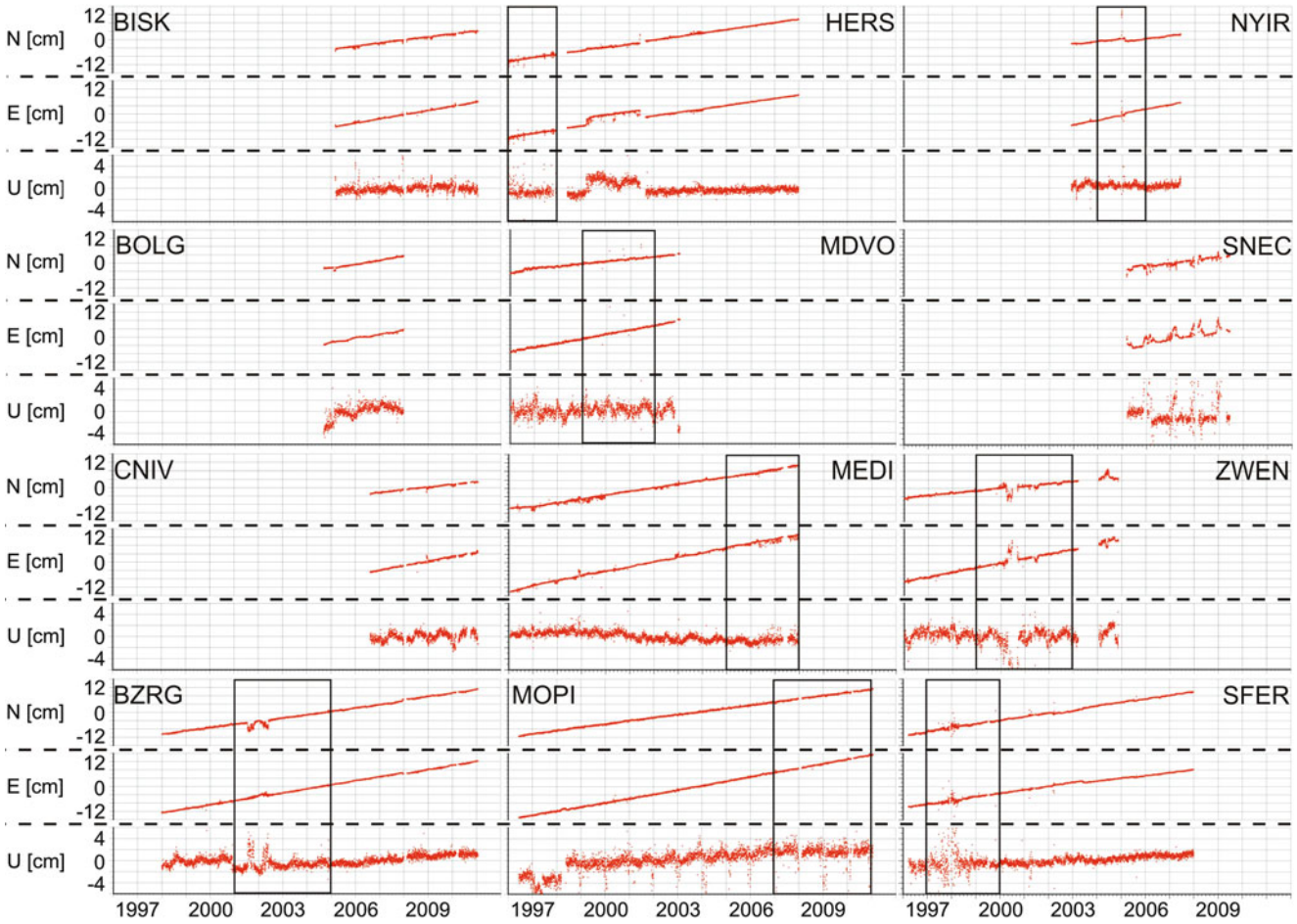

Fig. 1 The time series (in the ITRF2005) with the highest amount of outliers taken for the removal analyses. For shorter time series, all data were analyzed, for longer ones – only the data in the black boxes were considered. Some of the time series are quite consistent and there are just few of outliers. For others, all data are spread (SNEC, ZWEN) and noise estimation can be disturbed by them

To use the *MAD* value in a similar way as the standard deviation for the normal distribution, we multiply it by 1.4826 (Ruppert 2011). Later in this paper, whenever we use *MAD* it is actually $3 \cdot 1.4826 \cdot MAD$, what makes the values of median absolute deviation close to 3 times the standard deviation, but never equal to. Twelve extremely noisy EPN stations (BISK, BOLG, CNIV, BZRG, HERS, MDVO, MEDI, MOPI, NYIR, SNEC, ZWEN, SFER) were chosen to investigate how the outliers influence noise estimation (Figs. 1 and 2).

The number of outliers removed from the twelve of the analyzed stations reaches the greatest value of 4% for ZWEN station with the 3 sigma criterion, whereas it is larger than 15% for *MAD* for the same station (Fig. 3). The MLE was performed after outliers removal with 3σ, 5σ, *MAD* assuming the white plus power-law noises. As the result, the spectral indices and noise amplitudes with uncertainties were obtained (Fig. 4a–c).

The spectral indices for twelve of analyzed stations range between -2 and 0. The noise amplitudes for stations with spread time series reach quite odd and unrealistic values (HERS, SNEC, SFER). The noise amplitude uncertainties in case of no removal of outliers are too large and unacceptable. All stations prove the necessity of outliers removal. The disputable issue here is the criterion. No removal or 5σ criterion brings unacceptable results for stations with just a few of outliers (BISK; BOLG; CNIV; BZRG; HERS – the North and East components; MDVO; MEDI; MOPI; NYIR; ZWEN). The noise amplitudes obtained after 3σ or *MAD* criterion are smaller than $10\ mm \cdot yr^{\kappa/4}$ and quite close to each other at the same time for the consistent time series. The situation changes in case of spread time series. Here, the *MAD* criterion results in smaller noise amplitudes and uncertainties as well. The most interesting time series with extremely spread values for both horizontal and vertical changes comes definitely from the SNEC station. The spectral index for SNEC was estimated as close to random-walk what may be interpreted as changes related to the monument instability. As stated by King and Williams (2009) random-walk

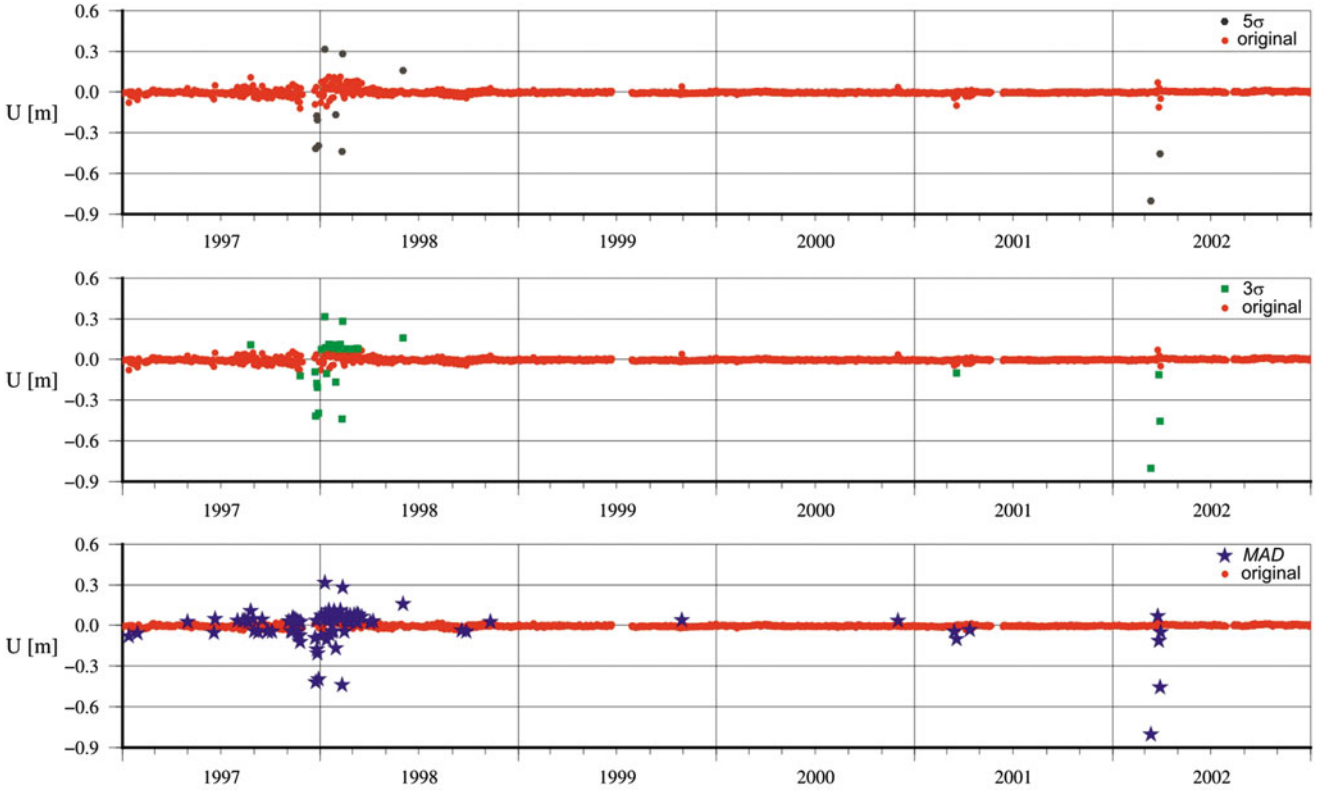

Fig. 2 The removed values with 3σ, 5σ and *MAD* criteria for SFER station, here – Up component was presented, data in the ITRF2005

Outliers - 3 sigma			
Station	N [%]	E [%]	U [%]
BISK	3.00	2.02	1.20
BOLG	2.42	0.30	0.61
CNIV	1.82	1.17	0.51
BZRG	3.69	2.33	2.81
HERS	2.13	1.97	4.43
MDVO	0.66	0.66	0.66
MEDI	0.47	2.69	1.64
MOPI	0.80	1.04	2.71
NYIR	1.29	1.13	1.45
SNEC	2.68	1.04	2.85
ZWEN	4.19	4.01	3.21
SFER	1.67	1.91	1.67

Outliers - 5 sigma			
Station	N [%]	E [%]	U [%]
BISK	0.16	0.33	0.65
BOLG	0.20	0.00	0.10
CNIV	0.15	0.73	0.07
BZRG	0.00	0.24	0.16
HERS	1.15	0.82	0.33
MDVO	0.55	0.55	0.22
MEDI	0.12	0.23	0.00
MOPI	0.00	0.32	1.36
NYIR	1.29	0.48	1.45
SNEC	0.00	0.00	0.09
ZWEN	0.45	0.71	0.00
SFER	0.72	0.60	0.72

Outliers - MAD			
Station	N [%]	E [%]	U [%]
BISK	5.62	1.80	1.42
BOLG	4.65	0.10	0.40
CNIV	3.14	1.68	0.36
BZRG	9.62	2.33	2.81
HERS	10.82	2.95	8.03
MDVO	1.55	0.77	0.55
MEDI	1.52	2.69	1.29
MOPI	0.80	0.56	3.83
NYIR	1.61	1.13	1.45
SNEC	7.96	0.26	3.37
ZWEN	15.06	5.17	3.30
SFER	5.26	3.35	3.82

Fig. 3 The percentage of outliers removed from the analysed time series using the 3σ, 5σ and *MAD* criteria. The results are presented for topocentric components in the North, East, Up order

amplitudes for well monumented stations are probably no higher than 0.5 $mm \cdot yr^{-0.5}$. The SNEC station with such a spread time series reaches the highest noise amplitude. It is still too large even after *MAD* outliers removal. Now, the BZRG station with quite consistent time series with two periods of strong reflexes from trend. No removal of outliers, 5σ and 3σ criteria result in similar values of amplitudes, while the *MAD* criterion results in smaller and interpretable noise parameters. It causes the reduction of amplitudes to around 10 $mm \cdot yr^{\kappa/4}$ with the increment of spectral index to -1 for the Up component. Bearing in mind, that the type and amplitude of noise takes part in estimation of the linear parameters from the time series, one has to understand the values he obtains. Sometimes they do not strictly reflect the existence of the noise, but they can simply be the effect of the wrong or even lack of data pre-analysis.

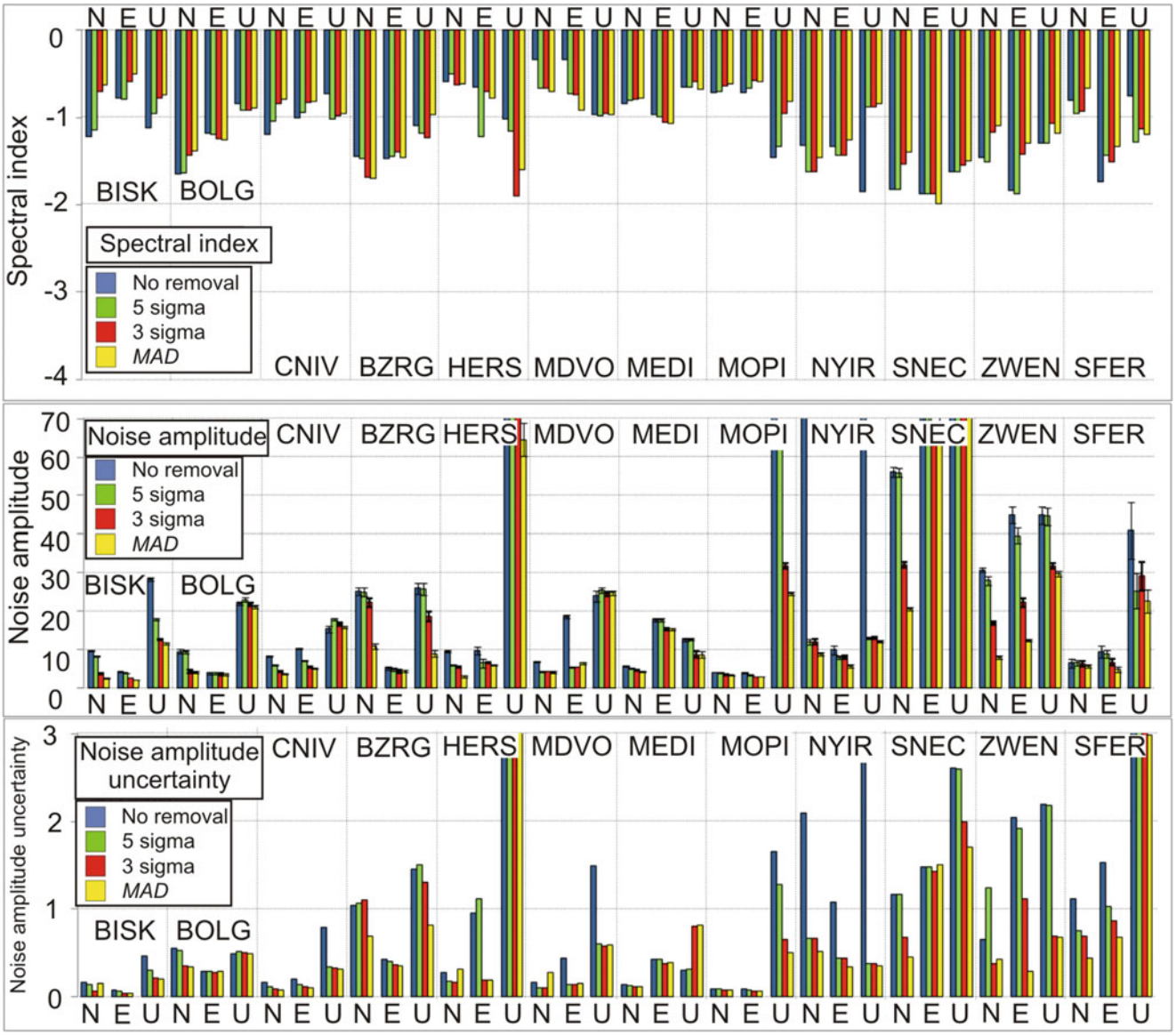

Fig. 4 The spectral indices (**a**), noise amplitudes (with one sigma error bars) (**b**) and their uncertainties (one sigma error bars, presented apart from noise amplitudes) (**c**) estimated for all of analyzed stations using the MLE method. The amplitudes are presented in $mm \cdot yr^{\kappa/4}$. The results are presented with respect to the analyzed stations. The *blue colour* indicates no removal of outliers, green stands for the 5σ criterion, red for 3σ, and yellow for *MAD*. In all cases no interpolation of removed data was performed

4 The Probability Analysis

The probability analysis was conducted beyond the noise analysis. The point is whether treating the time series as normally distributed for the GNSS time series and therefore using the 3σ criterion for outliers removal is appropriate or some robust method (here *MAD*) should be used. The analysis was performed by estimation of moments of the data's probability density function (PDF) that are the skewness and kurtosis. Their advantage in this study, however, is high sensitiveness to outliers.

The asymmetry of PDF's shape can be described by the skewness:

$$S = \frac{E(x - \overline{x})^3}{\sigma^3} \tag{5}$$

where $\overline{x}$ is the mode of x, σ is the standard deviation of the data and E is the expected value. If the classic Gaussian

Station	Skewness											
	N				E				U			
	No removal	5σ	3σ	*MAD*	No removal	5σ	3σ	*MAD*	No removal	5σ	3σ	*MAD*
BISK	-1,01	1,04	1,06	1,11	1,00	1,10	1,11	1,16	3,11	1,13	1,11	1,14
BOLG	-1,03	1,04	1,19	1,15	1,03	1,07	1,15	1,15	0,76	1,10	1,12	1,14
CNIV	1,05	1,04	1,08	1,11	1,03	1,07	1,08	1,14	3,32	1,07	1,10	1,12
BZRG	-1,04	1,02	1,04	1,09	1,01	1,09	1,13	1,16	3,05	1,09	1,15	1,14
HERS	1,01	1,05	1,12	1,13	-0,95	1,07	1,20	1,24	3,34	1,01	1,04	1,22
MDVO	1,08	1,07	1,08	1,15	2,17	1,02	1,02	1,18	0,38	1,09	1,12	1,15
MEDI	1,01	1,04	1,09	1,14	-1,00	1,04	1,07	1,11	1,65	1,07	1,13	1,15
MOPI	1,00	1,08	1,13	1,14	-1,02	1,09	1,13	1,13	-2,19	1,04	1,07	1,11
NYIR	8,50	1,22	1,18	1,17	1,24	1,04	1,14	1,14	-12,26	1,02	1,02	1,08
SNEC	1,12	1,05	1,09	1,15	0,79	1,53	1,50	1,36	2,93	1,34	1,20	1,36
ZWEN	-1,16	1,04	1,05	1,12	-0,74	1,12	1,10	1,18	-2,63	1,04	1,07	1,12
SFER	-0,43	1,02	1,02	1,13	-1,08	1,06	1,12	1,12	-14,47	1,02	1,02	1,13
Station	Kurtosis											
	N				E				U			
	No removal	5σ	3σ	*MAD*	No removal	5σ	3σ	*MAD*	No removal	5σ	3σ	*MAD*
BISK	1,03	1,09	1,16	1,30	1,01	1,31	1,31	1,45	29,71	1,38	1,30	1,40
BOLG	1,09	1,11	1,56	1,44	1,07	1,19	1,40	1,40	3,91	1,27	1,33	1,39
CNIV	1,52	1,10	1,21	1,30	1,10	1,21	1,21	1,38	45,89	1,20	1,27	1,33
BZRG	1,13	1,06	1,11	1,24	1,02	1,26	1,36	1,44	32,69	1,26	1,41	1,40
HERS	1,02	1,14	1,32	1,37	1,57	1,21	1,61	1,86	52,27	1,04	1,12	1,64
MDVO	1,35	1,20	1,23	1,41	13,10	1,06	1,06	1,52	5,94	1,24	1,34	1,41
MEDI	1,03	1,11	1,24	1,38	1,01	1,12	1,18	1,30	3,69	1,19	1,37	1,42
MOPI	1,00	1,22	1,36	1,38	1,07	1,26	1,36	1,36	6,80	1,09	1,17	1,29
NYIR	99,63	1,78	1,49	1,45	2,44	1,12	1,40	1,40	152,23	1,06	1,06	1,23
SNEC	1,72	1,13	1,23	1,41	3,16	2,77	2,62	2,10	10,69	2,24	1,65	2,20
ZWEN	1,60	1,10	1,15	1,33	2,11	1,39	1,30	1,54	11,64	1,10	1,18	1,33
SFER	23,42	1,05	1,06	1,33	1,29	1,17	1,33	1,33	435,72	1,05	1,07	1,36

Fig. 5 The values of skewness and kurtosis (with no removal, 5σ, 3σ and *MAD* criteria) for analyzed stations for the North, East and Up components, data in the ITRF2005

distribution is considered, its skewness is equal to zero. If not, the distribution is skewed right for values greater than zero or skewed left for values below zero. The standard error of skewness (*SES*) can be computed by (Cramer 1977):

$$SES = \sqrt{\frac{6n\,(n-1)}{(n-2)\,(n+1)\,(n+3)}} \tag{6}$$

where n is the number of data in the time series. In this paper, $SES = \pm 0.06$. The value of $3 \times SES = \pm 0.18$ was assumed here as the boundary value for normal distribution.

The kurtosis is a measure of the probability distribution "peakedness" of a real-valued random variable. The kurtosis is computed by the formula:

$$K = \frac{E(x-\overline{x})^4}{\sigma^4} \tag{7}$$

If the kurtosis is equal to 3 we deal with the normal distribution. High kurtosis means that the peak near the mean is distinct, and probability distribution decline rather rapidly. The standard error of kurtosis can be estimated by (Cramer 1977):

$$SEK = \sqrt{\frac{n^2-1}{(n-3)\,(n+5)}} \tag{8}$$

where n is the number of data in the time series. Here, $SEK = \pm 0.12$ and $3 \times SEK = \pm 0.36$ were assumed as the boundary values for the normal distribution. The skewness and kurtosis put together can indicate the normally distributed time series.

Firstly, the skewness and kurtosis were calculated for data with no removal of outliers. Then, for the 5σ, 3σ and *MAD* criterion. The usage of 5σ brought the unexpectedly good betterment in the analyzed values (even though there were just few values exceeding this limit), what proved that the skewness and kurtosis are really sensitive to outliers (Fig. 5). The differences in the skewness values after removal of outliers with 3σ and *MAD* criteria are mostly within 3 times of *SES* for the horizontal components what proves that the use of removal criterion does not change the probability distribution. Three stations (HERS, SNEC, SFER) in case

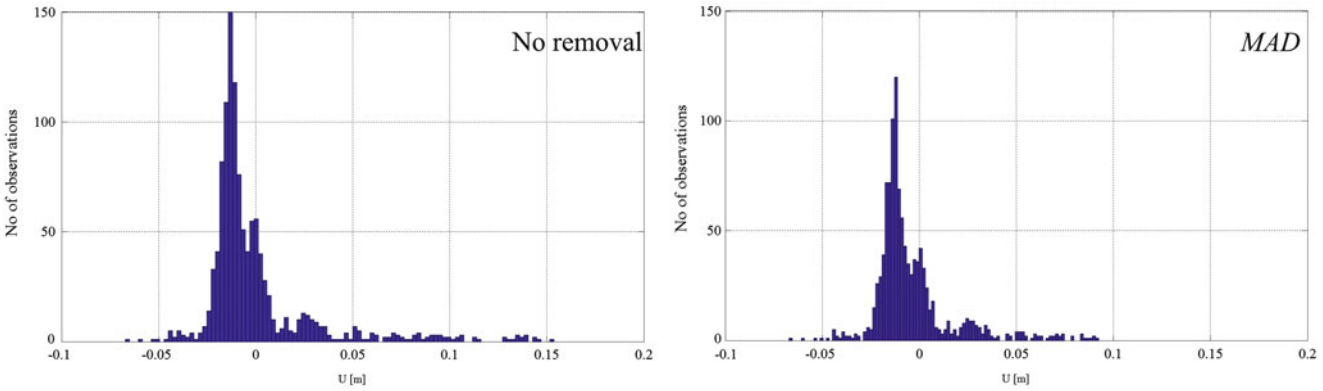

Fig. 6 The probability density function for the SNEC station – the Up component with no removal (*left*) and after *MAD* (*right*) outliers removal

of the Up component show quite large differences between skewness after 3σ and *MAD*. The differences between the kurtosis values after 3σ and *MAD* removal in most cases fall into 3 times the *SEK*. However, the differences are greater for few stations: HERS (the East and Up components), MDVO (the East component), SNEC (the East and Up components), SFER (the North and Up components). One of the kurtosis interpretations is the precision of data gathered. If kurtosis is high, precision is also high – the peak near the mean is very distinct (but only if the skewness is equal to 0). In case of the inappropriate criterion of outliers removal and no analyses of skewness, remaining outliers can have a significant impact on kurtosis values and therefore lead to falsified conclusions. The example of data stated as highly precised (without analysing its skewness) is presented in the Fig. 6. However, it is well known that high values of kurtosis can also mean heavy tails, which is exactly what would be expected if outliers are present. Thus, the large value of kurtosis obtained without outliers removal is entirely expected. Therefore the data pre-analysis is so essential before any further estimations.

5 Discussion and Conclusions

Our main goal in this research is to show how the proper removal of outliers affects the estimation of kurtosis and skewness and therefore our understanding of the nature of the data. The pre-analysis of data that includes outliers removal has to be well-chosen to the type of time series. The commonly used 3σ criterion seems to fail in case of spread GNSS time series, due to the fact that the standard deviation is calculated from the whole data set. Otherwise, the *MAD* criterion seems to be more appropriate for outliers removal, since it is calculated from the median value and therefore is much more robust for outliers than sigma-based methods. The obvious issue is that the outliers have to be removed, while further analyses that are to be conducted could be really sensitive to them. As showed in this research, although the MLE method resulted in quite consistent spectral indices, the amplitudes of noises were unacceptable in a few cases. They did not even differ in the range of their uncertainties, what may result in the variety of wrong interpretations. To show how the outliers can affect any further estimations, the probability analysis was performed, since skewness and kurtosis are highly sensitive to outliers. We showed that the wrongly-chosen criterion leads to the misinterpretation on the time series distribution and also data precision. A few of differences of skewness and kurtosis showed in this research were higher than the set value of 3 times the *SEK* and *SES*. It proved that sometimes the use of 3σ criterion is not proper enough to remove outliers since the analyzed time series do not strictly reflect the normal distribution. On the basis of the results, the usage of the *MAD* criterion is recommended for the GNSS data. Its advantages over commonly used sigma-based criteria are quite obvious, according to the presented paper. Being less sensitive to outliers, it removes greater number of them, providing in this way better interpretation of real effects. The presented paper discusses the univariate time series. In the future, authors plan to expand the work for multivariate cases as in Feng (2012).

Acknowledgments This research was financed by the Faculty of Civil Engineering and Geodesy MUT statutory research.

References

Agnew DC (1992) The time-domain behaviour of power-law noises. Geophys Res Lett 19(4):333–336

Altamimi Z, Collilieux X, Legrand J, Garayt B, Boucher C (2007) ITRF2005: a new release of the International Terrestrial Reference Frame based on time series of station positions and earth orientation parameters. J Geophys Res Solid Earth 112(B9). doi:10.1029/2007JB004949

Beavan J (2005) Noise properties of continuous GPS data from concrete pillar geodetic monuments in New Zealand and comparison with data from U.S. deep drilled braced monuments. J Geophys Res 110:B08410 doi:10.1029/2005JB003642

Bergstrand S, Schnereck H-G, Lidberg M, Johansson JM (2007) (2007): BIFROST: Noise properties of GPS time series. Dyn Planet Int Assoc Geodesy Symposia 130:123–130. doi:10.1007/978-3-540-49350-1_20

Bogusz J, Kontny B (2011) Estimation of sub-diurnal noise level in GNSS time series. Acta Geodynamica et Geomaterialia 83(163)273–281

Bos MS, Fernandes RMS, Williams SDP, Bastos L (2008) Fast error analysis of continuous GPS observations. J Geodesy 82:157–166. doi:10.1007/s00190-007-0165-x

Bruyninx C, Gurtner W, Muls A (1996) The EUREF permanent GPS network. Ankara, Turkey, May 22–25 1996, EUREF Publication No. 5, Veröffentlichungen der Bayerischen Kommission für die Internationale Erdmessung der Bayerischen Akademie der Wissenschaften, pp 123–130

Cramer D (1977) Basic Statistics for Social Research. Step-by-step calculations and computer techniques using. Routledge, Minitab. ISBN 0-419-12004-7

Dach R, Hugentobler U, Fridez S, Meindl M (eds) (2007) Bernese GPS software version 5.0. Astonomical Institute, the University of Bern, Bern

Dong D, Fang P, Bock Y, Webb F, Prawirodirdjo L, Kedar S, Jamason P (2006) Spatiotemporal filtering using principal component analysis and Karhunen-Loeve expansion approaches for regional GPS network analysis. J Geophys Res 111:B03405. doi:10.1029/2005JB003806

Feng Y (2012) Regression and hypothesis tests for multivariate GNSS state time series. J Global Positioning Syst 11(1):33–45

Johansson JM, Davis JL, Schnereck H-G, Milne GA, Vermeer M, Mitrovica JX, Bennett RA, Jonsson B, Elgered G, Elosegui P, Koivula H, Poutanen M, Ronnang BO, Shapiro LI (2002) Continuous GPS measurements of postglacial adjustment in Fennoscandia J Geodetic results. J Geophys Res 107(B8):2157. doi:10.1029/2001JB000400

Johnson HO, Agnew DC (1995) Monument motion and measurements of crustal velocities. Geophys Res Lett 22(21):2905–2908. doi:10.1029/95GL02661

King MA, Williams SDP (2009) Apparent stability of GPS monumentation from short-baseline time series. J Geophys Res 114:B10. doi:10.1029/2009JB006319

Klos A, Bogusz J, Figurski M, Kosek W (2014) Uncertainties of geodetic velocities from permanent GPS observations: the Sudeten case study. Acta Geodyn Geomat 11/3(175):201–209. doi:10.13168/AGG.2014.0005

Mandelbrot B (1983) The fractal geometry of nature. W.H. Freeman, San Francisco, 466 pp

Mandelbrot B, Van Ness J (1968) Fractional Brownian motions, fractional noises, and applications. SIAM Rev 10:422–439

Mao A, Harrison CGA, Dixon TH (1999) Noise in GPS coordinate time series. J Geophys Res 104(B2):2797–2816

Mosteller F, Tukey J (1977) Data analysis and regression. Addison-Wesley, Upper Saddle River

Peinke J, Bottcher F, Barth S (2004) Anomalous statistics in turbulence, financial markets and other complex systems. Ann Phys 13:450–460

Ruppert D (2011) Statistics and data analysis for financial engineering. Springer, New York, Dordrecht, Heidelberg, London. doi:10.1007/978-1-4419-7787-8

Sachs L (1984) Applied statistics: a handbook of techniques. Springer-Verlag, New York, p 253

Sura P, Gille ST (2003) Interpreting wind-driven Southern Ocean variability in a stochastic framework. J Mar Res 61:313–334

Sura P, Gille ST (2010) Stochastic dynamics of sea surface height variability. J Phys Oceanogr 40(7):1582–1596. doi:10.1175/2010JPO4331.1

Teferle FN, Williams SDP, Kierulf KP, Bingley RM, Plag HP (2008) A continuous GPS coordinate time series analysis strategy for high-accuracy vertical land movements. Phys Chem Earth 33(2008):205–216. doi:10.1016/j.pce.2006.11.002

Williams SDP (2003) The effect of coloured noise on the uncertainties of rates estimated from geodetic time series. J Geodesy 76:483–494. doi:10.1007/s00190-002-0283-4

Williams SDP (2008) CATS: GPS coordinate time series analysis software. GPS Solutions 12:147–153. doi:10.1007/s10291-007-0086-4

Williams SDP, Bock Y, Fang P, Jamason P, Nikolaidis RM, Prawirodirdjo L, Miller M, Johnson D (2004) Error analysis of continuous GPS position time series. J Geophys Res 109:B03412. doi:10.1029/2003JB002741

Real-Time Precise Point Positioning Using BeiDou

Javier Tegedor, Kees de Jong, Xianglin Liu, Erik Vigen, and Ola Øvstedal

Abstract

Satellite positioning is evolving rapidly, with the deployment of Galileo and BeiDou systems, in addition to the modernisation programmes for GPS and GLONASS. At the time of writing, the BeiDou constellation consists of 5 Geostationary Orbit (GEO), 5 Geosynchronous Orbit (IGSO) and 4 Medium-Earth Orbit (MEO) satellites. The constellation design is particularly interesting as it allows visibility of a sufficient number of BeiDou satellites over Asia for autonomous positioning. In this paper, possibilities for real-time precise point positioning (PPP) using BeiDou are explored.

For real-time generation of orbit and clock products, observation data from Fugro's proprietary station network are used, together with data from the IGS Multi-GNSS Experiment (MGEX). In order to perform orbit estimation, the NAPEOS (Navigation Package for Earth Orbiting Satellites) software has been extended for processing BeiDou data.

Satellite orbits are generated every hour and include a predicted part which can be used for real-time positioning. In order to estimate the accuracy of the real-time orbit, a validation with post-processed products is presented.

A Kalman filter has been extended to process BeiDou observation data, in order to estimate satellite clock biases in real-time.

For precise point positioning, Fugro's kinematic PPP engine is used. The engine is fed with real-time orbits and clocks, as well as observation data from test receivers. Kinematic PPP results are presented, in real-time and post-processing, including BeiDou standalone and in combination with GPS.

Keywords

BeiDou • Orbit Determination • Precise Point Positioning • real-time

1 Introduction: BeiDou Status

BeiDou, the Chinese satellite navigation system, started with the experimental phase from 2000 to 2003. During this period, three geostationary satellites were put in orbit, known as Beidou 1B, 1C and 1D, which constituted the initial regional phase of the system, known as Beidou-1.

The operational system, known as Compass/Beidou-2 is well under development. The constellation has been designed to provide augmented navigation services over China, thanks to Inclined Geosynchronous Orbit (IGSO) and Geostationary

J. Tegedor (✉) • O. Øvstedal
Norwegian University of Life Sciences, Ås, Norway
e-mail: javier.tegedor@nmbu.no; ola.ovstedal@nmbu.no

K. de Jong • X. Liu
Fugro Intersite BV, Leidschendam, The Netherlands
e-mail: k.djong@fugro.nl; x.liu@fugro.nl

E. Vigen
Fugro Satellite Positioning AS, Oslo, Norway
e-mail: e.vigen@fugro.no

© Springer International Publishing Switzerland 2015

C. Rizos, P. Willis (eds.), *IAG 150 Years*, International Association of Geodesy Symposia 143,
DOI 10.1007/1345_2015_118

Table 1 Operational BeiDou satellites in August 2013 (source: www.celestrack.org)

PRN	Common name	Launch date	COSPAR ID	NORAD ID	Position
C01	Beidou G1	2010-01-16	2010-001A	36287	140.0° East
C02	Beidou G6	2012-10-25	2012-059A	38953	80.0° East
C03	Beidou G3	2010-06-02	2010-024A	36590	84.7° East
C04	Beidou G4	2010-10-31	2010-057A	37210	160.0° East
C05	Beidou G5	2012-02-24	2012-008A	38091	58.8° East
C06	Beidou IGSO 1	2010-07-31	2010-036A	36828	
C07	Beidou IGSO 2	2010-12-17	2010-068A	37256	
C08	Beidou IGSO 3	2011-04-09	2011-013A	37384	
C09	Beidou IGSO 4	2011-07-26	2011-038A	37763	
C10	Beidou IGSO 5	2011-12-01	2011-073A	37948	
C11	Beidou M3	2012-04-29	2012-018A	38250	Plane B/slot 4
C12	Beidou M4	2012-04-29	2012-018B	38251	Plane B/slot 3
C13	Beidou M5	2012-09-18	2012-050A	38774	Plane A/slot 7
C14	Beidou M6	2012-09-18	2012-050B	38775	Plane A/slot 8

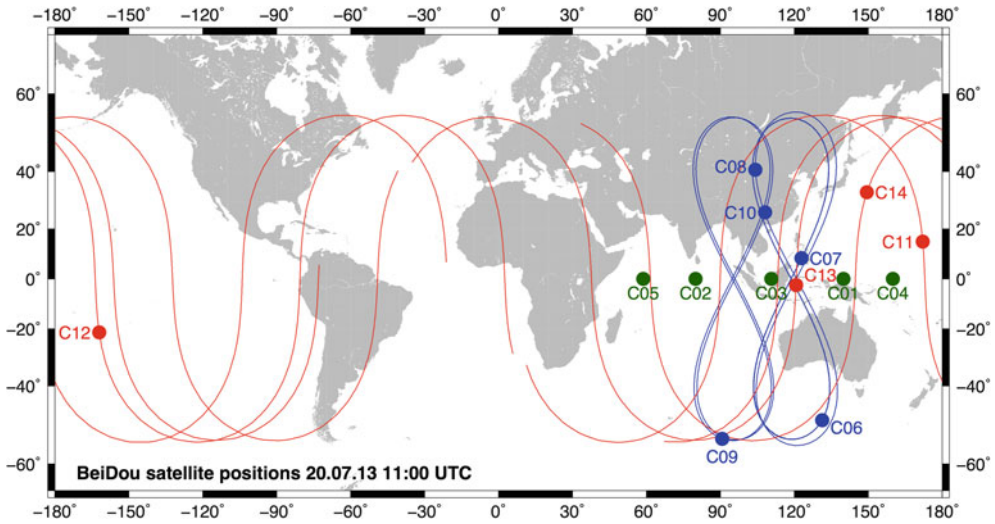

Fig. 1 Ground track for BeiDou constellation, as of July 20th 2013. IGSO satellites in *blue*, MEO satellites in *red* and GEO satellites in *green*

Orbit (GEO) satellites, in addition to Medium Earth Orbit (MEO) satellites for providing global coverage. At the time of writing, the constellation consists of 14 operational satellites, whose characteristics are detailed in Table 1. The ground track is depicted in Fig. 1. The second phase of BeiDou foresees the operation of up to 27 MEO satellites before 2020, offering worldwide positioning coverage.

BeiDou has been designed for transmitting three carrier frequencies: 1589.74 MHz (B1), 1207.14 MHz (B2) and 1268.52 MHz (B3) (Grelier 2007). The Interface Control Document for the open-service signals on the B1 carrier was released in December 2012 (CSNO 2012).

BeiDou has drawn the attention of the scientific community since its very beginning. Shortly after the first MEO M1 satellite was launched in 2007, ranging codes were obtained thanks to the use of high-gain antennas and advanced signal processing techniques (Grelier 2007; Wilde et al. 2007; Gao et al. 2009). Initial results for orbit determination of M1 satellite using Satellite Laser Ranging (SLR) were presented in Hauschild et al. (2011), together with clock estimates obtained using microwave observations from two GNSS receivers.

Initial positioning results using a reduced 3-GEO and 3-IGSO constellation were presented in Shi et al. (2012). Using experimental broadcast ephemerides, accuracies of tens of meters were achieved with absolute positioning. Regarding relative positioning, accuracy below decimeter level was obtained in a short baseline configuration. A characterization of triple-carrier ionosphere-free linear combination for BeiDou frequencies was presented in Montenbruck et al. (2012). In the same study, ambiguity resolution was also attempted in a short baseline configuration making use of the extra wide-lane observations with the signals on the B2 and B3 frequencies.

The first assessment on precise orbit determination using GNSS data for GEO and IGSO satellites was presented in Steigenberger et al. (2013), where several solar radiation pressure parametrisations were assessed. In that study,

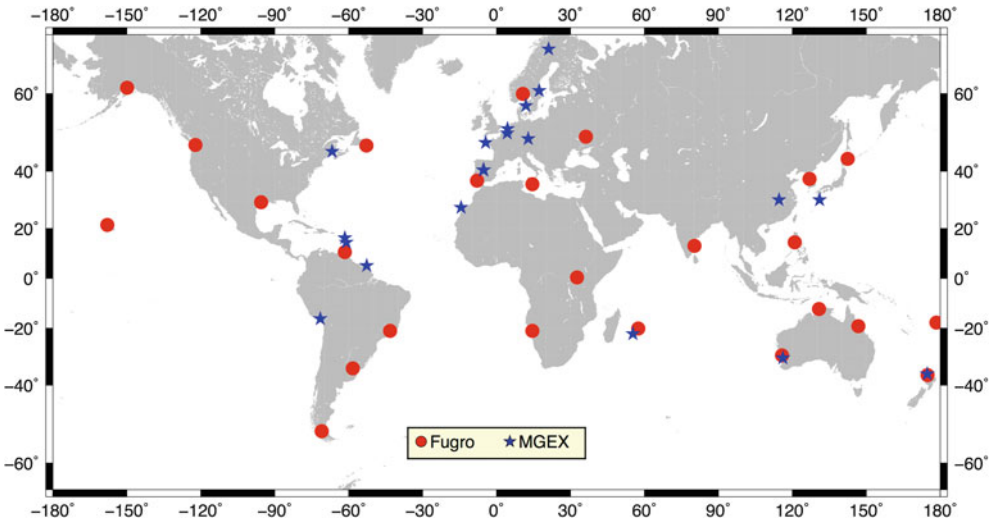

Fig. 2 BeiDou tracking network, including Fugro and MGEX stations (August 2013)

the GEO orbit accuracy was limited to few meters due to the reduced size of the tracking network available. Further results using an extended network are available in He et al. (2013), where sub-meter orbit errors were achieved for the first time.

In this study, we assess the possibility of real-time navigation with BeiDou, using the Precise Point Positioning technique (Zumberge et al. 1997). For the generation of satellite orbit and clock estimates, a global GNSS tracking network is used, which is described in Sect. 2. Section 3 presents the processing strategy for real-time PPP. In Sect. 4, BeiDou orbit results are given. BeiDou standalone positioning results are presented in Sect. 5, and combined GPS and BeiDou positioning is discussed in Sect. 6. Conclusions are summarized in Sect. 7.

2 BeiDou Tracking Networks: MGEX and Fugro

In 2010, the International GNSS Service (IGS) (Dow et al. 2009) started the MGEX campaign (Rizos et al. 2013), in order to provide the scientific community with tracking data for the new GNSS signals and systems, using state-of-the art geodetic equipment. At the time of writing, a subset of the stations in the network are equipped with BeiDou-capable equipment, including Trimble NETR9, Javad Delta G3T and Septentrio PolaRx4 geodetic receivers.

In parallel, Fugro has upgraded the Trimble NETR9 receivers in its proprietary reference station network in order to support new constellations, on top of the existing commercial G2 PPP service based on GPS and GLONASS (Melgard et al. 2009).

Table 2 BeiDou-capable receivers available from Fugro and MGEX networks

Receiver type	Fugro	MGEX	B1	B2	B3
Trimble NETR9	25	13	✓	✓	✓
Septentrio PolaRx4	0	7	✓	✓	
Javad Delta G3T	0	1	✓	✓	

In order to obtain the highest possible accuracy in orbit and clock estimation, all available stations from both networks are used. Figure 2 shows the combined station network, and the receiver type distribution is summarized in Table 2. Although many of the stations are located in Europe, the network is still reasonably well distributed, thus providing worldwide tracking of BeiDou with an adequate level of redundancy.

Regarding the observation types available, it has been found that not all MGEX receivers available are tracking BeiDou satellites; this depends not only on the receiver type, but also on particular firmware installed in each receiver. A summary of the receivers available with BeiDou observations is displayed in Table 2. Regarding observations types, all Trimble NETR9 receivers are providing pseudorange and carrier-phase observables in the three BeiDou carrier frequencies, B1, B2 and B3. However, Javad Delta G3T and Septentrio PolaRx4 receivers are not providing tracking data in B3, due to a current limitation in the receiver hardware and/or firmware. In order to maximize data availability for the orbit computation, B1 and B2 frequencies are used in this study, which are processed using the well-known ionosphere-free linear combination.

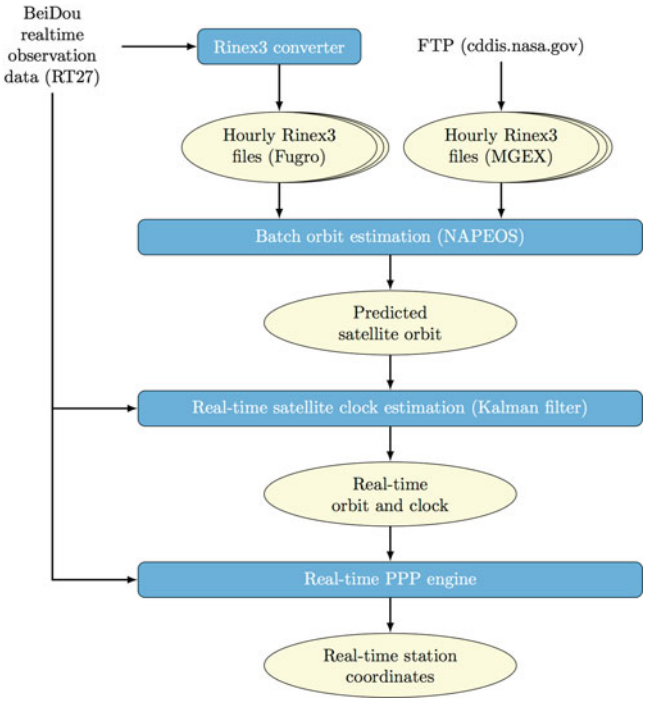

Fig. 3 Processing strategy for real-time PPP

3 Processing Strategy

The processing strategy for real-time PPP is depicted in Fig. 3, where BeiDou data is processed together with GPS. The NAPEOS software package (Springer and Dow 2009) is used to generate an orbit prediction suitable for real-time applications. The software has been enhanced in order to process BeiDou observation data via RINEX3 format (IGS and RTCM-SC104 2013). For the orbit estimation, hourly observation files from both Fugro and MGEX stations are used. MGEX station data is downloaded from the CDDIS data centre (ftp://cddis.nasa.gov). The Fugro data arriving in real-time via Trimble's RT27 format is converted to RINEX3 using a specific converter. The predicted orbit, based on NAPEOS batch-runs using 48 h of observation data, is updated every hour, in order to ensure short prediction times and thus avoiding large orbit errors for real-time PPP.

For generation of real-time satellite clocks, a Kalman filter has been developed where both BeiDou- and GPS-data are processed using the predicted orbits as fixed values. The Kalman filter also estimates ancillary parameters, such as station clock biases, wet tropospheric delays and carrier-phase ambiguities. GPS-BeiDou intersystem biases are estimated as part of the orbit adjustment, and kept fixed for real-time clock estimation. The Kalman filter is fed with observation data coming from the Fugro network, which is available in real-time with few seconds latency.

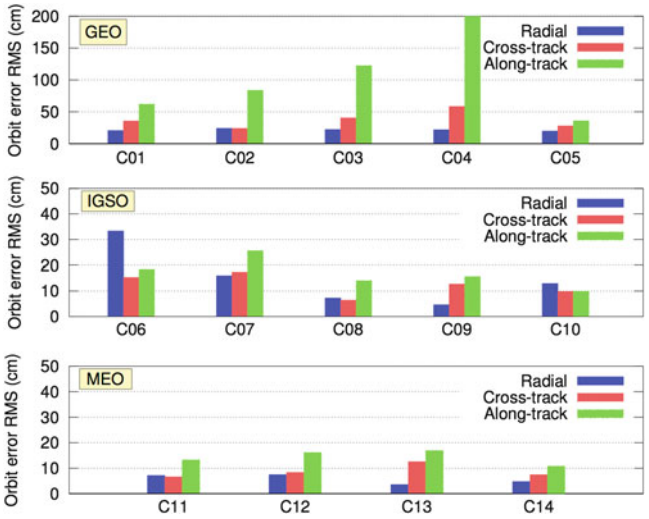

Fig. 4 Orbit comparison results (real-time vs post-processed) on August 17th, 2013

Finally, orbit prediction and real-time clock estimates are injected into Fugro proprietary PPP engine, together with observation data from the RT27 streams, in order to obtain station coordinates in real-time making use of BeiDou satellites.

4 Orbit Results

In an attempt to assess the accuracy of the BeiDou orbits, the real-time estimates are compared against a post-processed product stemming from 24 h of observation data. It is assumed that the post-processed orbit has higher accuracy, therefore this comparison is a good assessment of the accuracy of the real-time orbit, which is later used in PPP.

Daily statistics of the orbit comparison are presented in Fig. 4. The accuracy of IGSO and MEO satellites is very good, down to sub-decimeter level. However, the orbit accuracy of GEO satellites is worse, at decimeter level, including some meter-level outliers, specially for the along-track orbit component. The reason for the lower orbit accuracy for GEO satellites is mainly the lack of geometry variation for these satellites, as they appear static in the sky observed from each reference station. These poor geometry conditions weaken the observability of the orbit dynamics, affecting the estimated orbit parameters. These results are consistent with the analysis previously presented in He et al. (2013).

The radial and cross-track orbit components are still very good, and the GEO satellites can be used in PPP.

It should be noted that there are still a number of factors limiting the orbit quality in the network adjustment. These are mainly due to modeling uncertainties, such as precise satellite antenna phase center corrections for BeiDou

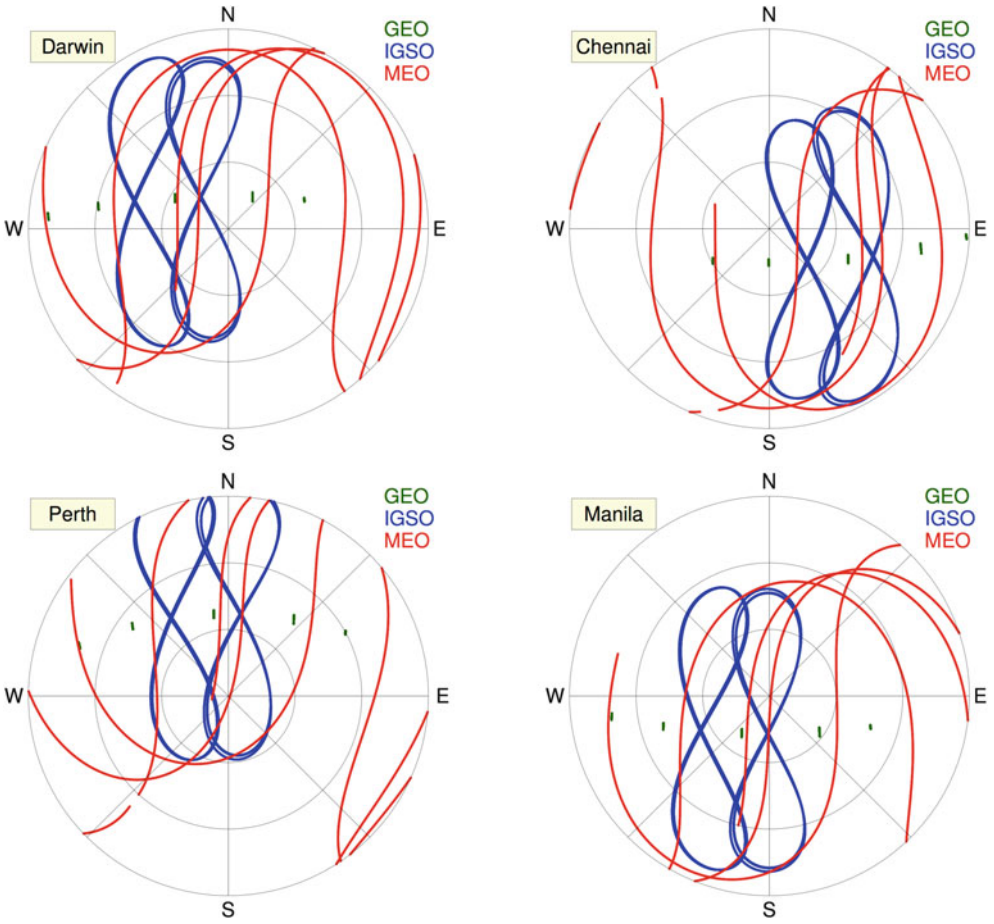

Fig. 5 Polar visibility plot for Fugro stations in Darwin, Chennai, Perth and Manila

satellites, which are available for GPS (Schmid et al. 2005). For the BeiDou satellites, the antenna phase center offsets proposed in the MGEX campaign have been used, namely [0.6 0.0 1.1] meters in XYZ in the satellite body-fixed reference frame. For the BeiDou frequencies, antenna phase center corrections are not yet publicly available for receiver antennas. Furthermore, BeiDou satellite modeling needs to be improved, in particular regarding solar radiation pressure and attitude modeling. In this study, CODE empirical model with 5 parameters has been used for solar radiation pressure. Finally, ambiguity resolution is a promising way to improve the orbit quality, in the same way as it can be done for GPS (Ge et al. 2005). The assessment of ambiguity resolution for BeiDou goes beyond the scope of this article, as it needs an extensive characterization of BeiDou signals.

5 BeiDou Standalone PPP

In order to assess PPP performance, several Fugro reference stations in the Asia-Pacific region are selected, as they have full visibility of the BeiDou constellation, including also GEO and IGSO satellites, and data can be processed in real-time via data streams in RT27 format.

In particular, stations located in Chennai (India), Manila (Philippines), Darwin and Perth (Australia) are selected for this analysis. Polar visibility plots for these stations are depicted in Fig. 5.

Precise point positioning results for station Perth are represented in Fig. 6, where the PPP engine is run in kinematic mode using 10 s observation sampling. These results were obtained in real-time using BeiDou-standalone PPP on August 17th, 2013. The good visibility of the BeiDou constellation allows to have enough satellites in view for continuous positioning. However, the satellite geometry is occasionally suboptimal as can be observed in the increased values for horizontal and vertical dilution of precision (HDOP and VDOP) in the second half of the day. Horizontal positioning errors for the three other stations are presented in Fig. 7.

In order to compare real-time versus post-processed solutions, the PPP engine has also been run using the post-processed orbit and clock solution mentioned in Sect. 4. The PPP configuration between the real-time and the

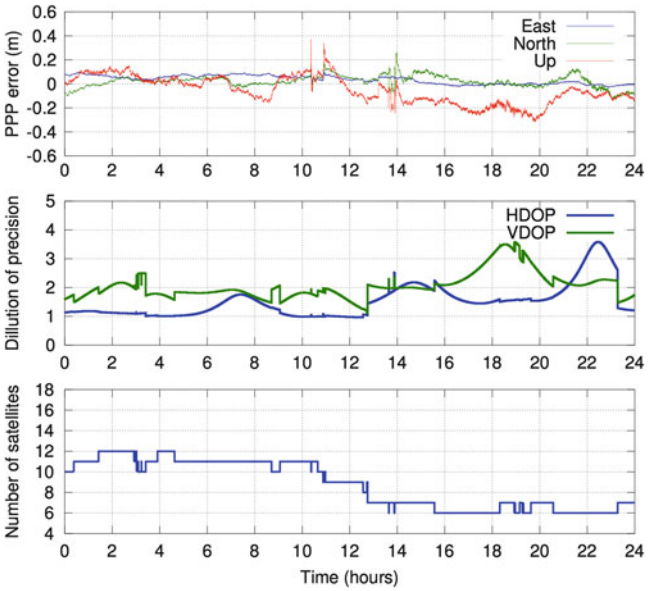

Fig. 6 Real-time BeiDou-standalone PPP results for Perth, on August 17th, 2013

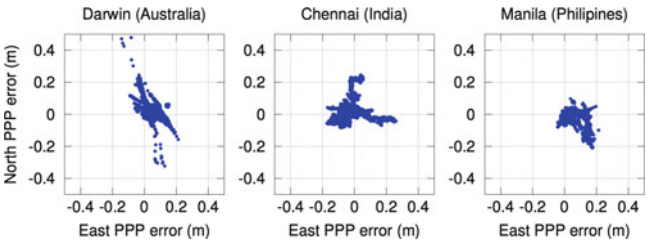

Fig. 7 Real-time horizontal results for BeiDou PPP, on August 17th, 2013

post-processed solution is identical, the only difference is the source of orbit and clocks. Positioning statistics for the four stations are summarized in Table 3. The post-processed solution is significantly more accurate than the real-time one; the reason is mainly the higher quality of the post-processed orbit and clock estimates.

6 GPS+BeiDou PPP

In this section the contribution of BeiDou on top of GPS-based PPP is addressed. In order to obtain positioning statistics in different configurations, the PPP engine is run in post-processing using the satellite orbit and clocks obtained in real-time, as described in Sect. 3.

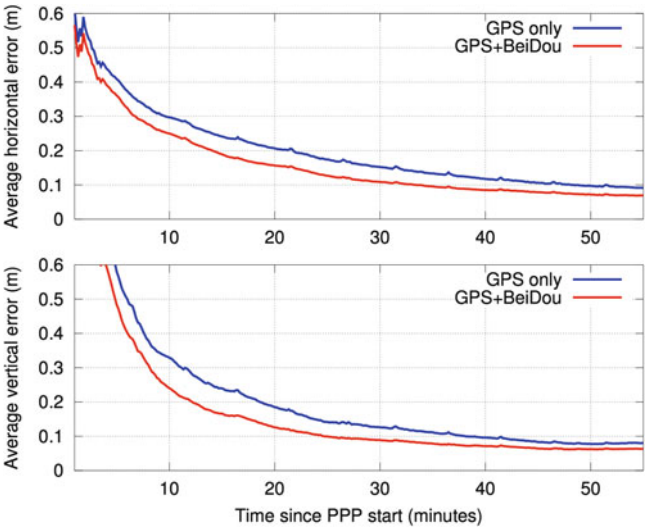

Fig. 8 Convergence time analysis for GPS standalone and BeiDou+GPS

Additionally, the PPP engine is restarted every hour, in order to observe the improvement in convergence time when adding BeiDou on top of GPS. Figure 8 represents average position error as a function of time since PPP start, for all four stations from 18th to 22nd of August 2013. A total of 480 independent PPP runs have been performed for this analysis.

It is interesting to observe that adding BeiDou on top of GPS systematically improves PPP position accuracy and reduces convergence time by several minutes. These results are very encouraging, taking into account the current limitations on BeiDou tracking data and satellite modelling.

7 Conclusions

In this article, the first real-time PPP results using BeiDou have been presented. Using a well distributed station network, real-time orbit accuracy can be achieved at decimeter level for MEO and IGSO satellites, and around meter-level for GEO satellites. The accuracy of GEO orbits is mainly limited due to lack of geometry change, resulting in poor observability of the orbit dynamic parameters.

Table 3 BeiDou standalone PPP statistics (RMS), on August 17th 2013

Station location	Real-time			Post-processing		
	East (cm)	North (cm)	Up (cm)	East (cm)	North (cm)	Up (cm)
Darwin (Australia)	6.09	5.88	16.14	4.24	4.40	7.81
Perth (Australia)	4.73	5.27	12.63	1.31	3.75	4.44
Chennai (India)	8.68	5.90	15.25	3.41	1.63	8.02
Manila (Philippines)	7.60	4.68	13.60	3.38	1.59	8.71

The real-time positioning accuracy using BeiDou PPP standalone is around 5 cm horizontal and 15 cm vertical, for stations with good visibility of IGSO and GEO satellites. Post-processed PPP results are significantly better thanks to the higher quality of post-processed orbits and clocks. Regarding convergence time, it has been observed that combined GPS and BeiDou PPP converges faster than GPS standalone, thanks to the enhanced visibility and satellite geometry when adding the new constellation.

The overall BeiDou accuracy is currently limited by the number of receivers with BeiDou tracking capability, as well as modeling limitations for BeiDou, such as antenna phase center corrections, solar radiation pressure and attitude modelling. Taking these limitations into account, the positioning results are very promising and will likely be improved following the further development of the BeiDou constellation, as well as further improvements in the processing models for these satellites.

References

CSNO (2012) BeiDou Navigation Satellite System. Signal In Space Interface Control Document. Open Service Signal B1I. BDS-SIS-ICD-1.0. China Satellite Navigation Office

Dow J, Neilan R, Rizos C (2009) The International GNSS Service in a changing landscape of global navigation satellite systems. J Geod 83(3):191–198

Gao GX, Chen A, Lo S, Lorenzo DD, Walter T, Enge P (2009) Compass-M1 Broadcast Codes in E2. IEEE J Sel Top Sign Proces 3(4):599–612

Ge M, Gendt G, Dick G, Zhang FP (2005) Improving carrier-phase ambiguity resolution in global GPS network solutions. J Geod 79(1–3):103–110

Grelier T (2007) Initial observations and analysis of compass MEO satellite signals. Inside GNSS May/June:39–42

Hauschild A, Montenbruck O, Sleewaegen J-M, Huisman L, Teunissen PJG (2011) Characterization of compass M-1 signals. GPS Solutions 16(1):117–126

He L, Ge M, Wang J, Wickert J, Schuh H (2013) Experimental study on the precise orbit determination of the BeiDou navigation satellite system. Sensors (Basel, Switzerland) 13(3):2911–28

IGS and RTCM-SC104 (2013) Rinex (The Receiver Independent Exchange Format) Version 3.02. Available at ftp://igs.org/pub/data/format/rinex302.pdf

Melgard T, Vigen E, de Jong K, Oerpen O (2009) G2 – the first real-time GPS and GLONASS precise orbit and clock service. In: Proceedings of the 22nd International Technical Meeting of the Satellite Division of the Institute of Navigation (ION GNSS 2009), pp 1885–1891

Montenbruck O, Hauschild A, Steigenberger P, Hugentobler U, Teunissen P, Nakamura S (2012) Initial assessment of the COMPASS/BeiDou-2 regional navigation satellite system. GPS Solutions 17(2):211–222

Rizos C, Montenbruck O, Weber R, Weber G, Neilan R, Hugentobler U (2013) The IGS MGEX experiment as a milestone for a comprehensive multi-GNSS servicele. In: Proceedings of the ION 2013 Pacific PNT Meeting, Honolulu, Hawaii, pp 289–295

Schmid R, Rothacher M, Thaller D, Steigenberger P (2005) Absolute phase center corrections of satellite and receiver antennas. GPS Solutions 9(4):283–293

Shi C, Zhao Q, Hu Z, Liu J (2012) Precise relative positioning using real tracking data from COMPASS GEO and IGSO satellites. GPS Solutions 17(1):103–119

Springer T, Dow J (2009) NAPEOS Mathematical Models and Algorithms 1.0. European Space Agency, DOPS-SYS-TN-0100-OPS-GN

Steigenberger P, Hugentobler U, Hauschild A, Montenbruck O (2013) Orbit and clock analysis of compass GEO and IGSO satellites. J Geod 87(6):515–525

Wilde WDE, Boon F, Sleewaegen JM, Wilms F (2007) More compass points tracking China's MEO satellite. Inside GNSS July/August:44–48

Zumberge JF, Heflin MB, Jefferson DC, Watkins MM (1997) Precise point positioning for the efficient and robust analysis of GPS data from large networks. J Geophys Res 102(1):5005–5017

GFZ Global Multi-GNSS Network and Data Processing Results

Maik Uhlemann, Gerd Gendt, Markus Ramatschi, and Zhiguo Deng

Abstract

The Helmholtz Centre Potsdam GFZ German Research Centre for Geosciences (GFZ) is operating a worldwide Global Navigation Satellite Systems (GNSS) station network since many years. With recent developments in receiver technology and new upcoming navigation satellite systems like Galileo an upgrade of our stations was needed to track all GNSS. We will present the current status and setup of our station network and the plan for future upgrades. All modernized stations are presently contributing to the Multi-GNSS EXperiment (MGEX) of the International GNSS Service (IGS) as well as to the COoperative Network of GNSS Observations (CONGO). Selected results from a combined GPS/Galileo data processing will be shown. The used data were taken mainly from the public available MGEX network whereas the focus of analysis lies on precise orbit and clock determination of Galileo In-Orbit-Validation (IOV) satellites. Quality assessments are given which are based on orbit overlap statistics, clock stabilities as well as comparisons with external solutions. Additionally an independent validation of the orbits is derived through Satellite Laser Ranging (SLR) measurements. Furthermore some initial results of BeiDou data processing are shown which were derived with an experimental set of MGEX data.

Keywords

BeiDou • Galileo-IOV • MGEX • Multi-GNSS • POD

1 Introduction

The landscape of GNSS is rapidly changing since several years. The full operational systems GPS and GLONASS are going to be modernized and new global available systems will be deployed and are already providing initial services, e.g. the European Galileo or the Chinese BeiDou. The last mentioned system provides a interesting constellation, which differs from all other GNSS and consists of satellites in Geostationary-Earth-Orbit (GEO), Inclined-Geo-Syncronus-Orbit (IGSO) and of course the typical Medium-Earth-Orbit (MEO) (Steigenberger et al. 2013b). It is expected that in 2020 around 100 navigation satellites will be operational. The new constellations, signals and frequencies opens possibilities for new scientific research areas, but this initiates also a competition to track all possible signals and also to adapt existing software packages to handle the new systems. For this reason the IGS started the MGEX campaign in 2012 (Montenbruck 2013) where Multi-GNSS station data from a global ground tracking network are collected and made public to the community. Several Analysis Centres (ACs) of the IGS are currently using these observation data to produce precise satellite orbit and clock products. These are routinely or campaign-wise available and give the possibility for further experiments and studies in the

M. Uhlemann (✉) • G. Gendt • M. Ramatschi • Z. Deng
Section 1.1 GPS/Galileo Earth Observation, Helmholtz Centre Potsdam, GFZ German Research Centre for Geosciences, Telegrafenberg, 14473 Potsdam, Germany
e-mail: uhle@gfz-potsdam.de

© Springer International Publishing Switzerland 2015

C. Rizos, P. Willis (eds.), *IAG 150 Years*, International Association of Geodesy Symposia 143,
DOI 10.1007/1345_2015_120

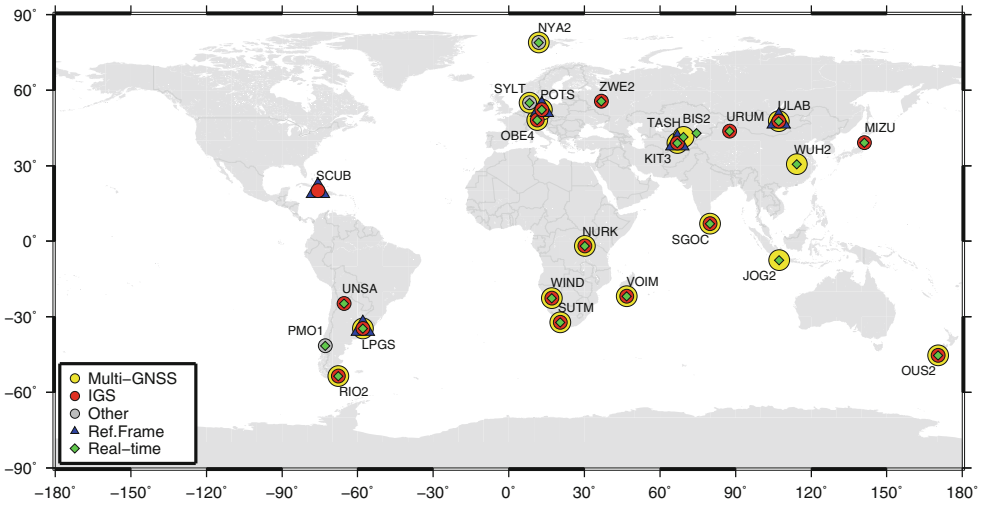

Fig. 1 Global network of GNSS sensor stations operated by GFZ. Modernized Multi-GNSS stations are marked *yellow*, IGS stations red and real-time stations *green*

challenging and exiting world of Multi-GNSS, e.g. for precise point positioning techniques or GNSS remote sensing. The following article will present the contribution of GFZ to MGEX. This comprises the current status and setup of the GFZ Multi-GNSS station network and the plan for future upgrades. Furthermore some selected results from a combined GPS/Galileo data processing with 10 weeks of data are shown. The quality of the orbit and clock products are assessed by means of orbit overlap statistics, clock stabilities as well as comparisons with external solutions. Additionally an independent validation of the orbits is derived through SLR measurements. Finally some initial results of a BeiDou data processing are shown which were derived from an experimental set of 3 weeks of MGEX data.

2 GFZ Multi-GNSS Station Network

GFZ is operating a global GNSS station network (currently ∼30 stations, the most important ones are shown in Fig. 1) since the early 1990s to support scientific research activities like crustal dynamics, precise satellite orbit and clock determination, and nowadays also GNSS remote sensing. With recent developments in receiver technology and new upcoming navigation satellite systems like Galileo an upgrade of our stations was needed to track all GNSS to support as much as possible research activities. Through the in-house development of GNSS sensor stations a reliable network performance can be ensured and even a fast adaption to unusual requirements from scientific projects is possible.

2.1 Current Status

Almost all of the 17 modernized stations are currently contributing to the MGEX campaign of the IGS as well as to the CONGO network which is led by German Aerospace Center (DLR). They are equipped with *JAVAD TRE_G3TH DELTA* receivers and high performance *JAV_RINGANT_G3T* choke-ring antennas. Actually the receivers are operated with firmware version 3.4.7 and are tracking the signals of GPS (L1/L2/L5), GLONASS (L1/L2), Galileo (L1/L5) and recently also from the Japanese QZSS (L1/L5) at five stations. The new installed antennas are individually calibrated using the anechoic chamber of the University of Bonn (Germany). All these stations provide real-time measurements in JAVAD proprietary format and in RTCM-3 format. For post-processing purposes the observation data are stored in RINEX-2 Gurtner and Estey (2005) and RINEX-3 IGS and RTCM-SC104 (2013) format to support as much as possible user needs in ongoing and future projects. The stations are designed to host any kind of commercial GNSS receiver; they use a PC with low power consumption and can be controlled fully remotely via a secure VPN connection.

2.2 Planned Network Upgrade

The plan for the near future comprises the upgrade of the majority of the GFZ operated stations to fulfill Multi-GNSS capability with focus on South- and Central America.

3 Galileo Data Processing Setup

3.1 Motivation

One of the main goals of this study is the demonstration of what is possible with the current MGEX tracking network. The focus lies on precise orbit and clock determination of the four Galileo In-Orbit-Validation (IOV) satellites and also

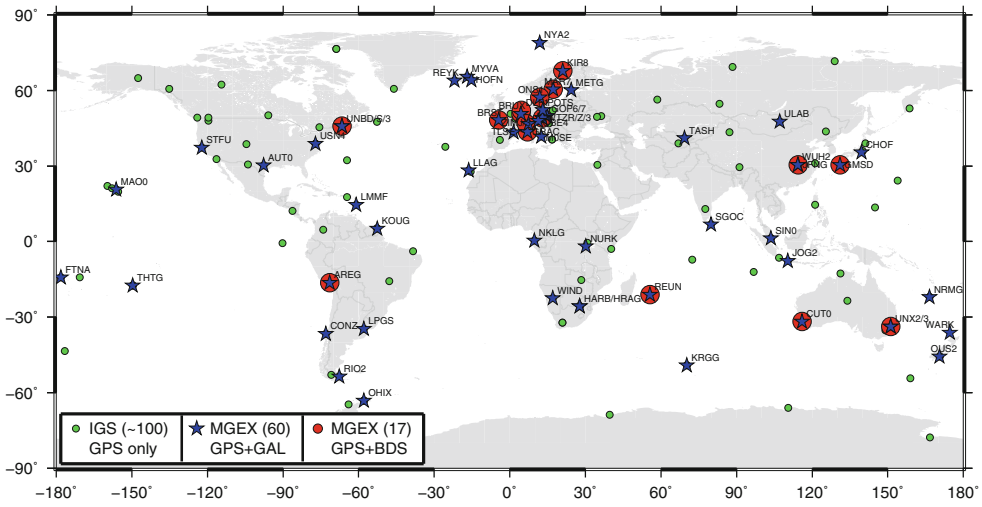

Fig. 2 Global network of IGS (*green*) and MGEX stations, which were set up for data processing. The 60 Galileo-MGEX stations (*blue*) realize a good global coverage for practical Galileo orbit determination purposes, whereas most of BeiDou-MGEX stations (*red*) are still located in Europe

the investigation of station tracking behavior and orbit issues. Initial experiences of Galileo orbit determination based on the CONGO network were already presented in Uhlemann et al. (2012).

3.2 Data Set and Products

The observation data were collected by Galileo-capable stations of the IGS MGEX network (Fig. 2). These files in RINEX-3 format were downloaded from the CDDIS MGEX data archive[1] for the time period of GPS-weeks 1738–1747 (27/04 to 07/07/2013).

DLR kindly provided corrected data files for their stations, which were affected by missing Galileo E1 observations due to a bug in the RINEX converter.

All orbit, clock and bias products (file extensions *.sp3, *.clk, *.bia) generated in this study are available at the CDDIS MGEX product archive.[2]

3.3 Processing Scheme

The general processing strategy is similar to the one used for the routine processing within the IGS-AC at GFZ. Most relevant information and parameter are summarized below:

- Fully combined GPS/Galileo processing with GFZ software package EPOS.P8
- Technique: Ionosphere-free linear combination, undifferenced carrier phase and pseudo range observations
- Observation types used: see Table 1.
- Sampling rate: 5 min; Elevation cut-off angle: 7°

Table 1 Defined RINEX-2/3 observation types for the combined GPS/Galileo data processing

Network	Type	GPS	Galileo	#Sta
IGS	RINEX-2	L1/L2	–	∼100
MGEX	RINEX-3	L1W/L2W	L1X/L5X or L1C/L5Q	∼60

The Galileo frequencies were chosen according their most frequently availability

- Orbit model: 5 SRP parameter (D, Y, B, sin/cos B)[3]; 3-day long-arcs
- Troposphere: hourly zenith total delay, daily north/east gradients
- Ambiguity fixing: GPS and Galileo
- Satellite and station clock: per epoch
- Inter System Bias (ISB): One bias parameter per station and day
- Satellite antenna phase centre offset: No estimated, use of confidential ESA values

4 Galileo Results and Comparisons

4.1 Orbit Overlaps

A first orbit quality assessment can be derived from overlapping time intervals at day boundaries determined from the final 3-day solution (Fig. 3). This long arc solution was chosen to improve the quality of the orbit and to overcome some problems which might occur due to the revolution period of approx. 14 h of the Galileo satellites. As a matter of fact, under this conditions the station geometry varies from day to day which might lead to decreased orbit qualities. This effect is typically much more pronounced when the global

[1] ftp://cddis.gsfc.nasa.gov/gnss/data/campaign/mgex.

[2] ftp://cddis.gsfc.nasa.gov/pub/gps/products/mgex.

[3] Sun-oriented coordinate system, D: axis from satellite to the Sun, Y: axis parallel to solar panel, B: completing right-hand system.

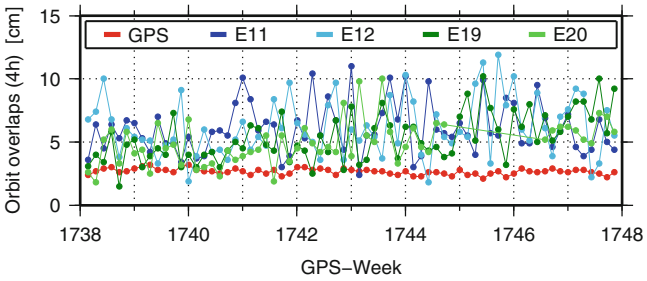

Fig. 3 Orbit overlap RMS (4 h) of Galileo satellites. For GPS the median of all satellites is given (∼3 cm)

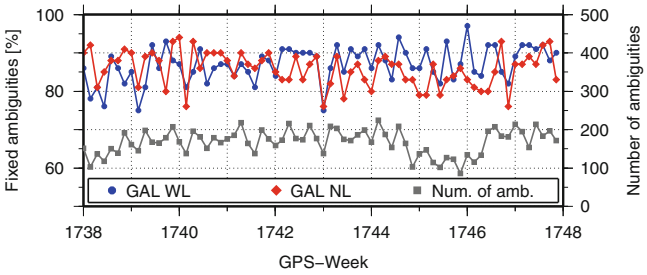

Fig. 4 Galileo ambiguity fixing success rates for wide-lane (*blue*) and the corresponding narrow-lane (*red*) ambiguities as well as the total number of ambiguities (*black*)

station distribution is uneven. Nevertheless, due to the longer arc length the possibility is given to uses an 4-h interval for the overlap statistics. It is shown that an average orbit accuracy (repeatability) of 6 cm can be achieved, whereas larger variations are still present, which typically depend on the availability of 'important' tracking sites, e.g. in the Pacific region.

4.2 Ambiguity Fixing

The integer carrier-phase ambiguities are fixed according to Ge et al. (2005) for the systems GPS and Galileo separately. Baseline lengths up to 4,000 km were allowed in both cases. To resolve the double-difference ambiguities for Galileo the available stations were grouped according their (receiver-dependent) observation types:

– Group 1: L1C/L5Q (e.g. BRUX)
– Group 2: L1X/L5X (e.g. POTS)

Only between stations belonging to the same group it was in a first step allowed to select the linear independent baselines until afterwards all remaining baselines were defined. The statistic of the Galileo wide-lane (WL) and narrow-lane (NL) ambiguities is given in Fig. 4. It can be seen that, despite their low overall number, it is possible to fix the Galileo ambiguities with a success rate of only about 85%. This may be a result from the very long baseline lengths, because only max. 30% of the baselines are shorter then 1,000 km,

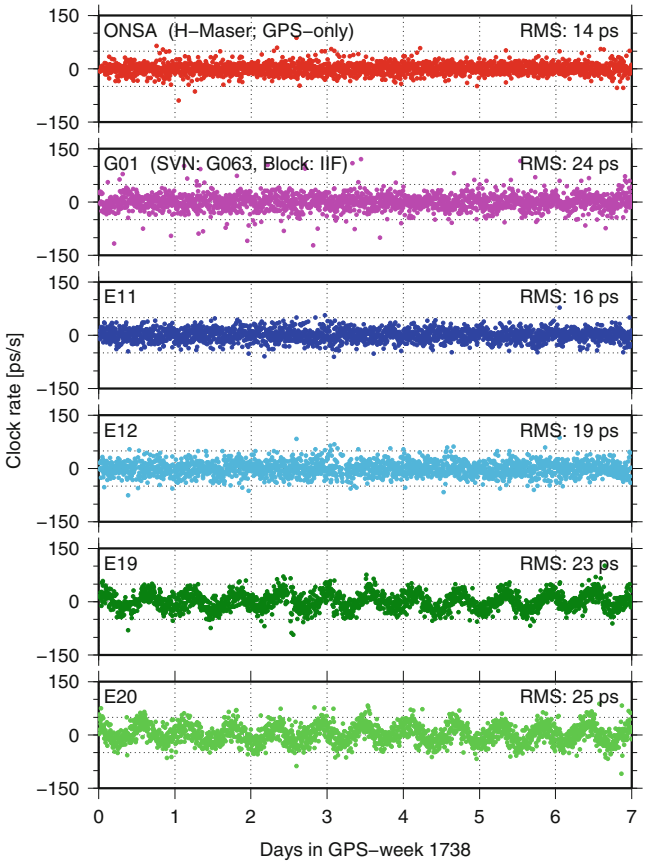

Fig. 5 Clock rates as first derivative of the adjusted clock corrections (de-trended) for one ground station (ONSA), one GPS satellite (G01) and all four Galileo-IOV satellites

or it may come from the different observation types which are given in the network. These effects will be studied further.

4.3 Clock Performance

During the test period all Galileo satellites were operated on modern Passive Hydrogen Masers (PHM) which are announced to be the most precise atomic clocks ever flown in space. In Fig. 5 it is depicted that the IOV satellite clock behavior is comparable to modern GPS Block IIF and also to H-Maser operated on ground. All IOV satellites are well performing, but clear pattern are visible in the clock rates for E19 and E20 which are obviously orbit modeling problems because of the correlation between radial orbit and clock errors. The reasons for the mis-modeling might be issues with the SRP model, outgassing effects or even thermal effects once per revolution. In the selected period (GPS-week 1738) both satellites (which are flying on the same orbital plane) are crossing the Earth shadow (angle of the Sun above the orbital plane (beta) is ∼0°).

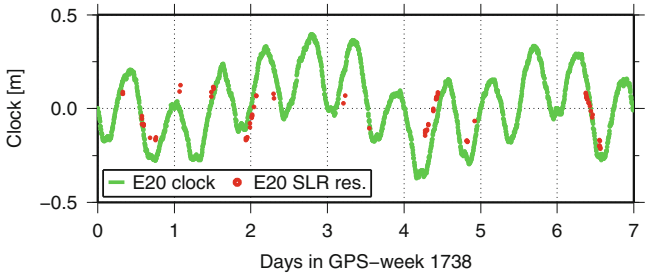

Fig. 6 Estimated satellite clock (de-trended) compared to SLR residuals (*red*) for satellite E20

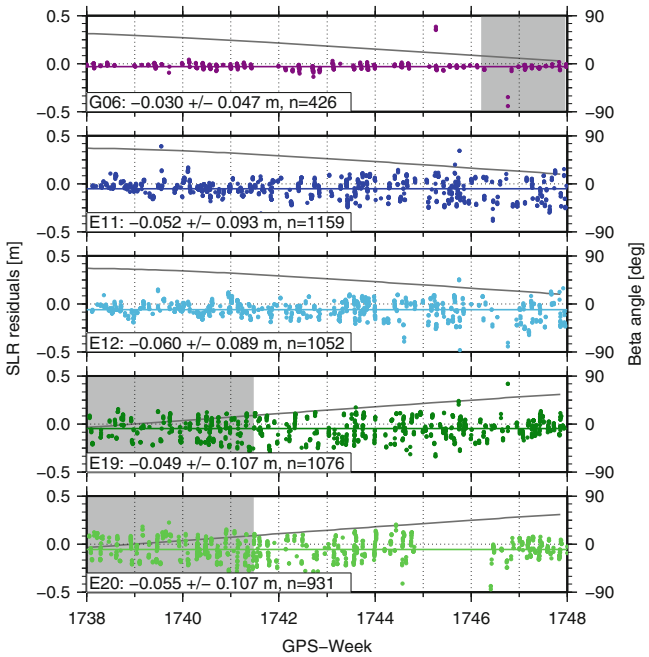

Fig. 7 SLR residuals for GPS and Galileo satellite orbits (threshold for outlier test: 0.5 m). Eclipse periods and beta angle are plotted in *grey*

The existence of these problems during eclipse seasons manifests when comparing the estimated satellite clocks with the (inverse) SLR residuals. This is exemplarily shown in Fig. 6 for the satellite E20.

4.4 Orbit Validation Using SLR

Fortunately, all Galileo-IOV satellites are equipped with laser reflectors thus an independent validation of the determined satellite orbits (mainly the radial component) can be assessed via SLR measurements (Fig. 7). The residual time series show the performance of all IOV satellite orbits and indicate orbit accuracies of ∼10 cm. A systematic bias of about −5 to −6 cm is obvious, as well as the dependency of the residuals with respect to beta angle. Comparable results were also reported by Steigenberger et al. (2013a).

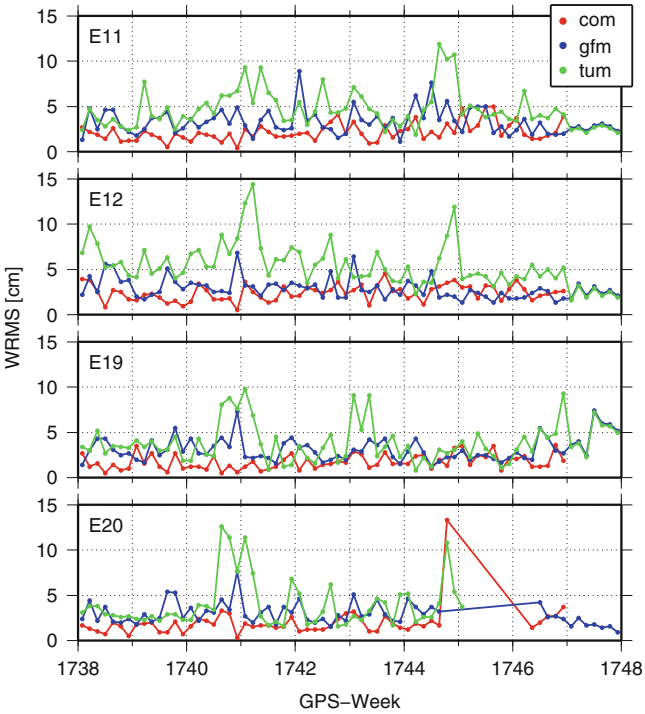

Fig. 8 Weighted RMS (WRMS) of individual MGEX-AC orbits with respect to the combined result for all Galileo-IOV satellites (Note: E20 out-of-service around GPS-week 1745)

4.5 Orbit Combination Results

To quantify and compare the accuracy of orbit products an orbit combination of three individual MGEX-AC solutions was performed. This was done with an adopted version of the ORBCMB software, which is every day used for the generation of the official combined IGS products.

The following three MGEX-ACs were used for this comparison, which generate Galileo orbit products:

– GFZ,
– Center for Orbit Determination in Europe (CODE),
– Technische Universität München (TUM).

The also available CNES/CLS (GRG) Galileo orbit solutions were skipped from the comparison due to lower quality. All of the mentioned products can be downloaded from the CDDIS MGEX archive. The plots in Fig. 8 show the agreement for each of the MGEX-AC orbit solutions with respect to the combined orbit. Except for single outliers the agreement of the orbits is in the range of 3–10 cm but in general below 5 cm. The GFZ (gfm) and CODE (com) solution agree very well which might be an effect of the 3-day long-arc orbit strategy and the rigorous GPS/Galileo processing scheme, whereas TUM (tum) is using a two step approach. Further details regarding the processing strategies of CODE and TUM can be found in Prange et al. (2013) and Steigenberger et al. (2013a), respectively.

5 BeiDou Data Processing Setup

5.1 Experimental Data Set

Currently the Chinese BeiDou constellation provides observation data of five Geostationary-Earth-Orbit (GEO) satellites, five Inclined-GeoSynchronous-Orbit (IGSO) satellites and four Medium-Earth-Orbit (MEO) satellites. In this experiment totally 12 operational satellites are involved:

GEO	-	C01, C02, C03, C04, C05
IGSO	-	C06, C07, C08, C09, C10
MEO	-	C11, C12

Based on tracking data of BeiDou-capable receivers from the MGEX network up to 20 global distributed stations (highlighted with red circles in Fig. 2) are selected to estimate orbit and clock parameters of the BeiDou satellites. The orbit analysis is based on a time period of 3 weeks, namely GPS-weeks 1743–1745 (01/06 to 23/06/2013).

5.2 Processing Scheme

An upgraded version of EPOS.P8 software is used for the processing of dual-frequency GPS and BeiDou data together. The general processing strategy is similar to the above mentioned Galileo processing scheme, but no ambiguity-fixing was set up for BeiDou. The ionosphere-free linear combination of B1 (1561.098 MHz) and B2 (1207.140 MHz) is used and the a priori orbits are taken from the broadcast navigation message files provided by the MGEX. The observation data are processed in daily batches and normal equations (NEQs) are kept to generate 3-day solutions.

5.3 Initial Results

To check the orbit quality the RMS of the orbit overlap differences in along-track, cross-track and radial directions are taken. The statistic results are given in Table 2 and Fig. 9. Most GEOs have a larger RMS than IGSOs and MEOs. The IGSOs have the smallest RMS except C08, where the source of this effect is unknown, but seems to be related to data availability (data cleaning). The GEO orbit determination suffers clearly from the weak observation geometry and the lack of orbit dynamics and results in higher RMS values, but nonetheless the radial orbit component is equivalent to the IGSOs. The individual results of the two MEOs are more homogeneous then the others which is related to our orbit modeling experiences for this kind of satellites. The satellite antenna phase centre correction was set to zero and the satellite attitude control is unknown actually, which can cause larger RMS errors in across-track and radial directions. Further studies will be carried out in the next step.

Table 2 RMS of orbit overlap differences for different BeiDou satellite types

Satellite type	Along (cm)	Across (cm)	Radial (cm)
GEO	86.7	84.5	27.9
IGSO	50.8	60.7	41.0
MEO	60.5	81.6	54.8

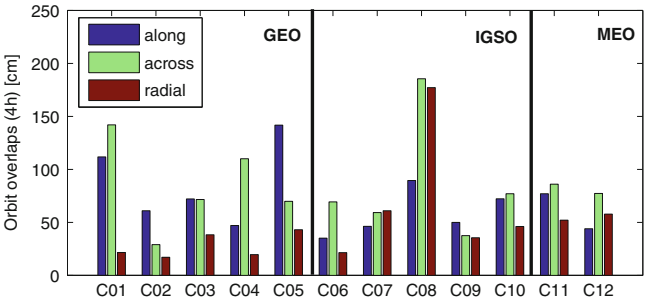

Fig. 9 Orbit overlap RMS (4 h) of BeiDou satellites in along, across and radial direction

6 Summary

GFZ is operating modern Multi-GNSS sensor stations to support the scientific community with observation data of the new GNSS. These data are provided within the MGEX to the users.

Galileo satellite orbit and clock parameter were derived with data of the MGEX tracking network. It was demonstrated that the orbits can be determined with accuracies of 5–10 cm, which was additionally underlined through comparisons with external solutions. In so far is the contribution of SLR measurements very useful to identify the source of the periodic variations in the clock estimates. (This might be one reason, why the laser reflectors will find their way back on board of future GPS III satellites Miller et al. 2013.) The adjusted satellite clocks and their stabilities are in a level of about 20 ps and suffer only from obvious orbit modeling problems during eclipsing periods. The attitude behavior as well as the improvement of the Galileo ambiguity fixing strategy will need future investigations.

First results of a BeiDou data processing were also presented and the orbit quality checked. For this system orbit accuracies in a level of 30–80 cm can be derived. The sparse tracking network and the special orbit characteristics of the GEOs causes known deficiencies in the orbit determination

process during the test period. This will be part of further studies in this field.

Acknowledgements The efforts of the IGS (Dow et al. 2009) in providing Multi-GNSS observation data are kindly acknowledged.

References

Dow J, Neilan R, Rizos C (2009) The International GNSS Service in a changing landscape of Global Navigation Satellite Systems. J Geod 83(3–4):191–198. doi:10.1007/s00190-008-0300-3

Ge M, Gendt G, Dick G, Zhang FP (2005) Improving carrier-phase ambiguity resolution in global GPS network solutions. J Geod 79(1–3):103–110. doi:10.1007/s00190-005-0447-0

Gurtner W, Estey L (2005) RINEX: the receiver independent exchange format, version 2.11. Technical Report, IGS Central Bureau

IGS, RTCM-SC104 (2013) RINEX: the receiver independent exchange format, version 3.02. Technical Report, IGS Central Bureau

Miller JJ, LaBreque J, Oria A (2013) Expert advice: laser reflectors to ride on board GPS III. GPS World http://gpsworld.com/expert-advice-laser-reflectors-to-ride-on-board-gps-iii/

Montenbruck O (2013) Multi-GNSS working group. In: Dach R, Jean Y (eds) IGS Technical Report 2012, IGS Central Bureau, Jet Propulsion Laboratory, pp 163–170

Prange L, Lutz S, Dach R, Schaer S, Jäggi A (2013) MGEX data analysis at CODE – current status. In: EGU General Assembly 2013

Steigenberger P, Hackel S, Hugentobler U, Montenbruck O (2013a) One year of galileo IOV orbit and clock determination. In: EGU General Assembly Conference Abstracts, vol 15, p 2616

Steigenberger P, Hugentobler U, Hauschild A, Montenbruck O (2013b) Orbit and clock analysis of compass GEO and IGSO satellites. J Geod 87(6):515–525. doi:10.1007/s00190-013-0625-4

Uhlemann M, Ramatschi M, Gendt G (2012) GFZ's global multi-GNSS network and first data processing results. In: IGS Workshop 2012, Olsztyn, Poland

A Conditional Equation for Minimizing the GDOP of Multi-GNSS Constellation and Its Boundary Solution with Geostationary Satellites

Shuqiang Xue, Yuanxi Yang, Yamin Dang, and Wu Chen

Abstract

The Walker-delta constellation has been widely used in GNSS (Global Navigation Satellite System). As a key index to measure the positioning configuration, the GDOP minimization plays an important role in GNSS constellation design with a fixed number of satellites. In this paper, we analytically solve this criterion by revealing the geometry of GDOP minimization. Firstly, the graph composed of the GNSS constellation and the unknown point is established and the geometrical conditions for minimizing the GDOP are revealed by introducing two kinds of GDOP. As to the Walker-delta constellation applied in GNSS, a conditional equation is then given to analytically solve the GDOP minimization involved in multi-GNSS constellation optimization. It shows that: relative to the optimal inclination 54.75° for single GNSS constellation, the inclination of the inclined orbits from the multi-GNSS constellation mixed with a certain number of geostationary satellites should be increased to realize the GDOP minimization which is determined by the number of geostationary satellites and the number of inclined orbits. Ultimately, the multi-GNSS constellation design is performed to show the validation of the conditional equation.

Keywords

Combined GNSS • GDOP • GNSS • Mixed constellation • Positioning configuration • Walker constellation

1 Introduction

In navigation, GDOP (Geometric Dilution of Precision) is the common used index to measure the positioning configuration and it determines the scale of the spherical error of the positioning (Langley 1999; Massatt and Rudnick 1990; Yarlagadda et al. 2000). GDOP is aslo used as a criterion to optimally select satellites for the purpose of fast positioning (Kihara and Okada 1984; Phatak 2001; Zhang and Zhang 2009). Based on the GDOP minimization criterion, GNSS constellation design has been discussed (Dufour et al. 1995). In GNSS constellation design, one aim is to seek an optimal constellation with the lowest GDOP on the Earth surface under some boundary conditions, such as a fixed number of satellites used (this involves the system cost and the practically computational issues), a certain number of

S. Xue (✉)
School of Geological and Surveying Engineering, Chang'an University, Yanta Road, Xi'an 710054, China

Chinese Academy of Surveying and Mapping, Beijing 100830, China
e-mail: xuesq@casm.ac.cn

Y. Yang
National Key Laboratory for Geo-information Engineering, Xi'an Research Institute of Surveying and Mapping, Xi'an 710054, China

Y. Dang
Chinese Academy of Surveying and Mapping, Beijing 100830, China

W. Chen
The Hong Kong Polytechnic University, Hung Hom, Kowloon, Hong Kong, China

© Springer International Publishing Switzerland 2015

C. Rizos, P. Willis (eds.), *IAG 150 Years*, International Association of Geodesy Symposia 143,
DOI 10.1007/1345_2015_30

geostationary satellites involved, the lowest GDOP coverage in low latitude zones, maximum GDOP allowed. Moreover, many scientific applications need the isotropic coverage of the Earth to study the Earth's rotation, troposphere and ionosphere and so on. Particularly for some applications, small or large orbital inclination is needed, such as the use of large inclination orbits in optimally determining the motion of the Earth mass center (Dong et al. 2003).

The Walker-delta constellation is one kind of basic constellations in GNSS design (Príz et al. 2005). Slightly different from the GPS, the new developing Chinese COMPASS will use a Walker-delta constellation mixed with a certain number of geostationary satellites and inclined geosynchonous orbits (Yang et al. 2011). Basically, the problem of designing a multi-satellite constellation exhibits a lot of parameters with many possible combinations (Lansard et al. 1998). Although the Walker-delta constellation has been widely adopted by GNSSs to perform the Earth coverage, the optimality of single GNSS as well as multi-GNSS needs to be further discussed. This is a base to discuss the impact of the new orbits introduced to the Walker constellation.

Nowadays, there are many simulation GDOP analyses to perform GNSS constellation design. In fact, GDOP minimization is a particular geometry problem and it can be accurately modeled and might be analytically solved by the graph theory and group theory. The graph theory used in geodetic network has been widely discussed (Chebotarev 2011; Okeke and Krumm 1998). A new perspective of GPS networks based on principles from graph theory to describe connectivity properties of GPS networks was demonstrated and the relevant algorithm was proposed (Even-Tzur 2001). A broad perspective of the application of graph theory to establishment of GPS control networks has been achieved (Katambi et al. 2002). New developments show that the GNSS algebraic structure might appeal to the algebraic graph theory and the algebraic number theory (Lannes and Gratton 2009; Lannes and Teunissen 2011). The optimality of the dynamic configuration integrating the continuous observations over time has been revealed that the symmetry of the configuration is very important to identify the systematic errors such as the clock-offset (Xue et al. 2014a). However, slightly different from the dynamic configuration optimization, the single GNSS constellation or multi-GNSS constellation design mainly aims to realize the high performance of real time positioning and then the continuously tracking positioning will be good performance if the positioning configuration always keeps the optimal graph in time.

We try to analytically solve the GDOP minimization in multi-GNSS constellation design especially involved a certain number of geostationary satellites. In Sect. 2, the graph presentation and two kinds of GDOP are introduced. In Sect. 3, geometrical conditions for minimizing the GDOP are given to reveal the relation between the GDOP minimization and the homogeneous of the constellation. The connection between GDOP minimization and the D-optimization are given. In Sect. 4, a conditional equation is proposed to analytically solve the GDOP minimization of the combined Walker-delta constellations, and then the problem involved geostationary satellites are discussed. By the conditional equation the GNSS constellation are simulated to show the GDOP distribution on the Earth surface to verify the main results proposed.

2 Graph of Single-Point-Positioning Configuration and Its GDOP Metric

In navigation, to determine unknown position based on pseudo-ranging measurements, the receiver clock bias which cannot be computed from the prior information is implemented as an unknown parameter (Grafarend and Shan 2002). From pseudo-distance measurements l_i ($i = 1, \ldots, n$), we can get a nonlinear equation system as (Xue et al. 2014b)

$$l_i = d_i(\mathbf{x}) + c\Delta t + \varepsilon_i \qquad i = 1, \cdots, n \tag{1}$$

where Δt is the clock-offset and c is the signal velocity, $d_i(x) = \sqrt{\sum_{j=1}^{m} (x_j - x_{i,j})^2}$ is the Euclidean distance from the unknown position $\mathbf{x} = [x_1, \cdots, x_m] \in \mathbb{R}^m$ to known point $\mathbf{x}_i = [x_{i,1}, \cdots, x_{i,m}] \in \mathbb{R}^m$, ε_i is the observation error, the subscript i is to index the known point number while j represents the coordinate component.

Graph theory can be used to model pairwise relations between objects (West 2001). In m-dimensional space ($m = 2$ or 3), the positioning configuration, which is composed of the unknown point $\mathbf{x}$ and the known points $\mathbf{x}_i$ ($i = 1,2, \ldots, n$), can be then modeled by a graph as (Lannes and Gratton 2009; Lannes and Teunissen 2011)

$$\mathcal{G}_{n,m} = (\mathbf{x}, \Theta) \tag{2}$$

where $\Theta = \{\mathbf{x}_i \,|\, i = 1, 2, \ldots, n\}$ is the control (points) configuration.

As to GNSS applications, the nonlinearity of the equation system (1) is usually low and the linearization takes a good approximation around the approximate value of the unknown position (Lannes and Teunissen 2011; Xue et al. 2014a, b). Applying the law of error propagation to the linearized equation system, the GDOP represents the scale to measure the spherical error of the positioning which is determined by the number of the visible satellites, the distribution of these satellites, and the measuring precision. To discuss the GDOP minimization with a fixed number of satellites and to reveal the best distribution of these satellites, two kinds of GDOP will be used in the following discussion

where the first kind of GDOP is defined by (Levanon 2000)

$$GDOP'\left(\mathcal{G}_{n,m}\right)=\sqrt{\mathrm{tr}\left[\left(\mathbf{J}'^{\mathrm{T}}\mathbf{J}'\right)^{-1}\right]} \tag{3}$$

in which tr is the trace of the matrix $\left(\mathbf{J}'^{\mathrm{T}}\mathbf{J}'\right)^{-1}$, $\mathbf{J}'=\left[\mathbf{e}_1^{\mathrm{T}}\ \mathbf{e}_2^{\mathrm{T}}\cdots\mathbf{e}_n^{\mathrm{T}}\right]^{\mathrm{T}}$ and $\mathbf{e}_i=\left[c_{i,1}-x_1\ \cdots\ c_{i,m}-x_m\right]\Big/\|\mathbf{c}_i-\mathbf{x}\|_2$ is the line of sight, the second kind of GDOP is defined by

$$GDOP''\left(\mathcal{G}_{n,m}\right)=\sqrt{\mathrm{tr}\left[\left(\mathbf{J}''^{\mathrm{T}}\mathbf{J}''\right)^{-1}\right]} \tag{4}$$

in which $\mathbf{J}''=\left[\mathbf{J}'\ \mathbf{k}_n\right]$, $\mathbf{k}_n=\left[1\ \ldots\ 1\right]^{\mathrm{T}}$.

The first-kind GDOP is the geometrical strength criteria to the positioning configuration using distances as measurements while the second-kind GDOP is the geometrical strength criteria involved pseudo-distance measurements. The first-kind GDOP is an intermediate variable for the convenience of discussion.

3 General Conditions of Minimizing GDOP

The following will show a set of general conditions for minimizing the GDOP and reveal the role play of the fist kind GDOP for minimizing the second kind GDOP.

3.1 First Kind GDOP Minimization

Let $\mathrm{N}'=\mathbf{J}'^{\mathrm{T}}\mathbf{J}'$, with the singular value decomposition

$$\mathrm{N}'=\mathbf{S}^{\mathrm{T}}\,\mathrm{diag}\left(\lambda_1,\lambda_1,\cdots,\lambda_1\right)\mathbf{S} \tag{5}$$

where $\lambda_1,\lambda_2,\ldots,\lambda_m$ are the eigenvalues, $\mathbf{S}$ is orthogonal transform, we have (Seber 2008)

$$\mathrm{tr}\left(\mathbf{N}'\right)=\sum_{i=1}^{m}\lambda_i=n \tag{6}$$

where n is the number of the visible satellites. With regard to the relation (6), by the basic inequality we have

$$\begin{aligned}GDOP'^2\left(\mathcal{G}_{n,m}\right)&=\prod_{i=1}^{m}\lambda_i^{-1}\geq m\sqrt[m]{\prod_{i=1}^{m}\lambda_i^{-1}}\geq m^2\Big/\sum_{i=1}^{m}\lambda_i\\&=m^2/n\end{aligned} \tag{7}$$

where the equality holds if and only if $\lambda_1=\lambda_1=,\ldots,=\lambda_m=\frac{n}{m}$, namely the condition

$$\mathbf{N}'=\frac{n}{m}\mathbf{S}^{\mathrm{T}}\mathbf{I}\mathbf{S}=\frac{n}{m}\mathrm{I} \tag{8}$$

results in $\min GDOP'\left(\mathcal{G}_{n,m}\right)=m\Big/\sqrt{n}$.

3.2 Second Kind GDOP Minimization

Let $\mathbf{N}''\ :=\ \mathbf{J}''^{\mathrm{T}}\mathbf{J}''$ and $\mathrm{s}_n\ :=\ \mathrm{k}_n^{\mathrm{T}}\mathbf{J}'$, then the inversion $\mathbf{N}''^{-1}$ can be given by the Gauss-Jordon elimination algorithm as the follows steps: (Meyer 2000):

1. Structure the augment matrix as

$$\left[\mathbf{N}''\middle|\mathbf{I}\right]=\left[\begin{array}{cc|cc}\mathrm{N}' & \mathrm{s}_n^{\mathrm{T}} & \mathbf{I} & \mathbf{0}\\ \mathrm{s}_n & \mathrm{k}_n^{\mathrm{T}}\mathrm{k}_n & \mathbf{0} & 1\end{array}\right] \tag{9}$$

2. The second row of (9) is added by the first row left multiplied $-\mathrm{s}_n\mathrm{N}'^{-1}$, that

$$\left[\begin{array}{cc|cc}\mathrm{N}' & \mathrm{s}_n^{\mathrm{T}} & \mathbf{I} & \mathbf{0}\\ \mathrm{s}_n & \mathrm{k}_n^{\mathrm{T}}\mathrm{k}_n & 0 & 1\end{array}\right]\Rightarrow\left[\begin{array}{cc|cc}\mathrm{N}' & \mathrm{s}_n^{\mathrm{T}} & \mathbf{I} & \mathbf{0}\\ \mathbf{0} & a_0 & -\mathrm{s}_n\mathrm{N}'^{-1} & 1\end{array}\right] \tag{10}$$

where $a_0\ :=\ \mathrm{k}_n^{\mathrm{T}}\mathrm{M}\mathrm{k}_n$ is a nonnegative constant, $\mathbf{M}=\left(\mathbf{I}-\mathbf{J}'\mathbf{N}'^{-1}\mathbf{J}'^{\mathrm{T}}\right)$ is the orthogonal projection operator.

3. The first row of (10) is added by the second row left multiplied $-\mathrm{s}_n^{\mathrm{T}}a_0^{-1}$, that

$$\begin{aligned}&\left[\begin{array}{cc|cc}\mathrm{N}' & \mathrm{s}_n^{\mathrm{T}} & \mathbf{I} & \mathbf{0}\\ \mathbf{0} & a_0 & -\mathrm{s}_n\mathrm{N}'^{-1} & 1\end{array}\right]\\&\Rightarrow\left[\begin{array}{cc|cc}\mathrm{N}' & \mathbf{0} & \mathbf{I}+a_0^{-1}\mathrm{s}_n^{\mathrm{T}}\mathrm{s}_n\mathrm{N}'^{-1} & -a_0^{-1}\mathrm{s}_n^{\mathrm{T}}\\ \mathbf{0} & a_0 & -\mathrm{s}_n\mathrm{N}'^{-1} & 1\end{array}\right]\end{aligned} \tag{11}$$

4. The first row and the second row of (11) are respectively multiplied by N'^{-1} and a_0^{-1}, that

$$\mathbf{N}''^{-1}=\left[\begin{array}{cc}\mathbf{N}'^{-1}+a_0^{-1}\mathbf{N}'^{-1}\mathbf{s}_n^{\mathrm{T}}\mathbf{s}_n\mathbf{N}'^{-1} & -a_0^{-1}\mathbf{N}'^{-1}\mathbf{s}_n^{\mathrm{T}}\\ -a_0^{-1}\mathbf{s}_n\mathbf{N}'^{-1} & a_0^{-1}\end{array}\right] \tag{12}$$

From the definition of the second kind GDOP, by (12) we obtain the relation

$$GDOP''^2=\mathrm{tr}\left(\mathbf{N}'^{-1}\right)+\mathrm{tr}\left(a_0^{-1}\mathbf{N}'^{-1}\mathbf{s}_n^{\mathrm{T}}\mathbf{s}_n\mathbf{N}'^{-1}\right)+a_0^{-1} \tag{13}$$

Connecting the definition of the first kind GDOP will results in

$$GDOP''^2=GDOP'^2+a_0^{-1}\left[\mathrm{tr}\left(\mathbf{N}'^{-1}\mathbf{s}_n^{\mathrm{T}}\mathbf{s}_n\mathbf{N}'^{-1}\right)+1\right] \tag{14}$$

With regard to the nonnegative definite matrices involved, by the inequality

$$\mathrm{tr}\left(\mathbf{N}'^{-1}\mathbf{s}_n^{\mathrm{T}}\mathbf{s}_n\mathbf{N}'^{-1}\right) \geq 0 \tag{15}$$

we can obtain the following inequality as

$$GDOP''^2 \geq GDOP'^2 + a_0^{-1} \tag{16}$$

where the equality holds if and only if

$$\mathrm{s}_n = \mathrm{k}_n^{\mathrm{T}}\mathbf{J}' = \mathbf{0} \tag{17}$$

Connecting with the first kind GDOP minimization condition (8), we have $\min GDOP'' = \sqrt{(m^2+1)/n}$ if and only if

$$\begin{cases} \mathbf{J}'^{\mathrm{T}}\mathbf{J}' = n\mathbf{I}/m \\ \mathrm{k}_n^{\mathrm{T}}\mathbf{J}' = \mathbf{0} \end{cases} \tag{18}$$

The geometrical meaning of the GDOP minimization is that the columns of the design matrix are orthogonal to each other while the lengths (norm) should be equal to each other (except for the $\|\mathrm{k}_n\| = \sqrt{n}$). By the Hadamard inequality (Meyer 2000)

$$\det\mathbf{N}' \leq \prod_{i=1}^{m}\|\mathbf{n}_i\|,\ \det\mathbf{N}'' \leq \sqrt{n}\det\mathbf{N}' \tag{19}$$

where $\mathbf{n}_i$ is the ith column of $\mathbf{N}'$. The equality in (19) holds if and only if the vectors are orthogonal to each other and this indicates the condition (18). The determinant maximization and the GDOP minimization are essentially equivalent in unconstrained optimizations and the condition $\mathrm{k}_n^{\mathrm{T}}\mathbf{J}' = \mathbf{0}$ indicates that the configuration symmetry plays a key role in identifying the clock-offset.

4 Conditional Equation for Minimizing the GDOP of Combined GNSS Constellation

4.1 Graph Representation of Walker-Delta Constellation

In two-dimensional space, regular polygon is the positional configuration with the lowest GDOP (Levanon 2000). In three dimensional space, the regular tetrahedron has been frequently quoted and used in technical papers (Kihara and Okada 1984). Besides the regular tetrahedron, it has been proved that the cube, regular octahedron, regular icosahedron, and regular dodecahedron are all optimal configurations in there-dimensional space (Craig 1979; Gilmore and McKern 1972; Kihara and Okada 1984; Levanon 2000; Shim and Yang 2010; Yuksel 2011; Xue et al. 2014a). However, these regular polyhedrons can hardly applied to the satellite constellation design because the satellites must obey the Newton's law of motion. For this reason, we next discuss the optimality of the Walker-delta constellation widely adopted in GNSSs.

As shown in the Fig. 1a, the Walker-delta constellation proposed by Walker (1984) is usually denoted as $\alpha : T/P/F$ where α is the inclination, T is the total number of satellites, P is the number of equally spaced planes, F is the relatively spacing between satellites in adjacent planes. The walker-delta constellation $0 : T/T/0$ can be treated as T satellites equally spaced in an equatorial orbital plane. GPS is a Walker-delta constellation 55°:24/6/1 constellation, GLONASS is 64.8°:24/3/1, GALILEO is 56°:27/3/1 and COMPASS (MEO) is 55°:24/3/1.

The positioning configuration composed of the Walker-delta constellation and the unknown point can be then denoted by the graph as

$$\mathcal{W}_{T,3}^{\alpha,P,F} = (\mathbf{x}, \{\mathbf{x}_i \,|\, i = 1, 2, \ldots, T\}) \tag{20}$$

where $\mathbf{x}_i$ is the position of the ith satellite and $\mathbf{x}$ is the unknown point. According to the definition of the Walker-delta constellation, the longitude of ascending node and the argument of latitude (in degree) satisfies:

$$\Omega_j = \frac{360}{P}(j-1), \quad \omega_{j,q} = \frac{360}{S}(q-1) + \omega_{j,0} \tag{21}$$

where $j = 1, 2, \ldots, P$ is to index the jth orbit plane, $S = T/P$ is the total number of satellites in each orbit plane, $q = 1, 2, \ldots, S$ is to index the qth satellite in the jth orbit plane, $\omega_{j,0} = F(j-1)360/T$ is a constant in each orbit plane where F is the phase factor.

As shown in the Fig. 1b, combining N Walker-delta constellations we obtain a multi-constellation configuration as

$$\sum_{k=1}^{N}\mathcal{W}_{T_k,3}^{\alpha_k,P_k,F_k} := \left(\mathbf{x}, \bigcup_{k=1}^{N}\left\{\mathbf{x}_i^k \,|\, i = 1, 2, \ldots, T_k\right\}\right) \tag{22}$$

where $\cup$ is the union of the satellites set, T_k is the number of satellites in the kth Walker-delta constellation.

4.2 GDOP Minimization to the Single-Constellation

Around the point with the lowest GDOP, there are a series of level curves (see e.g., Levanon 2000). For this, the GDOP on the Earth surface is evenly distributed if the GDOP at the geocenter gets the minimum because the Earth radius is relatively small compared to the GNSS orbit radius.

At the geocenter, the Jacobin matrix of single Walker constellation reads

$$\mathbf{J} = \left[\mathbf{J}_1^{\mathrm{T}}\ \mathbf{J}_2^{\mathrm{T}}\ \ldots\ \mathbf{J}_P^{\mathrm{T}}\right]^{\mathbf{T}} \tag{23}$$

where (Xu 2007)

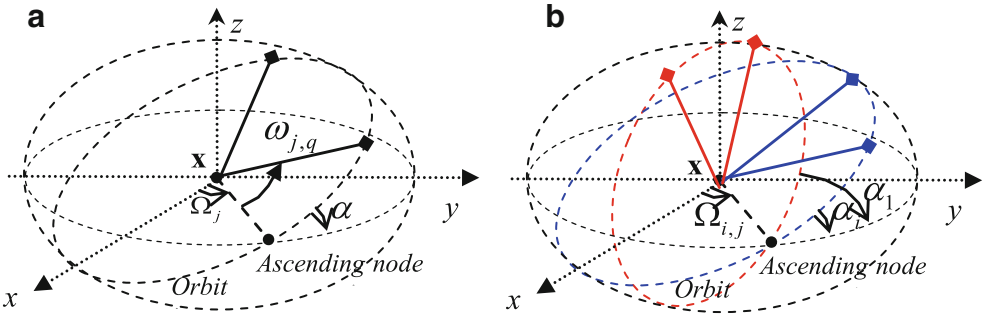

Fig. 1 Single Walker-delta and combined Walker-delta constellation
(**a**) Single-constellation
(**b**) Multi-constellation

$$\mathbf{J}_j = \begin{bmatrix} \cos\omega_{j,1}\cos\Omega_j - \sin\omega_{j,1}\sin\Omega_j\cos\alpha & \cos\omega_{j,1}\sin\Omega_j + \sin\omega_{j,1}\cos\Omega_j\cos\alpha & \sin\omega_{j,1}\sin\alpha & 1 \\ \cos\omega_{j,2}\cos\Omega_j - \sin\omega_{j,2}\sin\Omega_j\cos\alpha & \cos\omega_{j,2}\sin\Omega_j + \sin\omega_{j,2}\cos\Omega_j\cos\alpha & \sin\omega_{j,2}\sin\alpha & 1 \\ \vdots & \vdots & \vdots & \vdots \\ \cos\omega_{j,S}\cos\Omega_j - \sin\omega_{j,S}\sin\Omega_j\cos\alpha & \cos\omega_{j,S}\sin\Omega_j + \sin\omega_{j,S}\cos\Omega_j\cos\alpha & \sin\omega_{j,S}\sin\alpha & 1 \end{bmatrix} \tag{24}$$

is the Jacobin matrix of sub-constellation in the jth orbit plane, $S = T/P$ is the number of satellites in each orbit plane. Let $\mathbf{N}_j = \mathbf{J}_j^{\mathrm{T}}\mathbf{J}_j$, then

$$\begin{cases} \mathbf{N}_{j,1,1} = \cos^2\Omega_j\sum\limits_{q=1}^{S}\cos^2\omega_{j,q} + \sin^2\Omega_j\cos^2\alpha\sum\limits_{q=1}^{S}\sin^2\omega_{j,q} - \sin 2\Omega_j\cos\alpha\sum\limits_{q=1}^{S}\sin\omega_{j,q}\cos\omega_{j,q} \\ \mathbf{N}_{j,2,2} = \sin^2\Omega_j\sum\limits_{q=1}^{S}\cos^2\omega_{j,q} + \cos^2\Omega_j\cos^2\alpha\sum\limits_{q=1}^{S}\sin^2\omega_{j,q} + \sin 2\Omega_j\cos\alpha\sum\limits_{q=1}^{S}\sin\omega_{j,q}\cos\omega_{j,q} \\ \mathbf{N}_{j,3,3} = \sin^2\alpha\sum\limits_{q=1}^{S}\sin^2\omega_{j,q},\ \mathbf{N}_{j,4,4} = S \end{cases} \tag{25}$$

and

$$\begin{aligned} \mathbf{N}_{j,1,2} &= \sum_{q=1}^{S}\left(\cos\omega_{j,q}\cos\Omega_j - \sin\omega_{j,q}\sin\Omega_j\cos\alpha\right) \\ &\quad\times\left(\cos\omega_{j,q}\sin\Omega_j + \sin\omega_{j,q}\cos\Omega_j\cos\alpha\right) \\ &= \tfrac{1}{2}\sin 2\Omega_j\sum_{q=1}^{S}\cos^2\omega_{j,q} - \tfrac{1}{2}\cos\alpha\sin^2\Omega_j\sum_{q=1}^{S}\sin 2\omega_{j,q} \\ &\quad + \tfrac{1}{2}\cos^2\Omega_j\cos\alpha\sum_{q=1}^{S}\sin 2\omega_{j,q} \\ &\quad - \tfrac{1}{2}\cos^2\alpha\sin 2\Omega_j\sum_{q=1}^{S}\sin^2\omega_{j,q} \end{aligned} \tag{26}$$

$$\begin{aligned} \mathbf{N}_{j,1,3} &= \sum_{q=1}^{S}\left(\cos\omega_{j,q}\cos\Omega_j - \sin\omega_{j,q}\sin\Omega_j\cos\alpha\right) \\ &\quad\times\sin\omega_{j,q}\sin\alpha \\ &= \tfrac{1}{2}\cos\Omega_j\sin\alpha\sum_{q=1}^{S}\sin 2\omega_{j,q} \\ &\quad - \tfrac{1}{2}\sin\Omega_j\sin 2\alpha\sum_{q=1}^{S}\sin^2\omega_{j,q} \end{aligned} \tag{27}$$

$$\begin{aligned} \mathbf{N}_{j,1,4} &= \sum_{q=1}^{S}\left(\cos\omega_{j,q}\cos\Omega_j - \sin\omega_{j,q}\sin\Omega_j\cos\alpha\right) \\ &= \cos\Omega_j\sum_{q=1}^{S}\cos\omega_{j,q} - \sin\Omega_j\cos\alpha\sum_{q=1}^{S}\sin\omega_{j,q} \end{aligned} \tag{28}$$

$$\begin{aligned} \mathbf{N}_{j,2,3} &= \sum_{q=1}^{S}\left(\cos\omega_{j,q}\sin\Omega_j + \sin\omega_{j,q}\cos\Omega_j\cos\alpha\right) \\ &\quad\times\sin\omega_{j,q}\sin\alpha \\ &= \tfrac{1}{2}\sin\Omega_j\sin\alpha\sum_{q=1}^{S}\sin 2\omega_{j,q} \\ &\quad + \tfrac{1}{2}\sin 2\alpha\cos\Omega_j\sum_{q=1}^{S}\sin^2\omega_{j,q} \end{aligned} \tag{29}$$

$$\begin{aligned} \mathbf{N}_{j,2,4} &= \sum_{q=1}^{S}\left(\cos\omega_{j,q}\sin\Omega_j + \sin\omega_{j,q}\cos\Omega_j\cos\alpha\right) \\ &= \sin\Omega_j\sum_{q=1}^{S}\cos\omega_{j,q} - \cos\Omega_j\cos\alpha\sum_{q=1}^{S}\sin\omega_{j,q} \end{aligned} \tag{30}$$

Table 1 GDOP at the center and on the surface of the Earth

Graphs	$GDOP''_{center}$	E($GDOP''_{surf}$)	D($GDOP''_{surf}$)	max($GDOP''_{surf}$)	Dead zones
$\mathcal{W}_{24,3}^{55^\circ,6,0}$	0.64550	1.78027	0.52516	∞	112cells around the earth poles
$\mathcal{W}_{24,3}^{55^\circ,6,1}$	0.64550	1.79211	0.17449	4.67658	No
$\mathcal{W}_{24,3}^{64.8^\circ,3,0}$	0.65240	1.87248	0.16669	2.74891	No
$\mathcal{W}_{24,3}^{64.8^\circ,3,1}$	0.65240	1.81085	0.12538	2.77988	No
$\mathcal{W}_{30,3}^{a\tan\sqrt{2},3,0}$	0.57735	1.56679	0.03822	2.29009	No
$\mathcal{W}_{30,3}^{a\tan\sqrt{2},3,1}$	0.57735	1.56348	0.03166	1.97388	No

$$\mathbf{N}_{j,3,4} = \sin\alpha \sum_{q=1}^{S} \sin\omega_{j,q} \tag{31}$$

By the relations in (21), we have (Spiegel 1968)

$$\begin{aligned} &\sum_{q=1}^{S} \sin\omega_{j,q}\cos\omega_{j,q} = 0, \sum_{q=1}^{S} \sin\omega_{j,q} = 0, \sum_{q=1}^{S} \cos\omega_{j,q} = 0, \\ &\sum_{q=1}^{S} \sin^2\omega_{j,q} = \sum_{q=1}^{S} \cos^2\omega_{j,q} = \frac{S}{2} \end{aligned} \tag{32}$$

$$\begin{aligned} &\sum_{j=1}^{P} \sin\Omega_j\cos\Omega_j = 0, \sum_{j=1}^{P} \sin\Omega_j = 0, \sum_{j=1}^{P} \cos\Omega_j = 0, \\ &\sum_{j=1}^{P} \sin^2\Omega_j = \sum_{j=1}^{P} \cos^2\Omega_j = \frac{P}{2} \end{aligned} \tag{33}$$

Substituting the relations in (32) and (33) into the Eqs. (25)–(31) results in

$$\begin{aligned} \mathbf{J}^{\mathrm{T}}\mathbf{J} = \sum_{j=1}^{P} \mathbf{N}_j = diag\big(&T/4 + T/4\cos^2\alpha,\ T/4 \\ &+ T\cos^2\alpha/4,\ T\sin^2\alpha/2,\ T\big) \end{aligned} \tag{34}$$

Compared (34) with (18), if and only if

$$\sin\alpha = \sqrt{2/3} \tag{35}$$

namely, $\alpha = \operatorname{asin}\sqrt{2/3} \approx 54.74^\circ$ is the only one solution to ensure the lowest GDOP at geocenter.

To verify this conclusion above, we simulate the constellations $\mathcal{W}_{24,3}^{55^\circ,6,0}$, $\mathcal{W}_{24,3}^{55^\circ,6,1}$, $\mathcal{W}_{24,3}^{64.8^\circ,3,0}$, $\mathcal{W}_{24,3}^{64.8^\circ,3,1}$, $\mathcal{W}_{30,3}^{a\tan\sqrt{2},3,0}$ and $\mathcal{W}_{30,3}^{a\tan\sqrt{2},3,1}$ with the following assumptions:

1. All orbits are circular and the orbital altitude is 20,000 km;
2. $GDOP''_{center}$ is defined as the second kind GDOP at the geocenter;
3. On the Earth surface, satellites are visible if the altitude angle is greater than 0;
4. The Earth surface is divided into 625 cells and the mean GDOP is defined as

$$\mathrm{E}\left(GDOP''_{surf}\right) = \sum_{i=1}^{n} GDOP''_i/n \tag{36}$$

where $GDOP''_i$ is the second kind GDOP in the ith cell, n is the total number of the cells in which the GDOP should be smaller than 100. The variance of the surface GDOP is defined as

$$\mathrm{D}\left(GDOP''_{surf}\right) = \sum_{i=1}^{n} \left(GDOP''_i - \mathrm{E}\left(GDOP''_{surf}\right)\right)^2 \Big/ (n-1) \tag{37}$$

and max($GDOP''_{surf}$) is defined as the maximum GDOP on the Earth surface.

5. The cell is called as "Dead Zone" if the GDOP is great than 100.

The relevant statistics are given in the Table 1. It shows that: The closer the inclination to $\alpha = \operatorname{atan}\sqrt{2} \approx 54.74^\circ$, the closer the $GDOP''_{center}$ will get the theoretical minimum $\sqrt{(m^2+1)/n}$ and the smaller the D($GDOP''_{surf}$) will be. This indicates that the GDOP on the Earth surface is approximately evenly distributed when the GDOP is minimized at the center of the Earth. Although the E($GDOP''_{surf}$) of $\mathcal{W}_{24,3}^{55^\circ,6,F}$ is smaller than that of $\mathcal{W}_{24,3}^{64.8^\circ,3,F}$, as shown in the Fig. 2, the GDOP coverage from $\mathcal{W}_{24,3}^{64.8^\circ,3,F}$ is more remarkable for covering the high latitudes. Moreover, the factor F is helpful to improve the GDOP homogeneity on the Earth surface as well as to improve the average GDOP. GALILEO adopts a similar constellation with $\mathcal{W}_{30,3}^{\operatorname{atan}\sqrt{2},3,0}$ or $\mathcal{W}_{30,3}^{\operatorname{atan}\sqrt{2},3,1}$ as shown in the last two rows of the Table 1. It shows that: relative to GPS and GLONASS the increased number of the satellites can improve all GDOP indexes involved in the Table 1.

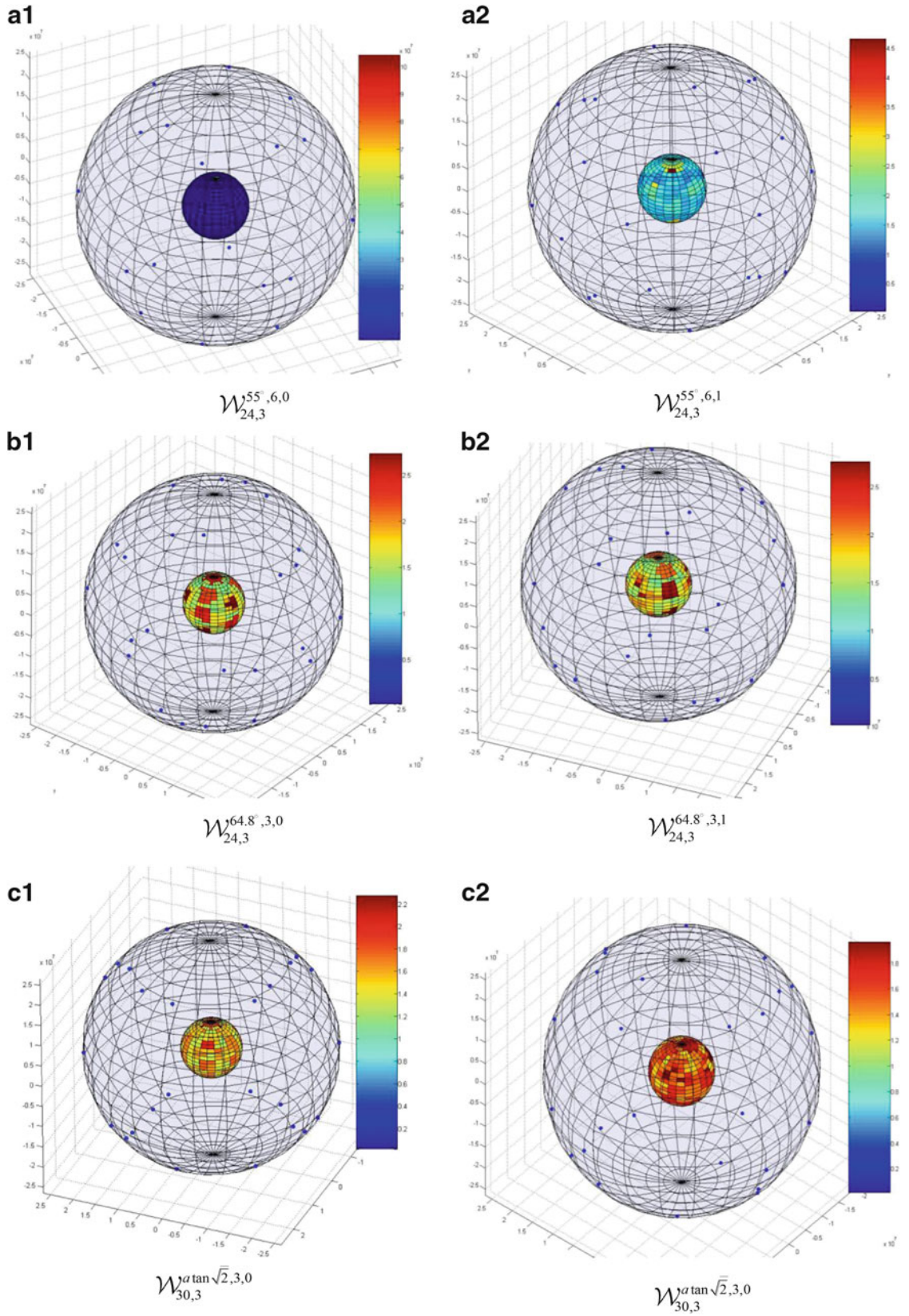

Fig. 2 Second kind GDOP on the Earth surface

Table 2 GDOP at the center and on the surface of the Earth

Graphs	$GDOP''_{center}$	E($GDOP''_{surf}$)	D($GDOP''_{surf}$)	max($GDOP''_{surf}$)
$\mathcal{W}_{24,3}^{64.8^\circ,3,0}+\mathcal{W}_{6,3}^{64.8^\circ,1,0}$	0.58991	1.66011	0.14393	2.68034
$\mathcal{W}_{24,3}^{64.8^\circ,3,1}+\mathcal{W}_{6,3}^{64.8^\circ,1,0}$	0.58991	1.61058	0.09788	2.69865
$\mathcal{W}_{24,3}^{64.8^\circ,3,0}+\mathcal{W}_{6,3}^{0^\circ,6,0}$	0.57739	1.61851	0.13585	2.33987
$\mathcal{W}_{24,3}^{64.8^\circ,3,1}+\mathcal{W}_{6,3}^{0^\circ,6,0}$	0.57739	1.56284	0.08396	2.33987

For the constellation $\mathcal{W}_{24,3}^{55^\circ,6,0}$, because of the practically visible condition use in the simulation assumption (3), as shown in the Table 1 there are some dead zones around the Earth poles. This problem can be partly solved by the factor $F=1$, but there still exists relatively large GDOP converge zones at high latitudes. However, since GLONASS adopts three orbital planes with larger inclination such that the number of visible satellites increases at high latitude zones, these dead zones no longer exist and the maximum GDOP is relatively small.

4.3 GDOP Minimization of the Multi-Constellation

Next a conditional equation for minimizing the GDOP of the multi-constellation $\sum_{k=1}^{N}\mathcal{W}_{T_k,3}^{\alpha_k,P_k,F_k}$ defined by (22) will be given. With the information matrix (34), the total information matrix of the combined Walker-delta constellation (22) can be expressed as

$$\mathbf{N}=\sum_{k=1}^{N}\left(\mathbf{J}^{\mathrm{T}}\mathbf{J}\right)_k=\operatorname{diag}\left(\sum_{k=1}^{N}\left[\frac{T_k}{4}+\frac{T_k}{4}\cos^2\alpha_k\right],\sum_{k=1}^{N}\left[\frac{T_k}{4}+\frac{T_k}{4}\cos^2\alpha_k\right],\sum_{k=1}^{N}\frac{T_k}{2}\sin^2\alpha_k,\sum_{k=1}^{N}T_k\right) \tag{38}$$

where $(\mathbf{J}^{\mathrm{T}}\mathbf{J})_k$ is the information matrix of the kth constellation. Comparing (38) with (18), we obtain a conditional equation as

$$\sum_{i=1}^{N}\left[\frac{T_i}{4}+\frac{T_i}{4}\cos^2\alpha_i\right]=\sum_{i=1}^{N}\frac{T_i}{2}\sin^2\alpha_i \tag{39}$$

Simplifying the Eq. (39) results in

$$\sum_{i=1}^{N}T_i\cos^2\alpha_i=\frac{1}{3}\sum_{i=1}^{N}T_i \tag{40}$$

The Eq. (40) is undetermined, namely, and it can only be solved by introducing a series of boundary conditions. For example, let $N=2$, $\alpha_1=0^\circ$, then from the conditional equation (40), we have

$$\cos^2\alpha_2=1/3-2T_1/(3T_2) \tag{41}$$

If and only if $0\le T_1/T_2\le\frac{1}{2}$, there will be a real number α_2 satisfying the Eq. (41), and $\cos^2\alpha_2<\frac{1}{3}$. Under the Eq. (41), properly selecting the ratio T_1/T_2 we can obtain the optimal inclination α_2.

GLONASS constellation isn't optimal for minimizing the GDOP at the geocenter, but as discussed above GLONASS constellation improves the high latitude coverage. According to the conditional equation (40), to improve the global performance, the GLONASS constellation can be optimized by introducing five or six geostationary satellites. To verify this conclusion we compare the following strategies:

1. Introducing an inclined orbit as $\mathcal{W}_{6,3}^{64.8^\circ,1,0}$;
2. Introducing a geostationary orbit as $\mathcal{W}_{6,3}^{0^\circ,6,0}$.

The GDOP performances of $\mathcal{W}_{24,3}^{64.8^\circ,3,0}+\mathcal{W}_{6,3}^{64.8^\circ,1,0}$, $\mathcal{W}_{24,3}^{64.8^\circ,3,1}+\mathcal{W}_{6,3}^{64.8^\circ,1,0}$, $\mathcal{W}_{24,3}^{64.8^\circ,3,0}+\mathcal{W}_{6,3}^{0^\circ,6,0}$ and $\mathcal{W}_{24,3}^{64.8^\circ,3,1}+\mathcal{W}_{6,3}^{0^\circ,6,0}$ are shown in the Table 2 and in the Fig. 3. It shows that the geostationary orbit $\mathcal{W}_{6,3}^{0^\circ,6,0}$ is better than the inclined orbit $\mathcal{W}_{6,3}^{64.8^\circ,1,0}$ in improving the $GDOP''_{center}$, E($GDOP''_{surf}$), D($GDOP''_{surf}$) and max($GDOP''_{surf}$). Comparing Fig. 2(b1,b2) with Fig. 3, we can find that the gain from the new introduced geostationary orbit mainly focus on the lower or middle latitudes. However, the inclined orbit $\mathcal{W}_{6,3}^{64.8^\circ,1,0}$ breaks the symmetry of the surface GDOP distribution and this may go against the aim of improving the global performance. For this, geostationary satellites or symmetrical orbits with small inclination are significant to improve the global performance of GLONASS. As to the COMPASS constellation where five geostationary satellites have been available, if the inclination α of the 27 MEO satellites and 3 IGSO satellites satisfies $5\cos^2 0^\circ+30\cos^2\alpha=\frac{35}{3}$ namely $\cos\alpha=\frac{1}{3}\sqrt{2}\approx 61.87^\circ$, the full constellation will be approximately achieved with the lowest GDOP on the Earth surface.

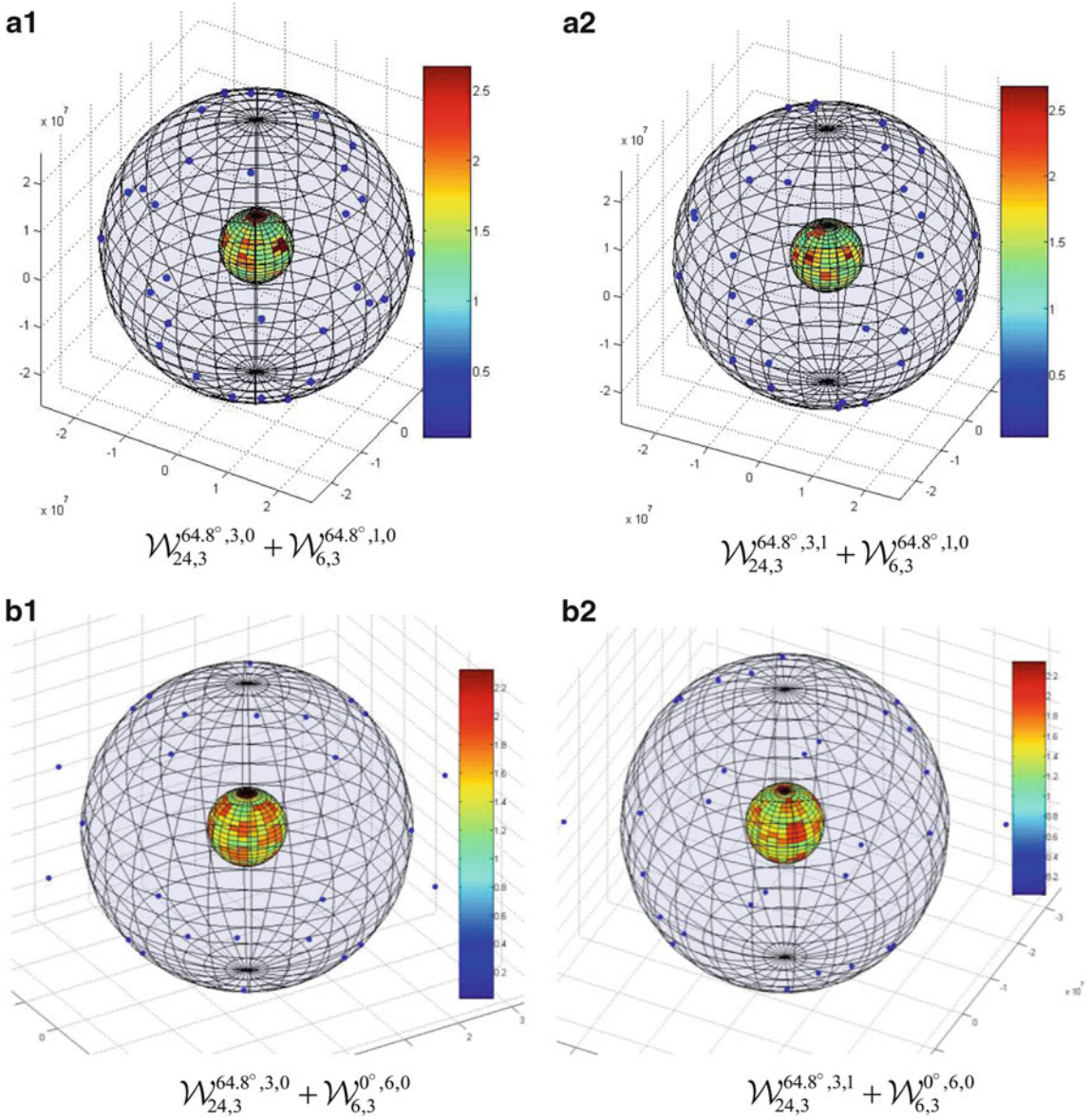

Fig. 3 Second kind GDOP on the Earth surface

5 Conclusions

The orbital inclinations used in GPS, GALILEO and COMPASS MEO orbits are very close to the optimal angle 54.74°. However, to achieve isotropic coverage of the Earth, using the same inclination might not be always optimal, such as under the background of high latitude applications or the Earth mass center determination which needs large inclination. On the contrary, the inclination 64.8° of GLONASS constellation is helpful to improve the high latitude applications. By the conditional equation proposed, the current GLONASS constellation can be easily modified to be optimal to improve the global performance by introducing a certain number of geostationary satellites or small inclined orbits.

With regard to the current use of geostationary satellites in Chinese COMPASS system, India IRNSS (Indian Regional Navigational Satellite System) and Japan QZSS (Quasi-Zenith Satellite System), in the future, multi-GNSS applications might need more orbits with large inclination than the standard 54.74°. For independently developing GNSSs, we recommend that these systems adopt mixed constellation and employ the conditional equation proposed to achieve the GDOP minimization to improve the isotropy of the single Walker-delta constellation. Then, the optimality achieved in each independent GNSS can ensure the optimality and the best benefit for multi-GNSS applications. The other

potential applications of the conditional equation proposed is to maintain the single or multi-GNSS constellation when the precession phenomenon decreases or increase the ascending node, the flattening and the inclination of the orbital planes.

The conditional equation proposed indicates a best solution to coordinate GNSSs development to save space resource that: small inclination GNSS orbits are mainly developed and maintained by the low latitude countries or zones; median inclination GNSS orbits are mainly developed and maintained by the median latitude countries or zones and the high inclination GNSS orbits even the polar orbits are mainly developed and maintained by the high latitude countries or zones. It is practically significant that the GDOP minimization and the isotropy are not conflict with each other, but may be harmonious in some senses.

Acknowledgements This work is partly supported by National Science Foundation of China (Grant Nos. 41020144004, 41104018), National High-tech R&D Program (Grant Nos. 2009AA121405, 2013AA122501, 2012BAB16B01), GFZX0301040308-06 and Fujian provincial key laboratory of coast and island management technology study (201403).

References

Chebotarev P (2011) A class of graph-geodetic distances generalizing the shortest-path and the resistance distances. Discrete Appl Math 159:295–302

Craig RJ (1979) Tetrahedral redundant inertial reference unit. Google Patents

Dong D, Yunck T, Heflin M (2003) Origin of the international terrestrial reference frame. J Geophys Res Solid Earth 108(B4)

Dufour F, Bertrand R, Sarda J, Lasserre E, Bernussou J (1995) Constellation design optimization with a dop based criterion. In: 14th International symposium on space fligt dynamics

Even-Tzur G (2001) Graph theory applications to GPS networks. GPS Solutions 5:31–38

Gilmore JP, McKern RA (1972) A redundant strapdown inertial reference unit (SIRU). J Spacecr Rockets 9(1):39–47

Grafarend EW, Shan J (2002) GPS solutions: closed forms, critical and special configurations of P4P. GPS Solutions 5(3):29–41

Katambi S, Guo J, Kong X (2002) Applications of graph theory to gross error detection for GPS geodetic control networks. Geo Spat Inf Sci 5:26–31

Kihara M, Okada T (1984) A satellite selection method and precision for the global positioning system. Navigation 31:8–20

Langley RB (1999) Dilution of precision. GPS World 10:52–59

Lannes A, Gratton S (2009) GNSS networks in algebraic graph theory. J Glob Position Syst 8:53–75

Lannes A, Teunissen PJG (2011) GNSS algebraic structures. J Geod 85:273–290

Lansard E, Frayssinhes E, Palmade JL (1998) Global design of satellite constellations: a multi-criteria performance comparison of classical walker patterns and new design patterns. Acta Astronaut 42:555–564

Levanon N (2000) Lowest GDOP in 2-D scenarios. IEE Proc Radar Sonar Navig 147:149–155

Massatt P, Rudnick K (1990) Geometric formulas for dilution of precision calculations. Navigation 37:379–391

Meyer CD (2000) Matrix analysis and applied linear algebra, vol xii. Society for Industrial and Applied Mathematics, Philadelphia, p 718

Okeke F, Krumm F (1998) Graph, graph spectra and partitioning algorithms in a geodetic network structural analysis and adjustment. Boll Geod Sci Affi LVII:1–24

Phatak MS (2001) Recursive method for optimum GPS satellite selection. IEEE Trans Aerosp Electron Syst 37:751–754

Príiz R, Martín-Peiró B, Romay-Merino M (2005) The Galileo constellation design: a systematic approach. In: Proceedings of the 18th international technical meeting of the satellite division of the Institute of Navigation (ION GNSS 2005), Long Beach, CA, pp 1296–1306

Seber GAF (2008) A matrix handbook for statisticians, vol xix, Wiley series in probability and statistics. Wiley-Interscience, Hoboken, p 559

Shim D-S, Yang C-K (2010) Optimal configuration of redundant inertial sensors for navigation and FDI performance. Sensors 10(7):6497–6512

Spiegel MR (1968) Mathematical handbook of formulas and tables, Schaum's outline series. McGraw-Hill, New York, p 271

Walker JG (1984) Satellite constellations. J British Interplanet Soc 37:559–571

West DB (2001) Introduction to graph theory. Prentice Hall, Upper Saddle River, p 588

Xu G (2007) GPS: theory, algorithms, and applications. Springer, Berlin, p 340

Xue S, Yang Y, Dang Y, Chen W (2014a) Dynamic positioning configuration and its first-order optimization. J Geod 88(2):127–143

Xue S, Yang Y, Dang Y (2014b) A closed-form of Newton method for solving over-determined pseudo-distance equations. J Geod 88(5):441–448

Yang Y, Li J, Xu J, Tang J, Guo H, He H (2011) Contribution of the compass satellite navigation system to global PNT users. Chin Sci Bull 56(26):2813–2819

Yarlagadda R, Ali I, Al-Dhahir N, Hershey J (2000) GPS GDOP metric. IEE Proc Radar Sonar Navig 147:259–264

Yuksel Y (2011) Design and analysis of inertial navigation systems with skew redundant inertial sensors. UCGE Report, 20328

Zhang M, Zhang J (2009) A fast satellite selection algorithm: beyond four satellites. IEEE J Sel Top Sign Process 3:740–747

Near Real-Time Coordinate Estimation from Double-Difference GNSS Data

A Case Study for the National Multi-Hazard Early Warning System in the Sultanate of Oman

Daniel Arnold, Simon Lutz, Rolf Dach, Adrian Jäggi, and Jens Steinborn

Abstract

Real-time and near real-time coordinate estimation become increasingly important in many applications like, e.g., environmental hazard monitoring. The typical approach is based on a Precise Point Positioning (PPP), which has the advantage that all stations can be processed independently and, therefore, the processing of monitoring networks with a large number of stations becomes efficient due to parallelization. However, a PPP requires external satellite clock corrections and the accuracy of the obtained coordinates strongly depends on the consistent usage of these clock corrections and on their quality. Since the processing time for real-time products is strictly limited, it is clear that, in general, the quality of such clock corrections is degraded w.r.t. post-processed products.

The purpose of this article is to demonstrate that the classical double-difference network approach, where no accurate satellite clock corrections are needed, has a lot of potential also for near real-time applications, when a latency of a few minutes is acceptable. The presented results were obtained in the framework of the establishment of a National Multi-Hazard Early Warning System in the Sultanate of Oman.

Keywords

Ambiguity resolution • Double-difference analysis • GNSS • Hazard monitoring • Near real-time • NMHEWS

1 Introduction

An increasing number of monitoring, sensing and surveying applications rely on the processing of data from Global Navigation Satellite Systems (GNSS). Many of these applications require a rapid availability of resulting station coordinates, asking for real-time or near real-time data processing. An example of such an application is, among many others, the German Indonesian Tsunami Early Warning System (GITEWS, Falck et al. 2010).

In many cases the station coordinate estimation is based on an undifferenced Precise Point Positioning (PPP). This obviates the need for reference stations and each station can be processed independently. Therefore, a PPP is especially attractive when an application needs the processing of data of a large number of stations.

However, the PPP also has some drawbacks. First of all, very accurate satellite clock corrections are needed. The precision of the coordinates strongly depends on the quality and consistent usage of these clock corrections. Unlike for satellite orbits, satellite clocks cannot be predicted over a sufficient long time span, nor can they be interpolated well enough. The real-time service of the International GNSS Service (IGS, Caissy et al. 2013), officially launched on April 1, 2013 and reaching its full operational capability by

D. Arnold (✉) • S. Lutz • R. Dach • A. Jäggi
Astronomical Institute of the University of Bern, Sidlerstrasse 5, CH-3012 Bern, Switzerland
e-mail: daniel.arnold@aiub.unibe.ch

J. Steinborn
SpaceTech GmbH, Seelbachstr. 13, DE-88090 Immenstaad, Germany
e-mail: jens.steinborn@spacetech-i.com

© Springer International Publishing Switzerland 2015

C. Rizos, P. Willis (eds.), *IAG 150 Years*, International Association of Geodesy Symposia 143,
DOI 10.1007/1345_2015_173

mid of 2014, offers the possibility to obtain satellite clock corrections with a relatively short latency via data streams.

Furthermore, the ambiguity resolution (AR) becomes much more involved in the zero-difference case (e.g., Laurichesse et al. 2009) as compared to a double-difference processing. If one chooses to perform a PPP using an ambiguity float solution, the convergence time for reaching high accuracies is often quite long (Grinter et al. 2013).

While a lot of progress has been and is made to overcome the above problems and to improve, e.g., the availability of real-time products, the classical double-difference coordinate estimation is still a viable approach, not afflicted by the requirement of accurate satellite clock corrections and with much easier AR. The purpose of this article is to show that this approach has a potential also for near real-time applications if a latency of a few minutes is acceptable.

The methods summarized here will be applied to the GNSS data processing in the framework of a National Multi-Hazard Early Warning System (NMHEWS) in the Sultanate of Oman, established by SpaceTech GmbH in cooperation with the German Research Centre for Geosciences Potsdam (GFZ) and the Astronomical Institute of the University of Bern (AIUB). After giving a short overview on this system, we describe the processing strategy, based on double-difference coordinate estimation. Since the GNSS network of the NMHEWS is not yet built up, a number of stations of the European Permanent Network (EPN)[1] were selected to assess the performance of our approach. Furthermore, we also applied our processing scheme to data from the GITEWS, gathered by its GNSS stations during the May 2010 Northern Sumatra Earthquake. The results of these tests will be presented at the end.

2 A National Multi-Hazard Early Warning System in the Sultanate of Oman

2.1 Overview

After the disastrous tsunami on December 26, 2004 in the Indian Ocean, a lot of effort has been undertaken to plan and realize tsunami early warning systems. As one of the first reactions, already in 2005 the GITEWS was initiated by the German government. Its establishment was coordinated by the GFZ and it was successfully handed over to the Indonesian partner institutions in 2011 (Münch et al. 2011).

In 2009, UNESCO signed an agreement with the Sultanate of Oman to establish a NMHEWS.[2] The German company SpaceTech GmbH Immenstaad is commissioned to coordinate the setup of the GNSS sector, in cooperation with the GFZ and the AIUB. While the GFZ will contribute its expertise for the engineering, maintenance and operation of the GNSS stations, the AIUB provides the expertise for the GNSS data processing.

The NMHEWS will be composed of several sensor networks, with seismic stations, GNSS stations, meteorological stations, and tide gauges as the main components.

2.2 The GNSS Network

The GNSS network consists of ten permanent stations, equipped with Septentrio PolaRx4 receivers and NavXperience 3G+C antennas providing real-time data. Only GPS data is planned to be processed. Figure 1 shows the locations of the GNSS stations in Oman. The purpose of the network is the monitoring of land deformation to cross validate the possibility of a tsunami after a nearby submarine Earthquake. The requirement is to obtain the displacement vectors of the stations with a delay less than 2 min in case of an Earthquake.

3 The Processing Strategy

The processing of the GNSS data is performed with the Bernese GNSS Software v5.2 (Dach et al. 2007) as it is available to the user community, using the ultra-rapid orbits and Earth rotation parameters (ERPs) of the Center for Orbit Determination in Europe (CODE, Dach et al. 2009). To bypass the difficulties of a PPP mentioned in Sect. 1, it is based on double-difference GNSS data, where baselines are formed with an algorithm to maximize the number of common observations. For the rest of this report we use the term *warning stations* for the 10 GNSS stations of the NMHEWS, while by *reference stations* we denote additional stations from the IGS network with known coordinates in the IGb08 reference frame (Rebischung et al. 2013).

As a matter of fact, only very few reference stations are located in the region where the NMHEWS shall be established. Since they are far away from the warning stations and in order to become independent of the requirement that they provide real-time data, the data processing is split up into two main steps: a datum step (Sect. 3.1) and a near real-time step (Sect. 3.2).

3.1 The Datum Step

In the datum step a solution for the warning stations together with the reference stations is computed to monitor the stability of the warning stations w.r.t. the global reference frame.

[1] http://www.epncb.oma.be/.

[2] http://www.unesco.org/new/en/unesco/partners-donors/the-actions/sciences/national-multi-hazard-early-warning-system-nmhews/.

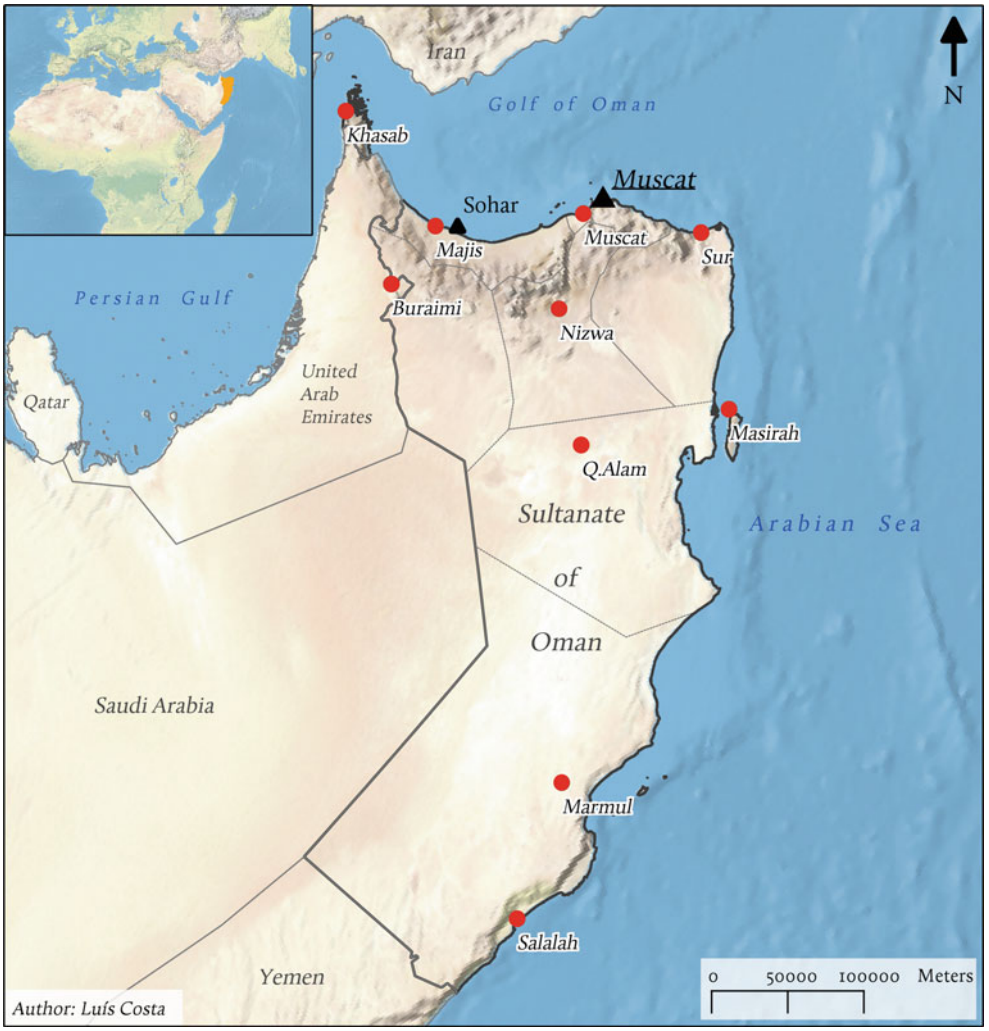

Fig. 1 Locations of the GNSS stations (*red dots*) and warning centers (*black triangles*) of the NMHEWS. By courtesy of Luís Costa

For this, a defined amount (e.g., 8 h) of the most recent data is used from the warning and the reference stations.

The preprocessing of the data involves an extended procedure for the AR to cope with the fact that the baselines to the reference stations may be very long. In particular, code- and phase-based wide-lane AR, code- and phase-based narrow-lane AR, Quasi-Ionosphere-Free (QIF) AR and direct L1/L2 AR is applied (a full description of these strategies is given in Dach et al. 2007). All strategies are optimized for post-processing and, compared to real-time strategies, need more data to reliably resolve the ambiguities (see also Sect. 4.3).

Finally, static coordinates for all stations are estimated with the full amount of data. The coordinates of the warning stations are estimated in a no-net-translation (NNT) minimum constraint solution w.r.t. the coordinates of the reference stations at the epoch of measurements. This step includes a verification of the consistency of the solution and the coordinates of the reference stations.

The datum step is repeated once per hour. The static coordinates of the warning stations are then used as a priori coordinates for the subsequent near real-time step.

3.2 The Near Real-Time Step

In the near real-time step (repeated every 2 min) only data from the warning stations is processed. To speed up the preprocessing, ambiguities are resolved using the QIF strategy only (which is applicable to baselines of lengths up to 1000–2000 km). For the AR, again a certain number of hours of the most recent data is obtained from the warning stations (we will investigate the impact of the amount of data in Sect. 4.3).

For the last 3 min of data, kinematic coordinates are estimated for the warning stations introducing the resolved ambiguities and using a NNT condition for each epoch w.r.t. the coordinates computed for the warning stations in the most recent datum step (Sect. 3.1). That means, for each epoch

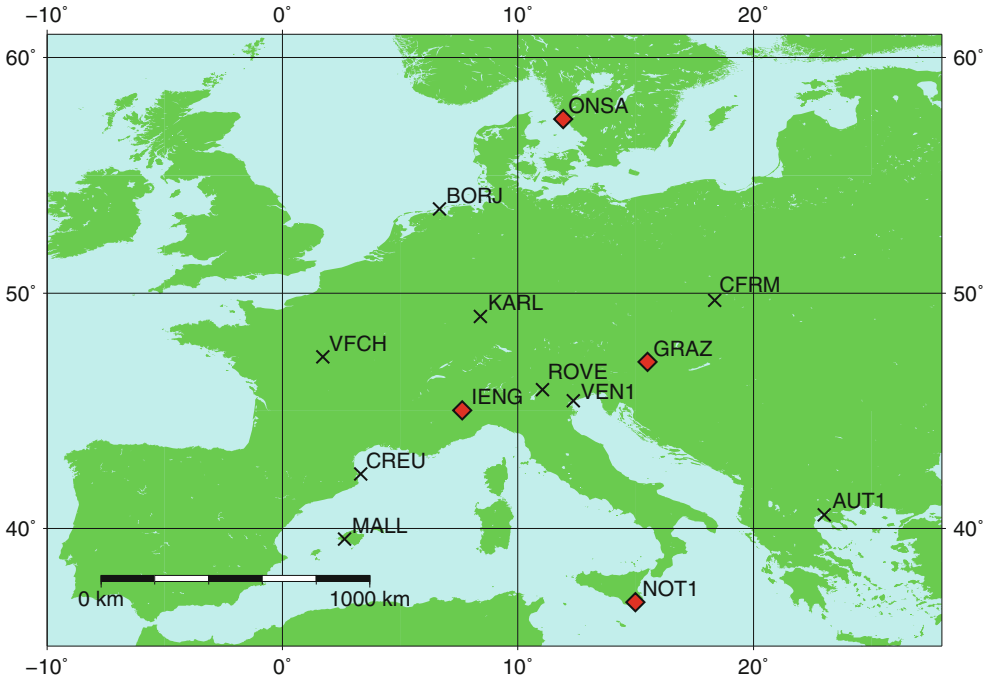

Fig. 2 The geographical distribution of the test network. *Crosses*: EPN (warning) stations. *Red diamonds*: IGb08 reference stations

the coordinates of the warning stations are shifted to keep the barycenter (the geometrical center) of the network at its a priori position. In a first step, all stations contribute to this datum definition. Then, the kinematic coordinates are screened w.r.t. their variances and the station(s) with the largest variance(s) are identified. The datum definition is then repeated without the maximally varying station(s). This strategy excludes stations from the datum definition that are affected by a displacement, avoiding that the displacement is partly absorbed in a shift of the other station coordinates (see also Sect. 4.5).

4 Results

4.1 The Test Setup

Since the GNSS stations for the NMHEWS are not yet installed, a network of European GNSS stations has been selected to develop the processing scheme and to proof its performance. It consists of 9 EPN stations providing real-time data (simulating the warning stations) and 4 IGb08 reference stations providing hourly RINEX files. Figure 2 shows the geographical distribution of these stations. The 1 Hz data from the EPN stations was streamed using the BKG Ntrip Client (BNC) v2.8 (Weber et al. 2007), the 30 s hourly RINEX files from the reference stations were downloaded every hour.

4.2 Kinematic Coordinates

Figure 3 shows 3 min of kinematic coordinates derived from GPS observations of the nine warning stations at a 5 s sampling, obtained through the processing steps described in Sect. 3. The differences to the a priori coordinates (as estimated in the datum step) are shown.

Possible sources of the observed offsets from the a priori coordinates are multipath effects during the selected interval of processing and correlations between station coordinate parameters with the unresolved ambiguities during very short intervals (all these parameters are nearly linear as long as the satellite geometry does not significantly change). These offsets are, however, not relevant, as one is only interested in the relative displacement of one or several stations in the case of an Earthquake.

Since the near real-time processing repeats every 2 min, two consecutive 3 min coordinate batches overlap for 1 min; the characteristics of these overlaps can be taken as an indicator for the quality and stability of the coordinate estimation (see Sect. 4.3). Figure 4 shows, as a typical example, for one of the EPN stations (MALL) three consecutive batches of kinematic coordinates. The batch of Fig. 3 corresponds to the first one shown in Fig. 4. It is apparent, that, at least in most overlaps, the coordinates of two consecutive batches do not match perfectly. Again, this mismatch is not relevant for the data post-processing, as long as two consecutive batches only show a not too large constant relative offset that can be removed to obtain continuous time series.

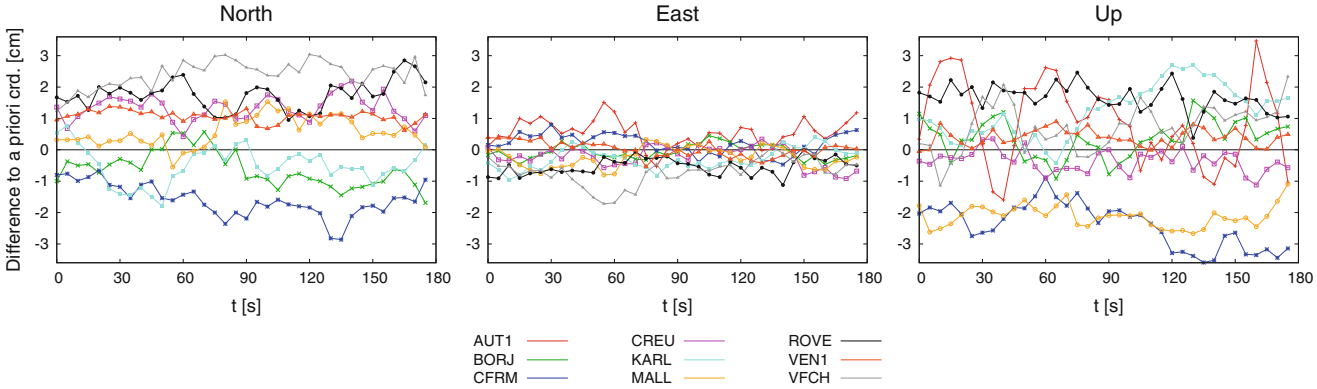

Fig. 3 Kinematic coordinates (3 min at 5 s sampling) for the warning stations. $t = 0$: August 06, 2013, 23:53:00 UT

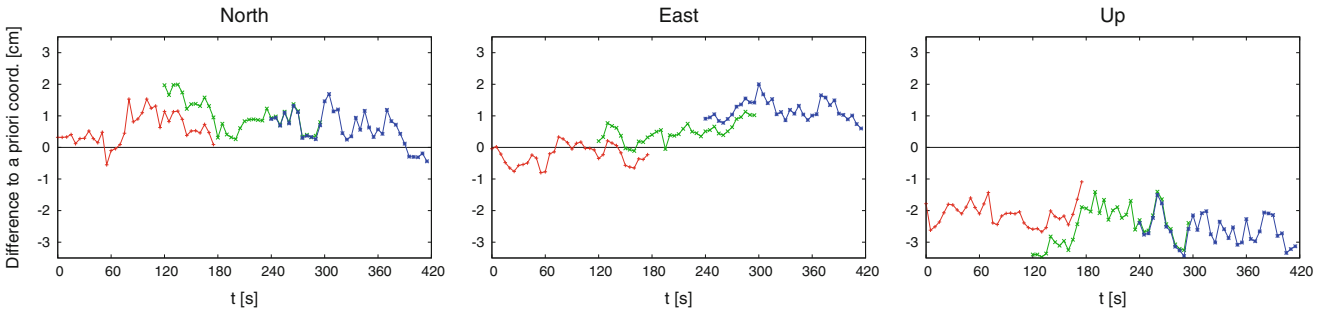

Fig. 4 Overlap of three consecutive 3 min coordinate batches for station MALL. $t = 0$: August 06, 2013, 23:53:00 UT

4.3 The Impact of the Amount of Data

In order to quantify the mismatch of two consecutive coordinate batches, the mean value and standard deviation of the differences of the kinematic coordinates during the overlaps can be calculated. On the one hand, a small standard deviation indicates that the two batches mostly show only an offset, quantified by the mean value. On the other hand, if the two batches show additional inconsistencies – e.g., if they are tilted or shifted in time w.r.t. each other – the standard deviation will become larger, indicating that the batches do not 'fit' anymore.

These two numbers – the mean value and the standard deviation of the coordinate differences – are quality parameters in general and can be used to show the dependence of the quality of the obtained kinematic coordinates on the total amount of data used for the processing. Figure 5a, b show, as a typical example, these two quantities for two consecutive coordinate batches of the EPN station VFCH, depending on the number of hours of data.

It is obvious that with only 1 or 2 h of data both the mean value and the standard deviation differ significantly from zero, indicating a coordinate estimation with a low quality and stability. With more data both values converge to zero. This is important: the processing of several hours of data (in this case more than 4 or 5 h) is necessary, even though one is only interested in estimating coordinates for the last few minutes.

The main reason for this is the dependence of the AR success-rate (the percentage of resolved ambiguities) on the total amount of data used to resolve them. Figure 5c shows this dependence for the QIF AR of the near real-time step. This plot again suggests that a significant number of hours of data is needed to obtain a sufficiently high AR success-rate in order to guarantee a stable solution.

4.4 Computing Time

It is worth mentioning that in both of the main processing steps – the datum step and the near real-time step – the preprocessing and the processing are consequently parallelized: For each step we need two inversions of the full normal equation system, beside that, the stations or baselines are treated independently. This allows for a very rapid processing. On an 8 core Intel XEON E5-2660 2.2 GHz server with 32 GB DDR3 memory the datum step with a data sampling of 30 s completed in approximately 90 s, while the near real-time processing with a data sampling of 5 s took around 60 s (8 h of data in both cases). This underlines the near real-time capability of the established processing scheme.

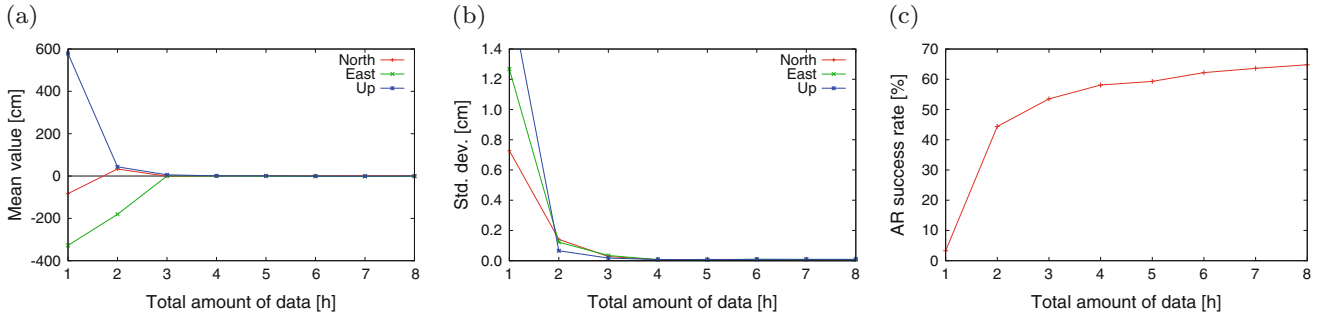

Fig. 5 The mean value (**a**) and the standard deviation (**b**) of the coordinate differences of two consecutive coordinate batches for the EPN station VFCH. (**c**) Percentage of ambiguities resolved by the QIF AR

Fig. 6 *Green triangles*: the nine GNSS stations at tide gauges of the GITEWS. *Yellow inverted triangles*: IGS reference stations. *Red circle*: the epicenter of the May 2010 Northern Sumatra Earthquake

4.5 The May 2010 Northern Sumatra Earthquake

On May 9, 2010 at 05:59:44 UTC a 7.2 magnitude Earthquake occurred off the island of Sumatra, 215 km from Banda Aceh (GEOFON 2010). At that time the GITEWS was operational, processing data from 9 real-time GNSS stations and 9 GNSS stations located at tide gauges. We analyzed the data of the 9 GNSS stations at tide gauges (Schöne et al. 2011) to assess the performance of our approach used for the data processing in the NMHEWS. In addition, four IGS reference stations were selected. The geographical distribution of the stations and the location of the epicenter are shown in Fig. 6.

The available data of all stations is at a 30 s sampling. Only GPS observations were used. Taking 8 h of data into account for both the datum and the near real-time step, the processing was performed as described in Sect. 3, however using the CODE final orbits and ERPs (due to lack of the ultra-rapid products from that time).

The kinematic coordinates of the warning stations indicated a displacement of the station MEUL, located closest to the epicenter of the Earthquake. Figure 7 shows the North, East and Up components of the coordinates of MEUL on May 9, 2010 from 05:50 to 06:10 UTC. To quantify the displacement, the mean values of the coordinates before and including 05:59:00 and after and including 06:01:00 were compared. The differences in the North (ΔN), East (ΔE) and Up (ΔU) components are shown in Table 1 for two different datum definitions: (a) for a datum definition in which all stations were included for the calculation of the barycenter and (b) one in which the station MEUL was excluded due to the high variance of the kinematic coordinates (as described in Sect. 3.2). The displacement in the former case turns out about 10 % smaller since here the physical displacement of MEUL reflects itself in small displacements of all the other station coordinates as well.

The comparison of two static solutions, one including data from 00:00 to 05:45 and one from 06:15 to 12:00 UTC, yielded $\Delta N = -4.2$ cm, $\Delta E = -2.6$ cm and $\Delta U = -0.5$ cm

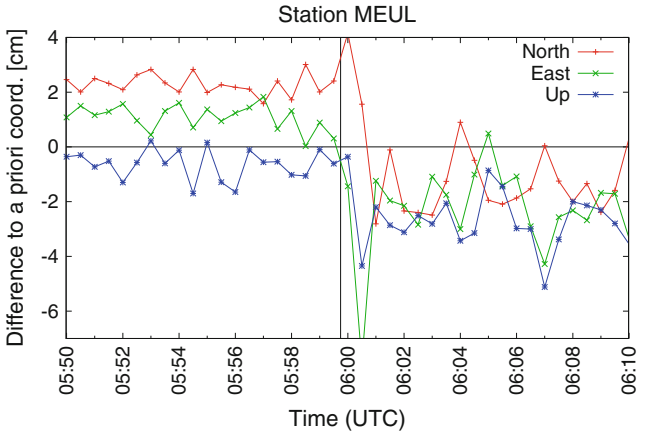

Fig. 7 Kinematic coordinates of station MEUL on May 9, 2010. *Vertical black line*: time of the Earthquake

Table 1 Displacements of station MEUL when including (a) and excluding (b) MEUL itself in the datum definition

Dat. def.	ΔN (cm)	ΔE (cm)	ΔU (cm)
(a)	−3.3	−2.8	−1.9
(b)	−3.7	−3.2	−2.1

for the station MEUL. This is very close to the values in Table 1. However, one has to keep in mind that the static solution displacements contain a larger fraction of the postseismic deformation.

A higher sampling of the data would be helpful to monitor the movement of the station at a higher temporal resolution. In our double-difference approach, data of higher sampling could easily be processed. Depending on the available clock corrections, this may not be the case for a PPP, where the sampling of the clock corrections sets the limit of the data processing.

5 Summary and Conclusion

The establishment of the GNSS sector of the NMHEWS in the Sultanate of Oman is coordinated by SpaceTech GmbH in cooperation with the GFZ and the AIUB, the latter contributing its expertise for the GNSS data processing. The processing is performed in a near real-time post-processing mode with the requirement to obtain the warning station displacements within less than 2 min after an Earthquake. To remain independent of accurate satellite clock corrections and to make usage of the AR, the processing is based on double-difference observations. It is split up into two parts: a datum step repeated every hour and a near real-time step repeated every 2 min.

Using the GPS observations of a network of EPN and IGb08 stations, the performance of the approach was tested. On our server the datum and the near real-time processing were completed within 90 and 60 s of computing respectively. It was found that, also for the estimation of 3 min of kinematic coordinates, 5 or more hours of data should be taken into account to guarantee a sufficient AR success rate.

The application of our processing scheme to data collected by GNSS receivers of the GITEWS during the May 2010 Northern Sumatra Earthquake showed that it is capable to detect warning station displacements of the order of a few centimeters.

Acknowledgements We are grateful to Tilo Schöne from the GFZ for interesting discussions and for providing us with the GITEWS data.

References

Caissy M, Agrotis L (2013) Real-time working group and real-time pilot project: IGS Technical Report 2012. In: Dach R, Jean Y (eds) AIUB. International GNSS Service: Technical Report 2012. IGS Central Bureau, pp 179–184

Dach R, Hugentobler U, Fridez P, Meindl M (2007) Bernese GPS Software 5.0. Astronomical Institute, University of Bern, Bern

Dach R, Brockmann E, Schaer S, Beutler G, Meindl M, Prange L, Bock H, Jäggi A, Ostini L (2009) GNSS processing at CODE: status report. J Geod 83(3–4):353–366

Falck C, Ramatschi M, Subarya C, Bartsch M, Merx A, Hoeberechts J, Schmidt G (2010) Near real-time GPS applications for tsunami early warning systems. Nat Hazards Earth Syst Sci 10:181–189

Grinter T, Roberts C (2013) Real time precise point positioning: are we there yet? In: IGNSS Symposium 2013, Outrigger Gold Coast, Qld, Australia, 16–18 July 2013

GEOFON (2010) http://dx.doi.org/10.5880/GEOFON.gfz2010jaei

Laurichesse D, Mercier F, Berthias JP, Broca P, Cerri L (2009) Integer ambiguity resolution on undifferenced GPS phase measurements and its application to PPP and satellite precise orbit determination. Navigation J Inst Navig 56(2):135–149

Münch U, Rudloff A, Lauterjung J (2011) Postface "The GITEWS Project – results, summary and outlook". Nat Hazards Earth Syst Sci 11:765–769

Rebischung P, Garayt B, Collilieux X, Altamimi Z (2013) IGS Reference Frame Working Group Coordinator Report 2012: IGS Technical Report 2012. In: Dach R, Jean Y (eds) AIUB. International GNSS Service: Technical Report 2012. IGS Central Bureau, pp 171–178

Schöne T, Illigner J, Manurung P, Subarya C, Khafid, Zech C, Galas R (2011) GPS-controlled tide gauges in Indonesia – a German contribution to Indonesia's Tsunami Early Warning System. Nat. Hazards Earth Syst Sci 11:731–740

Weber G, Mervart L (2007) The BKG Ntrip Client (BNC). EUREF Publication No. 17. Mitteilungen des Bundesamtes für Kartographie und Geodäsie, Band 42, London, 06–09 June 2007, pp 105–117

Analyzing the Variation of Precipitable Water Vapor with Ground-Based GPS Over Taiwan

Ta-Kang Yeh, Chuan-Sheng Wang, Jing-Shan Hong, and Tung-Yuan Hsiao

Abstract

Water vapor plays an important role in weather prediction. Thus, it would be helpful to use Precipitable Water Vapor (PWV) data from Global Positioning System (GPS) signals to understand weather phenomena. Approximately 100 ground GPS stations that cooperate with approximately 500 ground weather stations were used in this study. The hourly Zenithal Wet Delay (ZWD) values during the observation period of between 2006 and 2011 were estimated. The PWV which was converted from the ZWD variations were compared with the rainfall observations. The results indicated that the PWV amplitudes were between 10.98 and 13.10 mm and always occurred at the end of July. The magnitudes of the PWV annual growth rate were between 0.68 and 0.83 mm/year. Although the end of July with the greatest monthly average PWV values, the rainfall magnitude on this period is smaller than that during the typhoons, which only occurred for a few days. The PWV also increased during typhoons. Because this affect was short-term, it did not contribute to the PWV monthly average seriously.

Keywords

Ground-based GPS • Precipitable water vapor • Yearly variation

1 Introduction

GPS technology can provide nearly real-time, highly precise, and continuously varying PWV data across a wide coverage area. This ability is very important for improving the short-term weather forecast capability, especially in terms of thunderstorm forecasting and numerical weather forecast models. Currently, the ground-based GPS network of the National Oceanic and Atmospheric Administration (NOAA) of the United States can automatically estimate the variation of PWV above the network surface every 30 min. The Japanese GPS network, consisting of more than 1,000 stations, has also been used in functional ground-based GPS meteorological applications. Moreover, continuous GPS observations in China for 2004–2007 are used to produce PWV and the strong seasonal cycles are in summer with maximum water vapor and in winter with minimum water vapor are found (Jin et al. 2008). Furthermore, Roman et al. (2012) utilize ground-based GPS to retrieve the PWV in the U.S. Great Plains and Midwest and to detect a 1 mm/year PWV trend from 2000 to 2009. In this study, approximately 100 ground-based GPS stations that cooperated with approximately 500 ground weather stations from 2006 to 2011 were used to improve the understanding of the relationships between PWV and rainfall. Simultaneously, the seasonal and yearly variations of PWV and rainfall were also determined to discuss the greenhouse effect on Taiwan in these years.

T.-K. Yeh (✉) • C.-S. Wang
National Taipei University, New Taipei, Taiwan
e-mail: bigsteel@mail.ntpu.edu.tw; carlwang.cv87g@gmail.com

J.-S. Hong
Central Weather Bureau, Taipei, Taiwan
e-mail: rfs14@cwb.gov.tw

T.-Y. Hsiao
Hsing Wu University, New Taipei, Taiwan
e-mail: tungyuanhsiao@gmail.com

© Springer International Publishing Switzerland 2015

C. Rizos, P. Willis (eds.), *IAG 150 Years*, International Association of Geodesy Symposia 143,
DOI 10.1007/1345_2015_37

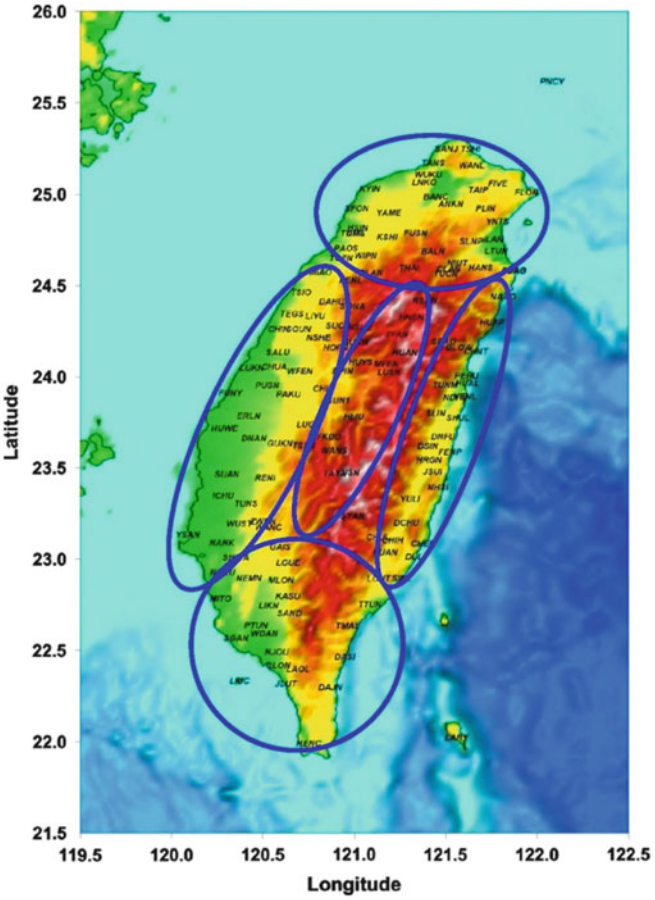

Fig. 1 The distribution of the GPS Continuously Operating Reference

2 Data Collection and Processing

Two types of data were collected in this study from between 2006 and 2011, including GPS measurements and rainfall data. The 30-second sample rate measurements from the 100 GPS stations were provided by the Central Weather Bureau, the Department of Land Administration and the Ministry of the Interior in Taiwan. The distribution of the GPS stations that were used in this study is shown in Fig. 1. The hourly recorded accumulated precipitation data from 496 weather stations around Taiwan were provided by the Central Weather Bureau. Because the locations of each weather station could not be matched to the individual GPS stations, the individual corresponding weather station for each GPS station was selected based on nearest distance to compare the PWV and rainfall data. The average nearest distance in this study was approximately 3 km.

In the data-processing procedure, the individual Zenithal Total Delay (ZTD) for each GPS station can be obtained after resolving the ambiguity with the least-squares method, which uses the double-difference strategy with GPS carrier phase measurements. By cooperating with the hydrostatic zenithal delay formula, the zenith dry delay and ZWD are separated from the ZTD. In this study, Bernese software was utilized. The L3 liner combination and the Global Ionospheric Maps of Total Electron Content (GIM-TEC) were used to reduce the ionospheric delay. The Niell model was utilized for mitigating the tropospheric delay. Moreover, the QIF method was adopted for the ambiguity resolving and the float ambiguities were taken into account with the ZWD solution (Yeh et al. 2013). To avoid eliminating the desired ZWD when eliminating the common error with differential calculation, we used the long baseline static relative positioning method to ensure that the obtained ZWD was the absolute value. In this study, the TSKB of Japan was chosen as the reference station and the baselines were produced from TSKB to all the other stations. At distances of more than 2,000 km, the atmospheric status between the two locations is assumed to be uncorrelated. By increasing the baseline distance between the main station and the calculation station, the atmospheric information can be preserved during the differential calculation. This process results in a more accurate ZWD (Yeh et al. 2014). Furthermore, due to the accuracy of the data and the comprehensive error correction, the output frequency of the ZWD was once per hour and 24 times per day per station. Thus, the temporal resolution of the GPS-deduced ZWD was 1 h, was easier to compare with the rainfall data.

To convert the ZWD data to PWV data, the relationship between the ZWD (ΔS_W) and PWV (P_W) based on the definition of precipitable water vapor is $P_w = \prod \times \Delta S_w$, where $\prod$ is the scale factor. The scale factor can be calculated as $\prod^{-1} = 10^{-6}\left[\rho R_w\left(k_3/T_m + k_2'\right)\right]$, where k_2 and k_3 are the experimental constants for atmospheric refraction, and $k_2 = 64.79\ K/hPa$, $k_3 = 3.766 \times 10^5\ K^2/hPa$, and $k_2' = k_2 - k_1 M_w/M_d = 16.52\ K/hPa$. The molar mass of the water vapor (M_w) is $18.015\,g/mol$, and $R_w = R/M_w = 461.524 J/kg \cdot K$. The scale factor $\prod$ is related to the temperature and changes in latitude, station height, season, and the weather. Therefore, the method used to determine the temperature is very important. In 1984, Davis et al. provided a solution to this problem and defined the weighted average temperature as follows: $T_m = \int_{h_s}^{\infty} \frac{e}{T} dh \Big/ \int_{h_s}^{\infty} \frac{e}{T^2} dh$, where e is the water vapor pressure, and T is the atmospheric temperature (K). From 586 radiosonde observations collected at the Taipei site from 1988 to 1997, Liou et al. (2001) revealed the linear relationship between the weighted average temperature T_m and the surface temperature T_s: $T_m = 1.07T_s - 31.5$. With these equations, the ZWD can be converted to PWV.

To avoid data loss during harmonic analysis of the relationships between PWV and rainfall, the hourly derived PWV data were averaged monthly. In addition, the rainfall

Table 1 The amplitudes, phases and annual growth rates for the monthly average PWV

Region	Amplitude (mm)	Time of peak* (month/day)	Increasing rate (mm/year)
North	12.10	7/26	0.68
West	13.10	7/23	0.83
South	12.88	7/27	0.71
East	11.53	7/30	0.67
Mountain	10.98	7/25	0.74

* is the peak time obtained from the phase

Table 2 The amplitude, phase and annual growth rate for the monthly average of accumulated precipitation

Region	Amplitude (mm)	Time of peak* (month/day)	Increasing rate (mm/year)
North	43.14	9/26	−3.55
West	139.72	7/15	−16.15
South	287.77	7/28	−7.27
East	157.21	9/14	7.95
Mountain	229.27	7/29	−17.44

* is the peak time obtained from the phase

data were summarized for each month between 2006 and 2011. Next, harmonic analysis was applied to compute the time series for each sub-region individually. The harmonic analysis that was used is $y(t) = \sum_{i=1}^{N} A_i \cos(v_i(t) - \phi_i)$, where A_i denotes the amplitude, ϕ_i represents the phase, and $v_i(t)$ is the frequency argument. Next, a least-squares analysis was performed to obtain the harmonic functions that represented the main components of the PWV and rainfall data. An essential assumption of harmonic analysis is that the time series of the data is periodic and is composed of harmonic functions with a limited number of known frequencies. Under this assumption, the amplitude and phase for PWV and rainfall can be obtained following harmonic analysis as shown in Tables 1 and 2. The amplitude shows the strength of the annual change. The phase value represents the time for the peak. The monthly slope of the PWV and rainfall were derived from the linear regression method. The annual growth rate for the PWV and rainfall was estimated by multiplying the monthly averages by 12, as shown in the last column of Tables 1 and 2.

3 Precipitable Water Vapor Analysis

First, the results of the PWV harmonic analysis in the Northern region are discussed as an example. The amplitude (12.10 mm) is presented in the first column of Table 1. The difference between the largest and smallest PWV in the Northern region was 24.20 mm. In addition, the phase was 203.87° (Table 1). The day of the year (207, equivalent to July 26th) can be derived by dividing the magnitude (203.87°) by 360° and then multiplying by 365 days. To analyze the variable PWV properties for each sub-region in Taiwan from 2006 through 2011, the monthly averages from the harmonic analysis and from the linear PWV slopes are analyzed. To analyze the differences between each wave peak sub-regions, wave troughs and the six year average, the harmonic analysis values were subtracted from the monthly averages. The monthly average exceeds 5 mm according to the harmonic analysis, which is denoted by the star sign in Fig. 2. Three of these times occurred in 2011. During the fourth time events, the monthly average only exceeded 5 mm in the Eastern region. In addition, during the last situation with monthly averages greater than 5 mm occurred in November, 2011. In addition, exceptionally greater PWV values always accompanied these rainfall events.

Monthly averages of less than 5 mm (according to the harmonic analysis) occurred between 2009 and 2011 and are depicted by triangle symbols in Fig. 2. Four of these events occurred in the winter season. The other two events occurred during the plum rain season. It is unlikely that months in which much lower PWV values occur will contain a heavy rainfall event. In summary, exceptionally greater values were more frequent during the plum rain season between 2006 and 2007. In addition, exceptionally low values occurred during the plum rain and winter seasons between 2009 and 2011 as the PWV increased from year to year in each sub-region. On the other hand, the annual rainfall growth rates in each sub-region were different from the annual PWV growth rates. Compared with the yearly accumulated precipitation of 2,500 mm, the annual growth rate only accounted from −0.6 to 0.3% of the precipitation. In summary, the above results show a slightly decreasing rainfall trend for Taiwan.

4 Conclusions

In summary, the largest PWV amplitude of 13.10 mm occurred in the Western region and was determined by the harmonic analysis. The second largest amplitude of 12.88 mm occurred in the Southern region. These results demonstrate that large seasonal PWV fluctuations occur in these two sub-regions. The Central Mountain region had the smallest amplitude of 10.98 mm because its higher altitude resulted in a lower PWV in comparison with the other sub-regions. In the winter, Taiwan is nearly always influenced by a northeast monsoon. This monsoon causes frequent rainfall events in the Eastern and Northern regions. Therefore, no obvious seasonal PWV fluctuations were observed. Moreover, the peak PWV always occurred at the end of July, which corresponded with the highest temperatures

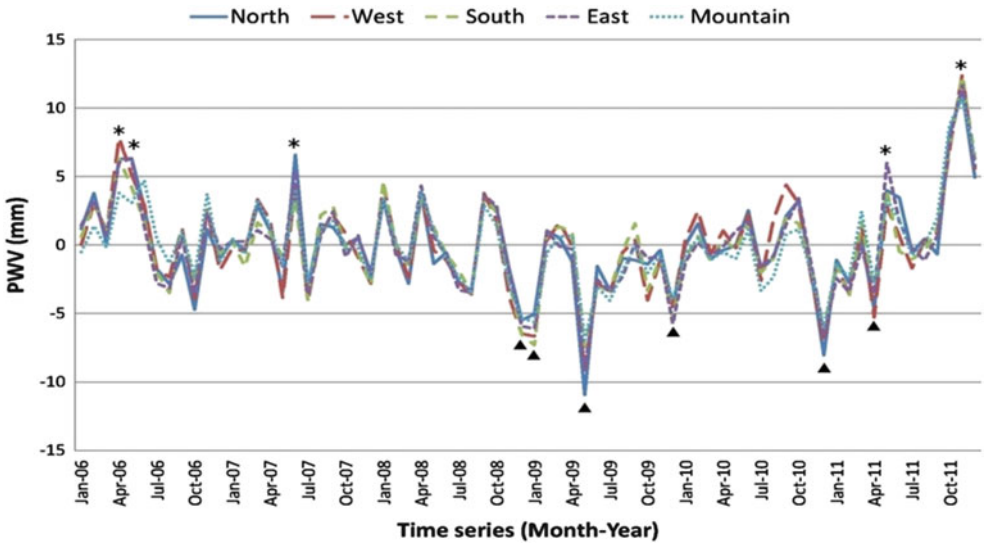

Fig. 2 The difference between the monthly average PWV and the harmonic analysis value. The monthly average of the PWV exceeds 5 mm. The harmonic analysis value is denoted by star and triangle signs for the values that are less than 5 mm

in each sub-region. The highest annual PWV growth rate was 0.83 mm/year, which occurred in the Western region. Although the PWV increased every year in each region, the PWV was exceptionally greater between 2006 through 2007. In contrast, exceptionally lower values occurred frequently between 2009 and 2011.

References

Jin SG, Li Z, Cho J (2008) Integrated water vapor field and multiscale variations over China from GPS measurements. J Appl Meteorol Climatol 47(11):3008–3015

Liou YA, Teng YT, van Hove T, Liljegren JC (2001) Comparison of precipitable water observations in the near tropics by GPS, microwave radiometer, and radiosondes. J Appl Meteorol 40(1): 5–15

Roman JA, Knuteson RO, Ackerman SA, Tobin DC, Revercomb HE (2012) Assessment of regional global climate model water vapor bias and trends using Precipitable Water Vapor (PWV) observations from a network of Global Positioning Satellite (GPS) receivers in the U.S. Great Plains and Midwest. J Climate 25:5471–5493

Yeh TK, Chen CH, Xu G, Wang CS, Chen KH (2013) The impact on the positioning accuracy of the frequency reference of a GPS receiver. Surv Geophys 34(1):73–87

Yeh TK, Hong JS, Wang CS, Hsiao TY, Fong CT (2014) Applying the water vapor radiometer to verify the precipitable water vapor measured by GPS. Terr Atmos Ocean Sci 25(2):189–201

Predicting and Correcting Scale Induced Biases Resulting from the Application of Regional Orbit and Clock Corrections

Lennard Huisman and Peter J.G. Teunissen

Abstract

Real-time orbit and clock corrections to GPS broadcast ephemeris, in short broadcast corrections (BCs), have become available as International GNSS Service (IGS) products through the IGS Real-time Service (RTS) in 2013. The BCs are distributed via the Network Transport of RTCM by Internet Protocol (NTRIP) according to RTCM State Space Representation standards. When applying the BCs in real-time Precise Point Positioning (PPP), user positions with sub-decimetre precision after convergence can be obtained. The IGS BCs refer to the International Terrestrial Reference Frame 2008 (ITRF2008). BCs in regional reference frames (RBCs) are available through regional NTRIP broadcasters in Europe, North-America, South-America and Australia.

The IGS RTS website states that: *Applying orbit and clock corrections from regional product streams in a real-time PPP solution automatically leads to regional coordinates. The PPP client would not need to transform coordinates because that is already done on the server side.* However, in contrast to the PPP-approach that uses BCs in ITRF2008 followed by a transformation to the local datum, the approach based on RBCs causes a bias in the PPP solution due to the scale factor between regional and global reference frames. This scale induced bias is satellite geometry dependent when the conventional 14-parameter transformation from the global to the regional reference frame is applied to the satellite position vectors in ITRF2008, to derive the RBCs from the IGS BCs. The size of the scale induced bias is significant. The bias is up to 8 cm for the Australian GDA94 and up to 0.5 cm for the North American NAD83.

Currently an additional satellite position dependent value is added to the satellite clock correction to deal with the scale induced biases of three RBCs, resulting in a transformed

L. Huisman (✉)
Kadaster, Apeldoorn, The Netherlands

Delft University of Technology, Delft, The Netherlands
e-mail: lennard.huisman@kadaster.nl

P.J.G. Teunissen
Curtin University, Bentley, WA, Australia

Delft University of Technology, Delft, The Netherlands
e-mail: p.teunissen@curtin.edu.au

© Springer International Publishing Switzerland 2015

C. Rizos, P. Willis (eds.), *IAG 150 Years*, International Association of Geodesy Symposia 143,
DOI 10.1007/1345_2015_117

clock correction (Weber, BKG Ntrip Client (BNC) Version 2.9 – Manual, 2013). Applying these transformed clocks results in a remaining scale induced bias of less then 10 mm for each RBC of ETRF2000, NAD83 and SIRGAS2000. For GDA94 the remaining scale induced bias is maximum 30 mm, this is caused by the large scale factor of GDA94 compared to other regional reference frames.

This contribution will show that the remaining bias in the PPP solution is practically independent from satellite geometry and depends mainly on the user position; hence the remaining bias can be predicted and corrected for at any location.

Keywords

Global and regional broadcast corrections • Global and regional reference frames • Real-time precise point positioning

1 Introduction

Before real-time orbit and clock corrections to broadcast ephemeris, the so-called broadcast corrections (BCs), became available, Precise Point Positioning (PPP) has been a technique that was mainly used in post-processing (Kouba 2009). Products of the International GNSS Service (IGS), such as orbits and clocks, are made available in the IGS realization of the International Terrestrial Reference Frame (ITRF), currently IGS08, which is aligned to ITRF2008 (Rebischung et al. 2012).

Users however, are often interested in positions in a Regional Reference Frame (RRF) such as ETRF2000, NAD83, GDA94, SIRGAS2000 or SIRGAS95 . The rigorous approach to obtain a position in the RRF is to first compute the PPP solution in the Global Reference Frame (GRF) and then to transform this solution, obtained using IGS products, to the required RRF. With the aim to have the PPP solution directly refer to a RRF, an alternative approach, based on transforming the input IGS products to RRFs, was suggested in Kouba (2002).

The BCs that are made available through the IGS Real-Time Service are available in IGS08 and made available through NTRIP (Caissy et al. 2012; IGS 2013). They are referred to as the Global BCs (GBCs). Next to these GBCs there are RRF-referenced Regional BCs available from regional NTRIP-casters (BKG 2013a; IGS 2013). Transforming IGS satellite position products to RRFs leads to a location and geometry dependent bias between the PPP solution obtained using the rigorous approach and the approach using RBCs (Huisman et al. 2012; Teunissen et al. 2012). The source of this bias lies in the scale difference between the GRF IGS08 and the RRFs.

Several approaches, such as the unscaled and scale-absorbed approach, have been proposed to overcome this bias. Currently, the available RBCs are based on the transformed clocks approach, which adds a satellite dependent value to the real-time clock correction, to take out the scale induced bias for a reference position in the validity area of the RRF. The assumption is that this satellite dependent correction will decrease the size of the scale induced bias within the whole region of the RRF.

This contribution will first describe the rigorous approach for obtaining a position using PPP with GBCs. Next, the scale induced bias caused by the RBCs will be identified in Sect. 3. Section 4 introduces the unscaled, the scale-absorbed and the transformed clocks approach and will show that the remaining scale-induced bias of the unscaled and scale-absorbed approach can be easily computed for any location and any epoch (present, past and future).

We also show that the remaining scale-induced bias of the transformed clocks approach can be approximated very well by that of the easily computable scale-absorbed approach. This is demonstrated in Sect. 5 by means of experimental results of the transformed clocks approach. Section 6 summarizes the findings on the theoretical and practical aspects of the transformed clocks.

2 Obtaining a Position in the RRF with GBCs

GBCs give corrections to broadcast ephemeris such that precise satellite positions and clock information can be obtained. On the server side precise satellite positions and clock offsets are estimated/predicted using data from a global network of GNSS-receivers (Hauschild and Montenbruck 2009). The difference between satellite positions and clock offset from broadcast ephemeris and the real-time process on the server side is sent to users via NTRIP (Weber et al. 2005; RTCM 2011). Broadcast ephemeris data is available on the user side as this information is transmitted by the GNSS-satellites. A user adds the received GBC information to the satellite positions and clock offsets computed

from broadcast ephemeris to obtain the precise positions and clock offsets from the server side. The GBCs can be used in the PPP algorithm to obtain precise results in real-time, for example with software such as the BKG NTRIP Client (BNC) (Weber 2013) and RTKLIB (Takasu 2010). A GRF-to-RRF coordinate transformation is then finally applied to obtain the receiver antenna position in the required RRF.

The GRF-to-RRF transformation is time-dependent so as to take various dynamics (e.g. tectonic movements) into account. For a specific epoch t, the 14-parameter GRF-to-RRF transformation reduces to a 7-parameter similarity transformation:

$$\mathbf{x}_R(t) = \mathbf{d}(t) + s(t)\mathbf{R}(t)\mathbf{x}_G(t) \tag{1}$$

where

$$\mathbf{d}(t) = \begin{bmatrix} d_x(t) \\ d_y(t) \\ d_z(t) \end{bmatrix}$$

$$s(t) = (1 + \Delta s(t))$$

$$\mathbf{R}(t) = \begin{bmatrix} 1 & -r_z(t) & r_y(t) \\ r_z(t) & 1 & -r_x(t) \\ -r_y(t) & r_x(t) & 1 \end{bmatrix}$$

with

$\mathbf{x}_G$: Coordinate vector in the global frame (GRF) x_G, y_G, z_G
$\mathbf{x}_R$: Coordinate vector in the regional frame (RRF) x_R, y_R, z_R
$\mathbf{d}$: Vector with translation parameters d_x, d_y, d_z
s : Scale factor between GRF and RRF
Δs : Increment of s to 1
$\mathbf{R}$: Matrix with differential rotation angles r_x, r_y, r_z

The transformation parameters are often considered to be dependent on time, in which case their time dependency needs to be known as well. Usually it is sufficient to only consider their linear time dependency. In that case the transformation is referred to as a 14-parameter transformation. The 14 parameters then consist of the 7 similarity transformation parameters, plus their 7 time-rates of change, all given at a certain reference epoch t_0. These 14 parameters can then be used to compute the 7 similarity transformation parameters for any epoch t as

$$\begin{aligned} \mathbf{d}(t) &= \mathbf{d}(t_0) + (t - t_0)\dot{\mathbf{d}}(t_0) \\ \mathbf{R}(t) &= \mathbf{R}(t_0) + (t - t_0)\dot{\mathbf{R}}(t_0) \\ \Delta s(t) &= \Delta s(t_0) + (t - t_0)\dot{\Delta s}(t_0) \end{aligned} \tag{2}$$

with

$\dot{\mathbf{d}}$: Rate of change of the translation vector
$\dot{\mathbf{R}}$: Rate of change of the rotation matrix
$\dot{\Delta s}$: Rate of change of the scale factor

3 The RBC Approach with Scale Induced Bias

In the RBC approach the GRF-to-RRF transformation is applied on the server side to the satellite positions. When a user applies the RBCs to the satellite positions from broadcast ephemeris the resulting positions are in the RRF. The RRF does not have the same scale as the observations, which is the case for the GRF. The receiver-to-satellite range, in a GRF, is computed as:

$$\rho^s_{r,G} = ||\mathbf{x}^s_G - \mathbf{x}_{r,G}|| \tag{3}$$

Substituting Eq. (1) into Eq. (3), taking the invariance of the norm with relation to the rotations into account, gives

$$\rho^s_{r,G} = \frac{1}{1 + \Delta s}||\mathbf{x}^s_R - \mathbf{x}_{r,R}|| = \frac{1}{1 + \Delta s}\rho^s_{r,R} \tag{4}$$

With

$$\frac{1}{1 + \Delta s} = 1 - \frac{\Delta s}{1 + \Delta s}$$

we may write

$$\begin{aligned} \rho^s_{r,G} &= ||\mathbf{x}^s_G - \mathbf{x}_{r,G}|| \\ &= ||\mathbf{x}^s_R - \mathbf{x}_{r,R}|| - \tfrac{\Delta s}{1+\Delta s}||\mathbf{x}^s_R - \mathbf{x}_{r,R}|| \\ &= ||\mathbf{x}^s_R - \mathbf{x}_{r,R}|| - \Delta s||\mathbf{x}^s_G - \mathbf{x}_{r,G}|| + \tfrac{\Delta s^2}{1+\Delta s} \\ &\quad ||\mathbf{x}^s_G - \mathbf{x}_{r,G}|| \\ &\approx ||\mathbf{x}^s_R - \mathbf{x}_{r,R}|| - \Delta s||\mathbf{x}^s_G - \mathbf{x}_{r,G}|| \\ &\approx \rho^s_{r,R} - \Delta s||\mathbf{x}^s_G - \mathbf{x}_{r,G}|| \end{aligned} \tag{5}$$

The size of $\frac{\Delta s^2}{1+\Delta s}||\mathbf{x}^s_G - \mathbf{x}_{r,G}||$ is at the micrometer level for currently existing RRFs and can therefore be ignored in Eq. (5). The presence of the last term in the above equation, $\Delta s||\mathbf{x}^s_G - \mathbf{x}_{r,G}||$, is the cause of the scale induced bias in the RBC approach. It has the following effect on the (simplified) observation equation,

$$\begin{aligned} p^s_r &= \rho^s_{r,G} + cdt_r - cdt^s + a^s_r + e^s_r \\ &= \rho^s_{r,R} - \Delta s||\mathbf{x}^s_G - \mathbf{x}_{r,G}|| + cdt_r - cdt^s + a^s_r + e^s_r \end{aligned} \tag{6}$$

with p^s_r the observation, cdt_r and cdt^s the receiver and satellite clock offsets in meters, a^s_r the atmospheric propagation delay and e^s_r denoting unmodelled errors and measurement

noise. As the scale induced bias is not parametrized in the PPP model, the bias $\Delta s||\mathbf{x}^s_G - \mathbf{x}_{r,G}||$ will be absorbed by the parameters which are solved for in the PPP algorithm, $\mathbf{x}_{r,R}$ and cdt_r.

4 Methods to Deal with the Scale Induced Bias

In the following three sections, methods are presented that deal with the scale induced bias, without the need of having to change the positioning algorithm. The residual biases of the three methods will also be described.

4.1 The Unscaled Approach

In the unscaled approach the scale induced bias is eliminated by ignoring the increment to scale. The applied transformation in the 'unscaled' case becomes

$$\mathbf{x}_{R'} = \mathbf{d} + \mathbf{R}\mathbf{x}_G \tag{7}$$

The relation between R- and unscaled R'-frame is (cf. Eq. (1)):

$$\mathbf{x}_R = \mathbf{x}_{R'} + \Delta s\ \mathbf{R}\ \mathbf{x}_G \tag{8}$$

Application of the unscaled transformation gives

$$\rho^s_{r,G} = ||\mathbf{x}^s_G - \mathbf{x}_{r,G}|| = ||\mathbf{x}^s_{R'} - \mathbf{x}_{r,R'}|| = \rho^s_{r,R} \tag{9}$$

and Eq. (6) becomes

$$p^s_r = \rho^s_{r,R'} + cdt_r - cdt^s + a^s_r + e^s_r \tag{10}$$

When using this observation equation, one solves the user position vector as $\mathbf{x}_{r,R'}$, implying that one is left with the following residual bias for the unscaled approach,

$$\begin{aligned} \mathbf{b}^{us}_r &= \mathbf{x}_{r,R'} - \mathbf{x}_{r,R} = -\Delta s\ \mathbf{R}\ \mathbf{x}_{r,G} \\ ||\mathbf{b}^{us}_r|| &= \Delta s||\mathbf{x}_{r,G}|| \end{aligned} \tag{11}$$

As shown in Huisman et al. (2012) and Teunissen et al. (2012), this remaining bias in the unscaled approach can be ignored for the horizontal component. Its vertical component is constant over large areas. In other words the remaining bias in the unscaled approach is location independent for practical purposes and only affects height.

4.2 The Scale-Absorbed Approach

As in the unscaled approach, the scale induced bias is eliminated by ignoring the increment to scale in the scale-absorbed approach. Additionally the bias of the unscaled approach, given in Eq. (11), is accounted for by adding this bias for a reference point to the translation vector. The applied transformation in the 'scale absorbed' case becomes:

$$\mathbf{x}_{R''} = \mathbf{d}' + \mathbf{R}\mathbf{x}_G \quad \text{with } \mathbf{d}' = \mathbf{d} + \Delta s\mathbf{R}\mathbf{x}_{*,G} \tag{12}$$

with $\mathbf{x}_{*,G}$ being the coordinate vector of a reference-point. The relation between R- and scale-absorbed R''-frame is (cf. Eq. (1)):

$$\mathbf{x}_R = \mathbf{x}_{R''} + \Delta s\ \mathbf{R}\ (\mathbf{x}_G - \mathbf{x}_{*,G}) \tag{13}$$

Application of the scale-absorbed transformation gives

$$\rho^s_{r,G} = ||\mathbf{x}^s_G - \mathbf{x}_{r,G}|| = ||\mathbf{x}^s_{R''} - \mathbf{x}_{r,R''}|| = \rho^s_{r,R''} \tag{14}$$

and

$$p^s_r = \rho^s_{r,R''} + cdt_r - cdt^s + a^s_r + e^s_r \tag{15}$$

with the bias of $\mathbf{x}_{r,R''}$, which is solved for in the scale-absorbed (sa) approach, following from (13) as

$$\begin{aligned} \mathbf{b}^{sa}_r &= \mathbf{x}_{r,R''} - \mathbf{x}_{r,R} = -\Delta s\ \mathbf{R}\ (\mathbf{x}_{r,G} - \mathbf{x}_{*,G}) \\ ||\mathbf{b}^{sa}_r|| &= \Delta s||\mathbf{x}_{r,G} - \mathbf{x}_{*,G}|| \end{aligned} \tag{16}$$

When $\mathbf{x}_{*,G}$ is chosen such that $||\mathbf{x}_{r,G} - \mathbf{x}_{*,G}|| < ||\mathbf{x}_{r,G}||$ for the region in which the RRF is valid, this bias is of course smaller than for the unscaled approach.

4.3 The Transformed Clocks Approach

In the transformed clocks approach the scale induced bias is accounted for by adding the scale induced effect of Eq. (5) to the satellite clock error, thus resulting in a transformed clock,

$$\widetilde{cdt}^s_R = cdt^s + \Delta s||\mathbf{x}^s_G - \mathbf{x}_{*,G}|| \tag{17}$$

To show the effect of $\widetilde{cdt}^s_R$ on the receiver position obtained using the PPP algorithm, first define

$$\tilde{\mathbf{x}}_{r,R} = \mathbf{x}_{r,R} - \Delta\mathbf{x}_R \quad \text{with } \Delta\mathbf{x}_R = \Delta s\mathbf{R}(\mathbf{x}_{r,G} - \mathbf{x}_{*,G}) \tag{18}$$

Then we have to first order (i.e. after linearisation):

$$\begin{aligned} ||\mathbf{x}^s_R - \tilde{\mathbf{x}}_{r,R}|| &= ||\mathbf{x}^s_R - \mathbf{x}_{r,R} + \Delta\mathbf{x}_R|| \\ &\approx ||\mathbf{x}^s_R - \mathbf{x}_{r,R}|| + (\mathbf{u}^s_{r,R})^T\Delta\mathbf{x}_R \\ &\approx ||\mathbf{x}^s_R - \mathbf{x}_{r,R}|| + \Delta s(\mathbf{u}^s_{r,G})^T(\mathbf{x}_{r,G} - \mathbf{x}_{*,G}) \end{aligned} \tag{19}$$

and

$$||\mathbf{x}^s_G - \mathbf{x}_{*,G}|| \approx ||\mathbf{x}^s_G - \mathbf{x}_{r,G}|| + (\mathbf{u}^s_{r,G})^T(\mathbf{x}_{r,G} - \mathbf{x}_{*,G}) \tag{20}$$

Table 1 Range of the predicted remaining scale induced bias for RBCs at August 9th 2013

RRF	Translation parameters d_x,d_y,d_z (mm)	Scale increment Δs (10^{-9})	Rotation angles r_x,r_y,r_z (mas)	Reference point $x_{*,G},y_{*,G},z_{*,G}$ (m)	Predicted bias maximum $\|\|\mathbf{b}_r^{tc}\|\|$ (mm)
NAD83	1004.6		−27.02	−1092950.0	
	−1912.4	−0.88	3.14	4383600.0	4
	−542.6		−10.75	4487420.0	
SIRGAS2000	2.0		0.17	3740860.0	
	4.1	0.00	−0.03	−4964290.0	0
	3.9		0.07	−1425420.0	
SIRGAS95	7.7		0.00	3135390.0	
	5.8	1.57	0.00	−5017670.0	9
	−13.8		−0.03	−2374440.0	
GDA94	−56.8		−29.88	−4052050.0	
	6.8	11.80	−25.43	4212840.0	30
	49.7		−25.04	−2545110.0	
ETRF2000	53.5		1.99	3661090.0	
	50.6	2.42	12.06	845230.0	6
	−83.0		−19.49	5136850.0	

with the receiver-satellite unit-direction vectors related as $\mathbf{u}^s_{r,R} = \mathbf{R}\mathbf{u}^s_{r,G}$.

Subtracting Δs times Eq. (20) from Eq. (19) gives

$$||\mathbf{x}^s_R - \tilde{\mathbf{x}}_{r,R}|| - \Delta s||\mathbf{x}^s_G - \mathbf{x}_{*,G}|| \approx ||\mathbf{x}^s_R - \mathbf{x}_{r,R}|| - \Delta s||\mathbf{x}^s_G - \mathbf{x}_{r,G}|| \tag{21}$$

The right-hand side we recognize as $\rho^s_{r,G}$ (see (5)). Thus to first order, we have

$$\rho^s_{r,G} = ||\mathbf{x}^s_R - \tilde{\mathbf{x}}_{r,R}|| - \Delta s||\mathbf{x}^s_G - \mathbf{x}_{*,G}|| \tag{22}$$

with the 2nd term on the right-hand side being the 'clock-correction'. Substitution of (17) and (22) into (6) gives

$$p^s_r = ||\mathbf{x}^s_R - \tilde{\mathbf{x}}_{r,R}|| + cdt_r - c\widetilde{dt}^s_R + a^s_r + e^s_r \tag{23}$$

This result shows that with the 'clock-correction' approach one is actually solving for $\tilde{\mathbf{x}}_{r,R}$. Comparing (13) with (18) shows that $\tilde{\mathbf{x}}_{r,R} = \mathbf{x}_{r,R''}$ and that in case of the transformed clock, to first order, one is actually solving for the same position as in de scale-absorbed approach. Hence, the 'transformed-clock' (tc) bias is approximated by

$$\mathbf{b}^{tc}_r \approx \tilde{\mathbf{x}}_{r,R} - \mathbf{x}_{r,R} = -\Delta s\mathbf{R}(\mathbf{x}_{r,G} - \mathbf{x}_{*,G}) = \mathbf{b}^{sc}_r \tag{24}$$

which is identical to the scale-absorbed bias.

4.4 Numerical Values of the Scale Induced Bias

From the previous sections two equations for the remaining scale induced bias are available. For the unscaled approach this is Eq. (11) and for both the scale-absorbed and transformed clock approach this is Eq. (16). Both equations show that if $\Delta s = 0$, i.e. if GRF and RRF have identical scale, then there is no positioning bias. As Δs is time dependent, so is the scale induced bias. Table 1 gives the transformation parameters to generate the RBCs for August 9th 2013, this is the date for which the experimental results in Sect. 5 have been generated. The last column of Table 1 gives the maximum predicted remaining scale induced bias for the transformed clock RBC. For SIRGAS2000 there should be no scale induced bias as $\Delta s = 0$. The remaining scale induced bias for the transformed clocks approach, according to Eq. (16), increases with the distance from the reference point $\mathbf{x}_{*,G}$. For NAD83, ETRF2000 and SIRGAS95 the bias is less than 10 mm. For GDA94 the bias is up to 30 mm on the mainland of Australia, due to the large scale factor of GDA94 compared to the other RRFs. This resulting scale induced bias is significantly less than the scale induced bias resulting from the RBC of 75 mm using only the GRF-to-RRF transformation and no transformed clock (Huisman et al. 2012). The maximum predicted remaining scale induced bias is one magnitude smaller than the decimetre level precision that can be achieved with real-time PPP (e.g. BKG 2013b), but is significant in post-processing applications where millimetre level precision is achieved (Kouba 2009).

5 Experimental Results with Transformed Clocks

For each of the RBCs one station in the region has been processed for August 9th 2013, a list of processed stations is given in Table 2. The RBCs available from regional NTRIP-

Table 2 Regional reference frame and location information for processed stations

Station	RRF	Latitude	Longitude	Height (m)
azu1	NAD83	34.1°N	117.9°W	135
braz	SIRGAS2000	15.9°S	47.9°W	28
conz	SIRGSA95	32.0°S	73.0°W	186
cut0	GDA94	32.0°S	115.9°E	28.5
dlf1	ETRF2000	52.0°N	4.4°E	67

Table 3 Predicted bias approach, mean bias using the (Eq. (16)) for the RBCs generated RBC in PPP and their differences with the transformed clocks

Station	Component	Predicted Bias (mm)	Mean Bias (mm)	Difference (mm)
azu1	North	−1.1	−2.0	−0.8
	East	−1.0	−1.0	−0.1
	Up	+0.2	+1.3	+1.1
	Total	+1.5	+2.6	+1.1
braz	North	−0.0	+0.1	+0.1
	East	−0.0	+0.1	+0.1
	Up	−0.0	+0.0	+0.0
	Total	+0.0	+0.1	+0.1
conz	North	+2.4	+2.3	−0.0
	East	+2.4	+2.4	+0.0
	Up	−0.6	−0.7	−0.1
	Total	+3.4	+3.4	+0.0
cut0	North	+9.1	+9.5	+0.4
	East	+21.4	+22.0	+0.6
	Up	−3.7	−5.0	−1.4
	Total	+23.5	+24.5	+1.0
dlf1	North	+0.6	+0.9	+0.3
	East	+1.3	+1.5	+0.2
	Up	−0.6	−0.0	+0.5
	Total	+1.6	+1.7	+0.2

casters are generated using a combination of GBCs, however the corresponding combined GBC is not available, which makes it impossible to compare results. Therefore RBCs have been generated with the BNC version 2.9 software using the IGS01 GBC as input. Besides generation of the RBCs also a GBC has been created using BNC 2.9, such that GBC and RBCs used in the data processing have the same sampling rate. BNC 2.9 has also been used to compute PPP solutions using the GBC and relevant RBC for each station. Table 3 and Fig. 1 summarize the remaining bias for the transformed clocks RBCs. The table shows for each station the predicted bias, given by the scale absorbed bias from Eq. (16), and the bias from the PPP processing. The figure gives the times series of the bias for station CUT0 in Perth, Australia. In all cases the bias is computed as $x_{r,RBC} - x_{r,GBC}$, where $x_{r,RBC}$ is the position obtained using the

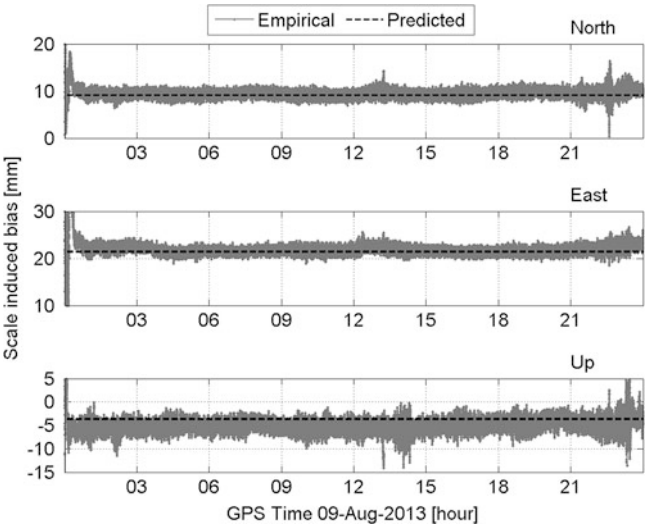

Fig. 1 Remaining scale induced bias using the transformed clocks RBCs at August 9th 2013, for station CUT0, Perth, Australia. *Gray line* gives the empirical bias from PPP processing, the *black dotted line* shows the predicted bias from (16)

RBC and $x_{r,GBC}$ is the position obtained from the GBC and then transformed to the RRF. The mean difference between the empirical bias from processing and the predicted bias is close to or less than 1 mm for all stations. The results show that the scale absorbed bias gives a good prediction for the transformed clock bias. As can be seen from Fig. 1, the transformed clock bias does not vary a lot with the 1 Hz observation rate of this dataset.

6 Conclusions

Using the 14-parameter transformation on the server side to generate RBCs causes scale induced biases in the PPP positions. Three methods have been given to deal with the scale induced bias, the unscaled, the scale-absorbed and the transformed clocks approach. For all three methods there are remaining residual scale induced biases. The bias for the unscaled and scale-absorbed approaches scan be computed / predicted exactly. This contribution has shown that the remaining bias in the transformed clocks approach can be approximated very well with the bias for the scale-absorbed approach. Using currently available RBCs causes scale induced biases of less than 10 mm in the case of ETRF2000, NAD83 and SIRGAS95. For SIRGAS2000 there is no scale induced bias, since in the generation of this RBC there is no increment to the scale factor. For GDA94 the remaining scale induced bias is maximum 30 mm, which is caused by the large scale factor of GDA94 compared to other RRFs.

Acknowledgements The second author is the recipient of an Australian Research Council (ARC) Federation Fellowship (project number FF0883188). Part of this work was done in the framework of the project 'New Carrier-Phase Processing Strategies for Next Generation GNSS Positioning' of the Cooperative Research Centre for Spatial Information (CRC-SI2).

References

BKG (2013a). http://igs.bkg.bund.de/ntrip/orbits

BKG (2013b). ftp://igs.bkg.bund.de/NTRIP/ppp/performance.13-08-09

Caissy M, Agrotis L, Weber G, Hernandez-Pajares M, Hugentobler H (2012) Innovation-coming soon-the international gnss real-time service. GPS World 23(6):52

Hauschild A, Montenbruck O (2009) Kalman-filter-based GPS clock estimation for near real-time positioning. GPS Solutions 13(3):173–182

Huisman L, Teunissen PJG, Hu C (2012) GNSS precise point positioning in regional reference frames using real-time broadcast corrections. J Appl Geod 6(1):15–23

IGS.org (2013) Real-time service. http://rts.igs.org/

Kouba J (2002) The GPS toolbox ITRF transformations. GPS Solutions 5:88–90. doi:10.1007/PL00012903. http://dx.doi.org/10.1007/PL00012903.

Kouba J (2009) A guide to using International GPS Service (IGS) products. Publication of the IGS Central Bureau, Online at http://igscb.jpl.nasa.gov/igscb/resource/pubs/UsingIGSProductsVer21.pdf

Rebischung P, Griffiths J, Ray J, Schmid R, Collilieux X, Garayt B (2012) IGS08: the IGS realization of ITRF2008. GPS Solutions 16(4):483–494. doi:10.1007/s10291-011-0248-2. http://dx.doi.org/10.1007/s10291-011-0248-2

RTCM (2011) RTCM-10410.1 Standard for Networked Transport of RTCM via Internet Protocol (Ntrip), Version 2.0 with Amendment 1, June 28, 2011

Takasu T (2010) Real-time PPP with RTKLIB and IGS real-time satellite orbit and clock. In: IGS Workshop

Teunissen PJG, Huisman L, Hu C (2012) Real-time precise point positioning in NAD83: global and regional broadcast corrections compared. J Surv Eng 139(1):1–10

Weber G (2013) BKG Ntrip Client (BNC) Version 2.9 – Manual. Federal Agency for Cartography and Geodesy (BKG). Frankfurt, Gemany

Weber G, Dettmering D, Gebhard H, Kalafus R (2005) Networked transport of RTCM via internet protocol (Ntrip)-IP-streaming for real-time GNSS applications. In: ION GNSS 18th International Technical Meeting of the Satellite Division, pp 13–16

Determination of Optimal Trajectories for an Inland Water Traffic Manoeuvre Guidance System Based on Sensor-Fused PNT-Data

Iván Herrera-Pinzón and Alexander Born

Abstract

The increasing traffic in vehicular river corridors as well as the growing demands on efficiency and positional accuracy for inland water transportation of goods have made the determination of position, navigation and timing (PNT) data including additional integrity information and the development of a driver assistance system for inland water vessels based on this PNT-data one of the most important challenges facing modern inland water transportation and a major practical problem for both navigators and geodesists. As the basis of a driver assistance system, this work describes the architecture of a system including the tightly-coupled sensor fusion of GNSS and IMU data for the determination of reliable PNT-data in real-time with inland water traffic purposes. Moreover, a simple mathematical model of vessel manoeuvring is presented. Optimisation approaches based on Interior Point Optimisation and Sequential Quadratic Programming are applied to search for the vessel trajectory considering several traffic conditions. Finally, first numerical results are presented and discussed.

Keywords

Manoeuvre guidance • PNT-data • Sensor fusion • Trajectory optimisation

1 Introduction

The goal of the Federal Ministry of Economics and Technology (BMWi) funded project PiloNav is the development of a generic location platform which can be used on different transport carrier to determine highly accurate PNT-data plus integrity information with the focus on rail and inland-water traffic. Therefore, carrier-specific sensors (IMU, radar, optical sensors, etc.) will be merged with position, navigation and timing information obtained by GNSS and therefore form an Integrated Navigation System (INS). In case of inland-water traffic this is referred to as a Positioning, Navigation and Timing-Unit (PNT-Unit) and in case of rail traffic as a Train Location Unit (TLU) respectively (Albrecht et al. 2013; Dai et al. 2011; Zachhuber et al. 2013). Figure 1 shows the PiloNav system on the example of the PNT-Unit (dashed box left).

On the application layer this PNT-data will be used as input for driver assistance and manoeuvre guidance systems which continuously provides reliable information and assists the driver with critical manoeuvres in order to optimise rail and inland-water traffic (dashed box right in Fig. 1) and to meet the requirements in terms of efficiency and environmental challenges (Albrecht et al. 2013; Vierhaus et al. 2012). This work, however, focuses on the inland water aspect and on the trajectory optimisation as part of the manoeuvre guidance system in particular.

The paper is structured as follows. Chapter 2 briefly reviews the state of the art for trajectory optimisation in inland water traffic. Chapter 3 shortly describes the components of the PNT-Unit as basis for the determination of

I. Herrera-Pinzón (✉) • A. Born
Department of Nautical Systems, Institute of Communications and Navigation, German Aerospace Center (DLR), 17235 Neustrelitz, Germany
e-mail: Ivan.HerreraPinzon@dlr.de; Alexander.Born@dlr.de

© Springer International Publishing Switzerland 2015

C. Rizos, P. Willis (eds.), *IAG 150 Years*, International Association of Geodesy Symposia 143,
DOI 10.1007/1345_2015_213

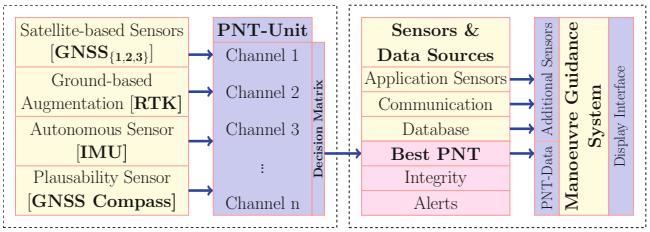

Fig. 1 Architecture of the PiloNav-System including the PNT-Unit (*left dashed box*) and the driver assistance system (*right dashed box*)

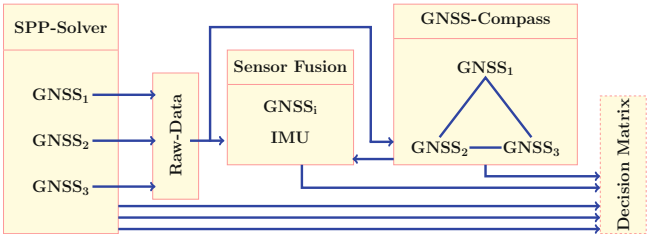

Fig. 2 Overview of PNT-Unit's Core

reliable and PNT-data and integrity information. The manoeuvre guidance is explained in more detail in Chap. 4. Before the paper concludes in Chap. 6, Chap. 5 presents results based on real data collected on measurement campaigns and numerical simulations.

2 Related Work

The topic of a real-time trajectory optimisation implementation has been extensively discussed by Miele and Wang (2005, 2006), Miele et al. (1999) and Tzeng (1998) with the provision of the so-called Multiple-Subarc Gradient Restoration Algorithm via the usage of realistic vessel's kinematic models (Miele and Wang 2003; Miele et al. 1974) plus complex – though effective – cost functional, demonstrating its suitability for maritime applications in open waters by virtue of its high performance and accuracy, lacking however of the use of autonomous sensors for the enhancement of the calculation of the vessel's position. With his work on the direct solution of optimal control problems via the sequential quadratic programming approach in Fabien (1998, 2008a,b, 2013a,b), Fabien has developed a robust set of efficient programming tools able to handle the trajectory optimisation problem allowing the definition of several functional and kinematic models dependent of user-defined variables, with an interesting susceptibility for the real-time applications. In his PhD work (Lutz 2011), A. Lutz goes further and proposes a collision detection system for inland waters with the use of modern technologies, such as GNSS and the Automatic Identification System (AIS), incorporating the use of hydrodynamic models to increase to adequacy of his models but missing the usage of autonomous and plausibility sensors, thus failing to address troubling scenarios and complex manoeuvres.

3 PNT-Data Generation

The core of the PNT-Unit is depicted in Fig. 2. Due to the favourable availability GNSS is used as primary sensor. To determine the attitude of the vessel, a system of three GNSS receivers is used (Dai et al. 2012). Before using the data, several tests are carried out to only use observations, which can be trusted on a very high level.

To achieve this, the three single point positioning processors (SPP-Solver in Fig. 2) are outfitted with a code based snapshot RAIM (Receiver Autonomous Integrity Monitoring), applying weights to the observations of each satellite. Consecutive measurements are checked if an unreasonably large step occurred (e.g. if the resulting velocity exceeds the maximum velocity/acceleration of the vessel) and also excluded according to the satellite health-status message. For safety-critical applications, such as the PiloNav driver assistance system, a 3D accuracy of 10 cm has to be guaranteed. Therefore the PNT-Unit uses real-time kinematics (RTK) as differential technique. To guarantee the accuracy, to increase the reliability of the PNT-data and to bridge short GNSS outages, caused by e.g. obstacles etc., an Inertial Measurement Unit (IMU) is used as autonomous, self-contained sensor.

The GNSS and IMU observations are fused in a tightly coupled approach, meaning the pseudo-range and Doppler observations derived by the initially defined primary GNSS sensor are used in an Extended Kalman Filter (EKF). The EKF is based on 17 states (positions: X, Y, Z; velocities: v_x, v_y, v_z; accelerations a_x, a_y, a_z; attitude parameters: roll, pitch, yaw with their according turning rates; receiver clock bias and receiver clock drift) and uses information from the attitude providing sensors aside the GNSS observations. This means, the classical measurement vector (containing pseudo-range and Doppler observations) is extended by introducing roll, pitch and yaw from a GNSS compass additionally. If the ship has a gyro-compass installed, the yaw angle derived from this is added as well. To increase the availability of the data the sensor-fusion is performed redundantly, i.e. parallel for each GNSS-sensor for the case the selected receiver is not providing data (Groves 2007).

Each traffic route can be segmented in areas with different requirements on quality parameters (accuracy, integrity, continuity and availability), represented by navigation modes. For example in some areas the accuracy itself is of interest, in other the reliability of the provided position or navigation data. Therefore, all possible combinations of the available sensors will be performed and the results, including the

corresponding individual quality information, collected in a so-called Decision Matrix (right box in Fig. 2). The best PNT-data, for the particular navigation mode, will be selected and forwarded to the application/driver assistance system. If the system cannot fulfil the requirements or provide integrity, the skipper will be informed to not rely on the provided information.

4 PNT-Based Manoeuvre Guidance

The availability of highly accurate PNT-data granted within the frame of the PiloNav project provides the unique opportunity to explore the determination of reliable trajectories for inland water vessels in near real-time, offering a wide range of maritime applications ranging from the precise docking manoeuvres to the efficient passing through lock chambers, with the aim to increase the safety in the navigation and to improve the efficiency in transportation.

The presence of static elements – locks, bridges and quay walls – as well as dynamic objects – e.g. incoming traffic – in river corridors poses an additional challenge for navigation and highlights the necessity to have efficient algorithms able to supply optimal trajectories while contributing with short-term risk collision detection. This task is accomplished by the Manoeuvre Guidance System using the so-called Optimal Control Theory.

4.1 Optimisation Model

For analysis purposes, the vessel is considering to move only in the $\mathbf{N}-\mathbf{E}$ plane with the orientation defined by the Course over the Ground (**CoG**) – relative to the **E** axis. Vessel's speed is defined by its velocity **v** in the direction of the **CoG**, with the acceleration **a** pointing also towards this direction. Vessel's angular velocity is regarded as the so-called **Rate of Turn** (**r**), $\dot{\mathbf{CoG}} = \mathbf{r}$. The tuple $\mathbf{y} = [\mathbf{N}, \mathbf{E}, \mathbf{v(t)}, \mathbf{CoG(t)}]'$ is know as the state variables, while the tuple $\mathbf{u} = [\mathbf{a(t)}, \mathbf{r(t)}]'$ is called control variables. Hence, the optimal control problem can be written as:

Cost Functional

$$\min_{\mathbf{t_f},\mathbf{a(t)},\mathbf{r(t)}} \left[\mathbf{c_1}\cdot\mathbf{t_f} + \int_{\mathbf{t_0}}^{\mathbf{t_f}} \left(\mathbf{c_2}\cdot\mathbf{a^2(t)} + \mathbf{c_3}\cdot\mathbf{r^2(t)}\right) \mathbf{dt} \right]$$

Subject to

$$\begin{aligned} \mathbf{y_0} &= [\mathbf{E_0}, \mathbf{N_0}, \mathbf{v(t_0)}, \mathbf{CoG(t_0)}]' \\ \mathbf{y_f} &= [\mathbf{E_f}, \mathbf{N_f}, \mathbf{v(t_f)}, \mathbf{CoG(t_f)}]' \\ \dot{\mathbf{y}} &= [\mathbf{v(t)}\cos(\mathbf{CoG(t)}), \mathbf{v(t)}\sin(\mathbf{CoG(t)}), \mathbf{a(t)}, \mathbf{r(t)}]' \end{aligned}$$

$$\mathbf{d(x, Obstacles)} \geq \varepsilon.$$

With $\mathbf{t_f}$ the final time of the manoeuvre, $\mathbf{y_0}$ the initial values of the state variables – origin, $\mathbf{y_f}$ the final values of the state variables – destination, $\dot{\mathbf{y}}$ the dynamic equations relating the state and the control variables by using the kinematics of a simple vessel in the 2D plane, and **d** the constraints of the trajectory wrt. the surrounding obstacles taking one of the following forms:

– For static obstacles:

$$\sqrt{(\mathbf{E}-\mathbf{E_{obst_i}})^2 + (\mathbf{N}-\mathbf{N_{obst_i}})^2} \geq \varepsilon_i$$

– For moving obstacles:

$$\sqrt{\begin{aligned}&(\mathbf{E}-(\mathbf{E_{obst_i}}-\mathbf{v_{obst_i}}\cos(\mathbf{CoG_{obst_i}})\mathbf{t}))^2 + \\ &(\mathbf{N}-(\mathbf{N_{obst_i}}-\mathbf{v_{obst_i}}\sin(\mathbf{CoG_{obst_i}})\mathbf{t}))^2\end{aligned}} \geq \varepsilon_i$$

With ε_i the safe margin to the obstacle i. Both state and control variables are bounded by the inequality constraints, determined for the PiloNav demonstration vessel in previous measurement campaigns as the average of the observed values for each variable, and defined as:

$$\begin{aligned} 0\ [\mathrm{m/s}] \leq \mathbf{v} \leq 5.5\ [\mathrm{m/s}], \\ -0.1\ [\mathrm{m/s^2}] \leq \mathbf{a} \leq 0.05\ [\mathrm{m/s^2}], \\ -120^\circ/\mathrm{min} \leq \mathbf{r} \leq 120^\circ/\mathrm{min}. \end{aligned}$$

The aforementioned model attempts to minimise time and effort by controlling sudden changes in velocity and **CoG** through the minimisation of **a** and **r**. More complex models including not only the 2D-kinematic of a vessel, but also its height component – for the clearance under bridges – as well as environmental factors – such as currents and winds – shall be considered to improve the reliability of the results.

The proposed problem is then solved within DLR's RTFramework (Gewies et al. 2012) using the optimal control problem solver OCP v1.0, available in Fabien (2013b), which transforms the system into a nonlinear programming problem by parameterizing the control variables and approximating the cost functional, to then use the sequential quadratic programming technique to solve the associated nonlinear programming problems (Fabien 2008a,b, 2013a).

5 Results

5.1 Numerical Simulations

To assess the robustness of the proposed optimisation model against PNT-data, a series of numerical experiments are

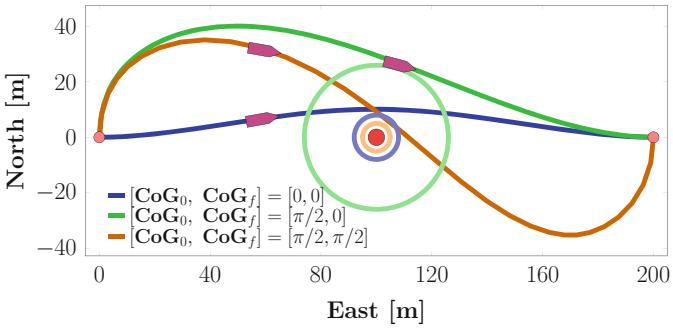

Fig. 3 Avoiding a static obstacle

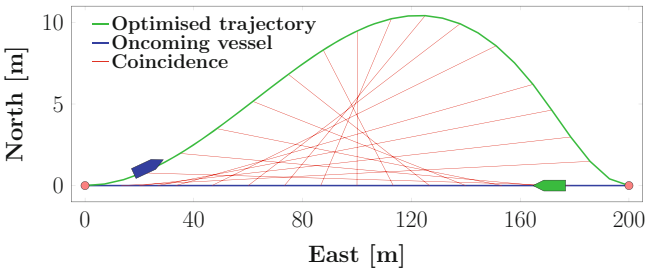

Fig. 4 Avoiding an oncoming vessel

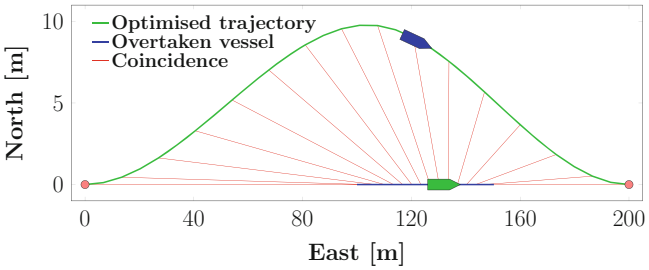

Fig. 5 Overtaking a slower vessel

conducted with the purpose of finding out a set of suitable constants for the cost functional adapting to the nature and needs of the described scenario.

In this regard, two main types of manoeuvres are addressed during this stage of the project, which, according to previous measurement campaigns, are the most frequent manoeuvres carried out when sailing inland river corridors. In the first place, the avoidance of a static obstacle located in the midpoint of the trajectory between two fiducial points has to be accomplished (Fig. 3). Therefore, it is required to find the optimal trajectory that will move the vessel from $\mathbf{y_0} = [0\ \text{m}, 0\ \text{m}, 2.5\ \text{m/s}, \mathbf{CoG}_0]'$ to $\mathbf{y_f} = [200\ \text{m}, 0\ \text{m}, 2.5\ \text{m/s}, \mathbf{CoG}_f]'$ minimising time, acceleration and rudder movements. Three different combinations of $[\mathbf{CoG}_0, \mathbf{CoG}_f]$, namely $[0, 0]$, $[\pi/2, 0]$ and $[\pi/2, \pi/2]$, and labelled as $\mathbf{CoG_a}$, $\mathbf{CoG_b}$ and $\mathbf{CoG_c}$, respectively, are tested.

Within this scenario different buffers around the obstacle has been defined as safely margins (5, 7, and 20 m). To meet this requirement the path constraint $\sqrt{(x-100)^2 + (y-0)^2} \geq \varepsilon_i$ is considered within the model.

Two scenarios involving dynamic obstacles (vessels) will be encompassed in the second place. On the one hand, an avoiding manoeuvre involving an oncoming vessel with constant velocity (4 m/s) and course over the ground ($\mathbf{CoG} = \pi$) will be taken into account (Fig. 4). The safety region for the avoiding vessel is defined by a buffer of 10 m. Therefore, it is sought the optimal trajectory that will take the vessel state from $[0\ \text{m}, 0\ \text{m}, 4\ \text{m/s}, 0]'$ to $[200\ \text{m}, 0\ \text{m}, 4\ \text{m/s}, 0]'$. A path constraint of the form $\sqrt{(x-(100-4\cdot t))^2 + (y-0)^2} \geq 7$ m is then included in the model.

On the other hand, an overtaking manoeuvre involving a slower vessel with constant velocity (2 m/s) and course over the ground ($\mathbf{CoG} = 0$) is considered (Fig. 5). The safety region for the avoiding vessel is defined by a buffer of 10 m. Hence, it is required to find the optimal trajectory that will take the vessel state from $[0\ \text{m}, 0\ \text{m}, 4\ \text{m/s}, 0]'$ to $[200\ \text{m}, 0\ \text{m}, 4\ \text{m/s}, 0]'$. A path constraint of the form $\sqrt{(x-(100+2\cdot t))^2 + (y-0)^2} \geq 7$ m is then included in the model.

In all the aforementioned scenarios the trajectories determined are feasible in terms of manoeuvring and accomplish the optimisation task showing a smooth transition between the initial and final points which guaranties their applicability to real cases.

5.2 Optimised Trajectories with Real PNT-Data

To evaluate the convenience and the numerical efficiency facing real-time data, the model discussed previously is tested in the demonstration area located on the river Moselle close to the lock of Koblenz, Germany, with an extension of about 3 km from the entrance of the river Moselle into the river Rhine until the head water of the lock Koblenz in the western direction.

Taking the skipper's experience into account, the most frequently followed trajectory – calculated as the average trajectory of those done by all the vessels sailing the channel over a period of 1 week – is set as the source of the final conditions for the optimised trajectories (green line in Fig. 6). This ideal trajectory, in the form of equidistant way points, is therefore used to establish the final coordinates and final

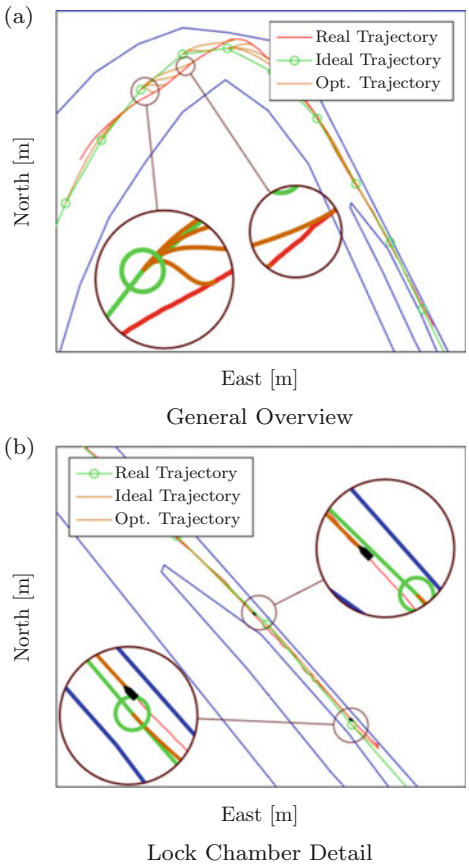

Fig. 6 Optimised trajectories for Koblenz Data. (**a**) General overview, (**b**) lock chamber detail

CoGs – regarded as the direction between two consecutive way points – at each stage of the navigation within the river corridor.

Under these assumptions the following scenario is proposed: it is required to find the optimal trajectory that will move the vessel state from $[\mathbf{E_k}, \mathbf{N_k}, \mathbf{v_k}, \mathbf{CoG_k}]'$ to $[\mathbf{E_w}, \mathbf{N_w}, \mathbf{v_k}, \mathbf{CoG_w}]'$, minimising time, acceleration and rudder movements. Here the subscripts k and w stand for Koblenz Data and the closest way point. In this case, it is assumed that the final velocity will be equal to the initial one.

Figure 6 shows a sample of the solutions for the proposed scenario. The actual trajectory of the vessel (red line) provides the initial conditions for the definition of the optimisation problem while, as it has been said, the ideal line (green line) supplies its final conditions. Orange lines represent the multi-stage optimised trajectories for points on the actual trajectory composed by a set of states which, if followed by the skipper, would take the vessel from its origin point (red line) to its destination (closest green point) together with the (minimum) time to accomplish the manoeuvre.

Table 1 Parameters of the solutions (average)

	Section of the channel		
	Open sky	Bridges	Lock
Solution time (s)	2.86	3.85	2.50
No. of iterations	56	106	92

The calculated trajectories follow the desired path while minimising effort and time for the navigation, but also the performance of their solution is applicable for near-real-time applications due to the low latency of its solution: 2–4 s per point, relatively high for real-time applications such as the PiloNav manoeuvre guidance system. Table 1 shows the average time and number of iteration needed for the calculation of the solutions based on a sample of 1,000 non-continuous points distributed along the channel. Although these indicators are grouped according their localisation within the channel, it is worth to mention that this distinction has no real significance on the calculation of the trajectories, which rely more in the relative geometry of the starting and ending points, but is more an inheritance of the determination of the position within the PNT-Unit related to the alerts generated for the integrity module.

Figure 7, displays the additional products obtained while calculating the optimal trajectories between two points. The remaining state variables, course over the ground and velocity, as well as the control variables, acceleration and rate of turn, are shown as a function of the time. While is obvious that for presentation purposes the exhibition of coordinates, velocity and **CoG** plays an important role, it is also clear that the data which will contribute the most to the precise manoeuvring are the control variables, both the acceleration and the **RoT**.

The adequacy of the model, for both functional and dynamics, can be seen in the fact that the state and control variables exhibit a smooth transition while meeting the limits and accomplishing the time optimisation (Fig. 7). Furthermore, the quality of the trajectories can be evaluated numerically by using the so-called Karush-Kuhn-Tucker (KKT) conditions implemented by the OCP v1.0 tool (Fabien 2008b). The KKT conditions give information on how the cost functional and the constraints of the optimisation problem behave at the solution point, becoming an useful mean to establish whether the just calculated trajectory constitutes a numerically stable solution and can be delivered as the sought optimal trajectory or must be rejected. A sample of this indicator for an arbitrary set of points within the channel can be seen in Table 2.

The appropriate analysis and combination of these conditions with the RAIM alerts given by the PNT-Unit, are the basis for the acceptance or rejection of the trajectories

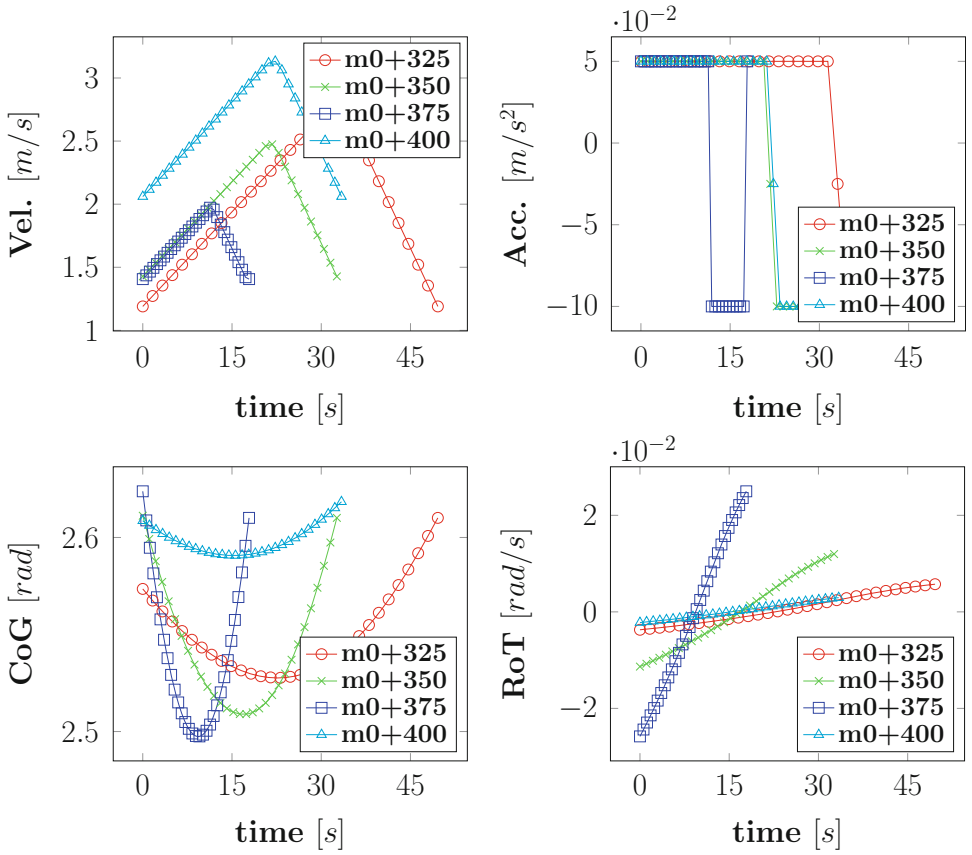

Fig. 7 Products of the trajectory determination

Table 2 Quality estimators

Selected point	Norm of the KKT conditions
m0 + 01	3.270×10^{-6}
m0 + 30	4.029×10^{-7}
m0 + 50	2.016×10^{-6}
m0 + 79	0.00030

and will become a key criteria for skippers when deciding whether to follow or not the suggested optimised path.

6 Discussion and Future Work

This work proposes the real-time calculation of optimal trajectories for inland-water vessels based on reliable and highly accurate PNT-data. The manoeuvre guidance system relies on the fusion of the autonomous sensor (IMU) and the GNSS data, while other carrier-specific sensors (such as radar and optical sensors) are used for providing traffic situation and performing plausibility checks. Sensor-fused PNT-data is then used as the source for the estimation of suitable trajectories for the efficient navigation through the use of the so-called optimal control theory. Adapting the aforementioned OCP v1.0 tool within DLR's RTFramework, in addition to the high quality data provided for DLR's PNT-Unit, have shown promising results concerning the improvement in the performance of the calculated paths, in both simulated and real scenarios, demonstrating the great potential of PNT-data and leading into complementary investigations for maritime purposes. Thus, in further stages of the project, factors such as the 3D optimisation of trajectories – required for the safe passing of bridges, environmental factors – such as river currents and winds – and the short-term collision detection in critical locations, such as bridges and locks, as well as in areas with high traffic confluence will be also considered and implemented.

Acknowledgements This work has been supported under grant number 19G10015A (keyword: PiloNav) by the Federal Ministry of Economics and Technology (BMWi) on the basis of a decision by the German Bundestag.

References

Albrecht T, Lüddecke K, Zimmermann J (2013) A precise and reliable train positioning system and its use for automation of train operation. In: IEEE International Conference on Intelligent Rail Transportation, Beijing

Dai Z, Ziebold R, Engler E (2011) The on-board maritime PNT Module: a focus on integrity monitoring and preliminary results. In: European Navigation Conference GNSS.

Dai Z, Ziebold R, Born A, Engler E (2012) Heading-determination using the sensor-fusion based maritime PNT Unit. In: IEEE/ION PLANS

Gewies S, Becker C, Noack T (2012) Deterministic framework for parallel real-time processing in GNSS applications. In: 6th ESA Workshop on Satellite Navigation Technologies, pp 1–7. IEEE Xplore, Piscataway

Groves PD (2007) GNSS technology and applications series. In: Principles of GNSS, inertial and multi-sensor integrated navigation systems. Artech House, Boston

Fabien BC (1998) Some tools for the direct solution of optimal control problems. Adv Eng Softw 29(1):45–61 [Elsevier Science Ltd.]

Fabien BC (2008a) Implementation of a robust SQP algorithm. Optim Methods Softw 23:827–846

Fabien BC (2008b) Direct optimization of dynamic systems described by differential-algebraic equations. Optimal Control Appl Methods 29:445–466

Fabien BC (2013a) Piecewise polynomial control parameterization in the direct solution of optimal control problems. ASME J Dyn Syst Meas Control 135(3):034506

Fabien BC (2013b) OCP: an optimal control problem solver. OCP v1.0 documentation. http://abs-5.me.washington.edu/ocp/. Accessed April 2013

Lutz A (2011) Kollisionserkennung und -vermeidung auf Binnenwasserstraßen. Universität Stuttgart

Miele A, Wang T (2003) Multiple-subarc gradient-restoration algorithm, part 1: algorithm structure. J Optim Theory Appl 116(1):1–17 [Plenum]

Miele A, Wang T (2005) Maximin approach to the ship collision avoidance problem via multiple-subarc sequential gradient-restoration algorithm. J Optim Theory Appl 124(1):23–53

Miele A, Wang T (2006) Optimal trajectories and guidance schemes for ship collision avoidance. J Optim Theory Appl 129(1):1–21

Miele A, Damoulakis JN, Cloutier JR, Tietze JL (1974) Sequential gradient-restoration algorithm for optimal control problems with nondifferential constraints. J Optim Theory Appl 13(2):218–255

Miele A, Wang T, Chao CS, Dabney JB (1999) Optimal control of a ship for course change and sidestep maneuvers. J Optim Theory Appl 103(2):259–282

Tzeng CY (1998) Collision avoidance by a ship with a moving obstacle: computation of feasible command strategies. J Optim Theory Appl 97(2):281–297

Vierhaus I, Born A, Minkwitz D (2012) Challenges on PNT-Unit and driver assistance systems in inland water. In: 14th IAIN World Congress 2012 Seamless Navigation

Zachhuber P, Herrera-Pinzón I, Born A, Hoppe M, Burmisova L, Heßelbarth A, Zimmermann J, Heidrich A, Richter R, Richter F, Michler O (2013) PNT-data generation as basis for guidance systems in inland water traffic. In: IEEE/Inertial Sensors and Systems - Symposium Gyro Technology

Application-Driven Critical Values for GNSS Ambiguity Acceptance Testing

Sandra Verhagen, Peter J.G. Teunissen, and Jingyu Zhang

Abstract

Integer ambiguity estimation and validation are crucial steps when solving the carrier-phase based GNSS model. For the validation, different ambiguity acceptance tests have been proposed. For those tests often fixed critical values are used, with the important disadvantage that the performance of the tests varies a lot depending on measurement set-up and circumstances. Therefore it is better to use model-driven critical values such that it is guaranteed that the failure rate will not exceed a user-defined threshold.

This contribution will study the model-dependency of the critical values for two well-known acceptance tests, the ratio test and difference test, and then specifically for a given application. This means that mainly the satellite-receiver geometry and number of epochs will be variable. It will be shown that critical values do exhibit a strong dependence on these factors, and it will not be possible to simply use a fixed (i.e., constant) application-driven critical value.

Keywords

Critical value • Integer acceptance test • Model-dependency

1 Introduction

Requirements on both precision and reliability depend on the GNSS application at hand, and drive the choice for receiver and measurement set-up. For (near) real-time applications, very precise positioning is only possible with carrier-phase based GNSS, and consequently relies on the carrier-phase integer ambiguities to be correctly estimated. Therefore both integer ambiguity estimation and validation are crucial steps.

S. Verhagen (✉) • J. Zhang
Department of Geoscience and Remote Sensing, Delft University of Technology, Delft, The Netherlands
e-mail: a.a.verhagen@tudelft.nl

P.J.G. Teunissen
GNSS Research Centre, Curtin University, Bentley, WA, Australia

Department of Geoscience and Remote Sensing, Delft University of Technology, Delft, The Netherlands
e-mail: p.teunissen@curtin.edu.au

For the validation, different ambiguity acceptance tests have been proposed. For those tests often fixed critical values are used, with the important disadvantage that the performance of the tests in terms of the failure rate and false alarm rate varies a lot depending on measurement set-up and circumstances. Therefore it is better to use model-driven critical values such that it is guaranteed that the failure rate will not exceed a user-defined threshold.

In Verhagen and Teunissen (2013) the model-dependency of the critical value of the popular ratio test was analysed and it was shown how the model-driven values can be determined. The results confirmed that in general it is not advisable to use a fixed critical value for all possible scenarios and/or measurement set-ups.

This contribution aims at analyzing application-driven critical values with the fixed failure rate approach, and to study the dependency on specifically the satellite-receiver geometry and number of observation epochs. The paper starts with a brief description of the procedure to solve the carrier-phase GNSS model, followed by a section on integer

© Springer International Publishing Switzerland 2015

C. Rizos, P. Willis (eds.), *IAG 150 Years*, International Association of Geodesy Symposia 143,
DOI 10.1007/1345_2015_36

acceptance testing. Here, the focus will be on two well-known tests, namely the ratio test and difference test. One specific measurement set-up will be used as an example in Sect. 4 to study the model-dependency of the critical values for both tests.

2 Solving the GNSS Model

The mixed integer GNSS linear(ized) model is defined as

$$\mathsf{E}(\boldsymbol{y}) = \boldsymbol{A}\boldsymbol{a} + \boldsymbol{B}\boldsymbol{b},\ \mathsf{D}(\boldsymbol{y}) = \boldsymbol{Q}_{yy} \tag{1}$$

where E and D denote the expectation and dispersion operators. $\boldsymbol{a} \in \mathbb{Z}^n$ is the integer carrier-phase ambiguity vector and $\boldsymbol{b} \in \mathbb{R}^p$ is the parameter vector with remaining unknown parameters, such as baseline parameters, residual zenith troposphere delays (ZTD) and ionosphere delays. The design matrices are $\boldsymbol{A} \in \mathbb{R}^{m\times n}$ and $\boldsymbol{B} \in \mathbb{R}^{m\times p}$ with $[\boldsymbol{A}\ \boldsymbol{B}]$ of full column rank. The observation vector $\boldsymbol{y} \in \mathbb{R}^m$ contains the double-difference (DD) code and phase observations and is assumed to be contaminated by normally distributed random errors with zero means and variance-covariance matrix $\boldsymbol{Q}_{yy}$. In general, a four-step procedure is employed to solve model (1).

Step 1: Float Solution The integer property of the ambiguities $\boldsymbol{a} \in \mathbb{Z}^n$ is disregarded and the so-called float solution,

$$\begin{bmatrix}\hat{\boldsymbol{a}}\\ \hat{\boldsymbol{b}}\end{bmatrix} \sim \mathrm{N}\left(\begin{bmatrix}\boldsymbol{a}\\ \boldsymbol{b}\end{bmatrix}, \begin{bmatrix}\boldsymbol{Q}_{\hat{a}\hat{a}} & \boldsymbol{Q}_{\hat{a}\hat{b}}\\ \boldsymbol{Q}_{\hat{b}\hat{a}} & \boldsymbol{Q}_{\hat{b}\hat{b}}\end{bmatrix}\right) \tag{2}$$

is computed with (recursive) weighted least-squares or Kalman filtering. Ideally, this step includes testing for outliers, cycle slips, or other modeling errors.

Step 2: Integer Estimation The float ambiguity estimate $\hat{\boldsymbol{a}}$ is used to compute its integer counterpart, denoted as

$$\check{\boldsymbol{a}} = \mathcal{I}(\hat{\boldsymbol{a}}) \quad \text{with} \mathcal{I} : \mathbb{R}^{\mathrm{n}} \mapsto \mathbb{Z}^{\mathrm{n}} \tag{3}$$

There are different choices of mapping function $\mathcal{I}$ possible, which correspond to different integer estimation methods. Integer rounding, integer bootstrapping and integer least-squares (ILS) are examples of such integer estimators. Of all choices, ILS is proven to be optimal as it achieves the lowest probability of incorrect fixing, referred to as failure rate (Teunissen 1999). ILS is efficiently mechanized in the LAMBDA method (Teunissen 1995; Verhagen and Li 2012).

Step 3: Integer Acceptance Test An integer acceptance test is devised to decide whether or not the integer solution from step 2 is sufficiently more likely than any other integer candidate. Several tests have been proposed in the literature and are currently used in practice. Examples are the ratio test, the difference test and the projector test. Ambiguity acceptance tests are discussed in Sect. 3. If the integer solution is accepted, it is possible to re-evaluate the validation of the GNSS model, since knowing the ambiguities strengthens the model.

Step 4: Fixed Solution The float solution of the baseline parameters is updated using the fixed integer parameters,

$$\check{\boldsymbol{b}} = \hat{\boldsymbol{b}} - \boldsymbol{Q}_{\hat{b}\hat{a}}\boldsymbol{Q}_{\hat{a}\hat{a}}^{-1}(\hat{\boldsymbol{a}} - \check{\boldsymbol{a}}),\ \ \boldsymbol{Q}_{\check{b}\check{b}} = \boldsymbol{Q}_{\hat{b}\hat{b}} - \boldsymbol{Q}_{\hat{b}\hat{a}}\boldsymbol{Q}_{\hat{a}\hat{a}}^{-1}\boldsymbol{Q}_{\hat{a}\hat{b}} \tag{4}$$

It is pointed out that the VC-matrix $\boldsymbol{Q}_{\check{b}\check{b}}$ is derived based on the error propagation law under the assumption that the integer solution $\check{\boldsymbol{a}}$ is deterministic. This holds true only when the probability of correct integer estimation is sufficiently close to 1. In that case, $\boldsymbol{Q}_{\check{b}\check{b}} \ll \boldsymbol{Q}_{\hat{b}\hat{b}}$, since after successful ambiguity fixing the carrier-phase measurements start to act as very precise pseudorange measurements. However, if the success rate is not sufficiently high, the fixed solution $\check{\boldsymbol{b}}$ is not necessarily better than the float solution $\hat{\boldsymbol{b}}$ (Verhagen et al. 2013).

3 Integer Acceptance Tests

Ambiguity acceptance testing concerns the third step in the procedure described in Sect. 2. It is common practice to use the ILS failure rate and/or a discrimination test to decide on acceptance or rejection of the integer ambiguity solution. Obviously, the ILS failure rate should be sufficiently close to 0, since incorrect fixing may lead to unacceptably large positioning errors. Apart from the ILS failure rate, a discrimination test allows to test whether or not the found integer solution is sufficiently more likely than any other integer candidate. Several tests have been proposed in literature (Abidin 1993; Chen 1997; Euler and Schaffrin 1991; Frei and Beutler 1990; Han 1997; Han and Rizos 1996; Landau and Euler 1992; Tiberius and De Jonge 1995; Wang et al. 1998; Wu et al. 2010). All these tests compare in one way or another the ILS solution $\check{\boldsymbol{a}}$ with a so-called 'second best' integer solution $\check{\boldsymbol{a}}_2$. Based on this comparison, the outcome of the discrimination tests is either to accept the integer solution $\check{\boldsymbol{a}}$, or to reject it in favor of the float solution $\hat{\boldsymbol{a}}$.

For all these tests the choice of the corresponding acceptance criterion is one of the challenges to which the recently developed integer aperture estimation theory provides an answer (Teunissen 2003). This theory namely allows to choose the critical value for the tests in such a way that the user gains control over the probability of incorrect fixing, the failure rate. This is referred to as the fixed failure

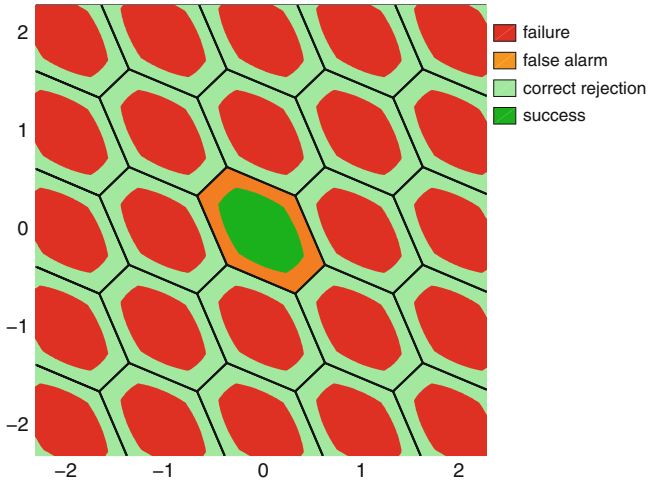

Fig. 1 Two-dimensional ILS pull-in regions (*black*) with acceptance regions. If the float solution resides in a *red* acceptance region, it will be incorrectly fixed (failure), if it resides in the (*dark green*) region it will be correctly fixed (success), otherwise it will be rejected (either a detection or false alarm)

rate approach. It should be stressed, that this is the failure rate *after* the acceptance test, which will be smaller than the ILS failure rate (the failure rate with unconditional acceptance).

The principle is illustrated in Fig. 1 for a two-dimensional example. The ILS pull-in regions are shown; these are regions centered at the integer grid points such that if the float solution resides in a specific pull-in region, the corresponding integer grid point is the ILS solution. The acceptance regions are contained by the ILS pull-in regions, and the size is determined by the critical value of the discrimination test. According to the fixed failure rate approach, the size is thus determined by choosing the maximum failure rate that one finds acceptable. From the figure it will be clear, that a smaller choice for the fixed failure rate will result in a smaller acceptance region.

One question still to be answered then is which discrimination (or acceptance) test to use. This choice will determine the 'shape' of the acceptance region. Interestingly, the integer aperture estimation theory now allows for defining an optimal test (Teunissen 2005). As can be seen from Fig. 1 the size of the acceptance region namely not only affects the failure rate, but the probability of correct fixing as well. The idea is then to define the test such that the probability of correct fixing is maximized for a given failure rate. Disadvantage of the optimal test remains the computational complexity and efficiency. In Verhagen (2005) and Verhagen and Teunissen (2006) the performance of the optimal test was compared with other acceptance tests, from which followed that especially the well-known ratio test and difference test (as defined below) generally exhibit close-to-optimal performance. Therefore these tests will be subject to further analysis in this contribution.

Let the squared norm of ambiguity residuals with respect to integer candidate i be given as

$$R_i = \|\hat{\boldsymbol{a}} - \check{\boldsymbol{a}}_i\|^2_{\boldsymbol{Q}_{\hat{a}\hat{a}}} = (\hat{\boldsymbol{a}} - \check{\boldsymbol{a}}_i)^T \boldsymbol{Q}^{-1}_{\hat{a}\hat{a}} (\hat{\boldsymbol{a}} - \check{\boldsymbol{a}}_i) \tag{5}$$

with

$$\check{\boldsymbol{a}}_i = \arg\min_{z \in \mathbb{Z}^n} \{\|\hat{\boldsymbol{a}} - z\|^2_{\boldsymbol{Q}_{\hat{a}\hat{a}}} \geq R_{i-1}, R_0 = 0\} \tag{6}$$

The ratio test (RT) is then defined as:

$$\text{Accept } \check{\boldsymbol{a}} \text{ iff: } \quad \frac{R_1}{R_2} \leq \mu_{\text{RT}}, \quad 0 \leq \mu_{\text{RT}} \leq 1 \tag{7}$$

The difference test (DT) is defined as:

$$\text{Accept } \check{\boldsymbol{a}} \text{ iff: } \quad R_2 - R_1 \geq \mu_{\text{DT}}, \quad \mu_{\text{DT}} \geq 0 \tag{8}$$

The critical values are denoted μ_{RT} and μ_{DT}.

In Verhagen and Teunissen (2013) the model-dependency of the ratio test was analyzed by considering many different scenarios. Furthermore, it was shown that using fixed critical values - as is common practice - will often lead to unnecessarily high false alarm rates (critical value is too conservative), implying longer times-to-fix, or conversely to high failure rates, which may lead to unacceptably large positioning errors.

4 Application-Driven Critical Values: Example

4.1 Scenario

In order to investigate whether application-dependent critical values for the ratio test and difference test can be determined, one specific scenario is selected here as an example. Table 1 presents an overview of the model parameters for this specific scenario. A medium-length single baseline scenario is considered, implying that the ZTD is estimated, and between-receiver single-difference ionosphere constraints are applied with a standard deviation of 1cm in zenith (see Fig. 2), cf. Odijk et al. (2012).

Table 1 Model parameters

System	All combinations of GPS, Galileo, BeiDou
# frequencies	2
Locations	Netherlands and Australia
Noise	See Fig. 2
# epochs	1, 2, 3, or 4
Atmosphere	Ionosphere-weighted model ZTD estimated
Fixed failure rate	0.1%

All results are based on simulations assuming the availability of the GPS, Galileo and BeiDou systems at full operational capability. All combinations of the three systems are considered as well, where double-differencing is employed per system (i.e., one reference satellite per system). For GPS the constellation as of July 2013 is used.

Two different geographic locations are considered, one in Europe at 50°N, and one in Australia at 18°S. The latter was chosen because of the excellent visibility of the BeiDou geostationary and inclined geosynchronous orbiting satellites (which are not visible in Europe). In order to study many different satellite-receiver geometries, more than 1,000 different observation times were selected over a 10-day period. The procedure for determining the critical values of an acceptance test based on simulations with many different models as described in Verhagen (2005) and Verhagen and Teunissen (2013) is used here.

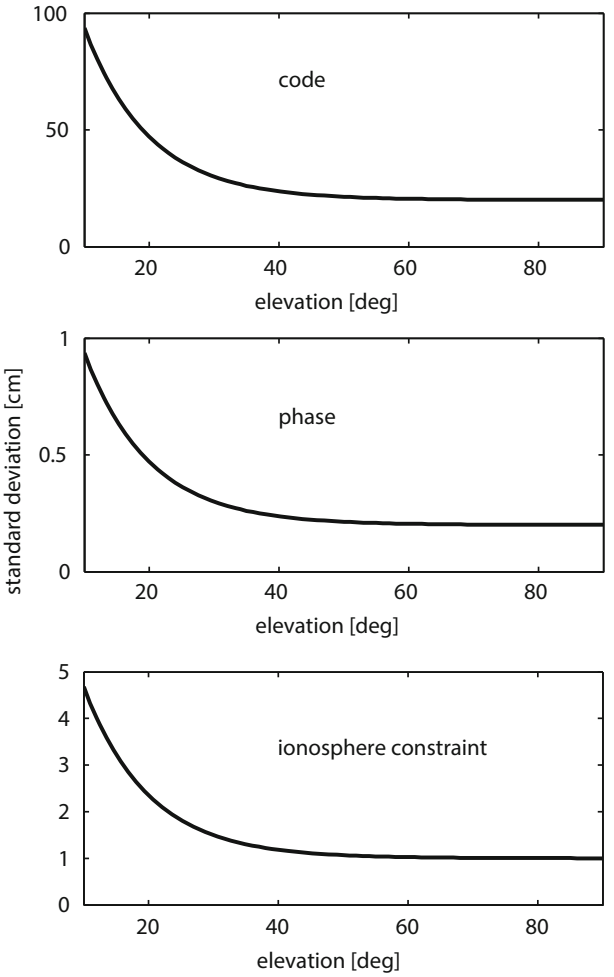

Fig. 2 Noise as function of elevation for code and phase observations, as well as for ionosphere constraints

4.2 Critical Values

Figures 3 and 5 shows the critical values of the ratio and difference test as function of number of satellites. Each marker corresponds to a specific satellite-receiver geometry. The corresponding number of systems is indicated by the marker-type. If the relation between critical value and number of satellites as shown in Figs. 3 and 5 is plotted per system and also per geographic location, this does not alter the pattern. Therefore, the results with different systems and locations are combined and not presented separately. In a specific measurement set-up, not only the satellite-receiver geometry will change, but also the number of epochs used to estimate the parameters. Here, the 1- up to 4-epoch models (from top to bottom) are considered.

Obviously, the satellite-receiver geometry is an important factor in most scenarios: there is quite some variability in the critical values for a given number of satellites.

For the 1-epoch scenarios, the model strength is generally poor. Even though the ratio test critical value shows less dependence on the satellite-receiver geometry for a given number of satellites, the corresponding fix rates (see Fig. 4) are generally low.

With the single-epoch model there are instances where the 3-system provides higher ILS failure rates than the 1- or 2-system constellation for the same time of observation; as a result the ratio test critical values can then be chosen larger with the 1- or 2-system constellation than with the 3-system (see Fig. 3: the **maximum** critical values with the 3-system are lower than the **maximum** values with the 1- and 2-systems). This implies that there is a dimensional curse: the much larger number of integer ambiguities to be estimated is not compensated sufficiently by improved float parameter precision due to better geometry and redundancy. This occurs for instance if the ILS failure rate with system A is very low, but with system B is very high; combining the two systems may then result in a higher ILS failure rate than with only system A.

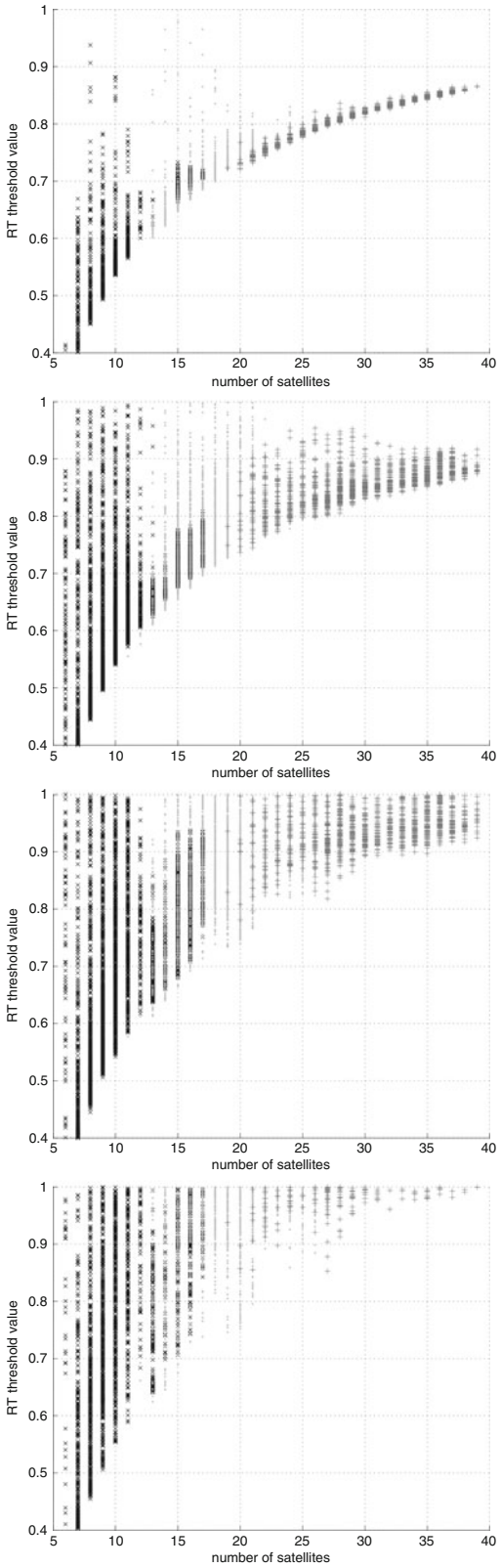

Fig. 3 Ratio test critical value with a fixed failure rate of 0.1% as function of number of satellites for many different times of observation and for all combinations of GPS, Galileo and BeiDou. From *top to bottom*: 1 to 4 epochs (*black crosses*: 1 system, *light grey filled circles*: 2 systems, *dark grey plus symbols*: 3 systems)

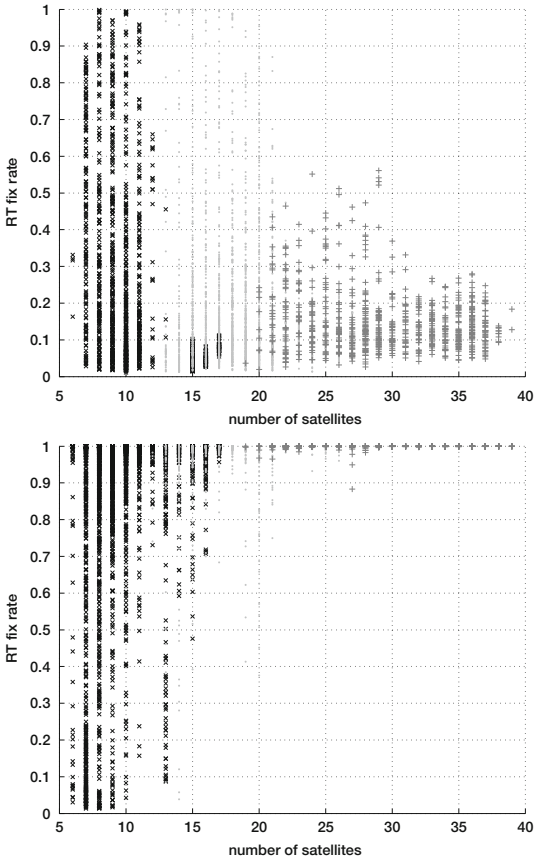

Fig. 4 Ratio test fix rate with a fixed failure rate of 0.1% as function of number of satellites for many different times of observation and for all combinations of GPS, Galileo and BeiDou. From *top to bottom*: 1 and 4 epochs (*black crosses*: 1 system, *light grey filled circles*: 2 systems, *dark grey plus symbols*: 3 systems)

For the ratio test it is clear that with increasing dimension, the minimum critical value over all satellite geometries is increasing as well. This is not per se related to more model strength, but also an effect of the dimension, i.e. number of ambiguities, itself. This is especially obvious for the 1-epoch models, where the fixing rate can be lower while the critical value is generally higher for larger number of satellites.

The relation between number of satellites and difference test critical value is not as obvious, as can be seen from Fig. 5; even for a fixed number of satellites, the variability in the critical value is very large.

The fix rates for the difference test are not separately shown, but show an almost similar pattern as for the ratio test in Fig. 4. With more epochs, the precision of the float solution will obviously improve. This implies that the acceptance regions can be chosen larger, which means a higher critical value for the ratio test and a smaller critical value for the difference test. As a consequence the fix rates will increase. The same applies if we would consider the same scenario but then for the triple-frequency case.

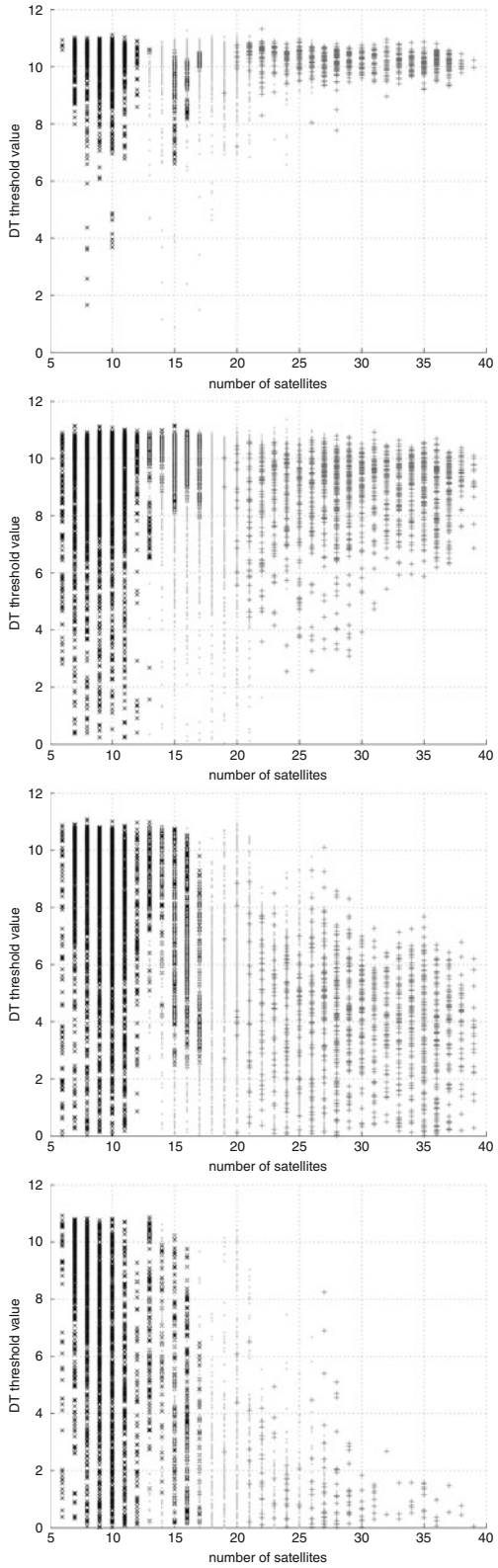

Fig. 5 Difference test critical value with a fixed failure rate of 0.1% as function of number of satellites for many different times of observation and for all combinations of GPS, Galileo and BeiDou. From *top to bottom*: 1 to 4 epochs (*black crosses*: 1 system, *light grey filled circles*: 2 systems, *dark grey plus symbols*: 3 systems)

5 Concluding Remarks

It is not advised to use a fixed critical value for the ratio test or difference test, even for a given application for which many model parameters will be fixed, such as the observation types (depending on system and frequencies), measurement noise, geographic region, and baseline length. The results in this contribution show that for a fixed failure rate, the corresponding critical values can be highly variable depending on satellite-receiver geometry and number of epochs.

For the ratio test the procedure as sketched in Verhagen and Teunissen (2013) can be used to devise look-up tables from which the appropriate critical value can be determined for a given dimension and ILS failure rate (these parameters can be determined prior to the actual IAR). The present contribution shows that it can be interesting to create such a table for the application (or: scenario) at hand and the required maximum allowable failure rate, i.e. the so-called fixed failure rate. In this way, users can determine the 'best' critical values for their needs.

The procedure is as follows. The GNSS model for many different satellite-receiver geometries and different numbers of epochs must be set-up. For each of these models, the critical value can then be empirically determined with a simulation procedure: generate a large number of float ambiguity samples for the model at hand, and tune the critical value such that the failure rate becomes equal to the required value. The current contribution shows an example for single baseline dual-frequency GNSS; future research will also address single- and multi-frequency scenarios, as well as PPP or multi-baseline processing.

For the difference test, a useful relation between critical value, and the dimension and ILS failure rate has not been found. In future work, it will be further investigated why this is different from the ratio test and also how it will be possible to efficiently determine the appropriate critical value for a fixed failure rate.

Acknowledgements This work has been executed in the framework of the Positioning Program Project 1.01 "New carrier phase processing strategies for achieving precise and reliable multi-satellite, multi-frequency GNSS/RNSS positioning in Australia" of the Cooperative Research Centre for Spatial Information.

References

Abidin HA (1993) Computational and geometrical aspects of on-the-fly ambiguity resolution. Ph.D. Thesis, Department of Surveying Engineering, Technical Report no.104, University of New Brunswick, 314 pp.

Chen Y (1997) An approach to validate the resolved ambiguities in GPS rapid positioning. In: Proceedings of the international symposium on kinematic systems in geodesy, geomatics and navigation, Banff

Euler HJ, Schaffrin B (1991) On a measure for the discernibility between different ambiguity solutions in the static-kinematic GPS-mode. In: IAG symposia no. 107, kinematic systems in geodesy, surveying, and remote sensing. Springer, New York, pp 285–295

Frei E, Beutler G (1990) Rapid static positioning based on the fast ambiguity resolution approach FARA: theory and first results. Manuscr Geod 15:325–356

Han S (1997) Quality control issues relating to instantaneous ambiguity resolution for real-time GPS kinematic positioning. J Geod 71:351–361

Han S, Rizos C (1996) Validation and rejection criteria for integer least-squares estimation. Surv Rev 33(260):375–382

Landau H, Euler HJ (1992) On-the-fly ambiguity resolution for precise differential positioning. In: Proceedings of ION GPS 1992, The Institute of Navigation, Fairfax, pp 607–613

Odijk D, Verhagen S, Teunissen PJG (2012) Medium-Distance GPS Ambiguity Resolution with Controlled Failure Rate. In: Kenyon S et al (eds) Geodesy for planet earth. International association of geodesy symposia, vol 136. Springer, Berlin, pp 745–751

Teunissen PJG (1995) The least-squares ambiguity decorrelation adjustment: a method for fast GPS integer ambiguity estimation. J Geod 70:65–82

Teunissen PJG (1999) An optimality property of the integer least-squares estimator. J Geod 73:587–593

Teunissen PJG (2003) Integer aperture GNSS ambiguity resolution. Artif Satell 38:79–88

Teunissen PJG (2005) GNSS ambiguity resolution with optimally controlled failure-rate. Artif Satell 40:219–227

Tiberius CCJM, De Jonge PJ (1995) Fast positioning using the LAMBDA method. In: Proceedings of DSNS'95, Bergen, paper no. 30

Verhagen S (2005) The GNSS integer ambiguities: estimation and validation. PhD thesis, Delft University of Technology, Netherlands Geodetic Commission, No. 58

Verhagen S, Teunissen PJG (2006) New global navigation satellite system ambiguity resolution method compared to existing approaches. J Guid Control Dyn 29:981–991

Verhagen S, Li B (2012) LAMBDA Software Package - Matlab implementation, version 3.0. Delft University of Technology and Curtin University, 39p

Verhagen S, Teunissen PJG (2013) The ratio test for future GNSS ambiguity resolution. GPS Solutions 17:535–548

Verhagen S, Li B, Teunissen PJG (2013) Ps-LAMBDA: Ambiguity success rate evaluation software for interferometric applications. Comput Geosci 54:361–376

Wang J, Stewart MP, Tsakiri M (1998) A discrimination test procedure for ambiguity resolution on-the-fly. J Geod 72:644–653

Wu Y, Jin SG, Wang Z, Liu J (2010) Cycle slip detection using multi-frequency GPS carrier phase observations: a simulation study. Adv Space Res 46(2):144–149

An Innovative Method to Predict and to Detect the False Fixing of the GNSS Ambiguity Phase

Paolo Dabove and Ambrogio M. Manzino

Abstract

One of the most critical points during the GNSS NRTK (Network Real Time Kinematic) positioning is the correct fixing of the ambiguity phase. This work wants to try to focus attention on the quality control of the real-time GNSS positioning, both from the point of view of what the network provides, and from one of the network products is used by the rover receiver. The quality of the positioning is a parameter that must be monitored in real time to avoid an incorrect ambiguity fixing, also called FF (false fixing), occurring; this can be due both to internal problems of the network software and, more often, to the environment (obstructions, multipath and so on) within which where the receiver works. To achieve this control a tool was designed that, starting from the data available in real time from a user connected to an NRTK positioning service, can identify with a certain probability threshold the effective presence, or the possibility, of a false fixing. The FF estimator will be composed of a neural network, trained a priori with some datasets, and will have, as a single output, the probability that the current fixing is a false fixing of the ambiguity phase.

Keywords

False fixing of ambiguity phase • GNSS • NRTK positioning • Quality control

Abbreviations

NMEA	National Marine Electronic Association
RTCM	Radio Technical Commission for Maritime Services

1 Introduction

The NRTK (Network Real Time Kinematic) positioning has undergone enormous development in recent years, thanks to the appearance of some networks of GNSS permanent stations. One of the main goals of these networks is to extend the real-time differential positioning beyond the limit of 10–15 km, allowing a positioning useful for applications such as surveying, monitoring, and precise navigation.

Considering this type of survey, the user can obtain a centimetre accuracy, which is usually achieved after a correct fixing of the ambiguity phase (Lachapelle et al. 2000). So the problem is that the unknown integer cycles of wavelength in the carrier phase measurements is very difficult to determine. Consequently, the integer ambiguity resolution and validation procedures have to be specifically dealt with for the purpose of reliable positioning and navigation (O'Keefe et al. 2006). Traditionally, ambiguity validation is carried out by statistical tests, such as the R-ratio test (Euler and Schaffrin 1991; Euler and Goad 1992; Ji et al. 2010; Feng and Wang 2011; Feng et al. 2012), F-ratio test (Frei and Beutler 1990), W-ratio test (Wang et al. 1998, 2000; Wang 2000), difference test (Tiberius and de Jonge 1995), and projector test

P. Dabove (✉) • A.M. Manzino
DIATI Department, Politecnico di Torino, C.so Duca degli Abruzzi, 24-10129 Turin, Italy
e-mail: paolo.dabove@polito.it; ambrogio.manzino@polito.it

© Springer International Publishing Switzerland 2015

C. Rizos, P. Willis (eds.), *IAG 150 Years*, International Association of Geodesy Symposia 143,
DOI 10.1007/1345_2015_19

(Han 1997; Wang et al. 1998; Teunissen 2003). Most of these statistical tests were derived from R1 and R2, which are two quadratic forms of ambiguity residuals related to the most likely integer ambiguity candidate and the second most likely integer ambiguity candidate. Major studies on these statistics were given in Teunissen (2003), Verhagen (2004, 2005), Verhagen and Teunissen (2006a, 2006b), and Li and Wang (2014). A common feature of these ambiguity validation tests is that a critical value is required from either the empirical value or the assumed distribution (Liu et al. 2014; Henkel and Günther 2012). Another promising trend of ambiguity validation is the introduction of the integer aperture (IA) estimation theory (Teunissen 2003; Teunissen and Verhagen 2009), which establishes a theoretical framework for ambiguity validation methods. The critical values for these statistical tests are then connected with user controllable fail-rates, which play the same role as the critical values, according to extensive simulation with the ambiguity VC matrix (Li and Wang 2014).

For various reasons, however, it is possible that the fixing of the integer ambiguities in the receiver may be unreliable. The primary purpose of this work is the correct fixing of the ambiguity phase in the double-difference approach, considering the rover receiver. The quality of the positioning is a parameter that must be monitored in real time to avoid an incorrect ambiguity fixing, also called FF (False Fixing), occurring; this can be due both to internal problems of the network software (i.e., the latency of communication between the Continuous Operating Reference Stations stations – CORSs and the software) and, more often, to the environment (obstructions, multipath and so on) where the receiver works. In order to do this, the idea is to develop an estimator that, starting from the data available in real time from a user connected to an NRTK positioning service, can identify with a certain probability threshold the effective presence, or the possibility of a false fixing in the position. This probability threshold can be chosen during the calibration phase of this tool (that concern both the training and the test phases of the algorithm) that depends on the type of receiver available. Some previous studies were made, considering only CORSs networks with inter-station distances of about 25–30 km and very good results were obtained Dabove and Manzino 2014. Now the goal of this work is to apply this revised method to CORSs networks with inter-station distances greater than the first ones (more or less 70 km, that is the typical distance of permanent stations for GNSS networks a national scale) in order to analyze if some other network parameters (i.e., ionospheric and tropospheric delays) must be considered for FF prediction.

2 Analysis of False Fixing

As it is usually said, FFs are unexpected errors that occur when the integer ambiguity estimation is wrong. First of all, it is important to understand what are the main factors that allow us to predict these events. So it is necessary to analyse which parameters, obtained by the rover and the network, are more sensitive to the fixing degradation. With regard to the rover parameters, only the information contained in the NMEA (National Marine Electronics Association) message or in the RTCM (Radio Technical Commission for Maritime Services) protocol are available in real time for the user. With the regard to the simplicity of decoding, only the information contained in the first type of message (in particular the GGA message) was considered while from the network software some different parameters were analysed:

- the latency of the differential correction
- number of GPS and GLONASS (satellites seen by the network stations for each epoch)
- number of GPS and GLONASS satellites which ambiguities is declared fixed by the network software for each epoch
- RMS (root mean square) of the network solution obtained in the current epoch, expressed in metres (σ_{ep})
- the value of the ionospheric delay expressed in ppm along the vertical direction. This index, that is a characteristic value of the GNSMART® software, is called I95 and is indicative of the error obtained from the global estimation of the ionosphere (Wübbena et al. 2004);
- the variation of the tropospheric delay (wet component) for each station in the network (expressed in percentage and derived by the modified Hopfield model).

Two different GNSS network configurations with different inter-station distances (shown in Fig. 1) have been considered, in order to also understand the impact of the inter-station distances on the FFs. About 20 days of data were acquired (RTK positioning with 24 h of session length, with an acquisition rate of 1 s) for each type of network, in order to test the major differential corrections used today (VRS, MAC and NRT – Nearest).

To try and assess whether any FF occurred during the measurement phase, the reference coordinates (obtained after an adjustment computed with the Bernese GPS 5.0 software in the ERTF2000 reference frame) were compared with those obtained in the NRTK survey by the rover receiver, considering only the positioning declared by the rover receiver as "fix" coordinates, where "fix" means that the ambiguity value of the carrier phase measurements were fixed to the

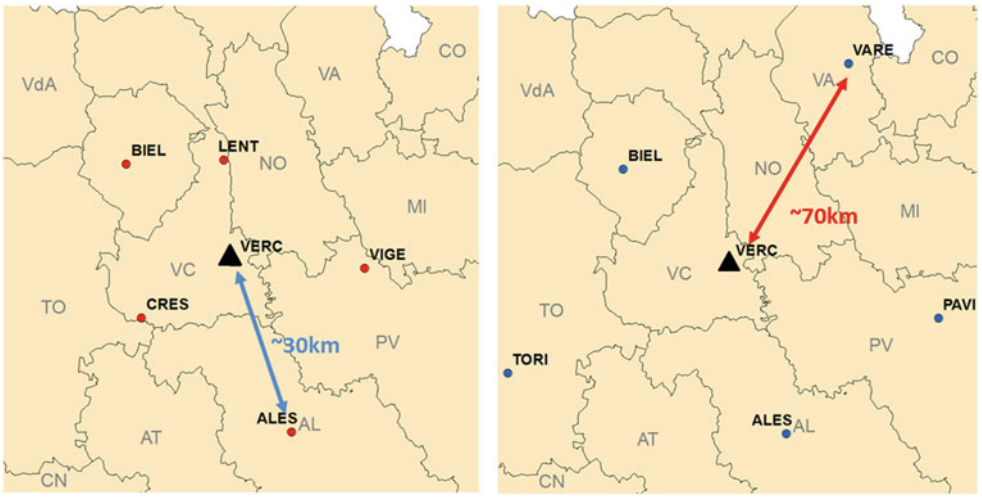

Fig. 1 Two network configurations: the small one on the left and the biggest on the right. The triangle shows the rover's position

integer correct value. As already mentioned, several geodetic receivers were tested, as well as different types of network products. From the studies carried out by Dabove and Manzino (2013) it is possible to conclude that, for networks with a mean inter-station distances of about 25–30 km, the following factors are the ones that induce an FF:

- latency of differential correction
- wrong ionospheric estimation (by the network software)
- high DOP (Diluition Of Precision) index variation
- high variation of number of satellites fixed by the network software.

Taking this into consideration, only the information available by the rover receiver was used in this work to train and to validate the FF estimator.

3 The FF Estimator

After the analysis of the types of false fix and the main factors that determine the occurrence of an incorrect fix, it was decided to develop an Artificial Neural Network (Fausett 1994), hereinafter ANN, that tries to predict the wrong fix of the ambiguity phase. To do this, a neural network toolbox, available in the Matlab® computer program, was used, but no appreciable results were obtained. So, some training and test algorithms were developed by the authors, still in Matlab®. Particular attention was devoted to the training phase: it is of fundamental importance to "train" the network correctly (Frean 1990), in such a manner that it is able to predict, after this phase, the possible false fixing of the ambiguity phase.

ANN are made up of *n* nodes, called artificial neurons, connected to each other, which are grouped into layers. There is one input layer consisting of a limited number of neurons, one output layer (in our case constituted by a single neuron that represents the decision about the FF), and one or more intermediate layers. Each neuron communicates with one or more neurons in a subsequent layer by means of directed communication links, each with an associated weight. The weights represent information being used by the net to solve the problem. Each neuron has an internal state called its 'activation' or 'activity level', which is a function of the inputs it has received. The first layer receives information from the input and returns it in the next layer through interconnections. The connections between one layer and the next do not transmit the output values derived from the previous layer directly, but transmit weighted values through weights w_{ij} that are assigned to each of these connections. These weights are the unknowns of the problem; to calculate them it is necessary to "train" the network. This means that you must provide a set of data (as input) for which you know the result in output. The neurons process the input through a certain function called *transfer function*: of all the transfer functions, the Hard Limit, the Linear and Log Sigmoid are the best known (Fig. 2). In addition to the transition function, each neuron is characterized by a threshold value. The threshold is the minimum value that must be present in input that allows the neuron to send something in output and is, therefore, active. Beyond this threshold value, the neuron transmits a value to the next layer that is the result of the application of the transfer function.

Generally, between one level and the next, all the neurons of the first level are connected with all the neurons of the second. It should be emphasized that there are neural networks in which there are also connections between neurons of the same level, but this does not happen in the case presented in this chapter. After the training phase, the effectiveness of the network is tested on a new set of data, called the *test set*. This set of data must be constituted by values of input and output never seen by the network. If the results offered by the network are close to the actual values, then the network can be considered valid. In these cases, it is said that the network is effective in generalization (Dabove 2013).

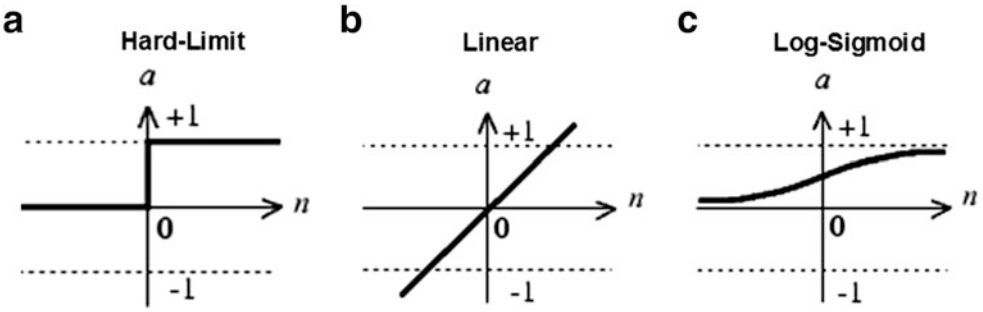

Fig. 2 Different types of transfer function

For the experiments shown in this paper, the input of ANN consists of a vector with three lines and one column that contain only the parameters available for the user in real time, that are contained into the NMEA message. This three parameters are, for all epochs, the values of the HDOP (Horizontal Diluition Of Precision) index, the latency of the correction, and the number of fix satellites (that means the satellites with fixed ambiguity phase) seen by the rover. The training set is constituted, for every epoch, by a Boolean vector consisting of 1, in the case of a false fix, and 0 otherwise. The hidden layer consists of ten neurons. As described in previous study (Dabove 2013) also in this case the dataset for training the network was divided as follows: 50% training; 30% validation; 20% testing. As mentioned, the control of what causes an FF is executed simultaneously in two respects: the verification of what is happening on the network at the time of the FF and the control of what the user can see on the rover receiver. The quality parameters, reported and considered significant to identify the reason for the FF, are extended for a period before and after the false fixing, established at 5-minute intervals (300 s). Almost always this period, especially before the false fixing, is sufficient to understand what is damaging the positioning.

4 Experiments

Four different methods were tested, depending both on the type of the input training file (each file was composed of 3 days of observations with an acquisition rate of 1 s), and the number of neurons considered in the hidden layer, as it is described in Dabove (2013), also for a CORSs network with a medium inter-station distances of about 70 km. This was made in order to understand if it is possible to generalize the results obtained both with a network with 'common' inter-station distances (about 30 km that represents the mean distance between two CORSs of the Italian regional networks) and with a one more larger (about 70 km that represents the mean distance of a national CORSs network).

So the ANN, for these experiments, was composed as follows (Fig. 3):

- ten neurons for hidden layer
- three layers
- transfer functions: log-sigmoid (first level) and linear (second level)
- training function: Levenberg-Marquardt backpropagation algorithm.

During the training phase, about 130 FFs were considered, that are mainly occurred due to HDOP index, latency of correction and number of satellites with fixed ambiguities. However some of them are unexplainable also seeing the report of the network software (also called state vector). Analyzing all these 130 FFs, it is possible to affirm that there isn't a parameter that cause more FFs respect to the others; in fact, for example if the latency had been the principal element that cause an FF, it would be possible to consider a threshold only on this parameter. But since it is not possible to find out a certain cause of all FFs, we have considered all this three parameters as input of ANN.

Considering the network with a mean inter-station distances of about 30 km (Fig. 1 – left), it is possible to affirm that the ANN identifies all the FFs, declaring 20% as certain FFs, while 80% are defined as possible FFs (hereinafter called 'warning'). More specifically, and choosing a random FF that occurred on that day, it is possible to see in Fig. 4 that this tool is able to predict an FF about 5 s in advance. In fact, the green and the red vertical bar represents the start and end epoch of the FF respectively while the green and blue points represent the decision of the ANN: green point when there is no FF, blue point when the ANN declare the present epoch as warning.

By means of a special program, developed in Matlab®, it was possible to analyse all those epochs when the estimated position differs by at least 20 cm (considered as certain FF because it is a static survey) from the "correct" one. It was also possible to create some statistics results, not on the quality of positioning but on the ability to predict and identify an FF in real time.

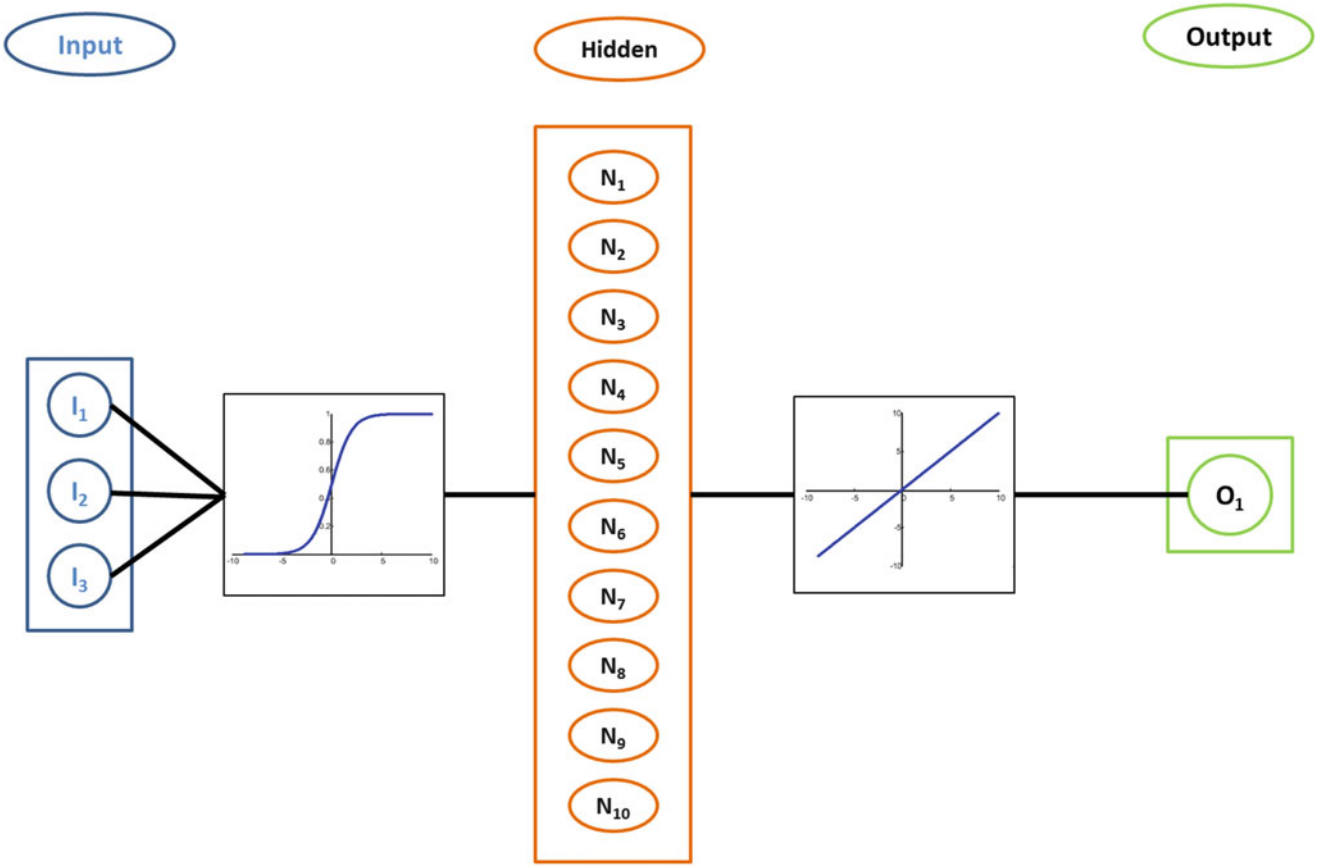

Fig. 3 ANN schema considered in this work

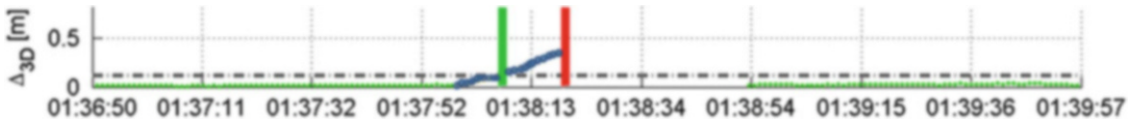

Fig. 4 Prediction of FF – an example

It is important to remark that an FF is very dangerous for the GNSS positioning so it is important to prevent this event. The prediction of this algorithm consists to indicate (as warning or as certain way) if an FF occours: in this regard the prediction is very useful even if a warning is the algorithm's output as said previously.

5 Discussion

As can be seen from Fig. 5, the neural network can be considered efficient, considering the MAC and VRS® corrections respectively, because 3 and 4% of cases report possible FFs that do not really occur, while never sure FF happen. So it is possible to affirm that the type of neural network and its training phase have proved effective. In this phase of the task, we only considered a few parameters obtained from the NMEA and RTCM messages, ignoring all the information derived from the network software that could further improve the results. Considering the network with mean inter-station distances of about 70 km (Fig. 1 – right), the results are quite different: as can be seen in Fig. 6, 66% of the FFs are due to the latency of the correction. In this case it is sufficient to put a threshold that reinitializes the ambiguity phase if the latency is up to 5 or 10 s.

Despite this, there are also 23% of FF that are wrong at the beginning and 21% that occur without apparent reason. Considering these results, we can affirm that it isn't useful in our opinion, to implement an ANN considering this type of CORSs network (mean inter-station distances of about 70 km) because the input parameters used for the first experiments are not significant for the other ones. We believe that it will be important to consider the network parameters in order to try to explain the other 21% of FF that, today, are

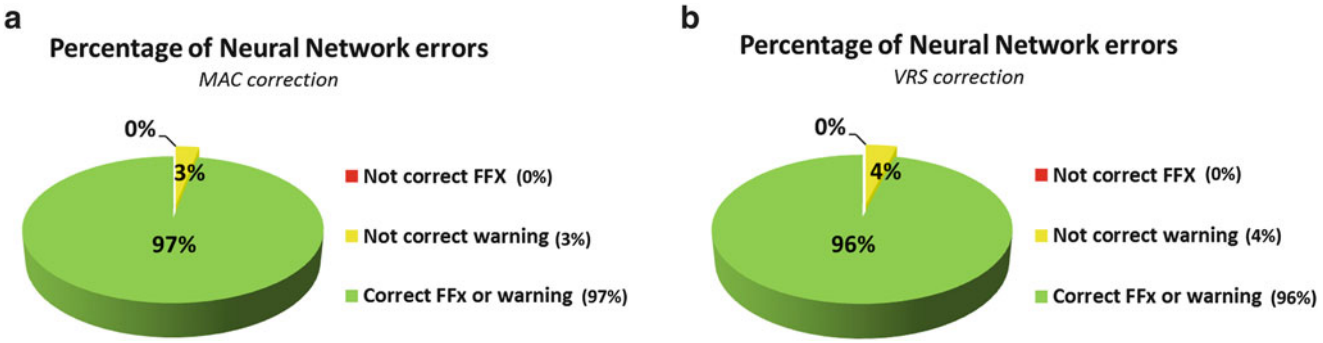

Fig. 5 Percentage of prediction errors considering MAC (*left* – **a**) and VRS (*right* – **b**) corrections

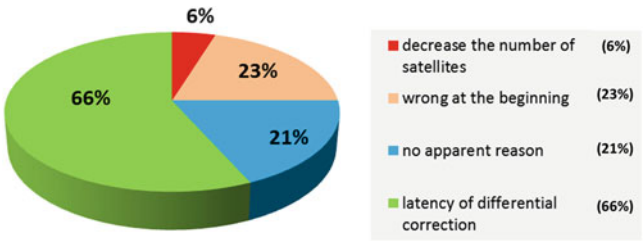

Fig. 6 Percentage of FF, considering different factors

unexplainable. Despite that, the ANN implemented is very useful for a CORSs network with inter-station distances of about 25–30 km (which is the typical distance of regional CORSs networks in some parts of the world, including Italy) while this can not be said for networks with greater inter-station distances (about 70 km, which is the typical distance of national CORSs networks, including Italy also in this case).

For this reason it is possible to affirm that the main factor that influence a fix of the ambiguity phase is the coupled receiver/antenna, because we have demonstrate that the developed algorithm is independent by the size of the network.

6 Conclusion and Future Development

As shown in the present work, it is not always possible to identify which parameter or its variation leads to a false fix. It is, however, possible to affirm that, according to the studies carried out, the significant quantities that allow the receiver to identify the presence of an FF with high probability, are:

- the latency of correction
- the noise of the RMS value (σ) of the three coordinates
- the DOP index and therefore the number of satellites used in parallel.

As it is known, an FF is very dangerous for the GNSS positioning so it is important to prevent this event. It is preferable re-initialize the ambiguity estimation respect to obtain a wrong estimation: in this regard the prediction is very useful even also a warning is the algorithm's output as said previously.

Considering networks with typical inter-station distances (30 km), the results obtained are very good and the developed tool is useful to detect and to predict FF. If the distances between the CORSs stations increase, the considered parameters are not useful to our goal: in fact, in 66% of cases the latency of the correction is the only factor that causes an FF. However it appears to be of great importance to consider the network parameters (such as ionospheric and tropospheric delays), in order to identify some FFs that today are unexplained. The input parameters of the network can be expanded. In addition, it is possible to affirm that the network can be trained for a "stop & go" positioning of the rover receiver or, with proper choice of these parameters, for a receiver in motion. The user will choose the type of survey and the receiver and, at the same time, the type of quality control of the survey. All these improvements will be made in the future.

References

Dabove P (2013) Quality control of the kinematic positioning into GNSS networks. Doctoral thesis, Politecnico di Torino

Dabove P, Manzino AM (2013) Analysis of ambiguity false fixing within a GBAS system. In: Ahmed HM (ed) Global navigation satellite systems – from stellar to satellite navigation. InTech, USA, p 27. doi:10.5772/55872. ISBN 9789535111627

Dabove P, Manzino AM (2014) GPS & GLONASS mass-market receivers: positioning performances and peculiarities. Sensors 14: 22159–22179

Euler H, Goad C (1992) On optimal filtering of GPS dual-frequency observations without orbit information. Bull Geod 65(2):130–143

Euler H, Schaffrin B (1991) On a measure for the discernibility between different ambiguity solutions in the static-kinematic GPS mode. In: IAG Symposia no 107, kinematic systems in geodesy, surveying, and remote sensing. Springer, Berlin, pp 285–295

Fausett L (1994) Fundamentals of neural networks: architectures, algorithms, and applications. Lavoisier, Paris

Feng Y, Wang J (2011) Computed success rates of various carrier phase integer estimation solutions and their comparison with statistical success rates. J Geod 85(2):93–103. doi:10.1007/s00190-010-0418-y

Feng S, Ochieng W, Samson J, Tossaint M, Hernandez M, Juan J, Sanz J, Aragon A, Ramos P, Jofre M (2012) Integrity monitoring for carrier phase ambiguities. J Navig 65(1):41–58

Frean M (1990) The upstart algorithm: a method for constructing and training feedforward neural networks. Neural Comput 2:198–209

Frei E, Beutler G (1990) Rapid static positioning based on the fast ambiguity resolution approach FARA: theory and first results. Manuscr Geod 15(4):325–356

Han S (1997) Quality control issues relating to instantaneous ambiguity resolution for real-time GPS kinematic positioning. J Geod 71(6):351–361

Henkel P, Günther C (2012) Reliable integer ambiguity resolution: multi-frequency code carrier linear combinations and statistical a priori knowledge of attitude. Navigation 59(1):61–75

Ji SY, Chen W, Ding XL, Chen YQ, Zhao CM, Hu CW (2010) Ambiguity validation with combined ratio test and ellipsoidal integer aperture estimator. J Geod 84(8):597–604

Lachapelle G, Alves P, Fortes LP, Cannon ME, Townsend B (2000) DGPS RTK positioning using a reference network. In: Proceedings of the 13th international technical meeting of the satellite division of the Institute of Navigation (ION GPS 2000), Salt Lake City (UT-USA), September 2000

Li T, Wang J (2014) Analysis of the upper bounds for the integer ambiguity validation statistics. GPS Solution 18:85–94. doi:10.1007/s10291-013-0312-1

Liu H, Chen Z, Ye W, Wang H (2014) GNSS carrier phase ambiguity resolution based on integrity restriction in ambiguity domain. Adv Space Res 53(8):1207–1218

O'Keefe K, Petovello M, Lachapelle G, Cannon ME (2006) Assessing probability of correct ambiguity resolution in the presence of time-correlated errors. Navigation (Washington, DC) 53(4):269–282

Teunissen PJG (2003) A carrier phase ambiguity estimator with easy-to-evaluate fail-rate. Artif Satel 38(3):89–96

Teunissen PJG, Verhagen S (2009) The GNSS ambiguity ratio-test revisited: a better way of using it. Surv Rev 41(312):138–151

Tiberius C, de Jonge P (1995) Fast positioning using the LAMBDA method. In: Proceedings of 4th international conference differential satellite systems, paper 30, Bergen, Norway, 24–28 April

Verhagen S (2004) Integer ambiguity validation: an open problem? GPS Solution 8(1):36–43

Verhagen S (2005) The GNSS integer ambiguities: estimation and validation. PhD thesis, Publications on Geodesy 58 Netherland Geodetic Commission, Delft

Verhagen S, Teunissen P (2006a) New global navigation satellite system ambiguity resolution method compared to existing approaches. J Guid Contr Dyn 29(4):981–991

Verhagen S, Teunissen P (2006b) On the probability density function of the GNSS ambiguity residuals. GPS Solution 10:21–28

Wang J (2000) Stochastic modeling for RTK GPS/glonass positioning. J US Inst Navig 46(4):297–305

Wang J, Stewart M, Tsakiri M (1998) A discrimination test procedure for ambiguity resolution on-the-fly. J Geod 72(11):644–653

Wang J, Stewart M, Tsakiri M (2000) A comparative study of the integer ambiguity validation procedures. Earth Planets Space 52(10):813–817

Wübbena G, Schmitz M, Bagge A (2004) GNSMART irregularity readings for distance dependent errors. Geo++White Paper

GNSS Antenna Impact on the Resulting Multipath Effects in Carrier-Phase and Signal Amplitude

M. Smyrnaios and S. Schön

Abstract

The impact of multipath propagation has attracted significant attention in the GNSS related studies and different approaches have been developed for the characterization of this phenomenon. In this paper, we present a new approach for the characterization of multipath effects in the GNSS observables where the impact of the receiving antenna is also considered. In modeling the receiving GNSS antenna by its gain pattern characteristics, we are able to calculate the relative amplitude between direct and indirect signal components. In this way, multipath effect on the GNSS carrier-phase can be simulated for complete satellite arcs. We present a simulation study on the impact that different GNSS antennas have on the resulting multipath errors. In a second step, the simulations are compared with GNSS data captured in a dedicated experiment. This investigation is the pre-step towards an in-depth quantification of the impact of multipath propagation on the GNSS observables.

Keywords

GNSS • Multipath • GNSS Antennas • Reflection Process

1 Introduction

In the presence of multipath, replicas of the direct signal reach the receiving antenna thought paths other than the line-of-sight (LOS) path and introduce biases in the observation domain. Different approaches can be found in GNSS literature for characterizing multipath effects. Georgiadou and Kleusberg (1988), derived a purely geometry related formulation. They showed that multipath effects can be identified by using double differenced (DD) phase observations. The analysis of C/N_0 observations has proven to be a very useful tool for the characterization of multipath effects (Axelrad et al. 1996; Bilich et al. 2008; Rost and Wanninger 2009).

Despite the different approaches developed, the impact of the receiving antenna in the process has not attracted much attention. The gain pattern characteristics of the receiving antenna are often unknown and they are not considered in the vast majority of multipath related studies for GNSS positioning. Aspects of GNSS antennas can be found in just recently publisted specialist textbooks on GNSS antennas (e.g. Rama Rao et al. 2013).

Furthermore, in recent years, due to the development of new scientific applications (e.g. GNSS remote sensing), reflected signal can be used as basic information and not as an unwanted bias (e.g. Nievinski and Larson 2013). For such applications, it would be better that the reflected signal components are received from the upper hemisphere of the antenna since GNSS antennas are designed in such a way that they suppress signals coming from below the horizon. Thus, the needs of such applications have led to the installation of GNSS antennas with different orientations. Furthermore, the use of left hand circular polarized (LHCP) antennas or even dual polarized antennas is often utilized for such applications (e.g. Löfgren, et al. 2010; Semmling, et al. 2012; Beckheinrich et al. 2012; Semmling et al. 2013). Since GNSS signal changes polarization upon reflection, LHCP

M. Smyrnaios (✉) • S. Schön
Institut für Erdmessung, Leibniz Universität Hannover, Schneiderberg Straße 50, 30167 Hannover, Germany
e-mail: smyrnaios@ife.uni-hannover.de

© Springer International Publishing Switzerland 2015

C. Rizos, P. Willis (eds.), *IAG 150 Years*, International Association of Geodesy Symposia 143,
DOI 10.1007/1345_2015_169

antennas will have an increased sensitivity to this type of incoming signal components while they will suppress right hand circular polarized (RHCP) signals, as the transmitted GNSS signals.

In this paper, we are characterizing the impact of the receiving antenna on the resulting signal amplitude of the direct and indirect signal components as well as on the resulting phase error. Apart from the computation of the relative amplitude of the incoming signal components, we also consider the phase shifts that occur due to the reflection process.

In the next section, the impact of multipath propagation on the signal amplitude and carrier phase will be summarized. The classical formulation of the phase error due to multipath is extended so that the relative amplitude between direct and indirect signals is calculated in an epoch-wise sense, as a function of the characteristics of the receiving antenna and the reflection process. Next, different antennas will be simulated, in terms of polarization (RHCP and LHCP) and orientation (i.e. looking upwards or downwards). Finally, results from a dedicated experiment will be presented where simulation results are compared against observed data. A discussion will conclude this paper.

2 Characterization of Multipath Effects

The impact of multipath propagation on the carrier phase is described as a function of the relative phase ($\Delta\Phi$) and the relative amplitude ($\boldsymbol{\alpha}$) between direct and indirect signal components. $\Delta\Phi$ can be calculated based on the geometry of the scenario as:

$$\Delta\Phi = \frac{2\pi\delta}{\lambda}, \tag{1}$$

where δ is the extra path delay in meters and λ is the wavelength of the carrier. If we assume a ground reflection from a horizontal reflector, the extra path length (δ) can be expressed as a function of the station height (h) and the satellite elevation (el) as:

$$\delta = 2hsin(el). \tag{2}$$

Assuming no noise, the phase error (ψ) due to multipath can be written as (Bishop et al. 1985; Georgiadou and Kleusberg 1988):

$$\psi = arctan\left(\frac{\alpha sin\Delta\Phi}{1+\alpha cos\Delta\Phi}\right), \tag{3}$$

where $\alpha = A_m/A_D$ with A_D the amplitude of the line-of-sight (LOS) component, A_m the amplitude of the multipath component (MPC) and $\Delta\Phi$ the relative phase between direct and indirect signal components. From Eq. (1) it can be noted that when the geometrical characteristics of the path of the incoming signal components are known, then a rough estimation for $\Delta\Phi$ is possible. Nevertheless, it should be corrected for the additional phase shifts resulting from the reflection process. On the other hand, the signal amplitudes of LOS (A_D) and MPC (A_m) signals are not directly accessible. An expression for the relative amplitude was presented in Smyrnaios et al. (2012), while a more detailed description of the approach can be found in Smyrnaios et al. (2013). This concept was adopted from wireless network simulations (Maltsev et al. 2011) and was adjusted to the needs of GNSS multipath scenarios by including the gain information and the rest of the parametrs from Friis transmission equation (i.e. free space path loss and transmitted signal power). The signal amplitudes for the ground multipath component (MPC) and for the LOS components are calculated as the absolute values of:

$$S_{MPC} = \vec{e}^{\,H}_{rec} H_{MPC} \vec{e}_{tran} S_T, \tag{4}$$

$$S_{LOS} = \vec{e}^{\,H}_{rec} H_{LOS} \vec{e}_{tran} S_T, \tag{5}$$

where $S_{MPC/LOS}$ are the received signal components, $\vec{e}^{\,H}_{rec}$ is the Hermitian conjugate of the Jones vectors of the receiving antenna, $\vec{e}_{tran}$ is the Jones vectors of the transmitting antenna and S_T is the transmitted signal power. The channel matrices for the case of a MPC and of LOS signal are:

$$H_{MPC} = A_{MPC} e^{-j\beta} H_{ref}, \tag{6}$$

$$H_{LOS} = A_{LOS} e^{-j\alpha}. \tag{7}$$

A_{LOS} and A_{MPC} account for the free space loss attenuation and $e^{-j\beta}$ and $e^{-j\alpha}$ are the phase changes for the LOS and MPC components, respectively, coming from the free-space propagation. Finally, H_{ref} is the channel polarization matrix for one single reflection (Smyrnaios et al. 2013). In Fig. 1 the geometric situation is depicted. In the current investigation, the link budget expression [Eqs. (4) and (5)] for the direct and indirect signal components are not evaluated as a whole due to algorithm implementation issues. We are only considering the gain information and the reflection process (for the MPC case). In a future publication it will be evaluated as a whole. No changes in the relative amplitude and the resulting phase error are expected.

The formulas used for the signal amplitude of the LOS and MPC signals as well as for the corrected $\Delta\Phi$ angle are:

$$A_D = |S_{LOS}|, \tag{8}$$

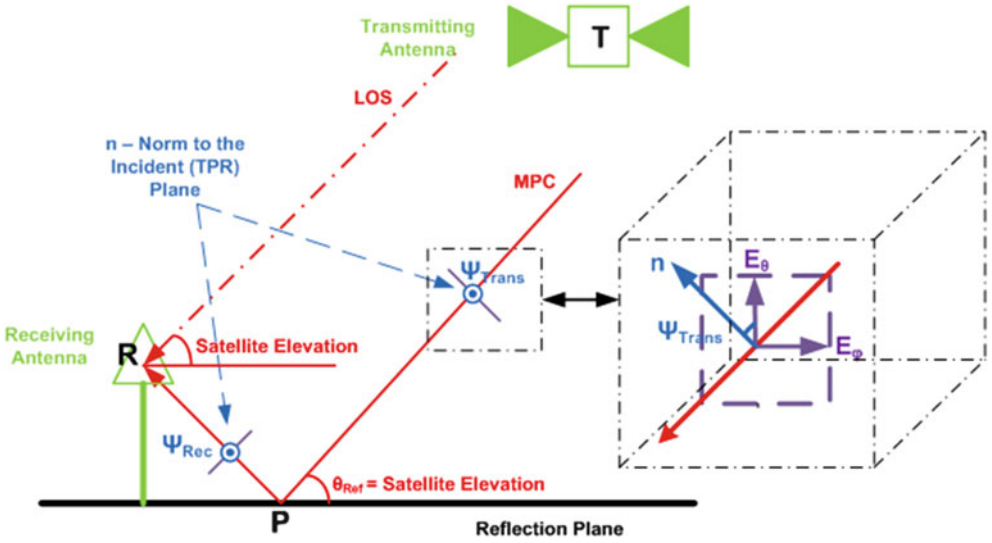

Fig. 1 Reflection geometry of ground reflection scenario. Adopted from Smyrnaios et al. (2013)

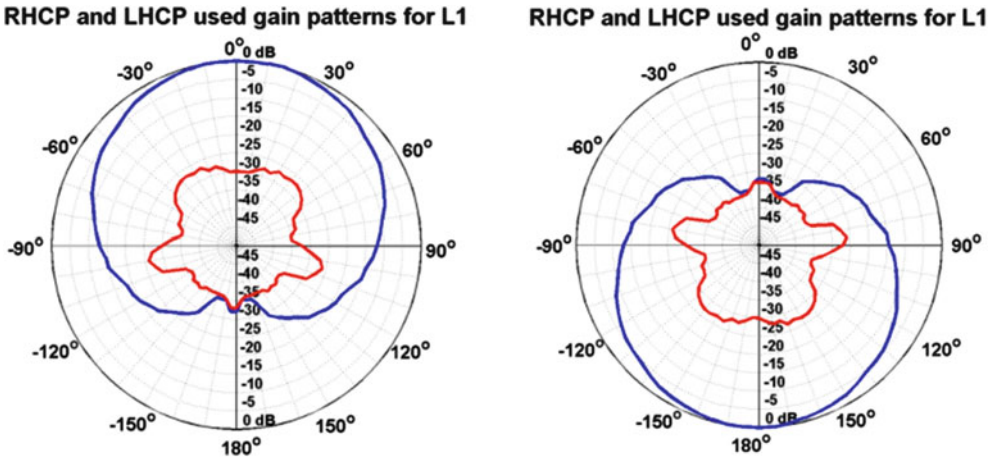

Fig. 2 Receiving GNSS antenna gain patterns (for RHCP in blue and for LHCP in *red*): (**a**) For a RHCP antenna looking upwards adopted from (Novatel), (**b**) For a RHCP antenna looking downwards

$$A_m = |S_{MPC}|\,, \tag{9}$$

$$\Delta\Phi_{\mathrm{cor}} = \mathrm{atan}\frac{\mathrm{Im}\,\{\mathrm{S_{MPC}}\}}{\mathrm{Real}\,\{\mathrm{S_{MPC}}\}}. \tag{10}$$

The integration of (8), (9) and (10) into (3) yields the final formula for the phase error due to multipath propagation.

$$\psi = \arctan\left(\frac{\left(\frac{|S_{MPC}|}{|S_{LOS}|}\right)\sin\left(\Delta\Phi_{cor}\right)}{1+\left(\frac{|S_{MPC}|}{|S_{LOS}|}\right)\cos\left(\Delta\Phi_{cor}\right)}\right). \tag{11}$$

3 Simulation Studies

3.1 Antenna Orientation and Polarization

In this part of the paper, we investigate the impact of the antenna polarization and orientation on the reflected signal's amplitude for four different reflectors. In Fig. 2 the gain patterns of the different antennas that were used for the simulations are plotted. The gain patterns of a Novatel 702 GG antenna (Novatel) for both orthogonal polarizations (RHCP and LHCP) were used (Fig. 2a). These antenna gain patterns were rotated by 180° to simulate a GNSS antenna

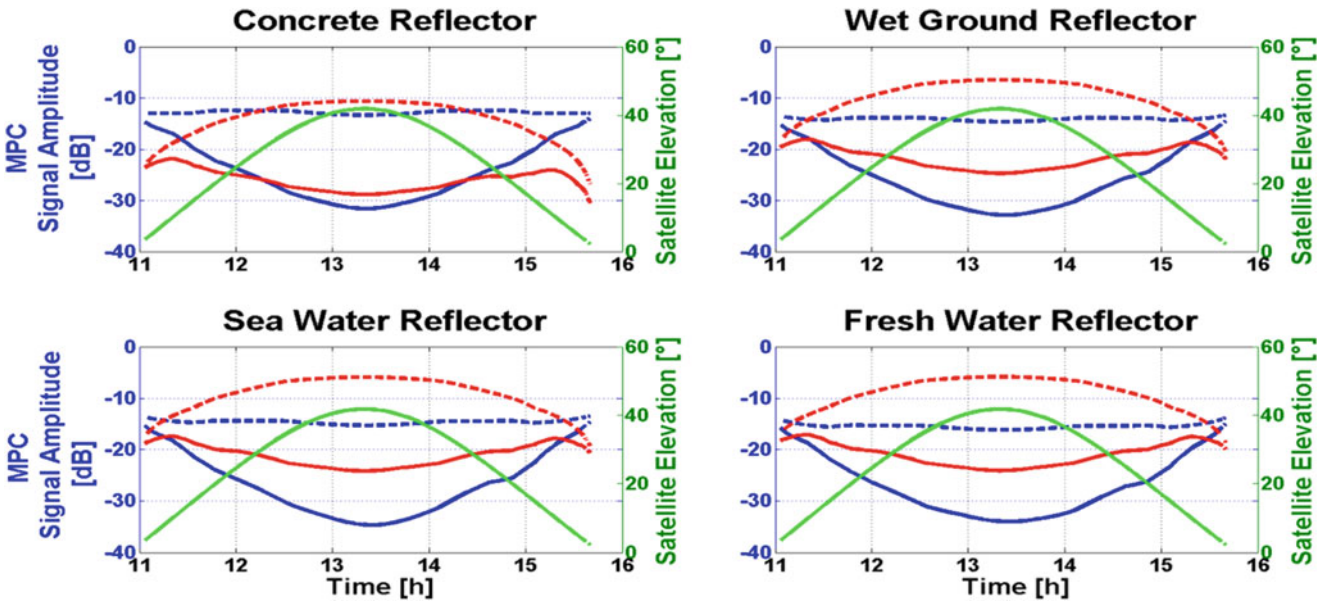

Fig. 3 MPC signal amplitude for: RHCP antenna looking upwards (in *solid blue*), RHCP antenna looking downwards (in *dashed blue*), LHCP antenna looking upwards (in *solid red*) and LHCP antenna looking downwards (in *dashed red*). For concrete, wet ground, sea water and fresh water reflectors

looking downwards. The gain patterns for the two orthogonal polarizations were reversed to simulate a LHCP antenna looking up- and downwards.

In Fig. 3 the normalized signal amplitude for the reflected signal [calculated with Eq. (9)] is plotted for each antenna. The satellite elevation changes from about 5° up to 40° and down to about 5°. The simulations are repeated for concrete, wet ground, sea water and fresh water reflectors, respectively. The intersection points of the dashed red curves with the dashed blue curves and the solid red curves with the solid blue curves indicate, in each plot, the situation where the reflection angles are equal to the Brewster angles. It should be mentioned that the reflection angle and the satellite elevation angle are equal for the scenario under investigation (see Fig. 1). For example, for a concrete reflector this angle is at 30° satellite elevation. For this reflection angle, the reflected signal is linear polarized. In other words, the magnitudes of RHCP component and of the LHCP component of the electric field vector are equal. Thus, the amplitude of the signal after a RHCP antenna or a LHCP antenna (with the same but reversed gain patterns) will be equal. The amplitude of a signal component coming from below the horizon of the antenna will be higher when the antenna is looking at the nadir direction. Finally, the amplitude of a signal reflected by a water reflector and received by a LHCP antenna looking to the nadir is bigger than the amplitude of a signal reflected by a concrete reflector. The opposite case can be noted in Fig. 3, if a nadir oriented, RHCP antenna (Fig. 2b) is used. Thus, it can be stated that GNSS signals reflected with reflection angles smaller than the Brewster angle will have larger amplitude when they are received by a RHCP antenna. On the contrary, signals reflected with reflection angles larger than the Brewster angle will have larger amplitude when they are received by a LHCP antenna. These properties are useful to select antennas either for multipath rejection or for sensing reflected signals.

3.2 GNSS Antenna Gain Pattern

In this section, the impact of the receiving antenna on the resulting phase error will be examined. Firstly, we simulate the phase error (ψ) and the ratio of amplitudes between the MP and the LOS signal components ($\boldsymbol{\alpha}$) for two antennas, using the antenna gain patterns shown in Fig. 4b, c. These two antennas have the same gain characteristics for positive elevation angles. For negative elevation angles, the antenna gain pattern, shown in Fig. 4c, suppresses signals coming from under the horizon to such an extent that they can be considered as negligible. Hence, the gain patterns for both orthogonal polarizations are set to a constant value of -45 dB for all possible angles of arrival (AoA) under the horizon of the antenna (see the lower hemisphere of Fig. 4c).

In Fig. 4a, the phase error, calculated from Eq. (3) and the relative amplitude, calculated as the ratio of Eqs. (9) and (8), are simulated for a satellite arc from 2° to 90°. The reflector is modeled as a concrete reflector. It can be noted that as the relative amplitude $\boldsymbol{\alpha}$ increases, the magnitude of the resulting phase error is also increasing. If the amplitude

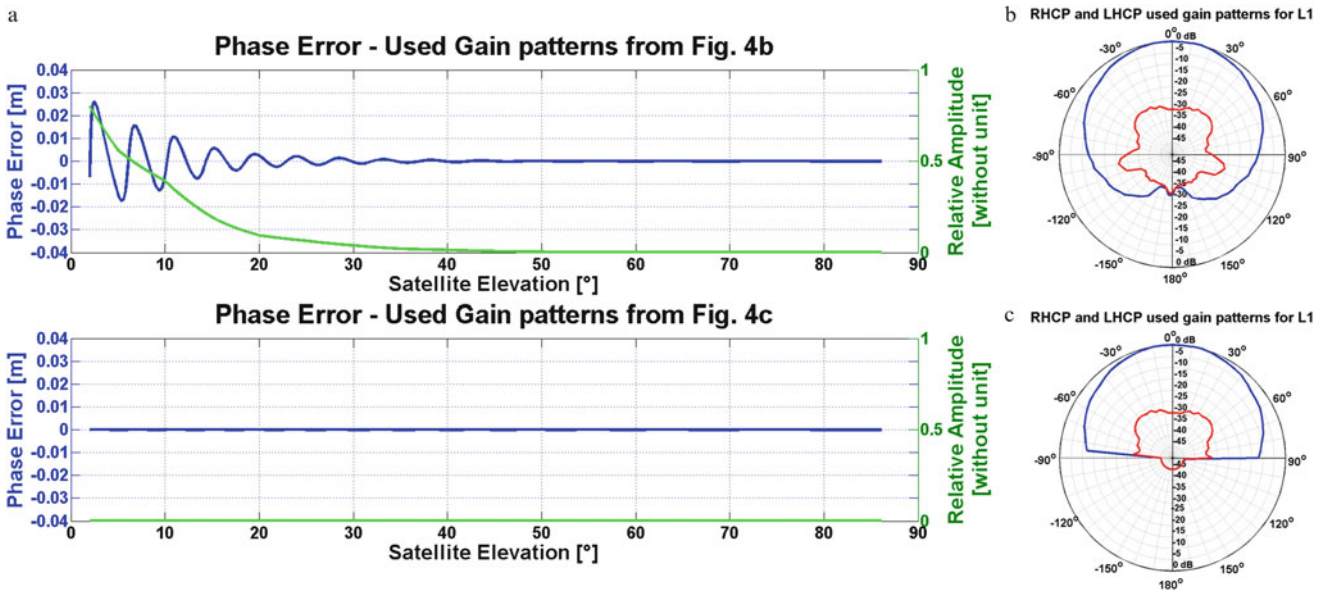

Fig. 4 Phase error (ψ) versus relative amplitude (a) between direct and indirect signal components. For the upper part of (**a**), the antenna gain patterns shown in (**b**) were used while for the lower plot of (**a**) the antenna gain patterns shown in (**c**) were used

of the direct and indirect signals would be equal ($\boldsymbol{\alpha} = 1$), then the phase error could reach its maximum value (i.e. a quarter of the wavelength). On the other hand, the phase error and the relative amplitude in the lower plot of Fig. 4a approaches zero. In this case, the amplitude of the reflected signal component is very low and can be consider negligible with respect to the amplitude of the LOS signal component (i.e. the relative amplitude $\boldsymbol{\alpha}$ is approaching zero). Unfortunately such a GNSS antenna, of Fig 4c, is hard to construct.

In this last part of the simulation study, different gain patterns with similar characteristics to GNSS antennas (Fig. 5a–d) are simulated and the resulting phase error due to one ground reflection is plotted in Fig. 5e. The satellite elevation varies from 2° to 40°. In this case, the simulations are performed for a concrete reflector and for the four different gain patterns plotted in Fig. 5a–d as well as for that one of Fig. 2b. The different gain patterns results in different multipath signatures. Small variations of the resulting error magnitude, as well as frequency and phase shifts between the different antennas can be observed. For example, at very low elevation the resulting error magnitude difference is in the order of 8 mm (Fig. 5e).

4 Experimental Set-Up and Results

In order to validate the previous described simulations, data sets were collected at the antenna reference open area test site at PTB Braunschweig. This particular area was chosen due to the flat terrain characteristics and the lack of any nearby potentially disturbing constructions for the receiving antennas. In this way, we were sure that (specular) reflections would only occur by the ground reflector which could be approximated as a planar and horizontal reflector. The two antennas of the observed baseline were mounted on tripods on a high-low antenna set-up in order to introduce asymmetry of the multipath effects for the two antenna locations. The antenna heights refer to the vertical distances between the mean phase centre of the antenna and the ground reflector plane. Observations from satellites above 0° were used for this investigation because ground multipath effects are much stronger at elevation angles less than 20°. The choice of this elevation mask, on the other hand, does not exclude diffraction effects by the trees in the surrounding area as can be seen in Fig. 6. A Leica AX1202GG and a Novatel 703GGG antenna were used together with two Leica GRX1200 + GNSS receivers for data capture (data rate 1 Hz). Absolute and individual antenna phase center corrections from IfE Hannover were taken into account during data processing. The experimental set up can be seen in Fig. 6. The antenna heights were 1.244 m (L) and 1.765 m (H), respectively.

In Fig. 7, the carrier phase double difference residuals (DD), computed from observed carrier phase measurements (PRN 9 as reference satellite), are plotted against the simulated phase error double differences of the same satellites. The observational period is from 4 up to 6h for the corresponding observed PRNs. The magnitude of the simulated phase error DD and the estimated carrier phase DD residuals is of the order of mm and within the noise

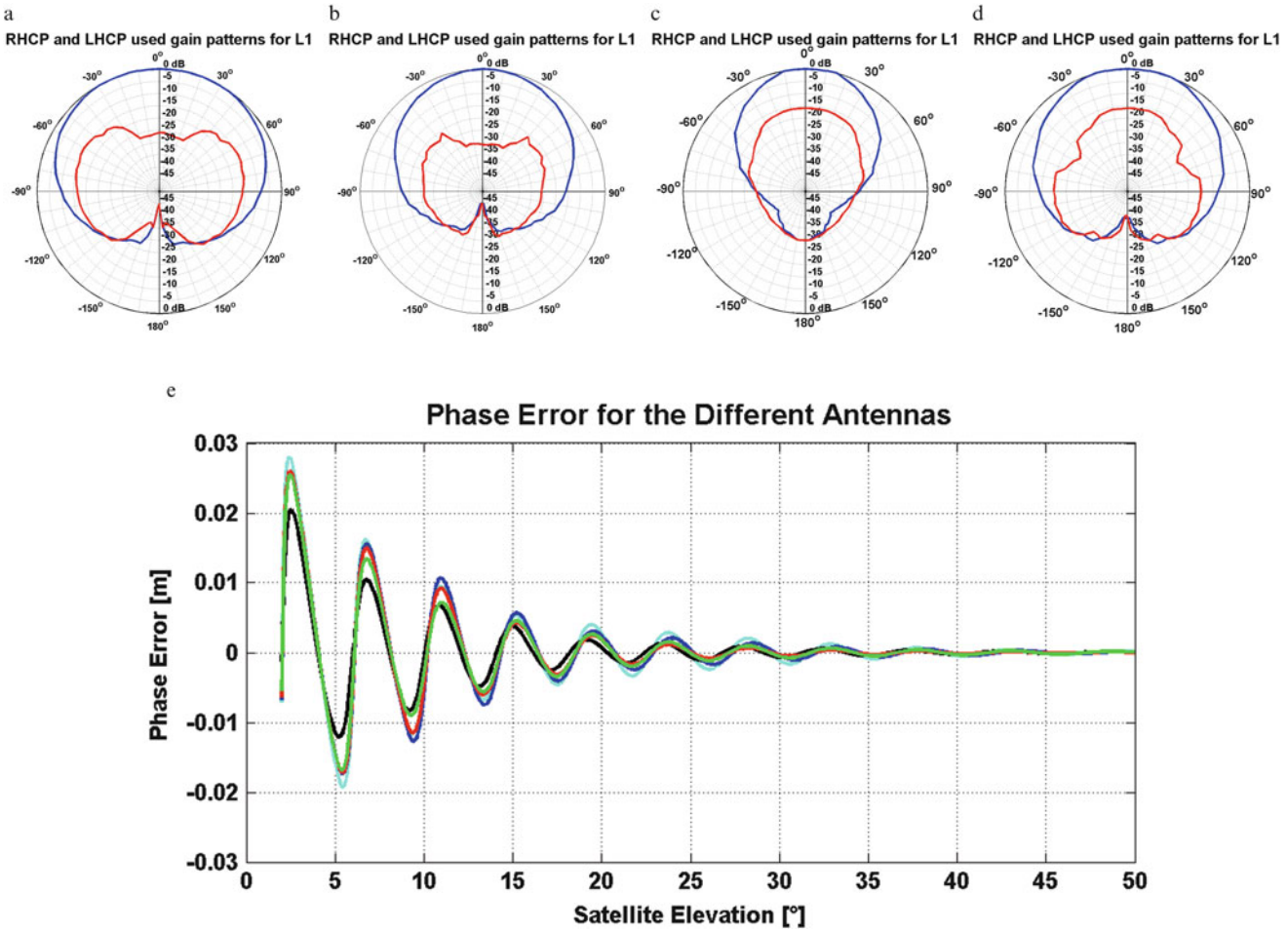

Fig. 5 (**e**) Phase error for GNSS antennas with different gain patterns. (**a**) Gain 1, (**b**) Gain 2, (**c**) Gain 3, (**d**) Gain 4

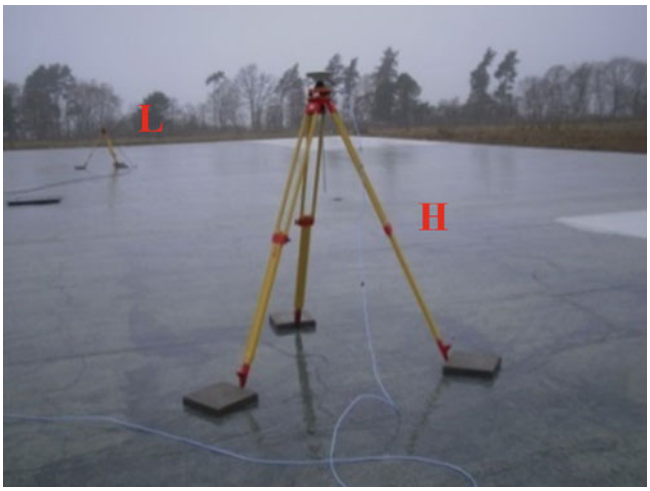

Fig. 6 Experimental set-up at PTB Braunschweig antenna reference open area test site

level for the vast majority of the observed epochs. The frequency and phase shifts that can be noticed between the observed and the simulated time series are attributed to several factors. One of them is that the ground reflector is not a horizontal reflector. Moreover for PRNs at very low elevation angles, diffraction effects will most probably occur and these effects are not considered in this investigation. Furthermore, differences between the real antenna gain pattern characteristics and the simulated one (e.g. azimuthal variations of the receiving antenna; especially of the side lobes under the horizon). Last but not least, phase center variations for the reflected MPC are not considered since the reception point, for both direct and indirect signal components, is considered to be at mean phase center of the antenna and is assumed identical for LOS and MP signal components.

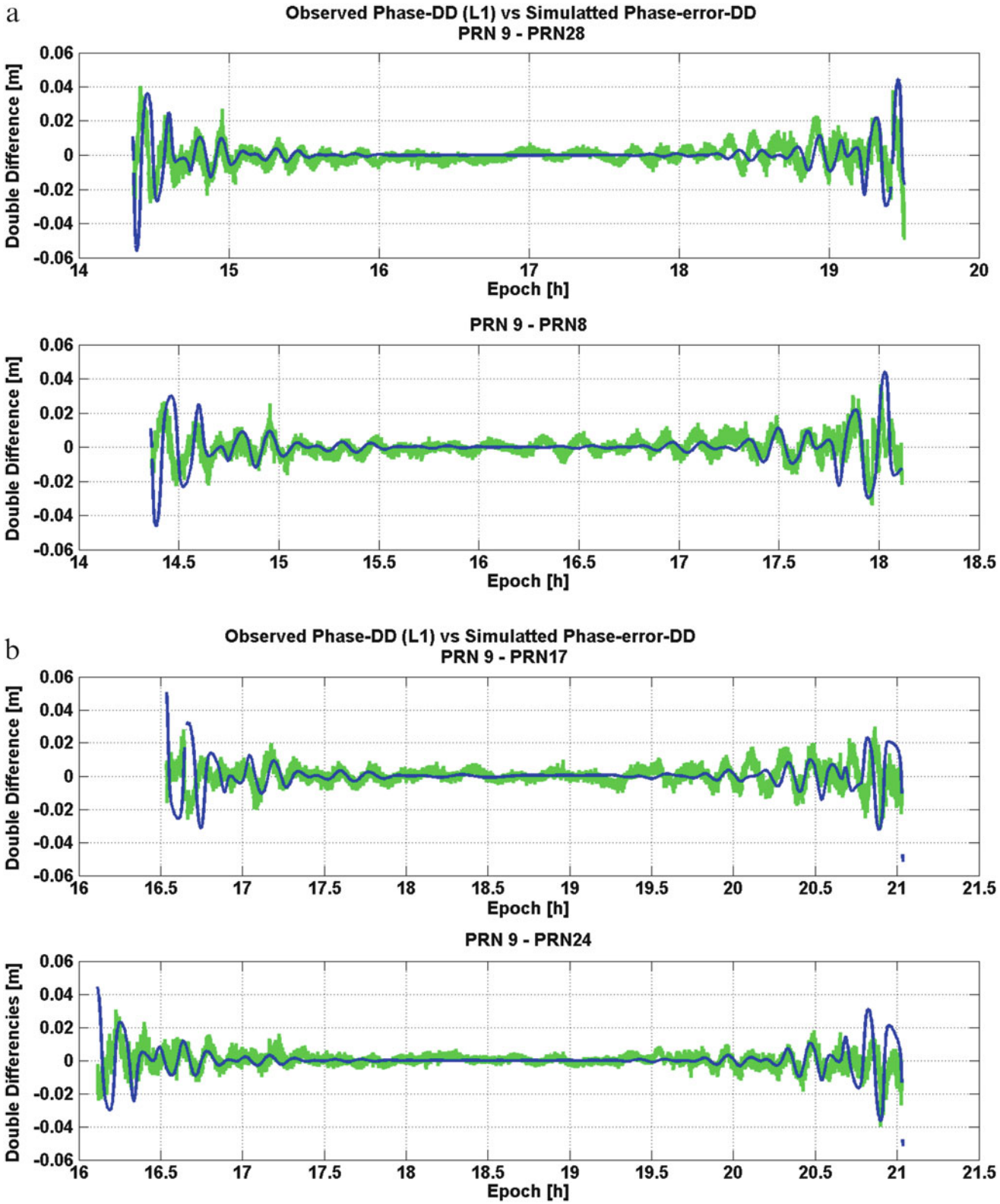

Fig. 7 Simulated DD phase-error (*green*) versus observed carrier-phase DD (*blue*) between: (**a**) PRN9–PRN28 (*upper plot*) and PRN9–PRN8 (*lower plot*) (**b**) PRN9–PRN17 (*upper plot*) and PRN9–PRN24 (lower plot)

5 Conclusions and Outlook

Simulations of multipath propagation effects on the GNSS carrier-phase and relative amplitude can be calculated as a function of the transmitting and receiving antenna gain patterns and the reflection process. The knowledge of the geometrical characteristics of the path of the reflected signal component is needed because the AoA of the received signals is a crucial parameter when the impact of the receiving antenna on the process is to be considered. Thus, for the implementation of the presented expression, apart from the geometry of the scenario, the gain patterns of the transmitting and receiving antennas are needed together with the material properties of the reflector. The developed algorithm makes use of the before-mentioned input information and calculates the corresponding phase error and relative amplitude for each observed satellite. In this way, we are able to simulate complete satellite arcs and to follow the magnitude of the resulting errors at mm level.

We presented a simulation analysis where the impact of the receiving antenna is characterized. RHCP and LHCP GNSS antennas as well as different orientations were simulated, since, different antenna orientation can be better for specific applications. Variations of the gain patterns show deviations of the phase error of up to 8 mm. In the last part of this paper observed data were compared with the simulation results. A 12 h experiment was conducted and the resulting carrier-phase DD agree with the simulated results with only a few mm difference.

In this investigation, we focused on the impact of the receiving GNSS antennas on the resulting phase error due to multipath. Whilst reflected signals are a limiting factor in high precision GNSS, they are also used as a primary observable in new GNSS scientific applications. Therefore GNSS antennas should not be considered as black boxes. Based on the radiation properties, they can be simulated and their impact can be taken into account. This investigation is the pre-step towards an in-depth quantification of the impact of multipath propagation on GNSS observables.

Acknowledgement This work has been realized within the BERTA project (50NA1012), funded by the Federal Ministry of Economics and Technology, and based on a resolution by the German Bundestag. The authors would like to thank Dr. Thorsten Schrader (PTB Braunschweig) for supporting the experiments at the antenna reference open area test site at PTB.

References

Axelrad P, Comp C, Macdoran P (1996) SNR-based multipath error corection for GPS differential phase. IEEE Trans Aerosp Electron Syst 32(2):650–660

Bilich A, Larson K, Axelrad P (2008) Modeling GPS phase multipath with SNR: case study from the Salar de Uyuni, Boliva. J Geophys Res 113:1–12

Bishop GJ, Klobuchar JA, Doherty PH (1985) Multipath effects on the determination of absolute ionospheric time delay from GPS signals. Radio Sci 20(3):388–396

Georgiadou Y, Kleusberg A (1988) On carrier signal multipath effects in relative GPS positioning. Manuscr Geodaet 13:172–179

Löfgren JS, Rüdiger H, Johansson JM (2010) Monitoring costal sea level using GNSS signal. Adv space Res 47(2):213–220

Maltsev A, Maslennikov R, Lomayev A, Sevastyanov A, Khoryaev A (2011) Statistical channel model for 60 Ghz WLAN systems in conference room enviroment. Radioengineering 20:409–422

Nievinski FG, Larson M (2013) Forward modeling of GPS multipath for near-surface reflectometry and positioning applications. GPS Sol. doi:10.1007/s10291-013-0331-y

Novatel: GPS-701-GG and GPS-702-GG antennas. http://webone.novatel.ca/assets/Documents/Papers/GPS701_702GG.pdf. Accessed 12 Oct 2013

Rama Rao B, Kunysz W, Fante R, McDonald K (2013) GPS/GNSS antennas. Artech House, Boston/London

Rost C, Wanninger L (2009) Carrier phase multipath mitigation based on GNSS signal quality measurements. J Appl Geod 3(2):81–87.103

Beckheinrich J, Beyerle G, Schön S, Apel H, Semmling AM, Wickert J (2012) WISDOM: GNSS-R based flood monitoring. In: Proceedings of the workshop on reflectometry using GNSS and other signals of opportunity, West Lafayette. IN, pp 1–6

Semmling AM, Schmidt T, Wickert J, Schön S, Fabra F, Cardellach E, Rius A (2012) On the retrieval of the specular reflection in GNSS carrier observations for ocen altimetry. Radio Sci 47, RS6007. doi:10.1029/2012RS005007

Semmling AM, Wickert J, Schön S, Stosius R, Markgraf M, Gerber T, Ge M, Beyerle G (2013) A zeppelin experiment to study airborne altimetry using specular Global Navigation Satellite System reflection. Radio Sci 48. doi:10.1002/rds.20049

Smyrnaios M, Liso M, Schön S, Kürner T (2012) Ray-tracing appraoch versus double differencies, multipath characterization in a multiple ray scenario. In: Proceedings of the 6th ESA wotkshop on satellite navigation technologies and European workshop on GNSS signals and signal processing, ESA ESTEC, Noordwijk

Smyrnaios M, Schön S, Liso M (2013): Multipath propagation, characterization and modeling in GNSS. In: Shuanggen J (ed) Geodetic sciences – observations, modeling and applications. Earth and planetary sciences series, InTech. doi:10.5772/54567

Attitude Determination and Relative Positioning for LEO Satellites Using Arrays of GNSS Sensors

Nandakumaran Nadarajah, Peter J.G. Teunissen, and Sandra Verhagen

Abstract

Global Navigation Satellite Systems (GNSS) have become ubiquitous in positioning, guidance and navigation. GNSS-based attitude determination and relative navigation are the important and promising applications. In this contribution we explore the potential of Low Earth Orbiting (LEO) satellite navigation in formation using arrays of GNSS sensors. We consider multiple LEO platforms in close formation, each equipped with multiple GNSS antennas/receivers. Platform processing involves precise attitude determination using the Multivariate Constrained Least-squares AMBiguity Decorrelation Adjustment (MC-LAMBDA) method effectively utilizing known antenna geometry in local body frame. Between-platform processing involves estimation of unconstrained baselines between platforms using array-aided relative positioning effectively exploiting the platform antenna geometry in improving between-platform ambiguity resolution and baseline estimates. Finally, we use nonlinear recursive filtering to further improve the attitude angular estimates and between-platform baseline estimates. Our hardware-in-the-loop experiment with space enabled Namuru GNSS receivers shows the potential of stand-alone, unaided, single-frequency attitude determination and relative positioning of LEO satellites.

Keywords

Attitude bootstrapping • Attitude determination • Carrier phase ambiguity resolution • Formation flying • GNSS • MC-LAMBDA

1 Introduction

Global Navigation Satellite Systems (GNSS) have become ubiquitous in positioning, guidance and navigation. As the potential of GNSS for space applications is discussed in Montenbruck et al. (2007), GNSS-based navigation for space vessels has been demonstrated in various space missions including engineering test satellite (ETS)-VII (Kawano et al. 2000) and prototype research instruments and space mission technology advancement (PRISMA) (Gill et al. 2007). GNSS attitude determination and relative navigation are the important and integral parts of spacecraft formation flying using GNSS observables. Spacecraft attitude determination using GPS receivers has been demonstrated in Duncan et al. (2007). GNSS based spacecraft relative positioning has

N. Nadarajah (✉)
Department of Spatial Sciences, GNSS Research Centre, Curtin University, Perth, WA 6845, Australia
e-mail: n.nadarajah@curtin.edu.au

P.J.G. Teunissen
Department of Spatial Sciences, GNSS Research Centre, Curtin University, Perth, WA 6845, Australia

Department of Geoscience and Remote Sensing, Delft University of Technology, 2600 GA Delft, The Netherlands

S. Verhagen
Department of Geoscience and Remote Sensing, Delft University of Technology, 2600 GA Delft, The Netherlands

© Springer International Publishing Switzerland 2015

C. Rizos, P. Willis (eds.), *IAG 150 Years*, International Association of Geodesy Symposia 143,
DOI 10.1007/1345_2015_26

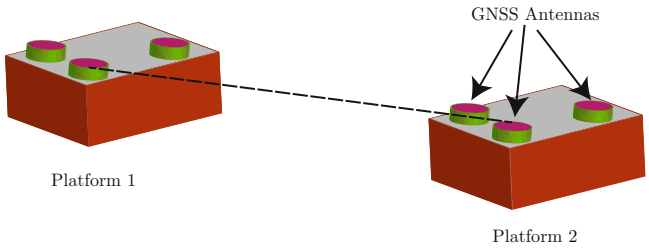

Fig. 1 LEO platforms in close formation

been explored in D'Amico and Montenbruck (2010). In this contribution we explore the potential of Low Earth Orbiting (LEO) satellite navigation in formation using *arrays* of GNSS sensors.

We consider multiple LEO platforms in close formation, each equipped with multiple GNSS antennas (Fig. 1). Platform processing involves precise attitude determination requiring successful resolution of the integer carrier phase ambiguities. Since antennas are rigidly mounted on the platform, the relative antenna geometry in the local body frame is known a priori and can be exploited for the purpose of increasing the probability of correct integer ambiguity estimation. In this contribution, we make use of the Multivariate Constrained Least-squares AMBiguity Decorrelation Adjustment (MC-LAMBDA) method (Teunissen 2007) effectively utilizing nonlinear geometrical constraints. By incorporating the known antenna geometry into its ambiguity objective function, this method has been shown to demonstrate reliable and instantaneous single-frequency integer ambiguity resolution.

Between-platform processing involves estimation of unconstrained baselines between platforms. In this contribution, we use array-aided relative positioning (Buist et al. 2011; Teunissen 2012) effectively exploiting the platform antenna geometry in improving between-platform ambiguity resolution. This method not only enhances the between-platform ambiguity resolution but also improves the between-platform baseline estimates. Finally, we use nonlinear recursive filtering to further improve the attitude angular estimates and between-platform baseline estimates. Our hardware-in-the-loop experiment with space enabled Namuru GNSS receivers (Parkinson et al. 2011) shows the potential of stand-alone, unaided, single-frequency attitude determination and relative positioning of LEO satellites.

2 Platform Processing

This section describes the platform processing involving attitude determination for a small-sized array of GNSS receivers/antennas with known local body frame antenna geometry. First the multibaseline attitude model is introduced using the multivariate formulation of Teunissen (2007). This formulation makes a frequent use of the Kronecker product $\otimes$ and the vec-operator (Harville 1997). Then we include the local body frame antenna-geometry and show how the constrained attitude model can be solved in a step-wise manner.

2.1 Instantaneous Attitude Determination

2.1.1 The Single-Frequency Multivariate Model

Let us consider the kth platform equipped with a set of $n_k + 1$ antennas simultaneously tracking m satellites. The set of linearized Double Difference (DD) GNSS phase and code observations obtained on the n_k baselines formed by these antennas at an observation epoch forms a *multivariate* Gauss-Markov model (Teunissen 2007):

$$\mathrm{E}(Y^k) = AZ^k + G^k B^k, \quad Z^k \in \mathbb{Z}^{m\times n_k} \tag{1}$$

$$\mathrm{D}(\mathrm{vec}(Y^k)) = Q_{y^k y^k} = P^k \otimes Q_{yy}, \quad B^k \in \mathbb{R}^{3\times n_k} \tag{2}$$

where $\mathrm{E}(\cdot)$ and $\mathrm{D}(\cdot)$ denote the expectation and dispersion operator, $\otimes$ denotes the Kronecker product, $Y^k = [y_1^k, \ldots, y_{n_k}^k]$ is the $2m \times n_k$ matrix of n_k linearized (observed-minus-computed) DD observation vectors, $y_j^k = [p_j^{k^T}\ \phi_j^{k^T}]^T$ consists of DD code and phase observations, $Z^k = [z_1^k, \ldots, z_{n_k}^k]$ is the $m \times n_k$ matrix of n_k unknown DD integer ambiguity vectors z_j, $B^k = [b_1^k, \ldots, b_{n_k}^k]$ the $3 \times n_k$ matrix of n_k unknown baseline vectors b_j, G^k is the $2m \times 3$ geometry matrix that contains the unit line-of-sight vectors, A is the $2m \times m$ matrix that links the DD data to the integer ambiguities, and P^k and Q_{yy} are known matrices of order $n_k \times n_k$ and $2m \times 2m$, respectively. Here, $\mathrm{vec}(\cdot)$ denotes the vec-operator, which transforms a matrix into a vector by stacking the columns of the matrix one underneath the other. Matrix P^k takes care of the correlation that follows from the fact that the n_k baselines have one antenna in common and matrix Q_{yy} takes care of the precision of the phase and code data. Note that, for the simplicity of the formulation, we assumed that all receivers/antennas track the same set of satellites. However, this restriction is relaxed in the software implemented using Matlab. Also, since the unit line-of-sight vectors of two antennas on a short baseline considered in this work ($\leq$10 km) to the same satellite are the same for all practical purposes, we have $G^k = G$.

2.1.2 The Body-Frame Antenna-Geometry as Multivariate Constraints

The strength of the above model can be increased by including information about the geometry of the antenna configuration. The known body-frame antenna-geometry can be included into the above model through the parametrization

$$B^k = R^k B_0^k \tag{3}$$

with the unknown $3 \times q_k$ orthogonal matrix R^k ($R^{k^T} R^k = I_{q_k}$) and the known $q_k \times n_k$ matrix B_0^k describing the known geometry of the antenna configuration in the body frame. Here, q_k is the degree of geometrical independence of the GNSS baselines, for example, $q_k = 1$ for co-linearly installed antennas, $q_k = 2$ for co-planarly installed antennas, and $q_k = 3$ for antennas installed not in a single plane. For $q_k = 3$, R^k is related to the Euler attitude angles $\xi = [\phi\ \theta\ \psi]^T$ as follows:

$$R(\xi) = \begin{bmatrix} c_\theta c_\phi & -c_\psi s_\phi + s_\psi s_\theta c_\phi & s_\psi s_\phi + c_\psi s_\theta c_\phi \\ c_\theta s_\phi & c_\psi c_\phi + s_\psi s_\theta s_\phi & -s_\psi c_\phi + c_\psi s_\theta s_\phi \\ -s_\theta & s_\psi c_\theta & c_\psi c_\theta \end{bmatrix} \quad (4)$$

with ϕ the heading, θ the elevation, ψ the bank, and where $s_\alpha = \sin(\alpha)$ and $c_\alpha = \cos(\alpha)$.

Substitution of (3) into (1), leads to the constrained GNSS attitude model (Giorgi et al. 2012; Teunissen 2012)

$$\mathrm{E}(Y^k) = AZ^k + GR^k B_0^k \qquad Z^k \in \mathbb{Z}^{m\times n_k} \quad (5)$$

$$\mathrm{D}(\mathrm{vec}(Y^k)) = Q_{Y^kY^k} = P^k \otimes Q_{yy} \qquad R^k \in \mathbb{O}^{3\times q_k} \quad (6)$$

Our objective is to solve for the attitude matrix R^k in a least-squares sense, thereby taking the integer constraints on matrix $Z^k \in \mathbb{Z}^{m\times n_k}$ and the orthonormality constraints on matrix $R^k \in \mathbb{O}^{3\times q_k}$ into account. Hence, the least-squares minimization problem that will be solved reads

$$\min_{\substack{Z^k\in\mathbb{Z}^{m\times n_k},\\ R^k\in\mathbb{O}^{3\times q_k}}} \left\|\mathrm{vec}\left(Y^k - AZ^k - GR^k B_0^k\right)\right\|^2_{Q_{Y^kY^k}} \quad (7)$$

with $||\cdot||^2_Q = (\cdot)^T Q^{-1}(\cdot)$. This is a mixed integer nonlinear least-squares problem that does not permit a closed-form solution. We now describe how (7) can be solved.

2.1.3 The Real-Valued Float Solution

The float solution is defined as the solution of (7) without the constraints. When we ignore the integer constraints on Z^k and the orthonormality constraints on R^k, the float solutions $\hat{Z}^k$ and $\hat{R}^k$, and their variance-covariance matrices are obtained from solving the system of normal equations:

$$\begin{bmatrix} Q_{\hat{z}^k\hat{z}^k} & Q_{\hat{z}^k\hat{R}^k} \\ Q_{\hat{R}^k\hat{z}^k} & Q_{\hat{R}^k\hat{R}^k} \end{bmatrix}^{-1} \begin{bmatrix} \mathrm{vec}(\hat{Z}^k) \\ \mathrm{vec}(\hat{R}^k) \end{bmatrix} = \mathcal{A}_k^T Q_{Y^kY^k}^{-1} \mathrm{vec}(Y^k) \quad (8)$$

with

$$\begin{bmatrix} Q_{\hat{z}^k\hat{z}^k} & Q_{\hat{z}^k\hat{R}^k} \\ Q_{\hat{R}^k\hat{z}^k} & Q_{\hat{R}^k\hat{R}^k} \end{bmatrix} = \left(\mathcal{A}_k^T Q_{Y^kY^k}^{-1} \mathcal{A}_k\right)^{-1}, \mathcal{A}_k = \begin{bmatrix} I_{n_k} \otimes A^T \\ B_0^k \otimes G^T \end{bmatrix}^T$$

The Z^k-constrained solution of R^k and its variance-covariance matrix can be obtained from the float solution as follows

$$\mathrm{vec}\left(\hat{R}^k(Z^k)\right) = \mathrm{vec}(\hat{R}^k) - Q_{\hat{R}^k\hat{z}^k} Q_{\hat{z}^k\hat{z}^k}^{-1} \mathrm{vec}\left(\hat{Z}^k - Z^k\right) \quad (9)$$

$$Q_{\hat{R}^k(Z^k)\hat{R}^k(Z^k)} = Q_{\hat{R}^k\hat{R}^k} - Q_{\hat{R}^k\hat{z}^k} Q_{\hat{z}^k\hat{z}^k}^{-1} Q_{\hat{z}^k\hat{R}^k} = \left(B_0^k P^{k^{-1}} B_0^{k^T}\right)^{-1} \otimes \left(G^T Q_{yy}^{-1} G\right)^{-1} \quad (10)$$

Using the above estimators, the original problem in (7) can be decomposed as

$$\begin{aligned} &\min_{\substack{Z^k\in\mathbb{Z}^{m\times n_k},\\ R^k\in\mathbb{O}^{3\times q_k}}} \left\|\mathrm{vec}\left(Y^k - AZ^k - GR^k B_0^k\right)\right\|^2_{Q_{Y^kY^k}} \\ &= \left\|\mathrm{vec}\left(\hat{E}^k\right)\right\|^2_{Q_{Y^kY^k}} + \min_{Z^k\in\mathbb{Z}^{m\times n_k}} \left(\left\|\mathrm{vec}\left(\hat{Z}^k - Z^k\right)\right\|^2_{Q_{\hat{z}^k\hat{z}^k}} \right. \\ &\quad \left. + \min_{R^k\in\mathbb{O}^{3\times q_k}} \left\|\mathrm{vec}\left(\hat{R}^k(Z^k) - R^k\right)\right\|^2_{Q_{\hat{R}^k(Z^k)\hat{R}^k(Z^k)}} \right) \end{aligned} \quad (11)$$

with $\hat{E}^k = Y^k - A\hat{Z}^k - G\hat{R}^k B_0^k$ being the matrix of least-squares residuals. Note that the first term on the right hand side is constant, as it does not depend on the unknown matrices Z^k and R^k.

2.1.4 The Integer Ambiguity Solution

Based on the orthogonal decomposition (11), the multivariate constrained integer minimization can be formulated as:

$$\check{Z}^k = \arg \min_{Z^k\in\mathbb{Z}^{m\times n_k}} C^k(Z^k) \quad (12)$$

where

$$C^k(Z^k) = \left\|\mathrm{vec}(\hat{Z}^k - Z^k)\right\|^2_{Q_{\hat{z}^k\hat{z}^k}} + \left\|\mathrm{vec}\left(\hat{R}^k(Z^k) - \check{R}^k(Z^k)\right)\right\|^2_{Q_{\hat{R}^k(Z^k)\hat{R}^k(Z^k)}} \quad (13)$$

with

$$\check{R}^k(Z^k) = \arg \min_{R^k\in\mathbb{O}^{3\times q_k}} \left\|\mathrm{vec}\left(\hat{R}^k(Z^k) - R^k\right)\right\|^2_{Q_{\hat{R}^k(Z^k)\hat{R}^k(Z^k)}} \quad (14)$$

The ambiguity objective function $C^k(Z^k)$ is the sum of two coupled terms: the first weighs the distance from the float ambiguity matrix $\hat{Z}^k$ to the nearest integer matrix Z^k in the metric of $Q_{\hat{z}^k\hat{z}^k}$, while the second weighs the distance from the conditional float solution $\hat{R}^k(Z^k)$ to the nearest orthonormal matrix R^k in the metric of $Q_{\hat{R}^k(Z^k)\hat{R}^k(Z^k)}$.

2.1.5 The Ambiguity Resolved Attitude Solution

Finally, we obtain the integer ambiguity resolved attitude solution by substituting $\check{Z}^k$ into (9), thus giving $\hat{R}^k(\check{Z}^k)$. The sought-for attitude angles $\xi^k\left(\check{Z}^k\right)$ are then given by reparametrized solution of (14). Using a first order approximation, the formal variance-covariance matrix of the attitude angles is given by

$$Q_{\xi^k\xi^k} \approx \left(J^T_{R^k,\xi^k} Q^{-1}_{\hat{R}^k(Z^k)\hat{R}^k(Z^k)} J_{R^k,\xi^k}\right)^{-1} \tag{15}$$

where J_{R^k,ξ^k} is the Jacobian of $\xi^k(R^k)$. As the results in the next sections show, this first order approximation works well. This can be explained by the fact that once the ambiguities have been resolved, the precision of the attitude solution is driven by the high precision of the carrier phase observations.

2.2 Recursive Attitude Filtering

The epoch-by-epoch MC-LAMBDA attitude solution is further processed using Unscented Kalman Filter (UKF) (Julier and Uhlmann 1997). For a nadir looking satellite (i.e., for small θ and ψ), the kinematic equations of the attitude angles are given as Nadarajah et al. (2012)

$$\xi_i = F\xi_{i-1} + v_{i-1} \tag{16}$$

where the state vector $\xi_i = \left[\phi_i\ \dot{\phi}_i\ \theta_i\ \dot{\theta}_i\ \psi_i\ \dot{\psi}_i\right]^T$ consists of attitude angles and angular rates, and the state transition matrix F is given as

$$F = I_3 \otimes \begin{bmatrix} 1 & T \\ 0 & 1 \end{bmatrix} \tag{17}$$

where T is the sampling interval. The process noise v_{i-1} has a zero mean normal distribution with variance-covariance matrix $Q_{vv,i-1}$, which is given as

$$Q_{vv,i-1} = \mathrm{diag}\left([\sigma^2_\phi,\ \sigma^2_\theta,\ \sigma^2_\psi]\right) \otimes \begin{bmatrix} T^3/3 & T^2/2 \\ T^2/2 & T \end{bmatrix} \tag{18}$$

with σ_ϕ, σ_θ, and σ_ψ the process noise standard deviations. The observation model reads

$$\zeta_i = h(\xi_i) + w_i \tag{19}$$

with ζ_i given by $\left(\hat{R}^k(\check{Z}^k)\right)$ at epoch i. The nonlinear observation function $h(\xi_i)$ is defined by (4), and the observation noise w_i is assumed to have a zero mean normal distribution with covariance matrix $Q_{ww,i}$, which is given by $Q_{\hat{R}^k(\check{Z}^k)\hat{R}^k(\check{Z}^k)}$ at epoch i.

3 Between-Platform Processing

This section describes the between-platform processing involving relative positioning between two platforms equipped with arrays of GNSS receivers/antennas. First the combined observation model for all independent baselines among all receivers on both platforms is described. Then we describe attitude-bootstrapping showing how platform arrays improve the between-platform baseline estimate.

3.1 Integrated Between-Platform Model

Let us consider two platforms carrying $n_1 + 1$ and $n_2 + 1$ receivers/antennas. The functional and stochastic models for the between-platform baseline formed by the first antennas (pivot antennas) read

$$\mathrm{E}(y^{12}) = Az^{12} + Gb^{12} \qquad z^{12} \in \mathbb{Z}^m \tag{20}$$

$$\mathrm{D}(y^{12}) = Q_{yy} \tag{21}$$

where y^{12} is the between-platform double difference observables, z^{12} is the unknown between-platform double difference ambiguities, and b^{12} is the unknown between-platform baseline. Note that, atmosphere delays are not considered in this formulation as troposphere delays are absent for LEO scenario and ionosphere delays can be ignored for short baseline (<10 km) considered in this work. However, these atmosphere delays must be taken into account for general long baseline scenarios (Teunissen 2012).

By combining between-platform observables in (20) and platform array observables in (5), the functional and stochastic models of the integrated system read

$$\mathrm{E}\left(\mathcal{Y}\right) = A\mathcal{Z} + G\mathcal{R}B_0 \tag{22}$$

$$\mathrm{D}\left(\mathrm{vec}(\mathcal{Y})\right) = P \otimes Q_{yy} \tag{23}$$

where

$$\mathcal{Y} = \begin{bmatrix} Y^1 & Y^2 & y^{12} \end{bmatrix} \tag{24}$$

$$\mathcal{R} = \begin{bmatrix} R^1 & R^2 & b^{12} \end{bmatrix} \in \mathbb{R}^{3\times(q_1+q_2+1)} \tag{25}$$

$$\mathcal{Z} = \begin{bmatrix} Z^1 & Z^2 & z^{12} \end{bmatrix} \in \mathbb{Z}^{m\times n_t} \tag{26}$$

$$B_0 = \begin{bmatrix} B^1_0 & 0 & 0 \\ 0 & B^2_0 & 0 \\ 0 & 0 & 1 \end{bmatrix} \tag{27}$$

$$P = \begin{bmatrix} P_{n_1} & 0 & \frac{1}{2}e_{n_1} \\ 0 & P_{n_2} & -\frac{1}{2}e_{n_2} \\ \frac{1}{2}e_{n_1}^T & -\frac{1}{2}e_{n_2}^T & 1 \end{bmatrix} \tag{28}$$

with $n_t = n_1 + n_2 + 1$ and e_{n_k} the n_k-vector of ones. The above system consists of attitude models of both platforms with unknowns Z^k and R^k, and between-platform baseline model with unknowns z^{12} and b^{12} . Even though these three subsystems do not have any parameter in common, they are correlated as in (28) due to the use of common observations from pivot antennas.

3.2 Attitude Bootstrapping

Attitude bootstrapping method (Buist et al. 2011; Teunissen 2012) uses decorrelation technique to decouple the combined system in (22) such that the subsystems still yield the optimal solution. This decorrelation keeps the platform processing intact as in (12), while between-platform ambiguity estimation becomes as

$$\breve{z}^{12} = \arg \min_{z^{12} \in \mathbb{Z}^m} \left\| \hat{z}'^{12} - z'^{12} \right\|^2_{Q_{\hat{z}'^{12}\hat{z}'^{12}}} \tag{29}$$

where

$$z'^{12} = z^{12} - \frac{e_{n_1}^T \otimes I_m}{n_1 + 1} \mathrm{vec}(Z^1) + \frac{e_{n_2}^T \otimes I_m}{n_2 + 1} \mathrm{vec}(Z^2) \tag{30}$$

with $\hat{z}'^{12}$ and $\breve{z}'^{12}$ having similar function, and

$$Q_{\hat{z}'^{12}\hat{z}'^{12}} = \eta Q_{\hat{z}^{12}\hat{z}^{12}} \tag{31}$$

with $Q_{\hat{z}^{12}\hat{z}^{12}}$ the variance-covariance matrix of float ambiguities for the standard relative positioning model in (20) and $\eta = \frac{n_t+1}{2(n_1+1)(n_2+1)}$ (Giorgi 2011). The ambiguity fixed baseline solution is then given as

$$\hat{b}'^{12}(\breve{z}'^{12}) = \hat{b}'^{12} - Q_{\hat{b}'^{12}\hat{z}'^{12}} Q^{-1}_{\hat{z}'^{12}\hat{z}'^{12}} \left(\hat{z}'^{12} - \breve{z}'^{12} \right) \tag{32}$$

with the associated variance-covariance matrix

$$Q_{\hat{b}'^{12}(z'^{12})\hat{b}'^{12}(z'^{12})} = \eta Q_{\hat{b}^{12}(z^{12})\hat{b}^{12}(z^{12})} \tag{33}$$

where

$$b'^{12} = b^{12} - \frac{e_{n_1}^T B_0^{1^T} \otimes I_3}{n_1 + 1} \mathrm{vec}(R^1) + \frac{e_{n_2}^T B_0^{2^T} \otimes I_3}{n_2 + 1} \mathrm{vec}(R^2)$$

with $\hat{b}'^{12}$ having similar function and $Q_{\hat{b}^{12}(z^{12})\hat{b}^{12}(z^{12})}$ is the variance-covariance matrix of ambiguity fixed baseline estimates for the standard relative positioning model in (20). Decorrelation allows first performing attitude determination for individual platforms and then estimating between-platform baseline with the help of reliable estimation of platform ambiguities using MC-LAMBDA method. The use of an array reduces the variance-covariance matrices of float ambiguities and ambiguity fixed baseline estimates by a factor of η. Note that, the between-platform baseline is now measured between centroids of antenna arrays (Teunissen 2012).

Table 1 Orbit specification for the simulated LEO satellites

Semi major axis	7,058.14 km
Inclination	98.0443°
Right ascension	−90.046°
Eccentricity	0
Mean anomaly	0°
Argument of perigee	0°

3.3 Recursive Baseline Filtering

The epoch-by-epoch baseline solution in Sect. 3.2 is further processed using UKF. Satellite relative motion in Earth-centered inertial frame is given by Park (2001)

$$\ddot{b} = \mu \left(\frac{r_1}{\|r_1\|^3} - \frac{r_1 + b}{\sqrt{\left(\|r_1\|^2 + 2r_1^T b + \|b\|^2 \right)^3}} \right) \tag{34}$$

where $\ddot{b}$ is the second derivative of baseline vector b, μ is the Earth gravitational constant, and r_1 is the absolute position of the first platform. Discretized model using the fourth-order Runge-Kutta method is used to filter the epoch-by-epoch baseline estimate in (32).

4 Results

This section describes the hardware-in-the-loop experiment with the Namuru receivers conducted at UNSW and it presents results of both attitude determination and between-platform baseline estimation. In the experiment, the NamuruV3.2Rx receiver was connected to a Spirent GSS6560 simulator tracking GPS signals. The simulated scenario is based on orbital parameters given in Table 1 having two LEO satellites 5 km apart. Figure 2 shows the trajectory of the satellites. These nadir looking satellites are equipped with three antennas/receivers forming the following antenna geometry

$$B_0^k = \begin{bmatrix} 1 & 0 \\ 0 & 1 \end{bmatrix} \quad [\mathrm{m}], \quad k = 1, 2 \tag{35}$$

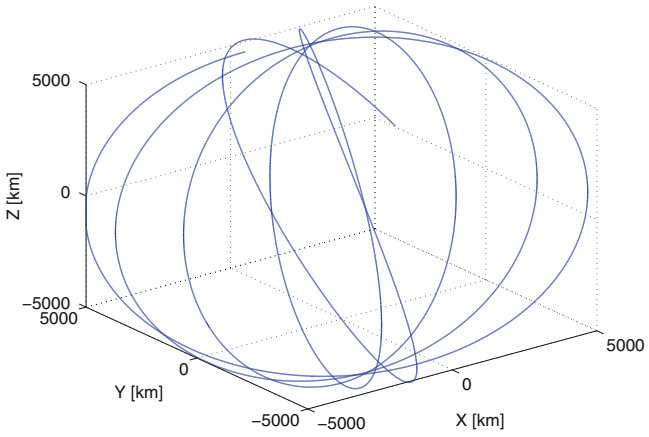

Fig. 2 Satellite trajectory in WGS84 coordinate system

Table 2 Empirical instantaneous ambiguity resolution success rate (%) for platform processing

Platform	LAMBDA	MC-LAMBDA
1	88.5	100
2	93.1	100

Table 3 Root mean square errors (RMSEs) for attitude estimates (deg)

	Platform	Heading	Elevation	Bank
Epoch-by-epoch	1	0.05	0.19	0.19
	2	0.04	0.16	0.16
Filtered	1	0.03	0.03	0.03
	2	0.02	0.05	0.05

Full GPS constellation with L1 frequency was simulated for about eight hours resulting in 27,962 epochs of data.

4.1 Attitude Results

Table 2 reports the single-frequency, single-epoch success rate of MC-LAMBDA method compared with that of standard LAMBDA method. As shown, the use of the known antenna geometry enhances the integer resolution success rate by about 10%. Table 3 reports the root mean squared errors (RMSEs) for the estimates. For recursive filtering, we used process noise standard deviations of $\sigma_\phi = 0.004°s^{-\frac{3}{2}}$ and $\sigma_\theta = \sigma_\psi = 0.0001°s^{-\frac{3}{2}}$. These choices can be justified by the very low variations of elevation and bank angles for a nadir looking satellite. For epoch-by-epoch solution, the heading angle, which is determined by horizontal position components, is estimated with highest precision. Filtering significantly improves the accuracy of the elevation and bank estimates. This is due to the use of the a priori knowledge of the attitude dynamics.

Table 4 Empirical instantaneous single-frequency ambiguity resolution success rate (%) for between platform processing

Standard baseline processing	Attitude bootstrapping
90.1	97.4

Table 5 Position accuracy: RMSE (cm)

	Standard baseline processing	Attitude bootstrapping
Float solution	230	137
Fixed solution	0.412	0.249
Filtered solution	0.213	0.141

4.2 Baseline Results

Table 4 reports the single-frequency, single-epoch success rate of attitude bootstrapping method compared with that of standard baseline processing demonstrating the improved success rate performance due to the use of an array of antennas. Table 5 summarizes baseline RMSE values for both standard baseline processing and attitude bootstrapping methods. Filtering further improves the baseline estimates. A factor of $\sqrt{3}$ improvement for three antennas per platform can be observed in the case of array-aided processing (33).

5 Conclusions

In this contribution, we explored the use of arrays of GNSS antennas for attitude determination and relative positioning of formation flying LEO satellites. The MC-LAMBDA method exploits the known antenna geometry to improve reliability of resolving platform ambiguities and hence to improve the estimation of the platform attitude. Furthermore, reliable estimation of platform ambiguities enables strengthening between-platform baseline model through attitude bootstrapping. Our analysis includes single-frequency epoch-by-epoch processing as well as recursive filtering using nonlinear filters. We demonstrated the improved performance of the proposed method using a hardware-in-the-loop experiment, consisting of two LEO satellites in formation with an inter-satellite distance of 5 km. Array-aided processing not only improves the ambiguity resolution success rate but also improves the position accuracy by a factor of $\sqrt{3}$ for three antennas per platform.

Acknowledgements This work is supported by the Australian Space Research Program GARADA project on SAR Formation Flying. The second author P.J.G. Teunissen is the recipient of an Australian Research Council Federation Fellowship (project number FF0883188). All this support is gratefully acknowledged. The authors also would like to thank Mr Mohammad Choudhury from the University of New South Wales for providing the data set used in this work.

References

Buist PJ, Teunissen PJG, Verhagen S, Giorgi G (2011) A vectorial bootstrapping approach for integrated GNSS-based relative positioning and attitude determination of spacecraft. Acta Astronaut 68(7–8):1113–1125

D'Amico S, Montenbruck O (2010) Differential GPS: an enabling technology for formation flying satellites. In: Sandau R, Roeser HP, Valenzuela A (eds) Small satellite missions for earth observation. Springer, Berlin, pp 457–465

Duncan SM, Hodgart MS, Unwin MJ, Hebden R (2007) In-orbit results from a space-borne GPS attitude experiment. In: Proceedings of the 20th international technical meeting of the satellite division of the institute of navigation (ION GNSS 2007), Fort Worth, pp 2412–2423

Gill E, Montenbruck O, D'Amico S (2007) Autonomous formation flying for the PRISMA mission. J Spacecr Rocket 44(3):671–681

Giorgi G (2011) GNSS carrier phase-based attitude determination estimation and applications. Ph.D. thesis, Delft University of Technology

Giorgi G, Teunissen PJG, Verhagen S, Buist PJ (2012) Instantaneous ambiguity resolution in Global-Navigation-Satellite-System-based attitude determination applications: a multivariate constrained approach. J Guid Control Dyn 35(1):51–67

Harville DA (1997) Matrix algebra from a statistician's perspective. Springer, New York

Julier S, Uhlmann J (1997) A new extension of the Kalman filter to nonlinear systems. In: Proceedings of Aerosense: 11th international symposium on aerospace/defense sensing, simulation and controls, Spie Bellingham, pp 182–193

Kawano I, Mokuno M, Miyano T, Suzuki T (2000) Analysis and evaluation of GPS relative navigation using carrier phase for RVD experiment satellite of ETS-VII. In: Proceedings of the 13th international technical meeting of the satellite division of the institute of navigation (ION GPS 2000), Salt Lake City, pp 1655–1660

Montenbruck O, Markgraf M, Garcia-Fernandez M, Helm A (2007) GPS for microsatellites – status and perspectives. In: Proceedings of 6th IAA symposium on small satellites for earth observation, Berlin, pp 165–174

Nadarajah N, Teunissen PJG, Buist PJ (2012) Attitude determination of LEO satellites using an array of GNSS sensors. In: 15th international conference on information fusion (FUSION) 2012, Singapore, pp 1066–1072

Park CW (2001) Precise relative navigation using augmented CDGPS. Ph.D. thesis, Stanford University

Parkinson KJ, Mumford PJ, Glennon EP, Shivaramaiah NC, Dempster AG, Rizos C (2011) A low cost Namuru V3 receiver for spacecraft operations. In: Proceedings of IGNSS symposium, Sydney, pp 1–8

Teunissen PJG (2007) A general multivariate formulation of the multi-antenna GNSS attitude determination problem. Artif Satell 42(2):97–111

Teunissen PJG (2012) A-PPP: Array-aided precise point positioning with global navigation satellite systems. IEEE Trans Signal Process 60(6):2870–2881

Combination of Ground- and Space-Based GPS Data for the Determination of a Multi-scale Regional 4-D Ionosphere Model

Wenjing Liang, Marco Limberger, Michael Schmidt, Denise Dettmering, and Urs Hugentobler

Abstract

In this paper, we present a four-dimensional (4-D) electron density model. The vertical distribution of the electron density is described by a F2-layer Chapman function combined with a plasmasphere layer function. The F2-layer peak density *NmF*2 and the peak height *hmF*2 are spatially and temporally modeled as 3-D series expansions in terms of localized B-spline functions depending on geographical longitude, latitude and time. The corresponding unknown series coefficients are estimated by a linearized model through an appropriate parameter estimation procedure. The input data are ground-based GPS data combined with electron density profiles retrieved from ionospheric GPS radio occultation measurements onboard the FORMOSAT-3/COSMIC, GRACE and CHAMP satellites, in order to compensate the insensitivity of the ground-based GPS data to the height parameter *hmF*2 as well as benefit from their different spatiotemporal resolutions. We verify our approach by measurements exemplarily over South and Central America for a selected time span during a solar minimum day 2008-07-01. Based on the B-spline method, we demonstrate an effective data compression by applying a multi-scale representation for the estimated coefficients derived from wavelet analysis.

Keywords

B-splines • Electron density • F2-layer • GPS • Ionosphere • Multi-scale representation • Radio occultation

1 Introduction

It is well known that the ionospheric delay is the most important error source for Global Navigation Satellite Systems (GNSS) such as the Global Positioning System (GPS). In contrast to dual-frequency GPS users, single frequency users have to eliminate the ionospheric error relying on an ionosphere model. With the rapid development of modern satellite missions, many efforts have been made for high precision ionosphere modeling. The 4-D electron density distribution is of the highest modeling interest since it is directly reflecting the actual state of the ionosphere. In order to reduce modeling difficulties, different mathematical representations have been exploited to describe the vertical structure of the ionosphere where the physics-motivated Chapman function (Davies 1990) is one of the most frequently used representations. Various modeling efforts have been made based on the Chapman function for a long time. For example, a Chapman function which assumes constant scale height along the whole profile is employed by e.g. Feltens (1998), Alizadeh (2013), and Reinisch et al. (2007) developed the Vary-Chap function with continuously varying scale height

W. Liang (✉) • M. Limberger • M. Schmidt • D. Dettmering
Deutsches Geodätisches Forschungsinstitut der Technischen Universität München (DGFI-TUM), Alfons-Goppel-Str. 11, 80539 Munich, Germany
e-mail: wenjing.liang@tum.de

U. Hugentobler
Forschungseinrichtung Satellitengeodäsie (FESG), Technische Universität München (TUM), Arcisstr. 21, 80333 Munich, Germany

© Springer International Publishing Switzerland 2015

C. Rizos, P. Willis (eds.), *IAG 150 Years*, International Association of Geodesy Symposia 143,
DOI 10.1007/1345_2015_25

to model the topside electron density. Without considering the height component, the modeling quantity can also be the 3-D spatiotemporal Vertical Total Electron Content (VTEC) which integrates the electron density along the vertical direction (e.g., Schaer 1999; Hernández-Pajares et al. 2009). The major input data for ionosphere modeling are GNSS observations due to their dense distribution. In order to take the advantage of individual sensitivity as well as different spatial and temporal resolutions, the combination of various techniques is applied in some research groups. For example, Todorova et al. (2007) combined GNSS observations and satellite altimetry data for global VTEC calculation; more recently Dettmering et al. (2011) calculated regional VTEC based on a combination of space-geodetic observations including ground-based GPS observations, radio occultation data from Low Earth Orbiters (LEO), dual-frequency radar altimetry measurements and data obtained by Very Long Baseline Interferometry (VLBI).

In this study, we apply an α-Chapman function for the F2-layer combined with a plasmasphere layer to describe the height dependency of the electron density (Jakowski 2005). B-spline functions are efficient for handling the data gaps due to their compactly supported features (Schmidt et al. 2011), the key parameters $NmF2$ and $hmF2$ are therefore represented regionally by tensor products of localized B-spline functions depending on geographical longitude, latitude and time. In this manner a 4-D electron density model is established considering some physical features. Ground-based GNSS observations provide the integrated ionospheric information in terms of Slant Total Electron Content (STEC). The insensitivity of STEC from GNSS data w.r.t. height parameter (e.g., $hmF2$) is compensated by pointwise vertical electron density profiles retrieved from space-based GNSS ionospheric radio occultation (IRO) measurements. We combine STEC from GPS observations with the electron density profiles from IRO data to solve the unknown model parameters. Since B-spline functions are applied, a multi-scale representation (MSR) can be derived from wavelet analysis which allows data compression (Schmidt 2007). In the following, we first introduce the modeling approach (Sect. 2) and then the input data (Sect. 3). After that we apply the developed model and evaluate the results in Sect. 4. Section 5 concludes the paper.

2 Modeling Approach

The electron density distribution $N_e(h)$ depending on height h is modeled by a Chapman layer whose topside is extended by a slowly decaying exponential term describing the plasmaspheric electron density with a fixed scale height, namely

$$\begin{aligned} N_e(h) \;&= NmF2 \cdot \exp\left(\frac{1 - z - \exp(-z)}{2}\right) \\ &+ \; N0P \cdot \exp\left(-\frac{|h - hmF2|}{HP}\right) \end{aligned} \tag{1}$$

with $z = (h - hmF2)/HF2$ and $HP = 10\,\text{km}$ for $h < hmF2$ (bottomside), and $HP = 10^4\,\text{km}$ for $h \geq hmF2$ (topside) (Jakowski 2005). It includes five key parameters, namely $NmF2$, $hmF2$, the scale height $HF2$, the plasmasphere basis density $N0P$ and the corresponding scale height HP. This paper deals with the two most important parameters $NmF2$ and $hmF2$, whereas the other three parameters are fixed. Specifically, $HF2$ and $N0P$ are taken from an existing model (e.g., the International Reference Ionosphere (IRI); see Bilitza and Reinisch 2007) with some reasonable assumptions. $HF2$ is calculated by the ionospheric slab thickness τ as $HF2 = \tau/4.13 = VTEC/(4.13 \cdot NmF2)$ according to Davies (1990), $N0P$ is assumed to be 1% of $NmF2$ to keep the plasmaspheric contribution in Eq. (1) small.

The two key parameters (e.g., $hmF2$) are modeled as the series expansion

$$\begin{aligned} &hmF2(\lambda, \varphi, t) \\ &\quad = \sum_{k_1=1}^{K_{J_1}} \sum_{k_2=1}^{K_{J_2}} \sum_{k_3=1}^{K_{J_3}} d_{k_1,k_2,k_3}^{J_1,J_2,J_3}\, \phi_{k_1}^{J_1}(\lambda)\, \phi_{k_2}^{J_2}(\varphi)\, \phi_{k_3}^{J_3}(t) \end{aligned} \tag{2}$$

in terms of tensor products of three 1-D base functions $\phi_k^J(x)$ with $x \in \{\lambda, \varphi, t\}$ depending on geographical longitude λ, latitude φ and time t with unknown series coefficients $d_{k_1,k_2,k_3}^{J_1,J_2,J_3}$; see Schmidt (2007). As we deal with a regional problem, we use endpoint-interpolating normalized quadratic B-splines as 1-D scaling functions of resolution level $J \in \mathbb{N}_0$ with shift $k = 1, \ldots, K_J$ and total number $K_J = 2^J + 2$ (Lyche and Schumaker 2001).

In this study observations are STEC from ground-based GPS data or electron density profiles from IRO measurements. Since $STEC$ is defined as the integral $STEC = \int_R^S N_e \cdot ds$ of the electron density N_e along the ray-path between satellite S and receiver R, these observations can be represented as a function of the two target parameters $NmF2$ and $hmF2$ based on Eq. (1), which in turn can again be written as a function of the B-spline scaling parameters according to Eq. (2). Since Eq. (1) is non-linear w.r.t. $hmF2$, a linearization is set up using the Taylor expansion and therefore initial values are necessary. To collect the total number $K_{J_1,J_2,J_3} = K_{J_1} \cdot K_{J_2} \cdot K_{J_3}$ of all series coefficients $d_{k_1,k_2,k_3}^{J_1,J_2,J_3}$ for $NmF2$ and $hmF2$ according to Eq. (2) in a vector $\boldsymbol{d}$, the unknown coefficient vector $\boldsymbol{d}$ is decomposed into an

initial coefficient vector $\boldsymbol{d}_0$ and a correction $\Delta\boldsymbol{d}$, i.e., $\boldsymbol{d} = \boldsymbol{d}_0 + \Delta\boldsymbol{d}$. The vector $\boldsymbol{d}_0$ can be derived from a known model (e.g., IRI-2007). To estimate the vector $\Delta\boldsymbol{d}$ we formulate a Gauss-Markov model for a certain observation group by introducing the stochastic part considering the given positive definite $n \times n$ weight matrix $\boldsymbol{P}_l$ of n observations and the unknown variance factor σ_l^2

$$\boldsymbol{l} + \boldsymbol{e}_l = \boldsymbol{A}\,\Delta\boldsymbol{d} \quad \text{with} \quad D(\boldsymbol{l}) = \sigma_l^2 \boldsymbol{P}_l^{-1} \tag{3}$$

with observation error vector $\boldsymbol{e}_l$. The vector $\boldsymbol{l}$ collects the differences between the observations and the initial values. As GNSS stations are heterogeneously distributed and the electron density profiles are rather sparse, prior information for the expectation vector $E(\boldsymbol{d}) = \boldsymbol{\mu}_d$ of the coefficients and the covariance matrix $D(\boldsymbol{d}) = \boldsymbol{\Sigma}_d = \boldsymbol{P}_d^{-1}$ are introduced. It means that in regions with data gaps the prior information can be interpreted as an additional observation technique. In this study we use IRI-2007 to derive both the priori information and the vector $\boldsymbol{d}_0$ for the linearization.

To combine STEC from GPS observations with electron density profiles from IRO data onboard different LEO satellite missions, an appropriate weighting scheme is applied to take different accuracy levels into account. The normal equation combining the p different observation groups and the prior information reads

$$\begin{aligned}\left(\sum_{m=1}^{p} \frac{1}{\sigma_m^2}\boldsymbol{A}_m^T\boldsymbol{P}_m\boldsymbol{A}_m + \frac{1}{\sigma_d^2}\boldsymbol{P}_d\right)\widehat{\Delta\boldsymbol{d}} \\ = \sum_{m=1}^{p} \frac{1}{\sigma_m^2}\boldsymbol{A}_m^T\boldsymbol{P}_m\boldsymbol{Y}_m + \frac{1}{\sigma_d^2}\boldsymbol{P}_d(\boldsymbol{\mu}_d - \boldsymbol{d}_0)\end{aligned} \tag{4}$$

(Dettmering et al. 2011). The unknown variance factors σ_m^2 and σ_d^2 indicate the different accuracy levels and can be either chosen empirically (manually) or estimated automatically within a variance component estimation (VCE), e.g., the fast Monte-Carlo implementation of the iterative maximum-likelihood VCE (Koch and Kusche 2002); the details about VCE implemented in the model are given by Limberger et al. (2013). With the estimated $\widehat{\Delta\boldsymbol{d}}$, the parameters *NmF*2 and *hmF*2 can be constructed everywhere within the investigated area and time interval based on the B-spline approach. Afterwards, the 4-D electron density can be calculated based on Eq. (1).

The B-spline functions are used as scaling functions as explained before, they can also be used for the generation of wavelet functions (Stollnitz et al. 1995), thus MSR can be performed starting from $\widehat{\Delta\boldsymbol{d}}$ estimated in Eq. (4). An important application of MSR is data compression. It can be very helpful for handling large datasets. The basic principle of MSR is to split an input signal into a smoothed version and a certain number of detail signals by successive low-pass filtering. Thus each detail signal is a band-pass filtered version of the input signal, which is represented as a series expansion in terms of wavelet functions with unknown wavelet coefficients. The procedure can be achieved by two steps, namely, the decomposition into level-dependent coefficients, and the reconstruction by means of the detail signals. The decomposition process can be realized by the highly effective pyramid algorithm (Fast Wavelet Transform, FWT). Figure 1 shows the 1-D pyramid generation; through a linear transformation of the scaling coefficient vector $\boldsymbol{d}_J$ estimated at the highest level J (if the B-spline model in Eq. (2) is a 1-D problem instead of 3-D, then $\boldsymbol{d}_J = \widehat{\Delta\boldsymbol{d}}$), the scaling coefficient vector $\boldsymbol{d}_{J-1}$ and the wavelet coefficient vector $\boldsymbol{c}_{J-1}$ at the adjacent lower level $J-1$ are acquired (Schmidt 2007). This procedure is repeated until the lowest level is achieved. Since the whole process is performed by linear transformations, covariance matrices for all the quantities are calculable by applying the law of error propagation. The algorithm for the multi-dimensional case is similar; more details are given by Schmidt (2012). In dependency on the signal energy, the absolute values of many wavelet coefficients are numerically very small due to the localizing property of wavelet functions. Therefore data compression can be applied effectively, e.g., through empirical thresholds or statistical hypothesis testing of significance.

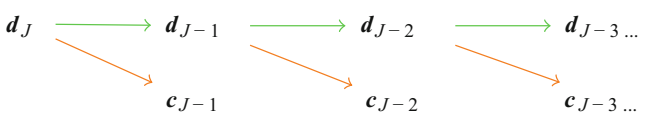

Fig. 1 1-D pyramid algorithm (from *left* to *right*): scaling coefficient vectors (*top*) and wavelet coefficient vectors (*bottom*). The *green arrows* indicate a low-pass filtering, the *orange arrows* a band-pass filtering

3 Input Data

The model is applied to South and Central America. On the one hand, there is an interesting phenomenon called equatorial anomaly; on the other hand, a dense GNSS network SIRGAS-CON (SIRGAS Continuously Operating Network) is available (Sánchez et al. 2013). We use dense GPS observations measured by the permanent reference stations of the SIRGAS-CON network and electron density profiles retrieved from IRO data onboard FORMOSAT-3/COSMIC (Taiwan's Formosa Satellite Mission #3/Constellation Observing System for Meteorology, Ionosphere and Climate, hereafter COSMIC) (Fong et al. 2009), GRACE (Gravity Recovery And Climate Experiment) (Tapley et al. 2004) and CHAMP (CHAllenging Minisatellite Payload) (Reigber et al. 2002), and regard them as four

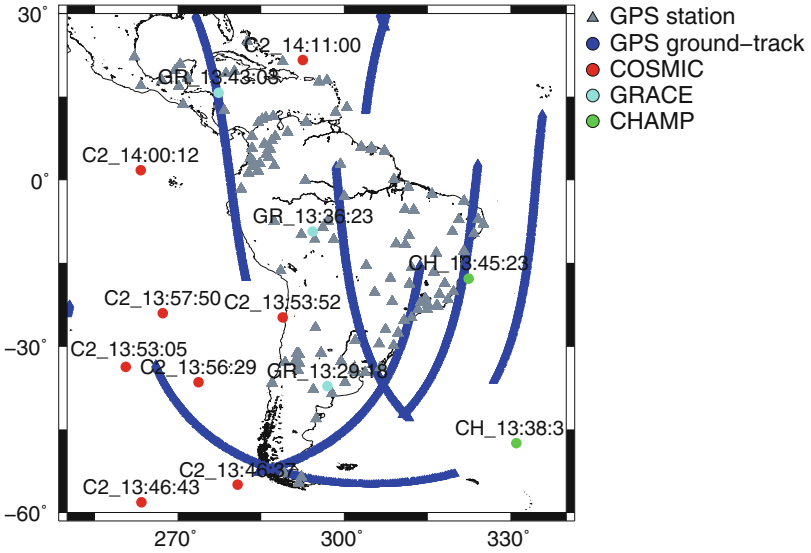

Fig. 2 Data distribution within the study area for the time interval [13, 15] UT on 2008-07-01. The observation time of the electron density profiles are labeled in UT

different groups described in Sect. 2, i.e. $p = 4$ in Eq. (4). To verify our procedure, we apply our model to the data with the selected time slot 13 to 15 UT (Universal Time) during a low solar activity day 2008-07-01. Figure 2 shows the distribution of all data used.

The geometry-free linear combination of the simultaneous GPS observations at the two carriers provides STEC (in unit of TECU, 1 TECU = 10^{16} el/m^2). In order to use the more accurate phase observations instead of more noisy code measurements without solving the ambiguity term, we apply phase leveling for the observations with elevation angle larger than 10° after data-screening. For a satellite pass which is defined by an uninterrupted data arc (without time gaps and cycle slips), a constant offset between the ionospheric path delays derived from code and phase measurements is calculated and used as correction for the phase data; the details about the algorithm used here can be found in Dettmering (2003). Differential code biases (DCBs) for satellites and receivers are estimated as additional unknowns by assuming daily constants per each satellite and each receiver. In order to avoid rank deficiencies, a zero-mean condition ($\sum DCB^S = 0$) is applied as constraint for satellite DCBs similar to the International GNSS Service (IGS) (Dow et al. 2009) method. As no realistic stochastic information about all observations is available, no correlations within the observation groups are introduced in the stochastic part of the Gauss-Markov model in Eq. (3). The amount of observations used is therefore reduced to 10 min sampling interval in order to decrease the temporal correlations. Consequently altogether 120 GPS stations and 9 satellites are available within the investigated time interval.

The vertical electron density profiles derived from IRO data onboard GRACE and CHAMP (Jakowski 2005) are kindly provided by the Institute of Communications and Navigation of the German Aerospace Center (DLR); the ones retrieved from COSMIC IRO data (Tsai et al. 2009) are processed by the Center for Space and Remote Sensing Research (CSRSR) of the National Central University (NCU) in Taiwan. Totally 14 vertical electron density profiles with 8 from COSMIC (2124 measurements), 3 from GRACE (63 measurements) and 2 from CHAMP (48 measurements) are used after eliminating outliers, see Limberger et al. (2013).

4 Numerical Investigation

In order to increase the stability of the linearized model we perform a sequential estimation, i.e., firstly we estimate only $NmF2$ and afterwards take them as the initial values to estimate $NmF2$ and $hmF2$ together. The estimated mean standard deviation of GPS observations is 1.84 TECU and the quantities for COSMIC, GRACE, CHAMP measurements are $2.03 \cdot 10^4$ el/cm^3, $2.91 \cdot 10^4$ el/cm^3 and $1.59 \cdot 10^4$ el/cm^3, respectively. The initial values $NmF2_0$ and $hmF2_0$ based on the vector $\boldsymbol{d}_0$ derived from IRI-2007 are depicted in the first row of Fig. 3. The second row displays the estimated corrections $\widehat{\Delta NmF2}$ and $\widehat{\Delta hmF2}$, and the third one visualizes the estimated final parameter values $\widehat{NmF2}$ and $\widehat{hmF2}$ (i.e., $\widehat{NmF2} = NmF2_0 + \widehat{\Delta NmF2}$, $\widehat{hmF2} = hmF2_0 + \widehat{\Delta hmF2}$), with B-spline levels $J_1 = J_2 = J_3 = 3$ in Eq. (2) for both parameters. It can be seen that significant corrections are obtained in areas with input data (see Fig. 2) and our final estimated parameters describe small-scale structures in comparison with the initial parameters from IRI-2007. For most regions $NmF2$ gets relatively large negative corrections up to $2 \cdot 10^5$ el/cm^3, which indicates that IRI-2007 overestimates $NmF2$ for the selected scenario, while $\widehat{\Delta hmF2}$ can be negative or positive for different regions and reaches minimum −57 km. Bilitza et al. (2012) compared IRI $hmF2$ with the ionosonde measurements at the two low latitude

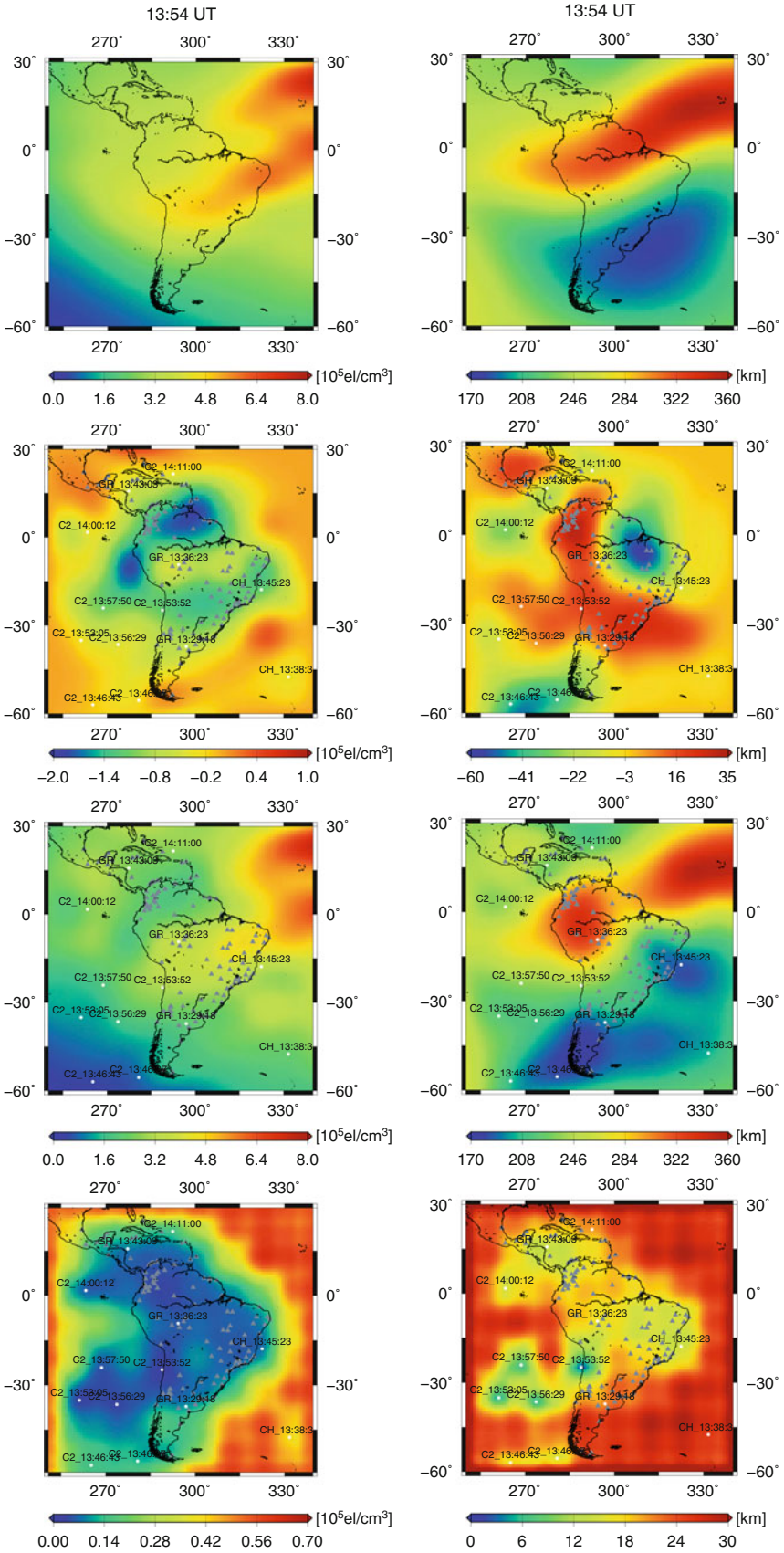

Fig. 3 (*Top*): initial $NmF2_0$ and $hmF2_0$ from IRI-2007; (*second row*): estimated corrections $\widehat{\Delta NmF2}$ and $\widehat{\Delta hmF2}$; (*third row*): estimated final parameters $\widehat{NmF2}$ and $\widehat{hmF2}$; (*bottom*): estimated standard deviations of $\widehat{\Delta NmF2}$ and $\widehat{\Delta hmF2}$ with B-spline levels $J_1 = J_2 = J_3 = 3$

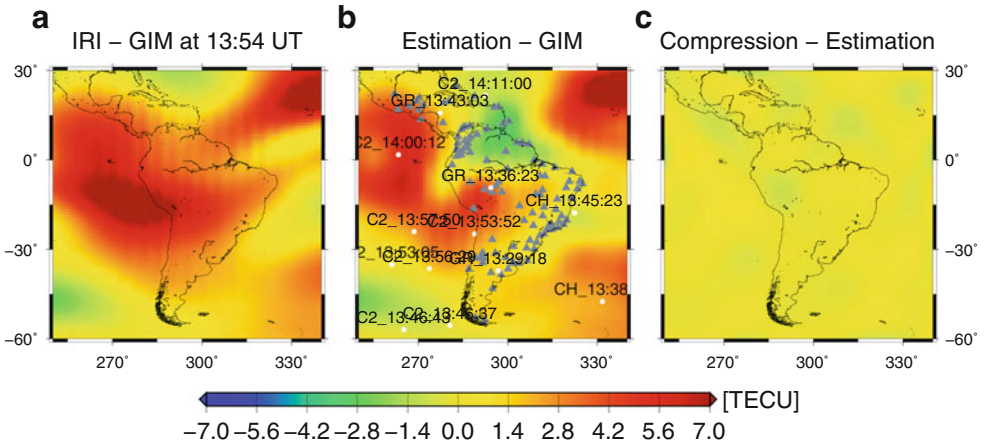

Fig. 4 VTEC comparison: IRI-2007 - GIM (**a**); $\widehat{VTEC}$ - GIM (**b**); $\widehat{VTEC}$ from compressed $NmF2$ - $\widehat{VTEC}$ (**c**)

Brazilian stations Sao Luis (at the magnetic equator) and Cachoeira Paulista (at the edge of the Equatorial Anomaly), and found that IRI overestimated $hmF2$ at Sao Luis by about 40 km and underestimated Cachoeira Paulista by about the same amount during the solar minimum. To look at the same locations, our estimation shows that IRI overestimates $hmF2$ at Sao Luis with a comparable amount of about 35.6 km and underestimates Cachoeira Paulista by a significantly smaller amount of 8.2 km. This exemplary validation indicates the potential of our model to provide reliable results. For a more reliable comparison with IRI, a large data basis should be used in future. If we look at the estimated standard deviations of the parameters shown in the last row, we can see that the precision of $\widehat{\Delta NmF2}$ is higher in the regions with input data and reaches the highest precision about $2.5 \cdot 10^3$ el/cm^3, whereas the precision is around $5 \cdot 10^4$ el/cm^3 over the oceans. The precision of $\widehat{\Delta hmF2}$ is highest of around 2.7 km over the coastline of Chile with one profile available at 13:54 UT and approximately 13 km is reached over the continents. The achieved precision is expected; STEC is insensitive to the $hmF2$ but electron density profiles are pointwise measurements and sensitive, accordingly the highest precision is in the regions with both STEC and electron density profiles available, followed by the areas with only profiles and then the locations with only GPS observations.

Based on $\widehat{NmF2}$ and $\widehat{hmF2}$, we construct $VTEC$ maps according to $\widehat{VTEC} = \int_{80}^{2000} N_e(\widehat{NmF2}, \widehat{hmF2}) \cdot dh$, and compare it with IRI-2007 and IGS GIM (Global Ionospheric Map) (Hernández-Pajares et al. 2009). The IGS GIM is a combination of several ionosphere models provided by IGS Associate Analysis Centres based mainly on GNSS observations from the IGS ground station network. Figure 4a shows the difference of IRI-2007 $VTEC$ and GIM at 13:54 UT with a RMS value of 3.42 TECU. Figure 4b displays the difference of the estimated $\widehat{VTEC}$ and GIM with a relatively smaller RMS value of 2.80 TECU. Comparing these two panels, it is clearly visible that our estimation is closer to GIM over the continent compared with the IRI model. Significant improvements are also shown in the areas with electron density profiles. Especially in the South Pacific Ocean around magnetic equator, the higher deviations (dark red) in the left panel has been improved notably (light red) in the middle panel. It is worth mentioning that the quality of our model depends on the distribution of the observations and the quality of the background model for deriving the prior information. If we look at the right upper corner, this becomes clear since similar large differences (dark red) are visible in both panels. Additionally, as mentioned in Sect. 3, DCBs have to be estimated. A comparison of the estimated DCBs to the IGS ones shows the quantities are quite close.

After the vector $\widehat{\Delta \boldsymbol{d}}$ is obtained from the adjustment system, we perform MSR for it. Figure 5 presents a graphical demonstration of the MSR exemplarily applied to the estimated $\widehat{\Delta NmF2}$ at 13:54 UT shown in Fig. 5a. The ordering of the panels is the same as the arrangement of the coefficient vectors of the pyramid algorithm in Fig. 1, and the panels are calculated from the corresponding quantities. Therefore, the panels b–d depict the low-pass filtered smoothed signals, and the band-pass filtered detail signals are shown in the panels e–g, which contain the information of the difference of the smoothed signals with two adjacent levels in Fig. 5a–d. Hence the sum of the smoothed signal at the lowest level (Fig. 5d) and the three detail signals yields the signal at the highest level (Fig. 5a), which reflects the principle of the MSR. It is obvious that the structures become coarser with decreasing levels.

Since more small-scale structures are contained in the higher-level detail signals, we apply level-dependent thresholds to neglect the coefficients in the wavelet coefficient vectors whose absolute values are smaller than a specified threshold. We choose the threshold $\varrho_{2,2,2}$ for the detail signal at levels $j_1 = j_2 = j_3 = 2$ (for 1-D case, the detail signal starts from $J - 1$ with the highest level $J = 3$) and apply a simple assumption $\varrho_{0,0,0} = 0.5 \cdot \varrho_{1,1,1} = 0.25 \cdot \varrho_{2,2,2}$ to get level-dependent thresholds. Since more wavelet

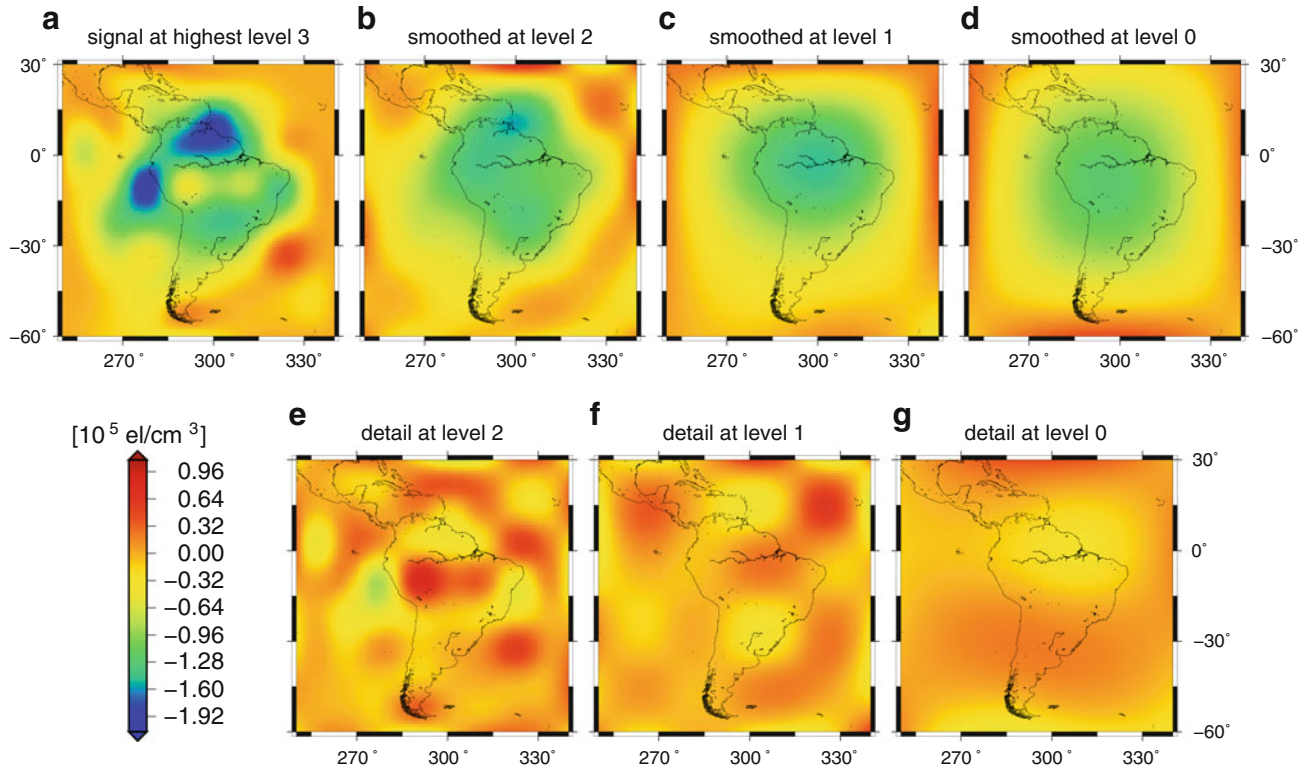

Fig. 5 MSR of estimated $\widehat{\Delta NmF2}$ at 13:54 UT: low-pass filtered smoothed signals (*top*: from left to right), estimated band-pass filtered detail signals (*bottom*: from left to right). (**a**) Signal at the highest level 3; (**b**) smoothed at level 2; (**c**) smoothed at level 1; (**d**) smoothed at level 0; (**e**) detail at level 2; (**f**) detail at level 1; (**g**) detail at level 0

coefficients can be neglected with increasing thresholds, higher compression rates are therefore achieved and more information will be lost. In order to get a high compression rate without losing significant information, we set $\varrho_{2,2,2} = 7 \cdot 10^3$ el/cm^3 and thus altogether 718 wavelet coefficients are neglected out of the total 973 wavelet coefficients (calculate by $K_{3,3,3} - K_{0,0,0} = (2^3+2)^3 - (2^0+2)^3 = 1{,}000 - 27 = 973$. In Fig. 1, the number of the scaling coefficients in $\boldsymbol{d}_J$ is equal to the sum of the number of the scaling coefficients $\boldsymbol{d}_{J-1}$ in the adjacent lower level and the number of the wavelet coefficients in $\boldsymbol{c}_{J-1}$), i.e., with the compression rate up to 73.8% (=718/973). Compared with the 1,000 scaling coefficients for *NmF*2 at the highest levels, just a small number of coefficients need to be stored, therefore an efficient data compression is achieved. To evaluate the quality, we calculate *VTEC* from compressed *NmF*2. The difference between the compressed *VTEC* and the constructed *VTEC* without compression is displayed in Fig. 4c, no significant difference can be seen there, and the RMS value is around 0.35 TECU. Therefore we just need to store a small number of wavelet coefficients without degrading the quality.

5 Conclusion and Outlook

In this paper we presented a linearized 4-D electron density model. The vertical structure is described by a physics-motivated Chapman function and a plasmasphere layer. The F2-layer parameters *NmF*2 and *hmF*2 in the Chapman function are modeled by series expansions in terms of localized B-spline functions depending on geographical longitude, latitude and time. In order to overcome the insensitivity of STEC derived from ground-based GPS observations to the height parameters (e.g., *hmF*2), a combination of ground-based GPS observations and pointwise electron density measurements retrieved from space-based GPS IRO data is performed. The performance of our model has been verified exemplarily over the South and Central American region for a selected time span during a low solar activity day. The exemplary comparison between our estimated corrections of *hmF*2 to the background model IRI and what Bilitza et al. (2012) have shown reveals that our model has a potential to provide reliable results. The estimated *VTEC* for the selected time epoch shows that our model is closer to GIM compared

with IRI-2007 in areas with input data. It has to be kept in mind that the presented results may differ in other regions and for other ionospheric conditions. Therefore the model should be validated by larger datasets for a longer time span and during different levels of solar activity in future. The joint estimation of the ionospheric parameters including the scale height $HF2$ as well as plasmaspheric parameters will also be exploited. The effective data compression from MSR has been demonstrated. Furthermore we will focus on improving the data compression technique statistically by a test of significance.

Acknowledgements This work is part of the project "MuSIK" funded by the German Research Foundation DFG. The authors would like to thank DFG for making this work possible and Laura Sánchez (DGFI/IGS RNAAC SIR), M. Mainul Hoque (DLR Neustrelitz) and Lung-Chih Tsai (CSRSR, NCU) for kindly providing the input data.

References

Alizadeh MM (2013) Multi-dimensional modeling of the ionospheric parameters using space geodetic techniques. Ph.D. thesis, Vienna University of Technology, Vienna, February 2013

Bilitza D, Reinisch BW (2007) International reference ionosphere 2007: improvements and new parameter. Adv Space Res 42(4):599–609

Bilitza D, Brown SA, Wang MY, Souza JR, Roddy PA (2012) Measurements and IRI model predictions during the recent solar minimum. J Atmos Sol Terr Phys 86:99–106

Davies K (1990) Ionospheric radio. Peter Peregrinus, London

Dettmering D (2003) The utilisation of the GPS for modelling the ionosphere in three dimensions. Ph.D. thesis, Universität Stuttgart, Germany (in German)

Dettmering D, Schmidt M, Heinkelmann R, Seitz M (2011) Combination of different space-geodetic observations for regional ionosphere modeling. J Geod 85(12):989–998

Dow JM, Neilan RE, Rizos C (2009) The international GNSS service in a changing landscape of global navigation satellite systems. J Geod 83:191–198. doi: 10.1007/s00190-008-0300-3

Feltens J (1998) Chapman profile approach for 3-D global TEC representation. In: Proceedings of the 1998 IGS analysis center workshop, ESOC, Darmstadt, 9–11 February 1998, pp 285–297

Fong CJ, Yen NL, Chu CH, Yang SK, Shiau WT, Huang CY, Chi S, Chen SS, Liou YA, Kuo YH (2009) FORMOSAT-3/COSMIC spacecraft constellation system, mission results, and prospect for follow-on mission. Terr Atmos Ocean Sci 20:1–19

Hernández-Pajares M, Juan JM, Sanz J, Orus R, Garcia-Rigo A, Feltens J, Komjathy A, Schaer SC, Krankowski A (2009) The IGS VTEC maps: a reliable source of ionospheric information since 1998. J Geod 83(3–4):263–275

Jakowski N (2005) Ionospheric GPS radio occultation measurements on board CHAMP. GPS Solut 9:88–95. doi: 10.1007/s10291-005-0137.7

Koch KR, Kusche J (2002) Regularization of geopotential determination from satellite data by variance components. J Geod 76(5):259–268

Limberger M, Liang W, Schmidt M, Dettmering D, Hugentobler U (2013) Regional representation of F2 Chapman parameters based on electron density profiles. Ann Geophys 31:2215–2227

Lyche T, Schumaker LL (2001) A multiresolution tensor spline method for fitting functions on the sphere. SIAM J Sci Comput 22(2):724–746

Reigber Ch, Lühr H, Schwintzer P (2002) CHAMP mission status. Adv Space Res 30(2):129–134

Reinisch BW, Nsumei P, Huang X, Bilitza DK (2007) Modeling the F2 topside and plasmasphere for IRI using IMAGE/RPI and ISIS data. Adv Space Res 39(5):731–738

Sánchez L, Seemüller W, Drewes H, Mateo L, González G, Silva A, Pampillón J, Martínez W, Cioce V, Cisneros D, Cimbaro S (2013) Long-term stability of the SIRGAS reference frame and episodic station movements caused by the seismic activity in the SIRGAS region. In: IAG symposia, vol 138. Springer, Berlin, pp 153–161

Schaer S (1999) Mapping and predicting the Earth's ionosphere using the global positioning system. Ph.D. thesis, Bern University

Schmidt M (2007) Wavelet modeling in support of IRI. Adv Space Res 39(5):932–940

Schmidt M (2012) Towards a multi-scale representation of multi-dimensional signals. Int Assoc Geod Symp 137:119–127

Schmidt M, Dettmering D, Mößmer M, Wang Y, Zhang J (2011) Comparison of spherical harmonic and B spline models for the vertical total electron content. Radio Sci 46:RS0D11

Stollnitz EJ, DeRose TD, Salesin DH (1995) Wavelets for computer graphics: a prime. IEEE Comput Graph Appl 15(3):76–84, part 1; 15(4):75–85, part 2

Todorova S, Schuh H, Hobiger T, Hernández-Pajares M (2007) Global models of the ionosphere obtained by integration of GNSS and satellite altimetry data. Vermessung und Geoinformation 2:80–89

Tapley BD, Bettadpur S, Watkins M, Reigber Ch (2004) The gravity recovery and climate experiment: mission overview and early results. Geophys Res Lett 31(9):L09607

Tsai LC, Liu CH, Hsiao TY (2009) Profiling of ionospheric electron density based on FormoSat-3/COSMIC data: results from the intense observation period experiment. Terr Atmos Ocean Sci 20(1):181–191

The Evaluation of Ground-Based GNSS Tropospheric Products at Geodetic Observatory Pecný

Jan Dousa and Pavel Vaclavovic

Abstract

The Geodetic Observatory Pecný (GOP) has developed and operated near real-time solutions for precise estimation of zenith total delays (ZTD) using data from the Global Navigation Satellite Systems (GNSS) permanent stations since 2001. The GOP tropospheric products have been assimilated into numerical weather prediction (NWP) models operated by Météo France and the UK Met Office and have been exploited in various ways by several other meteorological institutions. Over the last 3 years new developments consisted in the implementation and the assessment of (a) global hourly ZTD product, (b) regional ZTD products utilizing a common processing of the United States' GPS and the Russian GLONASS data, (c) real-time ZTD product. Original and new tropospheric products were evaluated with respect to reference ZTDs provided by the International GNSS Service (IGS) and the IAG Reference Frame sub-commission for Europe (EUREF). Near real-time ZTD estimations from the network approach can be characterized by a mean bias below 2 mm and a mean standard deviation of 3–6 and 3–8 mm for regional and global analysis, respectively. The quality of ZTDs from the global analysis in Europe is highly consistent with those from the regional products. A half-year evaluation of the real-time ZTD production, using the Precise Point Positioning strategy and the IGS real-time orbit and clock products, resulted in the standard deviations below 10 mm and the biases up to 20 mm. The real-time processing strategy and software are still under development and we expect further improvements.

Keywords

GNSS • Near real-time • Nowcasting • Numerical weather prediction • Zenith tropospheric delay

1 Introduction

For more than 12 years, the Geodetic Observatory Pecný (GOP) has estimated precise tropospheric parameters in near real-time (NRT) using data from Global Navigation Satellite System (GNSS) permanent stations. During this period, GOP products contributed to various projects in this domain in Europe such as COST-716 (Elgered 2001), TOUGH (Vedel 2003), E-GVAP I-III (E-GVAP 2015) and COST ES1206 (Guerova et al. 2013). Estimated zenith total delays (ZTD) have been disseminated on hourly basis via the Global Telecommunication System network to users worldwide. The GOP tropospheric products are assimilated into numerical weather prediction (NWP) models operated by Météo France and the UK Met Office and have been exploited in various ways by several other meteorological institutions. Until 2011, however, only data from the United States' Global Positioning System (GPS) were used in the operational processing at GOP.

J. Dousa (✉) • P. Vaclavovic
NTIS – New Technologies for Information Society, Research Institute of Geodesy, Topography and Cartography, Ústecká 98, 25066 Zdiby, Czech Republic
e-mail: jan.dousa@pecny.cz

© Springer International Publishing Switzerland 2015

C. Rizos, P. Willis (eds.), *IAG 150 Years*, International Association of Geodesy Symposia 143,
DOI 10.1007/1345_2015_157

Table 1 Operational tropospheric products provided by GOP in support of meteorology (PPP stands for the precise point positioning)

GNSS tropospheric solution	Software	Strategy	Period	Products
Regional GPS near real-time	Bernese	Network	2001–2013	IGS ultra-rapid orbits (GPS, official product)
Regional multi-GNSS near real-time	Bernese	Network	2011–2013	IGS ultra-rapid orbits (GPS+GLONASS, unofficial)
Global GPS near real-time	Bernese	Network	2010–2013	IGS ultra-rapid orbits (GPS, official product)
Regional GPS real-time	G-Nut/Tefnut	PPP	2013 (February–August)	IGS real-time orbits and clocks
Global GPS real-time	G-Nut/Tefnut	PPP	2013 (February–August)	IGS real-time orbits and clocks

New developments at GOP over the last 3 years consisted of (a) implementation and assessment of the global hourly ZTD product, (b) implementation of regional ZTD estimates using a common processing of data from the GPS and from the Russian GLONASS systems and (c) implementation of ultra-fast/real-time ZTD product. Basic characteristics of the original and new tropospheric product are summarized in Table 1. The first three products listed in the table were developed using the Bernese GNSS software V5.0 (Dach et al. 2007), the network solution approach and double-difference observations. The other two were developed exploiting the Precise Point Positioning (PPP) strategy (Zumberge et al. 1997), Kalman filter approach, the own software application G-Nut/Tefnut (Dousa and Vaclavovic 2014), and real-time orbit and clock products (Caissy et al. 2012) provided by the International GNSS Service (IGS) (Dow et al. 2009).

The paper evaluates new developments at GOP in terms of ZTD estimates with utilizing reference tropospheric products, such as available from the IGS (Byram et al. 2011) and from the International Association of Geodesy Reference Frame Sub-Commission for Europe, EUREF (Soehne et al. 2009). All the comparisons described in this paper were performed using the GOP-TropDB (Gyori and Dousa 2015) in terms of ZTDs only. This paper focuses on the assessment of specific aspects of near real-time solutions based on predicted precise orbits, in a regional or global scope and the use of GPS or GPS+GLONASS data.

ZTDs with respect to external data sources, such as radio sounding, were assessed in numerous studies, e.g. for regional results in Dousa (2001, 2003), Haase et al. (2003), Gendt et al. (2004), Pacione and Vespe (2008), and Seung-Woo et al. (2013) and for results in a global scope, see Wang (2008). Based on these and other studies an overall consistency with radio sounding data can be characterized with the accuracy of 1–3 mm in precipitable water which can be expressed in ZTD by using an approximate multiplication factor of 7. Other authors studied the internal GNSS quality of ZTDs with respect to the final GNSS products aiming mainly at assessing various aspects of near real-time processing. Such comparisons demonstrated a variable quality of NRT ZTD estimates dependent on a strategy implementation, software usage, overall processing robustness, the time period of comparison and many others. The first near real-time solution in Europe was developed in the German Research Centre for Geosciences (GFZ) applying the PPP strategy supported by their own hourly updated precise orbit and clock products. They demonstrating the accuracy of 1–2 mm of precipitable water (Gendt et al. 2004). This result was closely comparable to the GOP results using the network mode as presented in Dousa (2003). Both demonstrated that two different strategies were able to provide very similar results. Non-operational results of ZTD calculation with the accuracy of 10 mm in ZTD was also demonstrated in Hernandez-Pajares et al. (2001). Other operational NRT tropospheric solutions have been developed in different European countries since 2001. The tropospheric results were usually compared to the reference GNSS products and showed variable results, e.g. the accuracy of 1 mm in precipitable water in Karabatic et al. (2011), the ZTD mean bias of 0.5 mm and the standard deviation of 15 mm (Bosy et al. 2012).

The long-term production of various operational products and its consistent evaluations at GOP summarizes and compares different scenarios such as the global scope, multi-GNSS or ultra-fast production. Section 2 of the paper gives a long-term evaluation of near real-time GPS (2001–2013) and new multi-GNSS solution (2011–2013). Section 3 discusses results of the global NRT solution achieved during 2010–2013 and Sect. 4 evaluates initial results from the real-time demonstration campaign (February–August 2013) based on different software, strategies and products. The last section discusses and summarizes achieved results.

2 Near Real-Time GPS and GLONASS ZTD Products

The NRT regional GPS product has been produced since the COST-716 benchmark campaign in 2001 (van der Marel et al. 2004). Initial GOP developments were described in Dousa (2001), however, the strategy and precise models were updated several times. Also IGS ultra-rapid orbits (Springer and Hugentobler 2001) has been significantly improved since the beginning. The evolution of the original operational solution can be observed in Fig. 1 for the time series of monthly calculated mean ZTD biases and mean standard deviations

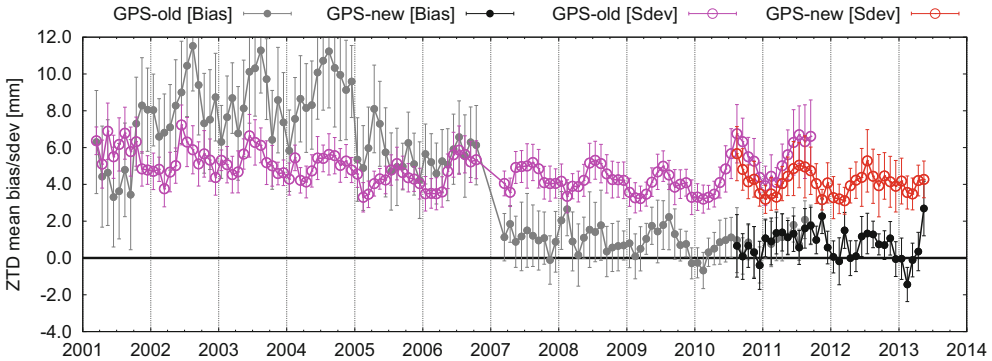

Fig. 1 Time series of monthly calculated ZTD bias and standard deviations from all stations and GOP NRT and EUREF tropospheric parameters differences

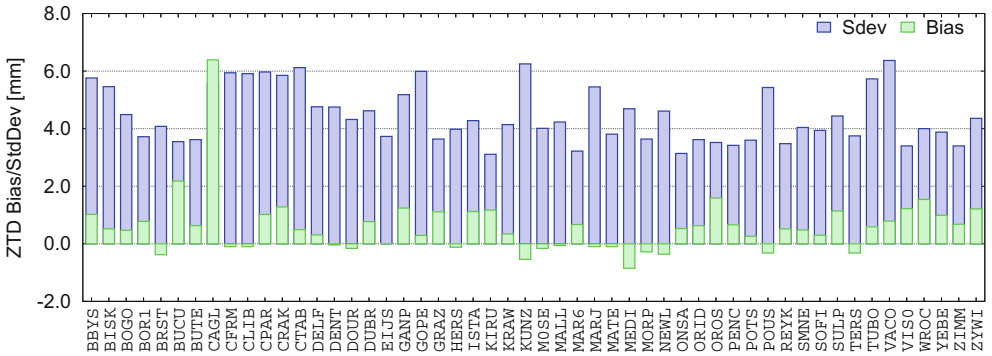

Fig. 2 ZTD statistics for all common stations and GOP NRT and EUREF tropospheric parameter differences

over all stations. The routine comparison is provided with respect to homogeneously reprocessed tropospheric product provided by EUREF.

An important update happened at the turn of 2006/2007 when the switch from the relative to absolute phase centre offset and variation model (PCO+PCV) together with the change to the ITRF2005 reference frame significantly reduced systematic errors in ZTDs, see Fig. 1. Additionally, new strategy was introduced in 2010 exploiting 4-h pre-processing interval instead of a single hour pre-processing. The new design was implemented together with developing a first hourly updated global ZTD solution at GOP, see Sect. 3. The strategy was tested during 2010–2011 and, in the end, brought a small but visible overall improvement.

Station by station ZTD statistics are provided in Fig. 2 showing that the bias is in most cases below 2 mm and the standard deviation below 6 mm. A single exception is the station CAGL (Sardinia) where a large bias was caused most probably due to an inconsistent contribution from a single analysis centre into the EUREF combination, clearly visible at the http://epncb.oma.be (tropospheric delays). On the other hand, we noticed that the GOP solution contains degraded ZTDs (by a factor of 1.5) for several national stations (BISK, CFRM, CPAR, CTAB, CRAK, GOPE, KUNZ, MARJ, POUS, TUBO and VACO) during 3 months in summer 2012. However, this problem is only marginally noticeable in the long-term statistics.

Rigorous multi-GNSS (GPS, GLONASS) ZTD solution was initially tested in 2009 following the development of the GOP ultra-rapid GNSS orbits as a new contribution (Dousa 2012) to the IGS. At that time a mean bias of 1.5 mm was identified between GPS and GLONASS ZTDs related to the inconsistencies in the IGS05 absolute PCO+PCV models for GPS and GLONASS satellites (Dilssner et al. 2010). Consequently, the implementation of a routine operation was postponed after the GPS week 1632 together with using the IGS08 absolute PCO+PCV model. The said modifications eliminated the bias and demonstrated an overall general better consistence between GPS and GLONASS estimated ZTDs (Dach et al. 2011). Actually, the multi-GNSS ZTD product runs in parallel to the GPS-only and it is expected to replace the current official GPS-only product in near future. The new ZTD multi-GNSS product is based on the unofficial GPS and GLONASS ultra-rapid orbits from the IGS, however, near real-time ZTDs estimated routinely achieved already a good quality and overall robustness.

Figure 3 shows monthly ZTD comparison during April 2011–April 2013 between GPS only and multi-GNSS constellations. Results has shown only minor improvements if GLONASS is included (half of all the stations processed by

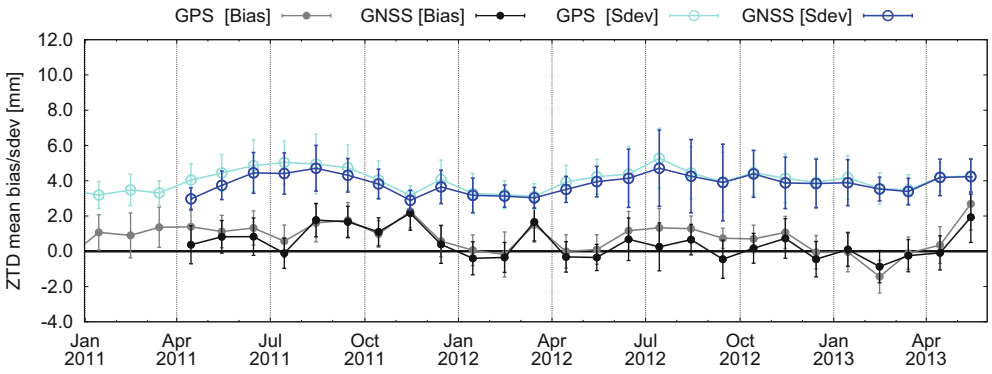

Fig. 3 Monthly comparison of GPS and GPS+GLONASS tropospheric parameters (all stations) during 2011–2013

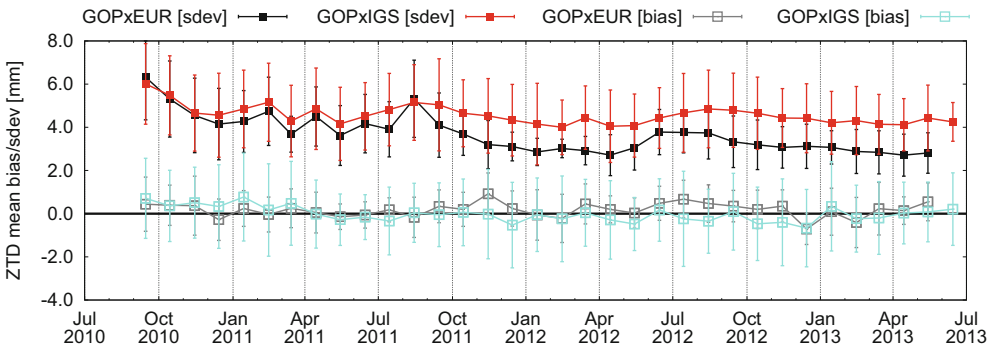

Fig. 4 Monthly calculated ZTD biases and standard deviations for all stations common to GOP NRT global product and EUREF and IGS product

GOP observe GPS only). Although GLONASS models and products have not achieved a comparable quality to those of GPS yet, we assume a small positive impact is due to the increased number of satellites and observations sensing the atmosphere in more directions and stabilizing the near real-time solution. A high consistency of standalone GPS and standalone GLONASS ZTD products for the IGS08 models was thus demonstrated.

3 Hourly Global ZTD Product

The GOP global ZTD product has been implemented on request of the meteorological institutions operating global numerical weather prediction models. The main differences in our global solution compared to regional ones consist in several specific aspects – (a) variable latency and instability (gaps) of data in a global station hourly data flow, (b) long baselines processing (up to 10,000 km), which cause several limitations – the decrease of common observations, the low success of resolved ambiguities, the higher impact of the orbit prediction errors (Dousa 2010) and some others; in general all isolated stations could not achieve the same quality as in a dense network and, finally, (c) global network covering areas with highly different climatic conditions (polar regions vs. equatorial areas).

The global ZTD product consisted of hourly updated ZTDs for more than 130 globally operated IGS stations. For more details on the new product description we refer to Dousa and Bennitt (2013). Based on a year assessment, the product was switched from the testing to the operational mode within the E-GVAP (October 2011). Since that time the product has been routinely assimilated into the global NWPs operated at Météo France and UK Met Office.

The global ZTD product was evaluated over the 3-year period (October 2010–August 2013) with respect to the reprocessing ZTDs from EUREF and IGS. Figure 4 displays monthly calculated ZTD biases and standard deviations over all stations common to the GOP near real-time global product and the EUREF and IGS products. Figure 5 shows geographical distribution of biases and standard deviations from the GOP near real-time global product compared to the IGS product. The comparison demonstrated that the quality of our NRT global product is similar to the results achieved from the regional solutions in Europe or the Northern hemisphere in general. Additionally, ZTD quality increased during the last 2 years when compared to the EUREF product for all stations processed in Europe. A lower quality (i.e. standard deviation up to 8 mm) is observed mainly for stations within equatorial areas or at isolated places. The former is influenced by a large volume and a higher variability of the water vapour in the tropical belt, while the latter is additionally

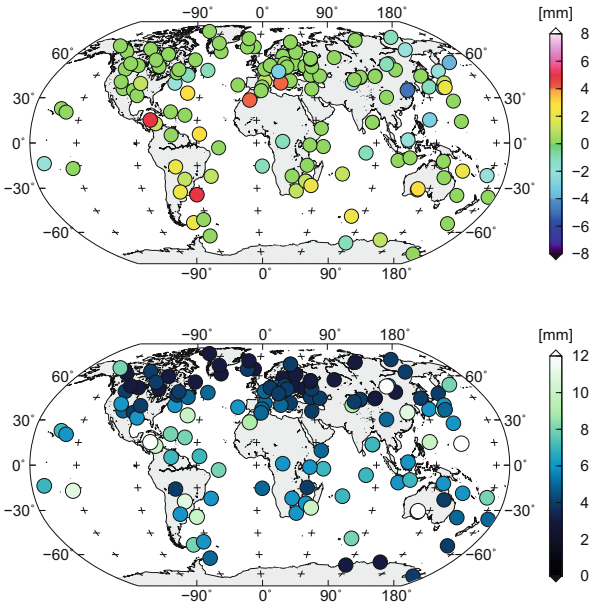

Fig. 5 Geographical distribution of ZTD biases (*top*) and standard deviation (*bottom*) from GOP near real-time global product compared to IGS final product

affected by specific aspects described at the beginning of this section.

4 Real-Time ZTD Product

The GOP real-time ZTD estimation was developed in 2012 in support of new meteorological applications like NWP nowcasting or severe weather monitoring aimed in the COST ES1206 project. The GOP real-time ZTD estimation has been implemented with our own G-Nut/Tefnut application. It is derived from the G-Nut software library (Vaclavovic et al. 2013) and, in 2013, it did not achieve a full compliance with all the IERS standards (Petit and Luzum 2010). The solution takes advantage of the IGS Real-Time Service orbit and clock corrections (Caissy et al. 2012) and utilizes the PPP strategy in contrast to all other GOP near real-time ZTD products. This new strategy was preferred for the real-time analysis because it supports an autonomous station by station processing, an epoch-wise real-time filtering and a high temporal resolution of ZTDs including horizontal tropospheric gradients or even direct slant delays from a receiver to all satellites in view.

In February 2013, we set up a real-time demonstration campaign in order to assess the software and new processing strategy. The campaign was based on selected 21 stations in Europe and 15 other stations in the world that provided real-time data and, additionally, reference ZTDs were available from the EUREF or IGS final tropospheric products. The campaign was updated on a monthly basis (if applicable) in order to support monitoring of the software development and optional strategy changes. The sampling rate for the estimating real-time ZTD and coordinates was 10 s. The processing delay of 80 s was applied in order to avoid clock and orbit extrapolations (global products were available with the latency of 40–50 s). The tropospheric model was initialized with zenith hydrostatic delay calculated using the Global Pressure and Temperature model (GPT) (Boehm et al. 2007) and zenith hydrostatic and wet delays were mapped to direct path delays using the Global Mapping Function, GMF1 (Boehm et al. 2006). The elevation angle cut-off 7° was applied and all observations were weighted with respect to the elevations using $1/(\cos z)^2$ function.

Figure 6 shows weekly ZTD comparison statistics, the mean biases and standard deviations, calculated for all stations common to the GOP real-time and EUREF/IGS solutions. The progressive improvement is clearly noticeable, however, during the initial period a poor quality was achieved due to an incorrect switching off the solid Earth tide model. This bug was fixed in April 2013 and reduced dramatically ZTD systematic errors as well as stabilized overall solution in terms of the precision. The ZTD results then steadily remained at the level of 7 mm for the ZTD standard deviation taking into account all compared stations – 21 in Europe and 36 in the world. The remaining systematic errors are mainly due to some incomplete models in the software, or other model inconsistencies, that needs to be implemented according to the latest IERS standards. Our first focus, however, aimed for achieving a stable precision because any remaining station specific errors, that are stable over a month or longer period, can be eliminated prior to the product assimilation as described in Bennitt and Jupp (2012).

Figure 7 displays ZTD biases and standard deviations for individual stations of the GOP real-time solution compared to EUREF and IGS products. The half-year evaluation demonstrated that minimum requirements for this product were already achieved. These were initially defined by the meteorological community within the TOUGH project (TOUGH 2013) such as the ZTD relative accuracy of 30 mm submitted with 60 min update and 30 min latency. In several aspects it already approached target user requirements, i.e. the relative accuracy of 6 mm in ZTD submitted with 5 min repetition cycle and 5 min ZTD latency. Besides improving precise models of the G-Nut/Tefnut application we expect further improvements in the optimizing our solution in balance of the requested timeliness and accuracy.

5 Summary

Since 2001, the Geodetic Observatory Pecný has developed and operated various tropospheric ZTD solutions for meteorological applications – regional and global, near real-time

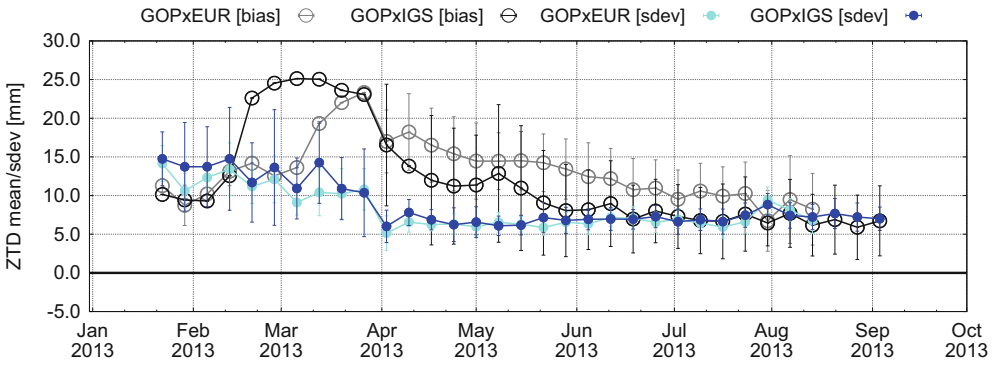

Fig. 6 Weekly ZTD comparison (mean biases and mean standard deviations) over all stations between GOP real-time solution and EUREF and IGS products

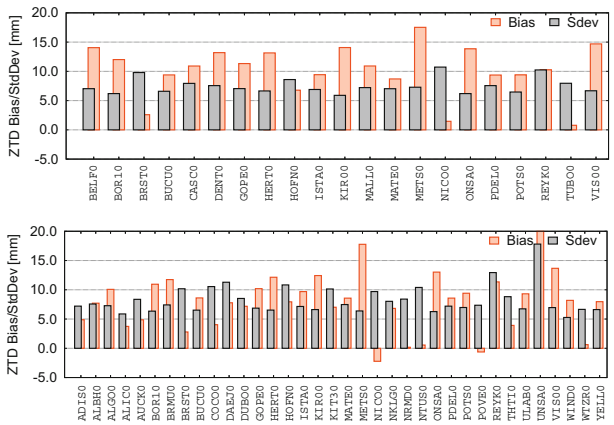

Fig. 7 ZTD comparisons (biases and standard deviations) for all common stations between GOP real-time solution and EUREF (*top*) and IGS (*bottom*) products

Table 2 Assessment of the products from a long-term comparisons

Tropospheric ZTD solution	Bias	Sdev	Remarks
Regional GPS near real-time	$\leq \pm 2$ mm	3–6 mm	Varies with season, station
Regional multi-GNSS near real-time	$\leq \pm 2$ mm	3–6 mm	Varies with season, station, GLONASS data availability
Global GPS near real-time	$\leq \pm 3$ mm	3–8 mm	Varies with season, station, region, latitude
Regional GPS real-time	$\leq \pm 20$ mm	6–10 mm	Varies with season, station, region
Global GPS real-time	$\leq \pm 20$ mm	6–10 mm	Varies with season, station, region, latitude

and real-time, GPS and multi-GNSS. Table 2 summarizes the results from our long-term evaluation of existing GOP ZTD products with respect to the EUREF and IGS homogeneously reprocessed ZTDs. The results provide an overview of various strategies of ZTD estimation as implemented at GOP, i.e. near real-time and real-time scenarios, different approaches (PPP and network), different scopes (regional and global) and different GNSS data (GPS and GLONASS). We should note here that the PPP ZTDs in the offline mode are comparable to the results from the double-difference network solution when precise models are consistently used between global products and a client software and if used global orbit and clock products are of the highest quality. The former is not yet fulfilled in the G-Nut/Tefnut software and the latter is rather challenging for a real-time ZTD production.

Near real-time ZTD estimations from the network approach can be characterized by the mean bias below 2 mm and the mean standard deviation of 3–6 and 3–8 mm for the regional and global analysis, respectively. The quality of ZTDs from the global analysis in Europe is highly consistent with those from the regional product. The half-year evaluation of the first real-time routine solutions, based on the PPP strategy and the IGS real-time orbit and clock products, resulted in the standard deviations below 10 mm, but still systematic errors up to 20 mm. Since biases are usually eliminated in a bias-reduction scheme prior to the assimilation process at meteorological agencies, the precision already fulfilled requirements for the NWP nowcasting. Real-time strategy and software are still under development and we expect further improvements.

Finally, the characteristics given in the table are expressed in terms of ranges since individual values vary with (1) the season due to the relation with the volume of water vapour, (2) individual station performance related to the data quality, latency and availability (GPS, GLONASS) and (3) the station location. The last is related to the latitudinal dependence (volume of water vapour, sub-daily pressure and water vapour variability in tropical areas), location at the network margins or at isolated places or regions with overall

the lower quality of global orbit and clock products due to the lack of global data.

Acknowledgements The development of the G-Nut/Tefnut software and real-time tropospheric product was supported by the Czech Scientific Foundation (P209/12/2207). The assessment of the real-time and multi-GNSS solutions was done within the COST ES1206 project (GNSS4SWEC-CZ, LD14102). Data from seven national GNSS permanent stations were collected with support of the CzechGeo project (LM2010008). We are thankful to wide EUREF and IGS communities for providing data and products used in this work. Finally, we thank all three anonymous reviewers for their valuable comments.

References

Bennitt G, Jupp A (2012) Operational assimilation of GPS zenith total delay observations into the UK met office numerical weather prediction models. Mon Weather Rev 140(8):2706–2719

Boehm J, Niell A, Tregoning P, Schuh H (2006) Global mapping function (GMF): a new empirical mapping function based on numerical weather model data. Geophys Res Lett 33(L07304):943–951

Boehm J, Heinkelmann R, Schuh H (2007) Short note: a global model of pressure and temperature for geodetic applications. J Geodesy 81(10):679–683

Bosy J, Kaplon J, Rohm W, Sierny J, Hadas T (2012) Near real-time estimation of water vapour in the troposphere using ground GNSS and the meteorological data. Ann Geophys 30:1379–1391

Byram S, Hackmann C, Tracey J (2011) Computation of a high-precision GPS-based troposphere product by the USNO. In: Proceedings of the 24th international technical meeting of the satellite division of the institute of navigation (ION GNSS 2011)

Caissy M, Agrotis L, Weber G, Hermandez-Pajares M, Hugentobler U (2012) Coming soon: the international GNSS real-time service. GPS World 23:52–58

Dach R, Hugentobler U, Fridez P, Meindl M (2007) Bernese GPS software version 5.0. User manual. Technical Report, Astronomical Institute, University of Bern

Dach R, Schmid R, Schmitz M, Thaller D, Schaer S, Lutz S, Steigenberger P, Wuebbena G, Beutler G (2011) Improved antenna phase center models for GLONASS. GPS Solutions 15, 49–65. doi:10.1007/s10291-010-0169-5

Dilssner F, Springer T, Flohrer C, Dow J (2009) Estimation of phase centre corrections for GLONASS-M satellite antennas. J Geodesy 84:467–480

Dousa J (2001) Towards an operational near-real time precipitable water vapor estimation. Phys Chem Earth A 26(3):189–194

Dousa J (2003) Evaluation of tropospheric parameters estimated in various routine analyses. Phys Chem Earth 29/2-3:167–175

Dousa J (2010) The impact of errors in predicted GPS orbits on zenith troposphere delay estimation. GPS Solutions 14(3):229–239

Dousa J (2012) Developments of the GLONASS ultra-rapid orbit determination at geodetic observatory pecny. In: Kenyon S, Pacino M, Marti U (eds) Geodesy of planet earth. International association of geodesy symposia, vol 136. Springer, Berlin, pp 1029–1036

Dousa J, Bennitt G (2013) Estimation and evaluation of hourly updated global GPS zenith total delays over ten months. GPS Solutions 17:453–464

Dousa J, Vaclavovic P (2014) Real-time zenith tropospheric delays in support of numerical weather prediction applications. Adv Space Res 53(9):1347–1358. doi:10.1016/j.asr.2014.02.021

Dow J, Neilan R, Rizos C (2009) The international GNSS service in a changing landscape of global navigation satellite systems. J Geodesy 83(3–4):191–198

E-GVAP (2015) The EUMETNET EIG GNSS water vapour programme. http://egvap.dmi.dk

Elgered G (2001) An overview of COST action 716: exploitation of ground-based GPS for climate and numerical weather prediction applications. Phys Chem Earth A 26(6–8):399–404

Gendt G, Dick G, Reigber C, Tomassini M, Liu Y, Ramatschi M (2004) Near real time GPS water vapor monitoring for numerical weather prediction in Germany. J Meteorol Soc Jpn 82:361–370

Guerova G, Jones J, Dousa J, Dick G, de Haan S, Pottiaux E, Bock O, Pacione R, Elgered G, Vedel H (2013) Advanced global navigation satellite systems tropospheric products for monitoring severe weather events and climate (GNSS4SWEC). In: 4th international colloquium scientific and fundamental aspects of the Galileo programme, Prague, Czech Republic, 4–6 December 2013

Gyori G, Dousa J (2015) GOP-TropDB development for tropospheric product evaluation and monitoring – design, functionality and initial results. In: Rizos PWC (ed) International association of geodesy symposia. Springer, Heidelberg

Haase J, Ge M, Vedel H, Calais E (2003) Accuracy and variability of GPS tropospheric delay measurements of water vapor in the western mediterranean. J Appl Meteorol 42:1547–1568

Hernandez-Pajares M, Juan J, Sanz J, Colombo O, van der Marel H (2001) A new strategy for real-time integrated water vapor determination in wadgps networks. Geophys Res Lett 28:3267–3270

Karabatic A, Weber R, Haiden T (2011) Near real-time estimation of tropospheric water vapour content from ground based GNSS data and its potential contribution to weather now-casting in Austria. Adv Space Res 47:1691–1703. doi:10.1016/j.asr.2010.10.028

Pacione R, Vespe F (2008) Comparative studies for the assessment of the quality of near-real-time GPS-derived atmospheric parameters. J Atmos Ocean Technol 25:701–714

Petit G, Luzum B (2010) IERS conventions (2010). Technical Report 36, IERS Convention Centre

Seung-Woo L, Kouba J, Schutz B, Kim D, Lee Y (2013) Monitoring precipitable water vapor in real-time using global navigation satellite systems. J Geodesy 87(10–12):923–934

Soehne W, Figurski M, Szafranek K (2009) Homogeneous zenith total delay parameter estimation from European permanent GNSS sites. In: Presented at EUREF 2009 symposium, Florence, 27–30 May

Springer T, Hugentobler U (2001) IGS ultra rapid products for (near-) real-time applications. Phys Chem Earth A 26(6–8):623–628

TOUGH – Targeting Optimal Use of GPS Humidity Measurement for Meteorology (2013) User requirements - D10. http://web.dmi.dk/pub/tough

Vaclavovic P, Dousa J, Gyori G (2013) G-Nut software library - state of development and first results. Acta Geodyn Geomater 10(4):431–436

van der Marel H, Brockmann E, de Haan S, Dousa J, Johansson J, Gendt G, Kristiansen O, Offiler D, Pacione R, Rius A, Vespe F (2004) COST-716 demonstration project for the near real-time estimation of integrated water vapour from GPS. Phys Chem Earth A/B/C 29(2–3):187–199

Vedel H (2003) TOUGH-team: targeting optimal use of GPS humidity measurements in meteorology. In: Proceedings of the international workshop on GPS meteorology, Tsukuba, 14–17 January

Wang JZL (2008) Systematic errors in global radiosonde precipitable water data from comparison with ground-based GPS measurements. J Climate 21(10):2218–2238. doi:10.1175/2007JCLI1944.1

Zumberge J, Heflin M, Jefferson D, Watkins M, Webb F (1997) Precise point positioning for the efficient and robust analysis of GPS data from large networks. J Geophys Res 102(B3):5005–5017

The CODE MGEX Orbit and Clock Solution

Lars Prange, Rolf Dach, Simon Lutz, Stefan Schaer, and Adrian Jäggi

Abstract

The Center for Orbit Determination in Europe (CODE) is contributing as a global analysis center to the International GNSS Service (IGS) since many years. The processing of GPS and GLONASS data is well established in CODE's ultra-rapid, rapid, and final product lines. With the introduction of new signals for the established and new GNSS, new challenges and opportunities are arising for the GNSS data management and processing. The IGS started the Multi-GNSS-EXperiment (MGEX) in 2012 in order to gain first experience with the new data formats and to develop new strategies for making optimal use of these additional measurements. CODE has started to contribute to IGS MGEX with a consistent, rigorously combined triple-system orbit solution (GPS, GLONASS, and Galileo). SLR residuals for the computed Galileo satellite orbits are of the order of 10 cm. Furthermore CODE established a GPS and Galileo clock solution. A quality assessment shows that these experimental orbit and clock products allow even a Galileo-only precise point positioning (PPP) with accuracies on the decimeter- (static PPP) to meter-level (kinematic PPP) for selected stations.

Keywords

CODE • Galileo • GNSS • IGS • MGEX

1 Introduction

The Center for Orbit Determination in Europe (CODE, Dach et al. 2013) is providing satellite orbits, satellite and receiver clock corrections, Earth rotation parameters, ionosphere maps, station coordinates, and troposphere products based on GPS since the start of the activities of the International GNSS Service (IGS, Dow et al. 2009) in the early 1990s. In the late 1990s the IGS ran the IGS GLONASS EXperiment (IGEX, Willis et al. 1999) to investigate the potential introduction of GLONASS into the IGS services. CODE contributed to the IGEX with a GPS and GLONASS orbit solution (Ineichen et al. 2003). In 2003 CODE started to provide a rigorously combined GPS and GLONASS solution in the final, rapid, and ultra-rapid product lines (Dach et al. 2009).

One decade later the GNSS community is again subject to considerable changes. The established GNSS GPS and GLONASS are under modernization: New signal types (e.g., L2C), a third frequency (L5), and new Block IIF satellites with improved atomic clocks are introduced for GPS. The next generation of spacecraft is already announced. The GLONASS constellation has been fully re-established and a new satellite generation (GLONASS-K) with code division multiple access capability is being tested. In addition, new GNSS (e.g., Galileo, BeiDou) and regional services [e.g., the Quasi-Zenith Satellite System (QZSS)] are

L. Prange (✉) • R. Dach • S. Lutz • A. Jäggi
Astronomical Institute of the University of Bern, Sidlerstrasse 5, 3012 Bern, Switzerland
e-mail: lars.prange@aiub.unibe.ch

S. Schaer
Bundesamt für Landestopografie swisstopo, Seftigenstrasse 264, 3084 Wabern, Switzerland
e-mail: stefan.schaer@aiub.unibe.ch

© Springer International Publishing Switzerland 2015

C. Rizos, P. Willis (eds.), *IAG 150 Years*, International Association of Geodesy Symposia 143,
DOI 10.1007/1345_2015_161

under development. The IGS reacted to these developments by launching the Multi-GNSS-EXperiment (MGEX, Montenbruck et al. 2013) and by the development of a new version of the Receiver INdependent EXchange data format (RINEX3, MacLeod and Agrotis 2013). The MGEX incorporates most components of the IGS processing chain consisting of data collection, data dissemination, data processing, and product combination.

CODE contributes to MGEX with a raw data monitoring since spring 2012, by providing orbit products since mid 2012 (Prange et al. 2012), and by providing clock products since late 2012 (Prange et al. 2013) based on MGEX data. The MGEX-related processing is currently run in a campaign-wise effort, but not yet with the fixed schedule as the other IGS-related products. The Bernese GNSS Software (Dach et al. 2007) and the processing algorithms used for generating the IGS products at CODE are step-by-step extended to be prepared for the new GNSS, new signals, and RINEX3 data format. The CODE MGEX orbits, Earth rotation parameters, satellite clock corrections, and inter-system biases (ISBs) are made available for public use via the MGEX product directory at the IGS data center CDDIS (see ftp://cddis.gsfc.nasa.gov/gnss/products/mgex\/, file name abbreviation for CODE results is "com").

The data basis and the tracking network used for the CODE MGEX analysis are introduced in Sect. 2. Section 3 describes the orbit solution and orbit validation. The clock solution and its results are presented in Sect. 4. A precise point positioning based on the CODE MGEX orbit and clock products is demonstrated in Sect. 5. The results are summarized in Sect. 6.

2 Data Basis and Network

The IGS-related processing schemes running at CODE make use of raw data of the IGS station network distributed by the global IGS data centers and of data from additional stations provided by some regional data centers. In early 2012 the data acquisition and monitoring of content and completeness of the RINEX observation files at CODE has been extended to data from the IGS-MGEX archives at CDDIS, BKG, and IGN. In addition the RINEX3 archive of the EUREF Permanent Network (EPN, Bruyninx et al. 2011), located at the BKG, is considered since day 80 of the year 2013. Selected results of the raw data monitoring are publicly available on the ftp server of the AIUB (Lutz et al. 2013, see ftp://ftp.unibe.ch/aiub/mgex/README.TXT for details).

Figure 1 shows that the number of monitored sites providing RINEX3 data increased from about 30 in spring 2012 to about 100 in mid 2013. The sudden increase around DOY (Day Of the Year) 80/2013 is due to the inclusion of EPN sites into the data monitoring, starting at that time. All stations are tracking GPS and nearly all GLONASS in addition. Galileo, BeiDou, QZSS, and SBAS are tracked by fewer sites. The best-supported new GNSS is Galileo. Most of the Galileo-tracking stations provide data on L1 (E1) and L5 (E5a), whereas other frequencies are only supported by a limited number of stations. The most commonly available Galileo signals are L1X/C1X and L5X/C5X. The focus of this article is on Galileo and its L1 and L5 signals.

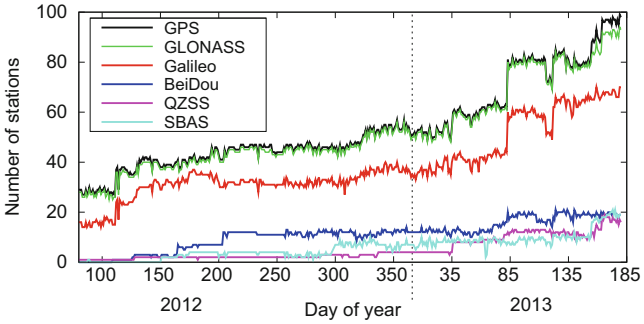

Fig. 1 Number of stations providing RINEX3 data considered in CODE's raw data monitoring

For the determination of GNSS satellite orbits and clock corrections not only the number of tracking stations is relevant, but also their spatial distribution. A homogeneous distribution of the tracking sites around the globe is preferable in order to achieve a redundant visibility all the time, which is especially important for the estimation of epoch-wise clock corrections (Bock et al. 2009). In 2012, when we started the MGEX processing, usually only 30 Galileo tracking sites were available. All of them were considered in the MGEX processing. Later on, data of more stations outside Europe became available. The additional inclusion of EPN sites into CODE's data monitoring in 2013 further increased the number of stations available for us, but also the imbalance of their global distribution (more sites than necessary in Europe vs. sparse station distribution in other regions). Therefore a station selection has been used since early 2013: All non-European plus a selection of European sites result in a network of about 35–45 Galileo tracking stations. In addition to the MGEX stations about 120 IGS stations providing only GPS and GLONASS measurements in RINEX2 format are included in the processing. The resulting station network selected for the CODE MGEX orbit and clock solutions is shown in Fig. 2.

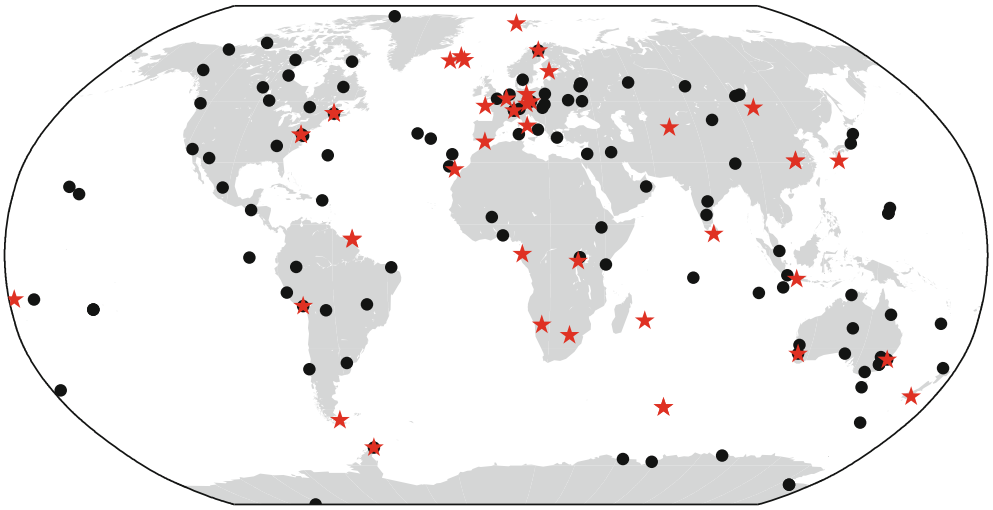

Fig. 2 Distribution of GNSS tracking stations contributing to the CODE MGEX orbit and clock determination (status mid 2013). *Black dots* represent stations tracking GPS (altogether 145–150 sites) and/or GLONASS (altogether about 125). *Red stars* represent stations tracking also Galileo (about 35–45)

3 CODE MGEX Orbit Solution

The CODE MGEX orbit processing scheme is a double-difference network solution that is consistent to the state-of-the-art GNSS processing standards following the IGS and IERS conventions (see code.acn, CODE 2013). The basic setup was extended to include Galileo L1 and L5 measurements and RINEX3 data. The fully integrated, triple-system (GPS, GLONASS, and Galileo) processing solves for satellite orbits, Earth orientation parameters, station coordinates, and troposphere parameters. Satellite orbits with arc lengths of 1 day and 3 days are computed. For the 3-day arcs the satellite positions of the middle day are provided in the result files. The orbits are available for the time interval DOY 145/2012 to DOY 180/2013 at the CDDIS.

The orbit quality is assessed (with the focus on Galileo) with different validation methods (see the statistics in Table 1). Orbit differences at the day boundaries (computed in the celestial reference frame) show the orbit misclosure between two consecutive daily orbits (naturally there should be no jumps of the orbits in the celestial reference frame). In a longarc fit a dynamical orbit (represented by the initial orbital elements plus coefficients of the radiation pressure model according to Beutler et al. 1994) is computed from the satellite positions at three consecutive days by numerical integration. The RMS of the orbit fit indicates how well the estimated orbit positions represent the physical orbit model within the integration time. It is also a measure for the continuity/smoothness of the estimated orbit. Both validation methods show clear advantages of 3-day orbits over 1-day orbits for all selected satellites (see Table 1 and Fig. 3).

Table 1 Orbit validation results: mean orbit differences at the day boundaries (1-day vs. middle day of 3-day arc solution), mean RMS of 3-day longarc fits through daily orbit positions (1-day vs. middle day of 3-day orbit), weekly mean bias and standard deviation of SLR residuals for orbits (middle day of 3-day arc) of selected satellites (unit is cm in all cases)

	Orbit differences		Longarc fit		SLR residuals	
Satellite	1-day	3-day	1-day	3-day	Bias	STD
G01	5.4	3.6	2.5	0.9	–	–
R24	10.1	3.5	3.5	1.9	–	–
E11	28.0	6.2	7.8	1.9	−5.9	8.4
E12	28.4	7.7	8.5	2.3	−6.0	8.0
E19	32.4	7.6	9.5	2.2	−3.6	9.4
E20	31.7	7.7	12.8	2.3	−4.6	8.3

The results in Table 1 show that Galileo benefits more than GPS and GLONASS from long arcs. This is due to the still more sparse and uneven station distribution of the Galileo tracking sites and the longer revolution period of the Galileo satellites. Galileo's long revolution period of more than 14 h has another side-effect: The Galileo groundtracks are shifted every day. This causes a changing observation geometry and observation number from 1 day to another, if the stations are unevenly distributed (which is still the case for the current MGEX network). As a result the quality of the estimated Galileo orbits may vary day by day. Longarcs significantly reduce this effect. Due to the clear advantage of the 3-day longarcs (especially for Galileo) only the middle days these orbits are considered in the following parts of this work and are made available for public use (see Sect. 1).

Satellite laser ranging (SLR) may provide a validation of mainly the radial component of GNSS orbits with an inde-

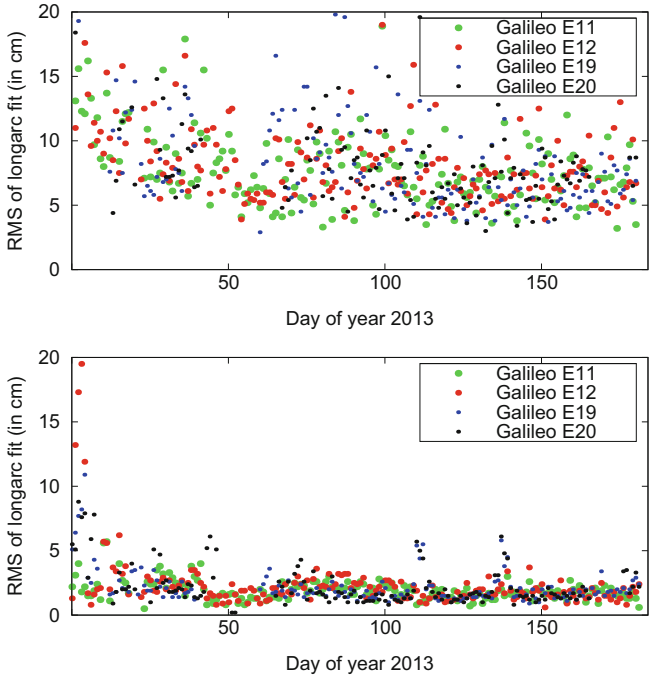

Fig. 3 RMS of 3-day longarc fits through orbit positions of three consecutive days. *Top*: 1-day arc solution. *Bottom*: Middle day of 3-day arc solution

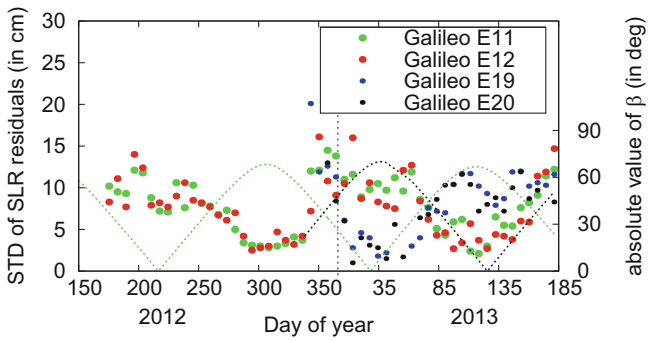

Fig. 4 Standard deviation of weekly SLR residuals of CODE MGEX Galileo orbits. *Green curve*: Absolute value of the Sun's elevation angle (β) w.r.t. the orbital plane of E11 and E12. *Black curve*: Absolute value of the Sun's elevation w.r.t. the orbital plane of E19 and E20

pendent space-geodetic technique (Flohrer 2008). About 15–20 SLR stations provide some hundred range measurements per week. From the residuals of each week the mean offset and standard deviation is computed per satellite. The values for the 3-day Galileo orbits are listed in Table 1. The SLR residuals of the Galileo In Orbit Validation (IOV) satellites show a correlation with the elevation angle of the Sun w.r.t. the orbital planes (named β in Fig. 4). Possible explanations are issues with the radiation pressure modeling (e.g., related to the area-to-mass ratio), deviations from the nominal attitude model, or outgasing effects. Further investigations are needed to understand this effect.

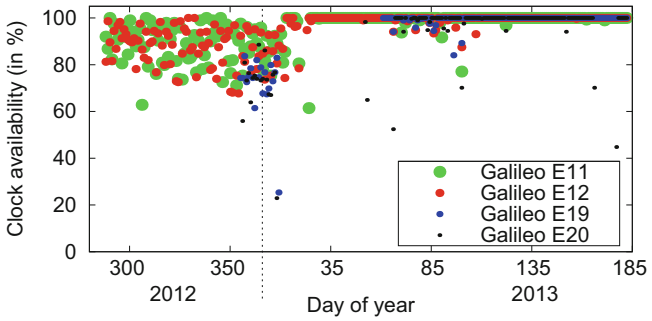

Fig. 5 Percentage of epochs, at which satellite clocks could be estimated

4 CODE MGEX Clock Solution

Like the orbit processing the CODE MGEX clock processing is consistent to the state-of-the-art GNSS processing standards following the IGS and IERS conventions (see code.acn, CODE 2013). Again the basic CODE setup was extended to make use of Galileo L1 and L5 measurements and RINEX3 data. The dual-system (GPS and Galileo) zero-difference processing scheme solves for epoch-wise satellite and receiver clock corrections (5 min sampling) and inter-system biases (ISB; one per combined GPS and Galileo tracking station and day). Orbits, Earth rotation parameters, troposphere parameters, and station coordinates are introduced from the double-difference solution (see Sect. 3) and kept fixed. They are defining the reference frame for the clock solution. The estimated clock corrections are provided in the clock-RINEX and SP3 format. The biases are provided in the CODE DCB and BIAS SINEX formats.

The estimation of satellite clocks is especially sensitive to the availability of redundant measurements at each observation epoch. Therefore, the completeness of the Galileo satellite clock corrections (see Fig. 5) benefits significantly from the contribution of new Galileo tracking sites outside Europe since early 2013, filling some gaps in the tracking network (see also Sect. 2).

One performance indicator for satellite clocks is the RMS of the daily linear fit through the epoch-wise clock estimates. It characterizes how close a clock comes to the ideal of a linear drift and is, e.g., suitable for monitoring the long-term (weeks, months, years) clock characteristics. The daily fit RMS of the estimated clocks of two GPS Block IIF satellites (G01 and G25) is shown in Fig. 6, top for comparison. The corresponding results for the Galileo IOV satellites are displayed in Fig. 6, bottom. The latter figure shows that the Galileo satellite clock estimates are correlated with the elevation angle of the Sun w.r.t. the orbital plane in the same way as the SLR residuals (see Fig. 4). Possible explanations are orbit errors being mapped into the satellite

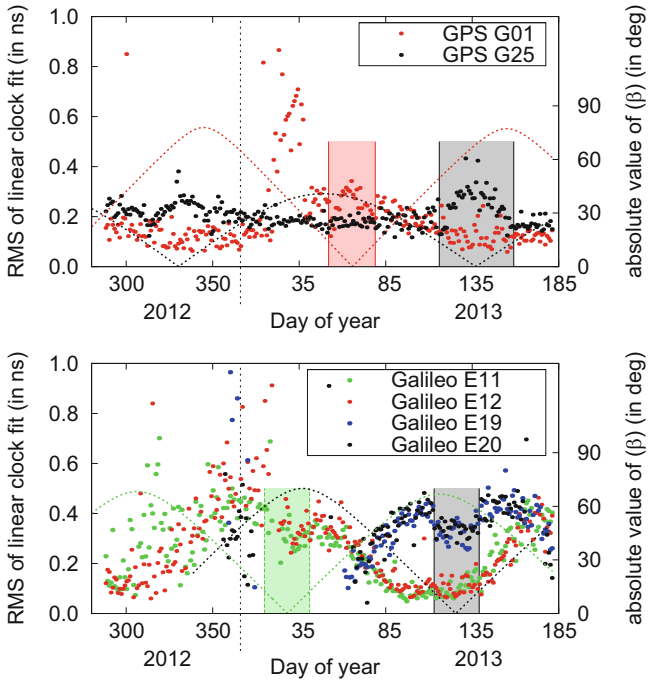

Fig. 6 RMS of daily linear fit through estimated epoch-wise satellite clocks (*big dots*). *Top*: Selected GPS Block IIF satellites. *Bottom*: Galileo IOV satellites. The *shaded areas* mark the eclipsing seasons of G01 (*top, red*), G25 (*top, black*), E11, E12 (*bottom green*), and E19, E20 (*bottom, black*). The *curves* show the absolute value of the elevation of the Sun w.r.t. the satellite's orbital planes (β) with the same color code as the boxes

clock estimates or effects affecting both (orbit estimates and clock corrections) in the same way (e.g., deviations from the nominal attitude model). Figure 6, top suggests that a correlation with the Sun's elevation angle exists also for GPS Block IIF satellite clocks, but it is less pronounced.

Montenbruck et al. (2012) reported an abnormal behavior of satellite clock corrections during eclipse phases (induced by increased orbit errors, thermal effects, and outgasing effects) for GPS SVN62 (currently PRN G25). This is confirmed by the linear clock fit RMS displayed in Fig. 6, top – indicating degraded clock estimates for G01 and G25 during the eclipse phases. In opposition to G01 and G25 the clock fit RMS is reduced during the eclipse seasons for the Galileo IOV satellites (see Fig. 6, bottom). Again, a similar behavior can be seen for the Galileo SLR residuals (see Fig. 4) – though less clearly. The reasons for the different characteristics of the estimated GPS Block IIF and Galileo IOV satellite clocks during eclipse seasons are unclear so far. Further investigations in the frame of MGEX could potentially bring more clarity on this issue.

The above-mentioned variability of the clock estimates accuracy due to eclipses and β-angle dependency makes it difficult to evaluate the true stability of the Galileo satellite clocks. Assuming a degradation of the satellite clock estimates due to the radiation pressure acting in radial direction for low β-angles the real performance of the satellite clocks is supposed to be represented better during periods with large β-angles. Figure 6, bottom shows that the linear clock fit RMS of the Galileo clocks is at a level of about 0.1–0.2 ns in such periods. This is comparable to the values obtained for GPS Block IIF satellites (see Fig. 6, top).

Another way to assess the clock quality are Allan deviations describing the clock stability over different time scales. They are, however, susceptible to clock jumps at the day boundaries and are more or less a snapshot of the clock characteristics at a certain moment. Notice that day-to-day changes in the Galileo network used to define the zero-mean condition for the GPS-Galileo ISBs affect exclusively the Galileo clocks and may contribute to day boundary jumps of the Galileo clock estimates. Figure 7 shows Allan deviations of CODE MGEX clock estimates of GPS Block IIF and Galileo IOV satellites at two different times. The clocks of the Block IIF satellites behave similar at both times. The characteristics of the Galileo clocks are apparently changing: Around DOY 180 the Galileo E11 and E12 clocks show a bulge indicating a once-per-revolution signal in the clocks. Around DOY 100, in contrast, E11 shows even better characteristics than the Block IIF clocks. Both snap-shots agree well with the time series of the linear clock fit RMS (see DOY 100 and 180 in Fig. 6).

The shown results suggest that the performance of the Galileo IOV clocks is at a level comparable to the clocks of the GPS Block IIF satellites. This is, however, not always reflected in the estimated clock corrections, which are affected by effects related to the Sun's elevation w.r.t. the orbital plane. It is worth to point out the different number of tracking stations contributing to the GPS and Galileo satellite clocks (150 for GPS vs. 35–45 for Galileo).

5 Precise Point Positioning

The quality of the generated MGEX orbits and satellite clock corrections is assessed by a precise point positioning (PPP, Zumberge et al. 1997). A set of MGEX stations is selected with the focus on maximum simultaneous visibility of all four Galileo IOV satellites within the time interval DOY 75–84/2013. A static and a kinematic PPP (epoch sampling 300 s) are performed using GPS only, GPS and Galileo together, and even Galileo only, respectively. The PPP-derived coordinates are compared to the coordinates obtained in the double-difference network solution of the same day. Both coordinate sets refer to the reference frame defined by the double-difference network solution. From the differences between network coordinates and PPP coordinates the mean value and standard deviation are computed per station. In order to prevent the statistics from

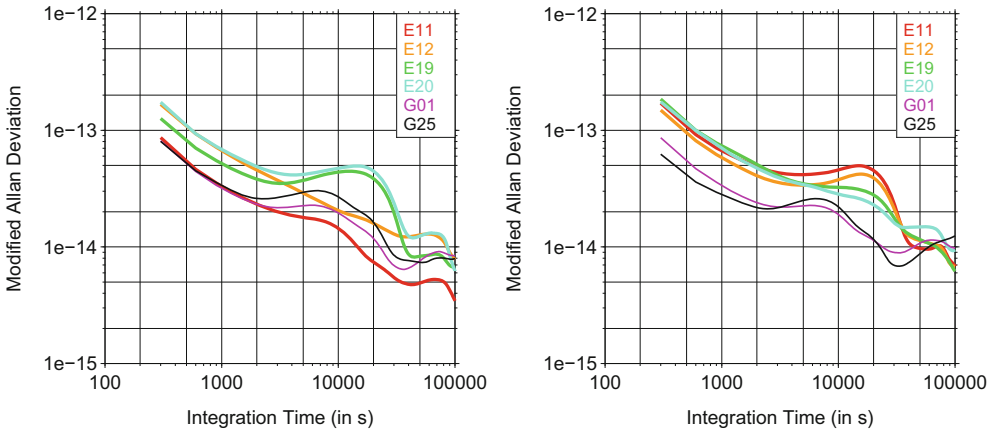

Fig. 7 Modified Allan deviation for 5-day time intervals (reference clock: BRUX). *Left*: Around DOY 100/2013. *Right*: Around DOY 180/2013

Table 2 Difference between PPP coordinates and network coordinates (in mm). Color code: **GPS and Galileo**, **GPS only**, **Galileo only**. *Top*: Static PPP (threshold 30 cm). *Bottom*: Kinematic PPP (threshold 10 m)

	North		East		Up	
Station	Mean	STD	Mean	STD	Mean	STD
OUS2	3.7	1.7	−2.8	2.1	−8.6	6.0
	3.2	1.3	−1.1	2.0	9.3	6.0
	37.9	135.6	33.8	34.4	−0.3	106.9
RIO2	1.7	1.2	−1.0	2.1	2.8	4.3
	1.9	1.2	1.6	2.0	3.2	3.7
	−27.2	62.7	−59.0	86.2	−9.7	50.8
TASH	0.3	1.1	2.8	2.4	1.9	4.1
	−0.4	0.8	1.2	2.0	3.4	4.4
	17.4	92.1	57.0	77.8	−43.3	101.3
ZIM3	2.5	1.0	1.0	1.7	−9.9	2.8
	−0.4	0.8	1.2	2.0	−9.5	3.4
	50.2	83.7	47.4	96.9	−65.9	91.9
OUS2	3.0	33.0	−7.8	38.1	210.1	112.1
	2.5	38.6	−7.2	47.7	216.8	119.9
	−104.6	1756.6	572.3	1036.7	−191.3	2251.3
RIO2	8.0	36.8	8.2	39.4	181.5	141.6
	7.8	43.9	12.2	47.5	185.7	149.0
	−223.0	1283.7	−18.9	516.1	−549.8	1539.8
TASH	1.5	19.4	0.9	26.6	112.1	92.8
	1.1	21.6	−2.2	29.6	114.2	95.0
	−326.2	1229.5	270.9	741.1	−7.2	1393.7
ZIM3	3.0	12.5	3.5	16.5	30.0	54.2
	3.3	13.2	1.0	17.0	30.3	55.1
	−112.2	690.3	13.8	369.2	246.7	944.6

being affected by few large outliers, coordinate differences exceeding a rejection threshold (30 cm in the static and 10 m in the kinematic case) are excluded from the statistics computation.

The comparison results in Table 2, top show that the GPS-only and combined solutions are on the same level of performance, i.e., the added Galileo observations do not contribute significantly to the static PPP. This is expected given the small number of Galileo measurements.

The four currently available Galileo satellites may, however, slightly contribute to a kinematic PPP (see Table 2, bottom). In this scenario the improved observation geometry achieved by the availability of additional satellites overcompensates for their reduced orbit and clock quality. Table 2, bottom shows also that a kinematic PPP using only the four Galileo IOV satellites is possible with standard deviations on the decimeter- to meter-level. Notice that due to the lack of redundancy these results represent mainly the satellite geometry. The Galileo-only kinematic PPP is of course limited to those time intervals when a tracking station has simultaneous visibility to all four IOV satellites (about 1–3 h per day for the selected stations in the time period DOY 75–84/2013).

6 Summary and Conclusion

The CODE analysis center contributes to the IGS MGEX with a triple-GNSS (GPS, GLONASS, and Galileo) orbit solution, and a dual-GNSS (GPS and Galileo) clock solution, which are publicly available. Galileo is currently the new GNSS that is best tracked by the MGEX network. The most commonly tracked Galileo frequencies are L1 (E1) and L5 (E5a). Therefore, the focus of our MGEX activities is on Galileo L1 and L5 signals so far.

The orbit validation shows that Galileo orbits benefit more than GPS and GLONASS orbits from long orbit arcs. Reasons are the Galileo tracking network with its still more sparse and inhomogeneous station distribution and the longer orbital period of the Galileo satellites (allowing less than two full revolutions per day). The CODE MGEX orbits made available to the public are therefore based on 3-day longarc solutions. The SLR validation of the Galileo orbits has a stan-

dard deviation of about 1 dm and shows a strong correlation with the Sun's elevation w.r.t. the orbital plane. The same correlation is observed for the estimated Galileo satellite clock corrections. These effects will be further investigated by CODE in the frame of MGEX.

The CODE MGEX orbit and clock products are used for a static and for a kinematic PPP. It is demonstrated that the Galileo products may slightly contribute to a combined kinematic PPP solution. Moreover a Galileo-only PPP is possible for limited time intervals and selected stations. The achieved accuracies on the meter-level reflect mainly the observation geometry because of the lack of redundancy.

The analysis of RINEX3 data provided in the frame of MGEX turned out to be very useful for extending, adapting, and testing the Bernese GNSS Software, CODE's raw data monitoring, and processing chains as a preparation for future IGS developments. It also helps to identify relevant topics for further investigations and improvements. We therefore thank the contributing station operators and data centers for providing the data. It is our plan to continue with further improvements of our analysis strategy and observation modeling, further studies about the characteristics of the new observations and satellites, support of additional GNSS, and occasional product releases.

References

Beutler G, Brockmann E, Gurtner W, Hugentobler U, Mervart L, Rothacher M (1994) Extended orbit modeling techniques at the CODE processing center of the international GPS service for geodynamics (IGS): theory and initial results. Manuscr Geodaet 19:367–386

Bock H, Dach R, Jäggi A, Beutler G (2009) High-rate GPS clock corrections from CODE: support of 1 Hz applications. J Geodesy 83(11):1083–1094. doi:10.1007/s00190-009-0326-1

Bruyninx C, Baire Q, Legrand J, Roosbeek F (2011) The EUREF permanent network (EPN): recent developments and key issues. Presented at EUREF 2011 symposium, Chisinau, Republic of Moldova

CODE (2013) http://igscb.igs.org/igscb/center/analysis/code.acn

Dach R, Beutler G, Bock H, Fridez P, Gäde A, Hugentobler U, Jäggi A, Meindl M, Mervart L, Prange L, Schaer S, Springer T, Urschl C, Walser P (2007) Bernese GPS software version 5.0: user manual. Astronomical Institute, Universtiy of Bern, Bern

Dach R, Brockmann E, Schaer S, Beutler G, Meindl M, Prange L, Bock H, Jäggi A, Ostini L (2009) GNSS processing at CODE: status report. J Geodesy 83(3–4):353–366. doi:10.1007/s00190-008-0281-2

Dach R, Schaer S, Lutz S, Meindl M, Bock H, Orliac E, Prange L, Thaller D, Mervart L, Jäggi A, Beutler G, Brockmann E, Ineichen D, Wiget A, Weber G, Habrich H, Ihde J, Steigenberger P, Hugentobler U (2013) Center for orbit determination in Europe (CODE). In: Dach R, Jean Y (eds) International GNSS service: Technical Report 2012 (AIUB), IGS Central Bureau, pp 35–46

Dow JM, Neilan RE, Rizos C (2009) The international GNSS service in a changing landscape of global navigation satellite systems. J Geodesy 83(3–4):191–198. doi:10.1007/s00190-008-0300-3

Flohrer C (2008) Mutual validation of satellite-geodetic techniques and its impact on GNSS orbit modeling. Geodätisch-geophysikalische Arbeiten in der Schweiz, vol 75. PhD Thesis, Astronomical Institute, University of Bern. ISBN:978-3-908440-19-2

Ineichen D, Springer T, Beutler G (2003) Combined processing of the IGS and the IGEX network. J Geodesy 75(11):575–586

Lutz S, Arnold D, Schaer S, Dach R, Jäggi A (2013) New RINEX file monitoring at CODE. Poster, EUREF symposium 2013, Budapest, 29–31 May

MacLeod K, Agrotis L (2013) IGS RINEX working group report 2011. In: Dach R, Jean Y (eds) International GNSS service: Technical Report 2012 (AIUB), IGS Central Bureau, pp 191–194

Montenbruck O, Steigenberger P, Schönemann E, Hauschild A, Hugentobler U, Dach R, Becker M (2012) Flight characterization of new generation GNSS satellite clocks. Navigation 59(4):291–302

Montenbruck O, Rizos C, Weber R, Weber G, Neilan RE, Hugentobler U (2013) Getting a grip on multi-GNSS: the international GNSS service MGEX campaign. GPS World 24(7):44–49

Prange L, Dach R, Lutz S, Schaer S, Meindl M, Jäggi A (2012) MGEX data analysis at CODE - first experiences. Presentation, IGS workshop 2012, Olsztyn, 23–27 July

Prange L, Lutz S, Dach R, Schaer S, Jäggi A (2013) MGEX data analysis at CODE - current status. Presentation, EGU general assembly 2013, Vienna, 7–12 April

Willis P, Beutler G, Gurtner W, Hein G, Neilan RE, Noll C, Slater J (1999) IGEX: international GLONASS experiment - scientific objectives and preparation. Adv Space Res 23(4):659–663. doi:10.1016/S0273-1177(99)00147-7

Zumberge JF, Heflin MB, Jefferson DC, Watkins MM, Webb FH (1997) Precise point positioning for the efficient and robust analysis of GPS data from large networks. J Geophys Res 102(B3):5005–5017

G-Nut/Anubis: Open-Source Tool for Multi-GNSS Data Monitoring with a Multipath Detection for New Signals, Frequencies and Constellations

Pavel Vaclavovic and Jan Dousa

Abstract

The GNSS software library G-Nut has been developed at the Research Institute of Geodesy, Topography and Cartography since 2011. Along with the PPP applications for positioning and troposphere monitoring, the third tool recently built using the new library is called Anubis. Its initial purpose is to provides quantity and quality monitoring for multi-GNSS data stored in RINEX 2.xx ($\leq$ 2.11) and 3.0x ($\leq$ 3.02) formats. Editing, cutting and splicing modes will be supported after implementing RINEX encoder in future. The Anubis is capable to handle all new emerging signals from all global navigation satellite systems and their augmentations (GPS, GLONASS, Galileo, BeiDou, SBAS and QZSS). Additionally, Anubis supports GPS, GLONASS and Galileo broadcast navigation messages, while others will be implemented soon. Supported with relevant navigation messages, Anubis performs single point positioning and provides GNSS data characteristics in elevation and azimuth dependencies. The pre-processing mode is used for the reconstructing observations affected by cycle slips or receiver clock jumps. A new algorithm was developed for code multipath detection supporting all signals, frequency bands and GNSS constellations. Being an open-source tool, Anubis is suitable for GNSS data providers as well as data and analysis centres for the quality and content monitoring prior to the data archiving, dissemination or a final GNSS analysis. The Anubis first version was released in the mid of 2013 under the GNU General Public Licence, version 3.

Keywords

Code multipath • Experimental data • MGEX • Multi-GNSS • Pre-processing • Quality checking

1 Introduction

The Geodetic Observatory Pecný (GOP) acts as analysis centre for precise GNSS data processing of various networks for coordinate and velocity estimation, troposphere monitoring and GNSS orbit determination. Data from national, European and global sites stemming from various sources are used for all these applications. Data are disseminated in the standard RINEX (Receiver Independent Exchange) format (Gurtner and Estey 2009), but usually without information on the data quality and content. Any corrupted file may cause unexpected behaviour in analyses requiring specific manual interventions.

Data quality monitoring provides information not only for data processing activities, but also for a high-quality data collection and archiving by individual providers or by scientific services such as the International GNSS Service (IGS) (Dow et al. 2009). New challenges arose with emerging many new GNSS signals, frequencies and constellations over past

P. Vaclavovic (✉) • J. Dousa
NTIS – New Technologies for Information Society, Research Institute of Geodesy, Topography and Cartography, Ústecká 98, 25066 Zdiby, Czech Republic
e-mail: pavel.vaclavovic@pecny.cz

© Springer International Publishing Switzerland 2015

C. Rizos, P. Willis (eds.), *IAG 150 Years*, International Association of Geodesy Symposia 143,
DOI 10.1007/1345_2015_97

years. The RINEX 3.0x format has been standardized for including all new data. Several programs for data quality checking exist, such as TEQC (Estey and Meertens 1999) and BKG Ntrip Client (Weber and Mervart 2009), but only the latter is open-source and supports the new RINEX 3.0x format. Experimental data, e.g. provided by the IGS MGEX campaign (Montenbruck et al. 2013) including a maximum of GNSS signals available in space, need to be properly monitored and tested prior to their use in operational analyses. This was the main motivation to develop a new open-source tool which we call Anubis.

The Anubis application is derived from the G-Nut software library (Vaclavovic et al. 2013) being developed at GOP of the Research Institute of Geodesy, Topography and Cartography. The library is designed for developing various GNSS end-user applications, e.g. for positioning, troposphere monitoring and others. It is written in C++ applying object-oriented programming approach for a high adaptability in future utilizations. Although it is designed for a command-line operation with a single input configuration file, a graphical user interface can be added in future.

The main purpose of the Anubis tool is currently the quantity and quality monitoring of all available GNSS data, i.e. signals, frequencies and satellite constellations. Editing, cutting and splicing modes will be supported after implementing RINEX encoder which is planned in future. Proper attention was paid recently to support RINEX 2.xx ($\leq$ 2.11) and RINEX 3.0x ($\leq$ 3.02) input formats. While the G-Nut library is not publicly distributed, the Anubis and other end-user applications are released under the GNU Public License v3 and the source code can be downloaded from the web http://www.pecny.cz/. The compilation and execution can be tested using the example data and configurations provided in an additional support area (see the web page). The software is designed as a multi-platform application with no extra need for specific developing libraries or programming frameworks. Although Anubis was successfully compiled on Windows and OS X, we currently support only Linux operating systems due to the presence of a few critical points for an easy compilation on other systems. However, this is expected to be resolved for any future release.

This paper aims for describing basic functionalities and algorithms of the first release of Anubis in August, 2013. The program configuration structure and setting options are described in the second section. Extraction output format including quantitative and qualitative statistics is discussed in the third section. Algorithms used for data quality monitoring, i.e. pre-processing and code multipath estimation, is described in the fourth and fifth section, respectively. In particular, the fifth section provides a new formula developed for the multi-signal, multi-frequency and multi-constellation code multipath detection. Summary and future Anubis developments are concluded in the last section.

2 User Configuration

Anubis can be executed from a command line with a single parameter defining the configuration file name in the Extensible Markup Language (XML) format or, alternatively, by reading XML configuration from the standard input (or via Linux pipe):

Anubis -x config.xml *(Anubis < config.xml).*

The XML format has been chosen because of its flexibility, extensibility and the support by many end-user editors. The format is applied for all end-user applications derived from the G-Nut library while different elements correspond to the specific application functionalities. The configuration file starts with sections common to all G-Nut's applications concerning the input, output and general settings. Additional XML elements are used by individual applications, such as $< qc >$ used by Anubis only. The example of a configuration is given below for a brief discussion:

```
<?xml version="1.0" encoding="UTF-8" standalone="yes" ?>
<!DOCTYPE config>
<config>

 <gen>
   <beg> "2013-02-09 00:00:00" </beg>
   <end> "2013-02-09 23:59:30" </end>
   <sys> GPS GLO GAL BDS SBS QZS </sys>
   <int> 30 </int>
   <rec> BRUX GOPE MATE </rec>
 </gen>

 <inputs>
   <rinexo> RINEX/mate0400.13o </rinexo>
   <rinexo> RINEX/gope0400.13o </rinexo>
   <rinexo> RINEX/brux0400.13o </rinexo>
   <rinexn> RINEX/brux0400.13n </rinexn>
   <rinexn> RINEX/brux0400.13g </rinexn>
   <rinexn> RINEX/brux0400.13l </rinexn>
 </inputs>

 <qc sec_sum="1"
     sec_hdr="1"
     sec_est="1"
     sec_obs="1"
     sec_gap="1"
     sec_bnd="2"
     sec_pre="1"
     sec_ele="1"
     sec_mpx="2"
     int_stp="1200"
     int_gap="600"
     int_pcs="1800"
     mpx_nep="15"
     mpx_lim="3.0" />

 <outputs verb="1" >
   <xtr> $(rec)_130400.xtr </xtr>
   <xml> $(rec)_130400.xml </xml>
   <log> /dev/stdout       </log>
 </outputs>
</config>
```

The section $< gen >$ defines general information, such as the beginning and the end epoch of data to be dealt with (*beg*, *end*), list of requested satellite systems (*sys*), sampling interval (*int*) and the list of marker names included in the processing (*rec*). The section $< inputs >$ defines all input files

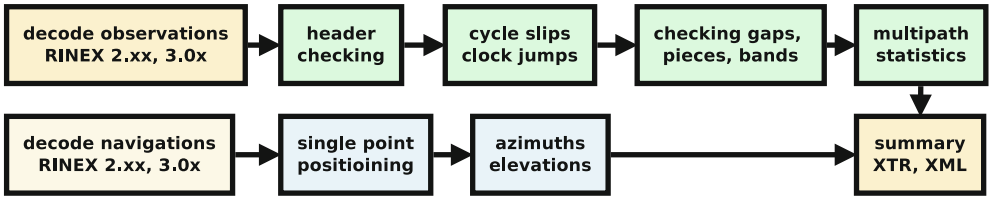

Fig. 1 Basic block diagram of Anubis operation

in specific formats, such as observation (*rinexo*) and navigation (*rinexn*) data. If navigation files are defined, extracted quantities are supported with azimuths and elevations.

The section $< qc >$ contains the level of verbosity settings for individual Anubis functions as shown in Fig. 1:
- summary information (*sec_sum*),
- meta data in header and from user requests (*sec_hdr*),
- overall observation statistics (*sec_obs*),
- data gaps and small data pieces (*sec_gap*),
- band counting from available observations (*sec_bnd*),
- cycle slip and clock jump detection (sec_pre),
- azimuth and elevation information (sec_ele),
- multipath estimation (sec_mpx).

Additional attributes concern specific procedure settings, such as (a) interval step in seconds for all time-specific characteristics (int_stp), (b) intervals in seconds for detecting gaps and small data pieces (int_gap, int_pcs) and (c) settings for the multipath estimation – the number of epochs used for the multipath calculation (mpx_nep) and the factor for sigma multiplication for internal cycle slip detection (mpx_lim). It should be noted, that this factor does not relate to the pre-processing part. In case of missing any specific setting, the default values are used.

The last section $< outputs >$ defines requested output files, which can be done uniquely for all processed sites (receivers) via applying a specific variable (rec). Along with the general log file (in our example the standard output), Anubis output can be stored in two extraction files (xtr) and (xml). While the former is an original Anubis format described in the next section, the latter is the XML format developed at the Center for Orbit Determination in Europe (CODE) (Lutz et al. 2013). As shown in the setting example, Anubis can be configured to process more RINEX files at once, e.g. all data stored in a directory.

3 Anubis Summary File

Results of the Anubis data quality and quantity analysis are summarized in the extraction file. Its format has been defined as a plain text divided into multiple sections containing similar structure and supporting easy information searching via defined keywords. The format also support epoch-wise and satellite-specific characteristics suitable for plotting; the former is organized in lines, the latter in a fixed column format. Table 1 shows three example segments of the extraction – (a) summary part, (b) observation quantitative statistics and (c) elevation and azimuth angles. Users decide how detailed information they require via the verbosity setting in the configuration file.

The observation section contains a list of available systems, satellites and signals. The summary contains two lists – the one reported in the header (e.g. *GPSHDR* keyword in Table 1) and the second from collecting real data (*GPSOBS* keyword). From such comparison the user can identify empty data records which is often the case in the EUREF and IGS experimental campaigns. The elevation and azimuth section is supported only if broadcast ephemerides are available.

For a brief user overview, the most important is the summary section which is explained in detail. Each line represents one GNSS or augmentation system and its relevant data summary quantification. The first three values provide an overview of the number of epochs – expected within a period and sampling (*ExpEp*), observed (*HavEp*) and usable (*UseEp*). The usable epoch is introduced if four or more satellites are observed with the minimum of two frequencies. The criterion of four satellites is applied only to global constellations, i.e. not the augmentation systems like SBAS or QZSS.

The next two values (*xCoEp* and *xPhEp*) count the amount of excluded measurements due to the presence of single-frequency code or carrier phase observations. Additional details are given in the *xCoSv* and *xPhSv* values summarizing the total number of satellites with only a single-band code and carrier phase observation, respectively. If the level of verbosity for the pre-processing is set to two or more, numbers of detected cycle slips and clock jumps are printed in *nSlp* and *nJmp* columns, while further event details are printed in the pre-processing section, see Table 2. The presence of data gaps and short data pieces, both defined by criteria in the settings, are summed up in the *nGap* and *nPcs*, respectively. The last columns (mpx) show mean values of multipath for individual frequencies over all signals.

4 Data Pre-processing Algorithm

Data pre-processing, i.e. searching and repairing clock jumps and phase cycle slips, is very important part of any software dealing with GNSS carrier phase data analysis. For

Table 1 Selected segments of the Anubis extraction from RINEX 3.01 observation and navigation data for GOP7 station, April 15, 2013

```
# gNut—Anubis [1.0.1] compiled: Nov  1 2013 09:52:48 ($Rev: 615 $)

#====== Summary (v.1)
#GNSSUM 2013—04—15 00:00:00 ExpEp HavEp UseEp xCoEp xPhEp xCoSv xPhSv  nSlp  nJmp  nGap  nPcs   mp1   mp2   mp5   mp6   mp7   mp8
=GPSSUM 2013—04—15 00:00:00  2880  2880  2880     0     0   430   424   219     0     0     0  47.7  53.5  23.5     —     —     —
=GALSUM 2013—04—15 00:00:00  2880   974     0   974   974     2     2     0     0     0     0  43.3     —  16.1     —     —     —
=GLOSUM 2013—04—15 00:00:00  2880  2880  2880     0     0   162   156     0     0     0     0  53.3  64.2     —     —     —     —
=QZSSUM 2013—04—15 00:00:00  2880    96    96     0     0     0     0     0     0     0     0     —     —     —     —     —     —
=SBSSUM 2013—04—15 00:00:00  2880  2880  2880     0     0 10226 10226     0     0     0     0     —     —     —     —     —     —

#====== Observations (v.1)
=GNSSYS 2013—04—15 00:00:00     5 GPS GAL GLO QZS SBS
=GPSSAT 2013—04—15 00:00:00    32 G01 G02 G03 G04 G05 G06 G07 G08 G09 G10 G11 G12 G13 G14 G15 G16 G17 G18 G19 G20 G21 G22 G23 G24
=GALSAT 2013—04—15 00:00:00     2   —   —   —   —   —   —   —   —   — E11 E12   —   —   —   —   —   —   —   —   —   —   —   —
=GLOSAT 2013—04—15 00:00:00    24 R01 R02 R03 R04 R05 R06 R07 R08 R09 R10 R11 R12 R13 R14 R15 R16 R17 R18 R19 R20 R21 R22 R23 R24
=QZSSAT 2013—04—15 00:00:00     1 J01   —   —   —   —   —   —   —   —   —   —   —   —   —   —   —   —   —   —   —   —   —   —
=SBSSAT 2013—04—15 00:00:00     4   —   —   —   —   —   —   —   —   —   —   —   —   —   —   —   —   —   — S20   —   —   — S24
=GALHDR 2013—04—15 00:00:00     6 C1X L1X S1X C5X L5X S5X
=GPSHDR 2013—04—15 00:00:00    15 C1C L1C S1C C1W L1W S1W C2X L2X S2X C2W L2W S2W C5X L5X S5X
=QZSHDR 2013—04—15 00:00:00     9 C1C L1C S1C C2X L2X S2X C5X L5X S5X
=GLOHDR 2013—04—15 00:00:00    12 C1C L1C S1C C1P L1P S1P C2C L2C S2C C2P L2P S2P
=SBSHDR 2013—04—15 00:00:00     3 C1C L1C S1C
=GPSOBS 2013—04—15 00:00:00    15 C1C C1W C2W C2X C5X L1C L1W L2W L2X L5X S1C S1W S2W S2X S5X
=GALOBS 2013—04—15 00:00:00     6 C1X C5X L1X L5X S1X S5X
=GLOOBS 2013—04—15 00:00:00    12 C1C C1P C2C C2P L1C L1P L2C L2P S1C S1P S2C S2P
=QZSOBS 2013—04—15 00:00:00     9 C1C C2X C5X L1C L2X L5X S1C S2X S5X
=SBSOBS 2013—04—15 00:00:00     3 C1C L1C S1C

#====== Elevation & Azimuth (v.1)
#GNSELE 2013—04—15 00:00:00    Mean x01 x02 x03 x04 x05 x06 x07 x08 x09 x10 x11 x12 x13 x14 x15 x16 x17 x18 x19 x20 x21 x22 x23 x24
 GPSELE 2013—04—15 00:00:00      36   —   —  46   —   —  67  11   —   —   —   —   —   —   —  10  61   —  51  24   —  56  34   —   —
 GPSELE 2013—04—15 00:15:00      40   —   —  53   —   —  74  11   —   —   —   —   —   —   —  12  57   —  55  30   —  49  41   —   —
 GPSELE 2013—04—15 00:30:00      40   —   —  60   —   —  80  11   —   —   —   —   —   —   —  13  51   —  56  36   —  43  48   —   —
 GPSELE 2013—04—15 00:45:00      35   —   —  67   —   —  85   9   9   —   —   3   —   —   —  14  44   —  56  43   —  37  54   —   —
 GPSELE 2013—04—15 01:00:00      34   —   —  73   —   —  81   7   9   —   —   9   —   —   —  13  38   —  54  49   —  31  60   —   —
 GPSELE 2013—04—15 01:15:00      35   —   —  77   —   —  74   4   8   —   —  14   —   —   —  11  31   —  50  56   —  25  64   —   —
 GPSELE 2013—04—15 01:30:00      34   4   —  76   —   —  67   0   7   —   —  20   —   —  10   —  24   —  46  63   —  20  67   —   —
 GPSELE 2013—04—15 01:45:00      36   9   —  72   —   —  60   —   5   —   —  26   —   —  15   —  18   —  41  69   —  14  67   —   —
 GPSELE 2013—04—15 02:00:00      32  15   —  65   —   —  53   —   2   —   —  32   —   —  21   —  11   —  35  75   —   9  64   —   —
 GPSELE 2013—04—15 02:15:00      32  20   —  58   —   —  46   —   —   —   —  38   —   —  26   —   5   —  29  78   —   3  60   —   —
 GPSELE 2013—04—15 02:30:00      38  26   —  51   —   —  39   —   —   —   —  45   —   —  32   —   —   —  23  77   —   —  54   —   —
 GPSELE 2013—04—15 02:45:00      34  32   —  44   —   —  32   —   —   —   —  51   —   —  36   —   —   —  18  71   1   —  48   —   —
```

high-accurate applications, only periods with uninterrupted satellite tracking can be used efficiently due to a single initial ambiguity set up for each satellite and frequency. If the continuity is broken for a particular satellite and a relevant cycle slip cannot be estimated, a specific ambiguity must be added to the solution implying additional estimated parameters.

Anubis exploits various time differentiated linear combinations that are compared with predefined thresholds. The cycle slip detection algorithm is based on Melbourne-Wuebbena (Wuebbena 1985) and geometry-free linear combinations due to their useful properties. The latter is usually denoted as L_4 and defined by the equation

$$\begin{aligned} L_4 = L_1 - L_2 &= \lambda_1 N_1 - \lambda_2 N_2 - I_1 + I_2 \\ &= \lambda_1 N_1 - \lambda_2 N_2 - I_1 \left(1 - \frac{f_1^2}{f_2^2}\right), \end{aligned} \tag{1}$$

where subscripts 1 and 2 stand for band numbers, L is the carrier frequency in meters, λ denotes wavelength, N initial ambiguity, I ionospheric delay and f frequency. The L_4 is independent of receiver clock errors and geometry (satellite/receiver position) and it contains only ionospheric delays and initial ambiguities for both frequencies. All other frequency-independent terms are neglected. The first two terms on the right site of Eq. (1) are constant in time meaning that any unexpected jump in L_4 must be caused by a cycle slip. The detection is based on the following criterion

$$L_4(t_2) - L_4(t_1) > k \cdot \sigma_{L4} + \Delta I_{max}. \tag{2}$$

The maximal ionospheric delay I_{max} is implicitly defined as 0.4 m/h in Anubis and the factor k is set to 4. The advantage of such approach is that it is based on carrier phase data only. On the other hand, it should be noted that in case of a positive test, we do not know whether any of L_1, L_2 or both are corrupted.

If dual-frequency carrier phase L and pseudorange P are available, the Melbourne-Wubbena linear combination (L_6) can be formed mixing wide-lane phase (L_W) and narrow-lane pseudorange (P_N) measurements

$$\begin{aligned} L_6 = L_W - P_N &= \frac{1}{f_1 - f_2}(f_1 L_1 - f_2 L_2) \\ &\quad - \frac{1}{f_1 + f_2}(f_1 P_1 + f_2 P_2) \\ &= \lambda_W N_W = \frac{c}{f_1 - f_2}(N_1 - N_2) \end{aligned} \tag{3}$$

where λ_W and N_W are called wide-lane wavelength and ambiguity, respectively.

The advantage of using the L_6 combination is due to the elimination of ionosphere, troposphere, geometry (satellite and receiver positions) and satellite and receiver clocks. The wavelength of this combination is approximately 86 cm. On the other hand, the inclusion of pseudorange observations increase the noise of the linear combination. Comparing L_6 for epochs t_1 and t_2 provides the information whether a slip occurs or not. It should be noted that slips on L_1 or L_2 cannot be checked directly, but their difference only. Due to a constant property of the right term in Eq. (3) we can check a presence of a cycle slip through the temporal differencing of L_6 observations. The detection is based on the criteria

$$L_6(t_2) - L_6(t_1) > k \cdot \sigma_{L6} \tag{4}$$

where the coefficient k is set to 4 and σ_{L_6} is the sigma of the L_6 observation. The coefficient k is introduced with assumption of normally distributed measurement linear combinations. Almost 99.9 cycle slips should be detected with k set up to 4. Sigmas for L_4 and L_6 are calculated according to the law of variance propagation from used observation sigmas. Since a cycle slip on any specific frequency cannot be detected, but only on $L_1 - L_2$ linear combination, any cycle slip common to L_1 and L_2 becomes undetectable. An improvement of the technique resides in the differencing L_6 from a single epoch and a mean value over all previous epochs since the last occurring cycle slip. This approach is planned for the next release.

The second purpose of the pre-processing consists of detecting and correcting for receiver clock jumps. Due to a low quality of some receiver oscillators, clocks are shifted by one or a few milliseconds when the clock bias becomes too large. Observations at a particular epoch as well as observations in all subsequent epochs are affected in the same way and must be corrected for. Otherwise ambiguity re-initialization and a new convergence interval would appear regularly. The principle of our algorithm resides in the pseudorange compensations of the clock jumps, while carrier phases for each satellite could still contain the same cycle slip (Guo and Zhang 2013). Fortunately, we know that the slip is exactly a millisecond or a few milliseconds, therefore, we can repair it precisely. Anubis can be thus used for recovering the coherency between range and phase data. One section of Anubis extraction provides results from the cycle slip and receiver clock jump detection, in which all values estimated and relevant epochs are reported. Values of cycle slips and clock jumps as well as epochs at which these occur are reported.

Table 2 shows an example of extracted results from the pre-processing. It starts with a summary of the number of detected cycle slips and clock jumps (*TotSlp* and *TotJmp*) followed by estimated values of slip cycles for each frequency and milliseconds of a clock jump in a particular epoch. As long as the cycle slip can not be calculated reliably, the 'n/a' flag is reported.

Table 2 Pre-processing sample output for station KUNZ (December 26, 2010)

```
#====== Preprocessing (v.3)
#PREPRO 2010-12-26 00:00:00 TotSlp[GPS] TotSlp[GLO]   TotJmp
=SUMPRP 2010-12-26 00:00:00           1           0      121

#GPSSLP 2010-12-26 00:00:00  PRN   SlipL1   SlipL2
 GPSSLP 2010-12-26 05:15:30  G10     -106    24694

#CLKJMP 2010-12-26 00:00:00  [ms]
 CLKJMP 2010-12-26 00:07:30   1
 CLKJMP 2010-12-26 00:19:30   2
 CLKJMP 2010-12-26 00:31:00   3
 CLKJMP 2010-12-26 00:42:30   4
 CLKJMP 2010-12-26 00:54:30   5
 CLKJMP 2010-12-26 01:06:00   6
 ...
```

5 Code Multipath Algorithm

The multipath affects both basic GNSS observations-pseudoranges and carrier phases, however, the former is much larger and variable among receiver types. The multipath error has a substantial contribution to the accuracy of observed pseudoranges, which are mainly used in a single point positioning technique (navigation, precise point positioning etc.). The knowledge of the multipath effect and pseudorange noise can be useful for a proper observation weighting. Such information can also provide specific characteristics of the receiver or about the station environment.

When dual-frequency data are available, pseudorange multipath is estimated from the linear combination eliminating the satellite-receiver geometry and all atmospheric effects. However, this combination does not eliminate ambiguities and any differential biases. While the latter is almost constant over time, this assumption is not always true for ambiguities due to a presence of cycle slips. The pre-processing (and optionally a cycle slip repair) is thus important for the multipath estimation. A simple cycle slip detection is already included in our algorithm independently of the Anubis's standard pre-processing algorithm (see above section) that does not still support all these signals.

We have developed a new general formula for Anubis supporting linear combination (*MP*) for pseudorange multipath estimates for all frequencies, available signals and GNSS constellations providing dual-frequency observations at least

$$MP_k = P_k - L_i - \beta(L_i - L_j) = P_k + \alpha L_i + \beta L_j, \tag{5}$$

Fig. 2 Pseudorange multipath estimated for all GNSS signals observed at the EUREF station AXPV (*top*) and BSCN (*bottom*) during January-November, 2013

with

$$\alpha = -\frac{(f_j^2 + f_k^2)}{(f_i^2 - f_j^2)}\frac{f_i^2}{f_k^2} \qquad \beta = \frac{(f_i^2 + f_k^2)}{(f_i^2 - f_j^2)}\frac{f_j^2}{f_k^2}, \tag{6}$$

where k, i and j are frequency (band) indexes. In the case of $k = i = 1$ and $j = 2$, the well-known equation for the code multipath at the first frequency can be obtained (Estey and Meertens 1999)

$$MP_1 = P_1 - L_1 - \frac{2f_2^2}{(f_1^2 - f_2^2)}(L_1 - L_2). \tag{7}$$

Similarly for $k = i = 2$ and $j = 1$ the code multipath for the second frequency is

$$MP_2 = P_2 - L_2 - \frac{2f_1^2}{(f_2^2 - f_1^2)}(L_2 - L_1). \tag{8}$$

Finally, for $k = 5, i = 1$ and $j = 2$ or any other frequency the code multipath can be expressed as follows

$$MP_5 = P_5 - L_1 - \frac{(f_1^2 + f_5^2)}{(f_1^2 - f_2^2)}\frac{f_2^2}{f_5^2}(L_1 - L_2). \tag{9}$$

The multipath statistics are then estimated as a standard deviation over a sequence of consecutive epochs (usually 15–30; mpx_int setting option) where the calculated mean represents all remaining biases. We do not require any specific pre-processing for all involved GNSS constellations because a simple cycle slip detection algorithm was implemented as a part of the statistics estimation based on multipath linear combinations only.

In the case of dual-frequency data, the multipath statistics are calculated applying the same formulas as used in other software, e.g. teqc and BNC. However, the results may differ due to tuning the estimation procedure which concerns of the cycle slip detection, observation window or others. The main advantage of the approach applied in Anubis relies in a flexible extension to all signals while keeping two carrier phase observations common to all multipath observables. Applying Eq. (5), we need to check two carrier phases for cycle slips only, which is used to speed up the algorithm.

Figure 2 shows the example of pseudorange multipath estimation calculated for two EUREF stations – AXPV (top) and BSCN (bottom). All GNSS signals for all available frequency bands are plotted for the period of January-November 2013. First, we can notice a stable multipath estimation during the whole interval, however, interesting is a progressive improvement for the BeiDou C7I signal.[1]

[1]For systems providing wide-band tracking (e.g. for Galileo E5a, E5b and E5a+E5b), the band/frequency number (n) in RINEX3 format is

Table 3 Multipath detection summary in the first verbose mode (example station GOP7)

#====== Code multipath (v.1)									
#GNSMxx	2013—04—15	00:00:00	mean	x01	x02	x03	x04	x05	x06 ...
=GPSM1C	2013—04—15	00:00:00	48.06	42	47	58	43	45	41 ...
=GPSM1W	2013—04—15	00:00:00	58.44	49	59	85	66	52	43 ...
=GPSM2W	2013—04—15	00:00:00	61.08	57	58	100	66	56	51 ...
=GPSM2X	2013—04—15	00:00:00	62.15	48	—	—	—	62	— ...
=GPSM5X	2013—04—15	00:00:00	27.55	15	—	—	—	—	— ...
=GALM1X	2013—04—15	00:00:00	45.33	—	—	—	—	—	— ...
=GALM5X	2013—04—15	00:00:00	18.58	—	—	—	—	—	— ...
=GLOM1C	2013—04—15	00:00:00	76.39	65	62	77	88	68	63 ...
=GLOM1P	2013—04—15	00:00:00	38.45	48	28	33	39	37	32 ...
=GLOM2C	2013—04—15	00:00:00	106.41	125	149	77	92	90	89 ...
=GLOM2P	2013—04—15	00:00:00	33.86	40	41	25	32	32	35 ...

Second, the lowest multipath effect can be observed for Galileo C8I signal (which was expected due to the AltBOC modulation), while the most worse performance shows the GLONASS C1C signal (visible at AXPV, but also typical for other stations). Two receivers, TRIMBLE NETR9 (AXPV) and LEICA GR25 (BSNC), show different quality of pseudorange observations in general. We can also notice the switch between X and Q tracking modes[2] at BSCN station for most of the GPS and Galileo signals. This is commonly observed at many other stations in the EUREF and IGS MGEX experimental campaigns. Finally, occasional interruptions of tracking GLONASS and Galileo satellites can be identified too.

Table 3 demonstrates multipath estimates for the undetailed verbose mode. Each line represents a single GNSS signal together with code multipath values for all available satellites as well as the mean over all of them.

6 Outlook and Conclusion

We have described initial functionality of the open-source tool Anubis for a qualitative and quantitative monitoring of new GNSS signals. The Anubis has been developed at GOP in particular for the monitoring of experimental GNSS data collected within the IGS MGEX and EUREF RINEX3 campaigns. A new development was demonstrated for the code multipath estimation based on a fully multi-signal, multi-frequency and multi-constellation approach. The software was released in August 2013 and updated in November, 2013. Some functionalities foreseen for near future implementations are presented below.

While data are retrieved from RINEX files, we started to implement RTCM decoder that will support input data from real-time streams too. On the other hand, after implementing RINEX encoder, users will be able to edit, cut or splice GNSS data as well as modify header records. Combining two above features, users will be able to read data from real-time streams and store them in RINEX files. As shown in examples in this paper, most of the functions already supports multi-GNSS operation. The exceptions remains in three functionalities: navigation message processing, single point positioning and azimuth/elevation calculation. Not all the satellite systems are fully operational, therefore Anubis is restricted to GPS-only and GLONASS-only single point positioning at the moment. The station position quantities relating to other constellation have to be calculated with support of GPS or GLONASS. Future development will thus aim to support also navigation messages from BeiDou, SBAS and QZSS along with currently supported GPS, GLONASS and Galileo. A real challenge then concerns developing new preprocessing algorithms in order to provide a general cycle slip detection, i.e. not only for additional GNSS constellations, but also for all available signals and bands. A significant rise of the computing time (from seconds to tens of seconds) was observed when processing large RINEX3 multi-GNSS data files. In this context, we will work on improving the efficiency of the source code to reduce the execution time for all new constellations, frequencies and signals. The station parallel processing will also help to support efficient control of many stations at a single place. Last, but not least, Anubis will be ready to support also users of Windows, OS X or other platforms in future.

Acknowledgements The development of the G-Nut software library was supported by the Czech Scientific Foundation (P209/12/2207). The data from two stations, GOP7 and KUNZ, used for the testing of Anubis were provided with support of the project CzechGeo (No. LM2010008). We thank three anonymous reviewers for their valuable remarks. We also thank to EUREF and IGS for supporting experimental data dissemination and to all individual contributors providing data in RINEX 3.0x format within the IGS MGEX and EUREF RINEX3 campaigns.

References

Dow J, Neilan R, Rizos, C (2009) The international GNSS service in a changing landscape of global navigation satellite systems. J Geod 83(3–4):191–198

Estey L, Meertens C (1999) TEQC: The multi-purpose toolkit for GPS/GLONASS data. GPS Solutions 3(1):42–49

Gurtner W, Estey L (2009) Receiver independent exchange format. Technical Report, Astronomical Institute, University of Bern (2009). Http://igscb.jpl.nasa.gov/igscb/data/format/rinex301.pdf

Guo F, Zhang X (2013) Real-time clock jump compensation for precise point positioning. GPS Solutions 18(1):41–50

Lutz S, Arnold D, Schaer S, Dach R, Jaeggi, A (2013) New RINEX file monitoring at CODE. In: Presented at EUREF symposium 2013, Budapest, Hungary, May 29–31, 2013

Montenbruck O, Rizos C, Weber R, Weber G, Neilan R, Hugentobler U (2013) The International GNSS Service MGEX Campaign. GPS World (2013)

assigned by its definition and not necessarily agrees with the official frequency, e.g. for Galileo, n=7 for E5b, n=8 for E5a+E5b (AltBOC).

[2]While I, Q (and others) represents two individual tracking modes, the X designates a dual-channel tracking mode and Z designates a triple-channel tracking mode.

Vaclavovic P, Dousa J, Gyori G (2013) G-Nut software library - state of development and first results. Acta Geodyn Geomater 10(4):431–436

Weber G, Mervart L (2009) The BKG Ntrip Client (BNC). In: Report on EUREF symposium 2007 in London, vol 42. Mitteilungen des Bundesamtes fuer Kartographie und Geodaesie (2009)

Wuebbena G (1985) Software development for geodetic positioning with GPS using TI 4100 code and carrier measurements. In: Proceedings 1st international symposium on precise positioning with the global positioning system, pp 403–012. Rockwille, Maryland

Precise Point Positioning with Partial Ambiguity Fixing and Optimal Subset Selection

Zhibo Wen, Patrick Henkel, and Christoph Günther

Abstract

Precise point positioning is attractive for numerous applications as it does not require the exchange of raw measurements between reference stations. In this paper, a Kalman filter is used to perform precise point positioning with dual-frequency code and carrier phase measurements, to estimate the receiver position, clock offset, tropospheric zenith delay, ionospheric slant delays and the absolute ambiguities. One improvement is to avoid the correlation between the height component and the tropospheric state by estimating the latter state with intervals. Additionally, a joint estimation of the ambiguity subset and their integer ambiguities is presented. The method differs from conventional partial fixing schemes by taking the stability of the float solution into account. The proposed method is tested with real GPS measurements, and a positioning accuracy in the order of a few centimeters is achieved.

Keywords

Kalman filter • Partial ambiguity resolution • Precise point positioning

1 Introduction

The concept of Precise Point Positioning (PPP) has been proposed by Zumberge et al. (1997), who determined the receiver position with precise satellite orbits and clocks. Kouba and Héroux (2001) proposed an approach with ionosphere-free code and phase measurements and listed the models for the necessary corrections which the user has to apply. The positioning accuracy has shown to be at cm level. Traditional approaches for PPP have been a two-step procedure, in e.g. Ge et al. (2008), Laurichesse et al. (2009), and Geng et al. (2012), to resolve undifferenced phase ambiguities. In a first step the widelane integer ambiguities are derived from the Melbourne-Wübbena combination, and reused in a second step to determine the receiver position, receiver clock offset and the narrowlane ambiguities with a wavelength of 10.7 cm from the ionosphere-free measurement combination

The Least-squares AMBiguity Decorrelation Adjustment (LAMBDA) method proposed by Teunissen (1995) has been used widely to perform the integer least-squares estimation for ambiguity fixing, which resolves all ambiguities at once. The integer bootstrapping estimator by Teunissen (2001) resolves the ambiguities in a sequential manner, and stops fixing under the constraint of the probability of wrong fixing by Verhagen et al. (2011). In the context of PPP, different convergence on the ambiguity estimates makes the correct fixing of all ambiguities less feasible. On the other hand, there is no full search over the ambiguity space for the integer bootstrapping. In this paper, the optimized selection of ambiguity subset is combined with the full search required by the integer least-squares estimation.

Z. Wen (✉) • P. Henkel
Institute for Communications and Navigation, Technische Universität München, München, Germany
e-mail: zhibo.wen@tum.de

C. Günther
Institute for Communications and Navigation, Technische Universität München, München, Germany
German Aerospace Center, Institute of Communications and Navigation, München, Germany

© Springer International Publishing Switzerland 2015

C. Rizos, P. Willis (eds.), *IAG 150 Years*, International Association of Geodesy Symposia 143,
DOI 10.1007/1345_2015_110

This paper proposes a PPP algorithm with Kalman filter which uses uncombined absolute dual-frequency measurements. The phase and code noise is thus amplified to by almost a factor of three in the ionosphere-free case, but at the expense of estimating more states. The paper begins with a general measurement model, which is simplified for a single station with precise corrections of orbit and clock as well as other deterministic corrections. A Kalman filter is suggested to estimate the receiver coordinates, the clock offset, tropospheric zenith delay, ionospheric slant delay and the ambiguities. Moreover, the tropospheric zenith delay is estimated with intervals and the initialization of the covariances between zenith delay and other states for the Kalman filter is derived. In the next section, a joint optimization of subset selection and integer least-squares estimation is proposed to perform partial ambiguity fixing.

2 Precise Point Positioning with a Kalman Filter

The model for absolute uncombined carrier phase $\lambda_m \varphi_{m,i}^k$ and pseudorange measurements $\rho_{m,i}^k$ for receiver i, satellite k on frequency m is suggested as follows by Günther (2013), under the assumption that the hardware biases can be separated with equality $b_{m,i}^k = b_{m,i} + b_m^k$ and $\beta_{m,i}^k = \beta_{m,i} + \beta_m^k$, i.e.

$$\begin{aligned}
\lambda_m \varphi_{m,i}^k &= \left\| (\mathbf{r}_i + \Delta\mathbf{r}_{\mathrm{et},i}) - \mathbf{r}^k \right\| + c\delta\tau_i - c\delta\tau^k - \frac{f_1^2}{f_m^2} I_{1,i}^k \\
&\quad + m_{\mathrm{T},i}^k T_{\mathrm{z},i} + \lambda_m N_{m,i}^k + \beta_{m,i} + \beta_m^k + \lambda_m \varphi_{\mathrm{pw},i}^k \\
&\quad + \varphi_{\mathrm{pcv}}^k + \varphi_{\mathrm{pcv},i} + \varphi_{\mathrm{mp},i}^k + \varepsilon_{m,i}^k \\
\rho_{m,i}^k &= \left\| (\mathbf{r}_i + \Delta\mathbf{r}_{\mathrm{et},i}) - \mathbf{r}^k \right\| + c\delta\tau_i - c\delta\tau^k + \frac{f_1^2}{f_m^2} I_{1,i}^k \\
&\quad + m_{\mathrm{T},i}^k T_{\mathrm{z},i} + b_{m,i} + b_m^k + \rho_{\mathrm{mp},i}^k + \eta_{m,i}^k, \qquad (1)
\end{aligned}$$

where $\mathbf{r}$ represents the coordinates of the phase center of the satellite or receiver depending on the index, $\delta\tau$ denotes the clock offset, I_1 denotes the ionospheric slant delay on frequency f_1, m_{T} and T_{z} are the tropospheric mapping function and zenith delay, the integer ambiguities are denoted by N, the phase and code biases are β and b, and the noise is respectively ε and η. The Niell mapping function proposed by Niell (1996) is used in this paper. The terms including the solid earth tides $\Delta\mathbf{r}_{\mathrm{et},i}$, phase wind-up $\varphi_{\mathrm{pw},i}^k$, and satellite and receiver phase center variations φ_{pcv}^k, and $\varphi_{\mathrm{pcv},i}$, can be modeled and corrected (see respectively Petit and Luzum 2010; Wu et al. 1993; Schmid et al. 2007). The effects of ocean tides and polar tides are neglected. The terms $\varphi_{\mathrm{mp},i}^k$ and $\rho_{\mathrm{mp},i}^k$ denote phase and code multipath delays (see Wen et al. 2013).

The code biases $b_{m,i}$ and b_m^k can be split into geometry- and ionospheric components (denoted by sub-indices g and I) in Wen et al. (2012), i.e.

$$b_{m,i} = b_{\mathrm{g},i} + \frac{f_1^2}{f_m^2} b_{\mathrm{I},i}, \quad \text{and} \quad b_m^k = b_{\mathrm{g}}^k + \frac{f_1^2}{f_m^2} b_{\mathrm{I}}^k, \qquad (2)$$

where $b_{\mathrm{g},i}$ is coupled with receiver clock offset and the same applies for b_{g}^k with satellite clock offset. The ionospheric components $b_{\mathrm{I},i}$ and b_{I}^k have the same coefficients with the ionospheric slant delay, and thus can be separated from it. Since the ionospheric slant delay also appears in the phase measurement equation, the mapped ionospheric code biases are then compensated in the phase biases.

For simplicity, the station index i is dropped from the above model when one station is analyzed at a time. Having the knowledge of the IGS precise satellite orbits and clock offsets, which have absorbed b_{g}^k, as well as other well-modeled corrections, one obtains the corrected carrier phase $\lambda_m \Delta\varphi_m^k$ and pseudorange measurements $\Delta\rho_m^k$ as

$$\begin{aligned}
\lambda_m \Delta\varphi_m^k &= \lambda_m \varphi_m^k + (\mathbf{e}^k)^{\mathrm{T}} \mathbf{r}^k + c\delta\tau^k - \lambda_m \varphi_{\mathrm{pw}}^k - \varphi_{\mathrm{pcv}}^k \\
&\quad - (\mathbf{e}^k)^{\mathrm{T}} \Delta\mathbf{r}_{\mathrm{et}} - \varphi_{\mathrm{pcv}} \\
&= (\mathbf{e}^k)^{\mathrm{T}} \mathbf{r} + c\delta\tau + m_{\mathrm{T}}^k T_{\mathrm{z}} - \frac{f_1^2}{f_m^2} I_1^k + \lambda_m \tilde{N}_m^k + \varepsilon_m^k \\
\Delta\rho_m^k &= (\mathbf{e}^k)^{\mathrm{T}} \mathbf{r} + c\delta\tau + m_{\mathrm{T}}^k T_{\mathrm{z}} + \frac{f_1^2}{f_m^2} I_1^k + \eta_m^k, \qquad (3)
\end{aligned}$$

with $\mathbf{e}^k$ being the unit vector from the satellite to the receiver, and the ambiguity term $\tilde{N}$ absorbing also the phase biases, namely $\tilde{N}_m^k \triangleq N_m^k + \beta_m + \beta_m^k$. The reason for the absorption is that the phase biases cannot be estimated separately from the integer ambiguities due to rank deficiency for a single station, unless there is prior information to correct the phase biases.

The absolute measurements on two frequencies are taken as input, where the initial outlier and cycle slip detections were performed to have clean data. Then after applying the necessary corrections, the states including the receiver coordinate, the receiver clock offset, the total tropospheric zenith delay, the ionospheric slant delays, and the ambiguities are estimated in a Kalman filter, as shown in Fig. 1. The measurement and state vectors read respectively

$$\mathbf{z} = \left(\lambda_1 \boldsymbol{\Delta\varphi}_1^{\mathrm{T}},\ \lambda_2 \boldsymbol{\Delta\varphi}_2^{\mathrm{T}},\ \boldsymbol{\Delta\rho}_1^{\mathrm{T}},\ \boldsymbol{\Delta\rho}_2^{\mathrm{T}}\right)^{\mathrm{T}}, \qquad (4)$$

$$\mathbf{x} = \left(\mathbf{r}^{\mathrm{T}},\ c\delta\tau,\ T_{\mathrm{z}},\ \boldsymbol{I}_1^{\mathrm{T}},\ \tilde{\boldsymbol{N}}_1^{\mathrm{T}},\ \boldsymbol{B}\tilde{\boldsymbol{N}}_2^{\mathrm{T}}\right)^{\mathrm{T}}. \qquad (5)$$

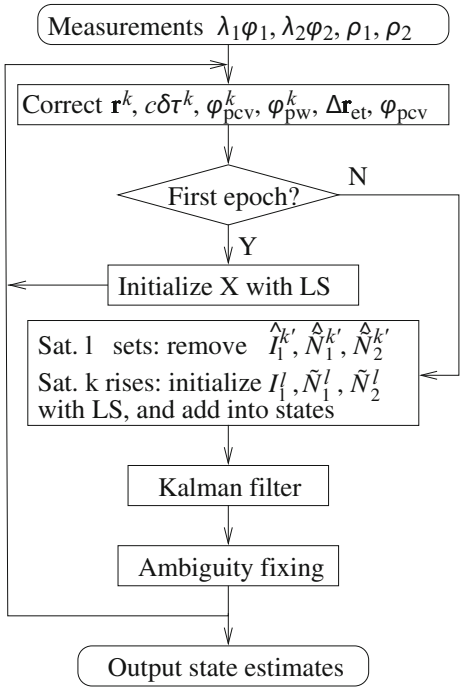

Fig. 1 The flow diagram for precise point positioning with absolute measurements using a Kalman filter

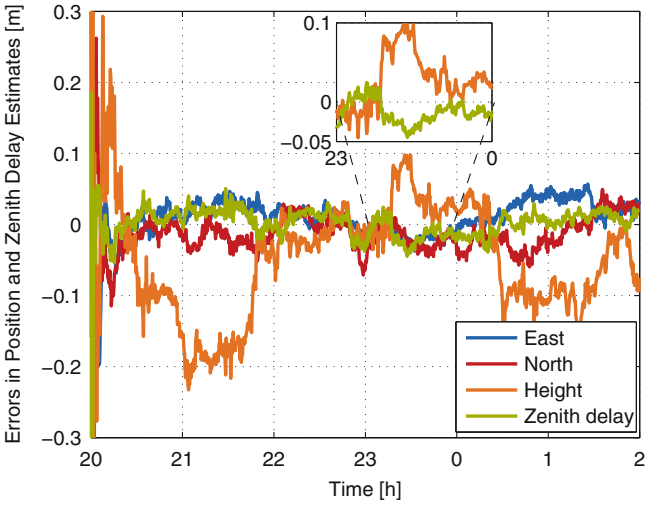

Fig. 2 The position errors and tropospheric zenith delay errors for IGS station KIRU, with the dual-frequency measurements taken from 20:00 to 02:00 on the first 2 days of 2011. The ambiguities are kept as float estimates

The dynamics of the rising and setting satellites have to be considered in the Kalman filtering. In the case for setting satellite, it is straightforward to delete the corresponding entries in the states and covariances, while for rising satellite the new introduced states should be estimated using existing state estimates as corrections. Taking an example of a rising satellite l, the new states contain ionospheric slant delay and ambiguities $\boldsymbol{x}^l = \left(I^l_1, \tilde{N}^l_1, \tilde{N}^l_2\right)^{\mathrm{T}}$, which are initialized correcting the existing estimates of $\hat{\boldsymbol{x}}_{\mathrm{c}} = \left(\hat{\mathbf{r}}^{\mathrm{T}}, c\hat{\delta\tau}, \hat{T}_{\mathrm{z}}\right)^{\mathrm{T}}$ multiplying with the design matrix $\boldsymbol{H}^l_{\hat{\boldsymbol{x}}_{\mathrm{c}}}$. Thus, the measurement model for the new satellite is given by

$$\boldsymbol{z}^l - \boldsymbol{H}^l_{\hat{\boldsymbol{x}}_{\mathrm{c}}}\hat{\boldsymbol{x}}_{\mathrm{c}} = \boldsymbol{H}^l_{\boldsymbol{x}^l}\boldsymbol{x}^l + \boldsymbol{\eta}_{z^l}, \tag{6}$$

with $\boldsymbol{\eta}_{z^l} \sim \mathcal{N}(\mathbf{0}, \tilde{\boldsymbol{\Sigma}}^l_{\mathrm{R}})$, and $\tilde{\boldsymbol{\Sigma}}^l_{\mathrm{R}} = \boldsymbol{\Sigma}_{\mathrm{R}} + \boldsymbol{H}^{l,\mathrm{T}}_{\hat{\boldsymbol{x}}_{\mathrm{c}}}\boldsymbol{\Sigma}_{\hat{\boldsymbol{x}}_{\mathrm{c}}}\boldsymbol{H}^l_{\hat{\boldsymbol{x}}_{\mathrm{c}}}$. The covariance matrices for measurements and states are denoted by $\boldsymbol{\Sigma}_{\mathrm{R}}$ and $\boldsymbol{\Sigma}$.

The least-squares (LS) estimates, along with its variances and covariances with $\hat{\boldsymbol{x}}_{\mathrm{c}}$ then read

$$\begin{aligned}
\hat{\boldsymbol{x}}^l &= \left(\boldsymbol{H}^{l,\mathrm{T}}_{\boldsymbol{x}^l}\tilde{\boldsymbol{\Sigma}}^{l,-1}_{\mathrm{R}}\boldsymbol{H}^l_{\boldsymbol{x}^l}\right)^{-1}\boldsymbol{H}^{l,\mathrm{T}}_{\boldsymbol{x}^l}\tilde{\boldsymbol{\Sigma}}^{l,-1}_{\mathrm{R}}(\boldsymbol{z}^l - \boldsymbol{H}^l_{\hat{\boldsymbol{x}}_{\mathrm{c}}}\hat{\boldsymbol{x}}_{\mathrm{c}}) \\
\boldsymbol{\Sigma}_{\hat{\boldsymbol{x}}^l} &= \left(\boldsymbol{H}^{l,\mathrm{T}}_{\boldsymbol{x}^l}\tilde{\boldsymbol{\Sigma}}^{l,-1}_{\mathrm{R}}\boldsymbol{H}^l_{\boldsymbol{x}^l}\right)^{-1} \\
\boldsymbol{\Sigma}_{\hat{\boldsymbol{x}}^l\hat{\boldsymbol{x}}_{\mathrm{c}}} &= -\boldsymbol{\Sigma}_{\hat{\boldsymbol{x}}^l}\boldsymbol{H}^{l,\mathrm{T}}_{\boldsymbol{x}^l}\tilde{\boldsymbol{\Sigma}}^{l,-1}_{\mathrm{R}}\boldsymbol{H}^l_{\hat{\boldsymbol{x}}_{\mathrm{c}}}\boldsymbol{\Sigma}_{\hat{\boldsymbol{x}}_{\mathrm{c}}}
\end{aligned} \tag{7}$$

The float ambiguity estimates are then input to the fixing block, where the temporal variation of the float estimates is observed over a time window. If the temporal variation is below a certain threshold, the ambiguity is fixed to the float value and eliminated from the state vector.

In the setting for the Kalman filter, the states are assumed to follow random walk processes, with the standard deviation of the process noise for the receiver position, receiver clock offset, tropospheric zenith delay, ionospheric slant delay, and ambiguities being 1 mm, 1 m, 5 mm, 2 cm, and 1 millicycle respectively. The measurement noise is assumed to follow zero-mean Gaussian distribution, with standard deviation being an exponential function of the elevation angle.

The algorithm is tested with GPS measurements on two frequencies collected from an IGS high-rate station KIRU. The position estimates are compared with the precise coordinates published by IGS SINEX product, while the tropospheric zenith delay estimate is compared with the Zenith Path Delay (ZPD) product. The errors in Fig. 2 show that the height component contributes the largest errors, i.e. in the range of ± 10 cm, and the east and north components along with the zenith delay errors are mostly below ± 3 cm. The large variation on the height error shows a strong negative correlation with the zenith delay error, which can be reduced by introducing a model for zenith delay between epochs and is discussed in the next section. Figure 3 shows the position and zenith delay errors, while the ambiguities are fixed to float numbers.

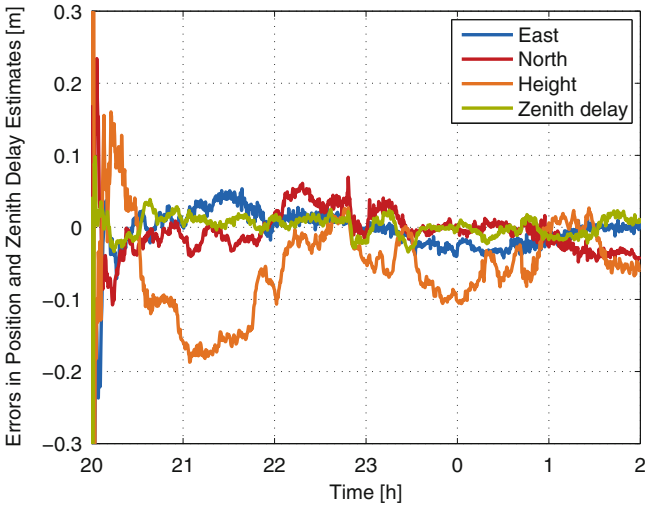

Fig. 3 The ambiguities whose temporal variations are small enough, less than 0.03 cycle over 1,800 epochs, are fixed to real values

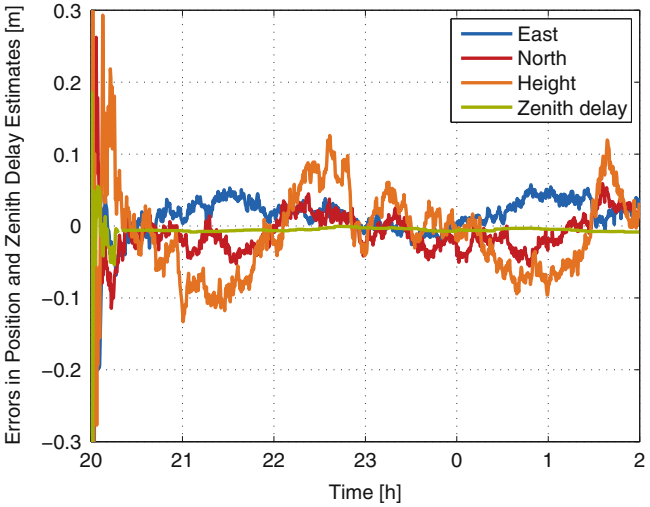

Fig. 4 The tropospheric zenith delay is not estimated epoch-wise, but with an interval of 300 s, which improves the positioning accuracy

3 Estimating Tropospheric Zenith Delay with Intervals

To overcome the high correlation between the height component of the receiver coordinate and the tropospheric zenith delay, it is reasonable to estimate the tropospheric zenith delay not epoch-wise, given that the zenith delay would not change rapidly. The state space model for the tropospheric zenith delay is described as

$$T_{z,n} = \begin{cases} T_{z,n-d} + w_{n-d} & n < n_0, \text{ or } n \bmod d = 0 \\ \hat{T}_{z,\lfloor n/d \rfloor \cdot d} & \text{else,} \end{cases} \tag{8}$$

with n_0 being the duration to allow convergence in the beginning, d representing the length of the interval without zenith delay estimate, and the process noise w_n being normal distributed as $w_n \sim \mathcal{N}(0, \sigma^2_{T_z})$.

Let Eq. (5) represent the case when the zenith delay is estimated, and let $\tilde{\boldsymbol{x}}$ denote the state vector without the tropospheric variable, i.e.

$$\tilde{\boldsymbol{x}} = \left(\mathbf{r}^{\mathrm{T}},\ c\delta\tau,\ \boldsymbol{I}_1^{\mathrm{T}},\ \tilde{\boldsymbol{N}}_1^{\mathrm{T}},\ \tilde{\boldsymbol{N}}_2^{\mathrm{T}}\right)^{\mathrm{T}}. \tag{9}$$

As the zenith delay is again included in the state vector, it is initialized with its last estimate according to Eq. (8), while the variance is then also initialized with its last variance. There exists correlation between the new introduced zenith delay and other state estimates $\hat{\tilde{\boldsymbol{x}}}$, since the last estimate has been used as a correction within the interval without the zenith delay state.

Given the measurement model and the state update equation of Kalman filter within the interval, with the Kalman gain $\boldsymbol{K}$ and measurement noise $\boldsymbol{v}$, i.e.

$$\begin{aligned} z &= \boldsymbol{H}_{\tilde{x}}\tilde{\boldsymbol{x}} + \boldsymbol{H}_{T_z} T_z + \boldsymbol{v} \\ \hat{\tilde{\boldsymbol{x}}}^{+} &= \hat{\tilde{\boldsymbol{x}}}^{-} + \boldsymbol{K}(z - \boldsymbol{H}_{T_z}\hat{T}_z - \boldsymbol{H}_{\tilde{x}}\hat{\tilde{\boldsymbol{x}}}^{-}), \end{aligned} \tag{10}$$

the covariance between zenith delay correction and the states can be derived as follows. Assume at epoch n the measurement is corrected for $\hat{T}_z$ at epoch $\lfloor n/d \rfloor \cdot d$ which is omitted in the derivation for simplicity.

$$\begin{aligned} \boldsymbol{\Sigma}^{+}_{\hat{\tilde{\boldsymbol{x}}}_n, \hat{T}_z} &= \mathbb{E}\left[\left(\hat{\tilde{\boldsymbol{x}}}^{+}_n - \tilde{\boldsymbol{x}}_n\right)\left(\hat{T}_z - T_z\right)^{\mathrm{T}}\right] \\ &= \mathbb{E}\Big[\Big(\hat{\tilde{\boldsymbol{x}}}^{-}_n + \boldsymbol{K}_n\Big(\boldsymbol{H}_{\tilde{x},n}\tilde{\boldsymbol{x}}_n + \boldsymbol{H}_{T_z,n}T_z + \boldsymbol{v}_n - \boldsymbol{H}_{T_z,n}\hat{T}_z \\ &\qquad -\boldsymbol{H}_{\tilde{x},n}\hat{\tilde{\boldsymbol{x}}}^{-}_n\Big) - \tilde{\boldsymbol{x}}_n\Big)\left(\hat{T}_z - T_z\right)^{\mathrm{T}}\Big] \\ &= \mathbb{E}\Big[\Big((\boldsymbol{I} - \boldsymbol{K}_n\boldsymbol{H}_{\tilde{x},n})\left(\hat{\tilde{\boldsymbol{x}}}^{-}_n - \tilde{\boldsymbol{x}}_n\right) - \boldsymbol{K}_n\boldsymbol{H}_{T_z,n} \\ &\qquad \left(\hat{T}_z - T_z\right) + \boldsymbol{K}_n\boldsymbol{v}_n\Big)\left(\hat{T}_z - T_z\right)^{\mathrm{T}}\Big] \\ &= \left(\boldsymbol{I} - \boldsymbol{K}_n\boldsymbol{H}_{\tilde{x},n}\right)\boldsymbol{\Sigma}^{-}_{\tilde{x}_n,T_z} - \boldsymbol{K}_n\boldsymbol{H}_{T_z,n}\boldsymbol{\Sigma}^{+}_{T_z}. \end{aligned} \tag{11}$$

The prediction for the a priori covariance is obtained as

$$\boldsymbol{\Sigma}^{-}_{\tilde{x}_n,T_z} = \boldsymbol{\Phi}\,\boldsymbol{\Sigma}^{+}_{\tilde{x}_{n-1},T_z}\boldsymbol{\Phi}^{\mathrm{T}} + \boldsymbol{\Sigma}_{\mathrm{Q},\tilde{x}_{n-1},T_z}, \tag{12}$$

where the state transition matrix $\boldsymbol{\Phi}$ is an identity matrix, and there is no process noise $\boldsymbol{\Sigma}_{\mathrm{Q}}$ assumed for the cross terms. With Eqs. (11) and (12), the initial covariance for the introduced zenith delay and other states can be calculated recursively.

Figure 4 shows the effect of estimating the zenith delay on the position errors, especially the height component. The

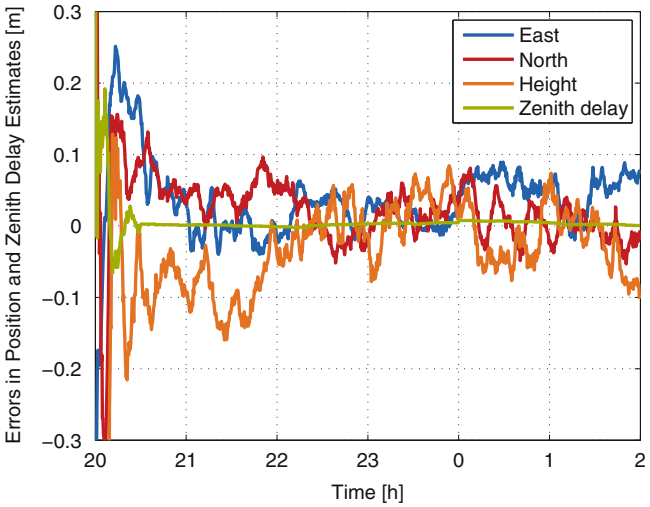

Fig. 5 The position and tropospheric errors for another IGS station MATE with the same data period as Fig. 4. The small variations on each estimates result from multipath effect

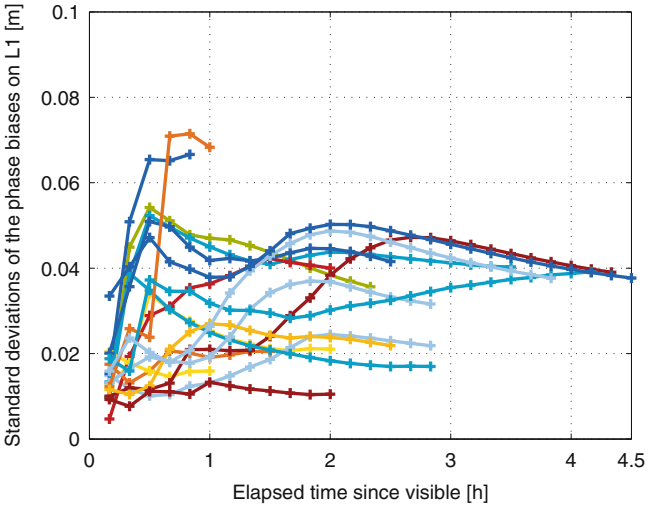

Fig. 6 The stability of the fractional parts of the L1 ambiguities from station KIRU

interval for correcting a priori zenith delay is set to 300 epochs (seconds). The errors of the zenith delay are dropped below 1 cm and most of the height errors are reduced to ±10 cm. In Fig. 5 the algorithm achieved similar position accuracy for another IGS station MATE.

4 Partial Ambiguity Fixing

In this section, we exploit the integer property of ambiguities to improve the PPP accuracy. We first analyze the stability of the float ambiguity estimates that are lumped with the receiver and satellite phase biases. We consider this ambiguity/bias term over a certain time window, i.e. we define the stability as the ratio of the standard deviation of the ambiguity/bias term to the time period of the window. The standard deviation is determined based on the ambiguity estimates and, thus, is much more realistic than the one obtained from covariance matrix from Kalman filtering which does not accurately model time correlation of the measurements. Figure 6 shows the standard deviation of the L1 phase bias estimates. The stability allows us to assume in this section that the phase biases are known (see Wen et al. 2011) and subtracted from the phase measurements.

It is difficult to fix all ambiguities correctly at once, since the convergence behaviors for the ambiguity estimates are different, and the variances coming from the Kalman filter are often too optimistic. Hence, trying to fix all might lead to wrong fixings, which would eventually project errors into the position estimates.

Consider a generalized carrier phase measurement model $\boldsymbol{\Psi} = \boldsymbol{H}\boldsymbol{\xi} + \boldsymbol{A}\boldsymbol{N} + \boldsymbol{\varepsilon}$, where $\boldsymbol{\xi}$ contains all real-valued parameters including position, clock offset, tropospheric and ionospheric delay, $\boldsymbol{N}$ represents the integer ambiguity vector, $\boldsymbol{H}$ and $\boldsymbol{A}$ are the corresponding design matrices, and $\boldsymbol{\varepsilon}$ is the phase noise. The squared error norm can be decomposed by Teunissen (1995) into three orthogonal terms

$$\begin{aligned}\|\boldsymbol{\Psi} - \boldsymbol{H}\boldsymbol{\xi} - \boldsymbol{A}\boldsymbol{N}\|^2_{\boldsymbol{\Sigma}_{\boldsymbol{\Psi}}^{-1}} &= \|\hat{\boldsymbol{N}} - \boldsymbol{N}\|^2_{\boldsymbol{\Sigma}_{\hat{\boldsymbol{N}}}^{-1}} + \\ &+ \|\check{\boldsymbol{\xi}}(\boldsymbol{N}) - \boldsymbol{\xi}\|^2_{\boldsymbol{\Sigma}_{\check{\boldsymbol{\xi}}(\boldsymbol{N})}^{-1}} + \|\boldsymbol{P}_{\bar{\boldsymbol{A}}}^{\perp}\boldsymbol{P}_{\boldsymbol{H}}^{\perp}\boldsymbol{\Psi}\|^2_{\boldsymbol{\Sigma}_{\boldsymbol{\Psi}}^{-1}}, \quad (13)\end{aligned}$$

with the float least-squares estimate $\hat{\boldsymbol{N}}$ and the fixed real-valued estimate $\check{\boldsymbol{\xi}}$. The last term is the error orthogonal to the solution spaces and is irrelevant. The orthogonal projection matrices $\boldsymbol{P}_{\boldsymbol{H}}^{\perp}$ and $\boldsymbol{P}_{\bar{\boldsymbol{A}}}^{\perp}$ are given by

$$\begin{aligned}\boldsymbol{P}_{\boldsymbol{H}}^{\perp} &= \boldsymbol{I} - \boldsymbol{H}(\boldsymbol{H}^{\mathrm{T}}\boldsymbol{\Sigma}_{\boldsymbol{\Psi}}^{-1}\boldsymbol{H})^{-1}\boldsymbol{H}^{\mathrm{T}}\boldsymbol{\Sigma}_{\boldsymbol{\Psi}}^{-1} \\ \boldsymbol{P}_{\bar{\boldsymbol{A}}}^{\perp} &= \boldsymbol{I} - \bar{\boldsymbol{A}}(\bar{\boldsymbol{A}}^{\mathrm{T}}\boldsymbol{\Sigma}_{\boldsymbol{\Psi}}^{-1}\bar{\boldsymbol{A}})^{-1}\bar{\boldsymbol{A}}^{\mathrm{T}}\boldsymbol{\Sigma}_{\boldsymbol{\Psi}}^{-1}, \ \bar{\boldsymbol{A}} = \boldsymbol{P}_{\boldsymbol{H}}^{\perp}\boldsymbol{A}. \quad (14)\end{aligned}$$

The ambiguity vector $\boldsymbol{N}$ shall now be divided into two subsets, one with integer-valued $\boldsymbol{N}^s = \boldsymbol{S}\boldsymbol{N}$ with $\boldsymbol{S}$ being the selection matrix, and one with real-valued ambiguities $\boldsymbol{N}^{\bar{s}} = \boldsymbol{N}\backslash\boldsymbol{N}^s$. The real-valued subset can be combined with the real-valued set $\boldsymbol{\xi}$, i.e. $\tilde{\boldsymbol{\xi}} = (\boldsymbol{\xi}^{\mathrm{T}}, \boldsymbol{N}^{\bar{s},\mathrm{T}})^{\mathrm{T}}$.

The squared error norm from Eq. (13) is adjusted to

$$\begin{aligned}\|\boldsymbol{\Psi} - \boldsymbol{H}\boldsymbol{\xi} - \boldsymbol{A}\boldsymbol{N}\|^2_{\boldsymbol{\Sigma}_{\boldsymbol{\Psi}}^{-1}} &= \|\hat{\boldsymbol{N}}^s - \boldsymbol{N}^s\|^2_{\boldsymbol{\Sigma}_{\hat{\boldsymbol{N}}^s}^{-1}} + \\ &+ \|\check{\tilde{\boldsymbol{\xi}}}(\boldsymbol{N}^s) - \tilde{\boldsymbol{\xi}}\|^2_{\boldsymbol{\Sigma}_{\check{\tilde{\boldsymbol{\xi}}}(\boldsymbol{N}^s)}^{-1}} + \|\boldsymbol{P}_{\bar{\boldsymbol{A}}}^{\perp}\boldsymbol{P}_{\boldsymbol{H}}^{\perp}\boldsymbol{\Psi}\|^2_{\boldsymbol{\Sigma}_{\boldsymbol{\Psi}}^{-1}}, \quad (15)\end{aligned}$$

over which the minimum shall be solved. The integer least-squares estimate $\check{\boldsymbol{N}}$ for the ambiguity subset is given by

$$\check{\boldsymbol{N}}^s = \arg\min_{\boldsymbol{N}^s \in \mathbb{Z}^s} \|\hat{\boldsymbol{N}}^s - \boldsymbol{N}^s\|^2_{\Sigma_{\hat{\boldsymbol{N}}^s}^{-1}}, \quad (16)$$

which can be obtained by a tree search in the decorrelated search space in Teunissen (1995). One applies the $\boldsymbol{L}\boldsymbol{D}\boldsymbol{L}^{\mathrm{T}}$ decomposition of the covariance matrix $\Sigma_{\hat{N}^s}$, and multiplies the error vector $\hat{\boldsymbol{N}}^s - \boldsymbol{N}^s$ with the matrix $\boldsymbol{L}$ to obtain the error of the conditional ambiguities, i.e.

$$\|\hat{\boldsymbol{N}}^s - \boldsymbol{N}^s\|^2_{\Sigma^{-1}_{\hat{N}^s}} = \sum_{l=1}^{k} \frac{(N^s_l - \hat{N}^s_{l|1,\ldots,l-1})^2}{\sigma^2_{\hat{N}^s_{l|1,\ldots,l-1}}} \leq \chi^2, \quad (17)$$

with the search space volume χ^2.

The inequality is solved for the k-th conditional ambiguity $\hat{N}^s_{k|1,\ldots,k-1}$,

$$\begin{aligned} N^s_k &\geq \hat{N}^s_{k|1,\ldots,k-1} - \sigma_{\hat{N}^s_{k|1,\ldots,k-1}} \sqrt{F_k(N^s)} \\ N^s_k &\leq \hat{N}^s_{k|1,\ldots,k-1} + \sigma_{\hat{N}^s_{k|1,\ldots,k-1}} \sqrt{F_k(N^s)}, \end{aligned} \quad (18)$$

with

$$F_k(N^s) = \chi^2 - \sum_{l=1}^{k-1} \frac{(N^s_l - \hat{N}^s_{l|1,\ldots,l-1})^2}{\sigma^2_{\hat{N}^s_{l|1,\ldots,l-1}}} - \|\boldsymbol{P}^{\perp}_{\bar{\boldsymbol{A}}} \boldsymbol{P}^{\perp}_{\boldsymbol{H}} \boldsymbol{\Psi}\|^2_{\boldsymbol{\Sigma}^{-1}_{\boldsymbol{\Psi}}}.$$

We applied a tree search for ambiguity fixing so far. It still leaves the choice of the subset open. We select the optimal subset such that the sum of the variances of the a posteriori position estimates is minimized with the constraint that the float ambiguity estimates of the subset are sufficiently stable over a predefined time window T_{w}, i.e.

$$\begin{aligned} &\hat{\boldsymbol{S}} = \arg\min_{\boldsymbol{S}} \operatorname{tr}\left(\boldsymbol{\Sigma}_{\hat{\mathbf{r}}(\check{N}^s)}\right), \text{ s.t.} \\ &\max_{t'}(\hat{N}^s_{t',k}) - \min_{t'}(\hat{N}^s_{t',k}) < \gamma, \ \forall k, \ \forall t' \in [t - T_{\mathrm{w}}, t], \end{aligned} \quad (19)$$

with tr denoting the trace function, the conditional variance $\boldsymbol{\Sigma}_{\hat{\mathbf{r}}(\check{N}^s)} = \boldsymbol{\Sigma}_{\hat{\mathbf{r}}} - \boldsymbol{\Sigma}_{\hat{\mathbf{r}}\hat{N}^s} \boldsymbol{\Sigma}^{-1}_{\hat{N}^s} \boldsymbol{\Sigma}^{\mathrm{T}}_{\hat{\mathbf{r}}\hat{N}^s}$, and t denoting the current epoch. Fixing all ambiguities would although give a minimum in the trace, yet not all ambiguities have converged well enough. It is therefore beneficial to consider the temporal variation jointly.

The estimation procedure is performed as follows: First a set of float ambiguities is selected whose temporal variations fulfill the constraint in Eq. (19). Then one minimizes the trace of the conditional variances of the position over all possible ambiguity combinations within the set, and obtains the subset containing the float ambiguity estimates. The fixed integer solution for the subset is obtained from the tree-search.

The algorithm is applied on the same data set from KIRU for epoch 9,000 which is 2.5 h. Figure 7 shows large variations on height component when all ambiguities are fixed to integers, while in Fig. 8 the optimal subset of ambiguities is fixed for PRN 8 and 28 on two frequencies.

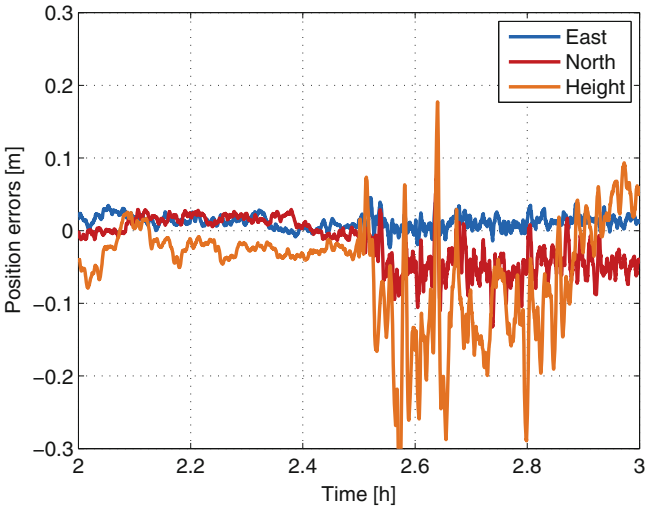

Fig. 7 All ambiguities are fixed to integers at epoch 2.5 h

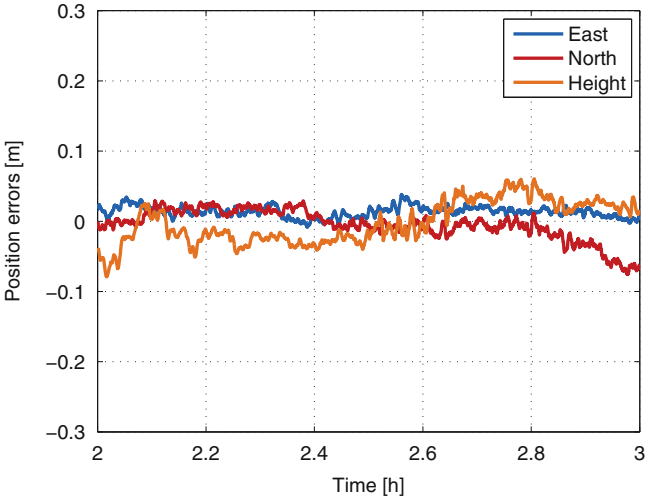

Fig. 8 The optimal subset is obtained for ambiguities from PRN 8 and 28 on two frequencies at epoch 2.5 h

5 Summary

In this paper, a PPP algorithm with uncombined undifferenced dual-frequency measurements with a Kalman filter has been proposed to estimate the receiver coordinate, clock offset, the tropospheric zenith delay, the ionospheric slant delay, and the ambiguities. It is foreseeable that the use of IGS rapid satellite orbit and clock products could enable it to function in realtime. The results have shown cm-level position accuracy, sub-cm accuracy on tropospheric

zenith delay. An algorithm of joint optimization on partial ambiguity fixing has also been proposed, and correct subset fixing has shown improved positioning accuracy.

References

Ge M, Gendt G, Rothacher M, Shi C, Liu J (2008) Resolution of GPS carrier-phase ambiguities in precise point positioning (PPP) with daily observations. J Geodesy 82(7):389–399

Geng J, Shi C, Ge M, Dodson AH, Lou Y, Zhao Q, Liu J (2012) Improving the estimation of fractional-cycle biases for ambiguity resolution in precise point positioning. J Geodesy 86(8): 579–589

Günther C (2013) Lecture notes on satellite navigation. Technische Universität München, München

Kouba J, Héroux P (2001) Precise point positioning using IGS orbit and clock products. GPS Solutions 5(2):12–28

Laurichesse D, Mercier F, Berthias JP, Broca P, Cerri L (2009) Integer ambiguity resolution on undifferenced GPS phase measurements and its application to PPP and satellite precise orbit determination. Navigation 56(2):135

Niell AE (1996) Global mapping functions for the atmosphere delay at radio wavelengths. J Geophys Res Solid Earth (1978–2012) 101(B1):3227–3246

Petit G, Luzum B (2010) IERS conventions 2010 (IERS Technical Note 36) rankfurt am Main: Verlag des Bundesamts für Kartographie und Geodäsie, p 179. ISBN 3-89888-989-6

Schmid R, Steigenberger P, Gendt G, Ge M, Rothacher M (2007) Generation of a consistent absolute phase-center correction model for GPS receiver and satellite antennas. J Geodesy 81(12):781–798

Teunissen P (1995) The least-squares ambiguity decorrelation adjustment: a method for fast GPS integer ambiguity estimation. J Geodesy 70(1–2):65–82

Teunissen P (2001) GNSS ambiguity bootstrapping: theory and application. In: Proceedings of international symposium on kinematic systems in geodesy, geomatics and navigation, pp 246–254

Verhagen S, Teunissen PJ, van der Marel H, Li B (2011) GNSS ambiguity resolution: which subset to fix. In: Proceedings of International Global Navigation Satellite Systems Society, IGNSS symposium, pp 1–15

Wen Z, Henkel P, Günther C (2011) Reliable estimation of phase biases of GPS satellites with a local reference network. In: Proceedings of 53rd IEEE international symposium ELMAR. IEEE, pp 321–324

Wen Z, Henkel P, Brack A, Günther C (2012) Satellite bias determination with global station network and best integer equivariant estimation. In: Proceedings of the 25th ION GNSS. Nashville, pp 3675–3682

Wen Z, Henkel P, Günther C (2013) Precise point positioning with estimation of code multipath subset. In: Proceedings of 55th IEEE international symposium ELMAR. IEEE, pp 345–348

Wu JT, Wu SC, Hajj GA, Bertiger WI, Lichten SM (1993) Effects of antenna orientation on GPS carrier phase. Manuscr Geodaet 18(2):91–98

Zumberge J, Heflin M, Jefferson D, Watkins M, Webb F (1997) Precise point positioning for the efficient and robust analysis of GPS data from large networks. J Geophys Res 102(B3):5005–5017

List of Reviewers

Joseph Adam
Jonas Ågren
Zuheir Altamimi
Matthew James Amos
Ole Baltazar Andersen
Dempster Andrew
Vassilios D. Andritsanos
Detlef Angermann
Graham Appleby
Kirco Arsov
Thomas Artz
Andrey Babeyko
Valerie Ballu
Yoaz Bar-Sever
Luisa M.C. Bastos
Oliver Baur
Matthias Becker
Battista Benciolini
Geoffrey Blewitt
Graeme Blick
Denizar Blitzkow
Heike Bock
Johannes Boehm
Manuela Bonano
Machiel Bos
Jaroslaw Bosy
Claudio Brunini
F.K. Brunner
Carine Bruyninx
Roland Bürgmann
Mark D. Butala
Alessandro Caporali
Stefano Casotto
Slawomir Cellmer
David Chadwell
Sylvain Charbonnier
Minkang Cheng
Mike Chin
Suelynn Choy
Sten Claessens
Xavier Collilieux
Brian Corey
Michael Craymer
David Crossley
John Dawson
Silvio R.C. de Freitas
Zhiguo Deng
Denise Dettmering
Thomas Dewez
Juan Carlos Fernandez Diaz
Steven Dickman
Robert Dill
Pavel Ditmar
Henryk Dobslaw
Hermann Drewes
Przemysław Dykowski
Bernd Eissfeller
João Encarnação
Saskia Esselborn
William Edward Featherstone
Yanming Feng
Luciana Fenoglio-Marc
Rui M.S. Fernandes
Rene Forsberg
Georgia Fotopoulos
Frederic Frappart
Jeff Freymueller
Mathias Fritsche
Yoichi Fukuda
Roman Galas Galas
Daniel Gambis
Pascal Gegout
Gerd Gendt
Olga Gitlein
Wenyu Gong
Barbara Görres
Alan Grant
Ronni Grapenthin

© Springer International Publishing Switzerland 2016

C. Rizos, P. Willis (eds.), *IAG 150 Years*, International Association of Geodesy Symposia 143,
DOI 10.1007/1345_2015

Richard Gross
Christian Gruber
Sanjeev Gunawardena Gunawardena
Rüdiger Haas
Matthias Hackl
Christine Hackman
Tomasz Hadas
Shin-Chan Han
Try Guoqi Han
Zhe He
Kosuke Heki
Patrick Henkel
Pierre Heroux
Thomas Herring
Thomas Hobiger
Catherine Y. Hohenkerk
Petr Holota
Nils Holzrichter
Melvin Hoyer
Jianliang Huang
Urs Hugentobler
C. Hwang
Sinem Elmas Ince
Shuanggen Jin
Jan Kaplon
Mio Kasai
Teruyuki Kato
Takahito Kazama
Ambrus Kenyeres
Matt A. King
Per Knudsen
Alexander V. Kopaev
Mamoru Koarai
Jan Krynski
Jacek Kudrys
Sebastien Lambert
John Langbein
Ruediger Lehmann
Bofeng Li
Xingxing Li
Martin Lidberg
Laurent Longuevergne
Scott B. Luthcke
Chopo Ma
Gerry Mader
Zinovy M. Malkin
Urs Marti
Michael Meindl
Xiaolin Meng
Stelios Mertikas
Bruno Meurers
Ulrich Meyer
Thierry Meyrath
J. Toby Minear
Juan Moirano
Terry Moore
Mark Morelande
Juergen Mueller
Wolfgang Niemeier
Takuya Nishimura
Jean-Mathieu Nocquet
Axel Nothnagel
Aboelmagd Noureldin
Pavel Novak
Dennis Odijk
Tönis Oja
Taku Ozawa
Rosa Pacione
Roland Pail
Béla Paláncz
Jihye Park
Erricos C. Pavlis
Nikolaos Konstantinos Pavlis
Jacek Paziewski
Mike Pearlman
Chris Pearson
Felix Perosanz
William Terry Petrachenko
Svetozar Petrovic
Lucia Plank
Christian Pock
Mike Poland
Arnaud Pollet
Rui Ponte
Eric Pottiaux
Peter Ramm
Elena Rangelova
John C. Ries
Roelof Rietbroek
Alberto Garcia Rigo
Ignacio Romero
Szabolcs Rózsa
Jean Rüeger
Axel Rülke
Fausto Sacerdote
David Salstein
Laura Sanchez
David Sandwell
Fernando Sanso
Alvaro Santamaria-Gomez
Marcelo Santos
Ralf Schmid
Michael Schmidt
Steffen Schön
Tilo Schöne
Harald Schuh

Josef Sebera
Florian Seitz
Kurt Seitz
Akbar Shabanloui
WenBin Shen
Manoochehr Shirzaei
Nagaraj Shivaramaiah
C.K. Shum
Lars E. Sjöberg
Wolfgang Söhne
Richard Stanaway
Guenter Stangl
Peter Steigenberger
Gabriel Strykowski
Hiroaki Takahashi
Felix Norman Teferle
Robert Tenzer
Peter J.G. Teunissen
Daniela Thaller
Maik Thomas
Gyula Toth
Paul Tregoning
Carl Christian Tscherning
Ilias Tziavos
Michel Van Camp
Henrik Vedel
Georgios S. Vergos
Sandra Verhagen
Martin Vermeer
Alfonso Vitti
Leonid F. Vitushkin
Jinling Wang
H. Wang
Yan Ming Wang
Lambert Wanninger
Shimon Wdowinski
Georg Weber
Robert Weber
Matthias Weigelt
Hanjiang Wen
Pawel Wielgosz
Philip Woodworth
Jicang Wu
Thomas Wunderlic
Guochang Xu
Yudan Yi
Kefei Zhang
Xiaohong Zhang

Author Index

© Springer International Publishing Switzerland 2016

C. Rizos, P. Willis (eds.), *IAG 150 Years*, International Association of Geodesy Symposia 143,
DOI 10.1007/1345_2015